

Materials

FY 2021 Annual Progress Report

Vehicle Technologies Office

(This page intentionally left blank)

Disclaimer

This report was prepared as an account of work sponsored by an agency of the United States government. Neither the United States government nor any agency thereof, nor any of their employees, makes any warranty, express or implied, or assumes any legal liability or responsibility for the accuracy, completeness, or usefulness of any information, apparatus, product, or process disclosed or represents that its use would not infringe privately owned rights. Reference herein to any specific commercial product, process, or service by trade name, trademark, manufacturer, or otherwise does not necessarily constitute or imply its endorsement, recommendation, or favoring by the United States government or any agency thereof. The views and opinions of authors expressed herein do not necessarily state or reflect those of the United States government or any agency thereof.

Acknowledgments

First and foremost, the Principal Investigators (PIs) from industry, academia, and the National Laboratories who supplied the content of these reports are to be acknowledged and commended. It is their work that moves our nation forward to improved and more affordable transportation, as well as increased energy security.

Thank you to the project managers at the National Energy Technology Laboratory for continued support administering these projects.

We would also like to acknowledge Idaho National Laboratory and Energetics for their help in preparing and publishing this report.

Sarah Kleinbaum

Program Manager
Materials Technology Program
Vehicle Technologies Office

Jerry L. Gibbs

Technology Development Manager
Propulsion Materials
Vehicle Technologies Office

Sarah Kleinbaum

Technology Development Manager
Automotive Metals & Multi-Material Joining
Lightweight Materials
Vehicle Technologies Office

H. Felix Wu, Ph. D

Technology Development Manager
Carbon Fiber and Polymer Composites
Lightweight Materials
Vehicle Technologies Office

Acronyms and Abbreviations

symbols

β	a phase in a metal alloy
ΔE	change in strain value
ΔH_m	change in enthalpy
δE_{cs}	coherency strain
ε	strain
$\varepsilon-N$	strain-number of cycles
κ	conductivity
η	order-parameter field value
γ'	precipitates that are ordered FCC ($L1_2$) structure and are coherent with the nickel-rich $\{\gamma\}$ matrix having an FCC structure.
λ	wavelength
μ	coefficient of friction (when referring to a measure of interaction between two surfaces).
μ_x	local diffusion potential for element “x”
μm	micrometer
Θ	designation used for micro-scale intermetallic precipitates mostly located at the grain boundaries in the as-cast state of aluminum.
Θ'	designation for nanoscale intermetallic precipitates present in the grain interiors of cast-aluminum alloy.
ρ	density
σ	standard deviation (when referring to statistical analysis).
σ	stress (or strength, when referring to physical properties).
σ	interfacial energy (when used in total energy calculations).
1D	one-dimensional
2BK	modeling parameter for double-baked.
2D	two-dimensional
3D	three-dimensional
3M	<u>M</u> innesota <u>M</u> ining and <u>M</u> anufacturing Company (company’s former name)
304	steel containing chromium (between 18% and 20%) and nickel (between 8% and 10.5%).
310	a medium carbon austenitic stainless-steel for high-temperature applications, such as furnace parts and heat-treatment equipment.

316L	the low carbon version of 316 stainless-steel commonly used in chemical and petrochemical industry, in food processing, pharmaceutical equipment, medical devices, in potable water, wastewater treatment, in marine applications and architectural applications near the seashore or in urban areas.
1040	a carbon (non-alloy) steel formulated for primary forming into wrought products
4140	a low alloy steel containing chromium, molybdenum, and manganese
4XT	4X Technologies
5xxx	series designation for aluminum alloyed with magnesium
6xxx	series designation for aluminum alloyed with magnesium and silicon
7xxx	series designation for aluminum alloyed with zirconium
A	
Å	angstrom
A316L	a chromium-nickel-molybdenum austenitic stainless-steel developed to provide improved corrosion resistance to Alloy 304/304L in moderately corrosive environments.
A319	aluminum alloy having a composition of 6% silicon and 3.5% copper alloy with 1.0 iron maximum that has excellent casting and machining characteristics and very good corrosion resistance and weldability.
A356	aluminum alloy with greater elongation, higher strength, and considerably higher ductility than Alloy 356 because of lower iron content that is typically used for airframe castings, machine parts, truck chassis parts, aircraft and missile components, and structural parts requiring high-strength.
A380	the most commonly specified aluminum alloy that has the best combination of casting, mechanical, and thermal properties; exhibits excellent fluidity, pressure tightness, and resistance to hot cracking; and is used for a wide variety of products including chassis for electronic equipment, engine brackets, gearbox cases, household furniture, power, and hand tools.
AA	aluminum alloy
AA	Aluminum Association (when used with a series e.g., AA1100 series)
AA1100	a pure aluminum alloy with excellent forming characteristics and machinability, especially when the alloy is machined in hard temper.
AA2024	a heat-treatable aluminum alloy with copper as the primary alloying element that is malleable when in the fully soft, annealed temper and can be heat-treated to high-strength levels after forming widely used in aerospace applications.
AA3003	aluminum alloy with moderate strength, which can be increased by cold working, and good corrosion resistance.
AA4043	a wrought aluminum alloy with good corrosion resistance typically used as filler material for welding of aluminum parts containing high amounts of 4.5% and 6.0% silicon.

AA5052	aluminum alloy most suited to forming operations, with good workability and higher strength than that of either 1100 or 3003. Although not heat-treatable, it is stronger than most of the 5xxx series of aluminums.
AA5182	wrought aluminum alloy with good corrosion resistance and weldability containing 4.5% Mg, 0.35% Mn, and the balance aluminum.
AA5356	an alloy in the wrought aluminum-magnesium family (5000 or 5xxx series) used primarily used as welding filler.
AA6022	heat-treatable low copper precipitation hardenable aluminum sheet alloy containing 0.8% to 1.5% silicon, 0.45% to 0.70% magnesium, and 0.25% zinc.
AA6061	precipitation hardening aluminum alloy containing 0.8% to 1.2% magnesium and 0.4% to 0.8% silicon as its major alloying elements.
AA6063	aluminum alloy consisting of aluminum, magnesium, and 0.5% silicon used for pipe, railings, furniture, architectural extrusions, irrigation pipes, and transportation.
AA6082	a medium strength alloy with excellent corrosion resistance and the highest strength of the 6000 series alloys used as a structural alloy.
AA6111	wrought aluminum alloy that is heat-treatable and possesses high-strength and excellent stretch-forming characteristics containing 0.6% to 1.1% silicon, 0.5% to 1.0% magnesium, 0.1% to 0.45% manganese, 0.5% to 0.9% copper, and 0.15% zinc.
AA7055	aluminum alloy containing zinc, magnesium, chromium, and copper as hardeners, as well as small amounts of iron, silicon, manganese, and titanium with the highest total strength, good fracture toughness, and a strong ability for fatigue crack propagation with a microstructure that is resistant to intergranular fracture and corrosion.
AA7075	aluminum alloy with strength comparable to many steels, good fatigue strength, and average machinability.
AA7085	a high-strength and high hardenability forging aluminum alloy that has excellent fracture toughness.
ABAQUS or Abaqus	software suite for finite element analysis and computer-aided engineering.
ABS	acrylonitrile-butadiene-styrene
ACEC	Advanced Combustion Engine and Emission Control
ACMZ	designation for aluminum alloys containing aluminum, copper, manganese, and zirconium
ACN	acrylonitrile
ACP	Advanced Carbon Products
AddUp	Additive Manufacturing Laser Powder Bed System
AET	Applied Engineering & Technology Integration, Inc.
AFA	Alumina-Forming Austenitics or Al ₂ O ₃ -forming austenitic alloys
AFM	antiferromagnetic
Ag	silver
AHSS	advanced high-strength steel

AI	artificial intelligence
AISI	American Iron and Steel Institute
Al	aluminum
Al ₂ Cu	aluminum-copper (2:1)
Al ₂ O ₃	aluminum oxide
Al ₈ Mn ₅	an intermetallic crucial for impurity control and corrosion resistance in aluminum alloys.
Alloy 380	one of the most commonly specified aluminum alloys with the best combination of casting, mechanical, and thermal properties that exhibits excellent fluidity, pressure tightness, and resistance to hot cracking and used for a wide variety of products including chassis for electronic equipment, engine brackets, gearbox cases, household furniture, power, and hand tools.
Alloy 422	a hardenable, martensitic stainless-steel designed for service temperatures as high as 1200°F
Alloy 626	a nickel-based superalloy that possesses high-strength properties and resistance to elevated temperatures.
Alloy 4043	a wrought aluminum alloy with good corrosion resistance typically used as filler material for welding of aluminum parts and contains between 4.5 and 6.0% silicon.
Alloy 4140	a chromium-, molybdenum-, and manganese-containing low alloy steel that has high fatigue strength, abrasion and impact resistance, toughness, and torsional strength.
Alloy 8620	a case-hardening steel alloy containing nickel, chromium, and molybdenum as alloying elements with good strength and toughness properties.
Al ₂ O ₃	aluminum oxide (or alumina)
Al-Si-Cu	aluminum-silicon-copper alloy is a cast-aluminum alloy widely used due to its high castability and low density.
Al-Ti	aluminum-titanium alloy
AM	additive manufacturing or additive manufactured (when referring to processes).
AM60	a castable magnesium alloy with excellent ductility, superior energy absorbing properties, and good strength and castability.
AMCOS	Active Monitoring of Composite Structures through Embedded Synthetic Fiber Sensor
AMIPC	additively manufactured interpenetrating phase composite
AMO	Advanced Manufacturing Office
ANL	Argonne National Laboratory
AOP	annual operating plan
AP	atmospheric plasma
APO	atmospheric plasma oxidation
APS	Advanced Photon Source (when referring to materials characterization)
APT	atom probe tomography

Ar	argon
AS	advancing side
ASM	American Society of Metals
ASTM	American Society for Testing and Materials
ASTM B221	American Society for Testing and Materials standard specification for aluminum and aluminum alloy extruded bars, rods, wire, profiles, and tubes (metric).
ASTM B820	American Society for Testing and Materials standard test method for bend testing copper and copper alloy strip samples to determine product formability or the ability to resist cracking when forming a bend around a specific radius.
ASTM D635	American Society for Testing and Materials standard test method for determining the rate of burning for plastics.
ASTM D638	American Society for Testing and Materials standard test method to determine the tensile strength of both reinforced and non-reinforced plastics.
ASTM D2344	American Society for Testing and Materials test standard designed to measure the short-beam strength of high modulus fiber-reinforced polymer matrix composites.
ASTM D3039	American Society for Testing and Materials standard test method for tensile strength of composite materials.
ASTM D3518	American Society for Testing and Materials standard test method for in-plane shear of composite materials.
ASTM D4541	American Society for Testing and Materials standard test method for pull-off strength of coatings using portable adhesion testers.
ASTM D5528	American Society for Testing and Materials standard test method for Mode I fracture toughness of composite materials.
ASTM D6641	American Society for Testing and Materials standard test method for compressive strength of composite materials.
ASTM D7905	American Society for Testing and Materials standard test method for Mode II fracture toughness of composite materials.
ASTM E290	American Society for Testing and Materials standard test method for determining the ductility of metals through bend testing to provide a visual indication of the material's ductility.
ASTM E8-16a	American Society for Testing and Materials standard test method for tension testing of metallic materials.
ASTM E1354	American Society for Testing and Materials standard test method for fire-test-response that measures the response of materials to a controlled level of radiant heat.
ASTM E1922	American Society for Testing and Materials standard test method for tensile and compressive translaminar fracture toughness.
ASTM G85	American Society for Testing and Materials test standard for cyclic acidified salt fog (spray) testing.
at. %	atomic percent

AUTO-SMART Accelent Technologies, Inc. is a product name for a sensor system that assists with vehicle self-sufficiency.

AZ31B most widely available magnesium grade alloy, high-strength-to-weight ratio with a composition of 2.5% to 3.5% aluminum and 0.7% to 1.3% zinc.

B

B boron

BA005 a standard aqueous binder from ExOne comprised of ~ 5.75% 2-butoxyethanol and ~ 17.5 wt% ethanediol use in additive manufacturing.

BAAM big area additive manufacturing

BaTiO₃ barium titanate

BCC or bcc body-centered cubic

BD build direction

BDGE bisphenol diglycidyl ether

BF basalt fiber

bhp brake horsepower

Bi bismuth

BJAM binder jet additive manufacturing

BK baked

BMEP brake mean effective pressure

BMS battery monitoring system

BMW Bayerische Motoren Werke AG; a German luxury automobile, motorcycle, and engine manufacturing company.

BP budget period (when referring to funding)

BP button pull-out (when referring to weld testing)

BSE backscattered electron

BX bias-extension

C

°C degrees Centigrade

C carbon

C300 a steel alloy with excellent resistance to cracking from impact and compression that is often used for dies and tooling.

Ca calcium

CaCl₂ calcium chloride

CA California

CA Composites Automation

CAD	computer-aided design
CAE	computer-aided engineering
CAFE	Corporate Average Fuel Efficiency
CALPHAD	<u>CAL</u> culat <u>ion</u> of <u>PHA</u> se <u>D</u> iagrams
CAN-CFRC	covalent adaptable network-based carbon fiber-reinforced composites
CCF	continuous carbon fiber
CCT	cyclic corrosion test
Cd	cadmium
Ce	cerium
CEL	Coupled Eulerian-Lagrangian
CEM	computational electromagnetics model (or modeling)
CEM Corp.	a company formed in 1979 by a <u>chem</u> ist, an <u>elect</u> rical engineer, and a <u>mech</u> anical engineer.
CF	carbon fiber
CFC	carbon fiber composite
CF8C-Plus	cast stainless-steel developed to provide higher temperature capability and reliability for advanced diesel engine components.
CFD	computational fluid dynamics
CFR	Code of Federal Regulations
CFRC	carbon fiber-reinforced composite
CFRP	carbon fiber-reinforced polymer
CFTF	Carbon Fiber Technology Facility
CG-MD	coarse-grained molecular dynamic
cm	centimeter
cm ²	square centimeter
CNF	carbon nanofiber
CNG	compressed natural gas
CNT	carbon nanotubes
Co	cobalt
CO ₂	carbon dioxide
COMSOL	a cross-platform finite element analysis, solver, and multiphysics simulation software that allows conventional physics-based user interfaces and coupled systems of partial differential equations.
CONVERGE	computational fluid dynamic software by Convergent Science Inc. with autonomous meshing capabilities that eliminates the grid generation problems from the simulation process.

COST507	(European) <u>C</u> ooperation in <u>S</u> cience and <u>T</u> echnology 507
COVID	C <u>O</u> rona <u>V</u> irus Disease
CP	coach peel
CP Al	commercially pure aluminum
CPEC	close proximity electromagnetic carbonization
CPFEM	crystal plasticity finite element models
Cr	chromium
CRADA	Cooperative Research and Development Agreement
Cr ₂ O ₃	chromium oxide
CRS	cold-rolled steel
CRSS	critical resolved shear strength
CT	computed tomography (when referring to an analytical method)
CT	cross-tension (when referring to a test configuration)
CTE	coefficient of thermal expansion
CTP	coal tar pitch
CTPM	coal tar pitch mesophase
Cu	copper
CYS	compressive yield strength
D	
D	distance (when referring to a process parameter)
DADPM	diamino diphenylmethane
DADPS	diamino diphenylsulfone
DAQ	data acquisition
DARPA	Defense Advanced Research Projects Agency
dB	decibels
DC	direct current (when referring to electricity)
DCM	dichloromethane (when referring to a solvent)
DCM	dielectric cure monitoring (when referring to a method to measure thermoset or composite cure state in real-time under actual process conditions.
DDT	dodecanethiol
DFT	density functional theory
DIC	digital image correlation
DICTRA	<u>D</u> iffusion- <u>C</u> ontrolled <u>T</u> RANSformations in multicomponent systems, a software diffusion module within ThermoCalc for accurate simulation of diffusion-controlled reactions in multicomponent alloy systems.

DIW	direct ink writing
DMA	dynamic mechanical analysis
DMC	dough molding compound
DMD	digital micro-mirror device
DNN	deep neural network
DOE	U.S. Department of Energy (when referring to the agency)
DOF	direction of fiber
DP	dual-phase
DP590	dual-phase steel with low tensile strength (590 MPa) and low yield frequently used in automotive body structure applications requiring high-energy absorption
DRX	dynamic recrystallized
DSC	differential scanning calorimetry
dtex	decitex
Dy	dysprosium

E

E	stiffness or elastic modulus or Young's modulus
EA	energy adsorption
EBM	Eagle Bend Manufacturing
EBSD	electron backscatter diffraction
ECAP	equal channel angular pressing
E-coat or e-coat	electrophoretic coating
ED	energy density (when referring to concentration of energy)
ED	extrusion direction (when referring to ShAPE™ processing)
EDM	electro-discharge machining
EDS	energy dispersive spectroscopy
e.g.	abbreviation meaning "for example"
E-EGR	enhanced exhaust gas recirculation
EERE	Office of Energy Efficiency and Renewable Energy
EFP	E-Form Plus
EGR	exhaust gas recirculation
EIS	electrochemical impedance spectroscopy
EM	electromagnetic
EMI	electromagnetic interference
EoP	error of prediction
E_p	pulse energy

EPA	Environmental Protection Agency
EPIKOTE™	EPIKOTE™ Resin 05475 with EPIKURE Curing Agent 05443: a system with low-viscosity, a relatively long injection window, excellent wetting and adhesion to CFs, and superior thermal and mechanical performance.
EPMA	electro probe micro-analyzer
Er	erbium
ESE Carbon	ESE Carbon company – supplier of carbon fiber composites and other services for tailored-fiber placement, high-pressure resin infusion, engineering design, and analysis.
et al.	abbreviation meaning “and others”
eV	electron volt
EV	electric vehicle (when referring to types of vehicles)
EWI	Edison Welding Institute
Exp.	experimental
<i>ex-situ</i>	off-site or out of place
F	
F	force
F_N	force normal to a plane
FADI-AMT LLC	a limited liability company that does testing of automotive materials; the name is a composite of the first name of the company’s president (Fadi Abu-Farha) and the abbreviation for automotive materials testing.
FARO	Frasier and Raab Orthopedics
FCA US LLC	Fiat Chrysler Automobiles U.S. Limited Liability Company
FCC or fcc	face-centered cubic
FDS	flow-drill screw
Fe	iron
FeCu	iron-copper alloy used for many applications due to its high-strength and electric and thermal properties.
FE	finite element
FEA	finite element analysis
FEI Company	Field Electron and Ion Company
FEM	finite element method (or model)
FIB	focused ion beam
FLC	forming limit curve
FLD	forming limit diagram
FLIR	forward-looking infrared

FMVSS	Federal Motor Vehicle Safety Standard
FSLW	friction stir linear welding
FSP	friction stir processing
F-SPR	friction self-piercing riveting
FTIR	Fourier-transform infrared spectroscopy
ft-lb	foot pound(s)
FY	fiscal year
G	
g	gram(s)
G _{IC}	Mode I interlaminar fracture toughness
G10	a glass fiber and epoxy composite material which is compressed under extremely high-pressure and heat cured to provide an extremely tough and durable material.
Ga	gallium
GB	grain boundary
g/cc or g/cm ³	grams per cubic centimeter
GDOES	glow discharge optical emission spectroscopy
Gd	gadolinium
GEM	gas emission model
GF	glass fiber
GG-MIT	Grossman Group at Massachusetts Institute of Technology
GHG	greenhouse gas
GHz	gigahertz
GM	General Motors LLC
GMT	glass mat thermoplastic
G/NG	go/no-go
GO	graphene oxide
GP	Guinier-Preston
GPa	gigapascals
GPC	gel permeation chromatography
GT-POWER	simulation software by Gamma Technologies Inc. used to predict engine performance quantities such as power, torque, airflow, volumetric efficiency, fuel consumption, turbocharger performance and matching, and pumping losses.
H	
h or hr	hour(s)

H13	a chromium, molybdenum, vanadium hot work tool steel with high hardenability and excellent toughness.
H ₂ O	water
H ₂ SO ₄	sulfuric acid
HAADF	high-angle annular dark-field
HAZ	heat-affected zone
HB	Brinell hardness
HC	honeycomb
HCF	high-cycle fatigue
HCP	hexagonal close-packed
HDDE	heavy-duty diesel engine
HDG	hot-dip galvanized (or hot-dip galvanizing)
HDPE	high density polyethylene
Hf	hafnium
HIP	hot isostatic pressing
HiSiMo	high silicon molybdenum
HK30Nb	a grade of cast stainless-steel with a composition of 25% chromium, 21% nickel, 1.75% silicon, 1.5% manganese, and trace amounts of carbon, phosphorus, sulfur, and molybdenum.
HMI	human-machine interface
HNO ₃	nitric acid
Ho	holmium
HPC	high-performance computing
HPDC	high-pressure die-casting
HP-RTM	high-pressure resin transfer molding
HRA	Honda R&D Americas
HRB	Hardness Rockwell – B scale
HRR	heat release rate
HR-STEM	high-resolution scanning transmission electron microscopy
HR-TEM	high-resolution transmission electron microscopy
HS	high-strength
HSLA	high-strength low alloy
HSLA 340	steel intended for general presswork, bending, and forming
HT	heat-treated
HTC	high-temperature carbonization when referring to carbon fiber
HV	Vickers hardness

Hz	hertz
I	
i.e.	abbreviation for “id est,” a Latin phrase meaning “that is”
i3	five-door urban electric vehicle
IACMI	Institute for Advanced Composites Manufacturing Innovation
ICE	internal combustion engine
ICME	integrated computational materials engineering
IDZ	interdiffusion zone
IE	Erichsen Index
IEEE	Institute of Electrical and Electronics Engineers
IF	interfacial
IFSS	interfacial shear strength
IIHS	Insurance Institute for Highway Safety
ILSS	interlaminar shear strength
IM7	a continuous, high-performance intermediate modulus, polyacrylonitrile-based carbon fiber manufactured by Hexcel Corporation.
IMC	intermetallic compound
IMR	internal mold release
in.	inch
in/min	inches per minute
in/sec	inches per second
<i>in-situ</i>	on-site or in place
IPF	inverse pole figure
ipm	inches per minute
ISO 5660	a test method for assessing the heat release rate and dynamic smoke production rate of specimens exposed in the horizontal orientation to controlled levels of irradiance with an external igniter.
ISS	ideal shear-stress
J	
J	joule
J/kg*K	joules per kilogram degree Kelvin
JCP	Joining Core Program
JOEL JEM-2200FS	a state-of-the art analytical electron microscope equipped with a 200kV field emission gun and an in-column energy filter that allows a zero-loss image resulting in clear images with high contrast manufactured by JOEL Ltd.

K

K	degree Kelvin
k Ω	kiloohm
K _{1C}	fracture toughness
K ₂ CO ₃	potassium carbonate
kDa	kilodalton
kg	kilogram
kgF	kilogram (force)
kg/m ³	kilograms per cubic meter
kHz	kilohertz
kJ	kilojoules
kJ/m ²	kilojoules per square meter
kJ/mol	kilojoules per mole
kN	kilonewton
kN/min	kilonewton per minute
kPa	kilopascal
Ksi, ksi, and kpsi	kilopound per square inch
kW	kilowatt
kWh	kilowatt-hour
kWh/kg	kilowatt-hour per kilogram
kW/l	kilowatt per liter
KY	Kentucky

L

L ₁₂	designation for the major strengthening phase precipitates of aluminum alloys
lb.	pound(s)
LCF	low cycle fatigue
LCCF	low-cost carbon fiber
LD	light-duty
LDH	limiting dome-height (when referring to materials testing)
LDPE	low density polyethylene
LFT	long fiber thermoplastic
Li	lithium
LiCl	lithium chloride
LIG	laser-induced graphene
LightMAT	Lightweight Materials Consortium

LiNO ₃	lithium nitrate
LLC	limited liability company
LLNL	Lawrence Livermore National Laboratory
L/min	liters per minute
LMP	Larson-Miller Parameter
LMPC	Light Metals Core Program
LPBF	laser powder bed fusion
LPPSC	low pressure precision sand-casting
LS	lap-shear
LS-DYNA	advanced, general-purpose, multiphysics simulation software package
LSTC	Livermore Software Technology Corporation
LSW	Lifshitz-Slyozov-Wagner
LSS	lap-shear strength
LTC	low-temperature carbonization
M	
m	mass
m	meter
m ²	square meter
M	milestone (with a number, e.g., M1 for the first milestone)
MΩ	milliohms
M2045	a vacuum-induction melted industrial-scale heat of Alloy 161
M42	a molybdenum series high-speed steel alloy with an additional 8 or 10 percent cobalt that is used in metal manufacturing industries because of its superior red hardness as compared to more conventional high-speed steels
Magna	Magna International Inc.
mAH	milliamp hours
MAP	microwave assisted plasma
MAS	micro-alloyed steel
MAT	material
MAT233+	a LS-DYNA material model for hexagonal closed packet metals capable of describing the yielding asymmetry between tension and compression for such materials and considers anisotropy
MATLAB	<u>MAT</u> rix <u>LAB</u> oratory, a multi-paradigm numerical computing environment and programming language
MAS	micro-alloyed steel
MC	multicomponent carbides

MCE	multi-cylinder engine
MD	molecular dynamic (when referring to computer simulation)
MD	machine direction (when referring to direction of fabric weave)
MDX	multidimensional luxury (Honda's three-row mid-size luxury crossover SUV)
MeOH	methanol
MESC	multifunctional energy storage composites
meV	millielectron volt(s)
MFI	materials flow through industry
Mg	magnesium
MgCO ₃	magnesium carbonate
MgO	magnesium oxide
Mg ₂ Si	magnesium silicide
Mg(OH) ₂	magnesium hydroxide
MgZn ₂	dizinc magnesium
MHHPA	methylhexahydrophthalic anhydride
MHz	megahertz
min	minute(s)
min.	minimum
MIT	Massachusetts Institute of Technology
mJ/m ²	milli-Joules per square meter
ML	machine-learning
m/min	meters per minute
mm	millimeters
mm/min	millimeters per minute
mm ³ /m	cubic millimeters per meter
mm ³ /Nm	cubic millimeters per nanometer
mm/sec or mms ⁻¹	millimeters per second
MMC	metal matrix composites
Mn	manganese
Mo	molybdenum
M _o	term used for the mobility of oxygen
MOOSE	multiphysics object-oriented simulation environment
MPa	megapascals
MPA	mercaptopropionic acid
MRD	multiples of random distribution

MSC	Materials Sciences Corporation
MSU	Michigan State University
M-TOW	multi-tow
MTS	Material Testing Systems
MTU	Michigan Technological University
mV	millivolts
mV/g	millivolt per gram
MX	a V- or W-rich carbide that has a face-centered cubic structure and commonly precipitates as fine disks on (100) alpha
MX or MXene	ceramics first discovered in 2011 that comprise one of the largest families of two-dimensional materials
N	
N	nitrogen
N ₂	diatomic nitrogen
N _f	number of cycles to failure
NaCl	sodium chloride
NaHCO ₃	sodium bicarbonate
NapDA	diaminonaphthalene
Nb	niobium
NBK	not baked
NCF	non-crimp fabric
Nd	neodymium
NDE	nondestructive evaluation
NETL	National Energy Technology Laboratory
Ni	nickel
nm	nanometer(s)
N/mm	newtons per millimeter
NMP	N-methylpyrrolidone
NMR	nuclear magnetic resonance
NN	neural network
NREL	National Renewable Energy Laboratory
NVH	noise, vibration, and harshness
nW/cc	nano Watts per cubic centimeter

O

O	oxygen
O ₂	diatomic oxygen
OPDA	4,4'-diaminodiphenyl ether
OEM	original equipment manufacturer
OM	optical microscopy
ON	Ontario
OPF	oxidized precursor fiber
OPP	out-of-plane printing
ORNL	Oak Ridge National Laboratory
OSU	The Ohio State University

P

P (or p)	pressure
PA	polyamide
PAA	poly(acrylic acid)
PA-6	polyamide 6 (or nylon 6)
PA-66	polyamide 66 (or nylon 66)
PALAPREG® P18-03	an unsaturated polyester resin derived from maleic acid and glycols, dissolved in styrene with medium viscosity and high reactivity
PAM-RTM	privileged access management - resin transfer molding
PAN	polyacrylonitrile
PAPSC	pressure-assistant precision sand-casting
Pb	lead
PC	polycarbonate
PDA	phenylene diamine
PDAS	primary dendrite arm spacing
PDF	probability density function
PE	polyethylene
PE-CAN	polyester-based covalently adaptable network
PEDOT:PSS	poly (3,4-ethylenedioxythiophene) polystyrene sulfonate
PEEK	polyether ether ketone
PEGDA	polyethylene glycol diacrylate
PEI	polyetherimide
PEL	potential energy landscape
PEN	polyethylene naphthalate

PET	polyethylene terephthalate
PFIB	plasma focused ion beam
pH	quantitative measure of the acidity or basicity of aqueous or other liquid solutions
PI	principal investigator
Pip	piperazine
PLC	Programmable Logic Controller
PM2.5	particulate matter smaller than 2.5 micrometers
PM10	particulate matter smaller than 10 micrometers
PMCP	Propulsion Materials Core Program
PNNL	Pacific Northwest National Laboratory
POM	polarized optical microscopy
PP	polypropylene (when referring to polymers)
PPA	polyphthalamide
PPG	Pittsburgh Plate Glass
p-PDA	para-phenylenediamine
PPM	Pinetree POSCO Mg (when referring to a source of magnesium)
PPS	pedestrian protection system
Pt	platinum
psi	pounds per square inch
PTFE	polytetrafluoroethylene
PTWA	Plasma Transfer Wire-Arc
PUSP	power ultrasonic-based surface processing
PVA	polyvinyl alcohol
PVDF	polyvinylidene difluoride
PZT	lead zirconate titanate

Q

Q	USAXS scattering vector
QEE-TECH [®]	a cell used for rapid production of complex-shaped continuous fiber composite reinforcements
QSP	quasi-static pole

R

R	radius
R	resistance
R ²	coefficient of determination or linear fit score

R ³	particle radius
rad/s	radian per second
RAMACO	Ramaco Carbon LLC
RAPID	a photopolymer resin that changes its physical properties when introduced to light
R&D	research and development
R&DD	research, development, and deployment
R/CPE	resistance-constant phase element
RE	rare-earth
ReaxFF	reactive force field
ReaxFF MD	reactive force field molecular dynamics
RF	radio frequency
RFI	resin film infusion (when referring to a type of process used in molding polymers)
RH	relative humidity
RIVTAC [®]	a high-speed process supplied by Bollhoff for joining aluminum, steel, plastics, and non-ferrous metals, as well as for mixed joints, multilayer joints, and hybrid joints of these materials
rpm or RPM	revolution(s) per minute
RR	Rolls Royce
RR350	an alloy that evolved from a World War II aircraft application by Rolls Royce
RS	retreating side
RS232	Recommended Standard 232, a standard for serial communication transmission of data
RSW	resistance spot weld (or welding)
r/t	radius to thickness ratio
RT	room temperature
RTM	resin transfer mold (or molding)
RVE	representative volume element
S	
S	seconds
S/cm	siemens per centimeter
S4CFRP	self-sensing, self-sustaining carbon fiber-reinforced polymer
SAE	Society of Automotive Engineers
SAE J404	Society of Automotive Engineers standard used for determining the chemical compositions of Society of Automotive Engineers alloy steels

SAE J2522	Society of Automotive Engineers Recommended Practice for Dynamometer Global Brake Effectiveness defining an Inertia Dynamometer Test procedure that assesses the effectiveness behavior of a friction material regarding pressure, temperature and speed for motor vehicles fitted with hydraulic brake actuation with the main purpose of comparing friction materials under the most equal conditions possible.
SAE J2334	SAE standard method which specifies the test conditions that are required to perform a cyclic corrosion test that replicates, on an accelerated basis, an outdoor exposure
SAXS	small-angle x-ray scattering
SBIR	Small Business Innovative Research
SBR	styrene-butadiene rubber
Sc	scandium
Scalmalloy®	a powder product designed to be processed using laser powder bed fusion additive manufacturing
SCE	single-cylinder engine (when referring to internal combustion engines)
SCF	stress concentration factor
SCF	solidification cracking susceptibility
SDAS	secondary dendrite arm spacing
SDF	Sudamericana De Fibras
SECCM	scanning electrochemical cell microscopy
SED	ShAPE™ extrusion direction
SEM	scanning electron microscope (or microscopy)
SF-TP	short-fiber-reinforced thermoplastic
ShAPE™	<u>shear-assisted processing and extrusion</u>
SHM	structural health monitoring
Si	silicon
SiC	silicon carbide
SiCP	silicon carbide precursor
SiO ₂	silicon oxide
SLIC	sustainable lightweight intelligent composite
SLPS	super solidus liquid phase sintering
Sm	samarium
SMC	sheet molding compound
S-N	stress-number of cycles
SNL	Sandia National Laboratories
SOC	state of charge
SOH	state of health

SPD	severe plastic deformation
SPG	specific gravity
SPH	smooth particle hydrodynamics
SPP	solid-phase processing
SPR	self-pierce riveting or self-piercing rivet
SRI	Southern Research Institute
SRNL	Savannah River National Laboratory
SRS	strain rate sensitivity
SRX	static recrystallization
SS	stainless-steel
SStAC	Stainless-Steel Alloy Corrosion (the name of a simulation tool)
STEM	scanning transmission electron microscope (or microscopy)
STF	strain to failure
SuRF	Scale-up Research Facility
SUT	shield under test
T	
t	time
T	temperature
T (with a number, e.g., 3T)	the thickness of the thinner of the two members being joined
T_c	crystallization temperature
T_d	degradation temperature
T_g	glass transition temperature
T_m	melting temperature
T5	temper designation for aluminum that is cooled from an elevated temperature shaping process then artificially aged
T6	temper designation for aluminum that is heat-treated at a temperature between 325°F and 400°F to increase the strength
Ta	tantalum
Tb	terbium
TBD	to be determined
TCF	Technology Commercialization Fund
TD	transverse direction
TEA	technoeconomic analysis
TEM	transmission electron microscope (or microscopy)

TFP	tailored-fiber placement
TGA	thermogravimetric analysis
T/H	temperature/humidity
ThermoCalc	software package for thermodynamic
Ti	titanium
Ti-6Al-4V	a Grade 5 alloy consisting of a two-phase $\alpha+\beta$ titanium alloy with aluminum as the alpha stabilizer and vanadium as the beta stabilizer
TiB ₂	titanium boride
TiO ₂	titanium dioxide or titania
Tl	thallium
Tm	thulium
TMD	transition metal dichalcogenide
TMF	thermomechanical fatigue
TMP	thermomechanical processing
TMPTA	trimethylolpropane triacrylate
TMS	The Minerals, Metals & Materials Society
TPA	terephthalic acid
TP	thermoplastic
TPM	thermal pseudo-mechanical
TPP	triphenyl phosphate
TPU	thermoplastic polyurethane
TRL	technology readiness level
T-S	traction-separation
TS	thermoset
TS	tensile strength
TuFF	<u>T</u> ailorable <u>u</u> niversal <u>F</u> eedstock for <u>F</u> orming
typ.	typical
TYS	tensile yield strength

U

UCLA	University of California – Los Angeles
UCS	ultimate compressive strength
UD	unidirectional
UD-CCM	University of Delaware Center for Composite Materials
UDRI	University of Dayton Research Institute
UF	University of Florida

UHMWPE	ultra-high molecular weight polyethylene
UIUC	University of Illinois at Urbana-Champaign
UJ	ultrasonic-based spot-joining
UK	United Kingdom
UM	University of Michigan-Dearborn
UMAT	<u>user-defined mechanical material</u> behavior - a user subroutine that can be used to define the mechanical constitutive behavior of a material
UNT	University of North Texas
UP or UPenn	University of Pennsylvania
UQ	uncertainty quantification
U.S.	United States
U.S. DRIVE	U.S. Driving Research and Innovation for Vehicle efficiency and Energy sustainability
USA	United States of America
USAMP	U.S. Automotive Materials Partnership
USAXS	ultra-small-angle X-ray scattering
USCAR	United States Council for Automotive Research
USFE	unstable stacking fault energy
USW	ultrasonic welding
UTS	ultimate tensile strength
UV	ultraviolet
UVA	University of Virginia
UW	University of Wyoming
V	
v	velocity
V	vanadium
V	volt or voltage (when referring to electricity)
V	volume (when referring quantity) or wear volume (when referring to wear rate calculations)
V/g	volts per gram
VaQ	vacancy activation energy
VARTM	vacuum-assisted resin transfer molding
VDA	Verband der Automobilindustrie
VFAW	vaporizing foil actuator welding
vol.	volume

vol.%	volume percent
vs.	versus
VTO	Vehicle Technologies Office

W

W	watts (when referring to electrical energy)
W	tungsten (when referring to the chemical element)
WAIM	water-assist injection molding
WAXD	wide-angle x-ray diffusion
WI	Wisconsin
WPI	Western Polytechnic Institute
WRI	Western Research Institute
W·s/mm	watts-second per millimeter
wt%	percent by weight

X

Xc	percent of crystallinity
XCB	cross car beam
Xe	xenon
X-FEM	extended finite element method
XPS	x-ray photoelectron spectroscopy
XRD	x-ray diffraction

Y

Y	yttrium
YAG	yttrium-aluminum-garnet
Yb	ytterbium
YS	yield strength

Z

ZAF	The most widely applied correction procedure for quantitative data about the sample composition derived from the different is peak intensities by an extensive mathematical process for matrix correction where the letters stand for and consider Z - atomic number, which affects the penetration of incident electrons into the material, A - absorption of X-rays in the specimen, on the path to the detector, and F - fluorescence caused by other X-rays generated in the specimen.
ZAXME11100	magnesium alloy with a composition of Mg-1.0Zn-1.0Al-0.5Ca-0.4Mn-0.2Ce by weight-percent
ZEK100	magnesium alloy composed of zinc, rare-earth elements, and zirconium

ZK60	magnesium wrought alloy consisting of primary matrix α (Mg) and the eutectic
Zn	zinc
ZOLTEK	a producer of commercial carbon fiber
Zr	zirconium
ZX21	magnesium alloy consisting of Mg-2Zn-1Ca
ZX30	magnesium alloy consisting of Mg-3Zn-0.2Ca
ZX31	magnesium alloy consisting of Mg-3Zn-1Ca

Executive Summary

The Materials Technology subprogram supports the Vehicle Technologies Office's mission to accelerate the deployment of clean energy technology toward achieving net-zero emissions in the transportation sector. The Propulsion Materials research portfolio seeks to develop higher performance materials that can deliver the required electrical, thermal, and strength properties needed to improve efficiency of vehicle powertrains including power electronics. Lightweight Materials research portfolio enables improvements in vehicle efficiency by providing properties that are equal to or better than traditional materials at a lower weight. Because it takes less energy to accelerate a lighter object, replacing cast-iron and traditional steel components with lightweight materials, such as advanced high-strength steels, magnesium (Mg) alloys, aluminum (Al) alloys, and fiber-reinforced polymer composites can directly reduce a vehicle's energy consumption. By 2025, the Materials Technology research activities seek to enable a 25% weight-reduction of the glider for light-duty vehicles including body, chassis, and interior as compared to a 2015 baseline at no more than a \$5/lb-saved increase in cost.

Propulsion Materials

In fiscal year (FY) 2021, the Propulsion Materials portfolio began transitioning research from materials for internal combustion engines to focus on materials improvements for electric vehicle powertrain components. The work presented in this report represents the conclusion of efforts in four main areas: (1) use of multiscale modeling to predict corrosion and oxidation of engine components and the material properties needed for future engines; (2) development of new lightweight alloys for high-temperature engine components; (3) additive manufacturing (AM) of powertrain alloys; and (4) lightweight high-efficiency engines for medium-duty (MD) vehicles. In addition to these four main thrusts, work was completed on several exploratory projects in novel materials, coatings, processing techniques, and characterization methods relevant to propulsion materials.

The environment within an engine and exhaust system during operation is extremely harsh, with high temperatures and pressures, combustion, and corrosive exhaust gases. This environment corrodes components, including engine intake and exhaust valves, valve seats, and exhaust manifolds. Three projects aim to develop practical and accurate models that can rapidly evaluate corrosion/oxidation of materials—such as stainless-steel, nickel-chromium (NiCr) based alloys, and cast-Fe—and predict the components performance. These new models will help decrease the time and cost of development as materials are selected for new engines that operate at higher temperatures.

Automotive applications need low-cost, lightweight, high-temperature alloys to enhance efficiencies in systems such as internal combustion engines. One project focuses on increasing the compositional range of the Al-Fe-silicon (Si) system via alloy design and non-equilibrium processing, such as AM. Another effort seeks to develop a fundamental understanding of the features that impart thermal stability to cast-Al precipitate microstructures, such as those found in Al-Cu and Al-Cu-Mn-Zr (ACMZ) alloys. Some components, such as exhaust valves, are exposed to even higher temperatures and the development of lower-cost, improved wrought-processed Ni-based alloys is needed to achieve the combination of yield and fatigue strengths, oxidation resistance, and cost specific to the operating characteristics and lifetime expectations. Pistons in heavy-duty (HD) diesel also have unique requirements and researchers are investigating existing commercial alloys, new developmental alloys, and alloys combined with thermal barrier coatings to enable increased operating temperature while requiring only moderate cost increases. Last, corrosion-resistant coatings are also being evaluated to determine whether the operating temperatures of alloys can be increased by improving cyclic oxidation resistance without impacting the alloy high-cycle fatigue behavior.

AM offers unprecedented possibilities to fabricate unique and complex near net-shape components leading to significant savings by decreasing tooling and materials cost, accelerating prototype development, offering

unique properties, and increasing system efficiency through advanced designs not achievable via conventional fabrication processes. In-depth understanding of the relationship between microstructure and processing parameters could result in unique microstructures and enhanced or geometrically tailored properties for a wide range of powertrain materials and components. Work in this area addresses the specific challenges and opportunities associated with AM for future LD and HD engine and electronic components. Key factors, such as cost, influence of feedstock characteristics, volatilization of species, cooling rates, non-equilibrium phases, materials properties, non-uniform geometry-dependent thermal history, thermal cycling, etc., are assessed for existing and new materials via both modeling and experimental studies.

While the market share of battery electric vehicles is increasing, most MD vehicles are projected to contain conventional or hybrid internal combustion engines well beyond 2030. Improvements in engine efficiency and reductions in powertrain weight have strong leverage to reduce vehicle-related CO₂ emissions for decades to come. Two continuing projects will use advanced materials and weight-savings technologies to demonstrate greater than 15% weight-reduction of the baseline engine while increasing efficiency. Approaches being investigated include development of new high-strength and heat-resistant materials that can be incorporated with novel metal casting and AM processes to produce highly durable engine structures to maximize performance of the materials and systems with minimum mass and cost.

Lightweight Materials

In FY 2021, the lightweight materials portfolio included research in the following three areas: (1) improving the properties and manufacturability of light metals, such as AHSS, Al alloys, and Mg alloys; (2) reducing the cost of carbon fibers (CFs) and developing Integrated Computational Materials Engineering (ICME) frameworks for manufacturing of polymer composites; and (3) developing novel joining methods to enable multi-material systems.

Substitution of light metals for mild steel can result in weight-savings of 25%–60% per component, which increases fuel efficiency. However, there are several challenges to the increased use of light metals including material cost, room temperature formability, and corrosion mitigation. In FY 2021, a new core research program focused on the local modification of properties through processing of lightweight metals was launched. Several projects in the Light Metals Core Program are working to lower the cost of Al by enabling the broader use of lower-cost alloys which also simplifies manufacturing logistics. Similarly, the use of high-performance Mg alloys in the automotive industry is currently limited due to the addition of costly rare-earth (RE) elements, need for high-temperature forming, and difficulties in corrosion mitigation. Four projects in this report address the challenges that Mg presents; one through alloy development and the other three through novel processing methods that address both formability and corrosion.

Polymer composites also have the potential to reduce component weight by more than 60%. One of the main barriers to widespread implementation is the high cost of CF, which is due in large part to the cost of input material (precursor) and the CF conversion process. In addition to a successfully commercialized plasma oxidation technology, several projects are addressing this challenge by developing higher throughput conversion of CF, thus further lowering manufacturing costs and increasing production rates. Two projects are investigating potential low-cost CF alternative precursors utilizing ICME models to guide their research to meet DOE's cost targets (no more than \$5 per pound) and four projects are developing alternate or recycled reinforcing fibers. Another challenge to implementation of polymer composites is related to the time required to manufacture components. Three projects are investigating new manufacturing methods including AM and tailored-fiber placement while additional projects are assessing opportunities to functionalize the fibers in automotive components for sensing, part consolidation and energy storage.

The most effective way to reduce the overall weight of a vehicle is to tailor the material selection to each component's needs. However, joining dissimilar materials to create a multi-material structure is a significant challenge. In FY 2021, the Joining Core Program renewed its efforts by extending joining methods previously developed to additional material pairs, advancing solid-state joining toward industry readiness, investigating surface modifications to improve adhesion and corrosion resistance, and using artificial intelligence for weld quality control. The methods developed in the Joining Core Program include solid-state welding, ultrasonic welding, novel methods for mechanical fastening, and adhesives. Solid-state welding, including an impact welding process investigated by one project, allows for joining materials with vastly different melting temperatures, which is not possible with fusion welding. The portfolio also includes three projects that model the effect of galvanic corrosion on a wide variety of joining methods and material combinations to predict the effect on joint strength and fatigue life and one project that predicts failure of Al to steel joints.

Table of Contents

Vehicle Technologies Office Overview	1
Annual Progress Report.....	1
Organization Chart	2
Materials Technology Program Overview.....	3
Introduction	3
Goals.....	3
State-of-the-Art	4
Program Organization Matrix.....	5
I Propulsion Materials.....	7
I.1 Modeling of Powertrain Materials.....	7
I.1.1 Multiscale Modeling of Corrosion and Oxidation Performance and Their Impact on High-Temperature Fatigue of Automotive Exhaust Manifold Components (Ford Motor Company).....	7
I.1.2 Multiscale Development and Validation of the Stainless-Steel Alloy Corrosion (SStAC) Tool for High-Temperature Engine Materials (University of Florida)	14
I.2 Automotive Metals	24
I.2.1 Metal Matrix Composite Brakes Using Titanium Diboride (Pacific Northwest National Laboratory).....	24
I.3 Powertrain Materials Core Program	31
I.3.1 Cost-Effective Lightweight Engine Alloys – Thrust 1	31
I.3.1.1 New Aluminum Alloys with Improved High-Temperature Performance (1A/1B).....	31
I.3.1.1.1 Fundamental Studies of Complex Precipitation Pathways in Lightweight Alloys (Task 1A1) (Oak Ridge National Laboratory).....	31
I.3.1.1.2 New Higher Temperature Performance Alloys (Task 1A2) (Oak Ridge National Laboratory).....	37
I.3.1.1.3 Properties of Cast-Al-Cu-Mn-Zr (ACMZ) Alloys (Task 1B) (Oak Ridge National Laboratory).....	43
I.3.2 Cost-Effective Higher Temperature Engine Alloys – Thrust 2.....	49
I.3.2.1 New Aluminum Alloys with Improved High-Temperature Performance (2A/2B).....	49
I.3.2.1.1 Development of Oxidation-Resistant Valve Alloys for 900–950°C (Task 2A1) (Oak Ridge National Laboratory)	49
I.3.2.1.2 Higher Temperature Heavy-Duty Piston Alloys (Task 2A2) (Oak Ridge National Laboratory).....	57
I.3.2.1.3 High-Temperature Coatings for Valve Alloys (Task 2A3) (Oak Ridge National Laboratory).....	63
I.3.2.1.4 Development of Cast, Higher Temperature Austenitic Alloys (Task 2B1) (Oak Ridge National Laboratory).....	69
I.3.2.1.5 Selective Material Processing to Improve Local Properties (Task 2B2) (Oak Ridge National Laboratory).....	76

I.3.3	Additive Manufacturing – Thrust 3.....	83
I.3.3.1	Development of Higher Temperature Alloys for Additive Manufacturing (3A/3B).....	83
I.3.3.1.1	Fundamental Development of Lightweight Alloys for Additive Manufacturing (Task 3A1) (Oak Ridge National Laboratory).....	83
I.3.3.1.2	Additively Manufactured Interpenetrating Phase Composites (AMIPC) via Hybrid Manufacturing (Task 3A2) (Oak Ridge National Laboratory).....	89
I.3.3.1.3	Overview of Fundamentals of Non-Equilibrium Processing Within the Powertrain Materials Program (Task 3A3) (Oak Ridge National Laboratory).....	95
I.3.3.1.4	Fundamentals of Austenitic Alloy Processing by Additive Manufacturing (Task 3B1) (Oak Ridge National Laboratory).....	103
I.3.3.1.5	Ferritic Alloys for Heavy-Duty Pistons via Additive Manufacturing (Task 3B2) (Oak Ridge National Laboratory).....	109
I.3.4	Advanced Characterization and Computational Methods – Thrust 4.....	117
I.3.4.1	Advanced Characterization (4A).....	117
I.3.4.1.1	Overview of Advanced Characterization Within the Powertrain Materials Program (Task 4A1) (Oak Ridge National Laboratory); (Task 4A2) (Argonne National Laboratory); and (Task 4A3) (Pacific Northwest National Laboratory).....	117
I.3.4.2	Advanced Computation (4B).....	136
I.3.4.2.1	Modeling of Light-Duty Engines (Task 4B2) (Oak Ridge National Laboratory).....	136
I.4	Modeling of Powertrain Materials.....	143
I.4.1	Next-Generation High-Efficiency Boosted Engine Development (Ford Research and Advanced Engineering).....	143
I.4.2	Low-Mass and High-Efficiency Engine for Medium-Duty Truck Applications (General Motors).....	153
I.4.3	Lightweight and Highly Efficient Engines Through Al and Si Alloying of Martensitic Materials (Oak Ridge National Laboratory).....	166
II	Lightweight Materials.....	169
II.1	Automotive Metals.....	169
II.1.1	Shear-Assisted Processing and Extrusion (ShAPE) of Lightweight Alloys for Automotive Components (Pacific Northwest National Laboratory/Magna International CRADA).....	169
II.1.2	Low-Cost Magnesium Sheet Component Development and Demonstration Project (Fiat Chrysler Automobile, U.S., LLC).....	176
II.1.3	New Technologies for High-Performance Lightweight Aluminum Castings (National Energy Technology Laboratory/General Motors).....	197
II.1.4	Room Temperature Stamping of High-Strength Aluminum Alloys (Pacific Northwest National Laboratory).....	204
II.1.5	Development of a Novel Magnesium Alloy for Thixomolding of Automotive Components (Oak Ridge National Laboratory).....	209
II.1.6	Laser Powder Bed Fusion Parameter Development for Novel Steel and Aluminum Powders Using <i>In-Situ</i> Synchrotron Imaging and Diffraction (Argonne National Laboratory).....	215

II.1.7	Light Metals Core Program: Thrust 1 Selective Processing of Aluminum Sheet Materials (Pacific Northwest National Laboratory).....	221
II.1.8	Light Metals Core Program: Thrust 2 – Selective Processing of Al Castings (Pacific Northwest National Laboratory).....	240
II.1.9	Light Metal Core Program - Thrust 3 - Selective Processing of Magnesium Castings - Localized Property Enhancement for Cast Magnesium Alloys (Pacific Northwest National Laboratory).....	260
II.1.10	Light Metals Core Program - Thrust 4 - Characterization, Modeling, and Lifecycle (Pacific Northwest National Laboratory).....	276
II.1.11	Solid-Phase Processing of Magnesium and Aluminum (Pacific Northwest National Laboratory).....	288
II.2	Carbon Fiber and Polymer Composites.....	298
II.2.1	Integrated Computational Materials Engineering Predictive Tools Development for Low-Cost Carbon Fiber for Lightweight Vehicles (University of Virginia)	298
II.2.2	Integrated Computational Materials Engineering Predictive Tools for Low-Cost Carbon Fiber (Western Research Institute).....	308
II.2.3	Functionally Designed Ultra-Lightweight Carbon Fiber-Reinforced Thermoplastic Composites Door Assembly (Clemson University).....	318
II.2.4	High-Temperature Carbon Fiber Carbonization via Electromagnetic Power (Oak Ridge National Laboratory)	333
II.2.5	Continuous Fiber, Malleable Thermoset Composites with Sub-1-minute Dwell Times: Validation of Impact Performance and Evaluation of the Efficacy of the Compression-Forming Process (Malinda LLC)	342
II.2.6	Ultra-Lightweight, Ductile Carbon Fiber-Reinforced Composites (Oak Ridge National Laboratory)	349
II.2.7	Carbon Fiber Technology Facility (Oak Ridge National Laboratory)	357
II.2.8	Low-Cost, High-Throughput Carbon Fiber with Large Diameter (Oak Ridge National Laboratory)	370
II.2.9	Self-Sensing Fiber-Reinforced Composites (Oak Ridge National Laboratory).....	376
II.2.10	Industrialization of Carbon Fiber Composite Wheels for Automobiles and Trucks (Oak Ridge National Laboratory)	383
II.2.11	LightMAT: A Novel Manufacturing Process of Lightweight Automotive Seats – Integration of Additive Manufacturing and Reinforced Polymer Composite (Oak Ridge National Laboratory)	388
II.2.12	Multi-Functional Smart Structures for Smart Vehicles (Ford Motor Company)	395
II.2.13	Development of Tailored-Fiber Placement, Multifunctional, High-Performance Composite Material Systems for High-Volume Manufacture of Structural Battery Enclosure (General Motors).....	415
II.2.14	Ultra-Lightweight Thermoplastic Polymer/Polymer-Fiber Composites for Vehicles (Pacific Northwest National Laboratory and Oak Ridge National Laboratory).....	436
II.2.15	Additive Manufacturing for Property Optimization for Automotive Applications (Oak Ridge National Laboratory)	443
II.2.16	Additively Manufactured, Lightweight, Low-Cost Composite Vessels for Compressed Natural Gas Fuel Storage (Lawrence Livermore National Laboratory).....	451
II.2.17	3D-Printed Hybrid Composite Materials with Sensing Capability for Advanced Vehicles (Oak Ridge National Laboratory)	457

II.2.18	New Frontier in Polymer Matrix Composites via Tailored Vitrimer Chemistry (Oak Ridge National Laboratory)	467
II.2.19	Adopting Heavy-Tow Carbon Fiber for Repairable, Stamp-Formed Composites (Oak Ridge National Laboratory)	473
II.2.20	Soft Smart Tools Using Additive Manufacturing (Savannah River National Laboratory)	480
II.2.21	Multi-Material, Functional Composites with Hierarchical Structures (Oak Ridge National Laboratory)	489
II.2.22	Efficient Synthesis of Kevlar and Other Fibers from Polyethylene Terephthalate (PET) Waste (Pacific Northwest National Laboratory)	495
II.2.23	Bio-Based, Inherently Recyclable Epoxy Resins to Enable Facile Carbon-Fiber- Reinforced Composite Recycling (National Renewable Energy Laboratory)	501
II.3	Multi-Material Joining.....	508
II.3.1	A Multiscale Computational Platform for Predictive Modeling of Corrosion in Al-Steel Joints (University of Michigan)	508
II.3.2	Phase-Field Modeling of Corrosion for Design of Next-Generation Magnesium- Aluminum Vehicle Joints (Worcester Polytechnic Institute).....	521
II.3.3	A Hybrid Physics-Based Data-Driven Approach to Model Damage Accumulation in Corrosion of Polymeric Adhesives (Michigan State University).....	529
II.3.4	High-Strength Steel-Aluminum Components by Vaporizing Foil Actuator Welding (The Ohio State University)	536
II.3.5	Machine-Learning for Automated Weld Quality Monitoring and Control - Joining Core Program (Oak Ridge National Laboratory).....	543
II.3.6	Prediction of Al-Steel Joint Failure (Pacific Northwest National Laboratory)	556
II.3.7	Extending High-Rate Riveting to New Material Pairs (Pacific Northwest National Laboratory).....	564
II.3.8	Solid-State Joining of Multi-Material Autobody Parts Toward Industry Readiness (Pacific Northwest National Laboratory and Oak Ridge National Laboratory).....	573
II.3.9	Surface Modifications for Improved Joining and Corrosion Resistance (Oak Ridge National Laboratory and Pacific Northwest National Laboratory).....	587
II.3.10	Ultrasonic-Based Multi-Materials Joining – Joining Core Program (Oak Ridge National Laboratory)	602
II.4	Small Business Innovation Research (SBIR)	609
II.4.1	Self-Sensing, Self-Sustaining Carbon-Fiber-Reinforced Polymer (S4CFRP) Composites for Next-Generation Vehicles (Newport Sensors, Inc.)	609
II.4.2	Integrated Self-Sufficient Structurally Integrated Multifunctional Sensors for Autonomous Vehicles (Acellent Technologies, Inc.)	616
II.4.3	Active Monitoring of Composite Structures through Embedded Synthetic Fiber Sensor (Intellisense Systems, Inc.)	625
II.4.4	Short-Fiber Preform Technology for Automotive Part Production – Phase II (Composites Automation, LLC).....	631
II.4.5	Multifunctional Composites for Vehicles (Trimer Technologies, LLC).....	641
II.4.6	Low-Cost Resin Technology for the Rapid Manufacture of High-Performance Fiber- Reinforced Composites – Phase II (Trimer Technologies, LLC)	647

List of Figures

Figure I.1.1.1. (a) Mass changes during cyclic oxidation trials. (b) Oxidation layer structures and thicknesses of static oxidation trials for HiSiMo-type alloys. Source: ORNL and Missouri Science and Technology.	9
Figure I.1.1.2. OM, SEM, and EDS characterization result of the samples after TMF testing showing that the “elephant skinning” structures with thick oxidation layers observed in (a) base HiSiMo alloys, while absent in (b) HiSiMo+1wt%Cr alloys and (c) HiSiMo+3wt%Al alloys. Source: Ford Motor Company.....	10
Figure I.1.1.3. Representative HR-TEM images of the layered structure of oxides right above HiSiMo + 1.0 wt% Cr alloy after TMF testing: (a) HR-TEM imaging; and (b)–(d) fast Fourier transformation images of the phases presented in (a). Source: Ford Motor Company.....	11
Figure I.1.1.4. Representative DFT calculation results showing (a) the adhesive strength or the interfacial energy of the iron/graphite interfaces with the presence of various impurity elements, as well as (b) the segregation energy of those impurity elements along the iron/graphite interfaces. Source: The Ohio State University.....	11
Figure I.1.1.5. DFT calculation results showing (a) the adhesive strength or interfacial energy of the iron/graphite interfaces with presence of various impurity elements, as well as (b) the segregation energy of those impurity elements along the iron/graphite interfaces. Source: University of Michigan.....	12
Figure I.1.2.1. Mass variation changes in the 23-8N and 21-2N alloys corroded in water-vapor/CO ₂ mixed atmosphere compared to those corroded in pure atmospheric CO ₂ at 700 °C for up to 925 hours. Source: University of Wisconsin–Madison.	16
Figure I.1.2.2. SEM-EDS cross-sectional characterization of 21-2N samples corroded at 700 °C for 50 hours. Low magnification SEM micrographs are shown in (a) for the water-vapor/CO ₂ atmosphere and in (c) for dry CO ₂ . EDS maps for Fe, Mn, Cr and O and C are shown in (b) for water-vapor/CO ₂ and in (d) for dry CO ₂ . Source: University of Wisconsin–Madison.	16
Figure I.1.2.3. STEM-EDS micrograph of the 21-2N samples corroded at 700 °C for 50 hours in (a) water-vapor/CO ₂ and in (c) dry CO ₂ . The EDS maps for C, Mn, Cr, Fe, and O in (b) water-vapor/CO ₂ and (d) dry CO ₂ . Source: University of Wisconsin–Madison.	17
Figure I.1.2.4. The GM 2.0L turbo platform being utilized for component-level validation mounted to a dynamometer in Cell 14 at the Plymouth Technical Center. Source: Tenneco, Inc.	18
Figure I.1.2.5. Simulation of oxidation using the meso-scale model in a 1D domain with fast or slow oxygen mobility: (a) the domain, initial conditions, and boundary conditions; (b) the thickness of the three oxide phases with time; (c) the integral of the component concentrations across the 1D domain—similar to the total amount in the entire domain—with time; and (d) total oxide thickness with time. Source: University of Florida.	19
Figure I.1.2.6. (a) Migration energy barriers for neutral and charged cation vacancies in MnCr ₂ O ₄ . (b) Illustration of the Cr vacancy migration pathway (top) and illustration of the Mn vacancy migration pathway (bottom). Source: University of Florida.....	21
Figure I.1.2.7. 2D simulation results showing (a) the Mn concentration profile in the metal (blue) and in the oxide (red) and (b) the Mn concentration profile near the oxide/metal interface along the white line shown in (a). Source: University of Wisconsin–Madison.	22

Figure I.1.2.8. Modeling the oxide (shown in red) growth with X-FEM in a 2-D axisymmetric valve model. A constant interface velocity is uniformly applied at the exterior surface of the valve. Source: Idaho National Laboratory.	23
Figure I.2.1.1. Conventional brake design utilizing an Al caliper and a cast-Fe brake disc. Source: PNNL.	25
Figure I.2.1.2. (a) Gravity cast plates of 5, 10, and 15 vol.% TiB ₂ reinforced A356 alloy. (b) Sub-scale rotors ready for friction/wear testing. (c) Machined pad samples fitted in the pad holder. Source: PNNL.	26
Figure I.2.1.3. (a) Brake friction pair test stand at PNNL. (b) Schematic of the test setup with corresponding locations of the pads, rotor, load cells and other measurement equipment. Source: PNNL.	26
Figure I.2.1.4. Summary of the wear rate test resulted obtained in the previous PNNL project [3]. Source: PNNL.	29
Figure I.3.1.1.1.1. Constructed supercell models of Al-Al ₃ X (top) and Al ₃ X-Al ₂ Cu (bottom) for DFT calculations. Shaded area indicates the interface between the two phases. Source: ORNL.	32
Figure I.3.1.1.1.2. DFT formation energies of Al-Al ₃ X (X=Li, Sc, Ti, Zr, and Hf) interface supercells with respect to reciprocal number of atoms. Source: ORNL.	34
Figure I.3.1.1.1.3. DFT formation energies of Al ₃ X-Al ₂ Cu (X=Li, Sc, Ti, Zr, and Hf) interface supercells with respect to reciprocal number of atoms. Source: ORNL.	35
Figure I.3.1.1.2.1. (a) A STEM image showing segregation of solutes to interfaces in a θ' precipitate. (b) The hardness stability of two ACMZ alloys (Al ₇ CuMnZr and Al ₅ CuNi) during long-term exposure at 300 °C compared to a commercial alloy (Al ₅ CuMg). Source: ORNL.	38
Figure I.3.1.1.2.2. The mean values and the standard error of Vickers hardness of each alloy in the as-aged state and after a 200-hour, 350 °C exposure are plotted as a function of the alloys' impurity Si content. Note that the x-axis is logarithmic. Source: ORNL.	39
Figure I.3.1.1.2.3. Representative microstructures of low, intermediate, and high Si impurity level alloys in this study after aging and after subsequent high-temperature exposure at 350 °C for 200 hours. The low Si impurity alloy and the high Si impurity alloy both exhibit fine θ' precipitates in the as-aged state and θ' to θ transformation upon extended thermal exposure. The intermediate Si alloy shows coarser θ' particles upon aging and no obvious θ' to θ transformation upon thermal exposure. Source: ORNL.	39
Figure I.3.1.1.2.4. Comparison of (a) room and elevated temperatures [(b) 100°C, (c) 200°C, (d) 300°C, and (e) 350°C] lattice strain evolution in the θ' precipitate for the experimentally measured results from neutron diffraction against predicted lattice strains from the model developed in FY 2020. For each experiment, the precipitate followed the predicted behavior until the yield point of the precipitate. Source: ORNL.	40
Figure I.3.1.1.2.5. CRSS of the θ' precipitates versus temperature measured using neutron diffraction. The precipitate yield strength decreases strongly with temperature. Source: ORNL.	41
Figure I.3.1.1.2.6. Lattice strain versus true strain curves for the θ' (211) crystallographic orientation, as well as the two extremes of matrix crystallographic grain orientations. Source: ORNL.	41

Figure I.3.1.1.3.1. (a) A backscatter electron SEM image showing numerous fractured bright contrast θ precipitates in a 9.0 Cu ACMZ alloy after tensile tests at RT. (b) A schematic of the synchrotron x-rays <i>in-situ</i> tensile test set up used to measure the fracture strength of θ precipitates. (c) A lattice stress evolution parallel to the loading axis in θ precipitates calculated with (200) planes as a function of macroscopic strain in which the arrows indicate the onset of θ precipitate fracture. (d) Average fracture stress in θ precipitates as a function of equivalent precipitate radius, R. Source: ORNL.	45
Figure I.3.1.1.3.2. (a) Double logarithmic plot of creep strain rate as a function of applied tensile or compressive stress at 300°C for 6.0 Cu and 9.0 Cu ACMZ alloys. (b) Creep strain accumulated as function of time at 300 °C. (c) Monotonic tensile stress-strain curve at 300 °C. The symbol ‘x’ indicates sample fracture. Source: ORNL.	46
Figure I.3.1.1.3.3. Cross-sectional SEM montages of fractured (a) 6.0 Cu and (b) 9.0 Cu tensile creep samples showing cavitation at grain boundary θ precipitates and the magnified views of the cavities are shown for the two alloys in (c) and (d), respectively. double-headed arrow, dashed arrow, and solid arrow indicate creep cavities, creep intergranular crack, and casting pores, respectively [4, 5]. Source: ORNL.....	46
Figure I.3.1.1.3.4. Thermal conductivity of cast ACMZ alloys (e.g., 6.0, 8.0, and 9.0 wt% Cu) and commercial cast-Al alloys A356 + 0.5 Cu and 319 as a function of temperature. Source: ORNL.....	47
Figure I.3.2.1.1.1. The microstructure of a solution-annealed and aged sample from H2078. (a) Inverse pole figure map showing the grain size and grain orientation. (b) (001), (011), and (111) pole figures showing no obvious preferred orientation. (c) Fine γ' precipitates present in the as-aged condition. Source: ORNL.	51
Figure I.3.2.1.1.2. The microstructure of a solution-annealed and aged sample from H2079. (a) Inverse pole figure map showing the grain size and grain orientation. (b) (001), (011), and (111) pole figures showing no obvious preferred orientation. (c) Fine γ' precipitates present in the as-aged condition. Source: ORNL.	51
Figure I.3.2.1.1.3. (a) The effect of aging for 48 h, 480 h, and 720 h of annealing time at 900 °C on the γ' size in M2078 and M2079. (b) Plot of R3- R03 as a function of time (h). Source: ORNL....	52
Figure I.3.2.1.1.4. The number of cycles to failure at 900 °C as a function of the ratio of applied stress to tensile strength for two ORNL developmental alloys designed for higher strength at higher temperatures, and for lower-cost than commercial higher temperature valve alloys. The arrow shows that the test was stopped without sample failure (runout). Source: ORNL.....	53
Figure I.3.2.1.1.5. (a) Newly designed alumina-forming alloys showed oxidation behavior comparable to commercial alumina-forming Ni-based alloys at 950 °C in air + 10% water-vapor. (b) Cross-section of a sample from ORNL-developed Alloy 6B tested for 5450 1-hr cycles showing presence of a thin Al-rich oxide scale. Source: ORNL.....	54
Figure I.3.2.1.1.6. Yield strength of the best new alumina-forming alloy exceeded FY 2021 target at 950 °C. Source: ORNL.	54
Figure I.3.2.1.1.7. Yield strengths of the most promising new alumina-forming polycrystalline alloy exceed those of several lower-cost ORNL-developed chromia-formers and alloy 751 over a wide temperature range. Source: ORNL.....	55
Figure I.3.2.1.2.1. Steel pucks in an industrial vacuum furnace for austenitization. Source: ORNL..	58

Figure I.3.2.1.2.2. (a) UTS and (b) thermal conductivity as a function of temperature for various developmental alloys as well as commercial Alloy 4140. Strength levels of Alloys 418 and 422 are also shown in (a). The steels are in the as-tempered condition. Alloy 212, filled pink circles, shows an exceptional combination of high-strength and relatively high thermal conductivity. Source: ORNL.	59
Figure I.3.2.1.2.3. Oxidation mass change as a function of time (1-h cycles) at (a) 650 °C and (b) 700 °C for medium Cr developmental alloys and commercial Alloys 4140 and 422. Source: ORNL.	60
Figure I.3.2.1.2.4. Optical micrographs of the oxide layers of medium Cr alloys (a) B and (b) D after 1,000 hours (1-hour cycles) at 650 °C in air plus 10% water-vapor. Developmental Alloy B shows a very thick oxide scale while Alloy D exhibits a very thin oxide scale barely visible between the alloy and copper plating, and characteristic of protective oxide behavior. Source: ORNL.	60
Figure I.3.2.1.2.5. (a) UTS and (b) thermal diffusivity of select high Cr developmental alloys, as well as commercial Alloy 422 (Alloy 4140 strength shown), all in the as-tempered conditions. Source: ORNL.	61
Figure I.3.2.1.2.6. Cyclic oxidation mass change (1h cycles) for high Cr developmental alloys, as well as commercial alloys 9Cr-1Mo and 422 at 700 °C in air plus 10% water-vapor: (a) shows overview and (b) shows a higher-resolution graph of the same data in (a). Source: ORNL.	61
Figure I.3.2.1.3.1. (a)–(b) Microstructure of the as-deposited Flame Spray, Inc., slurry aluminide coating on (a) ORNL-1 and (b) 31V. (c)–(d) Calculation of the coating chemistries based on phase identification by EDS and EPMA, as well as image analysis, (c) Al concentration, and (d) Cr, Fe, and Ti concentrations. Source: ORNL.	65
Figure I.3.2.1.3.2. BSE-SEM micrographs comparing the oxide products after cyclic oxidation testing at 900 °C in air + 10% water-vapor at the surface of: (a) uncoated ORNL-1 alloy; and (b) slurry coated ORNL-1 alloy. Source: ORNL.	66
Figure I.3.2.1.3.3. (a)–(b) BSE-SEM micrographs comparing coating microstructure evolution after cyclic oxidation testing at 900 °C in air + 10% water-vapor: (a) 31V coated alloy; (b) ORNL-1 coated alloy; and (c) calculation showing Al activity ratio in the coating to the substrate. Source: ORNL.	66
Figure I.3.2.1.3.4. 1 h cyclic oxidation behavior in air and 10% water-vapor of bare alloy and Flame Spray, Inc., slurry aluminide coated alloy: (a) Alloy 31V at 900 °C; (b) Alloy 31V at 950 °C; (c) Alloy 2687 at 900 °C; and (d) Alloy 2687 at 950 °C. Source: ORNL.	67
Figure I.3.2.1.4.1. Specific mass change in the laboratory-scale AFA5 base alloys after cyclic oxidation with 1 h cycles at (a)–(c) 950 °C and (d)–(f) 1,000 °C in air with 10% water-vapor. Source: ORNL.	71
Figure I.3.2.1.4.2. A comparison of creep-rupture lives of cast AFA5 alloys (e.g., laboratory-scale and industrial heats) and reference HK30Nb alloy tested at 900 °C and 50MPa. Source: ORNL.	72
Figure I.3.2.1.4.3. Optical micrographs and SEM-BSE images of the as-cast AFA5 alloys: (a)–(b) the original laboratory-scale alloy; and (c)–(d) the industrial heat #2. Source: ORNL.	74
Figure I.3.2.1.4.4. Comparison of RT tensile ductility of the laboratory-scale heats and the industrial heats plotted as a function of the analyzed Y contents. Source: ORNL.	74

Figure I.3.2.1.5.1. Previous fatigue testing results showing that significant improvements in fatigue performance can be achieved when applying FSP to cast–Al alloys [2]. Source: PNNL.....	77
Figure I.3.2.1.5.2. (a) Deck surface of an as-cast-Al block showing cast-in holes for head bolts above and below the interbore area. (b) Complex casting of an EV drive system, combined motor/transmission/differential housings. (c) The same casting showing the bolt flange areas. Source: (a) PNNL; (b) and (c) ORNL.....	78
Figure I.3.2.1.5.3. Casting mold design for generating different defects around core pins using (a) a steel book mold with core pins to create cast-in holes and (b) the details of the experimental plan. Source: PNNL.....	79
Figure I.3.2.1.5.4. Schematic diagram of FSP region healing porosity in the area later threaded for a fastener. Source: PNNL.....	79
Figure I.3.2.1.5.5. (a)–(c) Macrograph cross-sections of FSP processed regions adjacent to the edge of the hole left by the FSP tool. Different tool designs and processing create different characteristics (including width) in the defect-free processed region. Source: PNNL.....	80
Figure I.3.2.1.5.6. ABB IRB 7600 robot with an FSP end-effector. This configuration illustrates processing a cast-in hole that will be later drilled and tapped for a cylinder head bolt. Source: PNNL.....	81
Figure I.3.2.1.5.7. (a) Load versus position graphs for different speeds of the FSP tool showing that different processing conditions result in different tool loads. (b) Orientation for the travel shear and the rotation shear forces on a FSP tool in the tools frame of reference. Source: PNNL....	81
Figure I.3.3.1.1.1. Summary of key results from studies on AM Al-9Cu-6Ce-(1Zr) alloys with (a) representative microstructure of the Al-Cu-Ce alloy with refined Al ₈ Cu ₃ Ce intermetallic network, (b) YS, and (c) UTS of the AM Al-Cu-Ce-(Zr) alloys plotted relative to common AlSi10Mg and Scalmalloy® additively manufactured Al alloys from the literature. Source: ORNL.....	84
Figure I.3.3.1.1.2. A summary of key results for the assessment of the elevated temperature ductility dip in the AM Al-9Cu-6Ce alloy (a) tensile elongation and SRS measured at different temperatures. The dip in elongation was concomitant with the dip in the SRS (b) failure site observed during tensile testing at 300 °C. The failure initiated in the HAZ, which is a weak region in the microstructure formed during additive processing. Source: ORNL.....	85
Figure I.3.3.1.1.3. Summary of key results from high-temperature studies of an AM Al-11Ce-3Ni-1Mn alloy: (a–b) after aging at 300 °C or 350 °C for 200 h, the complex microstructure of the sub-micron intermetallic phases remained stable; (c) HR-STEM micrograph and associated EDS maps showing complex elemental distributions within the intermetallics; (d) tensile YS of the AM Al-Ce-Ni-Mn alloy compared to other AM alloys from the literature displaying excellent strength at elevated temperatures; and (e) tensile creep behavior of AM Al-Ce-Ni-Mn at 300, 350, and 400 °C. The alloy outperformed the most advanced cast high-temperature Al alloys from the literature and approached the performance of PM Al alloys. Source: ORNL.....	86

Figure I.3.3.1.1.4. Multiscale characterization of aged AM Al-9Cu-0.4Mn-0.9Zr performed using: (a) EBSD mapping showing individual grains and melt pool structures; (b) SEM imaging showing break down of the θ -Al₂Cu network; (c) STEM imaging showing metastable θ' -Al₂Cu precipitates; and (d) APT analysis showing 3D distribution of L1₂-Al₃Zr nanoprecipitates. (e) Creep testing of the alloy at 300 °C revealed superior creep resistance in the as-fabricated condition. Only after overaging at 400 °C for 200 h did the creep resistance of AM ACMZ fall below that of its cast counterpart. Source: ORNL..... 87

Figure I.3.3.1.2.1. Process for synthesizing AMIPCs using the PrintCasting technique. The model is printed using a selective laser melting process, filled with liquid metal using centrifugal casting, and then post-processed to optimize the properties. Source: ORNL. 90

Figure I.3.3.1.2.2. Results of employing HIP conditions of ASTM F3318-18 (i.e., 100 MPa at 510-530 °C for 3 hours) on: (a) a PrintCast sample with 30% volume 316L SS lattice with balance of cast A356; and (b) the HIP post-processing procedure mitigates the porosity in the A356 matrix. From the SEM analysis, the interface exhibits gaps (black regions) ranging between 50 and 100 μ m. Source: ORNL..... 91

Figure I.3.3.1.2.3. (a) Tensile measurements of pre-and-post-HIP of PrintCast samples at 40% volume fraction 316L SS with balance A356 Al. (b) FEA domain used to simulate measured interface gap in samples. (c) FEA results of a varied gap at the constituent interface. Source: ORNL. 92

Figure I.3.3.1.2.4. Hypervelocity measurements performed by Rice University [5] and the simulation of the impact's performance at ORNL using the calibrated FEA mode. Source: ORNL. 92

Figure I.3.3.1.2.5. FEA simulation of super-knock-loading of pistons using the calibrated FEA model for (a) cast-Al and (b) 40% 316L/356 SS Al PrintCast. Source: ORNL..... 93

Figure I.3.3.1.3.1. Schematic flowchart showing the approach used in this project. Source: ORNL.. 96

Figure I.3.3.1.3.2. Calculated solidification reactions and experimentally observed microstructure of Al-8.8Cu-5.91Ce wt. %: (a) calculated solidification path using the Scheil model; (b) liquid compositions (red line) superimposed onto the liquidus projection of Al-Cu-Ce system; (c) low magnification of the SEM/BES image; (d) enlarged image showing the feature in the white box; and (e) EDS mapping of Al, Cu, and Ce. Source: ORNL. 97

Figure I.3.3.1.3.3. (a) Calculated isothermal section of Al-Cu-Ce at 610 °C. (b) Microstructure of Al-8.8Cu-5.91Ce wt. %, which is the solid square in (a) in the as-annealed state at 610 °C for 2h. (c) Calculated isothermal section of Al-Cu-Ce at 540 °C. (d) Microstructure of Al-8.8Cu-5.91Ce wt. %, which is the solid square in (c) in the as-annealed state at 540 °C for 20h. Source: ORNL. 98

Figure I.3.3.1.3.4. Phase analysis in AM Al-7.78Cu-4.73Ce wt. % alloy: (a)–(b) low and high magnified SEM/BSE image showing the phases in the as-built microstructure; (c) APT results showing at least three phases coexisting in the microstructure with compositions in atomic %; (d) XRD results of as-built and as-annealed microstructure at 400 °C; and (e) calculated equilibrium mole fractions of phases as a function of temperature for the AM alloy. Source: ORNL. 99

Figure I.3.3.1.3.5. Calculated solidification reactions and experimentally observed microstructure of Al-4.13Ni-9.94Ce wt.%. (a) calculated solidification path using the Scheil model; (b) liquid compositions (red line) superimposed onto the liquidus projection of Al-Ni-Ce system; (c) low magnification of SEM/BES image; and (d) high magnification of SEM/BES image. Red dot: Al ₁₁ Ce ₃ ; purple dot: (Al); yellow box: eutectic of (Al)+ Al ₁₁ Ce ₃ ; and green box: eutectic of (Al)+ Al ₁₁ Ce ₃ + Al ₃ Ni. Source: ORNL.....	100
Figure I.3.3.1.3.6. (a) Calculated mole fraction of phases in the Al-4.13Ni-9.94Ce alloy as a function of temperature. (b) Microstructure in the as-annealed state at 620°C for 2 h. (c) Microstructure in the as-annealed state at 520°C for 20 h. Source: ORNL.....	101
Figure I.3.3.1.4.1. Inverse pole figure maps and corresponding {001} pole figure for the as-printed LPBF HK30Nb alloy (a) along the BD and (b) perpendicular to the BD. Source: ORNL and PNNL.....	104
Figure I.3.3.1.4.2. (a) STEM image of the as-printed HK30Nb alloy. (b) Corresponding EDS maps of Nb and Cr. (c) APT map showing the 30 at.% iso-concentration surface. (d) and (e) STEM images of as-printed CF8C+. (f)-(h) Corresponding EDS maps for: (f) Nb; (g) Cr; and (h) N. Source: ORNL and PNNL.....	105
Figure I.3.3.1.4.3. Comparison of the tensile properties between the LPBF and cast austenitic steels for (a) yield strength and (b) total deformation. “Per. To BD” = perpendicular to the build direction. Source: ORNL.....	105
Figure I.3.3.1.4.4. LMP plot comparing the creep properties of the LPBF austenitic steels along and perpendicular to the BD at 700 °C – 800 °C with the creep properties of cast counterparts. “Per. to BD” = perpendicular to the build direction. Source: ORNL.....	106
Figure I.3.3.1.4.5. Microstructure characterization of LPBF HK30Nb creep specimens tested at 700 °C, 120MPa: (a) optical image, BD; (b) optical image perpendicular to BD; (c) BSE-SEM micrographs, BD; and (d) BSE-SEM micrographs, perpendicular to BD. Source: ORNL.....	107
Figure I.3.3.1.5.1. Workflow used to setup the CALPHAD model based on powder feedstock and binder analysis [1]. Source: ORNL.....	110
Figure I.3.3.1.5.2. (a) TGA on the binder. (b) TGA on the H13 powder + binder mixed in 9:1 ratio. (c) Local C pickup at the interparticle region due to the binder residue. (d) Spatial evolution of volume fraction of liquid for varying binder saturations and sintering temperatures. (e) Liquid fraction curve calculated from ThermoCalc for H13 powder chemistry, H13 + 85% binder saturation, and H13 + 105% binder saturation [1]. Source: ORNL.....	112
Figure I.3.3.1.5.3. (a) Relative density, (b) liquid channel width, (c) bulk composition after cooling post sintering, and (d) shape loss estimates from contiguity [1]. X-axis labels indicate sintering temperature (°C) and binder saturation levels (wt.%). Source: ORNL.....	113
Figure I.3.3.1.5.4. Low magnification STEM image, along with the corresponding elemental maps of V, Mo, Cr, Fe, Mn, and the micro-XRD profile across two particles in the sample sintered at 1,380 °C with an 85% binder saturation. Source: ORNL and PNNL.....	114
Figure I.3.3.1.5.5. Diffraction pattern analysis of the carbides and APT C atom maps and proxigrams across the matrix and the carbide. Source: PNNL.....	114

Figure I.3.3.1.5.6. Phase fraction estimates for (a) H13 powder composition and (b) H13 powder composition after incorporating excess C pickup from the residual binder after burnout. Source: ORNL.	115
Figure I.3.3.1.5.7. Summary of yield strength of BJAM H13 in different conditions as compared with 4140 and MAS. Source: ORNL.	115
Figure I.3.4.1.1.1. HAADF- STEM images along the $\langle 001 \rangle$ α -Al zone axis of (a) the as-aged microstructure and after thermal exposure at 300 °C for (b) 200 h; (c) 2100 h; and (d) 5000 h. Two habits of θ' precipitates are seen edge-on, while a third indicated by arrows depict the plain view. High-resolution HAADF- STEM images of θ' precipitates in the (e) as-aged condition, and (f) after 5000 h thermal exposure at 300 °C. Source: ORNL.	120
Figure I.3.4.1.1.2. (a) STEM-derived volume fraction change in the θ' precipitates from the as-aged to 5000 h exposure condition. Most of the small reduction in volume fraction occurs in the first 200 h of exposure at 300 °C. Source: ORNL. (b) Synchrotron derived volume fractions for trace phases detected in the as-aged and 5000 h sample at 300 °C. This image is taken from Bahl et al. [2]. Source: ANL.	121
Figure I.3.4.1.1.3. (a)-(c) Coherent interface composition profiles for a low, intermediate, and high Si alloy exposed to 350 °C for 200 h after aging, respectively, calculated from APT data. The curve colors are given in the shared legend located in (d). (d) APT atom maps for an intermediate and high Si alloy used for the composition profiles in (b) and (c), respectively. The composition profile was calculated from the region marked by arrows in the high Si alloy using a proximity histogram from a 10 at.% Cu iso-concentration surface. Note that the positive distance values in (a)-(c) represent the region inside the precipitate and negative values represent the matrix. This image is taken from Shower et al. [7]. Source: ANL.	122
Figure I.3.4.1.1.4. (a) APT reconstruction of the ACMZ alloy after annealing at 350 °C for 4 hours where the θ' precipitate is highlighted using a 10 at.% Cu iso-concentration surface. (b) The compositional partitioning of Cu, Al, Mn, and Zr across the θ' and Al matrix is revealed using 2D compositional maps with a $36 \times 5 \times 46$ nm region of interest. A clear segregation of Mn and Zr at the θ' and Al matrix interface is evident after <i>in-situ</i> annealing. Source: PNNL.	123
Figure I.3.4.1.1.5. (a) SAED pattern along $[001]$ γ zone axis. Superlattice spots are shown in the red circles. (b) HAADF-STEM image. (c)-(h) EDS area maps showing elemental distribution within the γ and γ' . (i) A 3D reconstruction showing the γ' precipitates delineated by an iso-concentration surface (red) enclosing a region with more than 5 at.% Al. (j) Proxigram of major alloying elements. (k) Minor alloying elements showing the elemental partitioning across the γ - γ' interface. Source: ORNL.	125

- Figure I.3.4.1.1.6. TEM and APT analysis of a sample in the AA-HTA condition. (a) STEM image with the face-centered cubic matrix (γ) and the dark contrast primary γ' precipitates showing SAED patterns from the matrix (γ), and the precipitate (γ') aligned at $\{011\}$ direction. Faint super lattice spots are observed in SAED patterns from the matrix, while they are much more intense in the SAED patterns from the precipitate. Also shown are the color-coded EDS maps of Cr and Ni distribution, respectively, depicting the partitioning of Ni within the γ' precipitates. (b) APT 3D reconstruction showing a γ - γ' interface. The top portion of the figure has an interface demarked by a 5 at.% Al iso-concentration surface and the top proximity histogram shows the elemental partitioning across the interface of the matrix (γ) and coarse (γ'). The bottom APT reconstruction from the matrix region consists of fine γ' precipitates ($\sim 5\text{nm}$) that are not clearly discernable in TEM are also highlighted here within the matrix (γ). The proximity histogram shows the elemental partitioning across the interface of the matrix (γ) and fine (γ') precipitates. Source: PNNL. 126
- Figure I.3.4.1.1.7. (a) USAXS/SAXS data and model scattering contributions for chromia-forming alloy sample fatigue-tested at 900°C for 150 MPa. (b) SEM γ' size analysis with schematic overlay of Log-normal and LSW distributions from γ' modeling of USAXS data. Source: ANL..... 127
- Figure I.3.4.1.1.8. BSE image of carbides and a Mo-rich phase in CC282. Source: ORNL. 128
- Figure I.3.4.1.1.9. (a) Al-Cu-Ce-Zr phase in the Al matrix that is oriented to a low-index zone axis orientation. (b) Atomic column image at 10Mx direct magnification from the thin edge of the phase grain. (c) The projection of the $\text{Al}_{24}\text{Cu}_8\text{Ce}_3\text{Mn}$ proposed crystal structure in the $\langle 110 \rangle$ zone axis orientation. An image simulation and the crystal structure projection shown in the inset suggest a good match of the phase to the proposed crystal structure. Source: ORNL..... 129
- Figure I.3.4.1.1.10. (a) SEM-BSE image of the Al-11Ce-3Ni-1Mn (wt.%) fabricated by LPBF AM followed by stress relief annealing. The area marked in between the inner and outer circle was removed by Xe ion milling in PFIB to fabricate a micropillar. (b) A final micropillar fabricated using PFIB milling before micropillar compression test. (c) The stress-engineering strain curve along with the insets of the compression tester top and deformed pillar with the white arrows highlighting specific morphological changes on the pillar during compression at ambient temperature. Source: PNNL. 130
- Figure I.3.4.1.1.11. (a) RT tensile stress-strain curves of AA cast and as-fabricated additive ACMZ alloys. (b)-(c) Cross-sectional SEM images showing fractured θ precipitates in cast and additive ACMZ samples, respectively, after tensile tests. (d) Lattice stress in θ precipitates along the loading axis vs. macroscopic tensile strain calculated using (200) reflection from θ during *in-situ* tensile tests. Source: ORNL and ANL..... 131
- Figure I.3.4.2.1.1. Head temperature predictions starting from the baseline condition of 2,000 RPM and 21.9 bar BMEP, showing materials suites and cooling scenarios, along with the maximum service temperature of each alloy. Source: ORNL..... 139
- Figure I.3.4.2.1.2. Exhaust valve temperature predictions starting from the baseline condition of 2,000 RPM and 21.9 bar BMEP, showing materials suites and cooling scenarios, along with the maximum service temperature of each alloy. Source: ORNL..... 140
- Figure I.3.4.2.1.3. Exhaust valve temperature predictions starting from the baseline condition of 5,000 RPM and 17.7 bar BMEP. Temperature management is (a) without and (b) with protective enrichment. Source: ORNL. 140

Figure I.3.4.2.1.4. (a) Head and (b) piston temperature predictions starting from the baseline condition of 5,000 RPM and 17.7 bar BMEP. Source: ORNL.	141
Figure I.4.1.1. Specific power vs. maximum efficiency. Source: FEV, Ford.....	143
Figure I.4.1.2. The project development approach and work streams. Source: Ford.....	144
Figure I.4.1.3. Cylinder head made of AS7GU-T64-Al. Source: Ford.....	145
Figure I.4.1.4. Oil pan molds. Source: ORNL.....	146
Figure I.4.1.5. Cylinder head water jacket for a conventional core and a printed core. Source: Ford.....	146
Figure I.4.1.6. Design modifications resulting in lower stress. Source: Ford/FEV.....	147
Figure I.4.1.7. Tappet bore distortion comparison for: (a) Al; and (b) Mg. Source: Ford/FEV.....	147
Figure I.4.1.8. Comparison of component temperature with SAE 8620 and SAE 316L. Source: Ford.....	148
Figure I.4.1.9. Main bearing cap designs for (a) the initial prototype, (b) optimized steel, and (c) optimized cast-iron. Source: Ford/FEV.....	149
Figure I.4.1.10. Main bearing cap ladder frame and windage tray. Source: Ford/FEV.....	150
Figure I.4.1.11. Prototype ULTEMTM 1010 resin windage tray. Source: Ford/FEV.....	150
Figure I.4.1.12. The distribution of frictional losses in an engine. Source: Ford [1].	151
Figure I.4.1.13. Image of honed surface showing different levels of porosities: (a) PTWA1 (less than 2%); (b) PTWA2 (3-5%); (c) PTWA3 (6-8%); and (d) PTWA4 (>8%). Source: Ford [1].....	152
Figure I.4.2.1. Proposed advanced combustion system. Source: GM.....	155
Figure I.4.2.2. Proposed advanced combustion system application in hardware. Source: GM.....	155
Figure I.4.2.3. Proposed advanced combustion system cylinder head assembly – exhaust side view. Source: GM.....	156
Figure I.4.2.4. Proposed advanced combustion system cylinder head assembly – intake side view. Source: GM.....	156
Figure I.4.2.5. “Ultra” high-pressure injection system adapted to proposed advanced combustion system cylinder head assembly – exhaust side view. Source: GM.....	156
Figure I.4.2.6. E-EGR system adapted to development engine. Source: GM.....	157
Figure I.4.2.7. Variable charge motion accomplished with inserts. Source: GM.....	157
Figure I.4.2.8. Cooling jacket design. Source: GM.....	158
Figure I.4.2.9. Projected and completed GEM cycle operating points. Source: GM.....	158
Figure I.4.2.10. Two sets of CT porosity measurements of five ACMZ alloy compositions for two representative sections of end-chill sand-cast plate castings. Source: ORNL.....	159
Figure I.4.2.11. Predictions of fatigue strength distributions based on the porosity measurements outlined. Source: ORNL.....	160
Figure I.4.2.12. (a) The first cylinder head casting made by (b) the novel LPPSC process showing good quality in X-ray CT. Source: ECK.....	160

Figure I.4.2.13. An assembly of exhaust valve steel seat (red) with exhaust port sand core (blue) and deck face metal chill (yellow). Source: GM.	161
Figure I.4.2.14. Casting patterns and experimental supplies. Source: OSU.....	161
Figure I.4.2.15. Overcasting sample in an as-cast state: (a)-(b) BSE image and EDS scan of Zn-plated sample; (c) Al-Fin processed sample; (d) SEM image; (e) EDS scan; and (f) BSE image of the sample with no coating. Source: OSU.	162
Figure I.4.2.16. Additively manufactured pistons with an AlCeNiMnZr alloy. Source: ORNL.....	162
Figure I.4.2.17. (a) UTS, (b) creep properties, and (c) fatigue strength of Al-Ce based alloy at various temperatures. Source: ORNL.	163
Figure I.4.2.18. CA simulation of melt pool and solidified grain structure during AM with the refined grid size. Source: OSU.....	163
Figure I.4.2.19. Pictures showing (a) the hollow cast-steel crankshafts that were made, and (b) the longitudinal sectioning of a crank. Source: GM.	164
Figure I.4.2.20. Fatigue S-N data comparing the fatigue properties of cast-steel crank samples with the forged steel ones. Source: GM.	164
Figure I.4.3.1. Alternating stress vs. number of cycles from rotating beam fatigue data at 600 °C for six specimens of the developed alloy. Filled data points correspond to failed specimens and un-filled data points are from specimens that were removed prior to failure. Stress values are proprietary and actual values have been omitted. Source: ORNL/Cummins.	168
Figure II.1.1.1. ShAPE™ machine installed in PNNL's Solid-Phase Processing Laboratory. Source: PNNL.	170
Figure II.1.1.2. Schematic of ShAPE™ tooling and process. Source: PNNL.	171
Figure II.1.1.3. Examples of AA6063-T5 tubing extruded by ShAPE™. Source: PNNL.	172
Figure II.1.1.4. Briquette manufactured by Magna R&D from 6063 scrap. Source: Magna R&D. ...	173
Figure II.1.1.5. (a) Machined and assembled port-hole die. (b) 6063 tubing fabricated from cast billet using a port-hole bridge die. Source: PNNL.	173
Figure II.1.2.1. Project task interrelationships. Source: USAMP.....	177
Figure II.1.2.2. Total part fabrication, assembly, and paint costs per door (100,000 annual volume). Source: Camanoe.	179
Figure II.1.2.3. Task organization and data flows for the new Mg alloy development and modeling process. Source: USAMP.	180
Figure II.1.2.4. RT formability (IE values) vs. the YS of various alloys. For the age-hardening Alloy 2 Plus, AA6061, and AA6016 alloys, the IE was measured in the solution-treated condition, but the YS was measured in peak-aged condition. Source: The Ohio State University.	180
Figure II.1.2.5. Alloy 2 and Alloy 2 Plus sheets rolled to large reductions at 275 °C. Source: The Ohio State University.....	181
Figure II.1.2.6. EBSD image and (0001), (1010), and (1120) pole figures from Alloy 2 Plus asymmetric rolled at 275 °C (1:1.2, 56%) showing almost complete recrystallization. Source: ORNL.	182

Figure II.1.2.7. Mini-door assembly schematic (left) with three cut-outs as manufacturing features, full welded assembly (center), and close-up top and bottom views of welded area (right) for bare EFP Batch #3 material with no lubricant. Source: AET.....	186
Figure II.1.2.8. EFP mini-doors treated with (a) Xtalic zinc plating or (b) Henkel coil pretreatment and then coated with Quaker or Fuchs lubricant. Panels were pretreated with either a two-step or a three-step process; Cleaner 1 → Cleaner 2.4 → (opt.) Pretreatment 8 or Pretreatment 1, and then e-coated with a standard automotive e-coat and subjected to G-85 A2 filiform corrosion testing. Source: PPG.	187
Figure II.1.2.9. Corrosion performance of EFP, CRS, AA6111, and HDG steel after three weeks of ASTM G-85 A2 corrosion testing. Cleaner 2 or Cleaner 2.4 → Pretreatment 1 and C2.4 → Pretreatment 24 showed promise. CRS showed the most corrosion of all substrates. Source: PPG.....	187
Figure II.1.2.10. A good quality warm-formed EFP cross-form (upper left), approximately 470 mm square, and the Argus true strain maps. Source: EWI.....	189
Figure II.1.2.11. Comparison of Argus and MAT233/233+ major strains. Source: Vehma and InalTech.	190
Figure II.1.2.12. Comparison of Argus and MAT233/MAT233+ minor strains. Source: Vehma and InalTech.	190
Figure II.1.2.13. Plots from simulations with a MAT233+ card compared with Argus scan (left) and an FLD map of a cross-form (right). Source: Vehma and InalTech.....	191
Figure II.1.2.14. Simulations from the MAT233+ compared with FLC for 200 °C. Source: Vehma..	191
Figure II.1.2.15. Comparison of Argus scan to the MAT233+ and crystal plasticity simulations. Source: Vehma and InalTech.	192
Figure II.1.2.16. (a) Warm-formed door outer is a good quality panel. (b) The final forming process parameters. Source: Promatek.....	192
Figure II.1.2.17. (a) Warm-formed door inner is a good quality part. (b) The final forming process parameters. Source: Promatek.....	193
Figure II.1.2.18. (a) A split cross-form part. (b) A split door outer panel. Source: FADI-AMT and Promatek.	193
Figure II.1.3.1. New PAPSC process for manufacturing a cast-Al head. Source: GM.	199
Figure II.1.3.2. New PAPSC process fitted with a gravity fed in-gate for manufacturing a cast-Al head. Water-cooled chill is shown in blue. Source: Eck Industries, Inc.....	200
Figure II.1.3.3. Water-cooled chill: (a) fin-side; and (b) casting side. Wood form resides in the location of the cast-Al block. Source: NETL.....	200
Figure II.1.3.4. Water-cooled deckface chill: (a) combustion chamber/deckface side; and (b) water-cooled, fin-side. Source: NETL.....	200
Figure II.1.3.5. A typical V8 cylinder head (deckface/combustion chamber view). Source: Eck Industries, Inc.....	201

Figure II.1.3.6. An Al plate (21-A15) cast against the water-cooled chill showing the locations of the thermocouples (left) the thermocouple reading (right). Note that the water temperature readings are shown on the right vertical axes with water in Ch7 and water out Ch8. Source: NETL.....	202
Figure II.1.3.7. A more recent Al plate (21-A35) cast against the water-cooled chill. Note the restricted in-gate to minimize aspiration and addition of a successful riser (a). The surface in contact with the chill (b) exhibited what appeared to be flow lines which can be attributed to the liquid flowing across the chill and freezing in place sequentially. The cylinder head should not exhibit this since the liquid will flow up the chill rather than across it. Source: NETL.....	202
Figure II.1.4.1. Mechanical properties derived from tensile tests of AA7075 side impact beams before and after paint-bake treatment. Data from the as-received 7075-T6 sheet is also shown for comparison. Source: PNNL.....	207
Figure II.1.4.2. FEM displacement maps for baseline steel and AA7075 Temper #2 beams along the bending direction of the anvil. (Legend - U: Displacement; U3: Displacement along anvil direction). Source: PNNL.....	207
Figure II.1.4.3. FEM simulated von Mises stress maps of baseline steel and AA7075 side impact beam with end-of-simulation fracture patterns for left, center, and right regions of the beam. (Legend - S, Mises: von Mises stress at the bottom surface of the beam). Source: PNNL.....	207
Figure II.1.5.1. Schematic of the approach used in the project. Source: ORNL.....	211
Figure II.1.5.2. Schematic showing the three characteristics of interest for alloys used in the thixomolding process. Source: ORNL.....	212
Figure II.1.5.3. Schematic showing three characteristics of interest in alloys used in the thixomolding process [5]. Source: ORNL.....	213
Figure II.1.5.4. Schematic showing calculated values for liquidus, solidus, and melting range of several candidate alloys used for screening. Source: ORNL.....	213
Figure II.1.5.5. Photograph of several candidate alloys used for screening. Source: ORNL.....	213
Figure II.1.5.6. Schematic showing calculated values for liquidus, solidus, and melting range of several candidate alloys used for screening. Source: ORNL.....	214
Figure II.1.6.1. LPBF experimental setup at ANL's APS: (a) schematic of experimental setup; and (b) photograph of the experimental setup installed in the APS beamline [1]. Source: ANL.....	217
Figure II.1.6.2. X-ray images from <i>in-situ</i> LPBF experiments with Al-Si-Cu alloy, processed at 520 W laser power and at 800mm/s scan speed: (a) no powder; (b) with powder; and (c) thermal profile from IR data. Source: ANL.....	218
Figure II.1.6.3. X-ray images from <i>in-situ</i> LPBF experiments with AlTi alloy, processed at 520W laser power and at 800mm/s scan speed: (a) no powder; and (b) with powder. Source: ANL.....	219
Figure II.1.6.4. X-ray images of the melt pool and vapor cavity in FeCu alloy processes at 350W laser power and different scan speeds: (a) 300 mm/s; (b) 400mm/s; and (c) 500 mm/s. Source: ANL.....	219
Figure II.1.6.5. EBSD maps of cross-sectioned FeCu scans for: (a) the high scan speed (500 mm/s); and (b) the slow scan speed (300 mm/s). The BD is oriented vertically upward along the page. Source: ANL.....	220

Figure II.1.7.1. Thrust and project structure of the LMCP. Source: PNNL.....	222
Figure II.1.7.2. Schematic B-pillar showing properties needed in different areas of the part. Source: PNNL.	223
Figure II.1.7.3. Three projects with the associated PIs that make-up LMCP Thrust 1. Source: PNNL.	223
Figure II.1.7.4. (a) Multi-alloy extrusions opened into a sheet. (b) The variable properties extrusions opened into a sheet. (c) The variable wall thickness extrusions. Source: PNNL.....	224
Figure II.1.7.5. (a) Butt joints between 6061 and 7075 formed during ShAPE. (b) Cladding formed between 7075/2024 and 6061/1100 during ShAPE. Source: PNNL.....	226
Figure II.1.7.6. (a) Temperature and (b) hardness along the length of a 6061 ShAPE extrusion showing (c) the regions of locally modified properties achieved during ShAPE processing. Source: PNNL.	227
Figure II.1.7.7. (a) Design of system for controlling wall thickness during ShAPE extrusion. (b) Data showing wall thickness transitioning from 2 mm to 1 mm over a length of approximately 6 in. Source: PNNL.....	227
Figure II.1.7.8. Composition-dependent hot cracking index (defined in the inset) in the first deposited layer as a function of dilution of the wire with the 6111 substrate. Multiple points (N=10) at the same dilution reflect an allowance for random variation in the alloy composition within specification in the calculations for (a) Al 4043 and (b) Al 5356 wire. Source: ORNL.....	228
Figure II.1.7.9. Images of the demonstration part with approximate scale bars to show the size of the deposit. (a) IR image from the build process of the part, where coloring represents IR intensity. (b) As-built 4043 wall on a 6061-T6 billet. (c) Partially machined wall showing a hybrid- finished surface versus an as-built surface. Source: ORNL.	229
Figure II.1.7.10. (a) Tensile tests of the vertical 4043/6061-T6 SS-1 sample done at 0.002 s-1 overall strain rate. (b) Strain rate maps, showing strain rate localization as a function of time. Source: ORNL.	229
Figure II.1.7.11. r/t ratios for base alloys and highest formable FSP conditions for each alloy. Red denotes fractured samples, while green denotes samples with no cracks. The red line shows the transition from safe to failed samples. Base 6111-T4 benchmark r/t is 0.55. Source: PNNL.	231
Figure II.1.7.12. Load-displacement plots for 90° and 180° angle bend tests on the base alloy and FSP-processed 7085-T76, 6111-T6, and 5182-H111. Source: PNNL.	231
Figure II.1.7.13. FEM of two-roller bending and unbending sheet with support during entry with its (a) equivalent plastic strain and (b) side profile. (c) The equivalent experimental setup and (d) side view of the processed sheet. Source: ANL.....	232
Figure II.1.7.14. Microhardness distribution across the cross-section of the processed sheet where the minimum (deep blue) = 64.7 HV and the maximum (red) = 95.7 HV. Source: PNNL.	232
Figure II.1.7.15. FEM of three-roller bending and unbending sheet with its (a) equivalent plastic strain and (b) side profile. (c) The equivalent experimental setup and (d) overall view of the processed sheet. Source: PNNL.....	233
Figure II.1.7.16. (a) The Lumonics 702H/pulsed Nd:YAG 1064 nm laser system. (b) The translation stage. Source: ORNL.....	233

Figure II.1.7.17. Examples of local laser-treated AA7075T6 samples. Source: ORNL.....	234
Figure II.1.7.18. Results from tensile tests across the modified region. Source: ORNL.....	234
Figure II.1.7.19. The first set of experiments was performed using a grooved sonotrode tip and a grid patterned-anvil: (a) sonotrode, (b) anvil, (c) and (d) are the sonotrode and anvil sides of the samples processed for 0.3 s. Source: ORNL.....	235
Figure II.1.7.20. (a) Low magnification and (b) high magnification of the cross-sectional EBSD observations of the sonotrode side of the processed sample. Source: ORNL.....	235
Figure II.1.7.21. The second set of experiments was performed using a flat sonotrode tip and a flat patterned-anvil. (a) shows the sonotrode that was used, while (b) and (c) show the processed surfaces on the sonotrode and anvil sides of the sheets, respectively. The results from the (d) IR temperature measurement and (e) cross-sectional EBSD observations are also shown. Source: ORNL.....	236
Figure II.1.7.22. The third set of experiments. (a) The experimental setup. (b) The sonotrode side processed samples with the use of two different values of ultrasonic power. Source: ORNL.....	236
Figure II.1.7.23. Results from VDA-bending simulations with the strength middle section material scaled by a factor of 70%–150% relative to the base material. (a) The model after VDA-bending. (b) The load-t curve. (c) The principle strain contours after the simulations. Source: ORNL.....	237
Figure II.1.8.1. Thrust and project structure of the LMCP. Source: PNNL.....	241
Figure II.1.8.2. Three projects within the LMCP Thrust 2. Source: PNNL.....	242
Figure II.1.8.3. Microstructure of as-received HPDC A380 plate: (a) low magnification overview of the plate; (b) Al-Si eutectic phase at die-wall; (c) Al-Si eutectic phase at mid-wall; and (d) second-phase particulates. Source: PNNL.....	244
Figure II.1.8.4. Summary of tensile properties of FSP processed HPDC A380 material. (a) Location of various miniature specimens within the FSP region; A: AS, M: middle area, R: RS. (b) Representative engineering stress-elongation curves for FSP and HPDC material. (c) Summary of stress-elongation plots. (d) HCF properties of HPDC vs. FSP condition; increased fatigue life observed after FSP. Source: PNNL.....	247
Figure II.1.8.5. Experimental matrix including process conditions and tooling used in the first round of PUSP. Source: PNNL.....	249
Figure II.1.8.6. (a) A specially designed spherical power ultrasonic tool and the processed surfaces at (b) 1 kW for 0.1 s and (c) 2 kw for 0.1 s. Source: ORNL.....	249
Figure II.1.8.7. A micrograph showing uniform refinement of the microstructure on the processed surface using a spherical ultrasonic tool at 2 kW processing conditions. Source: ORNL.....	250
Figure II.1.8.8. PUSP modeling results using a sphere-shaped sonotrode: (a) finite element model; (b) temperature distribution on Al sheet at 0.1 s; (c) vertical displacement showing surface indentation; (d) residual stress in longitudinal direction; and (e) residual stress in transverse direction. Source: ORNL.....	250
Figure II.1.8.9. (a) FEM of A380 microstructure. (b) Distribution of deformation in a very LCF test at the 30th cycle. (c) Initiation of failure at the 45th cycle. The model size is 20 μm \times 20 μm . Source: ORNL.....	251

Figure II.1.8.10. (a) The efficiency of the accelerated fatigue model for HCF. The x and y axes correspond to actual simulated cycles and equivalent simulation cycles, respectively. Stress distribution at 10,000 cycles in an accelerated model solution is shown in (b) and the difference (absolute error, unit: MPa) from the reference solution is shown in (c), respectively. The model size is 20 μm \times 20 μm . Source: ORNL. 252

Figure II.1.8.11. The cooling rates during solidification at the hottest location in the Al casting as a function of the width of the casting for different initial mold temperatures and a mold wall thickness of 0.5 in. Source: PNNL. 253

Figure II.1.8.12. The coarse dendritic microstructure of the specimen cast without ultrasound is depicted in (a) an inverse pole figure (IPF) map, where each grain is identified by a color that corresponds to its crystallographic orientation according to the color scheme in (b). (c) An OM from the same region shown in (a). Source: PNNL. 254

Figure II.1.8.13. Two IPF maps of the specimen cast with ultrasound identify non-dendritic (a) globular grains and (b) very fine grains. The colors correspond to the crystallographic orientation of each grain according to the color scheme in (c). Source: PNNL. 254

Figure II.1.8.14. (a) A schematic of sectioned alloy 4043 wall deposited on an alloy A356.2 ingot. The extracted SS-J3 vertical, horizontal, and interface specimen locations are shown schematically with the labeled outlines. (b) Tensile test results corresponding to marked locations in (a). The lines show the average of all samples, while the bands show a ± 1 standard deviation. Source: ORNL. 255

Figure II.1.8.15. (a) Vickers hardness measurements as a function of height in the sample. The inset shows the location of the measurements. (b) Primary dendrite arm spacing (PDAS) and secondary dendrite arm spacing (SDAS) in the cast A356.2 and as-built AM 4043 as a function of build height. Source: ORNL. 256

Figure II.1.8.16. (a) An OM showing the interface region between cast A356.2 (bottom) and AM 4043 (top). (b) HAZ between layers. The upper dashed line represents the fusion zone of the upper layer, and the bottom dashed line represents the approximate boundary of the HAZ in the previous layer. Images are oriented with the BD upward and the wire travel direction out-of-plane with the page. Source: ORNL. 256

Figure II.1.9.1. Primary thrust areas for Project 3A: Surface Modification for improving Corrosion Properties and Project 3B: Improving Local Thermomechanical Treatments for Improving Mechanical Behavior of Mg Alloys. Source: PNNL. 261

Figure II.1.9.2. Schematic description of (a) laser, (b) plasma, and (c) thermal CO₂ treatments to achieve corrosion-resistant surfaces on AZ91D Mg alloys. Source: ORNL (Project 3A2 Surface Alloying – PNNL). 262

Figure II.1.9.3. (a) An OM image of the HPDC plate with riser, gate, and sample locations marked. (b) The porosity band, (c) the pores in the band, and (d) the SEM-BSE imaging of various phases in the AZ91 alloy (upper images). (e) The porosity band, (f) the pores in the band, and (g) the SEM-BSE imaging of various phases in the AM60. The higher magnification SEM-BSE images in (d) and (g) show the presence of the β phase, the solute segregation, and the Mg-Al matrix. Source: PNNL. 264

Figure II.1.9.4. AZ91D coupon with five linear laser treatments. Cross-sectional electron microscope images are also shown for the respective laser linear intensities. The fusion zone modeling results coupled with the three images were for the linear intensity conditions of 7.5, 2, and 0.75 W-s/mm, respectively. Source: ORNL.	265
Figure II.1.9.5. AZ91D coupons treated with four linear intensities for a 19 × 19 mm ² area. The sample with the 7.5 W-s/mm condition is as-laser-treated, while the other three specimens were surface-finished by 600-grit SiC paper to remove the surface roughness caused by the laser treatments. Source: ORNL.....	265
Figure II.1.9.6. (a) Corrosion reaction resistance of Li preloaded and CO ₂ thermal-treated AZ91D in comparison with the baseline 600-grit-finished AZ91D as a function of immersion time. (b) Hydrogen collection volume from two baseline AZ91D and Li-salt-loaded and CO ₂ -treated AZ91D as a function of immersion time. Source: ORNL.	266
Figure II.1.9.7. (a) XRD intensity spectra from the baseline AZ91D and two-step Li-salt-preloaded and CO ₂ -treated AZ91D samples. All CO ₂ thermal treatments were performed for 3 h at 350 °C. (b) Tilted cross-sectional view and EDS mapping of two-step Li-salt-loaded and CO ₂ -treated AZ91D sample. Li salt-loading was performed by 0.5% and 1% LiNO ₃ solutions in order. Source: ORNL.	267
Figure II.1.9.8. (a) and (b) Cross-sectional microstructure of cold sprayed sample and corresponding TEM-EDS maps of the interface showing MgO and Mg ₁₇ Al ₁₂ layers, and (c) a plot showing their composition of O, Mg, and Al and their respective thicknesses. Source: ORNL.	270
Figure II.1.9.9. (a) Post-SECCM microstructure showing measurement footprints. Measurements were performed from the Mg-side to the Al side with 250 μm step size. (b) Tafel plots correspond to point 1–11. Source: ORNL.	271
Figure II.1.9.10. (a) Cross-section microstructure of reactive Zn melted coating. (b) Post-SECCM microstructure showing measurement locations. Measurements were performed from the Mg side to the Zn side with a 200 μm step size. (c) Tafel plots correspond to points 1–8. Source: ORNL.	271
Figure II.1.9.11. Process parameter optimization for (a) AZ91 and (b) AM60. Tool temperature is plotted as a function of tool rotation speed and traverse rate in AZ91 and AM60. (c) Images of the top surface of the processed region. Source: PNNL.	273
Figure II.1.9.12. Transverse sections of AZ91 processed at (a) 450 °C and (d) 410 °C. Microscopic images of (b) the nugget and (c) the boundary region at 450 °C, and microscopic images of (e) the nugget and (f) the boundary region at 410 °C. Source: PNNL.....	273
Figure II.1.9.13. Summary of (a) hardness and (b) tensile properties of AZ91 for various processing conditions. (c) The fatigue properties of AZ91 for various processing conditions. Source: PNNL.	274
Figure II.1.10.1. (a) STEM images of MgZn ₂ precipitates and Al ₃ Zr precipitates in the Al7085-T78 alloy. (b) An APT analysis revealing the composition of nanoscale intragranular precipitates. (c) A STEM image revealing the reduction in precipitate density after FSP. (d) The APT result of the FSP Al 7085-T78 highlighting the absence of distinct nanoscale intragranular precipitates. Source: PNNL.	279

Figure II.1.10.2. Parallel coordinate plot showing combined modeling results for a range of process parameters. Each horizontal line represents a data point, each vertical axis represents a variable, and the value of the variable for each data point is determined by where it crosses the line. Lines are colored by the SCS. Source: ORNL. 280

Figure II.1.10.3. (a) Snapshot of a multilayer thermal simulation for 25-layer part, showing the heat accumulation in the substrate and deposited material. (b) Extraction of transient temperature history during the 25-layer deposition at the center of the substrate. Source: ORNL.. 280

Figure II.1.10.4. The maximum principal strain contour macroscopic 90°V-bending model of 1-mm-thick AA7075T6 alloy both (a) before and (b) after bending deformation with the bending radius of $r=0.5$ mm ($r/t=0.5$), (c) and (d) are corresponding images for 180° bending with the bending radius of $r=0.2$ mm ($r/t=0.2$). Source: ORNL. 281

Figure II.1.10.5. (a) The optical image of the as-received AA7075-T6 Al alloy after polishing. (b) The combined 90° V-bending simulation results showing images from the micro- and macro-models. (c) The micro-model expanded. (d) An optical image of the V-bending test results for $r/t=0.39$, which showed no surface cracking. (e) The combined image of the micro- and macro-model. (f) The simulation results of the 180°-bending micro-model. Source: ORNL..... 282

Figure II.1.10.6. (a) H₂O molecule adsorption sites on the Mg(0001) surface. (b) H₂O molecule adsorption sites near a substitutional defect on the doped Mg(0001) surface. Orange and gray spheres represent Mg and impure Al, Zn, and Ce atoms, respectively. F, H, T, and B mark the face-centered cubic hollow, hexagonal close pack hollow, and top and bridge sites, respectively. (c) Adsorption energies of a single water molecule on the pure (black circles) and doped Mg(0001) surfaces: Al (red diamonds), Zn (blue squares), and Ce (magenta triangles). Source: PNNL. 283

Figure II.1.10.7. (a) Comparison of the residual stresses from the TPM model with the experimental characterization data from an Al7075 FSP sample. (b) Comparison of the temperatures from finite element analysis and SPH along a line normal to the weld direction. Source: PNNL. 284

Figure II.1.10.8. (a) Two FSP processed Al samples used for residual stress measurement. (b) Three locations selected for the depth profile of residual stresses. (c) Example of through-thickness longitudinal residual stress measurements using hole-drilling and XRD on a 7075 FSP processed sheet. Source: PNNL..... 285

Figure II.1.11.1. (a) A diagram of the ShAPE process. (b) Photo of the 4-scroll die. Source: PNNL. . 289

Figure II.1.11.2. EBSD microstructural characterization: (a) IPF map of an-extruded sample on the surface parallel to the extrusion direction and (b) IPF map of the ShAPE-processed sample on the surface parallel to the ShAPE direction. (c) and (d) (0002) pole figures of EBSD micrographs, as shown in (a) and (b), respectively. Kernel average misorientation (KAM) maps for (e) as-extruded and (f) ShAPE-processed samples. (g) The grain size distribution plot; and (h) the KAM quantitative distribution plot for maps (e) and (f). Source: PNNL..... 291

Figure II.1.11.3. Microstructural characterization of as-cast, as-extruded, and ShAPE-processed AZ31B alloys. (a) SEM image of an as-cast sample. SEM images of (b) perpendicular and (c) parallel surfaces to the extrusion direction of the as-extruded alloy. SEM images of (d) perpendicular and (e) parallel surfaces to the SED of the ShAPE-processed alloy. (f) An elemental spectrum for the second-phase particle. (g) The second-phase particle size and (h) interparticle separation distance distribution for the as-extruded and ShAPE-processed samples on the perpendicular surfaces. Source: PNNL.....	292
Figure II.1.11.4. Tensile and compressive true stress-strain curves for (a) the as-extruded AZ31B vs. ShAPE and (b) the as-cast vs. ShAPE. Source: PNNL.....	292
Figure II.1.11.5. (a) Artificial aging curve. (b) Tensile property of flash-annealed plus T6 aged samples. Source: PNNL.....	294
Figure II.1.11.6. (a) Example of Al-MMC rod made by ShAPE process. (b) An optical observation of the remnant puck. (c) The extruded rod along the longitudinal direction. Source: PNNL.....	295
Figure II.1.11.7. (a) SEM backscatter micrographs of microstructure in the extruded rod of Al6061 matrix with different vol.% of Al ₂ O ₃ particles. (b) Engineering stress-strain curves of the Al6061 MMC by tensile tests. Source: PNNL.....	295
Figure II.2.1.1. (a) The continuous bath line with metal salt solution, (b) untreated nylon 6 fibers (left) and treated Nylon 6 fibers (right), and (c) the tow encased in epoxy immediately following bath draining to capture <i>in-situ</i> tow geometry and for diffusion. Source: University of Virginia.....	301
Figure II.2.1.2. (a) Fibers without adequate uniformity. (b) Fibers with adequate uniformity. Source: University of Virginia.....	301
Figure II.2.1.3. The ML algorithm was capable of predicting the properties of modulus prediction based on key processing parameters such as temperature and duration. Source: University of Virginia.....	302
Figure II.2.1.4. Damage progression of a single fiber with a pore. Source: University of Virginia.....	303
Figure II.2.1.5. Normalized fiber failures with different major and minor ellipsoid diameters. Source: University of Virginia.....	303
Figure II.2.1.6. Results of nano-additive precursors showing significant increase in elastic modulus in the nano-additive samples (MSB3, MSB4) compared to the neat baseline sample (MSB1). Source: University of Virginia.....	304
Figure II.2.2.1. Organization for the Consortium for Production of Affordable CFs in the U.S. Source: WRI.....	310
Figure II.2.2.2. A diagram showing the high-level approach to integrate the models at different size scales using NNs. Source: University of Wyoming.....	311
Figure II.2.2.3. A diagram showing the modeling efforts that were performed and integrated during this study. The molecules shown for the feedstock are representative for petroleum pitch. Source: Western Research Institute.....	311
Figure II.2.2.4. The top shows select PP molecules relative to LDI spectra and the bottom shows hypothetical PM molecules relative to LDI based on [2], [3], [4], and [5]. The inset box in the top depicts actual molecular structures identified in PP using imaging techniques described in [3]. Source: Western Research Institute.....	313

Figure II.2.2.5. Blue triangles show the relationship between density and elastic modulus produced by the models. Theoretical maximum in density for sp ² graphite is around 2.27 g/cm ³ (yellow dashed line). For the model to move towards higher densities additional sp ³ bonding must occur. The black squares are experimental data from graphitized CF. Red triangles show updated modeling for graphitized CF. Source: Massachusetts Institute of Technology.	314
Figure II.2.2.6. Evolution of the CG PAN-based CF in relation to synthesis parameters (input), chemical and structural parameters of intermediate compounds, and the final CF. Source: Massachusetts Institute of Technology.	315
Figure II.2.2.7. Correlative analysis between processing parameters and structural, chemical, and elastic characteristics of PAN-based fibers. Source: Massachusetts Institute of Technology. ..	315
Figure II.2.3.1. Inner frame CAD modification at three locations (1,2,3). Source: Clemson University.	319
Figure II.2.3.2. Design change of anti-intrusion beam hinge side bracket and lower reinforcement. Source: Clemson University.	320
Figure II.2.3.3. Overview of final CAD for structural and aesthetic components. Source: Clemson University.	320
Figure II.2.3.4. Normalize force-displacement plot of baseline and composite door under the QSP test. Source: Clemson University.	322
Figure II.2.3.5. (a) Thermal chamber equipped with a thermocouple data acquisition system; and (b) liquid nitrogen cooling for thermoforming tests and thermoforming setup showing Cu cooling channels and thermocouple location. Source: Clemson University.	324
Figure II.2.3.6. Thickness variation in the hat structure of: (a) Side 1; and (b) Side 2, which are represented as average thickness ± standard deviation. Predicted thickness from simulation measured for the three experimental forming trials. Source: Clemson University.	324
Figure II.2.3.7. Fiber orientation in degree as observed in thermoforming trials and simulation at marked locations of the hat structure. Source: Clemson University.	325
Figure II.2.3.8. (a) Dimensions of the bonded hat section part; and (b) the experimental setup for the three-point bend test showing the hat structure, supports, and punch. Source: Clemson University.	325
Figure II.2.3.9. (a) Force-displacement plot of three experimental trials. (b) Force-displacement plot for the three-point bend test comparing experimental response with numerical prediction. Source: Clemson University.	326
Figure II.2.3.10. Deformation comparison between the experimental trials and the numerical simulations: (a) deformation side view showing a close match with experimental trial 3; and (b) top view comparison with stress contour plot. Encircled are the damage initiation locations on the structure. Source: University of Delaware.	326
Figure II.2.3.11. (a) Inner beltline stiffener blank strategy; and (b) the blank size (1240 × 860) obtained from the supplier. Source: Clemson University.	327
Figure II.2.3.12. (a) Initial tool concept of the inner beltline stiffener. (b) Thermoforming simulation of the inner beltline stiffener. (c) Before forming. (d) Cavity driver touch lower tool. (e) Tool closed condition. Source: Clemson University.	328

Figure II.2.3.13. Blank strategy for inner frame. Source: Clemson University.....	329
Figure II.2.3.14. (a) Initial tool concept of inner beltline stiffener. (b) Thermoforming simulation of inner beltline stiffener. (c) Before forming. (d) Cavity driver touch lower tool. (e) Tool closed condition. Source: Clemson University.	329
Figure II.2.3.15. Cost distribution of the individual parts of the door. Source: Clemson University..	330
Figure II.2.3.16. Normal distribution of total cost of door. Source: Clemson University.	331
Figure II.2.4.1. A set of conventional LTC and HTC furnaces of the existing pilot line from ORNL. This set of furnaces was refurbished prior to its relocation at 4XTechnologies. Laboratory space has been altered and ancillary equipment installed to make this system operational. (NOTE: Portions of this photograph have been covered due to export control requirements.) Source: ORNL.	337
Figure II.2.4.2. Density measurements of seven tows processed with “CPEC-4 Configuration #2” with several residence times of process. The density of 1.76 g/cc can be achieved with this device with long residence times (economically unrealistic). Source: ORNL.....	338
Figure II.2.4.3. Full carbonization test where the performance of the existing EM process operating at 100% of its available power is compared with a modified conventional process. During this test, the EM LTC setup was tested with seven tows (only mechanical properties of tows A, D, and E are reported), whereas the conventional process was limited to a single tow by design (series “Conventional”). Tension per tow in both systems is comparable. Several residence times were tested. The mechanical properties of the OPF feedstock material are indicated at time = 0. Over the time span investigated, the EM process underperforms the altered conventional process. At short residence times, due to technical reasons, no data is available with the conventional process. At long residence time, none of these two processes is economically viable. Source: ORNL.	338
Figure II.2.4.4. Theoretical values of $S_{1,1}$, the coefficient of reflection. The green frame represents the band of operation of the generator system. The CEM modeling allows parametric studies. This figure shows a parametric study where a minimum of reflection goes lower while shifting to lower frequencies. In this configuration, $S_{1,1}$ can reach -17.5 dB while being relatively broad and remaining in the band of interest. Source: ORNL.	339
Figure II.2.4.5. Calculated S_{11} parameter values of the future reactor across a frequency spectrum at a point where the material becomes conductive. Each curve represents the calculation of the S_{11} parameter for a given position of the tuning system of the cavity. This figure shows that it will be still possible to find bands of low reflection in the band of operation (green frame) of the generator system until the end of the process. Source: ORNL.	339
Figure II.2.4.6. Pattern prediction of energy deposition on a ribbon of 4 tows of 50k filaments each. Propagation of the tows is along u, width along v, and thickness along w axes. Image generated by CEM modeling. Source: ORNL.	340
Figure II.2.5.1. Dynamic test data comparing Mallinda CF material with commercial GMT. Source: ORNL.	344
Figure II.2.5.2. Dynamic compressive stress-strain curves of unidirectional composite for (a) in-plane and (b) out-of-plane. Source: SNL.	345
Figure II.2.5.3. Effect of impact velocity (strain rate) on flexural modulus. Source: SNL.....	345

Figure II.2.5.4. Entropy images of all three specimens in this study. <i>Hf, g</i> images for specimens (a) SB01, (b) SB02, and (c) SB03. Source: SNL.	346
Figure II.2.5.5. A joint signal energy image of all three specimens in this study. <i>Hf, g</i> images for specimens (a) SB01, (b) SB02, and (c) SB03. Source: ORNL.	347
Figure II.2.6.1. (a) Optical path diagram of the infinity-corrected projection system. (b) Segmentation of a single projection image. (c) A schematic of the large-area high-resolution projection stereolithography system. (d) The current optical system with adjustable projection area/resolution. Source: ORNL.	351
Figure II.2.6.2. (a) Plate-lattices having a range of relative densities. (b) A stress-strain curve of the plate-lattices with different relative densities. (c) A comparison of the stiffness between plate-lattices and truss lattices. Source: ORNL.	351
Figure II.2.6.3. Design, fabrication, and evaluation of bi-material isotropic cubic+octet plate-lattice. (a) Each plate is designed as a sandwich plate (CFRP-soft-CFRP). (b) Post thermal curing fused the soft-stiff phase. The unit cell has a relative density of 30% after injection. (c) The absorbed energy, U , under compression of bi-material isotropic cubic+octet plate-lattices having different volume fractions of the soft phase for several relative densities. (d) Assessment of energy absorption performance against previously reported materials. Source: ORNL.	352
Figure II.2.6.4. (a) Schematic of the multi-material exchanging system, cleaning system, and resin recycling system. (b) The overall system setup. (c) Ram extruder and custom extrusion nozzles with multiple outlets. (d) A large antenna array made of two different resins and copper was deposited onto the charged resin. Source: ORNL.	353
Figure II.2.6.5. (a) Hierarchical CFRP truss-lattice materials ($l = 18$ cm, strut radius of $150 \mu\text{m}$). (b) CFRP plate-lattice materials ($l = 10$ cm). Source: ORNL.	354
Figure II.2.6.6. (a) Demonstration of the high-strength of the cubic+octet plate-lattice ($4 \times 4 \times 2$). The lattice weighs only 20 g, and it can withstand the weight of an adult. The schematic below shows the unit cell design of such a group of plate-lattice. (b) Simulated compressive stress-strain curves of the cubic+octet plate-lattices for different relative densities, $\rho = 10\%$, 20% , and 30% . (c) UCS and specific strength of the plate-lattices (The data points correspond to the simulated cases with different relative densities). Source: ORNL.	355
Figure II.2.7.1. CF manufacturing process and cost analysis. Source: ORNL.	358
Figure II.2.7.2. Embodied energy for PAN and coal pitch precursor and CF manufacturing. Source: ORNL.	360
Figure II.2.7.3. Multiscale R&D approach. Source: ORNL.	361
Figure II.2.7.4. Pitch-based precursor processed through the CFTF CF line. Source: ORNL.	362
Figure II.2.7.5. Melt-spun petroleum mesophase pitch fibers of different diameters. Source: ORNL.	363
Figure II.2.7.6. (a) DSC analysis of the commercial Polyamide 6 sample. (b) Isotherms in nitrogen at different temperatures (TGA). (c) Rotational shear rheology temperature sweeps of Polyamide 6 material. Source: ORNL.	364
Figure II.2.7.7. Melt-spun Polyamide 6 fibers using a single-single filament and a multi-filament extruder. At the laboratory-scale and a multi-filament extruder at CFTF scale. Source: ORNL.	365

Figure II.2.7.8. Microscopy Images and measurement of the fiber diameter at the laboratory and CFTF scale. Source: ORNL.	366
Figure II.2.7.9. Single fiber mechanical test results. Source: ORNL.....	366
Figure II.2.7.10. CF produced with the OPF at CFTF. Source: ORNL.	367
Figure II.2.7.11. (a) Thermogravimetric analysis of silicon carbide precursor polymers in nitrogen (10° C/min), (b) DSC profile of silicon carbide precursor polymers on heating (10° C/min). Source: ORNL.	367
Figure II.2.7.12. Single fiber mechanical test results. Source: ORNL.	369
Figure II.2.9.1. SEM images of TiO ₂ on CF after a dip-coating process with mixtures containing: (a) 0 wt.%; (b) 1 wt.%; (c) 2 wt.%; (d) 3 wt.%; and (e) 4 wt.% TiO ₂ nanoparticles [2]. Source: ORNL.	378
Figure II.2.9.2. Results of the interlaminar shear strength testing showing: (a) the representative strength vs. strain curves; and (b) the average strength values versus the nanoparticle concentration in the coating mixture. The error bars signify one standard deviation [2]. Source: ORNL.	378
Figure II.2.9.3. (a) Electroded sample schematic in which the CFs run in the x-direction and the thickness is in the y-direction. (b) An overlay of the different strains placed on the composite beam. (c) Representative curves of the electrical resistance in response to the different strain cycles. (d) Overlap of a representative input strain and the electrical resistance response [2]. Source: ORNL.	379
Figure II.2.9.4. (a) Relative resistance change versus percent strain. (b) Gauge factor for each composite averaged over all the strain levels tested. Error bars signify one standard deviation [2]. Source: ORNL.	380
Figure II.2.9.5. Plot of the different composites showing the average interlaminar shear strength versus the average gauge factor. The dashed lines show the values for the composite without nanoparticles with the highlighted region signifying simultaneous improvements in both properties [2]. Source: ORNL.	380
Figure II.2.9.6. Schematic design of the fan blade assembly prototype where the multifunctional composites will be integrated. Source: Dronesat.	381
Figure II.2.9.7. (a) Schematic of the hybrid multifunctional composite. (b) Picture of the flexing test method with c) the corresponding voltage output from the composite. Source: ORNL.....	381
Figure II.2.10.1. Showing prepared compression samples with linear strain gauges, compression testing using CLC fixture, and through-thickness failure mode. Source: ORNL.....	385
Figure II.2.10.2. Mesh and static analysis results of cornering fatigue showing stiffness of 400 kN-m/rad. Source: ESE.....	386
Figure II.2.10.3. Curb impact analysis of the composite wheel without the tire. Source: ESE.....	386
Figure II.2.10.4. Radial (pothole) impact analysis of the composite wheel with the tire. Source: ESE.	386
Figure II.2.10.5. Iosipescu samples strain gauged and ready for testing. Source: ORNL.....	387

Figure II.2.11.1. An innovative approach for seatback manufacturing that integrates adaptive lattice structure generation, AM preform with controlled deposition direction, and overmolding on metal inserts. Source: ORNL. 389

Figure II.2.11.2. Design developed in a previous FY involving a novel hybrid manufacturing process using overmolding of polymer AM onto metal AM. Source: ORNL..... 390

Figure II.2.11.3. Design of several metal AM parts. (a) Meshes with different unit cell sizes. (b) Meshes for tensile tests. Source: ORNL. 391

Figure II.2.11.4. Experimental shear test setup and the apparatus of manufacturing shear test samples. Source: ORNL. 391

Figure II.2.11.5. (a) Metal mesh AM using (b) a metal powder laser AM system (AddUp) with the LFT. Source: ORNL. 391

Figure II.2.11.6. Overmolding process (a) AM metal mesh; (b) AM LFT preform on top of the AM metal mesh; and (c) compression overmolding. Source: ORNL..... 392

Figure II.2.11.7. Optimization process for the molding parameters. (a) Excess pressures and temperatures. (b) Good consolidation; however, excess materials flash. Source: ORNL. 392

Figure II.2.11.8. (a) Cross-section for the 4-mm depth overmolded sample showing good material penetration into the mesh. (b) Cross-section of a 13-mm depth mesh with poorly penetrated polymer on the back side. Source: ORNL. 393

Figure II.2.11.9. AM preform made of long carbon fiber-reinforced PA66 (356-mm × 356-mm). Source: ORNL. 393

Figure II.2.11.10. Preliminary design of a seatback with the new optimized subpart for hybrid manufacturing technologies. Source: ORNL. 394

Figure II.2.12.1. Project task breakdown. Source: Ford..... 396

Figure II.2.12.2. Instrument panel XCB system to be adapted to accommodate the new multifunctional XCB structure. Source: Ford..... 397

Figure II.2.12.3. CAD rendering of a representative instrument panel structure highlighting surrounding system hardware. Source: Ford. 398

Figure II.2.12.4. (a) CAE design and (b) analysis of instrument panel XCB. Source: Ford..... 399

Figure II.2.12.5. Design sections proposed for the WAIM and sensor placement. Source: Ford..... 400

Figure II.2.12.6. Input data screen for XCB technoeconomic analysis model. Source: Purdue. 401

Figure II.2.12.7. Electrical conductivity results for conductive filler materials. Source: Ford..... 402

Figure II.2.12.8. Electrical conductivity measurements of candidate fillers compounded in PA66. Source: Ford. 402

Figure II.2.12.9. Mechanical testing results for the reinforcement materials. Source: Ford..... 403

Figure II.2.12.10. Conductive materials mechanical testing results. Source: Ford. 403

Figure II.2.12.11. Thermal conductivity results for conductive materials. Source: Ford. 403

Figure II.2.12.12. Technology demonstrator mold for (a) the moving half and (b) the fixed half. Source: Ford. 404

Figure II.2.12.13. Technology demonstrator components. (a) Transition features on both ends of the part that manage the water injection and coring out of the part during processing. (b) A part that has been cut down the length of the component revealing the hollow cavity. (c) A batch of 30 parts produced as a part of the process capability study. Source: Ford.	405
Figure II.2.12.14. Thermoplastic prepreg tapes produced for continuous tow development. Source: Ford.	406
Figure II.2.12.15. Integrated functionality in continuous tow reinforcements. Source: Ford.	406
Figure II.2.12.16. Screen printed silver ink and poly (ethylenedioxythiophene) on a polyethylene terephthalate (PET) substrate behind 15 wt.% GF/PA6. Source: Ford.....	407
Figure II.2.12.17. Design volume and key load cases for the XCB structure. Source: Ford.	408
Figure II.2.12.18. 3D printed meshes produced for injection overmolding. Source: Ford.....	408
Figure II.2.12.19. W tool for sub-scale tow retention prove-out. Source: Yanfeng.....	409
Figure II.2.12.20. Fixture to conduct preliminary end-effector capability studies. Source: Yanfeng.	410
Figure II.2.12.21. Fixture to conduct preliminary end-effector capability studies. Source: Yanfeng.	411
Figure II.2.12.22. Data recording for a standard injection molding cycle. Source: Yanfeng.	412
Figure II.2.13.1. Hybridization of fiber commingling in (a) a tow, (b) a layer, and (c) a laminate. Source: GM.....	416
Figure II.2.13.2. Stress versus strain measured for glass, carbon, and Hexion material systems considered in the study. Source: GM.....	418
Figure II.2.13.3. Radar chart of performance/SPG for various other metrics. Source: GM.....	419
Figure II.2.13.4. Radar chart of performance/cost for various other variables. Source: GM.....	419
Figure II.2.13.5. Bias-extension results of various preform materials. Source: GM.....	420
Figure II.2.13.6. Bias-extension results with various backing materials through final downselection. Source: GM.....	420
Figure II.2.13.7. Hybrid Lattice™ preform with thermocouple wire (yellow) taped into place. Source: GM.....	421
Figure II.2.13.8. Temperature versus time data for one experiment. Source: Michigan State University.	421
Figure II.2.13.9. (a) Molding tool and (b) instrumentation setup. Source: Michigan State University.	422
Figure II.2.13.10. Flow front progression for molded panels with different amounts of injected resin. Source: Michigan State University.....	422
Figure II.2.13.11. Process repeatability and dimensional checks for a 200 g injected at 50 g/sec. Source: Michigan State University.	423
Figure II.2.13.12. (a) In-tool pressure signature summary at the middle of two samples from a 200 g injection at 50 g/sec with no patch. (b) Images of Sample 1 (top) and Sample 2 (bottom). Source: Michigan State University.	423

Figure II.2.13.13. Molding experiment target parameters with accidental addition of a patch. Source: Michigan State University.	424
Figure II.2.13.14. Results of flow rate reductions on dry spot area. Source: Michigan State University.	424
Figure II.2.13.15. FEM representation of the plaque (mesh size 2.5 mm). Source: Michigan State University.	425
Figure II.2.13.16. Pressure as function of time at the middle sensor. Source: Michigan State University.	426
Figure II.2.13.17. Multiscale model development. Source: Michigan State University.	427
Figure II.2.13.18. Description of the meso-scale model developed for the tensile load case. Source: Michigan State University.	427
Figure II.2.13.19. Force vs. displacement for the hybrid composite subjected to tensile load case. Source: Michigan State University.	428
Figure II.2.13.20. Description of the meso-scale model developed for the flexural load case. Source: Michigan State University.	428
Figure II.2.13.21. Force vs. displacement plot for the hybrid composite subjected to flexural load. Source: Michigan State University.	429
Figure II.2.13.22. Unit cell model for CF/GF hybrid composites (showing fiber tows). Source: Michigan State University.	429
Figure II.2.13.23. Different load cases studied with the unit cell analysis. Source: Michigan State University.	430
Figure II.2.13.24. Force vs. displacement for the three load cases in the RVE analysis. Source: Michigan State University.	430
Figure II.2.13.25. Plot of resistance versus strain in the composite. Source: Michigan State University.	431
Figure II.2.13.26. Plot of resistance versus strain in the composite wire and CF tow. Source: Michigan State University.	431
Figure II.2.13.27. Difference between temperature measured using surface-mounted and embedded thermal sensor. Source: Michigan State University.	432
Figure II.2.13.28. Predicting PDF of Poisson ratio conditioned on experimental observations of moduli, energy, maximum force, and displacement. Source: Michigan State University.	433
Figure II.2.13.29. Predicting PDF of tensile strain at failure (input to LS-DYNA) conditioned on experimental observations of moduli, maximum force, and displacement. Source: Michigan State University.	434
Figure II.2.14.1. Surface energy of PP fiber treated by low power oxygen plasma at varying durations. Source: PNNL.	438
Figure II.2.14.2. (a) Nominal IFSS vs. embedded length for untreated (black) vs. treated (red) PP fiber in a HDPE matrix. (b) Untreated PP fiber. (c) Plasma-treated PP fiber pulled out from HDPE matrix. Source: PNNL.	439

Figure II.2.14.3. A summary of tensile data on panels fabricated by film stacking method with untreated fibers. Source: PNNL.	440
Figure II.2.14.4. UHMWPE solution/gel preparation, fiber spinning, and hot drawing process. Source: ORNL.	441
Figure II.2.14.5. (a) A picture of the UHMWPE fiber being tensile tested. (b) The stress-strain curve monitored at the strain rate of 20 mm/min. The Young's modulus was determined at 0.2% strain. Source: ORNL.....	442
Figure II.2.15.1. DMA properties in a frequency sweep for (a) Xenoy and (b) TPU and CF/ABS blends (90/10 blends and 80/20 blends). Source: ORNL.	445
Figure II.2.15.2. Moduli of ABS/CF/TPU blend materials. Circle data are from the experiments. Source: ORNL.	446
Figure II.2.15.3. Deformation–force curves during loading bumpers made of the blend material and Xenoy. The bumper with the blend material is slightly (~11%) stiffer than the bumper with Xenoy. Source: ORNL.	446
Figure II.2.15.4. Bumper subcomponent printed with property optimized material combinations. The image of the 3D printed bumper was blurred due to proprietary info of Ford's design. Source: ORNL.	447
Figure II.2.15.5. (a) Load cases and deflection requirement for a door arm rest. (b) Stress distribution via FEA. (c)Topology optimization with 30% volume fraction target. (d) Final shell design. Source: ORNL.	447
Figure II.2.15.6. Performance simulation of the optimized design. The maximum deflection for the given load cases (6.8 mm) satisfies the requirement (<15 mm). Source: ORNL.	448
Figure II.2.15.7. Simulation workflow for lattice crush using FEA. Source: ORNL.	448
Figure II.2.15.8. Crush simulation on six different lattice orientations and comparison with experiments. Source: ORNL.	449
Figure II.2.15.9. Compressive responses with various cell wall thicknesses. (a) Honeycomb ($\theta=30^\circ$) lattice with CF/ABS/TPU blends. (b) Honeycomb ($\theta=30^\circ$) lattices with Formlab Tough. (c) Honeycomb ($\theta=30^\circ$) lattices with TMPTA. (d) Isogrid ($\theta=-30^\circ$) lattice. (e)–(f) Box Infill ($\theta=0^\circ$) lattice with CF/ABS/TPU blends. Source: ORNL.	449
Figure II.2.16.1. Schematic of an AM-CNG storage vessel concept. (a) External rigid structural layers of the vessel: load bearing resin filaments (blue) filled with short and continuous CF (white). (b) Continuous filament material is applied to the midbody yielding maximum hoop strength. (c) Short-fiber extrusion used to fabricate complex end caps. (b) and (c) Flexible and cross-linkable polymer compositions reinforced with nanoplatelets will be printed to serve as the inner layers of a vessel (yellow and blue layers represent the inner gas barrier and transition to structural layers respectively). Source: LLNL.	452
Figure II.2.16.2. Project schedule. Source: LLNL.....	453

Figure II.2.16.3. Rotational rheometry of a range of base and modified resins. The ‘Hexon EPON’ and ‘SWE2.0’ are unmodified epoxy and cyanate ester bases respectively. ‘MAW 0.5–1.5’ are 0.5 wt.%–1.5 wt.% dispersions of GO in cyanate ester. Note that the DIW modified GO resins have a clear thixotropic response with a shear-thinning profile at higher shear rates. Note that ‘SWE’ and ‘MAW’ are notebook tracking names for test formulations based in the initials of the researchers who produced the samples Source: LLNL.....	454
Figure II.2.16.4. Experimental shear test setup and the apparatus of manufacturing shear test samples. Source: ORNL.....	454
Figure II.2.16.5. Tensile stress vs. STF of DIW cyanate ester resins modified with up to 30 wt.% nanofibers. Source: LLNL.....	455
Figure II.2.16.6. Overmolding process (a) AM metal mesh; (b) AM LFT preform on top of the AM metal mesh; and (c) compression overmolding. Source: ORNL.....	456
Figure II.2.17.1. Schematic of fiber modification showing surface silanization followed by crosslinking with epoxy. Source: ORNL.....	460
Figure II.2.17.2. Schematic of the data-driven ML model used to precisely predict the interface adhesion properties and identify imperfections along interfaces from FEA. The modeling and actual data are compared for the separation and displacement on a test composite strip. Source: ORNL.....	461
Figure II.2.17.3. (a) SEM images of chopped CFs and their incorporation into the epoxy matrix. (b) A strength of 207 MPa and a Young’s modulus of 2.88 GPa were achieved. The printing and layering method is prepared over several coats of the materials. Failure mechanism can be attributed to a slip-disk model. Source: ORNL.....	462
Figure II.2.17.4. (a) 3D printing of epoxy and chopped CF was demonstrated for the ability to scale-up the process. EPON 826, EPIKURE 3140, EPIKURE W, and silica nanoparticles were added with the CF. (b) Loading of CF at 40 wt.% gave a tensile strength of 73 MPa and a modulus at 2.8 GPa, but elongation decreased to 3%. The toughness is maximized at 20 wt.%. These results were obtained for multi-material 3D printing with CF mat prepreg sheets. Source: ORNL.....	463
Figure II.2.17.5. (a) Process for 3D printing inks for embedded sensors. (b) Fabrication of Zn-anode based with carbon black particle additives and PVDF. (c) SEM and fluorescence spectroscopy imaging of the composite. Full characterization by electrochemical methods: (d) high reaction kinetics with increasing surface area; (e) no significant difference in series resistance; Zn-plate with high charge transfer resistance; (f) high specific capacity of 650 mAh/g at 0.2 A/g C-rate; and (g) stable and high-capacity 3D anode maintained in the long-term stability test. Source: ORNL.....	465
Figure II.2.18.1. Mechanical properties of ORNL vitrimer. (a) Tensile stress-strain curves; three different weight ratios of A to epoxy resins: 1:2 (pink), 1:1 (blue) and 2:1 (red). (b) Summarized tensile strength and strain values [1]. Source: ORNL.....	469
Figure II.2.18.2. Dynamic properties: (a) storage modulus, (b) tan delta versus temperatures, (c) normalized relaxation modulus of the dynamic epoxy and the ORNL vitrimer networks at 160 °C, (d) linear Arrhenius behavior of the dynamic epoxy and the dynamic ORNL vitrimer networks [1]. Source: ORNL.....	470

- Figure II.2.18.3. Reprocessing by hot-pressing. (a) Traditional epoxy samples with cross-linked unexchangeable bonds were processed in a hot press at 200 °C and 500 psi for 5 minutes, resulting in broken pieces. (b) Dynamic epoxy specimens were processed at the same hot-pressing conditions as traditional epoxy and formed a compact film. (c) ORNL vitrimer pristine samples were hot-pressed at 160 °C and 100 psi for 1 minute to obtain a recycled compact film. The ORNL vitrimer film was easily cut to dumbbell-shaped specimens. (d) Summarized tensile strength values of reprocessed dynamic epoxy (red) and ORNL vitrimer samples (green) [1]. Source: ORNL 470
- Figure II.2.18.4. Thermoformation of cured composite laminate. (a) Three individual CF fabric composite sheets with the ORNL vitrimer. (b) After being hot-pressed at 160 °C and 500 psi for 1 minute to obtain a compact multilayered composite sheet. Reshaping the multilayered film under hot-pressing: (c) bottom view and (d) top view of multilayered composite sheet [1]. Source: ORNL 471
- Figure II.2.18.5. Mechanical properties of the unidirectional CFRPs. Representative stress-strain curves obtained from (a) the short-beam shear and (b) flexural tests for pristine and repaired samples of epoxy composite, dynamic epoxy and ORNL vitrimer composites [1]. Source: ORNL. ... 472
- Figure II.2.19.1. Representative photographs of (a) the continuous CF tow processing system and (b) the spooled thermoplastic tow-preg. Source: ORNL..... 475
- Figure II.2.19.2. (a) Representative stress-strain plots of the prepared tow-pregs. (b) TGA thermograms, showing 12 wt.% to 17 wt.% CF loading in composites. Source: ORNL..... 475
- Figure II.2.19.3. Electron micrograph of (a)-(b) pristine, (c)-(d) mild treated, and (e)-(f) excessively treated CF surfaces. Source: ORNL. 476
- Figure II.2.19.4. Tensile stress-strain profile of composites from unsized discontinuous filaments from heavy-tow CF. Treated fiber composite specimens (red) are stronger and tougher than the control composite specimens (blue). Source: ORNL. 476
- Figure II.2.19.5. Plot showing crystallization half-time vs. crystallization temperature, suggesting crystallization rates become faster with increasing fiber loadings for all temperature ranges studied. Source: ORNL..... 477
- Figure II.2.19.6. Wide-angle X-ray diffractograms of PP and CF composites. Source: ORNL. 477
- Figure II.2.19.7. POM images showing (a) spherulitic crystal growth in neat PP and (b) fiber surface with transcrystallinity due to an abundance of nucleation sites, leading to restricted crystal growth around fiber. Source: ORNL. 478
- Figure II.2.19.8. Schematic of the fabrication process for multilayered composite structures: (a) the hot-pressing process for fabricating the multilayered CF-PP composite and (b) an SEM micrograph of the CF-PP microstructure. Source: ORNL. 479
- Figure II.2.20.1. Diagram of 3D printing equipment for CCF composites: Source: SRNL..... 482
- Figure II.2.20.2. (a) 2D rendering of the top and side build path and slicing diagrams of dog bones and (b) CCF 3D-printed dog bone. Source: SRNL 482
- Figure II.2.20.3. Microwave annealing of chopped CF dog bones shows enhancement of tensile properties after five minutes of irradiation at constant power. Source: SRNL. 483

Figure II.2.20.4. (a) Tensile strength measurements and (b) heat transfer measurements for 3D-printed CCF composite dog bone samples showing the effect of EM annealing (inset) forward-looking infrared (FLIR) camera images of 3D-printed CCF composite samples on a hotplate set to 200°C. Source: ORNL.....	484
Figure II.2.20.5. (a) Metal mesh AM using (b) a metal powder laser AM system (AddUp) with the LFT. Source: ORNL.	484
Figure II.2.20.6. (a) Voltage response of the thermocouple to temperature where the thermocouples and strain gauge were consecutively printed on a 3D-printed three-point bend bar. (b) Change in resistance as a function of bend angle in a silver three-point bend apparatus with a printed strain gauge. Source: Clemson University.....	487
Figure II.2.21.1. SEM images of (a) as-received basalt (with commercial sizing) and (b) BF coated with BaTiO ₃ particles using the 2 wt.% BaTiO ₃ coating bath [2]. Source: ORNL.....	490
Figure II.2.21.2. (a) Representative stress versus strain plots for selected composites. (b) The average apparent interlaminar shear strength for each composite [2]. Source: ORNL.....	491
Figure II.2.21.3. (a) Schematic of the composite layering. (b) Schematic of the composite electroding scheme. Pictures of the (c) sensing setup configuration and (d) energy-harvesting setup [2]. Source: ORNL.	492
Figure II.2.21.4. (a) The voltage generated from the composite in the sensing setup under three different input accelerations. (b) The voltage and power generated from the composite in the energy-harvesting setup from 0.7 g of acceleration [2]. Source: ORNL.....	492
Figure II.2.21.5. (a) The loss tangent from the dynamic mechanical analyzer testing of the 0.0 wt.% and 0.5 wt.% BaTiO ₃ samples as a function of temperature. (b) Representative stress versus strain curves for the 0.0 wt.% and 0.5 wt.% BaTiO ₃ chopped fiber samples. Source: ORNL.	493
Figure II.2.22.1. Direct depolymerization of PET waste and concerted repolymerization. Source: PNNL.	496
Figure II.2.22.2. Direct polycondensation of TPA and aromatic amines. Source: PNNL.....	497
Figure II.2.22.3. Representative example of aramid polymer synthesis from TPA (Kevlar is illustrated herein). Source: PNNL.....	497
Figure II.2.22.4. Structures of various amines employed in the synthesis of polymers P1–P15. Source: PNNL.	497
Figure II.2.22.5. Stacked ¹ H NMRs of polymers P1–P4 and P11. Source: PNNL.	499
Figure II.2.22.6. TGA plots of polymers P1–P4 and P11. Source: PNNL.	499
Figure II.2.23.1. Project overview. Source: NREL.	502
Figure II.2.23.2. Design developed in a previous FY involving a novel hybrid manufacturing process using overmolding of polymer AM onto metal AM. Source: NREL.....	503
Figure II.2.23.3. DMA of (a) an industry-relevant epoxy–amine CFRC and (b) the bio-derivable PE-CAN. Source: NREL.	503
Figure II.2.23.4. The depolymerization, wash, and repolymerization process was repeated for a total of three material generations. (a) The fiber alignment in various depolymerization techniques. (b) TGA results, demonstrating the removal of resin. Source: NREL.	505

Figure II.2.23.5. Results of the depolymerization, wash, and repolymerization process for (a) Generation I ($E'=28.7$ GPa); (b) Generation II ($E'=32.3$ GPa); and (c) Generation III ($E'=30.1$ GPa). Source: NREL.	506
Figure II.3.1.1. Variations of shear-stress and stacking fault energy as a function of engineer strain for fcc Al in (a) and (b) and for bcc Fe in (c) and (d), where the red symbols representing ISS (τ_{IS}) and USFE (γ_{US}). Source: Penn State University.....	509
Figure II.3.1.2. (a) Correlation between the DFT-predicted USFE (γ_{US}) and ISS (τ_{IS}) with the linear fit R^2 score = 0.78. (b) Correlation between the DFT-predicted vacancy activation energy VaQ and the experimental measured Brinell hardness HB with a linear fit R^2 score = 0.79. Source: Penn State University.....	510
Figure II.3.1.3. Calculation of material properties using atomic-level predicted ISS and USFE. Source: Penn State University.....	510
Figure II.3.1.4. Response surfaces for material losses over different input parameters: (a) pH and crevice gap; (b) conductivity and crevice gap; and (c) pH and conductivity. Source: University of Illinois Urbana Champaign.	512
Figure II.3.1.5. The integration of the atomic-phase and meso-scale predictions in FEM of a lap- shear test. Source: University of Michigan.....	512
Figure II.3.1.6. S-N charts of the nominal stress range versus failure life for non-corroded and corroded samples: (a) RSW and (b) SPR. Source: University of Michigan.	514
Figure II.3.1.7. S-N chart correlation for (a) the nominal stress, (b) the structural stress without considering corrosion effects, and (c) the structural stress considering corrosion effects. Source: University of Michigan.....	515
Figure II.3.1.8. Illustration of Mode A and Mode B fatigue failure modes. Source: University of Michigan.....	516
Figure II.3.1.9. Degradation of the fatigue resistance illustrated through fitted curves of the nominal stress range versus fatigue life for (a) RSW and (b) SPR. Source: University of Michigan..	516
Figure II.3.1.10. Failure characteristics of SPR joints. Source: University of Michigan.....	516
Figure II.3.1.11. S-N chart correlation for: (a) structural stress without considering corrosion effects; and (b) structural stress considering corrosion effects. Source: University of Michigan.....	517
Figure II.3.1.12. Integrative platform for prediction of the location and extent of corrosion in Al-steel joints and its impact on joint strength and fatigue life. Source: University of Michigan and University of Georgia.....	518
Figure II.3.2.1. FSW tool used to weld Al and Mg sheet and the Al side of the linear FSW Al-Mg welded panel. Source: PNNL.....	523
Figure II.3.2.2. Load vs. displacement plots for coupons cut from two welded panels showing improvement in lap-shear strength and consistency between samples welded in (a) May vs. (b) July. Source: PNNL.....	523
Figure II.3.2.3. (a) FSW joint coupons used as CCT sample geometries with varying surface area ratios of 6022 Al (bottom) to ZEK100 Mg (top). (b) Weight change during CCT testing by sample ID. Source: WPI.....	524

Figure II.3.2.4. Hardness distribution map of an Al-Mg FSW joint cross-section dilated in the vertical direction, with each box measuring 1 mm horizontal by 0.4 mm vertical. Source: WPI. 524

Figure II.3.2.5. Linear FSW cross-section (top image) with Al sheet on top and Mg beneath, and model geometry (bottom image) showing region of reduced strength in the Al nugget. Source: WPI. 525

Figure II.3.2.6. The SEM studies of the 6022 Al side of the joint polished down. (a) The EBSD orientation map showing distribution of grain sizes and texture. (b) The EDS map of Mg concentration. Source: ORNL. 525

Figure II.3.2.7. (a) Transmission Kikuchi diffraction image quality and (b) phase map with the identified phases from a FIB lift-out in an Al-Mg interfacial region of the Al nugget. Source: ORNL. 526

Figure II.3.2.8. Output of FEA mechanical failure model of Al-Mg FSW joint (Al sheet on top, Mg sheet on bottom) showing mesh and von Mises stress at initial, intermediate, and final stages of elongation. Source: WPI. 526

Figure II.3.2.9. (a) Predicted and (b) actual corroded and uncorroded load-extension curves. Source: WPI. 527

Figure II.3.3.1. The proposed model is validated through three different aging times and three different aging temperatures for black polyurethane. Source: Michigan State University. 531

Figure II.3.3.2. The proposed model is validated against rubric of environmental conditions for black polyurethane. Source: Michigan State University. 532

Figure II.3.3.3. Validation of proposed model on thermo-oxidative aging of black polyurethane. Source: Michigan State University. 534

Figure II.3.4.1. Illustrations of the two-shot VFAW showing: (a) the first shot welds the flat interlayer to the deformed target; and (b) the second shot welds the flyer to the welded flyer-target stack-up. Source: The Ohio State University. 538

Figure II.3.4.2. Prototype weld head test: (a) the fixture during welding; and (b) the AA 5183-HSLA340 coupon welds created by the system. Source: The Ohio State University. 538

Figure II.3.4.3. Pedestal welder with automated part handling, adhesive dispense, and cleaning. Source: The Ohio State University. 539

Figure II.3.4.4. Robotic prototype system: (a) a schematic of VFAW prototype production showing a 4.2kJ capacitor bank, robotic arm, prototype welding head, prototype components, and fixture table; (b) procured KUKA 6-axis welding robot; and (c) a holding fixture. Source: The Ohio State University. 540

Figure II.3.4.5. Regions of arcing issues and redesign solutions: (a) the terminal connection to the coaxial cable; (b) the hot bus bar area where there are lots of close edges of the bar and the anvil; and (c) the terminals on the welding head where the two through holes caused arcing from the hot copper terminal to the anvil and copper bar to the metal screw. Source: The Ohio State University. 541

Figure II.3.4.6. VFA-welded thick 5000 series Al coupon with HSLA 340 subcomponents: (a) steel side shows no damage; and (b) Al side shows successful welds of first weld (yellow) and second weld (blue). Source: The Ohio State University. 541

Figure II.3.5.1. Summary of 2T weld stack-ups in terms of materials, thicknesses, and surface treatments. Source: ORNL.....	544
Figure II.3.5.2. Two approaches to establish associations among process parameters, weld attributes, and weld performance. Source: PNNL/ORNL.....	545
Figure II.3.5.3. (a) Summary sheet showing the GM weld stack-ups analyzed by the unified ML model, and box plots of (b), (c), and (d) showing the EoP for weld mechanical performance of peak load, extension at break, and total energy, respectively, of both training and validation testing. Source: ORNL.....	546
Figure II.3.5.4. Validation testing results of ML prediction in comparison with experiment measurement for the mean value of (a) peak load, (b) extension at break, and (c) total energy, respectively, for each individual weld in the 15 analyzed GM's weld stack-ups. The high-value of Pearson's correlation coefficient for peak load, extension at break, and total energy indicates the DNN model learns the high-dimensional correlations between weld attributes and weld performance. Source: ORNL.....	547
Figure II.3.5.5. Validation testing results of ML prediction in comparison with experiment measurement for mean value and standard deviation of (a) peak load, (b) extension at break, and (c) total energy, respectively, for GM's 15 weld stack-ups. Source: ORNL.....	548
Figure II.3.5.6. The ML model reveals that the adhesive leads to reduced peak load when an Al-steel resistance spot weld is not baked. Source: ORNL.....	549
Figure II.3.5.7. The ML model identifies the thickness-dependent baking effect on weld mechanical performance of (a) peak load, (b) extension at break, and (c) total energy. (d) Solid mechanics simulation provides the mechanistic understanding of the ML-identified baking effect. Source: ORNL.....	550
Figure II.3.5.8. Peak load predictions made by the Random Forest model contrasted against the experimental data spread showing the accuracy of the ML model. Source: PNNL.....	551
Figure II.3.5.9. Importance scores of the Random Forest nodes corresponding to the independent process variables that were used to make the 6022/LCS and X626/LCS coach peel peak loads with ~80% accuracy. Source: PNNL.....	551
Figure II.3.5.10. Observed and predicted coach peel test peak loads for AA6022/LCS and X626/LCS samples as a function of the different RSW heating stages. Source: PNNL.....	552
Figure II.3.5.11. Importance of scores for Random Forest model with (a) 41 predictors and (b) 10 predictors. Source: PNNL.....	553
Figure II.3.5.12. Representative parametric space explored for the 5,000 completed experiments for: (a) the maximum and minimum current used in preheating stage of the RSW process; (b) the number of pulses and clamp load applied on the joint during RSW; (c) the peak load; and (d) the total energy predicted by the Random Forest models developed using the predictors with the 10 highest importance scores. (e) A schematic depicting the various process conditions corresponding to the hierarchy shown in the key to be used for manufacturing AA6022/LCS RSW joints with the highest peak loads and total energies. Source: PNNL.....	554

Figure II.3.6.1. Example of initial Al fracture strain curves estimation. (a) Equivalent plastic strain from a simulated model for OBK condition with 160% tensile fracture strain. (b) Stress-strain curve comparison between simulation and experiment for OBK condition. (c) Equivalent plastic strain from a simulated model for 2BK condition with 60% tensile fracture strain. (d) Stress-strain curve comparison between simulation and experiment for OBK condition. (e) Initially assumed Al fracture stress-strain curves based on tensile simulations. Source: PNNL.	559
Figure II.3.6.2. Examples of early load-displacement curve simulation versus experimental results for the (a) CP, (b) CT, and (c) LS tests. Source: PNNL.....	560
Figure II.3.6.3. Examples of load-displacement curves and failure mode simulation versus experimental tests after refinement activities for (a) CP, and (b) LS. Source: PNNL.	561
Figure II.3.7.1. LSS of non-treated and air plasma-treated metal/metal, metal/CFRP, and CFRP/CFRP combinations. The in-plane dimension of each material is 25 mm × 100 mm with a 645 mm ² bond area. Source: PNNL.	565
Figure II.3.7.2. Colorized surface morphology of non-treated and air plasma-treated CFRP after LS failure. The PA66-A6061 and PA66-A5052 combinations are shown on the left and right, respectively. The CFRP surface is shown in blue, while the adhesive remaining on the surface is shown in pink. Source: PNNL.	566
Figure II.3.7.3. (a) The degree of cure of the adhesive at different cure rates. (b) Model vs. experimental data at a rate of 10 °C/min. Source: ORNL.....	566
Figure II.3.7.4. (a) RT shear profile of adhesive subject to flow. (b) Viscosities of adhesive at increasing temperatures. Source: ORNL.	567
Figure II.3.7.5. (a) Concept of HVR. (b) Optical cross-section of 6061-T6 bonded using a commercial rivet. Source: PNNL.	567
Figure II.3.7.6. Results of the 150 m/s rivet speed, 6 mm solid rivet, and 1.5-mm deep die with a 3.5 mm hole for (a) the experimental value, (b) the temperature profile, (c) the pressure profile, and (d) the material damage. Source: PNNL.	568
Figure II.3.7.7. (a) An AA6061 plate joined to a CFRP plate with a steel rivet showing the extrusion of the two plates. Yellow and pink labels show the areas of contact and gap areas between the two plates, respectively, (b) AA6061 plates combined with an AA7075 rivet showing the areas of perfect contact. Source: PNNL.....	569
Figure II.3.7.8. (a) LS load-extension curves for 1040 steel flat head rivets. (b) Commercial nail LS tests. (c) 6061-T6 commercial nail with and without adhesive bonding. Source: PNNL.	569
Figure II.3.7.9. (a) Schematic demonstrating the HFR process for multi-material stack-ups. (b) A micrograph of the cross-section of an Al/CFRP joint comprising AA6022 joined to three CFRP plates using an AA7075-T6 rivet. (c) Top and side views of an Al/Al HFR joint made with an HS C300 alloy steel rivet. (d) Orthogonal and side views of the Al/steel HFR joint with AA6061 and DP590 plates, as well as an M42 steel rivet. Source: PNNL.	570
Figure II.3.7.10. LS tensile load of Al/steel joints manufactured using HFR as a function of joint extension. Source: PNNL.	571
Figure II.3.8.1. Material arrangements for the four material stacks to be joined and characterized. Source: PNNL.	574

Figure II.3.8.2. Overview of project approach. Source: ORNL.....	574
Figure II.3.8.3. (a) Robotic platform (inset: the baseline tool). (b) T-peel sample welding. (c) Linear lap weld. (d) Curve weld. (e) Clamping scheme for the T-peel sample. Source: PNNL.....	575
Figure II.3.8.4. Load per unit width vs. cross-head displacement plot for 3T FSLW joints: (a) LS; (b) T-peel; and (c) bar chart compilation of several tested samples. Source: PNNL.....	576
Figure II.3.8.5. Representative fracture mode for both LS and T-peel of (a) and (b) the 7055-7055-6022 stack; (c) the 6111-6111-6022 stack; and (d) the optical micrograph of the 7055-7055-6022 stack (e.g., 1350 rpm at 0.5 m/min). Source: PNNL.....	577
Figure II.3.8.6. Comparison of welding time (including plunge-in and traverse time) per plunging speed. Source: PNNL.....	578
Figure II.3.8.7. (a) The approach that was used starting with the material properties and (b) using a finite element model to determine (c) the structure-property relationships in a FSWL joint. (d) The simulated and experimentally determined strengths of the T-peel joints of various weld lengths. Source: PNNL.....	578
Figure II.3.8.8. Process modeling of an Al-Al F-SPR joint to optimize rivet tip and die cavity depth. (a) The computational approach by 3D CEL model and a 2D axisymmetric model. (b) The simulated rivet shape for a different tip angle and die cavity. Source: ORNL.....	580
Figure II.3.8.9. Performance modeling of Al-Al F-SPR joint for the LS test: (a) the von Mises stress [Pa] in a joint with a regular rivet; (b) the effect of rivet strength on LSS; (c) the von Mises stress [Pa] in a joint with a heat-treated and larger-shank rivet; and (d) the effect of interlocking distance on joint strength. Source: ORNL.....	581
Figure II.3.8.10. Cross-tension modeling of an Al-Al F-SPR joint to optimize rivet head and material strength: (a) the rivet under combined torque and compression load; (b) the von Mises stress [Pa] distribution at peak load of cross-tension; (c) the plastic strain localization at the fillet region of the rivet; and (d) the dependence of joint load on rivet head thickness and tensile strength. Source: ORNL.....	582
Figure II.3.8.11. Summary of mechanical joint performance for F-SPR Al7055-Al7055 joints from (a) lap-shear tensile testing and (b) cross-tension testing. Source: ORNL.....	583
Figure II.3.8.12. (a) Optical image of the Al7055-Al7055 F-SPR joint cross-section. (b) Magnified optical image at the joint interface (yellow box) showing grain refinement and solid-state bonding between the upper and lower Al sheet (horizontal white box), as well as the steel rivet and surrounding Al sheets (vertical white box). (c) Magnified optical image at flared rivet tip and bottom Al sheet, showing grain refinement of the Al sheet at the cap near the joint interface (left white box) and solid-state bonding between the steel and the bottom Al sheet (right white box). Source: ORNL.....	583
Figure II.3.8.13. Summary of mechanical joint performance for F-SPR TS CFRC-Al7055 joints from (a) LS tensile and (b) cross-tension testing. Source: ORNL.....	584
Figure II.3.8.14. Optical image of TS CFRC-Al7055 F-SPR joint cross-section, showing mechanical interlocking between the flared rivet leg and bottom Al7055 sheet, as well as the crack-free joint on the Al sheet. Source: ORNL.....	585
Figure II.3.9.1. (a) The Nd:YAG laser system at ORNL. (b) The atmosphere plasma system at ORNL. (c) The atmosphere plasma jet from the nozzle. Source: ORNL.....	589

Figure II.3.9.2. Optical images of laser-surface-treated Al7075 with different laser pulse energies: (a) $E_p=1.2\text{J}$; and (b) $E_p=1.6\text{J}$. The areas in dotted boxes are approximately (a) 1×0.5 in. and (b) 1×1.0 in. Source: ORNL.	589
Figure II.3.9.3. Summary of surface roughness on (a) as-received Al7075, (b) 600-grit surface-finished Al7075, and (c) laser-treated Al7075 at $E_p=1.2\text{J}$. (d) Summary of R_a (arithmetical mean deviation of the measured surface profiles) and R_z (maximum peak to valley height of the measured profile) for four different surface conditions. Source: ORNL.	590
Figure II.3.9.4. Optical images of AP-treated AA7075 with different nozzle heights ranged from 0.5 in. to 1.0 in. at a fixed scan speed of 32 ipm. Source: ORNL.	591
Figure II.3.9.5. (a) Nyquist plots of laser-treated (1.2 J) and baseline 600-grit finish Al7075 surfaces with the exposure area of 0.833 cm^2 . (b) A comparison of corrosion reaction resistance values from laser-treated (1.2, 1.4, and 1.6 J) samples and the baseline Al7075. Source: ORNL. .	591
Figure II.3.9.6. Nyquist plots of AP-treated Al7075 with the scanning speed of (a) 5 and 10 ipm and (b) 20 and 32 ipm in comparison with the baseline 600 grit finish Al7075. Source: ORNL.	592
Figure II.3.9.7. Cross-section STEM bright-field micrographs of the (a) as-received Al7075, (b) the laser-processed Al7075 at 1.2J, and (c) the AP-processed Al7075. The AP sample shows a band under the formed surface film that is depleted of GP zones. Source: ORNL.	593
Figure II.3.9.8. STEM/EDS data from the Al7075 as-received base metal sample. The native oxide film contains O, Mg, Cu, and Si. Source: ORNL.	594
Figure II.3.9.9. STEM/EDS data from the Al7075 1.2 J laser-processed sample. The formed film contains O, Mg, Cu, and Si. Source: ORNL.	594
Figure II.3.9.10. STEM/EDS data from the Al7075 1.8 kW AP-processed sample. The formed film contains O, Mg, Cu, and Si. Source: ORNL.	595
Figure II.3.9.11. Surface energy stability of (a) Al6061 and (c) CFRP-PA66 as a function of time in air and the wetting envelopes of (b) Al6061 and (d) CFRP-PA66. Dotted lines of surface energy plots indicate total, polar, and dispersive component of as-received surfaces. Source: PNNL.	596
Figure II.3.9.12. XPS Al2p spectra of Al6061 and CFRP-PA66 before and after air plasma treatment: (a) Al6061_AR, as-received; and (b) Al6061_air plasma. O1s: (c) Al6061_AR; and (d) Al6061_air plasma. C1s: (e) CFRP-PA66_AR; and (f) CFRP-PA66_air plasma. N1s: (g) CFRP-PA66_AR; and (h) CFRP-PA66_air plasma. Source: PNNL.	597
Figure II.3.9.13. Tafel plots measured on pre- and post-plasma-treated surfaces of Al5052, Al6061, and DP590 steel. Source: PNNL.	598
Figure II.3.9.14. Nyquist plots measured on pre- and post-plasma-treated surfaces of Al5052 and Al6061 sample and their equivalent circuit diagram used for resistance value calculation. Source: PNNL.	598
Figure II.3.9.15. Potentiodynamic curves of the different Al alloys and steel that are being used for the JCP 2.0 project. Source: PNNL.	599
Figure II.3.9.16. (a) The current density of the rivet and sheet for the AA5052, AA5182, AA6063, AA5083, and AA6061 alloys with distance. (b) The current density map at the rivet region for the AA5083 and AA6063 alloys. Source: PNNL.	600

Figure II.3.10.1. (a) Single-joint LS coupons welded by varying ultrasonic energies. (b) Peak LSS as a function of ultrasonic energy. Source: ORNL.	604
Figure II.3.10.2. (a) Multi-joint sample that was welded using a constant ultrasonic energy input at 2500J. (b) Peak lap- shear strength of each USW joint that was cut out of the large coupon and tested individually. Source: ORNL.	605
Figure II.3.10.3. Measured and predicted temperature fields when surface temperature reaches the maximum during the welding of each joint as labeled w1–w5. Source: ORNL.....	605
Figure II.3.10.4. Prediction of similar temperature fields when making joints at different locations using different ultrasonic energies of: (a) 7,800 J; and (b) 2,300 J. Source: ORNL.....	606
Figure II.3.10.5. Adaptive energy inputs used to make consistent USW joint quality throughout the entire large coupon. Source: ORNL.	606
Figure II.3.10.6. Peak LSS of each USW joint (e.g., A through E) cut out of the large multi-joint coupon, as shown in Figure II.3.10.5, and the comparison with the peak strength obtained on the single-joint coupons. Source: ORNL.....	607
Figure II.4.1.1. Concept of S4CFRP composite system. Source: Newport Sensors, Inc.....	610
Figure II.4.1.2. Circuit block diagram of the proof-of-concept system. Source: Newport Sensors, Inc.	610
Figure II.4.1.3. Process for fabrication of test specimens. Source: Newport Sensors, Inc.	611
Figure II.4.1.4. Experimental evaluation setups: (a) fixture for free vibration, (b) fixture for damage from stylus, and (c) setup for impact with a hammer. Source: Newport Sensors, Inc.....	611
Figure II.4.1.5. Measured piezoelectric signals of the specimens from: (a) the free vibration test, (b) the impact test, and (c) the impact during free vibration. Source: Newport Sensors, Inc.....	612
Figure II.4.1.6. Energy-harvesting results at (a) 8 Hz and (b) 11 Hz. Source: Newport Sensors, Inc.	613
Figure II.4.1.7. (a) Damage detection test setup and (b) results of the damage detection test. Source: Newport Sensors, Inc.	613
Figure II.4.1.8. Simultaneous sensing and energy-harvesting result. Source: Newport Sensors, Inc.	614
Figure II.4.2.1. SMART Layer sensors. Source: Acellent.....	618
Figure II.4.2.2. Circuit block diagram of the proof-of-concept system. Source: Acellent.	618
Figure II.4.2.3. Voltage impulse received upon an impact with a golf club. Source: Acellent.	619
Figure II.4.2.4. Experimental evaluation setups: (a) fixture for free vibration, (b) fixture for damage from stylus, and (c) setup for impact with a hammer. Source: Acellent.	619
Figure II.4.2.5. (a) The 3,650 mAh pouch cell that underwent cycle life aging; (b), (c), and (d) schematics of the experimental guided wave propagation inspection setup in Li-ion batteries; and (e) the indicative results for the SOH [7]. Source: Stanford University.	620
Figure II.4.2.6. Experimental setup showing the battery cycler connection to the 3,650 mAh battery and the DAQ. Source: Stanford University.	621
Figure II.4.2.7. MESC battery monitoring components and layout. Source: Stanford University.....	622

Figure II.4.3.1. (a) Heat transfer model for the oven composite structure. (b) Heat source (100 W/cm ²) on one face of the material block. (c) Thermal heatmap of the improved nylon sample showing a temperature of approximately 163°C around the center of the panel. Source: Intellisense Systems, Inc.	627
Figure II.4.3.2. (a) Connectorized fibers of the composite test panel. A comparison of impact points from two tests using (b) 500 Hz and (c) 4,000 Hz sampling rates on the DAQ board. Both were impact tests in an Instron Dynatup machine with an impact energy of <10 joules. The impact caused the resistance to spike downward, and after a delay of several seconds, the resistance returned to its initial position. Source: Intellisense Systems, Inc.	628
Figure II.4.3.3. (a) Layup of the tensile panel with sensor lines exiting through the blue backing paper. (b) The composite panel containing six tensile coupons, three thermal coupons, and two reference coupons in which the sensor ends have been cleaned and connectorized. Source: Intellisense Systems, Inc.	628
Figure II.4.3.4. (a) Tensile coupon made by leading the sensor out the sides rather than threading through the top, eliminating the need for cutting. (b) One of the three new sensor coupons in which the end tabs were adhered to the coupon after fabrication. This may have reduced the gripping strength of the end tabs and adhesive. The sensor lines and end tabs were covered in tape, and a spackle dot pattern was sprayed along the front of the coupon. (c) A control coupon mounted in the Instron tensile clamps. Source: Intellisense Systems, Inc.	629
Figure II.4.3.5. (a) A graphical representation of the resistance, load, and strain data versus time. (b) Impact coupon loaded into the uncompressed test frame, with a breather cloth to protect the sensors. A hole was cut in the center where the tip impacts the coupon. (c) Impact test results. (d) Thermal ramp-step test, repeated. The chamber was heated from 20°C to 60°C at 10°C intervals, and back down to 40°C and 20°C. Each step involved a brief heating or cooling period, followed by a 60-min. waiting period. Source: Intellisense Systems, Inc.	629
Figure II.4.4.1. Fiber length investigation for: (a) the Vartega T-800 waste fiber; and (b) the ZOLTEK P35 fiber. Source: Composites Automation, LLC.	634
Figure II.4.4.2. TuFF processing using the (a) T-800 waste fiber, (b) ZOLTEK P35, and (c) Vartega recycled fiber. (NOTE: Proprietary information is covered by the white squares). Source: Composites Automation, LLC.	635
Figure II.4.4.3. Electrospinning of PVA with (a) a laboratory-scale four-needle electrospinning apparatus, (b) the SEM image of a 0.1 gsm electrospun PVA on TuFF preform, and (c) the TuFF material with 0.1 gsm PVA showing 50% stretching. Source: Composites Automation, LLC.	636
Figure II.4.4.4. Results of the compaction studies of the TuFF material that has been stabilized with PVA electrospun material (1% by weight). Source: Composites Automation, LLC.	637
Figure II.4.4.5. Results of the rheology study of Axiom resin. (a) Viscosity as a function of temperature for a heating ramp of 1°C/minute and (b) percentage conversion versus time predictions for isothermal cure temperatures ranging from 100°C to 150°C. Source: Composites Automation, LLC.	637
Figure II.4.4.6. Wet compression equipment: (a) Indexing table, high-pressure RTM, and twin press; and (b) the high-pressure RTM head, ready for dispensing epoxy on TuFF preform. Source: Composites Automation, LLC.	638

Figure II.4.4.7. TuFF processing with Axiom film: (a) prepregging TuFF with film; (b) locating the prepreg in a heated press with caul plates; and (c) application of heat and pressure to cure the panel. Source: Composites Automation, LLC.	639
Figure II.4.4.8. Fiber alignment properties of TuFF panels produced using T-800 waste fiber and ZOLTEK P35. Source: Composites Automation, LLC.	639
Figure II.4.5.1. (a) Laser-induced graphene on a Kapton polyimide film and IM7/8552 prepreg with the transferred graphene (note the transfer process yields the mirror of the graphene) and PEEK/IM7 prepreg coated with an LIG array. (b) SEM image of the graphene structure form on the PEEK matrix. Source: Trimer LLC.....	642
Figure II.4.5.2. (a) Experimental setup of the piezoresistive LIG strain sensor and (b) a Micro-Measurements strain gauge with a gauge electrically connected via a set of magnet wires bonded to the beam using silver paint. Source: Trimer LLC.	643
Figure II.4.5.3. (a) Voltage amplitude as a function of acceleration showing device sensitivity, which was 2.5 times greater for the LIG sensor than a commercial strain gauge, and (b) the time domain response to a sinusoidal excitation. Source: Trimer LLC.....	644
Figure II.4.5.4. EMI shielding effectiveness test configuration. Source: Trimer LLC.	645
Figure II.4.5.5. (a) Testing configuration using both antenna and (b) the EMI shielding effectiveness testing results showing both horizontal and vertical polarization. Source: Trimer LLC.....	645
Figure II.4.6.1. Tensile strength of the neat resin tested according to ASTM D638, demonstrating high-strength of the resin. Source: Trimer LLC.....	649
Figure II.4.6.2. Tensile strength after a 24-hour immersion in common automotive solvents. Source: Trimer LLC.....	650
Figure II.4.6.3. Dielectric cure monitor data from the molding of a 28-mm-thick composite part demonstrating a 90-second cure time. Source: Trimer LLC.	652
Figure II.4.6.4. Fatigue testing of fiberglass composites manufactured. Source: Trimer LLC.....	652
Figure II.4.6.5. Propane torch testing on a 3-mm-thick fiberglass composite panel with a 60-second flame exposure, after which the composite was able to self-extinguish in under 10 seconds. Source: Trimer LLC.	653

List of Tables

Table I.1.1.1. DFT Calculation Results	12
Table I.1.2.1. Chemical Composition of the Two Different Alloys 21-2N and 23-8N Studied in Weight-Percent (wt%) With Fe in Balance	15
Table I.1.2.2. Vacancy Formation Energy of Each Species i in the Oxide Film Reported in eV.....	21
Table I.1.2.3. Cation Substitution Energy of Each Species in the Oxide Film Reported in eV	21
Table I.2.1.1. Summary of the Wear Rate Tests	28
Table I.3.1.1.1.1. DFT Calculated Lattice Parameters of fcc Al and $L1_2$ -Al ₃ X	33
Table I.3.1.1.1.2. DFT Calculated Lattice Parameters of Al ₂ Cu and $L1_2$ -Al ₃ X	33
Table I.3.1.1.1.3. DFT Interfacial and Strain Energies of Al/Al ₃ X.....	34
Table I.3.1.1.1.4. DFT Interfacial and Strain Energies of Al ₃ X-Al ₂ Cu	35
Table I.3.2.1.1.1. Target Properties and Metrics.....	50
Table I.3.2.1.3.1. DFT Calculated Lattice Parameters of fcc Al and $L1_2$ -Al ₃ X	64
Table I.3.2.1.4.1. Analyzed Alloy Composition of the Industrial AFA5 Heats	73
Table I.3.3.1.1.1. Summary of New Al Alloys and Status for AM	87
Table I.3.3.1.4.1. Measured Chemistries of LPBF Austenitic Steels.....	103
Table I.3.4.2.1.1. Materials Suites Used in the Study.....	138
Table I.3.4.2.1.2. Effect of Diffusivity Temperature Dependence on Predicted Maximum Materials Temperatures	139
Table I.4.1.1. Material Properties	148
Table I.4.1.2. Main Bearing Cap Optimized Deflection Results	149
Table I.4.1.3. Mass Comparison for Cast-Fe and PTWA Liners.....	151
Table I.4.2.1. Primary Engine Architecture Selection Summary Pugh Chart.....	154
Table II.1.1.1. Tensile Properties of 2-mm-Thick Tubing Extruded by ShAPE from 6063 Cast Billets Compared to the Relevant ASTM [13] and ASM [14] Standards	172
Table II.1.1.2. Tensile Properties of 2-mm-Thick Tubing Extruded by ShAPE from 6063 Briquettes Compared to the Relevant ASTM [13] and ASM [14] Standards.....	173
Table II.1.2.1. Status of Project Tasks and Milestones at the End of FY 2021	178
Table II.1.2.2. Summary of Process Conditions used for Three Rolling Trials at ORNL	181
Table II.1.2.3. PPG Cleaning and Pretreatment Processes Evaluated for EFP Mini-door Compatibility.....	186
Table II.1.5.1. Die-Casting Alloys, Compositions, and Mechanical Properties.....	212
Table II.1.6.1. List of Alloys and Laser Parameters Used for Testing	217
Table II.1.7.1. Base Alloy Properties Listed for Comparison	230

Table II.1.7.2. Optimal FSP Parameters for Selected Al Alloys	230
Table II.1.8.1. Summary of Various Microstructural Features Seen in HPDC A380 Die-Cast Plates	245
Table II.1.8.2. Summary of Tensile Properties on Miniature Specimens of HPDC A380 Both Before and After FSP	248
Table II.1.9.1. Corrosion Reaction Resistance Determined by EIS for Laser-Treated AZ91D with Four Energy Intensities	266
Table II.1.9.2. Corrosion Reaction Resistance Determined by EIS For Plasma-Treated AZ91D With Four Varying Process Conditions.....	268
Table II.1.9.3. Trials Performed in Collaboration with PSU	269
Table II.1.9.4. Summary of the AZ91 and AM60 Tensile Properties	272
Table II.1.10.1. Summary of the AZ91 and AM60 Tensile Properties.....	278
Table II.1.11.1. Comparisons of Mechanical Properties of As-Extruded AZ31B vs. ShAPE of Extruded AZ31, and As-Cast AZ31 vs. ShAPE of Cast AZ31.....	293
Table II.1.11.2. Tensile Properties of ShAPE-Extruded Rods and Standard Deviation (σ)	294
Table II.2.1.1. Project Parameters and Requirements	300
Table II.2.2.1. Project Parameters and Requirements	309
Table II.2.2.2. Milestones for BP3	310
Table II.2.2.3. Model Integration Predictions Related to Experimental Data with Associated Errors for Bio-PAN CF Produced in This Study.....	312
Table II.2.2.4. Model Integration Predictions Related to Experimental Data with Associated Errors for Pitch-Based CF Produced in This Study	312
Table II.2.3.1. Project Participants.....	319
Table II.2.3.2. Static Performance of Composite Door.....	321
Table II.2.3.3. Results for the QSP Test.....	322
Table II.2.3.4. Results for Deformable Barrier Dynamic Load Cases Compared to Target Baseline Door.....	323
Table II.2.3.5. Comparison of Weight and Cost Distribution of Composite Door (Production Version) with the Baseline Door	330
Table II.2.4.1. Phased Approach to HTC Project	335
Table II.2.5.1. Process Parameters for Panel Set #2	346
Table II.2.7.1. Alternative Precursor and Advanced Conversion Processing Estimated Reduced Cost and Embodied Energy	359
Table II.2.7.2. Task 3 Milestones, Task Descriptions, and Status.....	361
Table II.2.7.3. Petroleum Mesophase Property	363
Table II.2.7.4. Polyamide 6 Tensile Properties	366
Table II.2.8.1. Plasma Oxidized/Conventional Carbonized 2.2 dtex Precursor	373

Table II.2.8.2. Plasma Oxidized/Conventional Carbonized 3.3 dtex Precursor	374
Table II.2.8.3. Plasma Oxidized/Conventional Carbonized 5.5 dtex Precursor	374
Table II.2.8.4. Steam Stretched, Conventionally Converted 2.2 dtex Precursor	374
Table II.2.8.5. Steam Stretched, Conventionally Converted 3.3 dtex Precursor	375
Table II.2.10.1. Fiber Properties (From Manufacturer) and Mechanical Testing Properties of the Plaques Provided by ESE.....	384
Table II.2.12.1. Milestones for Task 1 Work Stream Activities	396
Table II.2.12.2. Task 1.2 CAE Iterations in Support of the XCB Structural Design.....	398
Table II.2.12.3. Task 3 Milestones for Budget Period 1.....	404
Table II.2.12.4. Task 4 Milestones for Budget Period 1.....	405
Table II.2.12.5. Materials Used in the Initial Molding Trial	407
Table II.2.12.6. Task 5 Milestones for Budget Period 1.....	407
Table II.2.12.7. Task 6 Milestones for Budget Period 1.....	409
Table II.2.12.8. Task 7 Milestones for Budget Period 1.....	410
Table II.2.12.9. Task 9 Milestones for Budget Period 1.....	411
Table II.2.12.10. Task 10 Milestones for Budget Period 1	411
Table II.2.12.11. Thermal Characterization of Pellet Materials	413
Table II.2.12.12. Thermal and Mechanical Properties of Injected Molded Samples	413
Table II.2.12.13. Task 11 Milestones for Budget Period 1	413
Table II.2.13.1. Material Systems Considered for the Study	418
Table II.2.13.2. Process Parameters	425
Table II.2.13.3. Equivalent Permeability of the Surrounding Channel	425
Table II.2.13.4. Fiber and Resin Volume Fraction Information in the Unit Cell Model	427
Table II.2.14.1. FY 2021 PNNL Milestones.....	437
Table II.2.14.2. List of Fabricated Panels, Material Details, and Normalized Mechanical Properties Based on 50 wt% Fiber Content	440
Table II.2.14.3. FY 2021 ORNL Milestones.....	440
Table II.2.15.1. Modulus Evaluated for Five Materials Printed on Large-Scale AM System	445
Table II.2.16.1. Percentage Increase in Tensile Strength and Stiffness of a Cyanate Ester Based, Printed Short CF Composite as a Function of GO Loading.....	455
Table II.2.19.1. FY 2021 Milestones	474
Table II.2.20.1 Milestones and Go/No-Go	481
Table II.2.20.2 Specific Heat Capacity at Key Temperature Points.....	486
Table II.2.22.1 Amines and Conditions Employed in the Preparation of Aramid Polymers	497

Table II.2.23.1 Technoeconomic and Supply Chain Analysis Results for the PE-CAN Resin 504

Table II.3.5.1 Split in Training and Testing Data Portions in the AA6022/LCS RSW Data Set to Determine the Prediction Error in the Random Forest Model for Predicting Peak Load 550

Table II.3.5.2 Random Forest Coefficients Used for Building Total Energy Models Using 41 and Top 10 Most Important Predictors 553

Table II.3.7.1. Normalized Peak Stress and Normalized Fracture Energy of Various Al/Steel HFR Joints with and without Adhesive as Compared to An Al/Steel Joint Manufactured Using RSW as the Baseline 571

Table II.3.8.1. Effect of Rivet Design/Die Cavity Depth on Predicted Mechanical Interlocking Distance 580

Table II.3.9.1. Resistance Values Calculated from EIS Using the Equivalent Circuit Diagram 598

Table II.4.4.1. Tensile Properties of TuFF Panels Produced Using T-800 Waste Fiber and ZOLTEK P35 640

Table II.4.6.1. Comparison of Trimer’s RTM Polymer with Current Low-Cost Rapid-Cure Resins..... 648

Table II.4.6.2. Material Properties Form VARTM E-Glass Composites 651

Vehicle Technologies Office Overview

Vehicles move our national economy. Annually, vehicles transport 12 billion tons of freight—more than \$38 billion worth of goods each day¹—and move people more than 3 trillion vehicle-miles.² Growing our economy requires transportation, and transportation requires energy. The transportation sector accounts for approximately 27% of total U.S. energy needs,³ and the average U.S. household spends over 17% of its total family expenditures on transportation,⁴ making it, as a percentage of spending, the most costly personal expenditure after housing. Transportation is critical to the overall economy, from the movement of goods to providing access to jobs, education, and healthcare.

The Vehicle Technologies Office (VTO) funds research, development, demonstration, and deployment (RDD&D) of new, efficient, and clean mobility options that are affordable for all Americans. VTO leverages the unique capabilities and world-class expertise of the National Laboratory system to develop new innovations in vehicle technologies, such as advanced battery technologies (including automated and connected vehicles as well as innovations in efficiency-enhancing connected infrastructure); innovative powertrains to reduce greenhouse gas and criteria emissions from hard-to-decarbonize off-road, maritime, rail, and aviation sectors; and technology integration that helps demonstrate and deploy new technology at the community level. Across these technology areas and in partnership with industry, VTO has established aggressive technology targets to focus RDD&D efforts and ensure there are pathways for technology transfer of federally supported innovations into commercial applications.

VTO is uniquely positioned to accelerate sustainable transportation technologies due to strategic public-private research partnerships with industry (e.g., U.S. DRIVE, 21st Century Truck Partnership) that leverage relevant expertise. These partnerships prevent duplication of effort, focus DOE research on critical RDD&D barriers, and accelerate progress. VTO advances technologies that assure affordable, reliable mobility solutions for people and goods across all economic and social groups; enable and support competitiveness for industry and the economy/workforce; and address local air quality and use of water, land, and domestic resources.

Annual Progress Report

As shown in the organization chart (below), VTO is organized by technology area: Batteries & Electrification R&D, Materials Technology R&D, Advanced Engine & Fuel Technologies R&D, Energy Efficient Mobility Systems, and Technology Integration. Each year, VTO's technology areas prepare an Annual Progress Report (APR) that details progress and accomplishments during the fiscal year. VTO is pleased to submit this APR for Fiscal Year (FY) 2021. The APR presents descriptions of each active project in FY 2021, including funding, objectives, approach, results, and conclusions.

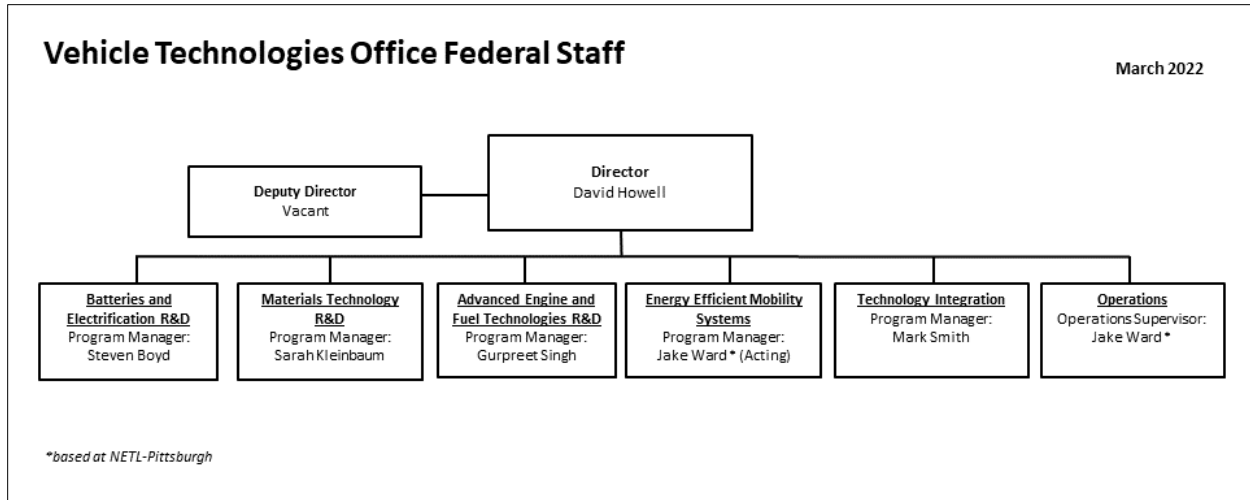
¹ U.S. Department of Transportation, Freight Analysis Framework Version 5.0 Data Tabulation Tool.

² U.S. Department of Transportation, March 2022 Traffic Volume Trends, Figure 1.

³ U.S. Energy Information Administration. Monthly Energy Review, 2022, <https://www.eia.gov/totalenergy/data/monthly/index.php>.

⁴ Davis, Stacy C., and Robert G. Boundy. Transportation Energy Data Book: Edition 39. Oak Ridge National Laboratory, 2020, <https://doi.org/10.2172/1767864>.

Organization Chart



Materials Technology Program Overview

Introduction

The Materials Technology subprogram supports the VTO goals of achieving 100% decarbonization of the transportation sector by 2050. This ambitious goal will be realized through the increased deployment of electric and hydrogen fuel cell vehicles. Materials play an important role in increasing the efficiency of electric vehicles through weight-reduction as well as enabling additional functionality such as faster charging and new sensing technologies. Lighter weight vehicle structures and electric drivetrains will require fewer batteries to achieve the same range, which in turn reduces battery cost, material needs, and reduces the greenhouse gas emissions from battery production. Functional materials with improved properties such as electrical conductivity, thermal conductivity, and unique sensing capabilities will enable innovations in charging and autonomous vehicles. The materials and manufacturing methods used to make vehicles also contribute to greenhouse gases and the Materials Technology subprogram supports research, development, and deployment to increase recyclability and reduce the overall embodied energy of vehicles. The Materials Technology subprogram accomplishes its technical objectives through research programs with academia, National Laboratories, and industry.

The Propulsion Materials portfolio is closely aligned with other VTO subprograms to identify critical materials needs for next-generation high-efficiency powertrains for both HD and LD vehicles. Strategies for achieving high-efficiency powertrains includes addressing key challenges in electrical conductivity, thermal conductivity, magnetic materials, and high-temperature operation currently limiting advances in electric powertrains and wireless charging. The Powertrain Materials Core Program is a national laboratory consortium that targets critical powertrain components based on thermal loading, structural, and electrical requirements and utilizes an ICME approach to link advanced characterization to high-performance computing methods to accelerate development of new material families. In FY 2021, the program has partnered with the Electrification subprogram to focus new materials development efforts on challenges facing power electronics for electric vehicles.

The Lightweight Materials team works closely with industry through the U.S. DRIVE partnership to understand LD vehicle structural weight-reduction goals and to identify technical challenges that prevent the deployment of lightweight materials. The most promising and likely approach for lightweighting is a multi-material structure, which focuses on the use of the right material for the application. The Lightweight Materials research portfolio addresses significant technology gaps for each family of structural materials: Mg, AHSS, Al, and polymer composites. Gaps include raw material costs, formability, manufacturing cycle time, ability to model and predict failure, corrosion mitigation, and incorporation of new materials into manufacturing plants. In addition, research efforts investigate dissimilar material joining in order to enable the reliable assembly of these multi-material systems.

Goals

The Materials Technology subprogram supports the VTO's mission to accelerate the deployment of clean energy technology toward achieving net-zero emissions in the transportation sector. Lighter vehicles with more efficient powertrains reduce energy use, decrease greenhouse gas (GHG) emissions, and save consumers money. The structural and powertrain systems that we target to improve are limited by materials performance. By improving the properties of powertrain and structural materials, we can enable a significant improvement in energy efficiency for future vehicles. Increasing the thermal and electrical conductivity of low-cost materials will enable increased electric vehicle efficiency while improving properties in structural materials, such as stiffness, strength, joinability, and crash-energy absorption—all with lower-cost, will accelerate the

deployment of lightweight materials in the automotive market. The specific performance and cost targets for the Materials Technology subprogram are to enable a 25% weight-reduction for LD vehicle gliders including body, chassis, and interior as compared to a 2015 baseline at no more than a \$5/lb.-saved increase in cost by 2025.

State-of-the-Art

Automakers are seeking to improve fuel economy, increase electric vehicle range, or reduce battery size while improving or maintaining vehicle performance and safety. Lighter weight vehicle structures and electric drivetrains will require fewer batteries to achieve the same range, which in turn reduces battery cost, material needs, and reduces the greenhouse gas emissions from battery production. Functional materials with improved properties such as electrical conductivity, thermal conductivity, and unique sensing capabilities will enable innovations in charging and autonomous vehicles. For structural components, the market is shifting from traditional steel components to lighter weight materials such as AHSSs, Al alloys, Mg alloys, and polymer composites.

In order to support the transition to all electric light-duty vehicles by 2035, research is needed to increase efficiency and decrease manufacturing cost of electrified powertrains. Development of new alloys with improved electrical/mechanical properties and enhanced resistance to corrosion/oxidation of components operating in harsh environments such as electrical bus bars, lightweight gears, underbody suspension, and brakes will address the future properties needs of electric and hydrogen fuel cell vehicles. Expanded development and characterization of materials supporting electrification such as lightweight conductors, ferrites, and high Si-steels are also important for challenging components such as inverters, motors, and gear-train. However, inadequate databases, modeling, and design tools are significant barriers for further development of new materials. By evaluating existing computational tools, and identifying gaps that must be overcome to achieve seamless integration across multiple-length scales and increasing understanding of the basic behavior of the material (effects of solute at the atomistic level, microstructural development, microstructure/property relationships, fracture and failure mechanisms, durability, temperature-dependent behavior, etc.), more accurate design tools and predictive models can be established. Characterization and multiscale computational materials methods will accelerate discovery and early-stage development of cutting-edge materials and innovative production techniques like AM for lighter and more efficient powertrains.

AHSS is the most mature lightweight material in terms of widespread use in industry due to its compatibility with existing manufacturing infrastructure and vehicle materials. Application of third-generation high-strength steel has the potential to reduce component weight by up to 25%, particularly in strength-limited designs. However, technical challenges remain to improve weldability and weight-reduction is dependent on the ability to maintain stiffness at reduced gauges. Al continues to see steady growth in market share in the automotive industry⁵ despite issues of material cost, room temperature (RT) formability, and limitations within the existing manufacturing infrastructure. This is due to the 40% weight-savings that can be achieved with Al along with the well-established domestic supply chain. Mg has the potential to significantly reduce vehicle component weight by 55% or greater; however, there are several significant technical barriers preventing increased use of this material in vehicle designs. Mg has high raw material costs and price volatility, relatively low specific stiffness, difficulty in forming sheet at low temperatures, low ductility of finished components, and a limited alloy set, among other challenges. CF and other polymer composites have the potential to reduce component weight by more than 60%. The main barriers to widespread use are the high cost to manufacture the CF, lack of high-volume composite manufacturing methods, and a need for reliable predictive tools for both part design and performance prediction.

5. Giampieri, A., J. Ling-Chin, Z. Ma, A. Smallbone, and A. P. Roskilly, 2020, "A review of the current automotive manufacturing practice from an energy perspective," *Appl. Energy*, Vol. 261, Art. 114074.

When combinations of the above lightweight materials are used, the resulting multi-material structures have challenges of their own. Traditional joining methods used in automotive assembly, such as resistance spot-welding and riveting, are inefficient for joining of dissimilar metals and for some combinations, infeasible. In the near-term, friction stir scribe welding and resistance spot riveting are showing promising advances for the joining of AHSS and Al (the more mature lightweight metals). An additional challenge posed by multi-material structures is the increased risk of corrosion due to galvanic coupling. As the barriers to introduction of Mg and CF are overcome, breakthroughs in joining technology will also be necessary.

Program Organization Matrix

The Materials Technology subprogram is led by Program Manager, Sarah Kleinbaum.

- Propulsion Materials focuses on:
 - Materials for Electric Vehicle Powertrain Components (Jerry Gibbs) – which includes addressing key challenges in electrical conductivity, thermal conductivity, magnetic materials, and high-temperature operation.
- Lightweight Materials consists of three research portfolios:
 - Light Metals (Christopher Schooler) – which includes research on property improvement and processing advances for AHSS, Al, and Mg.
 - Polymer Composites (Felix Wu) – which includes research on low-cost production of CF, novel processing methods for polymer composites, and predictive performance models of CF and other fiber-reinforced or hybrid composites.
 - Joining of Dissimilar Materials (Christopher Schooler) – which includes research on solid-state, mechanical, and chemical joining methods, as well as galvanic corrosion mitigation.

All the activities within the Materials Technology subprogram utilize computational methods for material discovery, prediction of structure, understanding failure mechanisms including corrosion, and the effects of processing on properties.

(This page intentionally left blank)

I Propulsion Materials

I.1 Modeling of Powertrain Materials

I.1.1 Multiscale Modeling of Corrosion and Oxidation Performance and Their Impact on High-Temperature Fatigue of Automotive Exhaust Manifold Components (Ford Motor Company)

Mei Li, Principal Investigator

Ford Motor Company
2101 Village Road
Room 2014
Dearborn, MI 48124
E-mail: mli9@ford.com

Jerry L. Gibbs, DOE Technology Manager

U.S. Department of Energy
E-mail: jerry.gibbs@ee.doe.gov

Start Date: October 1, 2018 End Date: September 30, 2021
Project Funding (FY 2021): \$1,840,000 DOE share: \$1,260,000 Non-DOE share: \$580,000

Project Introduction

Corrosion and oxidation of exhaust manifold components made from cast-Fe or steel under typical service conditions can be very severe and are a chief concern within the automotive industry, yet an understanding remains elusive as of today [1]. This is partly due to the lack of knowledge regarding the failure in structural components having been built upon either corrosion/oxidation or mechanical loads independently. In real applications, however, materials are susceptible to experiencing corrosion/oxidation in synergy with mechanical loads, which is more severe than the effects produced by these two mechanisms independently.

In this project, it is proposed to develop a multiscale computational model to predict:

1. The oxidation/corrosion performance of two different categories of iron-based materials used for exhaust manifold in Advance Combustion Engine and Emission Control (ACEC) gas compositions at two different temperatures (e.g., 805°C and 1050°C). This model—spanning from the atom level to the microstructure level—aims to study the oxidation/corrosion susceptibility of materials of interest to ACEC gas, as well as the diffusion-controlled growth of oxidation/corrosion production.
2. The lives of exhaust manifold components, based on a comprehensive database of high-temperature corrosion/oxidation and fatigue durability data, and a thorough and detailed investigation of the physical mechanisms that cause damage in high-temperature fatigue, with special consideration of the synergy effects of corrosion/oxidation.

Objectives

- To develop multiscale computational models capable of predicting the location and extent of high-temperature corrosion/oxidation of automotive exhaust manifold materials (e.g., cast steels, nickel [Ni]-resistant, cast-iron [Fe]) in ACEC gas compositions for temperatures up to 1050°C.
- To conduct static and thermal cycling corrosion/oxidation trials in controlled atmosphere and demonstrate the model capable of predicting the corrosion/oxidation performance of the exhaust manifold materials exposed to high temperatures and realistic combustion gases to within 10% of experimental measurements.

- To develop a robust computational model to predict the high-temperature fatigue life of the material under corrosive/oxidizing conditions, and demonstrate the model can predict the corrosion/oxidation-fatigue performance of exhaust manifold materials exposed to high temperatures and realistic environment to within 10% of experimental measurements.
- To demonstrate the predictive utility of the developed corrosion/oxidation-fatigue model in accelerating the development of new exhaust manifold alloys.

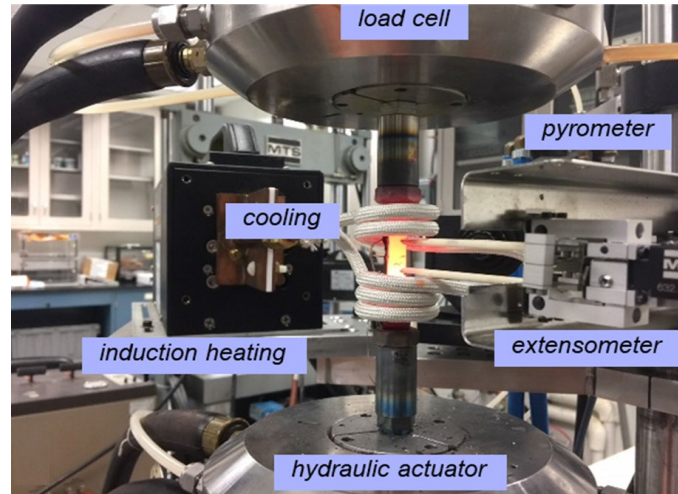
Approach

- Develop a multiscale simulation method that integrates atomistic and mechanistic models to understand the influence of composition, microstructure, and environment on the corrosion/oxidation performance of iron-based materials in combustion gases.
- Validate the corrosion/oxidation performance models using static and thermal cyclic corrosion/oxidation trials in controlled, realistic combustion gases.
- Develop and validate the corrosion/oxidation-fatigue model for exhaust manifold components.
- Demonstrate success of the project by quantifying the acceleration of developing new exhaust manifold alloys with the computational tools.

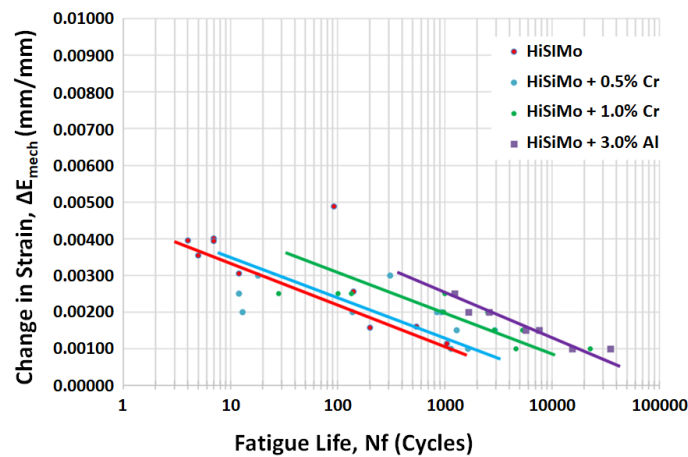
Results

In FY 2021, experimental progresses were made in quantification of the thermomechanical fatigue (TMF) performance of high silicon molybdenum (HiSiMo)-type alloys in ambient environments and understanding the influence of the alloying elements—including chromium (Cr) and Al—on microstructural evolution during TMF testing, which will be used to calibrate corrosion/oxidation-fatigue model. Regarding the corrosion/oxidation performance model, the main efforts were made to integrate density function theory (DFT) and potential energy landscape (PEL) into reactive force field molecular dynamics (ReaxFF MD) [2, 3], in aiming to develop a more robust computational framework that can be used to assess the impacts of alloying elements on oxidation resistance for HiSiMo-type alloys.

The TMF life of HiSiMo-type alloys with alloying of 0.5wt%Cr, 1.0wt%Cr, and 3.0wt%Al were tested using a servo-hydraulic fatigue testing machine with a high-frequency inductive heating device. As described in Figure I.1.1.1(a), the state-of-art TMF machine consists of an inductive heating coil and a cooling fan to generate thermal strain cycles, a servo-hydraulic load cell to create mechanical strain cycles, and a recording unit of extensometer and pyrometer to measure strain and temperature, respectively. The in phase (e.g., temperature peaks are according with load peaks) thermal cycling between 170°C and 800°C was selected because this is the target temperature range for this alloy in-service. The samples were machined and surface-polished before testing to obtain non-oxidized surface conditions. The TMF results are illustrated in Figure I.1.1.1(b). The fatigue life, N_f , was shown to decrease with an increase in strain, ΔE , which is used to represent the maximum strain reached during testing. More importantly, alloying 1 wt% Cr or 3 wt% Al into base HiSiMo alloys can significantly increase the TMF life, following the tendency as HiSiMo+3.0%Al (purple) > HiSiMo+1.0% Cr (green) > HiSiMo+0.5% Cr (blue) > base HiSiMo (red). For instance, the base HiSiMo alloys can only obtain 1000 cycles at total strain level of 0.1%, while the alloys with addition of Cr or Al can achieve 20,000 cycles at the same total strain level. The improved TMF performance of HiSiMo base alloys by addition of Cr or Al can potentially increase the operating temperatures for exhaust manifold application, thus increasing internal combustion engine fuel efficiency.



(a)



(b)

Figure I.1.1.1. (a) Mass changes during cyclic oxidation trials. (b) Oxidation layer structures and thicknesses of static oxidation trials for HiSiMo-type alloys. Source: ORNL and Missouri Science and Technology.

To further understand the mechanism leading to the improved TMF life by the alloying elements, an optical microscope (OM), a scanning electron microscope (SEM), and an energy dispersive spectrometer (EDS) were employed to characterize the samples after TMF testing. First, “elephant skinning” can be observed in the base HiSiMo alloys, while such surface structures are absent in HiSiMo+1.0% Cr, and HiSiMo+3.0% Al, as shown in Figure I.1.1.2. In addition, the examination of fracture surfaces confirms that the cracks always initiate in the swell of the “elephant skinning” surface structures. This indicates that the low TMF life for base HiSiMo alloys are correlated with the formation of those “elephant skinning” surface structures. And then, the longitude sections for the base alloys and the alloys with an addition of Cr or Al were characterized by SEM and EDS to understand the formation mechanism of the “elephant skinning” surface structures. The SEM imaging and EDS mapping of the base HiSiMo with ΔE of 0.15% are shown in Figure I.1.1.2(a). Clearly, the oxidation layer penetrated deeply toward the inner sections of the samples. The deep penetrations of the oxidation layers at those specific locations are mainly caused by the repeated formation and rapture of the brittle oxidation products under both thermal and mechanical strains. After the brittle oxidation products rapture under applied stress, the fresh metals are exposed to oxidation environment again for further oxidation. Eventually, such phenomenon could occur in multiple locations, thus resulting in the formation of “elephant skinning” surface structures. On the other hand, the SEM and EDS results of HiSiMo + 1.0% Cr and HiSiMo +

3.0% Al alloys are also exhibited in Figure I.1.1.2(b) and Figure I.1.1.2(c), respectively. The oxidation layers are much thinner in these two alloys, compared to the base HiSiMo alloys. More importantly, the “elephant skinning” surface structures are absent from those samples and the TMF are thus improved significantly.

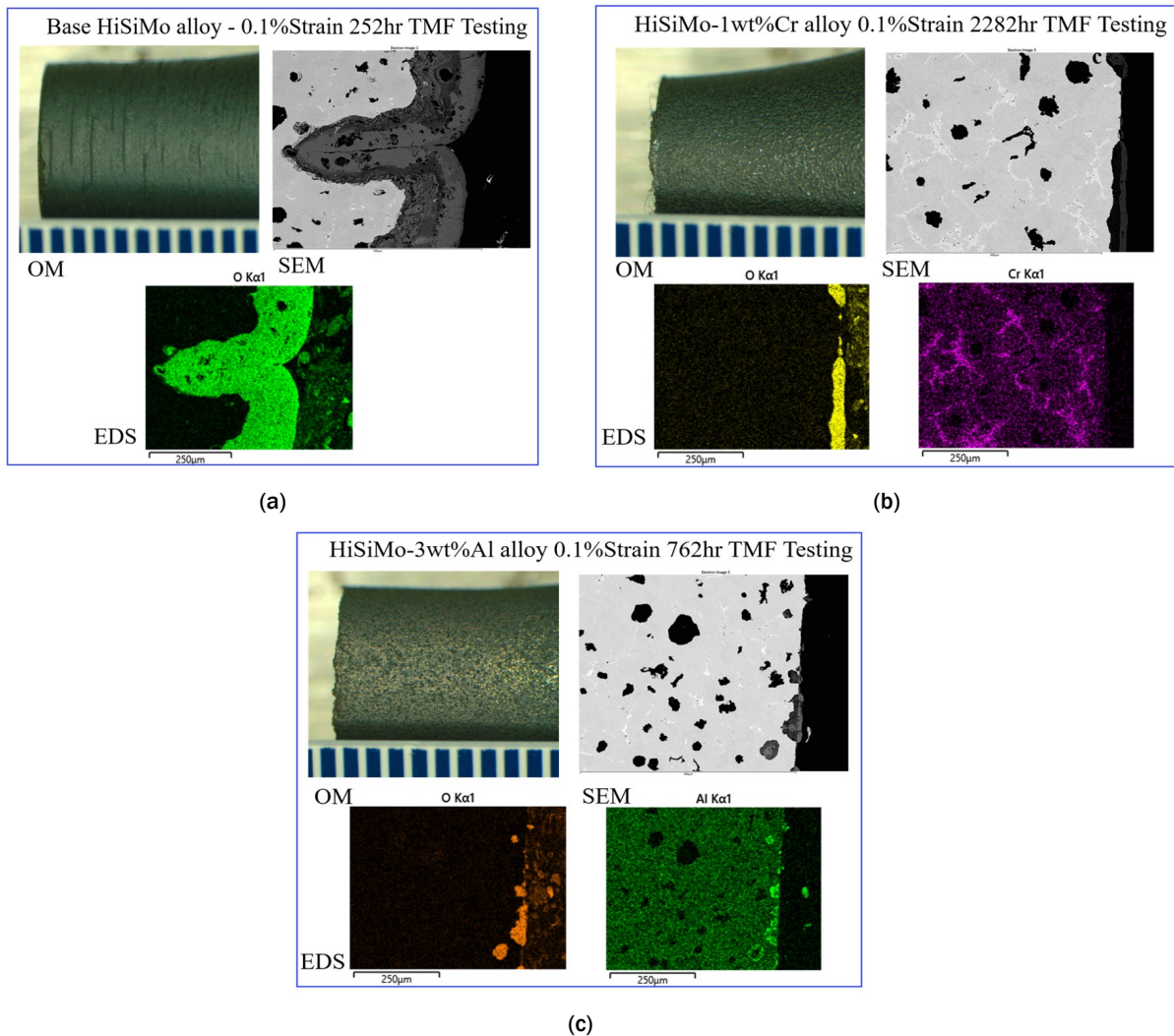


Figure I.1.1.2. OM, SEM, and EDS characterization result of the samples after TMF testing showing that the “elephant skinning” structures with thick oxidation layers observed in (a) base HiSiMo alloys, while absent in (b) HiSiMo+1wt%Cr alloys and (c) HiSiMo+3wt%Al alloys. Source: Ford Motor Company.

High-resolution transmission electron microscopy (HR-TEM) was also used to reveal the evidence that the alloying elements inhibit the “elephant skinning” surface structures. Figure I.1.1.3(a) is a selected HR-TEM image of the interface region between the substrate and scale for HiSiMo + 1 wt% Cr alloy after TMF testing. The substrate was shown and marked on the right-hand side of the image. Adjacent to the substrate is the silicon (Si)-rich oxide layer, which is amorphous according to the fast Fourier transformation analysis shown in Figure I.1.1.3(c). If continuous, this amorphous layer can help inhibit the diffusion of oxygen (O) and perhaps is more effective because there are no grain boundaries like those observed in the adjacent crystalline oxide layers. The crystal structure of the Cr- and manganese (Mn)-rich oxide layers were identified in Figure I.1.1.3(b) and Figure I.1.1.3(d), respectively, with the Cr-rich oxide layer right above the Si-rich oxide layer and the Mn-rich oxide above the Cr-rich oxide. Thus, it is the segregation of Cr likely promotes the formation of the Si amorphous layers.

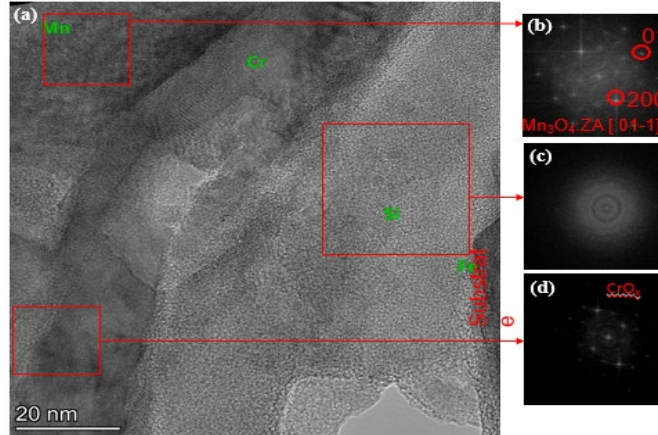


Figure I.1.1.3. Representative HR-TEM images of the layered structure of oxides right above HiSiMo + 1.0 wt% Cr alloy after TMF testing: (a) HR-TEM imaging; and (b)–(d) fast Fourier transformation images of the phases presented in (a). Source: Ford Motor Company.

ReaxFF MD was successfully developed to study the early-stage of the oxidation process for the HiSiMo-type alloys in the exhaust environment. However, the alloys studied in the previous ReaxFF MD simulation are random solid solutions without considering the iron/graphite interfaces and the segregation of alloying elements, which are the most important microstructural features to affect oxidation resistance. As a result, DFT calculations were first performed to assess the energetic properties of iron/graphite interfaces, including the adsorption energy, segregation energy, and interfacial energy, as well as adhesive strength. Some selected results are summarized in Figure I.1.1.4 and Table I.1.1.1. The adhesive strength is defined as the work of separation and represents the amount of energy required to separate an interface into two free surfaces. The results of work of separation for iron/graphite interface with the presence of impurities are shown in Figure I.1.1.4(a). Results indicate that substituting Fe by O, sulfur (S), Si, Al, and Mg could significantly decrease the interface strength, which reduces the interface stability, ultimately resulting in a vulnerable microstructural feature to oxidation species in a corrosive environment. On the other hand, the segregation energy of impurity elements along iron/graphite interfaces are also calculated and plotted in Figure I.1.1.4(b). Indications are that the segregation occurs when the impurity elements' size is smaller or comparable with the host Fe atom. These results will be used to calibrate the force field employed in ReaxFF MD to improve the modeling robustness.

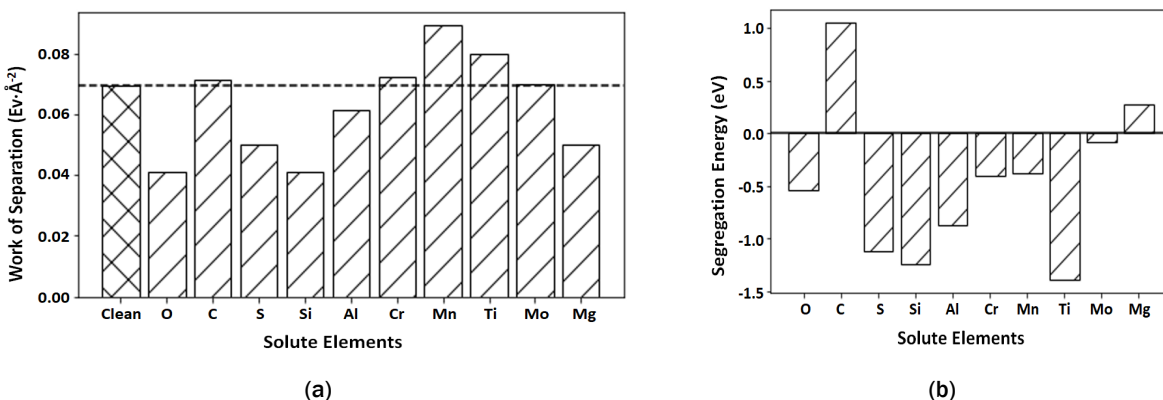


Figure I.1.1.4. Representative DFT calculation results showing (a) the adhesive strength or the interfacial energy of the iron/graphite interfaces with the presence of various impurity elements, as well as (b) the segregation energy of those impurity elements along the iron/graphite interfaces.

Source: The Ohio State University.

Table I.1.1.1. DFT Calculation Results

Trace Elements	$d_{x-c}(\text{\AA})$	$E_{seg}(\text{eV})$	$\Delta W_{adh}(\text{eV}/\text{\AA}^2)$	$E_{int}(\text{eV}/\text{\AA}^2)$
Clean	2.088	-	-	-0.0123
O	2.884	-0.542	0.0284	0.0319
C	3.252	1.048	-0.0020	0.0814
S	2.832	-1.121	0.0192	0.0196
Si	2.811	-1.243	0.0282	0.0372
Al	2.582	-0.872	0.0080	0.0196
Cr	2.14	-0.406	-0.0028	0.0251
Mn	2.089	-0.378	-0.0199	0.0135
Ti	2.215	-1.388	-0.0104	0.0272
Mo	2.25	-0.086	-0.0006	0.0541

Moreover, the PEL method was further developed to study the Cr segregation along grain boundaries (GBs) with consideration of different GB angles. The main objective of this research is to provide more realistic structures with ReaxFF MD simulation to capture the oxidation processes more. The widely used bi-crystal set up protocol [4, 5] was created with incorporating different GB-misorientation angles. An embedded atom method interatomic potential [6] was employed to be compatible with the applied periodic boundary conditions. The initial states of the samples were set as solid solutions by randomly assigning Fe, Cr, and Ni atoms to the lattice sites. A Monte Carlo metropolis algorithm was then applied to explore the thermodynamically favored states that correspond to the stable segregated structures. As shown in Figure I.1.1.5(a), the total energy of the system gradually decreases with the Monte Carlo steps. Eventually, the universal segregations of Cr at GBs are observed in Figure I.1.1.5(b). In addition, the latest results [7] also indicate the energetic and kinetic of Cr segregation can be well predicted by the local electronegativity and free volume of atomic packing, allowing for an expedient alloy design more efficiently. Finally, it is worthy to emphasize the demonstration and implementation of HiSiMo + 1.0 wt% Cr and HiSiMo + 3.0 wt% Al has been initiated for several exhaust manifold components used in HD trucks through collaborations with the tier-1 supplier.

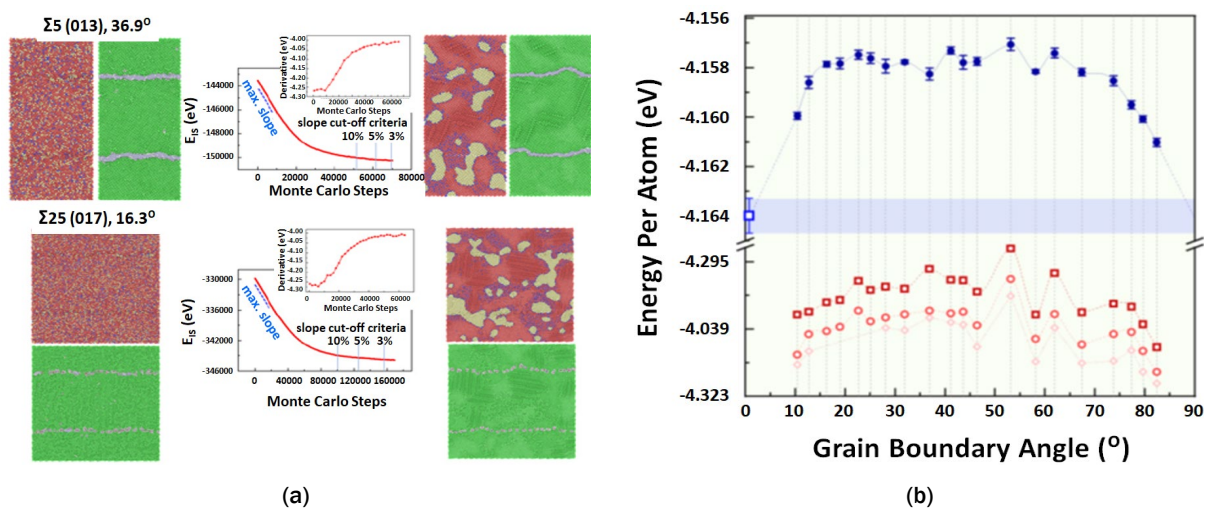


Figure I.1.1.5. DFT calculation results showing (a) the adhesive strength or interfacial energy of the iron/graphite interfaces with presence of various impurity elements, as well as (b) the segregation energy of those impurity elements along the iron/graphite interfaces. Source: University of Michigan.

Conclusions

TMF testing for base HiSiMo alloys, HiSiMo + 0.5 wt% Cr, HiSiMo + 1.0 wt% Cr, and HiSiMo + 3.0 wt% Al was conducted in an ambient environment. Clearly, addition of 1.0 wt% Cr or 3.0 wt% Al can achieve 20 times the improvement in TMF life, as compared to the base HiSiMo alloys. The microstructure characterization using OM and SEM indicate that the “elephant skinning” surface structures are developed in base HiSiMo alloys during TMF testing, which serve as the crack initial site to degrade TMF performance. The additions of Cr or Al can effectively inhibit the formation of “elephant skinning” surface structures by forming Si amorphous layers that can prevent further diffusion of oxidation into the substrates. The demonstration and implementation of HiSiMo + 1.0 wt% Cr and HiSiMo + 3.0 wt% Al alloys is ongoing for several exhaust manifold components.

The DFT calculation was completed to study the energetic properties of the iron/graphite interface with the presence of impurity elements, such as O, Si, Al, Cr, and Mn. The data collected in the DFT calculation can be used to validate the force field employed in the ReaxFF MD simulation to increase the modeling robustness. The PEL method was further developed to provide more realistic segregated structures to ReaxFF MD simulation and to capture the oxidation process more accurately. In addition, by combining with a physics-based machine-learning algorithm, the energetic and kinetic complex chemistries and microstructures can be reasonably predicted with respect to the local electronegativity and atomic packing environment.

Key Publications

1. Kim, Y., and C. Taylor, 2021, “Molecular dynamics of the early-stage of high-temperature corrosion,” *Phys. Rev. Mater.*, Vol. 5, Art. 113402.
2. Wang, Y., B. Ghaffari, C. Taylor, S. Lekakh, M. Li, and Y. Fan, 2021, “Predicting the energetics and kinetics of Cr atoms in Fe-Ni-Cr alloys via physics-based machine-learning,” *Scr. Mater.*, Vol. 205, No. 114177.
3. Zhu, W., B. Pint, Y. Huo, L. Godlewski, B. Ghaffari, S. Lekakh, C. Englar, and M. Li, 2021, “The oxidation on the HiSiMo cast-iron with Cr/Al at 800°C,” submitted to *Oxid. Met.*

References

1. Ekström, M., 2015, “Oxidation and corrosion fatigue aspects of cast exhaust manifolds,” Doctoral dissertation, KTH Royal Institute of Technology, Stockholm, Sweden. Available at: <http://kth.diva-portal.org/smash/get/diva2:810259/FULLTEXT01.pdf> (last accessed 13 December 2021).
2. Zou, C., Y. K. Shin, A. C. T. van Duin, H. Fang, and Z.-K. Liu, 2015, “Molecular dynamics simulations of the effects of vacancies on nickel self-diffusion, oxygen diffusion and oxidation initiation in nickel, using the ReaxFF reactive force field,” *Acta Mater.*, Vol. 83, pp. 102–112.
3. Shin, Y. K., H. Kwak, A. V. Vasenkov, D. Sengupta, and A. C. T. van Duin, 2015, “Development of a ReaxFF reactive force field for Fe/Cr/O/S and application to oxidation of butane over a pyrite-covered Cr₂O₃ catalyst,” *ACS Catal.*, Vol. 5, No. 12, pp. 7226–7236.
4. Tschopp, M., S. Coleman, and D. McDowell, 2015, “Symmetric and asymmetric tilt grain boundary structure and energy in Cu and Al (and transferability to other fcc metals),” *Integr. Mater. Manuf. Innov.*, Vol. 4, pp. 176–189.
5. Bai, Z., G. H. Balbus, D. S. Gianola, and Y. Fan, 2020, “Mapping the kinetic evolution of metastable grain boundaries under non-equilibrium processing,” *Acta Mater.*, Vol. 200, pp. 328–337.
6. Bonny, G., N. Castin, and D. Terentyev, 2013, “Interatomic potential for studying aging under irradiation in stainless steels: The Fe-Ni-Cr model alloy,” *Model. Simul. Mat. Sci. Eng.*, Vol. 21, No. 8, Art. 085004.
7. Wang, Y., B. Ghaffari, C. Taylor, S. Lekakh, M. Li, and Y. Fan, 2021, “Predicting the energetics and kinetics of Cr atoms in Fe-Ni-Cr alloys via physics-based machine-learning,” *Scr. Mater.*, Vol. 205, Art. 114177.

I.1.2 Multiscale Development and Validation of the Stainless-Steel Alloy Corrosion (SStAC) Tool for High-Temperature Engine Materials (University of Florida)

Michael Tonks, Principal Investigator

University of Florida
158 Rhines Hall
Gainesville, FL 32611
E-mail: michael.tonks@ufl.edu

Jerry L. Gibbs, DOE Technology Manager

U.S. Department of Energy
E-mail: jerry.gibbs@ee.doe.gov

Start Date: October 1, 2018	End Date: February 28, 2022	
Project Funding (FY 2021): \$617,474	DOE share: \$492,474	Non-DOE share: \$125,000

Project Introduction

The environment within an engine cylinder during operation is extremely harsh, with high temperatures, combustion, and corrosive exhaust gases. This environment corrodes engine components, including exhaust valves and exhaust valve seats. Current engine materials, such as stainless steels, resist corrosion during normal operation. However, as new engines are pushed to higher temperatures, the material can undergo microstructure evolution that sensitizes the material to corrosion, resulting in premature failure.

Companies that design and build engine parts do not typically employ models of corrosion; rather, they employ standard temperature ranges and allowable fuels for which each alloy can be employed when making material selection decisions for a specific part and customer. These standards are based on conservative physical properties of the alloy and on successful deployment history. This reliance on conservative standards can result in over-design and increased cost. In addition, if a new advanced engine design results in conditions significantly different from the deployment history, these standards may not be applicable. This can lead to a vastly increased time and cost of development.

Objectives

The goal of this project is to create a simulation tool to assist in part design, reducing costs by eliminating the need for conservative material selection, and enabling alloy optimization to improve corrosion resistance. Thus, it will help reduce costs for existing engines and will assist in the material selection and engine design for the engines of the future, reducing development time by years. To meet our stated goal, we have developed the SStAC tool, which:

- Can model corrosion of valve steels in an engine environment at temperatures up to 800°C.
- Can simulate the corrosion of an engine valve in one dimension (1D) for a fast estimate of the corrosion rate and in two dimensions (2D) and three dimensions (3D) for more detailed simulations that represent the valve geometry and predict the precise location and rate of corrosion.
- Was implemented using the Multiphysics Object-Oriented Simulation Environment (MOOSE).
- Includes a corrosion model that is being developed to describe the fundamental mechanisms of corrosion, including the impact of microstructure and alloy composition.

At the completion of the project, the SStAC tool will be able to predict the corrosion rate of engine valves with no more than 10% error.

Approach

The SStAC tool is being developed using a combination of macro-scale model development, meso-scale, and atomic-scale simulations to define the impact of microstructure on alloy corrosion and an experimental campaign to inform and validate the models. This work is being carried out during three budget periods (BPs). BP1 ended in February 2021 and our primary focus was the development of an initial corrosion model. BP2 ended in February 2021 and focused on the creation of the SStAC tool using the MOOSE framework. BP3 began in March 2021 and encompassed the completion and preliminary validation of the SStAC tool. The tasks for BP3 were:

- **Task 3.1 – Third Experimental Campaign:** Additional separate effects corrosion tests were carried out and the samples characterized to determine the effect of water-vapor and thermal cycling. Corroded valves from engine tests were characterized.
- **Task 3.2 – Validate and Apply the Meso-scale Model:** Atomic-scale simulations calculated that additional material properties also were needed for the meso-scale model and the SStAC tool. The meso-scale corrosion model was validated and then applied to obtain the microstructure-sensitive parameters needed by the macro-scale corrosion model in the SStAC tool.
- **Task 3.3 – Validation and Release of the SStAC Tool:** The SStAC tool was completed, incorporating all the information from the lower length scale simulations. Its predictions were validated and then it was released on GitHub.com.

Results

Task 3.1 – Third Experimental Campaign

Samples of 21-2N and 23-8N valve steel alloys, which primarily vary in their Mn, Cr, and Ni compositions, were exposed to a mixed water-vapor and carbon dioxide (CO₂) gas, with a 50/50 volume ratio, at atmospheric pressure at 700°C, and time-lapse corrosion data were collected. Samples were characterized before and after corrosion by various techniques, such as SEM, scanning transmission electron microscopy (STEM), and EDS. The composition of these two alloys is presented in Table I.1.2.1.

Table I.1.2.1. Chemical Composition of the Two Different Alloys 21-2N and 23-8N Studied in Weight-Percent (wt%) With Fe in Balance

	Cr	Mn	Ni	C	Mo	Si
21-2N	20.25	8.5	2.13	0.55	0.5	0.25
23-8N	23	1.5	8	0.38	0.5	1

The studied samples were removed from the furnace after 50, 150, 346, 500, and 800 hours. Oxidation kinetics of the mixed water-vapor experiment were compared to the one obtained from samples previously corroded in dry CO₂, as shown in Figure I.1.2.1. Both the 21-2N and 23-8N alloys showed a significant increase in weight gain in water-vapor/CO₂ atmosphere ~ 10 times higher than in a dry CO₂ atmosphere. Also, the samples after removal from the furnace showed some powder particles on the surface, which is a sign of spallation, indicating even higher oxidation kinetics than the ones reported in Figure I.1.2.1. Similar to the behavior in a dry CO₂ atmosphere, the 21-2N weight gain was lower than that of the 23-8N alloy. In this study, we focused on characterizing the 21-2N Mn alloy to obtain more information about the oxide composition and thickness by using cross-sectional SEM-EDS characterization and TEM-EDS. Figure I.1.2.2(a) shows a cross-sectional SEM micrograph of the 21-2N corroded up to 50 hours in CO₂-H₂O at 700°C. Elemental composition of the area in Figure I.1.2.2(a) was completed by EDS maps, as shown in Figure I.1.2.2(b). The EDS maps show the formation of an outer MnFe oxide scale, a CrMn oxide at the scale/alloy interface, and a depletion region of Mn in the substrate ahead of the oxide. For comparison, previous data on the same alloy exposed to dry CO₂ for the same time and temperature are shown in Figure I.1.2.2(c) and (d). The oxide thickness is clearly higher in mixed water-vapor/CO₂ environment than in dry CO₂, and a notable difference is that the oxide contains Fe.

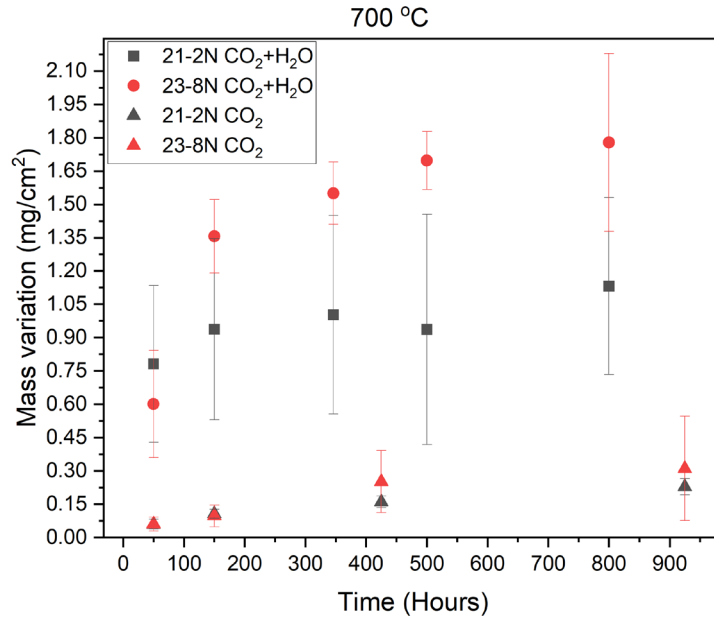


Figure I.1.2.1. Mass variation changes in the 23-8N and 21-2N alloys corroded in water-vapor/CO₂ mixed atmosphere compared to those corroded in pure atmospheric CO₂ at 700 °C for up to 925 hours.
 Source: University of Wisconsin–Madison.

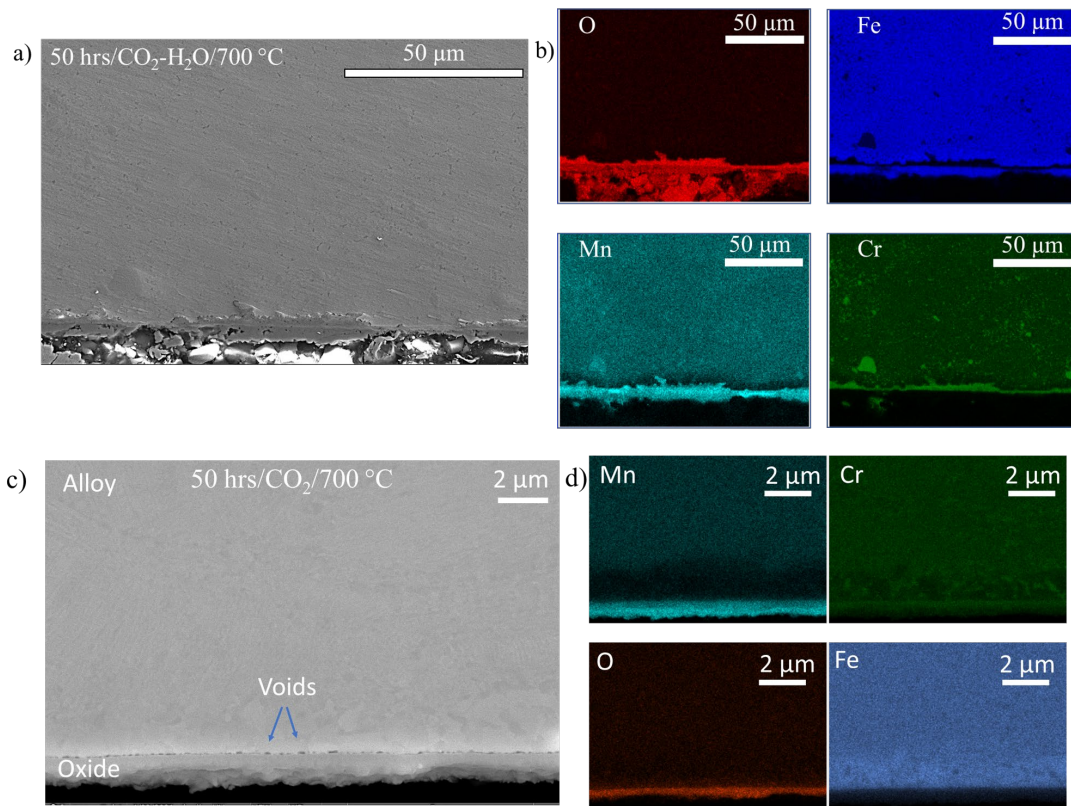


Figure I.1.2.2. SEM-EDS cross-sectional characterization of 21-2N samples corroded at 700 °C for 50 hours. Low magnification SEM micrographs are shown in (a) for the water-vapor/CO₂ atmosphere and in (c) for dry CO₂. EDS maps for Fe, Mn, Cr and O and C are shown in (b) for water-vapor/CO₂ and in (d) for dry CO₂.
 Source: University of Wisconsin–Madison.

To obtain a detailed examination of the oxide scale formation, STEM-EDS analysis was completed on a $20 \times 20 \mu\text{m}$ lamellae. Figure I.1.2.3(a) shows the STEM micrograph of the 21-2N corroded in water-vapor/ CO_2 at 700°C for 50 hours. In this figure, voids are located inside the oxide layer, as well as at the scale/alloy interface, with a possible crack detected inside the oxide scale. The outer scale is composed of large grains that are identified by EDS maps in Figure I.1.2.3(b) as FeMn oxide. The EDS maps also show the transition between the FeMn oxide and MnCr oxide at the scale/alloy interface. Further analysis is being performed to understand the oxide scale formation mechanism and its main difference compared to a dry CO_2 environment. Again, for comparison, previous data collected on the same alloy exposed to dry CO_2 for the same time and temperature is shown in Figure I.1.2.3(c) and Figure I.1.2.3(d).

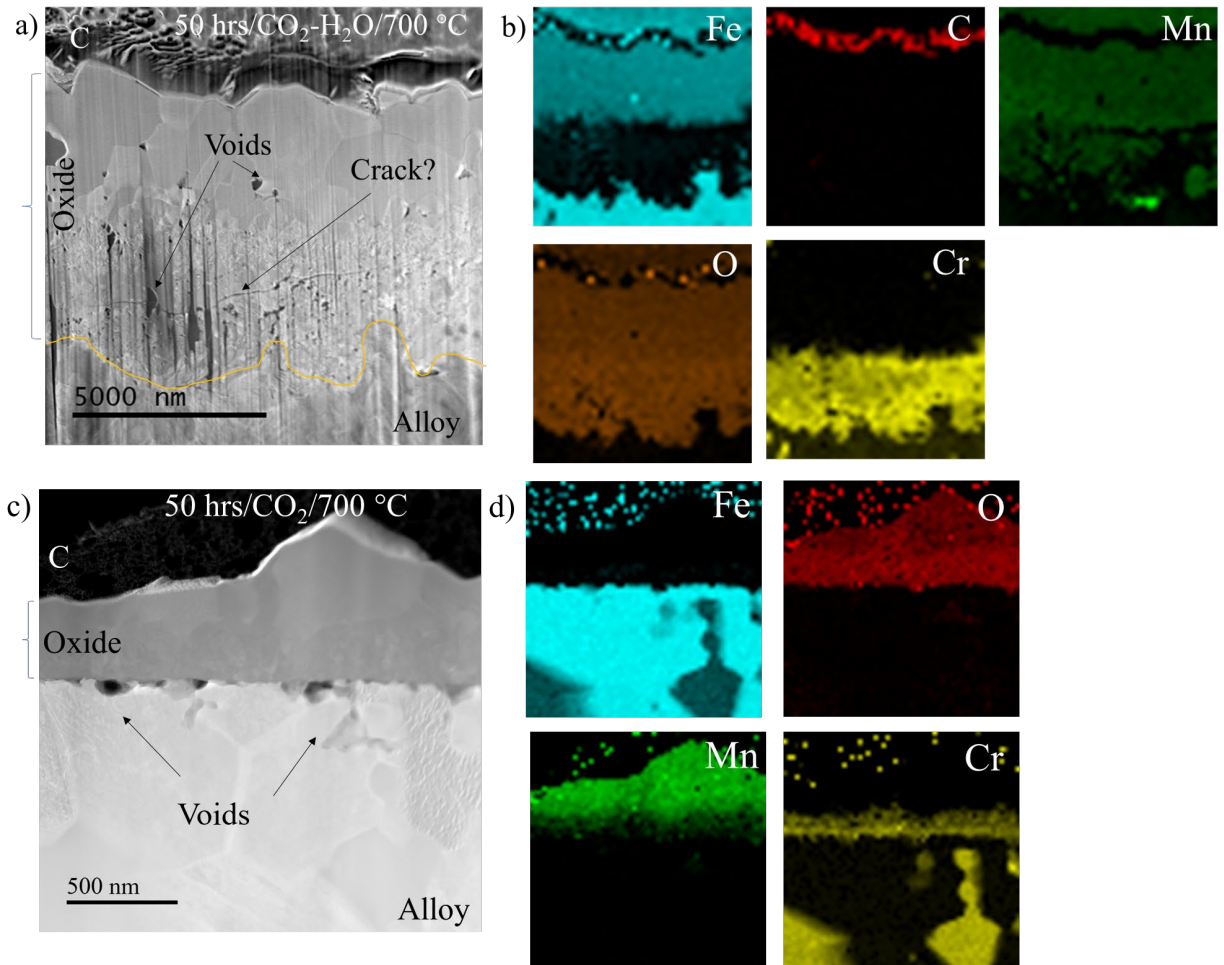


Figure I.1.2.3. STEM-EDS micrograph of the 21-2N samples corroded at 700°C for 50 hours in (a) water-vapor/ CO_2 and in (c) dry CO_2 . The EDS maps for C, Mn, Cr, Fe, and O in (b) water-vapor/ CO_2 and (d) dry CO_2 . Source: University of Wisconsin–Madison.

Component-level validation of the SStAC-based simulation tools will require engine testing of valves manufactured from the stainless-steel alloys under investigation. The platform chosen for this purpose, a General Motors (GM) turbocharged 2.0-liter four-cylinder gasoline engine, is in pre-operation checks in a dynamometer cell at Tenneco's Plymouth Technical Center, as observed in Figure I.1.2.4. This engine provides a unique capability to expose the valves to a particularly extreme environment owing to its performance capabilities and high-power density in a single-cylinder bank architecture. Calibrations of the engine control module are in progress. Valves composed of the 21-2N and 23-8N alloys that are being studied in laboratory-scale testing will be confirmed by Tenneco. Dedicated temperature check runs will follow

finalization of the engine control module calibration to map the thermal profiles in individual valves, which will be required for validation of the SStAC tool. Engine runs will follow a “split test” approach, in which each test cylinder head will be populated with valves of the different materials rather than a specific material for each engine operating cycle since the demanding nature of the durability tests will require several fully assembled engine blocks and numerous replacement cylinder heads over the course of the tests.



Figure I.1.2.4. The GM 2.0L turbo platform being utilized for component-level validation mounted to a dynamometer in Cell 14 at the Plymouth Technical Center. Source: Tenneco, Inc.

Task 3.2 – Validate and Apply the Meso-scale Model

Meso-scale Model Development

A phase-field corrosion model has been developed to simulate the formation of multiple oxide phases in valve steel in oxygen at 700°C, which has been implemented using the finite element method in MOOSE. The model includes five phases—including an alloy phase, three oxide phases, and a gas phase—and five components—including Fe, Cr, Mn, oxygen, and metal vacancies—and is based on the Kim-Kim-Suzuki (KKS) approach [1]. The three oxide phases are MnCr_2O_4 , Cr_2O_3 , and Mn_3O_4 , based on the dry CO_2 lab testing results. The Gibbs energies were modeled using a CALculation of PHase Diagram (CALPHAD) approach. Specifically, the sub-regular solution model, compound energy formulation, and Van der Waals Helmholtz energy model with a polynomial approximation were used for approximating the phase energies of the alloy, oxide, and gas phase, respectively. The diffusion mobilities were calculated through an interdiffusion mobility equation in a fixed-volume frame, which is related to the atomic mobilities of the different elements, and therefore is also related to tracer diffusivities available from the literature [2]. Since the diffusion mobility values are drastically different between components, a few approximations were made to benefit the simulation convergence. For example, the larger mobilities were reduced to only two orders of magnitude higher than the smaller mobilities without significantly impacting the results because the corrosion rate is limited by the smaller mobilities.

Since the oxygen mobilities in the oxides were not available in the literature, two corrosion simulation results with different oxygen mobilities (M_o) were performed to investigate its impact. In the fast diffusion case, the oxygen mobility M_o was set equal to the smallest metal component mobility; in the slow case, it was 0.2 times the fast M_o . The simulations were run in a 2.8 μm long 1D domain with an initial layer of each oxide and a larger layer of metal on the far left and of the gaseous environment on the far-right. The initial sizes of each layer, as well as the boundary conditions, are shown in Figure I.1.2.5(a). The simulations were run until all the metal was consumed by the oxide growth.

Left boundary condition:

$$\eta_{alloy} = 1$$

$$\mu_{Fe} = -59.26 \text{ eV nm}^3$$

$$\mu_{Mn} = -82.80 \text{ eV nm}^3$$

$$\mu_{Cr} = -55.06 \text{ eV nm}^3$$

$$\mu_{oxygen} = -128.94 \text{ eV nm}^3$$

Right boundary condition:

$$\eta_{gas} = 1$$

$$\mu_{oxygen} = 0 \text{ eV nm}^3$$

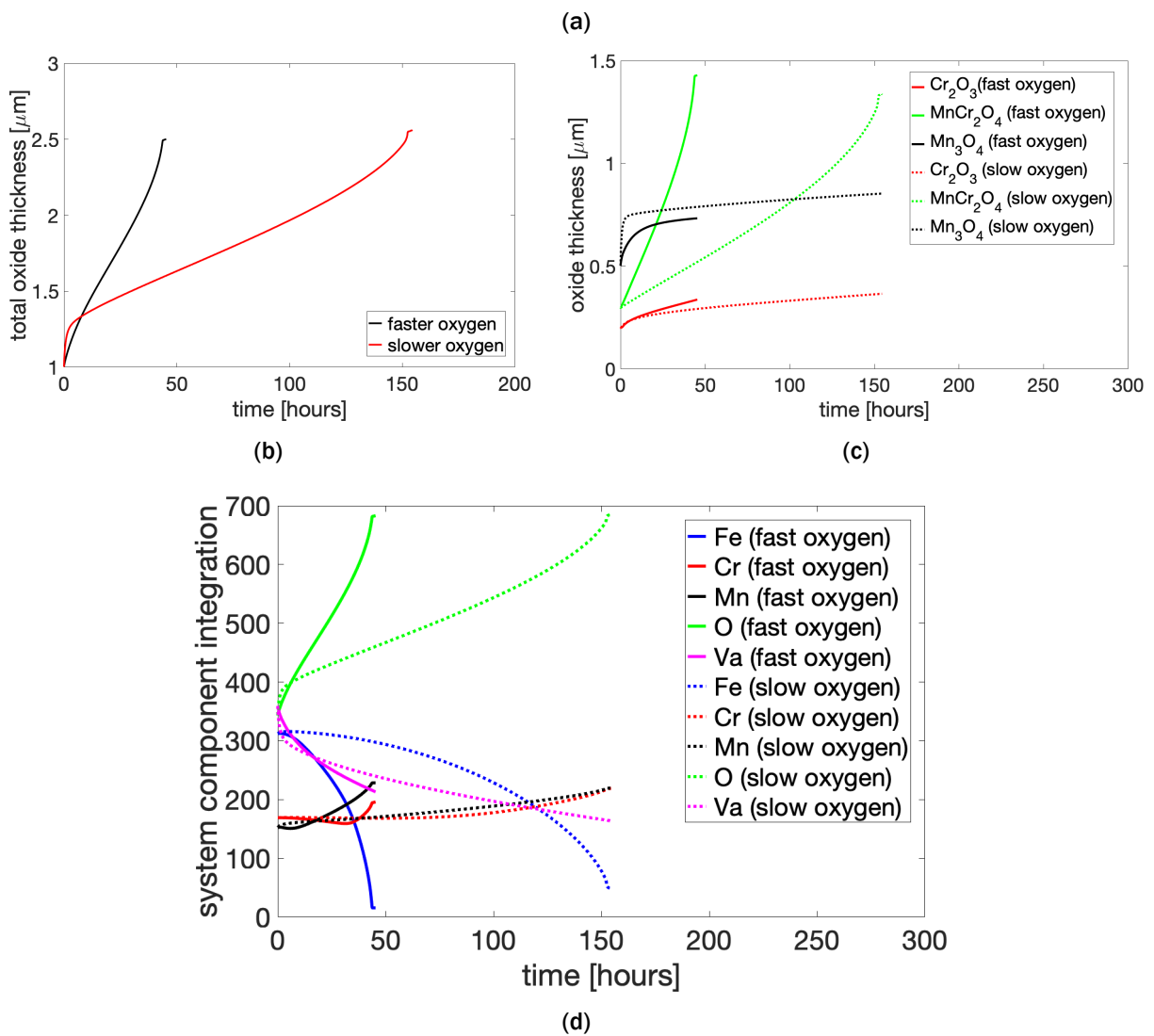
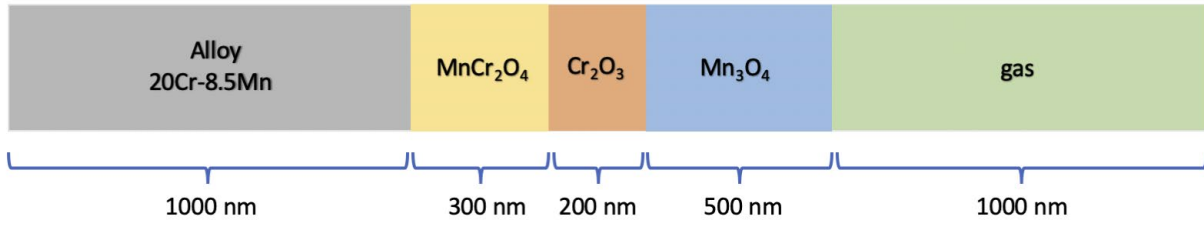


Figure I.1.2.5. Simulation of oxidation using the meso-scale model in a 1D domain with fast or slow oxygen mobility: (a) the domain, initial conditions, and boundary conditions; (b) the thickness of the three oxide phases with time; (c) the integral of the component concentrations across the 1D domain—similar to the total amount in the entire domain—with time; and (d) total oxide thickness with time. Source: University of Florida.

The results from the two cases are also shown in Figure I.1.2.5. The metal was consumed around three times faster with the fast oxygen mobility than with the slow mobility, as observed in Figure I.1.2.5(b), resulting in much faster oxide growth, though the final oxide thickness was nearly the same in the two cases. The relative growth of the different oxide layers, shown in Figure I.1.2.5(c), varied somewhat in the two cases; the MnCr_2O_4 and Cr_2O_3 layers were thicker with the fast oxygen mobility, while the Mn_3O_4 layer was thinner. To quantify the total amount of the different components in the system, we integrated them across the length and plotted the results versus time, as shown in Figure I.1.2.5(d). Since the boundary conditions were open, the compositions changed with time. Irrespective of the O mobility, O, Mn, and Cr entered the system and Fe and vacancies left the system. The total amount of all components changed faster with the faster O mobility. The final amount of O and Mn in the system were the same in the two cases. The total amount of Cr and Fe were smaller with the fast O mobility and the total amount of vacancies was larger. Thus, the O mobility has a large impact on the oxide growth kinetics, but it also changes the final oxide composition.

In addition, a new KKS model solving approach was developed in the MOOSE framework to reduce the computational cost of the meso-scale simulations. This approach removes the phase concentration variables from the nonlinear variable vector, and instead solves them locally at each quadrature point. The local solve approach has been shown to decrease the simulation wall time, the degrees of freedom of the system, and the memory usage compared with the standard approach for solving the KKS model in MOOSE.

Atomic-Scale Development

During FY 2021, the atomistic calculation campaign has produced valuable defect formation and migration energy values required to predict the growth rates of each phase in the oxide film. Collaboration with the experimental team has resulted in a refined understanding of the composition of this oxide film enabling more in-depth analysis. A significant extension from past results has been the inclusion of charge effects when evaluating migration and formation energies in oxide systems.

Figure I.1.2.6 depicts the energy barriers of the most favorable diffusion pathways for cation vacancies in the MnCr_2O_4 spinel layer. The 2^+ and 3^+ charge states on the defects were chosen for this analysis following an exhaustive set of calculations to evaluate the defect transition levels associated with each vacancy. It was determined that both Mn and Cr vacancies are more favorable in these charge states relative to the neutral state near the conduction edge of the band gap. The effect of charge on Cr vacancy migration is small—on the order of meV. However, for the case of Mn, the difference in barrier height between the neutral and charged states is as much as 0.2 eV. Additionally, Figure I.1.2.6 shows that the migration of Mn is significantly more favorable than Cr. Combining this information with prior knowledge that the formation energies for these defects are similar, we can conclude that Mn is the more mobile cation in the spinel phase.

Table I.1.2.2 and Table I.1.2.3, respectively, enumerate the vacancy formation and cation substitution energies of all phases observed by the experimental Glow Discharge Optical Emission Spectroscopy (GDOES) measurements on the 21-2N samples. The general trend across all oxides favors the formation of cation vacancies relative to the oxygen vacancies, except for Fe_2O_3 . The most readily formed cation vacancy is Mn in the outer Mn_3O_4 oxide, which is in-line with the experimental observations that show the Mn_3O_4 phase being consumed at the expense of the intermediate MnCr_2O_4 spinel phase as corrosion proceeds. Having established a trend of cation vacancy favorability, substitution energies mediated by such defects can provide valuable information regarding the interphase mobility of each species. Table I.1.2.3 shows that the energy cost of substituting Cr onto a tetrahedral site that would typically be occupied by Mn in the MnCr_2O_4 phase is very low. This finding suggests that MnCr_2O_4 can sustain an excess amount of Cr migrating from the bulk alloy. Experimentally, the MnCr_2O_4 phase is observed to form in contact with the bulk alloy and just below the Cr_2O_3 . This indicates that it is reasonable for the Cr_2O_3 phase to form after MnCr_2O_4 as the Cr can leave the bulk alloy and migrate directly through the spinel.

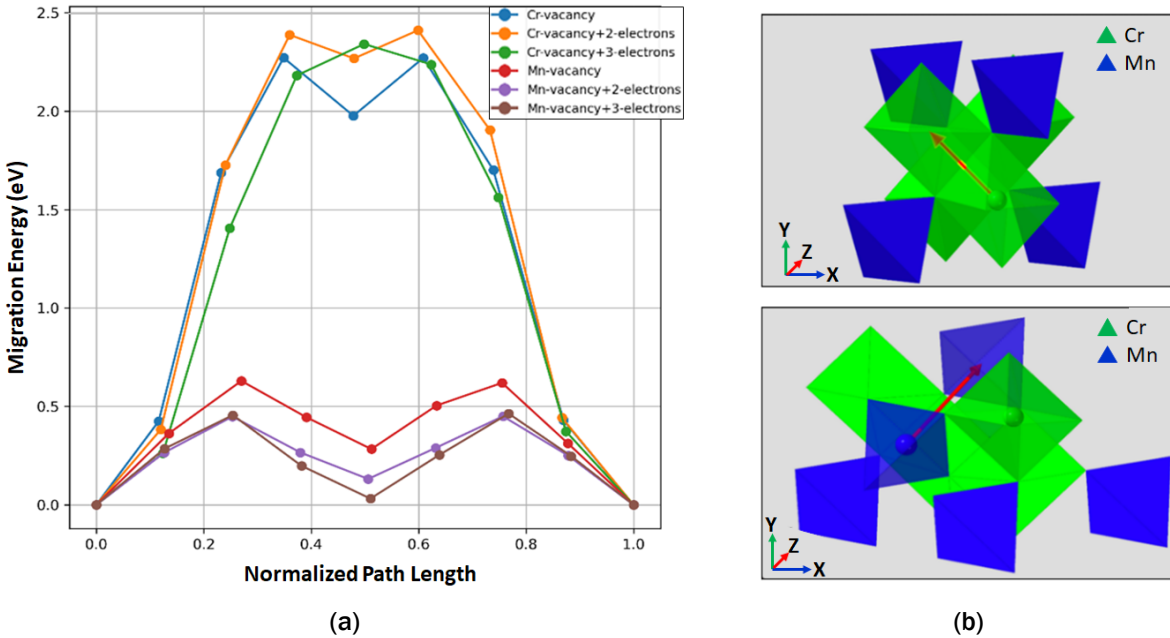


Figure I.1.2.6. (a) Migration energy barriers for neutral and charged cation vacancies in MnCr₂O₄. (b) Illustration of the Cr vacancy migration pathway (top) and illustration of the Mn vacancy migration pathway (bottom). Source: University of Florida.

Table I.1.2.2. Vacancy Formation Energy of Each Species *i* in the Oxide Film Reported in eV

	Mn	Cr	O	Fe
Mn ₃ O ₄	2.68	-	-	7.03
Cr ₂ O ₃	-	4.44	-	5.63
Fe ₂ O ₃	-	-	3.61	3.24
MnCr ₂ O ₄	3.52	3.91	-	5.45
Alloy	1.52	1.18	1.36	-

Table I.1.2.3. Cation Substitution Energy of Each Species in the Oxide Film Reported in eV

	Mn	Cr	Fe
Mn ₃ O ₄	-	1.17	1.80
Cr ₂ O ₃	1.99	-	2.07
MnCr ₂ O ₄ (Mn)	-	1.01	2.84
MnCr ₂ O ₄ (Cr)	1.80	-	1.97

Task 3.3 – Validation and Release of the SStAC Tool

The Coupled-Current Charge Compensation corrosion model was adapted for the corrosion of steel 21-2N. The model was developed for the corrosion in a CO₂ atmosphere using external experimental data. The oxide was modeled as an outward-growing, double-layered MnCr₂O₄-Mn₃O₄ scale with its growth limited by the diffusion of Cr and Mn from the alloy to the oxide/metal interface. The parametrization of the model was done by fitting the GDOES Cr and Mn diffusion profiles in the alloy. Decreasing diffusion coefficients were found to best fit the experimental data. This decrease is likely due to grain growth in the alloy.

Two methodologies were implemented in the SStAC tool to predict oxide layer growth. In the first approach, the model is based on the diffusion of species in the alloy—from bulk to the oxide/metal interface—and does not explicitly represent the oxide layer. Consequently, no moving interface was modeled, and the extended finite element method (X-FEM) was not used. The model can run in 1D, 2D, and 3D for non-planar interfaces. The Cr and Mn diffusion profiles were solved independently, and oxide thicknesses and weight gain can be estimated from their values. Using the parameters obtained by fitting the experimental diffusion profiles in the metal, the model yields oxidation kinetics in terms of oxide thickness and weight gain, as shown in Figure I.1.2.7, which are in good agreement with the experimental values. The formation of a body-centered cubic (BCC) phase resulting from Mn depletion in the underlying substrate can also be predicted by the model. As the BCC phase is believed to be more brittle, this gives valuable insight to predict the valve's mechanical behavior.

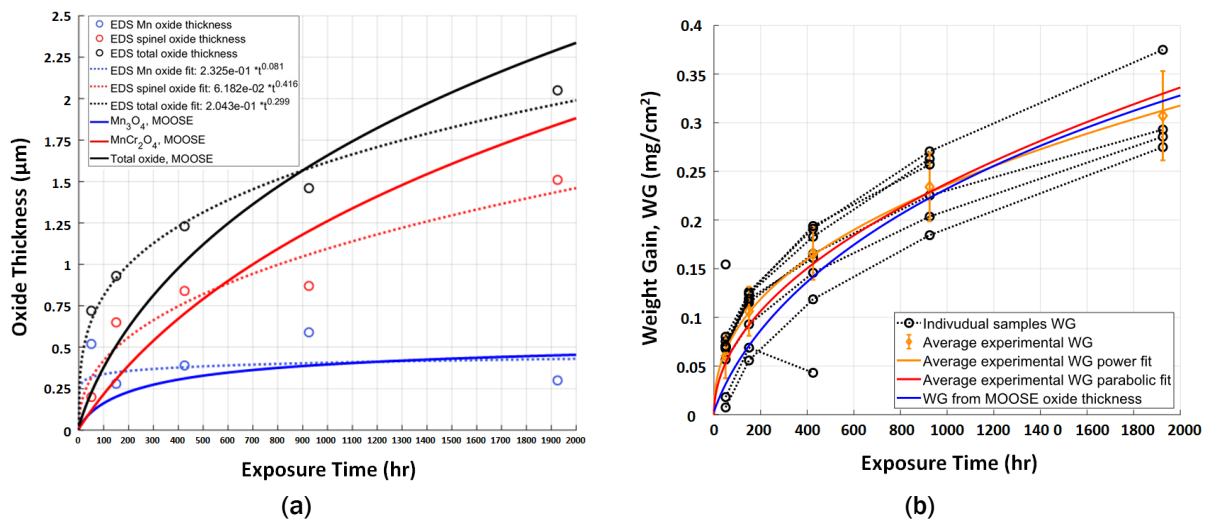


Figure I.1.2.7. 2D simulation results showing (a) the Mn concentration profile in the metal (blue) and in the oxide (red) and (b) the Mn concentration profile near the oxide/metal interface along the white line shown in (a). Source: University of Wisconsin–Madison.

In the second approach, the growth of the oxide layer is explicitly modeled with X-FEM. This approach provides the ability to couple with mechanics for studying how oxidation impacts mechanical properties under a corrosion environment. A new capability of modeling curved moving interface with X-FEM was developed in MOOSE that uses a lower-dimensional mesh to represent the material interface. The interface velocity is computed to update the interface using the solutions of the temperature and concentration extracted from the interface. To model the outward oxide growth, the mesh needs to be artificially extended on the exterior of the domain to leave some space for the oxide to grow into it. Figure I.1.2.8 demonstrates the modeling of the oxide growth with the X-FEM in a 2D axisymmetric valve model.

Ongoing work is focused on the coupling of thermal and diffusion to predict corrosion kinetics for realistic valve geometries. Documentation and examples also will be added before the final release.

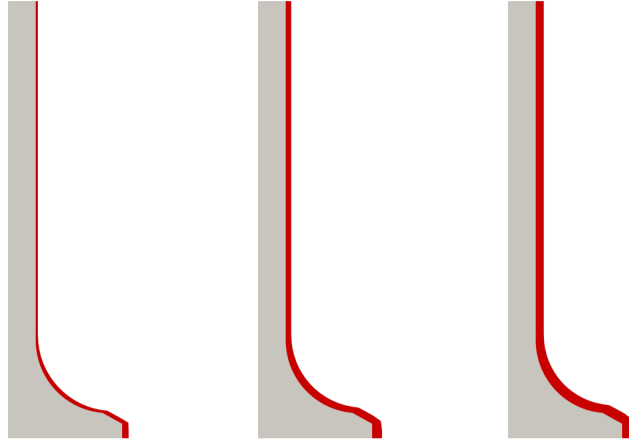


Figure I.1.2.8. Modeling the oxide (shown in red) growth with X-FEM in a 2-D axisymmetric valve model. A constant interface velocity is uniformly applied at the exterior surface of the valve.
Source: Idaho National Laboratory.

Conclusions

The overall objective of this project is to develop the SStAC tool for predicting the corrosion of 21-2N and 23-8N stainless-steel engine valves during engine operation. In BP3, testing was completed in a water-vapor/ CO_2 environment and the samples were characterized. These results have shown that corrosion is much faster with water-vapor than in dry CO_2 , and that Fe is present in the oxide, while it is not in dry CO_2 . The meso-scale oxidation model is being used to explore the impact of the kinetics of the various constituents on oxide formation. In addition, an alternative phase-field approach that is more computationally efficient is under development. Atomic-scale simulations have obtained formation and substitution energies of various constituents in the different oxide phases, provide insight into the behavior observed in the experiments. Two different approaches are available for modeling the oxide growth in 1D, 2D, and 3D in the SStAC tool—modeling just the metal transport and then estimating the oxide thickness and weight gain or directly modeling the oxide growth using X-FEM.

References

1. Kim, S. G., W. T. Kim, and T. Suzuki, 1999, “Phase-field model for binary alloys,” *Phys. Rev. E.*, Vol. 60, pp. 7186–7197.
2. N. Moelans, M., 2011, “A quantitative and thermodynamically consistent phase-field interpolation function for multi-phase systems,” *Acta Mater.*, Vol. 59, pp. 1077–1086.

Acknowledgments

All the work summarized in this report is due to the hard work of our research team composed of members from the University of Florida, University of Wisconsin–Madison, Tenneco, and Idaho National Laboratory.

I.2 Automotive Metals

I.2.1 Metal Matrix Composite Brakes Using Titanium Diboride (Pacific Northwest National Laboratory)

Glenn Grant, Principal Investigator

Pacific Northwest National Laboratory
902 Battelle Blvd.
Richland, WA 99352
E-mail: glenn.grant@pnnl.gov

Mert Efe, Co-Principal Investigator

Pacific Northwest National Laboratory
902 Battelle Blvd.
Richland, WA 99352
E-mail: mert.ef@pnnl.gov

Jerry L. Gibbs, DOE Technology Manager

U.S. Department of Energy
E-mail: jerry.gibbs@ee.doe.gov

Start Date: September 1, 2017	End Date: June 30, 2021	
Project Funding (FY 2021): \$660,800	DOE share: \$300,000	Non-DOE share: \$360,800

Project Introduction

There is currently no viable, cost-competitive alternative to cast-Fe brake rotors for the automotive market. While in past years, many weight-savings materials and designs have come to other parts of a vehicle, the brake assembly remains tied to near fifty-year-old technology, as observed in Figure I.2.1.1. Metal matrix composites (MMCs) present an opportunity to replace cast-Fe brakes in certain vehicles. By replacing cast-Fe rotors with lighter weight MMCs, the opportunity exists to reduce the unsprung weight of the brake assembly and adjacent components, such as the suspension arms and springs. A 50% savings in mass in a rotating and unsprung location can lead to a 0.25 mpg – 0.35 mpg fuel savings in a mid-sized internal combustion engine car or a 3 mile – 5-mile range increase in a 2-ton 400-mile range electric vehicle. In addition, Al-MMC brakes can offer lower wear rates. Lower wear also means fewer wear particles are generated during braking. These wear particles are the second largest source of particulate emissions from a vehicle. A recent report from the United Kingdom’s Air Quality Expert Group indicates that particles from brake wear, tire wear, and road surface wear currently constitute 60% and 73% (by mass), respectively, of primary PM_{2.5} and PM₁₀ emissions from road transport [1].

Barriers to more widespread use of MMCs for vehicle lightweighting are: (1) the costs of the feedstock, especially the insoluble reinforcement (e.g., particle, whisker, fiber) that is usually silicon carbide (SiC); (2) the cost of combining the reinforcement with the matrix in production, which requires cost and effort to insure the SiC particles are “sized” or coated correctly to promote wetting in molten Al; and (3) the cost of shaping/machining MMC components. One of the concepts to address the barriers above is to develop an alternative reinforcing particle. Titanium diboride (TiB₂) reinforcement offers an opportunity to improve wear resistance at a lower particle loading because of the improved ceramic–Al bonding. SiC reinforcement is costly when prepared for inclusion in an Al composite (e.g., particle size fraction constraints, SiO₂ coating, etc.). TiB₂ has much improved wetting with Al allowing for finer particle size and better homogeneity, and may prove to have a lower-cost overall due to lower particle loading required and reduced compositing time for the same friction and wear performance.



Figure I.2.1.1. Conventional brake design utilizing an Al caliper and a cast-Fe brake disc. Source: PNNL.

Recent improvements by Arconic to the TiB_2 production process may make it a more viable technical ceramic for MMCs than in the past. This LightMAT-funded project will utilize TiB_2 as a substitute for more traditional MMC efforts using SiC in an effort to improve performance, wear life, and cost in brake rotors.

Objectives

The objective of the project is to reduce the weight of brake rotors by $>50\%$ over the current cast-Fe materials and at the same time, improve brake performance, wear life, and life cycle cost over cast-Fe systems. The project will develop an Al-MMC material that shows the appropriate wear resistance, friction coefficient, and tribologic properties, as well as the potential for a cost/benefit ratio appropriate for commercial development.

Approach

The project proceeds through six tasks. The first five tasks were completed in previous years. As a part of the five tasks, A356- TiB_2 composites were produced by stir-casting. The stir-cast plates were then hot-rolled and aged to optimize the microstructure and minimize the porosity. Disk-shaped brake rotors were machined out of the rolled plates, as observed in Figure I.2.1.2(a) and (b).

The final task, as well as the primary focus of this year's efforts, are concentrated on the tribological performance of the composites. Rotors are tested with various pad materials, the stability of the friction pairs are evaluated, and the wear rates are determined. There were four rotors from the 5 vol.% and two rotors from the 10 vol.% composite with a 10 cm diameter and a 1.2 cm thickness. Despite the hot rolling, the 15 vol.% composite plate had significant open porosity, which prevented the machining of an intact rotor from the cast and hot-rolled plate. In addition, pad materials have been sourced and machined to fit in the pad holder, as shown in Figure I.2.1.2(c). The pad materials have been selected to be a range of properties that may produce different behaviors when applied against Al-MMC rotors. It was not the intention to develop a fully optimized friction pair during this testing, but the pad compositions were selected to give a range of friction coefficients and performance. Pad materials were: (1) Pagid racing pads designed to run against SiC ceramic brakes found in several high-performance cars; and (2) phenolic pads used against cast-Fe rotors, R705 (a manufacturer's designation for a pad thickness of 0.705-in.), which is a designation used by several manufacturers for HD vehicle brake pads. For a given pad material, three pad samples used for each test with an 8.7 x 8.7 mm length and width, and thickness ranging between 8 mm – 13 mm, depending on the pad material.

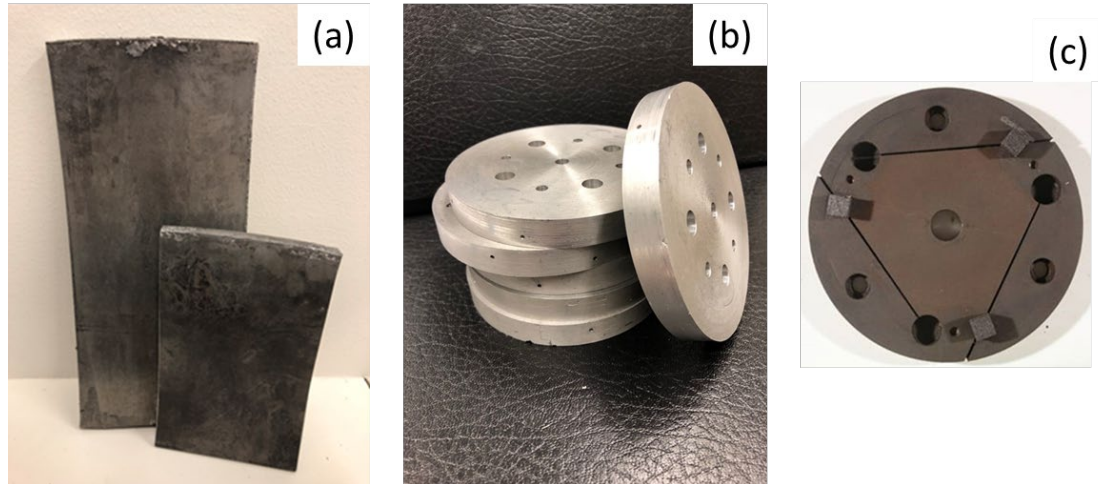


Figure I.2.1.2. (a) Gravity cast plates of 5, 10, and 15 vol.% TiB₂ reinforced A356 alloy. (b) Sub-scale rotors ready for friction/wear testing. (c) Machined pad samples fitted in the pad holder. Source: PNNL.

Wear testing is comprised of mounting the sub-scale rotors on an instrumented brake testing rig, as can be seen in Figure I.2.1.3, which can rotate the rotor or pad holder and apply clamping loads appropriate for automotive braking conditions. This rig is a reduced-scale brake dynamometer and based on the brake inertia dynamometers employed in Society of Automotive Engineers, SAE Standard J2522 for testing the effectiveness of a friction material regarding pressure, temperature, and speed [2]. However, in our rig, the pad holder rotates, but the rotor is stationary, as can be seen in Figure I.2.1.3(b). There is no flywheel between the spindle and pad holder, yet deceleration behavior can be simulated by controlling the speed of the spindle. Temperature can be controlled by adjusting the flow rate of water circulating in a copper cooling plate attached to the stationary rotor, as also can be observed in Figure I.2.1.3(b). Several energy profiles can be investigated including low-temperature, low-load continuous torque tests, and high-load, high-temperature transients. After testing, the data on loads, torque, power, and temperature are compiled, friction coefficients are calculated and correlated to test conditions.

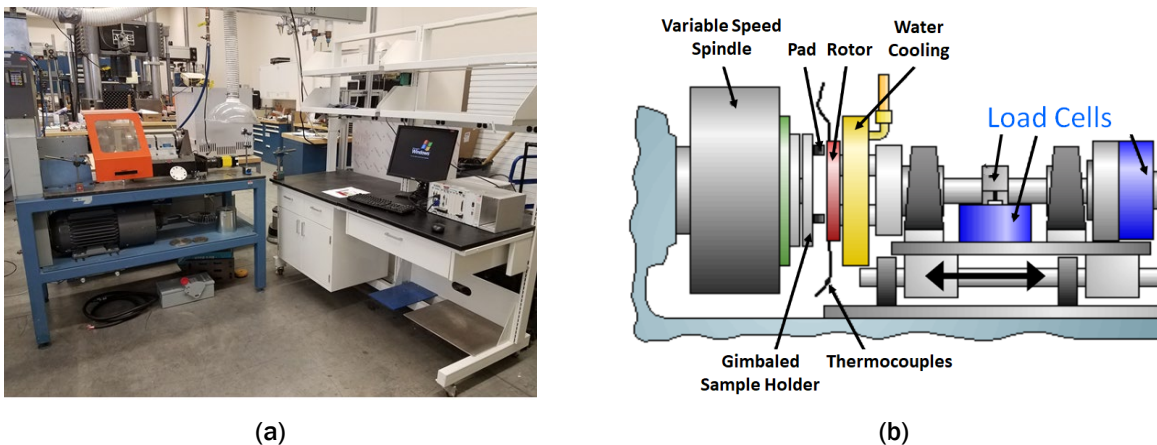


Figure I.2.1.3. (a) Brake friction pair test stand at PNNL. (b) Schematic of the test setup with corresponding locations of the pads, rotor, load cells and other measurement equipment. Source: PNNL.

Rotors and pads were measured and weighed with micrometers and high-precision scales before and after the wear tests to establish mass gain or loss for the wear rate calculations. The average mass loss of three pad samples was used for the calculations. The initial contact and burnishing steps were excluded from the weight

measurements. Some tests were repeated to check the repeatability of weight measurements and calculated wear rates. Overall, the weight measurements had enough precision (± 0.0001 g), which were also repeatable for a given test condition.

Results

This project focused on establishing the wear rates, rather than a complete performance evaluation of the friction pair. The wear rate tests were performed at 0.7 MPa, 4 m/s, and $150^\circ\text{C} \pm 15^\circ\text{C}$ for at least 20 minutes. These conditions somewhat represented expected highway braking conditions, and the data from the automotive manufacturers indicate that the sliding conditions of the front brakes of a full-size sedan moving at 100 km/h (60 mph) correspond to a temperature of 150°C [3]. An additional copper ring was placed between the rotors and the copper cooling plate, as observed in Figure I.2.1.3(b), to keep the temperatures in the desired range. Fixing the temperature around 150°C also enabled the comparison of the results obtained in this project to the previous one.

Specific wear rate is a commonly reported data obtained from the wear tests and can be easily benchmarked against the values available for other MMC rotors in the literature [4]. A specific wear rate (mm^3/m and mm^3/Nm) can be calculated from volume changes using Equation (1).

$$\text{Wear rate} = \frac{V}{d} \text{ or } \frac{V}{F_N d} \quad (1)$$

where V is the wear volume, F_N is the normal force, and d is the sliding distance. When calculating the wear rates, the rotor wear rates should be normalized using the ratio of the swept area on the rotor vs. the area of the three pads, as the contact area at a given time was the total area of the pads. Without normalization, the rotor wear rates appear to be smaller than the actual values. In addition to the volumetric specific wear rates in Equation (1), a thickness-based specific wear rate was also calculated to compare the results obtained in this project to the results obtained in Al-SiC MMC brake rotor work performed at PNNL in the early 2000s [3]. This wear rate, with units of in/ft, uses the change in the thickness of the pad and the rotor materials obtained by a micrometer or optical profilometer measurements and normalizes the change in thickness with the sliding distance [3]. In this project, thickness changes were calculated indirectly from the volume changes, as the micrometer measurements were found to be unreliable due to irregular thickness profiles of the pad samples.

Cast-Fe rotor tested with the R705 pads produced 8 times – 10 times lower specific wear rates as compared to the 5 vol.% and 10 vol.% Al-TiB₂ rotors. The R705/5% TiB₂ pair also resulted in slightly lower wear rates as compared with the R705/10% TiB₂ pair. This result is contrary to the expectations of higher volume fractions of reinforcing particles leading to lower wear rates. However, the 10 vol.% TiB₂ composite had higher porosity, which can explain its underperformance. The Pagid pads were more compatible with the MMC rotors, and they produced lower wear rates. However, when compared to the cast-Fe rotor tested with the Pagid pads, wear rates were still 2 times – 3 times higher for the 5 vol.% TiB₂ composite samples. In this case, the 10 vol.% TiB₂ composite sample had an excessive wear rate that was likely due to its higher porosity fraction.

Table I.2.1.1 summarizes the friction coefficient (μ) and the specific wear rate results obtained from the tests. Out of the total 30 tests performed, this subset corresponds to the final tests performed using the R705 and Pagid pad samples, as well as the selected test conditions. As a comparison, wear test results obtained in the previous PNNL project [3] are provided in Figure I.2.1.4, where both the MC21 static cast and F3S20S static cast rotors refer to Al359-20 vol.% SiC MMCs. The friction coefficient for cast-Fe rotors—0.37 for R705 and 0.39 for Pagid—are comparable to each other, as well as the results obtained in the previous project for the BBA2004 pads, where $\mu = 0.38$, and the Akebono PA533 pads, where $\mu = 0.36$. The Akebono PA533 pads were designed for the cast-Fe front brake rotors of a Toyota Camry. Only the R705/5% TiB₂ pair resulted in a similar friction coefficient ($\mu = 0.37$) as compared to the cast-Fe benchmarks, while the other pairs resulted in slightly lower coefficients. Variation of the friction coefficient from the 5 vol.% to the 10 vol.% composites

was higher for the R705 pads, while the Pagid pads produced similar values (e.g., 0.28 vs. 0.31). In addition, these values are comparable to the reported friction coefficients (~ 0.3) for the Al-SiC MMCs [3, 4]. Overall, the friction coefficients obtained for both the cast-Fe and Al-MMC rotors matched well to the literature values, despite the aim of this project was not to optimize any friction pairs to obtain the ideal friction coefficients.

Cast-Fe rotor tested with the R705 pads produced 8 times – 10 times lower specific wear rates as compared to the 5 vol.% and 10 vol.% Al-TiB₂ rotors. The R705/5% TiB₂ pair also resulted in slightly lower wear rates as compared with the R705/10% TiB₂ pair. This result is contrary to the expectations of higher volume fractions of reinforcing particles leading to lower wear rates. However, the 10 vol.% TiB₂ composite had higher porosity, which can explain its underperformance. The Pagid pads were more compatible with the MMC rotors, and they produced lower wear rates. However, when compared to the cast-Fe rotor tested with the Pagid pads, wear rates were still 2 times – 3 times higher for the 5 vol.% TiB₂ composite samples. In this case, the 10 vol.% TiB₂ composite sample had an excessive wear rate that was likely due to its higher porosity fraction.

Table I.2.1.1. Summary of the Wear Rate Tests

Friction Pair	Friction Coefficient	Component	Specific Wear Rate (mm ³ /Nm) x 10 ⁻⁵	Specific Wear Rate (mm ³ /m) x 10 ⁻⁴	Wear Rate (in./ft.) x 10 ⁻⁸
R705/ 5% TiB ₂	0.37	Pad	20.40	43.90	68.20
		Rotor	15.20	32.80	2.18
		Rotor Normalized	119.00	255.00	17.00
R705/ 10% TiB ₂	0.24	Pad	28.70	77.20	119.00
		Rotor	14.10	38.10	2.53
		Rotor Normalized	109.00	294.00	19.50
R705/ Cast-Iron	0.36	Pad	2.60	5.31	8.07
		Rotor	1.24	2.53	0.17
		Rotor Normalized	9.46	19.30	1.29
Pagid/ 5% TiB ₂	0.28	Pad	8.10	20.20	34.10
		Rotor	2.62	6.56	0.44
		Rotor Normalized	22.30	55.60	3.70
Pagid/ 10% TiB ₂	0.31	Pad	10.7	27.00	47.00
		Rotor	6.29	15.90	1.05
		Rotor Normalized	82.20	207.00	13.80
Pagid/ Cast-Iron	0.39	Pad	2.42	5.58	9.84
		Rotor	1.10	2.53	0.17
		Rotor Normalized	9.71	22.40	1.49

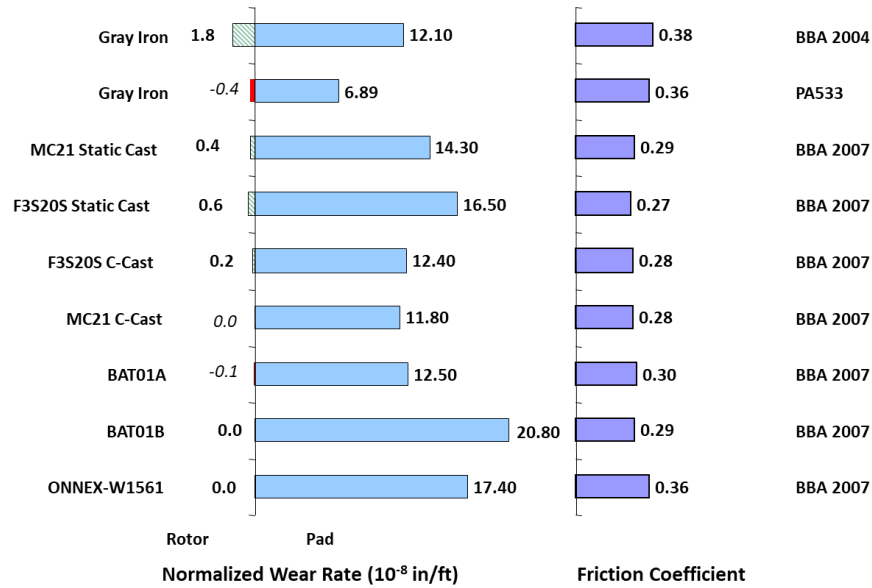


Figure I.2.1.4. Summary of the wear rate test resulted obtained in the previous PNNL project [3].
Source: PNNL.

Previous data on the cast-Fe rotors tested with the PA533 pads, as shown in Figure I.2.1.4, is comparable to the results obtained in this project. The pad wear rate was 6.68×10^{-8} in./ft. with the PA533/cast-Fe pair vs. 8.07×10^{-8} in./ft. for the current R705/cast-Fe friction pair. The rotor wear rate was -0.4×10^{-8} in./ft. (- sign indicates a build up rather than wear) in the previous project vs. 1.29×10^{-8} in./ft. for the current case. Due to the porosity issues and lower particle loads, the wear performance of Al-TiB₂ MMC is somewhat lower when compared to the previous Al-SiC MMC data, as observed in Figure I.2.1.4. The best MMC friction pair in this project was Pagid/5 vol.% TiB₂. The rotor wear rate is 3.70×10^{-8} in./ft. for this pair vs. 0.4×10^{-8} in./ft. for the MC21/BBA2007 pair and 0.6×10^{-8} in./ft. for the F3S20S/BBA2007 pair. Pad wear is 34.1×10^{-8} in./ft. for the current pair vs. 14.30×10^{-8} in./ft. for the MC21 and 16.50×10^{-8} in./ft. for the F3S20S tested with the BBA 2007 pads.

Conclusions

Future vehicle platforms have created opportunities to re-evaluate Al-MMC brakes. Light-weight brake rotors have an opportunity to contribute to vehicle lightweighting efforts and offer the possibility of a 50% weight-savings in rotating and unsprung mass in some vehicle applications. This project investigated a potentially lower-cost reinforcement than the more traditional SiC components by fabricating the TiB₂-reinforced sub-scale brake rotor components and testing their tribological performance. The Al-TiB₂ friction pairs had similar friction coefficients (~ 0.3) as compared to the Al-SiC data available in the previous projects and literature. The 10 vol.% composite resulted in higher wear rates of the pads and rotors than the 5 vol.% composite in almost all the tests, likely due to its higher porosity content remaining from the casting process. Wear rates were also 2 times – 3 times higher for the MMC friction pairs compared to the cast-Fe rotors benchmark tested with the same pads. This performance was similar to the Al-20 vol.% SiC composites benchmarked against cast-Fe rotors in the previous studies, where the Al-SiC MMC also yielded higher wear rates of the pads and rotors. However, these results are still promising given the porosity and lower reinforcement content of the Al-TiB₂ composites. Porosity free Al-TiB₂ rotors that is produced with high-pressure casting methods has the potential of performing better than the Al-SiC samples with the other added benefits of lower-cost and particle content. This may enable cost-competitive MMC brake rotors as an alternative to the cast-iron, which can lead to weight-savings and reduced wear particle emissions.

References

1. Air Quality Expert Group, 2019, “Non-exhaust emissions from road traffic,” U.K. Department for Environment, Food, and Rural Affairs. Available at: https://uk-air.defra.gov.uk/assets/documents/reports/cat09/1907101151_20190709_Non_Exhaust_Emissions_types_et_Final.pdf (last accessed 1 December 2021).
2. Society of Automotive Engineers International, 2014, “Dynamometer global brake effectiveness,” J2522_201409, Ground Vehicle Standard. Available at: https://doi.org/10.4271/J2522_201409 (last accessed 1 December 2021).
3. Herling, D., and G. Grant, 2003, “Friction Pair Testing of Candidate Metal Composite Brake Materials, Advanced Brake Systems for Heavy-Duty Vehicles: FY 2003 Annual Progress Report, Vehicle Systems Optimization and Truck Safety,” DOE–Office of Vehicle Technology.
4. Daoud, A., and M. T. Abou El-khair, 2010, “Wear and friction behavior of sand-cast brake rotor made of A359-20vol% SiC particle composites sliding against automobile friction material,” *Tribol. Int.*, Vol. 43, No. 3, pp. 544–553.

I.3 Powertrain Materials Core Program

I.3.1 Cost-Effective Lightweight Engine Alloys – Thrust 1

I.3.1.1 New Aluminum Alloys with Improved High-Temperature Performance (1A/1B)

I.3.1.1.1 *Fundamental Studies of Complex Precipitation Pathways in Lightweight Alloys (Task 1A1) (Oak Ridge National Laboratory)*

Dongwon Shin, Co-Principal Investigator

Oak Ridge National Laboratory
1 Bethel Valley Road
Oak Ridge, TN 37831
E-mail: shind@ornl.gov

Amit Shyam, Co-Principal Investigator

Oak Ridge National Laboratory
1 Bethel Valley Road
Oak Ridge, TN 37831
E-mail: shyama@ornl.gov

Jerry L. Gibbs, DOE Technology Manager

U.S. Department of Energy
E-mail: jerry.gibbs@ee.doe.gov

Start Date: October 1, 2018 End Date: September 30, 2023
Project Funding (FY 2021): \$350,000 DOE share: \$350,000 Non-DOE share: \$0

Project Introduction

Engineering of key interfaces between the Al matrix and strengthening precipitate phases to increase the temperature capability of lightweight Al alloys is the primary scientific driving force for this task. By explicitly utilizing modern materials science research capabilities (i.e., advanced characterization and the Oak Ridge Leadership Computing Facility), the ORNL team is significantly accelerating and promoting understanding of atomistic interfacial structures in Al alloys. The knowledge gained in the fundamental studies within this task are being applied in other program tasks to guide the design of advanced lightweight Al alloys capable of higher temperatures to enable automotive propulsion with higher efficiencies and reduced environmental impact.

Objectives

The focus of this FY 2021 low technology readiness level task was to develop a fundamental understanding of the interfacial energetics between the Al matrix and key precipitates in advanced Al alloys (i.e., θ' -Al₂Cu and L₁₂-Al₃X). We systematically investigated the two groups of pristine coherent (100) interfaces: Al and L₁₂ and θ' -Al₂Cu and L₁₂. As was previously shown, 3D transition metals that exhibit very low mobility in Al (e.g., Zr and Sc) have a propensity to segregate at the semi-coherent interface between Al and θ' -Al₂Cu, and consequently enhance the thermal stability of θ' [1, 2]. In addition, it was observed that Zr forms L₁₂ phases at the coherent interface of θ' -Al₂Cu, which contributes to stabilizing θ' to a further extent. We have broadly considered elements that are known to form L₁₂ Al₃X tri-aluminides (i.e., X=Li, Sc, Ti, Zr, and Hf) in the present study.

Approach

A supercell approach was employed within the context of first principles calculations based on DFT. Two supercells were constructed to represent the (100) coherent interfaces of Al/L₁₂-Al₃X and L₁₂-Al₃X/θ'-Al₂Cu, as illustrated in Figure I.3.1.1.1.1. These structural templates were used to calculate their total energies.

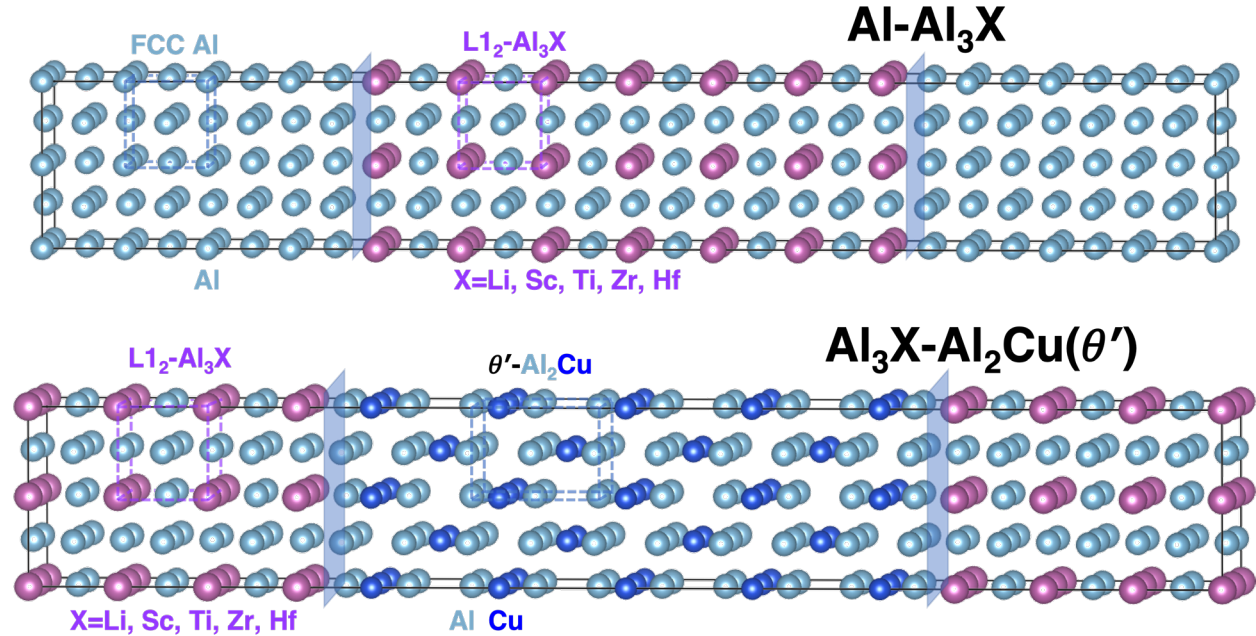


Figure I.3.1.1.1.1. Constructed supercell models of Al-Al₃X (top) and Al₃X-Al₂Cu (bottom) for DFT calculations. Shaded area indicates the interface between the two phases. Source: ORNL.

The formalism proposed by Wolverton et al. [3] was employed to deconvolute interfacial and coherency strain energies as shown in Equation (1).

$$\begin{aligned}\Delta E_f &= [E(\text{Al}_{m+3n}\text{X}_n) - mE(\text{Al}) - nE(\text{Al}_3\text{X})]/N, \\ \Delta E_f &= [E(\text{Al}_{2k+3l}\text{Cu}_k\text{X}_l) - kE(\text{Al}_2\text{Cu}) - lE(\text{Al}_3\text{X})]/N, \\ \Delta E_f &= \delta E_{\text{cs}}(\text{Al}, \text{Al}_3\text{X}) + 2\sigma A/N, \quad \Delta E_f = \delta E_{\text{cs}}(\text{Al}_3\text{X}, \text{Al}_2\text{Cu}) + 2\sigma A/N\end{aligned}\tag{1}$$

where E is the total energy of structure, $\text{Al}_{m+3n}\text{X}_n$ and $\text{Al}_{2k+3l}\text{Cu}_k\text{X}_l$ represent supercells for Al-Al₃X and Al₃X-Al₂Cu interfaces, N is the number of atoms in the supercell, δE_{cs} is the coherency strain, σ is the interfacial energy, and A is the surface area. The current approach requires creating different-sized supercells, while maintaining the same interfacial area. We have used 160, 224, and 288 atom supercells for the Al/Al₃X interface, and 108, 164, and 220 atom supercells for the Al₃X/θ'-Al₂Cu interface, respectively, by varying the number of unit cells (i.e., m and n for Al-Al₃X, k , and l for Al₃X-Al₂Cu) in each phase.

The structures were fully relaxed with respect to the volume, shape, and atomic positions to find the lowest energy states with special k -points sampling for the interfacial energy calculations. Total energies of reference states were calculated (i.e., face-centered cubic (fcc) Al, L₁₂, and θ') to derive formation energies of creating the supercell structures with specific interfaces. These reference states were fully relaxed and treated as bulk phases by invoking a sufficiently high number of k -points in all directions.

Results

The DFT calculations of all the reference phases were completed (i.e., pure fcc Al, θ' -Al₂Cu, and L1₂-tri-aluminides) to determine their total energy and equilibrium lattice parameters as references in deriving (100) coherent interfacial energy and lattice mismatch. Table I.3.1.1.1.1 summarizes the DFT lattice parameters of the fcc Al and L1₂-Al₃X phases considered in the present study.

Table I.3.1.1.1.1. DFT Calculated Lattice Parameters of fcc Al and L1₂-Al₃X

Phase	DFT Lattice Parameters (Å)	Experimental (Å)	Phase	DFT Lattice Parameters (Å)	Experimental (Å)	Lattice Mismatch (%)
fcc Al	4.014	4.05	Al ₃ Li	3.985	4.011	-0.71%
			Al ₃ Sc	4.074	4.104	1.51%
			Al ₃ Ti	3.948		-1.62%
			Al ₃ Zr	4.076	4.093	1.56%
			Al ₃ Hf	4.057		1.08%

In most cases, the DFT lattice parameters are slightly underpredicted, but they are in good agreement with the available experiments (e.g., within 1%). The (100) interface between the Al matrix and the L1₂ tri-aluminides is highly coherent as they both have a very similar cubical crystal structure. Nevertheless, the lattice mismatch is over 1%, which can be regarded as marginally high, except for Al/Al₃Li, which has a low mismatch. Thus, it is expected that the resultant strain energies of most of these interfaces may be significant.

The DFT lattice parameters of reference phases for the (100) coherent L1₂-Al₃X/ θ' -Al₂Cu are presented in Table I.3.1.1.1.2. As was the case in Al/Al₃X, DFT and experimental lattice parameters show good agreement where available, which supports the fidelity of the DFT approach to investigate atomic interfacial structures. The lattice parameter of the theta prime phase (4.045Å) is slightly higher than that of pure fcc Al (4.014Å). It is intriguing that L1₂-Al₃X/ θ' -Al₂Cu overall exhibits a much smaller lattice mismatch due to the similarity in their lattice parameters—as low as 0.28% for the Al₂Cu/Al₃Hf interface.

Table I.3.1.1.1.2. DFT Calculated Lattice Parameters of Al₂Cu and L1₂-Al₃X

Phase	DFT Lattice Parameters (Å)	Experimental (Å)	Phase	DFT Lattice Parameters (Å)	Experimental (Å)	Lattice Mismatch (%)
Al ₂ Cu	4.045	4.04	Al ₃ Li	3.985	4.011	-1.49%
			Al ₃ Sc	4.074	4.104	0.71%
			Al ₃ Ti	3.948		-2.39%
			Al ₃ Zr	4.076	4.093	0.77%
			Al ₃ Hf	4.057		0.28%

Next, the interfacial and strain energies of the two interface types were derived from the supercell total energy calculations. Figure I.3.1.1.1.2 compares these Al/Al₃X interface calculations. The slopes normalized with interfacial areas correspond to the interfacial energy and intercepts to the strain energy. Individual numerical values are summarized in Table I.3.1.1.1.3. Previous DFT-derived interfacial energies are also listed where available [4] (see references therein), and they are in good agreement with the present study. Overall, three different supercells show good convergence for all the L1₂ tri-aluminide forming elements. All the Al/Al₃X interface calculations show low strain energies. A threshold energy for an interface to be considered coherent is < 200 mJ/m²*, and each interface studied here exhibits relatively low interfacial energy. In particular, it is intriguing that the Al/Al₃Li and Al/Al₃Hf interfaces show almost negligible energy, both below 50 mJ/m².

* Generally accepted ranges to be regarded as a semi-coherent interface is 200~500 mJ/m², while the incoherent interface is >500 mJ/m².

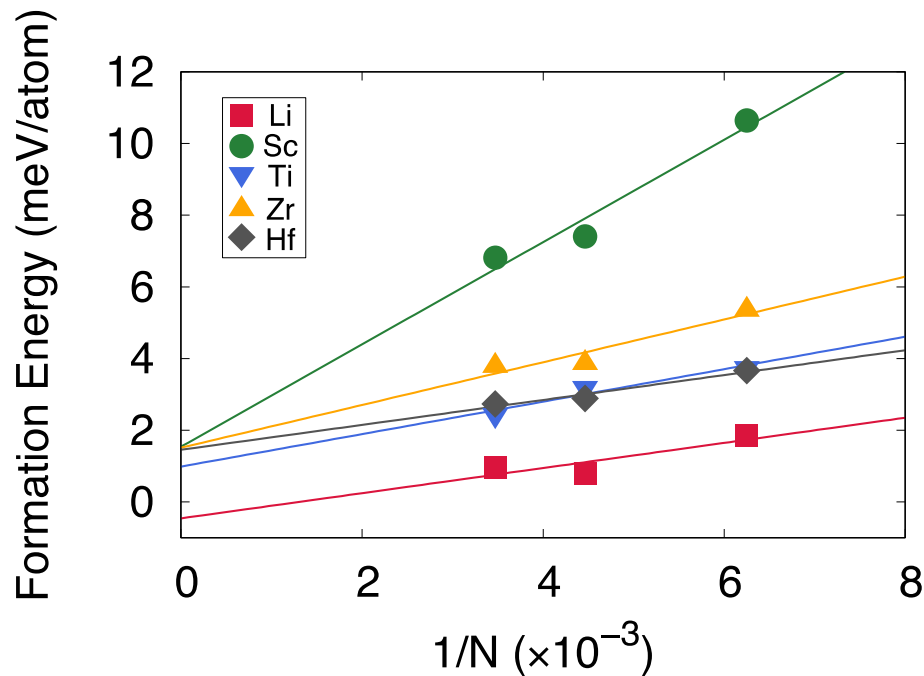


Figure I.3.1.1.1.2. DFT formation energies of Al-Al₃X (X=Li, Sc, Ti, Zr, and Hf) interface supercells with respect to reciprocal number of atoms. Source: ORNL.

Table I.3.1.1.1.3. DFT Interfacial and Strain Energies of Al/Al₃X

Interfaces	Interfacial Energy (mJ/m ²)	Reference [4]	Strain Energy (meV/atom)
Al-Al ₃ Li	44±8.45	16, 14, 12	-0.46
Al-Al ₃ Sc	174±13.07	192, 176, 165	1.54
Al-Al ₃ Ti	57±4.91		0.99
Al-Al ₃ Zr	73±8.01		1.51
Al-Al ₃ Hf	43±3.06		1.45

Figure I.3.1.1.1.3 and Table I.3.1.1.1.4 show the computed interfacial and strain energies of Al₃X-Al₂Cu interfaces. The degrees of convergence of formation energies with respect to the reciprocal number of atoms are slightly lower than the cases in Al-Al₃X. However, it should be noted that the overall magnitude of formation energies is relatively low, and the slopes (i.e., interfacial energies) are significantly lower than the previous case. Strain energies of Al₃X-Al₂Cu interfaces in comparison to Al-Al₃X are quite lower except for the Al₃Ti-Al₂Cu. Intriguingly, Al₃Zr-Al₂Cu shows the lowest interfacial energies and the second-lowest strain energy among the interfaces considered.

It has been experimentally demonstrated that adding both Ti and Zr to Al-Cu alloys as microsolutes has a favorable effect of further stabilizing θ' -Al₂Cu to higher temperatures by forming an adjacent Al₃(Ti_xZr_{1-x}) L1₂ phase as these elements segregate to the coherent Al- θ' -Al₂Cu interface [5]. This phenomenon can be explained by both Al₃Ti and Al₃Zr having a minimal energetic penalty in forming the interface, as well as low strain energy once formed. Based on this analysis, the present DFT studies suggest that adding other L1₂ forming elements (i.e., Li, Sc, and Hf) to the Al-Cu alloys may further enhance the stability of θ' -Al₂Cu at higher temperatures with the same mechanism. This hypothesis awaits further experimental validation.

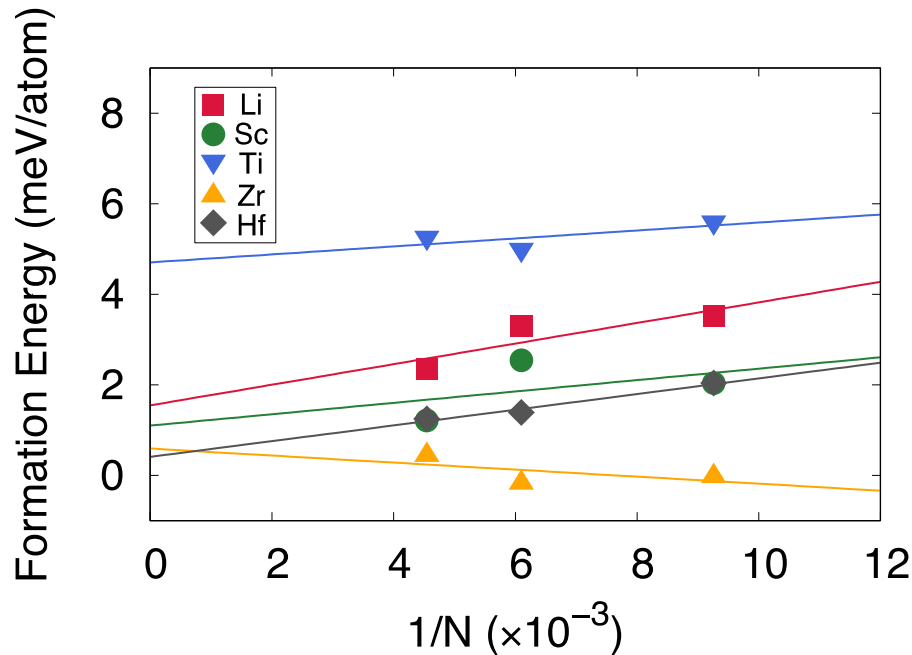


Figure I.3.1.1.1.3. DFT formation energies of Al₃X-Al₂Cu (X=Li, Sc, Ti, Zr, and Hf) interface supercells with respect to reciprocal number of atoms. Source: ORNL.

Table I.3.1.1.1.4. DFT Interfacial and Strain Energies of Al₃X-Al₂Cu

	Interfacial Energy (mJ/m ²)	Strain Energy (meV/atom)
Al ₃ Li-Al ₂ Cu	27±6.90	1.55
Al ₃ Sc-Al ₂ Cu	14±12.74	1.10
Al ₃ Ti-Al ₂ Cu	11±4.68	4.71
Al ₃ Zr-Al ₂ Cu	-9±5.54	0.59
Al ₃ Hf-Al ₂ Cu	21±1.44	0.41

Conclusions

A DFT supercell approach was applied to investigate the interfacial energetics of key precipitates in Al-Cu alloys (i.e., Al-Al₃X and Al₃X-Al₂Cu coherent interfaces), where X are elements known to form L₁₂ tri-aluminides in Al alloys (X=Li, Sc, Ti, Zr, and Hf). All the reference state single-phase calculations (i.e., fcc Al, L₁₂ Al₃X, and θ'-Al₂Cu) showed good agreements with the experiments and/or previous DFT simulations, where available. The calculated interfacial and strain energies of Al-Al₃X showed good convergence with respect to the number of atoms in the supercells. The magnitude of interfacial energies for all the Al/Al₃X combinations was in the range that was low enough to be regarded as coherent (e.g., below 200 mJ/m²). Another series of Al₃X-Al₂Cu interface calculations showed that the magnitude of interfacial and strain energies is significantly lower than the Al-Al₃X interface, which can be attributed to the lower lattice mismatch of Al₃X-Al₂Cu as compared to Al-Al₃X. Adding Ti and Zr in Al-Cu alloys has been shown to improve the thermal stability of θ'-Al₂Cu by forming Al₃(Ti_xZr_{1-x}) L₁₂ phase as they segregate to the coherent interface. The current DFT study suggests that adding other L₁₂ forming elements (i.e., Li, Sc, and Hf) to the Al-Cu alloys may further enhance the stability of θ'-Al₂Cu at higher temperatures.

Key Publications

1. Samolyuk, G. D., M. Eisenbach, D. Shin, Y. N. Osetsky, A. Shyam, and J. R. Morris, 2021, “Equilibrium solute segregation to matrix- θ' precipitate interfaces in Al-Cu alloys from first principles,” *Phys. Rev. Mater.*, Vol. 4, Art. 073801.
2. Poplawsky, J. D., B. K. Milligan, L. F. Allard, D. Shin, P. Shower, M. F. Chisholm, and A. Shyam, 2021, “The synergistic role of Mn and Zr/Ti in producing $\theta'/L1_2$ co-precipitates in Al-Cu alloys,” *Acta Mater.*, Vol. 194, pp. 577–586.
3. Peng, J., S. Bahl, A. Shyam, J. A. Haynes, and D. Shin, 2021, “Solute-vacancy clustering in aluminum,” *Acta Mater.*, Vol. 196, pp. 747–758.
4. Bahl, S., L. Xiong, L. F. Allard, R. A. Michi, J. D. Poplawsky, A. C. Chuang, D. Singh, T. R. Watkins, D. Shin, J. A. Haynes, and A. Shyam, 2021, “Aging behavior and strengthening mechanisms of coarsening resistant metastable θ' precipitates in an Al-Cu alloy,” *Mater. Des.*, Vol. 198, Art. 109378.
5. Chisholm, M. F., D. Shin, G. Duscher, M. P. Oxley, L. F. Allard, J. D. Poplawsky, and A. Shyam, 2021, “Atomic structures of interfacial solute gateways to θ' precipitates in Al-Cu alloys,” *Acta Mater.*, Vol. 212, Art. 116891.

References

1. Shyam, A., S. Roy, D. Shin, J. D. Poplawsky, L.F. Allard, Y. Yamamoto, J. R. Morris, B. Mazumder, J. C. Idrobo, A. Rodriguez, T. R. Watkins, and J. A. Haynes, 2019, “Elevated temperature microstructural stability in cast-Al-Cu-Mn-Zr alloys through solute segregation,” *Mater. Sci. Eng. A*, Vol. 765, Art. #138279.
2. Shin, D., A. Shyam, S. Lee, Y. Yamamoto, and J. A. Haynes, 2017, “Solute segregation at the Al/ θ' -Al₂Cu interface in Al-Cu alloys,” *Acta Mater.*, Vol. 141, pp. 327–340.
3. Vaithyanathan, V., C. Wolverton, and L. Q. Chen, 2004, “Multiscale modeling of θ' precipitation in Al-Cu binary alloys,” *Acta Mater.*, Vol. 52, pp. 2973–2987.
4. Mao, Z., W. Chen, D. N. Seidman, and C. Wolverton, 2011, “First principles study of the nucleation and stability of ordered precipitates in ternary Al-Sc-Li alloys,” *Acta Mater.*, Vol. 59, pp. 3012–3023.
5. Poplawsky, J. D., B. K. Milligan, L. F. Allard, D. Shin, P. Shower, M. F. Chisholm, and A. Shyam, 2021, “The synergistic role of Mn and Zr/Ti in producing $\theta'/L1_2$ co-precipitates in Al-Cu alloys,” *Acta Mater.*, Vol. 194, pp. 577–586.

Acknowledgments

This research used the resources of the Oak Ridge Leadership Computing Facility at the Oak Ridge National Laboratory, which is supported by the Office of Science of the U.S. Department of Energy under Contract No. DE-AC05-00OR22725. The authors also would like to thank Drs. A. Shyam, S. Bahl, and J. Poplawsky for helping with the experimental work and providing physical metallurgy insights.

I.3.1.1.2 New Higher Temperature Performance Alloys (Task 1A2) (Oak Ridge National Laboratory)

Amit Shyam, Co-Principal Investigator

Oak Ridge National Laboratory
1 Bethel Valley Road
Oak Ridge, TN 37831
E-mail: shyama@ornl.gov

Dongwon Shin, Co-Principal Investigator

Oak Ridge National Laboratory
1 Bethel Valley Road
Oak Ridge, TN 37831
E-mail: shind@ornl.gov

Jerry L. Gibbs, DOE Technology Manager

U.S. Department of Energy
E-mail: jerry.gibbs@ee.doe.gov

Start Date: October 1, 2018 End Date: September 30, 2023
Project Funding (FY 2021): \$350,000 DOE share: \$350,000 Non-DOE share: \$0

Project Introduction

Mechanisms that lead to improved thermal stability and other favorable attributes in lightweight Al alloys are emphasized in this task. Attributes are associated with mechanical and thermal properties of interest for various higher temperature powertrain components, such as light-duty engine pistons, cylinder heads, turbo compressors, and lightweight friction brake systems (particularly those for electric vehicles). An ICME approach was applied to understand and elucidate physical and metallurgical mechanisms of interest. This project report covers FY 2021 efforts for Task 1A2, “New Higher Performance Aluminum Alloys,” as a part of Thrust 1 for “New Aluminum Alloys with Improved High-Temperature Performance.”

Objectives

This task focuses on a fundamental understanding of the features that impart thermal stability to cast-Al precipitate microstructures. This is a low technology readiness level task to develop improved scientific understanding of this class of alloys and their key phenomena in order to leverage this understanding to identify design pathways for potential further improvements in high-temperature performance of Al-Cu and other Al alloys. These pathways include the identification of potential mechanisms for further improvement of thermal stability of favorable precipitates.

Approach

The emphasis of this task is on the establishment of microstructure and mechanical property associations of interest by linking experimental and simulation results. The approach relies on an interplay between advanced characterization and theoretical calculations that help to establish and understand the mechanisms. These in turn are utilized to develop improved high-temperature Al alloys that meet or exceed targeted industry needs. Within the precipitation-hardened alloys, there remains an emphasis on utilizing the non-equilibrium interfacial solute segregation mechanism and associated co-precipitate formation to improve the chemistry, heat treatments, and elevated temperature capability of cast-ACMZ alloys and variants with changing levels of impurities, especially the Si content. Neutron diffraction techniques are being applied to understand the deformation mechanisms in Al-Cu alloys of interest. Additionally, there are dispersion-hardened alloys under study and development, comprising alloys with improved elevated temperature properties, particularly alloys in the Al-Ni system.

Results

Thermal Stability Mechanisms

Our team continued to investigate the non-equilibrium interfacial solute segregation mechanism in order to extend the temperature limits of Al-Cu alloys and in particular the temperature limit of the ACMZ family of alloys. Work in previous years had revealed that solute segregation to strengthening precipitate interfaces was important in determining the higher temperature stability of ACMZ alloys. Figure I.3.1.1.2.1(a) shows the segregation of solutes to the interface of the strengthening θ' precipitate through a STEM image. In this case, the brighter solute atoms on the coherent interface are Zr atoms. This FY, it was quantitatively demonstrated by this task team that the slower diffusing Mn and Zr atoms determine the thermal stability of ACMZ alloys. The underlying theory of Ostwald ripening in the presence of slow-moving solutes proposed by Voorhees and co-workers [1] was found to apply. The resultant thermal stability of the strengthening precipitate in ACMZ alloys led to hardness stability with long-term thermal exposure at 300°C that is demonstrated in Figure I.3.1.1.2.1(b). As shown in this figure, the two ACMZ alloys (Al7CuMnZr and Al5CuNi) have a lower as-aged hardness but retain their hardness much better after extended exposure. The commercial alloy (Al5CuMg) has improved hardness in the as-aged state but continuously loses hardness with exposure due to unfavorable transformations that cannot be prevented in these alloys.

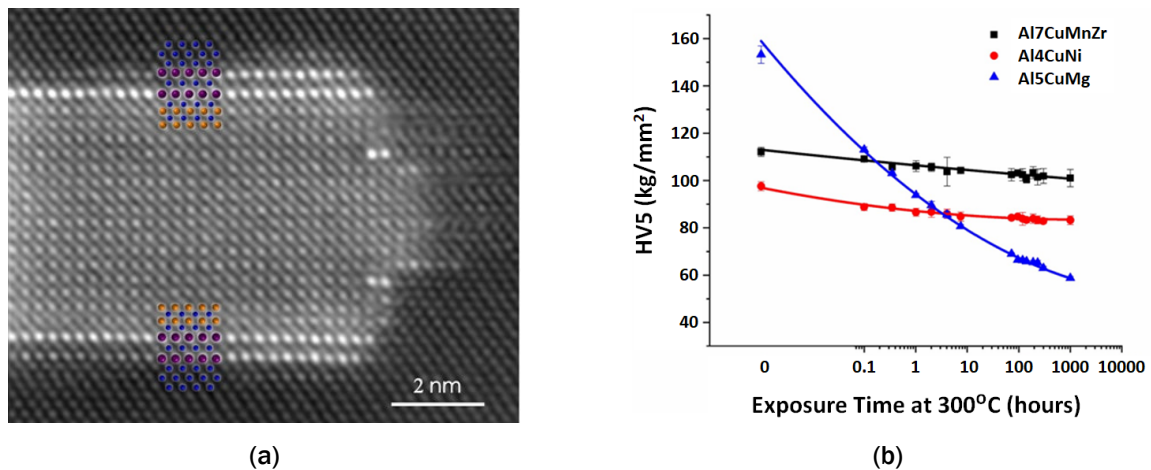


Figure I.3.1.1.2.1. (a) A STEM image showing segregation of solutes to interfaces in a θ' precipitate. (b) The hardness stability of two ACMZ alloys (Al7CuMnZr and Al5CuNi) during long-term exposure at 300 °C compared to a commercial alloy (Al5CuMg). Source: ORNL.

Another factor that was determined to be influential in the thermal stability of ACMZ alloys was the concentration of Si atoms. Si is typically considered an impurity in these alloys, but a systematic analysis of ACMZ alloys with a range of Si levels reveals that there is an optimum Si content for achieving the ideal high-temperature microstructural stability. In a study completed this FY, a combination of hardness testing and microstructural characterization was used to trace the relationship from Si content to aging response to thermal stability in ACMZ alloys. As shown in Figure I.3.1.1.2.2, which compares the as-aged hardness and 350°C - 200 hour exposed hardness of a series of ACMZ alloys with varying impurity levels of Si, an intermediate level of trace Si is most desirable for the hardness stability of the microstructure. The hardness stability is, of course, related to the thermal stability of the microstructure as shown in a series of SEM images in Figure I.3.1.1.2.3. It is shown that a Si level of 0.05 wt% to 0.1 wt% is optimal and corresponds to a reduced as-aged hardness, but a greater amount of hardness retained after thermal exposure to 350°C for 200 hours.

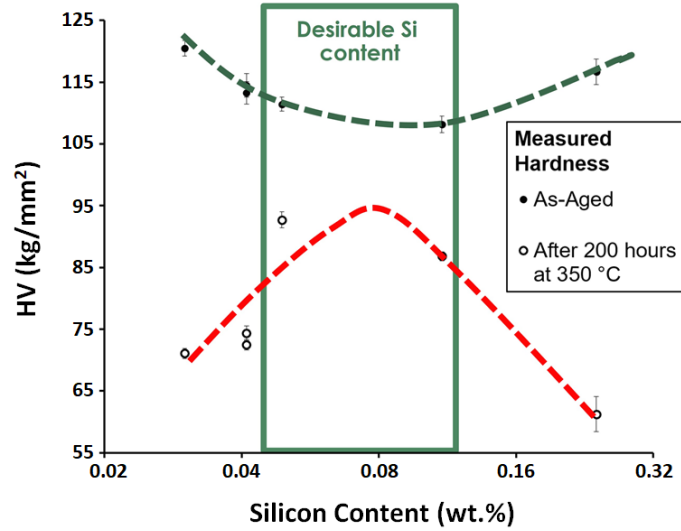


Figure I.3.1.1.2.2. The mean values and the standard error of Vickers hardness of each alloy in the as-aged state and after a 200-hour, 350 °C exposure are plotted as a function of the alloys' impurity Si content. Note that the x-axis is logarithmic. Source: ORNL.

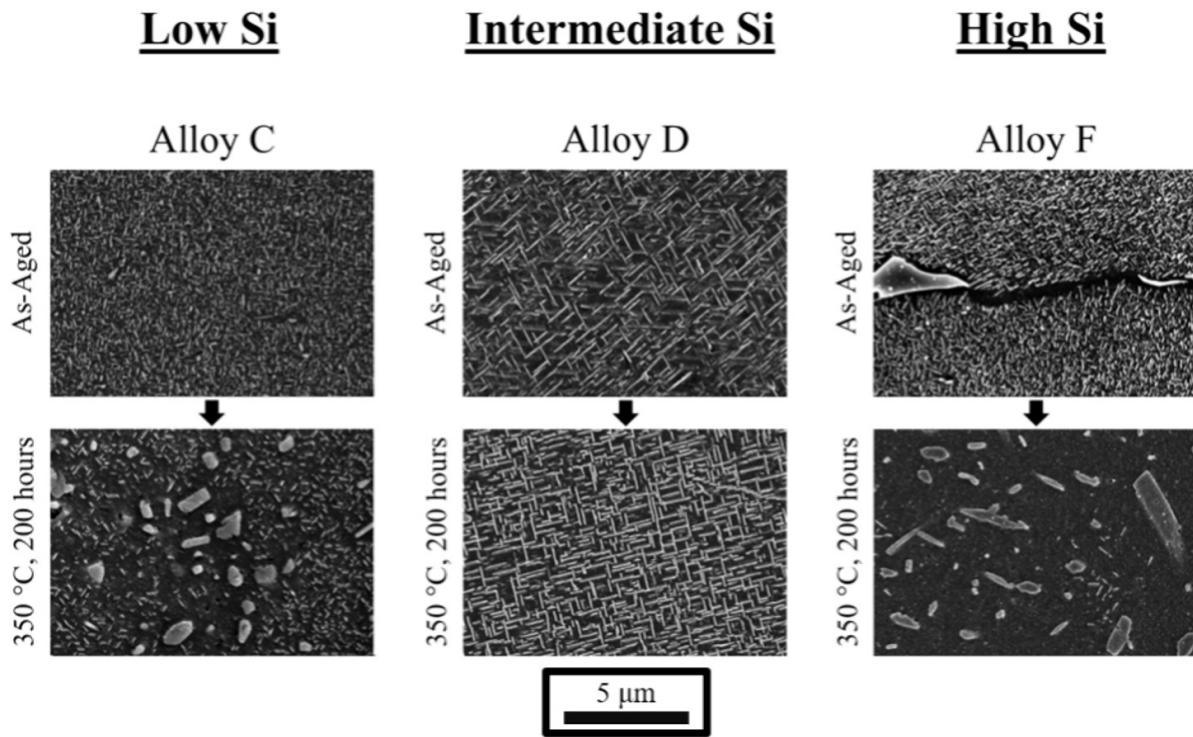


Figure I.3.1.1.2.3. Representative microstructures of low, intermediate, and high Si impurity level alloys in this study after aging and after subsequent high-temperature exposure at 350 °C for 200 hours. The low Si impurity alloy and the high Si impurity alloy both exhibit fine θ' precipitates in the as-aged state and θ' to θ transformation upon extended thermal exposure. The intermediate Si alloy shows coarser θ' particles upon aging and no obvious θ' to θ transformation upon thermal exposure. Source: ORNL.

Neutron Diffraction of Al-Cu Alloys

In FY 2020, we reported that the RT strain hardening rate in Al-Cu alloys was strongly orientation-dependent, which was modeled based on load-sharing between the precipitates and the matrix [2]. It was shown that certain grain orientations (e.g., $\langle 001 \rangle$) were more efficient at transferring load to the precipitate and had a lower strain hardening rate in the matrix. Conversely, other grain orientations (e.g., $\langle 111 \rangle$) did not transfer load to the precipitate as efficiently and they led to a higher strain hardening rate in the matrix. *In-situ* neutron diffraction experiments were performed on an elevated temperature Al-Cu alloy known as RR350, which evolved from a World War II aircraft application by Rolls Royce, from 20-350°C. The lattice strain evolution was recorded during tensile deformation. Lattice strain evolution for the (211) peak in θ' precipitate phase in RR350 alloy at five testing temperatures is shown in Figure I.3.1.1.2.4. The solid black line represents the predictions of a model reported in the last FY. Note that at 100°C and 200°C, the precipitates' lattice strain is reduced near the end of the experiment, suggesting yielding in the precipitates.

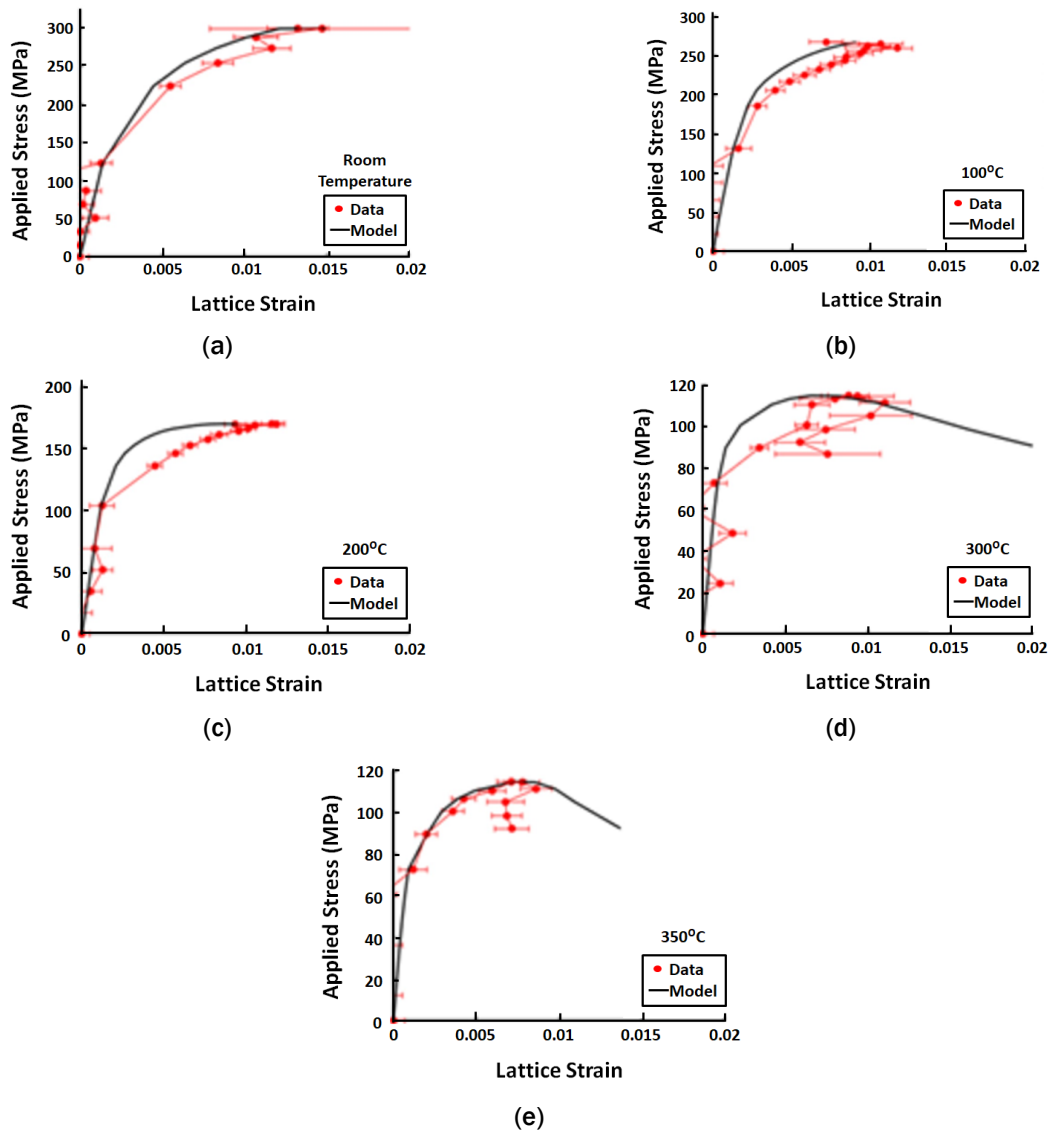


Figure I.3.1.1.2.4. Comparison of (a) room and elevated temperatures [(b) 100°C, (c) 200°C, (d) 300°C, and (e) 350°C] lattice strain evolution in the θ' precipitate for the experimentally measured results from neutron diffraction against predicted lattice strains from the model developed in FY 2020. For each experiment, the precipitate followed the predicted behavior until the yield point of the precipitate. Source: ORNL.

At 300°C and 350°C, the lattice strain hooks back during the later stages of deformation, signifying strain softening. The model effectively predicts precipitate behavior up to the yield point of the precipitate. This observation is consistent with fact that the model assumed that the precipitate does not yield. From the maximum stress reached, the critical resolved shear strength (CRSS) of the strengthening θ' phase could be calculated as a function of temperature, as shown in Figure I.3.1.1.2.5. This result is the first reported measurement of temperature dependence of CRSS for this vital strengthening precipitate.

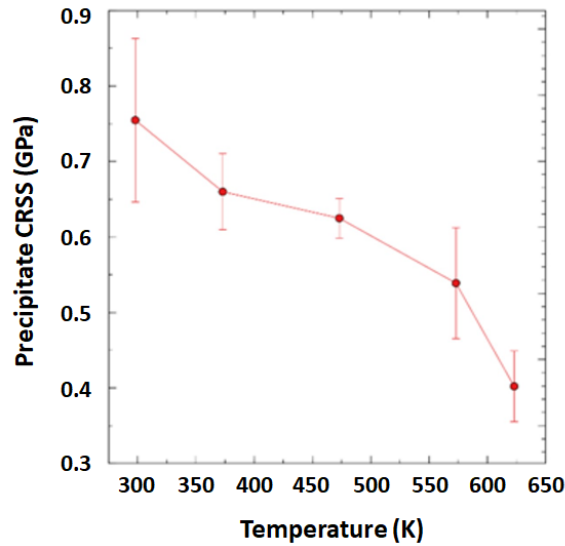


Figure I.3.1.1.2.5. CRSS of the θ' precipitates versus temperature measured using neutron diffraction. The precipitate yield strength decreases strongly with temperature. Source: ORNL.

Creep tests were also performed at 300°C for the same RR350 alloy and the important mechanism that was revealed is illustrated with the aid of lattice strain versus macrostrain curves for a number of stress levels as shown in Figure I.3.1.1.2.6. Note that the precipitate stresses are increasing over the course of the experiment, while the matrix stresses are decreasing, signifying load transfer. This degree of load transfer suggests that the primary precipitate-dislocation interaction is bypass via Orowan looping.

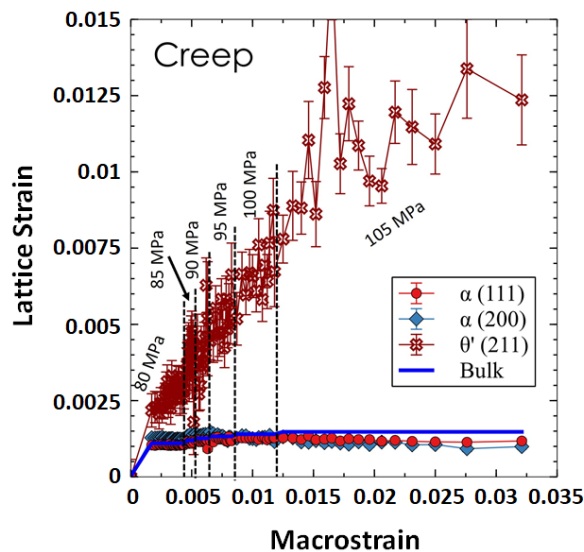


Figure I.3.1.1.2.6. Lattice strain versus true strain curves for the θ' (211) crystallographic orientation, as well as the two extremes of matrix crystallographic grain orientations. Source: ORNL.

Conclusions

- The effects of solute segregation and impurity Si levels on the thermal stability of key strengthening θ' precipitates in Al-Cu alloys were elucidated.
- *In-situ* neutron tensile tests determined the CRSS of the strengthening θ' precipitate as a function of temperature for the first time.
- *In-situ* neutron creep tests revealed the mechanism of creep-strengthening in Al-Cu alloys stemmed from Orowan looping of dislocations around strengthening precipitates.

Key Publications

1. Milligan, B., D. Ma, L. F. Allard, A. Clarke, and A. Shyam, 2021, “Dislocation- θ' (Al_2Cu) interactions during creep deformation of an Al-Cu Alloy,” *Scr. Mater.* (in review).
2. Milligan, B., D. Ma, L. F. Allard, A. Clarke, and A. Shyam, 2021, “Crystallographic orientation-dependent strain hardening in a precipitation-strengthened Al-Cu alloy,” *Acta Mater.*, Vol. 205, Art. 116577.
3. Bahl, S., L. Xiong, L. F. Allard, R. A. Michi, J. D. Poplawsky, A. Chihpin Chuang, D. Singh, T. R. Watkins, D. Shin, J. A. Haynes, and A. Shyam, 2021, “Aging behavior and strengthening mechanisms of coarsening resistant metastable θ' precipitates in an Al-Cu alloy,” *Mater. Des.*, Vol. 198, Art. 109378.
4. Shower, P., J. Poplawsky, S. Bahl, and A. Shyam, 2021, “The role of Si in determining the stability of the θ' precipitate in Al-Cu-Mn-Zr alloys,” *J. Alloys Compd.*, Vol. 862, Art. 158152.
5. Milligan, B. K., S. Roy, C. S. Hawkins, L. F. Allard, and A. Shyam, 2020, “Impact of microstructural stability on the creep behavior of cast-Al-Cu alloys,” *Mater. Sci. Eng. A*, Vol. 772, Art. 138697.
6. Shyam, A., S. Roy, D. Shin, J. D. Poplawsky, L. F. Allard, Y. Yamamoto, J. R. Morris, B. Mazumder, J. C. Idrobo, A. Rodriguez, T. R. Watkins, and J. A. Haynes, 2019, “Elevated temperature microstructural stability in cast Al-Cu-Mn-Zr alloys through solute segregation,” *Mater. Sci. Eng. A*, Vol. 765, Art. 138279.
7. Shyam, A., Y. Yamamoto, D. Shin, S. Roy, J. A. Haynes, P. J. Maziasz, A. Sabau, A. F. Rodriguez-Jasso, J. A. Gonzalez-Villarreal, J. Talamantes-Silva, L. Zhang, C. R. Glaspie, and S. Mirmiran, 2016, “Aluminum Alloy Compositions and Methods of Making and Using the Same,” U.S. Patent Application No. 15160926, filed May 20, 2016.
8. Shyam, A., J. A. Haynes, J. A. Gonzalez-Villarreal, A. F. Rodriguez-Jasso, G. T. Black, C. R. Glaspie, and S. M. Mirmiran, 2018, “Heat Treatments for High-Temperature Cast-Aluminum Alloys,” U.S. Patent Application No. 16171201, filed October 25, 2018.

References

1. Phillippe, T., and P. W. Voorhees, 2013, “Ostwald ripening in multicomponent alloys,” *Acta Mater.*, Vol. 61, No. 11, pp. 4237–4244.
2. Milligan, B., D. Ma, L. F. Allard, A. Clarke, and A. Shyam, 2021, “Crystallographic orientation-dependent strain hardening in a precipitation-strengthened Al-Cu alloy,” *Acta Mater.*, Vol. 205, Art. 116577.

Acknowledgments

The authors would like to thank the following individuals from Oak Ridge National Laboratory, who were instrumental in their support of the project: B. Milligan, J. D. Poplawsky, P. Shower, J. A. Haynes, D. Shin, S. Bahl, X. Hu, J. Cheng, J. Jun, H. Wang, S. Hawkins, D. McClurg, and D. Ma. The authors also acknowledged the assistance of A. Clarke from the Colorado School of Mines.

1.3.1.1.3 Properties of Cast-Al-Cu-Mn-Zr (ACMZ) Alloys (Task 1B) (Oak Ridge National Laboratory)

Amit Shyam, Co-Principal Investigator

Oak Ridge National Laboratory
1 Bethel Valley Road
Oak Ridge, TN 37831
E-mail: shyama@ornl.gov

J. Allen Haynes, Co-Principal Investigator

Oak Ridge National Laboratory
1 Bethel Valley Road
Oak Ridge, TN 37831
E-mail: haynesa@ornl.gov

Jerry L. Gibbs, DOE Technology Manager

U.S. Department of Energy
E-mail: jerry.gibbs@ee.doe.gov

Start Date: October 1, 2018 End Date: September 30, 2023
Project Funding (FY 2021): \$220,000 DOE share: \$220,000 Non-DOE share: \$0

Project Introduction

The primary focus of this task is to further develop high-temperature cast-Al alloys for internal combustion engine (ICE) applications (e.g., cylinder head and block, piston, turbocharger) with improved power density and efficiency, including lightweight high-power density range extenders for electric freight vehicles. This task focuses on improving the low-temperature ($T < 150^{\circ}\text{C}$) ductility and low cycle fatigue (LCF) properties of higher temperature (300°C capable) cast ACMZ alloys, while simultaneously achieving a balance of other highly relevant material properties (e.g., creep, thermal conductivity, hot-tearing resistance, corrosion resistance). Key microstructural levers, which control the relevant material properties will be identified with the aim of increasing the commercial impact of cast ACMZ alloys.

Objectives

This is a mid-technology readiness level task to develop the fundamental understanding of microstructural features that control ductility and LCF life (at $T < 150^{\circ}\text{C}$), creep, thermal conductivity, and corrosion behavior of cast ACMZ alloys. The target properties include ambient temperature ductility higher than 5% and LCF life higher than the baseline commercial Al alloys A356 + 0.5 Cu and commercial alloy 319. The key activities in the task are as follows:

- To identify microstructural features in ACMZ alloys that control relevant mechanical properties.
- To modify the identified features using chemistry or processing modifications.
- To report scientific studies in the literature to advance materials technology for ICE applications, such as high-power density range extenders for hybrid electric HD trucks.

Approach

The major secondary phases in ACMZ alloy microstructures are the stable θ -Al₂Cu and metastable θ' -Al₂Cu intermetallic precipitates. θ' precipitates are present as fine, coherent platelets located inside the Al grains where their main purpose is to strengthen ACMZ alloys. In contrast, the coarse θ precipitates are located at the GBs and do not contribute significantly to the strength of cast alloys. However, the brittle nature of θ precipitates turns them into potential crack initiation sites in the microstructure that can impact ductility and LCF life of Al-Cu alloys. θ precipitates may also influence the creep properties by strengthening or weakening

the GBs at elevated temperatures. A higher Cu content is desirable in ACMZ alloys from the standpoint of better hot-tearing resistance during casting [1], but the simultaneous increase in the volume fraction of θ precipitates at the GBs is also expected to impact the mechanical properties. A series of ACMZ alloys with controlled Cu contents of 6.0, 6.6, 7.3, 8.0, and 9.0 weight percentage (wt%) were fabricated with gravity casting to systematically investigate the effect of Cu content on the mechanical properties. The 6.0-9.0 wt% range of Cu content is such that only the volume fraction of θ precipitates changes, but the volume fraction of θ' precipitates within the grains remains constant for each alloy composition. Consequently, any change in the mechanical properties will be a function of only the θ precipitates. The cast alloys were homogenized at 540°C for 5 h followed by quenching in warm water at 80°C. The alloys were subsequently aged at 240°C for 5 h to form the intended θ' precipitates in the microstructure. Monotonic tensile tests were performed at temperatures between RT and 300°C, LCF tests at temperatures between 150°C and 250°C, and creep tests (tensile and compressive) at 300°C. Synchrotron x-ray *in-situ* tensile testing at RT were performed at the Advanced Photon Source (APS) of Argonne National Laboratory (ANL). Microstructures were characterized with SEM, EBSD, STEM, and APT. FEM was used to simulate and understand the fracture behavior under monotonic tensile and LCF loading. The influence of Cu content on thermal conductivity of cast ACMZ alloys was also evaluated as a function of temperature.

Results

Research within this task over the previous two years demonstrated that the ductility of ACMZ alloys in the RT to 250°C range decreases with an increase in the Cu content from 6.0 to 9.0 wt% while the strength remains constant. Decreased ductility is related to larger size of grain boundary θ precipitates in the higher Cu alloys. Microscopic evidence suggests that larger θ precipitates have a lower fracture strength, which favors crack initiation resulting in lower alloy ductility. Figure I.3.1.1.3.1(a) shows the profusely fractured θ precipitates in the vertical cross-section microstructure of a 9.0 Cu ACMZ alloy following tensile testing. The size-dependent fracture strength of θ precipitates is quantitatively validated with synchrotron x-rays *in-situ* tensile tests, as schematically depicted in Figure I.3.1.1.3.1(b). Figure I.3.1.1.3.1(c) shows lattice stress parallel to the loading axis in the θ precipitates as a function of macroscopic strain calculated with (200) planes of the precipitates. The decrease in lattice stress after a certain amount of strain, which are indicated by the arrows, marks the onset of extensive fracture of θ precipitates and this peak stress is taken as the precipitate fracture strength. The size dependency of precipitate fracture strength is validated by the inverse relationship between fracture strength and the square root of the equivalent precipitate radius, as shown in Figure I.3.1.1.3.1(d). Thus, the decrease in the ductility of ACMZ alloys with increasing Cu content is a result of larger but weaker θ precipitates.

Grain boundary θ precipitates can also influence the creep properties of the ACMZ alloys through changes in creep deformation mechanisms [2] and cavitation [3]. Analysis of creep deformation mechanisms and cavitation is difficult, as both processes occur simultaneously, but this issue can be resolved by comparing tensile and compressive creep properties as the latter is not influenced by cavitation. The tensile and compressive creep strain rates as a function of applied stress at 300°C for 6.0 and 9.0 Cu ACMZ alloys are shown in Figure I.3.1.1.3.2(a). During compression creep studies, which were collaboratively conducted by Northwestern University, 6.0 and 9.0 Cu alloys deform with similar rates indicating that changes in the volume fraction of grain boundary θ precipitates as a function of the Cu content has no significant influence on the creep deformation mechanisms. In contrast, 9.0 Cu alloy creeps faster than 6.0 Cu during tensile creep at stresses above 15 MPa and the difference in strain rates increases with the stress level. As the creep deformation mechanisms do not change, the faster tensile creep of 9.0 Cu alloy is attributed to enhanced cavitation relative to the 6.0 Cu alloy. Cross-sectional SEM montages in Figure I.3.1.1.3.3 show cavitation occurring at grain boundary θ precipitates via interfacial decohesion in both alloys. The larger size of θ precipitates in the 9.0 Cu alloy promotes greater cavitation resulting in faster creep rates. Thus, higher Cu content in ACMZ alloys increases creep strain rate at high tensile stresses but has no effect at low tensile stresses or in compression.

The effect of Cu content on the ductility of ACMZ alloys at 300°C differs compared to the effect at lower temperatures. At 300°C, the ductility is higher for 9.0 Cu alloy compared to 6.0 Cu alloy, while the opposite is true at lower temperatures. The higher ductility of 9.0 Cu alloy is seen during both creep, as can be seen in Figure I.3.1.1.3.2(b), and the monotonic tensile tests, as observed in Figure I.3.1.1.3.2(c). Failure at 300°C occurs due to cavitation at grain boundary θ precipitates, whereas it occurs by brittle fracture of these precipitate at lower temperatures. Although the larger size and volume fraction of the θ precipitates in the 9.0 Cu alloy favor cavity nucleation, a combined effect of their more irregular morphology and local strengthening of grain boundary regions delays subsequent cavity linkage resulting in improved ductility. The easier cavity linkage in the 6.0 Cu alloy leads to the formation of more elongated intergranular cracks resulting in lower ductility, as shown in Figure I.3.1.1.3.3.

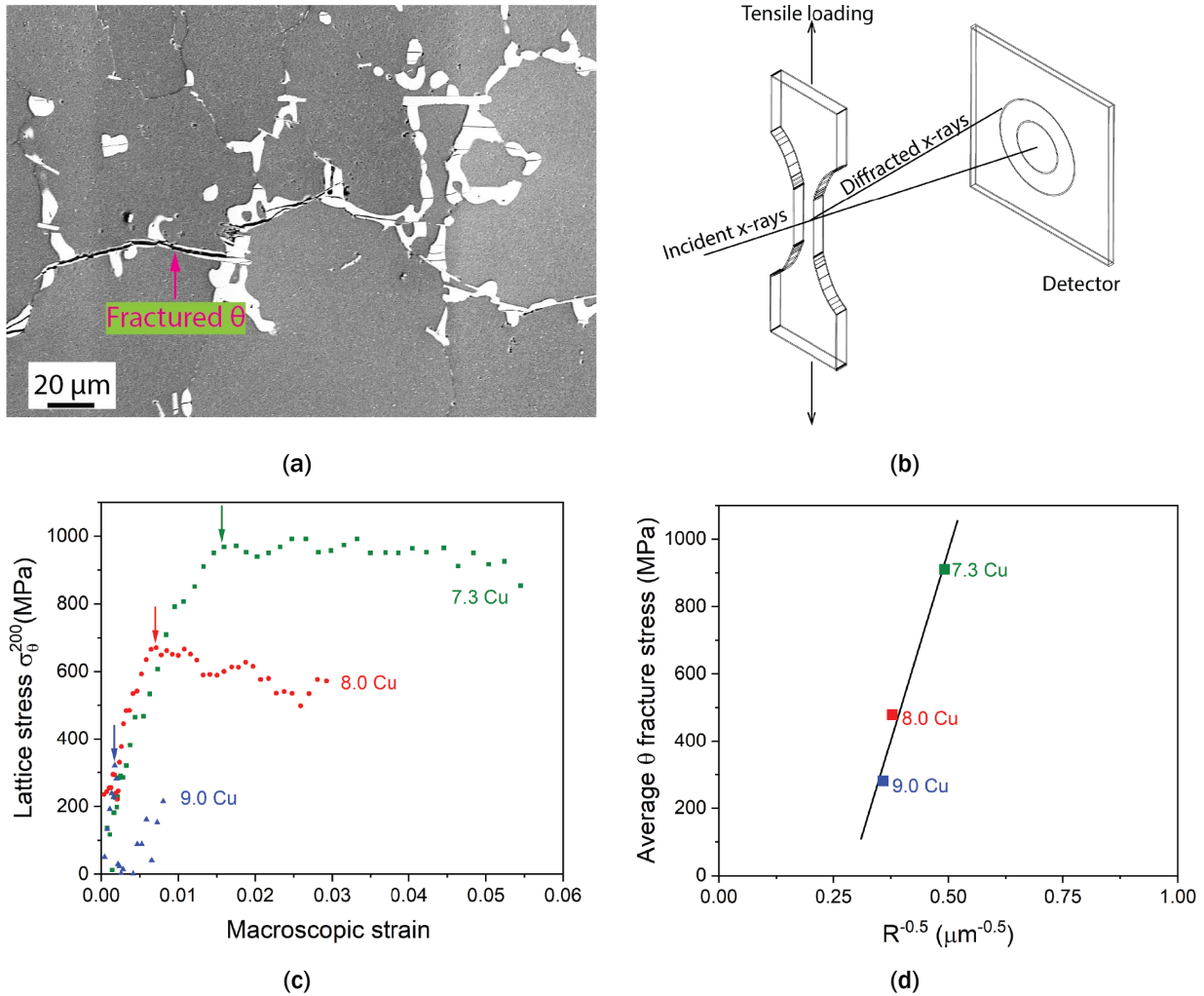


Figure I.3.1.1.3.1. (a) A backscatter electron SEM image showing numerous fractured bright contrast θ precipitates in a 9.0 Cu ACMZ alloy after tensile tests at RT. (b) A schematic of the synchrotron x-rays *in-situ* tensile test set up used to measure the fracture strength of θ precipitates. (c) A lattice stress evolution parallel to the loading axis in θ precipitates calculated with (200) planes as a function of macroscopic strain in which the arrows indicate the onset of θ precipitate fracture. (d) Average fracture stress in θ precipitates as a function of equivalent precipitate radius, R . Source: ORNL.

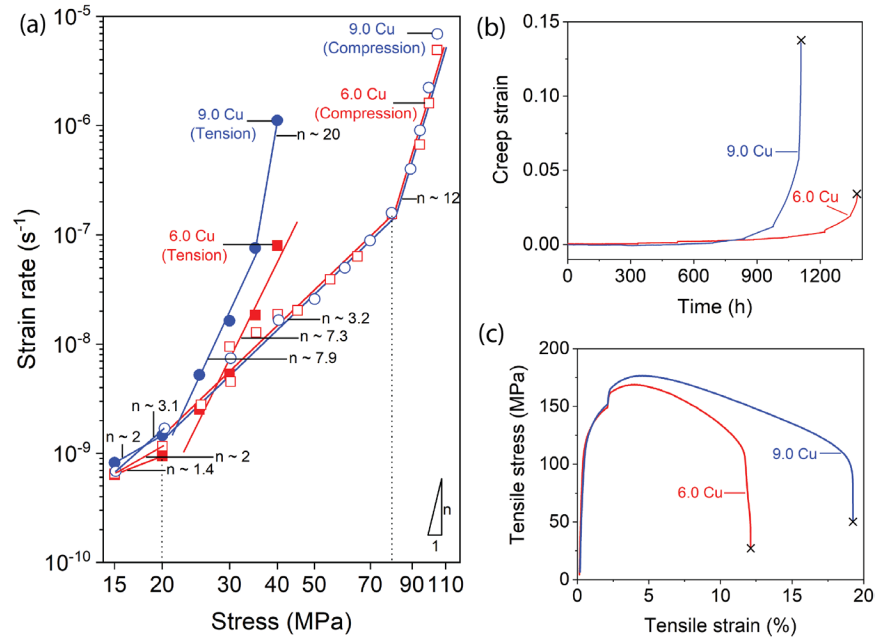


Figure I.3.1.1.3.2. (a) Double logarithmic plot of creep strain rate as a function of applied tensile or compressive stress at 300°C for 6.0 Cu and 9.0 Cu ACMZ alloys. (b) Creep strain accumulated as function of time at 300°C. (c) Monotonic tensile stress-strain curve at 300°C. The symbol 'x' indicates sample fracture.

Source: ORNL.

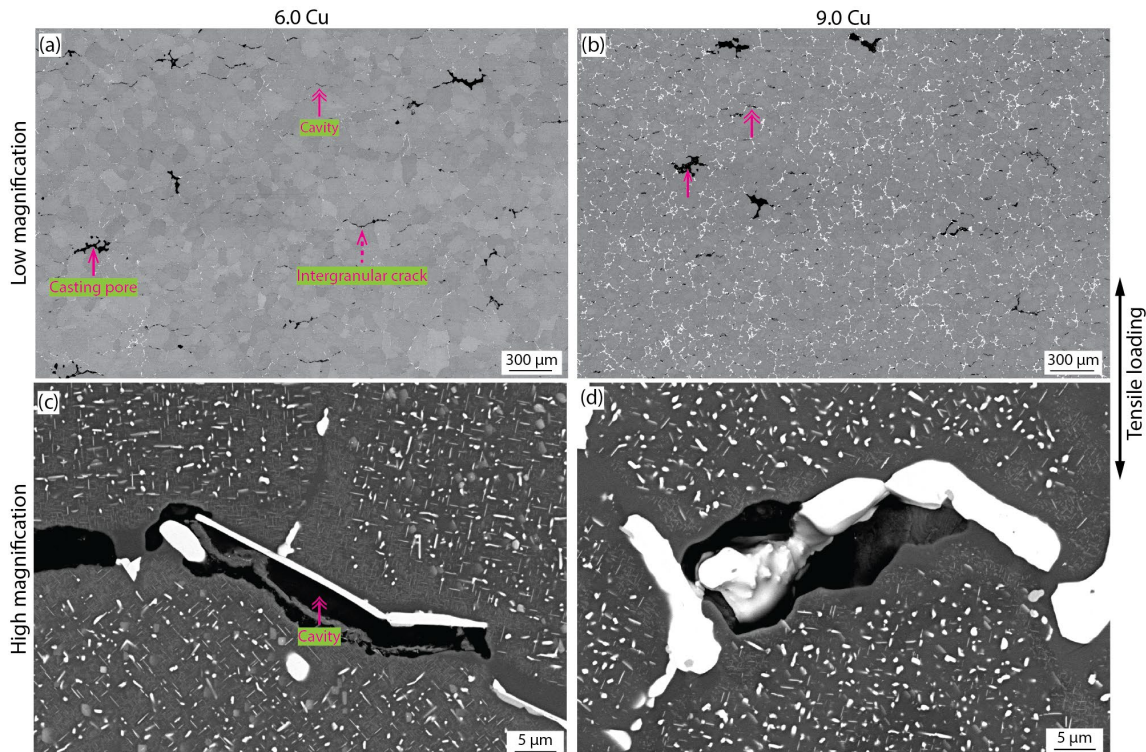


Figure I.3.1.1.3.3. Cross-sectional SEM montages of fractured (a) 6.0 Cu and (b) 9.0 Cu tensile creep samples showing cavitation at grain boundary θ precipitates and the magnified views of the cavities are shown for the two alloys in (c) and (d), respectively. double-headed arrow, dashed arrow, and solid arrow indicate creep cavities, creep intergranular crack, and casting pores, respectively [4, 5]. Source: ORNL.

Apart from the mechanical properties, thermal conductivity is an important property for the ICE applications. Figure I.3.1.1.3.4 shows thermal conductivity measured as a function of temperature for three ACMZ alloys with differing Cu contents and two commercial Al alloys. The change in Cu content of ACMZ alloys between 6.0 and 9.0 wt% does not influence their thermal conductivity and those values are comparable to commercial Al alloys, with thermal conductivity slightly higher than Alloy 319 and slightly lower than Alloy A356+0.5 Cu over most of the temperature range.

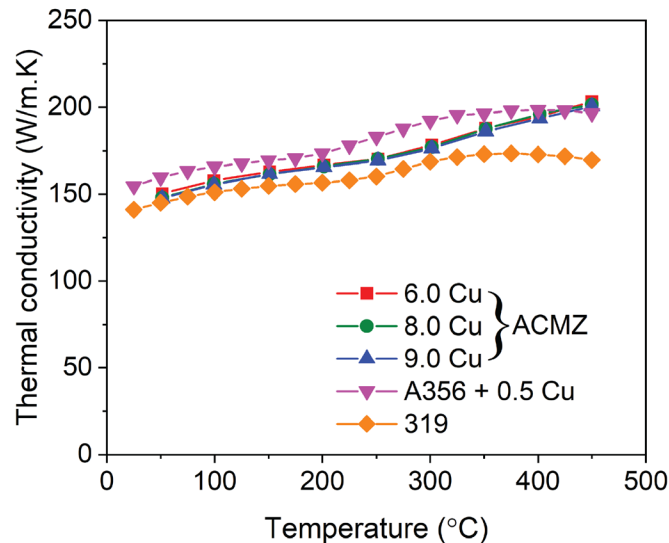


Figure I.3.1.1.3.4. Thermal conductivity of cast ACMZ alloys (e.g., 6.0, 8.0, and 9.0 wt% Cu) and commercial cast-Al alloys A356 + 0.5 Cu and 319 as a function of temperature. Source: ORNL.

Conclusions

- Synchrotron x-ray *in-situ* tensile tests showed that grain boundary θ precipitates weaken as their size increases with the Cu content (e.g., between 6.0 and 9.0 wt%) resulting in lower ductility of higher Cu ACMZ alloys.
- A higher Cu content results in faster creep only at tensile stresses above 15 MPa, but has negligible impact at lower tensile stresses or in compression.
- Thermal conductivity of the ACMZ alloys does not change with the Cu content and its value is comparable to commercial A356 + 0.5 Cu and 319 Al alloys up to 450°C.

Key Publications

1. Milligan, B., D. Ma, L. F. Allard, A. Clarke, and A. Shyam, 2021, "Crystallographic orientation-dependent strain hardening in a precipitation-strengthened Al-Cu alloy," *Acta Mater.*, Vol. 205, Art. 116577.
2. Bahl, S., L. Xiong, L. F. Allard, R. A. Michi, J. D. Poplawsky, A. Chihpin Chuang, D. Singh, T. R. Watkins, D. Shin, J. A. Haynes, and A. Shyam, 2021, "Aging behavior and strengthening mechanisms of coarsening resistant metastable θ' precipitates in an Al-Cu alloy," *Mater. Des.*, Vol. 198, Art. 109378.
3. Bahl, S., X. Hu, K. Sisco, J. A. Haynes, and A. Shyam, 2020, "Influence of copper content on the high-temperature tensile and low cycle fatigue behavior of cast-Al-Cu-Mn-Zr alloys," *Int. J. Fatigue*, Vol. 140, Art. 105836.
4. Bahl, S., X. Hu, E. Hoar, J. Cheng, J. A. Haynes, and A. Shyam, 2021, "Effect of copper content on the tensile elongation of Al-Cu-Mn-Zr alloys: Experiments and finite element simulations," *Mater. Sci. Eng. A*, Vol. 772, Art. 138801.

5. Milligan, B. K., S. Roy, C. S. Hawkins, L. F. Allard, and A. Shyam, 2021, “Impact of microstructural stability on the creep behavior of cast-Al-Cu alloys,” *Mater. Sci. Eng. A*, Vol. 772, Art. 138697.
6. Shyam, A., S. Roy, D. Shin, J. D. Poplawsky, L. F. Allard, Y. Yamamoto, J. R. Morris, B. Mazumder, J. C. Idrobo, A. Rodriguez, T. R. Watkins, and J. A. Haynes, 2019, “Elevated temperature microstructural stability in cast-Al-Cu-Mn-Zr alloys through solute segregation,” *Mater. Sci. Eng. A*, Vol. 765, Art. 138279.
7. Shyam, A., S. Bahl, J. A. Haynes, and Y. Yamamoto, 2021, “High-temperature cast-aluminum-copper-manganese-zirconium alloys with low-temperature ductility,” U.S. Patent Application No. 17/189,181, filed September 16, 2021.

References

1. Sabau, A. S., S. Mirmiran, C. Glaspie, S. M. Li, D. Apelian, A. Shyam, J. A. Haynes, and A. F. Rodriguez, 2018, “Hot-tearing assessment of multicomponent nongrain-refined Al-Cu alloys for permanent mold castings based on load measurements in a constrained mold,” *Metall Mater Trans B*, Vol. 49, No. 3, pp. 1267–1287.
2. Harris, J. E., 1973, “The inhibition of diffusion creep by precipitates,” *Met. Sci. J.*, Vol. 7, No. 1, pp. 1–6.
3. Nix, W. D., 1988, “Mechanisms and controlling factors in creep fracture,” *Mater. Sci. Eng. A*, Vol. 103, No. 1, pp. 103–110.
4. Preibisch, S., S. Saalfeld, and P. Tomancak, 2009, “Globally optimal stitching of tiled 3D microscopic image acquisitions,” *J. Bioinform.*, Vol. 25, No. 11, pp. 1463–1465.
5. Schneider, C. A., W. S. Rasband, and K. W. Eliceiri, 2012, “NIH Image to ImageJ: 25 years of image analysis,” *Nat. Methods*, Vol. 9, No. 7, pp. 671–675.
6. Milligan, B., D. Ma, L. F. Allard, A. Clarke, and A. Shyam, 2021, “Crystallographic orientation-dependent strain hardening in a precipitation-strengthened Al-Cu alloy,” *Acta Mater.*, Vol. 205, Art. 116577.

Acknowledgments

The synchrotron x-ray measurements were performed at the APS, a DOE–Office of Science User Facility operated for the DOE–Office of Science by ANL under Contract No. DE-AC02-06CH11357. The authors would like to thank the following individuals from ORNL, who were instrumental in their support of the project: S. Bahl, J. A. Haynes, D. Shin, X. Hu, J. Cheng, J. Jun, H. Wang, S. Hawkins, and D. McClurg. The authors also thank Y. Ren and A. Chihpin Chuang of ANL; and D. C. Dunand, J. U. Rakhmonov, and C. Kenel of Northwestern University.

I.3.2 Cost-Effective Higher Temperature Engine Alloys – Thrust 2

I.3.2.1 New Aluminum Alloys with Improved High-Temperature Performance (2A/2B)

I.3.2.1.1 Development of Oxidation-Resistant Valve Alloys for 900–950 °C (Task 2A1) (Oak Ridge National Laboratory)

Govindarajan Muralidharan, Co-Principal Investigator

Oak Ridge National Laboratory
1 Bethel Valley Road
Oak Ridge, TN 37831
E-mail: muralidhargn@ornl.gov

Bruce Pint, Co-Principal Investigator

Oak Ridge National Laboratory
1 Bethel Valley Road
Oak Ridge, TN 37831
E-mail: pintba@ornl.gov

Jerry L. Gibbs, DOE Technology Manager

U.S. Department of Energy
E-mail: jerry.gibbs@ee.doe.gov

Start Date: October 1, 2018 End Date: September 30, 2023
Project Funding (FY 2021): \$450,000 DOE share: \$400,000 Non-DOE share: \$50,000

Project Introduction

Improving the engine efficiencies and reducing emissions of passenger and commercial vehicles is a major goal of the U.S. DOE-EERE VTO. One potential approach to achieving improved engine efficiency, while reducing emissions, is through retaining more heat in the exhaust gas. This approach has been projected to increase exhaust gas temperatures from a current value of 760°C to values to at least 870°C, and very likely reach as high as 1,000°C in the longer term [1, 2]. High-performance exhaust valves, currently used at temperatures up to ~760°C, are fabricated using Ni-based alloys, such as commercial Alloy 751. Other higher performance Ni-based alloys primarily developed for aerospace applications have the potential to operate at temperatures of 1,000°C with the desired strength but may be both too expensive for automotive applications and are also extremely difficult to forge into valves via the existing manufacturing infrastructure. Another benefit of higher temperature valve alloys would be to better enable the future use of hydrogen as a low- or zero-carbon combustion fuel for HD reciprocating engines.

Objectives

The primary objective of this project is the development of cost-effective advanced alloys for exhaust valves, capable of operating at temperatures of at least 900°C, and up to 950°C. These alloys should have the appropriate combination of oxidation resistance and high-temperature mechanical strength required for the most-rigorous exhaust valve applications in both automotive and heavy-duty diesel engines. In collaboration with a recently established cooperative research and development agreement (CRADA) partner, Federal Mogul Powertrain/Tenneco, this project aims to demonstrate the suitability of a newly developed advanced alloy for use in exhaust valves by fabricating and testing prototype valves using an industrially produced heat of material in FY 2022.

Approach

Table I.3.2.1.1.1 shows the yield strength, fatigue life, oxidation resistance, and cost targets of materials needed for exhaust valves in next-generation high-efficiency engines. Two parallel approaches were pursued in the design strategy: (1) chromia-forming, lower-cost, higher strength Ni-based alloys; and (2) more-oxidation-resistant alumina-forming Ni-based alloys—including the development of alumina-forming high-strength polycrystalline alloys. The principal approach to achieving Ni-based alloys with adequate high-temperature mechanical strength in both approaches is through the use of γ' ($\text{Ni}_3(\text{Al},\text{X})$, $L1_2$ -type) precipitates for strengthening in a γ -matrix. In addition to controlling the volume fraction of γ' , a fine distribution of these precipitates must be achieved for optimum strengthening. One or more carbide phases, such as M_{23}C_6 , MC, and M_7C_3 may also be present for grain size control. Since at temperatures of 900°C and higher, diffusion rates can be significant, the key challenge in achieving the long-term mechanical properties is to ensure that the γ' precipitates remain stable over the expected lifetime of the alloys with relatively low rates of coarsening. It was anticipated that the alumina-forming alloys could achieve the targeted strength and oxidation resistance at temperatures up to 950°C. However, it is most likely that oxidation-resistant coatings would be needed at temperatures greater than 900°C to protect the higher strength chromia-forming alloys from the combustion environment. A separate task within this research thrust (e.g., Task 2A3) is pursuing the development of oxidation-resistant slurry aluminide and thermal spray coatings for the chromia-forming alloys in this project.

Table I.3.2.1.1.1. Target Properties and Metrics

Property	Final Target
Yield Strength	≥ 50 Ksi at 950 °C.
Fatigue Life	Fatigue life of new alloys > fatigue life of Alloy 751 at 900 °C–950 °C at 30–50 Ksi.
Oxidation Resistance	Mass change ≤2X commercial alumina-forming alloys at 950 °C.
Cost	≤ 1.25X of 751.

The approach used in this task to develop the two classes of alloys is outlined below:

- Chromia-forming alloys:** Previous work at ORNL has shown that the strengths in the heat-treated condition of new, lower-cost NiCrFe-based ORNL alloys are superior to that of Alloy 751, the current state-of-the-art valve alloy, at temperatures of 870°C and beyond [3, 4]. This subtask is partnering with industrial CRADA partner Tenneco to identify which alloy variants can maintain their long-term strength at 900°C and above. Microstructural evolution is being evaluated in a select group of alloys fabricated at the laboratory-scale. Larger-sized heats are being fabricated by the industrial partner. High-temperature fatigue properties of those heats are being evaluated. Prototype exhaust valves will be fabricated in FY 2022 using one or more downselected alloys, based upon the measured properties of the industrial heats. These prototype exhaust valves will be evaluated on a testing rig and/or in engine tests by the CRADA partner in their commercial facilities. Advanced characterization methods are being used to study γ' -precipitate evolution in the various alloys to determine how this behavior affects high-temperature mechanical properties related to both manufacturing (forging) and valve performance in higher efficiency engine designs. Advanced modeling is being used to predict microstructural evolution and will be validated to enable longer term predictions of alloy strength stability.
- Alumina-forming alloys:** The primary challenge in this new class of alloys is achieving the required high-temperature strength and fatigue resistance while maintaining the excellent oxidation resistance provided by the alumina scale. Commercially available polycrystalline alumina-forming alloys are much lower in strength than the chromia-forming alloys at temperatures beyond 900°C, and hence, new alloys are needed with improved strength for use at these higher temperatures. Computational thermodynamics are being used to design alloys with desired γ' contents while also achieving good alumina scale formability at the targeted temperature of 950°C. Kinetic modeling is being used to design alloys with appropriate γ' sizes. Models are being validated using TEM, APT, and ultra-small-angle/small-angle scattering in FY 2021.

Results

Chromia-forming alloys: Three different lower-cost ORNL alloys were identified in the original patent by the following compositions: (1) Alloy 161—nominal composition: 47Ni-27Fe-17.5Cr-1Co-1Mo-1.75Al-3.75Ti-0.03C, all in weight percentage, and heat M2045; (2) Alloy 200—nominal composition: 48Ni-26Fe-18Cr-2Co-1Mo-1.7Al-3.5Ti-0.04C, all in weight percentage, and heat H2078; and (3) Alloy 163—nominal composition: 48Ni-24Fe-17.5Cr-1Co-1.5Mo-1.75Al-3.75Ti-1Ta-0.5W-0.03C, all in weight percentage, and heat H2079. Each were successfully scaled-up in FY 2019, FY 2020, and FY 2021, respectively. Figure I.3.2.1.1.1 shows the microstructure of a solution-annealed and aged sample from H2078, while Figure I.3.2.1.1.2 shows the microstructure of a sample from H2079 after a similar heat-treatment. Note that both alloys show the presence of fine γ' precipitates, which is a prerequisite for achieving the designed higher strengths at temperatures beyond the $\sim 870^\circ\text{C}$ temperature limit of commercial alloys like IN751.

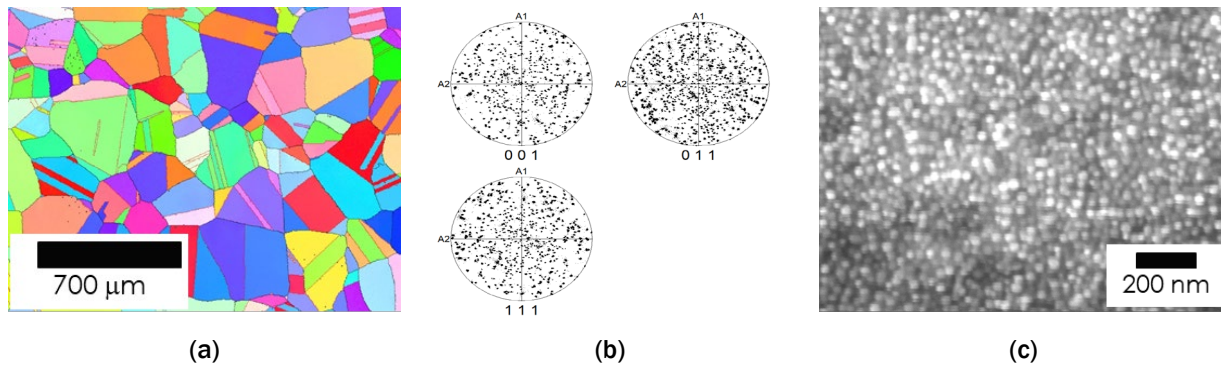


Figure I.3.2.1.1.1. The microstructure of a solution-annealed and aged sample from H2078. (a) Inverse pole figure map showing the grain size and grain orientation. (b) (001), (011), and (111) pole figures showing no obvious preferred orientation. (c) Fine γ' precipitates present in the as-aged condition. Source: ORNL.

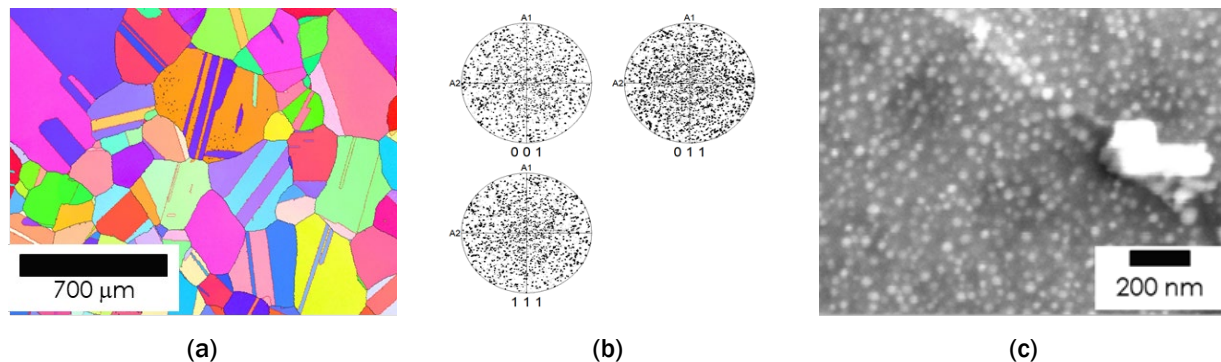
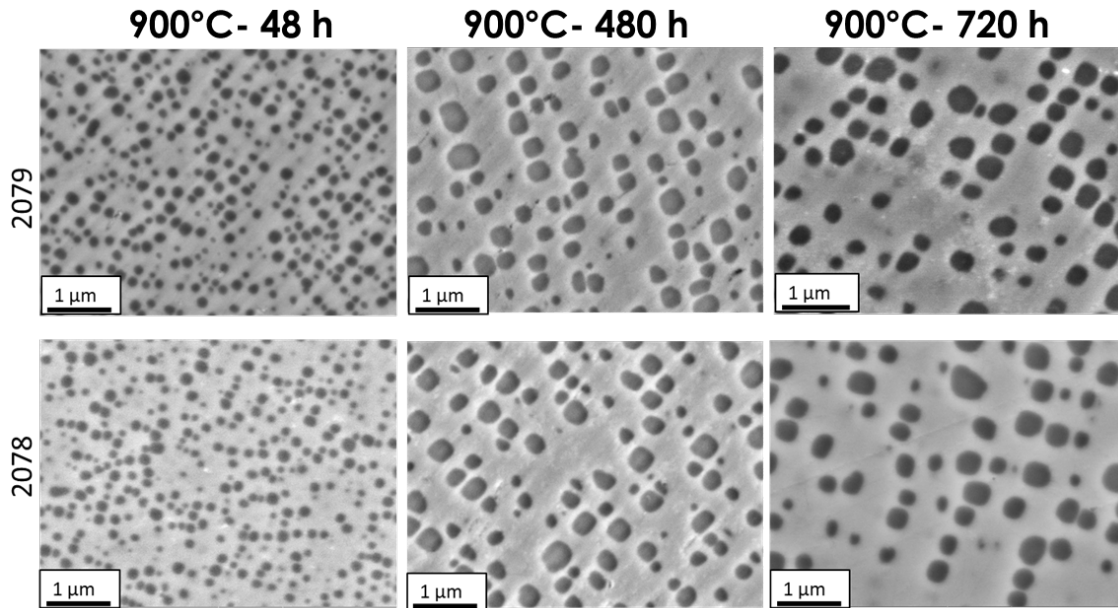


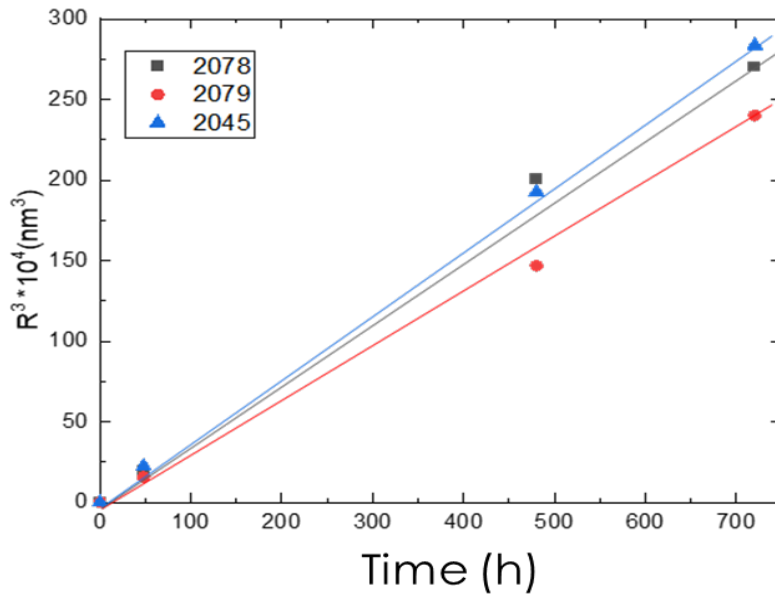
Figure I.3.2.1.1.2. The microstructure of a solution-annealed and aged sample from H2079. (a) Inverse pole figure map showing the grain size and grain orientation. (b) (001), (011), and (111) pole figures showing no obvious preferred orientation. (c) Fine γ' precipitates present in the as-aged condition. Source: ORNL.

Figure I.3.2.1.1.3(a) shows the effect of long-term aging at 900°C on the coarsening of γ' precipitates in the H2078 and H2079 samples. A plot of $R^3 - R_0^3$ as a function of time (h), as shown in Figure I.3.2.1.1.3(b), shows a linear relationship consistent with the Ostwald ripening with the rate of coarsening of γ' precipitates in the H2079 being lower than that of γ' precipitates in the H2078. Preliminary high-temperature fatigue testing results are presented in Figure I.3.2.1.1.4, which shows the number of cycles to failure at 900°C as a function of the ratio of applied stress to tensile strength for ORNL Alloys M2045 and H2079. The H2079 alloy did not fail even after >20 million cycles at 900°C and 125 MPa, resulting in a runout. By comparison, Alloy M2045 failed after less than 10 million cycles under the same conditions. The superior performance of the H2079 is

likely due to the lower coarsening rate of γ' precipitates, but further work is required to confirm this hypothesis. Additional fatigue tests are currently being performed both at ORNL and by Tenneco to assess the typical variation in fatigue lives at these conditions.



(a)



(b)

Figure I.3.2.1.1.3. (a) The effect of aging for 48 h, 480 h, and 720 h of annealing time at 900 °C on the γ' size in M2078 and M2079. (b) Plot of $R^3 - R_0^3$ as a function of time (h). Source: ORNL.

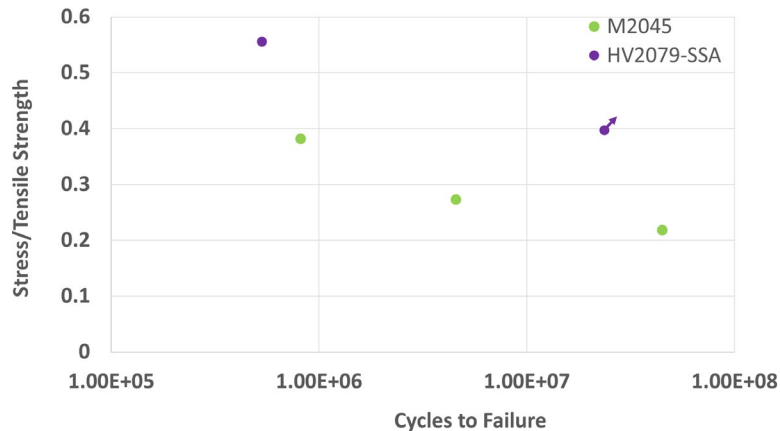
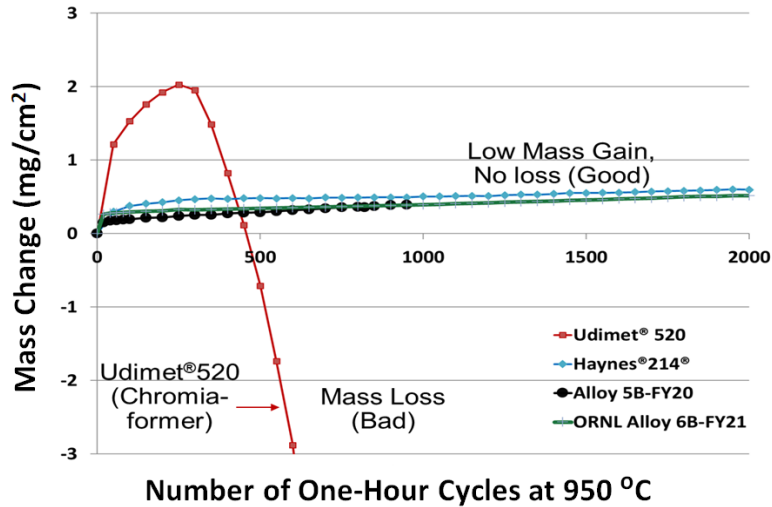


Figure I.3.2.1.1.4. The number of cycles to failure at 900 °C as a function of the ratio of applied stress to tensile strength for two ORNL developmental alloys designed for higher strength at higher temperatures, and for lower-cost than commercial higher temperature valve alloys. The arrow shows that the test was stopped without sample failure (runout). Source: ORNL.

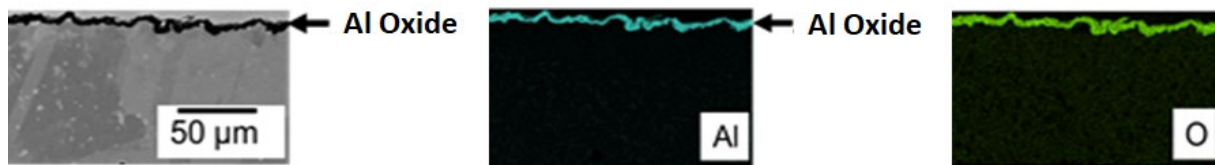
Alumina-forming alloys: Figure I.3.2.1.1.5(a) compares the mass change as a function of the number of one-hour cycles at 950°C in air plus a 10% water-vapor environment for one of the new alumina-forming ORNL alloys developed in FY 2020 (5B) and one new alloy developed in FY 2021 (6B) to that of an alumina-forming commercial alloy, Haynes®214®, as well as a commercial chromia-forming alloy, Udimet®520. The high-strength ORNL alumina formers show oxidation behavior comparable to that of the commercial 214 alloy. All alumina formers shown in Figure I.3.2.1.1.5 show oxidation behavior far superior to that of the chromia-former Udimet®520. Figure I.3.2.1.1.5(b) shows the cross-section of a sample from ORNL Alloy 6B tested for 5,450 1-h cycles with mass change, as shown in Figure I.3.2.1.1.5(a). Note the presence of a thin oxide scale that is rich in Al, confirming the presence of an adherent Al-rich oxide after over 5,000 h cyclic oxidation testing at 950°C.

Figure I.3.2.1.1.6 compares the yield strengths at 950°C of the new ORNL alloys developed in FY 2021 with those of alumina-forming alloys developed in previous fiscal years, commercial chromia-forming Udimet®520 and commercial alumina-forming Haynes®214®. Also shown in Figure I.3.2.1.1.6 are the FY 2020 and FY 2021 Go/No-Go decision point targets for yield strengths for the new alumina-forming alloys at 950°C. Note that substantial improvements were achieved in yield strengths measured at 950°C in FY 2021 as compared to those achieved in FY 2020. The FY 2021 targets were successfully exceeded while still achieving outstanding oxidation resistance at 950°C in air plus 10% water-vapor environment. Alloy 6B developed in FY 2021 achieved a yield strength of about 296 MPa, which although lower than the ultimate target of 345 MPa, represents an improvement over the ~267 MPa achieved in FY 2020 and ~250 MPa improvement over the commercial alloy 214 (~46 MPa yield strength at 950°C). Thus, this appears to be an unprecedented level of high-temperature strength for a polycrystalline alumina-forming alloy. Although further improvements are needed to attain the targeted yield strength values for this project, since the improvements in yield strength have been substantial, a commercial scale-up of an earlier version of the ORNL-developed alumina-forming alloy [2, 3] was completed this year to evaluate fatigue behavior of this class of alloys in FY 2022.

Figure I.3.2.1.1.7 shows that the improved strength of the ORNL-developed alumina-former is not restricted to 950°C only, but also shows better yield strength than commercial alloy 751 and several ORNL-developed lower-cost chromia-forming alloys over a wide temperature range. The improvements achieved this year suggest that further increases in high-temperature yield strength are possible using the current alloy design strategy. Additional alloys are currently being designed with the goal of achieving the ultimate target of 345 MPa.



(a)



(b)

Figure I.3.2.1.1.5. (a) Newly designed alumina-forming alloys showed oxidation behavior comparable to commercial alumina-forming Ni-based alloys at 950 °C in air + 10% water-vapor. (b) Cross-section of a sample from ORNL-developed Alloy 6B tested for 5450 1-hr cycles showing presence of a thin Al-rich oxide scale. Source: ORNL.

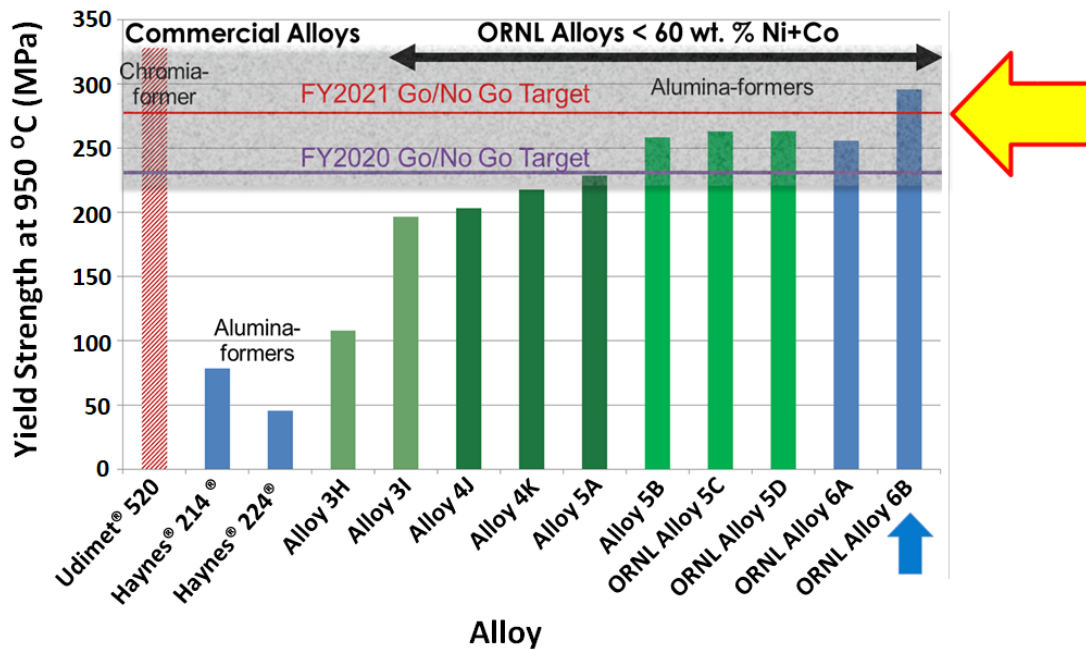


Figure I.3.2.1.1.6. Yield strength of the best new alumina-forming alloy exceeded FY 2021 target at 950 °C. Source: ORNL.

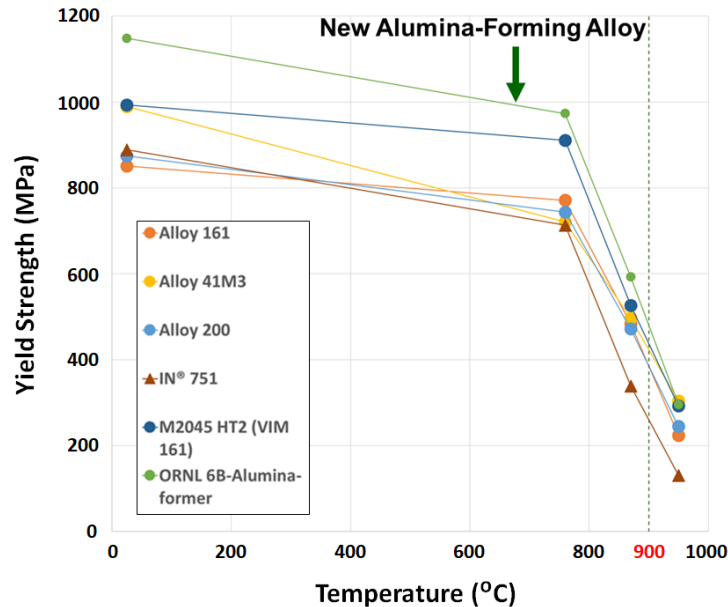


Figure I.3.2.1.1.7. Yield strengths of the most promising new alumina-forming polycrystalline alloy exceed those of several lower-cost ORNL-developed chromia-formers and alloy 751 over a wide temperature range. Source: ORNL.

Conclusions

Three new lower-cost chromia-forming alloys developed at ORNL have been successfully scaled-up using smaller, industrial-scale heats. High-temperature fatigue testing indicates good high-temperature fatigue properties and microstructural stability at 900°C. Additional chromia-forming ORNL alloys will be scaled-up in FY 2022 with guidance from CRADA partner Federal Mogul Powertrain/Tenneco. New ORNL alumina-forming alloys have been developed with remarkable yield strengths, with values at 950°C exceeding that of the current commercial valve alloy 751. These new high-strength alumina-forming polycrystalline alloys retain their excellent oxidation resistance after thousands of hours at 950°C due to alumina scale formation. Scale-up of one alloy alumina-forming composition was completed in FY 2021 to allow preliminary fatigue testing in FY 2022. These higher temperature alloys may also offer value in potential future hydrogen fueling scenarios.

Key Publications

1. Gwalani, B., S. Shukla, D. Leonard, J. D. Poplawski, D. T. Pierce, L. Kovarik, G. Muralidharan, and A. Devaraj, 2021, "Understanding the microstructural stability in a γ' -strengthened Ni-Fe-Cr-Al-Ti alloy," *J. Alloys Compd.*, Vol. 886, Art. 161207.
2. Muralidharan, G., and B. Pint, 2019, "Alumina-forming, high-temperature creep-resistant Ni-based alloys," U.S. Patent 10,174,408 B2, issued January 8, 2019.
3. Muralidharan, G., and B. Pint, 2021, "Alumina-forming creep-resistant Ni-based alloys," U.S. Patent No. 10,745,781, issued August 18, 2021.

References

1. DOE Vehicle Technologies Office, 2013, "Light-Duty Vehicles Technical Requirements and Gaps for Lightweight and Propulsion Materials," DOE VTO Workshop Report No. DOE/EE-0868, February 2013.
2. DOE Vehicle Technologies Office, 2013, "Trucks and Heavy-Duty Vehicles Technical Requirements and Gaps for Lightweight and Propulsion Materials," DOE VTO Workshop Report No. DOE/EE-0867, February 2013.
3. Muralidharan, G., and B. Pint, 2019, "Alumina-forming, high-temperature creep-resistant Ni-based alloys," U.S. Patent 10,174,408 B2, issued January 8, 2019.

4. Muralidharan, G., and B. Pint, 2020, “Alumina-forming creep-resistant Ni-based alloys,” U.S. Patent No. 10,745,781, issued August 18, 2020.
5. DOE Vehicle Technologies Office, 2021, “DOE Vehicle Technologies Materials FY 2020 Annual Progress Report,” DOE/EE-2336, April 2021.

Acknowledgments

The authors would like to acknowledge S. Shukla, J. Chiles, D. T. Pierce, D. Leonard, J. Poplawsky, J. A. Haynes, T. Muth, T. R. Watkins, D. Erdman, K. Hedrick, J. Moser, C. Hawkins, G. Cox, K. Hanson, D. Moore, C. Carmichael, I. Stinson, G. Garner, T. Lowe, and T. Geer from ORNL; M. Frith, J. Ilavsky, S. Lapidus, and D. Singh from ANL; and B. Gwalani, A. Devraj, and L. Kovanik from PNNL for their support in this work.

I.3.2.1.2 Higher Temperature Heavy-Duty Piston Alloys (Task 2A2) (Oak Ridge National Laboratory)

Dean Pierce, Co-Principal Investigator

Oak Ridge National Laboratory
1 Bethel Valley Road
Oak Ridge, TN 37831
E-mail: piercedt@ornl.gov

Govindarajan Muralidharan, Co-Principal Investigator

Oak Ridge National Laboratory
1 Bethel Valley Road
Oak Ridge, TN 37831
E-mail: muralidhargn@ornl.gov

Jerry L. Gibbs, DOE Technology Manager

U.S. Department of Energy
E-mail: jerry.gibbs@ee.doe.gov

Start Date: October 15, 2018 End Date: September 30, 2023
Project Funding (FY 2021): \$200,000 DOE share: \$200,000 Non-DOE share: \$0

Project Introduction

Quench and tempered 4140 martensitic steel and micro-alloyed 38MnVS6 steel are the primary materials used in pistons for heavy-duty diesel engines (HDDEs). A major pathway to increasing the efficiency and reducing emissions of future internal combustion engines—and perhaps including hydrogen fueled combustion engines—involves increasing both the peak cylinder pressure and combustion gas temperatures. However, these current piston materials are operating at their limits of mechanical and thermal loading in current HDDEs. The 4140 and micro-alloyed steel alloys are limited to an operating temperature of ~500°C. As such, current piston materials limits are a major barrier to increasing engine efficiency for the long-haul freight industry, which is expected to double in volume within the U.S. in the next decade.

Objectives

The objectives of this project are to investigate existing commercial alloys, as well as alloys being developed at ORNL, for use in HDDE pistons. Alloys that have the potential to enable increased operating temperatures and cylinder pressures, but require only moderate increases in materials and manufacturing costs over 4140 steels, are of particular interest. Specifically, the new alloys must meet the unique combinations of requirements for HDDE pistons, including high-temperature strength, high-cycle fatigue strength, cyclic oxidation resistance in a combustion environment, optimal thermal conductivity, wear resistance, machinability, friction weldability, microstructural stability, etc. These phenomena can act synergistically to cause failure or to create cost or manufacturing barriers. The targeted peak piston operating temperature within this task is > 600°C. Further key targets include ultimate tensile strength (UTS) levels of approximately 525 MPa at peak temperature and acceptable oxidation resistance at > 600°C.

Approach

Four major groups of alloys are being investigated to identify materials that are suitable from a performance and cost perspective for use in next-generation HDDE pistons: (1) commercial martensitic stainless steels; (2) ORNL developmental low-cost low Cr alloys with superior elevated temperature strength; (3) ORNL developmental alloys with medium levels of Cr and improved oxidation resistance; and (4) ORNL developmental advanced high Cr alloys for operation at between 650°C and 700°C. Evaluation of the low, medium, and high Cr developmental alloys occurred in FY 2021. However, most alloy development activities

were primarily focused on the high Cr group of alloys in FY 2021. The decision to focus on this group of alloys in FY 2021 is primarily due to these alloys being most ready for scale-up for prototype piston manufacture, as well as that this group of alloys exhibits what is believed to be the best combination of properties for pistons in next-generation HDDEs.

Results

Commercial Baseline Alloys

Two commercial baseline alloys were selected for evaluation of mechanical, oxidation, and thermal properties in the first stage of this project: (1) martensitic stainless-steel Alloy 418 (e.g., Fe-0.15C-0.25Mn-0.25Si-13Cr-2Ni-3W wt.%); and (2) martensitic stainless-steel Alloy 422 (e.g., Fe-0.23C-0.75Mn-0.35Si-1Mo-11.5Cr-0.8Ni-1W wt.%). After evaluating and testing the two commercial alloys, Alloy 422 was identified as having the best potential for piston applications. Based on the testing and evaluation of commercial alloys in this core program task, Alloy 422 was subsequently downselected for manufacturing of prototype pistons and engine testing as part of a satellite project with the U.S. Army Ground Vehicles Systems Center. Figure I.3.2.1.2.1 shows numerous 6 in. diameter Alloy 422 “pucks” in a vacuum furnace at an external heat-treatment facility prior to the austenitization, quench, and tempering heat-treatment. The Alloy 422 pucks will be manufactured into prototype pistons for welding and machining trials and ultimately, engine testing in a single-cylinder research engine, as part of the project with Army Ground Vehicles Systems Center.

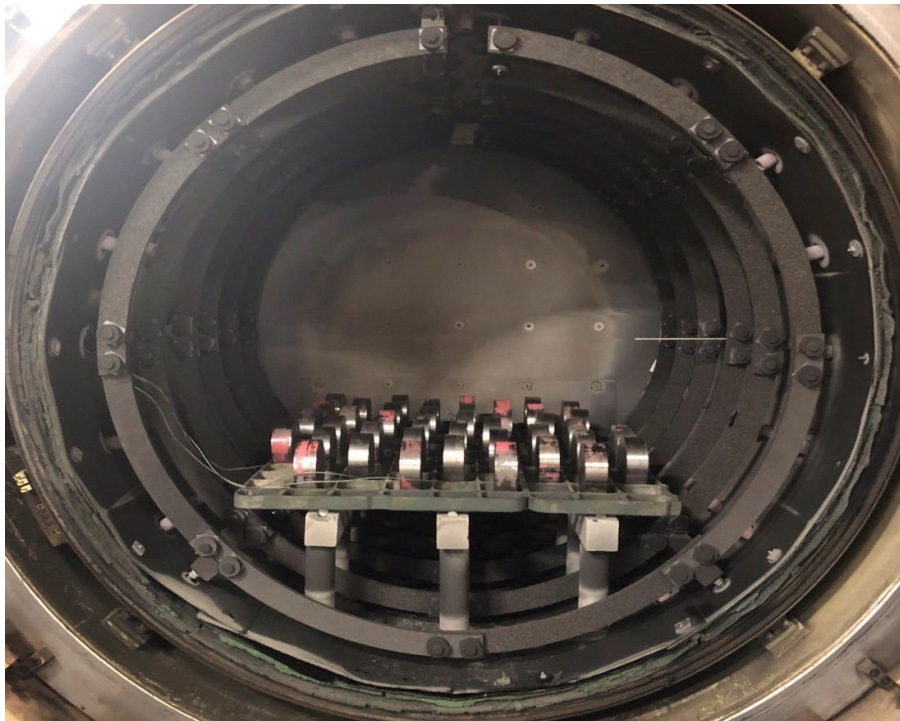


Figure I.3.2.1.2.1. Steel pucks in an industrial vacuum furnace for austenitization. Source: ORNL.

Low Cr Martensitic Development Steels

Alloy design concepts for steels with lower Cr levels for reduced cost applications have been developed. In addition, compared to steels with a higher alloy content, these steels offer higher thermal conductivity. Furthermore, these steels, targeted for operation at up to 550°C, show very high levels of strength compared to baseline commercial Alloys 422 and 4140. The UTS and thermal conductivity as a function of temperature are shown for a series of low Cr ORNL developmental alloys in Figure I.3.2.1.2.2 along with that of commercial Alloys 4140 (e.g., strength values are also shown for Alloy 422 and Alloy 418). One of the developmental alloys, designated Alloy 212, exhibits a UTS level exceeding 700 MPa at 600°C. This is notably superior to the target of 525 MPa, and thermal conductivity values greater than that of Alloy 4140, meaning the alloy will

operate at lower temperatures, potentially further enhancing the strength advantage over Alloy 4140. This superior balance of strength and thermal conductivity may enable new piston designs with certain functional advantages, such as thinner wall thickness, reduced weight, and/or lower surface temperatures. These alloys may increase engine efficiency, particularly for highly stressed pistons operating in engines with increased peak cylinder pressures. The low Cr steels show promise for advanced piston applications where peak metal temperatures do not exceed $\sim 550^{\circ}\text{C}$, due to excessive oxidation that may occur above this temperature for lower Cr alloys.

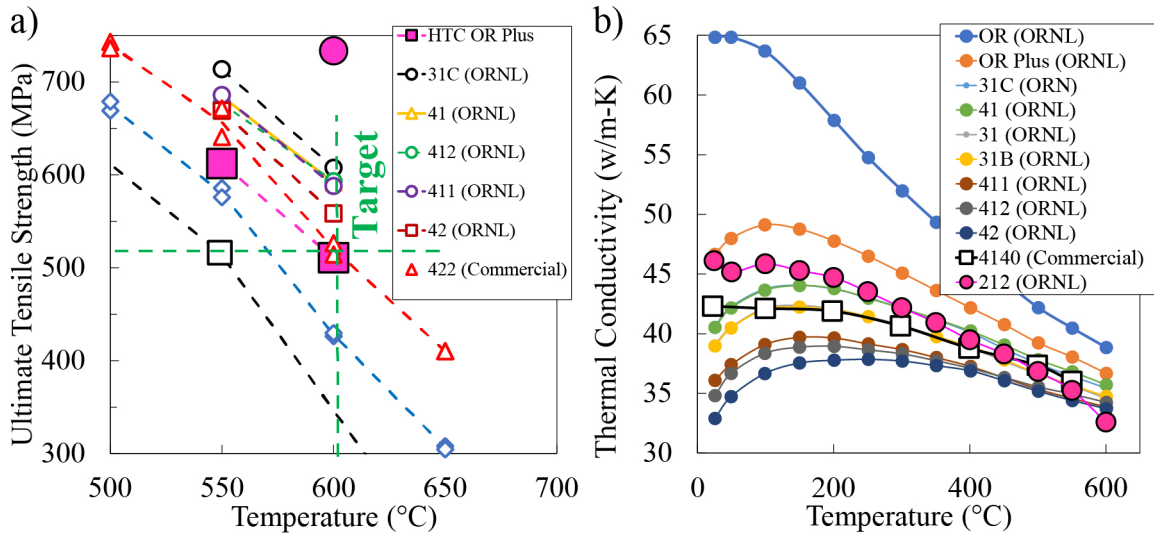


Figure I.3.2.1.2.2. (a) UTS and (b) thermal conductivity as a function of temperature for various developmental alloys as well as commercial Alloy 4140. Strength levels of Alloys 418 and 422 are also shown in (a). The steels are in the as-tempered condition. Alloy 212, filled pink circles, shows an exceptional combination of high-strength and relatively high thermal conductivity. Source: ORNL.

Low-Cost Medium Cr Developmental Steels

Alloy design efforts to achieve acceptable oxidation resistance at medium levels of Cr were undertaken to enable reduced raw material cost and higher thermal conductivity, as compared to higher Cr alloys, such as commercial Alloy 418 and Alloy 422 (nominally 12 weight percentage Cr). Reducing Cr, a relatively high cost element, directly lowers the raw material cost. These alloy design efforts have thus far been able to achieve improved oxidation resistance relative to Alloy 422 at significantly lower levels of Cr. Figure I.3.2.1.2.3(a) shows the mass gain due to oxidation at 650°C for medium Cr developmental Alloys B, C, and D, along with Alloy 422. The oxidation mass gain of Alloy 4140 is also shown at both 550°C and 600°C for comparison. Medium Cr alloys C and D exhibit 1-2 orders of magnitude less oxidation mass gain relative to 422°C at 650°C . Micrographs of the oxide layers of Medium Cr Alloys B and D after 1,000 h at 650°C are shown in Figure I.3.2.1.2.4. Figure I.3.2.1.2.3(b) shows the mass gain due to oxidation at 700°C for medium Cr developmental Alloys C, D, E, and F along with Alloy 422. Similarly, the oxidation mass gain of Alloy 4140 is also shown at both 550°C and 600°C for comparison. Medium Cr alloys D, E, and F show very low-mass gain and protective oxidation behavior at 700°C up to 1,000 h, whereas Alloy 422 steel exhibits break-away oxidation and accelerated mass gain after less than 200 1h cycles.

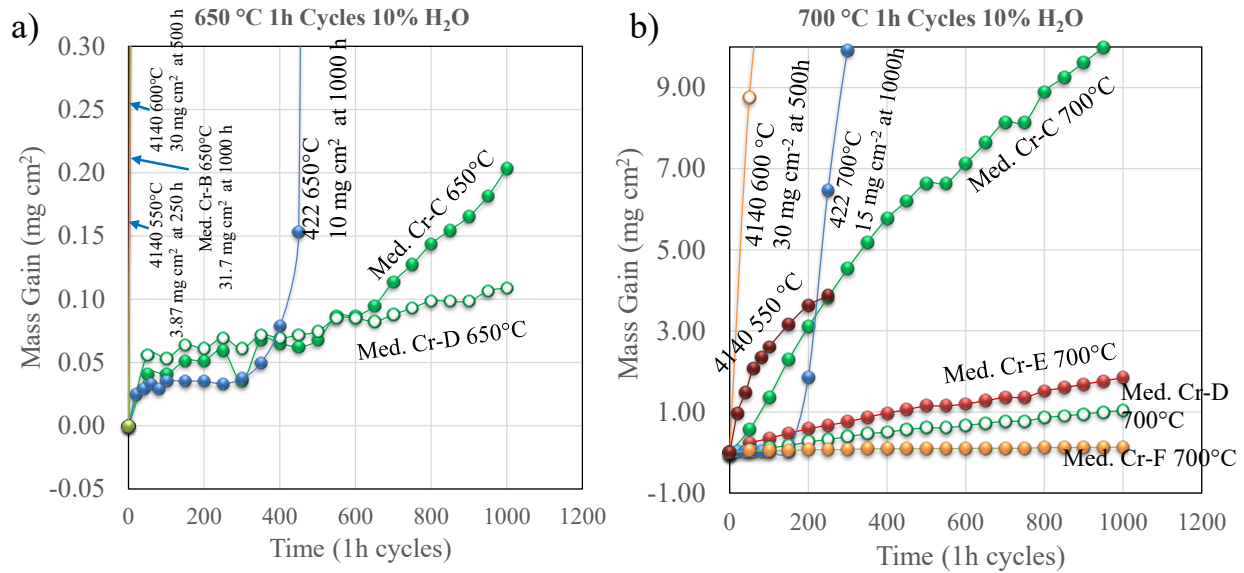


Figure I.3.2.1.2.3. Oxidation mass change as a function of time (1-h cycles) at (a) 650 °C and (b) 700 °C for medium Cr developmental alloys and commercial Alloys 4140 and 422. Source: ORNL.

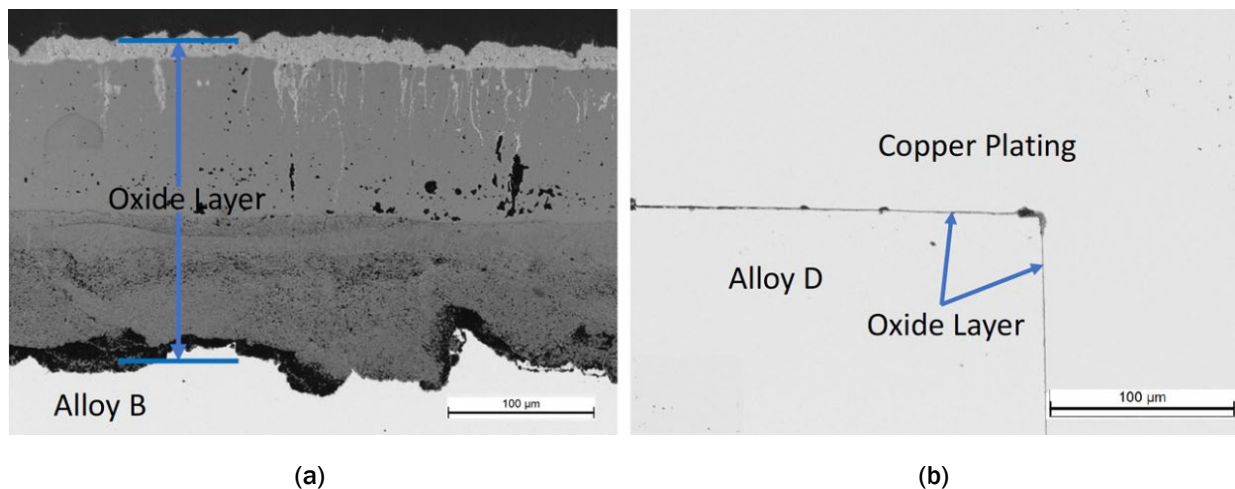


Figure I.3.2.1.2.4. Optical micrographs of the oxide layers of medium Cr alloys (a) B and (b) D after 1,000 hours (1-hour cycles) at 650 °C in air plus 10% water-vapor. Developmental Alloy B shows a very thick oxide scale while Alloy D exhibits a very thin oxide scale barely visible between the alloy and copper plating, and characteristic of protective oxide behavior. Source: ORNL.

High Cr Martensitic Developmental Steels

Alloy design concepts for advanced high Cr martensitic steels have been developed for higher operating temperatures of 650 °C to 700 °C. These steels are designed to possess improved strength, cyclic oxidation resistance, and thermal properties up to 700 °C relative to existing commercial martensitic stainless steels. The UTS and thermal diffusivity of the high Cr developmental alloys is shown in Figure I.3.2.1.2.5(a) and (b), respectively. Maximum strength and thermal diffusivity increase of 21% and 16% at 650 °C in the developmental alloys, respectively, relative to Alloy 422, have been achieved. In a single developmental alloy, strength increases of 21% and 8%, respectively have been realized. The cyclic oxidation mass gain at 700 °C of select high Cr developmental alloys along with commercial Alloys 422 and 9Cr-1Mo are shown in Figure I.3.2.1.2.6. It is noted that all the high Cr developmental alloys exhibit relatively low-mass gain consistent with protective oxide scale formation, whereas Alloys 422 and 9Cr-1Mo undergo break-away

oxidation at times substantially below 1,000 h. Elevated temperature strength, thermal conductivity, and oxidation resistance are often in conflict in steel alloys, and optimization of one property typically requires tradeoffs with one or more of the other properties. In the present work however, the development of alloy design strategies to substantially increase these three properties simultaneously in a single alloy, over current commercial Alloy 422, represents a significant step forward in potential piston performance for next-generation HD engines fueled by biodiesel, natural gas, green hydrogen, or some mixture.

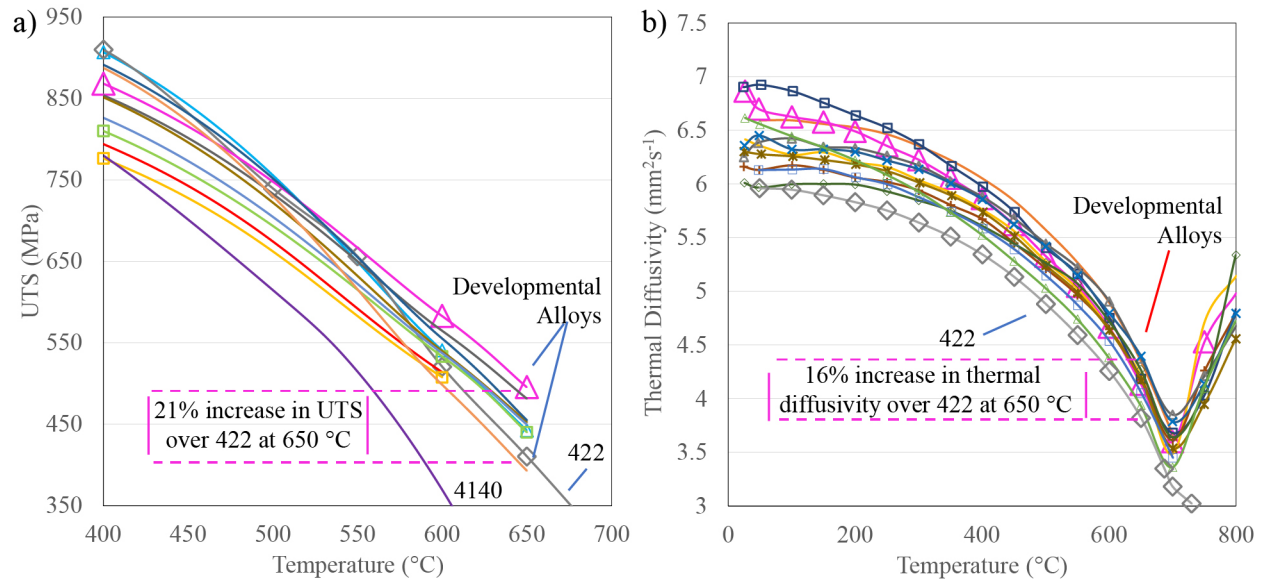


Figure I.3.2.1.2.5. (a) UTS and (b) thermal diffusivity of select high Cr developmental alloys, as well as commercial Alloy 422 (Alloy 4140 strength shown), all in the as-tempered conditions. Source: ORNL.

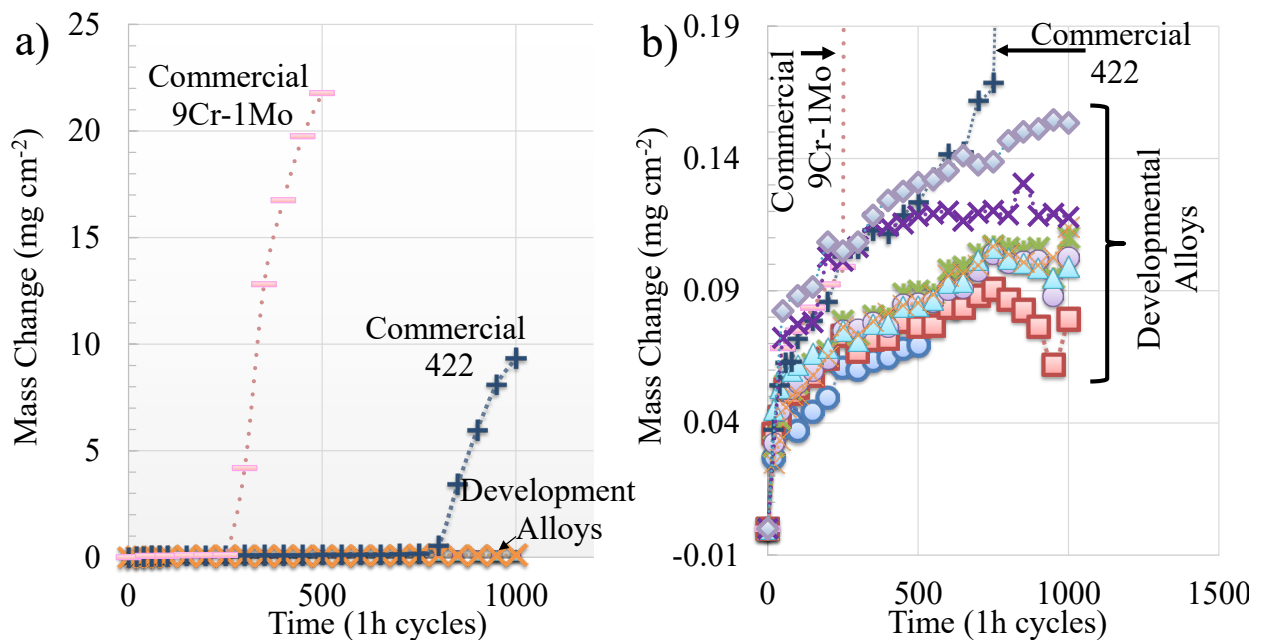


Figure I.3.2.1.2.6. Cyclic oxidation mass change (1h cycles) for high Cr developmental alloys, as well as commercial alloys 9Cr-1Mo and 422 at 700 °C in air plus 10% water-vapor: (a) shows overview and (b) shows a higher-resolution graph of the same data in (a). Source: ORNL.

Conclusions

Multiple high-temperature steel alloy development concepts have been investigated for piston peak temperature applications of 550°C – 700°C. These concepts target low, medium, and high Cr alloys with a variety of cost and performance ranges. Alloy design strategies have been developed to optimize strength and oxidation resistance characteristics that address the demanding combination of properties and performance requirements of pistons for future advanced HD engines for long-haul freight applications, including those potentially fueled by biodiesel, natural gas and/or green hydrogen. Some alloys from all groups investigated show an enhanced balance of strength and oxidation resistance over current commercial steels. Some alloys met all performance targets. The developmental high Cr alloys show enhanced properties relative to existing commercial stainless steels and are under consideration for scale-up and prototype piston manufacture.

Key Publications

1. Pierce, D., A. Haynes, J. Hughes, R. Graves, P. Maziasz, G. Muralidharan, A. Shyam, B. Wang, R. England, and C. Daniel, 2019, “High-temperature materials for heavy-duty diesel engines: Historical and future trends,” *Prog. Mater. Sci.*, Vol. 103, pp. 109–179.
2. Gingrich, E., D. T. Pierce, K. G. Byrd, K. Sebeck, V. Korivi, G. Muralidharan, H. Wang, J. Torres, A. Trofimov, J. A. Haynes, and M. Tess, 2022, “Evaluation of high-temperature martensitic steels for heavy-duty diesel piston applications,” SAE Technical Paper, 2022-01-0599, Preprint. Available at: <https://www.sae.org/publications/technical-papers/content/2022-01-0599/> (last accessed 22 February 2022).
3. Pierce, D. T., G. Muralidharan, A. Trofimov, J. Torres, H. Wang, J. A. Haynes, K. Sebeck, E. Gingrich, G. Byrd, and M. Tess, 2021, “Evaluation of thermal processing and properties of 422 martensitic stainless-steel for replacement of 4140 steel in diesel engine pistons,” *Mater. Des.*, Vol. 214, Art. 110373.

Acknowledgments

The authors would like to acknowledge the efforts of the following ORNL personnel: L. Allard, T. Muth, J. Poplawsky, J. A. Haynes, B. Pint, C. Carmichael, I. Stinson, H. Wang, E. Cakmak, K. Hedrick, G. Garner, S. Curlin, A. Trofimov, and Y. Yamamoto.

I.3.2.1.3 High-Temperature Coatings for Valve Alloys (Task 2A3) (Oak Ridge National Laboratory)**Sebastien Dreypondt, Co-Principal Investigator**

Oak Ridge National Laboratory
 1 Bethel Valley Road
 Oak Ridge, TN 37831
 E-mail: dreypondtsn@ornl.gov

Beth Armstrong, Co-Principal Investigator

Oak Ridge National Laboratory
 1 Bethel Valley Road
 Oak Ridge, TN 37831
 E-mail: armstrongbl@ornl.gov

Rishi Pillai, Co-Principal Investigator

Oak Ridge National Laboratory
 1 Bethel Valley Road
 Oak Ridge, TN 37831
 E-mail: pillairr@ornl.gov

Jerry L. Gibbs, DOE Technology Manager

U.S. Department of Energy
 E-mail: jerry.gibbs@ee.doe.gov

Start Date: October 1, 2018 End Date: September 30, 2023
 Project Funding (FY 2021): \$160,000 DOE share: \$160,000 Non-DOE share: \$0

Project Introduction

ORNL is developing lower-cost, higher strength Ni-based valve alloys in an associated task (Task 2A1) for operating conditions up to 950°C in advanced combustion environments. The chromia-forming versions of these alloys have excellent strength, but poor oxidation resistance above 900°C. One solution explored in Task 2A1 to improve the oxidation resistance of higher temperature valve alloys is to modify the alloy chemistry to form a thermally grown protective alumina scale without impacting the alloy mechanical strength, since alumina is more stable and protective than chromia above 900°C. This task—Task 2A3—is complementary to Task 2A1, and is focused on developing an alternative cost-effective solution, which is the deposition of alumina-forming protective coatings at the surface of ORNL's higher strength chromia-forming valve alloys. In collaboration with its academic and industrial partners, ORNL is evaluating a commercial MCrAlY overlay coating and developing lower-cost diffusion slurry aluminide coatings. Previous cyclic oxidation results at 900°C and 950°C in combustion-relevant environments (e.g., air + 10% water-vapor) on commercial alloy Pyromet 31V and high-strength ORNL-1 alloy demonstrated that a slurry coating application can significantly improve the oxidation behavior of both alloys [1].

Table I.3.2.1.3.1 shows the chemical compositions of each alloy. The oxidation rates were, however, higher for the ORNL-1 coated sample in comparison with the 31V coated coupon. These results also highlighted the importance of the slurry coating thickness—with mass losses, which is indicative of oxide scale spallation and observed for 20- μ m-thick coatings, but not for 40- μ m-thick coatings. A key focus in FY 2021 was, therefore, to conduct extensive characterization of the oxidized 31V and ORNL-1 coupons and determine the key factors impacting the oxidation performance of coated valve alloys. In-depth characterization of the coating and substrate microstructures after oxidation at 900°C and 950°C also enabled validation of an in-house coupled

thermodynamic and kinetics predictive model [1, 2]. Finally, high-cycle fatigue (HCF) testing was conducted at 900°C to assess coating impact on alloy mechanical behavior.

Table I.3.2.1.3.1. DFT Calculated Lattice Parameters of fcc Al and L1₂-Al₃X

Substrate	Ni	Fe	Cr	Ti	Al	Mo	C	Others
ORNL-1	47	27	18	3.8	1.8	1.2	0.03	1 Co
Pyromet 31V	57	13.6	22.7	2.3	1.3	2	0.04	0.9 Nb, 0.2 Si

Objectives

The main objectives of this task are to develop cost-effective oxidation-resistant alumina-forming coatings to increase high-strength valve operating temperatures in combustion environments up to 950°C. Cyclic oxidation and HCF testing were performed to evaluate the coating's effects at 900°C – 950°C. An ICME approach based on a coupled thermodynamic and kinetics model was developed and applied to accelerate the coating development and qualification process.

Approach

In collaboration with Flame Spray, Inc., a slurry aluminide coating was deposited on both commercial alloy 31V and ORNL's high-strength ORNL-1 alloy. Cyclic oxidation testing, in which the time at temperature per cycle is 1 h, was conducted in air + 10% water-vapor on bare and coated alloys at 900°C and 950°C for up to 1,000 h. Extensive backscattered scanning electron microscopy (BSE-SEM), EDS, and electro probe micro-analyzer (EPMA) characterization coupled with image analysis was performed to study oxide products and quantify phases in the coatings before and after oxidation testing. These results were used to determine the key factors impacting the oxidation behavior of coated Ni-based valve alloys and validate a new coupled thermodynamic and kinetics lifetime model. To assess the coating influence on the ORNL-1 alloy mechanical properties at high-temperature, HCF testing was carried out at 900°C on bare and coated ORNL-1 alloys. In addition to the 40- μ m-thick Flame Spray Inc. slurry aluminide coating, a commercial thermally sprayed NiCoCrAlYHfSi 35- μ m-thick Amdry 386 coating deposited by Stony Brook University's Thermal Spray Laboratory using high velocity oxygen fuel spraying was evaluated.

Results

As-Fabricated Coatings Deposited on 31V and ORNL-1 Alloys

Figure I.3.2.1.3.1 shows examples of BSE-SEM images of the as-fabricated coatings deposited on alloy ORNL-1, as observed in Figure I.3.2.1.3.1(a), and 31V, as can be seen in Figure I.3.2.1.3.1(b). These BSE-SEM images and corresponding EDS elemental distribution maps (not shown) enabled the determination by image analysis of the volume fraction and composition of each phase present in the coating outer layer and interdiffusion zone (IDZ). β -(Ni,Fe)Al, α -(Cr,Fe,Ni,Mo), and σ -phase were observed in the IDZ of both alloys but Ti-rich carbides and σ -phase were observed in the ORNL-1 IDZ while (Ti,Nb)-rich carbides and γ' phase were observed in the IDZ of the 31V coated coupon. These results were used to determine the average chemical composition of the coating as a function of the distance from the surface. As can be seen in Figure I.3.2.1.3.1(c) and (d), higher Al and Ti concentrations—in particular in the IDZ and at the IDZ/substrate interface—and lower Cr concentration were observed in the ORNL-1 coated sample, in comparison with the 31V coated sample. These results are consistent with the substrate chemistries, with greater Al and Ti concentrations in alloy ORNL-1 and higher Cr concentration in the 31V alloy.

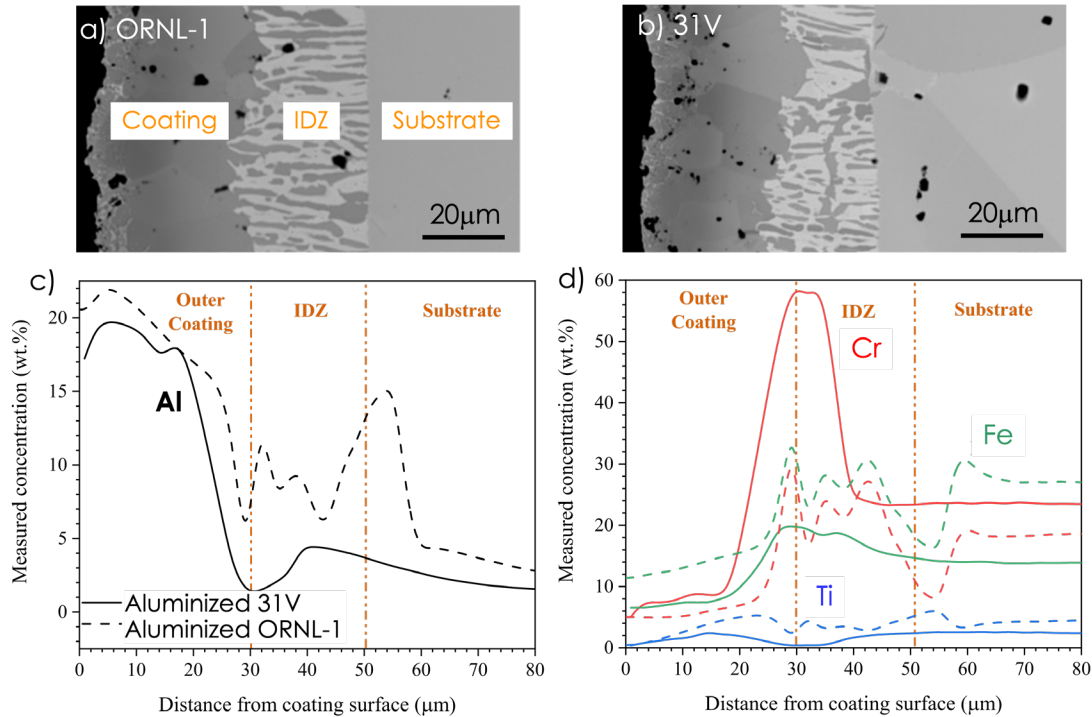


Figure I.3.2.1.3.1. (a)–(b) Microstructure of the as-deposited Flame Spray, Inc., slurry aluminide coating on (a) ORNL-1 and (b) 31V. (c)–(d) Calculation of the coating chemistries based on phase identification by EDS and EPMA, as well as image analysis, (c) Al concentration, and (d) Cr, Fe, and Ti concentrations.

Source: ORNL.

Oxidized 31V and ORNL-1 Coatings

The BSE-SEM images of the bare and aluminized ORNL-1 alloy after exposure in wet air at 900°C for 500 h and 1,000 h, respectively, are shown in Figure I.3.2.1.3.2. The uncoated ORNL-1 alloy exhibited extensive oxidation with Ti-rich oxides atop a chromia scale and internal oxidation of Al and Ti. Numerous TiN precipitates were also observed beneath the oxide scale. In contrast, the high Al concentration in the coating led to the formation of a thin continuous alumina scale at the surface of the aluminized ORNL-1 coupon, with the presence locally of NiCrFe spinel and Ti-rich oxides. Figure I.3.2.1.3.3 compares the microstructure of the coated ORNL-1 and 31V coupons exposed for 1,000h in wet air at 900°C. A compact external alumina scale formed on the aluminized 31V specimen, without the presence of NiCrFe spinel or Ti-rich oxides. Phase identification based on measured EDS compositions and thermodynamic calculations revealed significant differences between the ORNL-1 and 31V-coated specimens. The coating on the 31V coupon was completely depleted in the Al-rich β -(NiFe)Al phase, with the formation of a γ' layer at the specimen surface, precipitation of α -FeCr phase at the coating/oxide scale interface, and the presence of intermetallic σ -phase beneath the γ' layer. The intermetallic σ -phase and γ' precipitates were also observed in the coated ORNL-1 coupon, but a significant fraction of the β -(NiFe)Al phase was still present in the coating after 1,000 h at 900°C in wet air. Calculations based on our thermodynamic and kinetic model confirmed the faster rate of β -(NiFe)Al phase depletion for the 31V-coated coupon compared to the ORNL-1 coupon when exposed to wet air at 900°C. This difference in depletion rates can mainly be attributed to variation in chemical potential gradients and Figure I.3.2.1.3.3(c) shows calculated ratios for Al activity in the coating to the substrate. Values are significantly higher for the 31V coated sample, which should result in a faster diffusion of Al from the coating to the substrate, as observed experimentally. Slower β -(NiFe)Al phase depletion rate for the ORNL-1-coated sample should promote the formation of a protective alumina scale, but faster oxidation rates with scale spallation were measured for the ORNL-1 coated coupon in comparison with the 31V coated sample. The likely explanation is the higher concentration of Ti in the ORNL-1 alloy and the rapid diffusion of Ti to the coating surface, resulting in the formation of nonprotective Ti-rich oxides observed in Figure I.3.2.1.3.2.

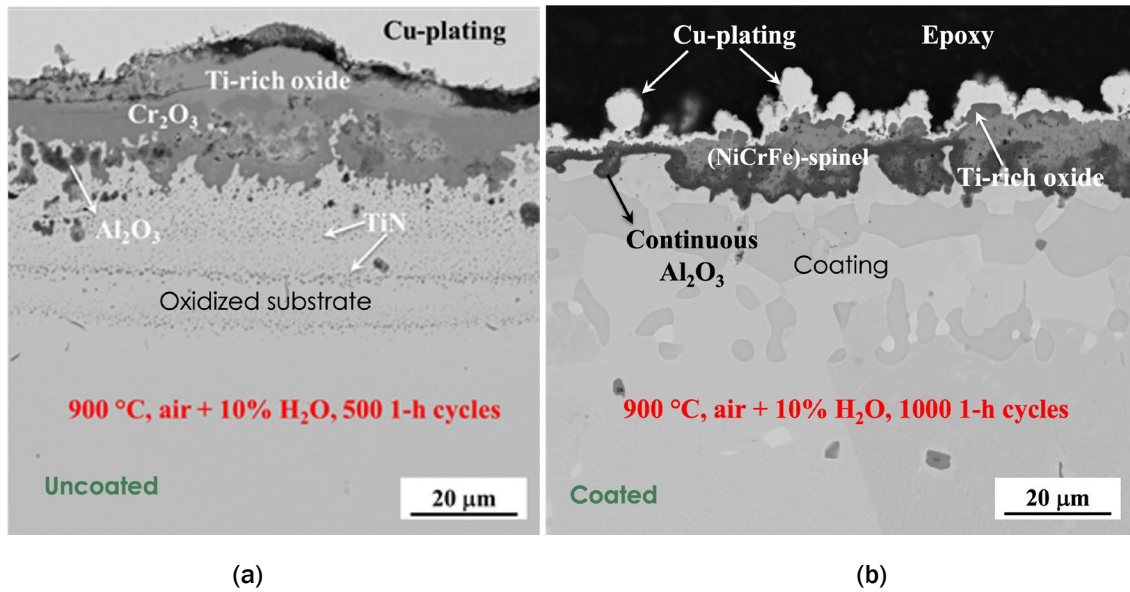


Figure I.3.2.1.3.2. BSE-SEM micrographs comparing the oxide products after cyclic oxidation testing at 900 °C in air + 10% water-vapor at the surface of: (a) uncoated ORNL-1 alloy; and (b) slurry coated ORNL-1 alloy. Source: ORNL.

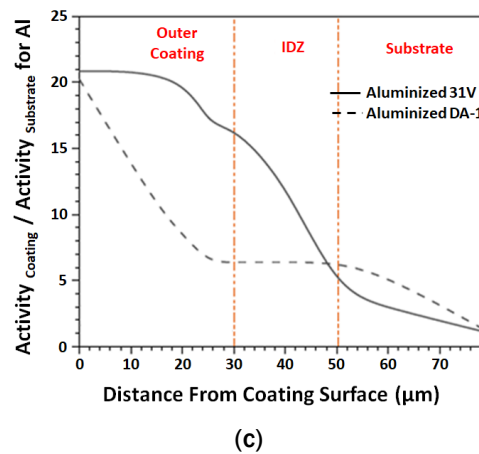
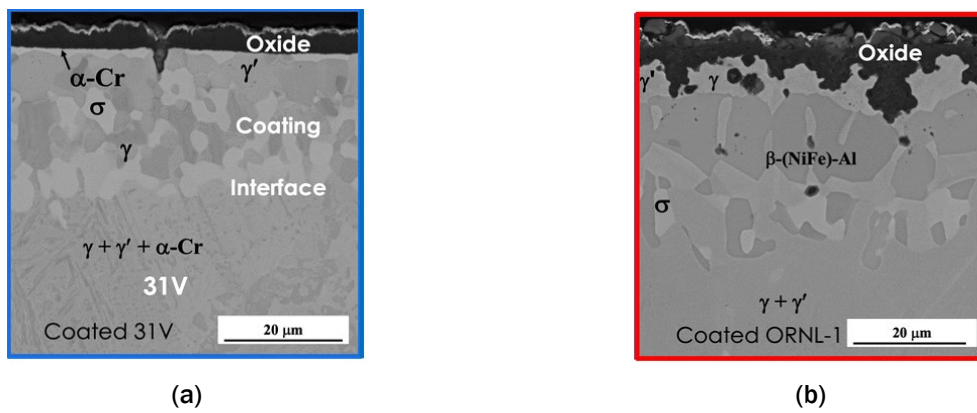


Figure I.3.2.1.3.3. (a)–(b) BSE-SEM micrographs comparing coating microstructure evolution after cyclic oxidation testing at 900 °C in air + 10% water-vapor: (a) 31V coated alloy; (b) ORNL-1 coated alloy; and (c) calculation showing Al activity ratio in the coating to the substrate. Source: ORNL.

Ti promotes the formation of a high-volume of strengthening γ' precipitates at high temperatures in valve alloys. Figure I.3.2.1.3.4(a) highlights that one of the alloys developed at ORNL exhibited similar high-temperature yield strength as alloy ORNL-1, but with Ti concentration approaching the Ti concentration in alloy 31V [3, 4]. Coating application on such a high-strength low Ti valve alloy might offer greater balance between mechanical strength and oxidation resistance. In any case, a better understanding of the impact of Ti concentration in the substrate on the oxidation behavior of a coated valve alloy is necessary to optimize the substrate and coating chemistries simultaneously. Four Ni-22wt%Cr model alloys with additions of 1 wt% Ti, 3 wt% Ti, 2 wt% Al-2 wt% Ti or 2 wt% Al-3 wt% Ti have been coated and will be oxidized at 900°C and 950°C. The goal of these experiments is to evaluate coated Ni-based alloy lifetime as a function of Ti and Al concentrations with a simplified substrate chemistry to facilitate result analysis.

HCF of Coated ORNL-1 Alloy

While the key objective of this coating project is to improve the alloy oxidation resistance, it is critical to verify that the presence of a high Al content coating does not have a deleterious effect on the substrate properties. Figure I.3.2.1.3.4(b) compares the HCF behavior of bare and coated ORNL-1 alloy in air at 900°C, 20 Hz, with applied stresses of 125 MPa or 150 MPa and an 0.1 load ratio. The results shows that both the Flame Spray slurry aluminide and overlay NiCoCrAlYHfSi coatings had no significant impact on the HCF numbers of cycles to rupture. It is worth noting that conducting similar tests in intensified combustion environments should result in significant improvement for coated specimens since severe oxidation will likely decrease the performance of the bare ORNL-1 alloy.

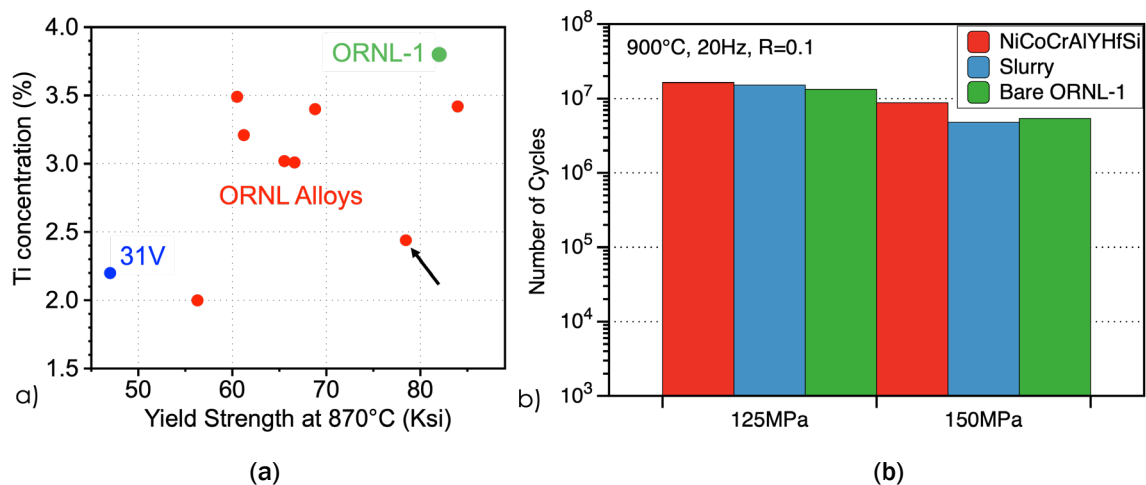


Figure I.3.2.1.3.4. 1 h cyclic oxidation behavior in air and 10% water-vapor of bare alloy and Flame Spray, Inc., slurry aluminide coated alloy: (a) Alloy 31V at 900°C; (b) Alloy 31V at 950°C; (c) Alloy 2687 at 900°C; and (d) Alloy 2687 at 950°C. Source: ORNL.

Conclusions

ORNL is developing and validating cost-effective, oxidation-resistant, alumina-forming coatings for lower-cost, higher strength valve alloys. Aluminide coatings deposited on valve alloys by Flame Spray, Inc., significantly improved the alloy oxidation resistance at 900°C and 950°C in combustion-relevant laboratory cyclic oxidation environments due to the formation of continuous alumina scales. Extensive characterization of the as-fabricated coatings highlighted the impact of the substrate chemistry on the coating composition. After oxidation for 1,000 h at 900°C, the coating deposited on a high-strength ORNL alloy retained a large fraction of an Al-rich β -(NiFe)Al phase, while the 31V coated coupon was completely depleted in a β -(NiFe)Al phase. These results were consistent with the calculated Al activities in the two coatings, indicating that more significant Al diffusion and depletion from the coating to the substrate should take place with the 31V alloy. However, the ORNL-coated sample exhibited more rapid oxidation rates than the 31V coated sample due to the higher Ti concentration in the former alloy leading to the formation of Ti-rich nonprotective oxides.

Coatings were deposited on model Ni-22 wt% Cr alloys with various Ti and Al additions, to improve the understanding of the impact of substrate Ti concentration on the coated alloy oxidation behavior. Finally, HCF testing at 900°C revealed that both types of coatings had no impact on the HCF behavior of these high-strength valve alloys. These results indicate that low-cost coatings are a very promising route for increasing the allowable temperature of high-strength valve alloys.

Key Publications

1. Pillai, R., S. Dryepontd, B. L. Armstrong, M. J. Lance, and G. M. Muralidharan, 2021, “Evaluating the efficacy of aluminide coatings to improve oxidation resistance of high-performance engine valve alloys,” *Surf. Coat. Technol.*, Vol. 421, Art. 127401.

References

1. Pillai, R., S. Dryepontd, B. L. Armstrong, M. J. Lance, and G. M. Muralidharan, 2021, “Evaluating the efficacy of aluminide coatings to improve oxidation resistance of high-performance engine valve alloys,” *Surf. Coat. Technol.*, Vol. 421, Art. 127401.
2. Pillai, R., W. Sloof, A. Chyrkin, L. Singheiser, and W. J. Quadackers, 2015, “A new computational approach for modeling the microstructural evolution and residual lifetime assessment of MCrAlY coatings,” *Mater. High Temp.*, Vol. 32, No. 1–2, pp. 57–67.
3. Muralidharan, G. M., 2017, “Low-cost Fe-Ni-Cr alloys for high-temperature valve applications,” U.S. Patent No. 9605565.
4. Muralidharan, G. M., 2017, “Low-cost high-strength Fe-Ni-Cr alloys for high-temperature exhaust valve applications,” U.S. Patent No. 9752468.

Acknowledgments

The authors would like to acknowledge M. Stephens, T. Lowe, and V. Cox for assisting with the experimental work. They also would like to acknowledge M. Lance for generating the EPMA analysis data and G. M. Muralidharan for providing the ORNL-1 material.

I.3.2.1.4 Development of Cast, Higher Temperature Austenitic Alloys (Task 2B1) (Oak Ridge National Laboratory)

Yukinori Yamamoto, Co-Principal Investigator

Oak Ridge National Laboratory
1 Bethel Valley Road
Oak Ridge, TN 37831
E-mail: yamamotoy@ornl.gov

Michael P. Brady, Co-Principal Investigator

Oak Ridge National Laboratory
1 Bethel Valley Road
Oak Ridge, TN 37831
E-mail: bradymp@ornl.gov

Jerry L. Gibbs, DOE Technology Manager

U.S. Department of Energy
E-mail: jerry.gibbs@ee.doe.gov

Start Date: October 1, 2018 End Date: September 30, 2022
Project Funding (FY 2021): \$305,000 DOE share: \$305,000 Non-DOE share: \$0

Project Introduction

Automotive engine exhaust components are anticipated to experience temperatures of $\geq 900^{\circ}\text{C}$ – 950°C in the near future to reach the engine efficiency targets. The ferrous cast alloys currently used for the turbocharger housings and the exhaust manifolds are at their upper-temperature limit for creep and/or oxidation resistance. Therefore, new, cost-effective alloys will be required to meet the increasing operating temperature requirements in higher efficiency engines, including potential future combustion engines fueled by hydrogen.

Objectives

The goal of this subtask is to increase the upper-temperature oxidation limit to $\geq 900^{\circ}\text{C}$ – 950°C for next-generation, cast, austenitic stainless-steel (SS) exhaust gas components. Candidate alloys will utilize an Fe(Ni) base with ≤ 25 wt.% – 30 wt.% Ni to remain cost-competitive, as well as to minimize the use of other costly alloying additions, such as Mo, Nb, W, etc. The cast SS alloys being developed in this task are referred to as Alumina-Forming Austenitics (AFA) and have the unique distinction of being designed to form an alumina (Al_2O_3) protective oxide scale on the surface during oxidation rather than the chromia (Cr_2O_3) oxide scales that form on most commercial SS alloys. Alumina scales are typically slower growing and more protective than chromia scales, particularly at higher temperatures, but alloy design and the casting of Al-containing SS alloys can be challenging.

Approach

Design exploration of second generation cast AFA alloys with ≤ 25 wt.% Ni has been pursued for use in exhaust components for up to 900°C operating temperature. The task leverages recent ORNL alloy development successes for wrought 25Ni-base AFA alloys for use in up to 850°C – 900°C and cast 35Ni-base AFA alloys for use up to 1150°C . Alloy design, development, and refinement in this Thrust 2 task are being guided by Thrust 4 projects, including advanced characterization of nano-micro-scale strengthening precipitates (e.g., Thrust 4A), as well as computational activities, including CALPHAD and machine-learning (ML) for alloy design (co-supported by Thrust 4B: Advanced Computation). In FY 2021, the focus has been on the evaluation of various alloying additions to influence oxidation resistance and creep-rupture properties of the alloys based on a downselected cast AFA alloy (e.g., AFA5, Fe-17Cr-22Ni-4Al-0.6Nb-0.15C base, wt.%). The deterioration of this alloy's outstanding creep-rupture performance after scaling to full industrial heats

(e.g., AFA5) is being evaluated, and the role of compositional modification to mitigate the performance deterioration issue is being addressed. Multiple laboratory-scale, arc-cast heats of AFA5 base alloys with variations of small alloying additions were prepared. Property screenings in the range of 900°C – 1,000°C were conducted at ORNL.

Results

Oxidation, creep, and tensile testing of laboratory-scale AFA5 base alloys with various alloying additions were conducted at ORNL. A total of 10 different additional alloys with variations of Ni, Nb, Y, Si, and Al contents were prepared to evaluate the contribution of these alloying additions on improving creep-rupture performance and RT ductility in the industrial-scale AFA5 heats, without interfering with the oxidation resistance. Under the developmental activities in previous years, it was found that the scaled-up, industrial AFA5 heats (e.g., total ~72 kg) prepared by a commercial foundry (MetalTek International, Waukesha, WI) by air-induction melting with an Ar cover gas exhibited significantly lower creep-rupture performance and reduced RT tensile ductility than those of the original laboratory-scale AFA5 alloys prepared by arc-casting at ORNL. The potential degradation mechanisms attributed to the scaled-up casting process, such as solidification defect formation, inclusions, microstructure evolution, compositional inhomogeneity (segregation), and non-optimized chemical composition for the air-melting process, must be resolved. The approach to optimize the chemical composition (e.g., compositional modification) was chosen by considering not only the potential property improvement, but also the evaluation of the compositional tolerance to achieve the target performance of the final products. The other factors described above were dominantly controlled by the air-induction melt and cast-process conditions (e.g., reduction of slag, component design, temperature control of pre-/post-solidification process), so that these issues were considered for improvement by process optimization and were separated from the contributions of the compositional modification.

Oxidation test results suggested that careful control of alloying additions in the AFA5 base alloys was necessary. Oxidation testing was conducted under aggressive conditions of 1 h cycles at 950°C and 1,000°C in air with 10% water-vapor to simulate engine exhaust gas conditions, up to 1,000 and 500 cycles, respectively. The mass gains as a function of total exposure time are summarized in Figure I.3.2.1.4.1, in which the plots were separated into three different groups for each test temperature for clarity. In all plots, the results of the original AFA5 alloy are plotted with a red filled circle symbol. The results for identical testing of a commercial cast SS alloy HK30Nb (chromia-forming cast austenitic SS, Fe-20Ni-25Cr base) at 950°C are also plotted for comparison. It should be emphasized that HK30Nb showed an abrupt mass loss in the early stages of oxidation testing, suggesting no promise of protectiveness at the 950°C test condition, as anticipated for this class of alloy. On the other hand, the original AFA5 demonstrated very slow oxidation kinetics at both 950°C and 1,000°C, indicating highly protective alumina formation, as previously reported. Among the alloying additions in the present study, reductions of Ni and Y contents had a strong negative impact on oxidation resistance of AFA. As the Ni content reduced from 22.2 to 18.3 wt.%, the mass loss occurred earlier and more aggressively at both test temperatures, as observed in Figure I.3.2.1.4.1(a) and (d), respectively. Thus, the results suggested that a minimum threshold of ~22 wt.% Ni would be required to achieve the desired protective behavior under these aggressive test conditions. The Nb contents between 0.30 to 1.08 wt.% did not show a significant influence on the oxidation resistance at 950°C, as shown in Figure I.3.2.1.4.1(b), whereas the lower Nb contents of 0.30 and 0.43 wt.%, respectively, resulted in a reduced mass gain at 1,000°C, as shown in Figure I.3.2.1.4.1(e). Although the mechanisms of these trends are still unclear, it is obvious that the range of the Nb additions in the present study do not exhibit obvious negative influences on the oxidation behavior of AFA. Increasing Si or Si+Al contents reduced the mass gains at 950°C, as observed in Figure I.3.2.1.4.1(c), although neither would be a likely industrial-scale alloy modification since both showed a negative impact on creep-rupture performance, as discussed in the latter part of this report. Reduction of the Y content was suggested in last year's report as a strategy for potential improvement of RT tensile ductility. However, reducing to 0Y resulted in a loss of oxidation resistance in the early-stage of exposure at 1000°C, as can be seen in Figure I.3.2.1.4.1(f). Increasing Y additions up to 0.19 wt.% positively improved the oxidation resistance, although RT ductility was reduced to nearly half of that at 0Y (e.g., 31% for 0Y to 17% for 0.19Y).

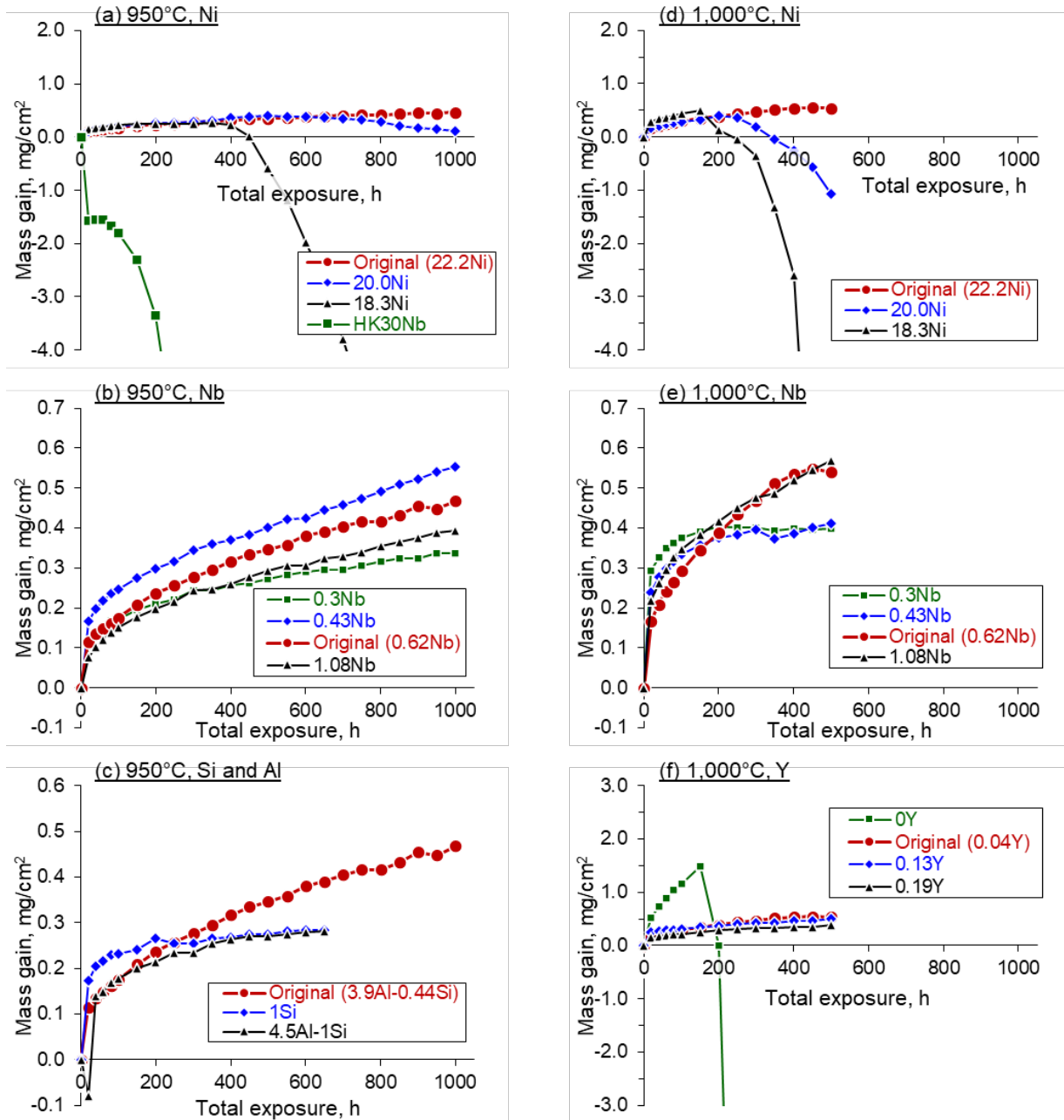


Figure I.3.2.1.4.1. Specific mass change in the laboratory-scale AFA5 base alloys after cyclic oxidation with 1 h cycles at (a)–(c) 950 °C and (d)–(f) 1,000 °C in air with 10% water-vapor. Source: ORNL.

Creep-rupture tests of all laboratory-scale AFA5 base alloys were also conducted at 900°C and 50 MPa, and the results were compared with the industrial AFA5 heats #1 through #3, as well as HK30Nb cast-in the same manner as the industrial AFA5, as summarized in Figure I.3.2.1.4.2. It should be noted that industrial heats #1 and #2 were the same as previously reported, while heat #3 was newly procured with “no Y addition.” This new alloy’s creep-rupture properties were measured in FY 2021.

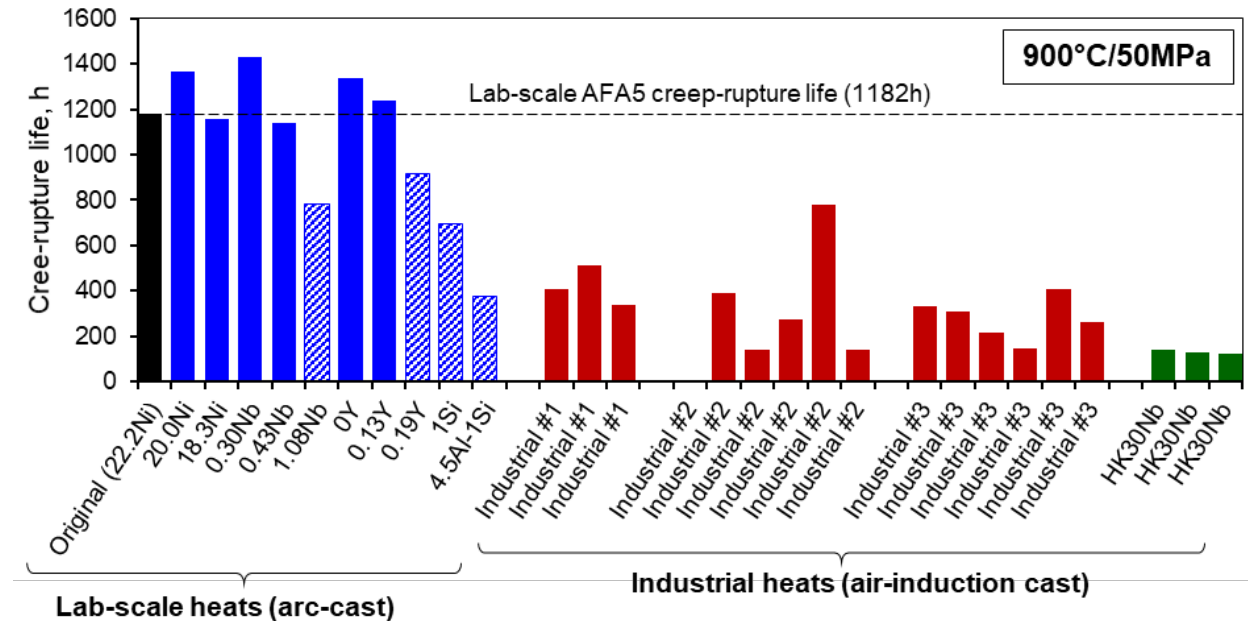


Figure I.3.2.1.4.2. A comparison of creep-rupture lives of cast AFA5 alloys (e.g., laboratory-scale and industrial heats) and reference HK30Nb alloy tested at 900 °C and 50MPa. Source: ORNL.

The creep-rupture life of the original, laboratory-scale AFA5 alloy was 1,182 h at the 900°C test condition, and many laboratory-scale alloys showed similar creep-rupture lives within $\pm \sim 200$ h despite wide variations of the alloying additions. However, the laboratory-scale alloys with 1.08Nb, 0.19Y, 1Si, and 4.5Al+1Si resulted in significant reduction of creep-rupture lives. These alloying additions are considered to deteriorate the creep-strengthening mechanism proposed for the AFA5 alloy design: (1) excess Nb addition significantly lowers the amount of the strengthening $M_{23}C_6$ phase; (2) excess Y addition introduces dispersions of a weak eutectic microstructure; and (3) excess Si addition promotes a G-phase (or Ni-Nb-Si-rich intermetallic compound) formation, which also negatively impacts the creep-rupture performance. When considered in combination with oxidation resistance and RT ductility, the alloys with lower Nb content—as low as 0.30 wt.%—would be within the allowable compositional variance, since the performance was comparable to the original AFA5 alloy.

In comparison to the laboratory-scale AFA5 alloys, the industrial-scale AFA5 heats also exhibited significantly reduced creep-rupture lives. Compositional offsets from the target chemistry were observed in the delivered industrial heats in the contents of Cr, Al, Mo, Si, W, Zr, Y, and B, as summarized in Table I.3.2.1.4.1. However, these compositional variations could not sufficiently explain the degree of reduction of creep-rupture lives, as well as the significant deviation of the test results within the same industrial heat. The amounts of internal defects were determined by density measurements, which revealed that the larger amount of the defects trended toward promoting shorter creep-rupture lives. But this observation did not fully explain the reduction of the creep-rupture performance. Based on these considerations, it was considered that microstructure evolution could be a dominant factor in the reduction of creep-rupture lives in the industrial heats. It is important to note that despite the reduction in creep-rupture lives for industrial cast AFA5 alloys vs. lab-cast AFA5, the creep resistance of the industrial alloys was still generally well in excess of that for the commercial alloy HK30Nb samples industrially cast-in the same manner as the AFA5.

Table I.3.2.1.4.1. Analyzed Alloy Composition of the Industrial AFA5 Heats

Alloy ID	Fe	Ni	Cr	Al	Mn	Mo	Nb	Si	W	Zr	Y	C	B	Remarks
AFA5	51.69	22.0	17.0	4.00	2.00	1.00	0.60	0.50	0.50	0.10	0.030	0.500	0.010	Target
#1 Rod	48.12	22.5	20.1	3.92	1.97	1.05	0.69	0.39	0.52	0.10	0.070	0.450	<0.005	#190201
#2 Rod	49.21	23.0	17.6	4.04	2.04	0.94	0.74	0.74	0.80	0.12	0.074	0.5033	0.031	#190894
#2 Keel Block	51.38	22.2	16.5	3.95	1.94	0.91	0.72	0.73	0.83	0.12	0.054	0.4982	0.023	
#2 Plate	51.78	22.0	16.4	3.87	1.95	0.91	0.74	0.74	0.77	0.12	0.061	0.4884	0.022	
#3 Rod	52.73	22.9	16.1	3.35	2.10	0.63	0.66	0.49	0.32	0.08	<0.005	0.5100	0.009	#210048, Y-free
#3 Keel Block	53.78	22.9	15.6	3.31	2.09	0.45	0.63	0.36	0.25	0.06	<0.005	0.5000	0.004	
#3 Plate	52.67	22.9	15.8	3.33	2.10	0.80	0.65	0.64	0.41	0.11	<0.005	0.5100	0.006	

Note: the yellow highlighted values represent values that are out of specification.

Coarse primary phases formed during solidification were found to be the most likely primary source of performance degradation and variance in the industrial heats. These larger industrial heats experienced slower solidification or cooling rates than the laboratory-scale alloys, since the former was cast into a sand mold, whereas the latter used a water-cooled Cu mold. Figure I.3.2.1.4.3 represents optical micrographs and SEM-BSE images showing typical microstructures of the laboratory-scale AFA5, as observed in Figure I.3.2.1.4.3(a) and (b), respectively, and the industrial heat #2, as can be seen in Figure I.3.2.1.4.3(c) and (d), respectively. Macroscopically, both displayed a coarse columnar grain structure with a size greater than a few millimeters. The grains consisted of a typical dendritic structure of austenite grains, although the typical dendrite arm spacings of the industrial heat (e.g., ~100 μm) were notably larger than those of the laboratory-scale heat (e.g., ~30 μm). Between the dendritic arms, primary phases including NbC, M_7C_3 , M_{23}C_6 (M: mainly Cr), and B2-NiAl were observed, while the size of these interdendritic phases in the industrial heat (e.g., > 10-20 μm) were significantly larger than those in the laboratory-scale heat (e.g., ~1-5 μm). The SEM-BSE images of the industrial heat also revealed a secondary M_{23}C_6 precipitation with a size of ~1 μm , surrounding the primary carbides. The high-temperature strengthening mechanism designed for AFA5 alloy strongly relies on nanoscale secondary M_{23}C_6 precipitation formed during the service conditions. However, the slow solidification and cooling process in the industrial heats allows the coarsening of the primary Cr-rich carbides, as well as the formation of the secondary M_{23}C_6 precipitation, resulting in a reduction of available strengthening M_{23}C_6 supersaturation in the austenite matrix. Although a quantitative analysis has not yet been performed, it appears that the reduction of the “effective” strengthening precipitates in industrial heat #2 degraded the alloy’s resistance to creep deformation, and therefore resulted in a shorter creep-rupture life, as compared to that of the laboratory-scale alloys.

Industrial heat #3 was designed with no Y addition (0Y), targeting the improvement of RT tensile ductility. However, the reduction of Y content did not significantly improve the ductility of the industrial heat compared to the laboratory-scale heats, as summarized in Figure I.3.2.1.4.4. The Y-free industrial heats showed an elongation of 6% – 12%, which was a slight improvement over the Y-containing heats (e.g., <5%). In contrast, the 0Y laboratory-scale heat exhibited >30% elongation. Since the compositional dependence of the ductility is quite mild in the industrial heats, the present results provide additional evidence that the casting process control for high-performance AFA alloys may be a more significant factor for achieving industrial heat property improvements than slight alterations in the base alloy compositions.

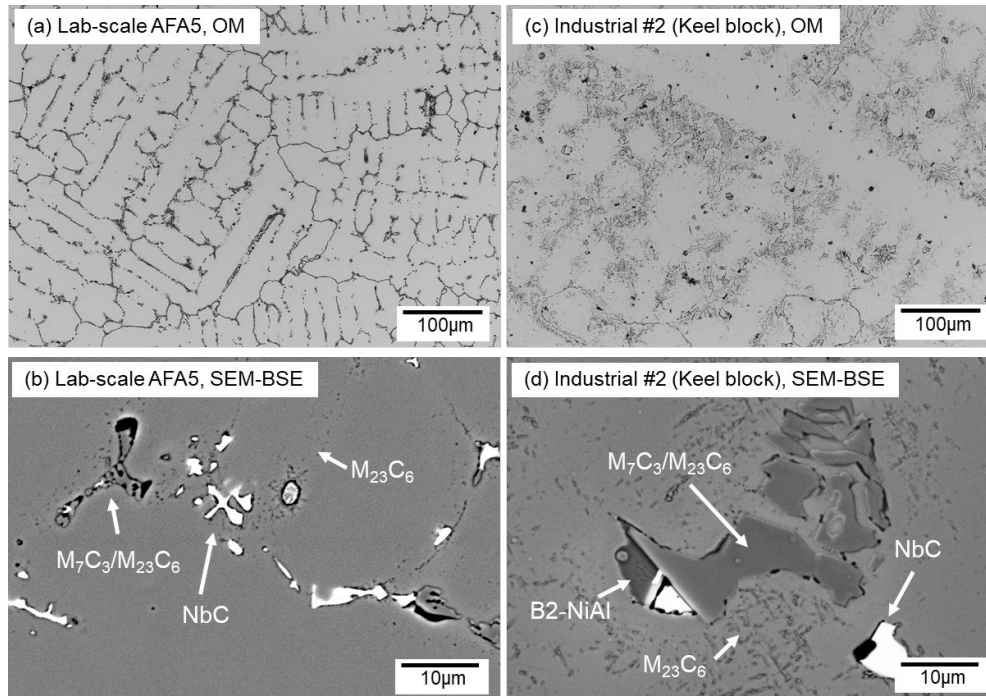


Figure I.3.2.1.4.3. Optical micrographs and SEM-BSE images of the as-cast AFA5 alloys: (a)-(b) the original laboratory-scale alloy; and (c)-(d) the industrial heat #2. Source: ORNL.

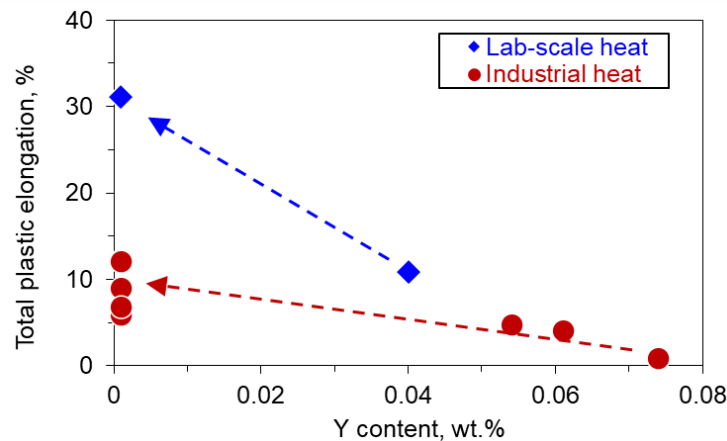


Figure I.3.2.1.4.4. Comparison of RT tensile ductility of the laboratory-scale heats and the industrial heats plotted as a function of the analyzed Y contents. Source: ORNL.

It is expected that a controlled solidification process with relatively rapid cooling rate should improve the mechanical properties of future industrial heats. Two approaches are proposed for additional investigation: (1) cast into a custom mold with a step-like morphology to evaluate the component thickness effect on the as-cast microstructure evolution and the mechanical response; and (2) apply an AM process that naturally solves the potential issue of a larger dendrite arm spacing or coarse primary phase formation due to a rapid solidification/cooling condition. These proposed next steps are anticipated to offer one or more solutions for the performance improvement of industrial-scale heats, which will be the major scope of the task's wrap-up activities in FY 2022.

Also, a series of ML studies to optimize the AFA alloy composition for the improved creep-rupture performance were conducted, leveraging a project under Thrust 4 of the DOE VTO PMCP Task 4B (led by Dongwon Shin, ORNL). A quality evaluation of the ability of the AFA creep-rupture database to predict the Larson-Miller Parameter was pursued. It was found that the prediction accuracy varied with the compositional variety, and even an existing small-size database was split by the types of the strengthening mechanisms that showed better prediction accuracy when the compositions in the database were homogeneously deviated. The downselection of the candidate AFA alloys to be experimentally evaluated is currently in progress.

Conclusions

Oxidation (e.g., 950°C and 1,000°C), creep (e.g., 900°C, 50 MPa), and tensile properties of newly prepared cast AFA5 base alloys were evaluated at ORNL. The laboratory-scale alloys with systematic variations of alloying additions revealed various positive/negative impacts on the high-temperature performance, as well as the RT ductility. It was found that the original cast AFA5 alloy possessed a very good combination of the desired properties, and the compositional variations of Ni, Nb, Y, Si, and Al could cause negative impacts on oxidation resistance, creep-rupture performance, or RT tensile ductility. The industrial AFA5 heats demonstrated significantly lower creep-rupture lives than the laboratory-scale alloys (albeit still better than the benchmark HK30Nb), despite no significant compositional variations in each industrial heat. It is suggested that the control of the solidification process with relatively faster cooling rate should improve the mechanical performance of the industrial AFA5 heats by refining grain size and precipitate scale. A more detailed evaluation of the cooling rate dependence is to be evaluated during the final phase of this study.

Key Publications

1. Pillai, R., S. Dryepont, B. L. Armstrong, M. J. Lance, and G. M. Muralidharan, 2021, "Evaluating the efficacy of aluminide coatings to improve oxidation resistance of high-performance engine valve alloys," *Surf. Coat. Technol.*, Vol. 421, Art. 127401.
2. Pillai, R., W. Sloof, A. Chyrkin, L. Singheiser, and W. J. Quadackers, 2015, "A new computational approach for modeling the microstructural evolution and residual lifetime assessment of MCrAlY coatings," *Mater. High Temp.*, Vol. 32, Nos. 1–2, pp. 57–67.

Acknowledgments

The authors would like to thank G. A. Cox, D. T. Moore, D. C. Heidel, K. O. Hanson, G. Garner, M. S. Stephens, T. Lowe, T. Jordan, C. S. Hawkins, J. L. Moser, and K. L. Hedrick for helping with the experimental work. The authors would also like to acknowledge Drs. A. Devaraj and B. Gwalani of Libor Kovarik for their collaborative support on the detailed alloy microstructure under Thrust 4A, as well as Drs. J. Peng, D. Shin, and S. Lee of ORNL for leading the ML efforts and Dr. G. Muralidharan of ORNL for his alloy design insights.

I.3.2.1.5 Selective Material Processing to Improve Local Properties (Task 2B2) (Oak Ridge National Laboratory)

Glenn Grant, Co-Principal Investigator

Pacific Northwest National Laboratory
902 Battelle Blvd.
Richland, WA 99352
E-mail: glenn.grant@pnnl.gov

Saumyadeep Jana, Co-Principal Investigator

Pacific Northwest National Laboratory
902 Battelle Blvd.
Richland, WA 99352
E-mail: saumyadeep.jana@pnnl.gov

Jerry L. Gibbs, DOE Technology Manager

U.S. Department of Energy
E-mail: jerry.gibbs@ee.doe.gov

Start Date: October 1, 2018 End Date: September 30, 2023
Project Funding (FY 2021): \$300,000 DOE share: \$300,000 Non-DOE share: \$0

Project Introduction

The project goal is to develop advanced hybrid manufacturing processes to locally improve the performance of parts and assemblies through selective microstructure modification. The concept includes the notion that, in general, strength requirements of an assembly are often driven by a limited number of highly loaded small areas on a complex part. Failure in these areas can drive global component section thickness or strength requirements leading to excessive and unnecessary part weight. If just those selected areas could be improved to meet the strength requirements—or more importantly the fatigue and toughness requirements—then overall material and/or cost-savings could be achieved.

This concept of applying a secondary process to selective areas to locally improve the properties where they are needed could allow for using lower-cost materials to achieve properties that meet or exceed current state-of-the-art materials. The added cost of the secondary process is offset by the lower base material cost, with the balance designed to achieve a total cost of no more than 10% higher than the current production process.

Selective area modification could also enable new high-performance alloys, local up-alloying, and improve the performance of parts made by advanced manufacturing techniques, such as laser or friction additive processes. In many cases, advanced alloys are designed to gain higher temperature performance, but often at the expense of another property, such as castability, fracture toughness, or fatigue performance. For these new alloy opportunities, local property improvement through selective processing and engineering could enable economical and better bulk material performance, while still addressing the extreme performance requirements in localized areas.

The project will investigate and demonstrate advanced processes—such as friction stir processing (FSP), cold spray, and others—with the potential to produce enhanced properties on local areas of complex propulsion material castings, forgings, or additively manufactured materials. FSP, for example, has been shown to provide dramatic improvements in fatigue performance to cast materials across a wide range of alloy systems [1], as observed in Figure I.3.2.1.5.1.

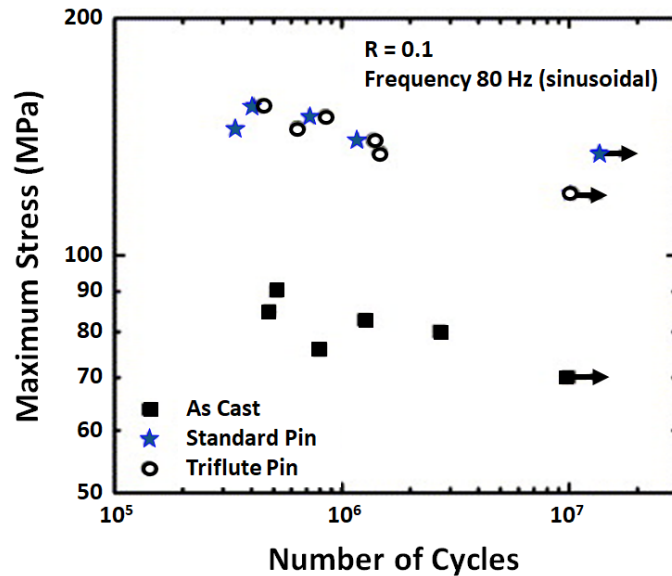


Figure I.3.2.1.5.1. Previous fatigue testing results showing that significant improvements in fatigue performance can be achieved when applying FSP to cast—Al alloys [2]. Source: PNNL.

Local material property improvements can be especially important in enabling new high-performance alloys. In some cases, alloys designed for higher temperature operations arrive at their performance through complex alloy chemistries that can show coarse second-phase precipitates or have castability issues leading to near-surface casting defects. FSP has been shown to be able to refine microstructure, heal casting defects, improve alloy homogeneity, and produce a wrought microstructure.

The focus of the project has been on the local modification of ICE castings, but the principals and performance improvements are equally valid for other powertrain materials, such as engine and driveline cases for electric vehicle (EV) propulsion. The current project will conclude at the end of FY 2021 as the Powertrain Materials Core Program (PMCP) moves to develop materials important for EV powertrains, but technologies developed here are expected to be useful in several new projects beginning in FY 2022 on brakes, gears, and electric motor materials.

Objectives

The objective of the project is to demonstrate through several solid-phase processing techniques that local material property improvements can contribute to the goals of increased materials strength and performance to enable increased engine efficiency. This project will investigate and demonstrate advanced FSP, cold spray, and other processes with the potential to produce enhanced properties on local areas of complex powertrain material castings, forgings, or additively manufactured materials. In some cases, it is expected that local secondary processing can enable lower-cost ferrous and non-ferrous alloys to achieve properties that meet or exceed the current state-of-the-art advanced materials. The objectives of this project are to demonstrate the enhanced property potential, to demonstrate the processes can be adapted to a robotic platform and to provide data usable by powertrain design engineers.

Approach

The project's approach has changed and was downscoped as the PMCP has shifted to a focus on materials for electric drivetrains. The primary task however, developing methods to improve the performance of drilled or cast-in holes for fasteners, remains a key research area. This topic addresses an issue of casting quality that is also of concern in EV powertrains as EV's often employ complex, combined motor/transmission/differential housings and casting integrity is still a concern.

The project approach during FY 2021 has focused on demonstrating FSP as a process capable of improving the microstructure and performance of Al structural castings, as observed in Figure I.3.2.1.5.2(a) and (b), respectively. This task focuses on improving the local microstructure and performance of areas within a casting that will undergo drilling and threading operations to receive threaded fasteners. It will also demonstrate the concept of improving the microstructure, healing potential casting defects near cast-in holes, and provide data on the pull-out strength of fasteners threaded in these holes. The concept is to process the region where a threaded hole will be drilled and tapped such that the microstructure created by FSP provides greater reliability for the later fastening operation. The requirement for casting integrity around fastener areas can be a driver of cost forcing complex die design and higher cost alloys.

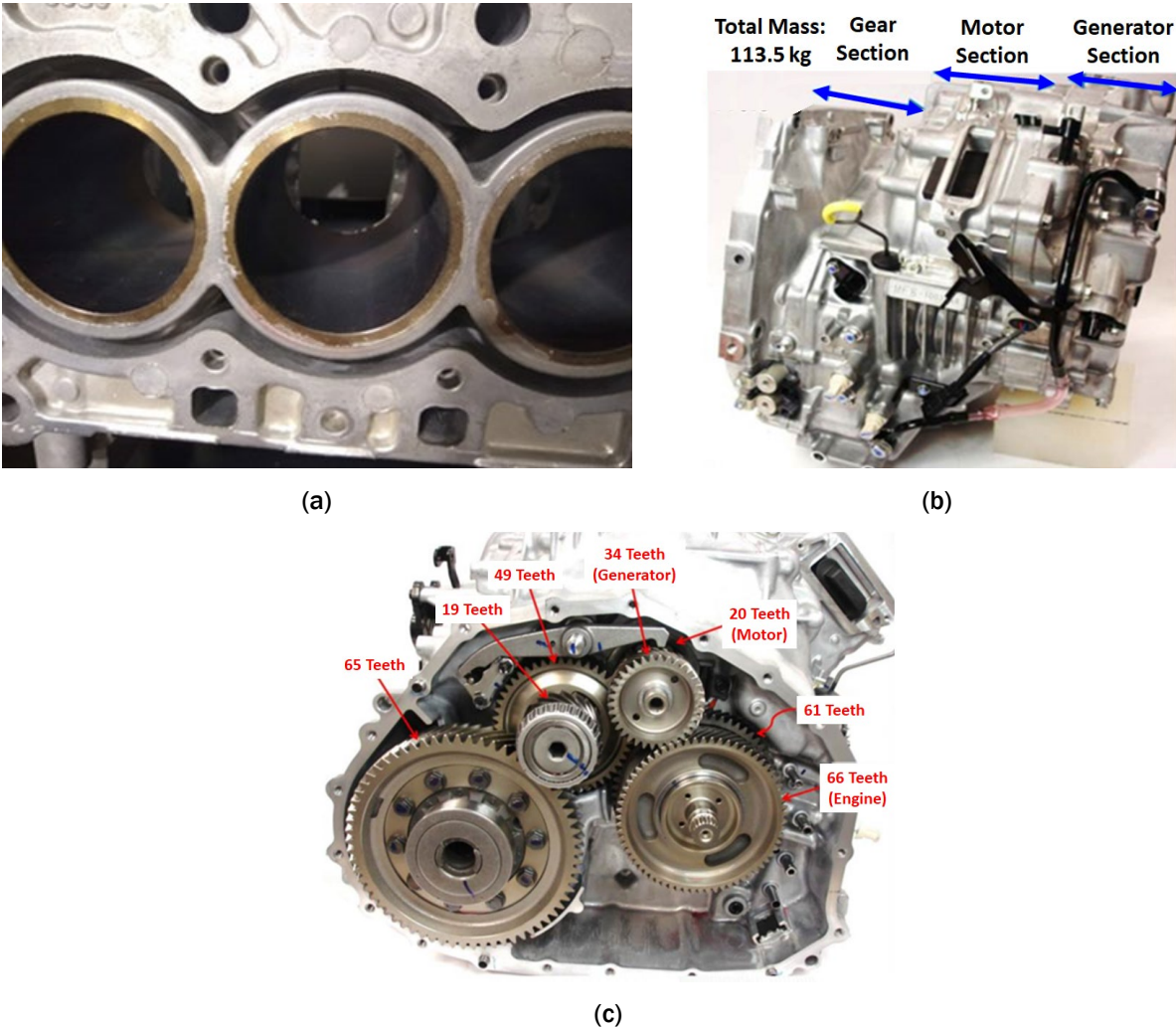
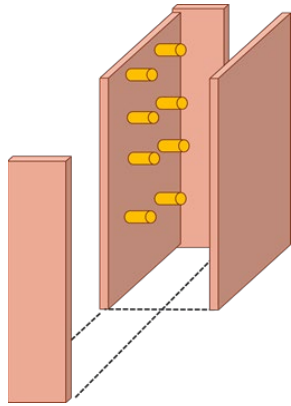


Figure I.3.2.1.5.2. (a) Deck surface of an as-cast-Al block showing cast-in holes for head bolts above and below the interbore area. (b) Complex casting of an EV drive system, combined motor/transmission/differential housings. (c) The same casting showing the bolt flange areas.

Source: (a) PNNL; (b) and (c) ORNL.

The experimental approach involves casting plates in book molds with replacable core pins mounted on one wall of the mold, as shown in Figure I.3.2.1.5.3(a), with the experimental plan shown in Figure I.3.2.1.5.3(b). These pins are designed to produce coupon-sized examples of the types and geometries of defects seen around cast-in holes, including pin holes, blow outs, and shrinkage pores. In addition, uncoated H13 core pins, or used core pins with failed coatings, will be used to simulate soldering defects seen when pin coatings break down.

Different pins will reflect a variety of conditions, including differing thermal conductivity and coating effects. Castings will be analyzed destructively to see which pin conditions create the defect styles most commonly seen in production, with consultation from vehicle manufacturers. From this information, the pin condition will be downselected, while a population of castings will be made with similar conditions.



(a)

Experimental Plan:

- Initial trials use a heterogeneous set of core pins to create different defect styles.
- Core pins with and without coatings, and core pins of different cooling rates and the potential for shrinkage porosity.
- Downselection of core pin with representative defects.
- Casting trials with downselected core pins.
- Samples are then cut from cast plate for drilling and tapping for fasteners.
- A population of plates will be processed using FSP prior to drilling and tapping to test the efficacy of selective processing.
- Processed and unprocessed samples will be subjected to bolt retention testing to quantify performance.

(b)

Figure I.3.2.1.5.3. Casting mold design for generating different defects around core pins using (a) a steel book mold with core pins to create cast-in holes and (b) the details of the experimental plan. Source: PNNL.

Casting alloys will be subjected to FSP using a narrow tool plunge and retract technique illustrated schematically in Figure I.3.2.1.5.4. This will produce a fine-grained microstructure and heal defects within a narrow region lining the hole. All plates will be drilled and tapped using standard procedures and cut into individual coupons that can be tested on a bolt retention test rig at Pacific Northwest National Laboratory (PNNL). The deliverables of this task will be reports documenting microstructure, mechanical properties, and threaded fastener pull-out strength as a function of processing parameters.

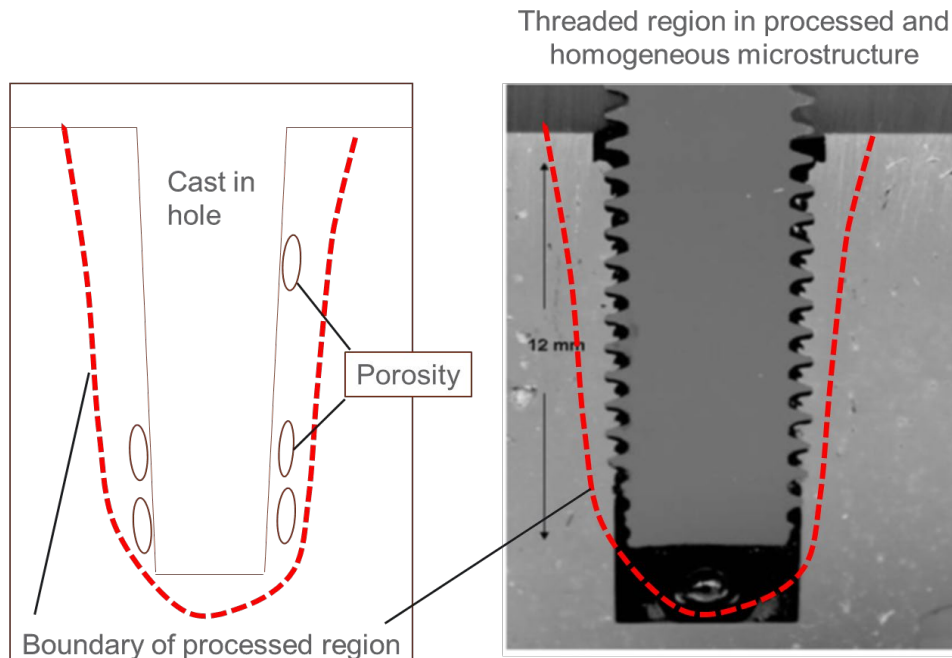


Figure I.3.2.1.5.4. Schematic diagram of FSP region healing porosity in the area later threaded for a fastener. Source: PNNL.

Results

Project work during FY 2021 focused on two tasks: (1) developing a FSP process capable of creating wrought microstructures of high-quality in typical cast-Al alloys; and (2) preliminary investigations into translating the process to a robotic platform. In the first task, efforts focused on a demonstration of defect elimination by FSP at the coupon level. This work demonstrated defect healing and porosity elimination by FSP in flat plate castings of a strontium-modified A356 alloy and in A380 plate castings. These regions were processed using a tool pin producing a processed depth of approximately 4 mm. Processed regions varied with tool design changes and with changes in process parameters, such as tool rotation rate. Figure I.3.2.1.5.5(a)–(c) show three cross-section macrographs showing the characteristics of the wall adjacent to a FSP tool after the tool is retracted. The macrographs show the processed region free of volumetric indication. Adjacent to the processed region, areas of original casting porosity can be observed. The macrographs also show three different tool and process conditions that resulted in large changes in process zone width. This width will be important to customization for bolt thread pitch and geometry for each threaded hole application.

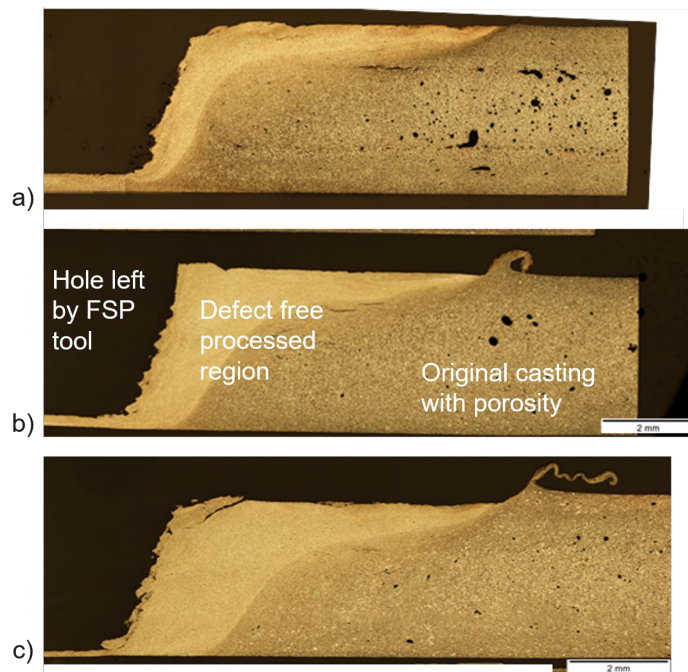


Figure I.3.2.1.5.5. (a)–(c) Macrograph cross-sections of FSP processed regions adjacent to the edge of the hole left by the FSP tool. Different tool designs and processing create different characteristics (including width) in the defect-free processed region. Source: PNNL.

Process development was also initiated on a robotic platform, as shown in Figure I.3.2.1.5.6. Translating the process to a robotic platform is an important consideration for commercial implementation. It is likely that increased industrial automation will take place in the powertrain assembly process as it is in the body structure assembly process. The processes proposed appear at first glance to be similar to robotic spot-welding, a process that locally welds sheet assemblies together using a self-reacting “C-gun” mounted on the end of the robot arm.

One significant difference between robotic spot-welding and robotic FSP is the forces exerted against the work piece with FSP are significantly higher, and are generally reacted by the part, not the “C-gun.” These higher forces combined with the fact that robots are very flexible platforms due to all of its joints and pivot points require additional effort to correctly compensate for deflection, while maintaining precise process loads, and in cases where short linear process zones are needed, precise paths to follow in 3D space.

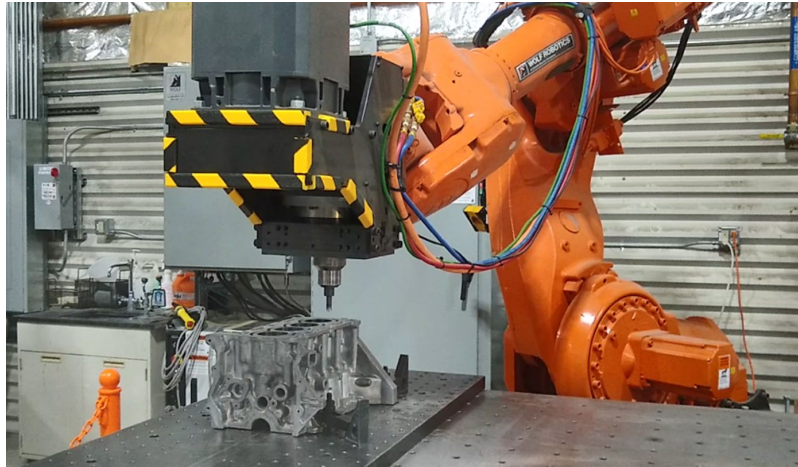


Figure I.3.2.1.5.6. ABB IRB 7600 robot with an FSP end-effector. This configuration illustrates processing a cast-in hole that will be later drilled and tapped for a cylinder head bolt. Source: PNNL.

Work began in FY 2021 to catalog these forces and deflections under process conditions with the eventual goal of providing feedback to path planning/programming and to develop a knowledge base from which deflection compensation can be programmed. Figure I.3.2.1.5.7 shows an example of load output measured from the FSP end-effector on the robot during runs made at different process conditions. As can be seen comparing the force plots from the three orthogonal directions, the revolutions per minute changes in the tool can result in different loads, which will cause the robot to deflect in different ways. Path planning must be adjusted to compensate.

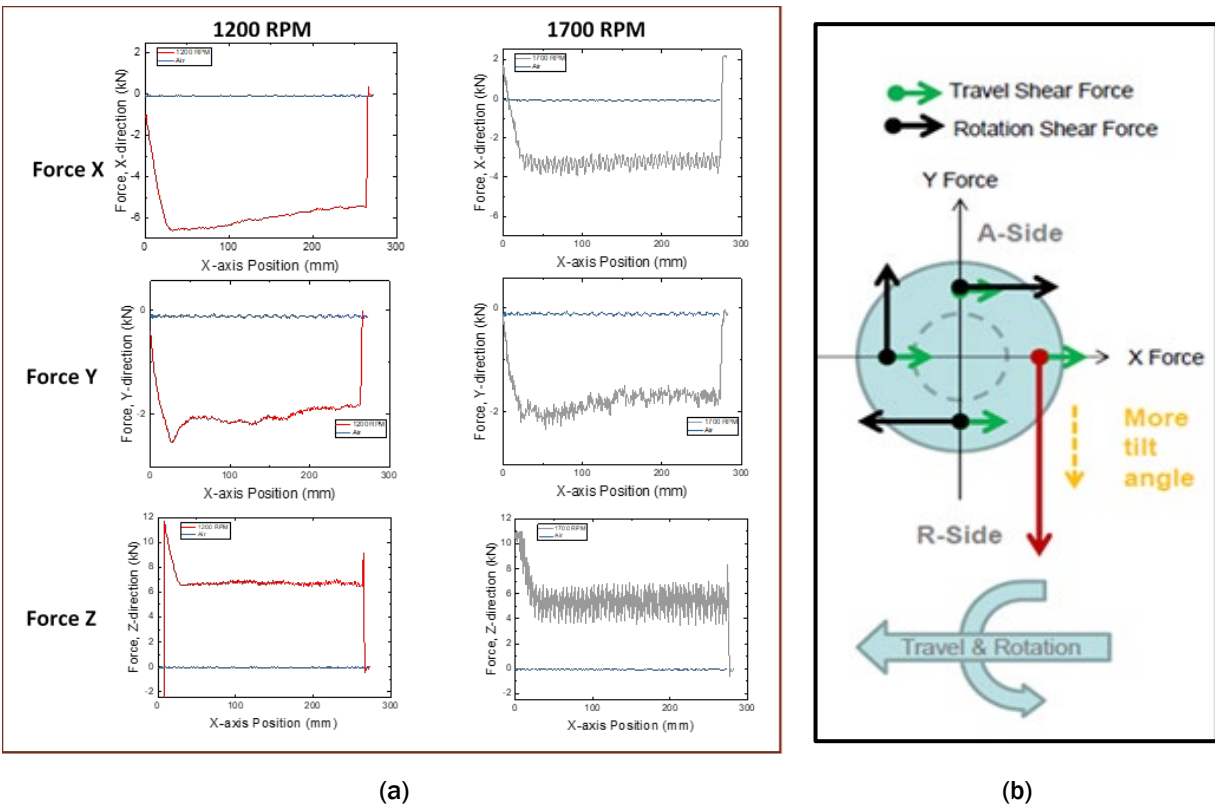


Figure I.3.2.1.5.7. (a) Load versus position graphs for different speeds of the FSP tool showing that different processing conditions result in different tool loads. (b) Orientation for the travel shear and the rotation shear forces on a FSP tool in the tools frame of reference. Source: PNNL.

Conclusions

During FY 2021, FSP trials were completed on A356 and A380, where selective FSP was demonstrated to completely heal casting defects. Process space also was discovered and tool designs and processes for maximum processed width were explored. Work began on translating the process to a robotic platform. This is the first robotic implementation of selective FSP processing for engine components. Completed tasks included programming, load path planning, FSP end-effector integration with robot controls, and shakeout testing. All work was done in close collaboration with an industry advisory group made up of GM Research and Development employees who provided all materials and automotive cast-Al engine blocks for testing.

References

1. Jana, S., R. S. Mishra, and G. J. Grant, 2016. *Friction Stir-Casting Modification for Enhanced Structural Efficiency: A Volume in the Friction Stir Welding and Processing Book Series*, Elsevier, Oxford, UK.
2. U.S. Department of Energy, Vehicle Technologies Office, Annual Merit Review, 2015, “Tailored Materials for Improved Internal Combustion Engine Efficiency.”

Acknowledgments

The project has benefited greatly from collaboration and discussions with B. Carlson and Q. Wang from GM R&D. In addition, GM-provided experimental materials including unmachined four-cylinder engine blocks and base alloy materials.

I.3.3 Additive Manufacturing – Thrust 3

I.3.3.1 Development of Higher Temperature Alloys for Additive Manufacturing (3A/3B)

I.3.3.1.1 Fundamental Development of Lightweight Alloys for Additive Manufacturing (Task 3A1) (Oak Ridge National Laboratory)

Amit Shyam, Co-Principal Investigator

Oak Ridge National Laboratory
1 Bethel Valley Road
Oak Ridge, TN 37831
E-mail: shyama@ornl.gov

Alex Plotkowsky, Co-Principal Investigator

Oak Ridge National Laboratory
1 Bethel Valley Road
Oak Ridge, TN 37831
E-mail: plotkowskiaj@ornl.gov

Jerry L. Gibbs, DOE Technology Manager

U.S. Department of Energy
E-mail: jerry.gibbs@ee.doe.gov

Start Date: October 1, 2018 End Date: September 30, 2023
Project Funding (FY 2021): \$375,000 DOE share: \$375,000 Non-DOE share: \$0

Project Introduction

Automotive companies are seeking to apply the immense interest and technical potential for AM to vehicle propulsion. Al alloys with improved specific strength at higher temperatures are an obvious starting point for applying AM to lightweight engine applications. The primary focus in this task is the development of new, printable, high-strength Al alloys with significant improvements in high-temperature strength while retaining appreciable ductility. The newly developed Al alloys studied in FY 2021 were within the following families: (1) precipitation-hardened alloys (e.g., ACMZ type alloys); (2) dispersion-hardened alloys (Al-Ce-Ni-Mn); and (3) a combination of the two concepts (e.g., ACMZ + Ce and Al-Ce-Ni-Mn + Zr). The primary applications are higher temperature, lightweight powertrain components, such as cylinder heads, pistons, turbochargers, etc. Smaller-bore pistons are a specific target application for AM to enable higher efficiency internal combustion engines. Printed high-performance components for lightweight, highly efficient, boosted engines—including possible future range extenders for hybrid electric freight trucks—are a targeted application.

Objectives

The objective is to fabricate defect-free Al alloys via laser powder bed AM with high-temperature YS from 250°C – 400°C that exceed existing high-volume wrought commercial Al piston alloys by at least 35%, while simultaneously maintaining adequate ductility, fatigue resistance, creep resistance, and RT strength for lightweight piston applications.

Approach

Several studies using laser powder bed AM were performed in FY 2021 to investigate AM of new Al alloys designed at ORNL, including alloys in the Al-Cu-Ce-(Zr), Al-Ce-Ni-Mn-(Zr), and ACMZ systems. In these alloy systems, the rapid cooling rates during AM were exploited to both refine the microstructure to achieve reduced spacings between the fine-strengthening particles) and super-saturate the matrix with a solute (e.g., Zr) that may precipitate into the fine intermetallics upon heat-treatment to provide further strengthening. The research approach included advanced characterization of the alloy microstructures, including high-resolution

scanning transmission electron microscopy (HR-STEM) and atom probe tomography (APT), measurement of mechanical properties (e.g., tensile and creep) at elevated temperatures, and thermodynamic and kinetics modeling. The resultant scientific findings were published in two high-impact journals, as can be seen in the Key Publications below, with a third submission currently in review. We also published insights from our work in a review article on high-temperature Al alloys for AM. At least five additional publications are in progress and will be submitted in FY 2022. Several new alloys are in the initial stages of analysis, with continuation of the studies planned for lightweight high-temperature brake applications for EVs in FY 2022.

Results

During FY 2021, two manuscripts were published related to this task's research on AM Al-9Cu-6Ce-(1Zr) wt.% alloys. The first manuscript, published in *Additive Manufacturing*, investigated the microstructural evolution and mechanical properties of the alloys. The rapid solidification conditions from AM processing resulted in a refined eutectic structure, as shown in Figure I.3.3.1.1(a). The nanometer scale and thermal stability of the microstructure resulted in good RT YS and excellent high-temperature strength at $T > 250^{\circ}\text{C}$, which significantly exceeded that of common AM Al alloys, such as AlSi10Mg and Scalmalloy[®], as observed in Figure I.3.3.1.1(b) and (c), respectively. The Al-Cu-Ce alloy containing Zr was age-hardenable, leading to a 125 MPa increase in RT strength from $L1_2$ -Al₃Zr precipitation upon aging at 350°C for 8 h. A key finding was the discovery of the Al₈Cu₃Ce phase, which constituted the dominant intermetallic phase in the as-fabricated alloys. This intermetallic was previously unreported in the literature. The addition of Zr to the alloy appeared to stabilize the Al₈Cu₃Ce phase, thus suppressing transformation to Al₈Cu₄Ce. Thermodynamic modeling is currently being performed on this system to evaluate the phase stability. Another key finding was the very good printability of Al-Cu-Ce-(Zr) alloys across a wide range of processing parameters, likely related to their low predicted susceptibility to hot-tearing. This property is being leveraged to build components with site-specific properties.

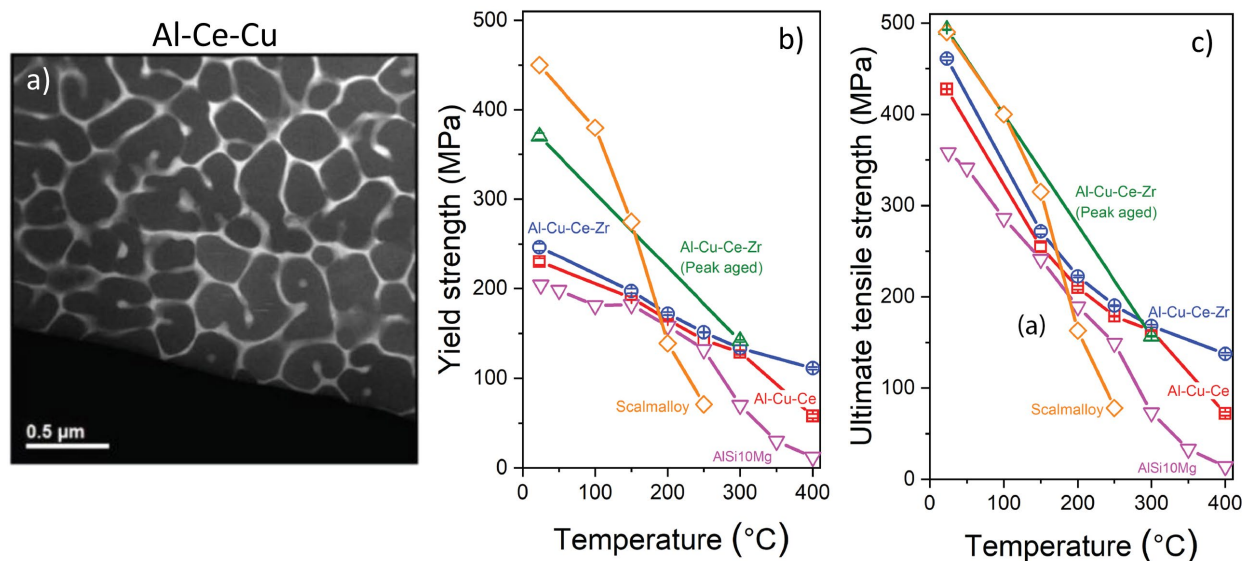


Figure I.3.3.1.1.1. Summary of key results from studies on AM Al-9Cu-6Ce-(1Zr) alloys with (a) representative microstructure of the Al-Cu-Ce alloy with refined Al₈Cu₃Ce intermetallic network, (b) YS, and (c) UTS of the AM Al-Cu-Ce-(Zr) alloys plotted relative to common AlSi10Mg and Scalmalloy[®] additively manufactured Al alloys from the literature. Source: ORNL.

The AM Al-Cu-Ce-(Zr) alloys exhibited a ductility dip at elevated temperatures, reaching a minimum ductility at 300°C, as shown in Figure I.3.3.1.2(a). The second FY 2021 manuscript on the AM Al-Ce-Cu system, published in *Acta Materialia*, investigated this behavior in-depth since it is of concern for potential elevated temperature applications. The ductility minimum at 300°C was found to correlate with a decrease in strain rate sensitivity (SRS) at this temperature, which led to strain localization and failure in the heat-affected zones

(HAZs) of the as-fabricated alloy, as observed in Figure I.3.3.1.1.2(b). The HAZs are areas in the microstructure that are weakened due to thermal fluctuations and remelting from building successive layers during AM processing and breaking up the refined eutectic network. At the other studied temperatures, a higher SRS slowed progression of strain localization such that failure was initiated at other microstructural features/defects. This study highlighted the importance of heterogeneous microstructural features in the deformation mechanisms of additively manufactured alloys, an area of research likely to receive great attention in the coming years.

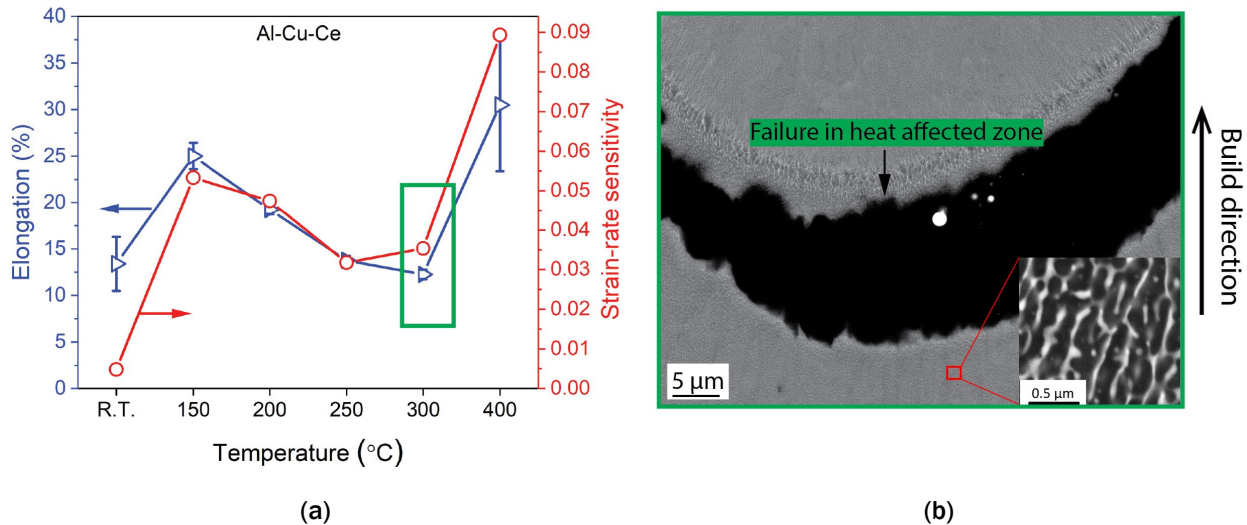


Figure I.3.3.1.1.2. A summary of key results for the assessment of the elevated temperature ductility dip in the AM Al-9Cu-6Ce alloy (a) tensile elongation and SRS measured at different temperatures. The dip in elongation was concomitant with the dip in the SRS (b) failure site observed during tensile testing at 300°C. The failure initiated in the HAZ, which is a weak region in the microstructure formed during additive processing. Source: ORNL.

A third submitted manuscript, currently under review, resulted from high-temperature studies of an AM Al-11Ce-3Ni-1Mn alloy. After a 2 h stress relief heat-treatment at 450°C, the microstructure of the alloy consisted of a complex mixture of sub-micron intermetallic phases with a combined volume fraction of ~35%, as shown in the SEM micrographs seen in Figure I.3.3.1.1.3(a) and (b), respectively, and the HR-STEM micrograph and associated EDS maps observed in Figure I.3.3.1.1.3(c). The compositions of the phases were quantified through APT analysis, with results used for another paper currently in preparation, where the effects of Mn additions to the Al-Ce-Ni system are evaluated using thermodynamic modeling. Upon aging at 300, 350, and 400°C for up to 200 h, the microstructure remained quite stable, with only slight coarsening of the intermetallics noted at 400°C. The high-temperature mechanical properties are especially promising for this alloy. Besides maintaining a yield stress of ~100 MPa up to 400°C, as observed in Figure I.3.3.1.1.3(d), the creep resistance of the alloy, over the range of 300°C – 400°C, was outstanding, which outperforms the most advanced cast high-temperature Al alloys, as can be seen in Figure I.3.3.1.1.3(e).

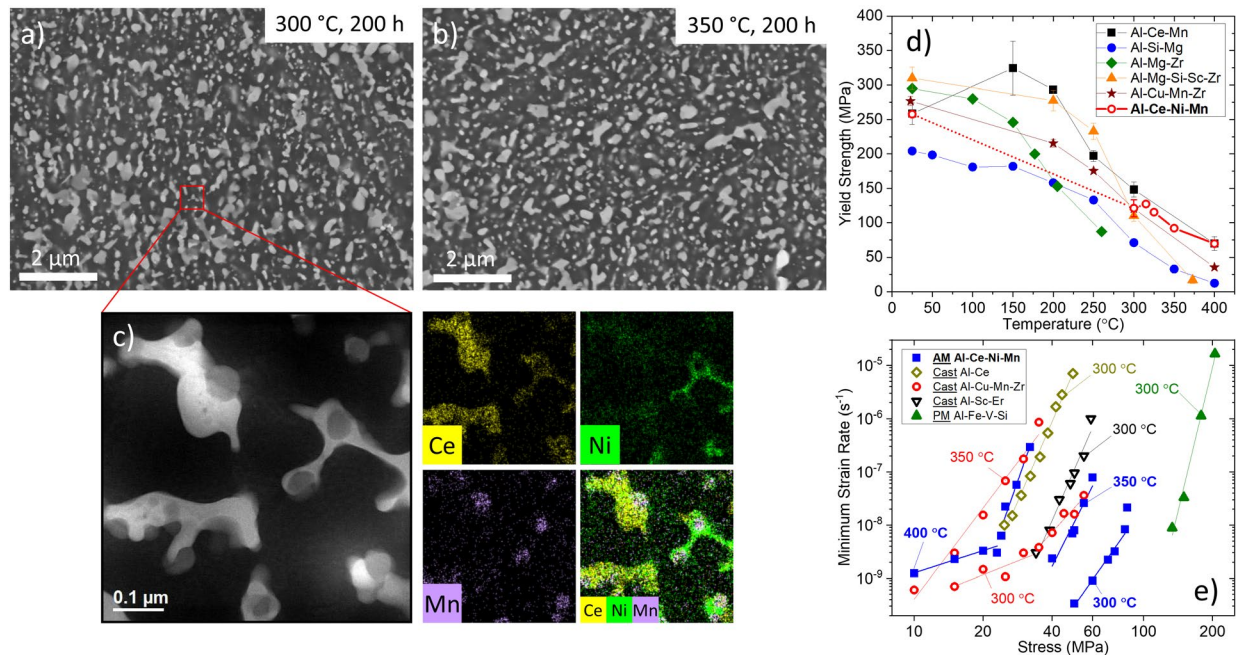


Figure I.3.3.1.1.3. Summary of key results from high-temperature studies of an AM Al-11Ce-3Ni-1Mn alloy: (a–b) after aging at 300 °C or 350 °C for 200 h, the complex microstructure of the sub-micron intermetallic phases remained stable; (c) HR-STEM micrograph and associated EDS maps showing complex elemental distributions within the intermetallics; (d) tensile YS of the AM Al-Ce-Ni-Mn alloy compared to other AM alloys from the literature displaying excellent strength at elevated temperatures; and (e) tensile creep behavior of AM Al-Ce-Ni-Mn at 300, 350, and 400 °C. The alloy outperformed the most advanced cast high-temperature Al alloys from the literature and approached the performance of PM Al alloys. Source: ORNL.

Characterization of an additively manufactured Al-9Cu-0.4Mn-0.9Zr alloy continued from FY 2020 into FY 2021, building on the previous published study of the as-fabricated alloy [1] with a focus this year on optimizing the aging of the alloy to improve the ambient- and high-temperature mechanical properties. Two manuscripts are in preparation and will be submitted in FY 2022. Figure I.3.3.1.1.4(a)–(d) show the extensive microstructural characterization performed on the alloy at multiple-length scales, from the micron-scale grain and melt pool structures down to the APT atom-by-atom analysis. The microstructural changes observed upon aging of the alloy were complex. Although the grain structure did not evolve significantly upon aging at 300, 350, or 400 °C, the refined and interconnected θ -Al₂Cu network formed upon printing broke down and spheroidized, metastable θ' -Al₂Cu precipitates formed *in-situ* during the build dissolved, and nanometric L1₂-Al₃Zr precipitated out of the matrix, which was supersaturated in Zr. These microstructural changes were used as an input for strengthening models to predict the YS after several different heat treatments. The tensile YS was increased by up to 62 MPa over the as-fabricated YS of 279 MPa by heat treating at 300 °C for 200 h, with negligible change in the measured 11% elongation. Some discrepancies in the measured vs. predicted YS, especially for the overaged 200 h heat-treatment at 400 °C, again pointed to the need for an increased understanding of heterogeneous microstructures in the AM alloys.

Creep testing of the AM ACMZ alloy at 300 °C revealed that the as-fabricated condition somewhat unexpectedly had the best creep resistance out of all heat treatments studied, as shown in Figure I.3.3.1.1.4(e). Except after a 200-h heat-treatment at 400 °C, the AM ACMZ alloy performed better, regardless of heat-treatment, than a cast ACMZ alloy with a similar composition. *In-situ* creep neutron diffraction studies were performed during creep to help elucidate the role of load transfer to the θ -Al₂Cu during creep. Results will be submitted to a journal in FY 2022.

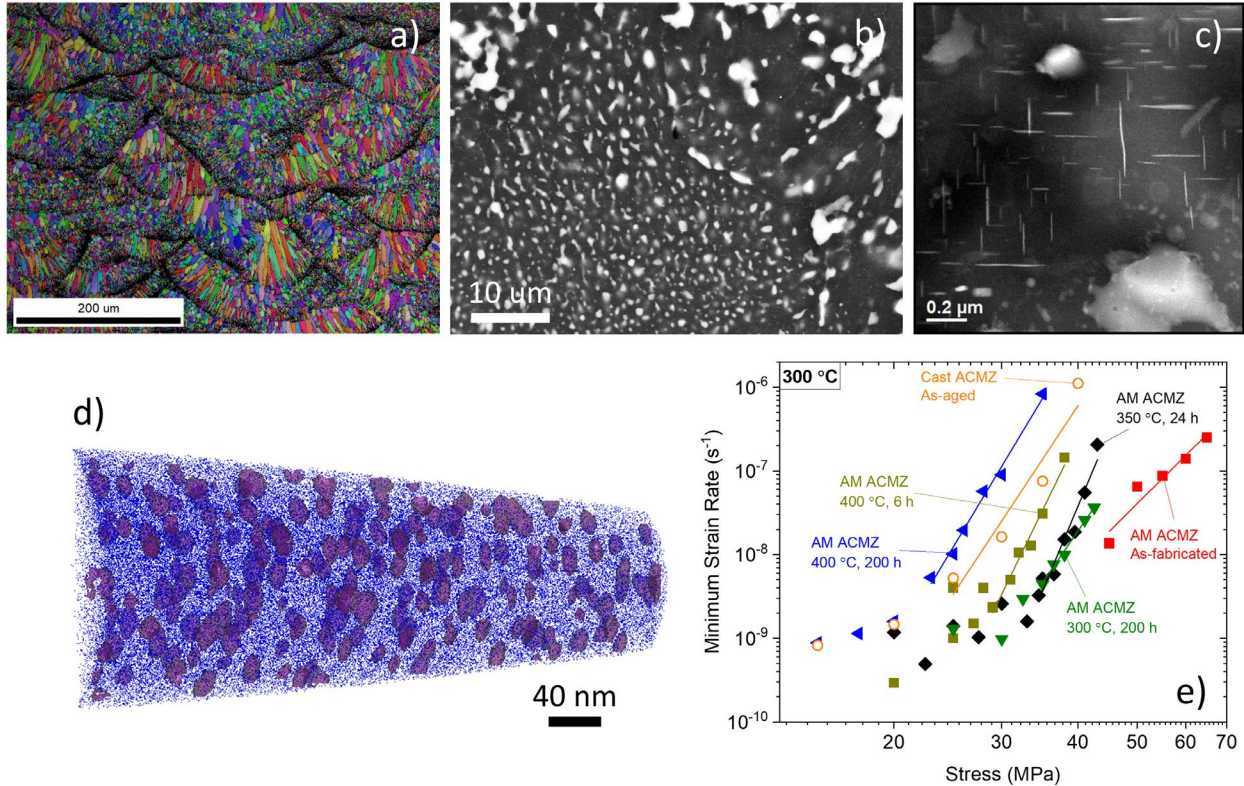


Figure I.3.3.1.1.4. Multiscale characterization of aged AM Al-9Cu-0.4Mn-0.9Zr performed using: (a) EBSD mapping showing individual grains and melt pool structures; (b) SEM imaging showing break down of the θ -Al₂Cu network; (c) STEM imaging showing metastable θ' -Al₂Cu precipitates; and (d) APT analysis showing 3D distribution of L1₂-Al₃Zr nanoprecipitates. (e) Creep testing of the alloy at 300 °C revealed superior creep resistance in the as-fabricated condition. Only after overaging at 400 °C for 200 h did the creep resistance of AM ACMZ fall below that of its cast counterpart. Source: ORNL.

Part building and characterization has begun for several new alloys listed in Table I.3.3.1.1.1, which shows both the nominal composition and measured powder composition of the additional alloys. Residual delays from COVID-19 postponed the building of parts from alloys Al-15Cu-0.5Mn-1Zr and Al-33Cu-0.5Mn-1Zr. There have been some initial issues with cracking during the printing of Al-9Cu-6Ce-3Zr, which are currently being addressed. Tensile bars for mechanical testing and pistons intended for engine testing at ORNL in FY 2022 have been printed from the Al-9Ce-4Ni-0.5Mn-1Zr alloy, and the initial results are extremely promising. This alloy is a modified version of the Al-Ce-Ni-Mn alloy reported above, with roughly half of the Mn content to avoid the formation of brittle intermetallics and the addition of Zr to promote age-hardening. After an aging treatment at 350 °C for 8 h, the YS at 200 °C is 195 MPa and negligible creep deformation was measured at 300 °C under 80 MPa tensile load.

Table I.3.3.1.1.1. Summary of New Al Alloys and Status for AM

Nominal Alloy Chemistry (wt.%)	Status	Measured Powder Chemistry (wt.%)							
		Al	Cu	Ce	Ni	Mn	Zr	Si	Fe
Al-9Cu-6Ce-3Zr	Issues with part cracking	Bal.	8.9	6.1	-	-	1.8	0.2	0.2
Al-9Ce-4Ni-0.5Mn-1Zr	AM parts built	Bal.	-	7.5	4.7	0.5	0.7	0.05	0.1
Al-15Cu-0.5Mn-1Zr	Atomized, ready for AM	Bal.	17.2	0.1	0.02	0.5	0.8	0.05	0.09
Al-33Cu-0.5Mn-1Zr	Atomized, ready for AM	Bal.	34.4	0.06	0.01	0.48	0.8	0.05	0.12

Conclusions

The research completed during this FY 2021 task has shown continued promise for the AM-facilitated development of Al alloys with microstructures and properties that cannot be achieved through conventional processing. Not only do the refined microstructures formed during AM processing provide appreciable strength at RT, but their thermal stability shows remarkable promise for high-temperature performance, as demonstrated in the creep and high-temperature results presented herein. Advanced characterization, extensive mechanical testing, and modeling of thermodynamics and kinetics of phase transformations in these alloys has helped us understand the critical mechanisms and non-equilibrium behavior of the alloys during processing and the consequences of these unique microstructural features on alloy properties. There are several areas that need attention in the future—particularly the effect of melt pool boundaries and other heterogeneous microstructural features on the mechanical behavior of additive alloys—and fatigue performance. Increasing scientific understanding in these areas will aid in the design of additional improved alloys for the future.

Key Publications

1. Bahl, S., A. Plotkowski, K. Sisco, D. N. Leonard, L. F. Allard, R. A. Michi, J. D. Poplawsky, R. Dehoff, and A. Shyam, 2021, “Elevated temperature ductility dip in an additively manufactured Al-Cu-Ce alloy,” *Acta Mater.*, Vol. 220, Art. 117285.
2. Bahl, S., K. Sisco, Y. Yang, F. Theska, S. Primig, L. F. Allard, R. A. Michi, C. Fancher, B. Stump, R. Dehoff, A. Shyam, and A. Plotkowski, 2021, “Al-Cu-Ce(-Zr) alloys with an exceptional combination of additive processability and mechanical properties,” *Addit. Manuf.*, Vol. 48, Art. 102404.
3. Michi, R. A., K. Sisco, S. Bahl, Y. Yang, J. D. Poplawsky, L. F. Allard, R. R. Dehoff, A. Plotkowski, and A. Shyam, 2021, “A creep-resistant additively manufactured Al-Ce-Ni-Mn alloy,” *Acta Mater.* (In review).
4. Michi, R. A., A. Plotkowski, A. Shyam, R. R. Dehoff, and S. Suresh Babu, 2021, “Towards high-temperature applications of aluminum alloys enabled by additive manufacturing,” *Int. Mater. Rev.*, (preprint) pp. 1–48. Available at: <https://doi.org/10.1080/09506608.2021.1951580>. Last accessed 6 December 2021.
5. Yang, Y., et al., 2022, “Thermodynamic modeling of Al-Cu-Ce system,” in preparation.
6. Bahl, S., et al., 2022, “High velocity laser processing of Al-Cu-Ce-Zr alloys,” in preparation.
7. Michi, R. A., et al., 2022, “Microstructural evolution and strengthening mechanisms in a heat-treated additively manufactured Al-Cu-Mn-Zr alloy,” in preparation.
8. Michi, R. A., et al., 2022, “Effects of load transfer on the creep behavior of an additively manufactured Al-Cu-Mn-Zr alloy: *In-situ* neutron diffraction experiments,” in preparation.
9. Yang, Y., et al., 2022, “Thermodynamic modeling of Al-Ce-Ni-Mn system,” in preparation.

References

1. Shyam, A., A. Plotkowski, S. Bahl, K. Sisco, L. F. Allard, Y. Yang, J. A. Haynes, and R. R. Dehoff, 2020, “An additively manufactured Al-Cu-Mn-Zr alloy microstructure and tensile mechanical properties,” *Materialia*, Vol. 12, Art. 100758.

Acknowledgments

The authors acknowledge the contributions of the ORNL team members for this subtask: A. Shyam, R. Dehoff, S. Bahl, R. Michi, Y. Yang, and L. Allard.

I.3.3.1.2 Additively Manufactured Interpenetrating Phase Composites (AMIPC) via Hybrid Manufacturing (Task 3A2) (Oak Ridge National Laboratory)

Derek Splitter, Principal Investigator

Oak Ridge National Laboratory
2360 Cherahala Boulevard
Knoxville, TN 37932
E-mail: splitterda@ornl.gov

Jerry L. Gibbs, DOE Technology Manager

U.S. Department of Energy
E-mail: jerry.gibbs@ee.doe.gov

Start Date: October 1, 2018 End Date: September 30, 2022
Project Funding (FY 2021): \$190,000 DOE share: \$190,000 Non-DOE share: \$0

Project Introduction

This work seeks to understand how the combination of metal AM with metal casting via ‘PrintCasting’ can be developed to create MMC structures that increase energy absorption and prevent failures of the ring land area of automotive pistons without significantly affecting the overall weight or thermal conductivity of the component. A key advantage of PrintCasting is that it leverages AM control over the reinforcing phase mesostructure. Therefore, the geometry and spatial distribution of the reinforcing constituent can be precisely controlled to create composites with geometries that realize improved energy absorbing behavior, as well as other tailored properties, with capability for locally controlled and varied properties across a component. It has been demonstrated that high levels of energy absorption can be achieved by creating a reinforcement geometry that converts the applied tensile load into local compression of the more brittle, cast-Al matrix. The printed reinforcement geometry is patterned with a topology designed to be bending-dominated, which upon axial loading collapses, thereby compressing the lightweight alloy matrix trapped in between. The project has the potential to provide solutions to overcome key barriers related to localized piston damage related to knock or pre-ignition in high-efficiency, turbocharged, spark-ignited engines. This novel concept also offers significant cross-cutting opportunities, as evidenced by its being licensed for non-transportation industries.

Objectives

This project aims to create AM metal-metal composites with high-energy absorption and tailorable local mechanical, thermal, and acoustic properties. Potential broader applications include energy absorption under tensile loading for scenarios that include impulse loading, blast containment, and load bearing structures—all of which are conditions relevant to automotive pistons in boosted spark-ignited engines prone to knock/pre-ignition. The objective is to understand the geometric factors, bonding, material selection, and processing aspects enabling development of multi-material hybrid systems suitable to high demand applications.

Approach

A powerful feature of metal AM is the ability to directly print net-shaped composites with high levels of architectural complexity, but most additive processes are limited to a single feedstock resulting in monolithic materials. In PrintCasting, the AM capabilities are leveraged with conventional casting such that a hybrid approach is used. Specifically, local control over composition is achieved through the AM portions by changing the printed lattice size and/or geometry, enabling gradients in composite composition and structure. Subsequently, the printed lattice is overcast and melt-infiltrated with a lower melting point, lightweight alloy—in this study, a cast-Al alloy A356. Lightweight cast A356 alloys have lower ductility due to casting porosity and experience brittle failure under tension, but can undergo very large plastic deformation under compression, whereas the AM 316L or Ti64 reinforcement lattice can undergo very high-strength and tensile ductility.

The A356/316L or Ti64/Al material systems are known to form brittle Fe-Al or Ti-Al intermetallic compounds when fused together [1], which motivated the design of the novel PrintCasting hybrid processing strategy. This approach combines AM of the higher melting point material lattice with casting of the lower melting point alloy to eliminate liquid phase mixing of the two alloys and thus avoids intermetallic formation, as highlighted in Figure I.3.3.1.2.1.

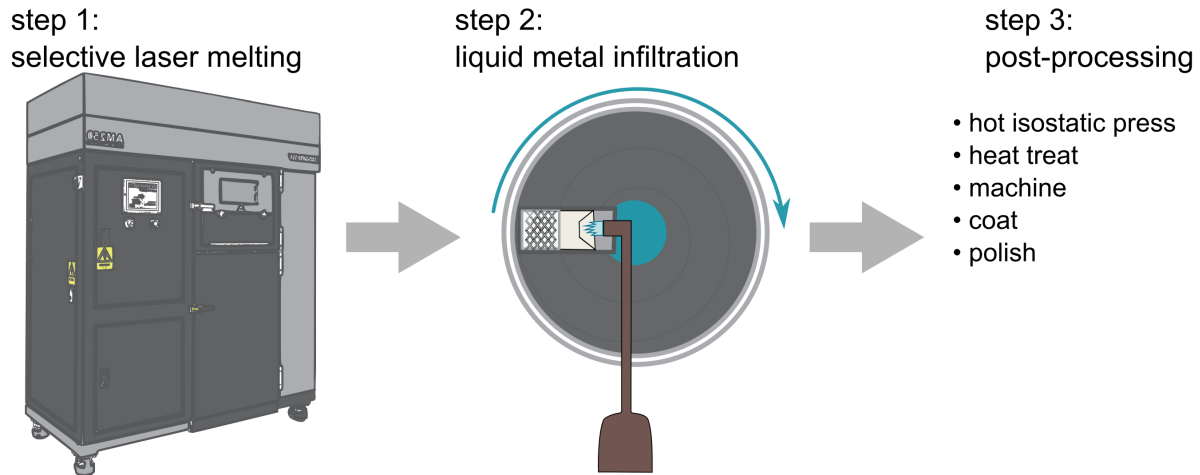


Figure I.3.3.1.2.1. Process for synthesizing AMIPCs using the PrintCasting technique. The model is printed using a selective laser melting process, filled with liquid metal using centrifugal casting, and then post-processed to optimize the properties. Source: ORNL.

The result of the PrintCast process is an interpenetrating phase composite (IPC) in which the two constituents form continuous and interconnected networks, but do not fuse and form Al-based intermetallics at the interfaces. It has been shown that an interpenetrating morphology can enable unique mechanical and thermal properties in a nonlinear blending of the properties of the constituents [2-5]. More specifically, it has been shown that fracture toughness can be increased by interconnecting the more ductile phase in a brittle/ductile system, which further improves energy absorption.

Results

Progress this year consisted of the completion of simulations and experiments focused on bonding between the constituents and energy absorption. A hypervelocity impact analysis from our partners at Rice University [5], as well as a hot isostatic pressing (HIP) analysis of the 316L/A356 samples, were our primary focus areas.

Initial progress on the PrintCast technology was tailored to understand the importance of the interface between the constituents. In FY 2020, the simulation results indicated this interface was critical to energy absorption in the PrintCast structures. To investigate the importance of this interface, various PrintCast materials were produced, with some samples from the same build lot being left in the “as-produced” condition, and others post-processed by HIP. The HIP process was tailored to close porosity in the A356 melt-infiltrated matrix material, including those along the printed lattice-cast-Al interfaces.

Figure I.3.3.1.2.2 shows the results of this approach employing the HIP conditions of ASTM F3318–18 (e.g., 100 MPa at 510-530°C for 3 hours), on a PrintCast sample with 30% volume 316L stainless-steel (SS) lattice with a balance of cast A356 Al. As Figure I.3.3.1.2.2 illustrates, the HIP post-processing procedure mitigates the porosity in the A356 matrix. It should be noted that HIP has minimal impact on 316L SS internal porosity (i.e., the HIP procedure primarily affects the Al under these selected conditions).

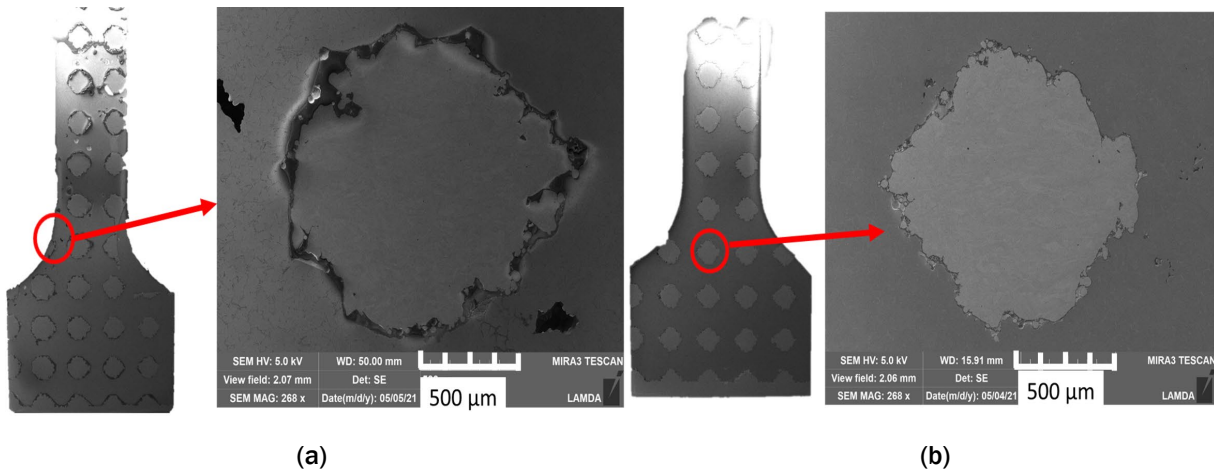


Figure I.3.3.1.2.2. Results of employing HIP conditions of ASTM F3318–18 (i.e., 100 MPa at 510-530 °C for 3 hours) on: (a) a PrintCast sample with 30% volume 316L SS lattice with balance of cast A356; and (b) the HIP post-processing procedure mitigates the porosity in the A356 matrix. From the SEM analysis, the interface exhibits gaps (black regions) ranging between 50 and 100 μm . Source: ORNL.

Using the HIP results, both the physical tensile bar testing and corresponding simulation were used to understand the importance of the interface between the constituents. As can be seen in Figure I.3.3.1.2.2, even with SEM magnification (in the far-right image), the as-produced sample exhibits a gap at the interface between the printed SS lattice element and the melt-infiltrated A356 Al. From the SEM analysis, the interface exhibits gaps (black regions) ranging between 50 and 100 μm . Likewise, the image from the same sample after HIP processing at a different lattice location in the sample shows very little gap to exist at the interface of the 316L SS and A356 Al. As such, a simulation effort varied the gap at the interface from 0 μm – 200 μm to understand the effect that such interface gaps have and to fully encompass the bounds of what was experimentally measured.

During FY 2020 research within this task, Cheng et al. [4] demonstrated a calibrated FEA simulation tool for exploring the effects of lattice geometry and materials performance to identify geometries of interest for mechanical testing. A key element of that approach was the employment of an interface gap model that could be varied independently. The interface gap enables tuning of the mechanical bonding of the constituents, significantly influencing the overall local and global deformation and energy absorption behaviors. This simulation approach was probed further in FY 2021 to better understand the complex and critical nature of the inter-constituent interface in the PrintCast technology. Key results from that effort are highlighted in Figure I.3.3.1.2.3 where measurements of pre- and post-HIP of the samples are shown, as well as a cross validated FEA domain for the interface gap between the constituents and the corresponding FEA results.

Using the developed and validated framework, the simulation effort was extended to hypervelocity impacts. Although hypervelocity impacts are not part of the technology being directly investigated for piston engines, the fundamental results of hypervelocity impact experiments by project collaborators at Rice University [5] were used as calibration measurements such that the performance of the PrintCast material and similar materials could be extended to engine-relevant conditions.

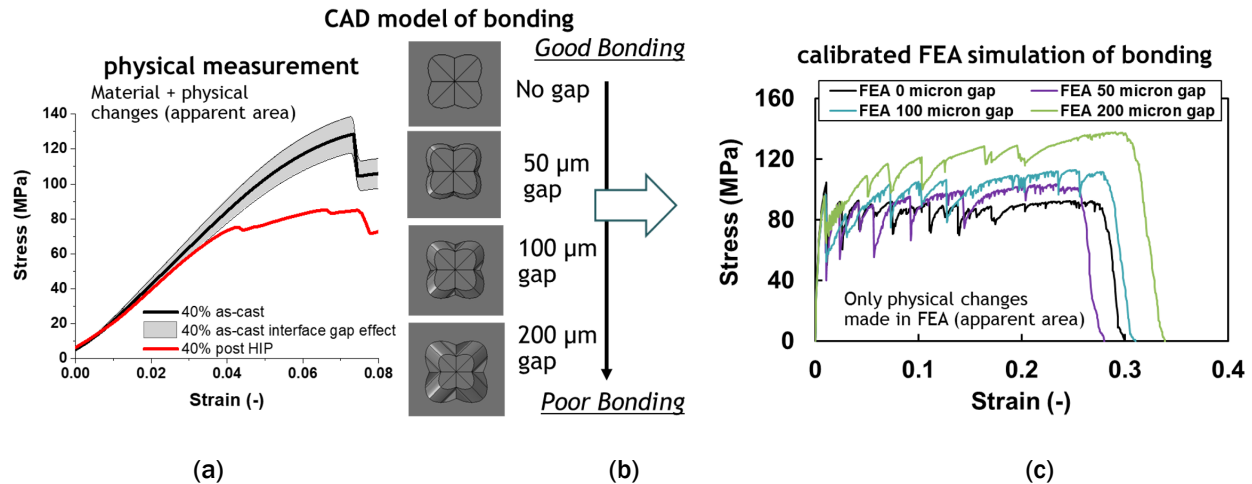


Figure I.3.3.1.2.3. (a) Tensile measurements of pre-and-post-HIP of PrintCast samples at 40% volume fraction 316L SS with balance A356 Al. (b) FEA domain used to simulate measured interface gap in samples. (c) FEA results of a varied gap at the constituent interface. Source: ORNL.

Figure I.3.3.1.2.4 demonstrates the physical hypervelocity impacts for three different materials, monolithic A356 Al, monolithic 316L SS, and a PrintCast sample with a 40% volume fraction 316L SS mesh, melt-infiltrated by A356 Al. Note that these samples were of various thicknesses such that total mass was conserved. In the impact testing, an Al sphere fired at 6.1 km/s (~Mach 18) impacted each surface at RT and pressure. The energy imparted by this approach is believed to be similar to that experienced during super knocking events that occur during stochastic pre-ignition events in downsized boosted engine operation. Thus, although a physical impact is not occurring in the engine scenario, the resulting detonation and or developing detonation and corresponding pressure profile imparted on the piston ring land is similar in energy deposition and duration.

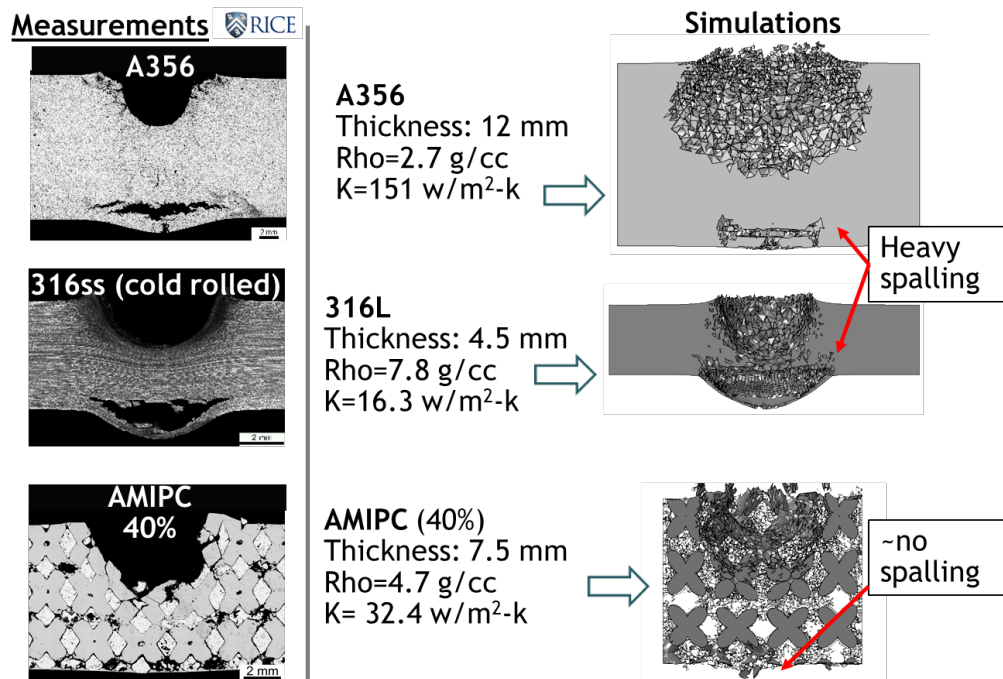


Figure I.3.3.1.2.4. Hypervelocity measurements performed by Rice University [5] and the simulation of the impact's performance at ORNL using the calibrated FEA mode. Source: ORNL.

Using this approach, the calibrated simulation assumed a 100 μm interface gap in the PrintCast sample, which is labeled as AMIPC in Figure I.3.3.1.2.4. Results show that the simulation effort mirrors the physical measurements well, capturing the spalling effects and eminent failure of the monolithic materials, as well as the performance improvements observed in the PrintCast structure. Specifically, the improved impact performance is complemented by improved energy to fracture, as shown in the integrated area under the tensile loading result in Figure I.3.3.1.2.3. Although not shown in Figure I.3.3.1.2.4, the source of the observed performance improvements is from energy dissipation between the material constituents and associated reduction in the peak load experienced in the PrintCast sample surfaces and shock reflection dynamics. This is an active area of our university partners' research as highlighted by Poole et al. [5] using the same physical samples and results shown in Figure I.3.3.1.2.4. Note that the simulations shown in Figure I.3.3.1.2.4 are not reported in Poole et al. [5].

After calibration with the hypervelocity impacts by Poole et al. [5], the simulation effort was extended to engine-relevant conditions. A shock-loading profile similar to what was observed in the engine experiments reported in [6], as well as what was reported to be representative-loading conditions by Splitter [7] in the DOE VTO Partnership for Advanced Combustion Engines (PACE) program experiments at ORNL. The results are presented in Figure I.3.3.1.2.5, where under the same shock impulse at nominal operating temperatures and pressures, the PrintCast piston is not predicted to fail when shock-loaded with the profile observed in the experiments. These results are not all-inclusive, but they do present initial indications of the impact absorption possibilities enabled by the PrintCast approach.

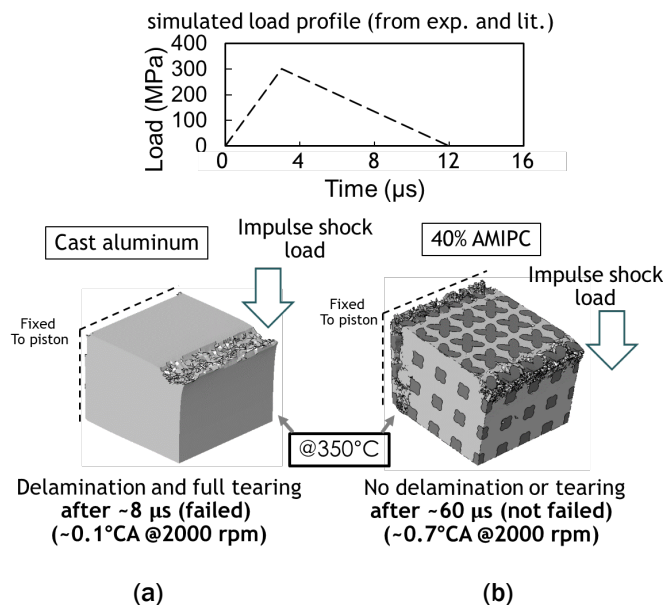


Figure I.3.3.1.2.5. FEA simulation of super-knock-loading of pistons using the calibrated FEA model for (a) cast-Al and (b) 40% 316L/356 SS Al PrintCast. Source: ORNL.

Conclusions

Research and analysis to understand the properties and potential of PrintCast metal-metal composites has continued. In addition, an effort to understand the lattice parameters and design was conducted to assess how the interface between the constituents affects energy absorption. The coupled approach of simulations and targeted experiments is systematically addressing the fundamental tradeoffs in the material performance of various PrintCast metal-metal composite systems. The goal is to research and demonstrate the potential breakthrough lightweight materials and manufacturing approaches for more robust materials solutions for automotive pistons and other associated high demand powertrain components in advanced, higher efficiency engines with extreme operating conditions, including pre-ignition and knock.

Key Publications

1. Allen, J., A. Moustafa, J. Cheng, X. Hu, D. Splitter, A. Shyam, and Z. Cordero, 2021, “Optimization of lattice structures for additively manufactured interpenetrating composites,” 13th International Conference on the Technology of Plasticity, 25–30 July 2021, Virtual Event.
2. Allen, J., J. Cheng, X. Hu, D. Splitter, M. Gussev, and A. Shyam, 2021, “The role of interface in additively manufactured interpenetrating composites,” 2021 Annual International Solid Freeform Fabrication Symposium, 2–4 August 2021, Virtual Event.
3. Allen, J., J. Cheng, X. Hu, D. Splitter, M. Gussev, and A. Shyam, 2021, “Interfaces in additively manufactured interpenetrating composites,” 2021 Annual International Solid Freeform Fabrication Symposium, 2–4 August 2021, Virtual Event.
4. Cheng, J., M. Gussev, J. Allen, X. Hu, A. R. Moustafa, D. A. Splitter, and A. Shyam, 2021. “Deformation and failure of PrintCast A356/316 L composites: Digital image correlation and finite element modeling,” *Mater. Des.*, Vol. 195, Art. 109061.

References

1. Hofmann, D. C., J. Kolodziejaska, S. Roberts, R. Otis, R. P. Dillon, J.O. Suh, Z. K. Liu, and J. P. Borgonia, 2014, “Compositionally graded metals: A new frontier of additive manufacturing,” *J. Mater. Res.*, Vol. 29, No. 17, pp. 1899–1910.
2. Moustafa, A. R., R. B. Dinwiddie, A. E. Pawlowski, D. A. Splitter, A. Shyam, and Z. C. Cordero, 2018, “Mesostructure and porosity effects on the thermal conductivity of additively manufactured interpenetrating phase composites,” *Addit. Manuf.*, Vol. 22, pp. 223–229.
3. Pawlowski, A. E., Z. C. Cordero, M. R. French, T. R. Muth, J. K. Carver, R. B. Dinwiddie, A. M. Elliott, A. Shyam, and D. A. Splitter, 2017, “Damage-tolerant metallic composites via melt infiltration of additively manufactured preforms,” *Mater. Des.*, Vol. 127, pp. 346–351.
4. Cheng, J., M. Gussev, J. Allen, X. Hu, A. R. Moustafa, D. A. Splitter, and A. Shyam, 2020, “Deformation and failure of PrintCast A356/316 L composites: Digital image correlation and finite element modeling,” *Mater. Des.*, Vol. 195, Art. 109061.
5. Poole, L. L., M. Gonzales, M. R. French, W. A. Yarberr III, A. R. Moustafa, and Z. C. Cordero, 2021, “Hypervelocity impact of PrintCast 316L/A356 composites,” *Int. J. Impact Eng.*, Vol. 136, Art. 103407.
6. Kalghatgi, G., 2018, “Knock onset, knock intensity, superknock, and pre-ignition in spark-ignition engines,” *Int. J. Engine Res.*, Vol. 19, No. 1, pp. 7–20.
7. Splitter, D., 2021, “Low speed pre-ignition,” DOE VTO PACE Program Annual Report.
8. Shyam, A., A. Plotkowski, S. Bahl, K. Sisco, L. F. Allard, Y. Yang, J. A. Haynes, and R. R. Dehoff, 2020, “An additively manufactured Al-Cu-Mn-Zr alloy microstructure and tensile mechanical properties,” *Materialia*, Vol. 12, Art. 100758.

Acknowledgments

The authors would like to acknowledge the following individuals who assisted in this effort: X. Hu, A. Shyam, J. Cheng, J. Allen, M. Gussev, and A. Moustafa of Rice University; and Z. Cordero of Rice University/Massachusetts Institute of Technology.

I.3.3.1.3 Overview of Fundamentals of Non-Equilibrium Processing Within the Powertrain Materials Program (Task 3A3) (Oak Ridge National Laboratory)

Ying Yang, Co-Principal Investigator

Oak Ridge National Laboratory
1 Bethel Valley Road
Oak Ridge, TN 37830
E-mail: yangying@ornl.gov

Allen Haynes, Co-Principal Investigator

Oak Ridge National Laboratory
1 Bethel Valley Road
Oak Ridge, TN 37830
E-mail: haynesa@ornl.gov

Jerry L. Gibbs, DOE Technology Manager

U.S. Department of Energy
E-mail: jerry.gibbs@ee.doe.gov

Start Date: October 1, 2021 End Date: September 30, 2023
Project Funding (FY 2021): \$140,000 DOE share: \$140,000 Non-DOE share: \$0

Project Introduction

AM offers unique opportunities to produce distinct microstructures that cannot be achieved from conventional casting methods—particularly considering the high cooling rates and heterogeneous cooling conditions in melt pools. However, the relationships between process parameters, heat transfer, and microstructural evolution are often convoluted and poorly understood. The ability to understand and control microstructural evolution in AM processing has the potential to revolutionize the design and control of AM alloy microstructures. This task was launched in FY 2021 and dedicated to address two major challenges in AM Al alloys. The first is limited knowledge of microstructural evolution—specifically phase stability—for materials fabricated via non-equilibrium processing conditions. The second is that newly designed AM alloys have limited phase diagram and thermodynamic property information. The lack of baseline knowledge in these new classes of Al alloys prevented accurate analysis on how kinetic factors affect the phase stability and phase transformations in non-equilibrium processing conditions.

The alloy systems investigated herein are an emerging class of AM Al alloys designed by ORNL. These alloys are primarily based on the Al-Ce eutectic system [1–4], but also include variants based on Al-Ni [5–7], and Al-Cu [8] eutectic systems. They were designed to resist hot cracking/hot-tearing based on the principle that the narrow solidification temperature range and large volume fraction of terminal eutectic can better fill the interdendritic regions that are typical initiation sites for hot-tearing/cracking. Apart from inherent resistance to hot-tearing, the rapid solidification conditions associated with laser powder bed AM processing refines the eutectic structures, resulting in improved mechanical properties in these binary eutectic systems. To further enhance the high-temperature strength, ternary eutectic alloys based on Al-M-Ce (M=Ni, Cu, Mn, Mg, Zr) are currently under investigation in this task. However, the microstructural characterization results from AM Al-Cu-Ce, Al-Cu-Ce-Zr, and Al-Ni-Ce-Mn alloys suggested that the phases present in the AM microstructures were either different from those phases reported in literature phase diagrams or there was lack of necessary phase stability knowledge in these multicomponent systems. Evaluation of the existing phase diagrams also showed inconsistencies between different sources. Therefore, in this work, we first established the baseline of phase stability for the Al-M-Ce (e.g., M=Cu, Mn, Ni, and Zr) systems, and then applied this knowledge to interpret the microstructures that were observed in the AM alloys.

Objectives

The objective of this task is to develop fundamental understanding of phase stability and thermodynamic models for newly designed AM Al-M-Ce (e.g., M=Cu, Mn, and Ni) alloys, and then couple with kinetic factors to interpret microstructural evolution under non-equilibrium AM processing conditions.

Approach

The approach is schematically shown in Figure I.3.3.1.3.1. For the Al-M-Ce (M=Cu,Ni) system, we first use the existing microstructural modeling tools—including CALPHAD-type thermodynamic databases, phase diagram calculation software, Scheil solidification models, etc.—and calculate the solidification pathways for a range of compositions based on the Scheil model. This model can describe the solidification process under relatively fast-cooling rates—if the composition at the solid-liquid interface can be maintained at equilibrium. Conventional copper mold casting methods generally fall into this cooling rate range. This model may not be directly applicable to AM conditions as the prerequisites of the solid-liquid interface composition at equilibrium may not be satisfied due to the fast-cooling rate. Nevertheless, it is still useful for screening purposes. The calculation results were subjected to examination based on alloy design criteria, such as how much eutectic fraction is needed for desirable AM alloys. Alloys that satisfied the design criteria were fabricated through both AM and conventional casting methods. Microstructural characterization results from conventional casting alloys were compared with the Scheil solidification modeling results. When they did not agree, thermodynamic property and phase diagram information from the literature were re-evaluated and re-modeled. Once the thermodynamic property and phase diagrams were validated by the experimental data, they were used to interpret the results obtained for the AM alloys. In this step, kinetic factors—such as solute trapping, competition in nucleation, and growth between stable and metastable phases—often need to be included to better understand the AM results. The modeling validation process often needs to iterate several times before the models can capture the key factors and satisfactorily describe microstructure evolution in AM alloys.

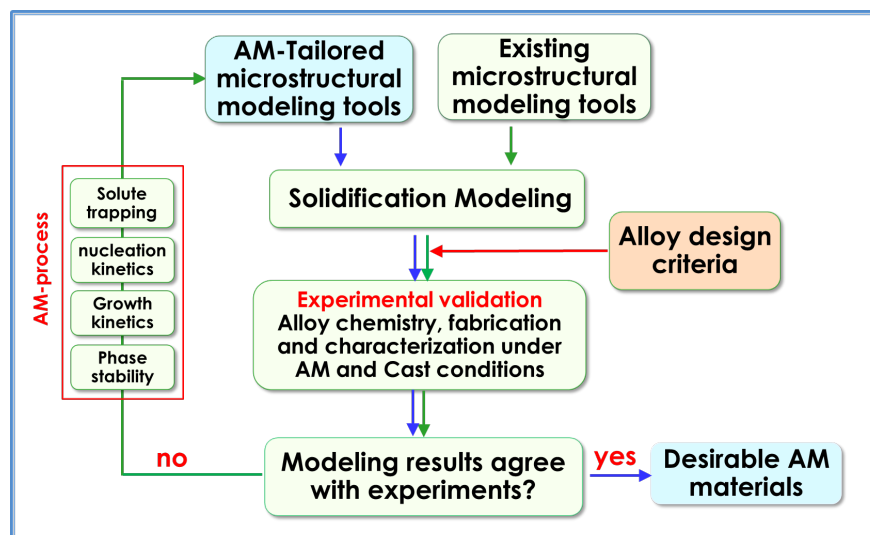


Figure I.3.3.1.3.1. Schematic flowchart showing the approach used in this project. Source: ORNL.

Results

Phase Stability in Al-Rich Al-Cu-Ce Ternary After Casting and AM

Solidification reactions and phase stability in the Al-rich Al-Cu-Ce ternary system have been carefully investigated in this task. The Al-9Cu-6Ce wt.% alloy was fabricated through both laser powder bed AM and conventional casting methods. The chemical analysis results of AM and cast alloys were Al-8.8Cu-5.91Ce and Al-7.78Cu-4.73Ce wt.%, respectively. Microstructural characterization was performed on the AM alloy for the as-built and heat-treated states at 400°C and on the cast alloy for the as-cast and heat-treated states at 610°C

and 540°C. The heat-treatment temperatures for the cast alloy were selected to understand the stabilities of the high-temperature phases. The solidification path simulated using the Scheil model is shown in Figure I.3.3.1.3.2(a) for the Al-8.8Cu-5.91Ce wt.% cast alloy following the sequential reactions of primary solidification of the (Al) phase, the two-phase eutectic solidifications of (Al)+Al₄Ce, (Al)+Al₈Cu₃Ce, and (Al)+Al₈Cu₄Ce, and finally the three-phase eutectic solidification of (Al)+Al₈Cu₄Ce+Al₂Cu. The liquid composition follows the red line that is superimposed onto the liquidus projection of the Al-Cu-Ce system, as observed in Figure I.3.3.1.3.2(b). It shows the composition starts in the (Al) primary phase region, then follows the eutectic valleys between (Al) and Al₄Ce, (Al)+Al₈Cu₃Ce, and (Al)+Al₈Cu₄Ce. Finally, it ends at the ternary eutectic composition of (Al)+Al₈Cu₄Ce and Al₂Cu. The microstructure in Figure I.3.3.1.3.2(c) clearly shows the primary Al phase, the two-phase eutectic of (Al)+Al₄Ce (i.e., the red box), and (Al)+Al₈Cu₃Ce (i.e., the yellow box). The (Al)+Al₄Ce eutectic is coarser than that of (Al)+Al₈Cu₃Ce. The EDS mapping clearly shows these two eutectics in Figure I.3.3.1.3.2(e). The eutectic microstructure of (Al)+Al₈Cu₄Ce cannot be observed in the microstructure, which is probably due to the very small fraction of this eutectic (i.e., less than 1%). The final ternary eutectic microstructure of (Al)+Al₈Cu₄Ce+Al₂Cu can be seen from the enlarged image of the white box. It is on the edge of the binary eutectic of (Al)+Al₈Cu₃Ce, as shown in the green box in Figure I.3.3.1.3.2(d). The phase compositions were confirmed by EDS analysis and the crystal structures were confirmed by Transmission Kikuchi Diffraction.

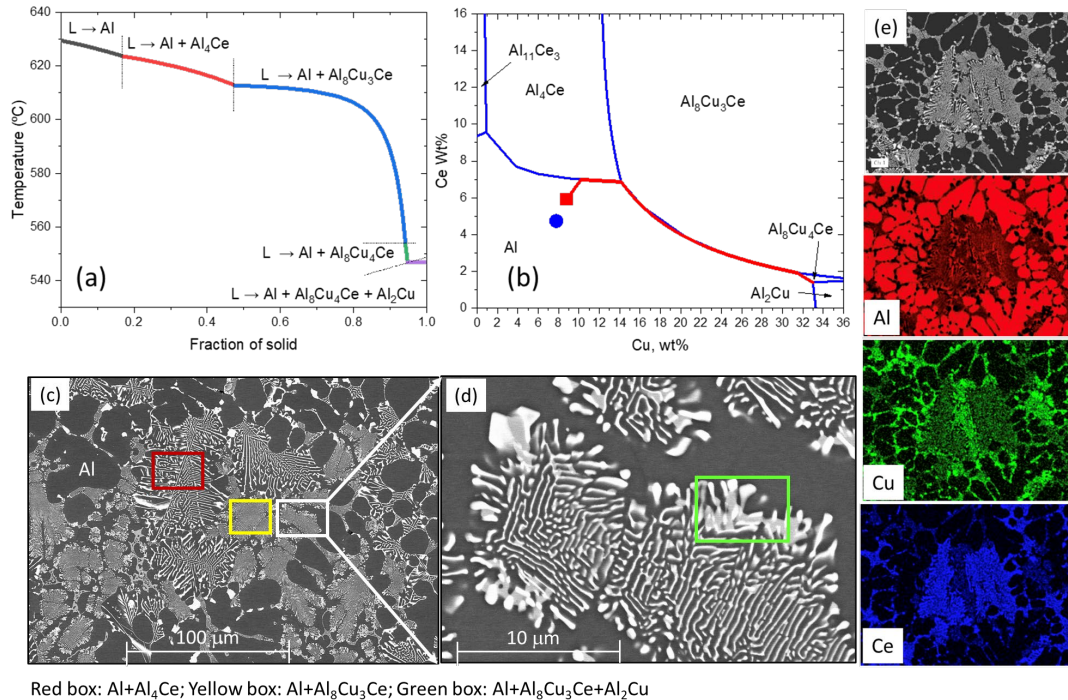


Figure I.3.3.1.3.2. Calculated solidification reactions and experimentally observed microstructure of Al-8.8Cu-5.91Ce wt.%: (a) calculated solidification path using the Scheil model; (b) liquid compositions (red line) superimposed onto the liquidus projection of Al-Cu-Ce system; (c) low magnification of the SEM/BES image; (d) enlarged image showing the feature in the white box; and (e) EDS mapping of Al, Cu, and Ce.

Source: ORNL.

Isothermal sections of the Al-Cu-Ce system at 610°C and 540°C were calculated, as shown in Figure I.3.3.1.3.3(a) and (c), respectively. The two experimental alloys are denoted by a solid square cast alloy and a solid circle AM alloy. Both alloys are located at the tie line between (Al)+Al₈Cu₃Ce. Any variation of local compositions can cause the alloy to move into the adjacent three-phase equilibria. In the 610°C-annealed sample, the two adjacent three-phase equilibria are (Al)+Al₈Cu₃Ce+Al₄Ce and (Al)+Al₈Cu₃Ce+liquid, as shown in the red region in Figure I.3.3.1.3.3(a). Four phases were observed in the microstructure of the

610°C-annealed alloy: (Al), $\text{Al}_8\text{Cu}_3\text{Ce}$, Al_4Ce , and liquid. This alloy was partially melted, suggesting the liquid phase is stable at 610°C. During the fast quench, the liquid formed a very fine eutectic, as denoted by the blue dotted region. In the 540°C-annealed sample, the two adjacent phase equilibria are (Al)+ $\text{Al}_8\text{Cu}_3\text{Ce}$ + Al_4Ce and (Al)+ $\text{Al}_8\text{Cu}_3\text{Ce}$ + Al_2Cu , as shown in the red region in Figure I.3.3.1.3.3(c). These four phases were confirmed in the 540°C-annealed microstructure of the cast alloy.

Combining thermodynamic calculations and experimental results, we clearly demonstrated that (Al), Al_4Ce , and $\text{Al}_8\text{Cu}_4\text{Ce}$ is the dominant ternary phase in the Al-Cu-Ce system. This is different from the current literature results where Bo et al. [9] suggested that (Al), $\text{Al}_{11}\text{Ce}_3$, and $\text{Al}_8\text{Cu}_4\text{Ce}$ are the dominant phases, while Belov et al. [10] suggested that (Al), $\text{Al}_8\text{Cu}_3\text{Ce}$, and Al_4Ce are the dominant phases. To further support our results, a DFT calculation on the enthalpies of formation of $\text{Al}_8\text{Cu}_4\text{Ce}$ and $\text{Al}_8\text{Cu}_3\text{Ce}$ were performed at zero degrees Kelvin. The DFT calculations suggested that the enthalpy of formation of $\text{Al}_8\text{Cu}_4\text{Ce}$ is about ~ 29 kJ/mole atoms, which is about two times of that of $\text{Al}_8\text{Cu}_3\text{Ce}$ (-14 kJ/mole atoms). This indicated that $\text{Al}_8\text{Cu}_3\text{Ce}$ is a stable phase only at high-temperature. It transforms into the $\text{Al}_8\text{Cu}_4\text{Ce}$ phase at low-temperature. This conclusion is supported by Figure I.3.3.1.3.3(d), where the $\text{Al}_8\text{Cu}_4\text{Ce}$ phase can be seen on the edge of $\text{Al}_8\text{Cu}_3\text{Ce}$. These results suggest the following solid-state reaction of (Al)+ $\text{Al}_8\text{Cu}_3\text{Ce}$ → $\text{Al}_8\text{Cu}_4\text{Ce}$. An isothermal section calculated at 227°C confirmed our conclusion that between these two phases, only the $\text{Al}_8\text{Cu}_4\text{Ce}$ phase is stable.

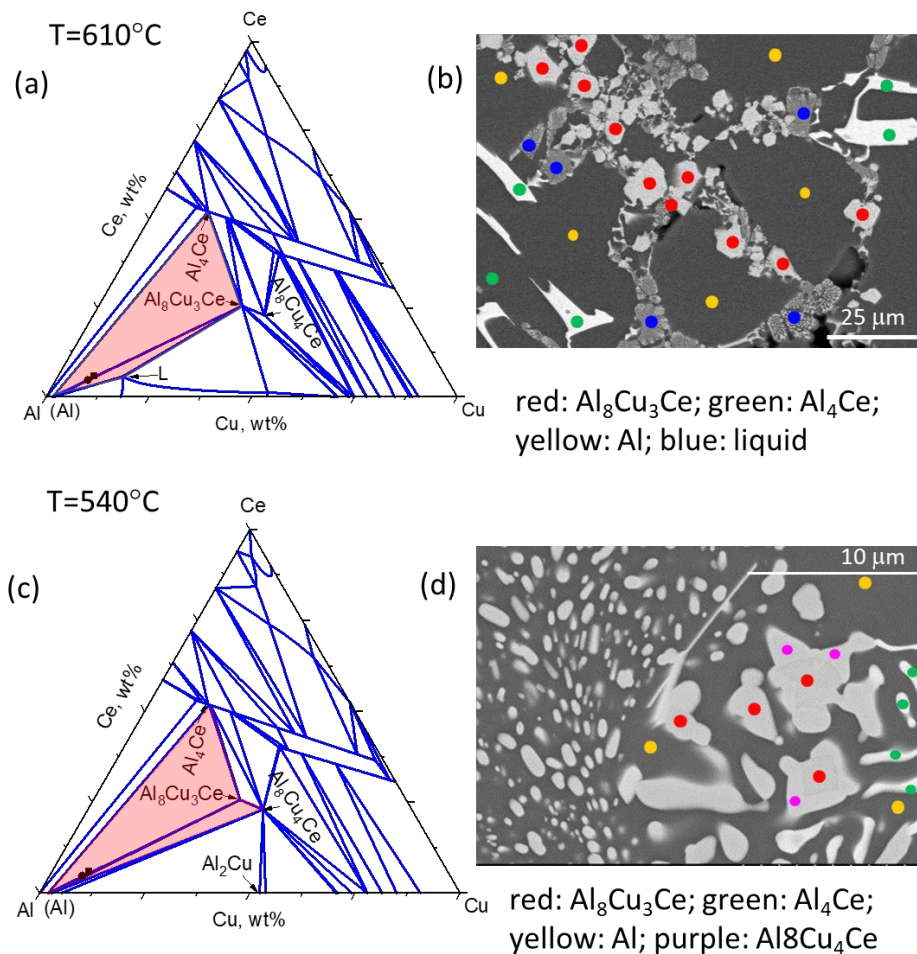


Figure I.3.3.1.3.3. (a) Calculated isothermal section of Al-Cu-Ce at 610°C. (b) Microstructure of Al-8.8Cu-5.91Ce wt.%, which is the solid square in (a) in the as-annealed state at 610°C for 2h. (c) Calculated isothermal section of Al-Cu-Ce at 540°C. (d) Microstructure of Al-8.8Cu-5.91Ce wt.%, which is the solid square in (c) in the as-annealed state at 540°C for 20h. Source: ORNL.

With the establishment of baseline thermodynamic models, we performed solidification and phase stability calculation for the AM alloy Al-7.78Cu-4.73Ce wt.%. The solidification path for the AM alloy is similar to that of the cast alloy, which is not surprising due to the similarities of the two compositions. The AM alloy shows a much more refined and less distinguishable binary eutectic and ternary eutectic microstructure, as shown in Figure I.3.3.1.3.4(a) and (b), respectively, as compared to that of the cast alloy shown in Figure I.3.3.1.3.2(c) and (d), respectively. However, the APT analysis, as provided in Figure I.3.3.1.3.4(c), shows the dominant phases in the AM alloy are the same as those in the (Al), Al₄Ce, and Al₈Cu₃Ce cast alloy. The phases of Al₈Cu₄Ce and Al₂Cu predicted from the model were not observed in the AM microstructure, which is possibly due to negligible amounts or less segregation in the AM conditions. The negligible amount or absence of Al₈Cu₄Ce in the as-built state is confirmed by the x-ray diffraction (XRD) results shown in Figure I.3.3.1.3.4(d). However, the XRD analyses also show that the Al₈Cu₃Ce transforms into Al₈Cu₄Ce when annealed at 400°C for 96 h. To account for the phase stability after annealing, we performed an equilibrium calculation of the phase amount vs. the temperature. The calculations suggested the transformation from Al₈Cu₃Ce to Al₈Cu₄Ce happens at ~530°C, which means if this alloy is annealed at any temperature below 530°C, this transformation can happen. The XRD results in Figure I.3.3.1.3.4(d) are consistent with the calculation. The transformation at 400°C has not completed even after 96 h annealing, thus suggesting slow transformation kinetics.

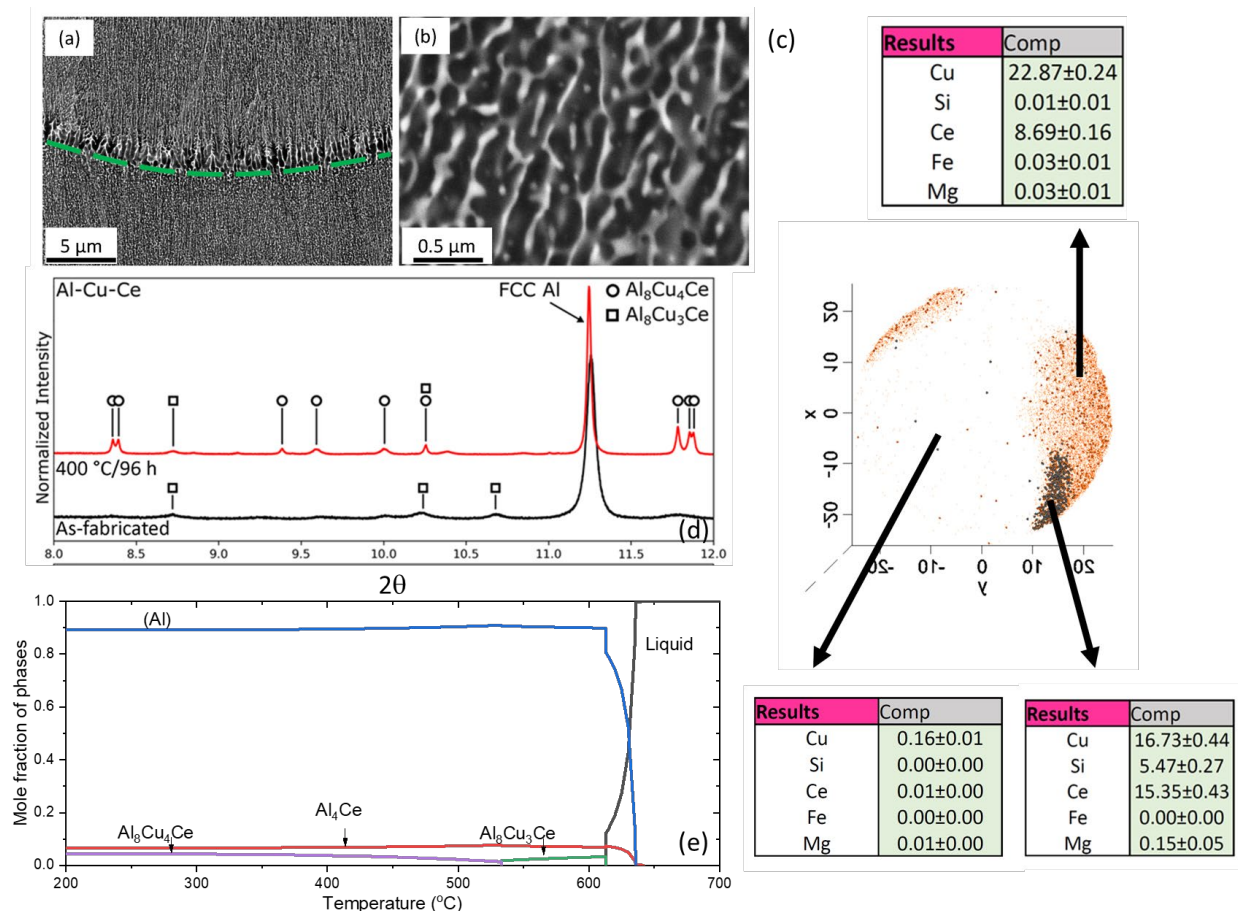


Figure I.3.3.1.3.4. Phase analysis in AM Al-7.78Cu-4.73Ce wt.% alloy: (a)–(b) low and high magnified SEM/BSE image showing the phases in the as-built microstructure; (c) APT results showing at least three phases coexisting in the microstructure with compositions in atomic %; (d) XRD results of as-built and as-annealed microstructure at 400°C; and (e) calculated equilibrium mole fractions of phases as a function of temperature for the AM alloy. Source: ORNL.

Phase Stability in Al-Rich Al-Ni-Ce Ternary After Casting

Following the same methodology as that for the Al-Cu-Ce system, a solidification path and phase stability analysis was performed for the Al-rich Al-Ni-Ce alloy, which is a necessary step to understand the microstructure of a recently developed (by ORNL) high-performance family of AM Al-Ni-Ce-Mn alloys. The cast alloy composition was Al-4.13Ni-9.94Ce wt.%, which was only slightly different from the nominal composition of Al-4.3Ni-10.5Ce wt.%. Microstructural characterization was performed on this alloy for the as-cast and heat-treated states at 620°C and 520°C. The solidification path simulated using the Scheil model is shown in Figure I.3.3.1.3.5(a) following the sequential reactions of primary solidification of $\text{Al}_{11}\text{Ce}_3$ phase, the two-phase eutectic solidifications of $(\text{Al})+\text{Al}_{11}\text{Ce}_3$, and finally the three-phase eutectic solidification of $(\text{Al})+\text{Al}_{11}\text{Ce}_3+\text{Al}_3\text{Ni}$. The liquid composition follows the red line that is superimposed onto the liquidus projection of Al-Ni-Ce system, as shown in Figure I.3.3.1.3.5(b). It shows the composition starts in the $\text{Al}_{11}\text{Ce}_3$ primary phase region, then follows the eutectic valley between (Al) and $\text{Al}_{11}\text{Ce}_3$. Finally, it ends at the ternary eutectic composition of $(\text{Al})+\text{Al}_{11}\text{Ce}_3+\text{Al}_3\text{Ni}$. The microstructure in Figure I.3.3.1.3.5(c) in low magnification and (d) in high magnification clearly shows the primary $\text{Al}_{11}\text{Ce}_3$ phase (i.e., the red dot), the two-phase eutectic of $(\text{Al})+\text{Al}_{11}\text{Ce}_3$ (i.e., the yellow box), and $(\text{Al})+\text{Al}_{11}\text{Ce}_3+\text{Al}_3\text{Ni}$ (i.e., the green box).

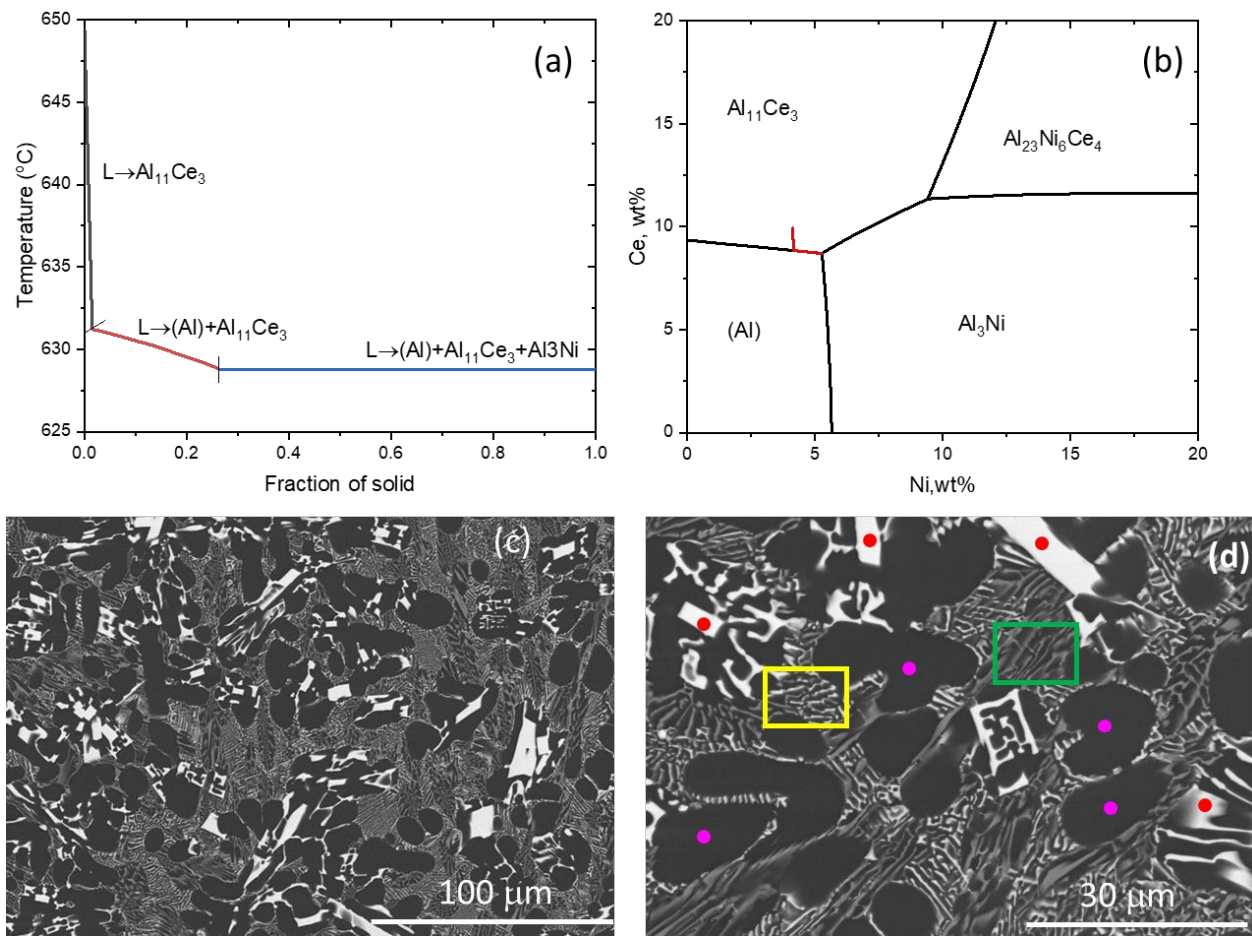


Figure I.3.3.1.3.5. Calculated solidification reactions and experimentally observed microstructure of Al-4.13Ni-9.94Ce wt.%. (a) calculated solidification path using the Scheil model; (b) liquid compositions (red line) superimposed onto the liquidus projection of Al-Ni-Ce system; (c) low magnification of SEM/BES image; and (d) high magnification of SEM/BES image. Red dot: $\text{Al}_{11}\text{Ce}_3$; purple dot: (Al) ; yellow box: eutectic of $(\text{Al})+\text{Al}_{11}\text{Ce}_3$; and green box: eutectic of $(\text{Al})+\text{Al}_{11}\text{Ce}_3+\text{Al}_3\text{Ni}$. Source: ORNL.

Mole fractions of equilibrium phases in Al-4.13Ni-9.94Ce as a function of temperature are plotted in Figure I.3.3.1.3.6(a), showing that the three-phase equilibria of (Al)+Al₁₁Ce₃+Al₃Ni are stable throughout the temperature range from 200°C to 650°C. Microstructural characterization results from the cast alloy annealed at 620°C, as observed in Figure I.3.3.1.3.6(b), and 520°C, as shown in Figure I.3.3.1.3.6(c), supported the calculation results. In both annealed states, the microstructure consists of three equilibrium phases: (Al) (i.e., the purple dot), Al₁₁Ce₃ (i.e., the red dot), and Al₃Ni (i.e., the green dot). The current thermodynamic models and experimental results are in general consistent with reports found in the literature [11]. It was originally planned to print an AM Al-Ni-Ce ternary alloy to compare to the cast-Al-Ni-Ce microstructure. However, due to the higher Mn content in the raw materials, a quaternary Al-Ni-Ce-Mn powder alloy resulted instead. The investigation of the Mn effect on the Al-Ni-Ce alloy is also under investigation. Results for AM Al-Ni-Ce-Mn alloys will be compared in future work.

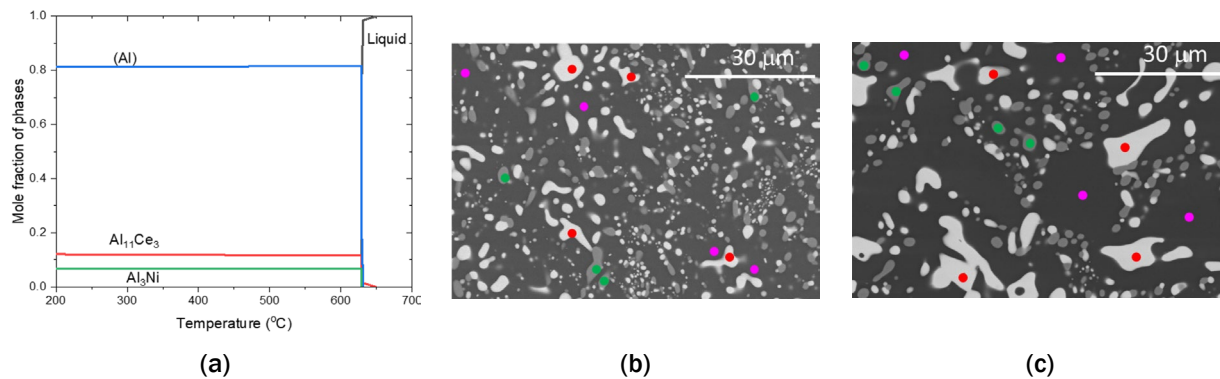


Figure I.3.3.1.3.6. (a) Calculated mole fraction of phases in the Al-4.13Ni-9.94Ce alloy as a function of temperature. (b) Microstructure in the as-annealed state at 620°C for 2 h. (c) Microstructure in the as-annealed state at 520°C for 20 h. Source: ORNL.

Conclusions

This task investigated the phase stability and solidification path of Al-Cu-Ce and Al-Ni-Ce alloys using a coupled approach of thermodynamic modeling and experimental study. The developed thermodynamic models for these two ternary systems have been validated by the newly obtained experimental data. The results from the Al-Cu-Ce system suggested incorrect descriptions within the prior data of phase stability in the Al-rich region of this system. Those for the Al-Ni-Ce system are consistent with the results reported in the literature. The validated thermodynamic models of the Al-Cu-Ce system were then used to interpret the results of the AM Al-Cu-Ce alloys. We found that despite the much more refined microstructure, the phases present in the AM alloy are the same as those in the cast alloy, suggesting that current AM processing conditions have a major role in refining microstructure, but can still maintain or approach the local equilibrium conditions at the solid-liquid interface of eutectic solidification in this alloy family. The validated thermodynamic models for the Al-Ni-Ce system will be incorporated into the thermodynamic models of the Al-Ni-Ce-Mn quaternary system for interpretation of phase stability in the AM Al-Ni-Ce-Mn alloys in future work.

Key Publications

1. Yang, Y., S. Bahl, K. Sisco, M. Lance, D. Shin, A. Shyam, A. Plotkowski, and R. R. Dehoff, 2020, "Primary solidification of ternary compounds in Al-rich Al-Ce-Mn alloys," *J. Alloys Compd.*, Vol. 844, Art. 156048.
2. Sisco, K., A. Plotkowski, Y. Yang, D. Leonard, B. Stump, P. Nandwana, R. R. Dehoff, and S. S. Babu, 2021, "Microstructure and properties of additively manufactured Al-Ce-Mg alloys," *Sci. Rep.*, Vol. 11, No. 1, Art. 6953.

3. Bahl, S., K. Sisco, Y. Yang, F. Theska, S. Primig, L. F. Allard, R. A. Michi, C. Fancher, B. Stump, R. Dehoff, A. Shyam, and A. Plotkowski, 2021, “Al-Cu-Ce (-Zr) alloys with an exceptional combination of additive processability and mechanical properties,” *Addit. Manuf.*, Vol. 48(B), Art. 102404.
4. Michi, R., K. Sisco, S. Bahl, Y. Yang, J. Poplawsky, L. Allard, R. Dehoff, A. Plotkowski, and A. A. Shyam, 2021, “A creep-resistant additively manufactured Al-Ce-Ni-Mn alloy,” *Acta Mater.*, Vol. 227, Art. 117699.
5. Yang, Y., R. Michi, K. Sisco, A. Plotkowski, A. Shyam, and R. Dehoff, 2022, “Effect of Mn on eutectic phase equilibria in Al-rich Al-Ce-Ni alloys,” *CALPHAD: Comput. Coupling Ph. Diagr. Thermochem.*, in preparation.
6. Perrin, A., S. Bahl, D. Leonard, K. Sisco, A. Plotkowski, A. Shyam, R. Dehoff, and Y. Yang, 2022, “Phase stability in AM and cast-Al-Cu-Ce alloy,” *J. Alloys Compd.*, in preparation.

References

1. Manca, D. R., A. Y. Churyumov, A. V. Pozdniakov, A. S. Prosviryakov, D. K. Ryabov, A. Y. Krokhin, V. A. Korolev, and D. K. Daubarayte, 2019, “Microstructure and properties of novel heat-resistant Al-Ce-Cu alloy for additive manufacturing,” *Met. Mater. Int.*, Vol. 25, No. 3, pp. 633–640.
2. Plotkowski, A., O. Rios, N. Sridharan, Z. Sims, K. Unocic, R. T. Ott, R. R. Dehoff, and S. S. Babu, 2017, “Evaluation of an Al-Ce alloy for laser additive manufacturing,” *Acta Mater.*, Vol. 126, pp. 507–519.
3. Plotkowski, A., K. Sisco, S. Bahl, A. Shyam, Y. Yang, L. Allard, P. Nandwana, A. Marquez Rossy, and R. R. Dehoff, 2020, “Microstructure and properties of a high-temperature Al-Ce-Mn alloy produced by additive manufacturing,” *Acta Mater.*, Vol. 196, pp. 595–608.
4. Sisco, K., A. Plotkowski, Y. Yang, D. Leonard, B. Stump, P. Nandwana, R. R. Dehoff, and S. S. Babu, 2021, “Microstructure and properties of additively manufactured Al-Ce-Mg alloys,” *Sci. Rep.*, Vol. 11, No. 1, Art. 6953.
5. Boussinot, G., M. Döring, S. Hemes, O. Stryzhyboroda, M. Apel, and M. Schmidt, 2021, “Laser powder bed fusion of eutectic Al-Ni alloys: Experimental and phase-field studies,” *Mater. Des.*, Vol. 198, Art. 109299.
6. Deng, J., C. Chen, X. Liu, Y. Li, K. Zhou, and S. Guo, 2021, “A high-strength heat-resistant Al–5.7 Ni eutectic alloy with spherical Al₃Ni nanoparticles by selective laser melting,” *Scr. Mater.*, Vol. 203, Art. 114034.
7. Thapliyal, S., S. Shukla, L. Zhou, H. Hyer, P. Agrawal, P. Agrawal, M. Komarasamy, Y. Sohn, and R. S. Mishra, 2021, “Design of heterogeneous structured Al alloys with wide processing window for laser powder bed fusion additive manufacturing,” *Addit. Manuf.*, Vol. 42, Art. 102002.
8. Shyam, A., A. Plotkowski, S. Bahl, K. Sisco, L. F. Allard, Y. Yang, J. A. Haynes, and R. R. Dehoff, 2020, “An additively manufactured Al-Cu-Mn-Zr alloy microstructure and tensile mechanical properties,” *Materialia*, Vol. 12, Art. 100758.
9. Bo, H., S. Jin, L. G. Zhang, X. M. Chen, H. M. Chen, L. B. Liu, F. Zheng, and Z. P. Jin, 2009, “Thermodynamic assessment of Al-Ce-Cu system,” *J. Alloys Compd.*, Vol. 484, No. 1–2, pp. 286–295.
10. Belov, N., and A. Khvan, 2007, “The ternary Al-Ce-Cu phase diagram in the aluminum-rich corner,” *Acta Mater.*, Vol. 55, No. 16, pp. 5473–5482.
11. Wang, H., Z. Li, Z. Chen, and B. Yang, 2016, “Thermodynamic optimization of the Ni-Al-Ce ternary system,” *J. Phase Equilibria Diffus.*, Vol. 37, No. 2, pp. 222–228.

Acknowledgments

This research was co-sponsored by the DOE-EERE AMO VTO Propulsion Materials Program. Collaborations from A. Plotkowski, A. Shyam, A. Perrin, B. Sumit, R. A. Michi, D. Leonard, K. Sisco, and R. Dehoff are acknowledged.

I.3.3.1.4 Fundamentals of Austenitic Alloy Processing by Additive Manufacturing (Task 3B1) (Oak Ridge National Laboratory)

Sebastien Dryepondt, Co-Principal Investigator

Oak Ridge National Laboratory
1 Bethel Valley Road
Oak Ridge, TN 37831
E-mail: dryepondtsn@ornl.gov

Peeyush Nandwana, Co-Principal Investigator

Oak Ridge National Laboratory
1 Bethel Valley Road
Oak Ridge, TN 37831
E-mail: nandwanap@ornl.gov

Jerry L. Gibbs, DOE Technology Manager

U.S. Department of Energy
E-mail: jerry.gibbs@ee.doe.gov

Start Date: October 1, 2018 End Date: September 30, 2023
Project Funding (FY 2021): \$205,000 DOE share: \$205,000 Non-DOE share: \$0

Project Introduction

AM allows for the design of complex high-temperature high-efficiency combustion engine components that offer the opportunity for significant performance improvement. In addition, very rapid cooling rates in AM processes often result in alloys with unique microstructure and properties [1, 2]. Turbocharger housings and exhaust manifolds require high-temperature austenitic steels, such as 310-type cast HK30Nb or 347-type cast CF8C+, but most of the prior AM studies on austenitic steels have been focused on lower temperature stainless steels, such as alloys 304 or 316L. Table I.3.3.1.4.1 provides the chemistries for these alloys. Our previous results showed that alloy HK30Nb could be produced crack-free by AM laser powder bed fusion (LPBF) with excellent yield and UTS up to 900°C. The superior alloy strength as compared to cast HK30Nb alloy was attributed to the unique microstructure of the printed alloy—in particular, the presence of cellular structures 0.5 to 1 μm in size with high dislocation density in the cell walls. Furthermore, a high density of NbC precipitates was observed in the cell walls leading to superior creep strength along the build direction (BD) for the LPBF HK30Nb in comparison to the cast counterpart. Significant reduction in creep strength was, however, observed perpendicular to the BD. Thus, in Fiscal Year 2021, the characterization of creep specimens was conducted to understand the specimen orientation effect on creep properties. In addition, we explored the fabrication of alloy CF8C+ by LPBF, since this alloy exhibits superior creep strength in comparison with cast HK30Nb due to its high nitrogen content and the resultant formation of nano Nb(C,N) strengthening precipitates.

Table I.3.3.1.4.1. Measured Chemistries of LPBF Austenitic Steels

Alloy	Fe	Cr	Ni	Mo	Mn	C	N	Nb	Si
HK30Nb	Bal.	25.4	20.5	0.27	0.2	0.2		1.37	1.14
CF8C+	Bal.	19	13	0.33	3.5	0.1	0.23	1	0.7

Objectives

The objective of this project was to fabricate by AM and characterize high-temperature austenitic steels for higher efficiency ICE applications. Castable and weldable austenitic steels currently used or considered for

engine components—specifically HK30Nb and CF8C+—were printed. Improving our understanding of the process-microstructure-properties relationships for these alloys is intended to enable the development of improved austenitic steels specifically designed for AM processing. By taking full advantage of the unique thermal profiles and microstructures achievable using AM alloys with unprecedented high-temperature strength are targeted for future development.

Approach

This project aims to fabricate high-temperature high-strength austenitic steels, such as-cast HK30Nb and CF8C+, using AM LPBF for powertrain components operating at temperatures up to 900°C. A design-of-experiment method was employed to determine processing windows leading to crack-free low-defect alloys. Extensive microstructure characterization, advanced image analysis, and mechanical testing along and perpendicular to the BD at temperatures up to 900°C were carried out to determine the impact of the AM unique microstructure on alloy properties. Based on these results, thermodynamic and kinetics modeling tools were used to develop advanced high-temperature, high-performance AM-specific austenitic steels.

Results

As-Printed LPBF Alloy Microstructure

A design of experiments approach was used to optimize printing parameters for alloys HK30Nb and CF8C+. Small cubes were fabricated using different printing conditions. Cube density was measured by pycnometry or from cross-sectional optical imaging. The optimum printing parameters were then used to fabricate rods and rectangular plates for extensive microstructure characterization and mechanical testing. The pole and inverse pole figures for the as-printed LPBF HK30Nb austenitic steel along and perpendicular to the BD revealed the typical chevron-type grain shape often observed in LPBF alloys, with no significant grain texture as shown in Figure I.3.3.1.4.1. The grain aspect ratio was 2-2.6:1 with elongated grains along the BD and grain size ranging from 1 μm to 90 μm . As can be seen in Figure I.3.3.1.4.2, the size of the cellular structure was similar in the LPBF HK30Nb and CF8C+ alloys with high dislocation density in the cell walls. As expected, different nanoprecipitates were observed, (Nb,Cr)-rich carbides in the LPBF HK30Nb alloy and Nb-rich carbonitrides in the LPBF CF8C+ alloy. APT conducted via a Thrust 4 advanced characterization project at PNNL confirmed the presence of (Nb,Cr)-rich carbides in the LPBF HK30Nb alloy with an Nb/Cr at.% ratio varying from 2:1 to 4:1.

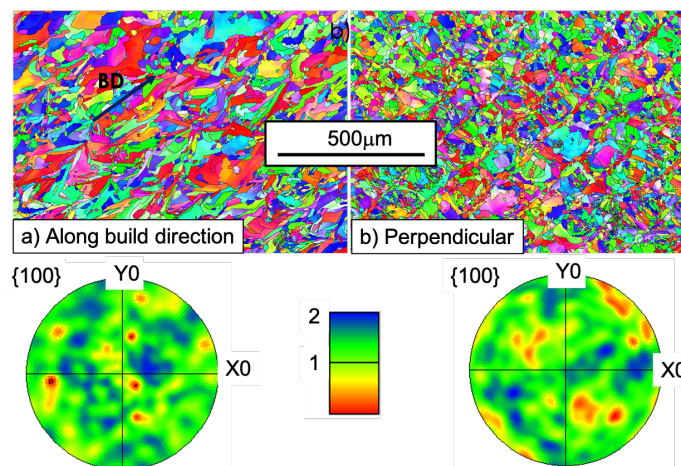


Figure I.3.3.1.4.1. Inverse pole figure maps and corresponding {001} pole figure for the as-printed LPBF HK30Nb alloy (a) along the BD and (b) perpendicular to the BD. Source: ORNL and PNNL.

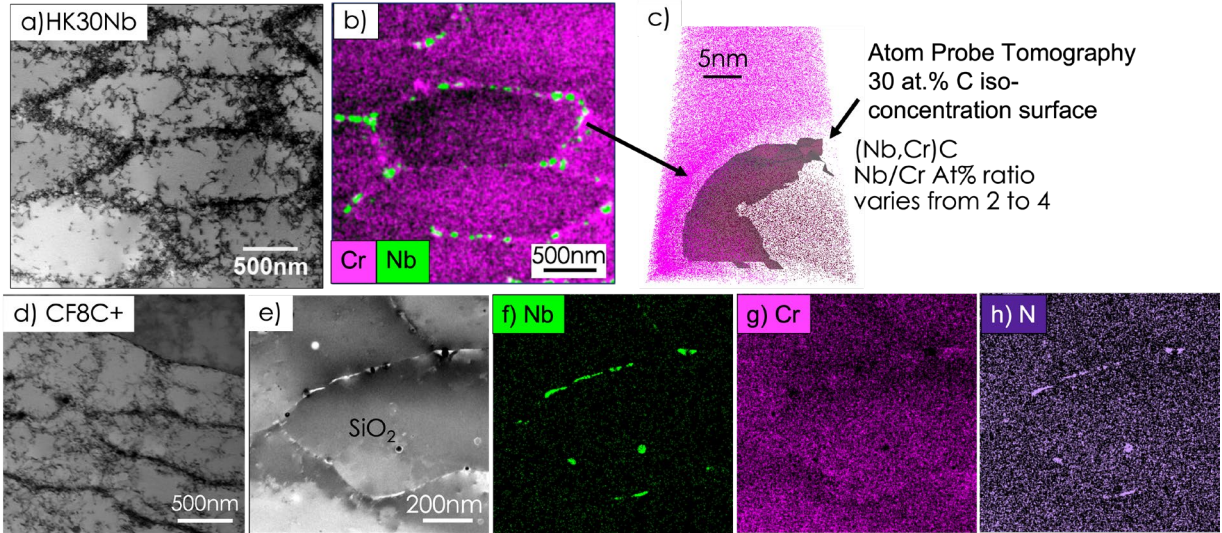


Figure I.3.3.1.4.2. (a) STEM image of the as-printed HK30Nb alloy. (b) Corresponding EDS maps of Nb and Cr. (c) APT map showing the 30 at.% iso-concentration surface. (d) and (e) STEM images of as-printed CF8C+. (f)-(h) Corresponding EDS maps for: (f) Nb; (g) Cr; and (h) N. Source: ORNL and PNNL.

LPBF Tensile Properties

The tensile properties at 20°C – 900°C of the LPBF HK30Nb and CF8C+ alloys along and perpendicular to the BD are compared in Figure I.3.3.1.4.3, along with the tensile properties of their cast counterparts. At all temperatures, the yield strength of the two LPBF alloys were similar and were both significantly higher than the yield strength of their cast versions, most likely because of the high dislocation density in the cellular walls. Similar yield strengths were measured along and perpendicular to the BD for both the HK30Nb and CF8C+ alloys, except at RT with higher yield strengths perpendicular to the BD. The total deformation at rupture decreased with increasing temperature for both the LPBF and cast alloys. Overall, the LPBF alloys exhibited higher ductility below ~700°C, but lower ductility above ~700°C in comparison with the cast alloys. Ductility was similar for the LPBF HK30Nb and CF8C+ alloys except for significantly lower deformation at rupture perpendicular to the BD for the LPBF CF8C+ alloy at temperatures higher than ~600°C.

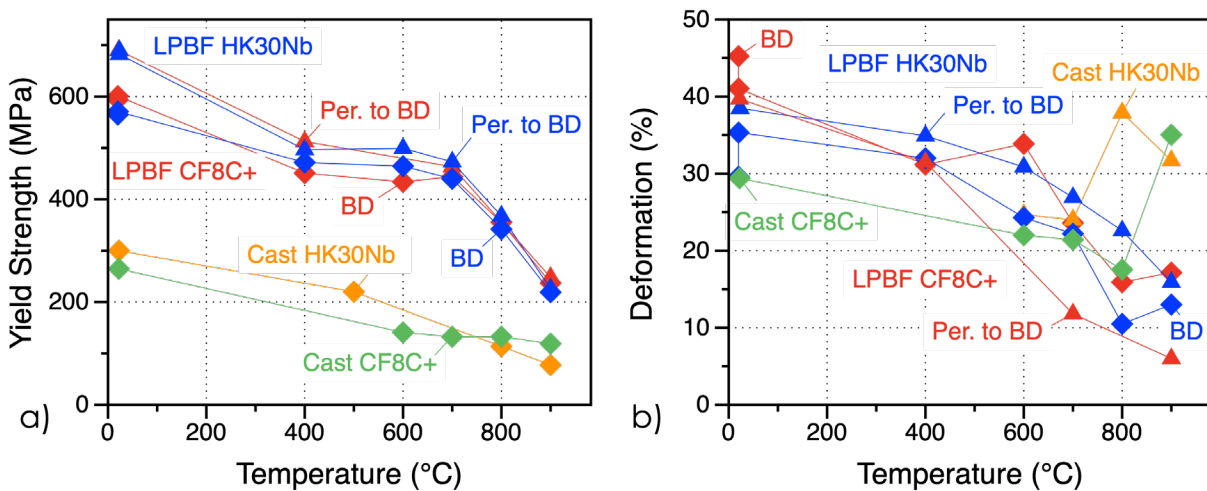


Figure I.3.3.1.4.3. Comparison of the tensile properties between the LPBF and cast austenitic steels for (a) yield strength and (b) total deformation. “Per. To BD” = perpendicular to the build direction. Source: ORNL.

LPBF Creep Properties

For high-temperature powertrain components, such as turbocharger housings, creep properties are critical to the component durability. Creep testing of the LPBF alloys was, therefore, conducted at 700-800°C along and perpendicular to the BD and the results are summarized in Figure I.3.3.1.4.4 using a Larson-Miller Parameter (LMP) versus the stress plot with $LMP = T(^{\circ}K) * (20 + \text{Log}(t_r))$, with T being the test temperature in Kelvin and t_r time to rupture.

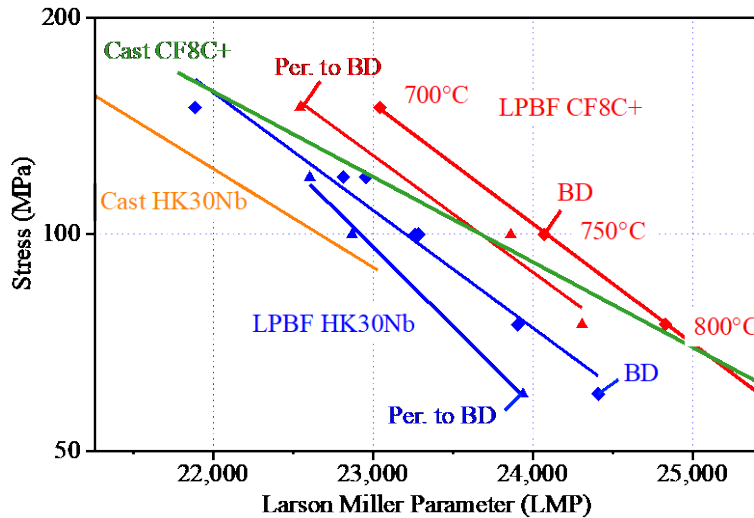


Figure I.3.3.1.4.4. LMP plot comparing the creep properties of the LPBF austenitic steels along and perpendicular to the BD at 700°C – 800°C with the creep properties of cast counterparts. “Per. to BD” = perpendicular to the build direction. Source: ORNL.

The LPBF HK30Nb alloy exhibited superior creep resistance at 700-800°C along the BD in comparison with cast HK30Nb alloy with an increase by a factor of ~3 in creep lifetime. The creep strength perpendicular to the BD was, however, much lower leading to creep lifetimes only slightly superior to the creep lifetimes of cast HK30Nb. Similar results were observed for the LPBF CF8C+ alloy with a drastic improvement of the creep lifetime along the BD compared to the cast counterpart at 700-750°C, by a factor of ~7 at 700°C. No improvement was observed at 800°C and, again, the alloy creep strength was much lower perpendicular to the BD.

Creep Specimen Characterization

Cross-section optical and BSE-SEM images of the LPBF HK30Nb creep specimens tested at 700°C with an applied stress of 120 MPa are shown in Figure I.3.3.1.4.5. Many cracks were present in the specimen tested perpendicular to the BD, which is the likely reason for the earlier rupture in the specimen in comparison with the specimen tested along the BD. Initial electron backscatter diffraction mapping revealed that many of these cracks were related to GBs. The BSE-SEM images in Figure I.3.3.1.4.5 also highlight the presence of large micron-size and needle-like Cr-rich precipitates, but no cellular structure. Fast-cooling rates during printing resulted in unique non-equilibrium microstructures. Consequently, significant microstructure evolution was expected at higher temperatures. In wrought 310-type or cast HK30Nb alloys, Cr-rich carbides or sigma phase are known to form at GBs above 650°C, leading to intergranular embrittlement [3, 4]. For the LPBF HK30Nb alloy, these precipitates nucleated both at the GBs and in the cellular structure walls. Ongoing work aims at quantification of these precipitates by image analysis in all creep specimens to determine their impact on creep-rupture and creep anisotropy.

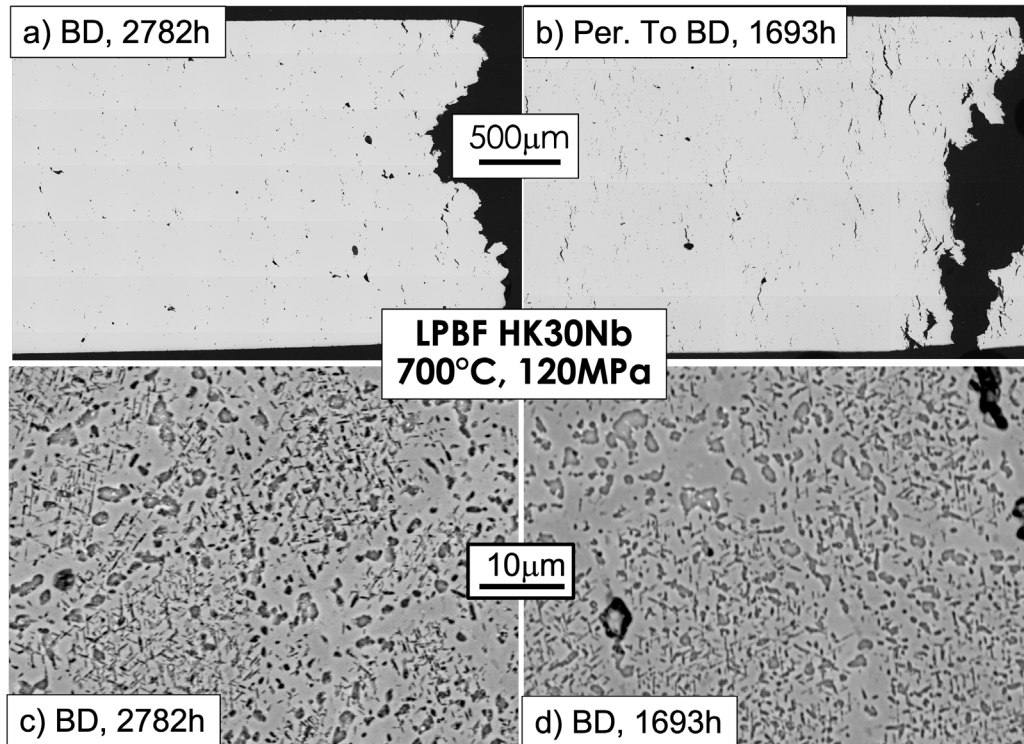


Figure I.3.3.1.4.5. Microstructure characterization of LPBF HK30Nb creep specimens tested at 700 °C, 120MPa: (a) optical image, BD; (b) optical image perpendicular to BD; (c) BSE-SEM micrographs, BD; and (d) BSE-SEM micrographs, perpendicular to BD. Source: ORNL.

Conclusions

Two higher temperature austenitic steels that had not been printed previously, HK30Nb and CF8C+, were successfully fabricated by LPBF. Very rapid cooling rates during printing led to the formation of cellular structures with high dislocation density within the cell walls, as well as (Nb,Cr)C and Nb(C,N) nanoprecipitates for alloys HK30Nb and CF8C+, respectively. These microstructural features resulted in very high tensile strength at 20-900°C in comparison with their cast counterparts. Exceptional creep properties were also measured at 700-800°C, along the BD with creep-rupture lifetime improvement by factors of 3 to 7 in comparison with the cast alloys. Reduced creep performance perpendicular to the BD was likely related to the specific orientation with respect to the BD of elongated grain and cellular structures. The superior high-temperature mechanical properties of LPBF austenitic steels could enable new, higher efficiency engine components with advanced designs only possible via AM. The ultimate goal of the project is to develop LPBF-specific austenitic steels that will take full advantage of the unique AM microstructural features to achieve unprecedented creep and oxidation performance at temperatures greater than 700°C.

Key Publications

1. Dryepontd, S., P. Nandwana, P. Fernandez-Zelaia, F. List, III, 2021, "Microstructure and high-temperature tensile properties of 316L fabricated by laser powder bed fusion," *Addit. Manuf.*, Vol. 37, Art. 101723.
2. Fernandez-Zelaia, P., T. Lee, Q. Campbell, S. Dryepontd, M. M. Kirka, and A. Marquez Rossy, 2021, "Microstructural digital image correlation: Statistical estimation of strain using spatial correlation functions," *Mater. Charact.* (In review).
3. Dryepontd, S., P. Nandwana, K. A. Unocic, R. Kannan, P. Fernandez-Zelaia, and F. A. List III, 2021, "High-temperature high-strength austenitic steel fabricated by laser powder bed fusion," *Acta Mater.* (In review).

References

1. Wang, Y. M., T. Voisin, J. T. McKeown, J. Ye, N. P. Calta, Z. Li, Z. Zeng, Y. Zhang, W. Chen, T. T. Roehling, R. T. Ott, M. K. Santala, P. J. Depond, M. J. Matthews, A. V. Hamza, and T. Zhu, 2018, “Additively manufactured hierarchical stainless steels with high-strength and ductility,” *Nat. Mater.*, Vol. 17, pp. 63–73.
2. Dryepontd, S., P. Nandwana, P. Fernandez-Zelaia, and F. List III, 2021, “Microstructure and high-temperature tensile properties of 316L fabricated by laser powder bed fusion,” *Addit. Manuf.*, Vol. 37, Art. 101723.
3. Vujic, S., R. Sandstrom, and C. Sommitsch, 2015, “Precipitation evolution and creep strength modeling of 25Cr20NiNbN austenitic steel,” *Mater. High Temp.*, Vol. 32, pp. 607–618.
4. Bai, X., J. Pan, G. Chen, J. Liu, J. Wang, T. Zhang, and W. Tang, 2014, “Effect of high-temperature aging on microstructure and mechanical properties of HR3C heat-resistant steel,” *Mater. Sci. Technol.*, Vol. 30, pp. 205–210.

Acknowledgments

The authors acknowledge the contributions of the following ORNL team members for this subtask: K. Unocic, R. Kannan, P. Fernandez-Zelaia, M. Lance, K. Hedrick, T. Lowe, and S. Hawkins. They also would like to thank A. Devaraj and J. Liu at PNNL for APT characterization.

I.3.3.1.5 Ferritic Alloys for Heavy-Duty Pistons via Additive Manufacturing (Task 3B2) (Oak Ridge National Laboratory)

Peeyush Nandwana, Co-Principal Investigator

Oak Ridge National Laboratory
1 Bethel Valley Road
Oak Ridge, TN 37831
E-mail: nandwanap@ornl.gov

Amy Elliott, Co-Principal Investigator

Oak Ridge National Laboratory
1 Bethel Valley Road
Oak Ridge, TN 37831
E-mail: elliottam@ornl.gov

Jerry L. Gibbs, DOE Technology Manager

U.S. Department of Energy
E-mail: jerry.gibbs@ee.doe.gov

Start Date: October 1, 2018 End Date: September 30, 2022
Project Funding (FY 2021): \$225,000 DOE share: \$225,000 Non-DOE share: \$0

Project Introduction

AM has garnered interest from the automotive sector due to its immense potential in unlocking novel designs and net-shaping capabilities, as well as offering the opportunity to print complex parts from classes of alloys that were previously considered difficult to fabricate. One of the limitations of AM is that it can be cost-prohibitive for very large volumes and low-cost-margins, such as those required in passenger vehicles. HD engines, such as those used in freight trucks, can prove to be early adopters of AM technologies due to their relatively lower manufacturing volumes and higher cost-margins as compared to those of passenger vehicles. The costs can be further reduced by using binder jet AM (BJAM), a powder bed-based AM technology that deposits green parts without the need for specialized build chambers or a power source, such as a laser or an electron beam source. The green parts can then be subjected to sintering for full densification to near net-shape geometries that can be subsequently machined to required surface finish. The potential to scale-up the operation arises from the fact that BJAM can have significantly larger build chambers as compared to other powder bed AM technologies. A further advantage is that conventional powder metallurgy and metal injection molding industries have already set the precedent for conducting sintering operations at scales that are economically viable for HD engine parts. The primary focus of this task is the fabrication of ferritic alloys via BJAM to enable future advanced pistons for higher efficiency, lower emissions HD truck applications in recognition of projected rapid growth in future freight demands.

Objectives

The objective of this task is to fabricate a ferritic/martensitic steel via BJAM, followed by sintering and post-sintering heat treatments to achieve higher room and elevated tensile strengths as compared to 4140 and micro-alloyed steels (MASs), which are the current commonly used alloys for pistons in HDDEs. An additional objective is to evaluate the oxidation behavior of the printed tool steel alloys to determine suitability for piston operation at anticipated higher engine operating temperatures.

Approach

The focus in FY 2021 was the evaluation of high-temperature tensile strength of binder jet printed H13 steel upon long-term thermal exposure to elevated temperature. Further, a thermo-kinetic model was developed to

predict the sintering behavior of binder jet 3D printed H13 steel that accounted for the local changes in C composition that impacts the sintering window. Finally, the as-sintered material fabricated on an ExOne Innovent binder jet system using gas atomized H13 powders and BA005 binder was evaluated using advanced characterization techniques, such as TEM and APT. A manuscript has been published on the thermo-kinetic calculations for the prediction of the sintering window, as well as two other publications that are currently being submitted to peer-reviewed journals.

Results

In FY 2021, we published an article on the use of CALPHAD models to predict the sintering window during supersolidus liquid phase sintering (SLPS) of H13 steel fabricated using binder jet 3D [1]. It was demonstrated that the changes in sintering temperature could be determined based on the local increase in C resulting from the binder, with reasonable accuracy. We validated the model based on the experimental results obtained from the sintering of binder jet 3D printed H13. Figure I.3.3.1.5.1 shows the overall workflow for setting up the CALPHAD model. Note that once the green part is heated to the binder burnout temperature, the binder leaves behind C-rich residue resulting in a C flux between the interparticle region and the bulk of the powder particle. This results in a local increase in C concentration at the interparticle regions. This thermodynamic phenomenon can be modeled with suitable inputs from feedstock, binder analysis, and the deposition process parameters. The key process parameters involved in BJAM are build time (t), droplet volume (V), printing speed (v), and droplet spacing (y), which affects the overall binder saturation in the system, density of the binder (ρ), mole fraction of C in the binder (x_c), and the molar mass of the binder (m_{binder}). Using these process parameters, binder flow rate, total binder volume deposited, and binder mass can be estimated, which gives:

$$\text{Mole fraction of C in binder} = x_c \frac{v}{y} V t \rho \quad (1)$$

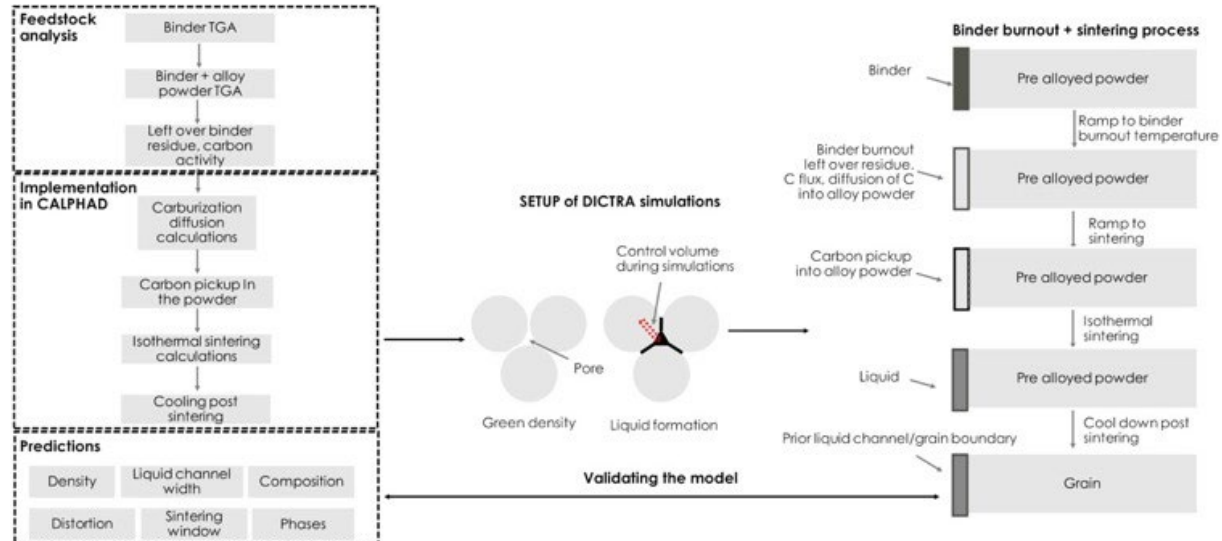


Figure I.3.3.1.5.1. Workflow used to setup the CALPHAD model based on powder feedstock and binder analysis [1]. Source: ORNL.

By performing thermogravimetric analysis (TGA) simulating the curing+debinding+sintering thermal cycle on the binder and binder+alloy powder in a predetermined ratio, the total fraction of the binder left behind as residue can be calculated, which can be used to determine the total mole fraction of C left behind. By using an ideal solution approximation, the activity of C will be equal to the mole fraction. Using the estimated C activity, a diffusion couple between the surface and the bulk of the powder particle can be set up, simulating the experimental thermal profiles using the DICTRA diffusion model add-on module to ThermoCalc software.

The calculations performed in this report were derived using the experimental thermal profile for binder burnout and sintering, BA005 binder, and H13 powder chemistry. Details of the powder are in [2].

Figure I.3.2.1.5.2(a) shows the TGA curve for the binder where complete binder burnout occurs at around 440°C, beyond which there is no change in the mass of the system. Figure I.3.2.1.5.2(b) shows the TGA of the H13 powder + binder, which was pre-mixed in the mass ratio of 9:1. If complete binder burnout were to occur, the mass of the system should have decreased by 10%, but from Figure I.3.2.1.5.2(b), it can be seen that in spite of testing to 1,400°C, incomplete binder burnout is observed. Similar to the TGA curve for the binder in Figure I.3.2.1.5.2(a), a rapid decrease in mass is observed up to 440°C, beyond which the rate of decrease in mass is significantly reduced. Thus, from Figure I.3.2.1.5.2(a) and (b), respectively, it can be concluded that incomplete binder burnout occurs during the ramp to binder burnout and the sintering cycle. This means that ash from the binder remains in the powder preform after burnout as residue, which results in excess C in the H13 powder, even to sintering temperatures. The activity of C leftover as residue was calculated to be 0.0397 and 0.0322 for 105% and 85% binder saturation respectively (i.e., the amount of binder deposited during the printing process), which can be used to compute the extent of C pickup by the H13 powder, as shown in Figure I.3.2.1.5.2(c). The total C picked up at the interface (>1%) is much higher than the bulk C content of H13 pre-alloyed powder, which is 0.471 wt.%. Figure I.3.2.1.5.2(d) shows the calculated local volume fraction of liquid formed at the end of isothermal hold during sintering. With the increase in sintering temperature and binder saturation, the total volume fraction of liquid at the interparticle boundary increases with a maximum volume fraction of around 80% during sintering at 1,400°C, while reaching a peak of 20% within the bulk of the powder particle. Figure I.3.2.1.5.2(e) compares the volume fraction of liquid calculated using the proposed approach and the volume fraction of liquid calculated based on the bulk H13 powder chemistry for the sintering temperatures and binder saturations considered in the present study. If bulk feedstock chemistry is used for calculating the sintering window without considering the effect of binder saturation, the total volume fraction of liquid can be underestimated, resulting in incomplete densification if the sintering temperature is low or in overestimation of the solidus temperature that can result in slumping of the part via formation of excess liquid.

To validate the predictions from the model, experimental data from the SLPS/BJAM of H13 powders published by Nandwana et al. were used [2]. Relative density, liquid channel width, composition after cooling, and shape loss due to excess liquid formation were extracted from the CALPHAD model and compared with the experimental measurements in Figure I.3.2.1.5.3(a). The predicted relative density based on the proposed approach agreed with the experimental measurements. At lower sintering temperatures, there is a discrepancy between the predicted density and the measured density, possibly because at lower temperatures, there could be incipient melting in the particles without melting the bulk particles, unlike in higher temperatures when melting in the bulk particles does occur [3], which may increase the overall liquid volume fraction in the system, and in turn, the density. Figure I.3.2.1.5.3(b) shows the comparison between the predicted liquid channel width and the experimental liquid channel width. The liquid channel widths predicted using the proposed approach are in reasonable agreement with the experimental liquid channel width measurements. The details of liquid channel width measurements can be found in Nandwana et al. [2]. A deviation between the predicted liquid channel width and the experimental liquid channel width is observed at both levels of binder saturation during sintering at 1,400°C, possibly because during sintering, abnormal grain growth of austenite and nucleation of new austenite grains during solidification can affect the liquid channel width as we have proposed in the previous reports. From Figure I.3.2.1.5.3(c), the predicted overall composition at the end of sintering and the measured bulk composition agreed reasonably well. Figure I.3.2.1.5.3(d) shows the variation in total volume fraction of liquid and contiguity, which provides an estimate of the critical liquid volume fraction above which shape loss occurs, with varying sintering conditions. In Figure I.3.2.1.5.3(d), contiguity is measured using the equations developed by Liu and German and Liu [3]. When the liquid volume fraction is above 22 vol.%, the contiguity drops below the critical contiguity required for preserving the shape. This drop in contiguity results in shape loss, which is in-line with the observed shape loss for different cubes, which were printed and sintered, as shown in the inset in Figure I.3.2.1.5.3(d).

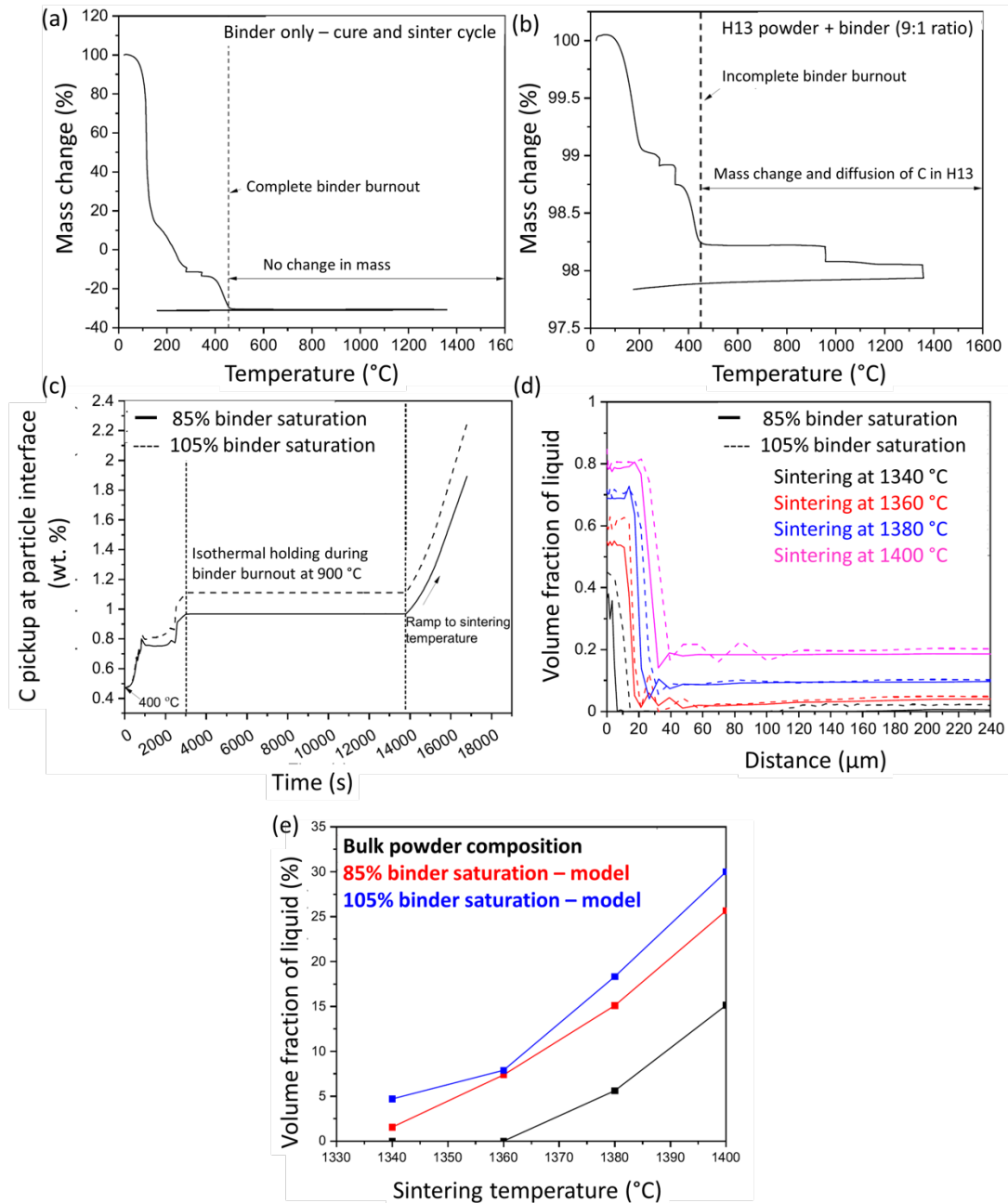


Figure I.3.3.1.5.2. (a) TGA on the binder. (b) TGA on the H13 powder + binder mixed in 9:1 ratio. (c) Local C pickup at the interparticle region due to the binder residue. (d) Spatial evolution of volume fraction of liquid for varying binder saturations and sintering temperatures. (e) Liquid fraction curve calculated from ThermoCalc for H13 powder chemistry, H13 + 85% binder saturation, and H13 + 105% binder saturation [1]. Source: ORNL.

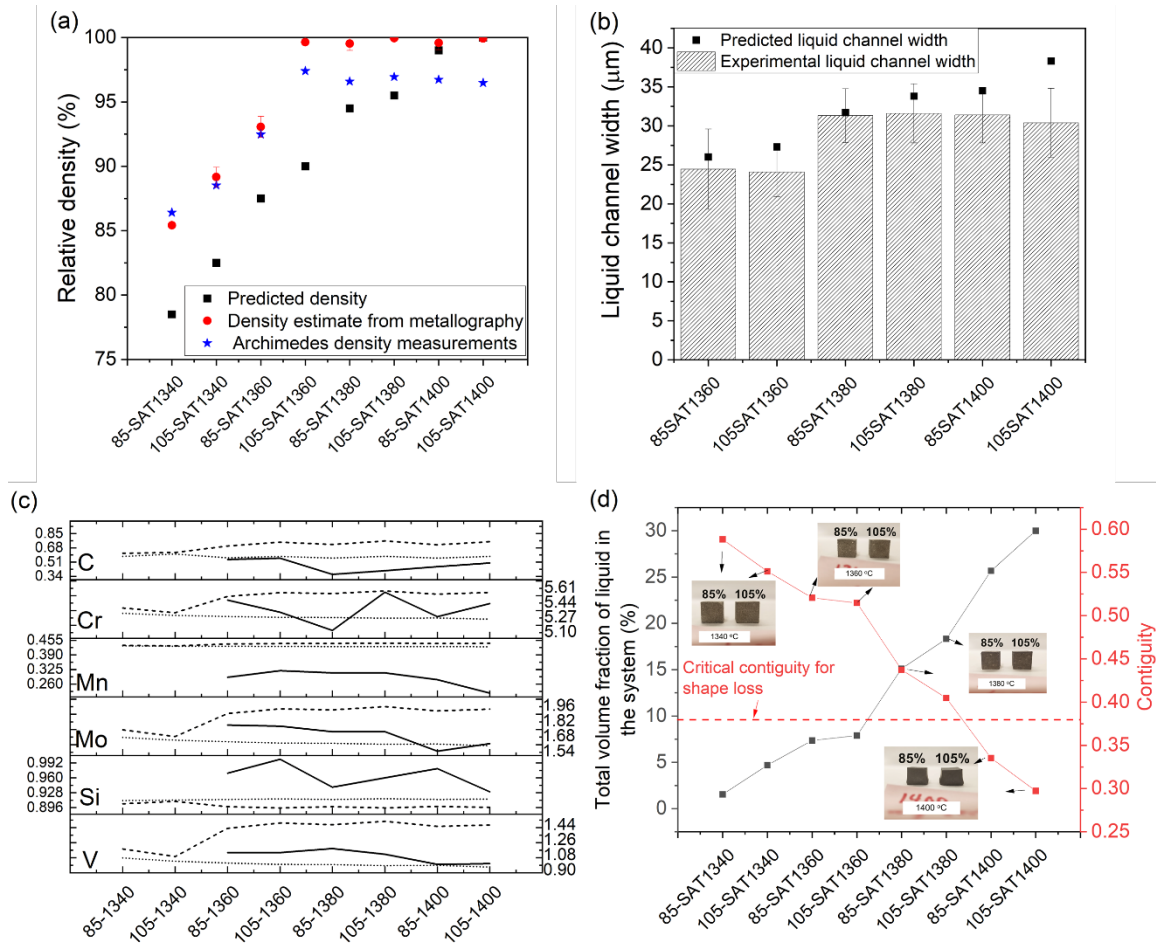


Figure I.3.3.1.5.3. (a) Relative density, (b) liquid channel width, (c) bulk composition after cooling post sintering, and (d) shape loss estimates from contiguity [1]. X-axis labels indicate sintering temperature (°C) and binder saturation levels (wt.%). Source: ORNL.

To further understand the phase evolution and distribution in the as-sintered state, the advanced characterization facilities at PNNL were leveraged through a Thrust 4 project. Micro-XRD, STEM, and APT were performed on the 85% binder saturated sample sintered at 1,380°C. Figure I.3.3.1.5.4 shows the low magnification STEM image along with corresponding V, Mo, Fe, Cr, and Mn concentration maps. Two types of V/Mo-based MX carbides are present. Rod-shaped MX is along the grain/interparticle boundaries, and cuboidal MX within the grain interiors. From the Cr map, there are few regions containing Cr-rich carbides, likely Cr_{23}C_6 , but the fraction is lower compared to the MX type carbides. The micro-XRD scan from one particle interior into the other along the interparticle boundary indicates that the ratio of relative intensity of fcc (220) and bcc (110) peaks increases near the interparticle boundary and drops down to 0 within the particle interiors. To get a better understanding of the phases present, selected area diffraction and APT were conducted. Figure I.3.3.1.5.5 shows the STEM diffraction pattern analysis and APT C atom maps and proxigrams. Based on the diffraction pattern analysis, both the grain boundary carbide (#1) and grain interior carbide (#2) are indeed MX with an fcc crystal structure. The APT data, along with the proxigrams, show that the MX carbide is predominantly (V,Mo,Cr)C enriched in V. The C atom map shows that though the carbides can appear discrete in the STEM images, which are 2D, the MX carbides can often be interconnected in 3D. Interconnected carbides are not desirable and can promote brittle failure prematurely. This result emphasizes the need for careful development of suitable post-fabrication heat treatments.

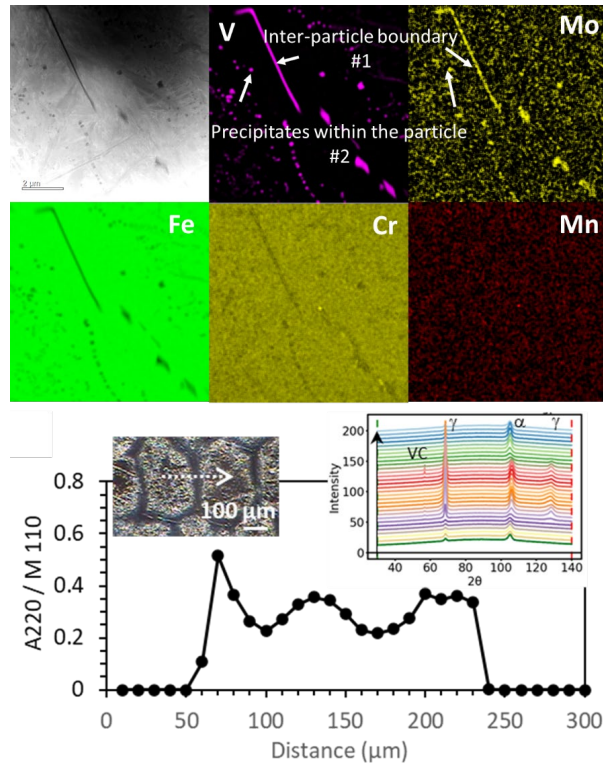


Figure I.3.3.1.5.4. Low magnification STEM image, along with the corresponding elemental maps of V, Mo, Cr, Fe, Mn, and the micro-XRD profile across two particles in the sample sintered at 1,380 °C with an 85% binder saturation. Source: ORNL and PNNL.

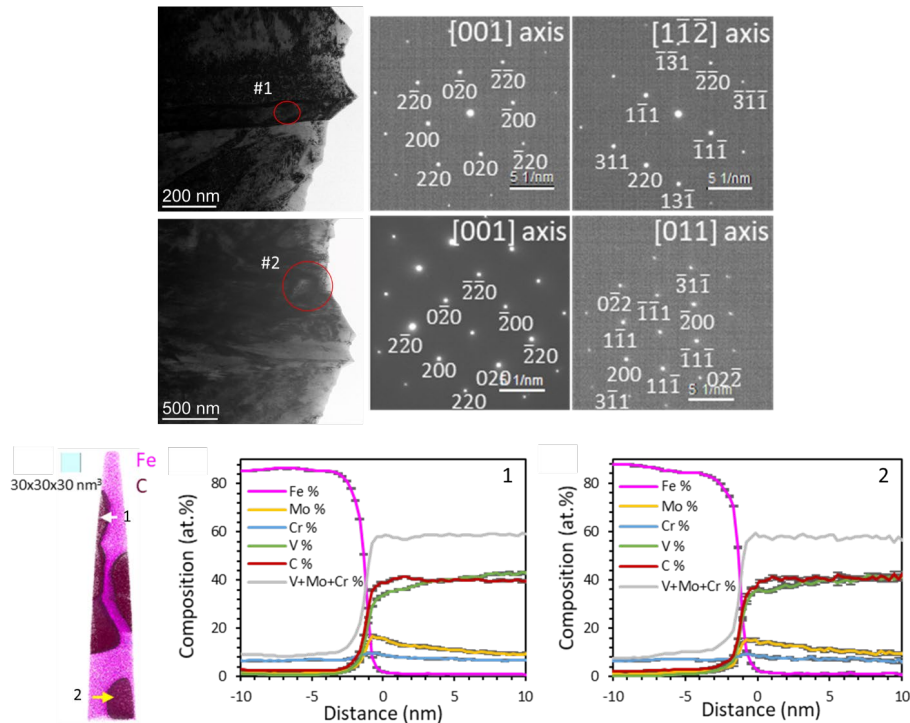


Figure I.3.3.1.5.5. Diffraction pattern analysis of the carbides and APT C atom maps and proxigrams across the matrix and the carbide. Source: PNNL.

The other observation from the STEM and APT data is the formation of eutectic MX in the liquid channel during solidification. Conventionally produced H13, as well as H13 produced by a laser/electron beam, have reported the absence of any eutectic MX during solidification. The presence of eutectic MX in H13 fabricated by SLPS/BJAM is likely due to C pickup during binder burnout and sintering operations. To validate this hypothesis, the local C concentration increases due to C pickup estimated using the CALPHAD model discussed above was used to calculate the phase fraction during solidification. Figure I.3.3.1.5.6(a) and (b), respectively, show the phase fraction evolution for H13 powder chemistry and the H13 powder chemistry after incorporating C pickup due to binder burnout, respectively. The C pickup due to binder burnout residue alters the solidification pathway from $L \rightarrow L + \delta \rightarrow \gamma$ to $L \rightarrow L + \gamma \rightarrow L + \gamma + MX \rightarrow \gamma + MX$ resulting in the formation of eutectic carbides near the interparticle boundaries.

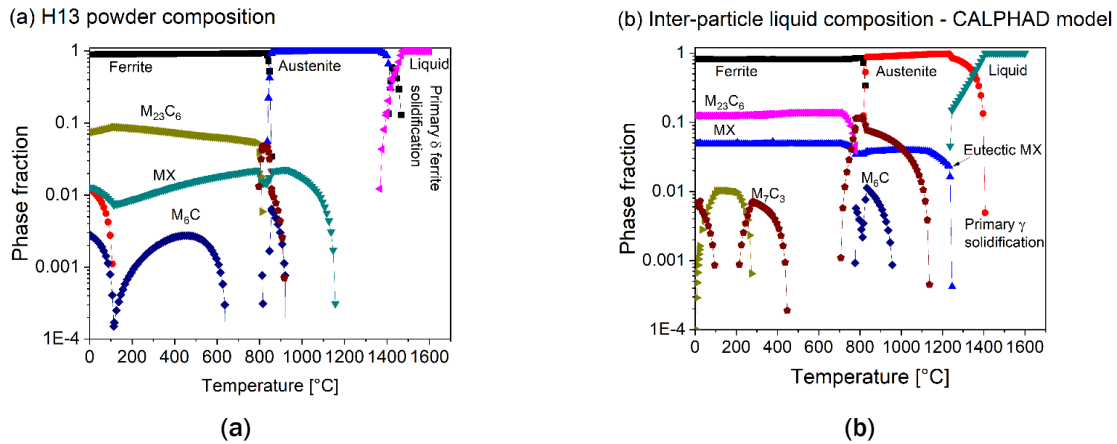


Figure I.3.3.1.5.6. Phase fraction estimates for (a) H13 powder composition and (b) H13 powder composition after incorporating excess C pickup from the residual binder after burnout. Source: ORNL.

Finally, building on the high-temperature testing conducted in FY 2020, the H13 samples were subjected to HIP and heat-treatment. They were then exposed to prolonged thermal preconditioning for 500 h at 600°C, followed by elevated temperature tensile testing at 550°C and 600°C. There was a substantial drop in the yield strength of the material, possibly due to coarsening of the carbides and the tempering of the martensite. The yield strength upon prolonged exposure is compared with high-temperature strength of H13 in as-sintered and HIP+HT conditions, as well as 4140 and MAS alloys without high-temperature preconditioning in Figure I.3.2.1.5.7. After the 500-hour preconditioning treatment the yield strength of the HIPed H13 alloys were similar to those of the MAS and 4140 alloys, suggesting an alloy with improved thermal stability may be desirable for piston applications approaching 600°C.

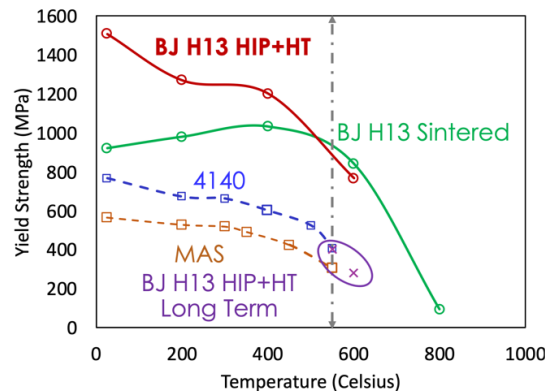


Figure I.3.3.1.5.7. Summary of yield strength of BJAM H13 in different conditions as compared with 4140 and MAS. Source: ORNL.

Conclusions

Research on BJAM H13 in FY 2021 has demonstrated that BJAM is a viable technique to fabricate complex tool steel components, possibly including HD pistons. While H13 has been historically used as a tool steel material, the near net-shape potential offered by BJAM can help minimize machining to that necessary to achieve final surface finish, compared to the extensive machining required while using forging blanks. We have shown that the CALPHAD models can be used to accurately predict the sintering windows to account for the local changes in C composition resulting from the deposition of binder in the interparticle regions during the 3D printing process. Further, we have conducted an in-depth characterization of the microstructural features that were rationalized using the CALPHAD models. The ability to make reasonable predictions using CALPHAD will be critical in evaluating the underlying causes for reduction in yield strength on long-term thermal exposure, as well as designing appropriate heat treatments to mitigate the notable drop in strength during long-term aging.

Key Publications

1. Nandwana, P., R. Kannan, and D. Siddel, 2020, “Microstructure evolution during binder jet additive manufacturing of H13 tool steel,” *Addit. Manuf.*, Vol. 36, Art. 101534.
2. Kannan, R., and P. Nandwana, 2021, “Predicting sintering window during supersolidus liquid phase sintering of steels using feedstock analysis and CALPHAD,” *Mater. Lett.*, Vol. 304, Art. 130648.
3. Liu, J., R. Kannan, D. Zhang, T. Liu, P. Nandwana, and A. Devaraj, 2021, “Processing-microstructure-property relationship of supersolidus liquid phase sintered binder jet additively manufactured H13 tool steel,” *Addit. Manuf.* (in submission).

References

1. Kannan, R., and P. Nandwana, 2021, “Predicting sintering window during supersolidus liquid phase sintering of steels using feedstock analysis and CALPHAD,” *Mater. Lett.*, Vol. 304, Art. 130648.
2. Nandwana, P., R. Kannan, and D. Siddel, 2020, “Microstructure evolution during binder jet additive manufacturing of H13 tool steel,” *Addit. Manuf.*, Vol. 36, Art. 101534.
3. Liu, J., and R. M. German, 1999, “Densification and shape distortion in liquid phase sintering,” *Metall. Mater. Trans. A.*, Vol. 30, pp. 3211–3217.

Acknowledgments

The authors acknowledge the contributions of the following team members for their assistance in this subtask: R. Kannan, D. Siddel, A. Rossy Marquez, K. Hedrick, D. Pierce, and S. Dryepondt from ORNL; and A. Devaraj, J. Liu, D. Zhang, and T. Liu from PNNL.

I.3.4 Advanced Characterization and Computational Methods – Thrust 4

I.3.4.1 Advanced Characterization (4A)

I.3.4.1.1 Overview of Advanced Characterization Within the Powertrain Materials Program (Task 4A1) (Oak Ridge National Laboratory); (Task 4A2) (Argonne National Laboratory); and (Task 4A3) (Pacific Northwest National Laboratory)

Thomas R. Watkins, Co-Principal Investigator

Oak Ridge National Laboratory
1 Bethel Valley Road
Oak Ridge, TN 37830
E-mail: watkinstr@ornl.gov

Dileep Singh, Co-Principal Investigator

Argonne National Laboratory
9700 S. Cass Avenue
Argonne, IL 60439
E-mail: dsingh@anl.gov

Arun Devaraj, Co-Principal Investigator

Pacific Northwest National Laboratory
902 Battelle Blvd.
Richland, WA 99354
E-mail: arun.devaraj@pnnl.gov

Jerry L. Gibbs, DOE Technology Manager

U.S. Department of Energy
E-mail: jerry.gibbs@ee.doe.gov

Start Date: October 1, 2019	End Date: September 30, 2023	
ORNL Project Funding (FY 2021): \$450,000	DOE share: \$450,000	Non-DOE share: \$0
ANL Project Funding (FY 2021): \$300,000	DOE share: \$300,000	Non-DOE share: \$0
PNNL Project Funding (FY 2021): \$300,000	DOE share: \$300,000	Non-DOE share: \$0
Total Project Funding (FY 2021): \$1,050,000	DOE share: \$1,050,000	Non-DOE share: \$0

Project Introduction

This report describes the activities performed during the third year of Thrust 4A, “Advanced Characterization,” within the DOE-EERE VTO PMCP. The goal of the PMCP, which was launched in October 2018, has been to accelerate design, development, demonstration, and deployment of new, cost-effective advanced alloy solutions via a modern ICME approach. The properties of these new materials are targeted to enable improvements in engine efficiency, lightweighting, and durability enhancement over the full range of on-road vehicle classes (e.g., Classes 1-8), including range extenders for future electric HD freight vehicles.

Objective

The overall objective for Thrust 4A is to provide advanced characterization support to obtain data and scientific understanding that will be applied to the development of new materials being performed under Thrusts 1, 2, and 3 of the PMCP.

Thrust 4A Objectives in Support of Tasks 1A1, 2A1, and 3A1

Thrust 4A supported the development of Task 1A1, “Fundamental Studies of Complex Precipitation Pathways,” at ORNL, which is within Thrust 1 of the PCMP, “Cost-Effective Lightweight High Temp Engine Alloys.” In FY 2021, Task 1A1 was supported by five advanced characterization projects conducted at ORNL, ANL, and PNNL that were focused on cast ACMZ alloys being developed by ORNL. This family of new alloys has shown remarkable strength at temperature (e.g., $> 300^{\circ}\text{C}$) due to the stability of small, high aspect ratio, metastable θ' intermetallic strengthening precipitates with chemistry of Al_2Cu . These and other precipitates in other precipitation-strengthened cast-Al alloys naturally coarsen with time and transform to undesirable, incoherent phases at temperatures above $\sim 230^{\circ}\text{C}$, which drastically reduces the strength and durability at more extreme operating temperatures required of higher efficiency and/or higher power density engine designs. ACMZ alloys have been designed to suppress these high-temperature phase transformations at temperatures up to 350°C . Work is underway in Task 1A1 at ORNL to develop additional variants of the ACMZ alloys to further improve or tailor performance. The objectives/achievements of the five supporting Thrust 4A projects described here are to characterize these experimental ACMZ alloys to understand the impact of the chemistry changes upon the thermal stability of these alloys.

Thrust 4A supported the development of Task 2A1, “Oxidation-Resistant Valve Alloys ($900^{\circ}\text{C} - 950^{\circ}\text{C}$),” at ORNL, which is within Thrust 2 of the PCMP, “Cost-Effective Higher Temp Engine Alloys.” In FY 2021, Task 2A1 was supported by four advanced characterization projects conducted at ORNL, ANL, and PNNL of precipitates in novel higher temperature, higher strength polycrystalline Ni-based superalloys being developed by ORNL for advanced exhaust valves. Ni-based alloys provide excellent high-temperature stability and good mechanical properties for many high-temperature applications (e.g., engine valves). As Ni and Co are expensive, Task 2A1 is exploring alternative lower-cost alloy compositions where Ni + Co is $\sim 45 \text{ wt.}\% - 50 \text{ wt.}\%$, instead of the more typical $65 \text{ wt.}\%$ or more. Novel Ni-Fe-Cr-Al-Ti-based alloys developed at ORNL [1] meet this compositional criterion and provide remarkable strength improvements over existing Ni-based commercial valve alloys at $900^{\circ}\text{C} - 950^{\circ}\text{C}$. The objective is to determine the effect of heat-treatment on the strengthening precipitates and subsequent stability of these precipitates after long-term exposure at higher temperatures.

Thrust 4A supported the development of Task 3A1, “Fundamental Development of Al Alloys for Additive Manufacturing,” at ORNL, which is within Thrust 3 of the PMCP, “Additive Manufacturing of Powertrain Alloys.” In FY 2021, Task 3A1 was supported by five advanced characterization projects conducted at ORNL, ANL, and PNNL, including a study of AM Al-Cu-Ce-X alloys where X is another element of interest, such as Mn or Zr. It was demonstrated that compared to casting, AM of the same alloy composition can produce a unique fine microstructure consisting of dispersoids such that AM processed alloys have significantly improved strength and, in some cases, ductility. As with Task 1A1, there is interest in retaining strength with extended exposure at elevated temperatures (e.g., $\geq 300^{\circ}\text{C}$). The objectives of the characterization activity supporting this task are to: (i) uncover the microstructural and chemical features behind the improvement in mechanical properties (e.g., strength, ductility, creep, and fatigue); and (ii) study the link between processing and mechanical properties for AM microstructures.

Approach

The advanced characterization of Thrust 4A is a multi-laboratory effort involving Task 4A1 at ORNL; Task 4A2 at ANL; and Task 4A3 at PNNL. To put Thrust 4A into programmatic context, the PMCP consists of five research thrusts: Thrust 1: “Cost-Effective, Lightweight (i.e., Al alloys) Engine Alloys;” Thrust 2: Cost-Effective, Higher Temperature Engine Alloys (i.e., Ni- and Fe-Based Alloys);” Thrust 3: “Additive Manufacturing of New Powertrain Alloys;” Thrust 4: “Advanced Characterization and Computational Methods;” and Thrust 5: “Exploratory Research for Emerging Technologies.” Thrust 4A addresses the advanced characterization needs of the various tasks within the three materials development thrusts (e.g., Thrusts 1–3). Advanced characterization activities may include STEM, APT, synchrotron x-rays, neutron scattering, and others. Thrust 4A provides additional advanced characterization support for the development tasks in Thrusts 1–3. This report discusses the advanced characterization activities completed by ORNL, ANL,

and PNNL as directed through Thrust 4A. In FY 2021, there were 26 Thrust 4A advanced characterization projects supporting 11 development tasks. A subset of Thrust 4A support projects for development tasks 1A1, 2A1, and 3A1 as described herein.

Thrust 4A Approach in Support of Tasks 1A1, 2A1, and 3A1

Tasks 1A1, 2A1, and 3A1 were supported by Thrust 4A activities at ORNL, ANL, and PNNL. The expertise and advanced characterization tools that were utilized in this effort included STEM with and without electron energy loss spectroscopy and *in-situ* and *ex-situ* APT and synchrotron x-rays to understand the multiscale microstructural phase composition and chemical features the new alloys. Both STEM and APT can determine the location of various elemental additions within the precipitates, matrix/precipitate interface and matrix, providing chemical and locational information on the atomic-scale. APT is a rare resource with about 100 instruments worldwide; both PNNL and ORNL have this resource. Both STEM and synchrotron x-rays provide crystallographic information, which determine the physical properties. The synchrotron source at ANL was essential due to its high flux (e.g., 1,000,000 times more intense than a laboratory x-ray machine) and high-energy (e.g., a large depth of penetration) allowing information for trace phases to be distinguished from the bulk matrix and higher volume precipitates. Small-angle x-ray scattering (SAXS) was used to determine average precipitate sizes and distributions.

Results

Thrust 4A Results in Support of Task 1A1

The ACMZ family of alloys were investigated using STEM, APT, and synchrotron x-rays to locate low fraction elements and phases on the atomic-scale, as well as phases on the bulk-scale, often as a function of time at temperature. One focus was the phase transition between the metastable θ' -Al₂Cu-strengthening phase, and the stable, but incoherent, θ -Al₂Cu phase. The θ' precipitates readily transform to θ precipitates during thermal exposure at temperatures above 250°C, but in the case of ACMZ alloys, this transformation is inhibited via the stabilizing effect of Mn and Zr solute segregation to the θ' /Al matrix interface at temperatures up to 350°C, resulting in superior elevated temperature strength.

Thus, an ACMZ alloy was examined to understand the thermal stability and strengthening mechanism of metastable θ' Al₂Cu precipitates with interfacial element segregation after prolonged thermal exposure [2]. Various θ' precipitate parameters including volume fraction, true diameter, true thickness, aspect ratio (diameter/thickness), equivalent radius, and number density per unit volume were determined [3] from high-angle annular dark-field (HAADF) images recorded on the aberration-corrected JEOL 2200FS STEM at ORNL. Five HAADF images at 50kx magnification, shown in Figure I.3.4.1.1.1, were analyzed per condition. The sample suite included an as-aged sample and three 300°C thermal exposure samples (e.g., 200 h, 2100 h, and 5000 h), as indicated in Figure I.3.4.1.1.1. The STEM imaging experiments also allowed determination of the average thickness of the thin-foil areas imaged [4], a necessary parameter for reliable measurements of the other precipitate parameters listed above. All imaging was conducted on Al matrix grains tilted to a precise $\langle 001 \rangle$ zone axis orientation (i.e., viewing the cubic Al structure along a cube-edge crystal direction). In this orientation, the Al₂Cu disk-shaped precipitates that lie on the three cube-face habits are seen either edge-on with two habits, a “needle” appearance, or in “plan view” looking normal to a faceted disk plane (e.g., this latter habit appears in low contrast, faint, and blurry) due to the thin crystal dimension and is indicated by red arrows in Figure I.3.4.1.1.1(c). Careful analysis of atomic-resolution images shown in Figure I.3.4.1.1.1(e) and Figure I.3.4.1.1.1(f) of the edge-on precipitates in the 5000 h-aged foil confirmed that the θ' crystal structure was fully maintained at this longest exposure time, with minimal precipitate coarsening. The insets show the diffractograms of the boxed regions inside the precipitates that confirm the body-centered tetragonal crystal structure of θ' precipitates [5]. An L1₂ Al₃Zr type phase started to co-precipitate on the θ' /Al coherent interface at 5000 h thermal exposure, as seen on the left-hand side interface of the θ' precipitate in Figure I.3.4.1.1.1(f), as depicted by the note arrow [6]. Both images were initially scaled relative to the $\langle 001 \rangle$ zone axis orientation of the Al matrix structure as an internal standard.

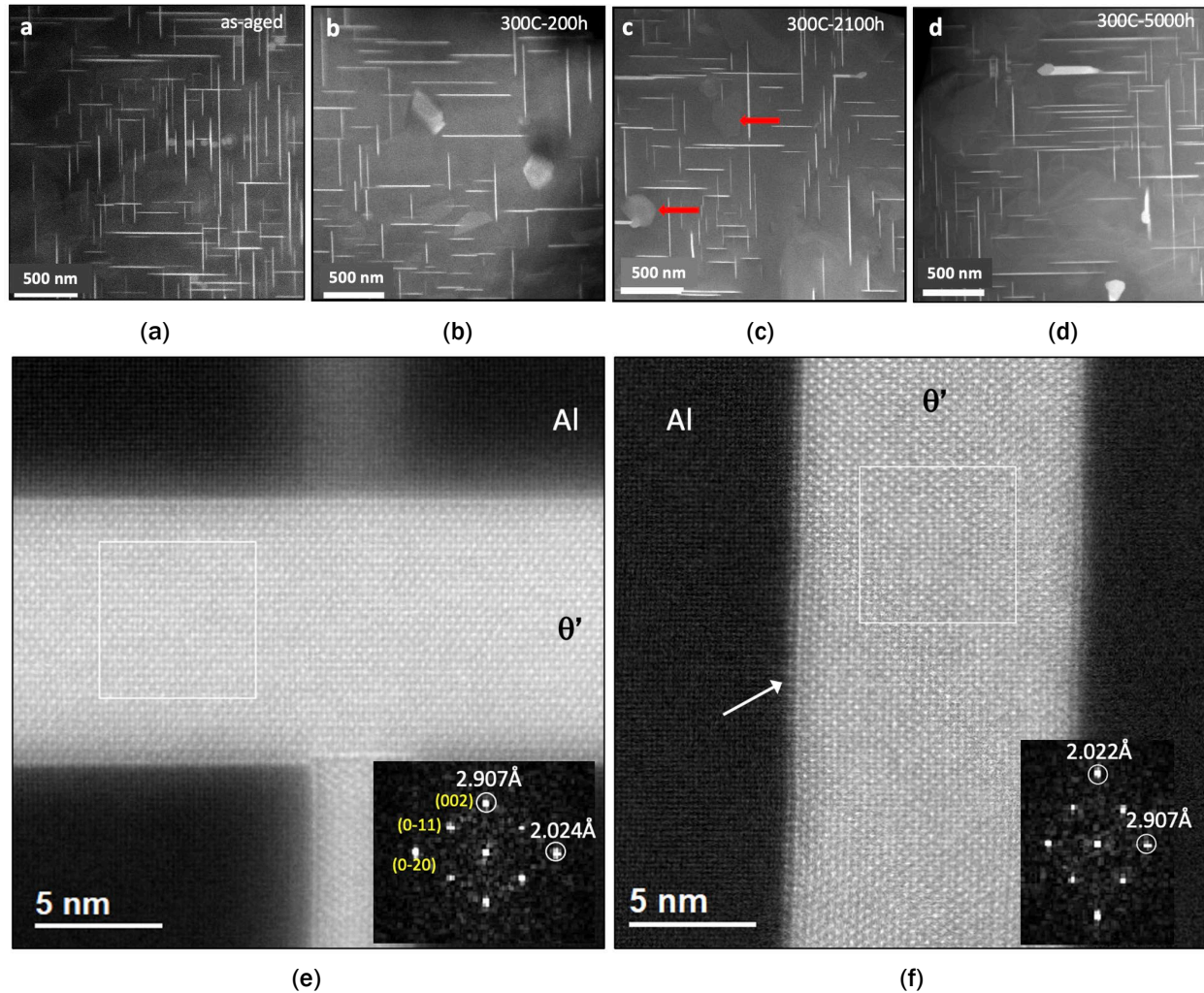
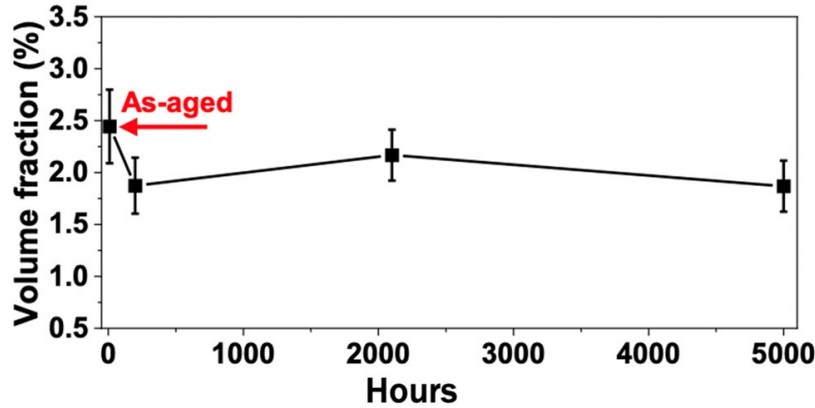


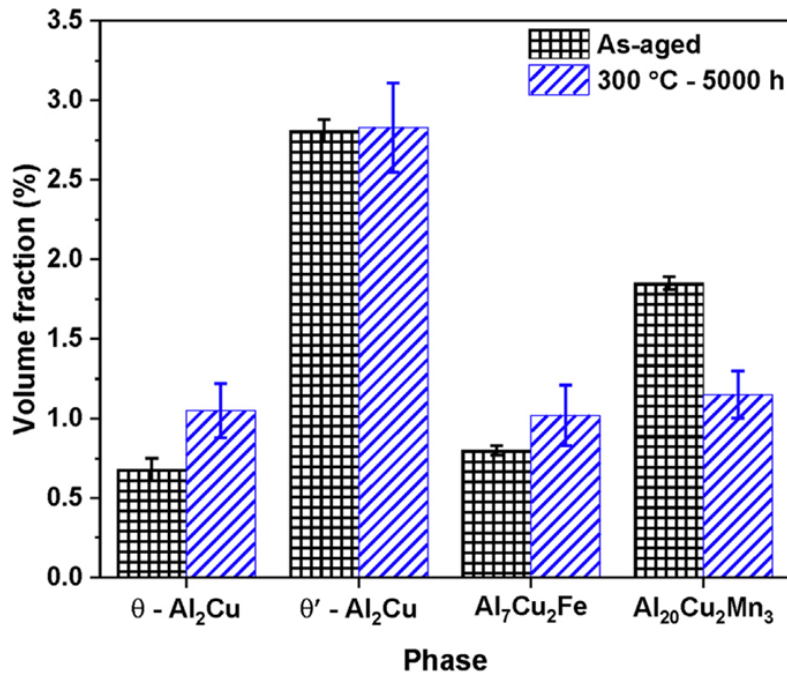
Figure I.3.4.1.1.1. HAADF-STEM images along the $\langle 001 \rangle$ α -Al zone axis of (a) the as-aged microstructure and after thermal exposure at 300 °C for (b) 200 h; (c) 2100 h; and (d) 5000 h. Two habits of θ' precipitates are seen edge-on, while a third indicated by arrows depict the plain view. High-resolution HAADF-STEM images of θ' precipitates in the (e) as-aged condition, and (f) after 5000 h thermal exposure at 300 °C. Source: ORNL.

Figure I.3.4.1.1.2(a) shows a typical measurement (e.g., volume fraction changes) resulting from the STEM imaging work and confirms that minimal phase transformation of the θ' occurred, even after 5000 h at 300°C, which is a remarkable outcome for a low-cost cast ACMZ alloy. Similar trends were obtained for all the other measurement parameters determined with STEM imaging.

At ANL's APS, the penetrating power of high-energy and high flux synchrotron x-rays were used to produce XRD patterns from ACMZ alloys. The θ' to θ phase transformation was examined in ACMZ alloys during extended thermal exposure at 300°C for up to 5000 h. The diffraction patterns were Rietveld refined to determine the fractions of crystallographic phases. Figure I.3.4.1.1.2(b) shows the fractions of trace phases, observable with APS's high flux, within an as-aged sample and one aged for 5000 h at 300°C. STEM and synchrotron results are in good agreement for the phase fractions [2]. Overall, the results partially illustrated in these figures suggest that most of the evolution in θ' precipitates from their starting as-aged condition occurred within the first 200 h of thermal exposure at 300°C, after which the precipitate distribution remained virtually constant, further supporting our understanding of the unusual high-temperature phase stability of these alloys.



(a)



(b)

Figure I.3.4.1.1.2. (a) STEM-derived volume fraction change in the θ' precipitates from the as-aged to 5000 h exposure condition. Most of the small reduction in volume fraction occurs in the first 200 h of exposure at 300 °C. Source: ORNL. (b) Synchrotron derived volume fractions for trace phases detected in the as-aged and 5000 h sample at 300 °C. This image is taken from Bahl et al. [2]. Source: ANL.

At ORNL, APT has been utilized to better understand the nanostructures in cast-Al-Cu alloys. The hardness of the Al-Cu alloys rely on a high number density of plate-shaped θ' (e.g., Al_2Cu) precipitates in the microstructure. Unfortunately, θ' is a metastable phase that typically coarsens and transforms to θ at temperatures $\geq 240^\circ\text{C}$, which softens most castable commercial Al-Cu alloys such that they are not useful for higher temperature applications. ORNL previously discovered that microsolite additions of Mn and Zr to Al-Cu alloys can result in an alloy that retains hardness after lengthy exposures to up to 350 °C. In FY 2020, APT revealed that Mn and Zr segregate to the θ' interfaces and synergistically stabilize the alloy through a reduction of interfacial energy, solute drag effects, and the eventual formation of $\text{L1}_2 \text{Al}_3\text{Zr}_x\text{Ti}_{1-x}$ along the θ' coherent interfaces [6].

Another important aspect of the alloy design of ACMZ for high-temperature stability is a trace Si addition between 0.05 wt.% and 0.10 wt.%. Within this range, the as-aged θ' microstructure displays the highest aspect ratio and lowest number density, which supports further improvements in stability of θ' . The inherent stability of the higher aspect ratio precipitates allows for more time for the slow diffusing Mn atoms to segregate to the interfaces and further stabilize the alloy. APT was performed on alloys with a low Si content (0.03 wt.%), an ideal Si content (0.09 wt.%), and a high Si content (0.23 wt.%) for trace. As shown in Figure I.3.4.1.1.3(a)–(c), the Mn and Zr segregation behavior to the θ' – Al matrix interfaces is relatively the same for all three conditions; however, clearly the θ' is more coarsened for the high Si case after the same heat-treatment, as can be seen in Figure I.3.4.1.1.3(d). The APT measured Si contents within θ' for the low Si content alloys and intermediate Si content alloys were the same in the as-aged microstructure, while the high Si content alloy contained more than 4 times the Si content. The higher number density of θ' in the low and high Si content alloys indicates that there are more θ' nucleation sites within these alloys compared to the intermediate Si alloys. θ' is known to nucleate on dislocation loops and Si clusters. The APT and microstructure evaluation results suggest that θ' nucleation transitions from a dislocation to a Si cluster mediated mechanism as the Si content is increased. The intermediate Si alloy has an ideal Si content as the Si is suppressing dislocation loops, while there is a low density of Si clusters. These results were published in Shower et al. [7].

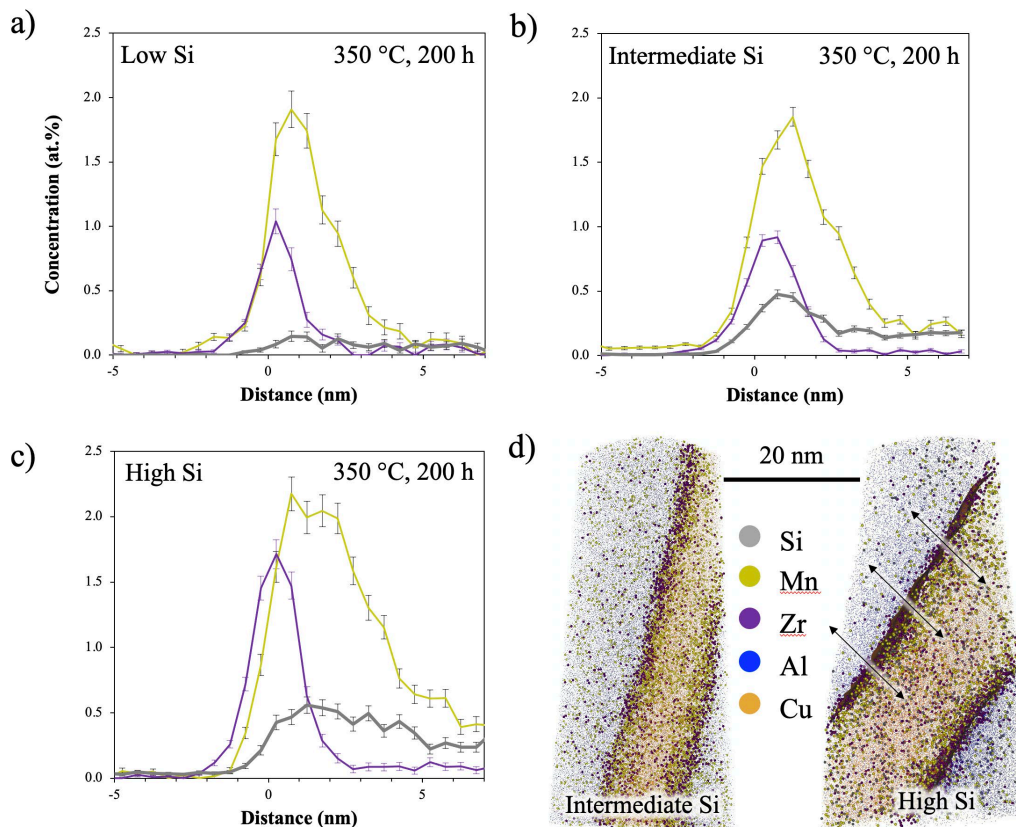


Figure I.3.4.1.1.3. (a)–(c) Coherent interface composition profiles for a low, intermediate, and high Si alloy exposed to 350 °C for 200 h after aging, respectively, calculated from APT data. The curve colors are given in the shared legend located in (d). (d) APT atom maps for an intermediate and high Si alloy used for the composition profiles in (b) and (c), respectively. The composition profile was calculated from the region marked by arrows in the high Si alloy using a proximity histogram from a 10 at.% Cu iso-concentration surface. Note that the positive distance values in (a)–(c) represent the region inside the precipitate and negative values represent the matrix. This image is taken from Shower et al. [7]. Source: ANL.

APT was also conducted at PNNL to analyze the evolution in compositional partitioning between the strengthening θ' precipitate and the Al matrix in the ACMZ alloy during *in-situ* high-temperature annealing, as shown in Figure I.3.4.1.1.4. The recently installed Thermo Fisher Scientific plasma focused ion beam (PFIB) system at PNNL was used for Ga-free APT sample preparation from the ACMZ alloys. The PFIB prepared APT needles, which were initially subjected to field evaporation in APT to clean the needle surface, were transferred into a custom developed environmental reactor chamber connected directly to the PNNL APT buffer chamber [8, 9]. In the reactor, these needles were subjected to annealing for 1 to 4 hours from 300°C to 350°C, and then promptly transferred back to the APT analysis chamber. The APT analysis results after the *in-situ* annealing experiments revealed a substantial increase in Mn and Zr segregation to the θ' and Al matrix interface, as shown in Figure I.3.4.1.1.4(b). These *in-situ* studies provided a comprehensive mechanistic understanding of the early stages of development of solute segregation responsible for microstructural stability of ACMZ alloys at high temperatures when correlated with prior *ex-situ* APT studies of ACMZ alloys annealed from 300°C to 350°C for long periods greater than 200 h.

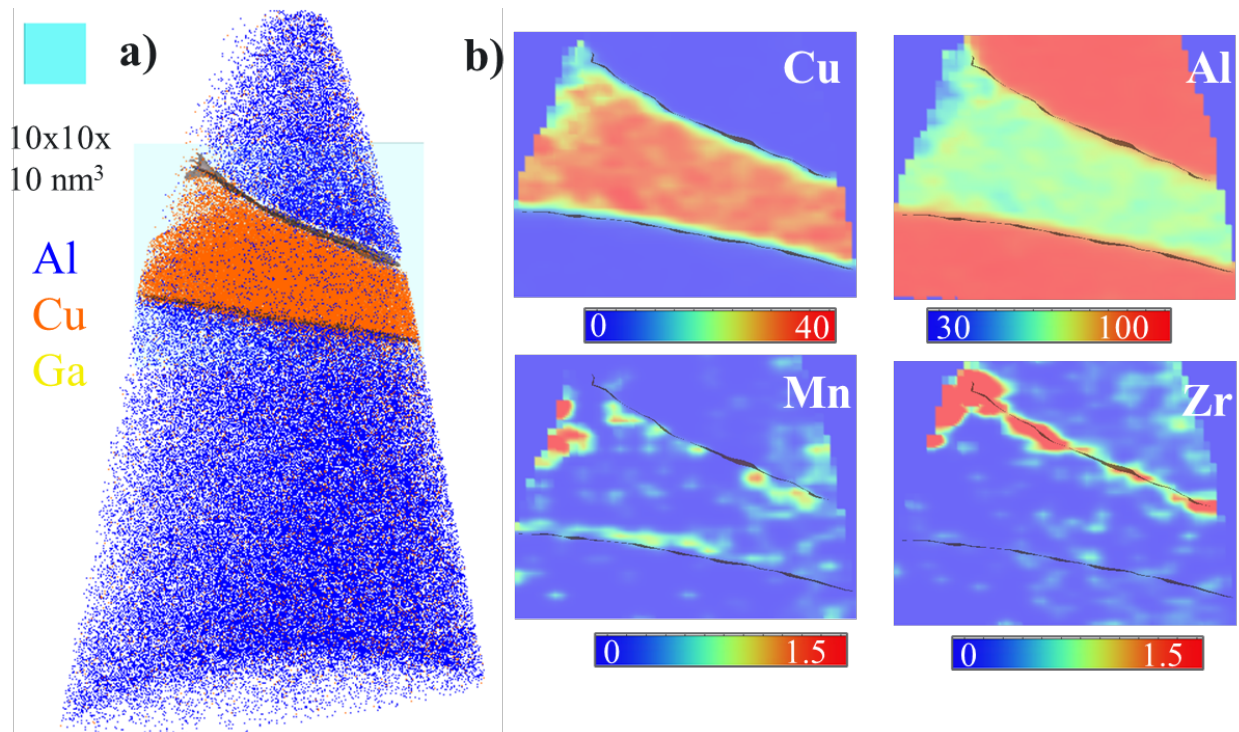


Figure I.3.4.1.1.4. (a) APT reconstruction of the ACMZ alloy after annealing at 350°C for 4 hours where the θ' precipitate is highlighted using a 10 at.% Cu iso-concentration surface. (b) The compositional partitioning of Cu, Al, Mn, and Zr across the θ' and Al matrix is revealed using 2D compositional maps with a $36 \times 5 \times 46$ nm region of interest. A clear segregation of Mn and Zr at the θ' and Al matrix interface is evident after *in-situ* annealing. Source: PNNL.

Thrust 4A Results in Support of Task 2A1

Since the compositions and size distributions of γ' precipitates and their long-term stability affect the high-temperature strength and fatigue properties of the novel Ni-Fe-Cr-Al-Ti-based chromia-forming alloys developed at ORNL, the characteristics of these precipitates were investigated using STEM at ORNL and PNNL, APT at ORNL and PNNL, and synchrotron SAXS at ANL. In addition, the effect of alloy composition and heat-treatment on the formation of undesirable topologically close-packed phases was also investigated using these advanced characterization techniques [10]. For these types of alloys, the matrix phase, γ , will precipitate out a strengthening phase, γ' , with heat-treatment.

The study focused on two conditions: as-aged (AA, 16 h at 760°C) and as-aged and high-temperature aging (AA-HTA, 16 h at 760°C then 250 h at 900 °C). Figure I.3.4.1.1.5 and Figure I.3.4.1.1.6 show the results of the detailed TEM with EDS and APT analyses, respectively, for both the AA and AA-HTA conditions. The selected area electron diffraction (SAED) patterns in both conditions, as observed in Figure I.3.4.1.1.5(a) and (b), respectively, indicate the presence of superlattice reflections at the $\{001\}$ and $\{011\}$ locations from the fine precipitates, consistent with an ordered γ' precipitate with the $L1_2$ structure. The EDS analysis corresponding to the HAADF-STEM images in Figure I.3.4.1.1.5(b) is shown in Figure I.3.4.1.1.5(c)–(h) for the AA condition's γ matrix and secondary γ' . EDS elemental maps indicate that the γ' precipitates were enriched in Ni, Ti, and Al, whereas Cr and Fe were partitioned to the γ matrix. Although there is an overlap in the images of the individual precipitates, the average diameter of the precipitates was estimated to be ~ 35 nm by using manual delineation of the precipitate-matrix interface. Similarly, Figure I.3.4.1.1.6(a) shows the results from the EDS analysis of the coarse γ' precipitates that range from 100 nm – 300 nm in diameter observed in the AA-HTA condition. These coarse γ' precipitates were formed through the growth of fine γ' precipitates observed in the AA condition.

Figure I.3.4.1.1.5(i)–(k) and Figure I.3.4.1.1.6(b) show the results from the APT examination of the matrix (γ), the fine precipitates in the AA, and the fine and coarse precipitates in the AA-HTA conditions, respectively. Figure I.3.4.1.1.5(i) represents a 3D reconstruction of the APT data with the fine γ' precipitates delineated by an iso-concentration surface shown in red enclosing a region with more than 5 at.% Al for the AA condition. The matrix is indicated by Cr atoms shown in green. Figure I.3.4.1.1.5(i) shows that in the region examined, the γ' shapes are approximately spherical in 3D, which is consistent with the results from the TEM study. The elemental variations across the γ - γ' interface are illustrated using the proxigrams, as shown in Figure I.3.4.1.1.5(j) and Figure I.3.4.1.1.5(k) along a cylinder of about 10 nm in length. Compositional analysis of the γ' showed that the average at.% precipitate composition was $\sim 72.90\text{Ni}/15.64\text{Ti}/9.10\text{Al}/1.74\text{Fe}/0.29\text{Cr}/0.28\text{Co}/0.02\text{Mo}$ with an average composition of γ' precipitates close to that of $\text{Ni}_3(\text{Al,Ti})$ stoichiometry along with minor quantities of Fe, Cr, and Co. The composition of the γ matrix at ~ 5 nm from the interface was $\sim 32.58\text{Ni}/0.34\text{Ti}/1.29\text{Al}/37.21\text{Fe}/26.71\text{Cr}/1.03\text{Co}/0.84\text{Mo}$ at.%. The elemental concentration profiles of minor elements shown in Figure I.3.4.1.1.5(k) demonstrate that Mo and Co are preferred in the γ matrix rather than in the γ' precipitate. Loomis et al. [11] observed that with an increase in the Ti content of the alloy, Mo preferentially partitioned to the γ matrix. This observation is consistent with the partitioning of Mo to the matrix observed in the current study since the alloy used in this study contains 4.4 at.% Ti.

The APT results for the AA-HTA condition, as shown in Figure I.3.4.1.1.6(b), were utilized to visualize and quantify the elemental partitioning of the elements in the two generations of the γ' precipitates and the matrix. The top image of Figure I.3.4.1.1.6(b) shows the APT reconstruction with the interface between the γ matrix and the secondary γ' delineated by a 5 at.% Al iso-concentration surface. The composition across this interface is illustrated in the adjacent proxigram: secondary γ' $\sim 60\text{Ni}/11\text{Ti}/7\text{Al}/12\text{Fe}/6\text{Cr}/<2(\text{Co}+\text{Mo})$ and γ matrix $\sim 35\text{Fe}/34\text{Ni}/20\text{Cr}/5\text{Ti}/4\text{Al}/<2(\text{Co}+\text{Mo})$ at.% at ~ 5 nm from the interface. Also, these precipitates are larger than those in Figure I.3.4.1.1.5(i). The fine γ' precipitates of ~ 5 nm in diameter had to be characterized using APT reconstruction of the matrix region devoid of the larger secondary γ' phase, as can be seen in the bottom image of Figure I.3.4.1.1.6(b). The adjacent proxigram shows the elemental partitioning across the matrix (γ) and ten randomly selected fine γ' precipitates: $\sim 56\text{Ni}/11\text{Ti}/10\text{Al}/14\text{Fe}/7\text{Cr}/<2(\text{Co}+\text{Mo})$ and γ matrix $\sim 34\text{Fe}/37\text{Ni}/20\text{Cr}/4\text{Ti}/4\text{Al}/<2(\text{Co}+\text{Mo})$ at.% at ~ 5 nm from the interface. Investigations focused on the elemental variation in various generations of γ' have demonstrated a small-size dependency of γ' composition [12, 13]. Further studies are needed to determine whether this is indeed a size effect.

Summarizing, the aging treatment of a novel Ni-Co alloy for 16 h at 760°C (AA) resulted in a microstructure consisting of fine spherical γ' precipitate in a γ matrix. The APT analysis confirmed the partitioning of Ni, Ti, and Al to the γ' precipitate while Fe, Cr, and Mo preferentially partitioned to the γ matrix. Subsequent long-term aging of the AA condition at 900°C for 250 h in the AA-HTA condition coarsened the γ' precipitates.

APT analysis of the AA-HTA condition sample also revealed the presence of very fine γ' precipitates, which may be formed during cooling from the heat-treatment temperature.

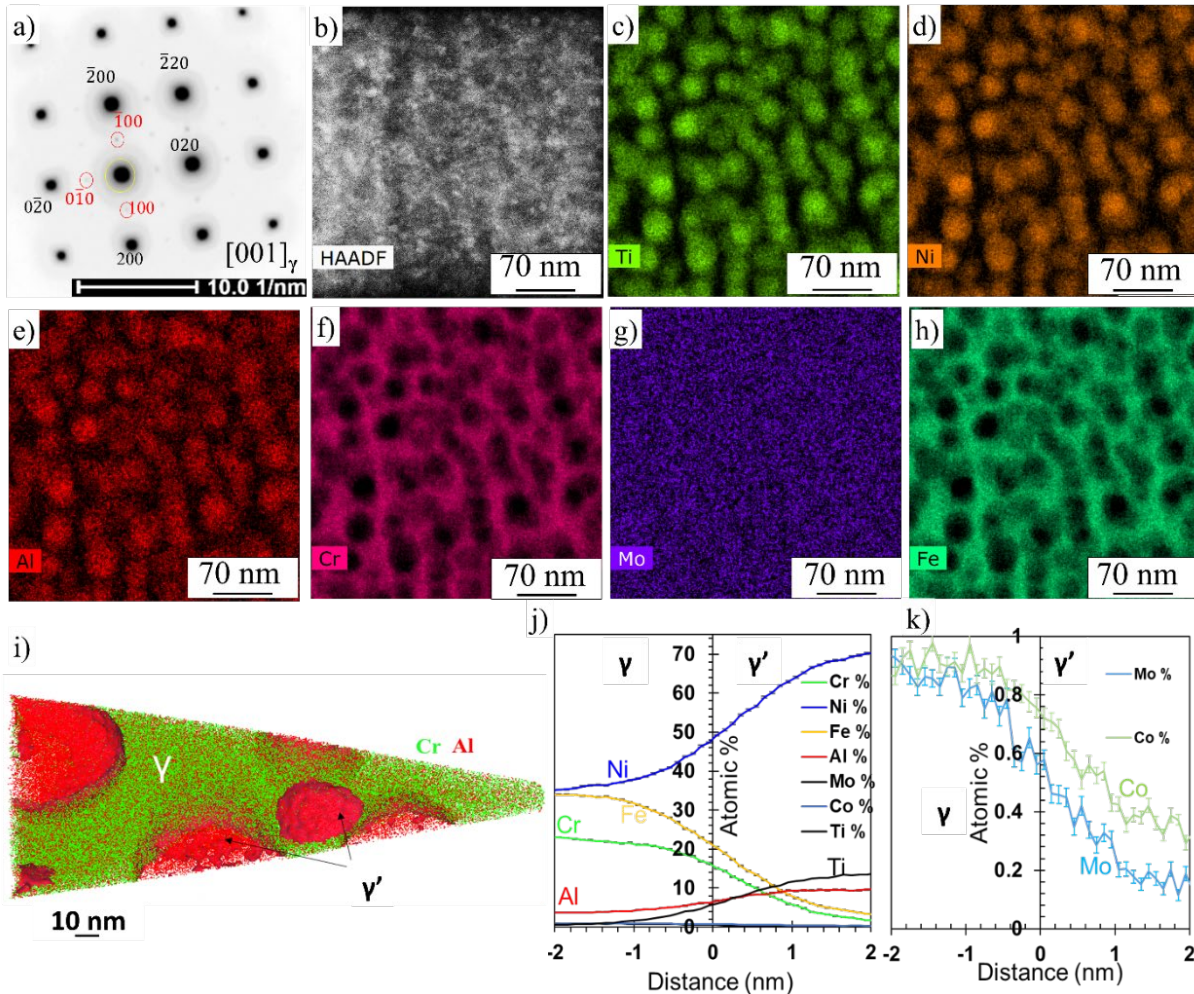


Figure I.3.4.1.1.5. (a) SAED pattern along $[001]_{\gamma}$ zone axis. Superlattice spots are shown in the red circles. (b) HAADF-STEM image. (c)-(h) EDS area maps showing elemental distribution within the γ and γ' . (i) A 3D reconstruction showing the γ' precipitates delineated by an iso-concentration surface (red) enclosing a region with more than 5 at.% Al. (j) Proxigram of major alloying elements. (k) Minor alloying elements showing the elemental partitioning across the γ - γ' interface. Source: ORNL.

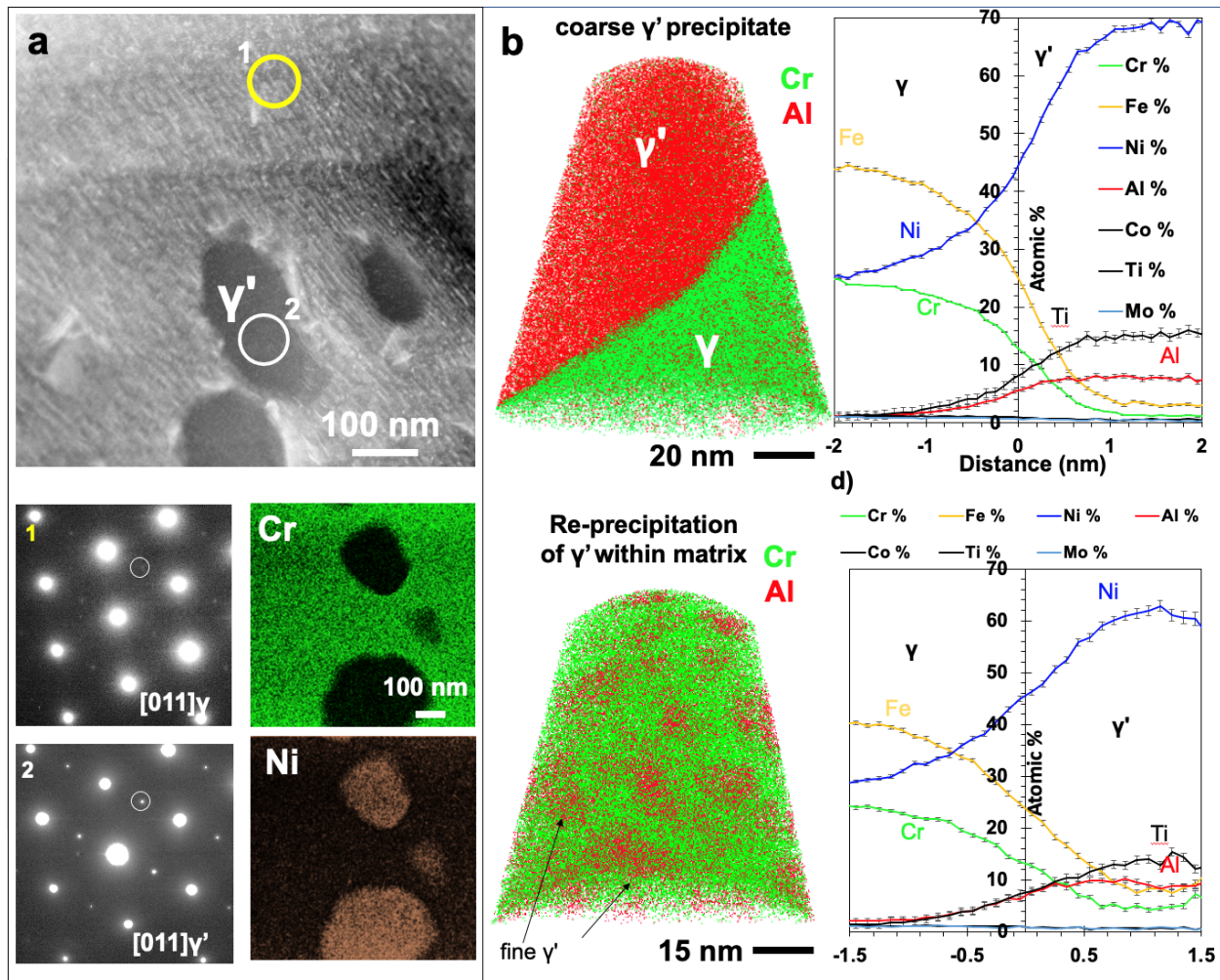


Figure I.3.4.1.1.6. TEM and APT analysis of a sample in the AA-HTA condition. (a) STEM image with the face-centered cubic matrix (γ) and the dark contrast primary γ' precipitates showing SAED patterns from the matrix (γ), and the precipitate (γ') aligned at $\{011\}$ direction. Faint super lattice spots are observed in SAED patterns from the matrix, while they are much more intense in the SAED patterns from the precipitate. Also shown are the color-coded EDS maps of Cr and Ni distribution, respectively, depicting the partitioning of Ni within the γ' precipitates. (b) APT 3D reconstruction showing a γ - γ' interface. The top portion of the figure has an interface demarked by a 5 at.% Al iso-concentration surface and the top proximity histogram shows the elemental partitioning across the interface of the matrix (γ) and coarse (γ'). The bottom APT reconstruction from the matrix region consists of fine γ' precipitates (~ 5 nm) that are not clearly discernable in TEM are also highlighted here within the matrix (γ). The proximity histogram shows the elemental partitioning across the interface of the matrix (γ) and fine (γ') precipitates. Source: PNNL.

Since the coarsening of γ' during high-temperature fatigue testing results in a loss of strength, *ex-situ* ultra-small-angle x-ray scattering (USAXS) was conducted at the APS to evaluate the γ' size distributions in another high-temperature chromia-forming alloy (M2045) samples after fatigue testing [14]. Here the high flux and monochromatic synchrotron x-ray beam coupled with a long-scan arm facilitate data to be collected rapid at very small angles (0.0003 to 0.3°), and therefore allowing larger precipitates to be quantified.

Figure I.3.4.1.1.7(a) provides an example of the data and fitting for the chromia-forming alloy sample fatigued at 900°C and 150 MPa. While both samples had two primary precipitate size distributions, USAXS data analyses show clear differences between the M2045 samples, which fatigue-tested at 900°C at 125 MPa and 150 MPa, fully reversible fatigue testing ($R=-1$). The curve in Figure I.3.4.1.1.7(a) was fit with two functions,

Log-Normal Population (LNP) and Lifshitz-Slyozov-Wagner (LSW), generating distributions that matched the SAXS data well. The M2045 sample fatigue-tested at 900°C for 125 MPa had LNP and LSW mean diameters of secondary γ' to be 50 ± 13 nm and 189 ± 4 nm, respectively. Similarly, the M2045 samples tested at 900°C for 150 MPa resulted in fits with LNP and LSW mean diameters of secondary γ' to be 26 ± 2 nm and 110 ± 12 nm, respectively, which are in the same range as those in Figure I.3.4.1.1.6(b). The fitting of the individual scattering contributions within the USAXS data produced results that were in good agreement with the precipitate distributions obtained from SEM, as observed in Figure I.3.4.1.1.7(b). Notably, the scattering data for these alloys systems is complex. Modeling of the 150 MPa samples required the inclusion of a contribution at high Q that is roughly equivalent to the inverse of the length (e.g., ~ 10 to 10000 Å) shown in Figure I.3.4.1.1.7. The observed humps in the SAXS curves were fit and correspond to an average reciprocal precipitate size. Knowledge of the system under study and experience with other alloy systems indicates that this high Q contribution is the result of scattering of very small particles or scattering from the surface roughness of particles. The source of the high Q contributions is below the particle size range accessible using SEM; therefore, the TEM/APT analyses are being pursued to fully characterize its origins.

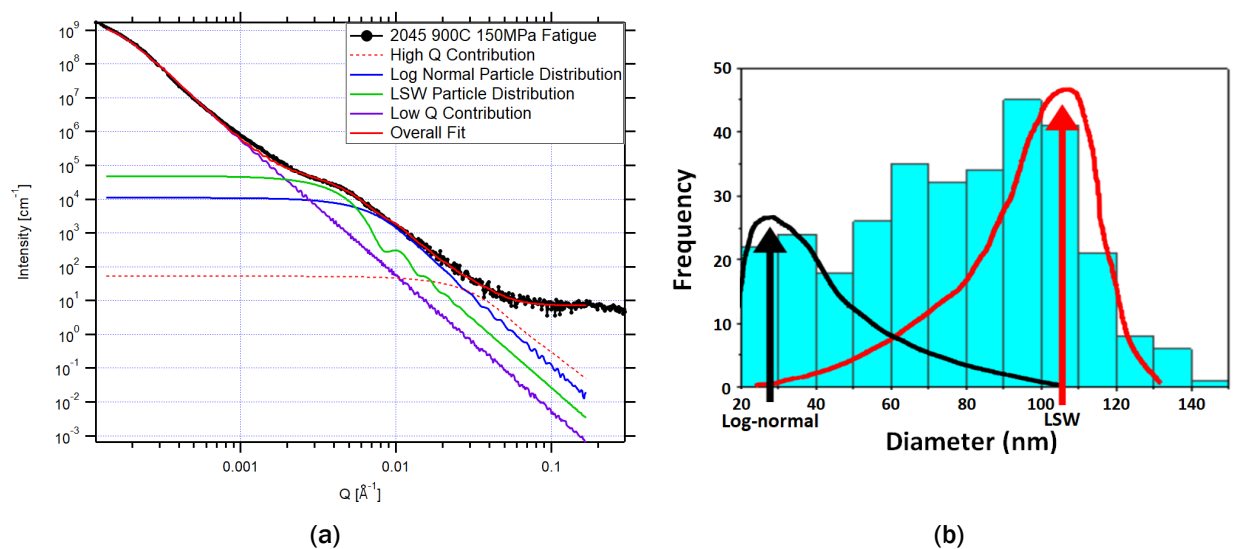


Figure I.3.4.1.1.7. (a) USAXS/SAXS data and model scattering contributions for chromia-forming alloy sample fatigue-tested at 900°C for 150 MPa. (b) SEM γ' size analysis with schematic overlay of Log-normal and LSW distributions from γ' modeling of USAXS data. Source: ANL.

At ORNL, characterization of carbides using electron probe microanalysis (EPMA) is currently being employed to study the role of carbides and surface oxides on fatigue life of ORNL-developed chromia-forming Ni-Fe-Cr-Al-Ti-based alloys. Preliminary work was performed on a carbide containing commercial alloy Haynes[®]282[®], which is currently being considered as an alternate candidate for exhaust valves. EPMA uses wavelength dispersive x-ray spectroscopy and has the sensitivity and accuracy to determine exact composition of carbides. Compositional analyses were acquired on an electron microprobe (JEOL 8200) equipped with five tunable wavelength dispersive spectrometers. The elements acquired using EDS were Ti, Cr, Co, Ni, Mo, Fe, Mn, Si, Al, and C. Pure standards were used to calibrate all elements, and a ZAF algorithm [15] was used for matrix correction. Figure I.3.4.1.1.8 shows a region of interest on Haynes[®]282[®] revealing the presence of carbides and a Mo-rich phase. EPMA point analysis with a 1- μ m spot size successfully characterized the composition of these phases with total weight percentages close to 100%, which is indicative of the accuracy of the measurement. The carbides were complex, $\sim 33\text{Ti}/15\text{Mo}/3\text{Cr}/2\text{Ni}/46\text{C}$ at.% and known to improve the fatigue properties of these alloys. The Mo-rich phase contained $\sim 33\text{Cr}/27\text{Mo}/27\text{Ni}/9\text{Co}/2\text{Si}$ at.%.

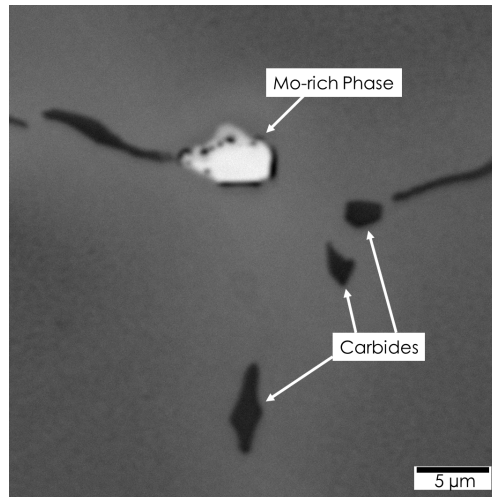


Figure I.3.4.1.1.8. BSE image of carbides and a Mo-rich phase in CC282. Source: ORNL.

Thrust 4A Results in Support of Task 3A1

New AM Al alloys that possess unique fine microstructures, which typically result in improved strength and ductility, are being developed by ORNL. Similar to Task 1A1, there is interest in developing durable alloys capable of retaining strength with extended exposure at elevated temperatures (e.g., $>300^{\circ}\text{C}$), with the difference being the alloys in Task 3 are being designed as a feedstock for 3D printing rather than casting. The new alloys include Al-Cu-Ce-X alloys (where X is another element of interest, such as Mn or Zr). Here, the phases within the microstructure and local mechanical properties were characterized.

At ORNL, the microstructure and crystal structure of phases present in AM Al-Cu-Ce(-Zr) alloys with an exceptional combination of additive processability and mechanical properties [16] were studied via atomic-level HAADF imaging techniques in the JEOL 2200FS STEM. HAADF images correlated to crystal structure models and image simulations can provide significant support for the analysis of crystal structure as suggested by XRD and other methods. Figure I.3.4.1.1.9 is an example of the determination of the structure of one of the phases in the additively manufactured Al-Cu-Ce-Zr alloy studied in this Thrust 4A project. In these HAADF images, atomic columns show contrast related to the average atomic number of elements in the column, so that the columns will show “brightness” nominally related by $Z^{1.7}$, where Z is the average atomic number. Columns of Ce atoms ($Z=58$) would therefore be greater than three times as bright as the columns of equal numbers of Cu atoms ($Z=29$), and 13 times as bright as the equal numbers of Al atoms ($Z=13$). Cerium contrast therefore dominates the HAADF images. In the study, the XRD results showed a diffraction pattern similar to the $\text{Al}_{24}\text{Cu}_8\text{Ce}_3\text{Mn}$ phase. The resulting lattice parameter of this phase was adjusted and then used for image simulations and structure matching. Although the $\text{Al}_{24}\text{Cu}_8\text{Ce}_3\text{Mn}$ phase was not anticipated to form in Al-Cu-Ce(-Zr) alloys based on existing thermodynamic databases, a “grain” was isolated in a region of the α -Al matrix and was tilted so that a strong “low-index” zone axis orientation was obtained, as observed in Figure I.3.4.1.1.9(a). The HAADF images were obtained at direct magnifications of 8-10Mx, as can be seen in Figure I.3.4.1.1.9(b). Comparison of the HAADF image in Figure I.3.4.1.1.9(c) with a crystal structure projection of the $\text{Al}_{24}\text{Cu}_8\text{Ce}_3\text{Mn}$ phase along the $\langle 110 \rangle$ zone axis orientation, as shown in Figure I.3.4.1.1.9(b) and the insets, reveal a good match with the general intensities of the atomic columns in the image to that of the model. A computed diffractogram (not shown) from the image also showed a good match of the periodicities of the computed pattern with those from the expected electron diffraction pattern from the structure. All the correlated results from the STEM imaging and XRD studies strongly support the idea that the general structure of the AM Al-Cu-Ce-Zr phase structure is consistent with that of $\text{Al}_{24}\text{Cu}_8\text{Ce}_3\text{Mn}$ (with Zr likely substituting for Mn in this alloy). This result was further supported by a similar analysis of a HAADF image from another zone axis orientation of this phase.

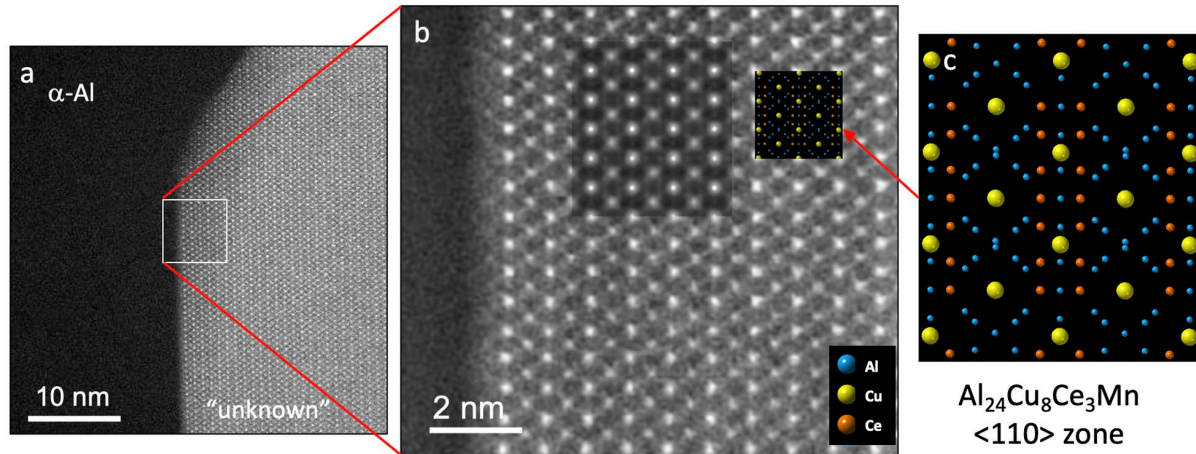


Figure I.3.4.1.1.9. (a) Al-Cu-Ce-Zr phase in the Al matrix that is oriented to a low-index zone axis orientation. (b) Atomic column image at 10Mx direct magnification from the thin edge of the phase grain. (c) The projection of the $\text{Al}_{24}\text{Cu}_8\text{Ce}_3\text{Mn}$ proposed crystal structure in the $\langle 110 \rangle$ zone axis orientation. An image simulation and the crystal structure projection shown in the inset suggest a good match of the phase to the proposed crystal structure. Source: ORNL.

At ONRL, APT has been extensively utilized in the characterization of an AM ACMZ alloy in the as-fabricated and aged conditions. The RT tensile strength of as-fabricated AM ACMZ is 50 MPa higher than its cast and aged counterpart. This increase in strength is maintained at elevated temperatures up to $\sim 300^\circ\text{C}$. In the as-fabricated condition, the eutectic θ structure and supersaturation of Zr (an L_{12} forming element) in the matrix, both results of the very rapid cooling rates resulting from the laser powder bed AM processes, are responsible for the ambient and elevated temperature properties of this alloy. While the θ network primarily contributes to the RT strength, the supersaturation of Zr allows for a high number density of coarsening resistant $\text{L}_{12}\text{-Al}_3\text{Zr}$ precipitates to form and stabilize the alloy at elevated temperatures. The use of APT allowed us to directly measure the size, number density, and volume fraction of the $\text{L}_{12}\text{-Al}_3\text{Zr}$ as a function of aging time and temperature, and the values were used as inputs for strengthening models. Although θ' is not the major strengthening precipitate in AM ACMZ, APT has also found similar Zr and Mn segregation to θ' interfaces as in the cast alloy, which could also contribute to thermal stability. APT has also been utilized to identify phase compositions in printed versions of Al-Ce-Mn, Al-Cu-Ce, Al-Cu-Ce-Zr, Al-Cu-Ce-Zr-Mn, Al-Ce-Ni-Mn, and Al-Ce-Mg-Zr alloys. These other alloy classes contain several phases that are difficult to identify, making compositional measurements from APT important for phase identification.

At PNNL, an Al-11Ce-3Ni-1Mn (wt.%) sample was fabricated by LPBF AM. When creep tested at 300°C , 350°C , and 400°C under applied tensile loads of ranging from 30 to 80 MPa, the alloy appeared to nucleate voids at the melt pool boundaries. To understand the mechanisms that may be leading to this mechanical behavior, as a part of Thrust 4A, an *in-situ* nanomechanical testing device, Bruker Hysitron PI89, installed inside a Thermo Fisher Scientific PFIB system was used to conduct site-specific nanomechanical testing of melt pool boundaries. First, without regard to melt pool locations, etc., the average hardness values of the alloy were found to be 1.63 ± 0.40 , 1.59 ± 0.12 , and 0.67 ± 0.07 GPa at ambient, 200°C , and 300°C , respectively. The small standard deviations suggest no significant change in hardness on the melt pool boundaries versus the interiors. Next, the melt pool boundaries and interiors were identified using SEM in the backscatter mode, as shown in Figure I.3.4.1.1.10(a), in preparation for site-specific testing. Two micropillars, each having a 1:2 (diameter to height) aspect ratio, were machined by milling the area between the inner and outer yellow circle marked using Xe ions in PFIB, as shown in Figure I.3.4.1.1.10(b). The engineering stress-strain curve recorded during the *in-situ* micropillar compression test along with images of the micropillar deformation are shown in Figure I.3.4.1.1.10(c). Initial testing indicated little difference in deformation between the melt pool boundaries versus interiors; the failure mode was mostly barrel type with many shear bands forming during deformation,

as observed by the white arrows shown in Figure I.3.4.1.10(c), denote the deformation bands that are a consequence of compression testing. The next steps of this project include comparing these site-specific micropillar compression test results with macro-scale creep test results of these additively manufactured alloys to ultimately help reveal the influence of local microstructural heterogeneity, such as the melt pool boundaries generated by AM on the macro-scale mechanical properties.

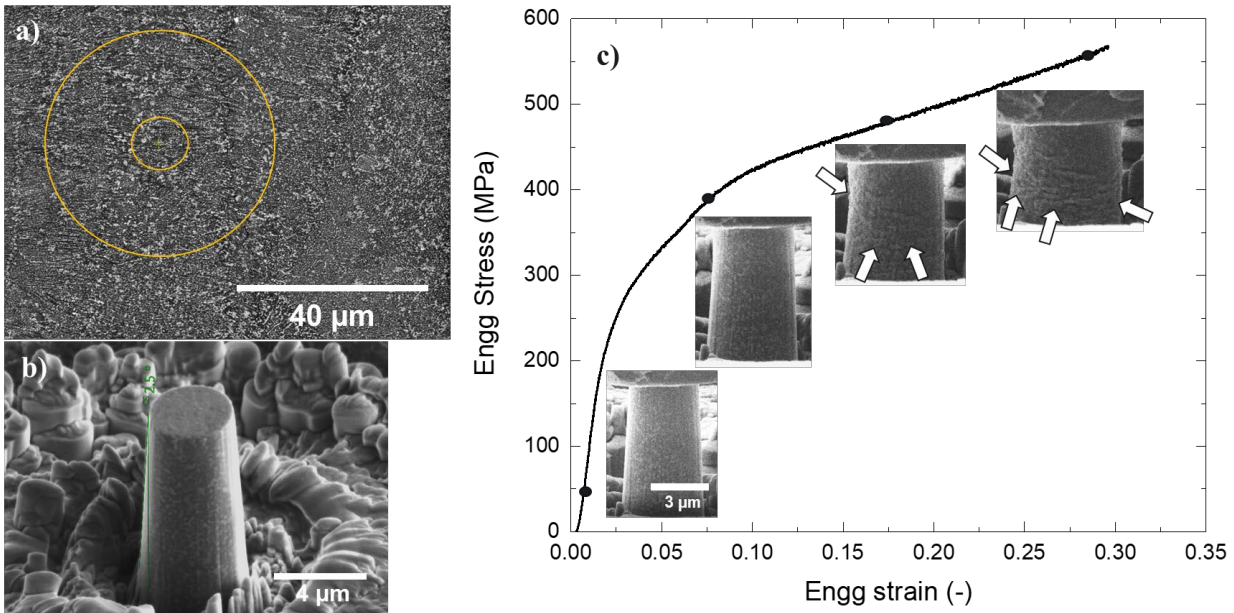


Figure I.3.4.1.1.10. (a) SEM-BSE image of the Al-11Ce-3Ni-1Mn (wt.%) fabricated by LPBF AM followed by stress relief annealing. The area marked in between the inner and outer circle was removed by Xe ion milling in PFIB to fabricate a micropillar. (b) A final micropillar fabricated using PFIB milling before micropillar compression test. (c) The stress-engineering strain curve along with the insets of the compression tester top and deformed pillar with the white arrows highlighting specific morphological changes on the pillar during compression at ambient temperature. Source: PNNL.

Rapid cooling rates during AM can generate vastly different alloy microstructures and resultant mechanical properties relative to their conventionally processed counterparts. Cast ACMZ are a new class of high-temperature Al alloys with an extended microstructural stability up to 350°C as compared to 250°C in commercial Al alloys [17]. An ACMZ alloy variant with a higher Cu content (such as 9 wt.%) is particularly amenable to additive processing owing to its excellent hot-tearing resistance [18]. AM leads to significant refinement in the size of stable θ -Al₂Cu and metastable θ' -Al₂Cu precipitates, as well as the matrix grain size in the AM ACMZ (Al-9Cu-0.45Mn-1Zr wt.%) alloy as compared to the cast ACMZ alloy of a similar composition (Al-9Cu-0.45Mn-0.2Zr wt.%) [19]. The additive ACMZ alloy exhibits both higher strength and ductility compared to the cast ACMZ in the RT to 300°C temperature range, as shown in Figure I.3.4.1.1.11(a) for RT; thus, overcoming the limitations of the typical strength-ductility tradeoff prevalent in metallic materials. The finer microstructure in additive ACMZ is consistent with enhanced strength, but it improves alloy ductility as well. Cross-sectional SEM images in Figure I.3.4.1.1.11(b) and Figure I.3.4.1.1.11(c) show widespread fracture of coarser θ intermetallic precipitates along the GBs in cast ACMZ but only limited fracture of the much finer, distributed θ precipitates in additive ACMZ, respectively. This suggests a size-dependent fracture strength of θ precipitates, which is confirmed with synchrotron XRD *in-situ* tensile tests at RT. Figure I.3.4.1.1.11(d) shows lattice stress evolution in θ precipitates as calculated using the (200) reflection from the θ parallel to the tensile loading axis vs. macroscopic strain. The coarser θ precipitates in cast ACMZ sustain much lower peak stress consistent with their widespread fracture compared to finer θ precipitates in additive ACMZ, which sustain a much higher peak stress, consistent with their limited fracture.

Thus, refinement in the size of brittle θ precipitates with high cooling rates in AM delays crack initiation and increases ductility of the additive ACMZ alloy compared to the cast ACMZ alloy with coarser θ precipitates and early crack initiation.

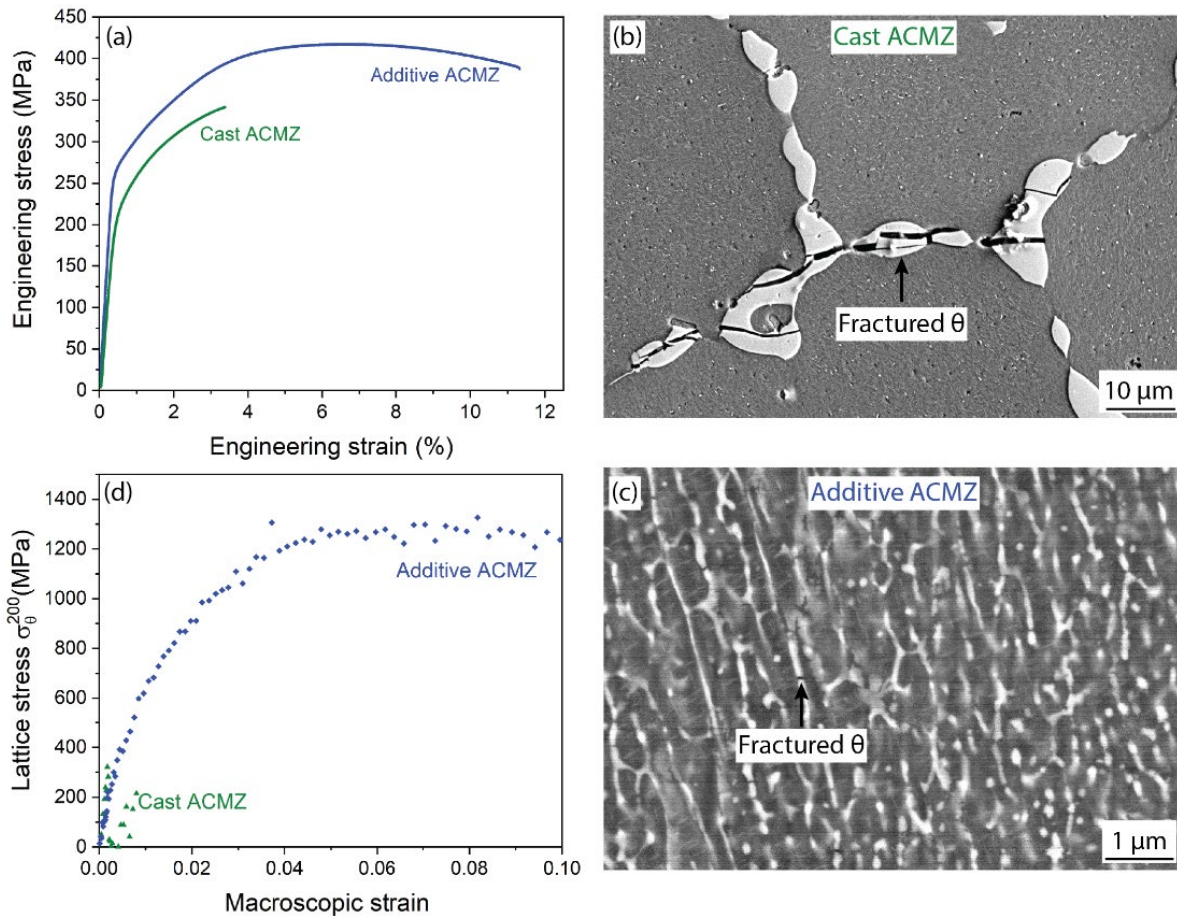


Figure I.3.4.1.1.11. (a) RT tensile stress-strain curves of AA cast and as-fabricated additive ACMZ alloys. (b)-(c) Cross-sectional SEM images showing fractured θ precipitates in cast and additive ACMZ samples, respectively, after tensile tests. (d) Lattice stress in θ precipitates along the loading axis vs. macroscopic tensile strain calculated using (200) reflection from θ during *in-situ* tensile tests. Source: ORNL and ANL.

Conclusions

Understanding the behavior of alloy systems under a variety of processing and use conditions requires a suite of advanced materials characterization techniques to clarify chemical, microstructural, and phase changes as a function of time, elevated temperature, pressure/loading, and other conditions. The advanced characterization techniques and examples of FY 2021 Thrust 4 projects highlighted here are proving essential for accomplishing the mission of accelerated development of new, advanced alloys under the PMCP. In short, high-resolution aberration-corrected STEM imaging allows direct imaging of crystalline phases and chemical information in the alloys being studied. Research utilizing the high intensity, high-energy, monochromatic synchrotron x-rays delivered quantification of trace phases/small precipitates. APT shows the placement of atoms at nanometer resolution within precipitates and at matrix-precipitate interfaces. This combination of advanced characterization tools from ORNL, ANL, and PNNL provide for essential, unique, and timely discovery, as well as the scientific understanding, which is enabling the rapid development of the next-generation of advanced materials for higher efficiency ground propulsion.

Key Publications

1. Bahl, S., L. Xiong, L. F. Allard, R. A. Michi, J. D. Poplawsky, A. C. Chuang, D. Singh, T. R. Watkins, D. Shin, J. A. Haynes, and A. Shyam, 2021, “Aging behavior and strengthening mechanisms of coarsening resistant metastable θ' precipitates in an Al-Cu alloy,” *Mater. Des.*, Vol. 198, Art. 109378.
2. Shower, P., J. Poplawsky, S. Bahl, and A. Shyam, 2021, “The role of Si in determining the stability of the theta ' precipitate in Al-Cu-Mn-Zr alloys,” *J. Alloys Compd.*, Vol. 862, Art. 158152.
3. Gwalani, B., S. Shukla, D. Leonard, J. D. Poplawsky, D. T. Pierce, L. Kovarik, G. Muralidharan, and A. Devaraj, 2021, “Understanding the microstructural stability in a gamma '-strengthened Ni-Fe-Cr-Al-Ti alloy,” *J. Alloys Compd.*, Vol. 886, Art. 161207.
4. Bahl, S., K. Sisco, Y. Yang, F. Theska, S. Primig, L. F. Allard, R. A. Michi, C. Fancher, B. Stump, R. Dehoff, A. Shyam, and A. Plotkowski, 2021, “Al-Cu-Ce(-Zr) alloys with an exceptional combination of additive processability and mechanical properties,” *Addit. Manuf.*, Vol. 48, Part B, Art. 102404.
5. Pillai, R., S. Dryepondt, B. L. Armstrong, M. J. Lance, and G. M. Muralidharan, 2021, “Evaluating the efficacy of aluminide coatings to improve oxidation resistance of high-performance engine valve alloys,” *Surf. Coat. Technol.*, Vol. 421, Art. 127401.
6. Peng, J. Y. Yamamoto, M. P. Brady, S. Lee, J. A. Haynes, and D. Shin, 2021, “Uncertainty quantification of machine-learning predicted creep property of alumina-forming austenitic alloys,” *JOM*, Vol. 73, pp. 164–173.
7. Poplawsky, J. D., R. Pillai, Q. Q. Ren, A. Breen, B. Gault, and M. P. Brady, 2022, “Measuring oxygen solubility in Ni grains and boundaries after oxidation using atom probe tomography,” *Scr. Mater.*, Vol. 210, Art. 114411.
8. Lee, Y., P. Nandwana, and S. Simunovic, 2021, “Powder spreading, densification, and part deformation in binder jetting additive manufacturing,” *Prog. Addit. Manuf.*, Vol. 1, No. 1, pp. 1–15.
9. Cakmak, E., P. Nandwana, D. Shin, Y. Yamamoto, M. N. Gussev, I. Sen, M. Hazar Seren, T. R. Watkins, and J. A. Haynes, 2019, “A comprehensive study on the fabrication and characterization of Ti-48Al-2Cr-2Nb preforms manufactured using electron beam melting,” *Materialia*, Vol. 6, Art. 100284.
10. Bahl, S., A. Plotkowski, K. Sisco, D. N. Leonard, L. F. Allard, R. A. Michi, J. D. Poplawsky, R. Dehoff, and A. Shyam, 2021, “Elevated temperature ductility dip in an additively manufactured Al-Cu-Ce alloy,” *Acta Mater.*, Vol. 220, Art. 117285.
11. Chisholm, M. F., D. Shin, G. Duscher, M. P. Oxley, L. F. Allard, J. D. Poplawsky, and A. Shyam, 2021, “Atomic structures of interfacial solute gateways to θ' precipitates in Al-Cu alloys,” *Acta Mater.*, Vol. 212, Art. 116891.
12. Milligan, B., D. Ma, L. F. Allard, A. Clarke, and A. Shyam, 2021, “Crystallographic orientation-dependent strain hardening in a precipitation-strengthened Al-Cu alloy,” *Acta Mater.*, Vol. 205, Art. 116577.
13. Yang, Y., S. Bahl, K. Sisco, M. Lance, D. Shin, A. Shyam, A. Plotkowski, and R. R. Dehoff, 2020, “Primary solidification of ternary compounds in Al-rich Al-Ce-Mn alloys,” *J Alloys Compd.*, Vol. 844, No. 5, Art. 156048.
14. Cheng, J., M. Gussev, J. Allen, X. Hu, A. Moustafa, D. A. Splitter, and A. Shyam, 2020, “Deformation and failure of PrintCast A356/316 L composites: Digital image correlation and finite element modeling,” *Mater. Des.*, Vol. 195, Art. 109061.
15. Bahl, S., X. Hu, K. Sisco, J. A. Haynes, and A. Shyam, 2020, “Influence of Cu content on the high-temperature tensile and low cycle fatigue behavior of cast-Al-Cu-Mn-Zr alloys,” *Int. J. Fatigue*, Vol. 140, Art. 105836.

16. Poplawsky, J. D., B. K. Milligan, L. F. Allard, D. Shin, P. Shower, M. F. Chisholm, and A. Shyam, 2020, "The synergistic role of Mn and Zr/Ti in producing Θ' /L12 co-precipitates in Al-Cu alloys," *Acta Mater.*, Vol. 194, pp. 577–586.
17. Peng, J., S. Bahl, A. Shyam, J. A. Haynes, and D. Shin, 2020, "Solute-vacancy clustering in aluminum," *Acta Mater.*, Vol. 196, pp. 747–758.
18. Plotkowski, A., K. Sisco, S. Bahl, A. Shyam, Y. Yang, L. Allard, P. Nandwana, A. Marquez Rossy, and R. R. Dehoff, 2020, "Microstructure and properties of a high-temperature Al-Ce-Mn alloy produced by additive manufacturing," *Acta Mater.*, Vol. 196, pp. 595–608.
19. Bahl, S., X. Hu, E. Hoar, J. Cheng, J. A. Haynes, and A. Shyam, 2020, "Effect of copper content on the tensile elongation of Al-Cu-Mn-Zr alloys: Experiments and finite element simulations," *Mater. Sci. Eng. A*, Vol. 772, Art. 138801.
20. Samolyuk, G. D., M. Eisenbach, D. Shin, Y. N. Osetsky, A. Shyam, and J. R. Morris, 2020, "Equilibrium solute segregation to matrix-precipitate interfaces in Al-Cu alloys from first principles," *Phys. Rev. Mater.*, Vol. 4, No. 7, Art. 073801.
21. Shyam, A., A. Plotkowski, S. Bahl, K. Sisco, L. F. Allard, Y. Yang, J. A. Haynes, and R. R. Dehoff, 2020, "An additively manufactured Al-Cu-Mn-Zr alloy microstructure and tensile mechanical properties," *Materialia*. Vol. 12, Art. 100758.
22. Milligan, B. K., S. Roy, C. S. Hawkins, L. F. Allard, and A. Shyam, 2020, "Impact of microstructural stability on the creep behavior of cast-Al-Cu alloys," *Mater. Sci. Eng. A*, Vol. 772, Art. 138697.
23. Shower, P., J. R. Morris, D. Shin, B. Radhakrishnan, L. F. Allard, and A. Shyam, 2019, "Temperature-dependent stability of θ' -Al₂Cu precipitates investigated with phase-field simulations and experiments," *Materialia*, Vol. 5, Art. 100185.
24. Allard, L. F., D. R. Leonard, J. D. Poplawsky, M. F. Chisholm, B. D. Eckhart, A. Shyam, F. S. Walden, B. B. Larson, R. Kelly, A. Stokes, and W. C. Bigelow, 2019, "The utility of Xe-plasma FIB for Preparing aluminum alloy specimens for MEMS-based *in-situ* double-tilt heating experiments," *Microsc. Microanal.*, Vol. 25, Suppl. 2, pp. 1442–1443.
25. Wang, J., N. A. Yousefzadi, J. D. Blanks, D. Shin, S. Lee, A. Shyam, H. Rezayat, and S. Shin, 2019, "Machine-learning for thermal transport analysis of aluminum alloys with precipitate morphology," *Adv. Theory Simul.*, Vol. 2, No. 4, Art. 1800196.
26. Shower, P., J. Morris, D. Shin, B. Radhakrishnan, J. Poplawsky, and A. Shyam, 2019, "Mechanisms for stabilizing Θ' (Al₂Cu) precipitates at elevated temperatures investigated with phase-field modeling," *Materialia*, Vol. 6, Art. 100335.
27. Wang, J., S. Shin, A. Y. Nobakht, and A. Shyam, 2019, "Structural deformation and transformation of θ' -Al₂Cu precipitate in Al matrix via interfacial diffusion," *Comput. Mater. Sci.*, Vol. 156, pp. 111–120.
28. Cakmak, E., N. Sridharan, S. V. Venkatakrishnan, H. Z. Bilheux, L. J. Santodonato, A. Shyam, and S. S. Babu, 2018, "Feasibility study of making metallic hybrid materials using additive manufacturing," *Metall. Mater. Trans. A-Phys. Metall. Mater. Sci.*, Vol. 49, pp. 5035–5041.
29. Shyam, A., S. Roy, D. Shin, J. D. Poplawsky, L. F. Allard, Y. Yamamoto, J. R. Morris, B. Mazumder, J. C. Idrobo, A. Rodriguez, T. R. Watkins, and J. A. Haynes, 2019, "Elevated temperature microstructural stability in cast Al-Cu-Mn-Zr alloys through solute segregation," *Mater. Sci. Eng. A*, Vol. 765, Art. 138279.

References

1. Muralidharan, G., “Low-cost, high-strength Fe-Ni-Cr alloys for high-temperature exhaust valve applications,” U.S. Patent 9,752,468 B2, September 5, 2017.
2. Bahl, S., L. H. Xiong, L. F. Allard, R. A. Michi, J. D. Poplawsky, A. C. Chuang, D. Singh, T. R. Watkins, D. Shin, J. A. Haynes, and A. Shyam, 2021, “Aging behavior and strengthening mechanisms of coarsening resistant metastable θ' precipitates in an Al-Cu alloy,” *Mater. Des.*, Vol. 198, Art. 109378.
3. Nie, J.-F., and B. C. Muddle, 2008, “Strengthening of an Al-Cu-Sn alloy by deformation-resistant precipitate plates,” *Acta Mater.*, Vol. 56, No. 14, pp. 3490–3501.
4. Roy, S., L. F. Allard, A. Rodriguez, W. D. Porter, and A. Shyam, 2017, “Comparative evaluation of cast-aluminum alloys for automotive cylinder heads: Part II-Mechanical and thermal properties,” *Metall. Mater. Trans. A–Phys. Metall. Mater. Sci.*, Vol. 48, No. 5, pp. 2543–2562.
5. Nie, J.-F., 2014, “Physical metallurgy of light alloys,” in: Laughlin, D. E., and K. Hono (eds.), *Physical Metallurgy (Fifth Edition)*, Elsevier, Oxford, U.K., pp. 2009–2156.
6. Poplawsky, J. D., B. K. Milligan, L. F. Allard, D. Shin, P. Shower, M. F. Chisholm, and A. Shyam, 2020, “The synergistic role of Mn and Zr/Ti in producing θ' /L1(2) co-precipitates in Al-Cu alloys,” *Acta Mater.*, Vol. 194, pp. 577–586.
7. Shower, P., J. Poplawsky, S. Bahl, and A. Shyam, 2021, “The role of Si in determining the stability of the θ' precipitate in Al-Cu-Mn-Zr alloys,” *J. Alloys Compd.*, Vol. 862, Art. 158152.
8. Lambeets, S. V., E. J. Kautz, M. G. Wirth, G. J. Orren, A. Devaraj, and D. E. Perea, 2020, “Nanoscale perspectives of metal degradation via *in-situ* atom probe tomography,” *Top Catal.*, Vol. 63, Nos. 15–18, pp. 1606–1622.
9. Kautz, E. J., B. Gwalani, S. V. M. Lambeets, L. Kovarik, D. K. Schreiber, D. E. Perea, D. Senior, Y. S. Liu, A. K. Battu, K. P. Tseng, S. Thevuthasan, and A. Devaraj, 2020, “Rapid assessment of structural and compositional changes during early stages of zirconium alloy oxidation,” *NPJ Mater. Degrad.*, Vol. 4, No. 1, Art. 29.
10. Gwalani, B., S. Shukla, D. Leonard, J. D. Poplawsky, D. T. Pierce, L. Kovarik, G. Muralidharan, and A. Devaraj, 2021, “Understanding the microstructural stability in a γ' -strengthened Ni-Fe-Cr-Al-Ti alloy,” *J. Alloys Compd.*, Vol. 886, Art. 161207.
11. Loomis, W. T., D. L. Sponseller, and J. W. Freeman, 1972, “Influence of molybdenum on γ' phase in experimental nickel-base superalloys,” *Metall. Trans.*, Vol. 3, No. 4, pp. 989–1000.
12. Chen, Y. Q., T. J. A. Slater, E. A. Lewis, E. M. Francis, M. G. Burke, M. Preuss, and S. J. Haigh, 2014, “Measurement of size-dependent composition variations for γ' precipitates in an advanced nickel-based superalloy,” *Ultramicroscopy*, Vol. 144, pp. 1–8.
13. Sudbrack, C. K., K. E. Yoon, R. D. Noebe, and D. N. Seidman, 2006, “Temporal evolution of the nanostructure and phase compositions in a model Ni-Al-Cr alloy,” *Acta Mater.*, Vol. 54, No. 12, pp. 3199–3210.
14. DOE, 2021, *DOE VTO Materials 2020 Annual Progress Report*, DOE/EE-2336, April 2021.
15. Waters, D., 2008, “Practical Aspects of Mineral Thermobarometry, Part 1. Electron Microprobe Analysis,” <https://www.earth.ox.ac.uk/~davewa/pt/pt01.html>.
16. Bahl, S., K. Sisco, Y. Yang, F. Theska, S. Primig, L. F. Allard, R. A. Michi, C. Fancher, B. Stump, R. Dehoff, A. Shyam, and A. Plotkowski, 2021, “Al-Cu-Ce(-Zr) alloys with an exceptional combination of additive processability and mechanical properties,” *Addit. Manuf.*, Vol. 48, Part B, Art. 102404.

17. Shyam, A., S. Roy, D. Shin, J. D. Poplawsky, L. F. Allard, Y. Yamamoto, J. R. Morris, B. Mazumder, J. C. Idrobo, A. Rodriguez, T. R. Watkins, and J. A. Haynes, 2019, “Elevated temperature microstructural stability in cast Al-Cu-Mn-Zr alloys through solute segregation,” *Mater. Sci. & Eng. A: Struct. Mater.: Prop. Microstruct. Process.*, Vol. 765, Art. 138279.
18. Sabau, A. S., S. Mirmiran, C. Glaspie, S. M. Li, D. Apelian, A. Shyam, J. A. Haynes, and A. F. Rodriguez, 2018, “Hot-tearing assessment of multicomponent nongrain-refined Al-Cu alloys for permanent mold castings based on load measurements in a constrained mold,” *Metall. Mater. Trans. B*, Vol. 49, No. 3, pp. 1267–1287.
19. Shyam, A., A. Plotkowski, S. Bahl, K. Sisco, L. F. Allard, Y. Yang, J. A. Haynes, and R. R. Dehoff, 2020, “An additively manufactured Al-Cu-Mn-Zr alloy microstructure and tensile mechanical properties,” *Materialia*, Vol. 12, No. 6, Art. 100758.

Acknowledgments

For development task 1A1, 2A1, and 3A1, the authors wish to acknowledge the contributions of the following individuals to this report:

- ORNL: L. F. Allard, S. Bahl, M. Lance, R. Michi, G. Muralidharan, A. Plotkowski, J. D. Poplawsky, S. Shukla, and A. Shyam
- ANL: A. C. Chuang, M. Frith, J. Ilavsky, J. Thomas, and L. Xiong
- PNNL: T. A. Ajantiwalay, B. Gwalani, L. Kovarik, S. Lambeets, and J. Liu.

I.3.4.2 Advanced Computation (4B)

I.3.4.2.1 Modeling of Light-Duty Engines (Task 4B2) (Oak Ridge National Laboratory)

Charles E. A. Finney, Principal Investigator

Oak Ridge National Laboratory
1 Bethel Valley Road
Oak Ridge, TN 37830
E-mail: finneyc@ornl.gov

Jerry L. Gibbs, DOE Technology Manager

U.S. Department of Energy
E-mail: jerry.gibbs@ee.doe.gov

Start Date: October 1, 2019 End Date: September 30, 2022
Project Funding (FY 2021): \$125,000 DOE share: \$125,000 Non-DOE share: \$0

Project Introduction

Internal combustion engines power most vehicles in LD applications and are projected to remain a primary powerplant for automotive propulsion for at least the next 20 years [1], even accounting for the current heavy emphasis on electrification. Automotive LD engines have evolved significantly over the past several decades [2] with specific power and emissions output targets being driven by fuel economy and pollutant emissions regulations, such as the Corporate Average Fuel Economy standards [3]. This rapid evolution has been enabled by advances in combustion control and boosting (e.g., turbocharging), which has allowed smaller, lighter engines to outperform their predecessors. However, the consequence of increased specific output via intensified combustion is more extreme engine operating conditions, resulting in both higher temperatures and pressures experienced by engine materials. An initial study performed by ORNL in 2018 identified several potential advantages to higher performance materials that enable even higher specific engine output (e.g., more power output per unit volume of engine displacement) [4].

As in cylinder temperatures continue to increase, they are presently nearing the practical operating limit for common commercial alloys used in pistons, valves, and cylinder heads. A projection of advanced LD engine performance into the coming decades has identified anticipated increased temperature ranges in the cylinder environment [5], but the required materials properties to operate in these environments are still unknown. This project seeks to inform materials selection and development by using a computational approach to estimate the thermomechanical environment at intensified operating conditions, as well as the resulting stresses, fatigue, and creep experienced by the respective materials in key engine components.

The primary focus is on higher temperature cast-Al and wrought steel alloys, particularly for use in the pistons, valves, and cylinder head. More advanced versions of these alloys are anticipated to be critical in allowing the continued development of high-efficiency internal combustion engines. The fundamental efforts in this project seek to predict the thermomechanical materials environment at projected future operating conditions. The required performance and properties can help guide alloy selection or alloy development targets for future boosted engines with higher power densities and superior efficiencies.

Objectives

This project focuses on understanding the thermal and mechanical stresses experienced by engine cylinder component materials at extreme operating conditions. Key targets are LCF and creep in the various alloys that comprise the piston, valves, and cylinder head. This low-to-mid-technology readiness level study will provide insight into projected operating conditions and suggest the needs and targets for future materials research.

Approach

A computational approach was employed to model combustion and heat transfer for LD internal combustion engines at several speeds and loads. Computational models were constructed based on measured design data. Limited engine validation data were used to tune and calibrate the models to match experimental engine performance. Once the combustion models were validated at known conditions and performance characteristics, operating points at intensified combustion regimes were simulated, and cylinder pressure and cylinder heat flux maps were calculated. These combustion outputs were then used as boundary conditions for a mechanical-loading model to evaluate the stresses and other materials responses to the combustion conditions. A multi-year plan beginning in FY 2019 aimed for the first year to assemble and validate the model components. The subsequent two years have focused on the exploration of potential operating scenarios using these models.

The target engine platform simulated was a GM 2.0 L turbocharged direct-injected LNF “Ecotec” engine, rated at 260 bhp, 260 ft-lb in stock trim. The engine is used by complementary activities funded by the DOE VTO in the Partnership on Advanced Combustion Engines program, which provides experimental validation data at a limited set of operating points. Both programs have the same computational models but use them much differently based on the programmatic goals.

The two computational models used herein for combustion simulations are a low-dimensional treatment and a high-dimensional treatment. Here, low-dimensional means that the properties of a component volume might be described by a single, mean value (0D), or simply along a characteristic length (1D), without accounting for variations in other directions (for instance, radially or circumferentially), whereas the high-dimensional (3D) treatment accounts for all variations with very fine (e.g., 0.5 mm – 4.0 mm) spatial resolution. Both models use design and engine operating data measured at ORNL. The low-dimensional model is implemented in the software code GT-POWER, an industry-standard system-level simulation suite with components catered for ICE modeling. The GT-POWER model incorporates high-fidelity geometrical surface data of the pistons, valves, and head as measured for use in conjugate heat transfer modeling to solve for materials temperatures. The high-dimensional model is implemented in the software code CONVERGE, an industry standard computational fluid dynamics (CFD) code with high-fidelity combustion and fluid dynamics models. The CONVERGE model also uses the measured geometrical data for conjugate heat transfer modeling.

The structural model for thermally and mechanically induced stresses in the materials has been implemented in ANSYS, an industry standard code based on finite element modeling. The code uses a solid model based on the same surfaces used in the combustion models. Cylinder heat flux maps and cylinder pressures from the high-dimensional combustion model were used as boundary conditions. Additionally, the thermal conditions of structural cooling boundaries—such as the head gallery, the water jacket, and the piston gallery—were specified or calculated using the CFD code. The relevant materials thermal and physical properties for each component were also included.

A key advantage of this study was the use of temperature-dependent thermal materials properties, such as thermal conductivity, specific heat capacity, and material density. These properties are integral to the material thermal diffusivity, which describes how heat dissipates through a medium. In many or most CFD simulations, a constant diffusivity, usually measured at RT, is used. However, thermal diffusivity can vary by up to 50% between RT and engine operating temperatures, and simulations that use only a constant thermal diffusivity can fail to calculate realistic temperatures in materials in engines operating at extreme conditions. This project had access to accurate, temperature-dependent thermal diffusivity data for engine-relevant alloys, either from the literature or measured at ORNL. Additionally, such properties data are available from ORNL measurements of the advanced powertrain materials, capable of significantly higher temperatures than the stock materials. These new materials developed under the VTO PMCP were used in these computational studies to examine the effects of materials substitution.

Results

In FY 2021, a large scoping study was conducted using the low-dimensional (GT-POWER) model. In this study, several operating conditions were examined—two engine speeds at three load points each—and two materials suites were studied. The first consisted of current, commercially available alloys, whereas the second consisted of the advanced alloys developed by ORNL under VTO sponsorship. A key objective was to gauge whether these new materials can withstand the higher temperatures and thermal loads predicted at the intensified conditions. The engine speeds were 2,000 revolutions per minute (RPM), as that was the speed at which the engine validation data had been acquired by the ORNL engine test cells in previous experimental studies, and 5,000 RPM, where some of the most intensive combustion occurs, usually under transient conditions. At both engine speeds, a peak load baseline was simulated, and two conditions, with 25% and 50% more power output, were simulated. Additionally, two cooling scenarios were simulated, with 50% less and 50% more cooling compared with the baseline to determine whether the current commercial engine materials could suffice under enhanced cooling, or whether advanced materials could survive with less cooling, and thus lower auxiliary loads, with attendant vehicle efficiency benefits.

The materials suites used in the study are shown in Table I.3.4.2.1.1. For each engine component, the service temperature limit was determined from either the literature or ORNL measurements of each alloy is listed. These service limits form the criterion for whether a material is suitable for a given component at a given operating condition. Details on how the materials and service limits were defined are available in a publication summarizing this study [6].

Table I.3.4.2.1.1. Materials Suites Used in the Study

Component	Commercial Alloy Suite	Service Limit [°C]	ORNL Alloy Suite (Developed under VTO)	Service Limit [°C]
Head	A356 + 0.5 Cu Cast-Al	230	ACMZ Cast Al-Cu-Mn-Zr	>300
Piston	M126 Cast Al-Si	325	Al-Ce-Ni-Mn 3D-printed Al	375
Exhaust Valves	IN751 Forged Ni-Cr	800–900	N21 Forged Ni-Fe-Cr	950
Intake Valves	Silchrome 1 Forged Stainless	538–590	2079 Forged Ni-Fe-Cr	Not determined
Block	319 Cast-Al	230	ACMZ Cast Al-Cu-Mn-Zr	>300

The importance of using temperature-dependent thermal properties is highlighted in Table I.3.4.2.1.2, where the maximum temperature in each component is reported for two baseline speed-load conditions. Two thermal diffusivity temperature dependences are examined: (1) using RT values at all temperatures (“constant diffusivity”); and (2) using measured thermal diffusivities that vary with temperature (“variable diffusivity”) from RT up to very high engine operating temperatures. The simulation software uses thermal diffusivity decomposed into thermal conductivity, specific heat capacity, and density as separate properties. For some components, such as the head, temperature dependence has a very small effect (5°C – 10°C), possibly due to the much higher thermal diffusivity of cast-Al alloys, as well as active fluid cooling. For the valves, however, the difference is quite pronounced (80°C – 100°C), partly because of the conductive geometry of the component and because of the very high temperatures that were experienced. A conclusion is that variable thermal diffusivity spanning a relevant temperature range should be used when available.

Table I.3.4.2.1.2. Effect of Diffusivity Temperature Dependence on Predicted Maximum Materials Temperatures

Component	Maximum Component Temperatures for the Commercial Alloy Suite [°C]			
	2,000 RPM 21.9 bar BMEP		5,000 RPM 17.7 bar BMEP	
	Constant Diffusivity	Variable Diffusivity	Constant Diffusivity	Variable Diffusivity
Head	195	191	234	227
Piston	263	260	309	304
Exhaust Valves	760	684	955	857
Intake Valves	635	592	709	653

Figure I.3.4.2.1.1 shows the predicted maximum temperatures in the cylinder head at the 2,000 RPM baseline load of 21.9 bar brake mean effective pressure (BMEP), as well as at 25% (27.4 bar) and 50% (32.9 bar) higher output loads. At this condition, the current state-of-the-art head material is predicted to be adequate at up to 25% load increase, but at higher loads, the materials temperatures could surpass the service limit, accounting for variabilities and uncertainties. The VTO-developed alloy, however, has more than adequate margin (around 70°C) even at a 50% load increase. A similar scenario is observed in Figure I.3.4.2.1.2, which shows exhaust valve temperature predictions at the baseline and intensified loads at 2,000 RPM. Here, current valve alloys are predicted to be sufficient at all levels of intensification at 2,000 RPM.

However, the higher fuel and heat loadings at 5,000 RPM is expected to tax stock valve materials significantly. A striking example of this is seen in Figure I.3.4.2.1.3, which shows the exhaust valve temperatures from the baseline condition at 5,000 RPM. Protective enrichment is a common strategy to reduce exhaust valve temperatures at higher loads by injecting extra fuel into the cylinder to lower the exhaust temperatures; this strategy adversely impacts fuel efficiency and emissions. Without enrichment, with all loads for the current stock materials, the exhaust valve temperatures would exceed their service limits, with higher potential for failure. However, using the VTO-developed valve alloys, all intensification strategies are tolerated by the exhaust valves. For the commercial alloys, increased levels of enrichment, with significant efficiency and pollutant emissions penalties, are required.

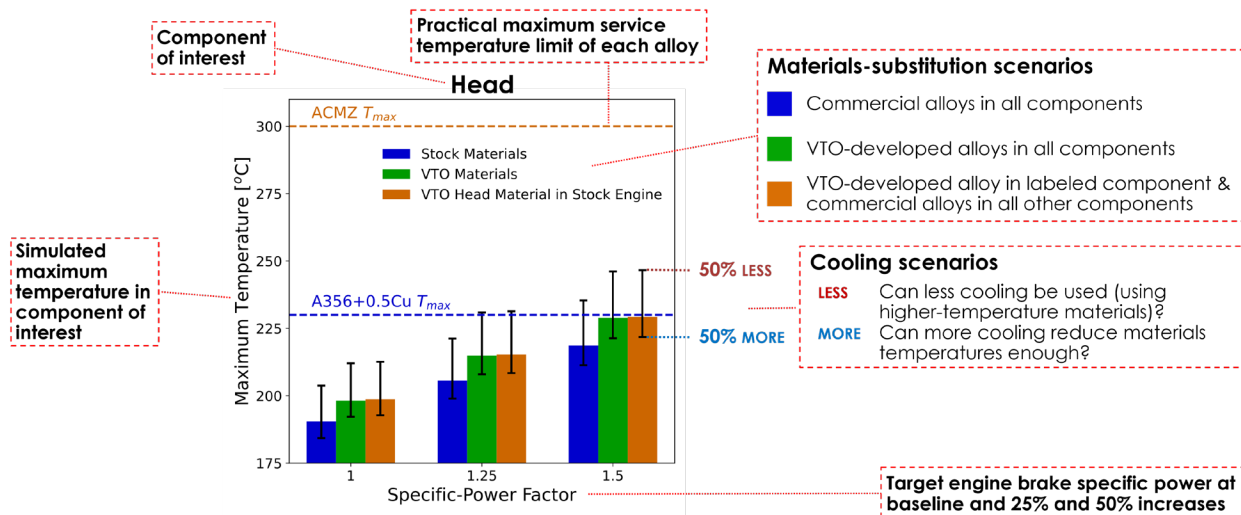


Figure I.3.4.2.1.1. Head temperature predictions starting from the baseline condition of 2,000 RPM and 21.9 bar BMEP, showing materials suites and cooling scenarios, along with the maximum service temperature of each alloy. Source: ORNL.

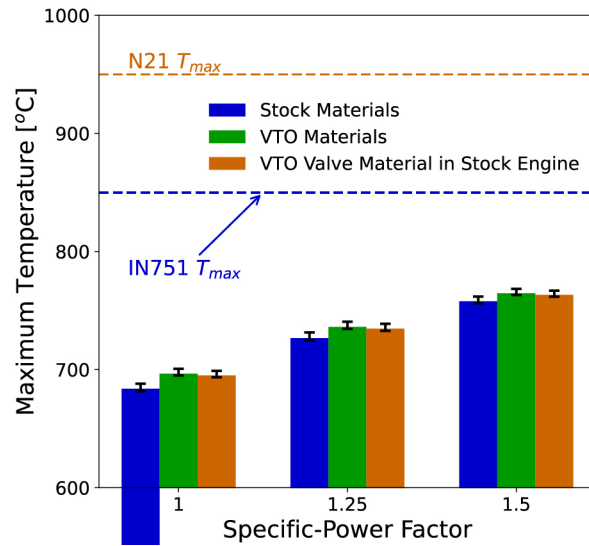


Figure I.3.4.2.1.2. Exhaust valve temperature predictions starting from the baseline condition of 2,000 RPM and 21.9 bar BMEP, showing materials suites and cooling scenarios, along with the maximum service temperature of each alloy. Source: ORNL.

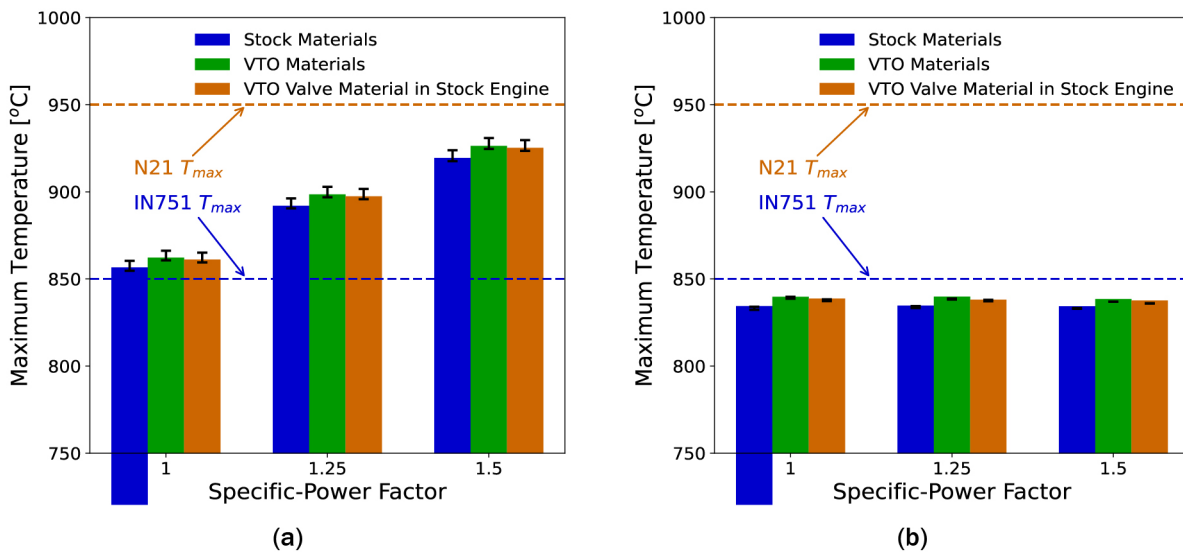


Figure I.3.4.2.1.3. Exhaust valve temperature predictions starting from the baseline condition of 5,000 RPM and 17.7 bar BMEP. Temperature management is (a) without and (b) with protective enrichment. Source: ORNL.

As seen in Figure I.3.4.2.1.4, commercial alloys are approaching their limits at the current levels of engine loading. With increased loading via specific output intensification, the VTO-developed alloys show significant promise for the higher temperatures and pressures projected to be experienced in future higher efficiency engines, or perhaps even future reciprocating engines fueled by hydrogen.

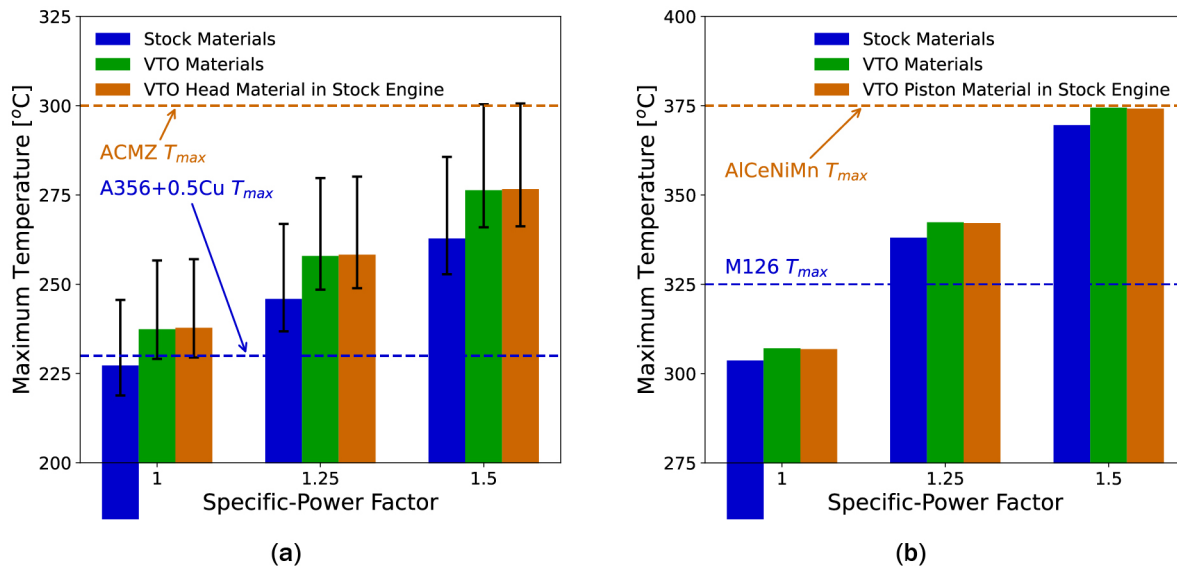


Figure I.3.4.2.1.4. (a) Head and (b) piston temperature predictions starting from the baseline condition of 5,000 RPM and 17.7 bar BMEP. Source: ORNL.

Conclusions

In this third project year, a scoping study of intensified combustion scenarios was conducted. This study showed that for some components, intensified combustion as projected in future engine operation will not pose a serious problem. However, for other components such as the piston crown, cylinder head, and exhaust valves, materials that can withstand the higher temperatures will need to be selected or developed. An additional finding was that emissions and efficiency penalties related to fuel enrichment at high loads could be eliminated by higher temperature engine materials. This knowledge will inform future materials selection and development for the next-generation of lightweight, high-efficiency ICEs, including future low-emissions range extenders for hybrid electric trucks, and perhaps future hydrogen fueled engines.

Key Publications

1. Reitz, R. D., H. Ogawa, R. Payri, T. Fansler, S. Kokjohn, Y. Moriyoshi, A. K. Agarwal, D. Arcoumanis, D. Assanis, C. Bae, K. Boulouchos, M. Canakci, S. Curran, I. Denbratt, M. Gavaises, M. Guenther, C. Hasse, Z. Huang, T. Ishiyama, B. Johansson, T. V. Johnson, G. Kalghatgi, M. Moike, S. C. Kong, A. Liepert, P. Miles, R. Novella, A. Onorati, M. Richter, S. Shuai, D. Siebers, W. Su, M. Trujillo, N. Uchida, B. M. Vaglieco, R. M. Wagner, and H. Zhao, 2019, "The future of the internal combustion engine," *Int. J. Engine Res.*, Vol. 21, No. 1, pp. 3–16.
2. Splitter, D., A. Pawlowski, and R. Wagner, 2016, "A historical analysis of the co-evolution of gasoline octane number and spark-ignition engines," *Front. Mech. Eng.*, Vol. 1, Art. 16.
3. U. S. National Highway Traffic Safety Administration (NHTSA) website, n.d., "Corporate average fuel economy." Available at: www.nhtsa.gov/laws-regulations/corporate-average-fuel-economy. Accessed 14 December 2021.
4. Mills, Z. G., C. E. A. Finney, K. D. Edwards, and J. A. Haynes, 2019, "Benefits of higher temperature operation in boosted SI engines enabled by advanced materials," *Proceedings of the 2018 Fall Technical Conference of the ASME Internal Combustion Engine Division*, 4–7 November 2018, San Diego, CA, USA. Paper ICEF2018-9739.
5. U. S. Department of Energy Vehicles Technologies Office website, 2013, "Light-duty vehicles technical requirements and gaps for lightweight and propulsion materials." Available at: www1.eere.energy.gov/vehiclesandfuels/pdfs/wr_ldvehicles.pdf. Accessed 14 December 2021.

6. Mills, Z. G., C. E. A. Finney, J. A. Haynes, A. A. Trofimov, H. Wang, D. T. Pierce, 2021, “Impact of materials properties on higher temperature engine operation,” SAE Technical Paper No. 2021-01-1142. DOI: 10.4271/2021-01-1142.

Acknowledgments

Co-investigators include Z. G. Mills and F. D. F. Chuahy of ORNL. A consulting contributor was J. A. Haynes of ORNL. Experimental validation data were provided by V. B. Colomer and D. A. Splitter of ORNL. Some materials thermal properties data were supplied by A. A. Trofimov, H. Wang, A. Shyam, D. T. Pierce, G. Muralidharan, Y. Yamamoto, and J. A. Haynes of ORNL.

I.4 Modeling of Powertrain Materials

I.4.1 Next-Generation High-Efficiency Boosted Engine Development (Ford Research and Advanced Engineering)

Michael Shelby, Principal Investigator

Ford Motor Company
 Research and Innovation Center
 2101 Village Road
 Dearborn, MI 48121
 E-mail: mshelby@ford.com

Jerry L. Gibbs, DOE Technology Manager

U.S. Department of Energy
 E-mail: jerry.gibbs@ee.doe.gov

Start Date: October 1, 2019 End Date: December 31, 2022
 Project continuation evaluated annually
 Project Funding (FY 2021): \$10,000,000 DOE share: \$7,566,730 Non-DOE share: \$2,433,270

Project Introduction

The next-generation high-efficiency engine development project is a 39-month DOE-EERE VTO-funded R&D effort. As shown in Figure I.4.1.1, the goal of the project is to combine advanced combustion system technologies, thermal management strategies, and advanced materials to demonstrate a turbocharged gasoline engine with peak efficiency exceeding the best of today’s hybrid electric vehicle (HEV) engines. While the market share of battery electric vehicles is increasing, most light-duty vehicles are projected to use conventional or HEV powertrains well beyond 2030. Improvements in engine efficiency and reductions in powertrain weight have strong leverage to reduce vehicle-related CO₂ emissions for decades to come. This project develops engine efficiency and weight-saving technologies that enable competitive, profitable internal combustion engines, targeting the highest production volume powertrains.

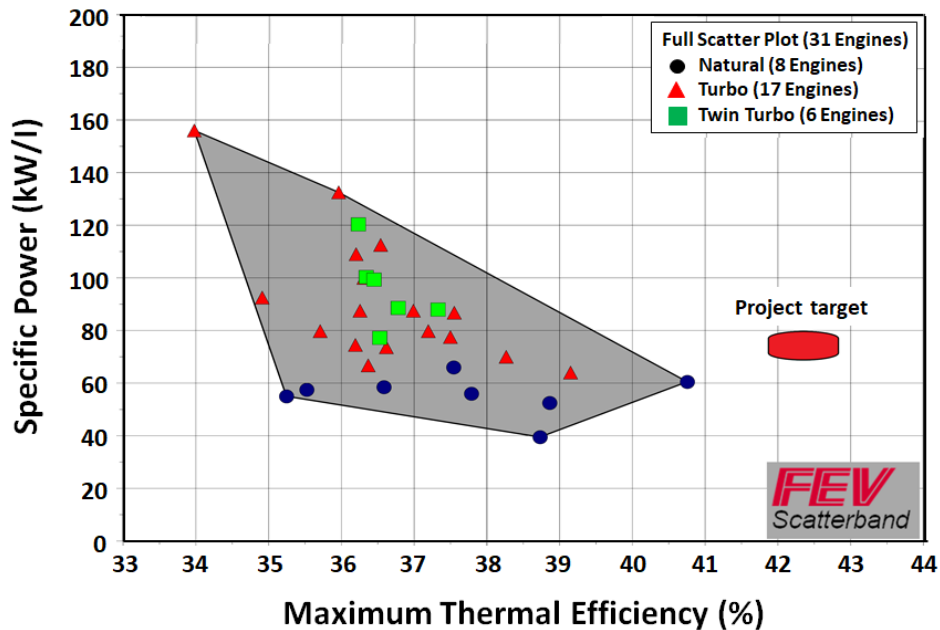


Figure I.4.1.1. Specific power vs. maximum efficiency. Source: FEV, Ford.

The project team consists of Ford Motor Company, FEV North America, and ORNL. Each partner brings different strengths to this collaboration, and the combined knowledge in powertrain, combustion, component design, analytical development, and manufacturing will ensure a successful project.

Objectives

The objective of this project is to develop an engine with advanced combustion technologies capable of achieving $\geq 23\%$ fuel efficiency improvement relative to a baseline 2016-model-year 3.5L V6 EcoBoost F150. The engine will be compliant with applicable U.S. Environmental Protection Agency (EPA) emissions standards and the fuel economy improvement will be demonstrated via engine dynamometer testing coupled to vehicle drive-cycle simulations. Advanced materials and weight-saving technologies will also be used to demonstrate the capability of $\geq 15\%$ weight-reduction of the baseline engine. These targets are particularly challenging given that the baseline engine is already a lightweight, downsized boosted engine.

FY 2021 concept design and analysis objectives are as follows:

- Continue combustion system modeling optimizing dilution tolerance, knock resistance, and burn rate.
- Continue single-cylinder engine (SCE) dynamometer studies supporting multi-cylinder engine (MCE) combustion and ignition design decisions and model validation.
- Complete all MCE design and analytical assessments required to finalize the design and support component hardware delivery by year-end.

Approach

To achieve the goals of the project, work will be divided into several overlapping workstreams as illustrated in Figure I.4.1.2. The technology selection process will be strongly guided by analytical tools, including 3D flow and combustion modeling, as well as structural and thermal analysis. Key items related to engine efficiency, outlined in the blue dotted circles of Figure I.4.1.2, will be demonstrated and developed using research SCEs. The final status of the fuel economy and weight targets will be demonstrated via dynamometer testing of a complete MCE—circled in yellow in Figure I.4.1.2—along with the regulatory drive-cycle simulations.

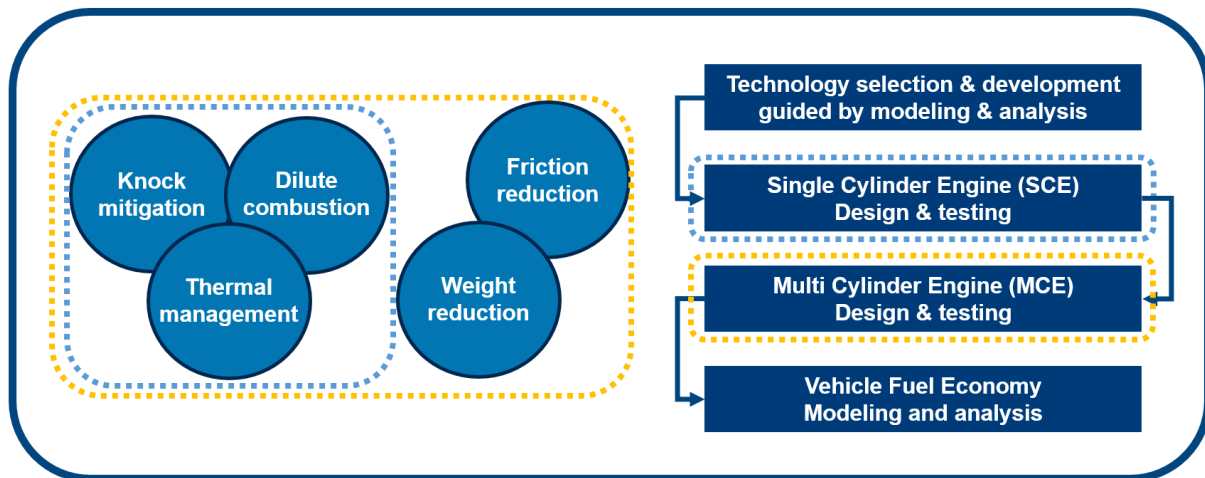


Figure I.4.1.2. The project development approach and work streams. Source: Ford.

This report will emphasize the materials aspects of the project. A second report has been prepared for the DOE Advanced Engine and Fuel Technologies annual report focusing on the combustion and efficiency portions of the project.

Results

Work during this reporting period has been focused in three areas: (1) optimization of the combustion system via modeling for improved dilution tolerance and knock mitigation, (2) manufacturing and testing of two SCEs intended to demonstrate the capabilities of the combustion system, and (3) completing design work on the MCE components targeting part availability in the fourth quarter of 2021.

Given the weight-reduction targets of the project, significant effort has been put into evaluating composite materials in place of Al for various engine components. Composites were considered for the oil pan, front cover, valve cover, rear main seal retainer, and engine mounts.

Structural Composite Oil Pan

As a part of the weight-reduction target for this project, a composite oil pan has been designed in collaboration with ORNL as a composite demonstration component. The oil pan was chosen because it has several design requirements that, if satisfied, will demonstrate suitability of the chosen material and process to other components. The pan must be lightweight, easy to manufacture, and be durable to the chemical, thermal, and mechanical boundary conditions present on the engine. The oil pan is also long and has a deep draw, which are challenging characteristics for some manufacturing processes.

The engine oil pan has been designed considering the material properties of composites to provide the structural capabilities needed for the powertrain system and reduced mass compared to conventional materials. The single-piece component, as shown in Figure I.4.1.3, is designed for an oil capacity of six quarts and a complete perimeter seal. In addition, it is a structural component of the powertrain providing a mechanical connection between the engine and the transmission. This mounting interface enhances the stiffness of the powertrain assembly for superior noise, vibration, and harshness (NVH) characteristics. A further structural feature is to provide a mounting location for the vehicle air-conditioning compressor. Providing a mounting boss directly on the pan saves weight by eliminating the need for a bracket and additional fasteners.

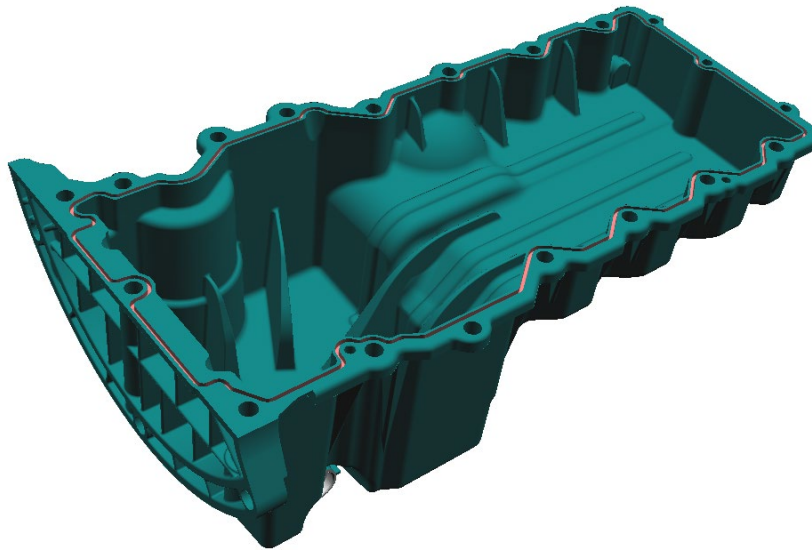


Figure I.4.1.3. Cylinder head made of AS7GU-T64-Al. Source: Ford.

Multiple molding processes were evaluated for the composite oil pan design, including injection molding, compression molding, blow molding, and thermoforming. These processes were evaluated for tooling costs, component durability, material capability, material properties, design complexity, sealing, and material recyclability. Extrusion compression molding was chosen as the best match to meet the form, function, and weight-reduction goals. It also more easily supports prototype timing and costs.

For extrusion compression molding, pellets of thermoplastic material reinforced with fibers are fed into a low shear extruder, which is used to plasticate the composite material into a “charge.” The charge is then transferred to a fast-acting press for the compression/consolidation process. While the use of AM to fabricate the tooling was to be the prime path, ultimately the tooling has been made using traditional methods of cutting blocks of Al to form both the upper and lower tool cavities, as shown in Figure I.4.1.4. This was due to the lack of availability of AM processing and the size of the actual molds that were needed to produce the pan. AM was used to make the bellhousing insert on the back of the pan, saving tremendous time and machining hours as the features of this area are complex and difficult to mold. The pan has at least three-degree draft angles to enable separation of the pan from the tool after molding. The draft angles were made possible by including the rear insert in the molding process, which otherwise was not feasible from a molding standpoint.

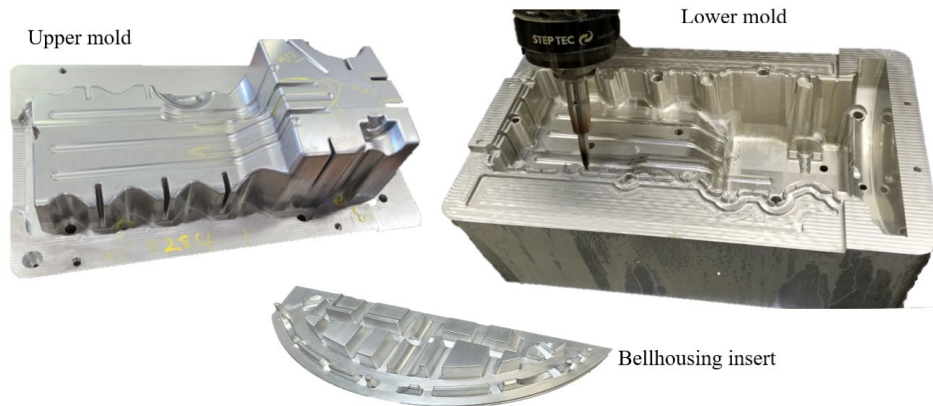


Figure I.4.1.4. Oil pan molds. Source: ORNL.

The material chosen for the oil pan is Solvay’s Amodel[®] PXM-18179, a highly filled glass fiber and recycled CF polyphthalamide (PPA) designed to work in the modern automotive environment and an excellent candidate for this project. This grade features high-heat deflection temperature, high-flexural modulus, and high tensile strength, as well as excellent creep resistance and low moisture absorption. Other available AM materials do not match the material properties of Amodel[®].

Valve Cover Design and Material Selection

Design work for the MCE valve cover has been completed and is shown in Figure I.4.1.5. The cover serves as the mount for the high-pressure fuel pump resulting in substantial cyclical forces and narrow sealing lands. As a result, it was not feasible to manufacture this component from readily available composite materials. The prototype parts will be manufactured from Al; however, several design iterations were required to reduce stress in the fuel pump mount area of the cover to acceptable levels, as seen in Figure I.4.1.6.

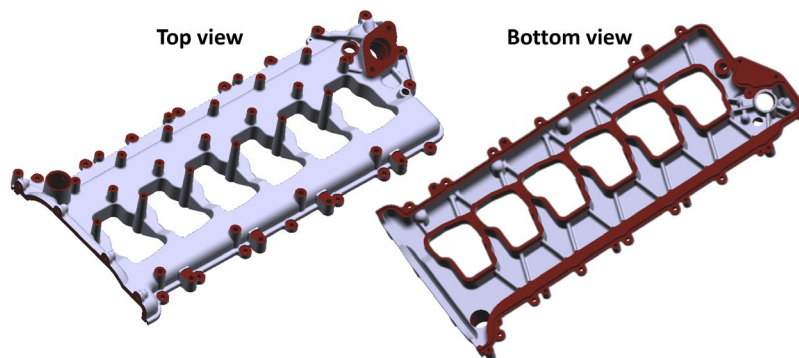


Figure I.4.1.5. Cylinder head water jacket for a conventional core and a printed core. Source: Ford.

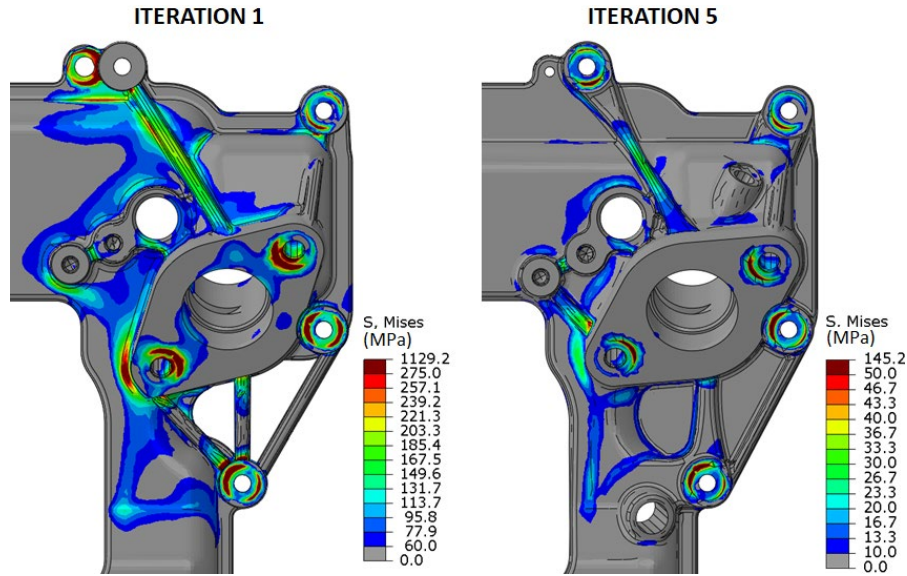


Figure I.4.1.6. Design modifications resulting in lower stress. Source: Ford/FEV.

Manufacturing the cover from Mg has also been investigated. Using Mg in place of Al results in an additional 1.4 kg of weight-savings but presents some challenges. Additional thread engagement is required with Mg, which can be accommodated in most locations. Another area of concern is the high-pressure fuel pump tappet bore. Figure I.4.1.7 shows a comparison of the expected tappet bore distortion due to assembly loads with the Al and Mg valve covers. Additional work would be required in the following areas to ensure durability:

- The required clearance and tolerancing between the bore and high-pressure fuel pump tappet have been well-developed for Al. Mg has a higher coefficient of thermal expansion (CTE) and would require verification and development to optimize.
- Mg may have a higher wear rate in the tappet bore than Al. Misalignment and distortion of the tappet bore can cause accelerated wear rates under some operating conditions.
- The reduced Young’s modulus of Mg results in increased deformation from the bolt clamp loads. This increased distortion reduces the oil film thickness between the bore wall and the pump roller tappet. The material compatibility between the tappet and Al is well-known, but material transfer from a Mg tappet bore has not been studied. Durability validation would be required.

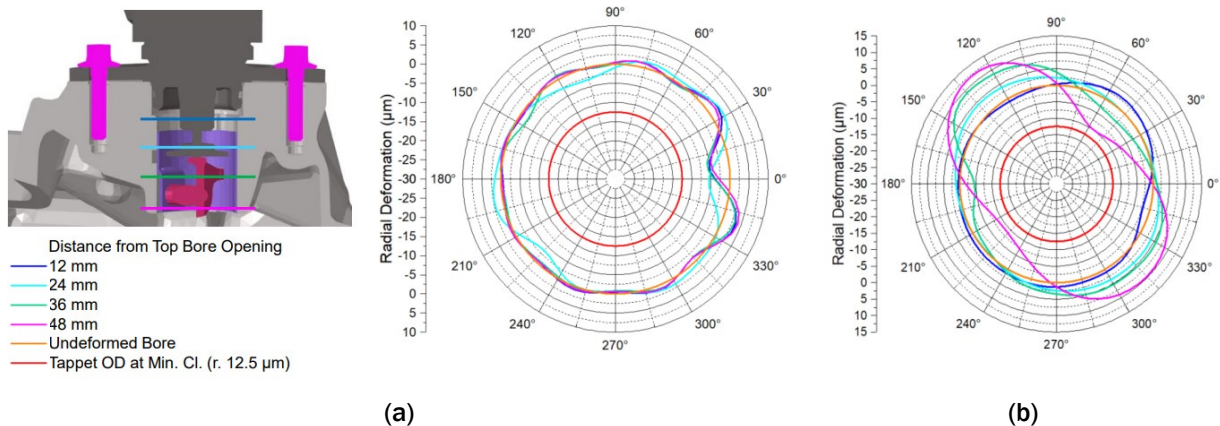


Figure I.4.1.7. Tappet bore distortion comparison for: (a) Al; and (b) Mg. Source: Ford/FEV.

Pre-Chamber Materials Selection

To meet the challenging engine efficiency target, an active pre-chamber ignition system was selected. This type of ignition system places a small combustion volume separate from the main combustion chamber. Air and fuel injectors are installed into this small chamber so that the residual mass fraction can be controlled separately from the main chamber. This allows an easily ignited mixture to be burned in the pre-chamber, sending hot reactive jets of gas into the main chamber. These jets act as a distributed, high-energy ignition source for the main combustion chamber, thereby facilitating efficient dilute combustion.

An active pre-chamber ignition system presents several challenges. An additional spark plug, fuel injector, and air injector must be packaged into the already crowded cylinder head. The pre-chamber is also subject to cyclical high-pressures and temperatures presenting material selection challenges.

To address the packaging challenges, the pre-chamber ignition system body was produced with an AM process, which facilitates complex geometric features that enable improved packaging and function. The materials available for AM are expanding but remain more limited than conventional manufacturing processes. For the main body of the pre-chamber, two materials were evaluated: AISI 8620 and AISI 316L. AISI 8620 was selected because of its superior heat transfer characteristics that result in reduced temperature of the pre-chamber tip, as observed in Figure I.4.1.8. Managing the tip temperature is important to avoid pre-ignition induced engine failures. Using AISI 8620 also provided temperature reductions at the pre-chamber fuel and air injector seal locations, which aids in maintaining injector seal durability. Table I.4.1.1 shows the material properties of several material composites.

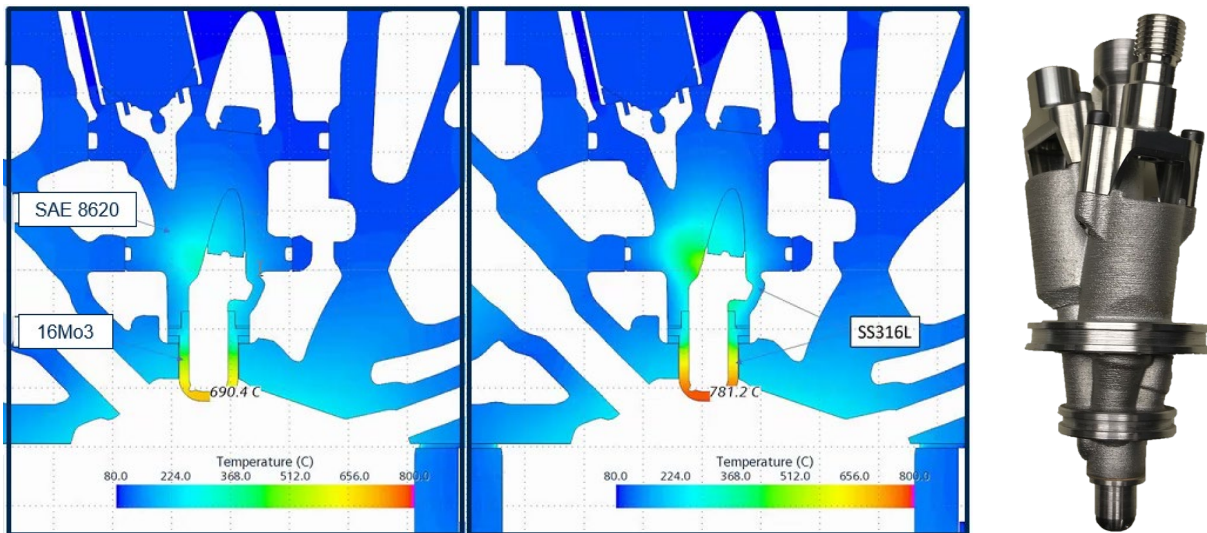


Figure I.4.1.8. Comparison of component temperature with SAE 8620 and SAE 316L. Source: Ford.

Table I.4.1.1. Material Properties

	AISI 316L (stainless-steel)	AISI 8620 (steel)	16Mo3 (steel)	UNS C11000 (copper)
Thermal conductivity [W/mK]	16.2	46.6	49	383
Density [g/cm ³]	7.9	7.87	7.85	8.89

Both the pre-chamber body and clamp were printed at the Ford Advanced Manufacturing Center using AISI 8620 steel powder on a LPBF technology metal 3D printing machine. This material was selected for its mechanical strength at elevated temperatures.

The pre-chamber tip was machined from 16Mo3 tool steel, which offers very good strength and wear resistance at elevated temperatures.

Main Bearing Cap Optimization

The main bearing caps are heavily loaded structural elements of the engine and contribute substantially to the mass of the engine. The initial prototype engines have been designed using SAE J404 4140 billet steel caps sufficiently strong to ensure reliable operation. To support the weight-reduction goals of the project, the main bearing cap design was further optimized considering alternate manufacturing methods and materials.

Using the design procured for the MCE as the baseline, the main bearing cap design was modified using topology optimization software to remove material not required to keep the vertical and lateral deflections of the main bearing cap within 10% of the baseline cap deflection. For the study, loads for bulkhead number two were used representing the worst-case loading condition. The shapes produced using topology optimization were further modified to improve manufacturability and are shown in Figure I.4.1.9.

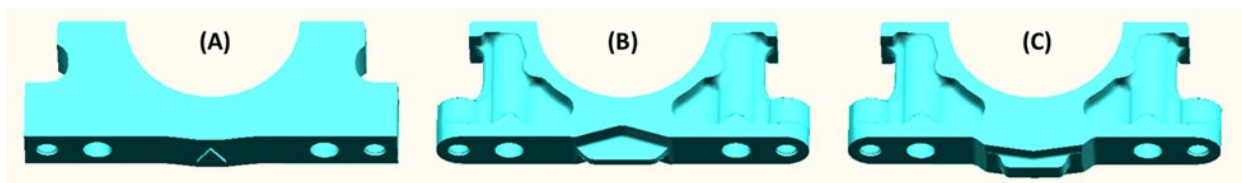


Figure I.4.1.9. Main bearing cap designs for (a) the initial prototype, (b) optimized steel, and (c) optimized cast-iron. Source: Ford/FEV.

The deflection analysis was repeated for the final alternative designs. As shown in Table I.4.1.2 meets the deflection targets and, when applied to all seven main bearing caps, provides 1.39 kg of weight-reduction. Design C offered even more mass reduction, but slightly exceeds the vertical deflection target and requires additional modifications to avoid interfering with the rear main seal retainer.

Table I.4.1.2. Main Bearing Cap Optimized Deflection Results

	Original Design A	Optimized Design B	Optimized Design C
Material	SAE J404 4140 (steel)	SAE J404 4140 (steel)	SAE J434 D550 (cast-iron)
Manufacturing Method	Billet Machining	Forging	Casting
Mass [g]	776	545	504
Vertical Deflection Increase	Baseline	8.6%	10.9%
Lateral Deflection Increase	Baseline	9.4%	8.7%

Windage Tray Design and Manufacture

Another innovative idea to reduce the mass of the engine was to separate the main bearing structural ladder frame from the windage tray features. The ladder frame connects the bottom of the main bearing caps to restrict fore and aft motion of the caps and supports the oil pump drive shaft, as observed in Figure I.4.1.10. The ladder frame weight was optimized utilizing modal analysis targeting a combined mode of the ladder frame and main bearing cap above 360 Hz.

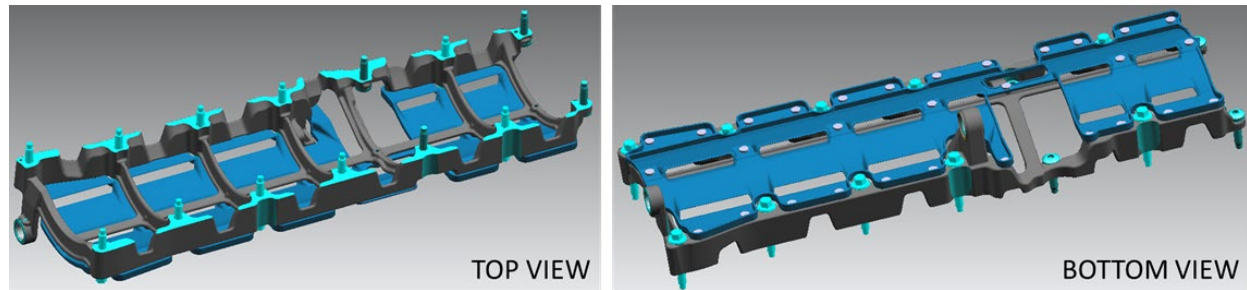


Figure I.4.1.10. Main bearing cap ladder frame and windage tray. Source: Ford/FEV.

Once the ladder frame design was finalized, and it was confirmed that additional stiffness from the windage tray was not required, alternative materials for the windage tray were investigated. ULTEM™ 1010 resin, a high-performance polyetherimide (PEI) thermoplastic was selected. This material has high-strength and excellent thermal properties and is capable of enduring engine oil temperatures for sustained periods. An additional advantage of ULTEM™ 1010 is that it can be machined from billet material or 3D-printed. The windage tray was printed at the Ford Additive Manufacturing Center and is shown in Figure I.4.1.11. Using a thermoplastic windage tray in place of an Al windage tray reduces engine mass by approximately 250 grams.

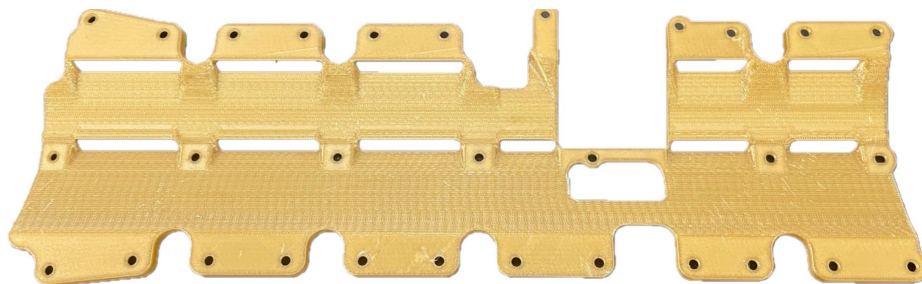


Figure I.4.1.11. Prototype ULTEM™ 1010 resin windage tray. Source: Ford/FEV.

Cylinder Bore Wall Material Selection

The power cylinders within the block—consisting of pistons, piston rings, and cylinder liners—contribute significantly to the overall efficiency of the engine. There are many system interactions that must be considered and carefully balanced to achieve the best results. The production of most Al cylinder blocks involves casting Al over a thick-wall cast-Fe liner to form the interface between the block and the sliding piston and ring pack. Cast-Fe is easily formed to near net-shape, has a low-cost, is durable, and provides a compatible interface for the piston and rings. Starting in the 1990s, Ford began pioneering the development of the Plasma Transfer Wire-Arc (PTWA) process for spraying a thin layer of cast-Fe or steel onto the inside of the pre-machined parent Al liner. PTWA coating results in a cast-Fe or steel liner thickness of approximately 0.15 mm versus the typical cast-in liner thickness of 2.2 mm – 3.0 mm. Several original equipment manufacturers (OEMs) have begun adopting some form of spray liner coating in the last decade including Nissan, Ford, BMW, Mercedes, and Audi. One benefit of this process is a significant weight-reduction of the block.

Relative to the baseline 3.5L V6 block with 3-mm-thick cast-Fe liners, the project's 3.7L PTWA block achieved 2.61 kg of mass reduction associated with forming the surface of the bores, as can be seen in Table I.4.1.3, where the mass of the baseline cast-Fe liners is compared to the mass of the Al and spray coating liners of the 3.7L engine. If the project engine is instead compared to a cast-Fe liner engine with the same displacement and bore-to-stroke ratio, the weight-savings of PTWA increases to 3.2 kg.

Table I.4.1.3. Mass Comparison for Cast-Fe and PTWA Liners

	3.5L With Cast-Fe liners	3.7L With PTWA liners
Al outer diameter (OD) [mm]	0	90
Al inner diameter (ID) [mm]	0	84.5
Liner OD [mm]	98.5	84.5
Liner ID [mm]	92.5	84
Liner length [mm]	130.4	161
Al volume [cm ³]	0	121.3
Cast-Fe volume [cm ³]	117.3	10.6
Al mass per liner [g]	0	333.57
Cast-Fe mass per liner [g]	844.6	76.7
Total liner mass per engine [kg]	5.07	2.46
PTWA mass savings [kg]	2.61	

In addition to reduced mass, PTWA bores provide an opportunity to reduce engine friction. It has been demonstrated that 50% to 60% of total engine friction is due to the interface between the pistons and piston rings with the cylinder liner, as shown in Figure I.4.1.12 [1].

A great deal of development time is spent attempting to optimize the piston liner interface for the lowest friction while meeting targets for scuff resistance, wear, blow by, NVH, and oil consumption. Most thermal spray bore applications are considered low porosity with pores occupying less than 2% of the surface area, which is made up of small open pores created during the plasma spray process. As a part of DOE project DE-EE0006901, Ford tested a wide range of PTWA porosity levels to enable reducing friction, as observed in Figure I.4.1.13.

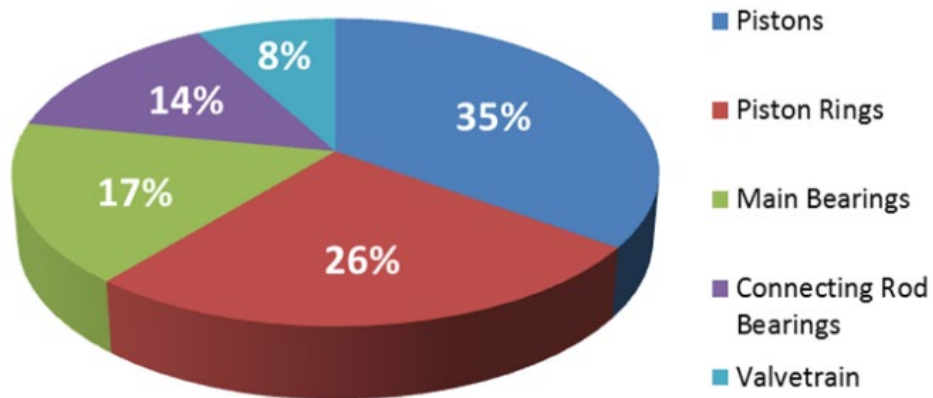


Figure I.4.1.12. The distribution of frictional losses in an engine. Source: Ford [1].

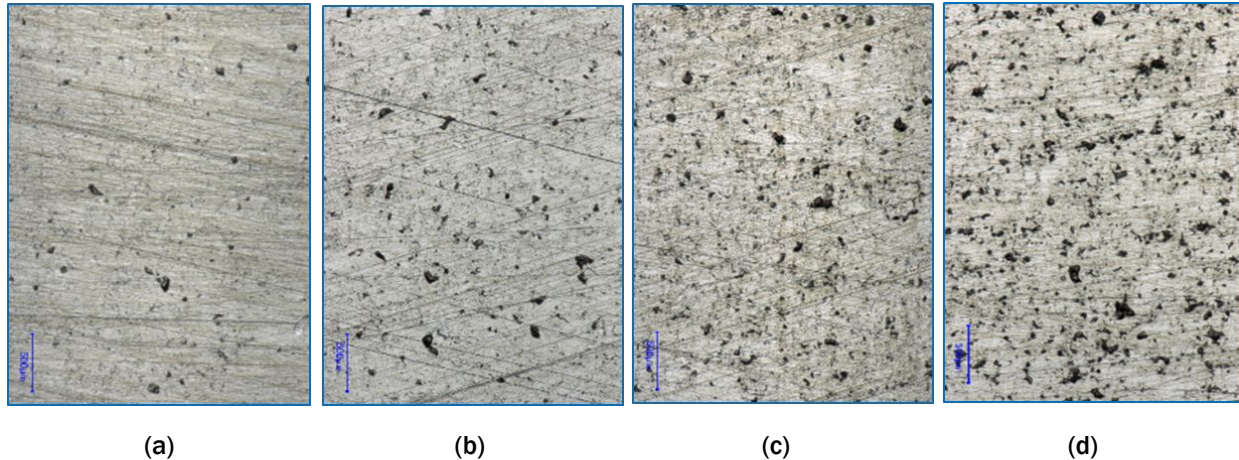


Figure I.4.1.13. Image of honed surface showing different levels of porosities: (a) PTWA1 (less than 2%); (b) PTWA2 (3-5%); (c) PTWA3 (6-8%); and (d) PTWA4 (>8%). Source: Ford [1].

Ford's previous experiments have focused on substituting the oil retention capabilities of porosity sites for the surface finish roughness normally required to meet this function, resulting in a smoother liner interface. With careful attention to balancing porosity level, surface finish, oil consumption, scuff and wear resistance, the team will be implementing a PTWA surface that is expected to achieve 0.8% to 1.0% metro-highway fuel economy improvement relative to a conventional honed cast-Fe liner.

Conclusions

Simultaneously meeting the fuel economy and weight targets of this project presents several materials-related challenges. In the second year of this project, we have reduced the mass of the oil pan and powertrain structure using extrusion compression molding to manufacture a composite oil pan. Advanced materials and manufacturing techniques have been applied to solve thermomechanical and packaging issues related to the pre-chamber ignition system. Unnecessary mass has been removed from the main bearing caps using topology optimization and the mass of the windage tray has been reduced by using a resin component for the non-structural elements of the tray. Finally, engine mass and friction have been reduced by implementing a PTWA cylinder liner in place of a cast-Fe cylinder liner. These efforts directly support the mass reduction and efficiency improvement goals of the project.

References

1. Gangopadhyay, A., 2021, "Power cylinder friction reduction through coatings, surface finish, and design." Final technical report, U.S. Department of Energy Award DE-EE0006901, June 2021.

Acknowledgments

The author would like to thank our partners at FEV North America and ORNL for their collaboration and support, as well as our National Energy Technology Project Manager, Ralph Nine, for his continued guidance.

I.4.2 Low-Mass and High-Efficiency Engine for Medium-Duty Truck Applications (General Motors)

Qigui Wang, Co-Principal Investigator

General Motors, LLC.
30003 Fisher Brothers Road
Warren, MI 48093
E-mail: qigui.wang@gm.com

Ed Keating, Co-Principal Investigator

General Motors, LLC.
28755 Louis Chevrolet Road
Warren, MI 48093
E-mail: ed.keating@gm.com

Jerry L. Gibbs, DOE Technology Manager

U.S. Department of Energy
E-mail: jerry.gibbs@ee.doe.gov

Start Date: October 1, 2019 End Date: December 31, 2023
Project Funding (FY 2021): \$1,875,664 DOE share: \$1,480,618 Non-DOE share: \$395,046

Project Introduction

With the increasing demand in lightweighting and reduction of fuel consumption, there is a need to develop a next-generation of high-efficiency, very low-emission ICEs. This requires a combination of new combustion strategies, advanced materials, and new materials processing techniques to further increase engine efficiency and reduce weight. The expected national economic, environmental, and energy security benefits of these next-generation engines and materials would be significant because most vehicles sold over the next two decades will still include an internal combustion engine. The availability of advanced lightweight engine designs will provide a significant positive impact on the fuel efficiency, environment, and competitiveness of the U.S. auto industry [1].

Objectives

The objective of this collaborative project between GM, Oak Ridge National Laboratory (ORNL), The Ohio State University (OSU), Michigan Technological University, and Eck Industries, Inc. (Eck), is to develop an advanced MD truck engine equipped with advanced materials and combustion technologies capable of $\geq 10\%$ fuel efficiency improvement and $\geq 15\%$ engine weight-reduction when compared to the 2015 Model Year GM L96 Vortec 6.0L V8 engine, compliant with applicable EPA emission standards with performance demonstrated via simulation coupled with engine dynamometer tests.

Approach

This project is proposed as a large-scale engine design and demonstration enabled by an advanced materials and manufacturing development program with a comprehensive plan spanning a period of four years. The project begins with engine architecture design and analysis activity, advanced materials and manufacturing process development, and downselection. It culminates in an engine test-cell evaluation with optimal materials and manufacturing solutions supporting final vehicle simulation. The final engine test will verify engine weight-reduction and performance to the objectives of the funding opportunity announcement [1].

Several advanced combustion technologies will be investigated including stoichiometric combustion, increased compression ratio, aggressive enhanced exhaust gas recirculation (E-EGR) dilution and load-point

optimization with a focus on an optimal cylinder deactivation, advanced valve train phasing and lift strategies, advanced fuel system strategies including “ultra” high-pressure direct injection, advanced ignition systems including pre-chamber spark plug, advanced EGR dilution systems including enhanced-EGR (E-EGR), Atkinson or Miller cycle strategies, variable induction system strategies, and combustion chamber cooling strategies.

In this project, high-strength and heat-resistant materials will be developed and incorporated with novel metal casting and AM processes to produce highly durable engine structures to maximize performance of the materials and systems with minimum mass and cost. The opportunity to include advanced materials and manufacturing in conjunction with high potential combustion systems and engine technologies also creates the chance to revisit the most appropriate engine specification to realize the desired efficiencies while reducing engine weight cost-effectively. A focus will be on the most cost-effective solution to promote wide market acceptance using the right materials in the right place and the right process for the right parts. Advanced material solutions for key engine components, such as head and block, will be investigated to achieve weight-reduction and performance requirements. Furthermore, ICME and computer-aided engineering tools will be fully used during the entire program to accelerate both the new material and manufacturing process development and optimization, as well as the complete engine design and manufacturing [2].

The project is planned for two phases over four BPs separated by distinct go/no-go decision points as follows:

- Phase 1—Technology R&D:
 - **BP1:** Identification of potential engine architecture designs and initial verification coupled with advanced technologies for combustion systems, materials, and manufacturing concepts for weight-savings and performance improvement through simulations and development.
 - **BP2:** Evaluation of proposed individual technology concepts using current equivalent architecture of GM development engines in conjunction with advanced materials and manufacturing process development of high-value weight-reduction and performance improvement strategies for components and subsystems.
- Phase 2—Technology Validation and Demonstration:
 - **BP3:** Design, procure, manufacture, assemble, and perform initial developmental testing of a proposed MD truck engine capable of meeting requirements.
 - **BP4:** Demonstration of performance and weight-reduction to meet requirements using engine test-cell and vehicle simulations.

Results

Based on the FY 2020 results obtained in BP1, engine architecture design, advanced combustion system and materials technologies, weight-savings simulations, and development, the normally aspirated large displacement V8 engine was selected as the focus for further development during the remainder of the project.

A Pugh chart denoting the performance to requirements and other attributes of interest of the two investigated engine architectures is shown in Table I.4.2.1. This chart illustrates our projection that either architecture can meet the project requirements using the identified fuel economy and weight-reduction technologies. While both architectures show a clear potential to meet the objectives of the project, our projection is that the normally aspirated large displacement V8 will do so much more cost-effectively. Therefore, this architecture has been chosen for further development.

Table I.4.2.1. Primary Engine Architecture Selection Summary Pugh Chart

Requirement/Attribute	Normally Aspirated Large Displacement V8	Downsized Boosted L6
-----------------------	--	----------------------

+10% Fuel Economy	MEETS	MEETS
-15% Engine Weight	MEETS	MEETS
Estimated Engine Cost	BASELINE	+37%
Performance	MEETS	MEETS

Task 2.1. Design and Build Hardware to Evaluate Advanced Combustion Technologies and Weight-Reduction Techniques Using Current Equivalent Architecture GM Development Engine and Incorporating Components Produced in Task 2.3

Work during FY 2021 focused on the evaluation of proposed individual technology concepts using a current equivalent architecture GM development V8 engine in conjunction with advanced material and manufacturing process development of high-value weight-reduction and performance improvement strategies for the components and subsystems.

Subtask 2.1.1— Hardware was designed and acquired to evaluate the advanced combustion system, as shown in Figure I.4.2.1, Figure I.4.2.2, Figure I.4.2.3, Figure I.4.2.4, and Figure I.4.2.5, respectively.

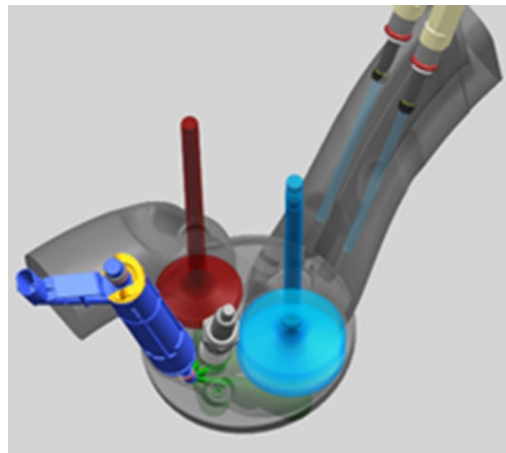


Figure I.4.2.1. Proposed advanced combustion system. Source: GM.

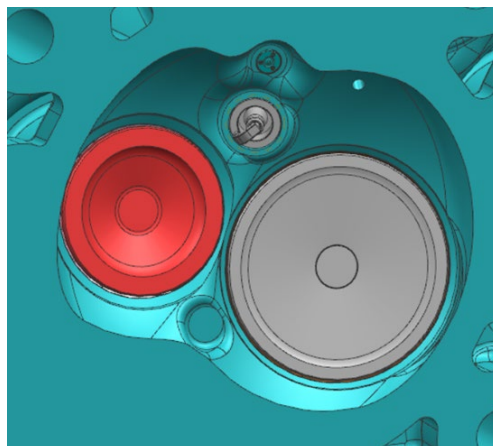


Figure I.4.2.2. Proposed advanced combustion system application in hardware. Source: GM.

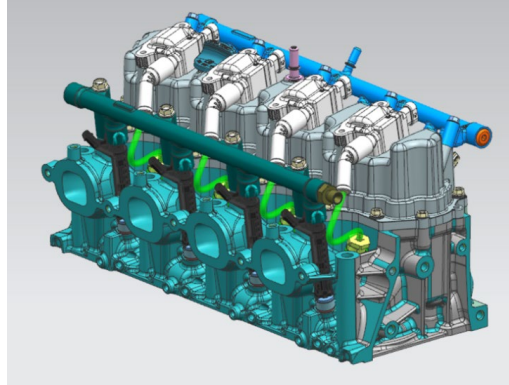


Figure I.4.2.3. Proposed advanced combustion system cylinder head assembly – exhaust side view.
Source: GM.

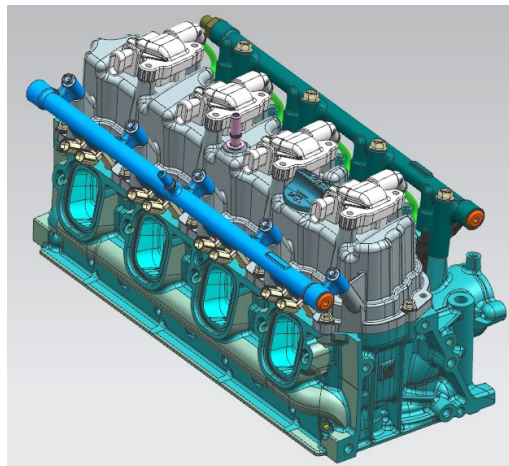


Figure I.4.2.4. Proposed advanced combustion system cylinder head assembly – intake side view.
Source: GM.

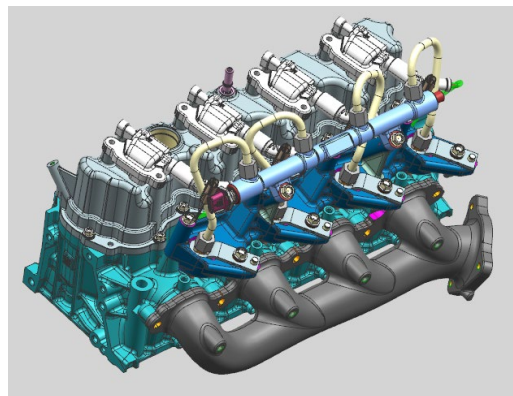


Figure I.4.2.5. "Ultra" high-pressure injection system adapted to proposed advanced combustion system cylinder head assembly – exhaust side view. Source: GM.

Subtask 2.1.2—As GM has a developed full authority cylinder deactivation system for a large displacement overhead valve V8 engine architecture, design and hardware acquisition was not required to evaluate optimal cylinder deactivation strategies analyzed.

Subtask 2.1.3—Hardware was designed and acquired to evaluate “ultra” high-pressure fuel injection using the advanced combustion system, as shown previously in Figure I.4.2.5.

Subtask 1.1.4—Opportunities to implement a high-value combustion system technology into both engine concept layouts have been explored and design studies have been completed to package this technology into both engine concept layouts. The list of high-value combustion system technologies is shown in Figure I.4.2.2.

Subtask 2.1.4—Hardware was designed and acquired to evaluate advanced ignition systems—a passive pre-chamber spark plug. The investigation of a potential radio frequency corona discharge ignition system is progressing.

Subtask 2.1.5—Hardware to implement an E-EGR system using EGR produced in dedicated cylinders was designed and acquired, as shown in Figure I.4.2.6.

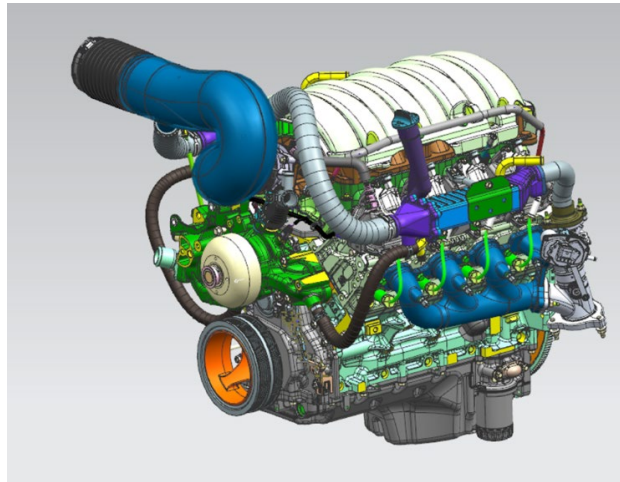


Figure I.4.2.6. E-EGR system adapted to development engine. Source: GM.

Subtask 2.1.6—Hardware to evaluate advanced Atkinson or Miller cycle strategies in conjunction with advanced variable valve duration and/or lift concepts was designed and acquired. Intake valve lift profiles and camshaft phasing hardware capable of implementing an Atkinson cycle strategy were implemented into the design and acquisition of components supporting the advanced combustion development engine.

Subtask 2.1.7—A variable charge motion concept was conceived and designed to evaluate advanced variable induction system strategies. Hardware was acquired to evaluate this concept using induction system inserts to increase charge motion based on strategic port blockage, as shown in Figure I.4.2.7.

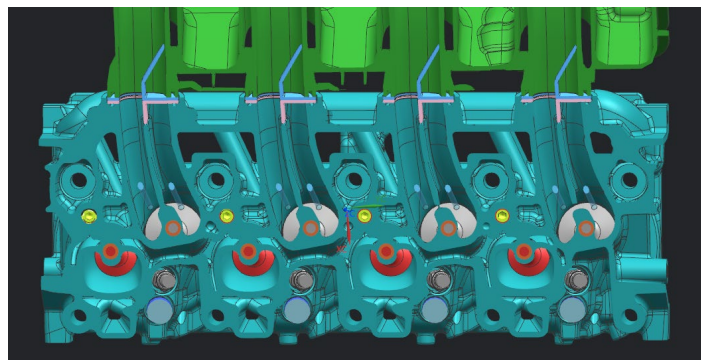


Figure I.4.2.7. Variable charge motion accomplished with inserts. Source: GM.

Subtask 2.1.8—A high velocity coolant jacket has been developed including key drillings to significantly improve cooling uniformity, as shown in Figure I.4.2.8.

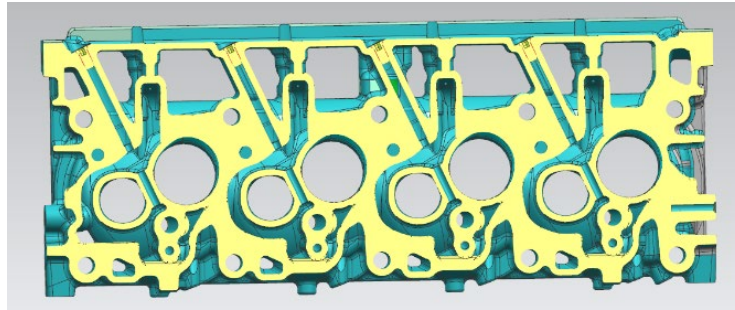


Figure I.4.2.8. Cooling jacket design. Source: GM.

Subtask 2.1.9—Additional components that were required to implement the key technologies described in Subtasks 2.1.1 through 2.1.8 were designed and acquired.

Task 2.2. Test-Cell Evaluation of Advanced Combustion Technologies and Weight-Reduction Techniques Using a Current Equivalent Architecture GM Development Engine

Subtask 2.2.1—The baseline L96 V8 engine was installed in the test-cell. Initial performance testing was completed.

Subtask 2.2.2—The development engine was updated with new basic combustion systems. Engine performance evaluation is progressing. Multiple delays in this activity have been experienced due to transition of work from within GM to a development partner. Projected Greenhouse Gas Emissions Model (GEM) points and evaluation status are shown in Figure I.4.2.9.

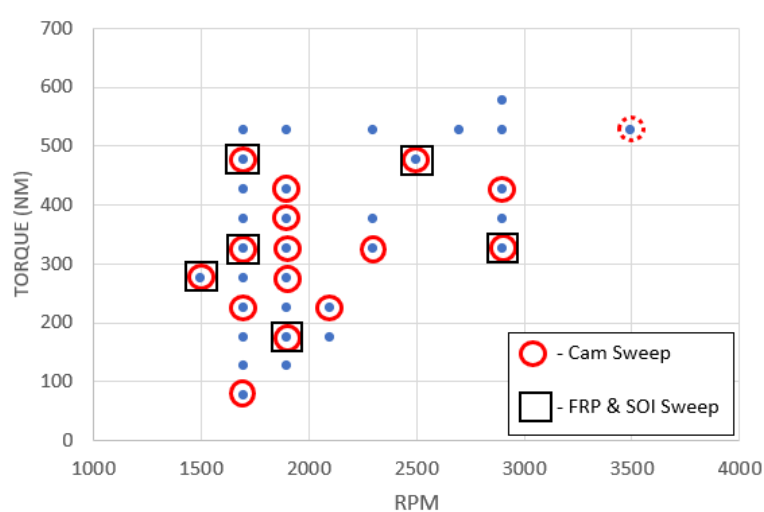


Figure I.4.2.9. Projected and completed GEM cycle operating points. Source: GM.

Subtask 2.2.3—For cylinder deactivation strategy, no test was required at this development phase as GM had developed hardware to implement this technology using an overhead valve V8 engine architecture.

Subtask 2.2.4—The development engine design has been updated with advanced fuel systems including “ultra” high-pressure direct injection. Hardware is ordered. Performance evaluation is planned.

Subtask 2.2.5—The development engine has been updated with advanced ignition systems. A pre-chamber ignition concept has been acquired. Performance evaluation is planned.

Subtask 2.2.6—The development engine design has been updated with advanced dilution systems. Performance evaluation is planned.

Subtask 2.2.7—The development engine was updated with advanced Atkinson cycle hardware. Advanced variable valve duration and/or lift hardware was not shown to be beneficial in conjunction with cylinder deactivation during simulations in BP1, so hardware was not acquired.

Subtask 2.2.8—The development engine has been updated with advanced variable induction system hardware. Performance evaluation is underway.

Task 2.3. Development of Advanced Material and Manufacturing Solutions for Mass Savings and Performance

Work during FY 2021 was focused on the development and downselection of new materials and manufacturing solutions for key engine components, such as a cast-Al engine block, a cast-Al head, a cast-steel crankshaft, a nodular-Fe crankshaft, and a piston fabricated with AM.

Subtask 2.3.1—Five ACMZ alloys with copper contents of 6.0, 6.6, 7.3, 8.0, and 9.0 wt.% were evaluated in terms of porosity population with two sets of end-chill sand-cast plates using X-ray computed tomography (CT). Two representative sections in the plates were measured: (a) Section 1 (0-15 mm from the chill end) corresponding to the deck face in the cylinder head and the bulkhead in the engine block microstructure, and (b) Section 2 (45-60 mm from the chill end) corresponding to the head bolt boss microstructure. Porosity measurements were performed with a CT scan technique. In the second set of X-ray CT scanning, a higher-resolution X-ray CT scanner was used for the samples next to the chill. Pores larger than 10 μm were detected and quantified. The total porosity of two sets of measurements in the two sections for the five evaluated alloys is summarized in Figure I.4.2.10.

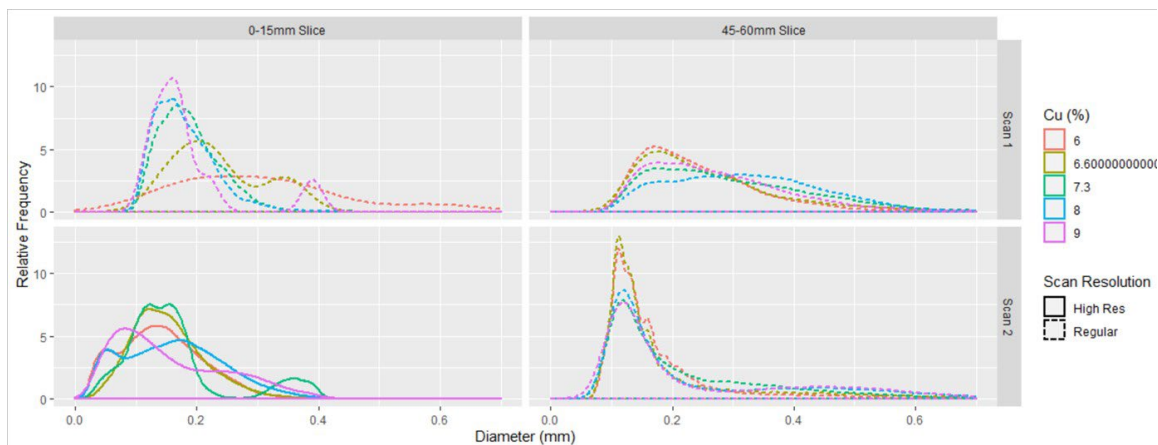


Figure I.4.2.10. Two sets of CT porosity measurements of five ACMZ alloy compositions for two representative sections of end-chill sand-cast plate castings. Source: ORNL.

Following Zhu et al. [3], fatigue limit was predicted with the pore size distribution and Monte Carlo technique. The predicted fatigue strength variation for two sets of CT porosity measurements is plotted in Figure I.4.2.11. Based on the measured porosity distribution and fatigue strength variation predicted from the CT data on two locations of the end-chill plates, alloys with 6.6% or 9% Cu show better castability and quality than other three Cu levels. It is recommended to use 9% Cu as a cylinder head alloy and 6.6% Cu as an engine block.

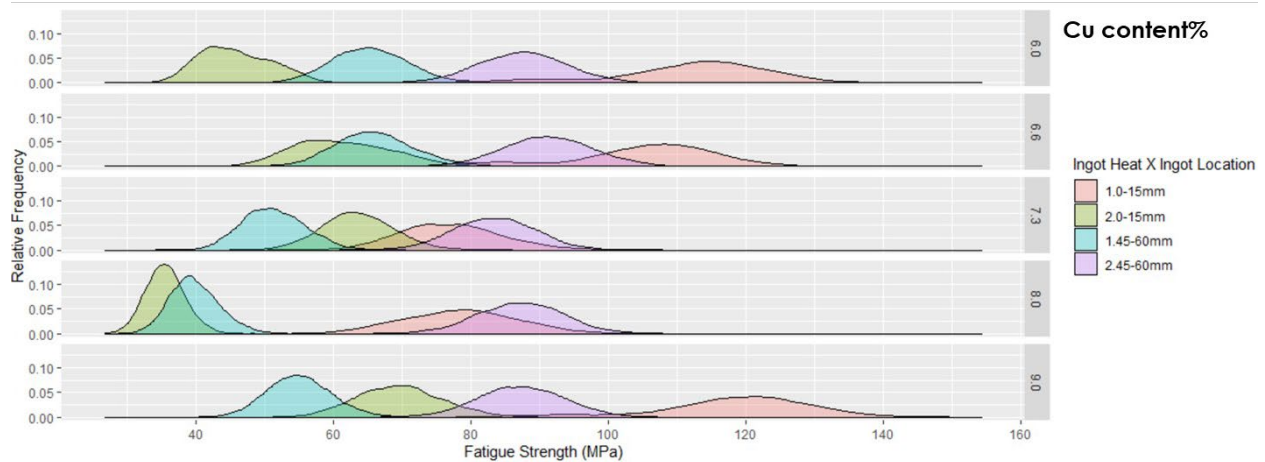


Figure I.4.2.11. Predictions of fatigue strength distributions based on the porosity measurements outlined. Source: ORNL.

A novel low pressure precision sand-casting (LPPSC) process has been proposed and investigated for cast high-quality Al cylinder head and engine block. After comprehensive casting process simulation and multiscale defect and microstructure modeling, gating, and riser system, as well as LPPSC process parameters were optimized for the cylinder head and engine block. The tooling work for the head casting was completed and the first set of cylinder heads with a baseline alloy were cast, as observed in Figure I.4.2.12. X-ray CT examination of the head showed good quality in meeting the requirement. Evaluation of mechanical properties and multiscale microstructure of the head is underway. Tool work for the engine block is under development.

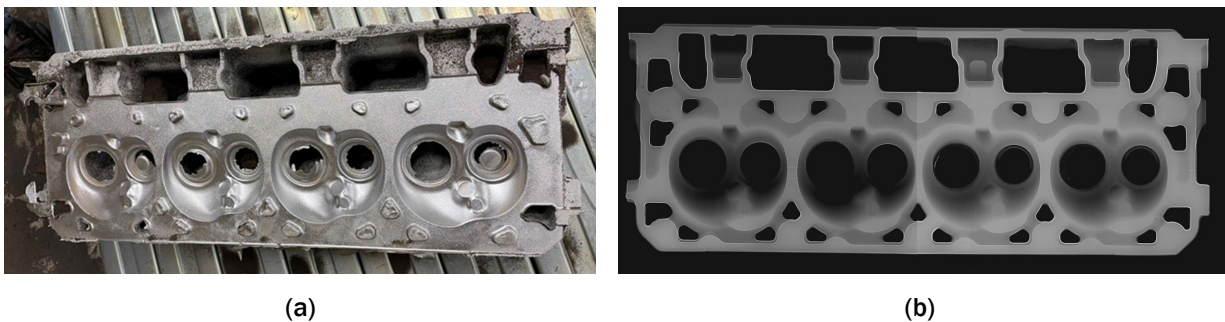


Figure I.4.2.12. (a) The first cylinder head casting made by (b) the novel LPPSC process showing good quality in X-ray CT. Source: ECK.

Subtask 2.3.2—Cast-in-place steel valve seat in cast-Al cylinder head was studied as one of the multi-material solutions for high-performance engine in this project. Figure I.4.2.13 shows an assembly of the newly designed exhaust valve steel seat with an exhaust port sand core and deck face metal chill for the cylinder head.

Comprehensive overcasting experiments and numerical modeling of steel valve seat with a cast-Al head alloy were performed. A variety of techniques have been studied to achieve good metallurgical bonding between the steel and cast-Al interface including steel surface oxide removal, steel surface coating, Al-fin processing, solid diffusion, special heat-treatment, etc. To evaluate the effect of mold design and filling, several iterations of mold design seen in Figure I.4.2.14 were used to identify key factors affecting metallurgical bonding at the bimetallic interface.

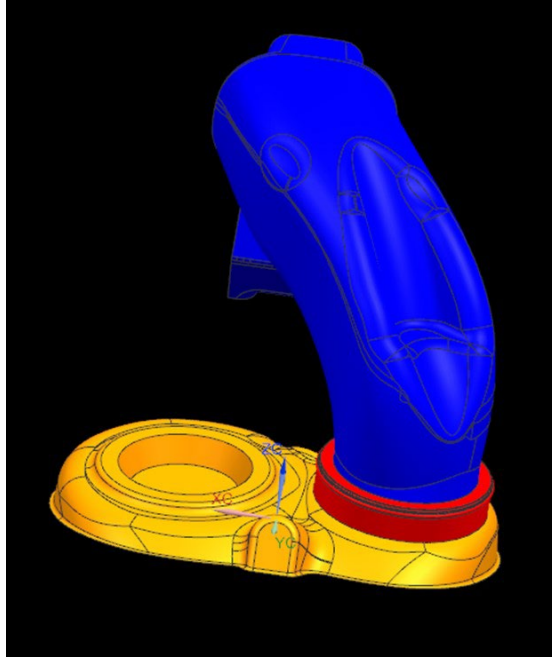


Figure I.4.2.13. An assembly of exhaust valve steel seat (red) with exhaust port sand core (blue) and deck face metal chill (yellow). Source: GM.

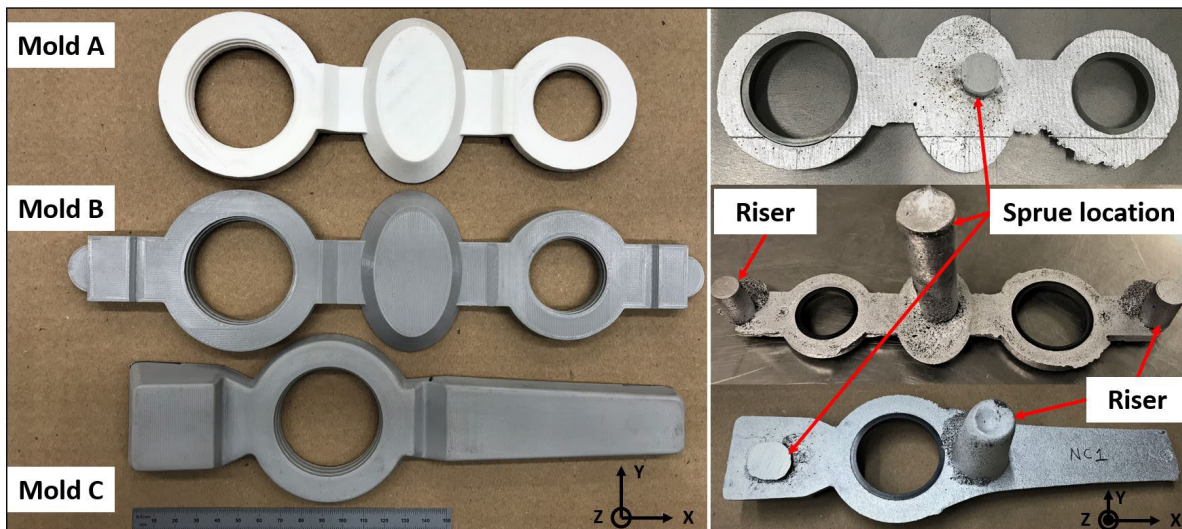


Figure I.4.2.14. Casting patterns and experimental supplies. Source: OSU.

After valve seat sample surfaces were well prepared, good metallurgical bonding had been achieved in both Zn-plated and Al-fin processed samples. As shown in Figure I.4.2.15(a) and (b), a roughly $3.5\ \mu\text{m}$ diffusion layer of Fe-Zn-Al was formed during the overcasting of the Zn-plated sample. Al-fin processed samples show intermetallic bonding where $\alpha\text{-Fe}_2\text{SiAl}_8$, $\beta\text{-FeSiAl}_5$, and $\theta\text{-FeAl}_3$ phases are observed between the Al and valve seat materials, but as indicated by the star in Figure I.4.2.15(c), some oxides are not broken down during the overcasting process. A sample with no coating, but well cleaned to remove the C-N-O layer, displayed a superior bonding interface. As shown in Figure I.4.2.15(d) and (f), the sample with no coating displayed a large clean interface with around a $1.9\ \mu\text{m}$ Al-Fe diffusion layer.

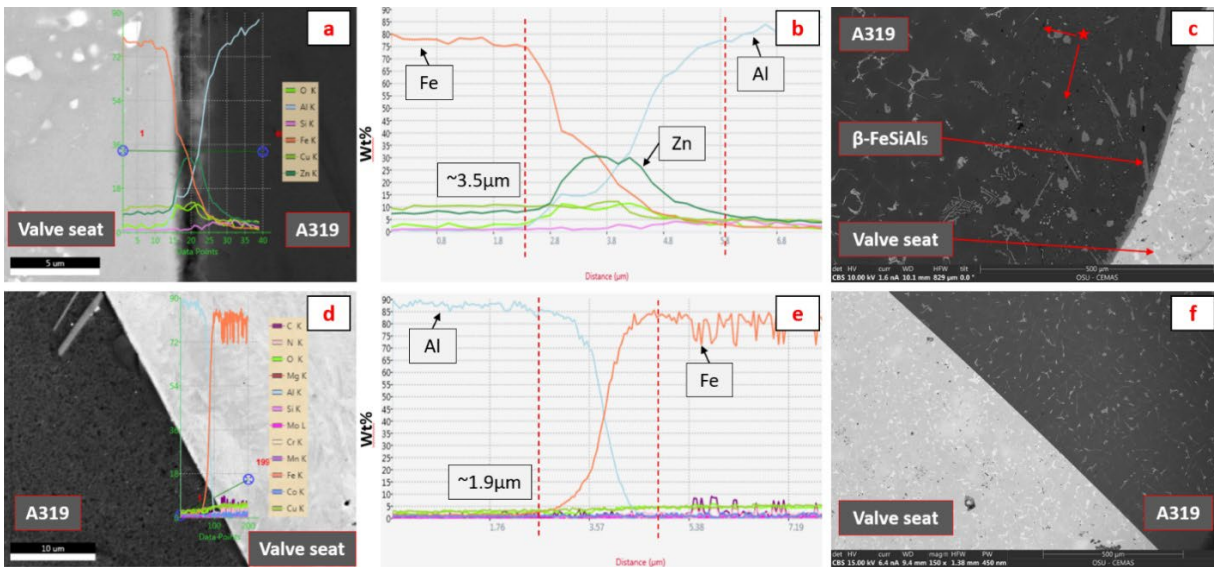


Figure I.4.2.15. Overcasting sample in an as-cast state: (a)-(b) BSE image and EDS scan of Zn-plated sample; (c) Al-Fin processed sample; (d) SEM image; (e) EDS scan; and (f) BSE image of the sample with no coating. Source: OSU.

Subtask 2.3.3—Design of the first engine piston for the AM process was completed. The first AM piston is slightly lighter (e.g., ~10 g) than a cast-Al production piston. Computer-aided engineering (CAE) analysis indicates that the AM piston design meets the piston safety factor (PSF) requirements. Al-Ce based alloy was downselected for printing the first set of pistons, as shown in Figure I.4.2.16. Figure I.4.2.17 shows the mechanical properties of as-printed Al-Ce based alloy tested.



Figure I.4.2.16. Additively manufactured pistons with an AlCeNiMnZr alloy. Source: ORNL.

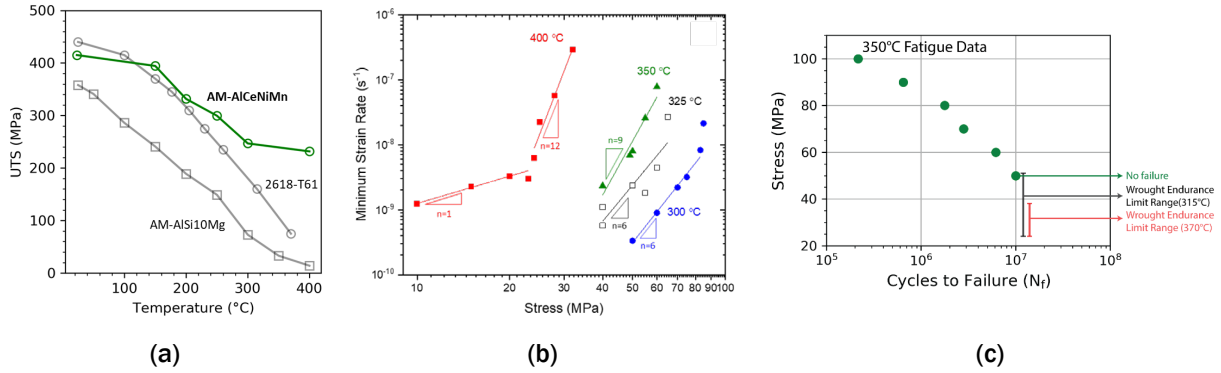


Figure I.4.2.17. (a) UTS, (b) creep properties, and (c) fatigue strength of Al-Ce based alloy at various temperatures. Source: ORNL.

To more accurately model microstructure evolution during powder bed fusion AM, thermal diffusion has been added to the current cellular automata model. The thermal profile in and around the melt pool strongly influences the formation of grains during solidification. Figure I.4.2.18 shows a new feature of the simulation. To simulate features less than 10 microns, the cellular automata domain in the melt pool is subdivided into a 1-micron grid, which reflects the experimental observation.

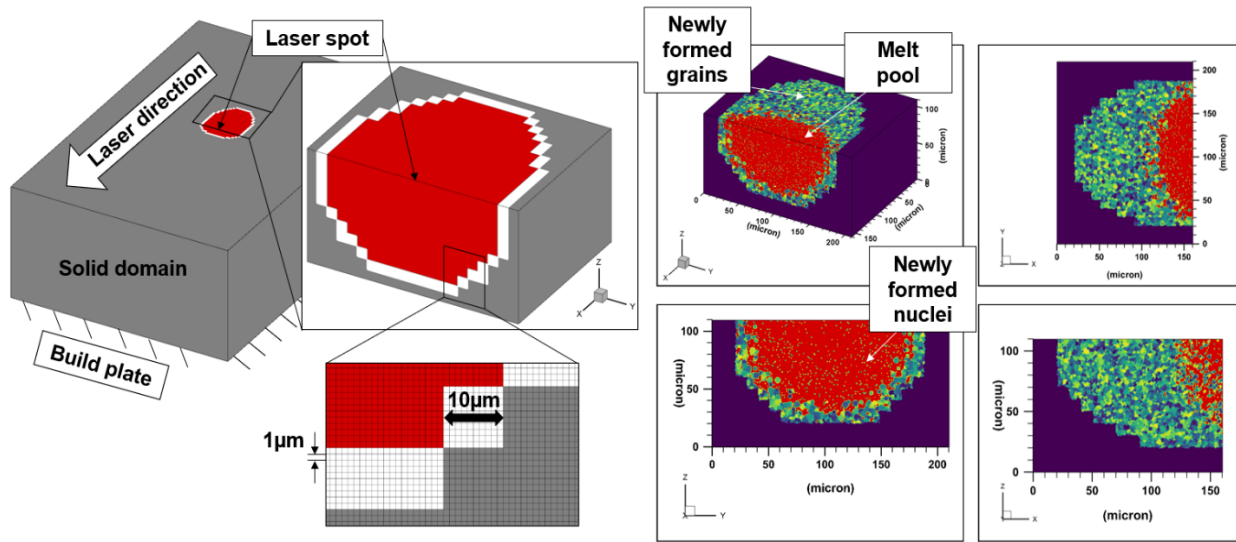


Figure I.4.2.18. CA simulation of melt pool and solidified grain structure during AM with the refined grid size. Source: OSU.

Subtask 2.3.4—GM34CrMoV cast-steel alloy was downselected to optimize the lightweight hollow crankshafts. Prototype crank sand molds were printed with the optimal gating/riser system and poured with the downselected alloy, as observed in Figure I.4.2.19(a). After casting, two cranks were sectioned showing no macro porosity, as shown in Figure I.4.2.19(b). The tensile properties of the cast-steel cranks exceed the targeted properties (e.g., yield strength: >800MPa, ultimate tensile stress: >900MPs, and elongation: >7%). Fatigue properties of samples taken from the cast-steel cranks are comparable with the forged steel crank samples, as seen in Figure I.4.2.20. It is noted, however, that there are micro shrinkage pores on the fracture surfaces of cast-steel crank samples, which leads to further development of optimizing crank casting process and gating/riser system design.

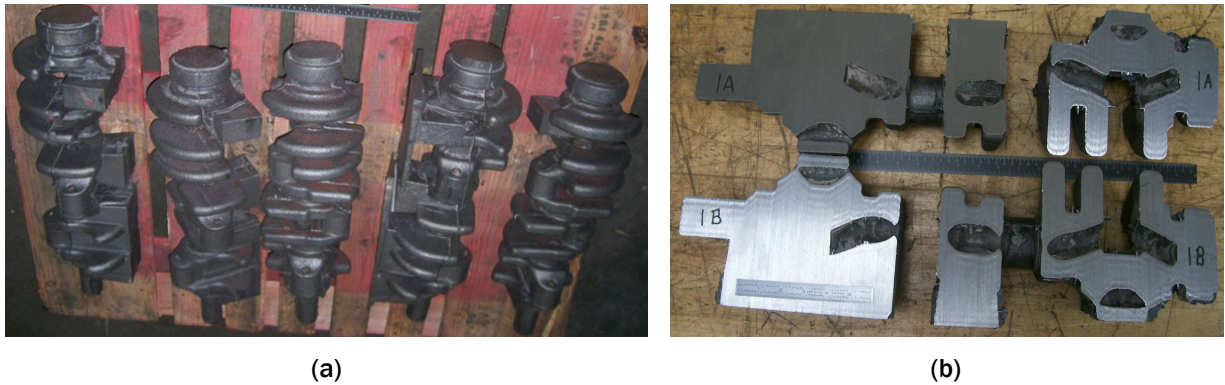


Figure I.4.2.19. Pictures showing (a) the hollow cast-steel crankshafts that were made, and (b) the longitudinal sectioning of a crank. Source: GM.

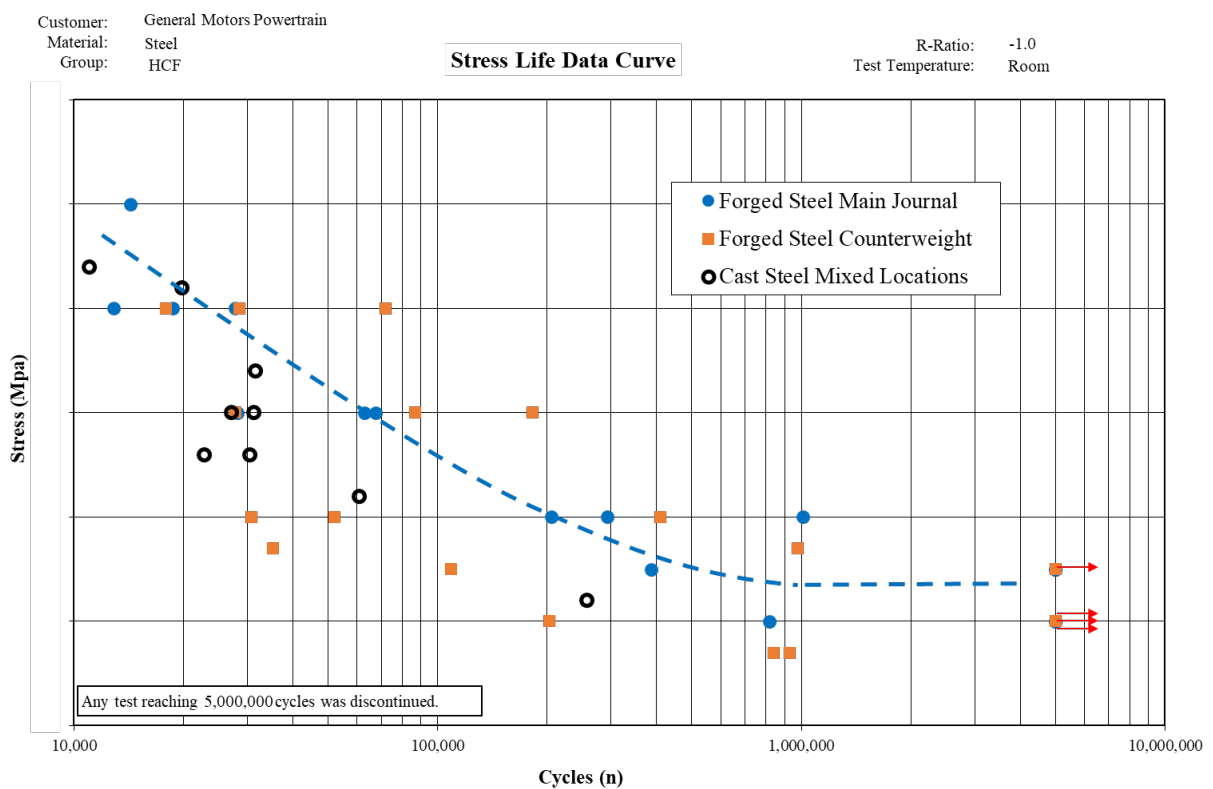


Figure I.4.2.20. Fatigue S-N data comparing the fatigue properties of cast-steel crank samples with the forged steel ones. Source: GM.

Conclusions

Advanced combustion technologies are being evaluated using a current equivalent architecture GM development V8 engine in conjunction with advanced material and manufacturing process development of high-value weight-reduction and performance improvement strategies for components and subsystems. The project is generally progressing well. Some Phase 1 activities are still ongoing due to challenges from the impact of COVID-19-related delays and the transition of work from within GM to a development partner. Phase 1 activities are expected to be completed in the first quarter of FY 2022.

Key Publications

1. Moodispaw, M. P., C. Gu, A. A. Luo, and Q. G. Wang, 2021, “Cellular automaton simulation of three-dimensional microstructure evolution during powder bed fusion additive manufacturing,” Materials Science and Technology Conference (MS&T21), 17–20 October 2021.

References

1. DOE-EERE, 2019, “Fiscal Year 2019 Advanced Vehicle Technologies Research Funding Opportunity Announcement,” DE-FOA-0002014, Washington, D.C., USA. Available at: <https://eere-exchange.energy.gov/FileContent.aspx?FileID=25f7a4dd-9874-4aee-9606-2ab52fe9cc18>. Accessed 25 February 2022.
2. Wang, Q. G., P. Jones, Y. Wang, and D. Gerard, 2011, “Advances in computational tools for virtual casting of aluminum components,” in: Allison, J. E., P. M. Collins, and G. Spanos (eds.), *Proceedings of the 1st World Congress on ICME*, TMS 2011, pp. 217–222.
3. Zhu, X., J. Z. Yi, J. W. Jones, and J. E. Allison, 2007, “A probabilistic model of fatigue strength controlled by porosity population in a 319-type cast-aluminum alloy: Part I. Model development,” *Metall. Mater. Trans. A–Phys. Metall. Mater. Sci.*, Vol. 38, No. 5, pp. 1111–1122.

Acknowledgments

The PIs would like to thank DOE-EERE VTO for the opportunity to work on this important project, especially Mr. K. Howden, Mr. J. Gibbs, and Mr. R. Nine at DOE for their project oversight. The PIs are also very grateful to Mr. S. Campbell (contract manager at GM) and the GM Project and Management Team; Dr. A. Shyam, and his team at ORNL; Prof. A. Luo, and his team at OSU; Prof. P. Sanders, and his team at Michigan Technological University; and Mr. D. Weiss, and his team at Eck Industries, Inc., for their extreme support and dedication to the project.

I.4.3 Lightweight and Highly Efficient Engines Through Al and Si Alloying of Martensitic Materials (Oak Ridge National Laboratory)

Yong-Ching Chen, Co-Principal Investigator

Cummins Technical Center
1900 McKinley Avenue
Columbus, IN 47201
E-mail: yong-ching.c.chen@cummins.com

Dean Pierce, Co-Principal Investigator

Oak Ridge National Laboratory
1 Bethel Valley Road
Oak Ridge, TN 37831
E-mail: piercedt@ornl.gov

Jerry L. Gibbs, DOE Technology Manager

U.S. Department of Energy
E-mail: jerry.gibbs@ee.doe.gov

Start Date: May 1, 2019	End Date: April 30, 2022	
Project Funding (FY 2021): \$313,447	DOE share: \$34,858	Non-DOE share: \$278,589

Project Introduction

This project began as a joint two-year project, funded by the DOE VTO LightMAT Program between ORNL and Cummins to develop and engine test a new steel alloy for pistons in diesel engines. The project brings expertise from both organizations to enable rapid development and specific optimization of the alloy's properties for the unique requirements of the piston application. The project was divided into Phase 1—focused on laboratory-scale alloy development—and Phase 2—focused on scaling the developed alloy, manufacturing a piston from the new alloy, and then engine testing the full-scale piston. Work in both phases of the project is being completed jointly by Cummins and ORNL, but ORNL executed the majority of the alloy development in Phase 1 while Cummins is primarily responsible for the majority of efforts relating to piston manufacture and engine testing in Phase 2. The project is currently in Phase 2. An extension of one-year with an additional \$125,000 in funds to ORNL and an additional \$80,000 cost-share commitment by Cummins was approved in FY 2021. The new project end date is April 2022.

The current piston materials for medium and HDDEs are quenched and tempered 4140 martensitic steel and grade 38MnVS6 micro-alloyed steel (MAS). These materials are cost-effective and have high-strength and acceptable oxidation resistance at temperatures up to ~500°C. A primary pathway to increase the efficiency of internal combustion engines involves increasing both peak cylinder pressure and combustion gas temperature. However, 4140 and MAS are currently operating at their temperature limits, which prevents further increases in efficiency by increasing combustion gas temperatures and pressures. Thus, new piston materials are required to overcome this barrier to increasing MD and HD diesel engine efficiency. Additional barriers to implementing new piston materials are cost and manufacturability. Some commercially available candidate materials that may possess the necessary elevated temperature properties are too expensive or have poor weldability and/or machinability resulting in additional costs and technical barriers.

Objectives

The objectives of this project are to develop and engine test new steel alloys for pistons. A new steel alloy must exhibit sufficient fatigue strength and oxidation resistance to be able to operate at peak temperatures of 600°C for extended periods of time. Furthermore, elevated temperature strength, oxidation resistance, and thermal conductivity are often in conflict with one another, and significant attention in this project is focused on how to balance these properties. An alloy must also be friction weldable to a piston-skirt material of 4140 steel or MAS and have reasonably good machining characteristics. In addition, the raw material cost of the new steel can only be incrementally greater than 4140 steel or the MAS. The steel must also have a high technology readiness level to enable the alloy to be commercially scaled and implemented in a relatively rapid timeframe, meaning the alloy should be similar enough to existing materials that it can be manufactured and processed with existing processes and equipment at steel mills and piston manufacturers. Therefore, while innovative alloying strategies are being pursued in this project, radical departures from current or candidate commercial materials are avoided in this three-year project. Cummins and ORNL have defined internal targets for strength, thermal conductivity, oxidation resistance, and cost for the new alloys.

Approach

This project is focused on the development of new alloys for piston materials. The 4140 steel was selected as the baseline alloy along with one additional commercial alloy, designated Alloy “C,” with higher heat resistance that may be suitable for 600°C operation in piston materials. These baseline alloys were used to evaluate performance improvements of the new developmental alloys. This project used computational alloy design methods to better facilitate identification of alloy chemistries that have the necessary mechanical and oxidation properties for piston applications operating at 600°C. Once alloy compositions were identified, the alloys were arc-melted, processed by hot rolling, heat-treated, tested, and characterized. Testing includes elevated temperature tensile testing, oxidation testing, thermal diffusivity measurements, and measurements of the CTE for select alloys. Samples were also aged at high temperatures for long periods of time to simulate thermal exposure during engine operation, and then tensile tested at elevated temperatures to evaluate each alloy’s resistance to aging. High-cycle rotating beam fatigue testing is also being performed. Microstructures were characterized by optical microscopy.

An iterative alloy development process was used, in which small batches of material were melted and tested, and the results used to guide the development of the next batch(es) of alloys. This process has resulted in an improved understanding of alloying effects on properties relevant to piston materials, continuous optimization, and downselection of promising alloy chemistries and processing routes. The same tests were performed on Alloy 4140 and Alloy C as were used in the developmental alloys to assess any improvement over the commercial alloys. CFD software was employed to evaluate how properties such as thermal conductivity affect piston temperatures and how predicted surface temperatures will change from alloy to alloy.

For the final phase of this project, a developmental alloy was downselected and then scaled-up at an external vendor to make sufficient amounts of material for fabrication of piston prototypes with a piston manufacturer. The prototype pistons are being manufactured and will undergo welding and machining trials and ultimately, pistons of the new material will be engine-abuse tested in FY 2022 to identify operational limits of the new alloy and its durability. After engine testing, pistons will be evaluated to further characterize the resistance of the material to aging and oxidation in a combustion atmosphere.

Results

The data generated in this project are proprietary and that which is provided is only relative to improvements over commercial Alloy C. Cummins and ORNL melted and tested a total of 24 developmental steels with varied compositions in the first 1.5 years of this project and downselected a single alloy composition for scale-up. The following important results and achievements occurred in FY 2021:

- An alloy with a good balance of cost, elevated temperature yield strength, oxidation resistance, and thermal conductivity was downselected for scaling up to a larger quantity.

- Intellectual property protection of the alloy was initiated.
- HCF testing of the developed alloy and Alloy C was conducted. The new alloy exhibits a 50% improvement in the fatigue limit at 600°C above the commercial baseline Alloy C. The normalized fatigue data is shown in Figure I.4.3.1.
- Cummins and ORNL are working with an external vendor to melt and rotary forge a 1,500 lb. ingot. The ingot has been melted and rotary forging is expected to occur in January 2022.

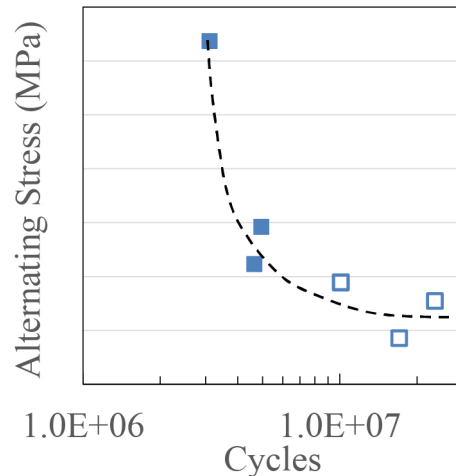


Figure I.4.3.1. Alternating stress vs. number of cycles from rotating beam fatigue data at 600°C for six specimens of the developed alloy. Filled data points correspond to failed specimens and un-filled data points are from specimens that were removed prior to failure. Stress values are proprietary and actual values have been omitted. Source: ORNL/Cummins.

Conclusions

In FY 2021, Cummins and ORNL downselected a promising alloy, confirmed it exhibits high elevated temperature fatigue strength, initiated intellectual property protection, and worked with an external vendor to melt a 1,500 lb. ingot of the alloy. The project received a one-year extension and prototype piston fabrication and engine testing is expected to occur in FY 2022.

Key Publications

1. Invention disclosure submitted in FY 2021.
2. Patent application submitted in FY 2021.

Acknowledgments

The following ORNL personnel are acknowledged for their contributions to this project: G. Muralidharan, A. Haynes, T. Muth, I. Stinson, G. Cox, D. Moore, D. Heidel, K. Hanson, V. Cox, H. Wang, A. Trofimov, K. Hedrick, and G. Garner. The following Cummins personnel are acknowledged for their contributions as well: C. Trobaugh, Q. Ma, J. Zhou, H. Savage, B. Wang, D. E. Richardson, and W. D. McNulty.

II Lightweight Materials

II.1 Automotive Metals

II.1.1 Shear-Assisted Processing and Extrusion (ShAPE) of Lightweight Alloys for Automotive Components (Pacific Northwest National Laboratory/ Magna International CRADA)

Scott Whalen, Co-Principal Investigator

Pacific Northwest National Laboratory
902 Battelle Blvd.
Richland, WA 99354
E-mail: scott.whelen@pnnl.gov

Tim Skszek, Co-Principal Investigator

Magna Services of America, Inc (Magna R&D)
750 Tower Dr.
Troy, MI 48098
E-mail: tim.skszek@magna.com

Sarah Kleinbaum, DOE Program Manager

U.S. Department of Energy
E-mail: sarah.kleinbaum@ee.doe.gov

Start Date: January 1, 2019	End Date: September 30, 2022
Project Funding (FY 2021): \$2,005,000	DOE share: \$1,005,000 Non-DOE share: \$1,000,000

Project Introduction

Lightweight automotive components made from Al alloys offer 25% weight-savings as compared to high-strength steel state-of-the-art components. Additionally, components made from 100% scrap offer >50% energy savings and >90% CO₂ savings during the manufacturing process as compared to conventional extrusion, since remelting during recycling and the use of primary Al can both be eliminated [1-2]. For this CRADA between PNNL and Magna R&D, ShAPE™ is being developed to convert Al scrap directly into a sub-scale EV battery support structure and chassis components. Extruded Al EV battery structures provide opportunity based on equal, or improved performance, at a reduced cost as compared to conventional extrusions.

The potential cost and environmental benefits associated with the use of a cast billet comprised of 100% secondary Al scrap are well-established [1-4]. However, the use of secondary scrap without the addition of a significant percentage of primary Al has not developed into an industry process due to fundamental material challenges associated with achieving full metallurgical bonding between interfaces [5] and uniform microstructure [6]. These process limitations have been overcome using severe plastic deformation (SPD) techniques [7], such as equal channel angular pressing (ECAP) [8]; however, although successful from a scientific standpoint, ECAP and other SPD processes are not scalable to an industrial level. The ShAPE process combines the microstructural advantages of SPD, with the scalability of a conventional extrusion process to offer a unique technology for converting Al scrap directly into automotive components. This report highlights the most noteworthy progress made toward this goal in FY 2021.

Objectives

The goal of this Magna R&D/PNNL CRADA is to demonstrate the feasibility of using PNNL's ShAPE technology to manufacture Al alloy tubular extrusions using billet feedstock comprised from 100% Al scrap. It is envisioned that by using the ShAPE process, billet feedstock comprised of 100% secondary scrap can be used to fabricate cross-members, engine cradles, roof rails, and EV battery support structures.

Approach

The scope of this work focuses on two discrete thrusts: (1) using ShAPE to extrude circular cross-sections from Al scrap to determine whether the process is technically feasible and (2) using ShAPE to extrude non-circular cross-sections using a port-hole bridge die approach to determine whether the process is adaptable to industry-relevant geometries. As a step toward non-circular cross-sections, round tubing is being extruded using a port-hole bridge die approach integrated into the ShAPE process. Magna R&D is primarily responsible for supplying feedstock material, tool fabrication, process modeling, and testing. PNNL is primarily responsible for tool design and integration, process development, microstructural characterization, publication, and project reporting. Figure II.1.1.1 shows PNNL's first-of-a-kind ShAPE machine, which is the manufacturing platform utilized for this project.



Figure II.1.1.1. ShAPE™ machine installed in PNNL's Solid-Phase Processing Laboratory. Source: PNNL.

Unlike conventional extrusion where the die is pressed against the billet using a strictly linear motion, the ShAPE extrusion process superimposes a rotational shear force by spinning the die, as observed in Figure II.1.1.2. The ShAPE process is described in detail elsewhere [9-12]; however, the basic operation for extruding hollow profiles is briefly described here for convenience. Contact between the billet and rotating die generates frictional heating at the die/billet interface along with heating within a thin layer of deforming material below the die face due to plastic deformation. The extent of heat generation and depth of the deformation zone is controlled by regulating rotational speed, motor torque, and ram speed. As a result, the heat required to soften the material is entirely derived by the process, and billet preheating in a separate furnace is not required. As the temperature increases, material plastically flows inward toward the extrusion orifice through individual spiral grooves machined into the die face. Upon exiting the grooves, the flow streams consolidate prior to entering the extrusion orifice where the material then flows between the mandrel and die-bearing surface to form a tube.

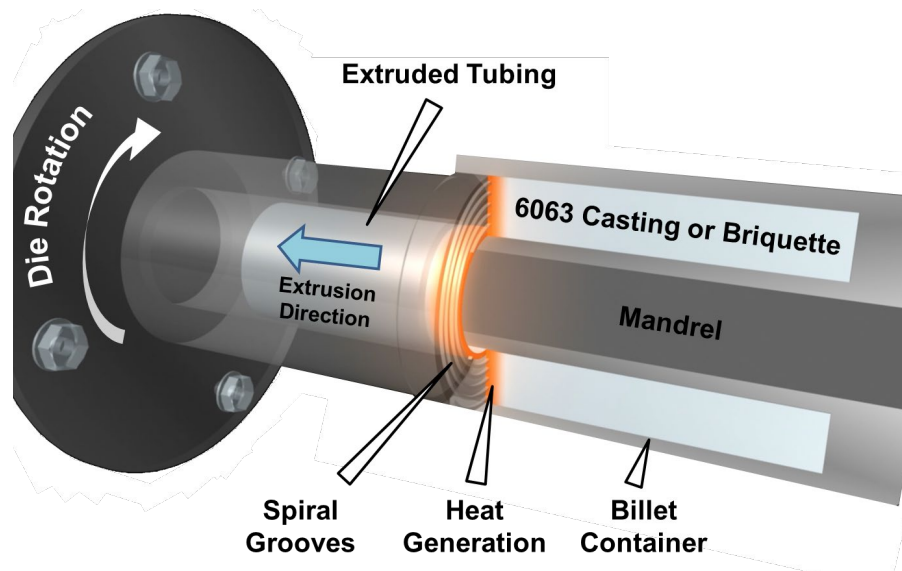


Figure II.1.1.2. Schematic of ShAPE™ tooling and process. Source: PNNL.

Results

The primary goals in FY 2021 were to: (1) demonstrate that ShAPE can extrude 100% Al scrap with adequate machinal properties for an EV battery tray structure application; and (2) demonstrate that a port-hole bridge die approach is feasible with ShAPE.

To demonstrate the extrusion of 100% Al 6063 scrap by ShAPE, Magna R&D provided PNNL with billets in the form of castings and cold-compacted briquettes. Castings were fabricated from 100% secondary scrap with small additions of Fe and Mg to explore the allowable upper limits for 6063, while briquettes were fabricated from engineered machining chips taken from 6063-T5 feedstock. It is worth noting that Magna R&D went through an extensive development cycle to determine the optimum cleaning, tooling, and pressing conditions for fabricating briquette billets with >99% density. PNNL extruded these cast and briquette billets using tooling designed by PNNL and fabricated by Magna R&D. Extrusions were performed at the maximum ram speed of the ShAPE machine (e.g., 0.36 m/min), which gave an extrusion speed of 4.5 m/min for tubing having a 12 mm OD and a 2-mm wall thickness. An extrusion ratio of 11.8 was utilized on this project. Prior work in FY 2020 determined that the extrusion temperature should be in the 500°C to 520°C range, as controlled by the rotational rate to achieve peak mechanical properties for ShAPE-extruded 6063. Water quenching of the extrusion was performed for extrusions made from cast billets, but was not available earlier in the year when the briquettes were extruded. Water quenching near the die exit is necessary to ‘press quench’ the extrusion to obtain the T6 properties (solution heat treating + quenching + artificial aging) with merely a T5 heat-treatment (quenching during extrusion + artificial aging), as it is typical of conventional extrusion. Figure II.1.1.3 shows an example of a 12-mm diameter tube with a 2-mm wall thickness extruded by ShAPE.

For extrusions made from cast billets, 150 mm long sections were cut from the tubes and artificially aged at 177°C for eight hours. No solution heat treating was performed prior to artificial aging to discover if press quenching was achieved during ShAPE extrusion of castings made from 100% scrap. The 150 mm long specimens were fitted with tapered pugs on each end per ASTM E8 and pulled at Magna on a Materials Testing Systems (MTS) 810 load frame with a 50-kN load cell at a rate of 2.3 mm/min, with a 50-mm extensometer measuring the gauge length. Eight replicates were tested for each billet type. Tensile test results are shown in Table II.1.1.1 and compared to the ASTM B221M-13 minimum standard [13] and American Society of Metals (ASM) typical values [14] for conventionally extruded 6063 tubes of this size in the T5 and T6 conditions.

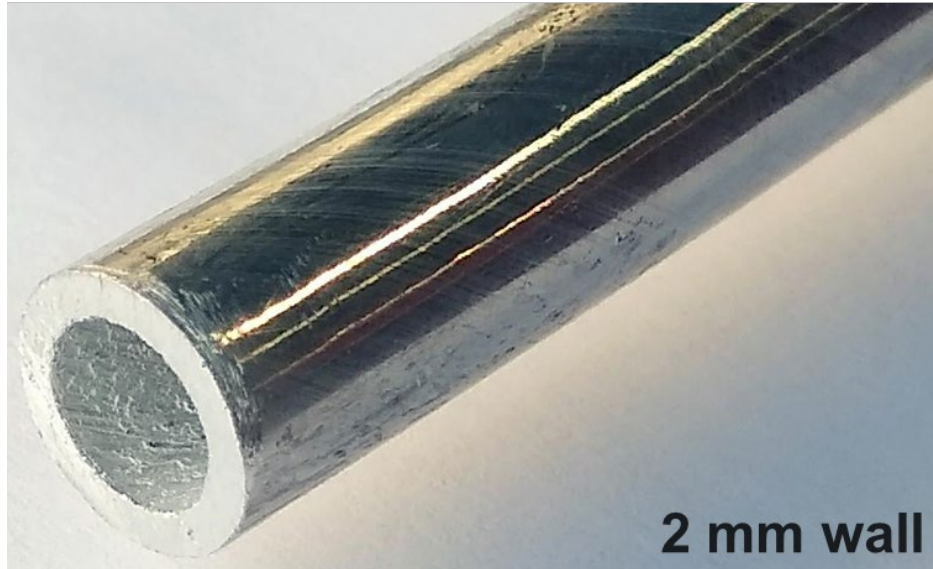


Figure II.1.1.3. Examples of AA6063-T5 tubing extruded by ShAPE™. Source: PNNL.

Table II.1.1.1. Tensile Properties of 2-mm-Thick Tubing Extruded by ShAPE from 6063 Cast Billets Compared to the Relevant ASTM [13] and ASM [14] Standards

Property	ShAPE 6063+Mg T5	ShAPE 6063+Mg+Fe T5	T5 Min. [13]	T5 Typ. [14]	T6 Min. [13]	T6 Typ. [14]
Yield Strength (MPa)	202 ± 10	191 ± 10	110	145	170	214
Ultimate Strength (MPa)	233 ± 9	226 ± 9	150	186	205	241

Table II.1.1.1 shows that yield and ultimate strengths for ShAPE-extruded 6063 castings, subsequently heat-treated to the T5 condition, are significantly higher than conventionally extruded 6063 in the T5 condition, per ASTM and ASM. This demonstrates that the Mg_2Si strengthening phase is driven into solution during extrusion and that press quenching was effective in minimizing Mg_2Si reprecipitation and coarsening. Additionally, yield and ultimate strength for ShAPE-extruded 6063 castings, subsequently heat-treated to the T5 condition, exceed that of the ASTM minimum standard for the T6 condition and approach the ASM typical values for T6. As such, this work validates that ShAPE can extrude 6063 casting made from 100% scrap with properties adequate for applications where conventionally extruded 6063 is a candidate.

For extrusions made from briquettes, 150-mm sections were cut from the tubes and artificially aged at 177°C for 8 hours to obtain T5. To obtain T6, specimens were solution heat-treated at 520°C for 1 hour, then immediately water-quenched, and followed by artificial aging at 177°C for 8 hours. Table II.1.1.2 shows that the yield and ultimate strengths for the ShAPE-extruded 6063 briquettes, as shown in Figure II.1.1.4, and subsequently heat-treated to the T5 condition, are higher than the ASTM minimum standard and on par with the ASM typical values for T5. For T6, the yield and ultimate tensile strengths for the ShAPE-extruded 6063 briquettes, and subsequently heat-treated to the T6 condition, are higher than the ASTM minimum standard, but slightly below the ASM typical values for T6. For all conditions, ShAPE extrusions have higher elongation due to refined and uniformly distributed second-phase precipitates as has been discussed in the literature [11, 12]. As such, this work validates that ShAPE can extrude 6063 briquettes made from 100% cold-compacted scrap, with properties adequate for applications where conventionally extruded 6063 is a candidate. Furthermore, the results demonstrate that adequate properties can be achieved from 100% scrap billets in cast or briquette form for 6063.

Table II.1.1.2. Tensile Properties of 2-mm-Thick Tubing Extruded by ShAPE from 6063 Briquettes Compared to the Relevant ASTM [13] and ASM [14] Standards

Property	ShAPE 6063 Briquette T5	ShAPE 6063 Briquette T6	T5 Min [13]	T5 Typ [14]	T6 Min [13]	T6 Typ [14]
Yield Strength (MPa)	149 ± 4	204 ± 9	110	145	170	214
Ultimate Strength (MPa)	191 ± 4	224 ± 8	150	186	205	241
Elongation (%)	22	17	8	12	8	12



Figure II.1.1.4. Briquette manufactured by Magna R&D from 6063 scrap. Source: Magna R&D.

Near the end of FY 2021, the project team developed a miniature port-hole die to demonstrate proof-of-concept, as shown in Figure II.1.1.5(a). An initial set of process parameters were developed that successfully extruded the tube as shown in Figure II.1.1.5(b) is currently undergoing microstructural characterization to determine the extent to which weld seams have been eliminated.

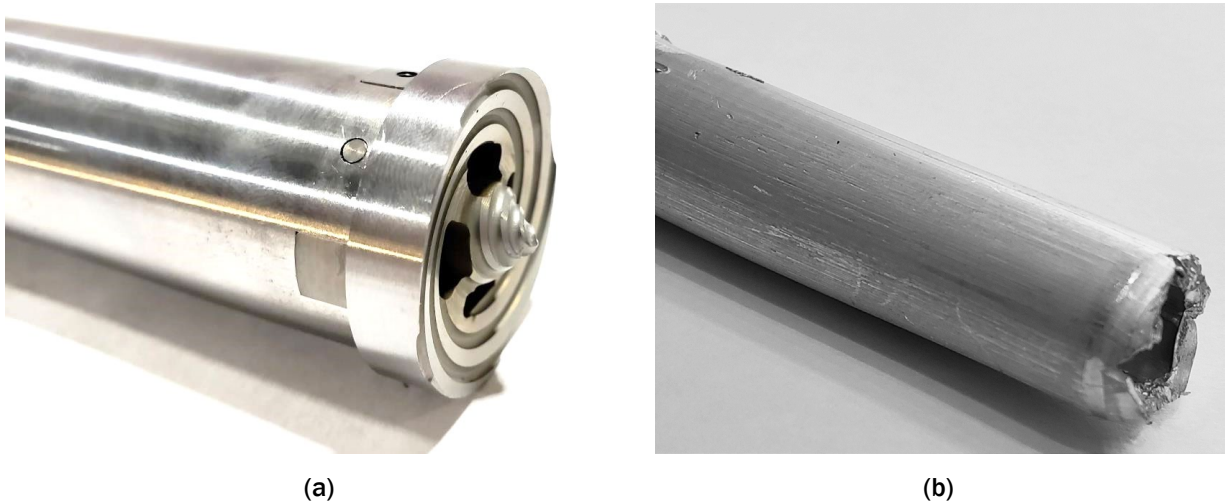


Figure II.1.1.5. (a) Machined and assembled port-hole die. (b) 6063 tubing fabricated from cast billet using a port-hole bridge die. Source: PNNL.

Conclusions

The joint PNNL/Magna R&D project team demonstrated that extrusion of 100% Al 6063 scrap in the form of castings and briquettes is possible using ShAPE. Tensile properties exceeding the ASTM minimum standard and ASM typical values for a T5 temper, and on par with a T6 temper, suggest that ShAPE-extruded castings and briquettes have viable properties for automotive applications where 6063 is of interest. A proof-of-concept was demonstrated for the port-hole die where a 12-mm diameter tube with a 2-mm wall thickness was extruded. Efforts in FY 2022 will focus on port-hole extrusion of non-circular profiles and additional work on briquettes from low-cost feedstock.

Key Publications

1. Taysom, B. S., N. Overman, M. Olszta, Md. Reza-E-Rabby, T. Skrzek, M. DiCiano, and S. Whalen, 2021, “Shear-assisted processing and extrusion of high-strength aluminum alloy 6063 tubing,” *Int. J. Mach. Tools Manuf.*, Vol. 169, Art. 103798.
2. Taysom, B. S., S. Whalen, Md. Reza-E-Rabby, M. DiCiano, and T. Skrzek, 2021, “Shear-assisted processing and extrusion of thin-walled AA6063 tubing,” *TMS 2021 Light Metals*, pp. 281–285.
3. Taysom, B. S., Md. Reza-E-Rabby, S. Whalen, M. DiCiano, T. Skrzek, and other co-authors, “Fabrication of aluminum alloy 6063 tubing from secondary scrap with shear-assisted processing and extrusion,” *TMS 2022 Light Metals* (accepted).

References

1. Mulholland, E., 2016, “Aluminum extrusion EPD background report,” Aluminum Extruders Council, Wauconda, IL, USA, September 6, 2016.
2. Bushi, L., T. Skrzek, and T. Reabum, 2019, “New ultra-light automotive door life cycle assessment,” *Int. J. Life Cycle Assess.*, Vol. 24, pp. 310–323.
3. Ab Rahim, S. N., M. A. Lajis, and S. Ariffin, 2015, “A review of recycling aluminum chips by hot extrusion process,” *Procedia CIRP*, Vol. 26, pp. 761–766.
4. Wan, B., W. Chen, T. Lu, F. Liu, and Z. Jiang, 2017, “Review of solid-state recycling of aluminum chips,” *Resour. Conserv. Recycl.*, Vol. 125, pp. 37–47.
5. Chiba, R., T. Nakamura, and M. Kuroda, “Solid-state recycling of aluminum alloy swarf through cold profile extrusion and cold rolling,” *J. Mater. Process. Technol.*, Vol. 211, pp. 1878–1887.
6. Guley, V., N. B. Khalifa, and A. E. Tekkaya, 2010, “Direct recycling of 1050 aluminum alloy scrap material mixed with 606 aluminum alloy chips by hot extrusion,” *Int. J. Mater. Form.*, Vol. 3, pp. 853–856.
7. Azushima, A., R. Kopp, A. Korhonen, D. Yang, F. Micari, G. Lahoti, P. Groche, J. Yanagimoto, N. Tsuji, A. Rosochowski, and A. Yangida, 2008, “Severe plastic deformation (SPD) processes for metals,” *CIRP Ann. Manuf. Technol.*, Vol. 57, pp. 716–735.
8. Hasse, M., N. Ben Khalifa, A. E. Tekkaya, and W. Z. Misiólek, 2012, “Improving mechanical properties of chip-based aluminum extrudates by integrated extrusion and equal channel angular pressing (iECAP),” *Mater. Sci. Eng. A*, Vol. 539, pp. 194–204.
9. Lavender, C., V. Joshi, G. Grant, S. Jana, S. Whalen, J. Darsell, and N. Overman, 2019, “System and process for formations of extrusion products,” U.S. Patent No. 10,189,063, January 29, 2019.
10. Whalen, S., N. Overman, V. Joshi, T. Varga, D. Graff, and C. Lavender, 2019, “Magnesium alloy ZK60 tubing made by Shear-Assisted Processing and Extrusion (ShAPE™),” *Mat. Sci. Eng. A*, Vol. 755, No. 7, pp. 278–288.

11. Taysom, B. S., N. Overman, M. Olszta, Md. Reza-E-Rabby, T. Skrzek, M. DiCiano, and S. Whalen, 2021, “Shear-assisted processing and extrusion of high-strength aluminum alloy 6063 tubing,” *Int. J. Mach. Tools Manuf.*, Vol. 169, Art. 103798.
12. Whalen, S., M. Olszta, Md. Reza-E-Rabby, T. Roosendaal, T. Wang, D. Herling, B. S. Taysom, S. Suffield, and N. Overman, 2021, “High-speed manufacturing of aluminum alloy 7075 tubing by Shear-Assisted Processing and Extrusion (ShAPE),” Vol. 71, pp. 699–710.

Acknowledgments

PNNL and Magna R&D thank the Vehicle Technologies LightMAT Program for supporting this project.

II.1.2 Low-Cost Magnesium Sheet Component Development and Demonstration Project (Fiat Chrysler Automobile, U.S., LLC)

Randy Gerken, Principal Investigator

Stellantis (formerly Fiat Chrysler Automobile, U.S., LLC)
800 Chrysler Drive, CIMS: 485-00-15
Auburn Hills, MI 48326
E-mail: randy.gerken@stellantis.com

Sarah Kleinbaum, DOE Program Manager

U.S. Department of Energy
E-mail: sarah.kleinbaum@ee.doe.gov

Start Date: October 1, 2016	End Date: July 31, 2021	
Project Funding (FY 2021): \$1,052,847	DOE share: \$736,993	Non-DOE share: \$315,854

Project Introduction

Most of the applications of Mg in lightweighting of commercial cars and trucks are die-castings rather than sheet metal, and automotive applications of Mg sheets have typically been experimental or low-volume serial production. The value of the U.S. Automotive Materials Partnership, LLC (USAMP), Low-Cost Mg Sheet Project to OEMs lies in the potential availability of a lower-cost, more formable Mg sheet alloy, as well as a reduced cost in using a Mg sheet in automotive applications due to: (a) improved formability at reduced temperatures; (b) improved corrosion protection; and (c) reduced coating costs because of improved forming lubricant and coating technologies. This five-year project, which was recently completed by USAMP and its research partners, pursued a comprehensive strategy to address these challenges.

Objectives

The overarching objective of the project was to research, develop, and demonstrate at least one large, challenging Mg sheet component on a model year (MY) 2013 or newer vehicle at a manufacturing cost of less than \$2.50 per pound of weight saved (\$5.50/kg saved).

The baseline components evaluated in this project were inner and outer panels from the front doors of two 2013 MY mid-size sedans: the Chrysler 200 and the Ford Fusion. These components were selected due to the numerous challenges involved in producing large Mg alloy-based panels that would meet industry requirements for formability, durability, joinability, stiffness, corrosion protection, and appearance. Whereas the Chrysler Mg-intensive door was used for technical cost-modeling, the Ford door was used for demonstration due to the ready availability of stamping tools.

Approach

The USAMP adopted a technical approach that integrated experimental studies with advanced computational tools based on ICME methods to develop new alloy chemistries and their thermomechanical processing that promise improved formability and lower forming temperatures. A penultimate task before finally forming the stampings was to incorporate actual microstructure parameters into models that would enable formability simulations. This approach has, for the first time, accounted for individual Mg grains moving in an anisotropic fashion unlike that for Al or steel that have isotropic properties upon which the current simulation tools are based. In separate activities, new coatings and lubricants to facilitate the forming and improved corrosion protection and joining strategies were developed to ensure the door could be successfully produced with the stated product requirements.

The following research activities were conducted concurrently: (1) technical cost guidance to identify key cost drivers associated with current Mg component production; (2) material characterization and modeling studies;

(3) rolling trials on ingots; (4) pretreatment, coating application, and lubrication studies; (5) forming studies; (6) scaling to warm-forming of large door components; and (7) exploratory joining studies. The task interrelationships are illustrated in Figure II.1.2.1 below.

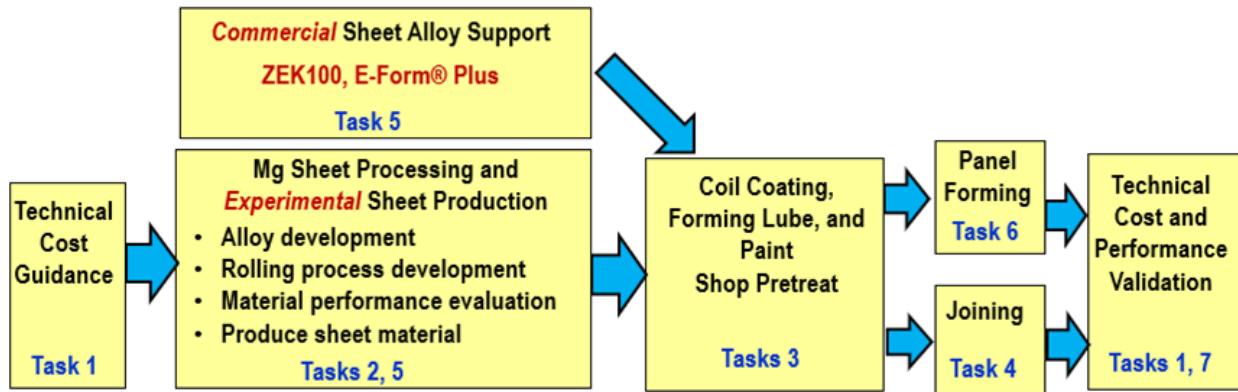


Figure II.1.2.1. Project task interrelationships. Source: USAMP.

Public data, experimental results, and the subtask and final reports developed on for the project are archived in the DataHUB repository established by the LightMAT Consortium accessible at <https://data.lightmat.org/project>.

The project participants included:

- Sub-awardees: Applied Engineering & Technology (AET) Integration, Inc.; Fuchs Lubricants Co.; Henkel Corporation; PPG Industries, Inc.; Quaker-Houghton Chemical Corporation; Vehma International of America, Inc.; Xtalic Corporation; The OSU; University of Florida (UF); University of Illinois at Urbana-Champaign (UIUC); University of Michigan (UM); and University of Pennsylvania (UPenn).
- Vendors: Bucciero & Associates, LLC; Camanoe Associates; Edison Welding Institute (EWI); FADI-AMT LLC; InalTech, Inc.; Korea Magnesium Industry; M-Tech International, LLC; POSCO and Pinetree Pos Magnesium (PPM).
- DOE National Laboratories: PNNL and ORNL.

Table II.1.2.1 lists the completion status of the project’s 11 milestones at the end of FY 2021.

Table II.1.2.1. Status of Project Tasks and Milestones at the End of FY 2021

BP	Milestone Number	Milestone Type	Task	Description	Status
1	1	Go/No-Go	Task 0: Project Management/Contracting	100% of purchase orders issued to subs.	Complete
	2	Technical	Task 1: Technical Cost Guidance	Baseline cost model for Mg sheet complete.	Complete
	3	Technical	Task 2: Alloy and Sheet Processing Development	New Mg alloy sheet composition(s) identified.	Complete
2	4	Technical	Task 2: Alloy and Sheet Processing Development	Constitutive model for textured Mg alloy completed and ideal texture suggested.	Complete
	5	Technical	Task 2: Alloy and Sheet Processing Development	Forming analysis completed on medium sheet.	Complete
	6	Technical	Task 3: Sheet Coatings and Lubricant Evaluation and Development	Forming lubricant composition identified.	Complete
	7	Go/No-Go	Task 5: Mg alloy Sheet Production	Manufacture and deliver experimental medium-width sheets.	Complete
3	8	Technical	Task 3: Sheet Coatings and Lubricant Evaluation and Development	Evaluation of corrosion protection coating completed.	Complete
	9	Technical	Task 5: Mg alloy Sheet Production	Delivery of wide sheet.	Complete
	10	Technical	Task 6: Mg alloy Large Body Component Production	Mg alloy panels formed to specifications.	Complete
	11	Technical	Task 7: Component(s) Demonstration	Final delivery and performance evaluation completed.	Complete

Results

In spite of the continuing COVID-19 pandemic, USAMP achieved all eleven project milestones and closed out this project in FY 2021. Most research tasks concluded in February 2021, followed by data analysis and subtask report reviews, a closeout review with DOE sponsors in May 2021, disposition activities and preparation and archival of final closeout reports. All remaining technical work was completed in July 2021.

Additional material testing over three strain paths and elevated temperatures was performed to support formability simulation studies in order to validate the project's final deliverable, which was an enhanced constitutive model and material card MAT233+ that factored evolving anisotropy in Mg sheet.

Task highlights and representative results for the work completed in FY 2021 are summarized in the following relevant sections.

Development of Technical Cost Model

From the initial analysis of cost drivers reported in FY 2020, Camanoe found that Mg assemblies are more expensive because material and assembly costs relative to baseline steel designs outweigh gains from lower mass and part count reduction. The material costs are primarily driven by high raw material production costs.

In FY 2021, Camanoe's process-based cost-modeling analysis of the FCA Chrysler 200 Mg door used two scenarios of producing Mg, considering that primary Mg from China (produced using the Pidgeon process) is about half as expensive as that made in the U.S. using the (electrolytic process). Total costs included parts

production, assembly, and paint. As shown in Figure II.1.2.2, the comparison of producing a Mg door to a steel door showed that the China-produced Mg door’s lightweighting cost of \$4.26/kg saved was under the project target of \$5.50 (derived from the industry standard cost to produce large assemblies from Al), whereas the U.S.-produced Mg scenario had a lightweighting cost of \$6.60. The cost of the coated Mg alloy sheet is a key driver of the results. A 10% decrease in the cost of using Mg sheets produced in the U.S. would lead to it being within the project’s lightweighting cost target. The mass of the Mg-intensive door is 9.1 kg (54%) less than that of a steel door.

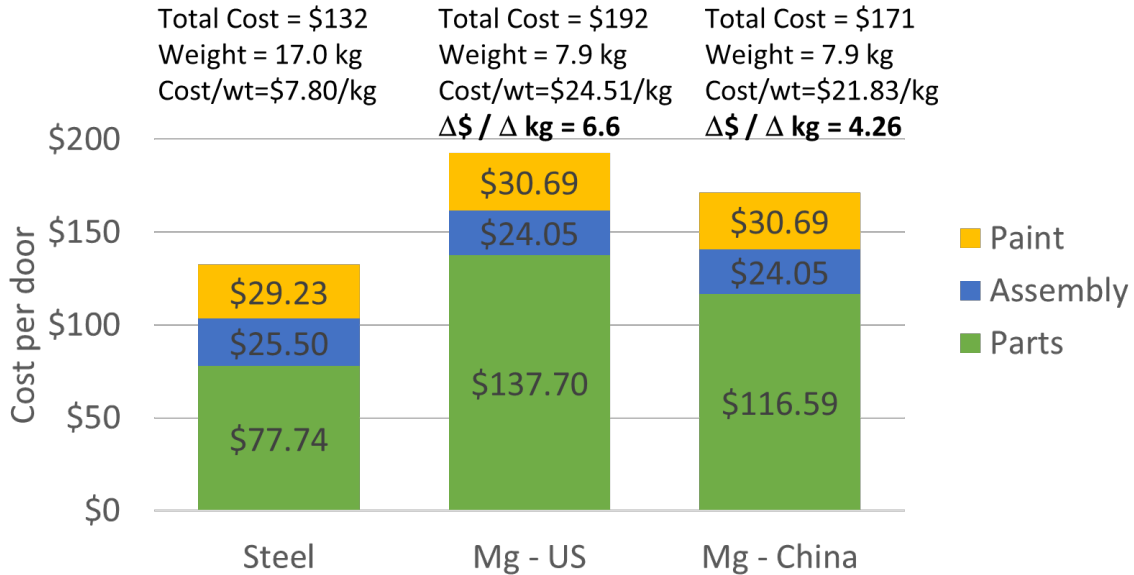


Figure II.1.2.2. Total part fabrication, assembly, and paint costs per door (100,000 annual volume). Source: Camanoe.

While larger parts in the Mg-intensive door design are cost-competitive based on the cost target, smaller parts have relatively high lightweighting costs, and the Al casting is heavier and significantly more expensive than the equivalent three steel parts. This indicates there is opportunity to further optimize the design of the Mg door.

Alloy Development and Modeling Studies

Figure II.1.2.3 illustrates the types of data that are generated and the inputs that are provided to modeling by each performing organization in sample fabrication and characterization.

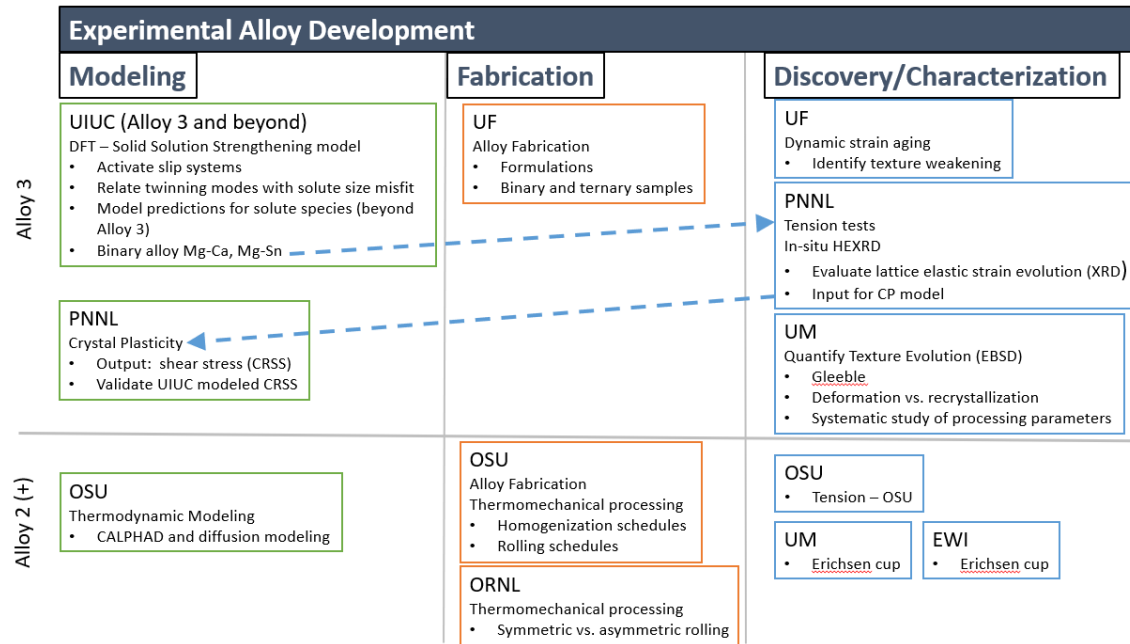


Figure II.1.2.3. Task organization and data flows for the new Mg alloy development and modeling process. Source: USAMP.

Alloy and Sheet Processing Developments

The UIUC, UF, UM, and PNNL groups completed their respective subtasks on development and evaluation of USAMP Experimental Alloy 3 (e.g., various combinations of binary and ternary Mg alloys) using guidance from the ICME models developed from the UIUC’s energy landscape computations of a range of elemental solutes systematically identified by the team.

ICME tools were also used by OSU, as reported in prior project years, to design a new Mg sheet alloy, ZAXME11100 (USAMP Alloy 2 Plus - Mg-1.0Zn-1.0Al-0.5Ca-0.4Mn-0.2Ce by weight), whose performance in RT formability was tested in Index Erichsen (IE) cup draw experiments and the yield strength (YS) was found to be similar to a 6000-series Al sheet, as shown in Figure II.1.2.4.

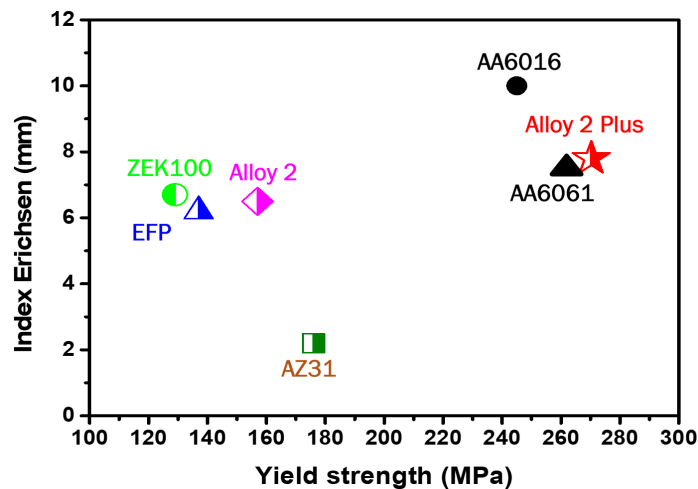


Figure II.1.2.4. RT formability (IE values) vs. the YS of various alloys. For the age-hardening Alloy 2 Plus, AA6061, and AA6016 alloys, the IE was measured in the solution-treated condition, but the YS was measured in peak-aged condition. Source: The Ohio State University.

In FY 2021, ORNL performed three laboratory-scale shear-rolling trials on Alloy 2 and Alloy 2 Plus to evaluate thermomechanical processing parameters for warm-rolling the new Mg alloys developed on this project. The results are reported in the next subsection.

Symmetric and Asymmetric Rolling with a Shear-Rolling Mill

Rolling trials were conducted on Alloy 2 and Alloy 2 Plus ingots using a shear-rolling mill at ORNL after the appropriate homogenization treatments. Table II.1.2.2 shows the rolling temperatures and velocity ratios used.

Table II.1.2.2. Summary of Process Conditions used for Three Rolling Trials at ORNL

Temperatures	Velocity Ratios	Reduction	Passes
135 °C	1:1 (symmetric)	10%–73%	Single-pass
275 °C	1:2 1:4	(Total reduction)	Multi-pass

Figure II.1.2.5 shows that both Alloy 2 and Alloy 2 Plus could be rolled to large reductions at 275°C. The edge quality of Alloy 2 Plus was better than that for Alloy 2. Symmetric rolling at 275°C with a targeted ~35% reduction in thickness resulted in cracking along the center of the rolled piece in Alloy 2, but the piece could be successfully rolled using asymmetric rolling. Thus, asymmetric rolling was beneficial in targeting larger reductions—especially in Alloy 2 Plus—and provided the desired weak basal texture of multiples of random distribution (MRD) = 5.9 with a tendency towards a random texture, as observed in the EBSD image seen in Figure II.1.2.6.



Figure II.1.2.5. Alloy 2 and Alloy 2 Plus sheets rolled to large reductions at 275 °C. Source: The Ohio State University.

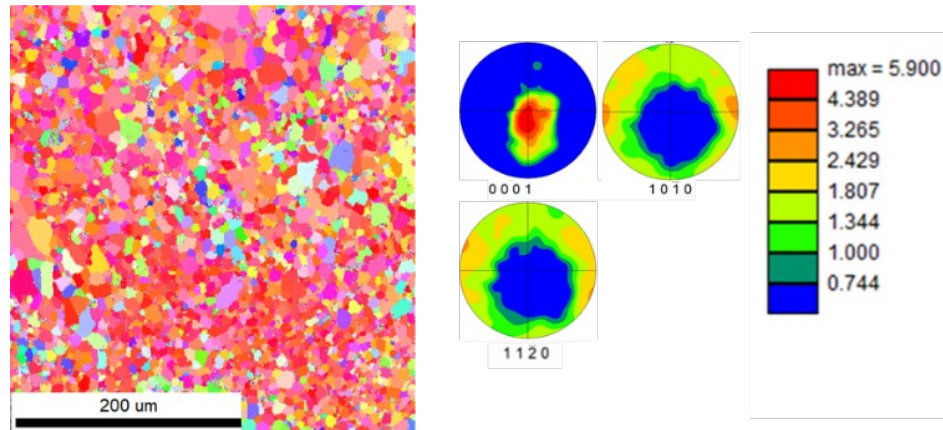


Figure II.1.2.6. EBSD image and (0001), (1010), and (1120) pole figures from Alloy 2 Plus asymmetric rolled at 275 °C (1:1.2, 56%) showing almost complete recrystallization. Source: ORNL.

The following summarizes ORNL's findings:

1. The Alloy 2 and Alloy 2 Plus developmental alloys were successfully rolled using warm rolls and different velocity ratios. Rolling could be accomplished at much lower temperatures (e.g., 275°C vs. 360°C) with heated rolls than with alloy preheating only.
2. Asymmetric rolling was critical in achieving larger reductions in Alloy 2.
3. Basal pole distributions were broader and a decrease in texture intensity (to MRD = 5.9) was observed in the asymmetrically rolled samples.
4. Observation of dynamic recrystallization after asymmetric rolling was correlated with a decrease in texture intensity, but further work is required to separate contributions from asymmetric rolling.

ICME-Based Simulations to Compute the Energy Landscape for Solute and Support Alloy Development

Atomistic simulations were utilized by UIUC to develop predictive models for Mg alloy chemistries with increased isotropic deformation and greater ductility stemming from solid solution strengthening. In general, solutes with a large size mismatch with Mg (either undersized or oversized) are the most effective at strengthening the individual deformation modes and lowering the plastic anisotropy ratios for improved ductility. Specifically, the RE solutes Gd, Tb, Dy, Nd, Ho, Er, Tm, Yb, and Sm are the most promising for increasing the strength and ductility of hexagonal close-packed (HCP) Mg, with the solutes listed here in decreasing order of effectiveness. Other solutes, such as Y and Sc (not treated here as RE solutes due to their behavior in computational calculations, which differs from the aforementioned RE solutes), Pb, Ca, Ag, Bi, Tl, Zn, Li, Ga, Al, and Cd, may also increase strength and ductility of HCP Mg, with the solutes listed here in decreasing order of effectiveness. These elements will benefit alloy formability only if they possess sufficient solubility in Mg. Accordingly, solubility analysis was extended to eight ternary Mg alloy systems utilizing the COST507 database. Solubility limits for Mg-Al-Cu, Mg-Al-Li, Mg-Al-Mn, Mg-Al-Si, Mg-Al-Zn, Mg-Cu-Si, Mg-Cu-Y, and Mg-Cu-Zn were determined by scanning the temperature-composition space to determine the maximum solubility of each solute in the HCP phase of Mg. Since large solutes are the most effective strengtheners in Mg, it is generally expected that in the most promising ternary alloys, the smaller of the two solutes will increase the solubility of the larger solute. In the Mg-Al-Li system, Al increases the solubility of Li and Li increases the solubility of Al. Adding a small amount of Li to Mg-Al, can increase the yield stress of the non-basal deformation modes by up to 25% while reducing the ratios of the non-basal to basal yield stresses by up to 10%. For the other seven ternary systems, the addition of a second solute either has a negligible effect on the solubility of the second solute or reduces the solubility depending on the alloy.

The UIUC work has advanced the state-of-the-art in atomistic modeling in a variety of ways:

1. Development of predictive models of solute chemistry on deformation in Mg.
2. Suggested routes for alloy chemistry of Mg alloys with improved formability.
3. Increased computationally efficient routes to map out the solute energy landscape for other alloy systems.

These methodologies that were developed to predict solute-defect interactions more efficiently and accurately from a smaller subset of calculations can be extended to other alloy systems in the future. The approach of combining accurate defect geometry calculations, solute misfits, and parameterized interaction models permits the identification of chemical trends, as well as the determination of energy landscapes with a fraction of computational effort needed for direct calculations. While elements of this approach have been used in the past, this is the first application for so many deformation modes and the majority of the periodic table.

Development of Experimental Alloy 3

The UF-led development of a viable USAMP Experimental Alloy 3 consisted of an investigation of binary and ternary alloys with a range of alloying elements of Ca (from 0.1 wt.%–1 wt.%) and Zn (from 0 wt.%–4 wt.%). The subtask accomplishments and conclusions are summarized as follows:

1. Mg-0.1Ca and Mg-0.1Ca-0.5Zn wt.% were characterized by positive SRS values; thus, no dynamic strain aging (DSA) occurred at 200° and 250°C from 10^{-3} to 10^{-1} /s. This can be related to the low amount of Ca in the Mg matrix of 0.1 wt.%. On the other hand, compositions of higher amounts of Ca (i.e., 0.35Ca wt.%) were characterized by negative SRS at 200° and 250°C from 10^{-3} to 10^{-2} /s. These results correlate to findings that demonstrate that increasing the solute content broadens the range of conditions at which DSA occurs.
2. The addition of 0.5 wt.% Zn to Mg-0.35Ca reduced the average grain size, which in turn increased the critical stress for twinning and subsequently reduced the volume fraction of twins after deformation.
3. The sole addition of Ca to the α -Mg matrix does not result in significant texture changes after deformation under DSA at 200°C. Nonetheless, the absence of RE-type texture in Mg-0.35Ca may be attributed to the absence of dynamic recrystallization which is considered necessary for the formation of the RE-texture component in extrusions of the Mg-0.5Ca (wt.%) binary alloy.
4. Additions of 0.5 wt.% Zn to Mg-0.35Ca decreased the recrystallization texture significantly after compression under DSA and non-DSA conditions and static recrystallization. However, no significant texture changes were observed between samples of Mg-0.35Ca-0.5Zn compressed under DSA and non-DSA conditions.
5. A higher area fraction (~ 12% more) of recrystallized grains with a weak RE-type of texture was observed after static recrystallization of Mg-0.35Ca-0.5Zn previously deformed under DSA, in contrast with the sample deformed under non-DSA conditions. These results partially support our hypothesis that processing dilute Mg-Ca-Zn alloys inside the DSA regime will lead to RE-texture components that enhance formability.
6. It is evident from these results and the literature that combinations of both Ca and Zn in solution reduce Mg basal texture intensity after deformation and static recrystallization. Therefore, Mg-Ca-Zn alloys represent promising RE-free alloys for production of low-cost Mg sheets for the automotive industry.

Recrystallization, Texture, and Grain Growth Studies of New Alloys

As culmination of the UM's subtasks, desirable spread basal textures with a low texture intensity were produced in Mg-Zn-Ca sheet alloys through a combination of a 10-pass deformation schedule and a final recrystallization annealing treatment. Ca content of at least 0.1 wt.% is required to produce the desired textures, while Zn content strongly affected the texture in the as-deformed and annealed conditions. The three higher Zn ternary Mg-Zn-Ca alloys (e.g., ZX21, ZX30, and ZX31) showed a significantly reduced basal texture intensity in the as-deformed condition (max ~ 4 MRD) as compared to the unalloyed and Mg-Ca

binaries and the low Zn ternary (ZX0p50) (max intensities > 12 MRD). Annealing for 30 minutes at 350°C did not alter the strong texture in the dilute alloys nor did static recrystallization appreciably change the as-deformed texture in the ZX21 alloy. Significant basal texture evolution was observed during static recrystallization in the ZX30 and ZX31 alloys. The final weak texture of these two alloys exhibited a desirable annular structure, with the c-axis tipped from the normal direction, which is a desirable texture for improved formability. Increasing the Ca content from 0.1 to 0.3 wt.% did not lead to any appreciable differences in texture but did lead to an increase in secondary phase particles.

While the high Zn ternary alloys show promisingly weak textures, it is important to note that improper processing can lead to strong basal textures in these “good” alloys as well. Increasing the strain rate from 0.5/s to 1/s leads to a much stronger basal texture in the 10-pass ZX30. In addition, a longer intermediate annealing step leads to increased basal texture intensities.

Limiting static recrystallization (SRX) and grain growth until the final annealing treatment is essential to producing a weak texture. A high strain rate increases the SRX kinetics, thus allowing for increased recrystallization during the intermediate annealing passes. A longer intermediate annealing treatment allows for recrystallization and potentially grain growth to occur. While limiting SRX during processing leads to improved textures, processing needs to promote dynamic recrystallization (DRX). This work demonstrates that the small, likely DRX grains have random orientations and that they exist through processing from the original deformation pass to the last. To optimize the texture, it is important to control their nucleation and growth. In contrast to the recrystallization grains, the deformed grains tend to have a more basal orientation. During annealing, the volume fraction of the deformed grains decreases, leading to a decrease in basal texture intensity observed in the Mg-3.2Zn-Ca alloys. In the Mg-Zn-Ca system, annealing leads to texture reduction rather than proliferation of the basal texture due to modified recrystallization kinetics.

Determine and Model Constitutive Behaviors of New Mg Alloys

PNNL’s research at the meso-scale established the fundamental relationships between the alloy compositions and the microstructural attributes, resulting from processing for the new Mg alloy compositions identified by the university team in the program, thereby providing the quantitative multiscale linkages for sheet formability simulations. They focused on two tasks: (1) microstructure-based ductility and formability predictions; and (2) small-scale *in-situ* experiments for model input and validations. Key accomplishments are summarized below.

The deformation mechanisms of the binary alloys Mg-0.2 at.%Ca (0.33 wt.% Ca) and Mg-1.5at.% Sn (6.92 wt.% Sn) were studied by *in-situ* neutron diffraction, synchrotron XRD, and SEM/EDS/EBSD, all of which provided detailed information about the microstructure and the available slip and twin deformations that are activated at RT under tensile load.

Furthermore, RT tensile deformation mechanisms and texture evolution of E-Form Plus (EFP) samples were investigated by the above techniques to better understand and characterize the alloy that was prominently utilized by the other tasks in this project. Notably, the much smaller grain size and higher ductility of EFP as compared to the binary alloys allowed the *in-situ* experiments to provide valuable inputs for the modeling efforts, for which the binary alloy results were not sufficient. The above experimental information, as well as first principles calculations from UIUC, were used to inform Crystal Plasticity Finite Element Models (CPFEM) for these alloys. Deformation of the binary alloys under tensile loading was modeled and favorably compared with experimental results, thereby providing validation for the first principles calculations.

In conclusion of this subtask, the CPFEM samples representative of the microstructure and texture of two binary Mg alloys—Mg-0.2at.%Ca and Mg-1.5at.%Sn—were modeled using crystal plasticity parameters from the literature for pure Mg and Taylor model values for EFP and modified using the change in CRSS calculated by UIUC using DFT simulations. A key goal of the CPFEM simulations was to understand the impact of individual microstructure features and parameters on bulk behavior. The study demonstrated the large impact of what might seem to be a small difference in grain size (67 μm to 48 μm between the two binary alloys) on

the bulk behavior of the sample. The smaller grains allow for additional hardening to occur, given the same material model properties, enhancing the simulated material yield and UTS by a factor of ~3. The second goal was to determine whether incorporating the changes in CRSS values calculated by DFT resulted in stress-strain response that matched the *in-situ* measurements. While using the CRSS values from DFT did match the stress levels of micro-yield, yield, and ultimate stress measured, the strain values were lower. The micro-yield stress value was most impacted by the changes in CRSS for the basal slip systems. This is to be expected as deformation is dominated by basal slip. The changes in CRSS values for the prismatic and pyramidal could be seen in changes to the yield and ultimate stress values. Additional investigation needs to be conducted to determine appropriate model parameters to capture the strain levels observed experimentally.

Material Property Measurements for Modeling Formability of EFP

This subtask on additional testing of EFP Batch #4 at elevated temperature for three strain paths was added towards the end of the project, after the USAMP reviewed the outcomes of multiple crystal plasticity-based finite element cross-forming simulations performed by InalTech using the new MAT233+ card and compared the results with the Argus strain map of the cross-form.

It was concluded that while simulations with both MAT233 and 233+ cards identified and correlated with areas of the cross-form with the highest strains, the models are unable to explain why the simulation results do not predict the fracture areas. A corresponding study of door panel fracture surfaces performed by FADI-AMT LLC concluded that there are no significant differences in thinning behavior between rolling direction and transverse direction.

InalTech recommended additional material testing and data-gathering be completed, which would help support new simulation runs and model calibrations, and thereby augment the team's knowledge on the forming limit diagrams (FLDs) for the EFP sheet. Based on the findings in literature, increasing the strain rate seems to be decreasing the formability for Ca/Ce-added Mg alloys. This is contradictory to everything known so far, especially for materials with a positive SRS, such as the EFP Mg alloy.

FADI-AMT performed custom formability testing on EFP Batch #4 sheets with digital image correlation to generate FLDs from three points: (1) uniaxial tension; (2) plane strain tension; and (3) balanced biaxial tension to develop accurate FLCs for the material at 200°C and at three different strain rates. These test results may correlate better when exploring different time-steps for peak strain values, which may also explain the strain levels and fracture locations. The formability (i.e., FLD₀) of EFP Batch #4 sheet at 200°C decreases from 0.42 to 0.18 as the strain rate of testing increases from 0.01 to 1.0 /s.

ICME Modeling of EFP Formability

In FY 2021, polycrystalline simulations partly fit to available experimental data for EFP were used to estimate the parameters that determine the material-symmetry rotations in the plastic flow relations, and the simulations for Batch #1 were carried out. The final step was to build the finite element user material (UMAT) model designated as *MAT233+, to extend the Cazacu-Plunkett-Barlat [1] flow rule to account for material-symmetry rotations (microstructural rotations) for Batch #1. The deliverable UMAT for *MAT233+ enhanced the USAMP team's capabilities for the cross-form simulations, but due to tight project schedule remaining, there was insufficient time to incorporate the model into an updated version of LS-DYNA that could be released for Vehma's door product and forming process modelers to run simulations and compare with warm-forming trials. This effort is expected to continue after conclusion of this project.

Welding Process Advances on Mg Sheet

AET concluded welding process trials in FY 2021 and produced 17 "mini-door" assemblies with RSW and laser welds to support PPG's corrosion studies, as shown in Figure II.1.2.7. The welding processes used for producing these "mini-doors" were mostly those that had been developed and optimized in previous RSW and laser weld process development work with some modifications to improve repeatability of the laser welds.

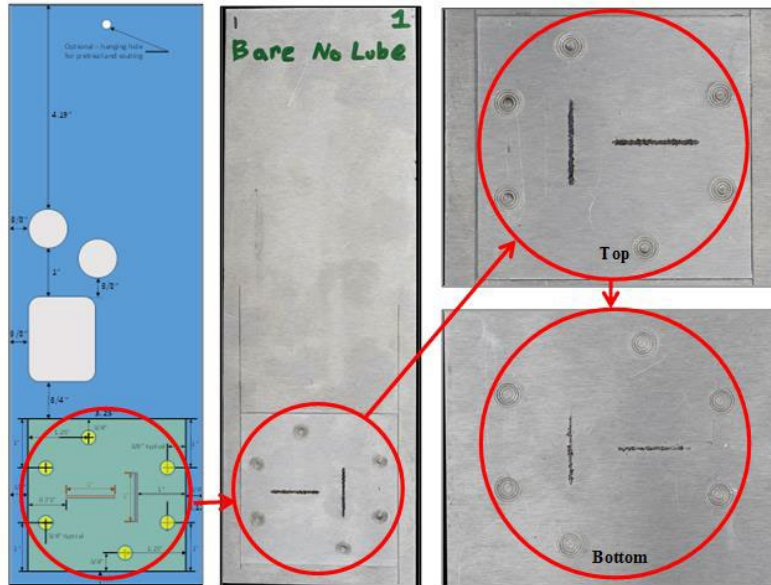


Figure II.1.2.7. Mini-door assembly schematic (left) with three cut-outs as manufacturing features, full welded assembly (center), and close-up top and bottom views of welded area (right) for bare EFP Batch #3 material with no lubricant. Source: AET.

EFP Mini-Door Evaluation in Corrosion Performance

Table II.1.2.3 lists the different top performing PPG-developed cleaning and pretreatment processes that were evaluated in FY 2021 on Xtalic/Fuchs, Xtalic/Quaker, Henkel/Fuchs, and Henkel/Quaker EFP panels that were welded, cut, and bent to form mini-doors. The Xtalic EFP mini-doors went through four weeks of G-85 A2 filiform corrosion testing, while the Henkel EFP mini-doors went through ten weeks of G-85 A2 corrosion testing. There was a loss in performance with the Xtalic coil-coated EFP panels, which were removed from corrosion testing after four weeks due to surface blistering and perforations through the metal. The Henkel coil pretreatment performed well in up to ten weeks of corrosion testing and did not have perforations through the metal. Figure II.1.2.8 visually summarizes the corrosion test results.

Table II.1.2.3. PPG Cleaning and Pretreatment Processes Evaluated for EFP Mini-door Compatibility

Condition	Coil Coating	Lubricant	Cleaning Steps	PPG Treatment System
1	Henkel	Quaker	Cleaner 1 (C1)	Cleaner 2.4
2	Henkel	Quaker		Cleaner 2.4 → Pretreatment 8
3	Xtalic	Quaker		Cleaner 2.4
4	Xtalic	Quaker		Cleaner 2.4 → Pretreatment 1
5	Henkel	Fuchs		Cleaner 2.4
6	Henkel	Fuchs		Cleaner 2.4 → Pretreatment 8
7	Xtalic	Fuchs		Cleaner 2.4
8	Xtalic	Fuchs		Cleaner 2.4 → Pretreatment 1

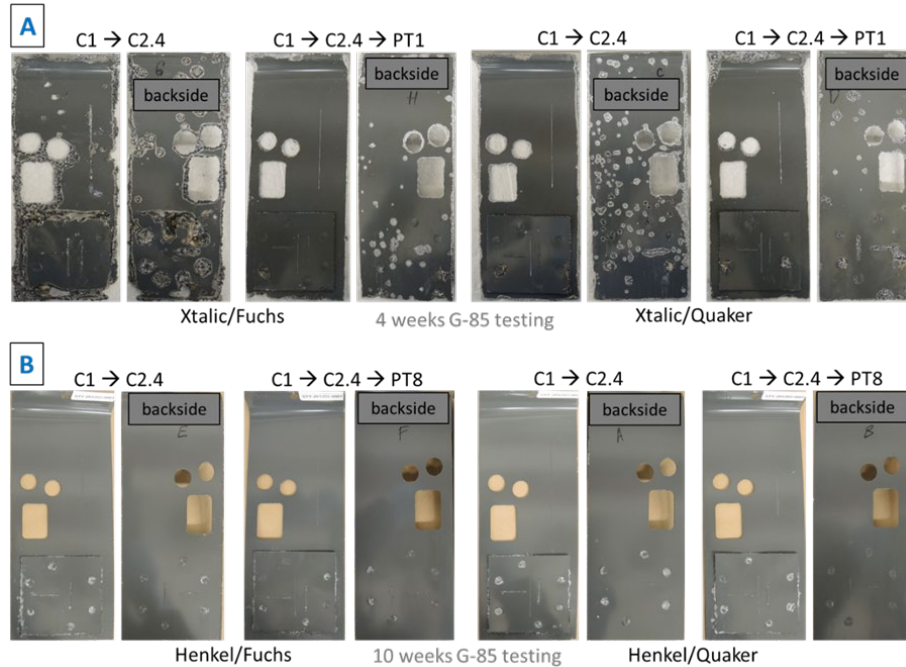


Figure II.1.2.8. EFP mini-doors treated with (a) Xtalic zinc plating or (b) Henkel coil pretreatment and then coated with Quaker or Fuchs lubricant. Panels were pretreated with either a two-step or a three-step process; Cleaner 1 → Cleaner 2.4 → (opt.) Pretreatment 8 or Pretreatment 1, and then e-coated with a standard automotive e-coat and subjected to G-85 A2 filiform corrosion testing. Source: PPG.

Optimization of Corrosion Cleaners and Pretreatments on Mg Alloys in Multi-Metal Systems

PPG also completed their optimization of PPG metal pretreatments for EFP in multi-metal systems in FY 2021 by evaluating the corrosion and adhesion performance of the pretreatment processes on non-joined panels and those joined (using rivets plus adhesion prior to cleaning) with EFP, cold-rolled steel (CRS), Al alloy 6111 (AA6111), and hot-dip galvanized (HDG) steel. The example results of tests on non-joined panels are summarized in Figure II.1.2.9. The AA6111 panels performed the best, while CRS performed the worst. Out of the pretreatment systems tested, Cleaner 2 or Cleaner 2.4, followed by Pretreatment 1, showed the best performance. Pretreatment 24 followed by Pretreatment 1 was also promising, although variability in the EFP samples was observed.

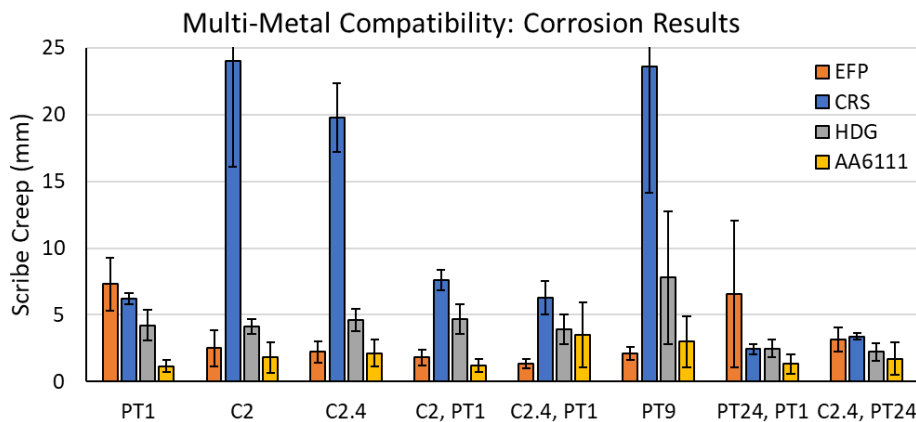


Figure II.1.2.9. Corrosion performance of EFP, CRS, AA6111, and HDG steel after three weeks of ASTM G-85 A2 corrosion testing. Cleaner 2 or Cleaner 2.4 → Pretreatment 1 and C2.4 → Pretreatment 24 showed promise. CRS showed the most corrosion of all substrates. Source: PPG.

PPG also determined the level of galvanic corrosion in multi-metal couples using rivets plus adhesive prior to cleaning of EFP, CRS, HDG steel, and/or AA6111. The top performing cleaning and pretreatment processes were evaluated to select systems that protect all metals. In this work, couples that were joined with adhesive and rivets prior to cleaning and pretreatment were evaluated.

The task of developing a cleaner and metal pretreatment prior to paint shop processes was approached by considering the entire process from cleaning and surface preparation to pretreatment formulation to sealers and post-rinses for gaining maximum corrosion protection. The following conclusions were reached:

1. Cleaner 1, an alkaline cleaner, was much more effective than the acidic cleaners at cleaning the Mg panels and removing lubricants. Mg dissolution is not directly related to the bath pH.
2. Pretreatment 2 and Cleaner 2 pretreatments impart good corrosion protection of e-coated ZEK100 and EFP. For both alloys, Cleaner 2.4 was a top performing pretreatment, showing promise as a stand-alone pretreatment.
3. Both, the two-step and three-step Cleaner 2.4 pretreatment processes were effective in protecting the coil-coated and lubricated EFP from corrosion, and in some cases, also improving the adhesion performance.
4. The PPG cleaners/pretreatments help afford corrosion protection to welded Mg mini-door samples.
5. Cleaners 2.21 and 2.32 provide sufficient corrosion protection for both Mg and steel, suggesting that the multi-metal systems might be processed successfully without increasing the number of steps beyond that currently found in typical automotive paint shops (i.e., one cleaning step plus one pretreatment step prior to the e-coat).

Forming Simulations and Correlation Studies

Vehma used material cards provided by the UPenn and InalTech team to conduct initial warm-forming simulations of the cross-form part, the door inner panel, and the door outer panel. The simulation subtasks performed by Vehma and InalTech included the following:

1. Forming simulations and correlation of cross-form panels.
2. Forming simulations of door outer and inner panels.
3. Door outer and inner die modifications.

The simulation software being used prior to the start of this project was not able to effectively handle the asymmetric behavior of Mg alloys at warm-forming temperatures. The USAMP team collaborated with Livermore Software Technology Corporation (LSTC) to modify the LS-DYNA software to include tables for temperature and strain rate. LSTC provided both training version and revised production software to Vehma. The MAT233 material card was used for cross-form simulations to calibrate and prepare for scale-up to door panel simulations. The new MAT233+ material card was also used for cross-form simulation; however, unlike the MAT233, it was excluded from the door forming analysis to meet project timing. MAT233+ relied on the development of the phenomenological model, which was not complete at the time the door simulation commenced, thus the MAT233+ simulation was used only for comparisons to measure the improvement gained when including the evolving symmetry axis. The simulations were compared to the Argus scan from an experimental good quality cross-form stamping, as shown in Figure II.1.2.10, for the optimum process window recommended by EWI's cross-forming trials at the end of FY 2020 for the Fuchs/Bare EFP panels.

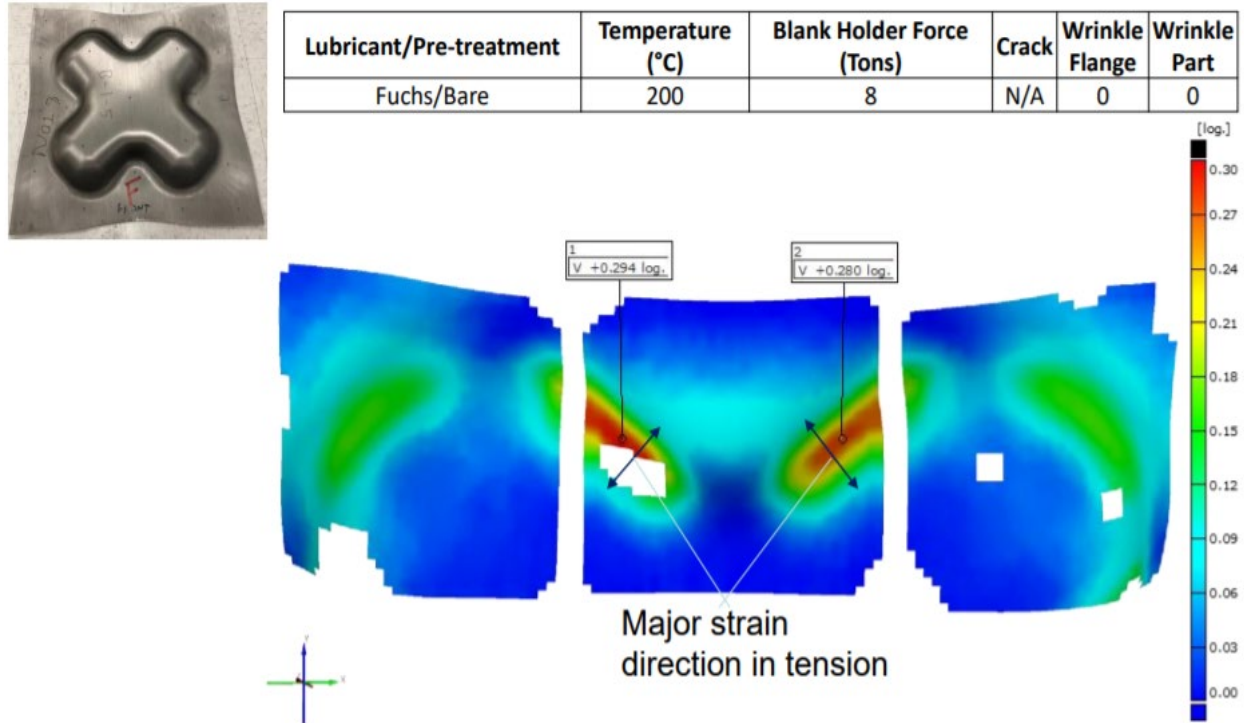


Figure II.1.2.10. A good quality warm-formed EFP cross-form (upper left), approximately 470 mm square, and the Argus true strain maps. Source: EWI.

Due to the plastic behavior of the material model, the strain values did not correlate between Argus measurement and simulation; however, the locations of the major strain did show adequate correlation, meeting the criteria that is typically required for automotive component production. Since the adaptive mesh feature was not available on the developer version of the software used in this task, the simulations were performed for two finite element mesh sizes—3 mm and 6 mm—as observed in Figure II.1.2.11. At the larger mesh size, the MAT233 model shows a peak major strain location that does not match the Argus scan, while the MAT233+ simulation is a significant improvement showing a peak major strain location that does match. For the smaller mesh size, both simulations show major strain locations matching the Argus scan and the MAT233+ results in a slight improvement in the peak value. For the minor strains, the simulations all predicted a smaller peak value and a different location of the peak as compared to the measured data, as shown in Figure II.1.2.12.

The strain values at various points of the cross-form panel were obtained and compared to the corresponding locations in the forming simulations. These points were then plotted relative to the forming limit curve (FLC), as observed in Figure I.4.2.13 and Figure I.4.2.14. The experimental strains and simulation strains were in the safe region when compared to the FLC. The areas that were prone to splitting during the experiment were FLD-safe.

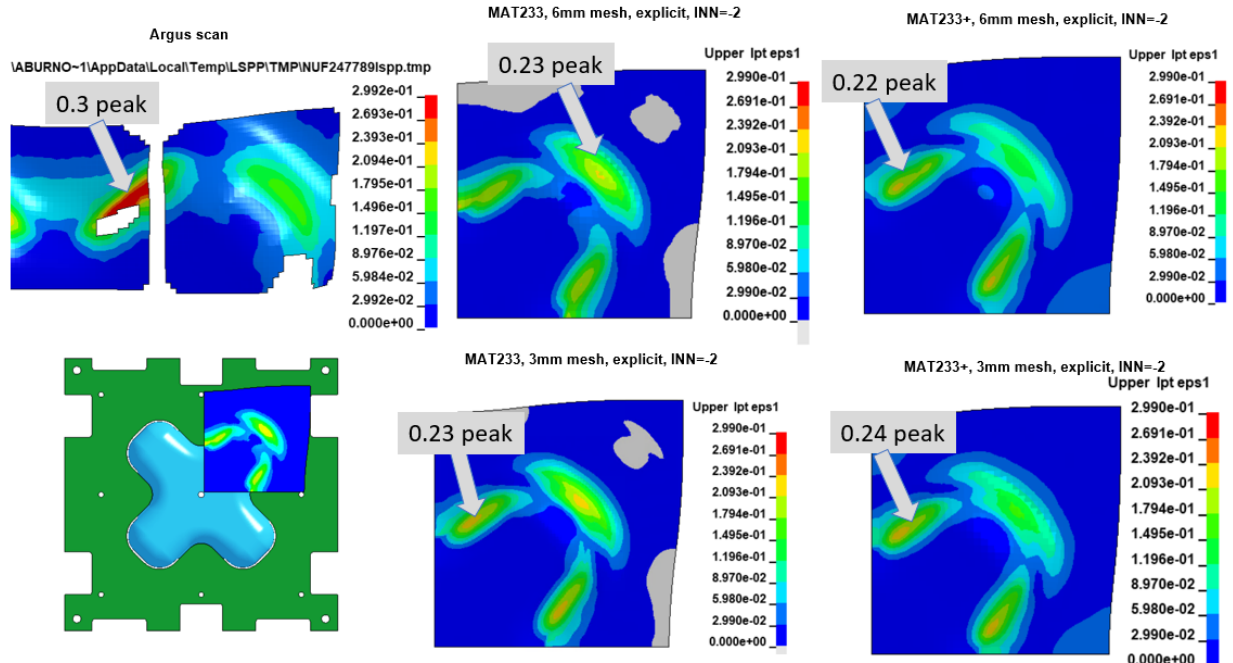


Figure II.1.2.11. Comparison of Argus and MAT233/233+ major strains. Source: Vehma and InaTech.

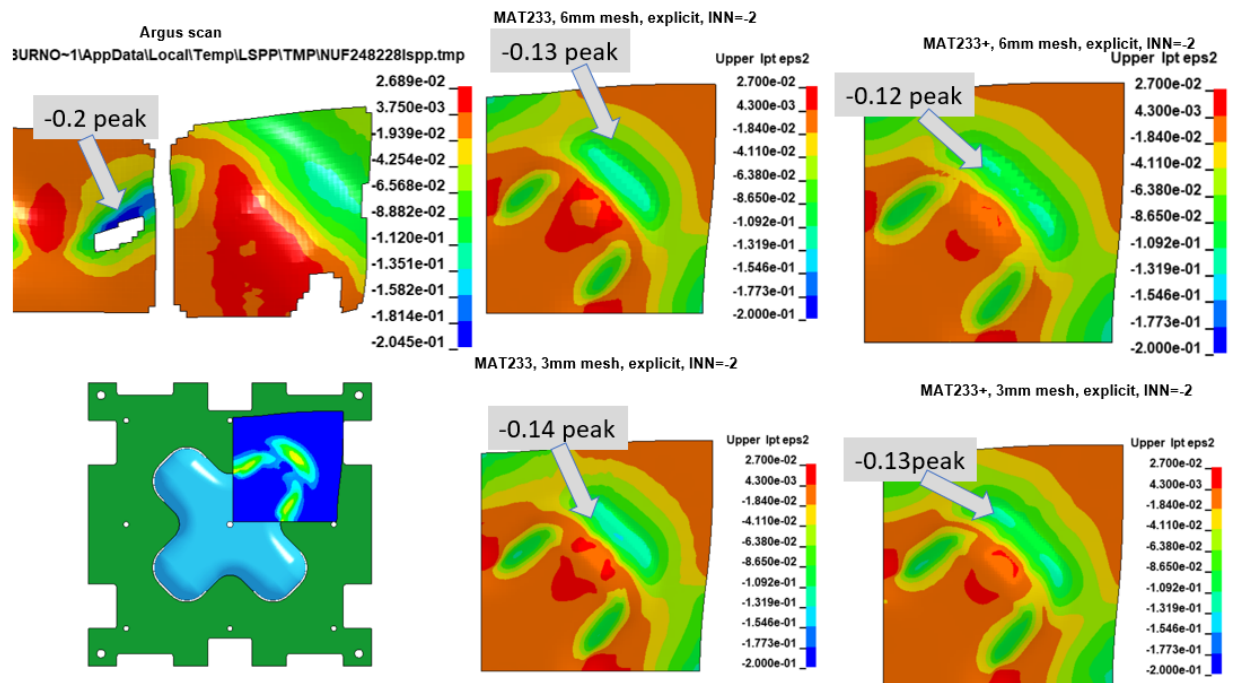


Figure II.1.2.12. Comparison of Argus and MAT233/MAT233+ minor strains. Source: Vehma and InaTech.

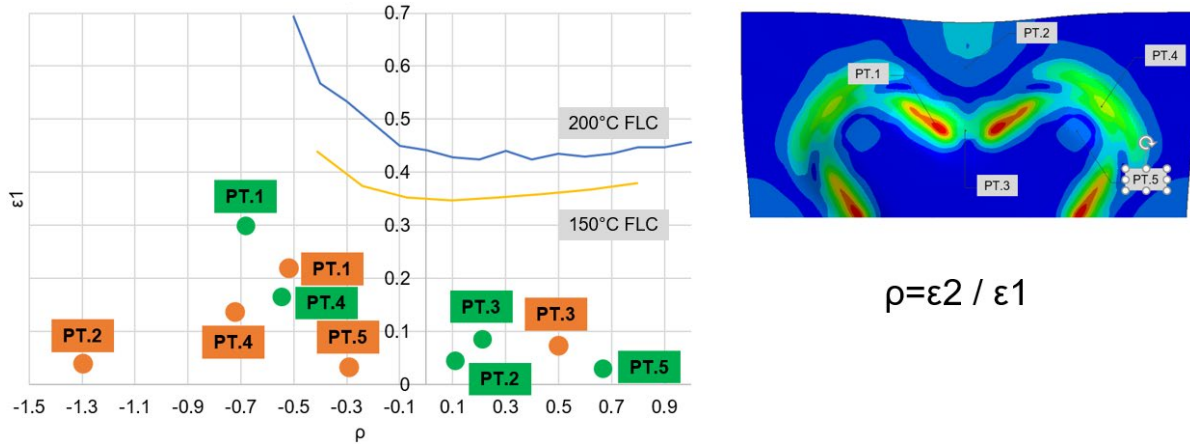


Figure II.1.2.13. Plots from simulations with a MAT233+ card compared with Argus scan (left) and an FLD map of a cross-form (right). Source: Vehma and InalTech.

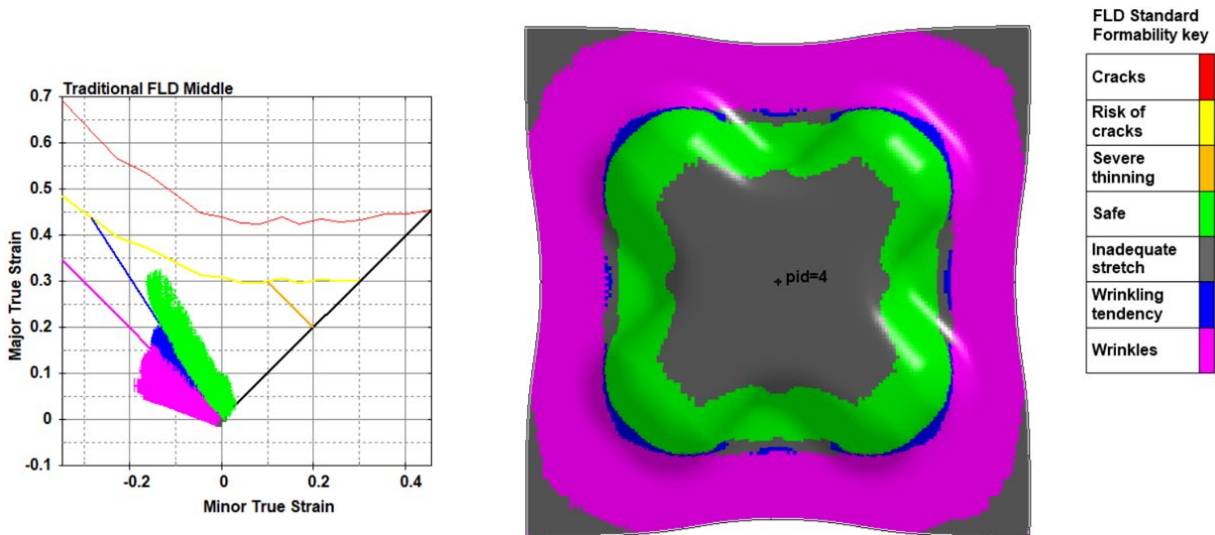


Figure II.1.2.14. Simulations from the MAT233+ compared with FLC for 200°C. Source: Vehma.

Cross-form Simulation Using the Crystal Plasticity Model

InalTech performed a simulation of the cross-form part using the crystal plasticity model developed in this program. Due to the large amount of computational processing power required to do this simulation (e.g., one run required five days even with 192 parallel processors), it is not yet practical for commercial part development; hence, this study was completed as an additional step to validate the previous LS-DYNA simulations. The results from the crystal plasticity simulation bolstered the correlation activity yielding a similar strain map and peak minor strain compared to the simulation using the material card MAT233+, as shown in Figure II.1.2.15.

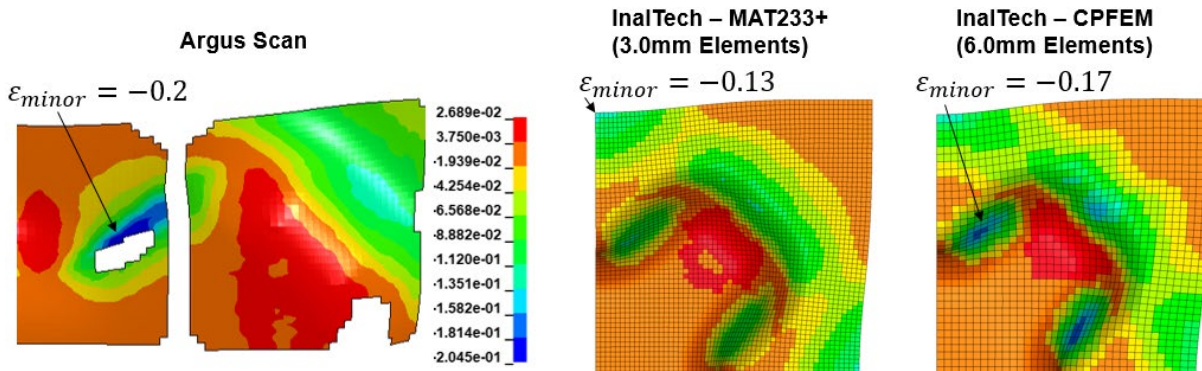


Figure II.1.2.15. Comparison of Argus scan to the MAT233+ and crystal plasticity simulations. Source: Vehma and InalTech.

Warm-Forming Demonstrations of Large Automotive Body Components

Stamping trials were conducted in FY 2021 at Promatek (Vehma’s metal forming division in Toronto) to develop processes for one-stage, warm-blank/cold die, stamping of 1.2 mm EFP Mg blanks into Ford Fusion door outer and inner panels. Blanks were coated with diluted Fuchs lubricants 278 or 1102 (per Fuchs recommended dilution ratios), allowed to dry, heated in an electric oven, robotically transferred to a press, and stamped at temperatures up to 250°C. As described in the previous year’s work, the dies had been modified from their original steel panel stamping-specific designs, based on Mg-forming simulations conducted by Vehma. Further modifications (i.e., reduction in height of draw beads and increase in radii of product features) were required to form split-free EFP door panels. When blank temperatures were reduced to 225°C and lower, splits were observed in the panels. Similarly, the Fuchs 278 lubricant, which was used with either water dilution or alcohol dilution, produced good quality panels, whereas the Fuchs 1102 lubricant used on Mg sheets with the same forming conditions produced splits.

Ten outer panels and sixteen inner panels of good quality were stamped using water-diluted Fuchs 278 blank lubricant and a blank temperature of 250°C. Figure II.1.2.16 and Figure II.1.2.17 show good quality outer and inner panels and associated final forming process parameters, respectively.



(a)

Final Forming Process Parameters	
Binder Gap	1.5 mm
Binder Tonnage	40 to 45 Ton
Binder Pressure	500 Psi
Oven Setting	280°C @ 85s
Blank Temperature	250°C
Press Tonnage	120 Ton
Lube	Al 278 (2=W, 1=L)
Bead	1.2 mm off the sides/ 1.5 mm off top and bottom

(b)

Figure II.1.2.16. (a) Warm-formed door outer is a good quality panel. (b) The final forming process parameters. Source: Promatek.



(a)

Final Forming Process Parameters	
Binder Gap	1.5 mm
Binder Tonnage	40 to 45 Ton
Binder Pressure	500 Psi
Oven Setting	280 °C @ 85s
Blank Temperature	250 °C
Press Tonnage	120 Ton
Lube	Al 278 (2=W, 1=L)
Bead	1.2 mm off the sides/ 1.5 mm off top and bottom

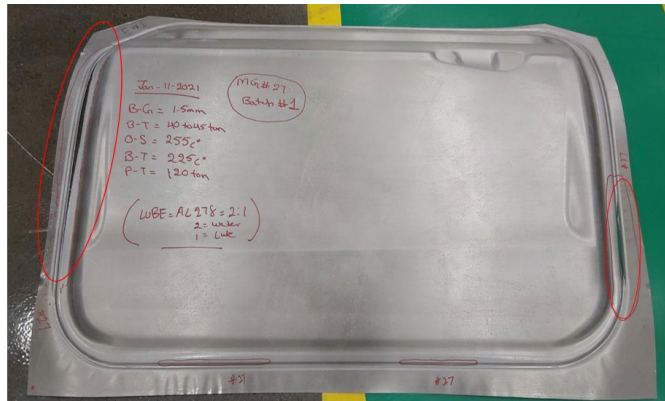
(b)

Figure II.1.2.17. (a) Warm-formed door inner is a good quality part. (b) The final forming process parameters. Source: Promatek.

For further examination of splits in panels, USAMP engaged FADI-AMT LLC to characterize fracture surfaces on four warm-stamped door outer panels, which cracked or split near draw beads during the stamping process, as observed in Figure II.1.2.18. The goal of this brief study was to understand the plastic deformation, fracture processes, and effects of temperature, orientation, and batch variations by taking careful thickness measurements near the cracks/splits and augmented by “cross-sectional metallography” of sections at the splits. This study concluded that there is no significant difference in thinning behavior between the rolling and transverse directions. Due to the short time remaining prior to project closeout, only the thinning measurements were made. A planned SEM study of these fracture surfaces could not be conducted.



(a)



(b)

Figure II.1.2.18. (a) A split cross-form part. (b) A split door outer panel. Source: FADI-AMT and Promatek.

Virtual Performance Validation of Components

CAE analyses were performed for stiffness and modal, denting and oil canning, check over and sag, and FMVSS 214 S-static pole, and mass comparison for a side door design based on the 2013 MY Ford Fusion baseline, but with Mg inner and outer panels and Al reinforcements. All engineering requirements were met at a door mass of 10.18 kg using a 1.2-mm-thick EFP inner and a 1.1-mm-thick EFP outer stamping, and a Nitto patch. The Mg alloy door panels achieve a 62% mass saving relative to the steel baseline panels. With no Nitto patches to enhance stiffness, the outer stamping needs to be 1.25-mm-thick, and the mass saving is reduced by 150 g (to 60%). If ZEK100-O were to be used instead of EFP, the outer panel could be down-gauged to 1.0 mm, with a resulting mass savings of 64% compared to the steel panels.

Conclusions

This project has demonstrated major material and process advances in Mg sheet technology across the entire automotive stamping value chain. The advances range from the computational design of new Mg alloys from atomistic levels to the casting of new experimental alloys and exploration of novel thermomechanical rolling processes to produce thin Mg sheet of desired texture to warm-forming demonstrations of large automotive components and the corrosion protection of assemblies. A new commercial Mg alloy sheet material, EFP, was sourced and pretreated with protective coil coatings, with its properties fully characterized. The Mg sheet was warm-formed using novel lubricants into intermediate size benchmark parts and full-size automotive door inner and outer panels. The project also explored conventional welding processes for Mg sheet joining, developed novel corrosion treatments for multi-metal assembly coatings, performed computer simulations of door panel forming using two new material cards based on crystal plasticity theory, and concluded with a door static and dynamic performance analysis. A technical cost model, which included parts production, assembly, and paint for a door specifically designed for an Mg sheet showed the cost penalty to be between \$4.26 to \$6.60/kg saved, which enveloped the project's cost targets. The cost of the coated Mg sheet was identified as the key driver for the cost penalty. The mass of the Mg-intensive door was 7.9 kg, which was 54% less than the baseline steel door.

Although the various elements of the project like new alloys, rolling processes, and coatings could not be incorporated into the sheet that made the demonstration door, the overall project generously funded by DOE demonstrated immense strides towards bringing an Mg sheet closer to a viable structural automotive application. The research that was completed will spur future work in areas such as enhancements to the computational modeling tools for virtual development and characterization of new alloys with still more randomized texture and enhancements to direct crystal plasticity models better optimized for complex stampings. Larger efforts are needed to scale-up the various promising technology components identified for high-volume implementation.

Key Publications

1. Buccholz, K, 2020, "USCAR broadens its research footprint," SAE Vehicle Engineering Technology e-Newsletter, 11/19/2020, Available at: <https://www.sae.org/news/2020/11/uscar-broadens-its-research-footprint> (Accessed 6 January 2022).
2. Sachdev, A., 2020, "Lightweighting with magnesium sheet," Virtual Oral Presentation at Inauguration of Global Magnesium Industrial Research Center (GMIRC), 10 December 2020, Suncheon City, Korea.
3. Berman, T. D., and J. E. Allison, 2020, "Relating texture and thermomechanical processing variables in Mg-Zn-Ca Alloys," in Jordon, J. B., V. Miller, V. Joshi, and N. R. Neelameggham, (Eds.), *Proceedings of 2020 Magnesium Technology*, TMS, Springer International Publishing, pp. 175–180.
4. Luo, A. A., R. Shi, J. Miao, and T. Avey, 2021, "Review: Magnesium sheet alloy development for room temperature forming," *JOM*, Vol. 73, pp. 1403–1418.
5. Zhao, D., R. Shi, R. P. Evans, A. A. Luo, and K. Y. Xie, 2021, "On the exceptionally high ductility of Mg-2Zn-0.3Ca-0.2Ce-0.1Mn alloy," *Mater. Sci. Eng.*, Vol. 819, Art. 141484.
6. Berman, T. D., and J. E. Allison, 2021, "Texture and microstructure evolution in thermomechanically processed Mg-Ca and Mg-Zn-Ca alloys," TMS Annual Meeting & Exhibition, 17 March 2021, Virtual.
7. Berman, T. D., and J. E. Allison, 2021, "Coupling thermomechanical processing and alloy design to improve textures in Mg-Zn-Ca sheet alloys," *JOM*, Vol. 73, pp. 1450–1459.
8. Berman, T. D., and J. E. Allison, 2021, "Evolution of texture and microstructure in Mg-Zn-Ca sheet alloys during thermomechanical processing," 12th International Conference on Magnesium Alloys and Their Applications, 15–18 June 2021, Virtual.
9. Berman, T. D., and J. E. Allison, 2021, "Texture evolution in Mg-Zn-Ca alloys," PRISMS Center Annual Workshop, 6 August 2021, Virtual.

10. Valdez, L., K. Allen, R. Harris, and R. Rock, 2021, “Novel magnesium pretreatment coatings offering excellent corrosion protection,” American Coatings Association Conference, 28–29 June 2021, Pittsburgh, PA, USA.
11. Sachdev, A., 2021, “Advances in magnesium alloys for automotive applications,” 12th International Conference on Magnesium Alloys and Their Applications, 15–18 June 2021, Virtual.
12. Ghaffari, B., 2021, “An ICME approach to development of a low-cost magnesium sheet component for automotive applications,” 6th World Congress on ICME (ICME 2021), Lake Tahoe, NV, USA, 14–18 November 2021.
13. Gerken, R., B. Ghaffari, A. Sachdev, M. Mehta, and J. Carter, 2022, “Magnesium sheet component development and demonstration project,” Invited Keynote Presentation, 2022 SAE World Congress, 5–7 April 2022, Detroit, MI, USA.

Patent and Invention Disclosures

- The OSU disclosed the following Subject Invention and pursued patent filing:
 - T2020-044, Inventor: Alan Luo, “A high-strength and high ductility magnesium sheet alloy for RT forming applications” – Application progress is below:
 - U.S. Provisional Application No. 62/908,077, filed 30 September 2019.
 - PCT application No. PCT/US/2020/053065, filed 28 September 2020.
 - PCT publication No. WO 2021/067782 A1, published 8 April 2021.
- PPG Industries disclosed via iEdison 13 Subject Inventions, each individually identifiable by the assigned T-number and their status is provided below:
 - **Patent Applications Filed:**
 - PCT/US2020/045656, “Control of etching by cleaner composition and organic pretreatment for magnesium substrate (Includes T-115306).”
 - PCT/US2020/045629, “ChemDeox 395 as a pretreatment-enhancing cleaner on magnesium alloy (includes T-115308, T-115816, T-118158, and T-118162).”
 - Application #63/228,756, “One-step multi-metal pretreatment for mg and steel (Includes T-120644)” – combined with T-124614 below.
 - Application #63/228,756, “Compact pretreatment for both CRS and Mg (Includes T-124614)” – combined with T-120644 above.
 - **Patent Applications in Preparation:**
 - T-117692, “Peroxide-free cerium pretreatment of magnesium substrates for longer bath life.”
 - T-122068, “Cerium pretreatment with oxidizer coupling on EFP magnesium.”
 - T-119012, “Corrosion protection of Mg alloys via orthophosphonic derivative based pretreatment.”
 - **Recession Letters Filed:**
 - T-117830, “Corrosion and adhesion improvement of ZB 1.5 on Mg-substrate with a pre-electrocoat bake – Recession 9/14/2020.”
 - T-118530, “Improvement of Mg-substrate corrosion performance with an Si-containing organic pretreatment – Recession 10/23/2020.”
 - T-122794, “Unique treated magnesium substrate using Chemdeox 395 and Nupal 435 – Recession 2/11/2021.”

References

1. Shi, R., J. Miao, T. Avey, and A. A. Luo, 2021, “A new magnesium sheet alloy with high tensile properties and RT formability,” *Sci. Rep.*, Vol. 10, No. 1, pp. 1–10.

Acknowledgments

This project was a collaboration with many researchers from Ford Motor Company, Fiat Chrysler Automobiles US LLC, GM, and sponsor/support/subrecipient/vendor organizations. The contributions of the following USAMP task leaders to this report are gratefully acknowledged: A. Adam and L. Decker (Stellantis); B. Ghaffari and M. Li (Ford Motor); L. Hector, A. Morales, and A. Sachdev (GM R&D); J. Carter and M. Mehta (M-Tech International LLC); and G. Bucciero (Bucciero and Associates).

II.1.3 New Technologies for High-Performance Lightweight Aluminum Castings (National Energy Technology Laboratory/General Motors)

Paul D. Jablonski, Co-Principal Investigator

National Energy Technology Laboratory
1450 Queen Ave SW
Albany, OR 97321
E-mail: paul.jablonski@netl.doe.gov

Qigui Wang, Co-Principal Investigator

General Motors
30003 Fisher Brothers Road
Warren, MI 48093-2350
E-mail: qigui.wang@gm.com

David Weiss, Co-Principal Investigator

Eck Industries
1602 North 8th Street
Manitowoc, WI 54220
E-mail: david.weiss@eckindustries.com

Sarah Kleinbaum, DOE Program Manager

U.S. Department of Energy
E-mail: sarah.kleinbaum@ee.doe.gov

Start Date: December 27, 2019	End Date: December 31, 2022	
Project Funding (FY 2021): \$500,000	DOE share: \$500,000	Non-DOE share: \$0

Project Introduction

Lightweight Al shape castings have widespread applications for structural components in the automotive, aerospace, and general engineering industries due to their excellent castability, corrosion resistance, and high-strength-to-weight ratio in a heat-treated condition. In the automotive industry, cast-Al alloys have been increasingly used to replace cast-Fe and steel in vehicle applications, such as engine blocks, cylinder heads, intake manifolds, brackets, housings, chassis, transmission parts, and suspension systems to reduce mass. Currently, over 400 lbs of Al alloys are used in a vehicle, while nearly 300 lb. are Al shape castings [1]. As many of the Al shape castings used in automobiles involve cyclic loading, the fatigue properties of the castings are critical to their success. The increasing use of lightweight Al cast components in critical structures requires improved integrity with more reliable and quantifiable performance. These goals are made more challenging by the complexity of shape casting processing, which involves many competing mechanisms, multiphysics phenomena, and potentially large uncertainties.

The understanding of mechanical performance of Al castings was summarized by Wang et al. [2, 3], who discussed the roles of porosity, oxide films, dendrite arm spacing, intermetallic and silicon particles, and matrix strength in tensile fracture, fatigue crack initiation, and propagation. One of the conclusions is that casting defects (e.g., porosity, oxides) are major microstructural heterogeneities that cause a significant reduction in the tensile and fatigue resistance of Al castings. Recent research results [4, 5] corroborate these findings. Under static loading, the volume fraction of defects dominates the tensile behavior. In dynamic loading, however, it is the defect size that controls fatigue performance. Reducing defect size increases fatigue properties. When the defect sizes are smaller than a critical size (~50 μm) [6], the eutectic particles and

persistent slip bands in the Al matrix become the fatigue crack initiation sites with a significant increase in fatigue life. To improve strength and fatigue performance of cast-Al alloys, casting defects should be minimized and eutectic particles should be refined and uniformly distributed in the microstructure. In Al castings, the size and population of multiscale defects and microstructure constituents depend not only on the alloy composition and melt quality, but also the casting process—including mold filling and solidification conditions.

Recently, there has been significant effort in developing high-temperature cast-Al alloys for high-performance cylinder head applications. The newly developed cast-Al alloys have shown significant improvement in tensile strengths at both room and elevated temperatures. The comparison of low cycle and HCF properties to those of a production alloy does not show significant improvement [7], which limits the application and implementation of the new high-temperature Al alloys. Fatigue resistance of Al castings is strongly dependent on microstructure (e.g., columnar grains) and particularly defects, such as porosity, oxides, and inclusions. The microstructure constituents and multiscale defects in Al castings are much more dependent on the casting process than on alloy composition or heat-treatment. This remains the biggest challenge for implementing any new high-performance Al alloys for improved engine efficiency and mass reduction. For instance, in cylinder head casting, a gravity-poured semi-permanent mold casting process is commonly used for mass production. Because of gravity pouring, a significant amount of Al oxides is produced and entrapped into the head casting during mold filling. The entrained oxides provide heterogeneous nucleation substrates for porosity and large eutectic particle formation during solidification. Furthermore, as liquid metal is introduced from the deck face and the riser is the last to fill in the gravity-poured semi-permanent mold head casting process, the riser feedability and microstructure soundness is poor, not to mention the resulting low metal yield. Rotacast® is considered as a premium casting process for making premium cylinder head casting. However, it is a very costly process (e.g., > 50% more expensive than gravity-poured semi-permanent casting). In Rotacast® heads, oxides are unavoidable due to gravity pouring of liquid metal into the Rotacast® pour ladle, and the casting quality is not much better than that of semi-permanent mold cast heads. Therefore, this project proposes to develop a novel casting process, “Pressure-Assistant Precision Sand-Casting (PAPSC)” [6, 7], for producing flawless cast-Al cylinder heads with minimum manufacturing and energy costs.

Objectives

The objective of this collaborative project between National Energy Technology Laboratory (NETL), GM, and Eck Industries, Inc. (Eck), is to develop a novel and cost-effective precision sand-casting process for producing high-quality and high-performance cast-Al cylinder heads with minimum porosity and oxides.

Approach

The proposed approach is to leverage GM, Eck, and NETL’s experience in producing high-quality metal castings through various microstructure control and defect elimination technologies, as well as comprehensive quantification of microstructure characteristics and mechanical properties. The project begins with the new precision sand-casting process technology development and demonstration at NETL. These new technologies will be used to make high-quality prototype cylinder head castings for thorough microstructure quantification and mechanical property evaluation. The final engine test will verify the cylinder heads made by the newly developed casting process technologies have superior performance in comparison with the current production heads. Four tasks have been proposed to achieve the objectives of the project:

- Task 1: Novel precision sand-casting process development.
- Task 2: Prototype casting of cylinder heads using the novel precision casting process.
- Task 3: Comprehensive evaluation of microstructure and mechanical properties of the head castings.
- Task 4: Cylinder head component and dynamometer durability testing.

Results

Task 1. Novel Precision Sand-Casting Process Development

Work during FY 2021 was focused on the development of the novel precision sand-casting process. However, much of the laboratory progress was delayed by the COVID-19 virus and associated laboratory closures so much of what is discussed here outlines the plans of work yet to be performed. The new PAPSC [4, 5] casting process is proposed to make a high premium cast-Al cylinder head. As illustrated in Figure II.1.3.1, two heads may be made in a production mold with a deck face metal chill and precision sand core boxes for enhanced productivity. Unlike a conventional gravity-poured semi-permanent mold casting, the head cavity will be bottom filled using low pressure or pumping mechanisms in the new process. After filling and roll over, the head casting will be solidified under low pressure applied to the riser with sand core pistons. The deckface chill is removed when the deckface material is solidified but other regions are still liquid. The deckface chill will then be extracted when it is thermally saturated and replaced with water spray to enhance cooling. More heat will be extracted from the solidified deckface and thus make other regions solidify quickly. The timing of chill extraction and pressurization profile during solidification may be optimized to deliver the best quality casting.

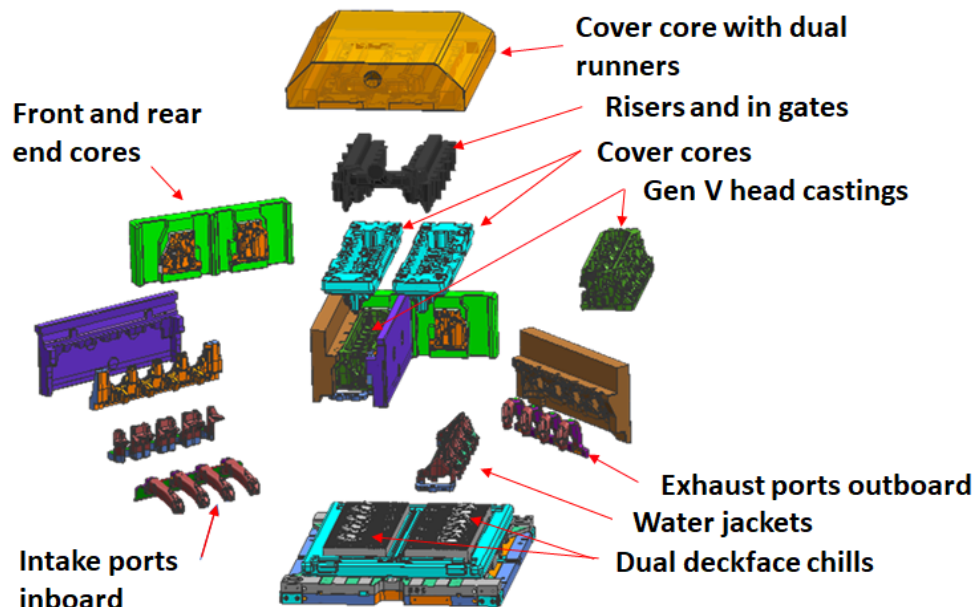


Figure II.1.3.1. New PAPSC process for manufacturing a cast-Al head. Source: GM.

In another version, the casting will be bottom gravity fed through a bottom in-gate while the deckface chill will be water-cooled and made of cast-Fe with protruding fins in a water-cooled cavity, as can be seen in Figure II.1.3.2. Following pouring, the chill fins will be flooded with water, the down sprue plugged, the mold rolled over, and hydrostatic pressure applied to the mold.

Initial trials have already begun on a simple plate casting incorporating a water-cooled chill and made of cast-Fe with protruding fins in a water-cooled cavity. Figure II.1.3.3 shows a photo of the pattern being used to form the chill plate. The fins protrude into a lower recess, which is plumbed for water-cooling. The simple plate casting will be formed on the upper side of the finned half of the chill. Critical variables include water temperature and water flow rate delay time before the start of water flow. Once the parameters are well-defined and good microstructural control is achieved, another chill will be utilized with an upper surface that forms the cylinder head deck surface and combustion chambers. Figure II.1.3.4 shows a photo of the deckface chill being used to form the casting side of the combustion chamber/deckface chill plate before finishing.

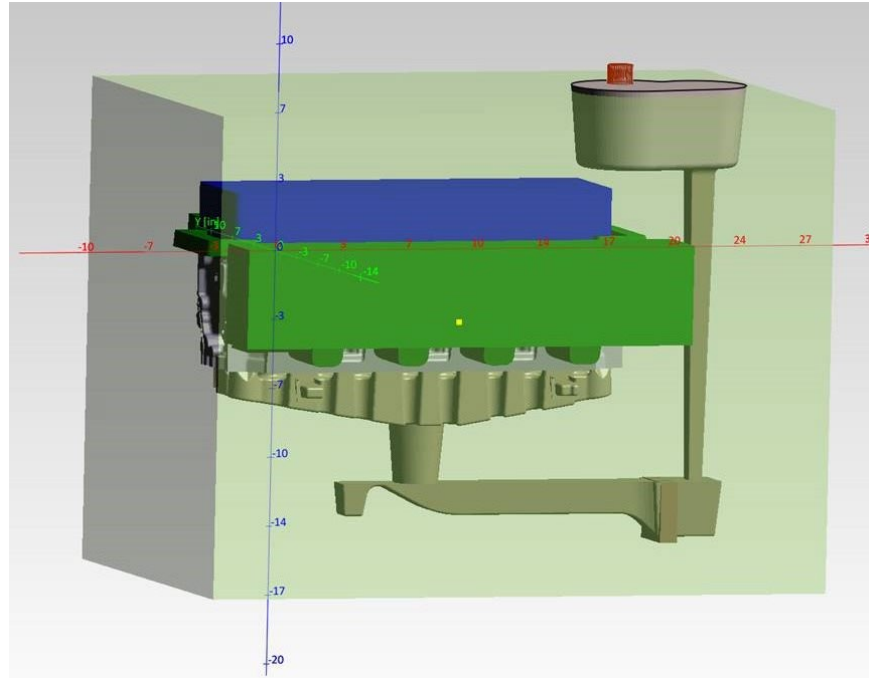


Figure II.1.3.2. New PAPSC process fitted with a gravity fed in-gate for manufacturing a cast-Al head. Water-cooled chill is shown in blue. Source: Eck Industries, Inc.



(a)

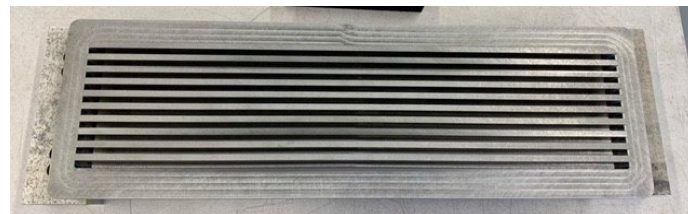


(b)

Figure II.1.3.3. Water-cooled chill: (a) fin-side; and (b) casting side. Wood form resides in the location of the cast-Al block. Source: NETL.



(a)



(b)

Figure II.1.3.4. Water-cooled deckface chill: (a) combustion chamber/deckface side; and (b) water-cooled, fin-side. Source: NETL.

Task 2. Prototype Casting of Cylinder Heads Using the Novel Precision Casting Process

Eck Industries Inc. will produce prototype cylinder head castings using the novel precision casting process technologies to be developed. Eck has done a lot of advanced work in cast-Al, such as ultrasonic degassing and grain refinement, nano-MMCs, etc. A recent relevant project is DOE contract DE-AC05-000R22725, subcontract 4000022893, “Development of an Advanced Squeeze Casting Process for the Production of High Integrity Truck Components.” Eck has advanced equipment and facilities in melting, melt quality control, casting process development and validation, heat-treatment, tensile testing, and nondestructive tests, including four available low pressure permanent mold machines and three airset molding lines, ultrasonic degasser, dye penetrant, and digital radiography.

The cylinder head selected for this project is a V8 head, as shown in Figure II.1.3.5, which is made of a 319-T7 alloy using state-of-the-art semi-permanent mold casting. One can see how the casting fits up with the deckface/combustion chamber chill shown in Figure II.1.3.4 with the bottom side of the intake runners being formed by sand mold patterns.

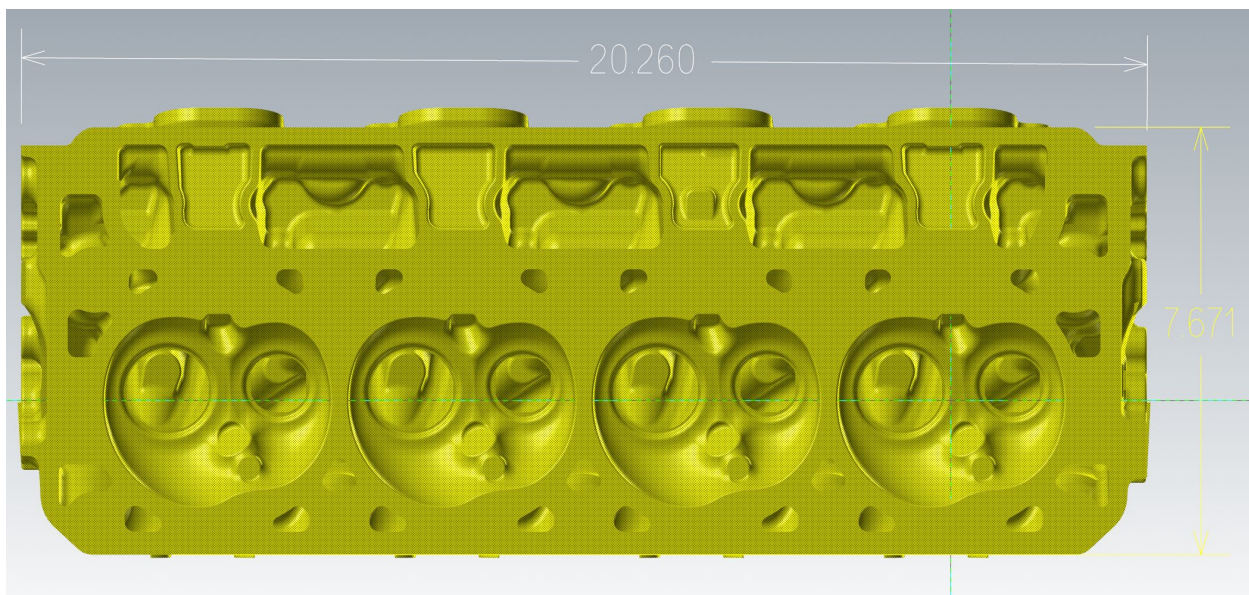


Figure II.1.3.5. A typical V8 cylinder head (deckface/combustion chamber view). Source: Eck Industries, Inc.

Several casting trials were made with either a 1 or $1.25 \times 4 \times 8$ in³ plate against the water-cooled cast-Fe chill. An early casting is shown in Figure II.1.3.6. This casting was made without a riser to get a thermal profile of the casting. As can be seen, the peak metal temperature ranged from 650°C to 550°C even though the pour temperature was 750°C. Over several trials, a number of process optimizations were made including restricting the in-gate, tapering the down sprue, controlling the moisture content of the sand, adding a riser, etc. A typical casting of this process is shown in Figure II.1.3.7. Here the pour temperature was 780°C and the maximum in mold temperatures were 695°C (inlet) and 600°C (outlet). A sound casting resulted. Subsequent trials will be made with the addition of mold rollover and pressurization utilizing the PAPSC process and water-cooled deck face chill. These castings will be utilized to complete Tasks 2-4.

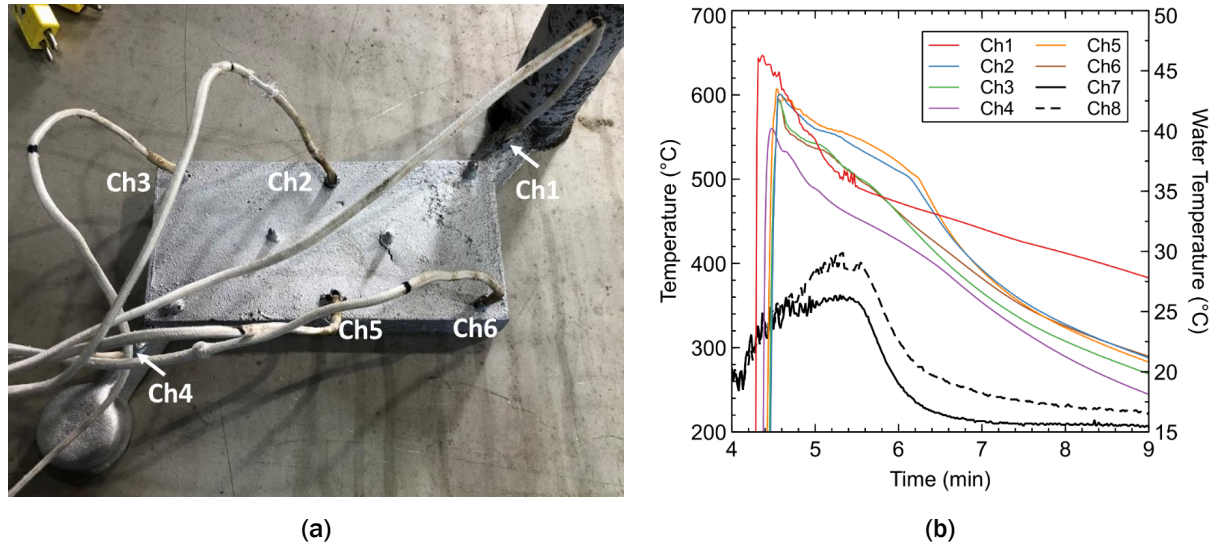


Figure II.1.3.6. An Al plate (21-A15) cast against the water-cooled chill showing the locations of the thermocouples (left) the thermocouple reading (right). Note that the water temperature readings are shown on the right vertical axes with water in Ch7 and water out Ch8. Source: NETL.



Figure II.1.3.7. A more recent Al plate (21-A35) cast against the water-cooled chill. Note the restricted in-gate to minimize aspiration and addition of a successful riser (a). The surface in contact with the chill (b) exhibited what appeared to be flow lines which can be attributed to the liquid flowing across the chill and freezing in place sequentially. The cylinder head should not exhibit this since the liquid will flow up the chill rather than across it. Source: NETL.

Conclusions

The new PAPSC [4-5] casting process is proposed to make a high premium cast-Al cylinder head. Water-cooled cast-Fe chills for both a simple plate, as well as the deck face/combustion chamber have been fabricated. Initial casting trials of the simple plate form have shown progress.

References

1. *Metallic Material Trends in North American Light Vehicles - Automotive Right-Weighting*, 2015, Ducker Worldwide, March 2015.
2. Wang, Q. G., D. Apelian, and J. R. Griffiths, 1998, in: Tiyakioglu, M., and J. Campbell (eds.), *Advances in Aluminum Casting Technology: Proceedings from Materials Solutions Conference '98 on Aluminum Casting Technology*, ASM International, pp. 217–223.

3. Wang, Q. G., 2003, “Microstructural effects on the tensile and fracture behavior of aluminum casting alloys A356/357,” *Metall. Mater. Trans. A*, Vol. 34, pp. 2887–2899.
4. McDowell, D. L., K. Gall, M. F. Horstemeyer, and J. Fan, 2003, “Microstructure-based fatigue modeling of cast A356-T6 alloy,” *Eng. Fract. Mech.*, Vol. 70, No. 1, pp. 49–80.
5. Houria, M. I., Y. Nadot, R. Fathallah, M. Roy, and D. M. Maijer, 2015, “Influence of casting defect and SDAS on the multiaxial fatigue behavior of A356-T6 alloy including mean stress effect,” *Int. J. Fatigue*, Vol. 80, pp. 90–102.
6. Wang, Q. G., D. Apelian, and D. A. Lados, 2001, “Fatigue behavior of A356-T6 aluminum cast alloys. Part I. Effect of casting defects,” *Journal of Light Metals*, Vol. 1, No. 1, pp. 73–84.
7. Wang, Q. G., M. Walker, D. Hess, and H. Doty, 2019, “Cast-aluminum alloys for high-performance cylinder heads,” *SAE World Congress, SAE International*, 9–11 April 2019, Detroit, MI, USA.
8. Cogan, C., Q. Wang, and M. Meyer, 2018, “Method of manufacturing metal castings,” Patent Application US20180016666.
9. Walker, M., J. Carter, and Q. Wang, 2017, “Mold assembly and method for manufacturing metal castings,” Patent Application US20190134704.

Acknowledgments

NETL would like to acknowledge the valuable assistance of E. Argetsinger, M. Detrois, and J. Mendenhall.

II.1.4 Room Temperature Stamping of High-Strength Aluminum Alloys (Pacific Northwest National Laboratory)

Aashish Rohatgi, Principal Investigator

Pacific Northwest National Laboratory
902 Battelle Blvd.
Richland, WA 99354
E-mail: aashish.rohatgi@pnnl.gov

Sarah Kleinbaum, DOE Program Manager

U.S. Department of Energy
E-mail: sarah.kleinbaum@ee.doe.gov

Start Date: October 1, 2016 End Date: September 30, 2022
Project Funding (FY 2021): \$1,425,000 DOE share: \$1,000,000 Non-DOE share: \$425,000

Project Introduction

This project addresses the challenge that high-strength Al sheet alloys possess limited formability at RT; therefore, these alloys are difficult to stamp into structural components with complicated geometries without cracking. Warm/hot forming can increase the formability of Al, but it is expensive due to the added costs of heated dies, forming lubricants, lubricant clean-up, etc. Unlike hot-stamped steels that undergo austenite to martensite phase transformation during quenching and achieve the high-strength at the end of the stamping process itself, Al alloy matrix does not undergo such phase transformation upon quenching. Hence, warm/hot forming results in lower post-formed strength such that heat-treatment, in addition to paint-bake, is needed (adding cost) to regain the strength. Thus, the use of an Al sheet is limited to lower strength Al alloys and/or simple-shapes (e.g., hood, deck lids, door inner, etc.) and many sheet components are still stamped in steel in the high-volume automotive industry. As such, the ability to form high-strength Al alloys cost-effectively (i.e., at RT) will expand Al use for structural components as well (i.e., crash beams, B-pillars, etc.), and has the potential to result in significant lightweighting. Additionally, microstructural modeling and component-level modeling can aid in expanding Al use. For example, modeling precipitation kinetics in high-strength Al alloys can help predict the YS evolution before and after the stamping process and assist in designing sheet tempers. Likewise, finite element modeling can simulate mechanical behavior at component-level without having to do full-scale testing.

Objectives

This project aims to develop processing techniques that will overcome the formability limitations of high-strength Al alloys and enable RT forming. Eventually, this knowledge must be leveraged to fabricate an automotive component. Thus, the project objectives are to:

- Identify automotive components that, if formed out of high-strength Al, can provide lightweighting, relative to if they were made of high-strength steels
- Develop constitutive relations and perform stamping simulations to determine the feasibility of stamping a selected component out of a high-strength Al alloy
- Integrate microstructure and mechanical property models for the selected Al alloy
- Fabricate and characterize the prototype component and perform simulations to analyze its deformation behavior under service conditions.

Approach

This project focuses on understanding the microstructure-formability-strength interplay in high-strength Al alloys with the expectation that microstructural control during processing could enable sufficient formability and strength in a prototypical automotive component. The project is structured to be performed in three phases. In the first, a door side impact beam was selected as the prototypical component for this project, while Al alloy AA7075 was selected as the high-strength alloy. Tempers specific to this alloy were developed through thermomechanical treatments and the properties were verified by tensile tests. In the second-phase, forming simulations with the AA7075, using temper-specific mechanical properties, were performed based on the design provided from an actual hot-stamped steel side impact beam. It was established from the simulations that the selected design made of AA7075 is stampable at the tempers developed in this project. During the third phase, which began in FY 2019, strength evolution in the AA7075 was predicted during natural aging and under stamping/straining conditions. *In-situ* and *ex-situ* SAXS and WAXS experiments were performed to quantify the evolution of microstructure (e.g., precipitation kinetics) during natural aging of the AA7075 sheet being used in the project. In FY 2020, starting with AA7075 sheets of different initial tempers, prototype side impact beams were successfully stamped at RT. These Al beams were ~38% lighter than the baseline steel beam. The mechanical properties of the beams were initially characterized by hardness measurements in various regions and the data showed that more than 80% of the measured values were within 10% of the T6 hardness in the as-stamped condition (i.e., without the necessity of imparting a post-forming heat-treatment). Furthermore, hardness measurements in aged and tensile deformed samples seemed to fluctuate with time and were mirrored in a separate set of samples by fluctuations in SAXS measurements of the precipitate sizes.

As a part of our continued third phase efforts in FY 2021, the RT stamped AA7075 side impact beams were characterized using mechanical testing. Some of the stamped beams were subjected to a simulated paint-bake heat-treatment (e.g., 180°C for 20 mins.). A total of seventeen samples with ASTM-E8 tensile geometry were cut using electro-discharge machining from each beam. These tensile samples were tested under constant cross-head speed control for a nominal strain rate of $5 \times 10^{-3} \text{ s}^{-1}$. An optical extensometer was used to track the fiducial marks within the gauge region.

To compare the potential performance of the beams under impact conditions in-service, bending behavior of the stamped non-paint baked Al beam and the baseline steel beam was modeled under three-point bend loading using FEM. The non-paint baked Al beam was selected for modeling as it showed the highest tensile strength and elongation relative to AA7075-T6 temper sheet. To date, such cold-stamping with T6 performance has not been reported. Since paint-bake lowers the strength, this indicates a need for some optimization in developing an appropriate temper that would be able to produce T6 performance in the stamped beam after pain-bake. Both simulated materials were assumed to be isotropic elastoplastic with isotropic hardening. Mechanical properties for AA7075 were obtained from the prior tensile tests and baseline steel beam properties were obtained from the literature [1]. Although hardness test data in the prior FY showed that the Al beams had greater hardness in the bent and edge regions relative to the remainder, the beams were modeled under the assumption of homogenous mechanical properties throughout the beam. The mechanical properties used for modeling were obtained from the tensile tested regions (flat portions of the beam) where the hardness was found to be 1-2 HRB lower than the average hardness over the entire beam. Thus, the modeled mechanical performance is expected to be conservative.

In the material model that describes deformation behavior after uniform elongation in a tensile test, a damage criterion was modeled under progressive degradation, which reduces the stress of the material after a critical plastic strain is reached. This critical plastic strain was determined from FLDs referenced from published work for both AA7075 and baseline steel [2, 3]. After the critical plastic strain is reached, the damage parameter is linearly proportional to the plastic strain.

The beams were meshed as a surface with shell elements of S4 and S4R. The thickness of the baseline steel beam was kept at 1.5 mm while the AA7075 beam was kept at 2.5 mm, corresponding to the initial blank

thickness. Both, the steel and Al blanks, undergo thickness changes during stamping. The thickness variation ranges from -8% to +4% for the beams. The strength of the beam should not vary more than 10% based on the hardness. Therefore, when comparing the respective bending behavior of the beams, assuming a uniform thickness throughout either beam was considered to be reasonable assumption to a first approximation. Each beam also had three drilled holes where the beam was supported using fixed boundary conditions to mimic beams bolted to the automobile car-door frame. Each bolt support was represented as a fixed area boundary condition where the beam is rigidly bolted. The anvil was also modeled as a rigid body that was free to move perpendicular to the surface of the beam. As the anvil moves down, the test beam bends downward and provides the displacement, strain and stress data, and fracture sites derived from the respective material properties of each beam. Anvil diameter of 25.4 cm (10 in.) was based on the U.S. Department of Transportation rigid pole side impact test protocol [4].

Results

Figure II.1.4.1 shows the summary of tensile mechanical properties of samples extracted from the stamped beams, where the beams were either in an as-stamped condition or had been given a simulated paint-bake treatment. Tensile data from the samples cut from the as-received AA7075-T6 sheet is also provided for comparison. The data shows that the UTS of the beam (labeled as Temper #2) after stamping and without any artificial aging heat-treatment is comparable to that of the as-received sheet that had been artificially aged to T6 temper. Additionally, the total elongation and uniform elongation of the Temper #2 beam is higher than that seen in the T6 aged condition, although the beam's YS is significantly lower (by ~110 MPa) than the T6 sheet. In other words, the beam can undergo extensive strain hardening such that even with a relatively lower YS than a T6 temper, the beam is able to achieve the UTS comparable to T6. Interestingly, after paint-bake treatment, both temper beams showed a decrease in UTS of ~80 MPa and a decrease in elongation, and yet, the YS was similar or somewhat higher than the beam without paint-bake treatment. This reduction in UTS after paint-bake treatment is likely due to over aging but requires additional microstructural analysis to confirm. The beams very likely continue to naturally age after stamping which increases the possibility of over aging upon subsequent paint-bake treatment. Thus, a possible remedy to avoid over aging during paint-bake is to control the time between the stamping and the paint-bake treatment.

Figure II.1.4.2 shows the FEM results of the displacement maps for the baseline steel beam and AA7075 Temper #2 beam just before fracture. Note that due to the coordinate system selected, the legend for Figure II.1.4.2 shows the bending displacement values along the anvil direction as negative. The baseline steel undergoes a maximum deflection of 13.73 mm before it starts to fracture, as compared to the maximum deflection of 34.25 mm for AA7075 beam. Thus, the AA7075 beam shows a larger bowing than the baseline steel before fracture.

Figure II.1.4.3 shows the final fracture locations of both the baseline steel and the AA7075 beams, the fracture being identified as when the force on the beams reduces to zero. The von Mises stress at the bottom surface of the beam is shown in the figures for reference. During bending, the fracture initiates at the center region of both beams. Subsequently, new cracks appear around the bolt holes in the left region of both beams while the fractures at the center of beam increases in size and density. Finally, the fracture starts to appear on the right region along the U-shape of the beam. Thus, both the beams show a similar fracture evolution. The simulations also show that the peak force supported by the Al and steel beams are ~440 kN and ~480 kN, respectively. In other words, the lightweight Al beam (e.g., 38% lighter than the steel beam) can support a peak bending load that is within 10% of the steel beam's performance and suggests that such a RT stamped AA7075 beam could serve as a lightweight alternative to the existing steel side impact beam.

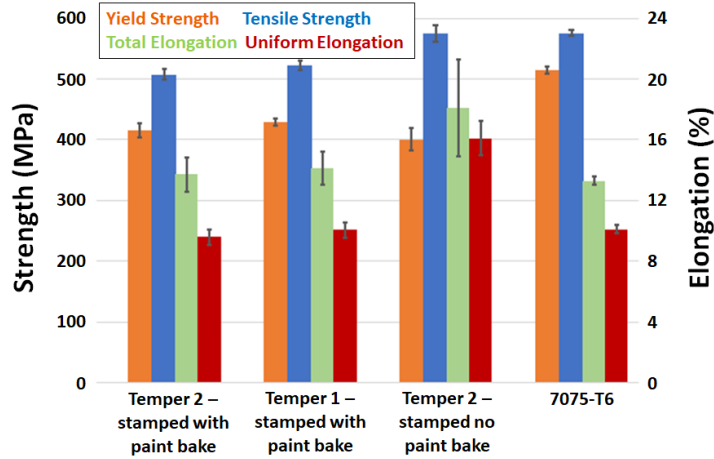


Figure II.1.4.1. Mechanical properties derived from tensile tests of AA7075 side impact beams before and after paint-bake treatment. Data from the as-received 7075-T6 sheet is also shown for comparison. Source: PNNL.

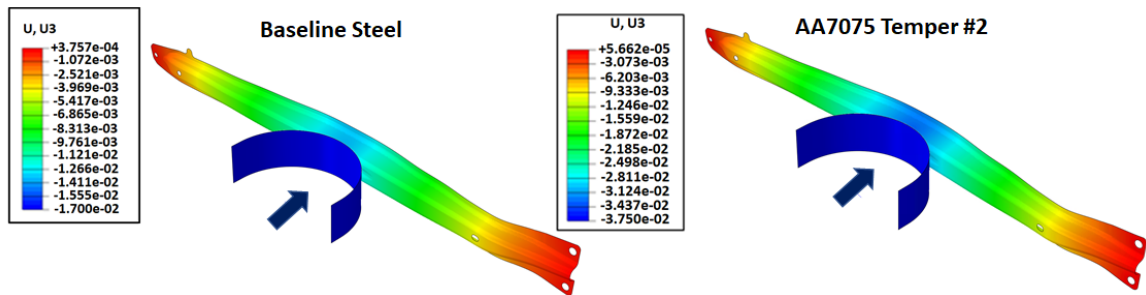


Figure II.1.4.2. FEM displacement maps for baseline steel and AA7075 Temper #2 beams along the bending direction of the anvil. (Legend - U: Displacement; U3: Displacement along anvil direction). Source: PNNL

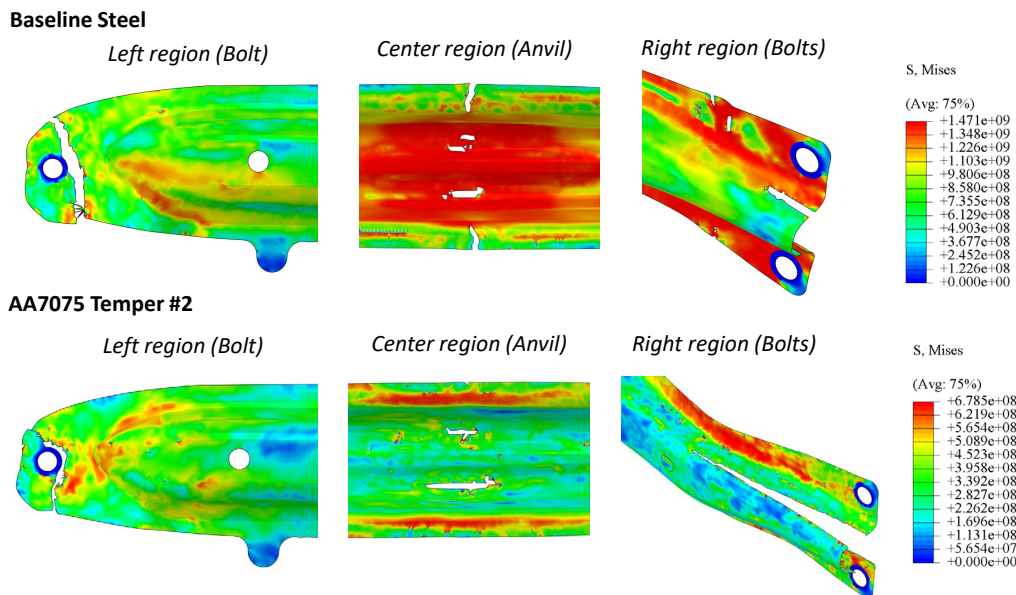


Figure II.1.4.3. FEM simulated von Mises stress maps of baseline steel and AA7075 side impact beam with end-of-simulation fracture patterns for left, center, and right regions of the beam. (Legend - S, Mises: von Mises stress at the bottom surface of the beam). Source: PNNL

Conclusions

Prototype side impact beams of AA7075 that had been stamped at RT were characterized through mechanical testing and FEM. Tensile samples extracted from the as-stamped AA7075 beams showed comparable UTS and higher elongation (total and uniform) than samples made from AA7075-T6 sheet. However, after paint-bake treatment, both temper AA7075 beams show a decrease in UTS and elongation (total and uniform) but the YS is similar or somewhat higher than the yield in an as-stamped condition, suggesting an overaged condition after paint-baking. Bending behavior of the stamped Al and the baseline steel beams, under three-point bending, was modeled using FEM to determine their potential performance under impact conditions in-service. Simulations show that the Al beam performed within ~10% of the baseline steel in terms of peak bending force. The Al beam also underwent a higher bowing displacement, relative to the steel beam, before fracture initiation. These FEM results show good potential of the RT stamped AA7075 beams as a lightweight replacement for baseline steel beams.

References

1. ArcelorMittal, *Stress-Strain Curves Hot Forming Steels -USIBOR(R) 1500 Treated*, 2016.
2. Behrens, B. A., et al. *Influence of the Quenching Rate and Natural Aging Duration on the Formability and Mechanical Properties of EN AW-7075*. in *Forming the Future*, 2021, Cham: Springer International Publishing.
3. Karbasian, H. and A. E. Tekkaya, 2010, "A review on hot stamping," *J. Mater. Process. Technol.*, Vol. 210, No. 15, pp. 2103–2118.
4. U.S. Department of Transportation, 2012, "Laboratory test procedure for FMVSS No. 214: Dynamic side impact protection," in *National Highway Traffic Safety Administration*.

Acknowledgments

Technical contributions of the PNNL staff supporting this research is gratefully acknowledged. In particular, we are grateful to Dr. M. Efe for leading the task on characterization of stamped beams; Dr. W. Nasim for the experimental and simulation analysis and report writing; Dr. S. S. Kulkarni for the FEM development; and to Mr. T. Roosendaal, Mr. M. Rhodes, and Mr. A. Ortiz in the Mechanical Testing Laboratory for their help in conducting the heat treatments, mechanical tests, and hardness measurements. We would like to thank the technical support provided by Mr. B. Kokosza and his team at Magna-Stronach Centre for the innovation for stamping operation, technical discussions, and support. We are also grateful to the technical staff at GM R&D—in particular, Mr. J. Carter and Dr. A. K. Sachdev, for their insightful comments, discussions, and providing the steel impact beam for this research, as well as providing information on lightweighting analyses for automotive components. Finally, we would like to thank PNNL staff that have provided valuable support over the course of this project: Dr. R. Davies, Ms. E. Stephens, Dr. A. Soulami, Dr. T. Mungole, Mr. M. Dahl, Mr. K. Mattlin, Dr. M. Olszta and Dr. K. Kruska.

II.1.5 Development of a Novel Magnesium Alloy for Thixomolding of Automotive Components (Oak Ridge National Laboratory)

Govindarajan Muralidharan, Co-Principal Investigator

Oak Ridge National Laboratory
1 Bethel Valley Road
Oak Ridge, TN 37831
E-mail: muralidhargn@ornl.gov

Bryan Macek, Co-Principal Investigator

Stellantis (formerly known as FCA US LLC)
1000 Chrysler Drive
Auburn Hills, MI 48326
E-mail: bryan.macek@stellantis.com

Nathan Sanko, Co-Principal Investigator

Leggera Technologies
87 Northpointe Drive
Orion Township, MI, 48359
E-mail: nathan@leggaretech.com

Sarah Kleinbaum, DOE Program Manager

U.S. Department of Energy
E-mail: sarah.kleinbaum@ee.doe.gov

Start Date: February 1, 2020	End Date: September 30, 2022	
Project Funding (FY 2021): \$300,000	DOE share: \$150,000	Non-DOE share: \$150,000

Project Introduction

Mg alloy die-castings are being increasingly used in the automobile industry as a means of providing cost-effective mass reduction, especially in systems where multiple components can be integrated into a single thin-wall die-casting. However, there is only one die-caster in North America capable of producing die-castings of the size needed for instrument panel structures, liftgate inner panels, swing gate inner panels, and similar components, thus making it difficult to negotiate competitive pricing and creating a supply chain risk. Furthermore, there are several component quality restrictions in thin-walled Mg die-castings, including variability in dimensional accuracy, part-to-part variation in mechanical properties, and porosity in the final part, which has limited the continued growth of die-cast components in the automobile industry.

An alternative to die-casting is the process of thixomolding. Widely used in the electronics industry, the thixomolding process has begun to make inroads into the automobile industry (e.g., 2018 Jeep Wrangler spare tire carrier) as a competing process to die-casting for producing complex thin-wall Mg components.

While the thixomolding process is somewhat similar to the die-casting process, it differs in at least one significant aspect. While the die-casting process relies on filling a mold at high speeds with the alloy in the completely molten state, the thixomolding process fills a mold with a thixotropic alloy in a semi-solid slurry state at a temperature between the liquidus and solidus temperatures. Ideally, the material should be ~30%–65% solid rather than being completely liquid at the beginning of the injection process. Advantages of the thixomolding process include a finer grain structure, lower porosity, improved dimensional accuracy,

improved part-to-part consistency, improved mechanical properties, particularly ductility in the component, the ability to reduce wall thickness for mass savings, and longer tool life due to lower process temperatures.

Although thixomolding offers improved mechanical properties over die-cast-Mg components, the mechanical properties obtained in the thixomolded parts are still not sufficient to broadly enable application in components where both strength and ductility are key requirements (e.g., crash critical components exposed to high-impact velocities and powertrain or chassis components subjected to high levels of cyclic loading). Currently, the mechanical properties are limited by the alloys being used, which are the same alloys used in the die-casting process. Thus, there is a need for the development of new alloys, which can achieve high-strength with improved ductility for use in components fabricated by the thixomolding process.

Objectives

The objective of this project is to develop a novel Mg alloy more suitable for thixomolded automotive structural components than current die-casting alloys. For this project, ORNL will assist Fiat Chrysler Automobiles U.S. LLC (FCA US LLC) and Leggera Technologies in the development of up to two new Mg alloys optimized for the thixomolding process with improved mechanical properties when compared to current die-casting alloys. The primary interest is in improving ductility and fatigue strength, as these are properties that are critical for use in body and chassis structural applications. Since good corrosion resistance is also desirable for this application, this property will also be considered when evaluating promising alloy compositions. Additionally, suitability for heat-treatment to further improve YS, tensile strength, and corrosion performance is of interest, since this capability is not available in current die-casting alloys.

Approach

In consultation with Leggera Technologies, FCA US LLC will establish the desired thixomolding processing parameters, target strength, ductility, and corrosion performance requirements of the new alloy. To understand the relationship between thixomolding process conditions, alloy composition, microstructure, and properties of the current alloys, ORNL will perform a baseline study of two industry standard Mg alloys suitable for thixomolding in collaboration with industrial partners. In the initial phase of the work, ORNL has initiated microstructural characterization of an existing thixomolded component fabricated with AM60 using optical and SEM and X-ray microchemical analysis to understand the effect of alloy composition and processing conditions on the microstructural evolution during the thixomolding process and its effect on strength and ductility.

Based on correlations developed in this part of the work, the team will initiate new alloy development by identifying favorable microstructural characteristics for the target mechanical properties. ORNL will establish the feasibility of using computational thermodynamic models to predict the observed microstructure and to simulate the effect of selected alloying element additions on the solidification behavior. ORNL will also identify alloy compositions that have the potential to be successfully fabricated using the thixomolding process while having the desired microstructure in the final thixomolded component. Laboratory-scale heats will be fabricated at ORNL, and the as-cast microstructure and tensile properties of the alloys will be evaluated to identify the required type and amount of alloying element additions. One or two alloys will be downselected for alloy ingot and chip production for use in the thixomolding process and a prototype component will be produced by Leggera Technologies. FCA US LLC will coordinate and complete material characterization tests for one new material from samples excised from the component produced by Leggera Technologies and will supervise computer-assisted engineering card development to support component modeling. Finally, FCA US LLC will conduct simulated component structural evaluation using the new properties developed for the computer-assisted engineering card. Figure II.1.5.1 provides a schematic of the approach used in the project.

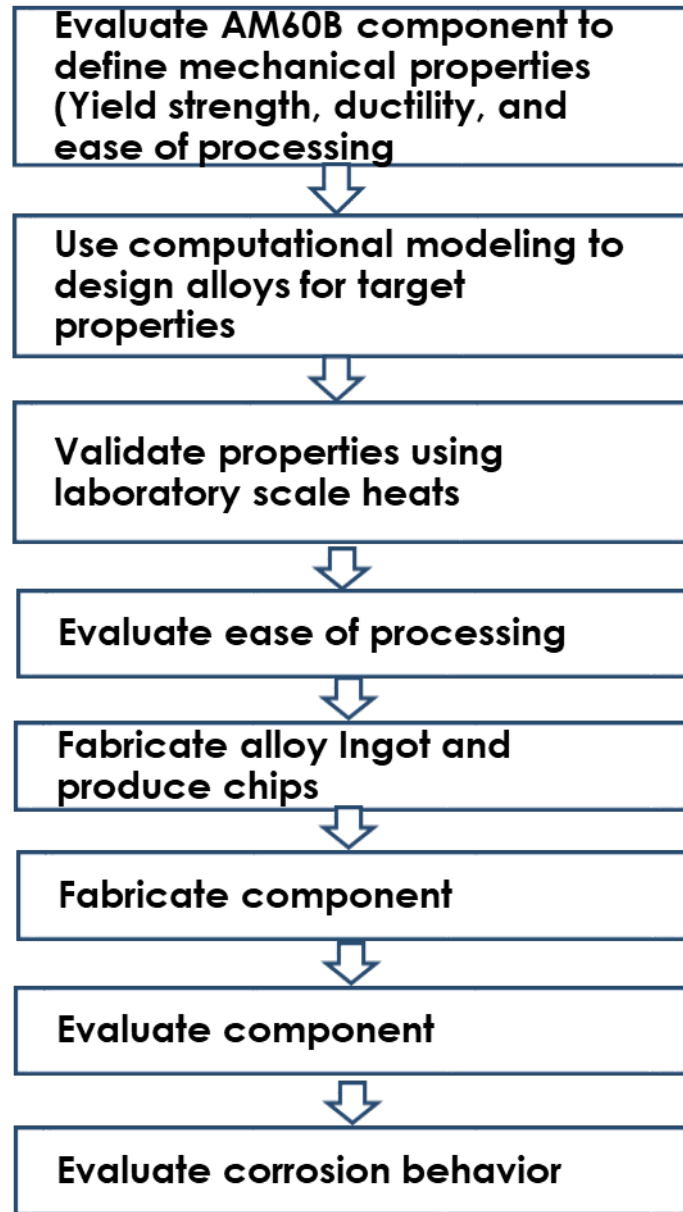


Figure II.1.5.1. Schematic of the approach used in the project. Source: ORNL.

Results

The aim of the alloy development effort used in this project was to develop new alloys for use in the thixomolding process that balance three major characteristics: (1) ease of processing; (2) strength, and (3) ductility. An alloy such as AZ91D can be processed more easily but lacks ductility. AM60B has good ductility and strength but would benefit from better processing characteristics in the thixomolding process. Table II.1.5.1 shows the nominal compositions of the alloys, their RT YS, and ductility [1-4]. Figure II.1.5.2 schematically shows the three required characteristics of the alloys and the current status of properties of AM60B and AZ91D.

Table II.1.5.1. Die-Casting Alloys, Compositions, and Mechanical Properties

Alloy	Mg	Al	Zn	Mn	Sr	YS (MPa)	% Elongation
AM60B	Bal.	6	0.2	0.3	0	121	16
AZ63A	Bal.	6	3	0.15	0	130	5
AJ52	Bal.	5	0	0.4	2	126	9
AZ91D	Bal.	9	0.7	0.3	0	158	6

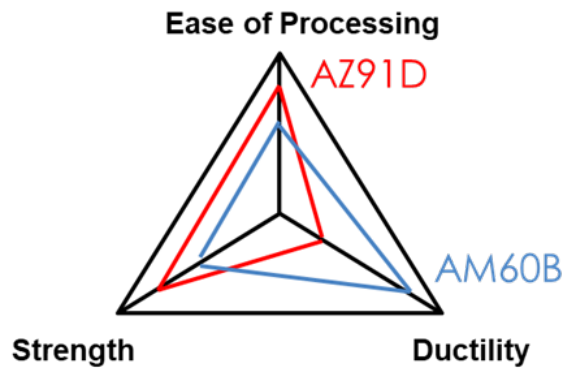


Figure II.1.5.2. Schematic showing the three characteristics of interest for alloys used in the thixomolding process. Source: ORNL.

For the alloy development effort, ease of processing was characterized by the liquidus, solidus, and the melting range (e.g., defined as the difference between the liquidus and solidus). Figure II.1.5.3 shows the solidus, liquidus, and melting range for several alloys of interest—including AZ91D and AM60B. Figure II.1.5.3 clearly shows that AZ91D has a significantly greater melting range and a lower solidus when compared to the AM60B with associated ease of processing. Hence, lower solidus and wider melting range were targeted for the new alloys.

Based on the desired liquidus and solidus temperatures and melting range, a wide range of alloy compositions were screened using computational modeling techniques. Figure II.1.5.4 shows that results of the screening process identified several alloys that could potentially meet the liquidus, solidus, and melting range requirements. Alloy compositions that had the potential to satisfy the strength and ductility criteria were downselected and five new alloys were cast-in the shape of 0.5 in. × 1 in. × 5 in. ingots in the laboratory-scale at ORNL and are shown in Figure II.1.5.5. Differential scanning calorimetry (DSC) was performed on the specimens removed from these alloys to compare the measured liquidus, solidus, and melting range. An example of this comparison is shown for AM60B. Based on the results from tensile tests, several new alloys for use in thixomolding applications have been identified; however, all their properties cannot be published at this time because of intellectual property considerations. Figure II.1.5.6 provides a schematic showing the calculated values for liquidus, solidus, and melting range of several candidate alloys used for screening. An invention disclosure of this new technology has been submitted.

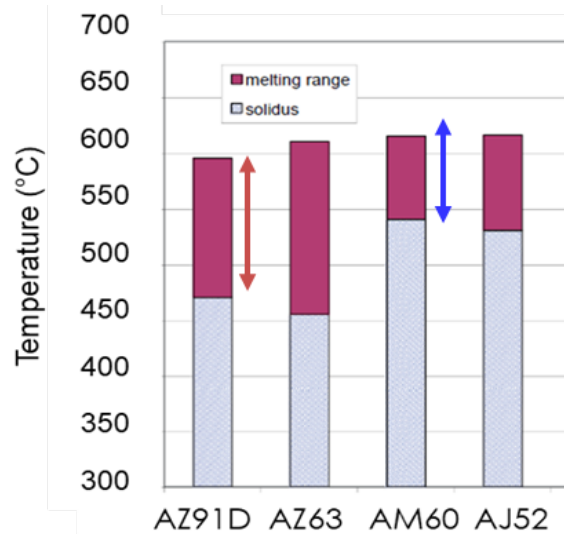


Figure II.1.5.3. Schematic showing three characteristics of interest in alloys used in the thixomolding process [5]. Source: ORNL.

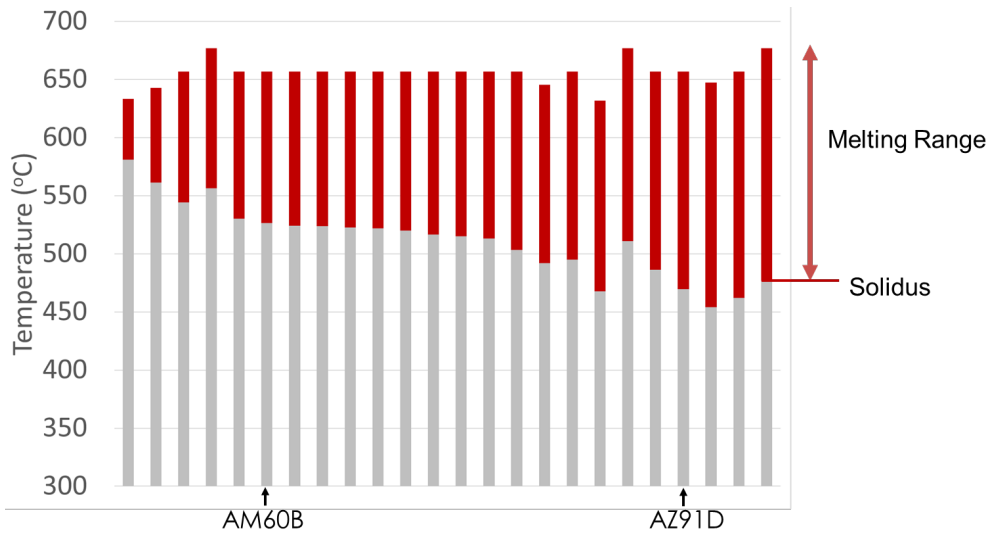


Figure II.1.5.4. Schematic showing calculated values for liquidus, solidus, and melting range of several candidate alloys used for screening. Source: ORNL.



Figure II.1.5.5. Photograph of several candidate alloys used for screening. Source: ORNL.

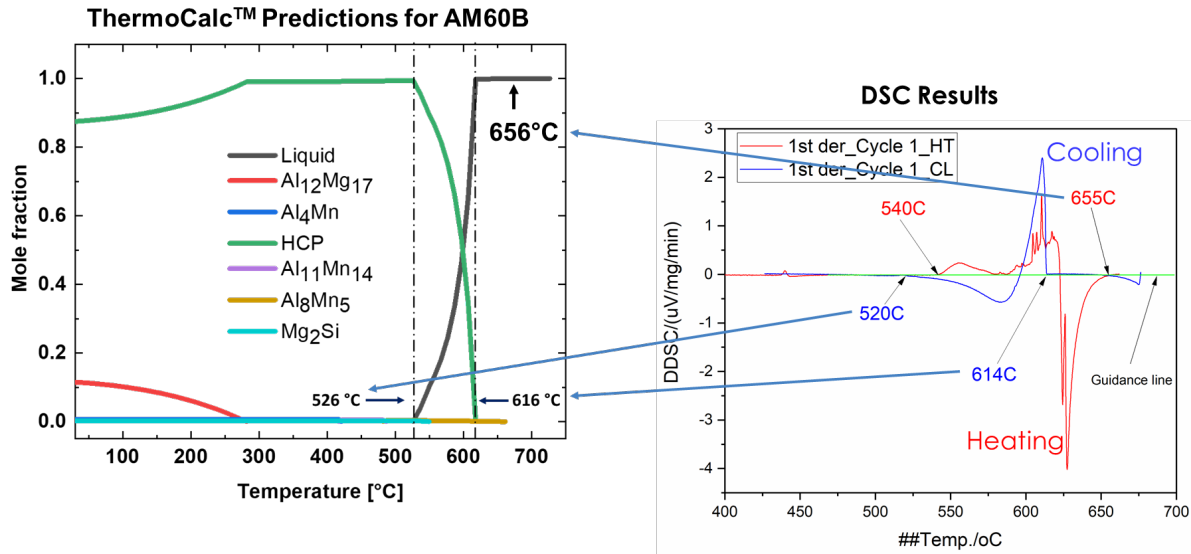


Figure II.1.5.6. Schematic showing calculated values for liquidus, solidus, and melting range of several candidate alloys used for screening. Source: ORNL.

Due to COVID-19 related delays, a no-cost extension has been requested until September 2022 to complete fabrication of a thixomolded component and evaluate properties of materials culled from the component.

Conclusions

New alloys required for thixomolding applications must balance ease of processing, strength, and ductility. Computational modeling has been used to screen alloys based on the liquidus, solidus, and melting range. Several alloys with the potential to satisfy the processing requirements and mechanical properties were identified. Laboratory-scale ingots were fabricated, properties were evaluated, and a subset of promising alloys were identified. An invention disclosure was also submitted. Future work will scale-up one alloy, fabricate a thixomolded component, and evaluate its properties.

Key Publications

1. Muralidharan, G., B. Macek, and N. Sanko, 2021, "New magnesium alloys for thixomolding applications," ORNL invention disclosure ID# 202104911, July 2021.

References

1. Luo, A. A., 2013, "Magnesium casting technology for structural applications," *J. Magnes. Alloy*, Vol. 1, pp. 2–22.
2. Patel, H. A., D. L. Chen, S. D. Bhole, and K. Sadayappan, 2010, "Microstructure and tensile properties of thixomolded magnesium alloys," *J. Alloys Compd.*, Vol. 496, No. 1–2, pp. 140–148.
3. Avedesian, M. M., and H. Baker (eds.), 1999, *Magnesium and Magnesium Alloys*, ASM International, Materials Park, OH, USA.
4. Moosbrugger, C. (ed.), 2017, *Engineering Properties of Magnesium Alloys*, ASM International, Materials Park, OH, USA.
5. Czerwinski, F., 2004, "Processing features of thixomolding magnesium alloys," *Die-Casting Engineer*, November 2004, pp. 52–58.

Acknowledgments

The authors would like to acknowledge the support of R. Davies, S. Shukla, T. R. Muth, C. Carmichael, I. Stinson, and T. Geer from ORNL.

II.1.6 Laser Powder Bed Fusion Parameter Development for Novel Steel and Aluminum Powders Using *In-Situ* Synchrotron Imaging and Diffraction (Argonne National Laboratory)

Aaron Greco, Co-Principal Investigator

Argonne National Laboratory
9700 S Cass Avenue
Lemont, IL 60349
E-mail: greco@anl.gov

Andrew Bobel, Co-Principal Investigator

General Motors
30470 Harley Earl Boulevard
RML 1-120, Research Metallurgical Laboratory
Warren, MI 48092
E-mail: andrew.bobel@gm.com

Sarah Kleinbaum, DOE Program Manager

U.S. Department of Energy
E-mail: sarah.kleinbaum@ee.doe.gov

Start Date: October 1, 2019	End Date: June 30, 2022	
Project Funding (FY 2021): \$500,000	DOE share: \$250,000	Non-DOE share: \$250,000

Project Introduction

Weight-reduction requirements in the automotive industry have led to an increased interest in the use of metal AM in vehicle body structures and powertrain components. Metal AM processes using LPBF and direct energy deposition have been demonstrated as viable methods for producing these metallic components. The benefits of these technologies—including greater design flexibility, accuracy, part consolidation, and significant weight-savings through topology-optimized design—are very attractive for automotive applications. Capturing the full value of AM for weight-reduction will include not only optimized component design, but also the use of unique low-cost additive materials, which will enable performance that would otherwise be impossible via current materials processing methods. The role of individual process parameters on the resulting microstructure and perceived material printability is unclear. This uncertainty translates to increased process parameter development time for exploring multiple processing conditions.

Objectives

This project will address this issue through the unique combination of *in-situ* X-ray imaging, temperature measurement, and phase transformation diffraction monitoring at ANL during the laser additive process on these new materials. These unique capabilities will significantly accelerate the process parameter development cycle using a scientifically motivated foundation. Specifically, the data generated will be used to validate CALPHAD alloy design modeling and create numerical models with sufficient fidelity to predict new AM lightweight alloys with properties that are better than existing alloys. This will greatly reduce the time taken from material conception to printing fully dense components in a manufacturing process that relies heavily on time-consuming trial-and-error iterative experimentation.

Approach

The proposed approach is to leverage ANL's unique facilities in ultra-high-speed synchrotron X-ray imaging of the metal LPBF process to guide and accelerate process optimization of manufacturing additive parts using innovative automotive-focused alloys identified and developed by GM. Recent successful efforts in measuring and understanding the LPBF process at ANL include the *in-situ* monitoring of melt pool dynamics, powder ejection, rapid solidification, phase transformation, and defect formation in Ti 6Al 4V.

Task 1: Specimen and Powder Procurement

In this task, GM will identify and supply an additive powder and base-plate material with a unique alloy chemistry identified and developed by GM for the automotive market to ANL. GM will supply powder of the chosen alloy chemistry with a particle size distribution suitable for the LPBF process to ANL. In addition, GM will prepare specimens to act as base plates for LPBF experiments of the same alloy chemistry. This task will be funded and performed by GM.

Task 2: Miniature Additive LPBF Builds

In this task, ANL will perform LPBF experiments on the supplied additive alloys and base plates [1, 2]. The purpose of this task will be to increase the print speed (i.e., minimize build time) while minimizing defect formation (e.g., porosity) for a range of process conditions. ANL will perform any final modifications to the supplied base plates (e.g., polishing) for use in the miniature laser powder bed system and will perform builds using the supplied powders. Builds will consist of laser scans that are 2 mm long using varied laser-parameter sets and powder-layer thicknesses. Each of the individual parameter sets identified will be tested and monitored using three different imaging capabilities at ANL: (1) ultra-high-speed dynamic X-ray imaging; (2) high-speed thermal imaging; and (3) high-speed XRD. The goal of this task is to couple the three imaging capabilities to fully understand the *in-situ* dynamic phenomena—such as vapor depression dynamics, powder spatter, void formation/incorporation into the build, rapid solidification, and directional grain growth that occur during LPBF.

Task 3: Image Analysis

In this task, ANL and GM will jointly post-process the high-speed image sets generated for each LPBF build. This task is critical because it will provide data needed to guide the selection of AM process parameters for the new alloys, guide AM process model development, and stimulate future alloy designs. For example, the X-ray imaging can supply data, such as melt pool depth and shape during the build process, porosity formation and movement within the melt, resulting build-layer thickness, and defect concentration in the build. In addition, the IR imaging will quantify temperature extremes experienced during the LPBF's rapid heating and cooling cycles, will enable correlation with the microstructure observed in Task 4, and will provide requisite inputs for CALPHAD modeling that will be conducted at GM. These experiments will reveal the physical basis of the formation of different defects and develop new parameters and materials that solve the challenge of manufacturing nearly defect-free automotive parts.

Task 4: Microstructure Analysis

In this task, GM will perform microstructural analyses of the as-built laser-processed base plates and materials newly built in Task 2. Task 4 will be funded and performed by GM. ANL will return the LPBF processed specimens to GM. GM will then use advanced metallographic techniques to prepare specimens to extract high-quality images and quantitative data on grains that span the nanometric- to micron-length scales. High-resolution SEM will be performed on the as-built samples to observe the resulting grain structure, intermetallic formation, and elemental segregation at locations throughout the laser scan area. In addition, SEM will be used to verify the melt pool depths and resulting HAZ produced by the laser scan process. EBSD will be used to quantify micron-scale grains and determine grain size and shape, phase information, misorientation, orientation, and their distributions. Where necessary, TEM will also be performed to identify nanoscale grain structure and precipitation within the as-built material. This task will identify the effects, such as columnar grain growth, of the laser parameters on as-built microstructures and drive new processing and alloy designs that avoid build failures, such as cracking and delamination.

Results

Because of the limited operation and restrictive access to ANL’s APS due to the ongoing COVID-19 pandemic, the effort during FY 2021 were primarily focused on APS data processing and microstructural characterization of the LPBF builds from the last period. Access to sectors 1-ID and 32-ID at the APS has been approved for early FY 2022 to complete this project. A no-cost extension for the project was also requested from DOE and granted due to the limitations experienced by the project. During FY 2021, the team completed APS experiments on four alloy types: (1) Al-Ti; (2) Al-Si-Cu; (3) Fe-Cu; and (4) Fe-393. In these experiments, the laser power and scan speed were varied to determine the effect of printing parameters on the formation of porosity defects during the print. Experiments were conducted with and without the corresponding powders spread on the surface prior to the laser scanning to represent the powder bed (glassy carbon plates were only used in scans with powders). In total, 106 experiments were performed. The parameters of the experiments are summarized in Table II.1.6.1.

Table II.1.6.1. List of Alloys and Laser Parameters Used for Testing

Material Tested	Laser Power Tested (W)	Laser Scan Speeds Tested (mm/s)
Al-Ti	260, 302, 395, 520	300, 800, 1000, 1300, 1600
Al-Si-Cu	260, 364, 520	800, 1300, 1400, 1600, 2000
Fe-Cu	213, 348	190, 300, 400, 500
Fe-393	213, 348	300, 400, 700

The experimental setup allowed for the direct observation of laser-material interaction, vapor cavity and melt pool formation in real-time using X-ray imaging, as well as for synchronized monitoring of the temperature during the LPBF process. Figure II.1.6.1(a) shows a schematic of the experimental setup and the actual setup is shown in Figure II.1.6.1(b).

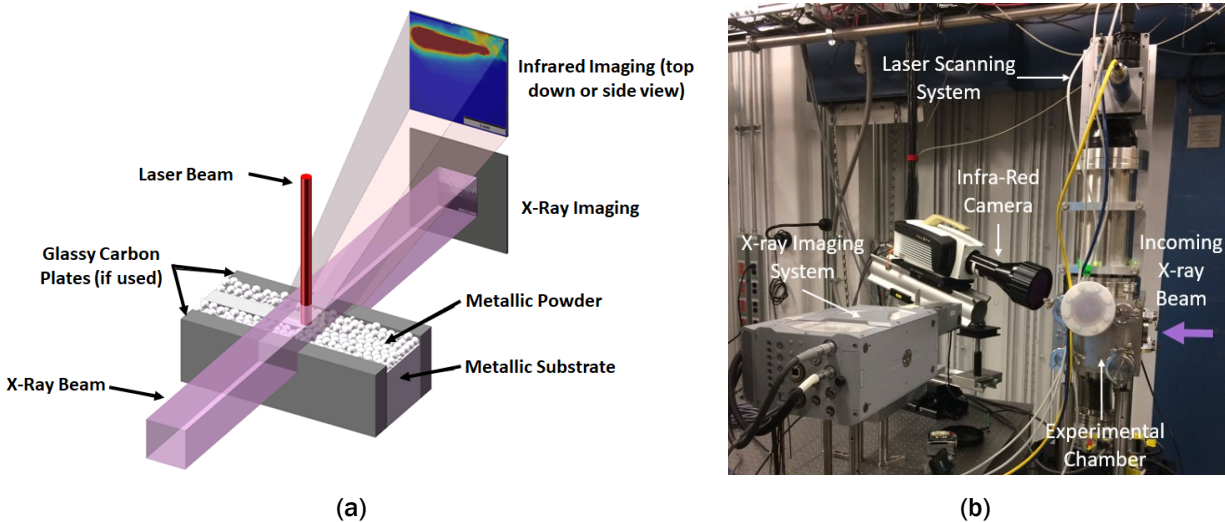


Figure II.1.6.1. LPBF experimental setup at ANL’s APS: (a) schematic of experimental setup; and (b) photograph of the experimental setup installed in the APS beamline [1]. Source: ANL.

The images shown in are representative single frames from the *in-situ* experiments, taken from the middle of the test run after the laser completed its pass from left to right. It is worth noting that these experiments are extremely fast, with a frame acquisition rate in the order of 60,000 per second. Although the laser processing is better visualized by videos, single frames of the experiments are shown here. The image in Figure II.1.6.2(a) is a representative frame of a test without powder, whereas Figure II.1.6.2(b) corresponds to the same material

and processing conditions with powder (e.g., Al-Si-Cu, 520W at 800mm/s). The glassy carbon plates used to contain the powders, as shown in Figure II.1.6.1(a), produce an edge effect observed in Figure II.1.6.2(b). No bonding or melting of the glassy carbon plates to the shims was observed, and no carbon transfer/reaction with the material is expected. In addition, no differences were observed between samples processed with and without glassy carbon plates, both exhibiting similar microstructure. Except for the edge effect and the presence of powder spatter, the melt pool and vapor depression have similar size and shape for the same material tested at the same conditions. Porosity formation was observed after the laser passes, due to gas entrapment shown as bubbles of variable size forming and moving up to the surface- indicated by red arrows. For each experiment, IR measurements were simultaneously taken to have the correlation between top surface thermal condition and subsurface defect formations, such as porosity. Figure II.1.6.2(c) shows the thermal profiles with time measured for the experiment shown in Figure II.1.6.2(a). IR calibration was performed via matching the melt pool geometry from the x-ray images to those of the IR images, and then setting the melt pool boundary temperatures to the material powder melting point. IR data is then extracted from each run using a 4-pixel subset from the center of the shim as the laser and melt pool pass across it.

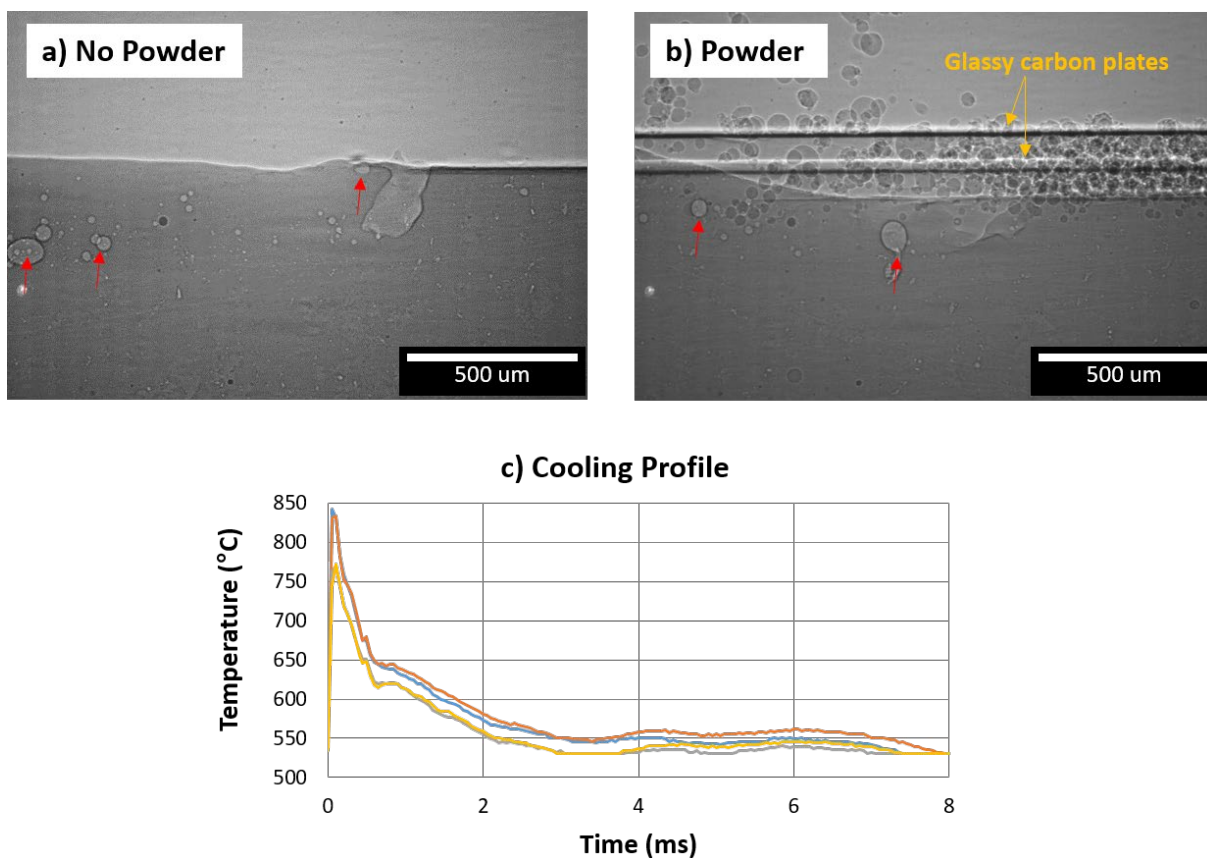


Figure II.1.6.2. X-ray images from *in-situ* LBPf experiments with Al-Si-Cu alloy, processed at 520 W laser power and at 800mm/s scan speed: (a) no powder; (b) with powder; and (c) thermal profile from IR data. Source: ANL.

Porosity formation during *in-situ* LBPf was more noticeable for Al alloys than for Fe-alloys. Fe-393 and Fe-Cu exhibited minimal porosity formation compared to Al-Ti and Al-Si-Cu. In addition, the fabrication method of the shim material also showed to have an effect. Porosity was more noticeable in the printed materials as compared to the cast samples. This may be due to the release of trapped oxide (or gas) introduced during the printing process in the Al alloys. Limited bubbling/porosity formation was observed in both cast and printed samples due to turbulent melting and cavity necking. However, only the printed Al samples exhibited a second type of porosity that occurred during the cooling process, which was hypothesized to be due to the presence of

oxide formed during the shim printing process. This was not observed in the printed steel shims, where less oxide formation is expected. Figure II.1.6.3 shows a casted versus a printed AlTi shim tested at the same conditions of laser power and speed (i.e., 520W and 1000 mm/s).

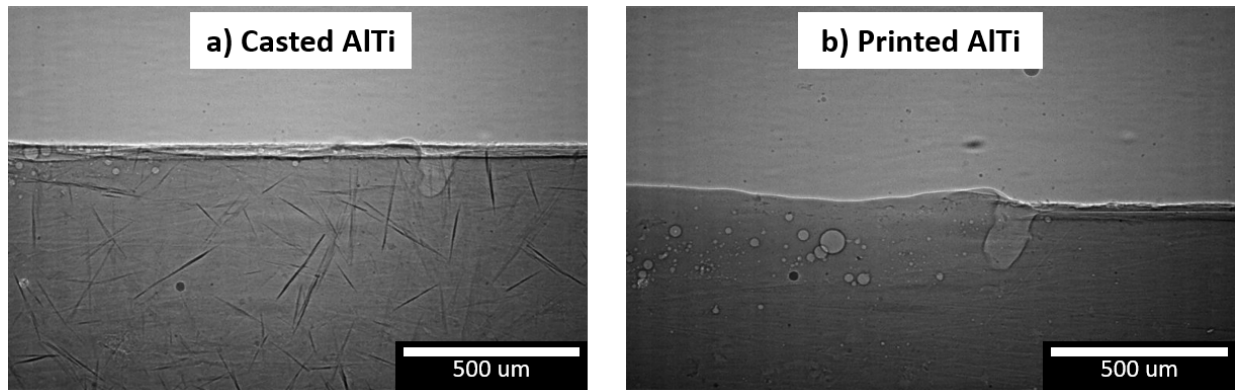


Figure II.1.6.3. X-ray images from *in-situ* LPPF experiments with AlTi alloy, processed at 520W laser power and at 800mm/s scan speed: (a) no powder; and (b) with powder. Source: ANL.

The shape of the melt pool and vapor depression are primarily controlled by the energy density, which increases with the energy input of the laser and decreases with the speed whereby the laser scans the surface for a fixed area (e.g., x-ray beam diameter), as expressed in Equation 1. Figure II.1.6.4(a)–(c), clearly illustrates that for a fixed laser power (e.g., 350W), both the melt pool, indicated by the red line, and the vapor depression, indicated by the blue line, decreased with speed. IR analysis of the thermal profiles indicated that slower scan speed allows for more heat dissipation. The cooling rate is found to increase with scan speeds or decreasing energy density for a given laser power. In addition, the heating rate is also observed to have a strong correlation with the laser scan speed, where the faster the scan speed, the faster the heating rate. The IR data in conjunction with the melt pool shape as measured during *in-situ* experiments can be utilized in computational modeling of the LPPF process, which is essential to explore processing parameter that allows for significant reduction in time and experimental effort for each of the studied alloys.

$$ED [J/(mm^2)] = (Laser\ Power [W]) / ((Scan\ Speed [mm/s] * Beam\ Diameter [mm])) \quad (1)$$

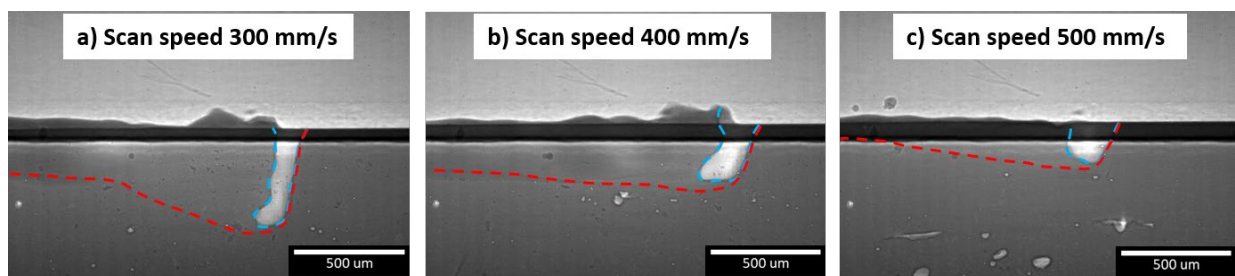


Figure II.1.6.4. X-ray images of the melt pool and vapor cavity in FeCu alloy processes at 350W laser power and different scan speeds: (a) 300 mm/s; (b) 400mm/s; and (c) 500 mm/s. Source: ANL.

EBSDF analysis from the cross-sections of *in-situ* LPPF line scans showed a higher microstructural anisotropy for the samples printed at faster scan speed, which agrees with faster heating and cooling rates observed at this condition. Figure II.1.6.5 shows an Inverse Pole Figure EBSDF map of the FeCu printed at low and high scan speed, with the BD up the page and the laser scan direction in and out of the page.

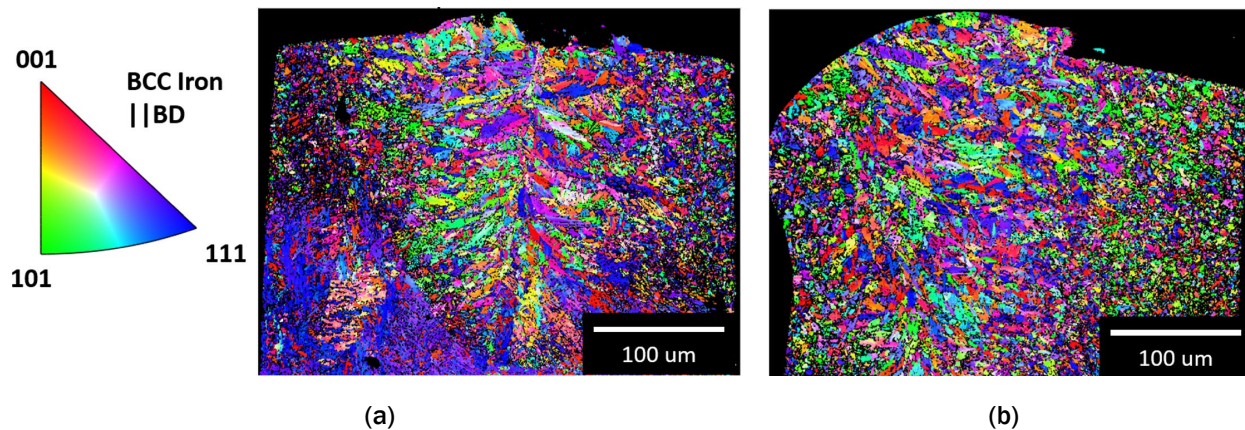


Figure II.1.6.5. EBSD maps of cross-sectioned FeCu scans for: (a) the high scan speed (500 mm/s); and (b) the slow scan speed (300 mm/s). The BD is oriented vertically upward along the page. Source: ANL.

Conclusions

Through our FY 2021 work, we demonstrated that advanced high-energy x-ray *in-situ* experimentation is effective at determining porosity formation in a wide set of alloys, fabrication methods, and processing parameters. Al-containing alloys and printed materials were more susceptible to secondary porosity formation, especially at high-energy density processing conditions. The combination of experimental data, *in-situ* x-ray radiographic images, and corresponding *in-situ* high-speed IR images yield relevant information to be utilized in laser-material modeling for additional insight into selection of appropriate laser parameters CALPHAD modeling for respective alloys.

References

1. Gould, B., S. Wolff, N. Parab, C. Zhao, M. C. Lorenzo-Martin, K. Fezzaa, A. Greco, and T. Sun, 2020, “*In-situ* analysis of laser powder bed fusion using simultaneous high-speed infrared and x-ray imaging,” *JOM*, Vol. 73, pp. 201–211.
2. Bobel, A., L. G. Hector, I. Chelladurai, A. K. Sachdev, T. Brown, W. A. Poling, and R. Kubic, 2019, “*In-situ* synchrotron x-ray imaging of 4140 steel laser powder bed fusion,” *Materialia*, Vol. 6, Art. 100306.

Acknowledgments

In addition to the PIs, the core project team also includes Dr. B. Gould, and C. L. Martin, Materials Scientists, in the ANL Applied Materials Division and Dr. L. Hector Jr. of GM R&D. The team would also like to recognize the contributions from Mr. M. Bohan, a DOE Science Undergraduate Laboratory Intern, and Dr. K. Fezzaa of ANL’s APS. The authors would like to thank the DOE VTO for funding this project through the LightMAT consortium, and Ms. S. Kleinbaum for her guidance. This research used the resources of the APS, which is a DOE–Office of Science User Facility operated for the DOE–Office of Science by ANL under Contract No. DE-AC02-06CH11357.

II.1.7 Light Metals Core Program: Thrust 1 Selective Processing of Aluminum Sheet Materials (Pacific Northwest National Laboratory)

Darrell Herling, Co-Principal Investigator

Pacific Northwest National Laboratory
908 Battelle Blvd.
Richland, WA 99354
E-mail: darrell.herling@pnnl.gov

Mert Efe, Co-Principal Investigator

Pacific Northwest National Laboratory
908 Battelle Blvd.
Richland, WA 99354
E-mail: mert.ef@pnnl.gov

Govindarajan Muralidharan, Co-Principal Investigator

Oak Ridge National Laboratory
1 Bethel Valley Rd.
Oak Ridge, TN 37831
E-mail: muralidhargn@ornl.gov

Alex Plotkowski, Co-Principal Investigator

Oak Ridge National Laboratory
1 Bethel Valley Rd.
Oak Ridge, TN 37831
E-mail: plotkowskiaj@ornl.gov

Scott Whalen, Co-Principal Investigator

Pacific Northwest National Laboratory
908 Battelle Blvd.
Richland, WA 99354
E-mail: scott.whelen@pnnl.gov

Sarah Kleinbaum, DOE Program Manager

U.S. Department of Energy
E-mail: sarah.kleinbaum@ee.doe.gov

Start Date: October 1, 2020 End Date: September 30, 2021
Project Funding (FY 2021): \$1,300,000 DOE share: \$1,300,000 Non-DOE share: \$0

Project Introduction

The Light Metals Core Program (LMCP), led by PNNL, is an integrated effort between PNNL, ORNL, and ANL. The overall program aims to develop and demonstrate scalable, cost-effective processing methods to locally enhance the properties of Al and Mg alloys to enable broader implementation of lightweight alloys in vehicles. The technical goal is to demonstrate that components and assemblies composed of commercially available alloys can be selectively modified to exhibit locally enhanced properties and deliver high materials performance in the most needed locations. This approach allows for significant improvements in

manufacturability, structural efficiency, and weight-savings in next-generation vehicles. Furthermore, the approach enables the right properties in the right locations and provides the opportunity to decrease the number of metal alloys required for new vehicle manufacture—reducing the challenges that automakers face today in managing supply chains, assuring sufficient materials sustainability, and efficiently recycling scrap metal.

Focused collaborative research thrusts have been established to develop local property modification strategies for each targeted metal system: high-strength Al sheet, Al castings, and Mg castings. Figure II.1.7.1 provides a brief description of these thrusts and how the principal manufacturing methodologies interact, as well as transition to higher technology readiness levels. Within those thrusts, individual projects explore and develop the science and process engineering to create spatially tailored properties in alloys and assemblies of target metal systems. A fourth, cross-cutting thrust provides overarching support in testing, characterization, and modeling.

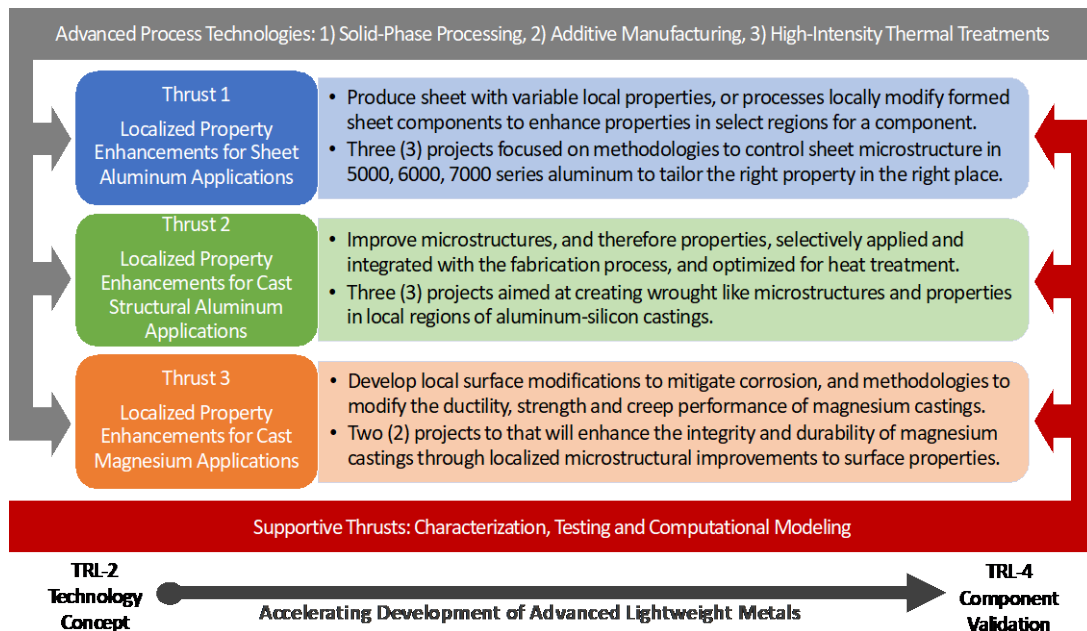


Figure II.1.7.1. Thrust and project structure of the LMCP. Source: PNNL.

The following report describes the FY 2021 technical efforts and results of Thrust 1, “Localized Property Enhancements for Sheet Aluminum Applications.”

Objectives

Sheet metal that is stamped or formed into components represent a material category that makes up the largest percentage of the glider in most designs. High-strength Al sheet offers the opportunity to significantly reduce the weight of the glider through downgauging and replacement of steel structures. However, multiple science and engineering challenges prevent more widespread use of high-strength Al. These challenges include the natural tradeoffs between high-strength, ductility, fracture toughness, and durability. High-strength Al sheets can suffer from low ductility, which in turn leads to poor RT formability, poor energy absorption during crash deformation, and if advantage of higher strength is taken to downgauge the sheet, then stiffness can become an issue in certain applications. A structural or hang-on component often requires one property in one location and a different property in another. Aligning with the overarching goal of the LMCP consortium, in this thrust, we will develop and demonstrate scalable, cost-effective processing methods to locally enhance the properties of wrought Al alloys to enable broader implementation of lightweight alloys in vehicles. Thrust 1 seeks to address these challenges by developing methodologies to locally modify Al sheets so that the right property is in the right place.

Specific engineering limitations with current commercial alloys include limited RT formability, edge effects that produce cracking in stamping, and the need to produce structures that can show local ductility in one area with extreme strength in another, as depicted in Figure II.1.7.2 [1]. Targeted applications include energy transfer structures, such as the A-B-C pillars or cross-body structures, and crush structures in the front or rear of the chassis.

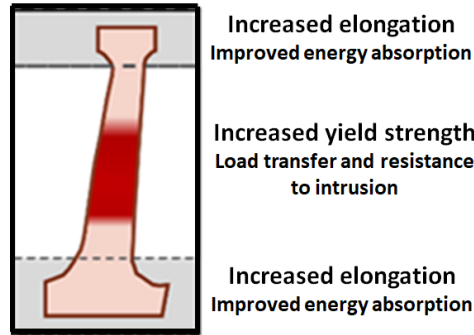


Figure II.1.7.2. Schematic B-pillar showing properties needed in different areas of the part. Source: PNNL.

Approach

Three LMCP Thrust 1 projects, as outlined in Figure II.1.7.3, will develop methodologies to locally change microstructure, stress-state, or geometry to address specific concerns for the part. These projects will develop specific methodologies to include high-shear solid-phase processing (SPP), hybrid additive deposition methods, and thermal surface treatments to address barriers to implementing a high-strength Al sheet.



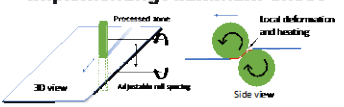
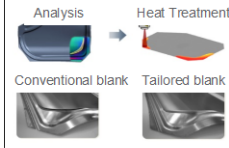

Project 1A	Project 1B	Project 1C
<p>Sheet Materials with Local Property Enhancement</p> <p>Shear Assisted Processing and Extrusion (ShAPE™)</p>  <p>AI 7075 AI 6061</p>  <p>Scott Whalen</p>	<p>Form-and-Print: Additive Manufacturing for Localized Property Enhancement of Al Sheet</p>  <p>Schematic of Form-and-Print approach for adding structural support or modifying sheet for joining.</p>  <p>Alex Plolkowski</p>	<p>Local TMP to Address Challenges to Implementing Aluminum Sheet</p>  <p>Roller Bend-Unbend Processing</p> <p>Mer Efe Piyush Upadhyay</p> <p>Friction Stir Processing</p>  <p>Sonic & Laser Processing</p> <p>G. Muralitharan</p>  <p>G. Muralitharan</p>

Figure II.1.7.3. Three projects with the associated PIs that make-up LMCP Thrust 1. Source: PNNL.

Project 1A: Sheet Materials with Local Property Enhancements

This project is developing techniques for fabricating extrusions via Shear-Assisted Processing and Extrusion (ShAPE™) with material properties that vary along the length [2–4]. In all three techniques shown in Figure II.1.7.4 and described in detail below, the extruded tubing is intended to be rolled into a sheet in preparation for subsequent stamping operations. Feedstock materials to be investigated include 5182, 6111, 6061, and 7075, all of which were identified in conversations with industry. General advantages of using ShAPE as compared to conventional extrusion include homogenization and refinement of microstructures for

improved formability and fatigue performance, variable hardening response to heat-treatment, and ability to tune materials properties at specific locations:

- Technique 1 – Multi-materials: Billets consisting of multiple Al alloys are ShAPE-extruded to form structures with different alloys along the length, as shown in Figure II.1.7.4(a).
- Technique 2 – Differential properties: Billets consisting of a single alloy are ShAPE-extruded while varying the process conditions to locally modify properties along the length, as shown in Figure II.1.7.4(b).
- Technique 3 – Variable thicknesses: The ShAPE tooling will be articulated during extrusion to actively control the wall thickness along the length, as shown in Figure II.1.7.4(c).
- Note Regarding Task 1: At the end of FY 2021, the LMCP determined that Task 1 was not fully aligned with the LMCP goals from a recyclability perspective. As a result, the multi-alloy extrusion task has been replaced with a tubular 6082 extrusion task targeting a known roof rail application.

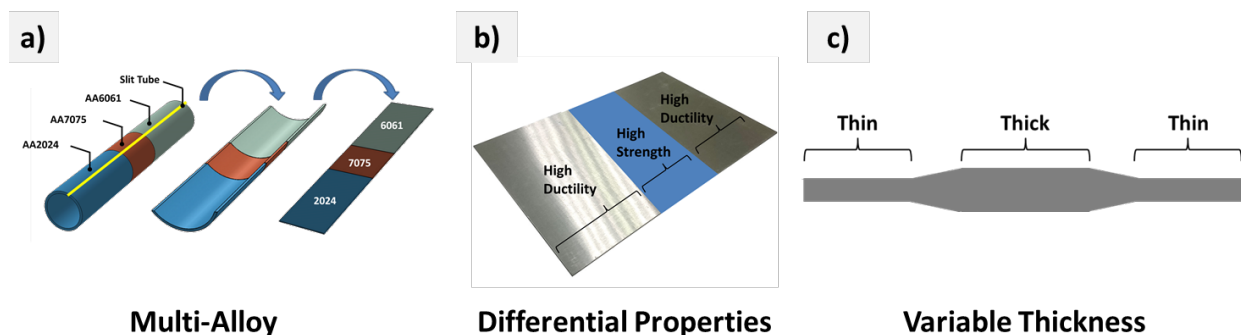


Figure II.1.7.4. (a) Multi-alloy extrusions opened into a sheet. (b) The variable properties extrusions opened into a sheet. (c) The variable wall thickness extrusions. Source: PNNL.

Project 1B: Form-and-Print - Additive Manufacturing for Localized Property Enhancement for Al Sheet

This second project involving AM techniques requires two main capabilities: (1) developing decision-making tools for evaluating candidate alloys for suitability for AM feedstock and their potential properties after AM processing; and (2) demonstrating laser hot-wire AM of the selected alloys on the representative substrates. The main objective in determining which alloys to use with the process was to maximize their processability, which in the case of depositing AM material on wrought Al alloys is primarily related to minimizing the susceptibility to hot cracking in the deposited material. The composition of the liquid alloy largely determines the hot cracking susceptibility, so a process model to predict dilution of the feedstock melt with the underlying substrate during fusion was combined with a CALPHAD-based thermodynamic calculation of the hot cracking susceptibility during solidification [5]. The simulation capabilities for these unique calculations are being developed in conjunction with Thrust 4 computational support at ORNL.

To demonstrate the feasibility of depositing material on wrought substrates, the selected material with the least hot cracking susceptibility (e.g., Al alloy 4043) was used to deposit a wall on an Al alloy 6061-T6 billet. A hybrid laser hot-wire machine was used to deposit a thin-wall of approximately 50 mm in height, 25 mm in length, and 10 mm in width. The wall was then sectioned into sub-scale tensile specimens in SS-J3 and SS-1 geometries [6], as well as specimens for microscopy. The tensile properties of the interface between the substrate and the deposited material itself were characterized to determine the feasibility of using laser hot-wire AM to deposit material in specified areas with satisfactory properties and minimal defects. The deposition was initially planned to be done on a novel Mazak hybrid laser hot-wire that was being delivered in FY 2021 to the ORNL Manufacturing Demonstration Facility. Due to manufacturer delays on the delivery and setup of the system, the initial demonstration (wall build) was instead conducted on a similar hybrid laser hot-wire system at the Mazak manufacturing facility in Florence, KY.

Project 1C: Local TMP to Address Challenges to Implementing Aluminum Sheet

This third project aims to develop new thermomechanical processing methods for improving the formability of commercial Al sheets locally. Four discrete techniques were pursued in FY 2021 to evaluate the effectiveness of each to modify local mechanical properties: (1) FSP; (2) roller bending-unbending; (3) laser treatment; and (4) power ultrasonic-based surface processing (PUSP). All start with an age- or work-hardened sheet and improve formability only where needed, without losing the high-strength elsewhere. Three alloys and temper conditions have been considered due to their potential use in automobiles if formability could be improved, including 7085-T76 for structural body-in-white parts, and 6111-T6 and 5182-H111 for closures. The maximum bending radius to thickness ratio (r/t) was used to gauge when failure occurred for the processed regions of the sheet metal, which is considered a performance indicator for general use in automobile applications that demand high local formability, such as stamping, deep drawing, hemming, edge stretchability, etc.

FSP is a localized SPP technique that uses a rotating tool head with a rod extension that gets inserted into a certain depth inside the sheet metal. The rotation causes local mixing introducing a high density of dislocations and high temperatures that forms dynamically recrystallized grains and reduces grain size improving the formability [7]. The FSP sheets were cut into bending samples using a hand shear tool at 25 mm width with the processed region centered on the bending sample. Bend testing according to the ASTM E290 standard was conducted on two modules: (1) a 90° bending angle for low formability alloys, such as 7085-T76; and (2) a 180° bending angle knife edge for high formability samples, such as 6111-T6 and 5182-H111. A pin with fixed radii can be attached to the module during testing and incrementally lowered to further reduce the r/t ratio. Some tests had to be continued on a vice to fail the samples where the pin was inserted into the folded sample and the vice was closed to ensure failure of the samples. For each pin size, a different sample was used, and tests were repeated for 2 to 4 times to pinpoint the minimum bend radius before cracking. The ASTM B820-18 standard was used to determine whether a sample had failed, where an optical stereoscope with a magnification of 34x was used to determine whether micro-cracks appeared on the surface, which established the minimum bending radius. Orange peeling or a rough surface were not considered to indicate a failure, and the bending radius for all the tests was measured afterward with the same stereomicroscope.

The second thermomechanical processing (TMP) method used in this study was a roller bending-unbending setup. This process has rolls that clamp to the blank and travel on the sheet to bend-unbend it locally without changing its shape and thickness [8]. Spacing between the rolls is adjustable to accommodate different sheet thicknesses and to change the level of deformation. During processing, an electrical current can also be passed through the rolls and the sheet, resulting in Joule heating of the processed zone. All tests were conducted on a simplified two-roller bending apparatus to test the feasibility of this process. A roller angle of ~15° was used for the two-roller setup. After successful testing, bending-unbending was transitioned to the three-roller setup with a roller angle of ~30°. Rockwell B hardness with a 1/16-in. ball indenter and 100 kgF was used to measure the macro-hardness along the processed surface to study the amount of plastic deformation of the sheet. A cross-section of the sheet was cut at the processed region and polished for Vickers' microhardness measurements. FEM of both the two- and three-roller systems were conducted by Abaqus to correlate plastic strain and dimensional and thickness changes of the sheets in the processed region with the experiments.

The final two techniques that were evaluated focused on the thermal treatment of the sheet metal only: (1) local heat-treatment to induce softening using a range of methods, including infrared heating, laser heating, and resistance heating techniques; and (2) localized modification using ultrasonic processing. These techniques can also be applied to improve edge stretchability of sheared automotive Al sheets by removing the shear-affected zone and edge damage using ultrasonic processing followed by rapid laser edge heating. Microhardness measurements and tensile properties obtained from the processed material were obtained from regions that have been locally modified and compared with properties obtained in the as-received condition. The effect of such microstructural modifications on RT formability was also evaluated by bend testing as described previously.

Results

Results for each of the three Thrust 1 projects are reported for FY 2021 as follows:

Project 1A: Sheet Materials with Local Property Enhancements

Task 1 Progress

Tooling and process parameters were developed to extrude 6061 and 7075 alloys in a butt-joint configuration, as shown in Figure II.1.7.5(a). This was accomplished by loading an alternating stack of 6061/7075 billets in the ShAPE machine container and extruding over a range of temperatures and speeds. The 6061/7075 transition was imaged using CT and metallurgical bonding was confirmed by SEM and EDS. Tooling and process parameters were also developed to extrude Al alloys in a cladding configuration, as shown in Figure II.1.7.5(b). This was accomplished by nesting billets in a concentric configuration. The 7075 and 2024 alloys were extruded in the interior with 6061 and 1100 alloys clad on the exterior as shown by the CT scan. Metallurgical bonding between the two materials was confirmed with SEM/EDS. Publication of full result details will be available in The Minerals, Metals and Materials Society (TMS) 2022 conference proceedings [9–10]. Provisional patents have been filed for the butt-joint and cladding techniques and industry partnerships are being pursued for the multi-alloy extrusions.

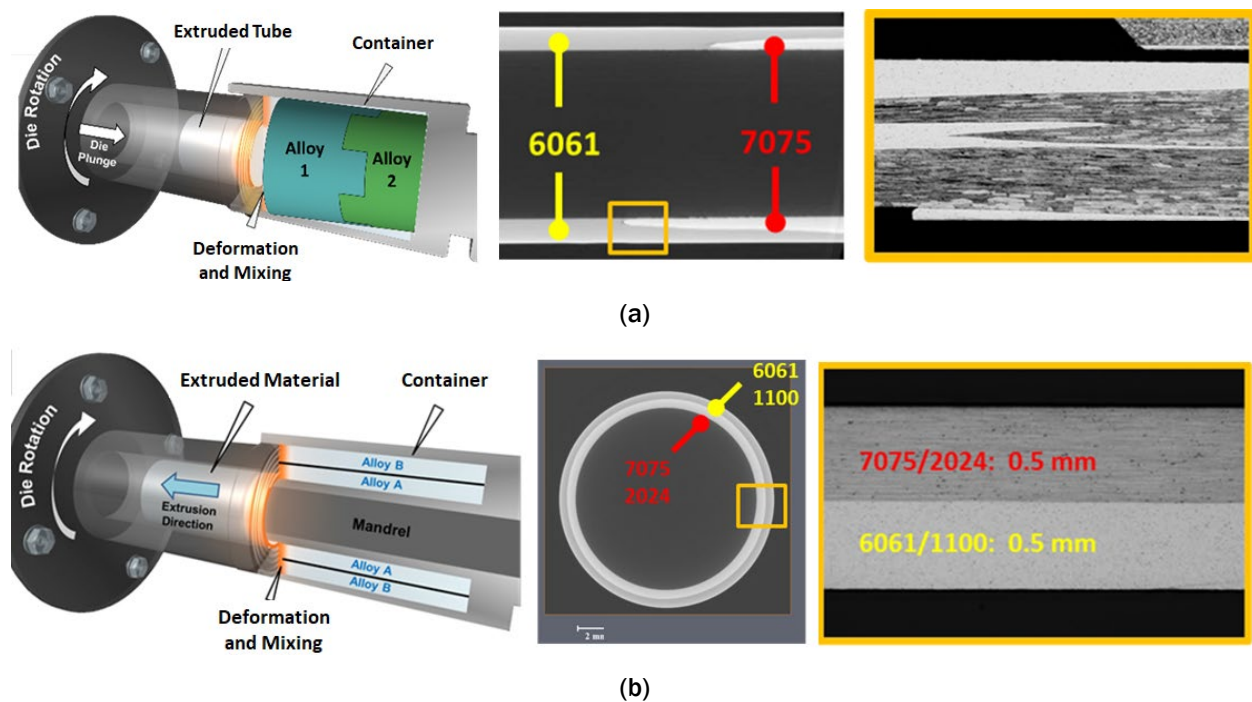


Figure II.1.7.5. (a) Butt joints between 6061 and 7075 formed during ShAPE. (b) Cladding formed between 7075/2024 and 6061/1100 during ShAPE. Source: PNNL.

Task 2 Progress

The tooling developed for Task 1 was utilized to extrude billets of 6061 where the temperature ranged from 300°C to 580°C along the length of a single extrusion, as shown in Figure II.1.7.6(a). This demonstrated that temperature could be controlled along the length of the extrusion, which is not possible with conventional extrusion [11]. Hardness along the length of the extrusion was then measured in the as-extruded and T5 conditions. Figure II.1.7.6(b) shows the relationship between process temperature, heat-treatment, and hardness, which illustrates that variable properties can be achieved in a single ShAPE extrusion.

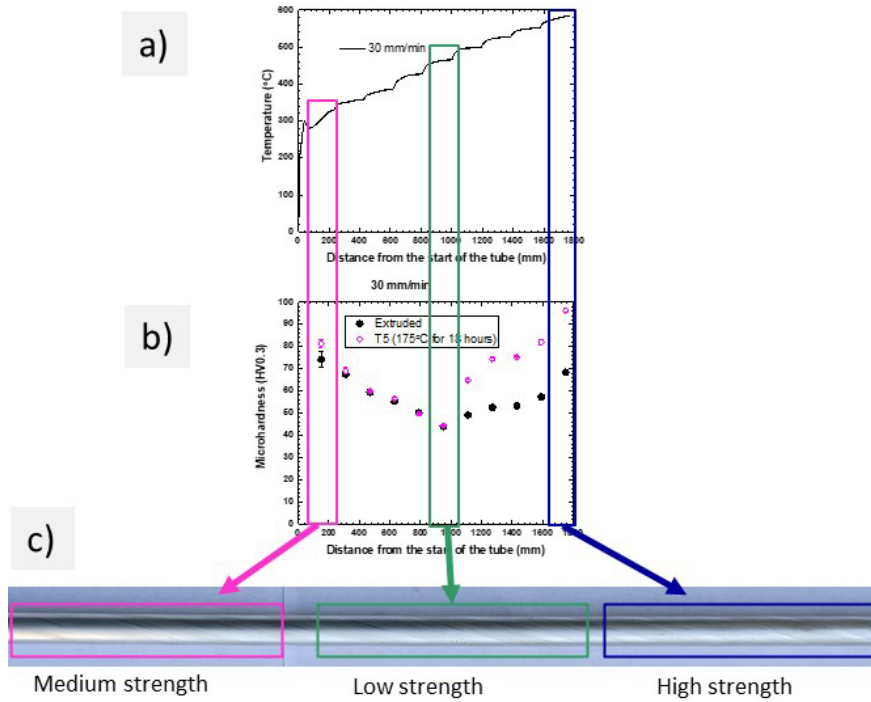


Figure II.1.7.6. (a) Temperature and (b) hardness along the length of a 6061 ShAPE extrusion showing (c) the regions of locally modified properties achieved during ShAPE processing. Source: PNNL.

Task 3 Progress

To control wall thickness during ShAPE extrusion, the position of a tapered mandrel must be precisely controlled within the die throat as the die plunges into the billet. A system controlling the mandrel position during extrusion has been fully designed, as shown in Figure II.1.7.7(a), with the piece parts and tooling being in various stages of procurement. The system consists of a linear servo actuator integrated with the ShAPE machine cross-head, control system, and tooling. Early in FY 2021, simple tests were performed with a stationary tapered mandrel to confirm that variable wall thickness was possible. Figure II.1.7.7(b) shows that the wall thickness transitioned from 2 mm to 1 mm over a length of approximately 6 in. This transition in wall thickness can be gradual or abrupt depending on the mandrel geometry and resolution on position control.

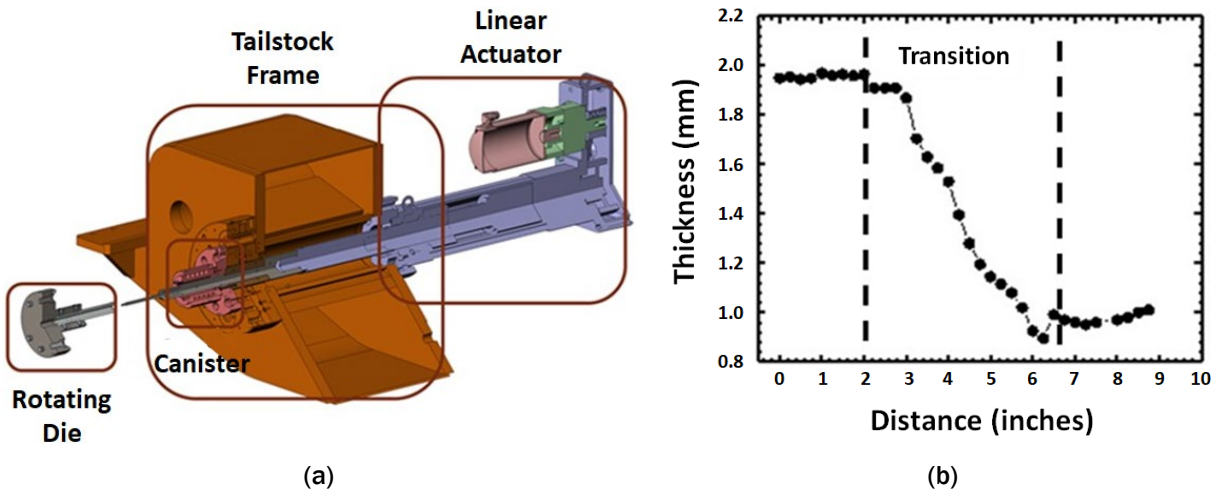


Figure II.1.7.7. (a) Design of system for controlling wall thickness during ShAPE extrusion. (b) Data showing wall thickness transitioning from 2 mm to 1 mm over a length of approximately 6 in. Source: PNNL.

Project 1B: Form-and-Print – AM for Localized Property Enhancement for Al Sheet

The CALPHAD simulations for hot cracking susceptibility are shown in Figure II.1.7.8 for 4043 and 5356 wire deposited on a 6111 sheet. While the demonstration build was done on a 6061 billet (rationale explained later), the 6111 sheet will be the substrate used for future work due to a specific interest from industry in 6111 as a substrate. The dilution percentage is defined as the percentage of base metal in the melt pool (i.e., 0% dilution is a melt pool with only wire feedstock material in it). In Figure II.1.7.8(a), shows that the 4043 wire has relatively low hot cracking susceptibility up to nearly 75% dilution. This indicates that the 4043 wire will produce a melt pool that is not particularly susceptible to hot cracking during solidification at reasonable levels of dilution with the substrate. Figure II.1.7.8(b) shows the relatively high susceptibility to solidification hot cracking in the 5356-wire deposited on a 6111 substrate. For the 5356 wire, the peak of solidification hot cracking susceptibility corresponds with observed hot cracking susceptibility in Al-Mg-Si alloys with compositions of approximately 1–3 wt% Mg and 0.5–0.75 wt% Si [12]. This indicates that the 5356 will require more precise control over the melt pool characteristics than the 4043, especially in the first few layers where the deposited material is diluted with the substrate. This analysis guided the decision to proceed with the 4043 alloy as the starting wire for the initial demonstration build.

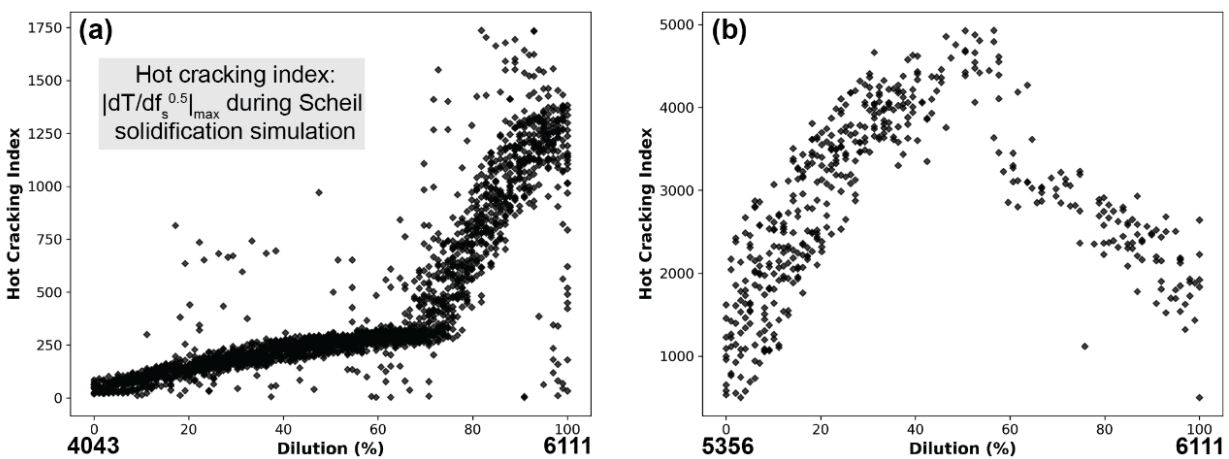


Figure II.1.7.8. Composition-dependent hot cracking index (defined in the inset) in the first deposited layer as a function of dilution of the wire with the 6111 substrate. Multiple points ($N=10$) at the same dilution reflect an allowance for random variation in the alloy composition within specification in the calculations for (a) Al 4043 and (b) Al 5356 wire. Source: ORNL.

The build demonstration consisted of building a 50-mm tall wall on a 6061-T6 billet due to lack of representative 6111 plate at the time and off-site location (as described previously) of the demonstration build. Both 6061 and 6111 are 6xxx series alloys used in the automotive industry, and they have similar compositions except for some small differences in the Si, Mg, and Cr content. Figure II.1.7.9(a) shows an infrared image of the build process near the middle of the part to show the wire, laser melting, and heat buildup in the deposit. The depositing layer is seen to be the hottest, as expected, and the lower layers are seen to reheat due to the deposition of the next layer. Figure II.1.7.9(b) shows the as-built wall part, with typical directed energy deposition AM surface roughness between layers and a few areas with pieces of partially melted wire that attached at the end of the layer. Figure II.1.7.9(c) shows benefit of the hybrid manufacturing process, with a similar 4043 wall machined on the front and top faces to highlight the difference in the surface finish. The allowance for hybrid machining in the same system as the AM deposition is promising for producing finished parts with accurate geometry. Hybrid manufacturing cell units of this type could eventually enable elements of the vehicle manufacturing process to shift from long assembly lines to island production, as envisioned in the 2021 USCAR Roadmap for Automotive Additive Manufacturing [13].

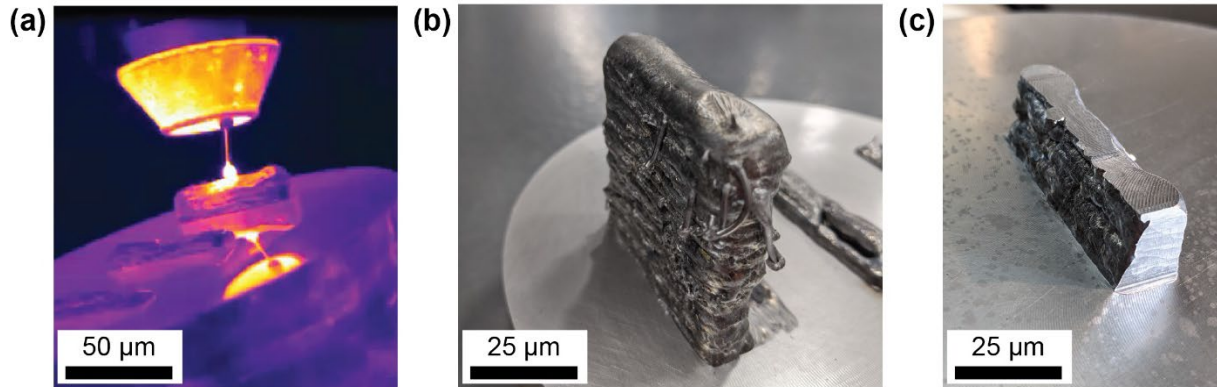


Figure II.1.7.9. Images of the demonstration part with approximate scale bars to show the size of the deposit. (a) IR image from the build process of the part, where coloring represents IR intensity. (b) As-built 4043 wall on a 6061-T6 billet. (c) Partially machined wall showing a hybrid-finished surface versus an as-built surface. Source: ORNL.

SS-1 tensile specimens were extracted using electro-discharge machining (EDM) across the interface to perform digital image correlation (DIC) during tensile testing, such that the length of the gauge section was parallel to the BD and the center of the gauge section was aligned with the substrate surface. Tensile tests were done at 0.002 s^{-1} strain rate and with the as-machined surface finish from EDM. The results are shown in Figure II.1.7.10(a) for the three SS-1 samples tested. The lighter gray lines show the raw data, while the black line shows the average of the datasets. The 0.2% offset YS is approximately 85 MPa and the UTS is approximately 175 MPa. Though the dissimilar materials at the interface prevent a direct comparison to literature values for the 4043 properties, it is interesting to note an increased yield and tensile strength as compared to the reported values of 70 MPa YS and 152 MPa tensile strength for wire-arc additively manufactured 4043 [14]. Figure II.1.7.10(b) shows the preliminary DIC results for one of the tensile tests indicating localized “hot spots” of strain rate. These discontinuous regions undergoing bursts of high strain rate indicate unusual plastic deformation behavior that is not typically observed in wrought alloys. Preliminary optical microscopy of the samples indicates there is likely a correlation between the hot spots of high strain rate and the melt pool boundaries formed during wall deposition. An analysis of these results and their applicability to other Al alloys deposited via the laser hot-wire process is ongoing.

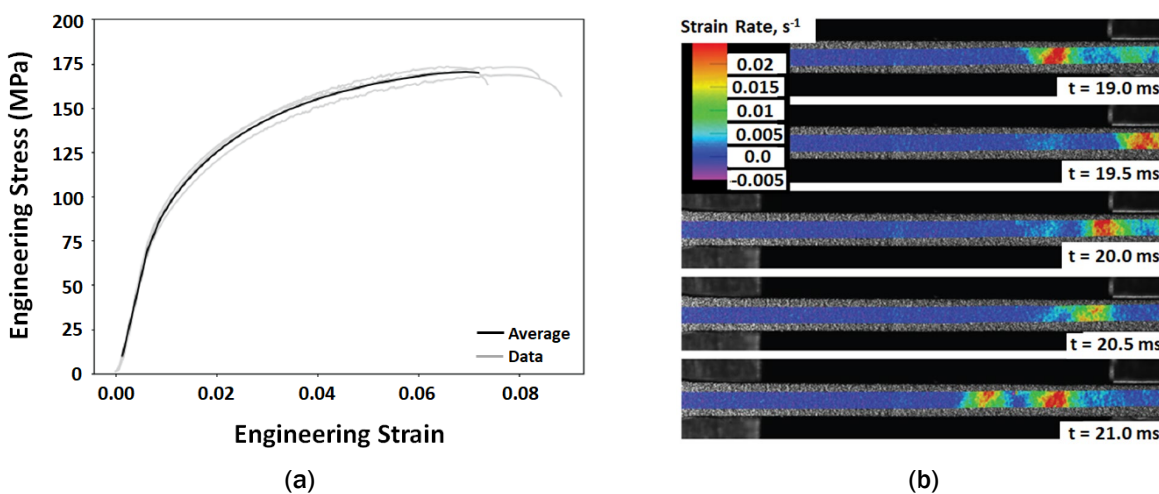


Figure II.1.7.10. (a) Tensile tests of the vertical 4043/6061-T6 SS-1 sample done at 0.002 s^{-1} overall strain rate. (b) Strain rate maps, showing strain rate localization as a function of time. Source: ORNL.

Project 1C: Local TMP to Address Challenges to Implementing an AI Sheet

The base alloy sheet thickness, hardness, and r/t ratio at failure have been listed in Table II.1.7.1 for comparison. The 7085-T76 had the least formability due to the highest r/t ratio, while the 6111-T4 had the most formability with the lowest r/t ratio. FSP was conducted on all alloys, except for the 6111-T4, which was used as a benchmark. Optimized FSP parameters were developed with the parameters shown in Table II.1.7.2, which includes RPM, welding speed, plunge depth, tilt angle, and measured temperature. Only the optimized FSP parameters that show the highest r/t improvement are shown here, but multiple conditions were tested for each alloy to find this optimum.

Table II.1.7.1. Base Alloy Properties Listed for Comparison

Alloy	Sheet Thickness (mm)	Hardness (HRB)	r/t at failure (mm/mm)
7085-T76	2.0	89.9 +/- 1.2	1.60
6111-T6	2.0	62.4 +/- 0.9	1.30
6111-T4	2.5	43.0 +/- 0.9	0.55
5182-H111	1.5	10.0	1.00

Table II.1.7.2. Optimal FSP Parameters for Selected AI Alloys

Alloy	Sheet Thickness (mm)	RPM	Welding Speed (m/min)	Plunge Depth (mm)	Tilt Angle (°)	Peak Temp (°C)
7085-T76	2.0	1800	3	1.94	2	465
6111-T6	2.0	600	0.75	1.93	2	435
5182-H111	1.5	500	0.5	1.40	2	---

Figure II.1.7.11 shows the r/t ratios plotted for all base and FSP alloys after bend testing, where the fractured samples are marked in red and the samples without cracks at 34x magnification are marked in green. Some optical stereograph images of FSP samples at failure are shown. FSP was able to successfully improve the formability of each base alloy by lowering the r/t ratio. Alloys showed an r/t improvement of 30% for the 7085-T76, 50% for the 6111-T6 and 19% for the 5182-H111. Figure II.1.7.12 shows the load-displacement plots of the bending tests for the non-fractured samples of the base alloys and their respective FSP samples to determine the loss of maximum force after FSP. It can be observed that the 7085-T76 and 5182-H111 showed a loss in force of ~500 to 600 N while the 6111-T6 did not show any loss in force after FSP. The differences in displacement are associated with the type of bend testing used, the 90° bend module tests only allowed displacements up to 10 mm and the test was stopped when the sample contacted the top fixture. The 180° bend angle tests had a displacement of 20 mm and above. The 180° angle bend tests were stopped when bending force was going towards 0 N, which showed it had folded completely. FSP has shown great promise in improving the local formability of sheet alloys and future work will involve improving r/t for less formable alloys such as the 7055-T6 and 7075-T6 alloys.

Figure II.1.7.13(a)–(d) shows the FEM simulation and experimental results of the two-roller bending-unbending setup at 15° roller offset angle with a 5182 sheet having a thickness of 1.5 mm. The equivalent plastic strain peaked at 6.6% strain in the local central region of the sheet. Adding support during the entry of the sheet mimicking experiments showed very little warping along the cross-section of the sheet. In the experiments, the bending-unbending was achieved by feeding the sheet once and then flipping the sheet over and running it again. Hardness measurements along the central deformed region of the sheet were measured. Macro-hardness increased from 18.6 ± 1.4 HRB in the base metal up to 47.0 ± 1.2 HRB in the processed region, corresponding to a 2.5x increase. This was compared with hardness measurements of tensile strained samples of 5182-O tempered samples at fixed strain increments to correlate strain with hardness. This resulted in an approximate equivalent plastic strain of 13%, which was over double the FEM predictions. Vickers'

hardness map of the cross-section showed a 48% increase in hardness at the roller contact region showing a large increase in plastic deformation that decreases further away from the roller shown in Figure II.1.7.14. Overall, the deformed region width of 4 mm was 2x the roller thickness of 2 mm.

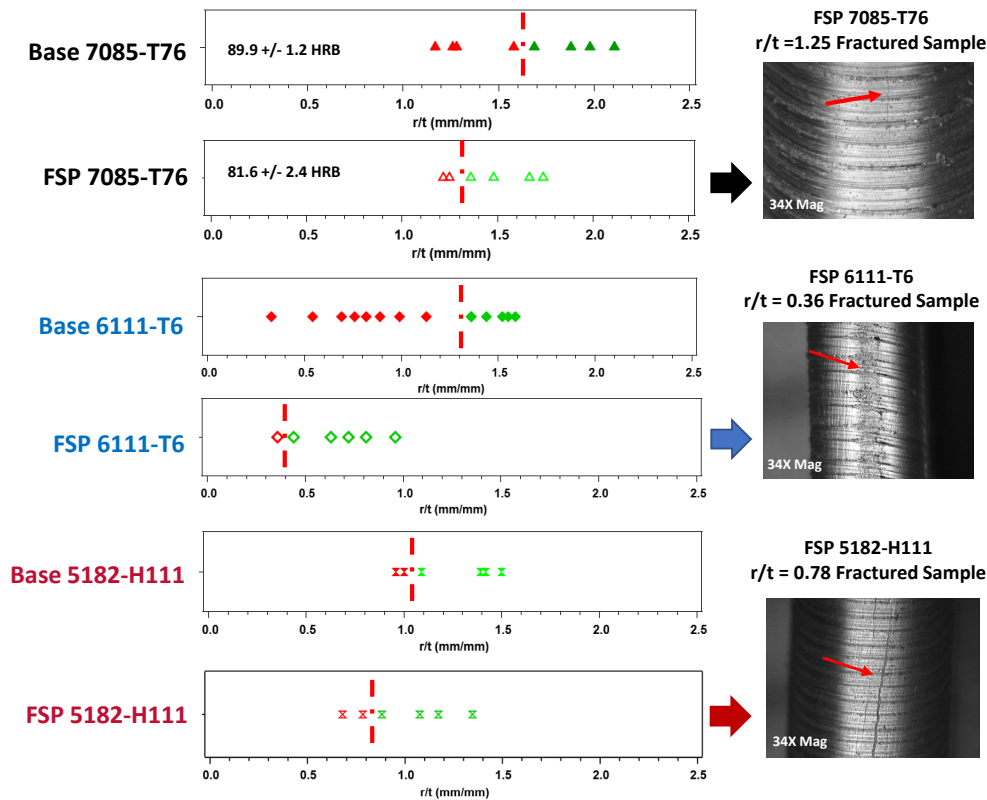


Figure II.1.7.11. r/t ratios for base alloys and highest formable FSP conditions for each alloy. Red denotes fractured samples, while green denotes samples with no cracks. The red line shows the transition from safe to failed samples. Base 6111-T4 benchmark r/t is 0.55. Source: PNNL.

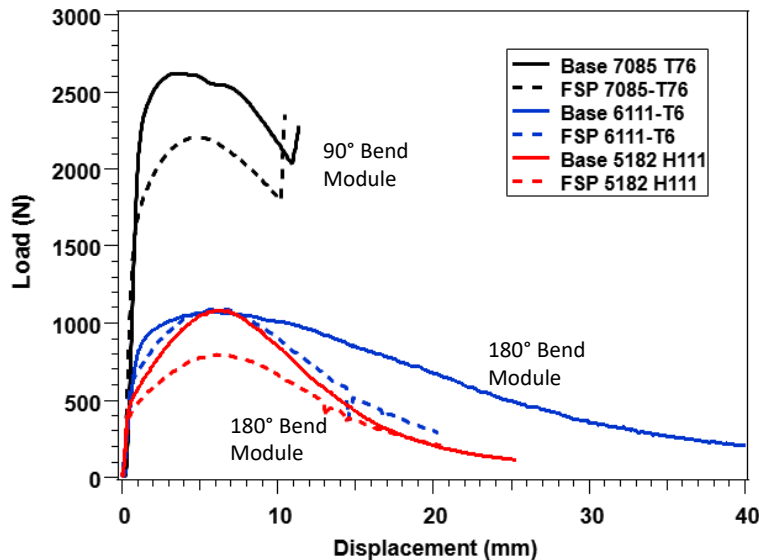


Figure II.1.7.12. Load-displacement plots for 90° and 180° angle bend tests on the base alloy and FSP-processed 7085-T76, 6111-T6, and 5182-H111. Source: PNNL.

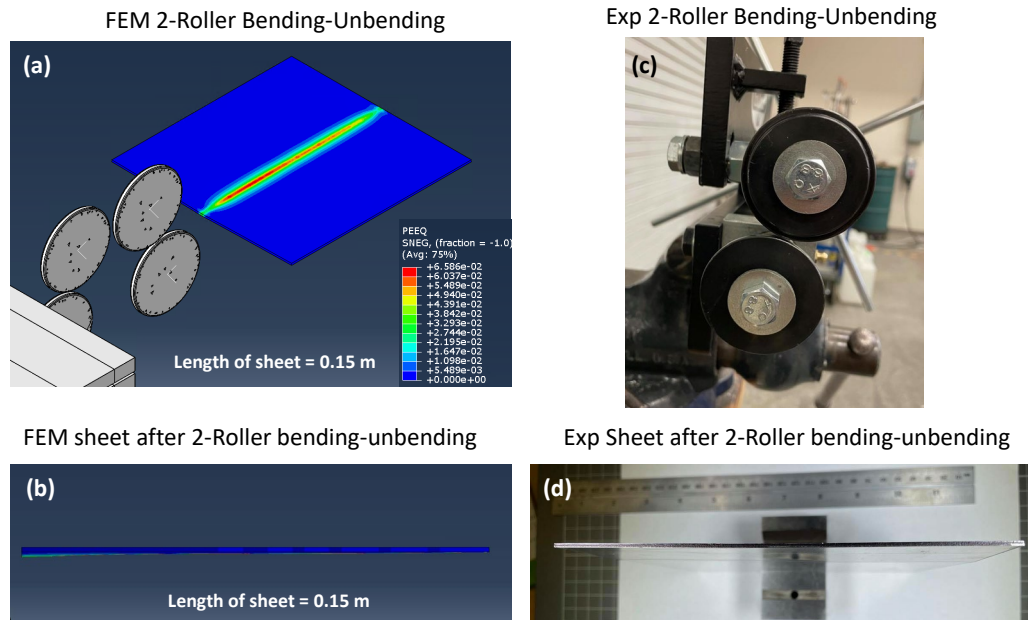


Figure II.1.7.13. FEM of two-roller bending and unbending sheet with support during entry with its (a) equivalent plastic strain and (b) side profile. (c) The equivalent experimental setup and (d) side view of the processed sheet. Source: ANL.

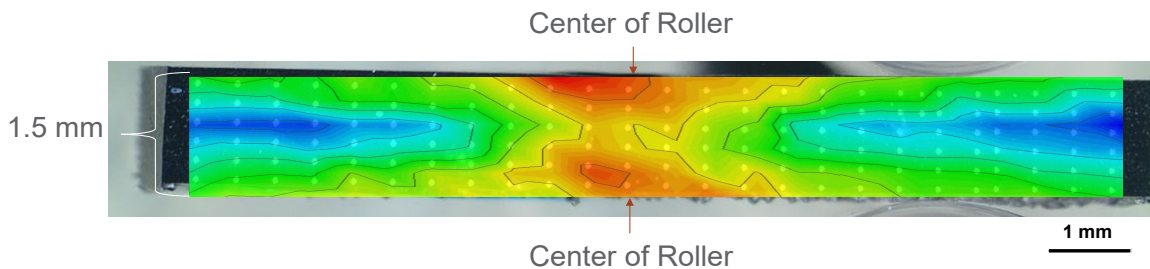


Figure II.1.7.14. Microhardness distribution across the cross-section of the processed sheet where the minimum (deep blue) = 64.7 HV and the maximum (red) = 95.7 HV. Source: PNNL.

Figure II.1.7.15(a) and (b) show the FEM of the three-roller case along with the experimental setup of the three-roller apparatus. In simulation, a representative material for the 5182-H111 sheets were used with a length of 2.5 m and a width of 0.25 m. FEM predicted a higher equivalent plastic strain of 96%. This is expected since the roller angle for the three-roller setup was at 30° and the two-roller angle was only at 15° . Most of the simulated deformation is centered along the rollers with some edge distortions at the entry and exit of the sheet. At this time, the experimental three-roller system has not been used for 5182-H111 testing, but the apparatus is ready for RT mechanical bending-unbending. As shown in Figure II.1.7.15(c), the experimental setup is similarly capable of achieving a 30° roller angle as was conducted in FEM. Figure II.1.7.15(d) shows the bending-unbending system has been attached to an electric drive motor with a gear system that will be used for automatic feeding of the sheet metal. For future work, 5182-H111 sheets will be used for experimental work in which the plastic strain and sheet morphology will be compared with the FEM work presented in this report to test the validity of the simulations. Furthermore, future work will also introduce a heating system to the experimental setup to increase the local formability while conducting mechanical bending-unbending of the sheet.

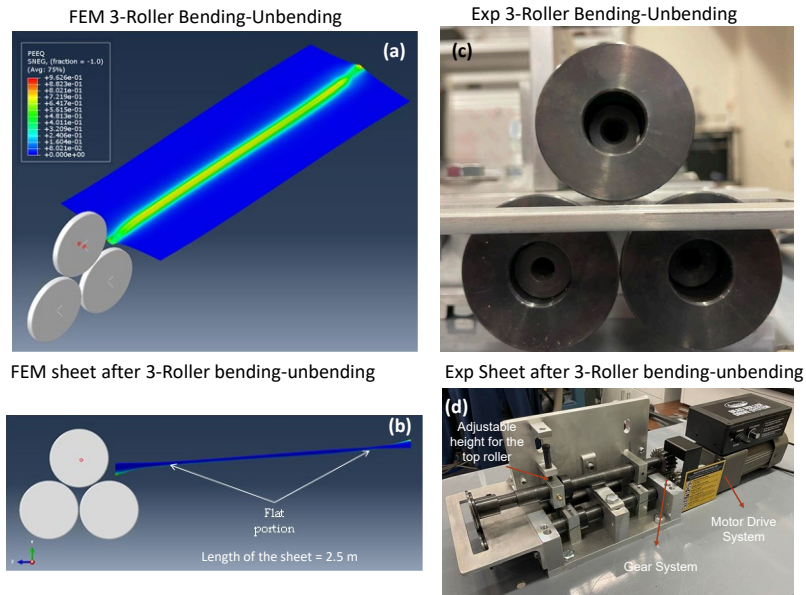


Figure II.1.7.15. FEM of three-roller bending and unbending sheet with its (a) equivalent plastic strain and (b) side profile. (c) The equivalent experimental setup and (d) overall view of the processed sheet.
 Source: PNNL.

Initial experiments to evaluate the effects of localized IR heating on microstructural modification were performed using physical masking to isolate the region of interest. However, with the experimental setup used for this work, the achieved heating rates were discovered to be too low, resulting in a potentially wide HAZs. Therefore, the IR heating was discontinued in favor of techniques such as laser heating, which can provide a higher heat input over a localized region thereby achieving much faster heating rates and a narrower HAZ. Initial experiments were performed using a Lumonics 702H/Pulsed Nd:YAG 1064 nm laser system shown in Figure II.1.7.16(a) and (b) with a translation stage having a maximum laser travel speed of 100 in. per second and a working envelope of 12×12×16 in.

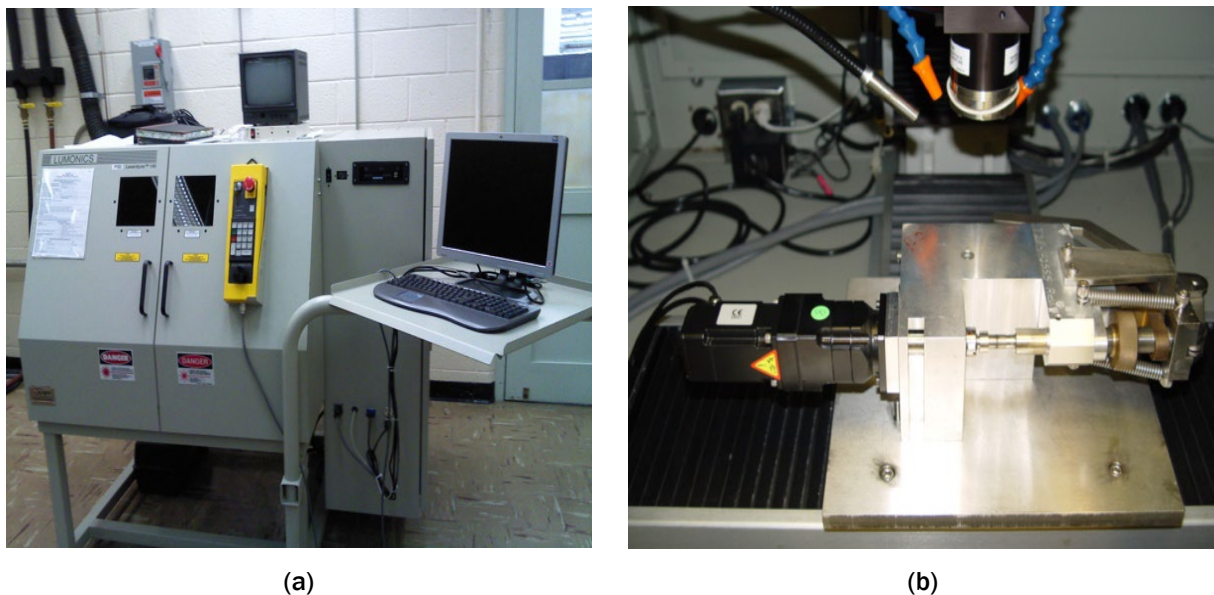


Figure II.1.7.16. (a) The Lumonics 702H/pulsed Nd:YAG 1064 nm laser system. (b) The translation stage.
 Source: ORNL.

Several experiments with a various combination of process parameters (e.g., power, number of laser pulses) were performed on 7075-T6 sheets along a line, as shown in Figure II.1.7.17. Figure II.1.7.18 shows the results from the tensile tests across the modified region in sample #7 revealing that the sheets containing the laser-treated region were softer than the as-received material. Bend tests are planned with the modified sheets.

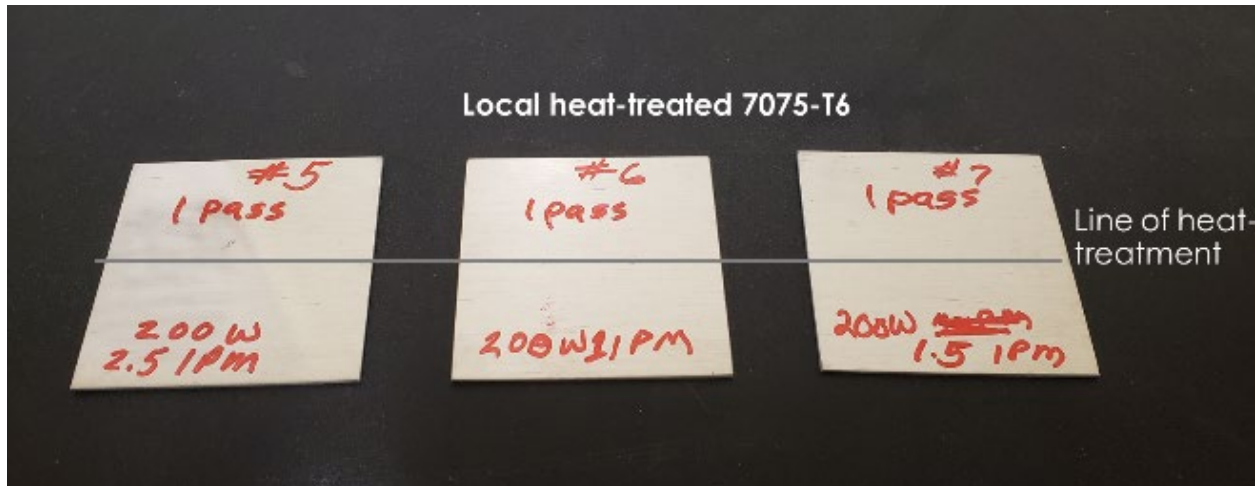


Figure II.1.7.17. Examples of local laser-treated AA7075T6 samples. Source: ORNL.

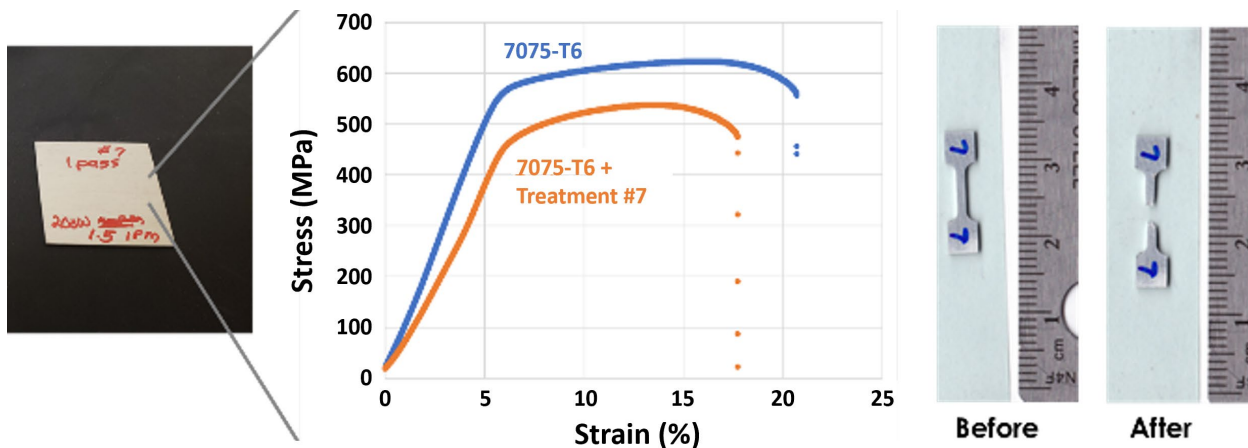


Figure II.1.7.18. Results from tensile tests across the modified region. Source: ORNL.

Three sets of local modification experiments were performed on 7075-T6 sheet surfaces using ultrasonic processing. The first set of experiments was performed with a grooved sonotrode tip ($7 \times 7 \text{ mm}^2$) which is generally used for ultrasonic welding, and a grid patterned-anvil. The ultrasonic power was fixed at 2.5kW and process times of 0.1, 0.2, and 0.3 seconds were used for the sequence of experiments. The pressure applied through the sonotrode was fixed at 90 psi. At the conclusion of these experiments, groove-like indentations were observed on the side of the Al sheet in contact with the sonotrode (henceforth referred to as the sonotrode side) and grid-like indentations were observed on the side of the sheet in contact with the anvil (henceforth referred to as the anvil side) on all processed sheets. These indentations were observed to increase in-depth with increasing process times.

Figure II.1.7.19(a)–(d) shows examples of sheets processed using a process time of 0.3 s. In the first experiment, charred regions were observed on the anvil side of the Al sheet suggesting that the temperatures may have been higher at that location. Another issue that was observed with these experiments was sticking between the sheets and the tools (e.g., both the sonotrode and the anvil). No sticking was observed when a

process time of 0.1 and 0.2 s were used for the same experiments. When the sheet was separated from the sonotrode and the anvil after the conclusion of the experiments, it was observed that some Al from the processed sheet was stuck to the anvil surface that was in contact with the sheet. Cross-sectional observation by EBSD of the sheet near the region in contact with the sonotrode shows the presence of a $\sim 20\text{--}50\ \mu\text{m}$ -thick layer with sub-micron-sized, recrystallized grains at the grooves of the indentation marks, as seen in Figure II.1.7.20(a) and (b). It was concluded that using a grooved sonotrode will result in significant roughness and poor surface quality of the processed sheet; hence, grooved sonotrodes cannot be used for localized surface modification using ultrasonic processing.

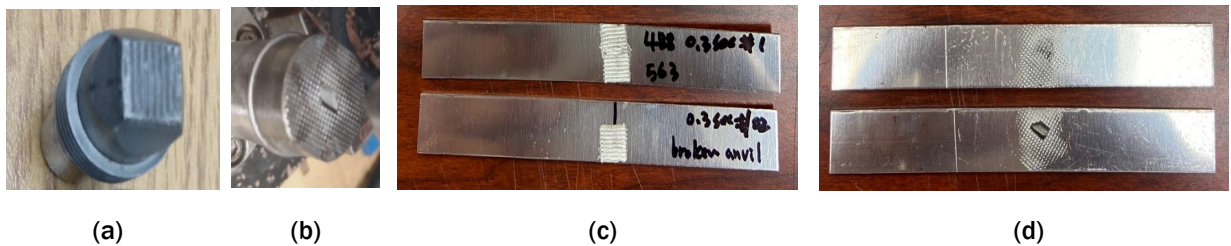


Figure II.1.7.19. The first set of experiments was performed using a grooved sonotrode tip and a grid patterned-anvil: (a) sonotrode, (b) anvil, (c) and (d) are the sonotrode and anvil sides of the samples processed for 0.3 s. Source: ORNL.

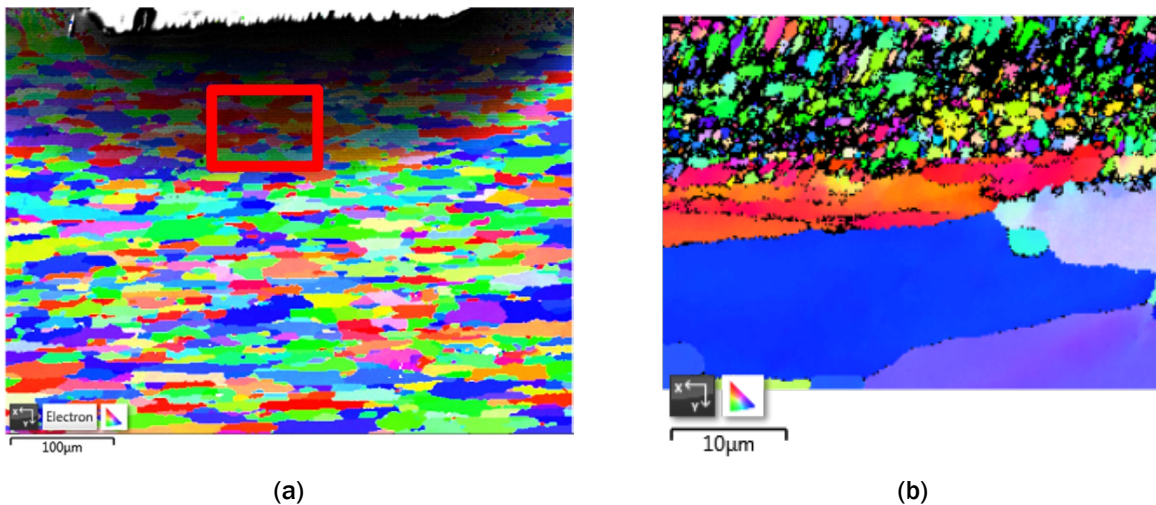


Figure II.1.7.20. (a) Low magnification and (b) high magnification of the cross-sectional EBSD observations of the sonotrode side of the processed sample. Source: ORNL.

The second set of experiments was performed using a flat tip sonotrode and a flat anvil, as shown in Figure II.1.7.21(a). It was hoped that the use of the flat sonotrode and flat anvil would eliminate the sticking observed in the previous experiments, thereby improving surface quality. The ultrasonic power was fixed at 3.5kW and pressure was set at 90 psi with the processing times ranging from 0.5 to 2 s. To understand the origin of charred regions observed in the previous experiments, an IR camera was utilized to measure the temperature of the specimens. However, contrary to expectations, there was evidence for sticking in these experiments as well. As shown in Figure II.1.7.21(b) and Figure II.1.7.21(c), it is evident that some of the Al material adhered to the tool surface after processing. The IR camera showed that the temperature outside the sonotrode/sheet contact region exceeded 240°C when the processing times were larger than 1 s (e.g., the temperature of the material directly under the sonotrode is not measurable using the current IR technique; it should be much higher), as shown in Figure II.1.7.21(d). EBSD showed the presence of large grains near the surface, indicating that the material might have undergone static recrystallization and grain growth, as shown

in Figure II.1.7.21(e). It is to be noted that one side of the as-received 1-mm-thick AA7075T6 was protected by a plastic film, while the other side was unprotected. Before the experiment, the film was peeled off to expose the protected fresh surface. The sonotrode was in contact with this fresh surface in the first two sets of experiments.

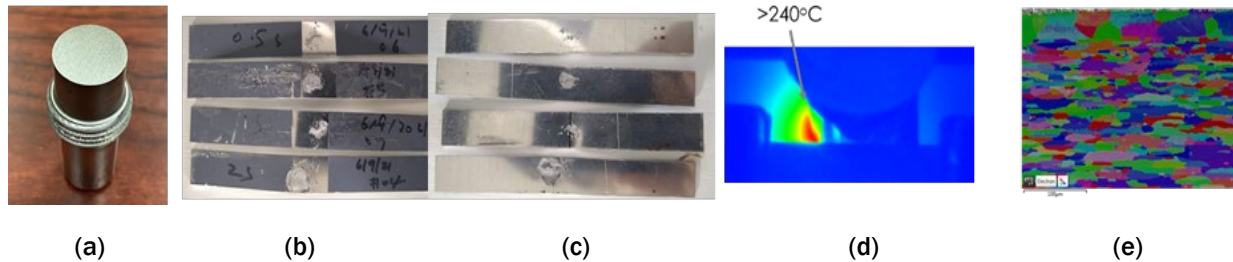


Figure II.1.7.21. The second set of experiments was performed using a flat sonotrode tip and a flat patterned-anvil. (a) shows the sonotrode that was used, while (b) and (c) show the processed surfaces on the sonotrode and anvil sides of the sheets, respectively. The results from the (d) IR temperature measurement and (e) cross-sectional EBSD observations are also shown. Source: ORNL.

The third set of experiments used a $\frac{3}{4}$ in. diameter hemispherical sonotrode/flat anvil combination, as shown in Figure II.1.7.22(a). Two tests were performed with this combination. The first had an unprotected side in contact with the sonotrode using an ultrasound power of 1 kilowatt (kW) and a process time of 0.1 s. The second was performed with the protected fresh surface contacting the sonotrode and a process time of 0.1 s. Ultrasonic power of 1 kW was used in the first experiment, but use of that power level on the fresh surface resulted in strong sonotrode/sheet adhesion and distortion of sheets. For the follow-on tests, ultrasonic power was reduced to 0.5 kW. The pressure was set at 90 psi in all cases. Figure II.1.7.22(b) shows that although a higher power was used in the first test with the unprotected side contacting the sonotrode, no sticking was observed. However, slight sticking of the sonotrode and significantly larger indentation marks were observed in the second test where the sonotrode contacted the freshly exposed surface. Thus, using the fresh surface (after removing the protective film) appeared to influence the surface-sonotrode interactions, leading to large indentation marks, possibly higher temperatures, and surface sticking. The cause for this is under investigation.

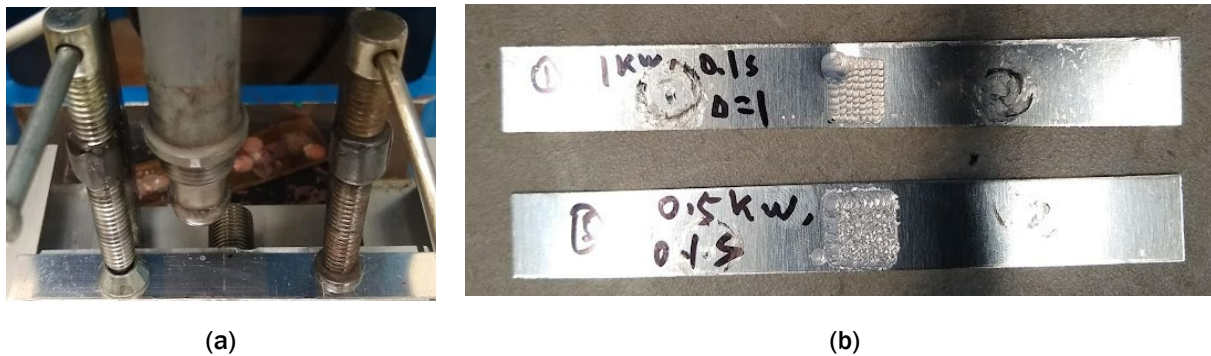


Figure II.1.7.22. The third set of experiments. (a) The experimental setup. (b) The sonotrode side processed samples with the use of two different values of ultrasonic power. Source: ORNL.

Bendability is an important indicator of formability of sheets, particularly for processes needing a small radii of bending, such as hemming. Bendability is usually classified by the critical r/t ratio below, in which cracks are observable, or a critical bending angle above which cracks are observable when r/t is fixed. Accurately predicting bendability is an important tool to guide the surface modification processes to have an optimized microstructure.

In the first simulations, the influence of local softening or hardening on bendability was through an evaluation using a FEM of the VDA-bending set up shown in Figure II.1.7.23(a). In this model, the middle section of the material was assigned a strength value different from the rest of the material. As shown in Figure II.1.7.23(b), this value ranged from 70%–150% of the baseline material. The results from the macro-micro multiscale modeling [15] show that the as-received 1 mm 7075 T6 material had very good bendability for $r/t=0.2-0.5$, which correlates well with the experiments. Another observation was that the largest strain achievable at the tension side of the surface is smaller when the strength of the middle section is 70% softer than the base material, as shown in Figure II.1.7.23(c). Predictions from these models will be validated in FY 2022 using the V-bend test fixture designed and manufactured in FY 2021.

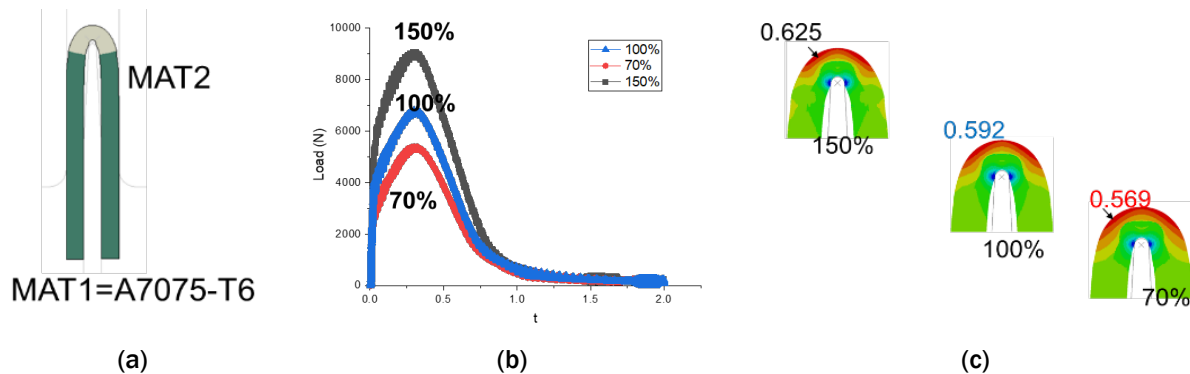


Figure II.1.7.23. Results from VDA-bending simulations with the strength middle section material scaled by a factor of 70%–150% relative to the base material. (a) The model after VDA-bending. (b) The load-t curve. (c) The principle strain contours after the simulations. Source: ORNL.

Conclusions

The culmination of FY 2021 tasks demonstrated that a variety of techniques are effective at locally and selectively modifying properties of Al sheet metal. Among the results, Project 1A demonstrated that multi-alloy extrusions could be fabricated using the ShAPE process. Proof-of-concept was shown for 6061 and 7075 joined in a butt-joint configuration. Proof-of-concept was shown for cladding 7075 and 2024 with 6061 and 1100. Extrusions with locally modified properties were fabricated by varying the rotational speed throughout the extrusion to control temperature. This resulted in substantial variations in hardness along the length in the as-extruded and T5 conditions. This suggests that mechanical properties can be tailored that ultimately result in sheet with locally modified properties. Proof-of-concept was also demonstrated to show that ShAPE is capable of variable wall thickness extrusions and design activities were completed on a system for actively controlling wall thickness.

For Project 2C, FSP showed an r/t improvement of 50% in 7085-T76, 30% in 6111-T6 alloys and 19% in 5182-H111. The overall maximum bending force of the alloys after FSP was still within 500-600N for 7085-T76 and 5182-H111 with their base alloys, while 6111-T6 force was still equivalent to the non-processed base alloy. FSP showed strong potential to improve the formability of Al sheets and will be applied to other low formable alloys such as 7075-T6 and 7055-T6 in future planned work. An experimental roller bending-unbending device, with 2- and 3-rollers, was successfully fabricated for RT mechanical processing. The device was able to successfully deform the local region at 13% and 96% plastic strain for 15° and 30° roller angles, respectively, and achieve significant hardness increases. High-temperature heating will be introduced into the 3-roller system in future work, to simultaneously deform and heat the sheets.

Results of Project 1C showed infrared heating achieves rapid heating rates and narrow HAZs, but it is not adequate for affecting formability. However, laser thermal treatments were successful in the local softening of 7075-T6 sheet, and bending simulations suggest that this softening can improve bendability. Local processing

and property modifications can also be achieved using ultrasonic vibrations with a sonotrode in contact with a sheet. The process parameters and tool geometry of the power ultrasonic process can be engineered to obtain different local microstructures and surface finishes. Although sonotrodes with grooved surfaces did not show promise for well-controlled local surface modifications, due to marking of the sheet surface, the use of a flat-faced sonotrode removed these surface markings. The initial surface condition of the sheet in contact with a sonotrode appeared to influence the surface response of the ultrasonically modified region. No sticking between the tool and the sheet was observed when the unprotected side of the sheet was in contact with the sonotrode. Conversely, sticking marred the surface of the sheet when the fresh surface (after peeling off the plastic protective film) was in contact with the sonotrode. Further experiments are in progress to understand the differences observed due to the initial surface condition of the Al sheet.

Key Publications

1. Milligan, B., M. Komarasamy, A. Battu, T. Varga, A. Guzman, and S. Whalen, 2022, “Multi-alloy aluminum tubing via Shear-Assisted Processing and Extrusion (ShAPE),” Accepted for Presentation at the TMS 2022 Annual Meeting, Anaheim, CA, USA, 27 February – 3 March 2022.
2. Komarasamy, M., S. Whalen, B. S. Taysom, and D. Herling, 2022, “Co-extrusion of dissimilar Al alloys via Shear-Assisted Processing and Extrusion (ShAPE),” Accepted for Presentation at the TMS 2022 Annual Meeting, Anaheim, CA, USA, 27 February – 3 March 2022.

References

1. EHFCV, 2018, “Multi-material joining B-pillar,” Available at: <https://ehfcv.com/multi-material-joining-b-pillar/> (last accessed 8 January 2022).
2. Lavender, C., V. Joshi, G. Grant, S. Jana, S. Whalen, J. Darsell, and N. Overman, 2019, “System and process for formations of extrusion products,” U.S. Patent No. 10,189,063, 29 January 2019.
3. Taysom, B. S., N. Overman, M. Olszta, Md. Reza-E-Rabby, T. Skszek, M. DiCiano, and S. Whalen, 2021, “Shear-Assisted Processing and Extrusion (ShAPE) of high-strength aluminum alloy 6063 tubing,” *Int. J. Mach. Tools Manuf.*, Vol. 169, Art. 103798.
4. Whalen, S., M. Olszta, Md. Reza-E-Rabby, T. Roosendaal, T. Wang, D. Herling, B. S. Taysom, S. Suffield, and N. Overman, 2021, “High-speed manufacturing of aluminum alloy 7075 tubing by Shear-Assisted Processing and Extrusion (ShAPE),” *J. Manuf. Process.*, Vol. 71, pp. 699–710.
5. Kou, S., 2015, “A criterion for cracking during solidification,” *Acta Mater.*, Vol. 88, pp. 366–374.
6. Gussev, M., J. Busby, K. Field, M. Sokolov, and S. Gray, 2015, “Role of scale factor during tensile testing of small specimens,” In: Sokolov, M. A., and E. Lucon (eds.), *Small Specimen Test Techniques: 6th Volume*. ASTM Stock #STP1576, ASTM International, West Conshocken, PA, USA.
7. Ma, Z. Y., 2008, “Friction stir processing technology: A review,” *Metall. Mater. Trans. A–Phys. Metall. Mater. Sci.*, Vol. 39, No. 3, pp. 642–658.
8. Han, S., T. Hwang, I. Oh, M. Choi, and Y. Moon, 2018, “Manufacturing of tailor-rolled blanks with thickness variations in both the longitudinal and latitudinal directions,” *J. Manuf. Process. Technol.*, Vol. 256, pp. 172–182.
9. Milligan, B., M. Komarasamy, A. Battu, T. Varga, A. Guzman, and S. Whalen, 2022, “Multi-alloy aluminum tubing via Shear-Assisted Processing and Extrusion (ShAPE),” accepted for presentation at the TMS 2022 Annual Meeting, Anaheim, CA, USA, 27 February – 3 March 2022.
10. Komarasamy, M., S. Whalen, B. S. Taysom, and D. Herling, 2022, “Co-extrusion of dissimilar Al alloys via Shear-Assisted Processing and Extrusion (ShAPE),” accepted for presentation at the TMS 2022 Annual Meeting, Anaheim, CA, USA, 27 February – 3 March 2022.
11. Kinsey, B., and X. Wu (eds.), 2011, *Tailor Welded Blanks for Advanced Manufacturing, 1st Edition*, Elsevier, Woodhead Publishing, Cambridge, U.K.

12. Dausinger, F., 2000, “Laser welding of aluminum alloys: From fundamental investigation to industrial application,” In: Chen, X., T. Fujioka, and A. Matsunawa (eds.), *High-Power Lasers in Manufacturing*, Proceedings Vol. 3888. Available at: <https://doi.org/10.1117/12.377044>.
13. U.S. Council for Automotive Research (USCAR), 2021, *Roadmap for Automotive Additive Manufacturing*, Southfield, MI, USA.
14. Miao, Q., D. Wu, D. Chai, Y. Zhan, G. Bi, F. Niu, and G. Ma, 2020, “Comparative study of microstructure evaluation and mechanical properties of 4043 aluminum alloy fabricated by wire-based additive manufacturing,” *Mater. Des.*, Vol. 186, Art. 108205.
15. Hu, X. H., M. Jain, P. D. Wu, D. S. Wilkinson, and R. K. Mishra, 2010, “A macro-micro-multi-level modeling scheme to study the effect of particle distribution on wrap-bendability of AA5754 sheet alloys,” *J. Mater. Process. Technol.*, Vol. 210, No. 9, pp. 1232–1242.

Acknowledgments

The PNNL and core program participants thank DOE VTO for support through the LMCP. PNNL staff members B. Milligan, M. Komarasamy, and B. S. Taysom are commended for their excellent task leadership on this project. Additionally, ORNL staff and postdoctoral researchers that supported this work are recognized, namely, Y. Yang, G. Knapp, T. Feldhausen, B. Stump, R. Kannan, M. Gussev, A. M. Rossy, and S. Graham. The PIs also acknowledge D. Wilson at Mazak Corporation and C. Agosti at Lincoln Electric for their technical assistance with the initial system parameters development. The authors would also like to acknowledge the contributions of S. Shukla, J. Allen, J. Cheng, J. Chen, and Y. C. Lim in their experimental and modeling support to the project.

II.1.8 Light Metals Core Program: Thrust 2 – Selective Processing of Al Castings (Pacific Northwest National Laboratory)

Glenn J Grant, LMCP Project Manager, Principal Investigator Thrust 2

Pacific Northwest National Laboratory
902 Battelle Blvd.
Richland, WA, 99352
E-mail: glenn.grant@pnnl.gov

Saumyadeep Jana, Principal Investigator 2A1

Pacific Northwest National Laboratory
902 Battelle Blvd.
Richland, WA, 99352
E-mail: saumyadeep.jana@pnnl.gov

Zhili Feng, Principal Investigator 2A2

Oak Ridge National Laboratory
1 Bethel Valley Road
Oak Ridge, TN 37831
E-mail: fengz@ornl.gov

Aashish Rohatgi, Principal Investigator 2B

Pacific Northwest National Laboratory
902 Battelle Blvd.
Richland, WA, 99352
E-mail: aashish.rohatgi@pnnl.gov

Alex Plotkowski, Principal Investigator 2C

Oak Ridge National Laboratory
1 Bethel Valley Road
Oak Ridge, TN 37831
E-mail: plotkowskij@ornl.gov

Jerry L. Gibbs, DOE Technology Manager

U.S. Department of Energy
E-mail: jerry.gibbs@ee.doe.gov

Start Date: October 1, 2020 End Date: September 30, 2023
Project Funding (FY 2021): \$1,450,000 DOE share: \$1,450,000 Non-DOE share: \$0

Project Introduction

The LMCP, led by PNNL, is an integrated effort between PNNL, ORNL, and ANL. The overall program aims to develop and demonstrate scalable, cost-effective processing methods with the direction of PIs from each of the three National Laboratories to locally enhance the properties of Al and Mg alloys to enable broader implementation of lightweight alloys in vehicles. The technical goal is to demonstrate that components and assemblies composed of commercially available alloys can be selectively modified to exhibit locally enhanced properties and deliver high materials performance in the most needed locations. This approach allows for significant improvements in manufacturability, structural efficiency, and weight-savings in next-generation

vehicles. Furthermore, the approach enables the right properties in the right locations and provides the opportunity to decrease the number of metal alloys required for new vehicle manufacture—reducing the challenges that automakers face today in managing supply chains, assuring sufficient materials sustainability, and efficiently recycling scrap metal.

New processing methodologies could allow high-strength Al sheet materials over 450 MPa yield stress to reach ductility over 15% or forming bend radii <2x thickness. Local processing of cast parts can produce regions on a casting that will show >5x fatigue life or doubling of the endurance limit stress. Inherent to the research plan is an underpinning science theme to understand the behavior of microstructure evolution during manufacturing and the resulting material performance in-service. Recognizing that metal microstructures are process dependent, controlling and optimizing the right microstructure will lead to desired property (e.g., ductility, strength, fatigue, corrosion resistance, etc.) in the right location of components. Focused collaborative research thrusts have been established to develop local property modification strategies for each targeted metal system: high-strength Al sheet, Al castings, and Mg castings. Figure II.1.8.1 provides a brief description of these thrusts and how the principal manufacturing methodologies interact, as well as transition to higher technology readiness levels. Within those thrusts, individual projects explore and develop the science and process engineering to create spatially tailored properties in alloys and assemblies of target metal systems. A fourth, cross-cutting thrust provides overarching support in testing, characterization, and modeling.

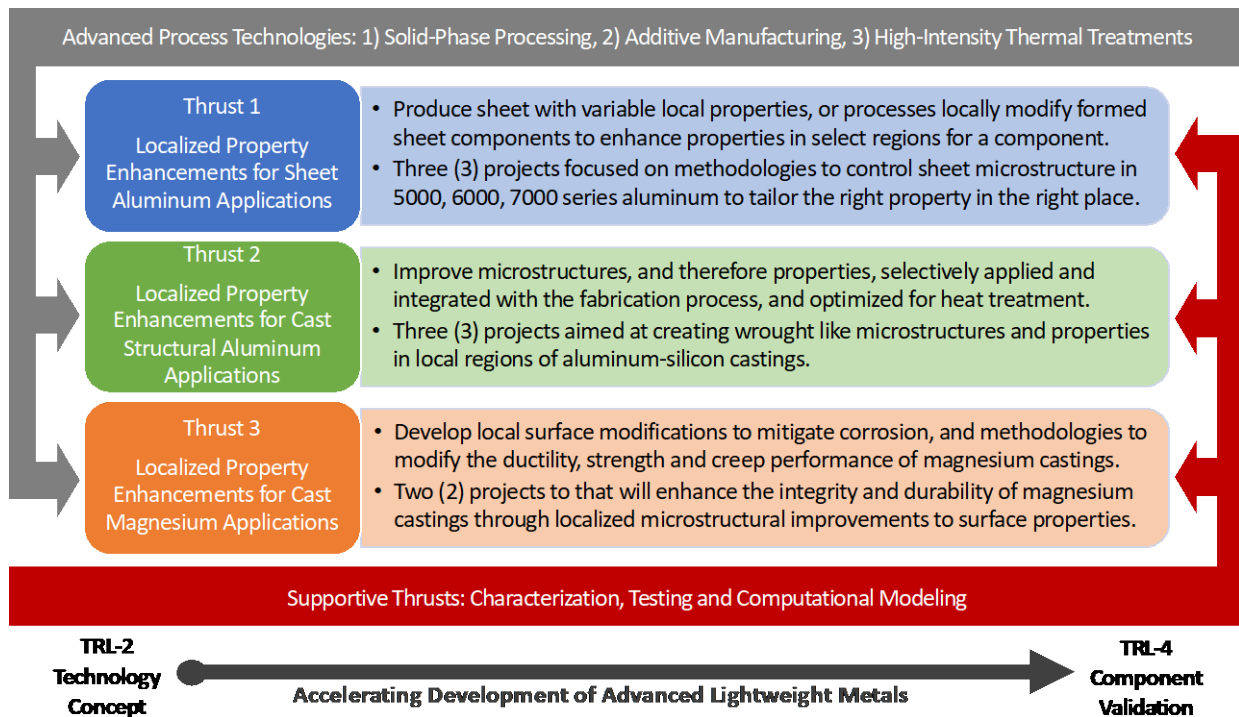


Figure II.1.8.1. Thrust and project structure of the LMCP. Source: PNNL.

The following report describes the FY 2021 technical efforts and results of Thrust 2, “Selective Processing of Aluminum Castings.”

Objectives

Al cast parts offer excellent opportunities for vehicle lightweighting, a reduced part count, and assembly costs. However, there are science and engineering challenges with the integration of castings into assemblies, including local ductility in the regions where castings are attached to other structures; fatigue in stress members; and the strength of high fluidity alloys. To enable further integration of lightweight castings into the

body-in-white, this thrust proposes to develop processes to locally modify cast parts so that single castings can satisfy the varying property requirements at different locations of the component.

Cast microstructures are inherently less homogeneous than the wrought materials, and their properties (e.g., fatigue, fracture performance, ductility, strength) are usually defined by local microstructural characteristics, such as porosity; second-phase distribution and morphology; and dendrite size and morphology. Castings are especially prone to durability challenges due to near-surface microstructural inhomogeneities. Through the development of manufacturing approaches to locally customize, optimize, and/or repair microstructures in the component to meet specific application performance requirements, it will become possible to consider Al castings for a much wider range of applications and to reduce wall thicknesses in existing cast parts to enable additional weight-savings. In addition, if local microstructures are modified for a better heat-treatment response, cast parts can be strengthened, enabling an even greater insertion of thin-wall castings into glider components. Thrust 2 will seek to enhance the local properties in cast-Al components through three projects: (1) using FSP or PUSP to create local regions of improved microstructure that exhibit better fatigue performance, and to fix locally defected microstructures at cold shots or in locations where die filling is challenging; (2) using an integrated high intensity thermomechanical approach that combines ultrasonics, Joule heating, and high-pressure waterjet peening to modify local microstructures for enhanced strength, fatigue resistance and ductility; and (3) using an AM cast-and-print process to locally improve microstructures and/or add structural features.

Thrust 2 is comprised of three individual projects, as shown in Figure II.1.8.2. Project 2A is a collaborative project between PNNL and ORNL (e.g., 2A1, 2A2) investigating FSP and PUSP to locally improve the strength, ductility, and fatigue performance of high-pressure die-cast (HPDC) Al alloys in thin-walled castings. Project 2B (PNNL) focuses on high intensity thermomechanical and thermal treatments to improve the properties of thicker wall (e.g., >2 mm) Al structural castings, and Project 2C (ORNL) focuses on using AM to make cast parts with local AM additions.

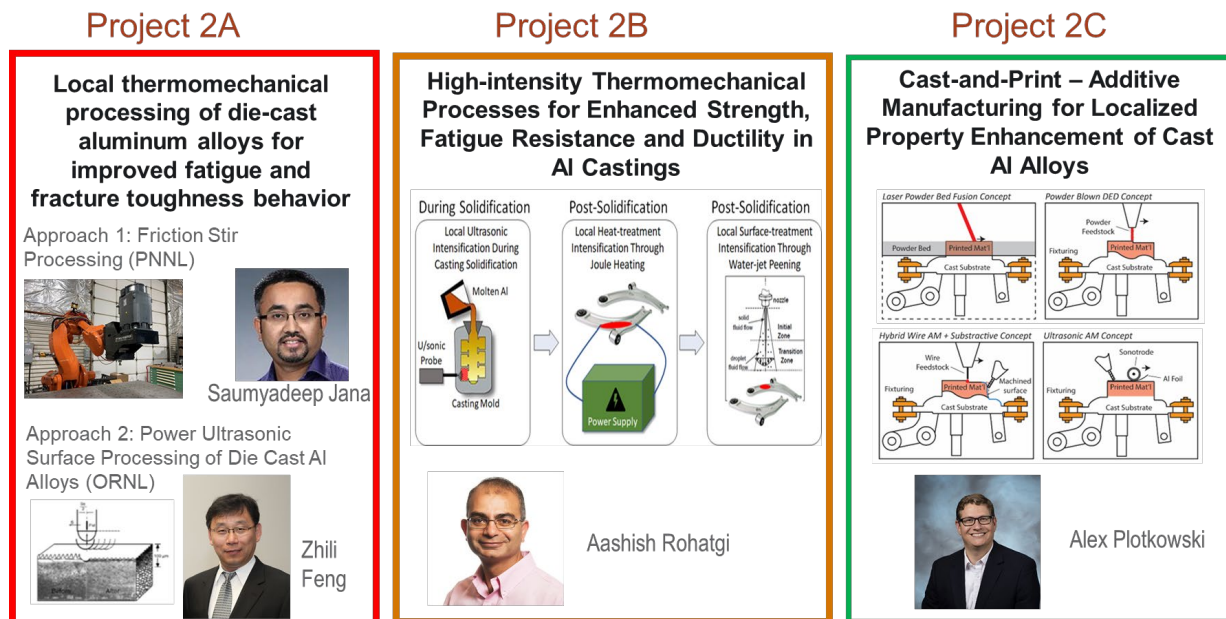


Figure II.1.8.2. Three projects within the LMCP Thrust 2. Source: PNNL.

Project 2A1: Friction Stir Processing of Die-Cast-Al Alloys (PNNL)

HPDC Al alloys provide a potential route to achieve lightweighting by using large, thin-wall and intricately shaped castings as structural members in a car body. HPDC components can help in part unitizing, have the potential to replace various pillars (e.g., B-pillar, C pillar, etc.), and can also be used in car-door structures. However, for HPDC components to reliably perform as structural members, they need to demonstrate a good combination of strength, ductility, fracture toughness, and in certain situations, high fatigue properties. Typical HPDC Al alloy composition contains high Fe (e.g., to prevent die soldering) together with casting induced microstructural features (e.g., porosity, inclusions, etc.) that negatively impact the mechanical properties, preventing their use as structural members [1]. Alloy development research has led to identifying some low-Fe-containing premium HPDC Al alloy compositions (e.g., Silafont, Castasil, Aural, etc.) with improved mechanical properties [2]. Similarly, improvements in die-casting technology using the vacuum-assisted HPDC method can help in reducing casting defects such as porosity [3]. However, the use of premium quality HPDC Al alloys and/or the use of an improved die-casting method carry a cost penalty that prevents widespread adoption.

Modification of the typical defect-containing HPDC microstructure, however, could be an alternative strategy to enable the use of HPDC Al alloy components as structural members. Selective local processing of the regular HPDC component can be carried out to remove defects/other microstructural features responsible for mechanical property depression, especially in areas that are prone to failure. If successful, this method would then allow for the structural use of Al alloy components made by the standard HPDC method, and not use premium HPDC Al alloy compositions or process, thus offering a significant step to achieve lightweighting in a cost-effective manner. In addition, typical recycled Al has high Fe content which can lead to reduced performance in castings. Enabling improved performance through selective modification in standard die-cast alloys will also potentially enable increased use of recycled Al in these alloys as well. In this study, we have utilized FSP, as one such tool for locally modifying the microstructure of a typical thin-wall HPDC Al alloy. This project develops the FSP process and evaluates the improved mechanical performance through coupon level mechanical testing. The objectives of this project are to: (1) demonstrate that FSP can reduce/remove casting porosity and achieve microstructural refinement in a HPDC Al alloy of choice; and (2) demonstrate that the combined effect of microstructural refinement together with the elimination of casting porosity results in improved mechanical properties (strength and ductility) in a FSP processed HPDC Al alloy.

Project 2A2: Power Ultrasonic Surface Processing (PUSP) of Die-Cast-Al Alloys (ORNL)

The goal of this subtask is to explore and develop PUSP technology to enhance surface properties of cast-Al alloys for auto body structures.

Project 2B: High Intensity Thermomechanical Processes (PNNL)

As-cast microstructures are typically dendritic, are inherently less homogeneous, and may contain porosity, resulting in lower mechanical performance as compared to wrought materials. Some enhancement in as-cast properties can be achieved through microstructural refinement by increasing the local cooling rate (e.g., by using chills) and/or enhancing the nucleation rate in the melt (e.g., by adding grain refiners). However, the use of chills is not always practical, and grain refiners are limited in how small a grain size that can efficiently be produced. Furthermore, castings are often heat-treated to achieve high-strength. However, heat treatments that require solutionizing at elevated temperatures are not always feasible in cases where the presence of entrapped gas porosity can create blistering, such as in HPDCs. Consequently, while Al casting technology is well-developed, many scientific and technical challenges remain. This project will develop advanced approaches to locally modify Al castings, and thereby satisfy the varying property requirements at different locations within the cast components. The objectives of this project are to: (1) improve the local tensile strength and ductility of cast-Al alloys; and (2) increase the local fatigue life of cast-Al alloys.

Project 2C: Cast-and-Print: Additive Manufacturing for Localized Property Enhancement (ORNL)

In this task, we are investigating cast-and-print technology, in which metal AM is used to locally deposit material onto cast substrates. This approach takes advantage of the high-throughput of conventional casting for automotive production volumes and combines it with the targeted application of AM technologies for localized

modification of geometry, microstructure, and properties. The properties of cast-Al alloys are largely determined by solidification cooling rates, which dictate their microstructural length scales [4]. Metal AM offers much more rapid cooling rates than casting processes with an associated decrease in microstructural length scale, providing opportunities for precise spatial control of microstructure and the ability to produce complex geometries [5, 6]. Combining casting and metal AM processes offers a route to maximize local control of microstructure and material properties while minimizing the added cost associated with AM components and enabling higher throughputs. The objective of this task is to add features to castings to enable unique advantages such as local strengthening through depositing material with enhanced material properties and part stiffening through geometry modification.

Approach

Project 2A1: Friction Stir Processing of Die-Cast-Al Alloys (PNNL)

FSP is a TMP technique that operates on similar principles as friction stir welding [7, 8]. During FSP, SPD imparted by the rotating tool on the workpiece refines the microstructure and eliminates porosity, thus improving the mechanical properties of cast alloys [9]. In this study, HPDC A380 plates of ~3.5 mm thickness were used for FSP trials. A380 (Al-8.5Si-3.3Cu-0.8Fe-0.6Zn-0.2Mn-0.1Mg, all in wt.%) is a common Al alloy heavily used in the die-casting industry for various non-strength critical applications. A representative through-thickness low magnification image of the HPDC A380 plate is shown in Figure II.1.8.3(a). The presence of a large number density of porosities can be seen, and the size and number density of porosity is location-specific. Material near the die-wall is relatively dense and contains smaller casting pores. On the other hand, material in the mid-wall region contains more pores, and they are larger in size. Higher magnification images of the as-cast HPDC A380 plate from specific locations are captured in Figure II.1.8.3(b) and Figure II.1.8.3(c). Changes in the size and morphology of eutectic Si particles, α -Al dendrites, and the vol. fraction of eutectic Al-Si phase is distinct between die-wall and mid-wall regions. Additionally, the presence of a variety of second-phase particles, marked by the blue arrows in Figure II.1.8.3(d), can be seen in the as-cast HPDC A380 material. Table II.1.8.1 provides a quantified summary of the various microstructural features observed in HPDC A380, indicating the high-level of microstructural heterogeneity present in as-received die-cast plates.

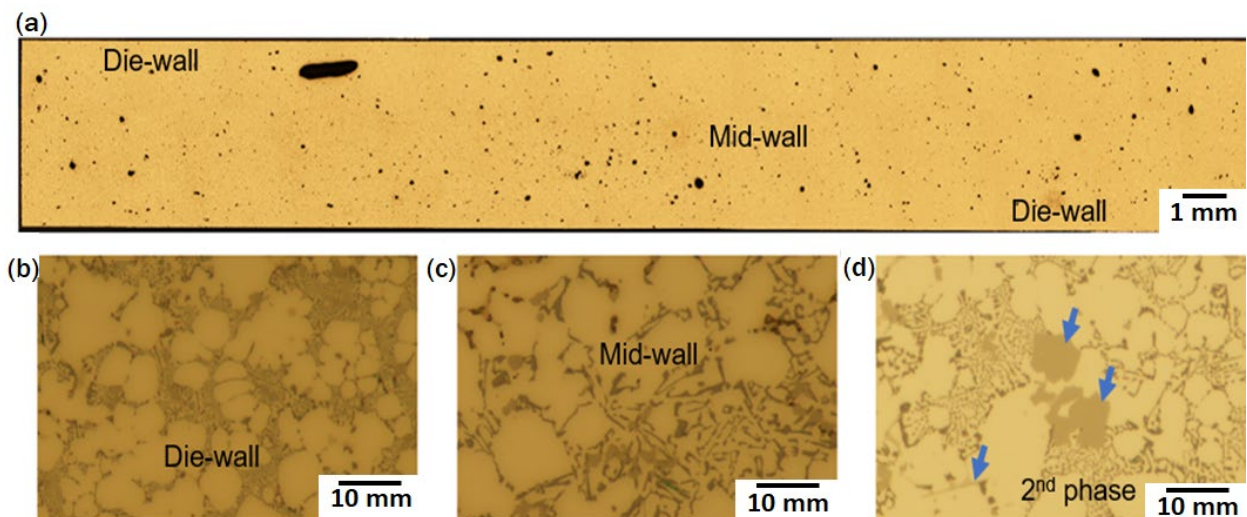


Figure II.1.8.3. Microstructure of as-received HPDC A380 plate: (a) low magnification overview of the plate; (b) Al-Si eutectic phase at die-wall; (c) Al-Si eutectic phase at mid-wall; and (d) second-phase particulates.

Source: PNNL.

Table II.1.8.1. Summary of Various Microstructural Features Seen in HPDC A380 Die-Cast Plates

Alloy	% Porosity Vol. Fraction	Avg. Porosity Size (< 50 μm)	Avg. Porosity Size (> 50 μm)	α -Al Dendrite Spacing, μm	Eutectic Si-Particle Size, μm	Si- Aspect Ratio	Second-Phase Size, μm
Die-Wall	0.7 \pm 0.3	3.8 \pm 1.5	61.8 \pm 9.5	5.7 \pm 1.5	1.6 \pm 0.9	4.6 \pm 2.2	2.3 \pm 2.1
Mid-Wall	2.2 \pm 1.7	5.8 \pm 5.4	90.9 \pm 57.5	9.5 \pm 3.2	5.5 \pm 2.8	14.5 \pm 8.1	2.9 \pm 2.3

FSP trials were conducted on flat HPDC A380 plates. A detailed design-of-experiment approach was taken to develop the right combination of process control variables—namely, tool rotational speed and tool travel speed to fabricate surface defect-free FSP plates that show the highest degree of microstructural refinement. To achieve a high-degree of microstructural refinement and casting porosity removal, two FSP passes were carried out on top of each other in the same direction. Based on our initial trials, a tool rotational speed of 450 RPM and the traverse velocity of 0.05 m/min were selected for characterization. Through a detailed microstructural characterization that involved the use of OM, SEM, and TEM imaging coupled with microstructural quantification, we established the role of FSP in modifying the HPDC A380 microstructure. The effect of microstructural modification imparted by FSP on tensile properties were established by testing miniature-sized tensile samples obtained from different locations of the FSP nugget region to establish location-specific mechanical properties within the FSP region.

Project 2A2: Power Ultrasonic-based Surface Processing Die-Cast-Al Alloys (ORNL)

PUSP is a relatively new concept at an early-stage of development. The underlying physics of PUSP suggest it has the potential to significantly reduce the process load, which is essential for single-side processing auto body components with a complex-geometry. The second potential advantage in using PUSP is its ability to create compressive surface residual stresses. It is well-known that compressive surface residual stress induced by laser shot peening can lead to significant improvement of fatigue life in Al alloy structures for aerospace applications.

The purpose of this subtask is to explore and develop PUSP technology to improve the local properties of cast-Al alloys for auto body structures. Specifically, we plan to demonstrate that surface property enhancements affected by power ultrasonics will lead to increased durability and fatigue life due to highly localized heating and SPD, which closes solidification porosity, refines the microstructure, and generates compressive residual stresses. In addition, the acoustic plastic softening effect will be investigated to reduce the required process load for one-side processing, thereby enabling integration with robotic auto body structure assembly systems.

A combined experimental process development and physics-based computational simulation method is used in this subtask. The multiscale modeling effort is designed to support the process development by studying heat generation, plastic deformation, and residual stresses, as well as the resulting microstructure, residual stress affected by PUSP, and enhanced durability or fatigue life of body structure components. The physics-based computational modeling framework integrates three types of analyses leading to the prediction of the fatigue life of PUSP processed parts. First, an ultrasonic joining process model previously developed [10] will be refined and applied to the ultrasonic processing by means of the thermomechanical finite element method. The process model will be applied to determine the effects of sonotrode geometry and processing conditions to the surface deformation and vibrational heating. Transient temperature, plastic strain, and stresses from the process model is used as input for the second computational analyses: recrystallization and microstructure simulation. Third, fatigue performance simulation is used to connect the process, microstructure changes, and residual stresses to the improvement in fatigue life by the ultrasonic processing.

Project 2B: High Intensity Thermomechanical Processes (PNNL)

This project is divided into three main tasks where each task will develop a different processing approach that may be used to improve the local properties of cast-Al automotive components at different stages of the manufacturing process. The first task will enhance the initial casting stage by applying local ultrasonic intensification during casting with the goal of refining the as-cast microstructure. The application of ultrasound

during casting can refine the microstructure through mechanisms such as enhanced heterogeneous nucleation and the fracture of dendrites [11–14]. The ultrasonically refined microstructure is expected to improve the as-cast strength, ductility, and fatigue life of the casting [15, 16]. Since castings are often heat-treated to improve their mechanical properties, the second task is designed to address the heat-treatment stage. The second task will enhance the heat-treatment stage by applying local thermal intensification with the goal of strengthening the as-cast microstructure. Thermal intensification will be applied through Joule heating and is expected to accelerate atomic-scale diffusion processes, which will decrease the time and/or temperatures required for post-solidification heat treatments. After heat treating, castings are sometimes subjected to a surface-treatment to improve fatigue life. Therefore, the third task will enhance the surface-treatment stage by applying local waterjet peening with the goal of imparting deep residual compressive stresses, which are expected to improve the fatigue life of the casting. Thus, these three main tasks address different stages during the production of a casting. Together, they are expected to produce high-performance Al castings where the local properties have been enhanced to meet the local property requirements.

Project 2C: Cast-and-Print: Additive Manufacturing for Localized Property Enhancement (ORNL)

The purpose of this task is to establish process-microstructure-property relationships for the Cast-and-Print approach to enable the design of automotive structural components. We will focus on fundamental development and a targeted application to commercial Al-Si and Al-Mg based alloys for HPDC and other potential casting methods of interest to automotive OEMs. The most impactful AM processes and corresponding feedstock materials will be selected to maximize the component performance benefits and process throughput while minimizing the cost and impact on recycling streams.

Results

Project 2A1: FSP of Die-Cast-Al Alloys (PNNL)

A low magnification overview of the FSP processed region (e.g., 450 RPM, 0.05 m/min, two-pass 100% overlap) is shown in Figure II.1.8.4. The formation of a basin-shaped process region is evident in this image, along with a distinct boundary that is present between the process region and the HPDC microstructure on the advancing side (AS). The boundary between the cast region and the FSP region is rather diffuse on the retreating side (RS). The processed region appears to be free of any visible porosity that is present in the as-received HPDC material on either side of the processed region. A closer look inside the FSP region through SEM EDS elemental mapping, which is marked by the dashed blue rectangle, revealed the degree of microstructural refinement attained by FSP. It appears that the Si particles are fragmented and dispersed uniformly within the process zone, thus eliminating the as-cast dendritic microstructure. Cu- and Fe-bearing second-phase particulates are refined extensively as well. Fe-bearing needle-shaped particles are especially detrimental to tensile/fatigue properties in cast-Al alloys, and it appears that FSP can efficiently refine such detrimental phases. Microstructural quantification indicated the porosity vol. fraction to be <0.1% in the FSP region. The as-received HPDC A380 alloy had an average porosity vol. fraction of ~1.2%, in contrast. Similarly, the average size of the Si particles and the aspect ratio within the FSP region were determined to be ~1.5 μm and ~2.0, which are ~60% and ~80% smaller as compared to the as-received die-cast material, where the average Si-particle size was ~3.5 μm and the aspect ratio measured ~9.5.

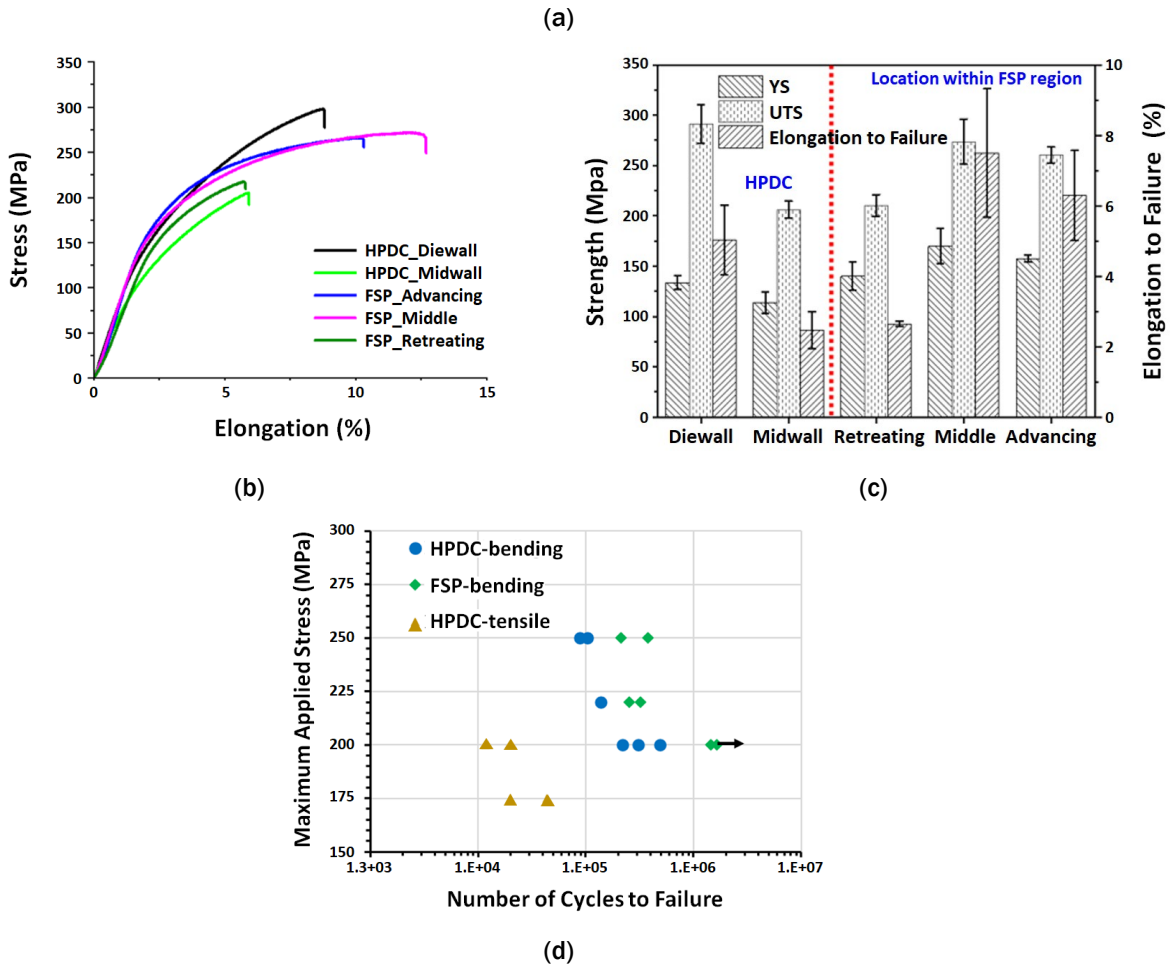
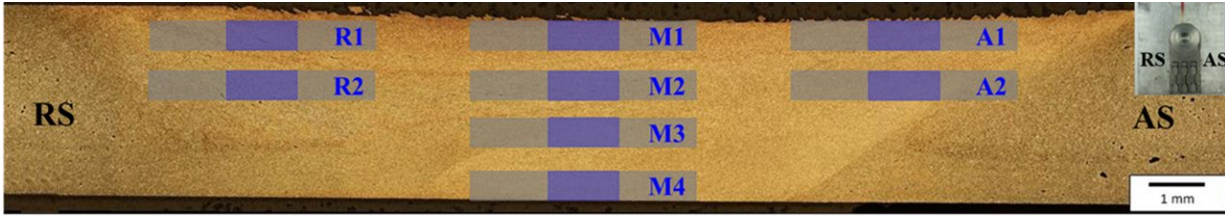


Figure II.1.8.4. Summary of tensile properties of FSP processed HPDC A380 material. (a) Location of various miniature specimens within the FSP region; A: AS, M: middle area, R: RS. (b) Representative engineering stress-elongation curves for FSP and HPDC material. (c) Summary of stress-elongation plots. (d) HCF properties of HPDC vs. FSP condition; increased fatigue life observed after FSP. Source: PNNL.

The effect of FSP-induced microstructural refinement, together with the elimination of casting porosity on mechanical properties of HPDC A380 alloy, was determined by carrying out tensile testing on miniature samples. The miniature tensile samples were extracted from the AS, middle, and RS areas of the FSP process zone, as depicted in Figure II.1.8.4(a). Tensile tests were performed using a computer-controlled tester at RT with a cross-head velocity of 0.005 mms^{-1} . Each miniature specimen had 4.3 mm in gauge length, 1.25 mm in gauge width, and 0.5 mm in gauge thickness. For effective comparison, miniature samples were also extracted from the die-wall and mid-wall regions of the as-received HPDC A380 plates. The representative engineering stress-elongation curves are shown in Figure II.1.8.4(b) for the different material conditions. The beneficial effect of FSP on increasing tensile ductility becomes immediately clear from this plot. A summary of tensile test results is pictorially represented in Figure II.1.8.4(c), with more details provided in Table II.1.8.2. From

the tensile test data, it is evident that the material in the die-wall regions of the HPDC A380 cast plate shows enhanced properties as compared to the mid-wall region. Enhanced properties observed in the skin/die-wall region are a well-known fact within the die-casting industry. This is because of faster solidification rates experienced in these areas and related refined microstructure. However, after FSP, the YS, tensile strength, and ductility increase by ~50%, 30%, and ~200% for certain test conditions. However, it seems that the tensile properties are not uniform within the FSP region with room for additional FSP parameter optimization.

Additionally, fatigue properties were determined in this study. Figure II.1.8.4(d) represents the S-N plot for various samples tested under different loading conditions. HPDC A380 alloy shows high fatigue life, especially when loaded in a 4-point bending configuration compared to tensile loading condition. However, after FSP, fatigue life increases significantly. In fact, for FSP samples tested at 200 MPa in bending mode, no failure was recorded even after $1.5 \times 1.0E6$ cycles, and the test was terminated due to lack of testing time. One should consider that such fatigue life improvement was achieved in a partially-optimized FSP microstructure, and the likelihood of achieving higher fatigue performance is very high with further FSP parameter optimization.

Table II.1.8.2. Summary of Tensile Properties on Miniature Specimens of HPDC A380 Both Before and After FSP

Test Condition	YS, MPa	TS, MPa	% Elongation
Die-Wall	133 ± 6.6	291.3 ± 19.3	5.0 ± 1.0
Mid-Wall	114 ± 10.7	206.2 ± 8.4	2.5 ± 0.5
FSP-AS	157.5 ± 3.5	260.5 ± 7.8	6.3 ± 1.3
FSP-Middle	170 ± 17.3	273.7 ± 22.5	7.5 ± 1.8
FSP-RS	140 ± 14.1	210.5 ± 10.6	2.7 ± 0.1

Project 2A2: Power Ultrasonic Surface Processing of Die-Cast-Al Alloys (ORNL)

The first year of research, development, and deployment (R&DD) in FY 2021 centered on demonstrating the feasibility of PUSP to achieve a targeted process load of 200 lb. to 300 lb., the formation of compressive surface residual stresses, and a meaningful surface microstructure refinement. The die-cast-Al alloy A380 was processed by PUSP under a wide range of process parameters and tool designs, assisted by process modeling. In addition, we developed a fatigue simulation acceleration approach that significantly improves simulation efficiency. This modeling tool makes it possible to simulate and interrogate within days—as opposed to weeks or months with standard simulation methods—the effect of microstructural features in cast-Al alloys, as well as the microstructure changes induced by PUSP, on fatigue deformation and fatigue life. The rate and quality of simulation are an essential tool to accelerate and assist the PUSP process development. The development in FY 2021 created a solid foundation for more comprehensive R&DD in Years 2 and 3.

Due to delays and staffing challenges related to the ongoing COVID-19 pandemic, the planned residual stress measurements and mechanical property testing was delayed and have been rescheduled to FY 2022.

PUSP Process Development

The PUSP process development was carried out in several rounds. The initial experiment in Round 1 was explored on die-cast-Al alloy A380 using ultrasonic tools for ultrasonic welding applications, with baseline process conditions listed in Figure II.1.8.5. As shown, one of the sonotrode tools had a square contact area of 7 mm × 7 mm and six parallel teeth, while the other had a circular contact area of $\Phi 12.4$ mm and 15 parallel teeth. Single-spot surface processing was initially performed on the samples using the different ultrasonic tools and a wide range of processing conditions (e.g., power ranges from 2500 W to 3500 W, processing time ranges from 0.1 s to 0.6 s, and a constant load level from 250 lb. to 300 lb.). The low loads required by these tools offer appealing opportunities for robotic arm manipulation and control for localized surface processing at high

rates. Tool surface dwell times will be brief, since it was noted that the ultrasonic tools begin to stick (weld) to the A380 surface with processing times of 0.3 s and longer.



	Power (W)	2500	2500	2500	2500	2500	2500
	Time (s)	0.1	0.2	0.3	0.4	0.5	0.6
	Power (W)	2500	2500	2500	3500	3500	3500
	Time (s)	0.1	0.2	0.3	0.1	0.2	0.3

Figure II.1.8.5. Experimental matrix including process conditions and tooling used in the first round of PUSP. Source: PNNL.

To achieve a deeper and more uniform surface region of grain refinement, a specially designed ultrasonic tool geometry with a spherical contact shape was used, as shown in Figure II.1.8.6(a). A short processing time of 0.1 s was used in all subsequent experiments to avoid tool sticking. Figure II.1.8.6(b) and Figure II.1.8.6(c) shows two examples of ultrasonic processed regions, which are about 10 mm long and 10 mm wide. Note that a spot ultrasonic tool was used to process the region in a spot-by-spot fashion with an approximate 20% to 40% overlap. The micrographs in Figure II.1.8.7 show the refinement of the microstructure near the surface. As can be seen in the micrograph, the modified sonotrode increased the depth of refinement to > 50 μm even at only 0.1 s of dwell time.

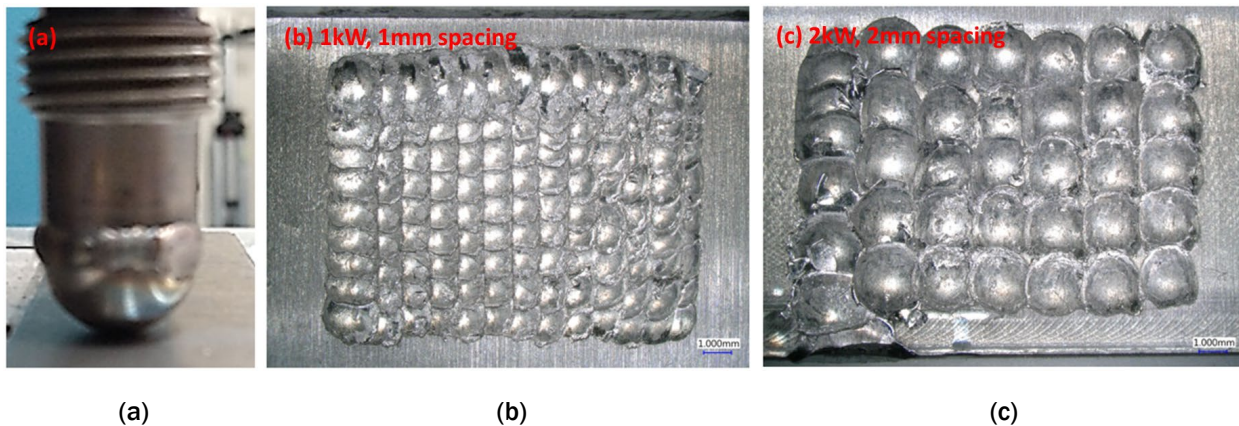


Figure II.1.8.6. (a) A specially designed spherical power ultrasonic tool and the processed surfaces at (b) 1 kW for 0.1 s and (c) 2 kw for 0.1 s. Source: ORNL.

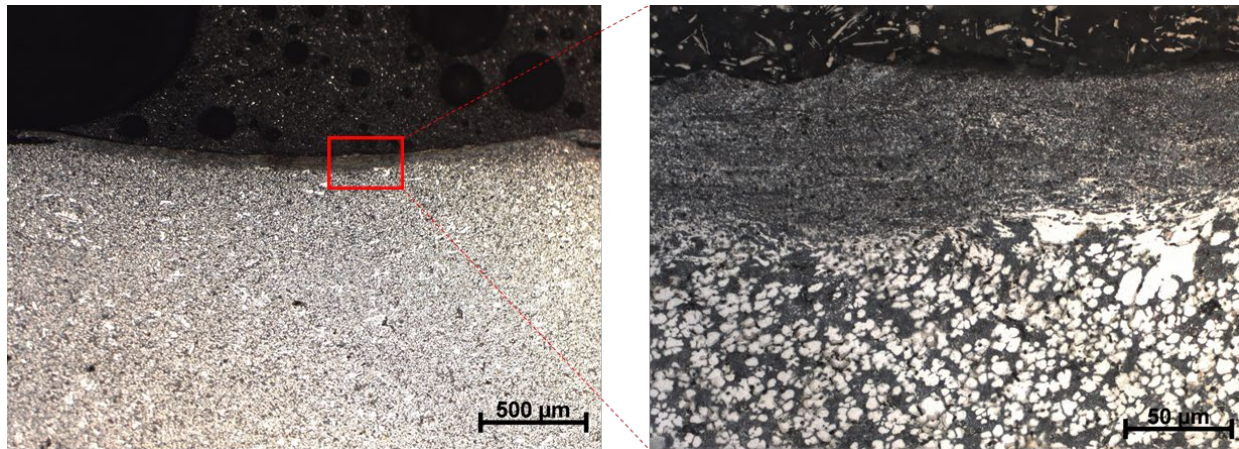


Figure II.1.8.7. A micrograph showing uniform refinement of the microstructure on the processed surface using a spherical ultrasonic tool at 2 kW processing conditions. Source: ORNL.

PUSP Process Development

The influence of ultrasonic processing on the distribution of surface residual stresses was studied for samples processed with a 2 kW condition, as shown in Figure II.1.8.8. A finite element numerical model [10] was applied to identify the process conditions to achieve a desirable surface residual stress distribution. The 2 mm spacing PUSP with the spherical sonotrode was simulated using the process model to understand the temperature and residual stress distribution. Figure II.1.8.8 shows that the temperature is below 100°C due to the short processing time of 0.1 s, while the surface indents (e.g., deformation/depression) in the sheet are more than 110 μm deep due to the small contact area. The large contact force and vibration shear load lead to residual compressive stresses from the A380 sheet surface to the middle thickness, with an average value of about 120 MPa. The PUSP process modeling results so far suggest that it is possible to introduce compressive surface stresses, which is important to enhance the fatigue life of the processed surfaces. The residual stress prediction will be validated by XRD measurement and used as an input for fatigue behavior simulation. Additional simulations will be carried out to assist the development and optimization of process conditions, such as spacing, processing time, and tool geometry, to enhance the PUSP effects on both residual stress and microstructures to improve the quality and efficiency of the surface processing.

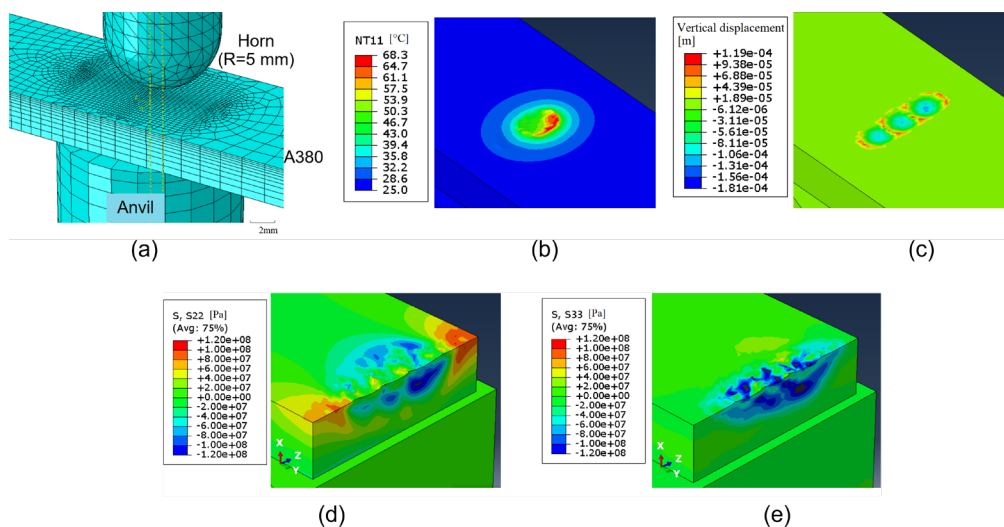


Figure II.1.8.8. PUSP modeling results using a sphere-shaped sonotrode: (a) finite element model; (b) temperature distribution on Al sheet at 0.1 s; (c) vertical displacement showing surface indentation; (d) residual stress in longitudinal direction; and (e) residual stress in transverse direction. Source: ORNL.

Development of an Ultrafast Fatigue Life Simulation Mode

To better understand the influence of microstructure (e.g., grain size and porosity) on the durability of the samples, meso-scale fatigue modeling was also investigated. Traditional fatigue life models used in industry are data-based approaches, such as the safe-life or damage-tolerance methods based on ϵ -N curves or S-N curves. These approaches do not consider the underlying microstructure and cannot provide guidance on how to improve the microstructure for optimized fatigue life. There are recent statistical fatigue life estimation models in literature [17, 18], but they are based on simplifications and only consider porosity, ignoring the interaction between porosity and other microstructure refinement. Furthermore, in actual application of the material in automobiles, the component often undergoes complex stress-state fatigue that is different from laboratory test conditions and leads to different fatigue behavior than measured from the experiments. The predictive model can therefore offer guidance for optimizing the local material modification by ultrasonic or other processing to improve fatigue performance in these complex situations. In this project, we developed a high-fidelity microstructure-based model to explicitly simulate the deformation, stress distribution, and failure occurrence under fatigue conditions for A380. Figure II.1.8.9(a) shows the microstructure finite element model constructed from SEM and OM, while Figure II.1.8.9(b) and Figure II.1.8.9(c) show the predicted deformation failure under a very LCF (e.g., test condition: applied max strain =1%, R=0) at the 30th and 45th cycles, respectively.

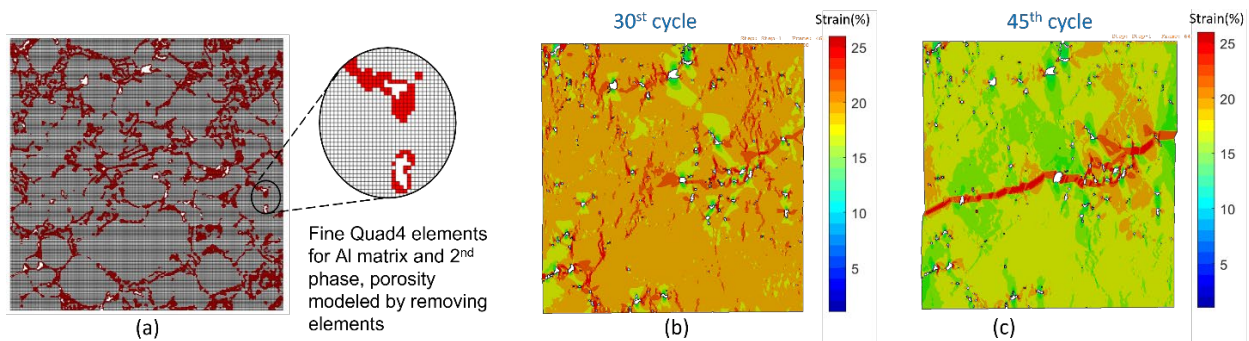


Figure II.1.8.9. (a) FEM of A380 microstructure. (b) Distribution of deformation in a very LCF test at the 30th cycle. (c) Initiation of failure at the 45th cycle. The model size is 20 μm × 20 μm. Source: ORNL.

The most difficult part of fatigue simulation is HCF in which failure often occurs at a few million cycles. Direct simulation of this number of cycles is computationally impossible using conventional finite element-based models, because such models need to explicitly simulate each cycle using fine time increments. In this project, we developed a fatigue simulation acceleration approach that improves simulation efficiency. This method takes advantage of the fact that deformation and stress redistributions over cycles evolves slowly during HCF. Consequently, slight changes of solution-dependent internal variables (i.e., plastic strain and damage variable for metallic materials) over blocks of cycles can be extrapolated using a Taylor-expansion. Based on the extrapolated internal variables, the displacement and stress solution after the jump can be obtained without solving the intermediate cycles, and the computational cost is reduced. Figure II.1.8.10(a) shows the efficiency of the accelerated fatigue simulation method in a benchmark test with the microstructure of A380 (e.g., test condition: load controlled, applied maximum load is 80% of material YS, R=0), where 6,000,000 cycles were simulated with the computation cost of 2500 normal cycles, and only takes four hours to finish using 16 central processing units. Figure II.1.8.10(b) shows the distribution of stress at 10,000 cycles using this acceleration model, while Figure II.1.8.10(c) shows the difference from the reference solution, which was simulated cycle-by-cycle using a conventional method. Nearly identical results were obtained with the accelerated model. This suggests that, within the variability of the processes modeled, the accelerated method can reach the same predictions with greater computational efficiency. With this modeling capability, the modification of microstructure features such as size, volume fraction of pores and intermetallic phases, and the depth of the processed zone will be analyzed to guide optimization of fatigue life.

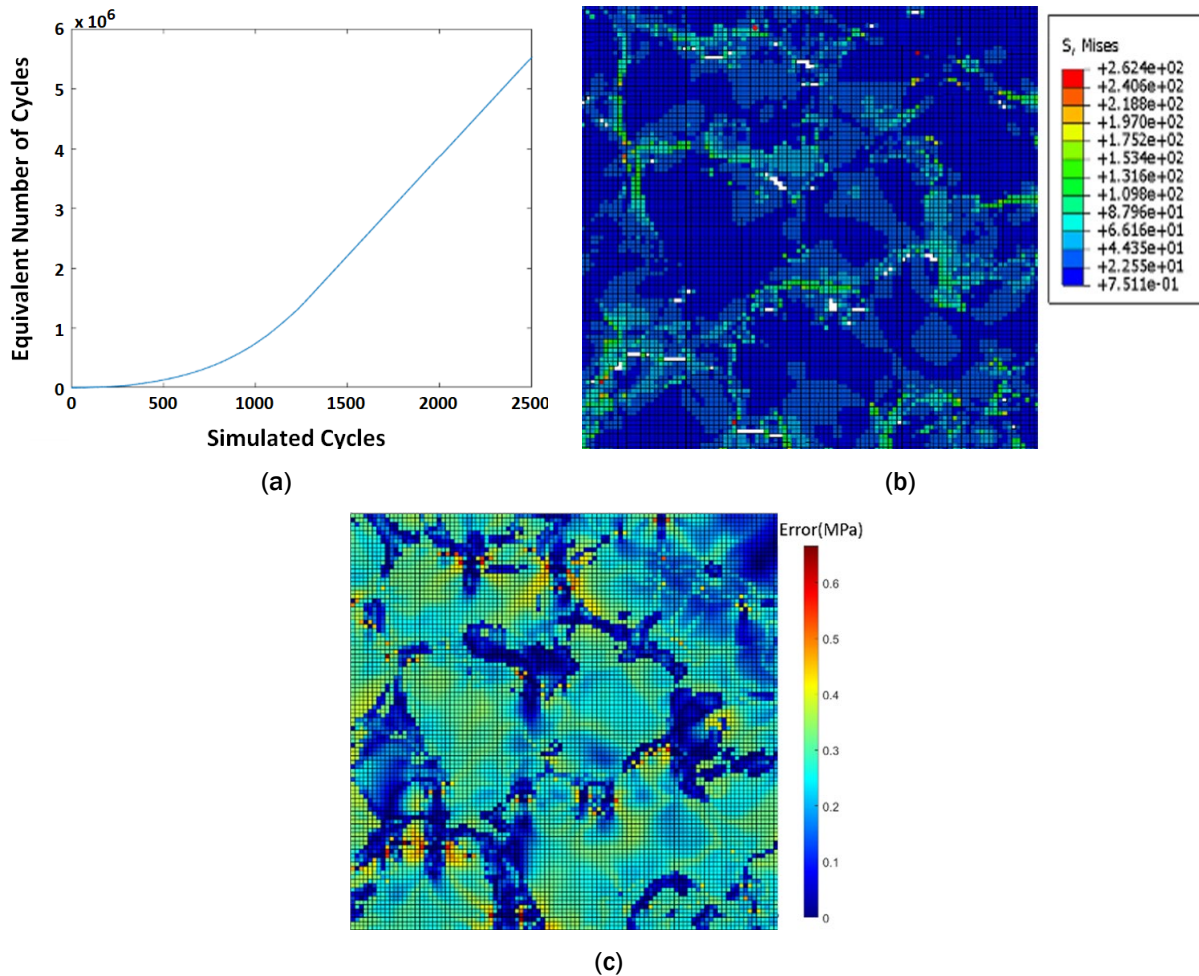


Figure II.1.8.10. (a) The efficiency of the accelerated fatigue model for HCF. The x and y axes correspond to actual simulated cycles and equivalent simulation cycles, respectively. Stress distribution at 10,000 cycles in an accelerated model solution is shown in (b) and the difference (absolute error, unit: MPa) from the reference solution is shown in (c), respectively. The model size is 20 μm \times 20 μm . Source: ORNL.

Project 2B: High Intensity Thermomechanical Processes (PNNL)

During FY 2021, the primary focus of this work was the first task (i.e., to refine the as-cast microstructure through the application of local ultrasonic intensification during casting). This task was accomplished through a combination of thermal modeling and casting experiments. The goal of thermal modeling was to help design a mold suitable for laboratory experiments and to achieve cooling rates relevant for automotive components cast through permanent mold casting techniques. Abaqus, a commercial finite element analysis software [16], was used to perform thermal transient simulations and guide the mold design for Al casting to achieve cooling rates during solidification in the approximate range of 0.3 to 1°C/s. These cooling rates are typically associated with permanent mold casting techniques used to produce cast automotive components [19] and should allow sufficient time for ultrasound to be applied during solidification. Parameters such as the initial mold temperature, mold wall thickness, and width of the casting were varied to identify the casting conditions that were achieved via cooling rates within the above-mentioned range. The initial temperature of the molten alloy was 700°C and the initial temperature of the steel mold was either 25, 250, or 400°C. The thickness of the steel mold was either 0.5 or 1 in. and the width of the casting varied from 0.25 to 6 in.

For the casting experiments, local ultrasonic intensification was applied during the solidification of A356 Al alloy by applying 20 kHz ultrasonic vibrations via a 0.5 in. diameter Ti-6Al-4V probe. The cooling rate during solidification was measured with a sacrificial K-type thermocouple placed inside the mold. Cast specimens, produced without the application of ultrasound, provided baseline microstructures for comparison against the microstructures produced with ultrasonic intensification. Both types of cast specimens were sectioned and polished using traditional metallographic techniques and the microstructures were analyzed using optical and electron microscopy.

Figure II.1.8.11 shows the cooling rates during solidification at the hottest location in the casting as a function of the width of the casting for various initial mold temperatures and for a mold wall thickness of 0.5 in. The thermal simulations show that the cooling rate during solidification decreases as the width of the casting increases and as the initial temperature of the mold increases. In other words, the cooling rate during solidification can be reduced by increasing the thermal mass (i.e., volume of molten Al) and/or by preheating the mold to reduce the thermal gradient during cooling. According to the thermal simulations, cooling rates of less than 1°C/s can be achieved by casting a plate at least 1 in. wide in a steel mold with 0.5 in. thick walls and an initial mold temperature of 400°C. Other combinations of casting width and initial mold temperature can also be selected to achieve a desired range of cooling rates.

For the casting experiments, two types of Al castings were produced: one without ultrasound to produce a baseline microstructure and one with the application of a local ultrasonic field to demonstrate the ability of this approach to produce a refined, non-dendritic, as-cast microstructure. The average cooling rate during solidification was measured to be ~2°C/s to 3°C/s. Although these cooling rates are somewhat higher than desired, they are of the right order of magnitude and can be further lowered by preheating the mold, as shown by the results of the thermal simulations presented in Figure II.1.8.11.

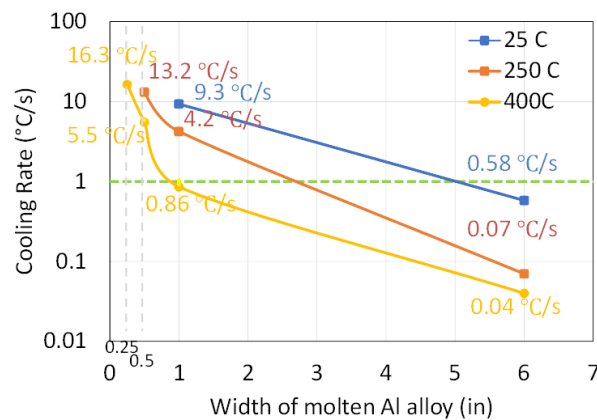


Figure II.1.8.11. The cooling rates during solidification at the hottest location in the Al casting as a function of the width of the casting for different initial mold temperatures and a mold wall thickness of 0.5 in.
Source: PNNL.

Figure II.1.8.12 shows that the specimen cast without ultrasound has a coarse dendritic as-cast microstructure that one would expect to see in a typical casting. The average grain size of the dendrites was measured to be 155 μm using electron backscatter diffraction and the average secondary dendrite arm spacing was measured to be 23 μm using OM. In contrast, Figure II.1.8.13 shows that the specimen cast with ultrasound has a non-dendritic as-cast microstructure with two distinct morphologies: (a) globular grains with an average grain size of 19 μm ; and (b) very fine grains with an average grain size of 9 μm . The globular grains are 88% smaller in grain size than the dendritic grains in the baseline microstructure, while the very fine grains are 94% smaller in grain size than the dendritic grains. The globular grains represent the majority of the non-dendritic microstructure, while the very fine grains were only observed within a few mm of the location of the ultrasound probe. The refined microstructural morphologies shown in Figure II.1.8.13 exemplify the goal of

the first task, while the rounded, globular grains are expected to provide increased strength, tensile ductility, and fatigue life as compared to the dendritic microstructures of conventional castings [14, 15]. Thus, these initial results successfully demonstrate the potential of ultrasonic processing to improve the as-cast microstructure. Work conducted in the next FY will measure the mechanical properties of ultrasonically refined microstructures to quantify expected improvement in mechanical properties. Additionally, the second task of developing a thermal intensification approach for local strengthening in a casting will be initiated.

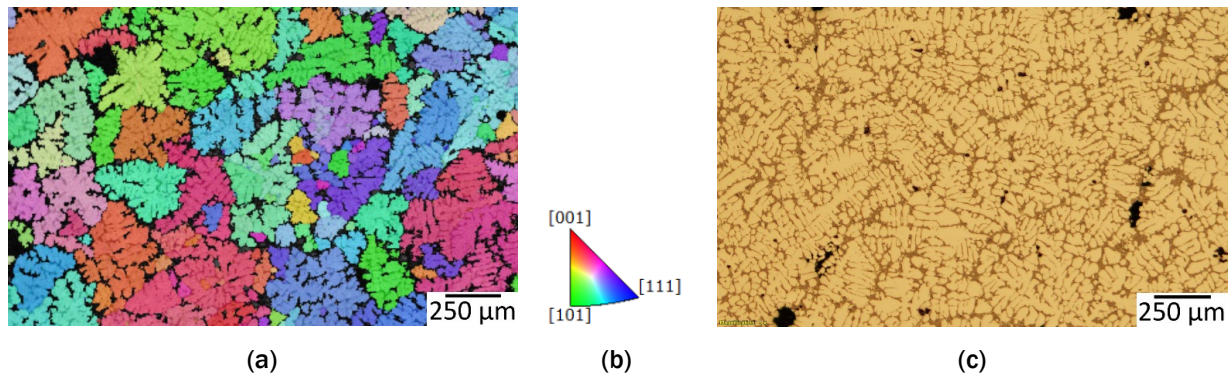


Figure II.1.8.12. The coarse dendritic microstructure of the specimen cast without ultrasound is depicted in (a) an inverse pole figure (IPF) map, where each grain is identified by a color that corresponds to its crystallographic orientation according to the color scheme in (b). (c) An OM from the same region shown in (a). Source: PNNL.

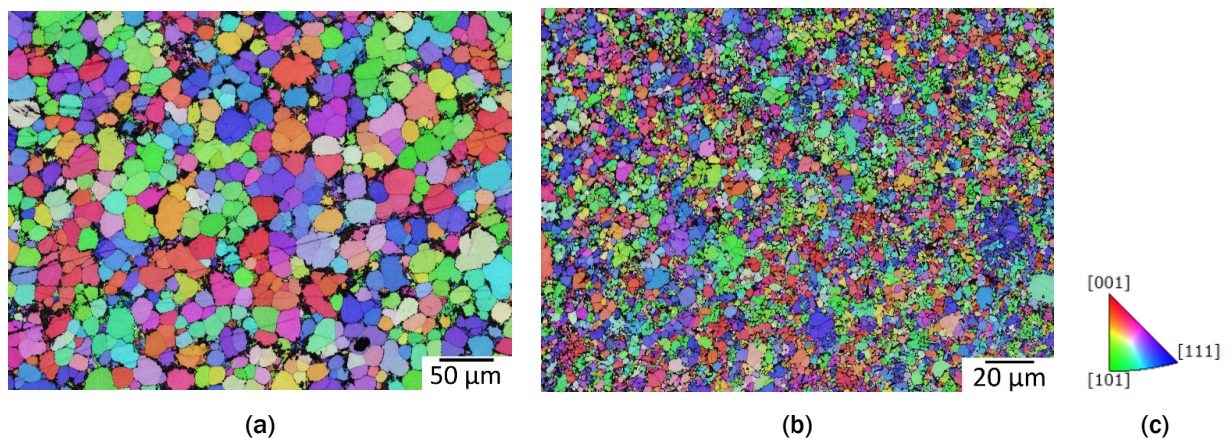


Figure II.1.8.13. Two IPF maps of the specimen cast with ultrasound identify non-dendritic (a) globular grains and (b) very fine grains. The colors correspond to the crystallographic orientation of each grain according to the color scheme in (c). Source: PNNL.

Project 2C: Cast-and-Print: AM for Localized Property Enhancement (ORNL)

The laser hot-wire AM process was used to deposit an approximately 25 mm tall, 25 mm long, and 10 mm wide 4043 wall on a section from an A356.2 die-cast ingot. The laser hot-wire processing parameters were 4000 W laser power, 104 W wire heating power, 88 in/min wire feed rate, 406 mm/min traverse rate, and 20L/min argon shielding gas flow. A notable amount of heat accumulation was noted during initial tests, so a one-minute forced convection cooling cycle was added between each layer using a fan machine tool attachment. The dilution of the AM melt pool by the substrate during cast-and-print processing was much less a concern than in the Thrust 1 form-and-print task for AM on wrought sheet alloys, since cast alloys are typically designed to possess inherently good resistance to hot cracking.

Sub-scale SS-J3 tensile specimens [20] were extracted for tensile testing. Metallographic sections for microscopic inspection were also removed. The partially sectioned specimen, substrate, and locations of the tensile specimens are shown schematically in Figure II.1.8.14(a). The interface specimen was cut so that the center of the gauge section was aligned with the top surface of the substrate. Figure II.1.8.14(b) shows the results of the tensile tests for the SS-J3 specimens machined from three areas of the build: (1) vertical (perpendicular to the BD, from within the deposited material); (2) horizontal (in the build plane of the deposited material); and (3) interface (vertical but centered on the interface of the AM deposit and cast substrate). The YS of the vertical sample is lower than the horizontal and interface samples, while the ductility of the vertical samples is higher. The strength of the interface and horizontal samples are similar, measuring approximately 95 MPa and 160 MPa for the YS and TS, respectively. All samples exhibited good ductility with over 15% elongation.

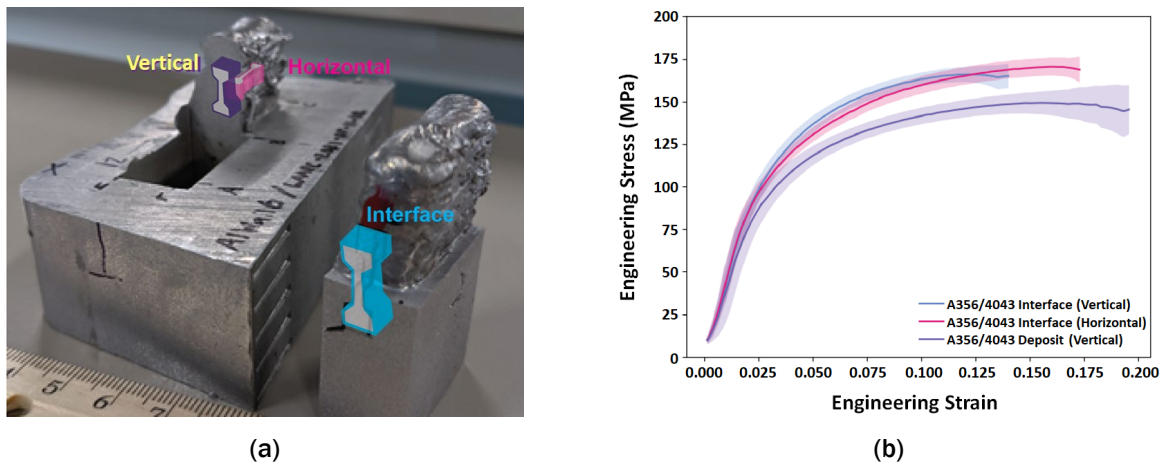


Figure II.1.8.14. (a) A schematic of sectioned alloy 4043 wall deposited on an alloy A356.2 ingot. The extracted SS-J3 vertical, horizontal, and interface specimen locations are shown schematically with the labeled outlines. (b) Tensile test results corresponding to marked locations in (a). The lines show the average of all samples, while the bands show a ± 1 standard deviation. Source: ORNL.

The reason for the modest difference in properties for the interface and vertical samples can be explained through the differences in the scale of the microstructure and the compositions of the deposited material. Figure II.1.8.15(a) shows the Vickers hardness of the material from microhardness testing using a 5 kg load. A decrease in hardness can be seen moving from the cast A356.2 substrate outward to the deposited material. Figure II.1.8.15(b) shows that the primary and secondary arm spacing of the cast material is much larger than that of the deposited 4043 material. This indicates that the higher hardness of the substrate is likely due to Mg_2Si precipitates rather than Hall Petch strengthening due to the scale of the microstructure. The deposited 4043 does not have Mg in its composition, so Hall Petch type strengthening due to the characteristic length of the microstructure is expected to be the main strengthening mechanism.

There are several microstructural features that correlate with the observed mechanical properties of the part. Figure II.1.8.16(a) shows the microstructure at the fusion zone boundary/interface of the A356.2 cast substrate and the deposited 4043 material. There is a stark difference in the size of the primary Al phase, as depicted by the light phase, and the eutectic structure, as depicted by the darker phase. Figure II.1.8.16(b) shows a region within the deposited material at the interface between two layers indicated as the area between the dashed lines. When the material on the top was deposited, the HAZ in the previous layer experienced a coarsened primary Al morphology and some apparent spheroidization of the eutectic silicon. While work is ongoing to characterize the properties of the HAZ, it is hypothesized that the increased ductility and reduced strength in the vertical direction is a consequence of these regions.

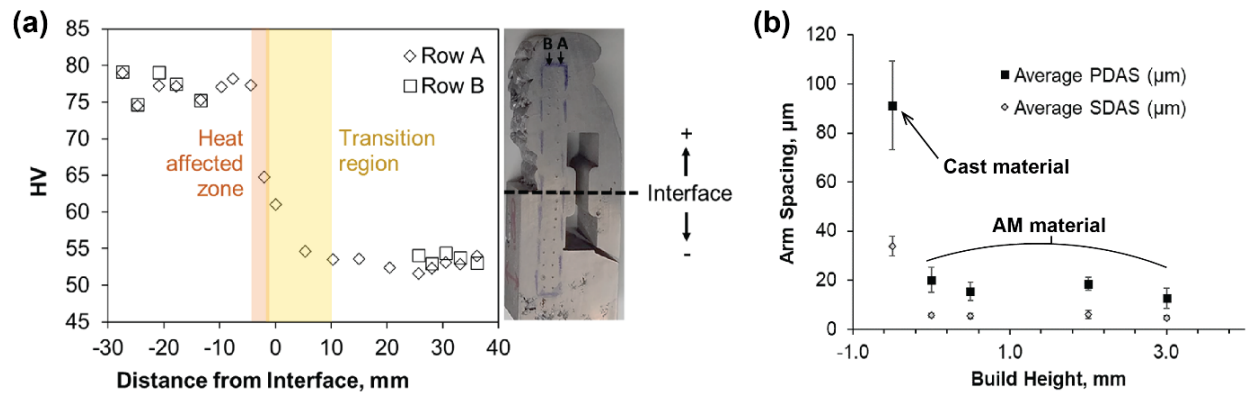


Figure II.1.8.15. (a) Vickers hardness measurements as a function of height in the sample. The inset shows the location of the measurements. (b) Primary dendrite arm spacing (PDAS) and secondary dendrite arm spacing (SDAS) in the cast A356.2 and as-built AM 4043 as a function of build height. Source: ORNL.

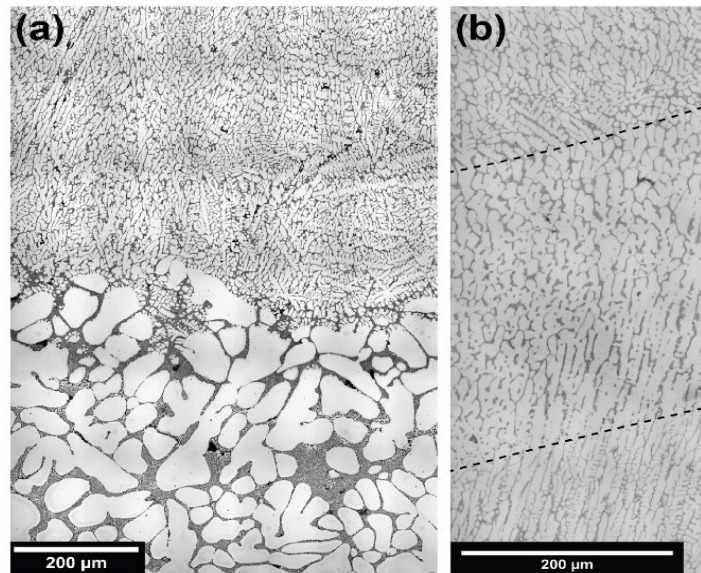


Figure II.1.8.16. (a) An OM showing the interface region between cast A356.2 (bottom) and AM 4043 (top). (b) HAZ between layers. The upper dashed line represents the fusion zone of the upper layer, and the bottom dashed line represents the approximate boundary of the HAZ in the previous layer. Images are oriented with the BD upward and the wire travel direction out-of-plane with the page. Source: ORNL.

Conclusions

Project 2A1: FSP of Die-Cast-Al Alloys (PNNL)

FSP has been evaluated as a TMP technique to locally induce microstructural changes in a thin-wall HPDC A380 alloy. FSP was carried out on flat plate geometry to evaluate the effect of processing on coupon level specimen properties. Microstructural characterization along with quasi-static and dynamic mechanical property evaluation indicates promising results for the viability of the FSP method. Two to ten times higher fatigue life and increased yield and elongation performance was demonstrated after FSP. This performance increase in some cases exceeded the performance of even the die-wall (skin) region known to have improved microstructures in HPDC materials. Current efforts have been aimed at understanding the effect of FSP in premium quality HPDC alloys (e.g., Aural-2).

Project 2A2: Power Ultrasonic Surface Processing of Die-Cast-Al Alloys (ORNL)

The following accomplishments were made in year one (FY 2021):

- Achieved the targeted PUSP process load of ~250 lb. to 300 lb. This is essential for future single-side localized processing of cast-Al component surfaces with a robotic system.
- Demonstrated considerable surface microstructure refinement by PUSP.
- Identified the process conditions by process simulations for compressive surface residual stress and microstructure refinements.
- Developed a novel ultrafast microstructure-based fatigue model, which makes it possible to conduct simulations of HCF and study the effect of surface modification on the fatigue life. This model will be used to provide guidance on the desired microstructure for surface processing and will reduce the cost and required amount of HCF experiments.

Project 2B: High Intensity Thermomechanical Processes (PNNL)

Thermal simulations show that cooling rates in the range of 0.3°C/s to 1°C/s can be achieved during solidification of an Al alloy plate through a combination of plate thickness and mold preheat temperature. Present simulations, using a steel mold with a wall thickness of 0.5 in. and a mold preheat temperature of 400°C, show that a plate with a thickness of 1 in. or more can serve as a test specimen where the cooling rates are in-line with the typical cooling rates of permanent mold casting techniques [19].

Casting experiments successfully demonstrated the feasibility of using ultrasound intensification to refine the as-cast microstructure. Al alloy A356 was cast with and without the application of a local ultrasonic field. Casting with a simultaneous application of ultrasound, both refined the size of Al grains and changed the morphology of the microstructure from dendritic to non-dendritic. The globular grains of the non-dendritic microstructure are 88% smaller than the grains of the dendritic microstructure, and the very fine grains of the non-dendritic microstructure are 94% smaller than the grains of the dendritic microstructure.

Work conducted in FY 2022 will compare the TS and ductility of the baseline dendritic microstructure to those of the ultrasonically modified, non-dendritic microstructure. Additionally, work will commence under Task 2 on the development of thermal intensification approaches to locally strengthen the casting through heat treatments.

Project 2C: Cast-and-Print: AM for Localized Property Enhancement (ORNL)

The deposition of 4043 on A356.2 substrate via the cast-and-print process produced a wall with reasonable strength and good ductility. The laser hot-wire process used for AM in the cast-and-print process produces a heterogeneous, fine microstructure due to the layer-by-layer nature of the deposition, which may be leveraged to improve part properties.

Key Publications

1. Samanta, A., et al., 2022, “Microstructural modification of a high-pressure die-cast A380 alloy through friction stir processing and its effect on mechanical properties,” Accepted for Presentation at the TMS 2022 Annual Meeting, Anaheim, CA, USA, 27 February – 3 March 2022.
2. PNNL, 2021, “Fabrication of castings with local application of ultrasound during solidification,” Invention Disclosure.

References

1. Hartlieb, M., 2013, “Aluminum alloys for die-casting,” *Die-Casting Engineer*, May 2013, pp. 40–43.
2. Casarotto, F., A. J. Franke, and R. Franke, 2012, “HPDC aluminum alloys for automotive applications,” in Rowe, J. (ed.), *Advanced Materials in Automotive Engineering*, Ch. 6, Woodhead Publishing, Sawston, U. K., pp. 109–149.

3. Niu, X. P., B. H. Hu, I. Pinwill, and H. Li, 2000, "Vacuum-assisted high-pressure die-casting of aluminum alloys," *J. Mater. Process. Technol.*, Vol. 105, Nos. 1–2, pp. 119–127.
4. Kurz, W., and D. J. Fisher, 1998, *Fundamentals of Solidification, 4th Edition*, Trans. Tech. Publications Uetikon-Zuerich, Switzerland.
5. Dehoff, R. R., M. M. Kirka, W. J. Sames, H. Bilheux, A. S. Tremsin, L. E. Lowe, and S. S. Babu, 2015, "Site-specific control of crystallographic grain orientation through electron beam additive manufacturing," *Mater. Sci. Technol.*, Vol. 31, No. 8, pp. 931–938.
6. Raplee, J., A. Plotkowski, M. M. Kirka, R. Dinwiddie, A. Okello, R. R. Dehoff, and S. S. Babu, 2017, "Thermographic microstructure monitoring in electron beam additive manufacturing," *Sci. Rep.*, Vol. 7, Art. 43554.
7. Thomas, W. M., E. D. Nicholas, J. C. Needham, M. G. Murch, P. Templesmith, and C. J. Dawes, 1991, "Friction welding," Great Britain Patent Application 9125978.8, December 1991.
8. Mishra, R. S., M. W. Mahoney, S. X. McFadden, N. A. Mara, and A. K. Mukherjee, 2000, "High strain rate superplasticity in a friction stir processed 7075 Al alloy," *Scr. Mater.*, Vol. 42, pp. 163–168.
9. Jana, S., R. S. Mishra, J. B. Baumann, and G. Grant, 2010, "Effect of friction stir processing on fatigue behavior of an investment cast-Al–7Si–0.6 Mg alloy," *Acta Mater.*, Vol. 58, No. 3, pp. 989–1003.
10. Huang, H., J. Chen, Y. C. Lim, Z. L. Feng, X. H. Hu, J. H. Cheng, and X. Sun, 2019, "Heat generation and deformation in ultrasonic welding of magnesium alloy AZ31," *J. Mater. Process. Tech.*, Vol. 272, pp. 125–136.
11. Wang, F., D. Eskin, J. Mi, C. Wang, B. Koe, A. King, C. Reinhard, and T. Connolley, 2017, "A synchrotron x-radiography study of the fragmentation and refinement of primary intermetallic particles in an Al-35 Cu alloy induced by ultrasonic melt processing," *Acta Mater.*, Vol. 141, pp. 142–153.
12. Zhang, Z., Wang, C., Koe, B., Schlepütz, C. M., Irvine, S., and Mi, J. 2021. "Synchrotron X-ray Imaging and Ultrafast Tomography *In-Situ* Study of the Fragmentation and Growth Dynamics of Dendritic Microstructures in Solidification Under Ultrasound." *Acta Mater.*, Vol. 209, No. 116796, pp. 1–12.
13. Khalifa, W., Y. Tsunekawa, and M. Okumiya, 2008, "Effect of ultrasonic melt treatment on microstructure of A356 aluminum cast alloys," *Int. J. Cast Met. Res.*, Vol. 21, No. 1–4, pp. 129–134.
14. Puga, H., J. Barbosa, S. Costa, S. Ribeiro, A. M. P. Pinto, and M. Prokic, 2013, "Influence of indirect ultrasonic vibration on the microstructure and mechanical behavior of Al-Si-Cu alloy," *Mater. Sci. Eng. A*, Vol. 560, pp. 589–595.
15. Eskin, G. I., 2001, "Broad prospects for commercial application of the ultrasonic (cavitation) melt treatment of light alloys," *Ultrason. Sonochem.*, Vol. 8, pp. 319–325.
16. Dassault Systemes, 2019, *Abaqus. V. 2019*, Windows/x-64, Dassault Systemes, Vélizy-Villacoublay, France.
17. Aigner, R., M. Leitner, M. Stoschka, and C. Hanneschälger, 2018, Modification of a defect-based fatigue assessment model for Al-Si-Cu Cast Alloys," *Materials*, Vol. 11, No. 12, Art. 2546.
18. Narayanan, G., 2021, "Probabilistic fatigue model for cast alloys of aero engine applications," *Int. J. Struct. Integr.*, Vol. 12 No. 3, pp. 454–469.
19. Lampman, S., 2018, "Permanent mold casting of aluminum alloys," In Anderson, K., J. Weritz, and J. G. Kaufman (eds.), *ASM Handbook 2A*, Materials Park, OH, USA, pp. 209–231.
20. Gussev, M., J. T. Busby, K. G. Field, M. A. Sokolov, and S. E. Gray, 2015, "Role of scale factor during tensile testing of small specimens," In Sokolov, M. A., and E. Lucon (eds.), *Small Specimen Test Techniques, 6th Volume*, ASTM International, West Conshohocken, PA, USA, pp. 31–49.

Acknowledgments

Project 2A1: FSP of Die-Cast-Al Alloys (PNNL)

The PI gratefully acknowledges the help and technical support from the following individuals during the execution of this project: A. Samanta, R. Seffens, A. Guzman, and T. Roosendaal. Technical discussions with G. Grant, D. Gothehold, D. Herling and Z. Feng are gratefully acknowledged as well. Finally, the PI extends his sincere thanks to the DOE Technology Manager, Ms. S. Kleinbaum, for her support to the LMCP Program.

Project 2B: High Intensity Therrmomechanical Processes (PNNL)

This project, and the LMCP Program, is a collaborative effort across several DOE National Laboratories. We are thankful for technical discussions with Drs. A. Sabau, A. Plotkowski and T. Watkins at ORNL and Drs. D. Singh, A. Chuang, and J. Thomas at ANL. Technical contributions of the PNNL staff supporting this research are gratefully acknowledged as well. In particular, we are grateful to Dr. K. Rader for leading the experimental task on ultrasonic processing. Dr. Rader was assisted by Mr. J. Helgeland and Dr. J. Darsell in his ultrasonic process development and casting experiments; Drs. K. Balusu and A. Soulami led the thermal modeling effort; Drs. M. Efe and X. Ma contributed to overall project coordination; and Mr. A. Guzman and N. Canfield assisted with metallography and microscopy. We also acknowledge discussions with Mr. D. Weiss at Eck Industries pertaining to Al casting practice and approaches to implement new processing techniques in industrial applications.

Project 2C: Cast-and-Print: AM for Localized Property Enhancement (ORNL)

We gratefully acknowledge R. Duncan and A. Marquez Rossy for their assistance in preparing and testing the tensile specimens used in this work.

II.1.9 Light Metal Core Program - Thrust 3 - Selective Processing of Magnesium Castings - Localized Property Enhancement for Cast Magnesium Alloys (Pacific Northwest National Laboratory)

Vineet V. Joshi, Co-Principal Investigator

Pacific Northwest National Laboratory
900 Battelle Blvd.
Richland, WA 99354
E-mail: vineet.joshi@pnnl.gov

Mageshwari Komarasamy, Co-Principal Investigator

Pacific Northwest National Laboratory
900 Battelle Blvd.
Richland, WA 99354
E-mail: mageshwari.komarasamy@pnnl.gov

Jlheon Jun, Co-Principal Investigator

Oak Ridge National Laboratory
1 Bethel Valley Rd.
Oak Ridge, TN 37831
E-mail: junj@ornl.gov

Sarah Kleinbaum, DOE Program Manager

U.S. Department of Energy
E-mail: sarah.kleinbaum@ee.doe.gov

Start Date: October 1, 2020	End Date: September 30, 2023
Project Funding (FY 2021): \$1,100,000	DOE share: \$1,100,000 Non-DOE share: \$0

Project Introduction

Being the lightest of structural materials, Mg and its alloys are extremely attractive for use in the transportation industry. Widespread utilization of these alloys will improve driving ranges and reduced greenhouse gas emissions [1, 2]. Owing to its ability to produce complex components quickly and at a low-cost, the HPDC process is generally used to fabricate cast-Mg alloy components. Almost 90% of the automotive Mg alloy cast components are currently manufactured via this process. The scientific and engineering challenges preventing more widespread adoption of Mg castings focus on the specific property requirements of the application. Mg castings have some of the same challenges as Al castings, but there are some differences that if overcome could result in Mg substitution for heavier, higher density materials. The primary technical challenges for Mg castings are corrosion, casting microstructural integrity (for durability and fatigue), the strength/ductility tradeoff for structural applications, low creep strength (in applications near elevated temperature engine, power electronics or battery locations), and an inherently low modulus relative to alternative materials. Under the umbrella of the LMCP, the projects under Thrust 3 focus on these scientific and engineering challenges that are preventing the more widespread adoption of Mg castings—and more specifically—susceptibility to corrosion-induced property degradation and fatigue and strength limitations due to anisotropy and microstructure defects.

Objectives

In alignment with the overarching goal of the LMCP consortium, in this thrust we will develop and demonstrate scalable, cost-effective processing methods to locally enhance the properties of Mg alloys to enable broader implementation of lightweight alloys in vehicles. Within this thrust, the project has two main objectives, which are: (1) the improvement of localized corrosion properties in Project 3A; and (2) the improvement of localized mechanical properties in Project 3B.

Approach

The projects within Thrust 3 are addressing these scientific challenges with two directions—one focused on local surface modification to enhance corrosion resistance, and the other on local TMP techniques to address the mechanical property shortcomings of typical commercial Mg alloy castings, as shown in Figure II.1.9.1. To accomplish this, processing strategies and techniques are being developed as described in Figure II.1.9.1 and guided by improved fundamental understanding of the underlying mechanisms using *ab initio* methods and advanced electrochemical potential measurement and microstructural characterization techniques. These efforts focus on HPDC AM60 and AZ91 alloy families but will also consider additional process or alloys based on automotive manufacturer and Tier 1 supplier input.

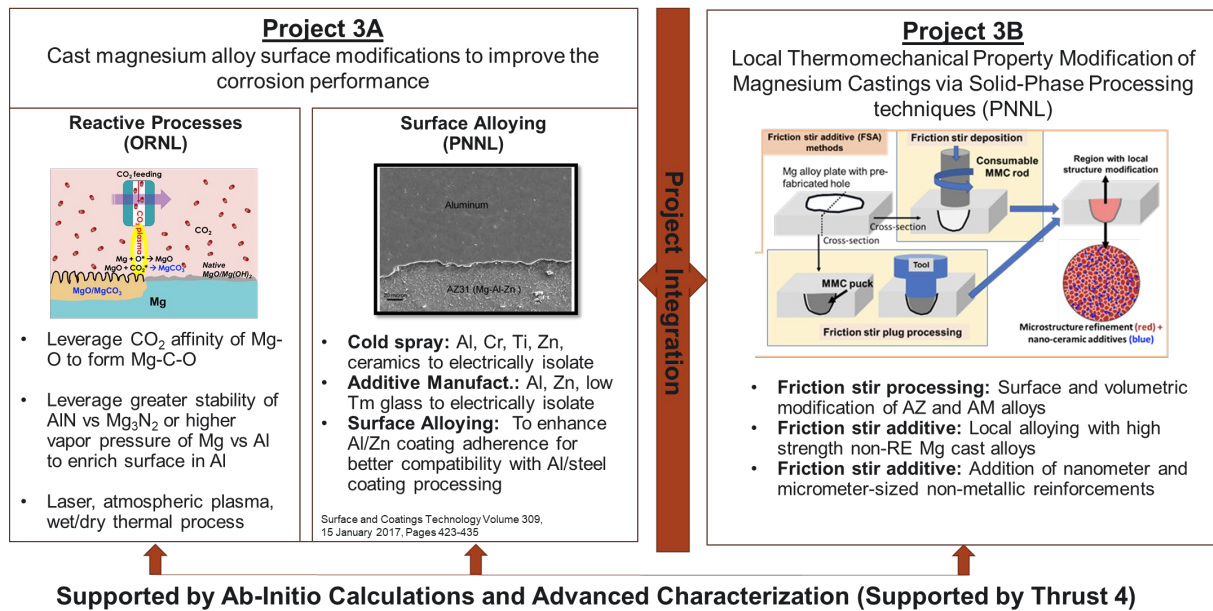


Figure II.1.9.1. Primary thrust areas for Project 3A: Surface Modification for improving Corrosion Properties and Project 3B: Improving Local Thermomechanical Treatments for Improving Mechanical Behavior of Mg Alloys. Source: PNNL.

Projects Under 3A

The projects within 3A perform localized surface modification in cast-Mg components to help improve their overall corrosion performance. The end goal of the project is to improve corrosion resistance, eliminate or minimize corrosion-induced fatigue, provide a better galvanic coupling interface for faying surfaces and, if needed, improve surface receptivity for subsequent top coating processes on Mg castings. In this ORNL/PNNL collaborative effort, we plan to accomplish the project goals by employing a multifaceted approach that relies on replacing the corrosion-susceptible MgO-Mg(OH)₂ native film, either directly or indirectly, by modifying the alloy surface composition. This project is further divided into two sub-projects—Project 3A1 and Project 3A2—which investigate the local surface modification using reactive processes and surface alloying, respectively. Within each project, different novel pathways are being explored and the most promising technique will be downselected for further development as described in the sections that follow.

Project 3A1 (Reactive Processes – ORNL)

The ORNL task team is pursuing three surface-treatment/modification pathways for cast-Mg: (1) Nd-YAG laser; (2) gas-ignited plasma; and (3) Li salt solution treatment + thermal CO₂ annealing. A schematic of each of these methods is shown in Figure II.1.9.2. The laser treatment method utilizes local heating to cause selective evaporation and redistribution of alloy elements in fusion zones, as well as microstructural evolution upon rapid cooling for higher corrosion resistance. The gas-ignited plasma torch provides activated gas molecules with local heating on the alloy surface to promote the formation of reaction layer(s) that can function as a corrosion barrier. CO₂ thermal treatment on preloaded Li salt on an AZ91D alloy is designed to form a Mg-, O-, and C-rich surface layer, including crystalline MgCO₃, which all have the potential to protect Mg alloys from corrosive environments.

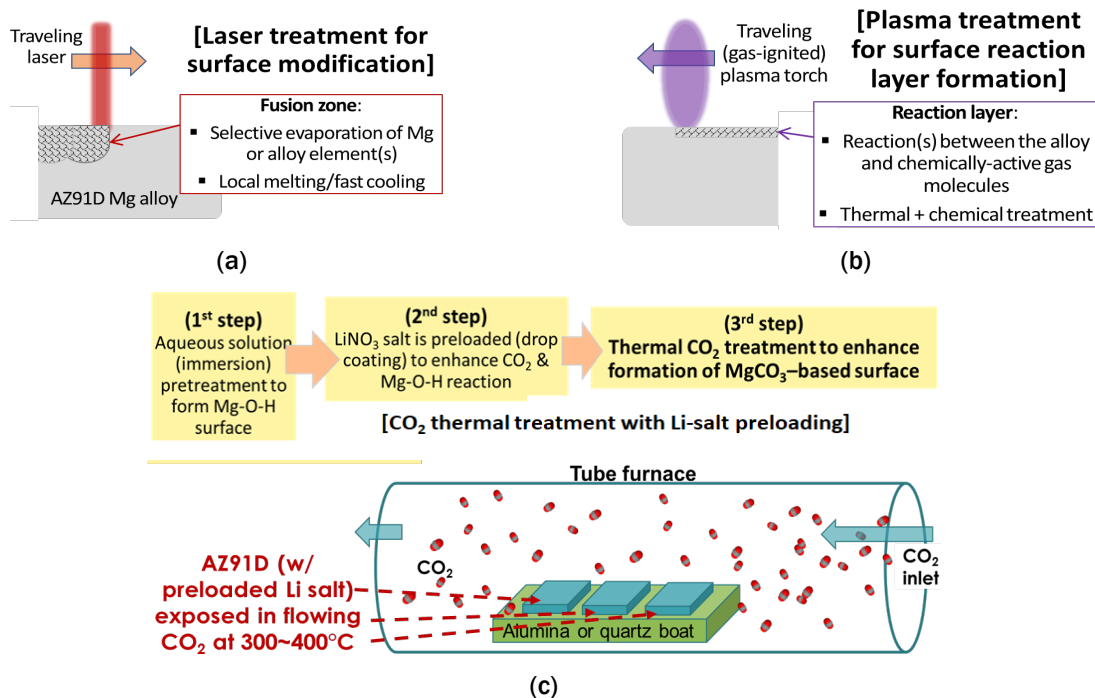


Figure II.1.9.2. Schematic description of (a) laser, (b) plasma, and (c) thermal CO₂ treatments to achieve corrosion-resistant surfaces on AZ91D Mg alloys. Source: ORNL (Project 3A2 Surface Alloying – PNNL).

The PNNL team is exploring two surface modification techniques by alloying using: (1) cold spray and (2) reactive melting deposition. Commercially pure (CP) Al and an Al6061 alloy are coated on top of cast-Mg alloys using the cold spray method, and then Zn is coated on the Mg alloys using the reactive melting coating method. Successfully doing this will completely change the corrosion characteristics of the component. These processes are more amenable to conventional conversion or plasma electrolytic and epoxy electro-coat techniques, while at the same time will mitigate the challenges associated with joining Mg-cast components with Al or steel components. Materials characterization of the coated and post-corrosion samples was accomplished using correlative multilength-scale microscopy and microanalysis and X-ray CT.

Complementing this work, micro-galvanic behavior was studied at the Mg-coating interfaces by scanning electrochemical cell microscopy (SECCM) [1, 2]. Measurement protocol was optimized for the SECCM measurement in the microscopic corrosion study to map the entire area across the interface of a welded joint. Corrosion evaluation of surface treated AZ91D samples were primarily performed by electrochemical impedance spectroscopy (EIS) measurement. The impedance data from the measurements were fitted by equivalent circuit models to determine corrosion reaction resistance, either R2 or R2 + R3.

Project 3B (Thermomechanical Property Modification – PNNL)

The purpose of this project is to perform localized enhancement of the mechanical properties, such as ductility and fatigue properties of the HPDC cast-Mg components, using FSP and friction stir additive methods. In addition, the project will develop ways for localized microstructure modification, measure the change in resultant properties, and demonstrate the property improvement in AZ91 and AM60 HPDC Mg-cast components. In order to understand the FSP processing parameters, the tool rotational speed and traverse rate were varied. The processing temperature was maintained between 400-450°C. Furthermore, single and overlapping double processing runs were carried out on both AZ91 and AM60 alloys. The processing runs that exhibited a defect-free surface were subjected to microscopy and mechanical property characterization. The transverse section of the processed regions is subjected to optical microscopy analysis to investigate the presence or absence of processing defects. Furthermore, post-aging heat treatments at 168°C for 16 hours and 200°C for 2, 4, 8, 12, and 24 hours, respectively, were carried out and then followed by hardness measurements. Tensile property was measured in the as-cast, as-processed, and in aged conditions. Fatigue property analysis in stress-controlled configuration with the fatigue ratio (e.g., the ratio of maximum to minimum stress) of $R=0.1$ is ongoing in the as-cast and as-processed conditions. SEM in BSE mode was completed using the Field Electron and Ion (FEI) Company™ Quanta 3D field emission gun dual beam FIB/SEM. Most of the presented results are for the AZ91 alloy.

Results

Microstructural Characterization of HPDC Mg Alloys

As-cast material characterization via optical microscopy and SEM are presented in Figure II.1.9.3. The riser, gate, and microscopy sample locations are shown on a HPDC cast-Mg plate, as presented in Figure II.1.9.3(a). Microscopy analysis of AZ91 and AM60 are presented in Figure II.1.9.3(b) through Figure II.1.9.3(d) and Figure II.1.9.3(e) through Figure II.1.9.3(f), respectively. Both the plates exhibited porosity bands as marked by the solid white arrows in Figure II.1.9.3(b), Figure II.1.9.3(c), Figure II.1.9.3(e), and Figure II.1.9.3(f). For the same casting configuration, AM60 exhibited a higher porosity fraction as compared to AZ91. The porosity fraction in the AZ91 and AM60 were ~1-1.6% and 2-2.8%, respectively. Similar levels of porosity were observed in the super vacuum HPDC AZ91 and AM60 shock tower [1]. Additionally, SEM-BSE imaging revealed the presence of $Mg_{17}Al_{12}$ (β phase, marked by red solid arrows) and solute segregation (marked by yellow dotted arrows) in the Mg-Al matrix, as observed in Figure II.1.9.3(d) and Figure II.1.9.3(g). Hardness measurements taken from 12 locations on the as-cast AZ91 and AM60 plates using microhardness testing and were averaged out to 74 ± 5 and 59 ± 6 HV0.2, respectively.

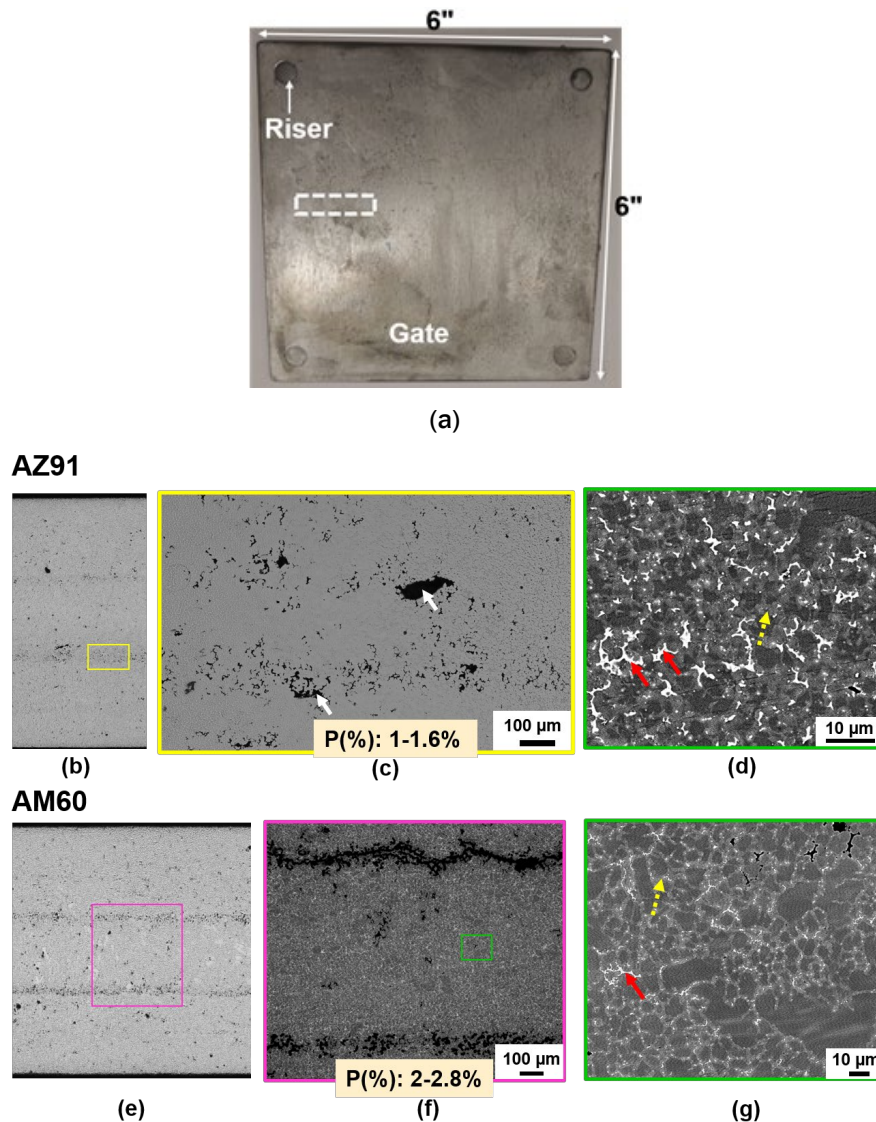


Figure II.1.9.3. (a) An OM image of the HPDC plate with riser, gate, and sample locations marked. (b) The porosity band, (c) the pores in the band, and (d) the SEM-BSE imaging of various phases in the AZ91 alloy (upper images). (e) The porosity band, (f) the pores in the band, and (g) the SEM-BSE imaging of various phases in the AM60. The higher magnification SEM-BSE images in (d) and (g) show the presence of the β phase, the solute segregation, and the Mg-Al matrix. Source: PNNL.

Project 3A1

Laser treatments on AZ91D Mg alloy coupons were performed by an industrial partner, Volunteer Aerospace (Knoxville, TN). The initial attempt used linear laser treatments, primarily varying laser beam size, power, and travel speed. Key characterization and modeling results are presented in Figure II.1.9.4 for four different linear energy intensities (i.e., the values of laser power divided by travel speed). The calculated maximum cooling rates are 4.5×10^4 , 5×10^5 , and 1.5×10^6 K/s for 7.5, 2, and 0.75 W·s/mm laser conditions, respectively. Also presented are cross-sectional microscope images with EDS mapping for the linear intensity condition of 0.833 W·s/mm. Fusion zone depth and porosity both increased by increasing the laser energy intensity. The simulation of fusion zone dimensions resulting from different laser energy input and calculated cooling rates showed reasonable agreement with the observed fusion zones. EDS mapping analysis of fusion zones after laser treatment with an energy intensity of 0.833 Ws/mm showed Mg and Al were intermixed uniformly, unlike the alloy matrix where Al-rich phases exist separately. Based on the results of the linear laser

treatments, four laser process conditions with 7.5, 2, 1.5, and 0.75 W·s/mm in energy intensities were used for the area treatments of the AZ91D coupons. Area-treated AZ91D by respective energy intensities of laser processes are presented in Figure II.1.9.5. As observed, the treated surface was not visually homogenous with randomly distributed darker spots. To remove surface roughness resulting from laser treatment, the top surface of some treated AZ91D specimens was finished by 600 grit SiC paper, as observed in Figure II.1.9.5. As the fusion zone is quite deep (up to 1 mm), 600 grit finish did not completely remove fusion zone depth. EIS measurements were conducted to evaluate the corrosion resistance of AZ91D surfaces after laser treatments with and without additional SiC paper finish. With the exception of a laser intensity of 7.5 Ws/mm exhibiting a higher R value, laser treatment can only produce marginal improvement under a narrow process window. Results are summarized in Table II.1.9.1. All the laser specimens are individual data. The average corrosion reaction resistance from the baseline 600 grit finished AZ91D is also presented. All data were from the impedance spectra after 1 h immersion in 3.5% NaCl solution.

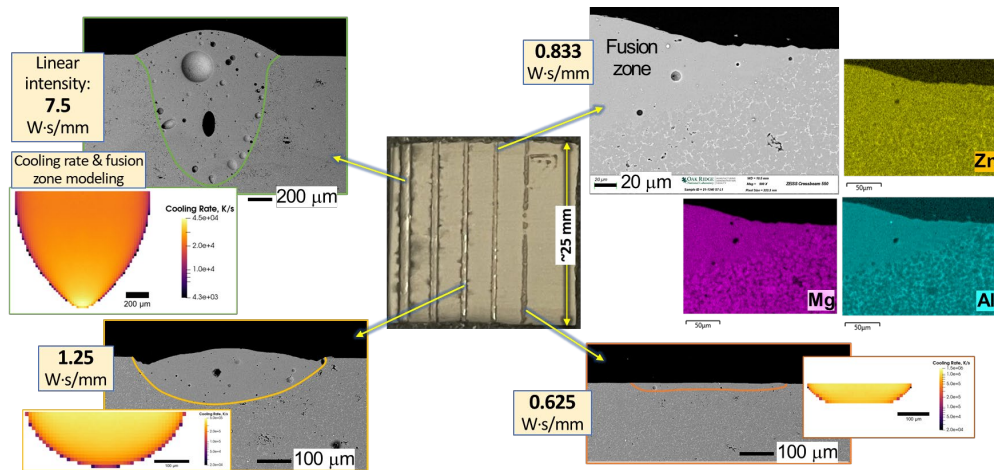


Figure II.1.9.4. AZ91D coupon with five linear laser treatments. Cross-sectional electron microscope images are also shown for the respective laser linear intensities. The fusion zone modeling results coupled with the three images were for the linear intensity conditions of 7.5, 2, and 0.75 Ws/mm, respectively. Source: ORNL.

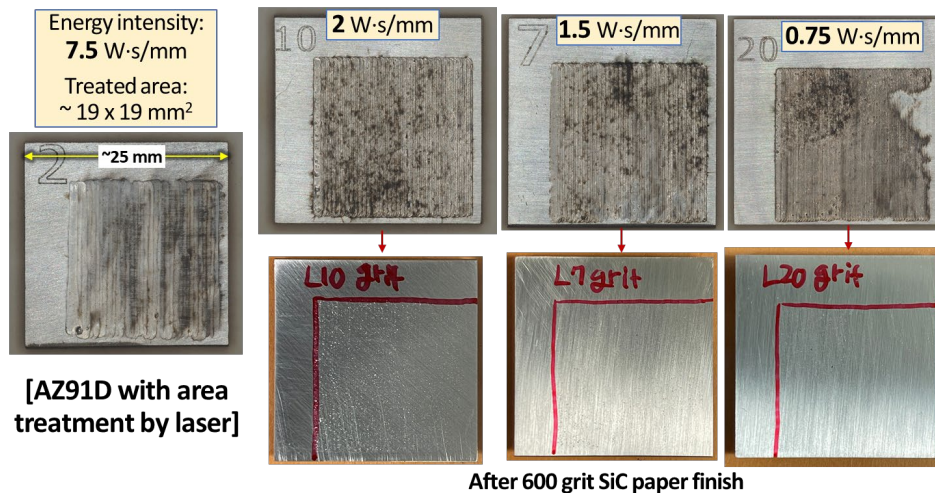


Figure II.1.9.5. AZ91D coupons treated with four linear intensities for a 19 × 19 mm² area. The sample with the 7.5 Ws/mm condition is as-laser-treated, while the other three specimens were surface-finished by 600-grit SiC paper to remove the surface roughness caused by the laser treatments. Source: ORNL.

Table II.1.9.1. Corrosion Reaction Resistance Determined by EIS for Laser-Treated AZ91D with Four Energy Intensities

Corrosion Reaction Resistance (ohm cm ²)	Laser processed	Laser Intensities	7.5 Ws/mm	2 Ws/mm	1.5 Ws/mm	0.75 Ws/mm
		As-treated	563	326	667	870
		Top-layer removed by 600 grit SiC	4000	1440	1842	1673
Untreated baseline 600 grit SiC finish		~2600±240 (average of 5 data)				

*Indicates without 600-Grit SiC finish on the laser-treated surfaces.

As noted in Table II.1.9.1, only one condition where AZ91D was treated by 7.5 W·s/mm laser and finished by 600-grit SiC paper showed marginally higher corrosion resistance than the baseline. On the other hand, the values of corrosion reaction resistance were notably lower in all the laser-treated samples with no 600-grit surface finish. This could be related to the increased surface roughness and surface area of the laser-treated samples. CO₂ thermal treatment of LiNO₃ preloaded AZ91D samples were used for EIS and hydrogen collection measurements. The results are presented in Figure II.1.9.6. During immersion testing in 3.5% NaCl solution over 100 h, CO₂-treated AZ91D with 5% LiNO₃ solution pretreatment showed a distinct improvement in corrosion reaction resistance up to ~7X as compared to the baseline AZ91D with a 600-grit SiC finish. With a 1% LiNO₃ pretreatment, AZ91D still exhibited high-corrosion reaction resistance, although one sample with a visually less uniform surface had a low resistance value. It is speculated that the sample with a less uniform surface did not have uniform loading of Li salt prior to CO₂ thermal treatment and resulted in insufficient local corrosion protection. The Li 2.5-2.5 and Li5.0-2.5 in Figure II.1.9.6(b) were treated by two-step salt-loading using 2.5 and 5% LiNO₃ solution. All CO₂ thermal treatments were performed for 3 h at 350°C.

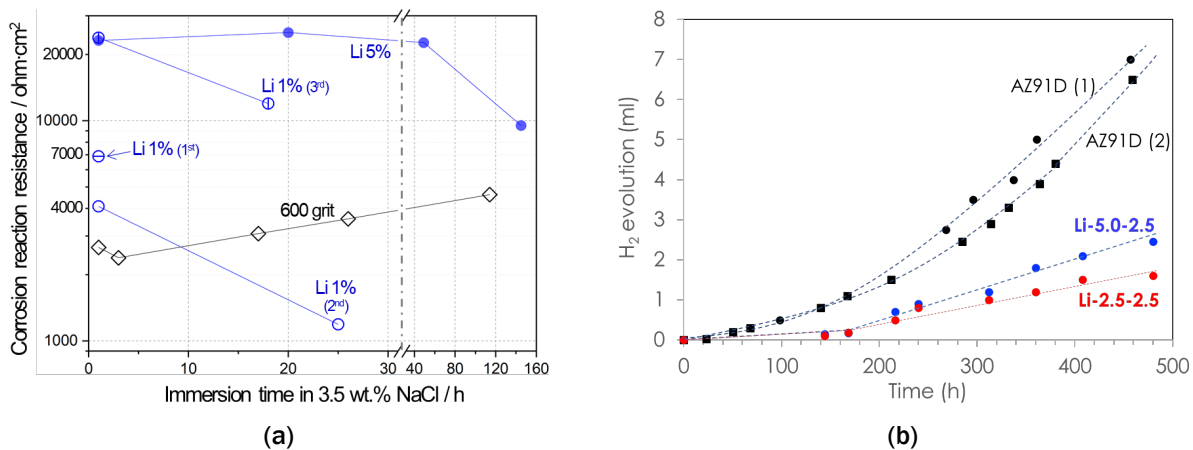
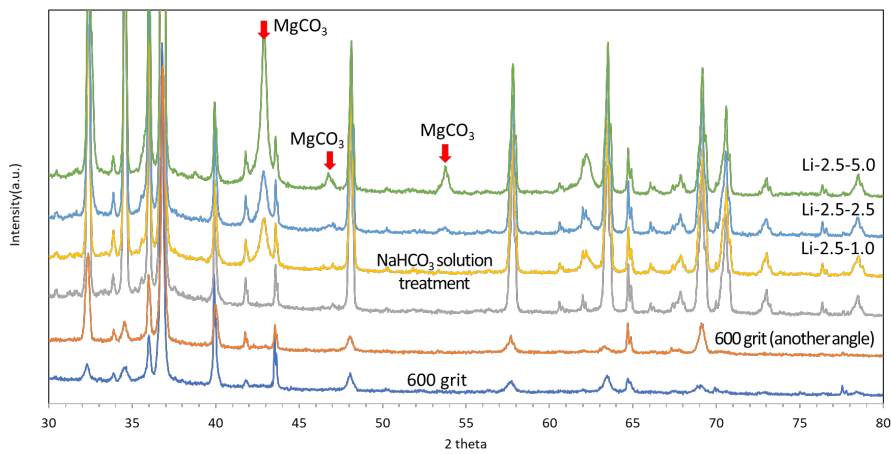


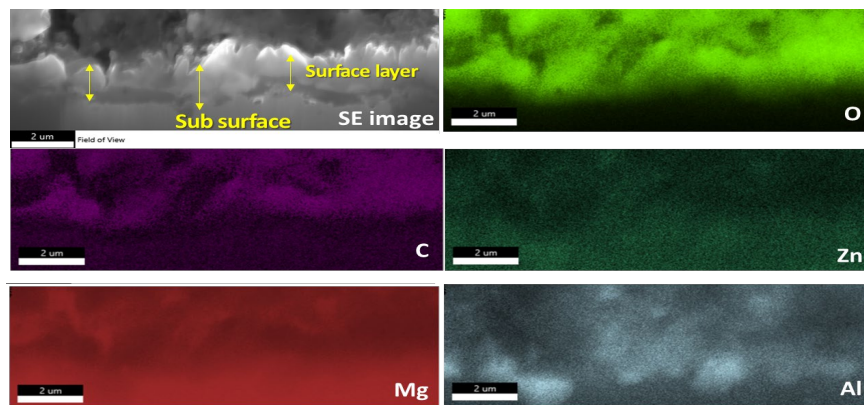
Figure II.1.9.6. (a) Corrosion reaction resistance of Li preloaded and CO₂ thermal-treated AZ91D in comparison with the baseline 600-grit-finished AZ91D as a function of immersion time. (b) Hydrogen collection volume from two baseline AZ91D and Li-salt-loaded and CO₂-treated AZ91D as a function of immersion time. Source: ORNL.

Meanwhile, the generated hydrogen volume (i.e., positively correlated with the cumulative Mg corrosion loss) was lower in the Li-salt-preloaded and CO₂-treated AZ91D samples than the baseline conditions, again highlighting the corrosion protection effect. Optimization of the Li salt preloading process and the CO₂ thermal treatment conditions is currently underway. Preliminary results from recently treated AZ91D samples indicated that the corrosion reaction resistance could be increased up to 20-fold after assessment by EIS.

Figure II.1.9.7(a) compares XRD intensity spectra from the AZ91D samples prepared by CO₂-treatment with Li salt preloading against the baseline AZ91D with a 600-grit surface finish. In all the Li-salt-loaded specimens, one predominant MgCO₃ peak at 43.5° was noticed, implying that the samples contained MgCO₃ crystals on the treated surface. In one Li-loaded sample—designated as Li-2.5-5.0—two more crystalline peaks of MgCO₃ were noted, suggesting that this sample contained a larger amount of MgCO₃ on its surface. Another Li salt-loaded and CO₂-treated specimen was prepared for characterization by FIB milling to reveal the local surface and subsurface structure. A secondary electron image and EDS mapping of the ion-milled specimen are presented in a tilted cross-sectional view in Figure II.1.9.7(b). The surface layer was a few microns thick and enriched in C, O, and Mg with some local enrichment of Al at the boundary of the layer and the subsurface region. These SEM and EDS characterization results, in addition to the previous XRD analysis, indicate that the surface layer formed by CO₂ thermal treatment is primarily composed of Mg, C, and O, which includes the MgCO₃ crystalline phases. More importantly, corrosion tests indicate that this Mg-, C-, and O-rich surface layer provides corrosion protection for the underlying AZ91D alloy, thus motivating further study and development of this approach.



(a)



(b)

Figure II.1.9.7. (a) XRD intensity spectra from the baseline AZ91D and two-step Li-salt-preloaded and CO₂-treated AZ91D samples. All CO₂ thermal treatments were performed for 3 h at 350 °C. (b) Tilted cross-sectional view and EDS mapping of two-step Li-salt-loaded and CO₂-treated AZ91D sample. Li salt-loading was performed by 0.5% and 1% LiNO₃ solutions in order. Source: ORNL.

Plasma treatments were performed with varying feed gases, air, and N₂, as well as with and without cover N₂ gas. The initial attempts used air feed plasma with no cover gas and open to lab air for AZ91D surface treatments. The corrosion reaction resistance values of AZ91D after this air plasma treatment were somewhat lower than the baseline samples. It was also found that the plasma-treated AZ91D surface contained Cu particles, which presumably originated from the Cu nozzle of the plasma device. Based on these observations, the next attempts used an Mg alloy nozzle to plasma-treat AZ91D samples. After switching to the Mg nozzle, AZ91D samples were plasma-treated using air or N₂ as feed gas. The samples had a 600 grit SiC finish before treatment. Unlike the samples resulting from the air plasma treatment, the AZ91D sample treated by N₂ plasma showed two impedance arcs with a greater impedance scale, suggesting that the N₂ plasma treatment enhanced the corrosion resistance of AZ91D surface. The corrosion reaction resistance value from the preliminary N₂-plasma-treated samples was 6341 ohm·cm². This was an improvement of 2.4 times over the baseline AZ91D with a 600-grit finish. The corrosion reaction resistance values of selected plasma-treated AZ91D samples are summarized in Table II.1.9.2. The N₂ plasma in open to air condition resulted in the notable increase of corrosion reaction resistance in both 1- and 1.5-inch nozzle distances. However, N₂ plasma combined with N₂ cover gas did not enhance corrosion resistance, suggesting that the formation of a corrosion-resistant surface film may require oxygen from the lab air. These preliminary results suggest that further exploration of plasma process parameters have the potential to achieve even higher corrosion reaction resistance for AZ91D type alloys.

Table II.1.9.2. Corrosion Reaction Resistance Determined by EIS For Plasma-Treated AZ91D With Four Varying Process Conditions

AZ91D Sample	Plasma Feed Gas	Plasma Cover Gas	Mg Nozzle Distance	Corrosion Reaction Resistance (ohm cm ²)
Baseline	N/A	N/A	N/A	~2600 (Avg.)
Air Plasma	Air	Open to Lab Air	1 Inch	~1654
N ₂ Plasma 1	N ₂	Open to Lab Air	1 Inch	~6341
N ₂ Plasma 2	N ₂	Open to Lab Air	1.5 Inch	~6412
N ₂ /N ₂ Plasma 1	N ₂	N ₂	1 Inch	~1444
N ₂ /N ₂ Plasma 2	N ₂	N ₂	1.5 Inch	~1950

Note: All data were from impedance spectra after 1 H immersion in 3.5% NaCl solution.

Project 3A2

Surface modification techniques using coatings are being utilized to improve corrosion properties by locally modifying the chemistry by surface alloying. Cold spray coating trials were performed on 25.4 mm × 25.4 mm AM60 and AZ91 coupon samples in collaboration with Pennsylvania State University (PSU). CP Al and Al6061 powders were spray-coated onto the Mg alloy coupons with a nitrogen carrier gas pressure of 6.55 MPa and gas temperatures of 375°C and 425°C, respectively. Al powders with an average particle size of 45 μm were used. Multiple trials were performed to obtain optimized parameters with the aim of improving the microstructure and to decrease porosity to less than 1% in the coating microstructure. The coating thicknesses that were obtained were on the order of 1 mm to 1.2 mm. Table II.1.9.3 provides information pertaining to the spray conditions, images of the cross-sections, and corresponding coating porosity for each of the coating trials performed at PSU. The porosity decreased significantly in the samples containing a CP Al bond coat. The coatings in each of these trials contain pancaked powder particles containing dark Mg₂Si phases at the boundaries and porosity/interparticle voids between particles. The Mg alloy matrix is seen to undergo localized deformation (e.g., ~30 μm in-depth) due to the impact of the particles during the coating process.

Table II.1.9.3. Trials Performed in Collaboration with PSU

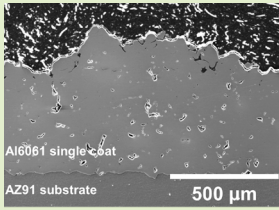
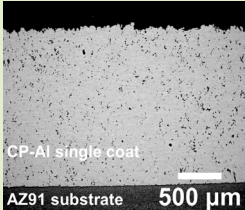
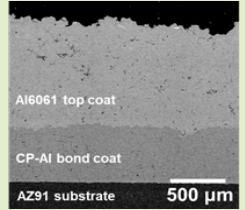
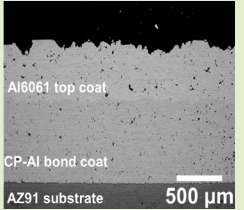
Cold Spray Settings	Trial 1	Trial 2	Trial 3	Trial 4
Spray Process	Single Coat of Solvus Al6061 Powders	Single Coat of Valimet H-15 CP Al Powders	Bond Coat Valimet H-15 CP Al Powders	Bond Coat Valimet H-15 CP Al Powders
			Solvus Al6061 Powders	Solvus Al6061 Powders
Gas Temperature (°C)	425	375	375 (for both CP Al and AA6061)	375 (CP Al); 425 (AA6061)
Porosity	3.4 ± 0.3%	0.5 ± 0.1%	0.5 ± 0.1% in CP Al Bond Coat and 0.2% in Al6061 Top Coat	0.5 ± 0.1% in CP Al Bond Coat and < 0.2% in Al6061 Top Coat
Cold Spray Coating Cross-Sections				

Figure II.1.9.8(a) shows the cross-sectional microstructure of an AZ91 substrate coated with CP Al and Al6061. The interfaces present between the individual layers are of particular interest as they determine the nature of the metallurgical bond created during the cold spray coating process. Figure II.1.9.8(b) and Figure II.1.9.8(c) contain high-resolution TEM-EDS information of the interface and EDS line scan showing the presence of thin layers of $Mg_{17}Al_{12}$ and MgO layers, respectively. Adhesion testing (ASTM D4541) of coatings was performed on the samples from Trial 2 the adhesion strength was determined to be 16.06 ± 0.39 MPa. Additionally, samples from Trial 4 showed 12 ± 4.1 MPa. The decrease in the strength and greater standard deviation is attributed to the fact that Trial 2 only had CP Al coating, while Trial 4 had CP Al and Al6061 coatings, which could lead to a higher likelihood of interface failure.

To test the corrosion performance of the coating with respect to the substrate, location-specific electrochemical measurements were performed on the coatings as well as the matrix. SECCM was used for microscopic corrosion measurement of the Mg-substrate coated with CP Al and Al6061. Potentiodynamic polarization measurements were performed from the substrate (Mg) to the coating (Al) side. Post-SECCM microstructure shows the measurement footprints along the lines, as depicted in Figure II.1.9.9(a), and across the interface. Figure II.1.9.9(b) shows the Tafel plots for all data points measured in both substrate and coating. Tafel data shows the coating is more cathodic as compared to the substrate (Mg). More SECCM work is underway on newly cold sprayed samples with lesser porosity to capture the transition of electrochemical properties across the interface. We have now transitioned the cold spray coating experiments to PNNL and are performing several trials to optimize the coating parameters, such as gas temperature, gas pressure, and powder feed rate to obtain high density, low roughness coatings, and higher adhesion strength.

A second approach to coating involved a coating of Zn on top of the Mg alloys by a reactive melting method. Mg alloy substrates were polished to remove the pre-existing oxide layer. Zn sheets of varying thicknesses (e.g., 0.1 mm to 1 mm) were placed on the Mg alloy substrates and a two-step heat-treatment protocol was performed for melting the Zn sheet and to perform diffusion, respectively. Figure II.1.9.10(a) shows the Mg-substrate coated with Zn. Two-step heating schedules (e.g., 400°C for 15 min and 350°C for 15 min) was used for melting the Zn powders and to diffuse through the Mg-substrate, respectively. Coating was performed in an Argon atmosphere. Similarly, Zn sheets with different thicknesses are also being used to create a cathodic coating on top of the Mg-substrate. Microscopic corrosion measurement was performed on the cross-section of

the Zn-coated Mg-substrate samples using SECCM. Potentiodynamic polarization scans were performed from the substrate (Mg) to the coating (Zn) side with a step size of 250 μm . Post-SECCM microstructure shows the measurement locations along the lines, as observed in Figure II.1.9.10(b) and across the interface.

Figure II.1.9.10(c) shows the Tafel plots for all data points measured in both the substrate and the coating. Tafel data shows the coating (Zn) is more cathodic as compared with the substrate (Mg). Additionally, EIS measurements indicate that the surface resistance to corrosion in the substrate (e.g., point 1 in the SECCM plot) is $3.2 \times 10^8 \Omega$, and in the coating (e.g., point 8 in the SECCM plot) is $1 \times 10^9 \Omega$, which is an order of magnitude increase. We are currently optimizing the heat-treatment parameters to control melting time/temperature and diffusion time/temperature. More SECCM work is also underway on new reactive Zn-coated samples to capture the transition of electrochemical properties across the interface.

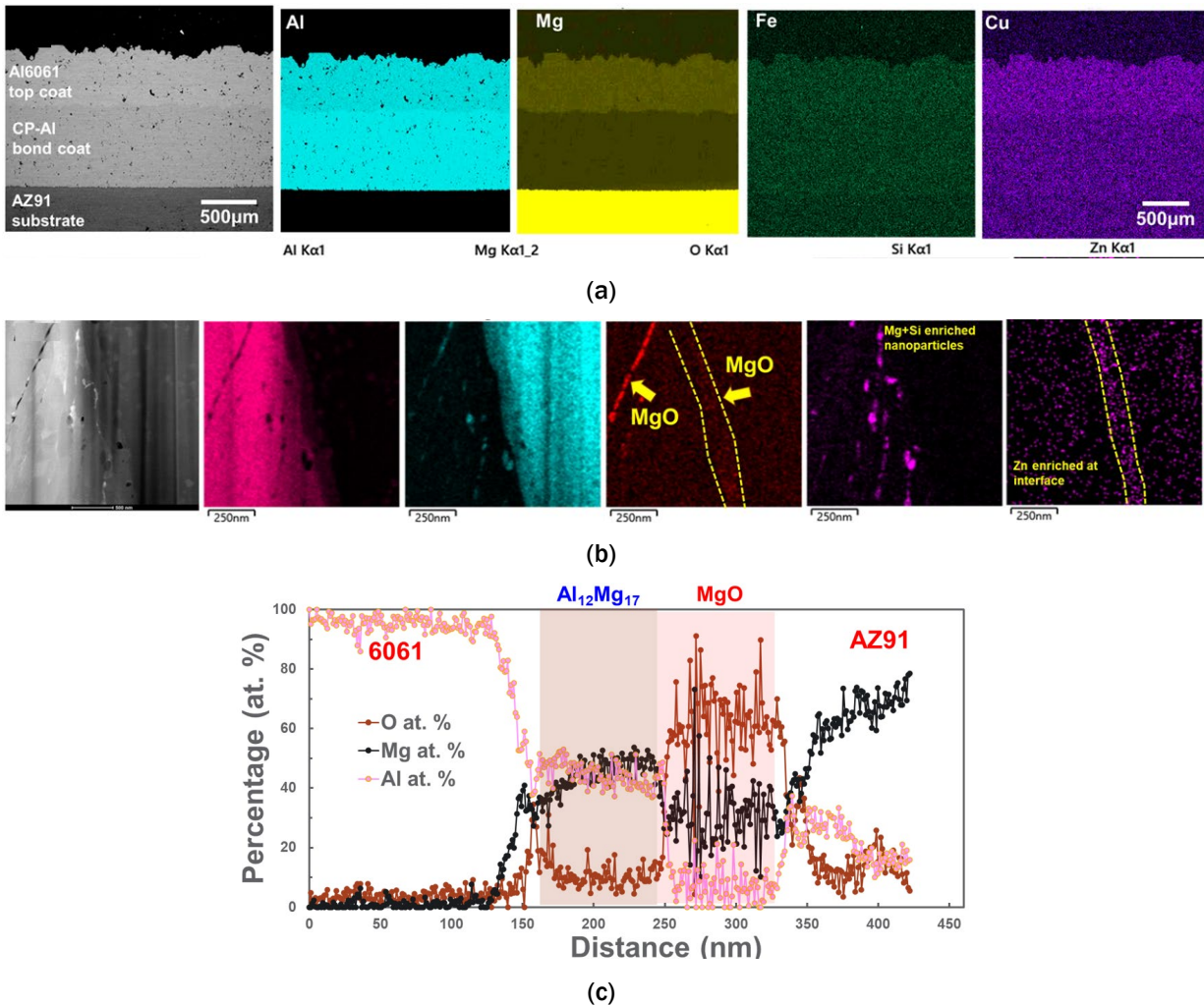


Figure II.1.9.8. (a) and (b) Cross-sectional microstructure of cold sprayed sample and corresponding TEM-EDS maps of the interface showing MgO and Mg₁₇Al₁₂ layers, and (c) a plot showing their composition of O, Mg, and Al and their respective thicknesses. Source: ORNL.

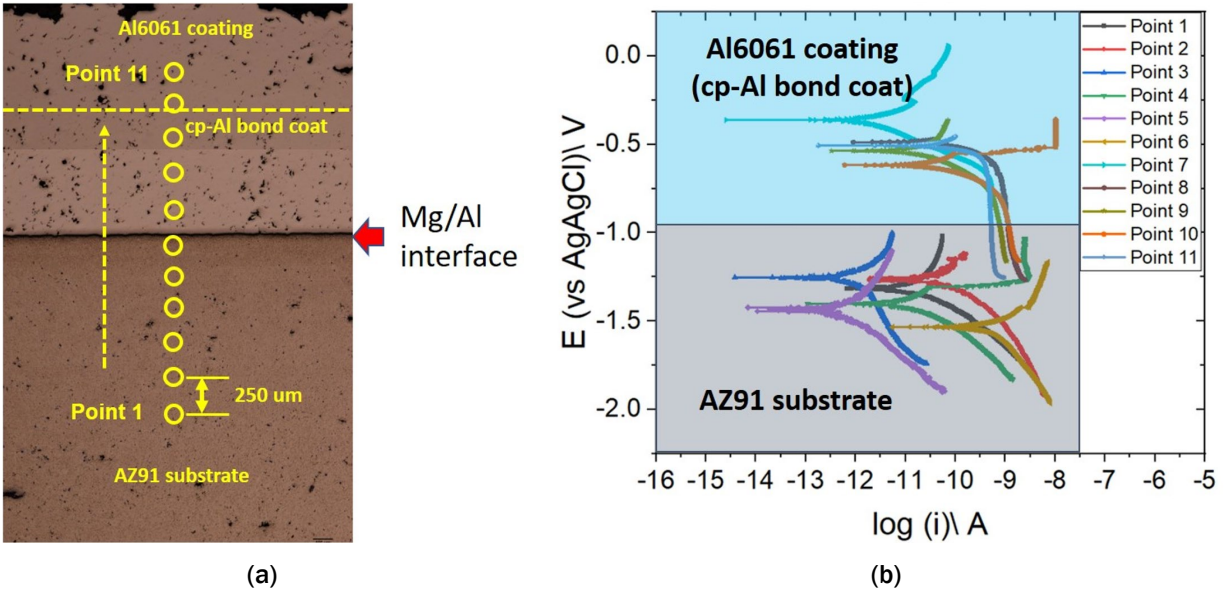


Figure II.1.9.9. (a) Post-SECCM microstructure showing measurement footprints. Measurements were performed from the Mg-side to the Al side with 250 μm step size. (b) Tafel plots correspond to point 1–11. Source: ORNL.

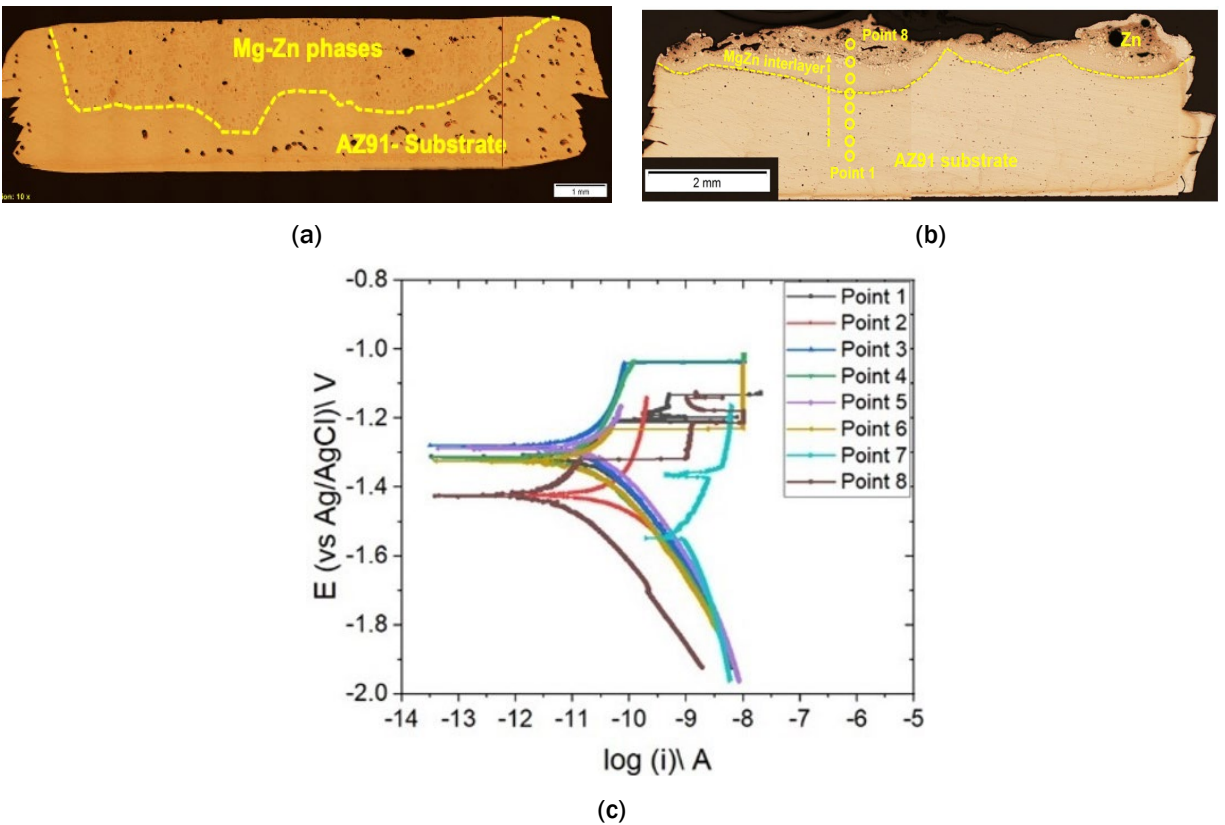


Figure II.1.9.10. (a) Cross-section microstructure of reactive Zn melted coating. (b) Post-SECCM microstructure showing measurement locations. Measurements were performed from the Mg side to the Zn side with a 200 μm step size. (c) Tafel plots correspond to points 1–8. Source: ORNL.

Project 3B

Summary of the as-cast AZ91 and AM60 tensile test results are presented in Table II.1.9.4. AZ91 exhibited an average YS of 192 MPa to 200 MPa, UTS of 227 to 257, and total elongation of 3.2% to 5.7%. AM60, on the other hand, exhibited YS of 98 MPa to 110 MPa, UTS of 201 MPa to 247 MPa, and elongation of 5.3% to 8.2%. As noted, the difference in UTS and YS was higher for the AM60 as compared to the AZ91 alloy. This could be due to the differences in the extent of work hardening and work hardening mechanisms.

Table II.1.9.4. Summary of the AZ91 and AM60 Tensile Properties

Sample Description		YS (MPa)	UTS (MPa)	UTS-YS (MPa)	Elongation (%)
AZ91	Parallel	192±4	227±25	35	3.2±2.1
	Perpendicular	200±4.2	257±18.3	57	5.7±2.3
AM60	Parallel	98±10.5	201±3.4	103	5.3±0.1
	Perpendicular	110±18.3	247±0.6	137	8.2±0.03

A summary of the processing parameter development for AZ91 and AM60 are presented in Figure II.1.9.11(a) and (b), respectively. Tool rotational speed and traverse rate also are presented with the corresponding tool temperature. The main objective was to obtain the processing envelope that does not have any surface processing defects. As noted, certain processing parameter combinations resulted in a defective surface while other combinations led to defect-free surfaces, as observed in Figure II.1.9.11(c). Once a set of processing conditions was established, both single and overlapping passes were completed to modify the microstructure. OM analysis of the transverse sections for the two conditions that did not exhibit surface processing defects are presented in Figure II.1.9.12. Figure II.1.9.12(a)–(c) and Figure II.1.9.12(d)–(f) correspond to processing carried out at 450°C and at 410°C tool temperature, respectively. In addition to the macro-overview of the transverse section, images of the processed region and the boundary region are provided. The processed region at 450°C did not have any remnant porosity; however, the processed region at 410°C indicated the presence of elongated defects. Therefore, the single and double overlapping passes performed at 450°C was subjected to tensile and fatigue property characterization.

The summary of the hardness and tensile property measurements for various conditions are presented in Figure II.1.9.13(a) and (b), respectively. The conditions are as-cast, single-pass, overlapping double passes, and post-aging at 168°C for 8 hours and at 200°C for 8 hours. Hardness of the as-cast material and aged condition was 74 and 79 HV0.2. The as-FSP hardness was ~71 in the single-pass and can be post-aged to ~89–94 HV0.2. Similar hardness values noted for the two double pass conditions (e.g., 450°C + 450°C and 450 + 410°C). And in the 450°C + 380°C double pass, both as-processed and aged conditions exhibited ~99 HV0.2. A similar trend was noted in the YS characterization as well. YS in the as-processed conditions varied from 160 MPa to 180 MPa. The double pass (e.g., 450°C + 450°C) condition exhibited a UTS and a total elongation of 18%, which were the highest among the as-FSP processed conditions. The highest YS was noticed for the 450°C + 380°C double pass, but the sample failed prematurely leading to the lowest total elongation of ~3%. Furthermore, a positive response to aging heat-treatment was noted for all processing conditions. Finally, fatigue testing of as-cast, single as-FSP, and double as-FSP conditions were carried out; the results are presented in Figure II.1.9.13(c). Both the as-cast and single-pass FSP sample exhibited significant scatter, while limited results show that double passes exhibited significantly improved fatigue lives. An initial fractography analysis indicated defect-controlled fatigue failure in some of the samples. More testing and analysis are underway.

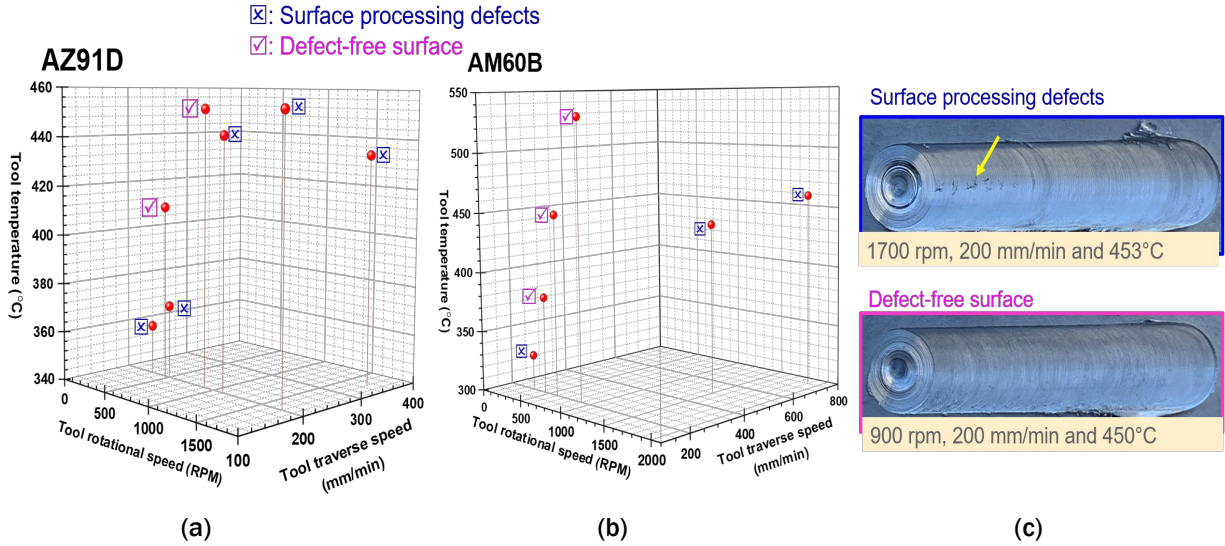


Figure II.1.9.11. Process parameter optimization for (a) AZ91 and (b) AM60. Tool temperature is plotted as a function of tool rotation speed and traverse rate in AZ91 and AM60. (c) Images of the top surface of the processed region. Source: PNNL.

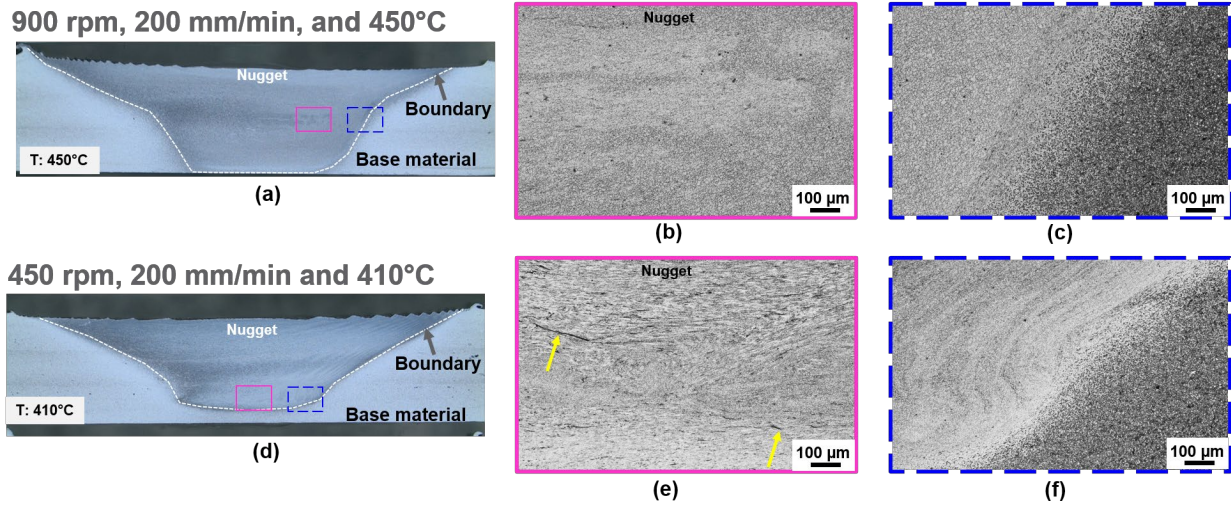


Figure II.1.9.12. Transverse sections of AZ91 processed at (a) 450 °C and (d) 410 °C. Microscopic images of (b) the nugget and (c) the boundary region at 450 °C, and microscopic images of (e) the nugget and (f) the boundary region at 410 °C. Source: PNNL.

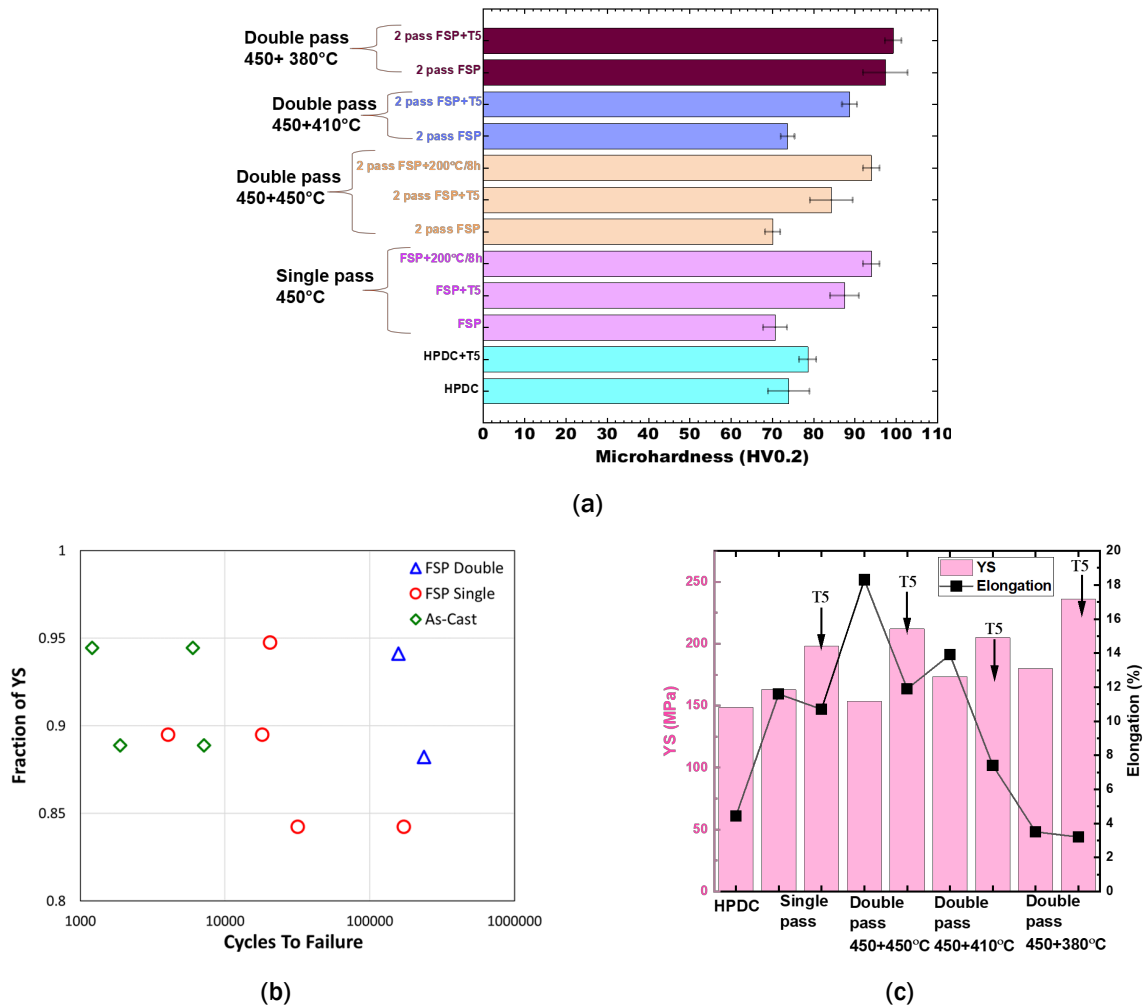


Figure II.1.9.13. Summary of (a) hardness and (b) tensile properties of AZ91 for various processing conditions. (c) The fatigue properties of AZ91 for various processing conditions. Source: PNNL.

Conclusions

Project 3A1

- Laser treatments with varying energy intensities resulting in different fusion zone depths, which were successfully simulated by computer modeling capability. However, only a marginal increase of corrosion resistance was achieved under laser processing.
- CO₂ thermal treatment with preloaded Li-based salts resulted in significant increases in corrosion resistance as evaluated by both EIS and hydrogen collection measurements. Analysis by SEM, EDS, and XRD indicated that Li-salt-preloaded AZ91D formed a Mg-, C-, and O-rich surface layer, containing crystalline MgCO₃, after CO₂ thermal treatment. The surface layer appears to function as an effective corrosion barrier. Downselection of techniques for future efforts will be based on the results of the corrosion reaction resistance as measured by EIS as well as H₂ collection results.
- A noticeable improvement in corrosion reaction resistance was achieved by N₂ plasma treatments in environments containing lab air, whereas the same N₂ plasma treatments in N₂ cover gas were not effective.

Project 3A2

- Al and Zn were successfully coated using cold spray and reactive melting methods respectively, on top of the cast-Mg-alloy substrates. In both methods, defects such as pores reduced significantly in the optimized coating condition and metallurgical bonding has been observed at the coating-substrate interfaces.
- Microscopic corrosion measurement using SECCM analysis shows the cathodic nature of coating as compared with the Mg-substrate. The cathodic nature of coatings (Al, Zn) will protect the Mg alloys from external corrosive environment and maintain the structural integrity of the components. EIS measurements also demonstrated significant increase in the resistance of the oxide scale.

Project 3B

- Porosity was reduced from ~2% in the as-cast AZ91 to no observable porosity in the FSP processed materials.
- Hardness of the processed region can be varied from 70 to 99 HV0.2, which is an increase of about 40%.
- Similarly, YS of the processed region can be varied from 165 to 235 MPa, which is about a 40% increase.
- Fatigue lives of the double pass were significantly higher than the as-cast material. Our first year effort is to map various FSP processed property pathways at the coupon level that could be transferred onto the part/component-level property modification.

Key Publications

1. Garcia, D., H. Das, X. Ma, T. Roosendaal, V. Joshi, D. Herling, M. Komarasamy, and G. Grant, 2022, "Exploring the microstructure-property relationship of Mg-Al-Mn alloys enhanced via friction stir processing," *Magnesium Technology 2022*, accepted for publication.
2. Kalsar, R., S. Niverty, A. J. Naccarelli, and T. Eden, 2022, "Correlation between microstructure, bond strength and corrosion properties of cold sprayed Al on cast-Mg alloys," manuscript in preparation.
3. Pang, Q., M. Song, R. Kalsar, V. V. Joshi, and P. V. Sushko, 2022, "Water adsorption and surface atom dissolution on Zn-, Al-, and Ce-doped Mg surfaces," *Magnesium Technology 2022*, accepted for publication.

References

1. Mordike, B. L., and T. Ebert, 2001, "Magnesium: Properties — applications — potential," *Mater. Sci. Eng.*, Vol. 302, No. 1, pp. 37–45.
2. Esmaily, M., J. E. Svensson, S. Fajardo, N. Birbilisi, G. S. Frankel, S. Virtanen, R. Arrabal, S. Thomas, and L. G. Johansson, 2017, "Fundamentals and advances in magnesium alloy corrosion," *Prog. Mater. Sci.*, Vol. 89, pp. 92–193.
3. Rettberg, L. H., J. B. Jordon, M. F. Horstemeyer, and J. W. Jones, 2021, "Low cycle fatigue behavior of die-cast-Mg alloys AZ91 and AM60," *Metall. Mater. Trans. A-Phys. Metall. Mater. Sci.*, Vol. 43, No. 7, pp. 2260–2274.

Acknowledgments

The authors from PNNL recognize D. Garcia, X. Ma, H. Das, A. Guzman, T. Roosendaal, R. Seffens, M. Rhodes, R. Kalsar, S. Niverty, V. Prabhakaran, L. Strange, C. B. Smith, D. Graff, G. G. Neuenschwander, A. J. Naccarelli, and T. Eden from Penn State University for processing and/or characterization activities for this project. The authors from ORNL recognize Y. C. Lim (ORNL, plasma treatment lead), G. G. Jang (ORNL, CO₂ thermal treatment lead), G. Knapp (ORNL, laser treatment modeling), A. Plotkowski (ORNL, laser treatment lead), D. Leonard (ORNL, microscopic characterization), A. Haynes (ORNL, program supervision) and Volunteer Aerospace (ORNL's industrial partner for laser treatment).

II.1.10 Light Metals Core Program - Thrust 4 - Characterization, Modeling, and Lifecycle (Pacific Northwest National Laboratory)

Arun Devaraj, Co-Principal Investigator

Pacific Northwest National Laboratory
902 Battelle Blvd.
Richland, WA 99354
E-mail: arun.devaraj@pnnl.gov

Ayoub Soulami, Co-Principal Investigator

Pacific Northwest National Laboratory
902 Battelle Blvd.
Richland, WA 99354
E-mail: ayoub.soulami@pnnl.gov

Thomas Watkins, Co-Principal Investigator

Oak Ridge National Laboratory
1 Bethel Valley Road
Oak Ridge, TN 37831
E-mail: watkinstr@ornl.gov

Dileep Singh, Co-Principal Investigator

Argonne National Laboratory
9700 South Cass Avenue
Lemont, IL 60439
E-mail: dsingh@anl.gov

Jeffrey S Spangenberg, Co-Principal Investigator

Argonne National Laboratory
9700 South Cass Avenue
Lemont, IL 60439
E-mail: jspangenberg@anl.gov

Sarah Kleinbaum, DOE Program Manager

U.S. Department of Energy
E-mail: sarah.kleinbaum@ee.doe.gov

Start Date: October 1, 2020 End Date: September 30, 2023
Project Funding: (FY 2021): \$1,150,000 DOE share: \$1,150,000 Non-DOE share: \$0

Project Introduction

This report describes the activities performed during the first year of the Characterization, Computation, and Life Cycle activity under Thrust 4 within the DOE VTO LMCP. The goal of the LMCP, which was launched in October 2020, is to combine multiscale modeling, rapid measurement of properties (i.e., high-throughput testing), and novel processing technologies (i.e., SPP, AM, and high intensity thermal treatment) to locally control material properties. Three materials development thrusts are included in the LMCP: Thrust 1 – Selective Processing of Aluminum Sheet; Thrust 2 – Selective Processing of Al Castings; and Thrust 3 – Localized Property Enhancement for Cast Magnesium Alloys. Thrust 4 supplements and supports the

advanced characterization, computational modeling, and life cycle needs of the various tasks within the three materials development thrusts. Advanced characterization activities include STEM, APT, synchrotron x-rays, neutron scattering, and other capabilities. The advanced characterization is a multi-laboratory effort involving ANL, PNNL, and ORNL. In the first year, PNNL conducted the STEM and APT studies. Beamline proposals have been submitted to ANL's APS for accessing synchrotron x-rays for diffraction. The modeling task includes high-performance computing, DFT, smooth particle hydrodynamics (SPH), multiscale modeling for understanding solidification, thermodynamic models, process models, and micro-macro-FEM for bendability. Modeling tasks have been conducted both at PNNL and ORNL. Residual stress characterization, prediction, and optimization tasks have been conducted at PNNL. Material life cycle studies have been conducted at ANL. This report will cover the results from the Thrust 4 efforts conducted at PNNL, ORNL, and ANL across all three of the following tasks: (1) advanced characterization and modeling; (2) residual stress characterization, prediction, and optimization; and (3) material life cycle in year 1 of this project.

Objectives

The objectives of this project are to: (1) bring together advanced microstructural characterization, local mechanical testing, and predictive modeling to help establish processing-microstructure-property/performance relationships; (2) characterize, predict, and optimize residual stresses introduced by the local processing approaches used to achieve intentionally heterogeneous microstructure; and (3) study recyclability of intentionally heterogeneous Al and Mg alloys.

Approach

The approach in this thrust is to leverage the unique combinations of experimental and computational science capabilities and expertise at these three National Laboratories in advanced characterization, modeling, residual stress studies, and material life cycle assessments. The LMCP PIs from Thrusts 1–3, all propose, compete, and obtain access to advanced characterization capabilities and modern computational tools and expertise through an internal proposal review process, issued twice in each financial year. During the review process of the Thrust 4 requests, emphasis is placed on cross-National Laboratory collaborations, especially integrating advanced characterization with computational studies from PNNL, ORNL, and ANL.

The access to advanced characterization and computation—as well as residual stress studies and material life cycle expertise enabled through Thrust 4—provides a unique opportunity to accelerate the development of Al- and Mg-based lightweight alloys with intentionally heterogeneous microstructure. Table II.1.10.1 provides all the advanced characterization, computation projects, residual stress, and life cycle projects funded and executed in FY 2021. The Results section focuses on describing the progress of these subtasks from each of the three tasks in Year 1.

Table II.1.10.1. Summary of the AZ91 and AM60 Tensile Properties

Task	Subtask Title	Relevant Thrust and Project	Lab Ownership
1. Advanced Characterization and Modeling	1.1. Advanced characterization of microstructure-mechanical property relationship in friction stir processed 7085-T78.	1C	PNNL and ANL
	1.2. Coupled thermodynamic and process modeling for AM Al alloys onto dissimilar cast or stamped parts.	1B & 2C	ORNL
	1.3. Multi-resolution macro-micro finite element modeling (FEM) to study the impact of local microstructures on the bendability of Al sheets.	1C	ORNL
	1.4. High-performance computing for DFT studies of cast Mg local corrosion mitigation.	3A	PNNL
2. Residual Stress Characterization, Prediction, and Optimization	2.1 Modeling of the residual stresses during FSP.	4	PNNL
	2.2 Experimental measurements of residual stress.		
3. Material Life Cycle	3.1 Material life cycle studies.	4	ANL

Results

Task 1: Advanced Characterization and Modeling

This task brought together the capabilities and expertise in advanced microstructural characterization and computational modeling at PNNL and ORNL for supporting requests under various subtasks from Thrusts 1–3 as described below.

Subtask 1.1: Advanced Characterization of Microstructure-Mechanical Property Relationship in FSP 7085-T78

PNNL researchers in Thrust 1, Project C, successfully processed Al 7085-T78 alloys using high-speed FSP. It is known that the stir zones after FSP reduced the load to the yield point in the bend tests. The focus of this subtask was to apply advanced microstructural characterization of nanoscale precipitates in base Al 7085-T78 alloy and FSP stir zone using aberration-corrected STEM and APT at PNNL to establish the FSP-microstructure-mechanical property relationships relative to the stir zones. A newly procured PFIB system at PNNL was instrumental in fabricating Gallium contamination free transmission electron microscopy and APT samples of these Al alloys. Figure II.1.10.1(a) and (b) show STEM imaging and APT results from the base Al 7085-T78 highlighting the presence of a high density of MgZn₂ precipitates and some Al₃Zr precipitates in the matrix. After FSP, the number density of the MgZn₂ precipitate was observed to decrease considerably as evident in the STEM image in Figure II.1.10.1(c) and the APT results in Figure II.1.10.1(d). Thus, advanced characterization revealed the reasoning for the reduced load to yield point during bend tests after FSP.

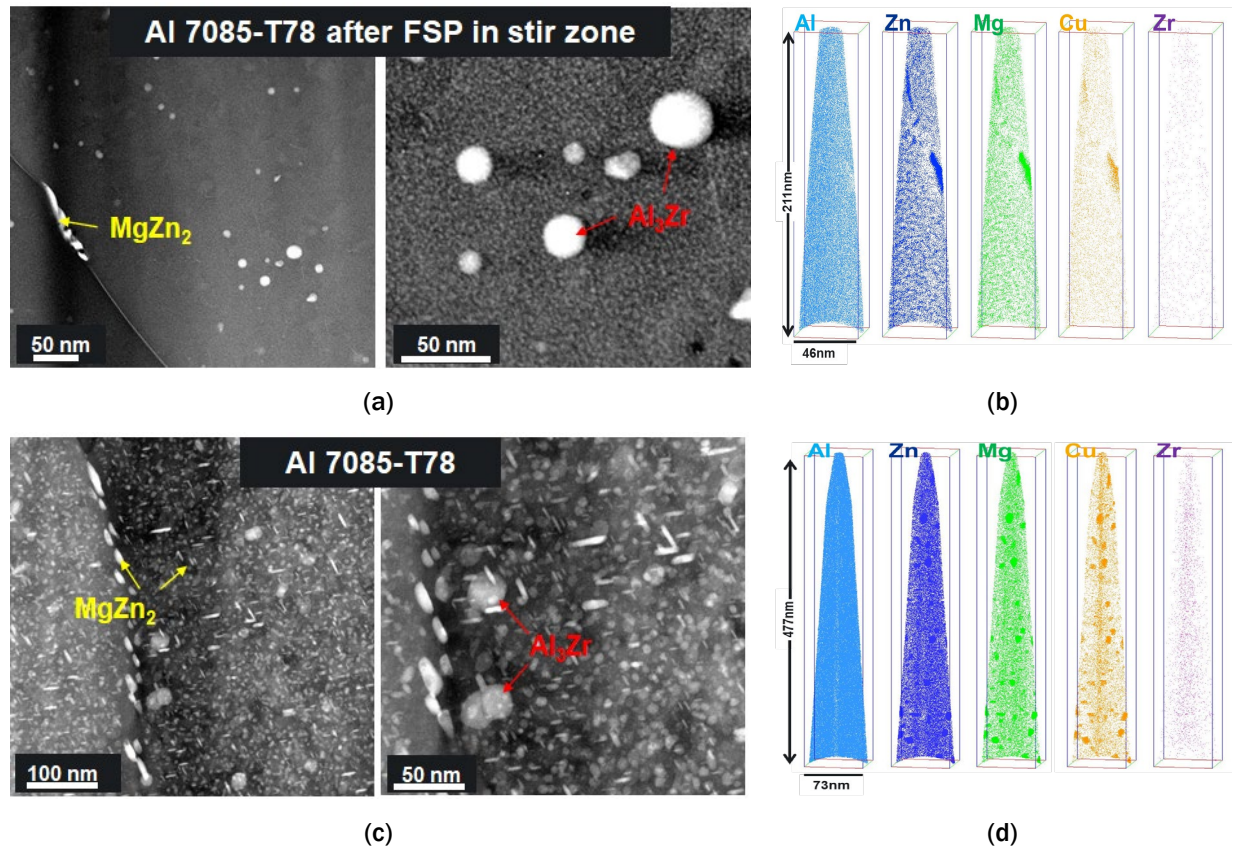


Figure II.1.10.1. (a) STEM images of MgZn₂ precipitates and Al₃Zr precipitates in the Al7085-T78 alloy. (b) An APT analysis revealing the composition of nanoscale intragranular precipitates. (c) A STEM image revealing the reduction in precipitate density after FSP. (d) The APT result of the FSP Al7085-T78 highlighting the absence of distinct nanoscale intragranular precipitates. Source: PNNL.

Subtask 1.2: Coupled Thermodynamic and Process Modeling for AM of Al Alloys onto Dissimilar Cast or Stamped Parts

In this subtask, thermodynamic and process modeling capabilities and expertise at ORNL were brought together to understand factors affecting the printability and heat-treatment response for AM of Al alloys on dissimilar cast or stamped parts. The printability of different alloys was determined by combining the composition-dependent solidification cracking susceptibility (SCS) criterion developed by S. Kou [1] with data on dilution, molten pool size, and cooling rates from analytical process models. One analytical process model incorporated an energy balance of the absorbed laser power, laser hot-wire power, energy used to melt the deposited material, and energy used to melt the substrate. Data from the laser hot-wire literature was used to calibrate the energy coupling efficiencies in the model [2]. Using the calibrated model, the ratio of AM deposited material to melted substrate material could be used to determine the dilution of the deposited material composition by the substrate material composition. This allows for calculations of the composition-dependent SCS using Scheil solidification simulations in Pandat, a software for applying calculation of phase diagram, (i.e., CALPHAD) methods. A second analytical model based on the analytical solution for a moving point source [3] was used to estimate the cooling rate along the trailing edge of the molten pool to provide a process dependent parameter related to hot cracking [4]. Using the aforementioned models and a multicomponent Al thermodynamic database developed at ORNL, a rich dataset was generated linking the process parameters, Scheil solidification phase composition, molten pool geometry, cooling rates, and SCS criterion. To visualize and interact with the highly dimensional dataset, parallel coordinate plotting [5] was applied. Figure II.1.10.2 shows the results of these calculations for a 5356 welding wire AM feedstock

deposited on a 6111 Al alloy substrate (e.g., a wire/substrate combination of interest for Task 1B). From these results, an initial process space for testing that specific wire/substrate combination was defined. An analysis of other alloys resulted in the understanding of the comparative ease of processing different alloy combinations, resulting in the Al alloy 4043 wire being chosen as the material to be used for demonstrating the feasibility of the laser hot-wire process.

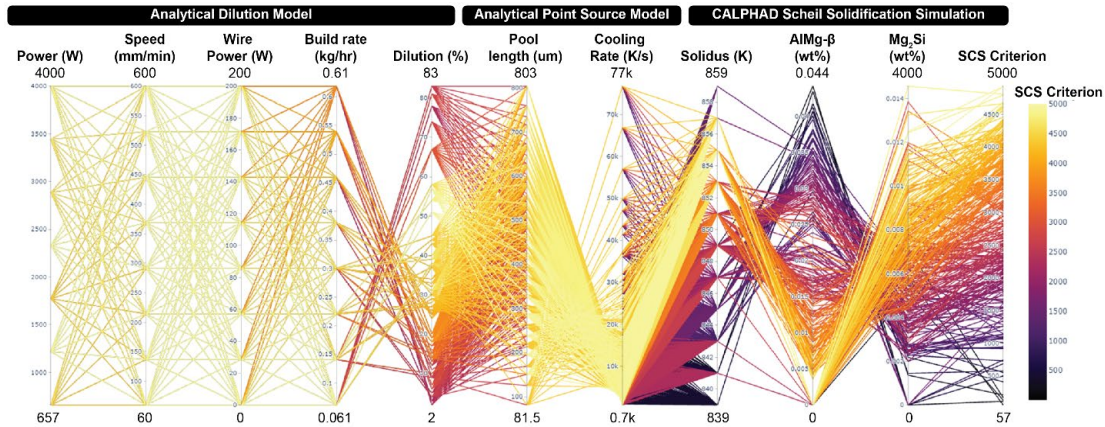


Figure II.1.10.2. Parallel coordinate plot showing combined modeling results for a range of process parameters. Each horizontal line represents a data point, each vertical axis represents a variable, and the value of the variable for each data point is determined by where it crosses the line. Lines are colored by the SCS. Source: ORNL.

In addition to the multimodal modeling for initial wire composition selection, numerical heat transfer simulations helped determine the thermal history experienced by different locations in the deposited geometry during the layer-by-layer deposition of laser hot-wire AM. An AM solver for OpenFOAM called “additiveFoam” [6], which was developed at ORNL, is being used for these simulations. Figure II.1.10.3(a) shows a snapshot of the predicted temperature field during a 25-layer simulation of wire deposited on a 305 mm × 305 mm × 5 mm-thick alloy 6111 substrate. Figure II.1.10.3(b) shows the temperature history of the center of the substrate as a function of time during the deposition. The 3D simulation of the temperature field during the deposition process enables thermal histories to be extracted at any point in the part and exported to thermodynamic and kinetic models for calculating the evolution of precipitation-strengthening phases. In future work, that coupling will form an analysis for determining the necessary heat treatments (if any) that will be necessary to achieve desired microstructure and properties in the final parts.

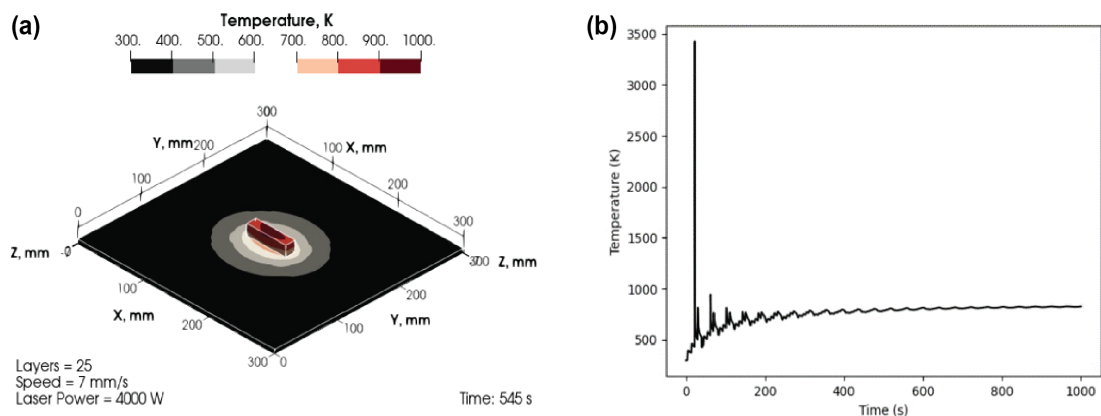


Figure II.1.10.3. (a) Snapshot of a multilayer thermal simulation for 25-layer part, showing the heat accumulation in the substrate and deposited material. (b) Extraction of transient temperature history during the 25-layer deposition at the center of the substrate. Source: ORNL.

Subtask 1.3: Macro-Micro FEM Scheme to Study Local Microstructure Influences on the Bendability of the AA7075T6 Alloys

The aim of this subtask was to use a macro-micro modeling approach to connect a component-level bending simulation with locally modified microstructures of the AA7075-T6 Al alloys. Bendability is an important indicator of the formability of sheets and is usually evaluated by the critical bend radius/sheet thickness (r/t) ratio before cracks are observable when the bending angle is fixed or a critical bending angle before cracks are observable when r/t is fixed. In this modeling approach, the macroscopic sample/component scale bending test model was first established for the finite element (FE) simulation. After the simulation, the local “hotspot” was identified, where the material will be most prone to failure. The displacement history of that location was then utilized to conduct a microstructure-based meso-scale micro-model where the local microstructure and its influences on bendability were studied. In this current work, this was applied to study the bendability of a 1-mm-thick AA7075-T6 alloy before and after local modification in the V-bending and 180°-bending tests [7].

The maximum principal strain of the macro-model of the 90° V-bend is shown in Figure II.1.10.4 both (a) before simulation and (b) after simulation for a bending radius of $r=0.5$ mm ($r/t=0.5$), while (c) and (d) show the results from the macro-model for a 180°-bending with $r=0.2$ mm ($r/t=0.2$). The highest tensile deformation was observed at the top-outer surface of both models. The 180° bending showed higher strains (0.592) than the V-bending model (0.415) due to its smaller r/t ratio and a larger bending angle.

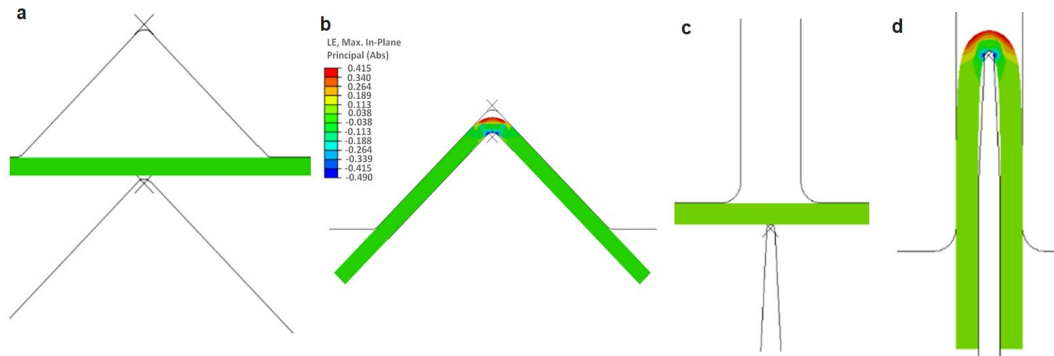


Figure II.1.10.4. The maximum principal strain contour macroscopic 90° V-bending model of 1-mm-thick AA7075T6 alloy both (a) before and (b) after bending deformation with the bending radius of $r=0.5$ mm ($r/t=0.5$), (c) and (d) are corresponding images for 180° bending with the bending radius of $r=0.2$ mm ($r/t=0.2$). Source: ORNL.

After obtaining the results of the macroscopic models, the displacement history at the boundary of this region was used as the boundary conditions for the microstructure-based meso-scale micro-model. Figure II.1.10.5(a) shows the microstructure of the as-received AA7075-T6 microstructure, which represents an area of 0.3×0.6 mm². The MATLAB image analysis showed that the volume fraction of the second-phase particles was less than 1%, and the particles were randomly distributed. In the microstructure-based model, ductile fracture was considered for the Al matrix material using the shear failure criterion in ABAQUS where the element was removed when the local equivalent plastic strain reached 1.7. On the other hand, a tension failure brittle fracture criterion was considered for the second-phase hard particles, where the element was removed when the local tensile hydrostatic stress reached 0.9 GPa. For the 90° V-bending ($r/t=0.5$), the results of the macro and micro-model are shown in Figure II.1.10.5(b), while the V-bending micro-model result is shown in Figure II.1.10.5(c). Cracking was not predicted, and this was attributed to the small volume fractions of the second-phase particles and the randomness of the particle distribution, which are both beneficial for the fracture resistance. Figure II.1.10.5(d) provides an optical image of the V-bending test results for $r/t=0.39$, which showed no surface cracking. For the 180° VDA-bending ($r/t=0.2$), the surface damage was observed on one location, which subsequently did not propagate through the thickness, as observed in Figure II.1.10.5(e) and Figure II.1.10.5(f). The model predictions of good bendability of the 1-mm as-received AA 7075-T6 Al alloy agreed well with the recent experiment of 90° V-bending with no observed cracking for $r/t=0.39$.

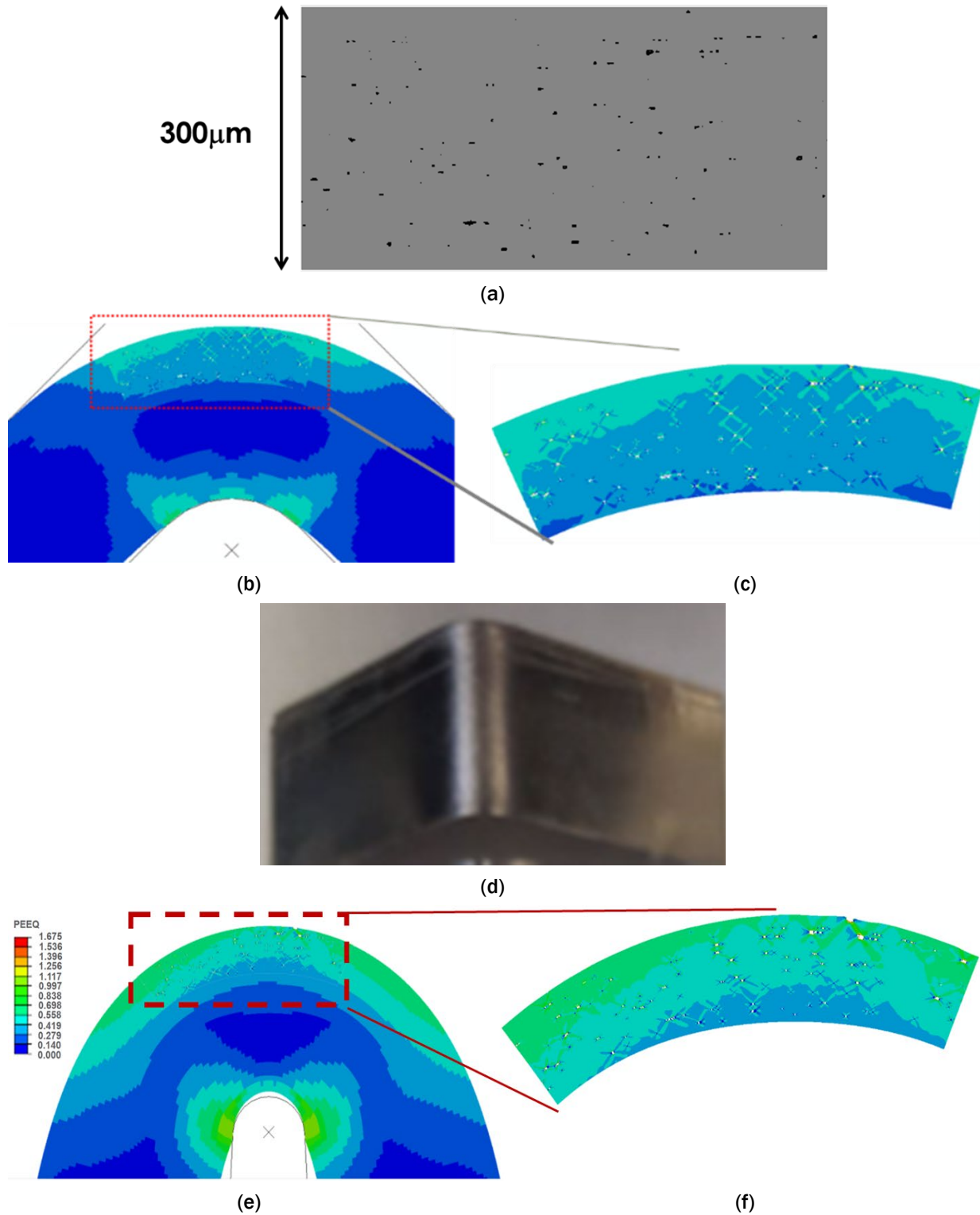


Figure II.1.10.5. (a) The optical image of the as-received AA7075-T6 Al alloy after polishing. (b) The combined 90° V-bending simulation results showing images from the micro- and macro-models. (c) The micro-model expanded. (d) An optical image of the V-bending test results for $r/t=0.39$, which showed no surface cracking. (e) The combined image of the micro- and macro-model. (f) The simulation results of the 180°-bending micro-model. Source: ORNL.

In contrast, the results of the V-bending test of the as-received 2.5-mm AA7075-T6 alloy showed clear cracking when $r/t=1.2$. This might be due to a different microstructure within the 2.5-mm-thick alloy; in particular, the second particle volume fraction and distributions. Future work will include microstructure examinations for input in the macro-micro modeling scheme to elucidate the reason of the different bendability of two AA7075-T6 Al alloys of different thicknesses.

Subtask 1.4: High-Performance Computing for DFT Studies of Cast-Mg Local Corrosion Mitigation

To provide the insights into understanding the corrosion mechanisms of Mg alloys and designing corrosion-resistant Mg alloys, the effect of dopants on the corrosion mechanism of Mg surfaces was investigated. In this subtask, the effect of dopants—including Zn, Al, and Ce—on the initial stages of water adsorption and surface atoms dissolution was investigated. Here, the role of Al, Zn, and Ce alloying elements in the initial stages of water adsorption on the Mg (0001) surface was investigated theoretically. Pure and alloyed Mg surfaces were represented using the periodic slab model with the surface area of 2.65 nm^2 ; the slab thickness was six atomic planes. DFT simulations were used to quantify the stability of the dopants, binding energies of the adsorbed water clusters containing up to 6 H_2O molecules, and the effect of the dopants on the orientations of the adsorbed molecules.

The simulations reveal noticeable charge transfer between the surface Mg and dopants, which affects the energetics and configurations of the adsorbed H_2O molecules. Moreover, the variety of the H_2O molecules binding sites is richer on the doped surfaces, as observed in Figure II.1.10.6(a) and (b). A single H_2O molecule is more stable on the Mg sites near Zn and Al than on the pure Mg surface. Interestingly, H_2O is the most stable when located on top of the Ce dopant site. In contrast, H_2O located on top of Zn and Al are less stable than on top of the Mg site, as summarized in Figure II.1.10.6(c). Notably, the Ce-water interaction is much stronger than that for the other three metals for all four considered surface sites. We also determined that the stability of adsorbed water molecules increases with increasing coverage due to the formation of hydrogen bonds. For the clusters containing six H_2O molecules, the adsorption energy per molecule is $\sim 30\%$ larger than that in the case of an isolated H_2O molecule. This strong adsorption may contribute to the surface Mg atom dissolution.

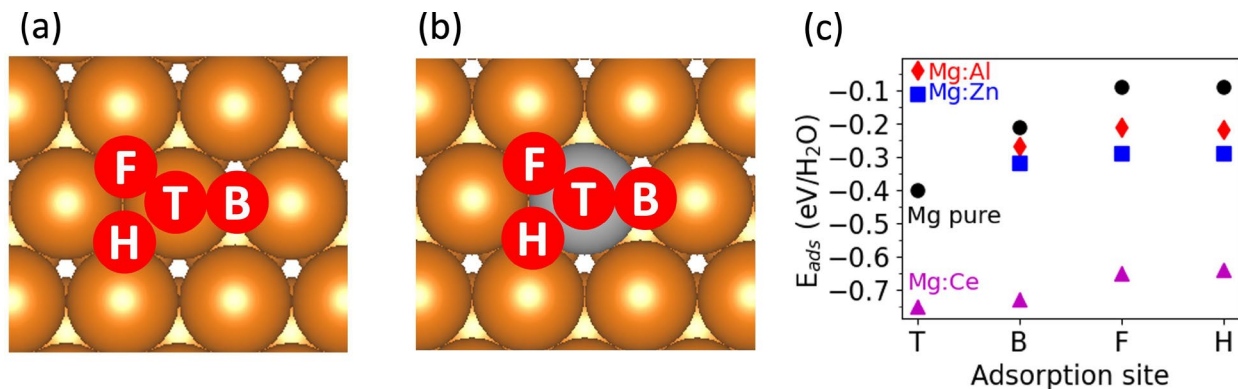


Figure II.1.10.6. (a) H_2O molecule adsorption sites on the Mg(0001) surface. (b) H_2O molecule adsorption sites near a substitutional defect on the doped Mg(0001) surface. Orange and gray spheres represent Mg and impure Al, Zn, and Ce atoms, respectively. F, H, T, and B mark the face-centered cubic hollow, hexagonal close pack hollow, and top and bridge sites, respectively. (c) Adsorption energies of a single water molecule on the pure (black circles) and doped Mg(0001) surfaces: Al (red diamonds), Zn (blue squares), and Ce (magenta triangles). Source: PNNL.

Task 2: Residual Stress Characterization, Prediction, and Optimization for Hybrid Property Assemblies

The aim of this task is to investigate residual stresses resulting from locally modified properties and provide support to other projects in the various Thrusts 1–3. The approach proposed in this project will combine the continuum-level models to predict the residual stresses, dimensional instability, and latent defects; with experimental measurements of the extent of residual stresses caused by the local enhancement methods. During FY 2021, predictive modeling tools were developed, and initial residual measurements were conducted validating the models. In FY 2021, the focus was on investigating residual stresses caused by FSP of Al sheets and Al castings.

Subtask 2.1: Modeling of the Residual Stresses during FSP

FSP enables local modifications to microstructures for local property enhancement. However, FSP also induces undesirable residual stresses that reduce fatigue life and cause part distortion. Therefore, the objective was to develop simulation capabilities that predict residual stresses arising during FSP and help establish optimum process parameters and conditions for residual stress mitigation.

During FSP, heat is generated through the friction between the tool and the specimen, and plastic work due to large deformation around the pin tool. The thermal pseudo-mechanical (TPM) model uses an analytical equation for heat generation instead of explicitly modeling the material flow. In this way, the tool can be treated as only a surface heat flux in the thermomechanical FE simulation.

Figure II.1.10.7(a) shows the residual stresses both longitudinal and transverse to the weld direction from the TPM simulation and experimental characterization (see Subtask 2.2) for an Al7075 FSP sample. The simulations can be seen to be predicting the peak stresses accurately. Longitudinal and transverse residual stress distributions were predicted but need improvement in the zones close to the weld line.

A way to improve simulation accuracy is to replace the analytical heat generation equation with a model that explicitly considers heat dissipation from the plastic flow associated with FSP. SPH was used to just simulate the heat generation rate from FSP, and this net heat generation was inserted as heat flux in the FE model. For validation of this proposed coupling of SPH and FE, a typical FSP process is simulated using SPH until a steady-state heat generation rate is achieved. This net heat generation rate is then transferred to the FE model. Now, at an instance, the simulated temperature fields from both the SPH and FE model methods are compared in Figure II.1.10.7(b). The close match in the peak temperatures and their distributions validates the thermal coupling aspect of the proposed SPH-FE approach.

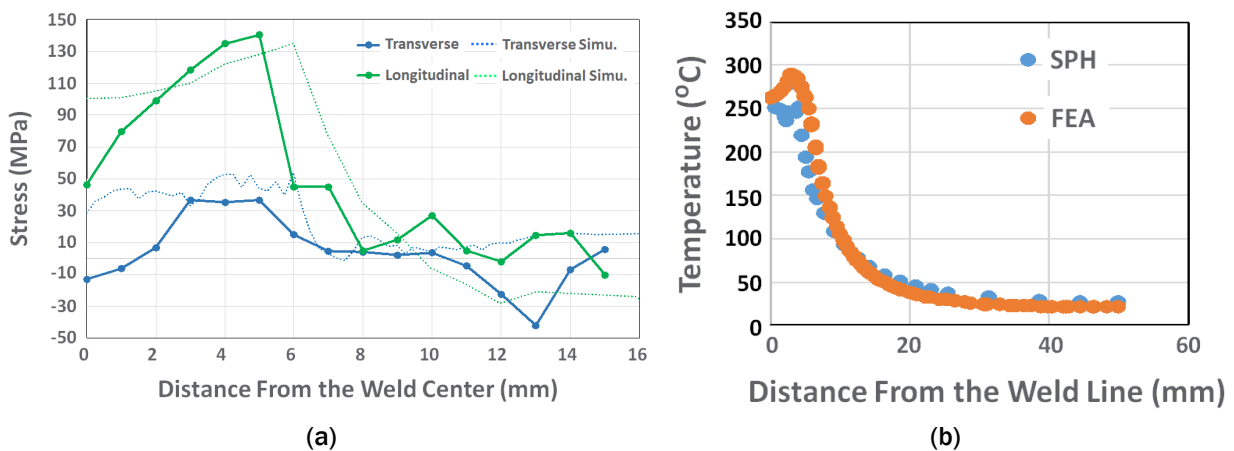


Figure II.1.10.7. (a) Comparison of the residual stresses from the TPM model with the experimental characterization data from an Al7075 FSP sample. (b) Comparison of the temperatures from finite element analysis and SPH along a line normal to the weld direction. Source: PNNL.

Future work would involve evaluating the accuracy and computational efficiency of the proposed combined SPH-FE approach in predicting residual stresses. In addition, the accuracy of residual stress prediction close to the weld center will be improved by modeling the material property evolution due to dynamic recrystallization.

Subtask 2.1: Experimental Measurements of Residual Stress

Experimental measurement of residual stresses were conducted on FSP processed samples obtained from two projects in Thrusts 1 and 2. An Al 7075 sheet and Al A380 casting samples were processed with FSP and residual stress measurements were conducted using hole-drilling and the XRD method. Samples were electropolished to remove material and through-thickness measurements were conducted using XRD.

Figure II.1.10.8(a) and (b) show the location of the measurements that were conducted at different depths. Figure II.1.10.8(c) shows a comparison between the two methods in the FSP processed 7075 sheet sample. Overall results show that general agreement beyond a depth of 50 μm is relatively good between the two methods. The measured residual stresses were used to validate the developed models.

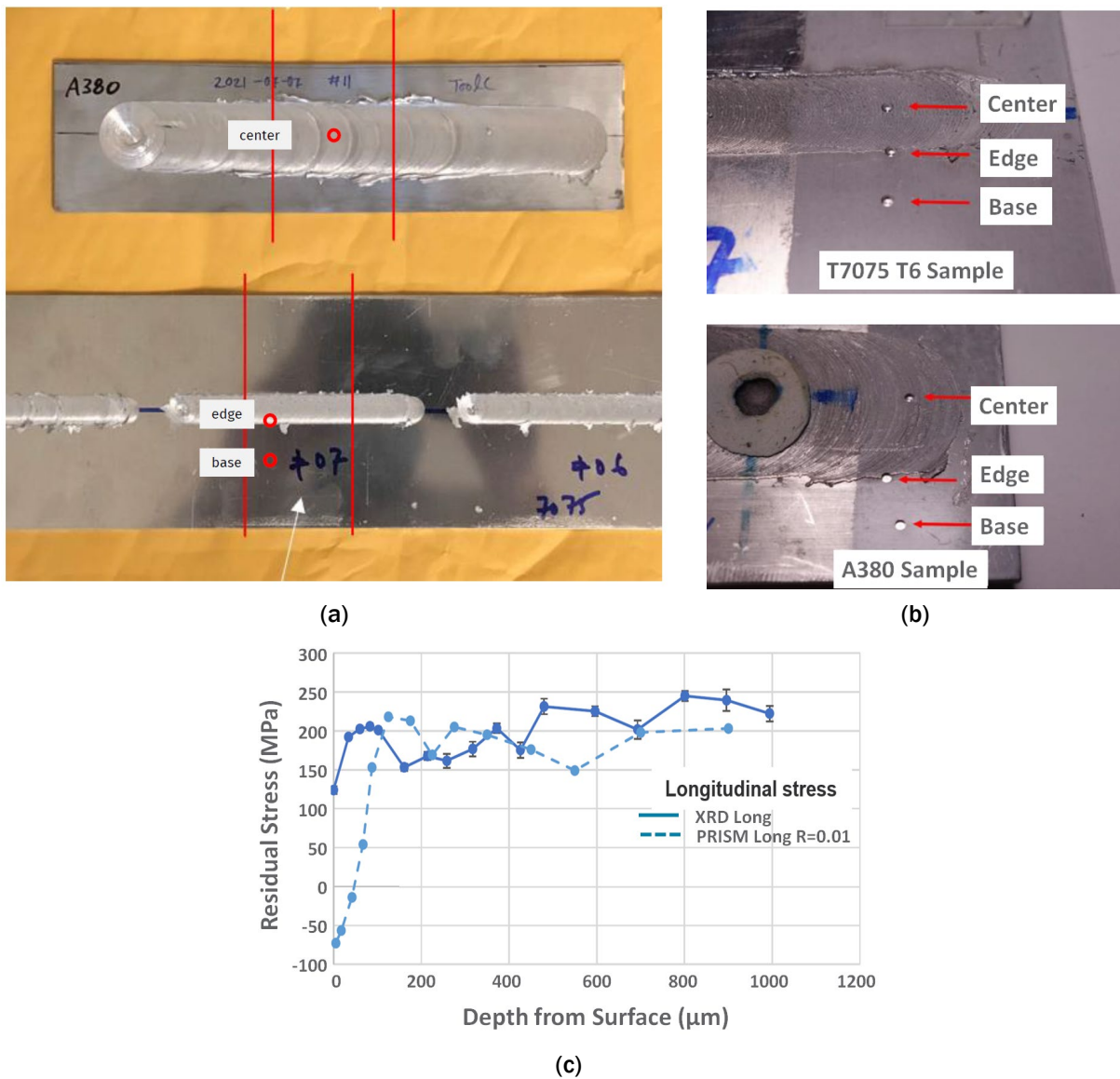


Figure II.1.10.8. (a) Two FSP processed Al samples used for residual stress measurement. (b) Three locations selected for the depth profile of residual stresses. (c) Example of through-thickness longitudinal residual stress measurements using hole-drilling and XRD on a 7075 FSP processed sheet. Source: PNNL.

Task 3: Material Life Cycle

It is uncommon for materials and products to be developed with much thought to sustainability and recyclability. The LMCP has deliberately provided focus on this area during the development process, which is to be commended. One of the main purposes of the program is to lightweight for vehicle efficiency. Without considering the sustainability of the manufacturing and end-of-life management, understanding the overall effect the materials have on sustainability is difficult. This first year of the program has been used to get a better understanding of the Al and Mg recycling landscape and to initially review how this program's efforts can help to increase sustainability and recyclability.

As this program focuses in on Al and Mg materials, the attention thus far, as related to sustainability, is the affect that these new materials—as well as a combination of materials—can have on the improvement of the sustainability at end-of-life. Understanding how these materials are recovered for recycling and how they are recycled is important. Vehicles are shredded with other metal-bearing scrap items at what is known as auto-shredders. The feed material is shredded to fist-sized pieces and then subjected to several unit operations to separate and recover metal materials for recycling. Al and Mg are typically recovered in a mixture of non-ferrous metals using eddy current separators. In the past, much of this material ended up being shipped out of the county to be sorted into furnace-ready fractions for recycling. Many of these countries have started to close their doors to this practice. This has resulted in the need to sort this non-ferrous metal mixture here in the U.S., and to recycle these metals in domestic secondary furnaces. This creates a great opportunity because now these materials are more likely to find purpose in the U.S.

There are a few ways to separate the mixed non-ferrous fraction into furnace-ready fractions. One of the most common methods is the use of dense media technologies. This process produces an Mg-rich fraction, an Al fraction, and a heavier metal fraction. Unfortunately, a measurable amount of Mg has not been recovered or recycled using this process in the U.S. This fraction is still sent overseas for further sorting and recycling. The Al fraction, on the other hand, can be further separated or used as is for inclusion as recycled content in new secondary production. In some instances, sensor sorting of metals by alloy is possible, but costs are still high—and therefore prohibitive—for many situations.

It has been challenging to get good, consistent information from industry on how the LMCP can improve the recyclability of Al back into vehicles. As mentioned, the mixed Al fraction can be sorted, though at high expense, into alloy categories. In most instances of dense media, the Al product is a mix of many alloys. A specific list of alloying elements, or melt contaminants, which would be good to eliminate from the mixture was not obvious. The general rule of thumb was to keep the broad list of alloying metals such as copper (Cu), silicon, Zn, manganese, and Mg as well as contaminants such as Fe, as low as possible so less dilution with new Al was necessary to reduce the levels to the desired product outcome.

Finally, there likely are many sustainability and recyclability wins to be highlighted. In many cases, this program will result in singular alloys or minimal alloys being used together to replace a part that would have used many more alloys or altogether different metals. The fewer alloys that are in a mixture help reduce the complexity of separations and recycling. In addition, this program will minimize the need for “over-building” a part because it requires high-performance in a small portion of the overall part. Improving performance at specific locations with the same or similar alloy results in more efficient use of material, which therefore reduces the embodied energy and CO₂ in the part.

Conclusions

Advanced characterization at PNNL using STEM and APT revealed a reduction in precipitate number density in Al-7085-T78 alloy after FSP, which in turn helped explain the observed improvement in the bendability of the FSP processed alloy.

Thermodynamic and process modeling was developed at ORNL under Subtask 1.2 to understand the factors affecting the printability and heat-treatment response for AM of Al alloys onto dissimilar cast or stamped Al

automotive parts. Under Subtask 1.3, the macro-micro FEM scheme was demonstrated to be valuable to predict local microstructure influences on the bendability of the AA7075T6 alloys.

The DFT studies in Subtask 1.4 revealed that the alloying elements reduced the stability of the Mg atoms next to them, with or without the adsorbed water molecules. It was also revealed that overall, the studied alloying elements enhance the water adsorption, dissociation, and dissolution of Mg atoms. The role of dopants in Mg surface corrosion might lie in facilitating surface passivation and eventually slow the corrosion rate.

Key modeling capabilities—such as the TPM model, SPH, and FE models, as well as the experimental methods—have now been developed to predict and evaluate residual stresses in friction stir processed alloys under Task 2.

Finally, in the material life cycle task under Task 3, early indications show that the LMCP has the capability to improve the overall environmental impact using parts that incorporate the technologies being developed in the program. This can be realized through the reduction of material demand, more effective vehicle lightweighting, and therefore vehicle use efficiency, increased recyclability, and recycle content in future vehicles.

Key Publications

All publications are currently under preparation or under peer review.

References

1. Kou, S., 2015, “A criterion for cracking during solidification,” *Acta Mater.*, Vol. 88, pp. 366–374.
2. Li, S., W. Xu, G. Xiao, and B. Chen, 2018, “Weld formation in laser hot-wire welding of 7075 aluminum alloy,” *Metals*, Vol. 8, No. 11, Art. 909.
3. Rosenthal, D., 1941, “Mathematical theory of heat distribution during welding and cutting,” *Weld J.*, Vol. 20, pp. 220–234.
4. Rappaz, M., J.-M. Drezet, and M. Gremaud, 1999, “A new hot-tearing criterion,” *Metall. Mater. Trans. A-Phys. Metall. Mater. Sci.*, Vol. 30, No. 2, pp. 449–455.
5. Inselberg, A., 2009, *Parallel Coordinates: Visual Multidimensional Geometry and its Applications*, Vol. 20. Springer Science & Business Media.
6. Coleman, J., A. Plotkowski, B. Stump, N. Raghavan, A. Sabau, M. Krane, J. Heigel, R. Ricker, L. Levine, and S. Babu, 2020, “Sensitivity of thermal predictions to uncertain surface tension data in laser additive manufacturing,” *J. Heat Trans-T ASME*, Vol. 142, No. 12, Art. 122201.
7. Wikipedia, “VDA 6.1.” Available at: https://en.wikipedia.org/wiki/VDA_6.1 (accessed 4 January 2022).

Acknowledgments

For Subtask 1.1, contributions from M. Song, C. Roach, T. Ajantiwalay, H. Das, M. Efe, and P. Upadhyay are acknowledged. We gratefully acknowledge ORNL staff and postdoctoral researchers G. L. Knapp, B. Stump, Y. Yang, J. Coleman, R. Kannan, and A. Plotkowski for their contributions to Subtask 1.2. Contributions by X. Hu and G. Muralidharan for Task 1.3 are acknowledged. We further acknowledge the contributions from Q. Pang, P. Sushko and V. Joshi for Subtask 1.4. For the Task 2 results, contributions by K. Balusu, K. S. Choi, and L. Li are acknowledged. The Environmental Molecular Sciences Laboratory (EMSL), which is a DOE PNNL National User Facility funded by biological environmental research, is acknowledged for the advanced microscopy facility access for this program.

II.1.11 Solid-Phase Processing of Magnesium and Aluminum (Pacific Northwest National Laboratory)

Vineet V. Joshi, Principal Investigator

Pacific Northwest National Laboratory
900 Battelle Boulevard
Richland, WA 99354
E-mail: vineet.joshi@pnnl.gov

Jerry L. Gibbs, DOE Technology Manager

U.S. Department of Energy
E-mail: jerry.gibbs@ee.doe.gov

Start Date: January 18, 2019 End Date: December 31, 2021
Project Funding (FY 2021): \$500,000 DOE share: \$500,000 Non-DOE share: \$0

Project Introduction

The primary goal of this project is to utilize SPP techniques to improve the properties of Mg and Al alloys for automotive application; thereby reducing the need to over-design the structure and add unnecessary weight to a vehicle [1, 2]. We aim to comprehend the detailed microstructural evolution in Mg [3, 4] and Al alloys [5] processed via novel solid-state processing, namely ShAPE™, and its role on corrosion and mechanical behaviors. The primary goal is to attain uniform microstructure, equiaxed grains, finer and homogeneously distributed precipitates, and chemical homogeneity along with desired texture to eliminate yield asymmetry and strength differential in these alloys.

Along with this, Al-MMC will also be utilized as a part of this study. Al-MMCs have always been limited by poor ductility—typically less than 1%. As a result, Al-MMC tubes and sheet products are difficult to manufacture and even more difficult to form into usable shapes for structural applications. Further, the poor ductility limits applications that require higher toughness and/or energy absorption characteristics. The upside is that by the addition of discrete ceramic particles to Al, the modulus can be increased significantly. For automotive applications where stiffness is critical, especially in higher strength materials where the desire is to decrease gauge thickness for maximum lightweighting, an Al-MMC can be beneficial. ShAPE will be used to produce an Al-MMC tube with either TiB₂ or Al₂O₃ particles to increase the modulus, which is increased linearly with the volume fraction of particles. Further, if sub-micron particles can be utilized, the strength of the metal composite should increase without a significant sacrifice of ductility. In addition, the ShAPE process was utilized for synthesizing Al-MMCs with discrete ceramic particulates.

Objectives

The objective of this project is to utilize SPP techniques to improve the properties of Mg and Al alloys for automotive applications; thereby reducing the need to over-design the structure and add unnecessary weight to a vehicle. In this project, the ability of SPP to uniquely modify the alloy microstructure and chemistry during fabrication of wrought materials will be investigated as a means to improve materials performance, and will demonstrate: (1) scalable SPP pathways for the manufacture of Mg and Al in semi-finished products and finished components; (2) that SPP methods can be used to robustly produce and tailor desired microstructures in the targeted materials; and (3) better properties and application-relevant performance for materials produced through SPP, relative to materials produced by conventional processing methods.

Approach

Commercially extruded AZ31B, as-cast AZ31, and cast ZK60 alloys were purchased from MetalMart International, Inc (Commerce, CA, USA). Canmet (Hamilton, ON, Canada) cast AZ31-2Si Mg-3Si alloy was cast at Brunel University (London, UK). Sourced Mg alloys were first machined into billets measuring approximately 31.7 mm in diameter by 18-mm-thick. The Mg alloy extruded billets were extruded into 5-mm diameter rods using ShAPE; a diagram of the apparatus is shown in Figure II.1.11.1. Commercially extruded Al alloys Al7075-T6 (AA7075) and Al6061-T6 (AA6061) that were procured from McMaster-Carr were machined into cylindrical billets measuring approximately 31.7 mm in diameter and 19 mm long. In all cases, these were subsequently extruded into 5-mm diameter rods using ShAPE at an extrusion ratio of ~40. MMCs were synthesized from a specially designed composite puck with 5 vol.% to 25 vol.% of hard ceramic particles (Al_2O_3). The Al_2O_3 powder with an average 1- μm particle size was used for dispersion in the Almatrix.

Prior to using ShAPE, the billet was loaded into a cylindrical container measuring 31.8 mm from the inside diameter and 20 mm tall that is held stationary, as shown in Figure II.1.11.1(a). A rotating die then was brought into contact with the material and an axial force applied. The combination of rotation and applied force causes heating due to friction between the tool and the material interface, as well as from plastic deformation of the material. An extrusion is formed as the softened material is pushed out of the die orifice due to axial pressure and motion of material flow from the scrolls. A 4-scroll die was used for this work, as shown in Figure II.1.11.1(b). ShAPE and feedstock materials in all cases will be tested for mechanical properties. Mechanical testing will provide YS, UTS, modulus, and elongation. A comparison of mechanical properties will be made with commercially available alloys with ShAPE-processed alloys. Advanced characterization will also be performed to correlate the mechanical and corrosion properties with microstructure.

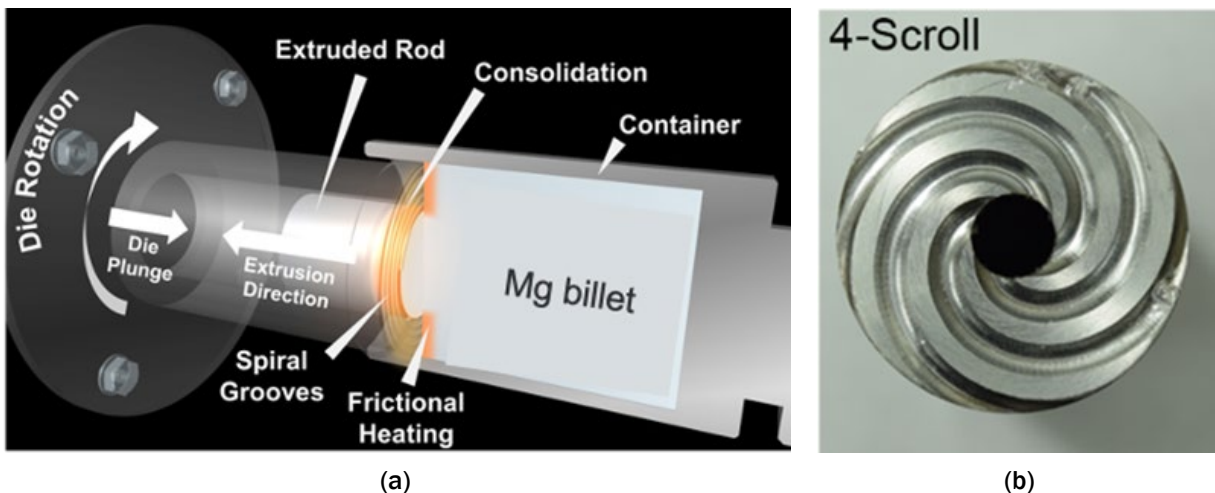


Figure II.1.11.1. (a) A diagram of the ShAPE process. (b) Photo of the 4-scroll die. Source: PNNL.

Results

ShAPE Processing of Mg Alloys: We successfully extruded several Mg alloys approximately 300 mm long and 5 mm in diameter. ShAPE processing can alter the grain size distribution and their orientations. Therefore, EBSD characterization was performed on the surfaces parallel (longitudinal) to the extrusion direction (ED) and ShAPE direction (SED) to understand the grain size distribution and texture evolution with processing. First, comparing the grain size distributions of both samples, the as-extruded sample shows a bimodal grain size distribution (i.e., elongated lamellar along the ED) and equiaxed sub-micron-size grains, as observed in Figure II.1.11.2(a). By comparison, the ShAPE-processed sample shows a distribution of equiaxed dynamic recrystallized (DRX) grains, as shown in Figure II.1.11.2(b). The grain size distribution map of both samples is represented in Figure II.1.11.2(g), which indicates that the average grain size of the ShAPE-processed sample is greater than the as-extruded sample. The formation of DRX grains during the ShAPE processing can be

attributed to the application of high force and temperature (e.g., $\sim 400^\circ\text{C}$). The texture analysis of the ShAPE-processed and as-extruded samples through the (0002) pole figures from planes normal (transverse) to the SED and ED in Figure II.1.11.2(c) through Figure II.1.11.2(d), which is the plane of interest for the corrosion study, show that the former has a tilted basal texture with the (0002) pole tilted by $\sim 30^\circ$ to 60° with the SED. Later, this same sample shows a fiber texture with most of the basal planes parallel to ED. These results can be further supported by the ED and SED IPF. Similar tilted basal and fiber textures in Mg alloys were earlier observed in the equal channel angular pressing and hydrostatic extrusion. The evolution of tilted basal texture in a ShAPE-processed sample from an as-extruded sample can be attributed to many factors. For instance, the activation of non-basal slips, such as prismatic slip at a high-temperature, not only acts as a principal mechanism for the motion of dislocation to form low and high-angle GBs, but also helps in rotation of newly formed DRX grains with variations in orientation. Additionally, it can be observed from the kernel misorientation map and its distribution plot that with the ShAPE processing, the overall misorientation that has reduced can be co-related to the overall reduction in residual strain.

Along with altering the grain size distribution and their orientations, ShAPE processing can also change the second-phase particle size and distribution. For the as-extruded and ShAPE-processed samples, surfaces both parallel and perpendicular (e.g., in the longitudinal/transverse sections) to the extrusion and ShAPE extrusion direction were observed. All images show the presence of a bright second-phase in the matrix, as shown in Figure II.1.11.3. The EDS spectrum for the bright phase, as observed in Figure II.1.11.3(f), shows it as an Al-Mn-based intermetallic, Al_8Mn_5 , which is similar to our earlier work. The size and spatial distribution of this intermetallic phase has been found to vary with processing conditions. Quantitative comparison of the particle size and their separation/distribution on surfaces that are perpendicular/longitudinal sections to the extrusion and ShAPE directions (e.g., the plane of interest for the corrosion study) shows that the large size particles in the as-extruded sample were fragmented into smaller size particles and distributed more homogeneously during the ShAPE processing. Visual observation from the SEM, as observed in Figure II.1.11.3(a), shows that the sizes of particles in the as-cast sample are larger than the other two condition samples. Further, with ShAPE processing, a uniform distribution of second-phase particles can be observed on the plane parallel to the ShAPE direction, which can be attributed to applied shear along with hydrostatic stress in the ShAPE process that can break the longitudinal alignment of particles. These two samples (except as-cast) were analyzed for their quantitative distribution plots because the as-extruded sample was the input feedstock for the ShAPE processing.

The mechanical behavior was investigated and compared for conventionally extruded AZ31B, ShAPE-processed extruded AZ31B, cast AZ31B, and ShAPE-processed cast-AZ31B. True stress-strain curves for both tension and compression were plotted in Figure II.1.11.4. For as-extruded AZ31B, the commonly observed YA and SD were present, with compressive yield stress (CYS) being much lower than the tensile yield stress (TYS), whereas the compressive flow stress rapidly increased after yielding, with ultimate compressive strength (UCS) significantly higher than UTS. In contrast, the tensile curve was well aligned with the compressive curve for ShAPE AZ31B, until the compressive strain level extended far beyond that of tensile strain.

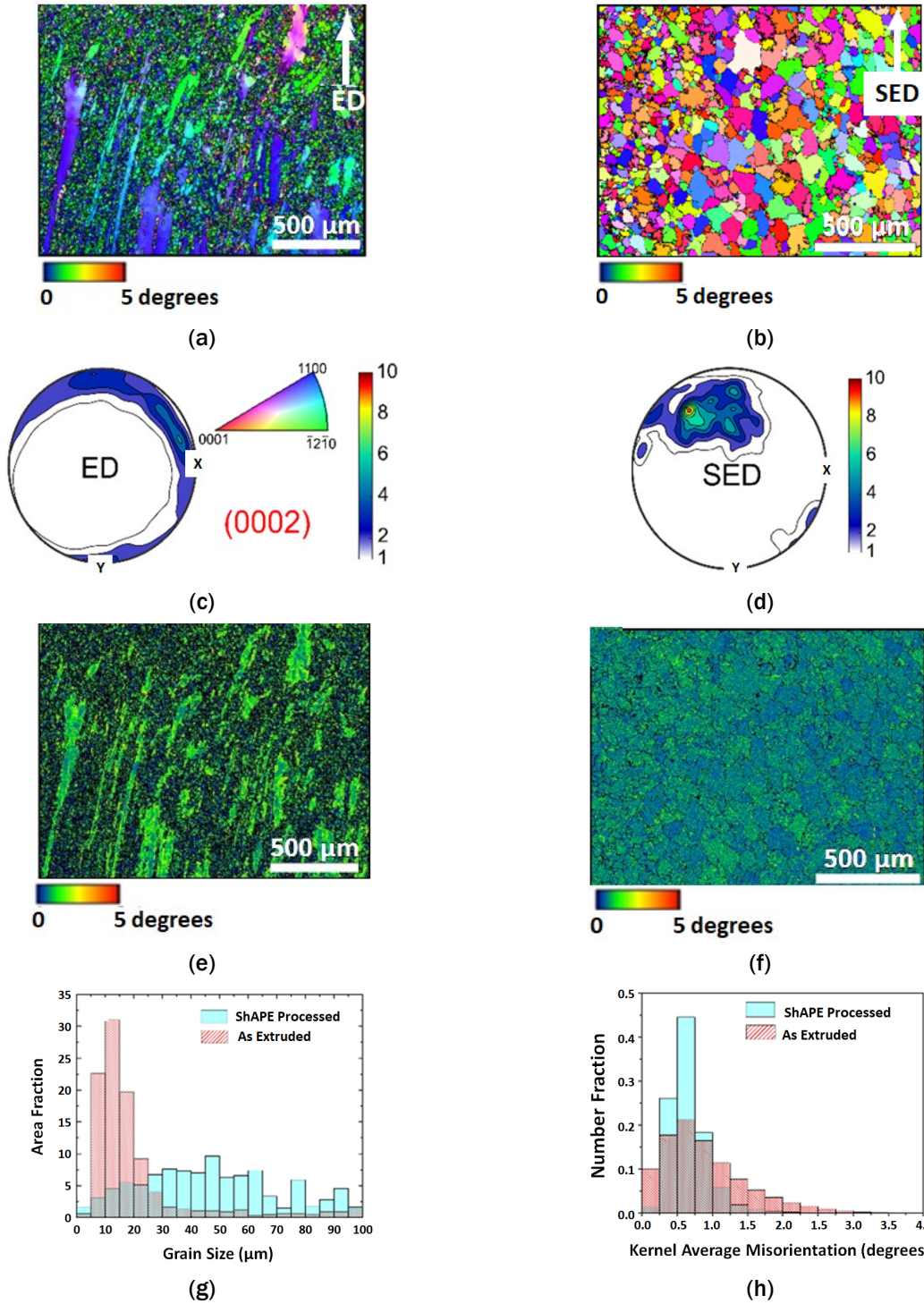


Figure II.1.11.2. EBSD microstructural characterization: (a) IPF map of an-extruded sample on the surface parallel to the extrusion direction and (b) IPF map of the ShAPE-processed sample on the surface parallel to the ShAPE direction. (c) and (d) (0002) pole figures of EBSD micrographs, as shown in (a) and (b), respectively. Kernel average misorientation (KAM) maps for (e) as-extruded and (f) ShAPE-processed samples. (g) The grain size distribution plot; and (h) the KAM quantitative distribution plot for maps (e) and (f). Source: PNNL.

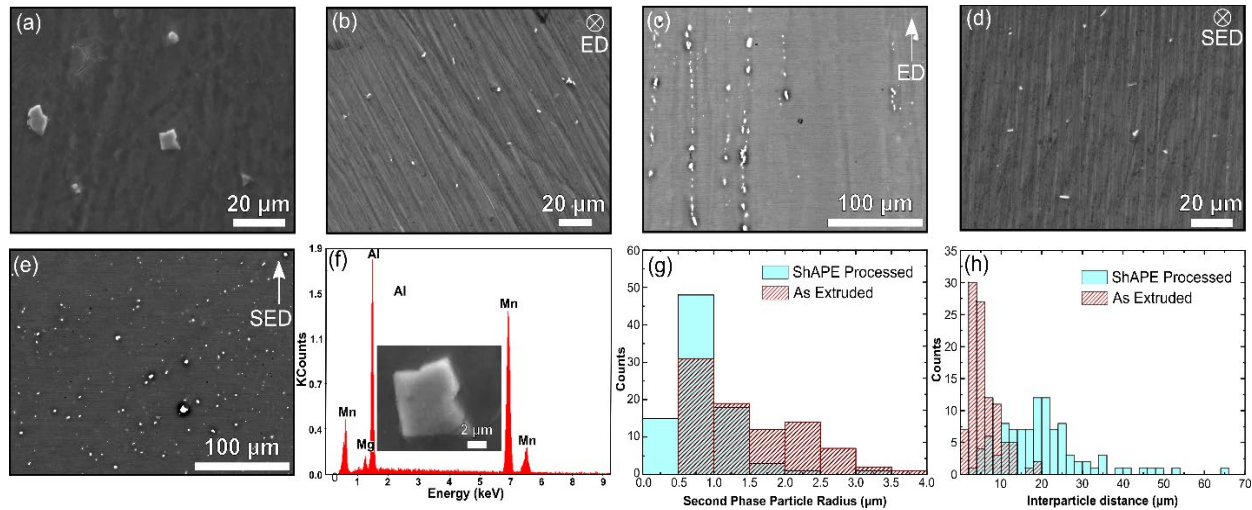


Figure II.1.11.3. Microstructural characterization of as-cast, as-extruded, and ShAPE-processed AZ31B alloys. (a) SEM image of an as-cast sample. SEM images of (b) perpendicular and (c) parallel surfaces to the extrusion direction of the as-extruded alloy. SEM images of (d) perpendicular and (e) parallel surfaces to the SED of the ShAPE-processed alloy. (f) An elemental spectrum for the second-phase particle. (g) The second-phase particle size and (h) interparticle separation distance distribution for the as-extruded and ShAPE-processed samples on the perpendicular surfaces. Source: PNNL.

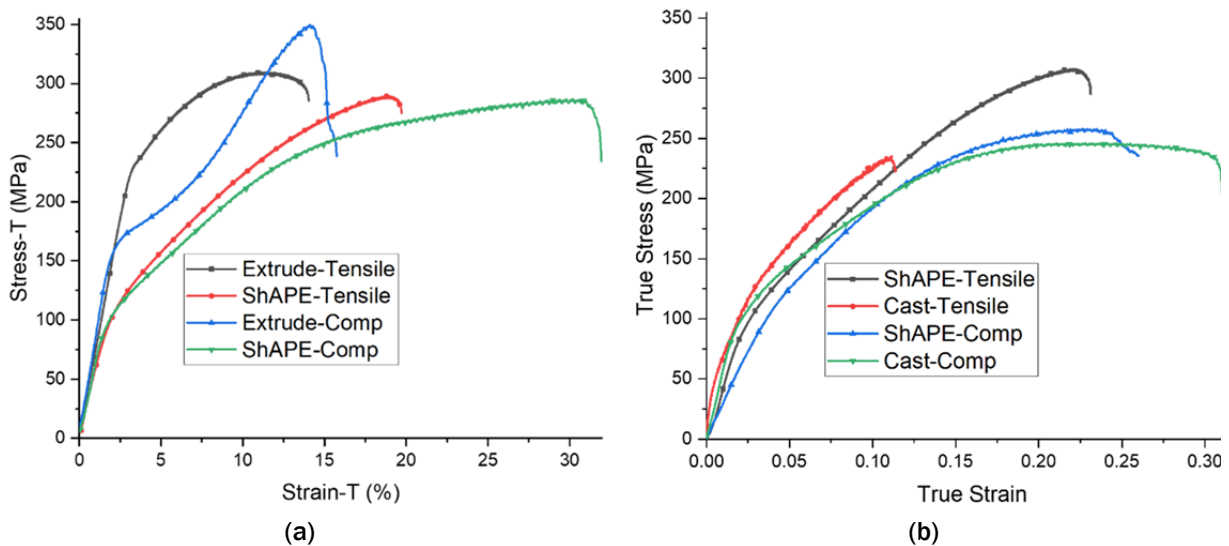


Figure II.1.11.4. Tensile and compressive true stress-strain curves for (a) the as-extruded AZ31B vs. ShAPE and (b) the as-cast vs. ShAPE. Source: PNNL.

The quantitative comparisons on YS, ultimate strength, strain at failure, and uniform elongation (for tensile tests only) were summarized in Table II.1.11.1 for the extruded, cast, and ShAPE AZ31B samples. ShAPE drives the CYS/TYS ratio to close to 1 in both cases. Also included are preliminary results of only ShAPE of cast ZK60 and ShAPE of cast-Mg-3Si. Preliminary data suggests ShAPE of cast ZK60 results in a CYS/TYS ratio of 1.03 to 1.30. ShAPE of cast-Mg-3Si ratios of 1.35 and 1.90 suggest less success in driving that to 1 in this alloy. One can notice CYS/TYS for ShAPE-extruded AZ31B was 1.05, whereas for as-extruded AZ31B, the value was 0.66. Similarly, UCS/TYS (not shown on the table) was 0.99 for the former, and 1.13 for the latter. Table II.1.11.1 shows that the ShAPE process improved CYS/TYS to closer to 1 for the cast case as well. The decrease in the compressive and TYS is associated with the basal plane orientation, which in the case

of the ShAPE-extruded sample was approximately 45 degrees to the extrusion axis. Notably, the ShAPE process significantly improved ductility, with uniform elongation almost doubled from 7.2% to 13.9% and the strength differential, typically observed in the Mg alloys, was completely eliminated. A similar analysis was performed for ShAPE-processed Mg-3Si and ZK60. The results can be found in the lower half of Table II.1.11.1. Here it is found that the CYS/TYS values for ShAPE-extruded ZK60 and ShAPE-extruded Mg-3Si were 1.30 and 1.35, respectively, suggesting a possible benefit to these alloys—especially in bumper beam applications.

Table II.1.11.1. Comparisons of Mechanical Properties of As-Extruded AZ31B vs. ShAPE of Extruded AZ31, and As-Cast AZ31 vs. ShAPE of Cast AZ31

Material	Sample ID	Yield Strength (MPa)	Ultimate Strength (MPa)	Ductility (%)	CYS/TYS
Extruded AZ31	Extrude Tensile	216.3	309.6	10.40	0.66
	Extrude Comp.	142.2	349.5	10.70	
	Extrude ShAPE Tensile	82.8	289.3	14.80	1.05
	Extrude ShAPE Comp.	87.1	286.7	27.20	
Cast AZ31	Cast-Tensile	33	235.3	10.10	1.94
	Cast-Comp	64	246.1	26.70	
	Cast-ShAPE-Tensile	71.7	308.7	16.40	1.03
	Cast-ShAPE-Comp	73.7	257.9	15.60	
ZK60	Cast-ShAPE Tensile	149	340	18	1.30
	Cast-ShAPE Comp	194	NA	NA	
Mg 3Si	Cast-ShAPE Tensile	52	174	13	1.35
	Cast-ShAPE Comp	70	NA	NA	

ShAPE Processing of Al Alloys and MMCs: Similar to Mg alloys, commercial AA7075 and AA6061 alloys were also extruded using ShAPE. Advantages of ShAPE-extruded microstructures over conventional extrusion were explored. To compare the effects of shear-processing on the AA7075-T6 microstructures to those of conventionally extruded microstructure, T6 aging was performed on both the ShAPE-extruded rods and conventionally extruded feedstock material. American Society for Testing and Materials (ASTM)-recommended T6 aging was performed on the feedstock material, where samples were solution-treated at 465°C for 40 min. For comparison, the ShAPE-extruded samples were solution-treated by flash-annealing them at 450°C for 15 min, which had been identified as optimal parameters. Artificial aging was performed at 120°C for solution-treated feedstock and ShAPE samples. Figure II.1.11.5(a) shows the artificial aging curves for both the conventionally extruded and ShAPE-extruded samples. Aging response in both conditions was very similar. This indicates that significantly lower solution treatment temperature and time were required for ShAPE-processed material to achieve peak aging strength than those for conventional extrusion materials. This corroborates the fact that ShAPE microstructures offer energy savings in post-processing heat-treatment.

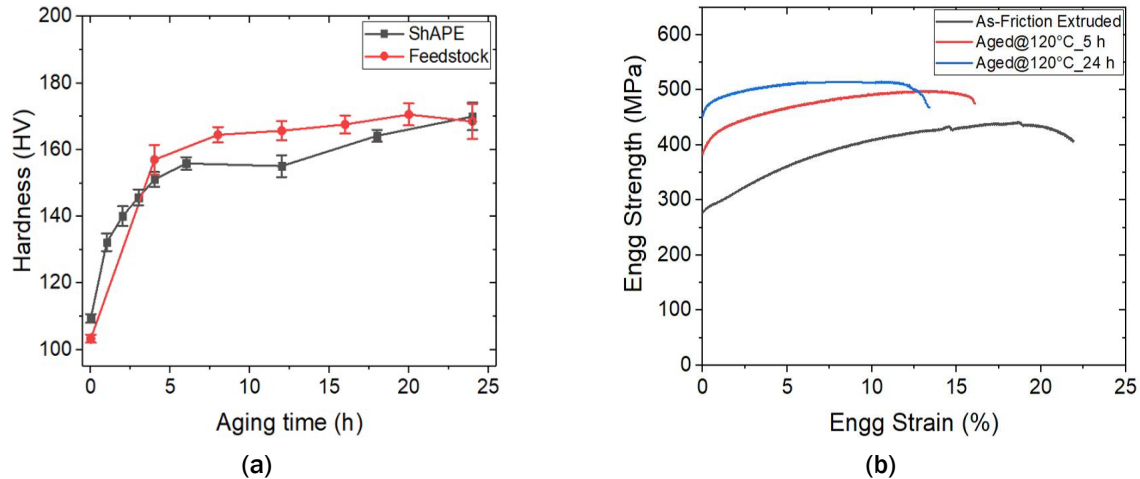


Figure II.1.11.5. (a) Artificial aging curve. (b) Tensile property of flash-annealed plus T6 aged samples. Source: PNNL.

Figure II.1.11.5(b) shows the engineering stress-strain curves of the as-ShAPE-processed and ShAPE+T6-aged samples. Flash-annealing was used for solution treatment: specimens were solution-treated at 450°C for 15 min. Artificial aging was performed at 120°C for 5 and 24 h. The as-ShAPE-processed sample showed a total elongation up to 22% and UTS around 440 MPa. However, after T6 aging, the total elongation decreased for both the aged samples. On the other hand, YS and UTS increased significantly. YS and UTS increased in the 24-h-aged sample compared to the 5-h-aged sample. Interestingly, the YS and UTS of the ShAPE-processed samples that were solutionized via flash-annealing technique at 450°C for 15 minutes and then aged at 120°C for 24 h met the ASTM T6 range of performance for the AA7075 alloy, as shown in Table II.1.11.2. In fact, the total elongation of these samples was beyond that specified for the ASTM samples. This shows that in addition to energy-efficient manufacturing pathways, ShAPE also serves to improve the performance of AA7075 alloys by retaining their strength while enhancing percent elongation.

Table II.1.11.2. Tensile Properties of ShAPE-Extruded Rods and Standard Deviation (σ)

Sample	YS (MPa)	UTS (MPa)	Total Elongation (%)
As Friction Extruded Processed	282 ± 7	437 ± 5	20.5 ± 2
Aged @ 120°C_5 h	399 ± 15	505 ± 10	13.3 ± 4
Aged @ 120°C_24 h	448 ± 25	523 ± 18	12.3 ± 2
ASTM-T6	430 - 480	510 - 540	5 - 11

We also successfully synthesized Al MMCs (i.e., Al alloy matrix plus discrete ceramic particles of 1 μm size embedded in the matrix) using the ShAPE process. A representative extruded 5-mm-diameter rod of Al6061 matrix with 5 vol.% Al_2O_3 MMC is shown in Figure II.1.11.6(a). Figure II.1.11.6(b) through Figure II.1.11.6(c) demonstrates the cross-section microstructure of the remnant puck and extruded rod by optical microscopy, showing a relatively uniform microstructure at the macroscopic scale. The darker color in the upper half of the remnant puck represents the processed zone during the ShAPE process. Figure II.1.11.7(a) shows the SEM backscatter micrographs of the cross-section of the MMC rod with different vol.% of the Al_2O_3 particles, all free of porosity or micro-voids in the microstructure, suggesting a good microstructure integrity is obtained after ShAPE processing. Importantly, all the rod microstructures exhibit the alternative distribution of particle dispersion, leading to a remarkable heterogeneity at the microscopic scale. The whiter periodic bands along the extrusion direction represent the regions where the particle content is less, and the grain size is relatively larger locally.

(a) Al6061 + 5 vol% Al₂O₃ MMC extruded rod by ShAPE



(b) Remnant puck after ShAPE extrusion



(c) Extruded rod (longitudinal direction)

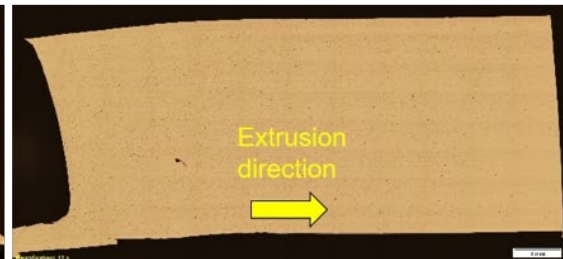


Figure II.1.11.6. (a) Example of Al-MMC rod made by ShAPE process. (b) An optical observation of the remnant puck. (c) The extruded rod along the longitudinal direction. Source: PNNL.

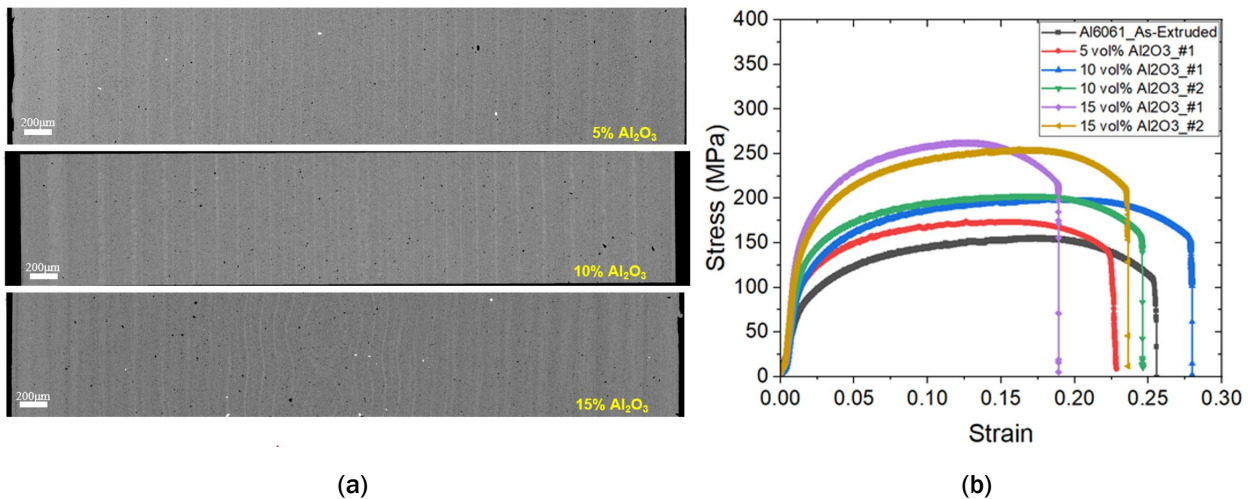


Figure II.1.11.7. (a) SEM backscatter micrographs of microstructure in the extruded rod of Al6061 matrix with different vol.% of Al₂O₃ particles. (b) Engineering stress-strain curves of the Al6061 MMC by tensile tests. Source: PNNL.

To test the mechanical properties of the produced MMC, uniaxial tensile tests were performed on those extruded rods with different vol.% of Al₂O₃ particles with the same testing condition. Figure II.1.11.7(b) shows the engineering stress-strain curves. Along with the MMC data, the as-ShAPE-processed 6061 is also presented in Figure II.1.11.7(b) as a benchmark for comparison. Strikingly, superior strength-ductility synergy is observed in the MMC products—both yield and ultimate strength increase significantly with the addition of Al₂O₃ particles without sacrificing the ductility. These encouraging results are expected to be closely related to the fine grain size and the development of hierarchical (wide distribution of second-phase particles) and heterogeneous (formation of alternating bands of particles and no particles) microstructures. All these factors contributed towards the exceptional strength, strain hardening, and elongation in these samples.

Conclusions

In this work, ShAPE was utilized to achieve improved properties in commercial Mg and Al alloys in the following ways:

- This work has shown that by using the optimized ShAPE process AZ series with and without silicon, ZK60 Mg alloys in as-received forms (e.g., as-cast or as-extruded) generated more uniform microstructure, equiaxed grains, finer and homogeneously distributed precipitates, and chemical homogeneity. The critical factors necessary to remove the yield anisotropy and minimizing the strength differential in Mg alloys was achieved using the ShAPE process. The ShAPE processes was responsible for tailoring the microstructure and is readily scalable to produce large parts relevant to automotive applications.
- The present study demonstrated fully consolidated, defect-free AA7075 rod extrusion using a shear-assisted processing method. This manufacturing method involves SPP of the AA7075 alloy with no melting or liquid phases formed during extrusion—even at local scale.
- Thoroughly homogenized, uniform microstructure was observed throughout the extruded rod. The measured average grain size in the ShAPE-extruded rod was $\sim 2.0 \mu\text{m}$, with precipitates uniformly distributed throughout the microstructure.
- ShAPE-extruded AA7075 alloy microstructure yielded advantages in reducing solution treatment time and temperature over those recommended per ASTM standard for conventionally extruded AA7075. Experimental results showed that lower solution treatment time and temperature were required before artificial aging to achieve maximum strength compared with those for conventional extrusion. Smaller precipitates and their uniform distribution in the microstructure may have also been important in reducing solution treatment time and temperature.
- Tensile data for samples that were flash-annealed and artificially aged after ShAPE processing showed exceptional increases in strength of UTS by over 19% and YS by over 59% as compared with an as-ShAPE-processed sample.
- MMC rods were successfully extruded over a fraction of 5 vol.% to 15 vol.% Al_2O_3 ceramic particles in an Al6061 and Al7075 matrix. Mechanical properties were evaluated for Al6061-(5 vol. % to 15 vol.%) Al_2O_3 extruded rods and more significantly the ductility of the MMC was same as that of the parent material. The strength of the MMC increased proportionally to volume fraction of ceramic particles added.

Key Publications

1. Darsell, J. T., D. Zhang, N. R. Overman, D. R. Herling, and V. V. Joshi, 2021, “Eliminating yield anisotropy and enhancing ductility in Mg alloys by shear-assisted processing and extrusion,” In: *Magnesium Technology 2021*, PNNL-SA-156766. The Minerals, Metals & Materials Society. Pittsburgh, PA, USA. pp. 91–99.
2. Beura, V., P. Garg, V. V. Joshi, and K. N. Solanki, 2020, “Numerical investigation of micro-galvanic corrosion in Mg alloys: Role of the cathodic intermetallic phase size and spatial distributions,” In: *Magnesium Technology 2020*, PNNL-SA-147890. Springer Nature. New York, NY, USA. pp. 217–223.
3. Beura V., D. Zhang, N. R. Overman, J. T. Darsell, D. R. Herling, K. N. Solanki, and V. V. Joshi, 2021, “Achieving excellent mechanical behavior and corrosion resistance in magnesium alloys through a novel solid-phase processing.” *Corros. Sci.* (submitted).
4. Kalsar, R., X. Ma, J Darsell, D. Zhang, K. Kappagantula, D. R. Herling, and V. V. Joshi, 2021, “Microstructure evolution, enhanced aging kinetics, and mechanical properties of Al7075 alloy after ShAPE,” *Mater. Sci. Eng. A* (submitted).

References

1. Joshi, V.V., S. Jana, D. Li, H. Garmestani, E. A. Nyberg, and C. A. Lavender, 2014, “High-shear deformation to produce high-strength and energy absorption in Mg alloys,” In: *Magnesium Technology 2014*, Proceedings of a Symposium Sponsored by the Magnesium Committee of the Light Metals Division of the Minerals, Metals & Materials Society (TMS), 143rd Annual Meeting & Exhibition, 16–20 February 2014, San Diego, CA, USA. pp. 83-88. John Wiley & Sons, Inc. Hoboken, NJ, USA.
2. Whalen, S., N. Overman, V. Joshi, T. Varga, D. Graff, and C. Lavender, 2019, “Magnesium alloy ZK60 tubing made by Shear-Assisted Processing and Extrusion (ShAPE),” *Mater. Sci. Eng. A*, Vol. 755, pp. 278–288.
3. Barnett, M. R., 2007, “Twinning and the ductility of magnesium alloys: Part I: ‘Tension’ twins,” *Mater. Sci. Eng. A*, Vol. 464, Nos. 1–2, pp. 1–7.
4. Zhang, D., H. Wen, M. A. Kumar, F. Chen, L. Zhang, I. J. Beyerlein, J. M. Schoenung, S. Mahajan, and E. J. Lavernia, 2016, “Yield symmetry and reduced strength differential in Mg-2.5Y alloy,” *Acta Mater.*, Vol. 120, pp. 75–85.
5. Whalen, S., M. Olszta, C. Roach, J. Darsell, D. Graff, M. Reza, E-Rabby, T. Roosendaal, W. Daye, T. Pelletiers, S. Mathaudhu, and N. Overman, 2019, “High ductility aluminum alloy made from powder by friction extrusion,” *Materialia*, Vol. 6, Art. 100260.

Acknowledgments

The PI at PNNL would like to acknowledge R. Kalsar, X. Ma, N. Overman, J. Darsell, D. Zhang, D. Herling, K. Kappaguntala, A. Guzman, M. Rhodes, V. Prabhakaran, V. Beura, and K. Solanki for processing and/or characterization activities for this project.

II.2 Carbon Fiber and Polymer Composites

II.2.1 Integrated Computational Materials Engineering Predictive Tools Development for Low-Cost Carbon Fiber for Lightweight Vehicles (University of Virginia)

Xiaodong (Chris) Li, Co-Principal Investigator

University of Virginia
122 Engineer's Way
Charlottesville, VA 22904
E-mail: xl3p@virginia.edu

Leonid V. Zhigilei, Co-Principal Investigator

University of Virginia
Wilsdorf Hall, Room 303D
Charlottesville, VA 22904
E-mail: lz2n@virginia.edu

Adri van Duin, Co-Principal Investigator

Pennsylvania State University
240 Research Building East
University Park, PA 16802
E-mail: acv13@psu.edu

James W. Klett, Co-Principal Investigator

Oak Ridge National Laboratory
1 Bethel Valley Road
Oak Ridge, TN 37831
E-mail: klettjw@ornl.gov

Desmond Cook, Co-Principal Investigator

Solvay Composite Materials, Carbon Fibers
50 Akron Drive
Greenville, SC 29602
E-mail: desmond.cook@solvay.com

Robert Hathaway, Co-Principal Investigator

Oshkosh Corporation
1917 Four Wheel Drive
Oshkosh, WI 54902
E-mail: BHathaway@oshkoshcorp.com

H. Felix Wu, DOE Technology Manager

U.S. Department of Energy
E-mail: felix.wu@ee.doe.gov

Start Date: October 1, 2017

End Date: March 31, 2021

Project Funding (FY 2021): \$1,319,900

DOE share: \$1,221,565

Non-DOE share: \$98,335

Project Introduction

In response to consumer demand for fuel-efficient vehicles and stringent vehicle emission regulations, automotive manufacturers are searching for alternative lightweight, high-strength materials to replace conventional metal structures in vehicle designs. Even compared to high-strength metal alloys, Carbon-fiber-reinforced polymer (CFRP) composites are a promising alternative due to their superior strength-to-weight ratio. Recent estimates have predicted that automotive weight reductions of 50% or greater will be necessary, in addition to enhanced engine and drivetrain efficiencies, to meet national and international emission standards [1, 2]. However, there are significant technical barriers that must be overcome to bring CFRP materials into widespread acceptance. CFRP materials are produced via a complex and expensive procedure and are often limited to small-scale production. A large portion of this cost is borne by the precursor material preparation—51% of the total CF cost may be attributed to the precursor fibers [3, 4]. Therefore, this project aims to develop low-cost alternative precursors and processing techniques through the implementation of an ICME framework to evaluate precursor conversion kinetics. This framework will be used to down-select precursors for laboratory- and pilot-scale production to validate resulting CFRP material properties and process cost-savings.

Currently, the highest quality CFs are produced from polyacrylonitrile (PAN) precursors, which have a high C yield and an ideal polymer structure for conversion into CFs with excellent mechanical properties. Typical yields are ~50 wt.% CF for the quantity of PAN precursor at the start of conversion. In literature, the highest quality commercially available CFs achieve strengths of up to 7 GPa (1000 ksi) [2, 5, 6]; however, PAN-derived CFs are expensive due to their high precursor cost- and energy-intensive processing, with costs of ~\$11/lb subject to petroleum-price fluctuations. Although advanced manufacturing techniques may further lower the price toward \$7/lb, PAN-derived fibers will likely remain too expensive for widespread adoption in the automotive industry [7, 8].

Therefore, the two most promising approaches to reduce the cost of CFs are to: (1) utilize new, low-cost precursors; and (2) reduce the energy requirements of CF processing. Project performance was planned to span three federal FY BPs. In FY 2019, Nylon 6 was identified as a promising low-cost alternative precursor. Laboratory-scale conversion of Nylon 6 into high-strength, low-cost CF was accomplished in FY 2020, and the ICME framework coupled with targeted experimentation was used to optimize the conversion process for reduced cost. FY 2021 was a two-quarter no-cost extension of the project through March 2021 due to delays caused by the COVID-19 pandemic. In the remaining two-quarters of the project, efforts to refine and scale the production of CFs derived from Nylon 6 continued alongside expanded characterizations of the fibers at all stages of the production process and ongoing advancement of the machine-learning-enhanced ICME framework.

Objectives

The first objective is to develop, integrate, and demonstrate an ICME framework and evaluate alternative precursors for suitability to manufacture low-cost CF. This ICME framework will predict CF properties, such as load to failure, failure mode, stiffness/deflection, dynamic performance, and microstructures. The framework must be capable of minimum modeling-element accuracies within 15% of measured properties, which would enable design, development, and optimization of precursor chemistry and kinetics associated with the CF conversion process. The ICME framework will also include methodologies to simulate manufacturing processes, including variability from both process and material.

The second objective is to research, develop, manufacture, and demonstrate CF precursor technology and processing techniques, where the CF will consist of thin, strong, multi-crystalline filaments of carbon used as a reinforcement material, especially in resins, capable of achieving the requirements in Table II.2.1.1.

Table II.2.1.1. Project Parameters and Requirements

Parameter	Requirement	
Cost	≤ \$5/pound	
Strength	≥ 250 Ksi	≥ 1.725 GPa
Modulus	≥ 25 Msi	≥ 172.5 GPa
Strain	≥ 1%	

Approach

The ICME framework was developed and validated around PAN-based CFs during FY 2018, and it can predict the properties of PAN-based CF within 15% error. This critical accomplishment supports the reliability of the assembled framework, which was extended to analyze alternative precursors in FY 2019. The ICME framework is constructed from Reactive Force Field (ReaxFF) simulations [9, 10], which predict the fiber chemistry during conversion, and large-scale MD simulations, which elucidate polymer matrix/fiber mechanics and properties [11, 12]. This framework requires key input parameters (i.e., precursor chemistry, chemical structure, and conversion parameters) and validation points (i.e., fiber chemistry, gaseous products, and mechanical properties), which are supplied by experimentation. Furthermore, experimentation has identified new conversion steps, such as mixing additives within the polymer, alternative conversion treatments, which are, in turn, investigated by the ICME framework to elucidate the underlying chemical mechanisms. Thus, our project structure is optimized for closed-loop research feedback in which each group receives and passes along information and data to the next as we investigate and optimize the conversion of low-cost CF.

Results

We previously demonstrated conversion of a pilot-scale Nylon 6 precursor fiber into CF, which met all our cost and mechanical property target metrics. During the final two-quarters of the project the team focused on three fronts: (i) studying the scalability of Nylon 6-derived CF production; (ii) experimental optimization and validation of CF performance via conversion process characterization; and (iii) development of a strategic framework for industrial production.

Scalability Study of CF Production

The scalability study was a critical bridge between the laboratory-scale testing conducted at the University of Virginia (UVA) and ORNL in FY 2019 and FY 2020 and industrial-scale production. This study was facilitated by pilot-scale production runs of Nylon precursor fibers facilitated by Solvay in FY 2019. These pilot runs assessed the feasibility of conversion methodologies for Nylon 6 precursors into CF and served as baseline references to assess the production cost of conversion.

A critical step in the demonstration of scaled production of Nylon 6-derived CF is the continuous metal salt solution treatment (pre-oxidation) of the fibers. A prototype continuous bath treatment line was designed and constructed over the course of FY 2020 and FY 2021, as shown in Figure II.2.1.1(a). Assembly of the prototype was completed in the second quarter of FY 2021 and 14 m of Nylon 6 precursor fibers were treated continuously. Spools of the untreated fibers are shown in Figure II.2.1.1(b). Samples of the tow were captured *in-situ* in epoxy at the entry, middle, and exit areas of the immersion to examine the progression of the metal salts through the fiber tow and individual fibers over the duration of the treatment process, as shown in Figure II.2.1.1(c). These segments were subsequently removed for characterization at a later date. This characterization provides a critical link with ReaxFF simulations, which predicted that the metal ion diffusion helped the efficiency of the subsequent stage of conversion.

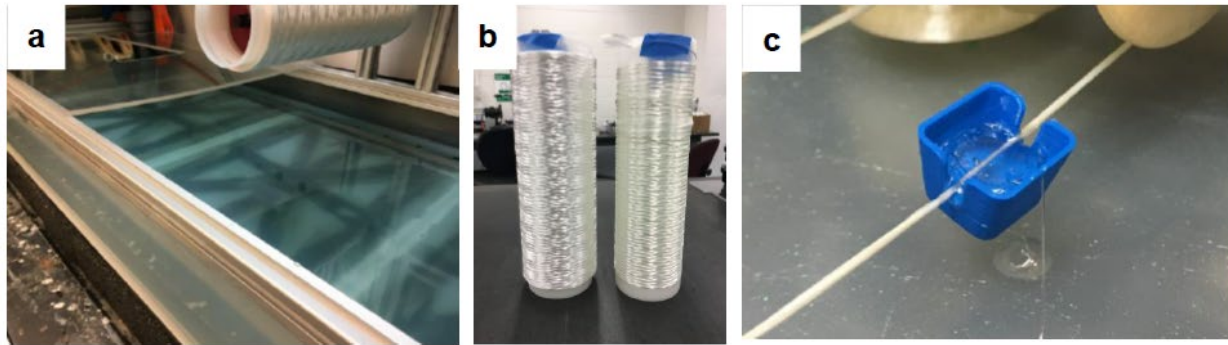


Figure II.2.1.1. (a) The continuous bath line with metal salt solution, (b) untreated nylon 6 fibers (left) and treated Nylon 6 fibers (right), and (c) the tow encased in epoxy immediately following bath draining to capture *in-situ* tow geometry and for diffusion. Source: University of Virginia.

Exploration of alternative conversion accelerating methodologies continued in the second quarter of FY 2021 with the exploration of photo-initiated crosslinking as a method of accelerating conversion. Alternative precursor fibers were coated with a photo-initiator and spun to incorporate the initiator into the fibers. This study found an alternative treatment to reduce the conversion time. We also worked with 4M Carbon Fiber Corporation and 4XTechnologies, LLC to investigate novel alternative treatments, and UVA characterized samples treated by these companies. This characterization found that the treatments were effective.

Experimental Validation of CF Properties

A new collection of thermomechanical testing and characterization techniques were performed on pilot-run and lab-synthesized fibers derived from alternative precursors. Experimental synthesis of alternative precursors explored the effects of conversion variables on fiber mechanical properties.

Efforts in FY 2020 were heavily focused on the optimization of alternative precursor-derived CFs. In FY 2021, results showed that the properties of the alternative precursor-derived CFs are highly sensitive to processing parameters. Figure II.2.1.2 shows fibers without adequate uniformity and fibers with adequate uniformity, suggesting that uniformity plays a critical role in fiber processing.

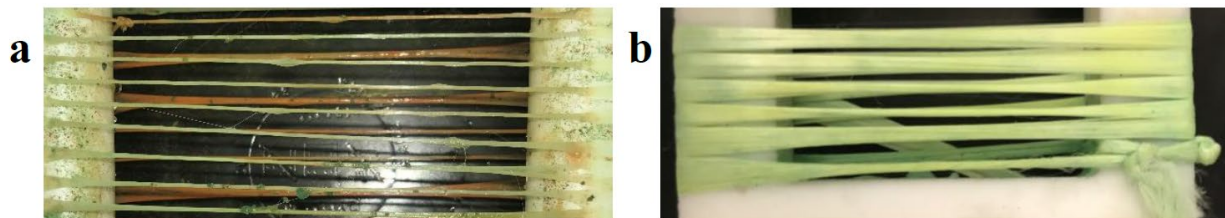


Figure II.2.1.2. (a) Fibers without adequate uniformity. (b) Fibers with adequate uniformity. Source: University of Virginia.

Conversion of Nylon 6 requires three stages: (1) peroxidation; (2) oxidation; and (3) carbonization, which were carefully optimized to achieve the target properties shown in Table II.2.1.1. Detailed characterization was performed to understand the mechanisms behind this conversion and thus inform future optimization. In FY 2021, the final properties of the Nylon 6-derived CFs were shown to be highly sensitive to processing parameters. The pre-oxidation stage poses a unique challenge for conversion, because impregnation of Nylon 6 precursors with water-insoluble metal salts is required. The water insolubility of the metal salts requires significant mixing and agitation during pre-oxidation to achieve loading uniformity throughout the Nylon 6 precursors. Figure II.2.1.2 illustrates the difference that pre-oxidation mixing makes in metal salt-loading uniformity in the fibers. Adequate mixing during pre-oxidation was found to consistently produce CFs of

acceptable quality, whereas a lack of mixing was found to result in a significant decrease in mechanical properties of the final CF. The carbon yield from fibers that underwent different accelerated treatments was measured by thermogravimetric analysis to study alternative accelerating conversion processes.

Strategic Framework for Industrial Production

The primary goal was to provide a deliverable that would be solely based on the experimental data provided from the synthesis and characterization portion of the project. However, a high-dimensional, low-error model with lab-scale experimental throughput would require testing capacity beyond the scope of this project. Therefore, the effort over FY 2021 was to develop the framework of an algorithm that could be easily expanded to high dimension space, while also being demonstratable in the scope of low-volume data. This was completed with success—the framework now stands capable of accepting any amount of recipe variables and returning predictions of any amount of resulting fiber properties. With the well-known caveat that more dimensions require higher densities of orthogonally-planned training data to produce a sound model, a small subset of the algorithm’s capability was validated with two recipe variations—the temperature and duration of a single step within a multi-step recipe.

Using this data, a model was generated by the algorithm using an optimization procedure that found the best fit across two supervised learning algorithm frameworks and eight respective hyper-parameters. The model was trained to be able to find nonlinear trends across the two-dimensional recipe parameterization with respect to fiber modulus and ultimate stress and demonstrates an ability to predict the optimal region to explore to increase mechanical properties. Figure II.2.1.3 provides an example of the modulus output.

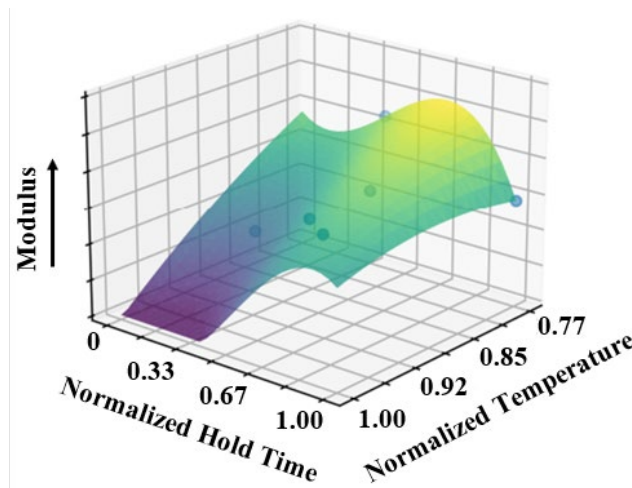


Figure II.2.1.3. The ML algorithm was capable of predicting the properties of modulus prediction based on key processing parameters such as temperature and duration. Source: University of Virginia.

Additionally, a continuum finite element model was developed to bridge the atomistic scale simulations to realistic fiber geometries. Prior electron microscopy and X-ray CT observed pores within the fiber microstructure, and atomistic mechanics simulations found these pores could contribute to large variations of tensile test results. Therefore, this modeling effort explored the effect of these defects on the stiffness and failure strength of the fiber.

The finite element model predicted the material behavior using a dynamic explicit analysis in conjunction with an element deletion technique in Abaqus 2020. The model predicted the failure load by removing the stiffness from the elements, which exceeded a damage criterion (i.e., the failure stress of a non-damaged fiber), as shown in Figure II.2.1.4.

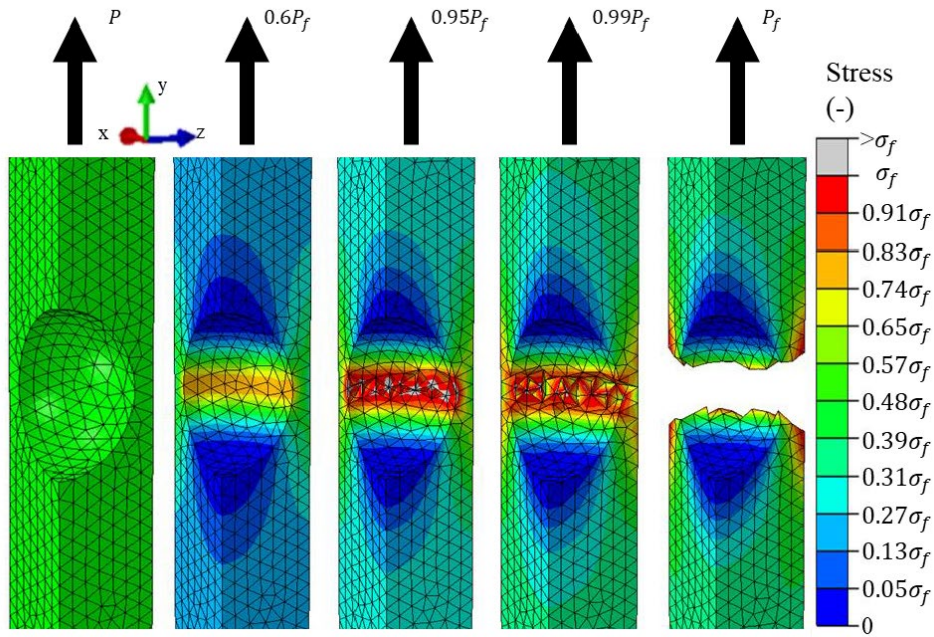


Figure II.2.1.4. Damage progression of a single fiber with a pore. Source: University of Virginia.

Pores of various shapes and sizes were incorporated. Figure II.2.1.5 shows the damage progression of a single fiber with a pore. This finding agrees with observations from atomistic mechanics simulations performed by Co-Principal Investigator, Zhiglei, in FY 2020. Clearly, Figure II.2.1.5 shows that there is very little impact to increasing the aspect ratio of a pore.

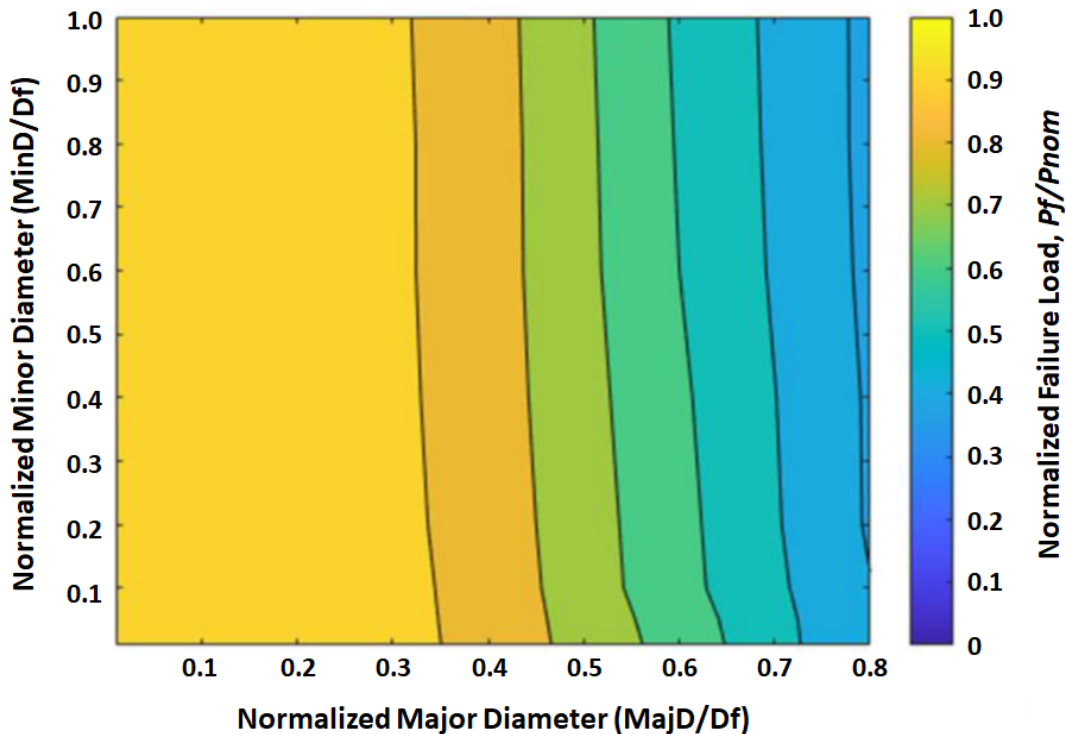


Figure II.2.1.5. Normalized fiber failures with different major and minor ellipsoid diameters. Source: University of Virginia.

The exploration of mechanical performance-enhancing nano-additives resumed in FY 2021 to demonstrate the fibers can be further improved. The pilot-scale precursor fibers were tensile tested to explore the effect of small nano-additive loadings, while alternative methods of nano-additive inclusion were explored. The nano-additive precursors showed a significant increase in mechanical performance, as shown in Figure II.2.1.6, and it is anticipated that with greater nano-additive loading the performance will be increased greatly.

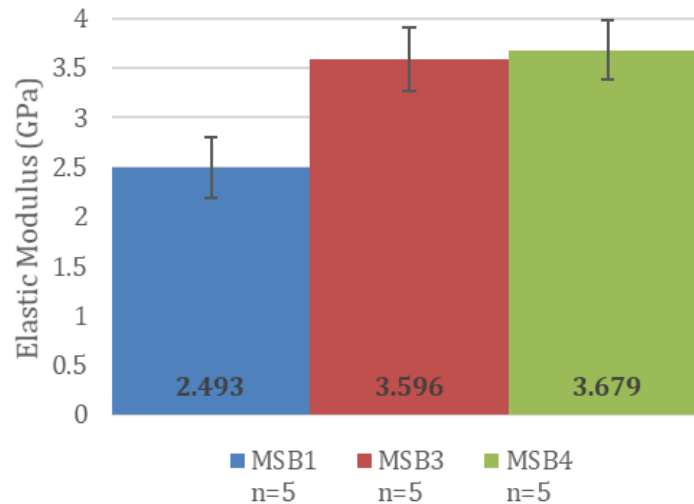


Figure II.2.1.6. Results of nano-additive precursors showing significant increase in elastic modulus in the nano-additive samples (MSB3, MSB4) compared to the neat baseline sample (MSB1).

Source: University of Virginia.

Conclusions

During the final two-quarters of this project at the beginning of FY 2021, the project team addressed questions of Nylon 6 conversion scalability to larger, continuous-production scales, expanded characterizations of the prototype fibers at all stages of the production process, and advanced the machine-learning-enhanced ICME framework. This ICME framework is built upon our success with ReaxFF simulations to uncover underlying chemistries, conduct atomistic simulations to investigate CF structure/property relationships, and perform laboratory-scale experimental CF conversion. Over the six-month extension period, the team packaged this wealth of data within a testbed software package, guided by ML, to present optimized Nylon CF conversion recipes and facilitate easy adoption of this technology within the CF and automotive industries. Importantly, we expect these tools, and the demonstration of Nylon-derived CF, will encourage the implementation of low-cost, high-strength CF within structural vehicular components to enable the manufacture of lightweight, energy-efficient vehicles.

Key Publications

1. Ashraf, C., A. Vashisth, C. E. Bakis, and A. C. T. van Duin, 2019, "Reactive molecular dynamics simulations of atomic oxygen impact on epoxies with different chemistries," *J. Phys. Chem. C*, Vol. 123, pp. 15145–15156.
2. Gao, Z., J. Zhu, S. Rajabpour, K. Joshi, M. Kowalik, B. Croom, Y. Schwab, L. Zhang, C. Bumgardner, K. Brown, D. Burden, J. Klett, A. C. T. van Duin, L. Zhigilei, and X. Li, 2021, "Graphene-reinforced carbon fibers," *Sci. Adv.*, Vol. 6, No. 17, Art. eaaz4191.
3. Rajabpour, S., Q. Mao, Z. Gao, M. K. Talkhonchek, J. Zhu, Y. Schwab, M. Kowalik, X. Li, and A. C. T. van Duin, 2020, "Polyacrylonitrile/graphene nanocomposite: Towards the next-generation of carbon fibers," 22 June 2020. Available at: <http://arxiv.org/abs/2006.11985> (last accessed 2 March 2022).
4. Joshi, K., M. Arefev, and L. V. Zhigilei, 2019, "Generation and characterization of carbon fiber microstructure in atomistic simulations," *Carbon*, Vol. 152, pp. 396–408.

5. Kowalik, M., C. Ashraf, B. Damirchi, D. Akbarian, S. Rajabpour, and A. C. T. van Duin, 2019, "Atomistic scale analysis of the carbonization process for C/H/O/N-based polymers with the ReaxFF reactive force field," *J. Phys. Chem. B*, Vol. 123, No. 25, pp. 5357–5367.
6. Kwon, H., S. Shabnam, A. C. T. van Duin, and X. Xuan, 2021, "Numerical simulations of yield-based sooting tendencies of aromatic fuels using ReaxFF molecular dynamics," *Fuel*, Vol. 262, Art. 116545.
7. Mao, Q., S. Rajabpour, M. Kowalik, and A. C. T. van Duin, 2021, "Predicting cost-effective carbon fiber precursor: Unraveling the functionalities of oxygen and nitrogen-containing groups during carbonization from ReaxFF simulations," *Carbon*, Vol. 159, pp. 25–36.
8. Ponomarev, I., A. C. T. van Duin, and P. Kroll, 2019, "A reactive force field for simulations of the pyrolysis of polysiloxanes into silicon oxycarbide ceramics," *J. Phys. Chem. C*, Vol. 123, pp. 16804–16812.
9. Vashisth, A., M. Kowalik, J. C. Geringer, C. Ashraf, A. C. T. van Duin, and M. J. Green, 2021, "ReaxFF simulations of laser-induced graphene (LIG) formation for multifunctional polymer nanocomposites," *ACS Appl. Nano Mater.*, Vol. 3, pp. 1881–1890.
10. Volkov, A. N., and L. V. Zhigilei, 2021, "Thermal conductivity of two-dimensional disordered fibrous materials defined by interfiber thermal contact conductance and intrinsic conductivity of fibers," *J. Appl. Phys.*, Vol. 127, Art. 065102.
11. Zhang, L., M. Kowalik, Z. Gao, C. Ashraf, S. Rajabpour, C. Bumgardner, Y. Schwab, B. Damirchi, J. Zhu, D. Akbarian, J. Klett, A. C. T. van Duin, and X. Li, 2019, "Converting PBO fibers into carbon fibers by ultrafast carbonization," *Carbon*, Vol. 159, pp. 432–442.
12. Zhu, J., Z. Gao, M. Kowalik, K. Joshi, C. Ashraf, M. Arefev, Y. Schwab, C. Bumgardner, K. Brown, D. Burden, L. Zhang, J. Klett, L. V. Zhigilei, A. C. T. van Duin, and X. Li, 2019, "Unveiling carbon ring structure formation mechanisms in polyacrylonitrile-derived carbon fibers," *ACS Appl. Mater. Interfaces*, Vol. 11, pp. 42288–42297.
13. Love-Baker, C. A., T. M. Harrell, K. R. Brown, C. H. Bumgardner, and X. Li, 2021, "Analyzing the effect of misalignment on single filament carbon fiber tensile testing via stereoscopic computer vision imaging," *Meas. Sci. Technol.*, Vol. 32, Art. 065904.
14. Rajabpour, S., Q. Mao, Z. Gao, M. Khajeh Talkhonchek, J. Zhu, Y. Schwab, M. Kowalik, X. Li, and A. C. T. van Duin, 2021, "Low-temperature carbonization of polyacrylonitrile/graphene carbon fibers: A combined ReaxFF molecular dynamics and experimental study," *Carbon*, Vol. 174, pp. 345–356.
15. Klett, J., Z. Gao, J. Zhu, S. Rajabpour, K. Joshi, M. Kowalik, Y. Schwab, L. Zhang, C. Bumgardner, B. Croom, D. Burden, K. Brown, Y. Murty, Q. Shi, B. Harmon, L. V. Zhigilei, A. C. T. van Duin, and X. Li, 2019, "Enhancement of Polyamid-6 derived carbon fibers with addition of graphene reinforcement," *Carbon Fibers and Their Composites and Applications Workshop*, 11–12 July 2019, ORNL, Oak Ridge, TN, USA.
16. Klett, J., L. Zhang, M. Kowalik, Z. Gao, J. Zhu, Y. Schwab, A. Chowdhury, B. Damirchi, C. Bumgardner, Y. Gu, Y. Murty, Q. Shi, B. Harmon, J. Batten, B. Epling, A. C. T. van Duin, and X. Li, 2019, "Conversion of poly(p-phenylene-2,6-benzobisoxazole) fibers to carbon fibers through processing optimization," *Carbon Fibers and Their Composites and Applications Workshop*, 11–12 July 2019, ORNL, Oak Ridge, TN, USA.
17. Kowalik, M., C. Ashraf, S. Rajabpour, B. Damirchi, D. Akbarian, Q. Mao, and A. van Duin, 2021, "Atomistic analysis of PBO carbonization process with ReaxFF reactive force field," *Bulletin of the American Physical Society*, 2–6 March 2021, Denver, CO, USA.

18. Li, X., 2019, “Graphene nanocomposites with exceptionally high-strength and toughness,” *International Symposium on Clusters and Nanomaterials (Energy and Medicine)*, 3–7 November 2019, Richmond, VA, USA.

References

1. Mainka, H., O. Täger, E. Körner, L. Hilfert, S. Busse, F. T. Edelmann, and A. S. Herrmann, 2015, “Lignin – An alternative precursor for sustainable and cost-effective automotive carbon fiber,” *J. Mater. Res. Technol.*, Vol. 4, No. 3, pp. 283–296.
2. Park, S.-J., and G.-Y. Heo, 2015, “Carbon fibers,” In: Park, S.-J. (ed.), *Carbon*. Springer Science & Business Media, Berlin, Germany.
3. Brown, S. F., 2013, “Carbon fiber, light and strong, arrives where it’s most needed,” *New York Times*, 14 July 2013. New York, NY, USA. Available at: <http://www.nytimes.com/2013/07/14/automobiles/carbon-fiber-light-and-strong-arrives-where-its-most-needed.html> (last accessed 2 March 2022).
4. Warren, C. D., 2007, “The development of lower-cost carbon fiber technologies for automotive applications,” *Proceedings of The Global Outlook for Carbon Fiber*, 23–25 October 2007, San Diego, CA, USA.
5. Fitzer, E., 1989, “PAN-based carbon fibers-present state and trend of the technology from the viewpoint of possibilities and limits to influence and to control the fiber properties by the process parameters,” *Carbon*, Vol. 27, No. 5, pp. 621–645.
6. Chen, J. C., and I. R. Harrison, 2002, “Modification of polyacrylonitrile (PAN) carbon fiber precursor via post-spinning plasticization and stretching in dimethyl formamide (DMF),” *Carbon*, Vol. 40, No. 1, pp. 25–45.
7. Pichler, D., 2016, ““Give us affordable carbon fiber!,”” *CompositesWorld*, 25 February 2016. Cincinnati, OH, USA. Available at: <http://www.compositesworld.com/columns/give-us-affordable-carbon-fiber> (last accessed 2 March 2022).
8. Rao, S., T. G. A. Simha, K. P. Rao, and G. V. V. Ravikumar, 2018, “Carbon composites are becoming competitive and cost-effective,” *Infosys*, Bengaluru, India. Available at: <https://www.infosys.com/engineering-services/white-papers/Documents/carbon-composites-cost-effective.pdf> (last accessed 2 March 2022).
9. Senftle, T. P., S. Hong, M. M. Islam, S. B. Kylasa, Y. Zheng, Y. K. Shin, and C. Junkermeier, 2016, “The ReaxForce-Field: Development, applications, and future directions,” *Npj. Comput. Mater.*, Vol. 2, Art. 15011.
10. Srinivasan, S. G., A. C. T. van Duin, and P. Ganesh, 2015, “Development of a ReaxFF potential for carbon condensed phases and its application to the thermal fragmentation of a large fullerene,” *J. Phys. Chem. A*, Vol. 119, No. 4, pp. 571–580.
11. Joshi, K., M. I. Arefev, and L. V. Zhigilei, 2019, “Generation and characterization of carbon fiber microstructure in atomistic simulations,” *Carbon*, Vol. 152, pp. 396–408.
12. Zhigilei, L. V., Z. Lin, and D. S. Ivanov, 2009. “Atomistic modeling of short pulse laser ablation of metals: Connections between melting, spallation, and phase explosion,” *J. Phys. Chem. C*, Vol. 113, No. 27, pp. 11892–11906.

Acknowledgments

The PIs would like to recognize contributions from Co-PI R. Hathaway and collaborator J. Batten, who have provided valuable input and carbon materials to the team. This input has helped the project remain focused on industry production needs and key material requirements.

The PIs would also like to recognize the contributions from Co-PIs B. Harmon, Q. Shi, D. Cook, J. Moskowitz, and V. Kumar at Solvay Composites. Mr. Harmon and Dr. Shi facilitated the pilot fiber production run at the conclusion of FY 2019 and provided guidance and feedback during the subsequent analysis and optimization during FY 2020. We would also like to thank Mr. Cook, Dr. Moskowitz, and Mr. Kumar for quickly onboarding as part of the project team and for their help critiquing the experimental and computational findings.

II.2.2 Integrated Computational Materials Engineering Predictive Tools for Low-Cost Carbon Fiber (Western Research Institute)

Jeramie J. Adams, Principal Investigator

Western Research Institute
3474 North Third Street
Laramie, WY 82072
E-mail: jeramie.adams@uwyo.edu

H. Felix Wu, DOE Technology Manager

U.S. Department of Energy
E-mail: felix.wu@ee.doe.gov

Start Date: October 1, 2017	End Date: July 31, 2021	
Project Funding (FY 2021): \$1,084,888	DOE share: \$351,825	Non-DOE share: \$733,063

Project Introduction

Significant weight-reduction for vehicles would have several economic and environmental advantages—most notably, reduced fuel consumption and greenhouse gas emissions. Additional cascading benefits would include reductions in infrastructure costs and maintenance by virtue of less stress applied to vehicles, roads, and other transportation infrastructure; reduction in vehicle weight making them safer and compensating for the greater weight of EVs [1]; and far-reaching geopolitical impacts, such as improved national security, by reducing the dependency of the U.S. on foreign crude oil.

One such way to reduce the weight of vehicles, while not sacrificing strength and crashworthiness, is to replace traditional stress bearing metal and body components with lightweight advanced materials and composites such as those made from CF. These advanced materials can be engineered to have physical strength properties 600% greater than steel at a fraction of the weight. By properly selecting materials and manufacturing protocols, very strong and flexible materials can be produced. CFs are used to produce materials used in a variety of applications, from spaceship nosecones to shafts of fly-fishing rods. This gives validity to pursuing CFs for future development of lightweight vehicles.

One difficulty in the large-scale deployment of CF for the commercial vehicle industry is the availability of large quantities of CF with appropriate physical properties at a reasonable cost. To address these limitations, academic, government, nonprofit, and commercial entities formed the Consortium for Affordable Carbon Fibers in the United States to study the feasibility of using large volume, low-cost natural resources to produce CFs of the appropriate quality and cost. Some of the most abundant natural resources are those from current biomass such as sugars derived from agricultural sources, or from ancient biomass such as coal and petroleum. The overarching vision of this study was to survey several types of feedstocks, and blends of these feedstocks, to provide a robust roadmap for potential materials. This study also considers the economic risks that can arise by becoming too dependent on any one material, which may itself be subject to climatic, environmental, geopolitical, and market variations. To mitigate these risks, no particular preference was given to any one feedstock and CFs were produced from coal-, petroleum-, and biomass-based feedstocks. Due to time and funding limitations, petroleum and biomass feedstocks were downselected at the end of the program.

Objectives

The objective of this research is to investigate the current landscape of appropriate raw starting materials from petroleum-, coal-, and biomass-based feedstocks to derive precursors to produce low-cost CF materials for lightweight vehicles in the U.S. This objective is divided into two complementary parts:

1. Develop, integrate, and demonstrate a suite of ICME modeling tools that predict CF properties within 15% of measured properties. This will enable the design, development, and optimization of precursor chemistry and molecular structure associated with conversion into CF and evaluate alternative precursors for their suitability to manufacture low-cost CF. The ICME models will also include methodologies to simulate the manufacturing processes, including variability from both process and material. All non-proprietary and non-business-sensitive public data and code—such as technical data used to support published journal articles or research code used for simulations—has been provided to the LightMAT Consortium for curation and hosting.
2. Develop, manufacture, and demonstrate CF precursor technology and processing techniques where CF is a material consisting of thin, strong, multi-crystalline filaments of C used as a reinforcement material, especially in resins, and capable of achieving the requirements in Table II.2.2.1.

Table II.2.2.1. Project Parameters and Requirements

Parameter	Requirement
Cost	≤ \$5/pound
Strength	≥ 250 Ksi
Modulus	≥ 25 Msi
Strain	≥ 1%

Approach

The approach will be to study readily available large volume feedstocks from biomass, coal, and petroleum to produce precursors of appropriate qualities that lend themselves to the production of CF with the appropriate physical properties and cost to be used in the commercial vehicle industry. The project will remove risk from this process by developing predictive models that can be used to guide the development of CF materials from new or blended feedstocks. To achieve this goal, a project team consortium was assembled including partners that have significant experience working with these different feedstocks, as well as experts in CF production, mechanical testing, and modeling from the molecular, micro, and macro levels. The team comprises:

- Western Research Institute (WRI): Prime recipient
- ORNL: Subrecipient, funded by a field-work proposal (FWP)
- Grossman Group at Massachusetts Institute of Technology (GG-MIT): Subrecipient
- Southern Research Institute (SRI): Subrecipient
- University of Wyoming (UW): Subrecipient
- Advanced Carbon Products (ACP): Subrecipient
- Ramaco Carbon LLC (RAMACO): Subrecipient
- Solvay Composites (Solvay): Industrial adviser
- Koppers: Industrial adviser.

Each member of the consortium brings a unique and complementary aspect necessary to build up fundamental scientific and industrially relevant understanding of the relationship between the chemistry and molecular structure of different organic feedstocks and subsequent precursor formation, while following the production chain up through CF tow level fabrication, mechanical characterization, and modeling. Figure II.2.2.1 shows a high-level depiction of the consortium organization and the primary strengths and responsibilities for each consortium member.

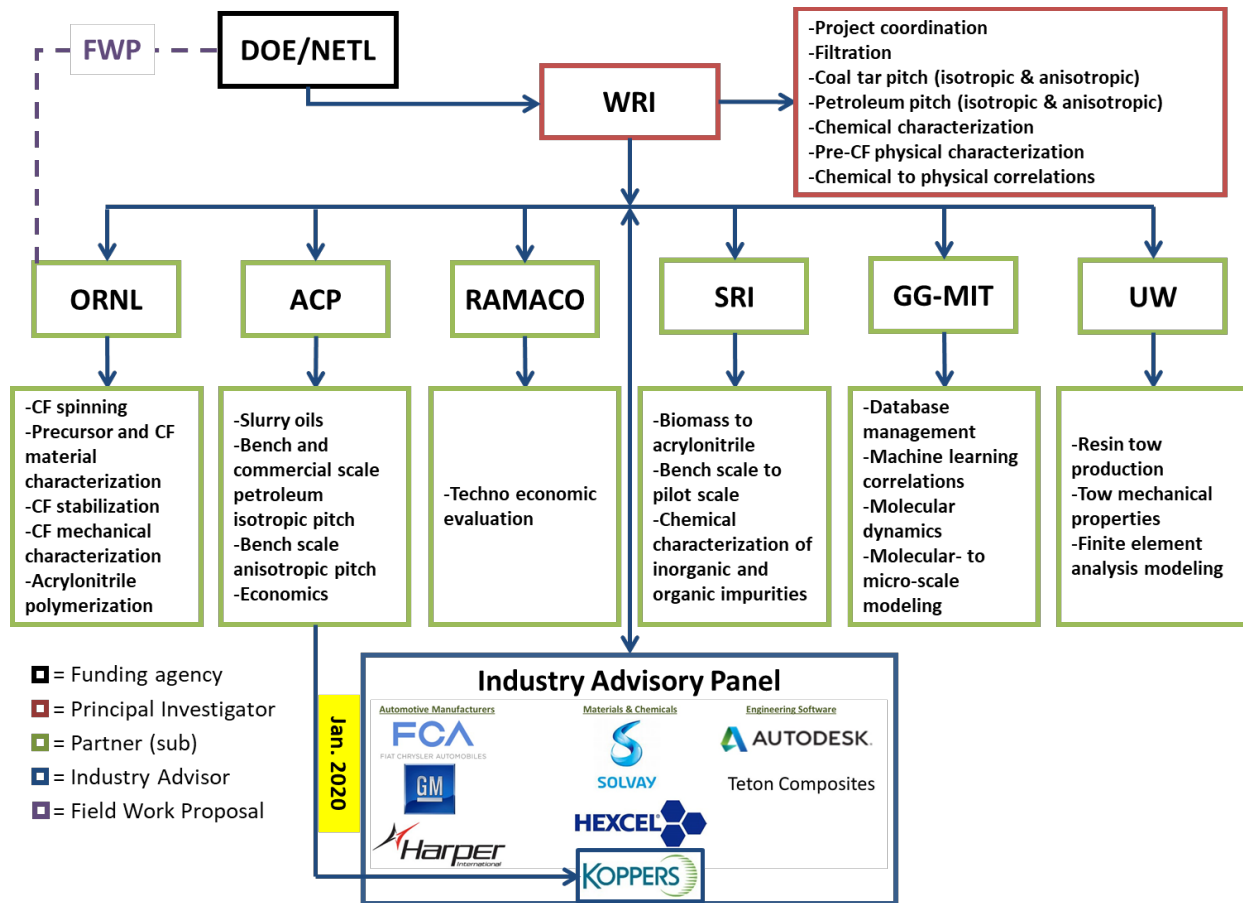


Figure II.2.2.1. Organization for the Consortium for Production of Affordable CFs in the U.S. Source: WRI.

The project was conducted in three BPs. This report summarizes the accomplishments achieved during BP3. The overall goals for BP3 are as follows:

BP3: Validation and Transfer of Models and Data to DOE ICME Program

The most promising CF materials will be further evaluated for producibility and to improve macro-level models while building a comprehensive performance database up to the tow level. Macro- and micro-level models will be integrated and validated for industry use. Models and data will be transferred to the DOE ICME program, and a final cost estimate will be produced. The milestones for BP3 are shown in Table II.2.2.2.

Table II.2.2.2. Milestones for BP3

Title	Type	Milestone Description	Verification
Validation of Integrated Micro-Macro-Models	Tech	Use empirical data to check accuracy of integrated Micro-Macro-models tools	Accuracy is ±15%
Verify CF Still Meet Strength and Cost Goals	Go/No-Go	Check that precursor production retains CF performance	Meets DOE strength goals at <\$5/lb
CF Meets Automotive Strength-to-Weight Ratio	Tech	Use test data to verify that CF tow test specimens achieve minimum strength-to-weight ratio	30% to 50% <steel
Validation of Macro-level Models	Tech	Check predictions against CF tow mechanical properties test results	Accuracy is ±15%

Results

A key effort of this work, within the ICME framework, is to integrate modeling of different size scales to link the micro- and macro-level modeling efforts. This integration was achieved by using neural networks (NN) to predict micro-level CF properties from feedstocks and precursors using atomistic modeling at the micro-level, which actually starts at the nanoscale, and modeling the tow level CF properties from epoxy composites at the macro-level using FEA. The linking of these various scales is shown in Figure II.2.2.2.

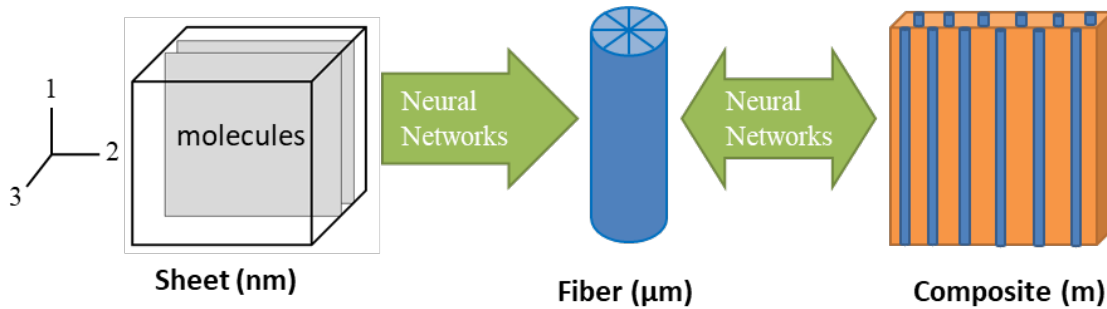


Figure II.2.2.2. A diagram showing the high-level approach to integrate the models at different size scales using NNs. Source: University of Wyoming.

Atomistic modeling was done through DFT, molecular dynamics, and using ReaxFF for pitch-based feedstocks; alternatively, coarse-grained molecular dynamics (CG-MD) was used to model the long repeating polymeric units of bio-based polyacrylonitrile (bio-PAN) produced from bio-based acrylonitrile (bio-ACN). Modeling of CF properties to tow level epoxy composite testing was accomplished using FEA. Figure II.2.2.3 shows a summary of the modeling efforts that were performed during this study for model integration, and which properties were linked using either ML or NN. To account for CF processing conditions to model CF properties from pitch chemistry and properties, an encryption method was developed to comply with export control laws and regulations.

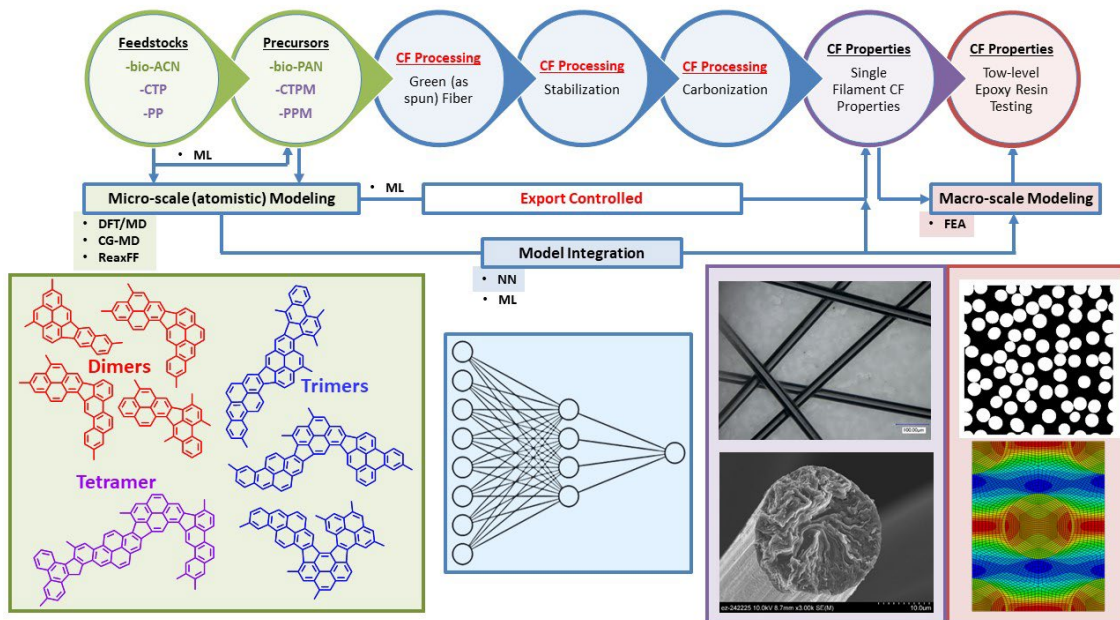


Figure II.2.2.3. A diagram showing the modeling efforts that were performed and integrated during this study. The molecules shown for the feedstock are representative for petroleum pitch. Source: Western Research Institute.

The results of the prediction tools for the macro-model and the micro-to-macro-model are summarized in Table II.2.2.3 and Table II.2.2.4 for the bio-PAN fibers and pitch-based fibers, respectively. The micro-to-macro-model utilizes the sheet properties, obtained from the MD atomistic simulations, to predict fiber properties that are then used to drive the prediction of the overall composite properties. The macro-model backs out predicted fiber properties given the more readily obtained experimental composite properties. Ultimately, both models yielded predicted properties that were in good agreement with experimental values and are significantly below the required $\pm 15\%$ error.

Table II.2.2.3. Model Integration Predictions Related to Experimental Data with Associated Errors for Bio-PAN CF Produced in This Study

Component	Model	Property	Predicted	Experimental	% Error
Fiber	Micro-Macro	E11 [GPa]	169.30	169.2	0.06
Fiber	Macro	E11 [GPa]	165.29	169.2	4.61
Composite	Micro-Macro	E11 [GPa]	81.94	81.0	1.17
Composite	Micro-Macro	E22 [GPa]	4.45	4.86	8.44
Composite	Micro-Macro	n12	0.33	0.33	0.00

Table II.2.2.4. Model Integration Predictions Related to Experimental Data with Associated Errors for Pitch-Based CF Produced in This Study

Component	Model	Property	Predicted	Experimental	% Error
Fiber	Macro	E11 [GPa]	300.73	298.58	0.72
Composite	Micro-Macro	E11 [GPa]	144.26	143.41	0.59

Experimental data from the isotropic petroleum pitch (PP) and mesophase (PPM), in conjunction with literature, was used to help construct proxy molecules as shown in Figure II.2.2.4. These molecules were then used with ReaxFF to model various degrees of hydrogen removal, using various rules to account for abstraction from the aromatic carbons and/or the methyl carbons to model various CF elastic properties. The models were successful in predicting CF properties well within $\pm 15\%$. These models were developed into temporary web pages to predict pitch to CF to composite properties simply using pitch proxy molecules and encrypted CF processing parameters using ML.

For PPM CF, the micro-scale modeling was improved to account for bonding configuration depending on the strategy adopted for CF fabrication, in particular, in achieving high modulus by increasing sp^3 carbon bonding (approaching a diamond type of structure), as opposed to strictly sp^2 graphitic type of bonding more common in traditional CF. Simulations showed that the sp^3 type of bonding can lead to much higher density fibers, while retaining high modulus, as illustrated in Figure II.2.2.5. Further investigation of the properties of the sp^3 fibers showed that a new type of CF should be able to be produced that would result also in a high compressive modulus. Within the proposed modeling framework, this fabrication method is not in conflict with a more conventional high-temperature fabrication process that relies on graphitization. The addition of simulated annealing within the framework can lead to a faithful reproduction of graphitized fibers, whose properties are validated with commercially available graphitized CFs with good agreement, as observed by the red triangles in Figure II.2.2.5. This is a testament to the extreme flexibility of the modeling framework developed through this project. Furthermore, the clear diversification in performance vs. density between graphitized and ungraphitized CFs points to clear differences in the role of CFs and potential alternative routes for CF synthesis. Graphitization is the current method to achieve very high modulus, and the effectiveness of the models here developed in capturing it is well represented by the asymptotic trend of the density to that of bulk graphite (2.266 g/cm^3).

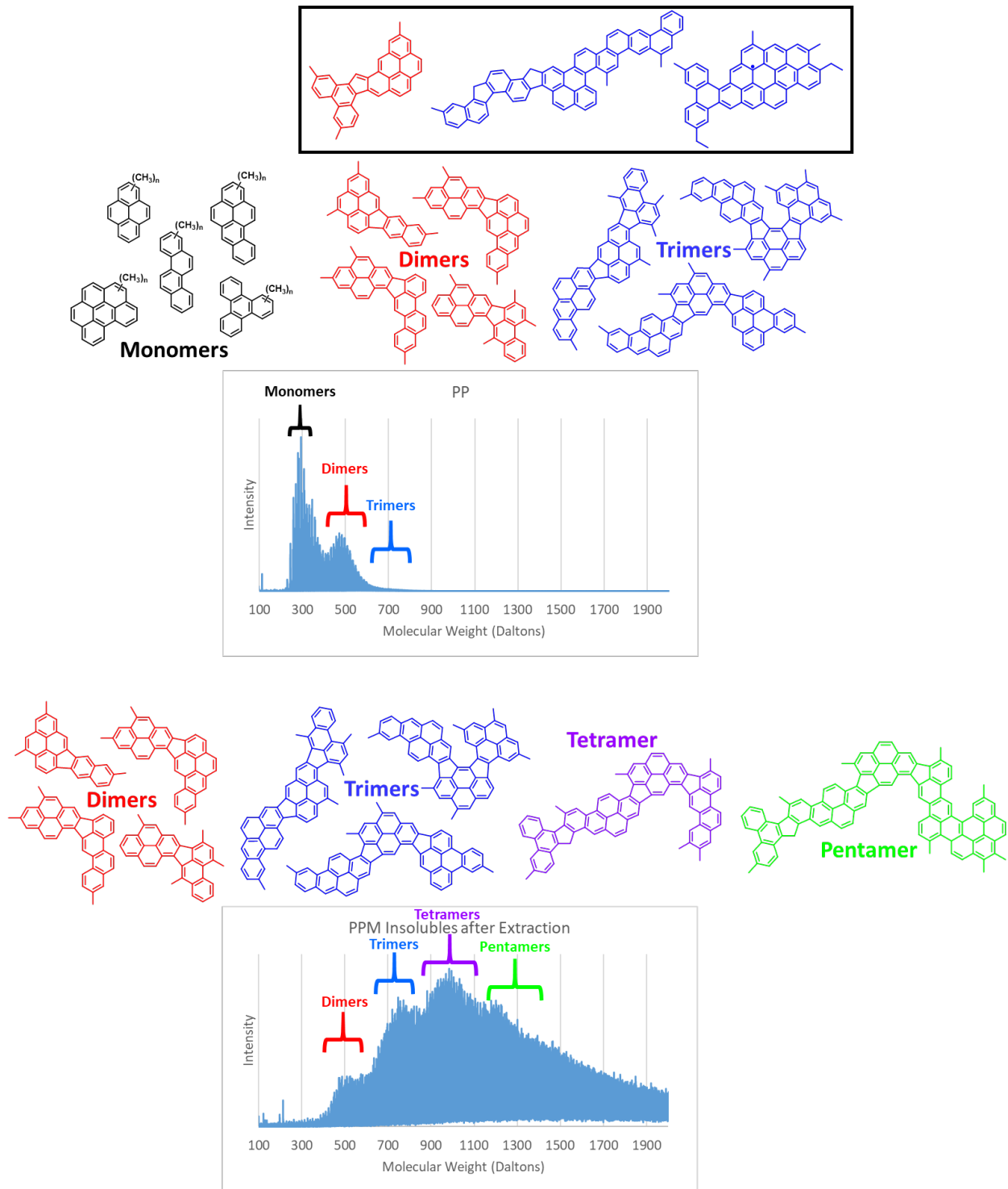


Figure II.2.2.4. The top shows select PP molecules relative to LDI spectra and the bottom shows hypothetical PM molecules relative to LDI based on [2], [3], [4], and [5]. The inset box in the top depicts actual molecular structures identified in PP using imaging techniques described in [3]. Source: Western Research Institute.

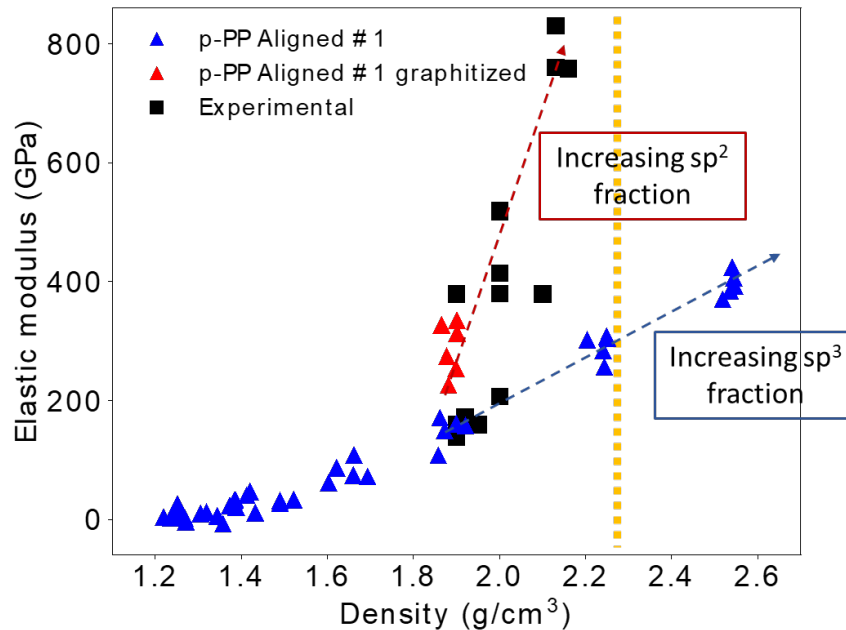


Figure II.2.2.5. Blue triangles show the relationship between density and elastic modulus produced by the models. Theoretical maximum in density for sp^2 graphite is around 2.27 g/cm^3 (yellow dashed line). For the model to move towards higher densities additional sp^3 bonding must occur. The black squares are experimental data from graphitized CF. Red triangles show updated modeling for graphitized CF. Source: Massachusetts Institute of Technology.

CG-MD modeling of bio-PAN, as shown in Figure II.2.2.6, was also further refined by taking the final CG configurations and reading all the hydrogen atoms. This resulted a fully atomistic model allowing complete relaxation of all the atoms. This corrected issues that occurred with overestimating some elastic properties. This method shows how it is possible to build a predictive framework from many different models. Figure II.2.2.7 shows some of the predictive frameworks and conclusions using this hybrid CG-MD/fully atomistic approach. Modeling of bio-PAN was extended to vary the stretching force, stabilization temperature, and stabilization time. This allowed for the models to actually predict processing conditions during CF production and could provide a tool for CF producers to target certain CF properties without trial-and-error approaches.

Scaled-up PPM and bio-ACN were able to produce CFs that met DOE targets. However, it was noticed that some variability in CF quality for PPM came from excess volatiles present in the mesophase which would cause defects in the fibers during the spinning process. It was also demonstrated that the amount of *n*-methyl-2-pyrrolidone insolubles (similar to quinoline insolubles) in the PP, prior to mesophase conversion, had a significant impact on CF quality. This was tested by using a PP with 2% to 3% insolubles and the same pitch with these insolubles removed and producing mesophase of the same softening point: 308°C . Using similar spinning conditions and appropriate CF processing it was shown that insolubles consistently produced larger diameter CF with a higher modulus but lower strength and elongation. This is likely the reason why some PPM could easily achieve the targeted modulus but were slightly low in strength, and especially in elongation. This is consistent with the insolubles increasing the defect density within the CFs.

A detailed technoeconomic analysis showed that scaled-up PPM and bio-PAN CF could be produced at less than $\$5/\text{lb.}$, meeting DOE's target. Various assumptions and aspects between the different materials need to be considered. The analysis shows that bio-PAN is less expensive than petroleum-based PAN because of buy-back credits for propylene glycol and ammonium sulfate, which are the two main coproducts. However, bio-PAN may be more attractive in the future as a way to reduce carbon emissions by producing CF from bio-based and renewable feedstocks, especially as carbon credits are more widely implemented and enforced.

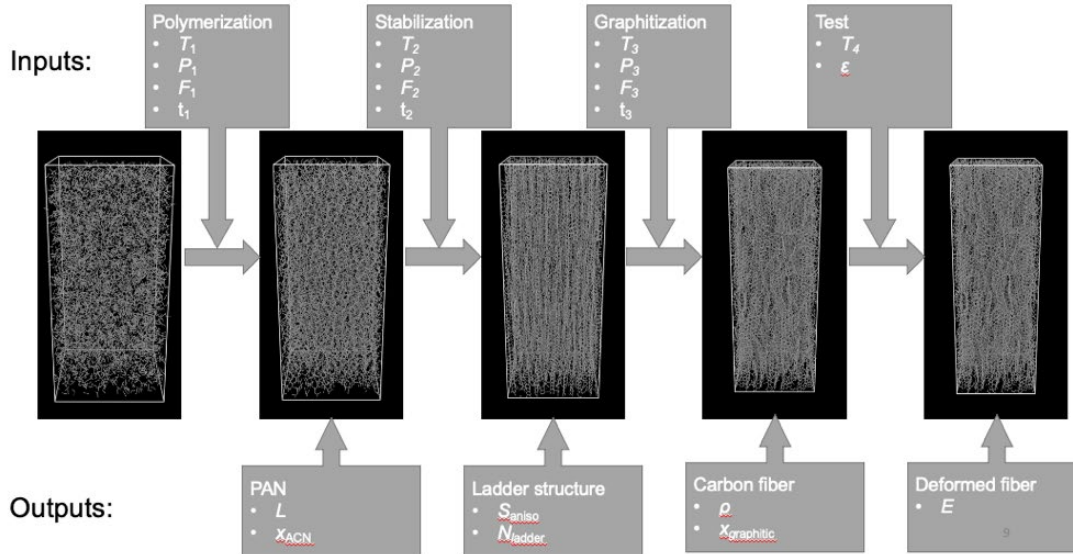
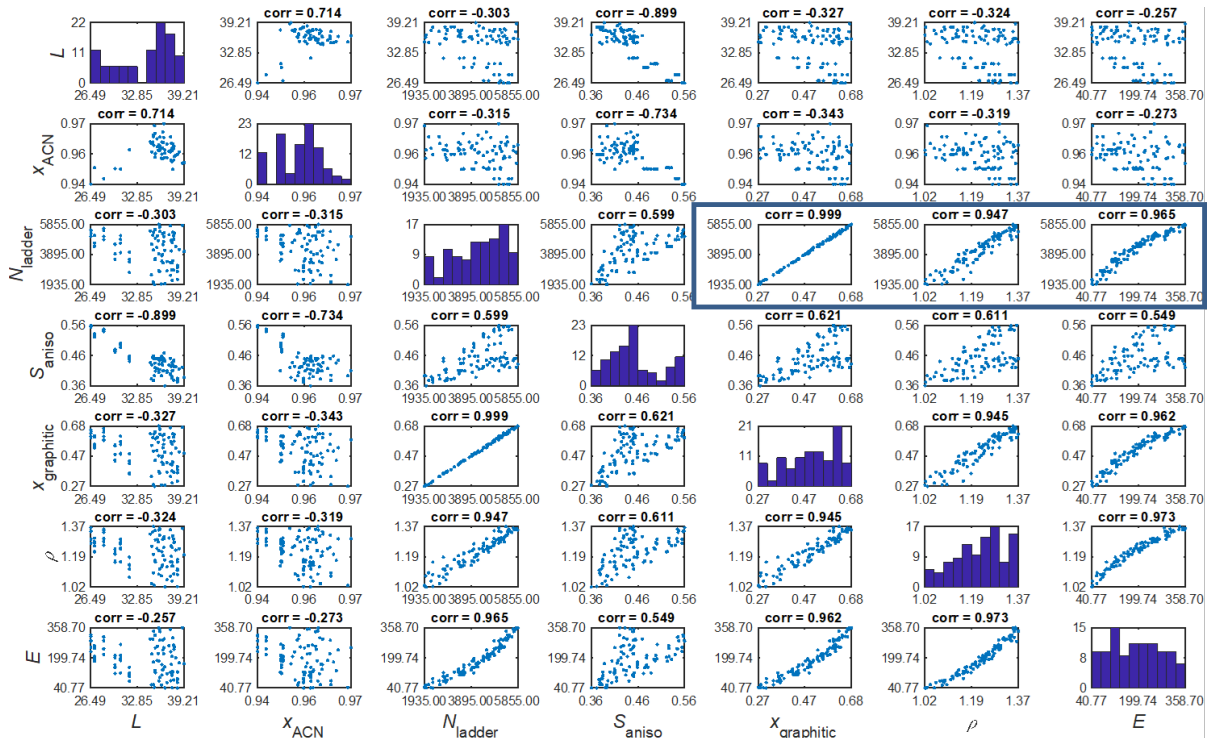


Figure II.2.2.6. Evolution of the CG PAN-based CF in relation to synthesis parameters (input), chemical and structural parameters of intermediate compounds, and the final CF. Source: Massachusetts Institute of Technology.



N_{ladder} = # of new bonds from stabilization, $X_{graphitic}$ = Fraction of aromatic content, ρ = Density, E = Young's modulus, X_{ACN} = Mole fraction of bio-ACN, S_{aniso} = x component of radius of gyration as alignment measurement, L = Average chain length of bio-PAN

Some Conclusions:

- N_{ladder} vs $X_{graphitic}$ = Ladder structure can be efficiently converted to the graphitic structure
- N_{ladder} vs ρ = More ladder structures also lead to higher density
- N_{ladder} vs E = Graphitic fraction and fiber density positively correlate with modulus
- CGMD models encompass a large set of process conditions. **This is not model but a predictive framework.**

Figure II.2.2.7. Correlative analysis between processing parameters and structural, chemical, and elastic characteristics of PAN-based fibers. Source: Massachusetts Institute of Technology.

Conclusions

Scaled-up PPM and bio-PAN CF were successfully prepared that meet DOE targets. Variability in PPM samples was related to the softening point and volatiles content in the samples, as well as insolubles present in the starting isotropic pitch. Other factors that affect variability are also likely responsible but additional investigation is needed to systematically identify all possible variables and the importance of these variables. Bio-ACN is a promising feedstock as it comes from renewable carbon, and it can be produced less expensively than petroleum-based ACN due to significant co-product credits. A thorough technoeconomic analysis showed that both bio-PAN and PPM could be produced at less than \$5/lb., even with a 20% increase in the costliest portion of the process.

Model integration was completed relating feedstock and precursor molecules to CF and composite properties. NNs were used to develop the relationships which were able to predict various elastic properties at less than 10% error, well within DOE targets of $\pm 15\%$. Advanced modeling strategies were developed which can account for CF processing conditions (stretching force, stabilization time, and stabilization temperature) to predict CF properties. These models and methods need additional levels of refinement and validation to determine their limitations. Some aspects which need to be further investigated are various CF morphologies (radial, random wave radial, random wave, pac-man motion, etc.), extension towards other more varied carbonaceous pitch-like feedstocks, and incorporation of other comonomer formulations for bio-PAN. Other more interesting outcomes would be to experimentally validate the PAN processing model and the mesophase CF with more sp^3 character for enhanced compressive modulus materials.

Key Publications

1. Annual Merit Review Meeting, June 22, 2021, “Consortium for the Production of Affordable Carbon Fibers (CPACF) in the U.S., Integrated Computational Materials Engineering (ICME) Predictive Tools for Low-Cost Carbon Fiber,” Project ID number: MAT125.
2. Jian, C., J. J. Adams, J. C. Grossman, N. Ferralis, 2021, “Carbon fiber synthesis from pitch: Insights from ReaxFF-based molecular dynamics,” *Carbon*, Vol. 176, pp. 569–579.
3. Annual Merit Review Meeting, June 22, 2021, “Consortium for the Production of Affordable Carbon Fibers (CPACF) in the U.S., Integrated Computational Materials Engineering (ICME) Predictive Tools for Low-Cost Carbon Fiber,” Project ID number: MAT125.
4. Annual Merit Review Meeting, June 22, 2021, “Consortium for the Production of Affordable Carbon Fibers (CPACF) in the U.S., Integrated Computational Materials Engineering (ICME) Predictive Tools for Low-Cost Carbon Fiber,” Project ID number: MAT125.
5. Annual Merit Review Meeting, June 19, 2018, “Consortium for the Production of Affordable Carbon Fibers (CPACF) in the U.S., Integrated Computational Materials Engineering (ICME) Predictive Tools for Low-Cost Carbon Fiber,” Project ID number: MAT125.

References

1. Shaffer, B., M. Auffhammer, and C. Samara, 2021, “Make electric vehicles lighter to maximize climate and safety benefits,” *Nature*, Vol. 598, pp. 254–256.
2. Burgess, W. A., J. J. Pittman, R. K. Marcus, and M. C. Thies, 2010, “Structural identification of the monomeric constituents of petroleum pitch,” *Energy Fuels*, Vol. 24, No. 8, pp. 4301–4311.
3. Chen, P., J. N. Metz, A. S. Mennito, S. Merchant, S. E. Smith, M. Siskin, S. P. Rucker, D. C. Dankworth, J. D. Kushnerick, N. Yao, and Y. Zhang, 2020, “Petroleum pitch: Exploring a 50-year structure puzzle with real-space molecular imaging,” *Carbon*, Vol. 161, pp. 456–465.
4. Esguerra, D. F., W. P. Hoffman, and M. C. Thies, 2014, “Liquid crystallinity in trimer oligomers isolated from petroleum and pyrene pitches,” *Carbon*, Vol. 79, pp. 265–273.

5. Thies, M. C., 2014, "Fractionation and characterization of carbonaceous pitch oligomers: Understanding the building blocks for carbon materials," *Polymer Precursor-Derived Carbon*, ACS Symposium Series, Oxford University Press, Oxford, U.K., Vol. 1173, Ch. 5, pp. 85–136.

Acknowledgments

The Consortium for Affordable Carbon Fibers in the U.S. would like to acknowledge DOE-EERE VTO Materials Technology Manager H. Felix Wu for his technical guidance. They would also like to acknowledge individuals who have contributed significantly to the technical success in several areas: Logan Kearney at ORNL for CF spinning, mechanical properties testing, and ACN polymerization; Nicola Ferralis at MIT for spearheading the computational work at the molecular level, ML, and database; Khalid Baig at WRI for analytical analysis, pitch filtrations, and conversion of isotropic PP and CTP to mesophase; Stacey McKinney, Brett Johnston, and Carl Muller at Koppers for providing CTP, PP, and PPM to the program; Charlie Atkins and Jim Dietz at Ramaco Carbon LLC for providing the detailed techno-economic analysis; Ray Fertig at UW for providing tow level tests and finite element analysis and other macro-level modeling; Amit Goyal at SRI for working to provide purified scaled-up batches of bio-ACN; and Girish Deshpande at Solvay for technical guidance for this program.

II.2.3 Functionally Designed Ultra-Lightweight Carbon Fiber-Reinforced Thermoplastic Composites Door Assembly (Clemson University)

Srikanth Pilla, Principal Investigator

Department of Automotive Engineering
 Department of Materials Science and Engineering
 Clemson University
 4 Research Drive, Suite 340
 Greenville, SC, 29607
 E-mail: spilla@clemson.edu

H. Felix Wu, DOE Technology Manager

U.S. Department of Energy
 E-mail: felix.wu@ee.doe.gov

Start Date: December 1, 2015	End Date: November 30, 2022
Project Funding (FY 2021): \$5,567,754	DOE share: \$2,449,994 Non-DOE share: \$3,117,760

Project Introduction

A promising route to achieve the 2025 Corporate Average Fuel Economy standards involves decreasing vehicular weight by incorporating lightweight materials, coupled with component redesign, to improve overall fuel efficiency. Indeed, one recent study indicates that the simple replacement of current metallic doorframes with CFRP composites can reduce the overall weight of the component by nearly 58% [1]. The objectives of this project are to achieve a weight-reduction of at least 42.5% as compared to the baseline door structure at the cost of less than \$5/lb., all while saving on energy metrics without compromising the fit, function, crash, and NVH requirements. The strategy for achieving these targets involves a holistic systems approach through the integration of unique designs, novel materials, manufacturing technologies, and joining/assembly of subsystems to ensure the developed technologies are ready for commercialization.

Objectives

The objective of this project is to reduce the weight of a door assembly by at least 42.5% compared to a baseline driver's side front door with an expected cost increase of less than \$5/lb. in weight saved. A 2016 Acura MDX sport utility vehicle's door with an assumed production volume of 20,000 vehicles annually is the basis for design. These criteria will either meet or exceed the fit, function, crash, and NVH requirements of the baseline door.

The intent is to: (1) enable a radical redesign of the baseline door via a holistic systems approach through the integration of unique designs; (2) use novel materials to render the door 100% recyclable; and (3) investigate manufacturing technologies and joining/assembly of subsystems to ensure the developed technologies are ready for commercialization. The partner organizations listed in Table II.2.3.1 are providing highly leveraged knowledge expertise to ensure the success of this effort.

Table II.2.3.1. Project Participants

Universities	Industry Partners	Computation Partners
Clemson University	Honda	Altair Engineering
	Tencate, Lanxess	Core-Tech Systems (Moldex 3D)
University of Delaware	Krauss Maffei, Trexel Inc.	MSC Software (Digimat)
	Proper Tooling	LS-Dyna

Approach

The project entails the use of a systems-level approach that begins with a systematic evaluation and benchmarking of the door and its subassemblies. In collaboration with our partnering companies and commercial suppliers, researchers are evaluating a variety of CF thermoplastic material forms for structural components (i.e., novel unidirectional and fabric prepregs, commingled fabrics, high aspect ratio discontinuous fibers, performance thermoplastic resins, novel fiber architectures, and localized reinforcements) and alternative solutions for glazing, trim, and other subcomponents. The initial focus involves creating the structural component and a materials database for all parts of the door structural assembly (i.e., outer shell, inner panel, carrier, and anti-intrusion beam[s]).

A two-phase integrated design and manufacturing optimization approach was adopted to obtain the optimal manufacturing process parameters of the thermoplastic materials and the optimal structural design parameters of the door. The PIs also conducted a top-level trade study to determine at least two candidate designs for optimization. The design parameters include: (a) thermoforming and injection molding parameters (e.g., pressure, temperature); (b) fiber parameters (e.g., material, length, diameter, volume fraction); (c) matrix parameters (e.g., material, volume fraction); (d) structural wall thickness; and (e) material density distribution. The research team will use four analysis tools—Moldex3D, Digimat, and LS-DYNA Implicit and Explicit—to construct the manufacturing-to-response analysis pathway [2–4]. The team will fabricate a door based on this optimal design for testing in accordance with OEM performance requirements.

Results

Concept Development

The team’s focus in the fifth FY was on manufacturability of the final door concept based on draping and tooling inputs from our material supplier and tooling partner. To achieve this, the team made several modifications to all components with an emphasis on the structural components. The composite inner panel, our most critical piece, underwent several rounds of modifications. The three major modifications are highlighted in Figure II.2.3.1.

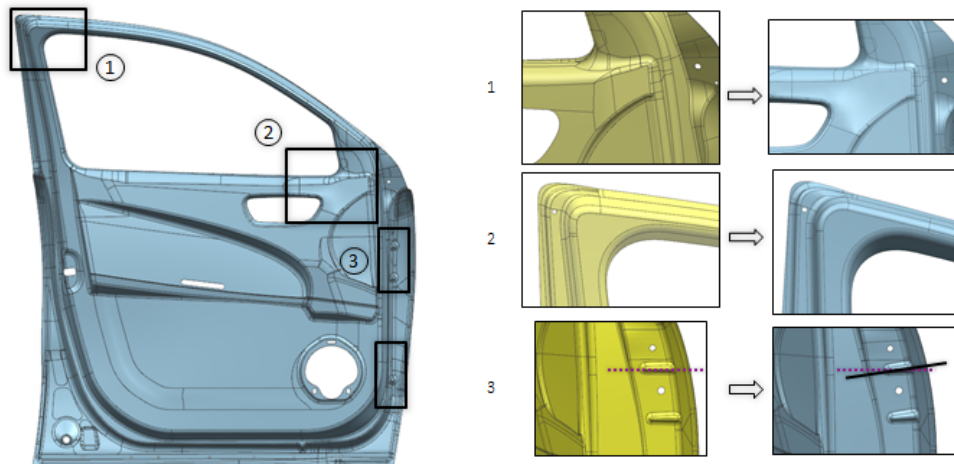


Figure II.2.3.1. Inner frame CAD modification at three locations (1,2,3). Source: Clemson University.

Similarly, significant computer-aided design (CAD) modifications were carried out on some of the mild steel and Al structural parts to improve manufacturability. Some examples include removing sharp corners and simplifying the surfaces to reduce shear-stress in the metal during the drawing operation, as shown in Figure II.2.3.2.

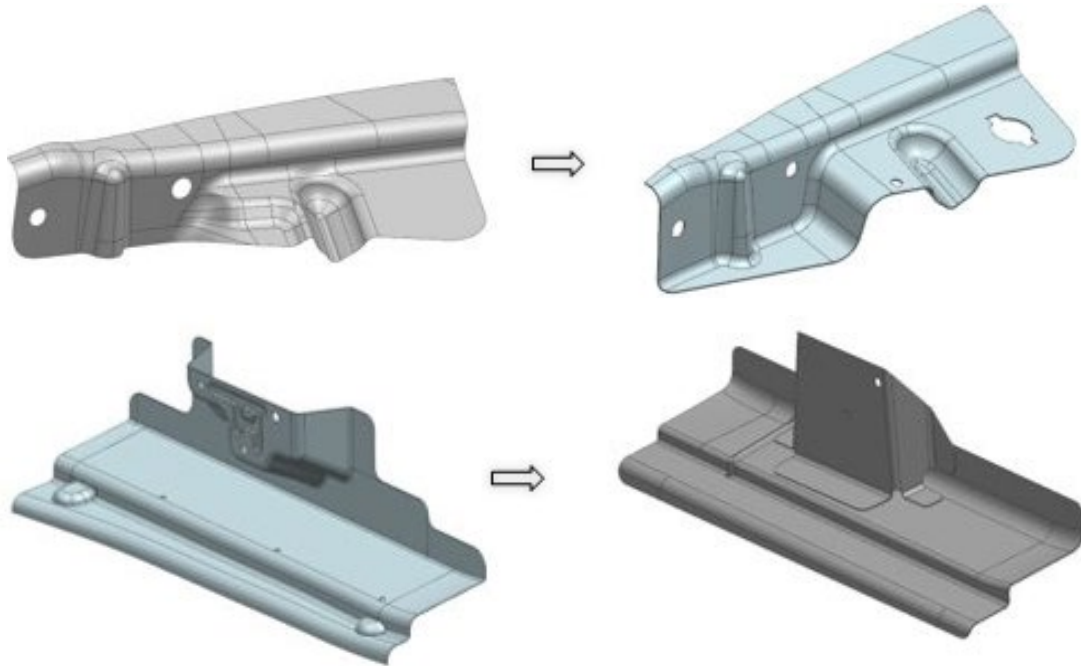


Figure II.2.3.2. Design change of anti-intrusion beam hinge side bracket and lower reinforcement. Source: Clemson University.

As a result of these changes, the team was able to achieve a 52% structural parts consolidation and a 45% structural weight consolidation due to innovative design strategic use of materials based on FEA and manufacturing simulation response, as illustrated in Figure II.2.3.3.

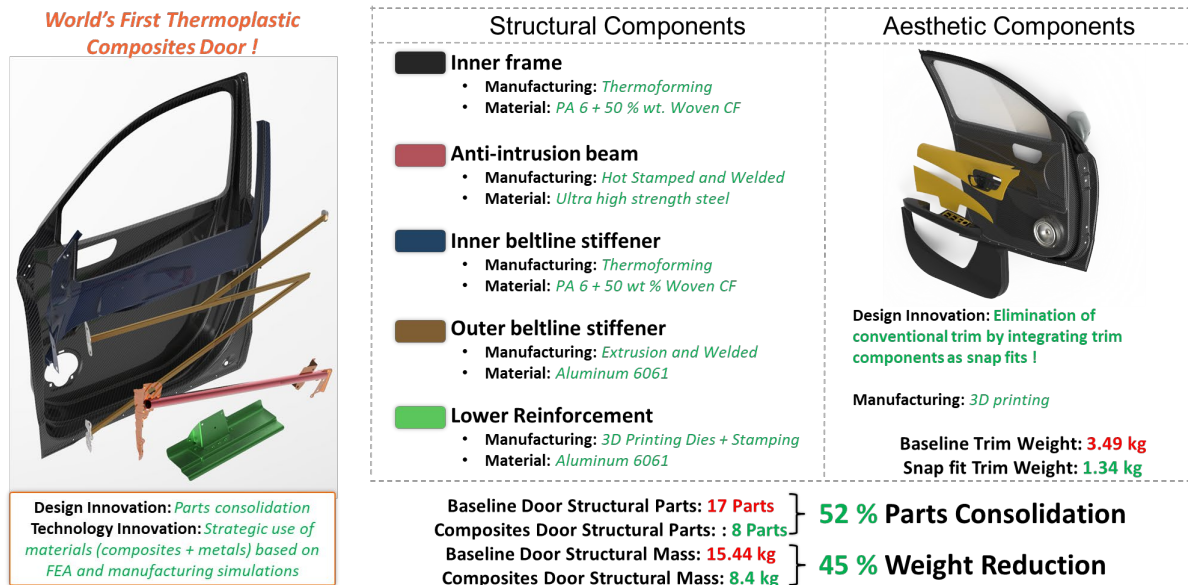


Figure II.2.3.3. Overview of final CAD for structural and aesthetic components. Source: Clemson University.

Summary of FEA Results

The team assessed the existing unidirectional (UD) + Woven ply design and decided to proceed with an entirely woven ply design having a uniform thickness of 3 mm for the inner panel and 2 mm for the inner beltline stiffener upon considering the geometric and thermoforming complexity of the inner panel. This configuration would greatly aid in simplifying the manufacturing effort by negating the need for equipment such as automated tape placement and simplifying material handling system while dramatically reducing tooling complexity.

The final door design is first optimized for linear static load cases, which represent daily use and misuse. These are: (1) door sag (two subcases); (2) sash rigidity (two subcases); (3) door over opening; (4) beltline stiffness; (5) outer panel stiffness; (6) mirror mount rigidity (two subcases); (7) speaker mount rigidity; and (8) window regulator stiffness. The composite door weight and deformation response under static loading is presented in Table II.2.3.2. The results are presented on the basis of the percentage relative difference between the baseline and the composite, where the negative sign indicates the reduction in the composite door response such as the mass or deformation from the target. The structural frame weight of the composite door is 45% lower than the target baseline weight while the total weight-reduction achieved is 37%, which is a little short of DOE's target of 42%. The deformation response of the composite door under static loading is lower than the target baseline for the majority of the load cases. The two load cases where the composite door response is slightly higher are mirror rigidity in X (+1%) and door over opening (+3%). However, these differences occur due to localized stress development near the hinges since the rigid body elements are used for modeling bolts. These differences can be easily eliminated during the door prototype fabrication by the usage of appropriate washers, therefore avoiding any major design change.

Table II.2.3.2. Static Performance of Composite Door

Serial No.	Target Category Subcase	Target (Unit)	% Relative Difference (Result - Target)/Target
1	Mass Target		
1.1	Structural Frame Weight	< Baseline (Kg)	-45%
1.2	Total Weight	< Baseline (Kg)	-37%
2	Frame Related		
2.1	Door Sag - Fully Open	< Baseline (mm)	-15%
2.2	Sash Rigidity at Point A	< Baseline (mm)	-10%
2.3	Sash Rigidity at Point B	< Baseline (mm)	-55%
2.4	Beltline Stiffness - IP	< Baseline (mm)	-79%
2.5	Window Regulatory (Normal)	< Baseline (mm)	-69%
2.6	Mirror Mount Rigidity in X	< Baseline (mm)	+1%
2.7	Mirror Mount Rigidity in Y	< Baseline (mm)	-67%
2.8	Door Over Opening	< Baseline (mm)	+3%
2.9	Speaker Mount Stiffness	< Baseline (mm)	-48%

The composite door was further tested under nonlinear load cases to evaluate crashworthiness. These load cases are: (a) the Federal Motor Vehicle Safety Standard (FMVSS) S214S quasi-static pole test (QSP), as shown in Table II.2.3.3; and (b) the deformable barrier test (Insurance Institute for Highway Safety [IIHS] Side Impact Moving Deformable Barrier). In addition to meeting the FMVSS and IIHS performance criteria, the requirements for individual load cases were provided by Honda based upon performance of a mass production door. The performance of the composite door under the QSP test is compared with the baseline door in the contact force vs. stroke plot, as presented in Figure II.2.2.4. The area under the curve of this plot gives the

energy absorbed during pole impact. The total energy absorbed by the composite door (e.g., solid orange curve) is clearly higher than that for the baseline door (e.g., solid black curve). There are three FMVSS requirements for the QSP test which are (i) initial average crush requirement stroke under 6 in. (represented by a dashed green curve), (ii) intermediate average crush requirement at under 12 in. (represented by a dashed blue curve), and (iii) peak average crush requirement under 18 in. (represented by a dashed horizontal line). The initial average crush for the composite door is higher by 7% to the actual FMVSS requirement, and the intermediate crush (up to 12 in.) is higher than the actual FMVSS requirement by 81%. The composite door also satisfies the maximum peak crush requirement (e.g., the horizontal line in the plot) and is higher by 101%.

Table II.2.3.3. Results for the QSP Test

Results	% Above FMVSS Requirement
Initial Average Crush	7%
Intermediate Average Crush	81%
Peak Crush	101%

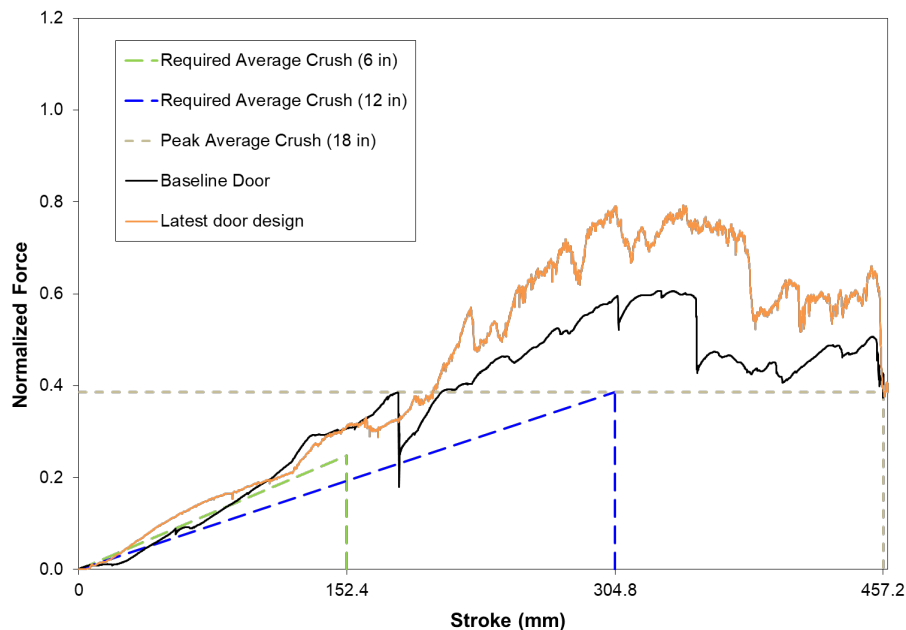


Figure II.2.3.4. Normalize force-displacement plot of baseline and composite door under the QSP test.
Source: Clemson University.

To evaluate the performance of the door under deformable barrier load case, the team listed five key performance indicators after discussions with Honda. A gauging matrix was further created to assess whether a composite door passed the Honda requirements or not. The gauging matrix is defined as: (a) successful (green) if the door response is better than the baseline; (b) tolerable (yellow) if the response is lower than the baseline, but it is within the 10% margin; and (c) failure (red) if the response is below 10% from the baseline door. Table II.2.3.4 presents the composite door response compared to that of baseline target on five performance indicators, which are maximum intrusions at roof, near windowsill, at front door dummy hip and near door lower level and safety survival space. The highlighted response in green color shows that three intrusion indicators are in successful range while one intrusion criterion at door lower level is in tolerable range. The safety survival space which is indicative of the occupant space left after the impact is also measured which improved by 1% when compared with baseline target.

Table II.2.3.4. Results for Deformable Barrier Dynamic Load Cases Compared to Target Baseline Door

Key Performance Indicator	Target	IIHS Side Impact Moving Deformable Barrier (Response/Target)
Max Roof Intrusion		3%
Max Windowsill Intrusion		12%
Front Door Dummy HIP Intrusion		25%
Max Door Level Intrusion		4%
Safety survival space		1%
Gauging Metrics		
Green (Success) - Below Baseline target values (<b).		
Yellow (Tolerable) - More than Baseline values but smaller than 10 % difference (>b, <b+10%).		
Red (Failure) - More than 10% above Baseline value (>b+10%).		

Subcomponent Manufacturing, Modeling, and Testing

To correlate and verify the crash simulations results to real-world behaviors, a hat profile structure was manufactured with a pre-existing mold using Nylon 6 reinforced with 50 vol.% woven CF supplied by our material partner, Lanxess. The forming setup, shown in Figure II.2.3.5(a), consists of two forming tools (e.g., the punch and die) and a blank holder apparatus accommodated in a thermal chamber. All forming tests were conducted on an Instron 5985 universal testing machine with a 250 kN 2580 series static load cell. Tests were performed using a cross-head speed of 5 kN/min until the preset load of 22 kN was reached. The entire set up—including the picture frame, composite material, and hat section tool—were placed in a furnace, thermocouples were placed on the punch, and the die, composite sheet, and furnace were heated. While cooling, the entire set up was cooled via forced convection until the composite material reached 100°C; then, liquid nitrogen was injected through Cu cooling channels in the tool to quench cool the part to RT. The intent of the quench cooling was to demonstrate the effect of cooling rate on the formation of residual stresses in the structure as shown in the graph of Figure II.2.3.5(b). The cooling channels were constructed in such a way that the composite part does not come into contact with the liquid nitrogen; any cooling seen on the material is due to conduction from the punch and the die.

The thickness variation and fiber orientations were experimentally measured after performing the thermoforming experiments and were compared with the numerical results. The thickness was measured at six different locations along the hat profile (or at three locations on each side) and the average thickness from the three experimental trials is presented in Figure II.2.3.6. The numerical thickness variation is predicted using a draping tool available in Altair Hyperworks software. A comparison between the measured thickness and the predicted thickness showed good agreement. Furthermore, the warp and weft tows of the composite sheet are referred to here as fibers in direction 1 and 2 initially 90° apart. These fibers of the composite sheet undergo reorientations as the sheet deforms to take the shape of the mold.

Figure II.2.3.7 shows a comparison of fiber orientations between the experiments and the simulation, where the change in angle between the two fiber directions was measured. The average fiber orientations from the three experimental trials were determined and compared with the numerical prediction, which showed good agreement. Next, the mechanical performance of the above thermoformed hat structure with the effect of residual stress was evaluated by carrying out a three-point bend test.

The hat structure samples were adhesively bonded to a 0.5-mm-thick PA 6 woven composite plate using the Plexus MA 530 adhesive system, as shown in Figure II.2.3.8(a). The experimental setup for the quasi-static mechanical test of the hat structure is shown in Figure II.2.3.8(b), which consists of two supports with a support span of 119.3 mm and a punch. The three-point bend tests were performed on an Instron 5985 universal testing machine with a 10 kN 2580 series static load cell using a modified Instron 2810 series flexure fixture and a cross-head speed of 1 mm/min on three samples.

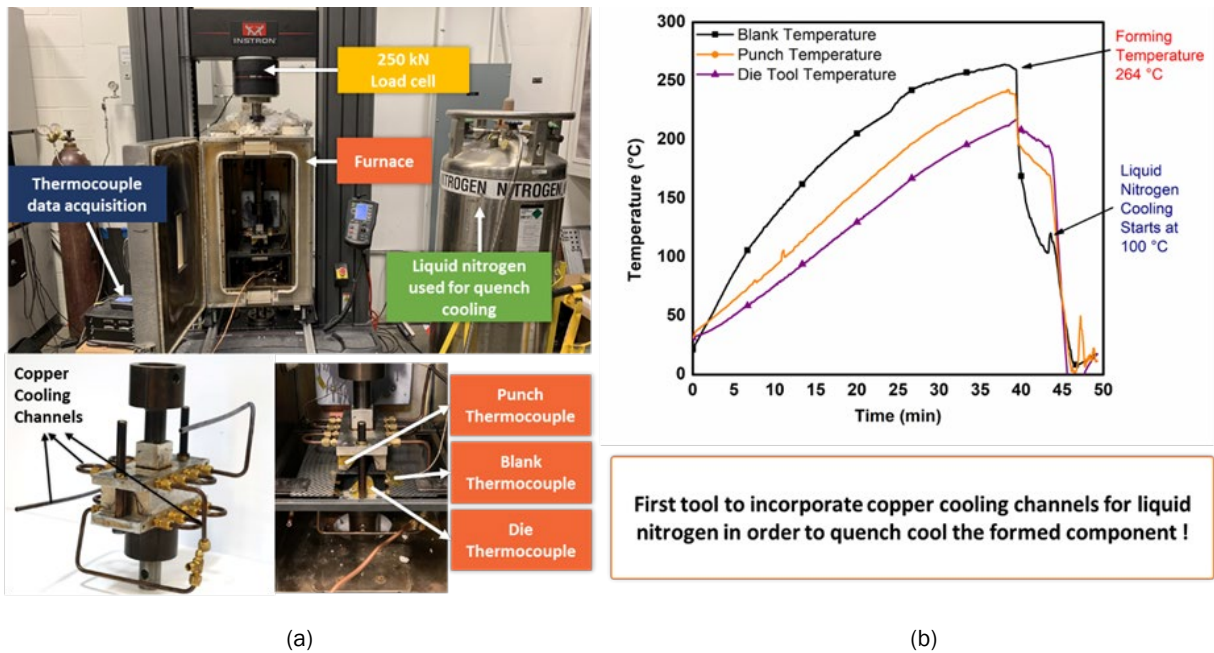


Figure II.2.3.5. (a) Thermal chamber equipped with a thermocouple data acquisition system; and (b) liquid nitrogen cooling for thermoforming tests and thermoforming setup showing Cu cooling channels and thermocouple location. Source: Clemson University.

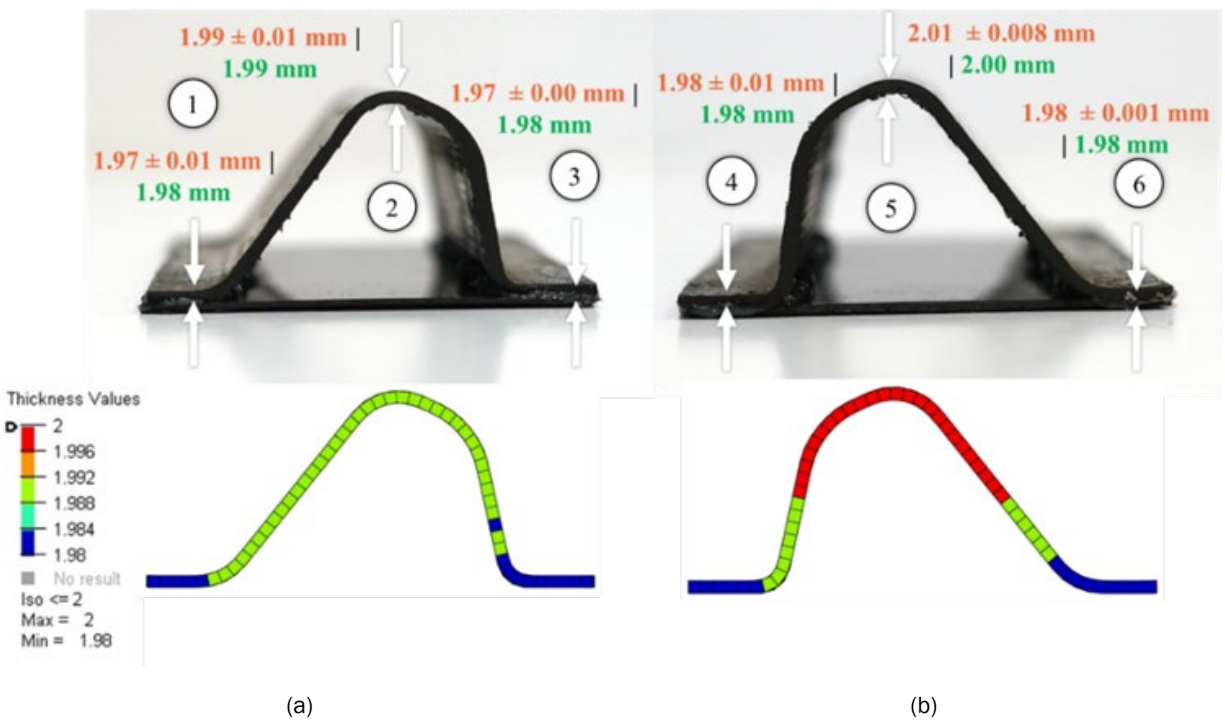


Figure II.2.3.6. Thickness variation in the hat structure of: (a) Side 1; and (b) Side 2, which are represented as average thickness \pm standard deviation. Predicted thickness from simulation measured for the three experimental forming trials. Source: Clemson University.

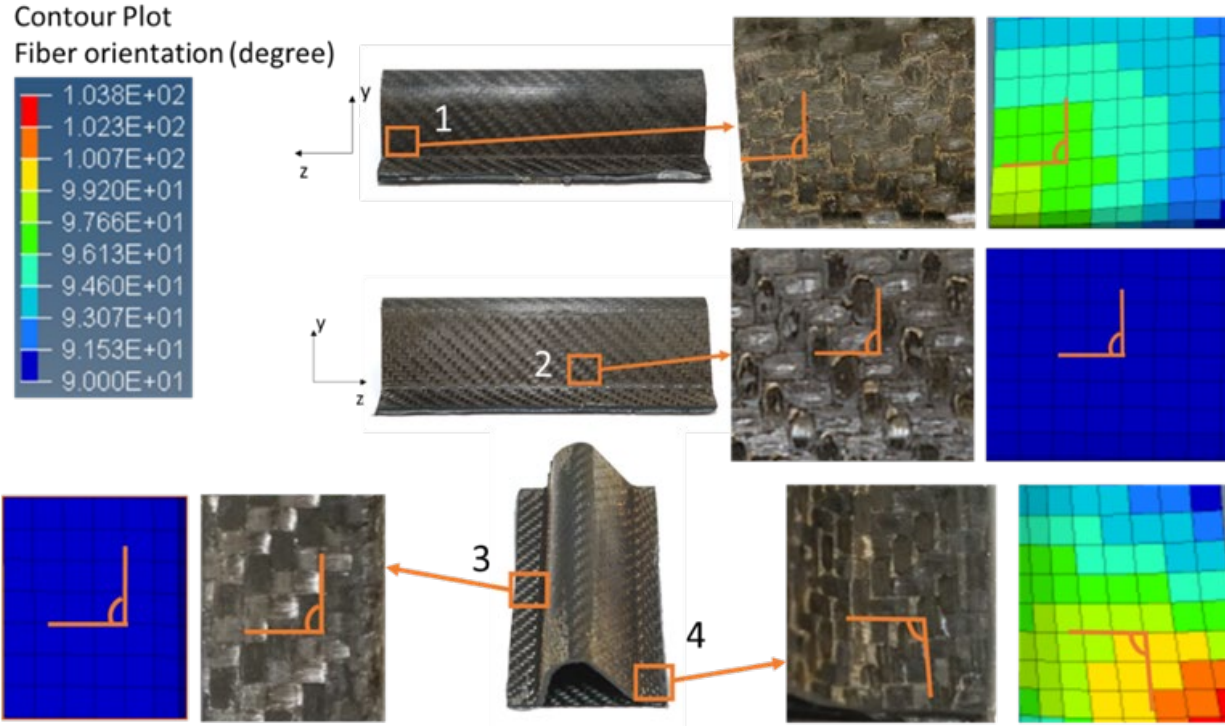


Figure II.2.3.7. Fiber orientation in degree as observed in thermoforming trials and simulation at marked locations of the hat structure. Source: Clemson University.

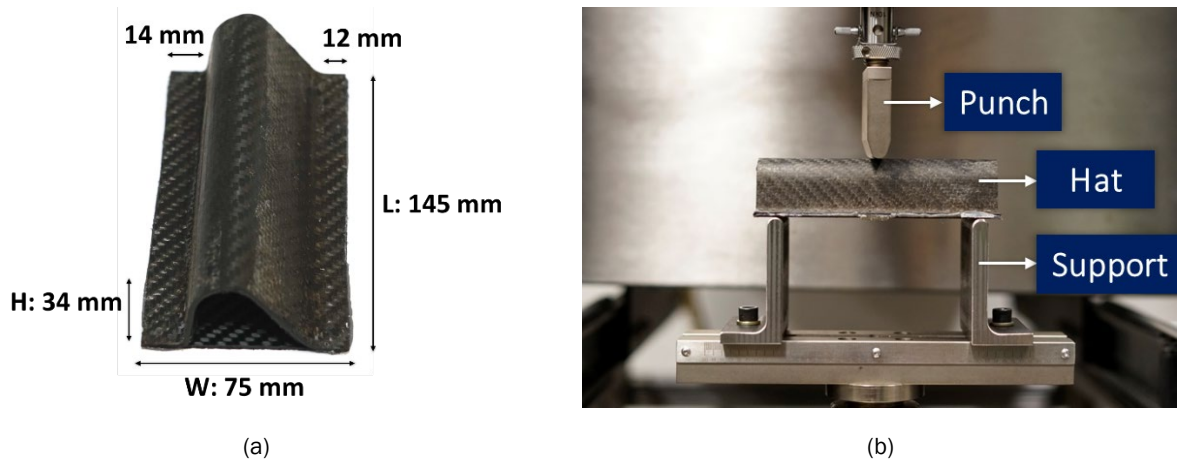


Figure II.2.3.8. (a) Dimensions of the bonded hat section part; and (b) the experimental setup for the three-point bend test showing the hat structure, supports, and punch. Source: Clemson University.

The force-displacement responses obtained from the three-point bend tests are presented in Figure II.2.3.9(a). A consistent and repeatable linear stiffness zone and failure initiation at an approximate 6 mm deflection is observed among all three trials. Additionally, the location, time, and displacement at which crack initiation occurs is extremely consistent across the three samples. The trials show a slightly varied force-displacement response post 7 mm deflection, with trial 1 exhibiting a peak load of ~ 5877 MPa at a 10 mm deflection and trials 2 and 3 show a load of 5272 MPa ~ 4652 MPa at the same deflection. The final shape and deflection of the crack vary slightly across the three samples, with trial 1 showing the least amount of damage in terms of

crack diameter and deflection and trial 3 showing the most damage. The numerical three-point bend test under a quasi-static loading condition is carried out using LS-DYNA after mapping the thermoforming effects. The force-displacement response is compared with the mean experimental results in Figure II.2.3.9(b), which show very good agreement until the onset of damage. The large deformation is observed at the impact location of the hat structure when the numerical predictions are compared with the three experimental trials.

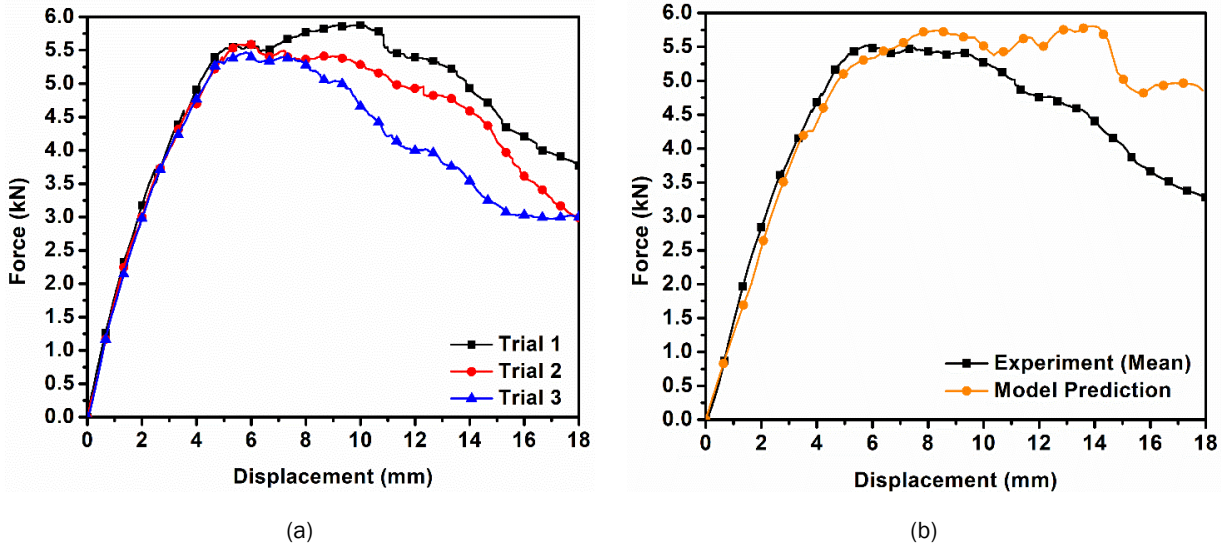


Figure II.2.3.9. (a) Force-displacement plot of three experimental trials. (b) Force-displacement plot for the three-point bend test comparing experimental response with numerical prediction.

Source: Clemson University.

Figure II.2.3.10(a) shows the side view, which closely matches the numerical prediction of deformation appearing in trial 3. Figure II.2.3.10(b) presents a top view of the hat structure along with the von Mises stress contour and encircled regions (appearing in red) that show the damaged locations. The damage behavior is consistent with the experimental results. However, it should be noted that delamination failure and damage propagation, which requires a detailed damage modeling strategy, are not considered in the study.

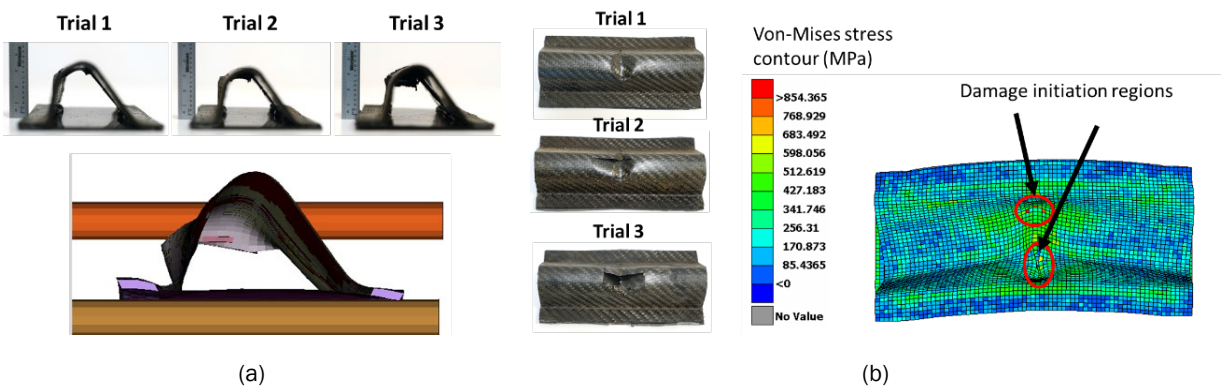


Figure II.2.3.10. Deformation comparison between the experimental trials and the numerical simulations: (a) deformation side view showing a close match with experimental trial 3; and (b) top view comparison with stress contour plot. Encircled are the damage initiation locations on the structure.

Source: University of Delaware.

Manufacturing of Door Components

As a result of COVID-19, the overall tooling effort has been delayed. Our tooling partner, Ventec, was unable to assist because of a ventilator project. As such, a detailed tooling and manufacturing strategy for all components were discussed with the material supplier, the tooling partner, and the team. With regards to the structural parts, the team would focus on the tooling and manufacturing of the smaller composite inner panel tool to implement simulated manufacturing strategies and apply these learnings to the target composite inner panel part. Tooling and manufacturing of the steel anti-intrusion beam, Al outer beltline stiffener and Al lower reinforcement will be spearheaded by Honda. The tooling strategy for each of the critical composite components is discussed below. The manufacturing for both strategies will begin with trials on PA 6 reinforced with 50 vol.% glass fiber to optimize material handling, process conditions, and cost-savings.

The team is considering two strategies for the manufacturing of the inner beltline stiffener. In the first, a blank of 2 mm thickness will be pre-cut in the shape of the final part, as shown in Figure II.2.3.11(a). This pre-cut blank will be thermoformed to form the final part without the need of post-processing operations. In the second, a 2-mm-thick pre-consolidated composite sheet of dimensions 1240 × 860 mm will be used as a blank to thermoform the part, as shown in Figure II.2.3.11(b). A post-processing process to cut out the trimline of the thermoformed part will be required in the second strategy. The team prefers the first strategy.



Figure II.2.3.11. (a) Inner beltline stiffener blank strategy; and (b) the blank size (1240 × 860) obtained from the supplier. Source: Clemson University.

The compression molding tool will accommodate both strategies. The tool will be 1200 mm × 850 mm × 450 mm in size made up of 5000 series Al material with a B3 surface finish. The tool will have the capability to rapidly heat (e.g., 150°C) and cool for improved surface finish and reduced cycle time. An initial tool concept is shown in Figure II.2.3.12(a) and (b). For manufacturing, both the horizontal (from the injection molders) and vertical presses (from Honda) are being considered. The pin shaped cavity drivers will be used to control the flow of material, as shown in the snapshots of simulation in Figure II.2.3.12(c)–(e).

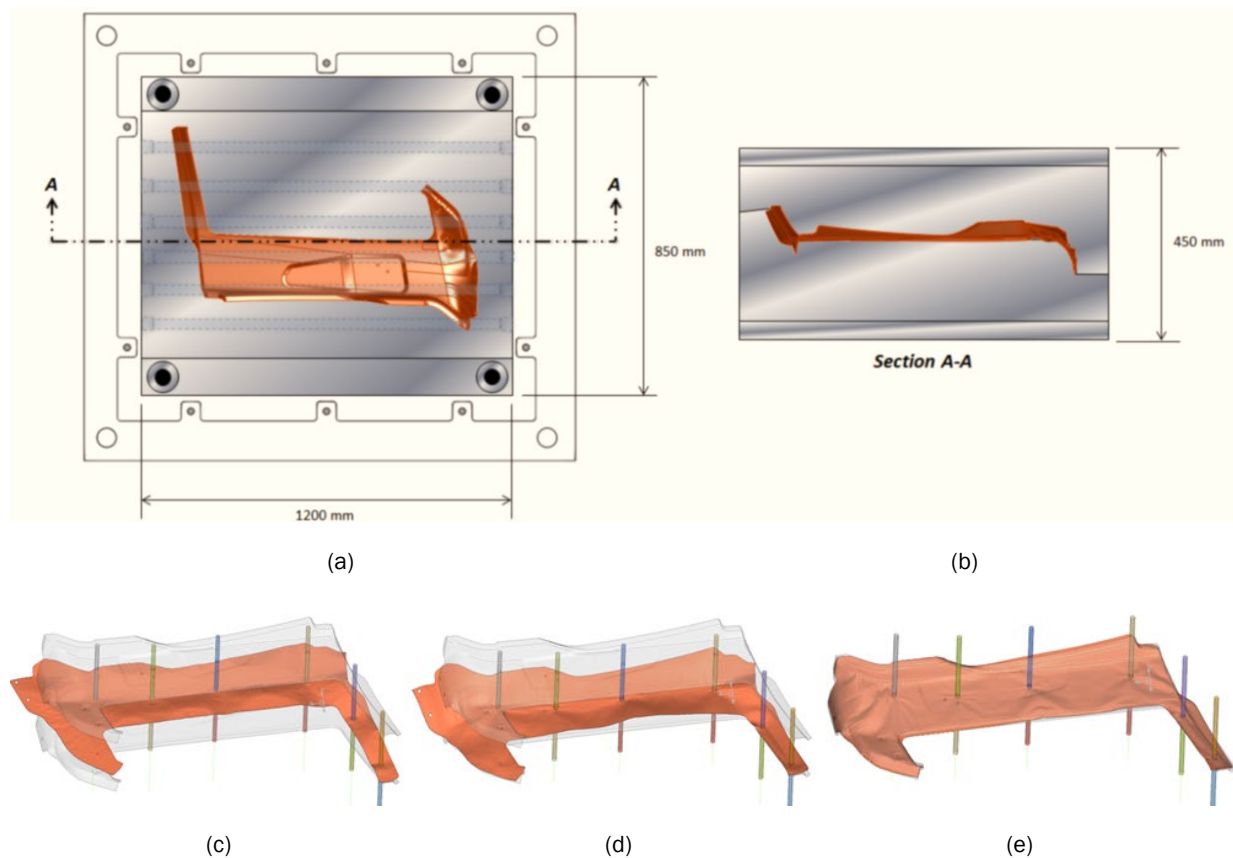


Figure II.2.3.12. (a) Initial tool concept of the inner beltline stiffener. (b) Thermoforming simulation of the inner beltline stiffener. (c) Before forming. (d) Cavity driver touch lower tool. (e) Tool closed condition.
 Source: Clemson University.

Composite Inner Frame

The size of the blank will be 1400 mm × 1540 mm × 3 mm made after the consolidation of three layers that are 1-mm-thick, as shown in Figure II.2.3.13. The compression tool, as shown in Figure II.2.3.14(a) and (b), for the inner frame (1930 mm × 1780 mm × 1130 mm) will be machined with 5000 series Al and A2 high polish.). This tool will also have the capability to rapidly heat (e.g., 150°C) and cool for improved surface finish and reduced cycle time. The tool will consist of a cavity driver forming window, door sash, and some panel areas to control the material flow during the thermoforming process. A simulation of the thermoforming steps is illustrated in Figure II.2.3.14(c)–(e). The manufacturing strategy will begin with trials on PA 6 reinforced with ~ 50 vol.% glass fiber to optimize the process conditions, specifically material handling, process conditions, and cost-savings. After completing the draping simulations, a forming simulation was conducted to calculate the residual stress and accurate ply rotations from which the mechanical performance of the structure was re-evaluated. During these forming simulations, process parameters (i.e., blank holder force, punch velocity, and clamping forces) were determined, as shown in Figure II.2.3.14(c)–(e). The virtual optimization of these process parameters will be useful in minimizing the risks during the prototyping phase. The blank will be held by a metallic frame using pneumatic grippers. The grippers will be controlled for the sequential release of the heated sheet, choreographed to properly form the inner panel. The concept is still under discussion with the material supplier. The snapshots of the initial simulation are shown in Figure II.2.3.14.

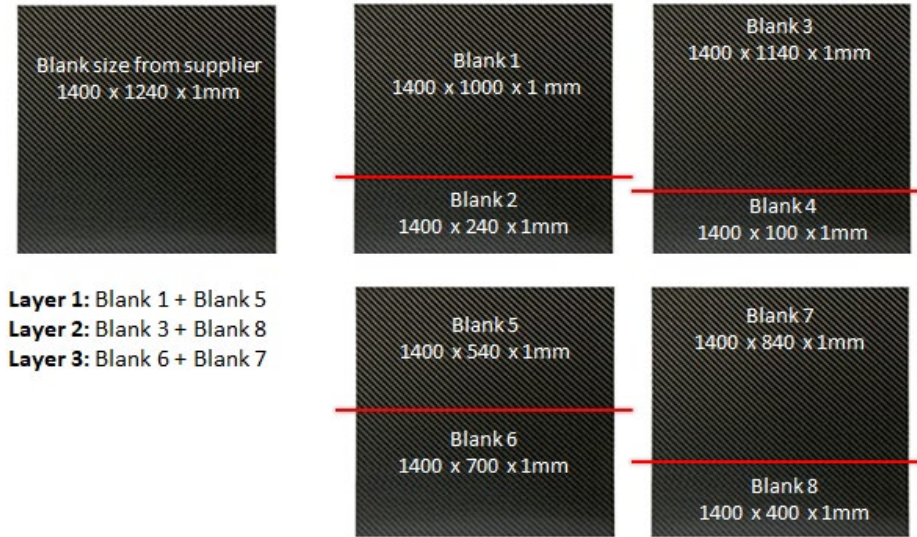


Figure II.2.3.13. Blank strategy for inner frame. Source: Clemson University.

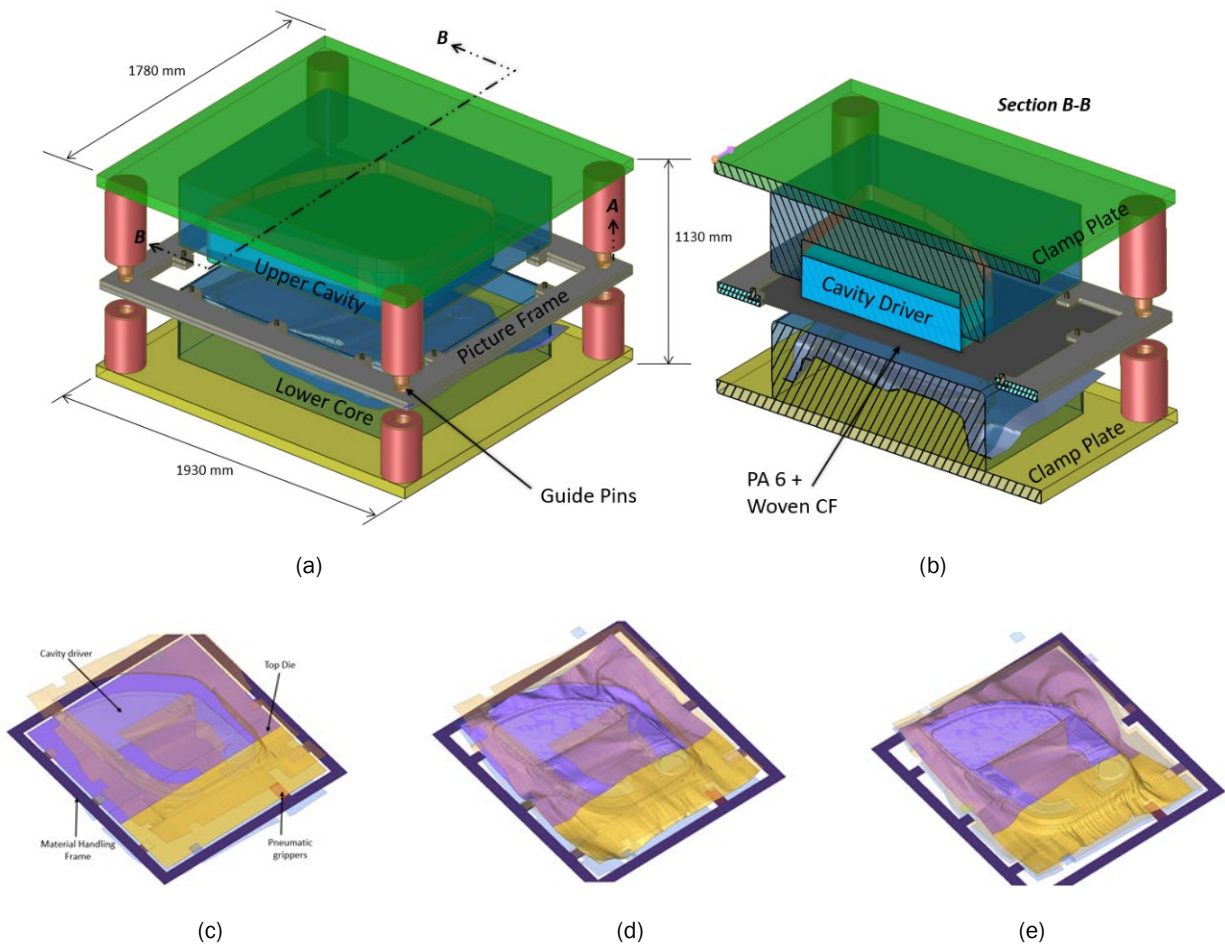


Figure II.2.3.14. (a) Initial tool concept of inner beltline stiffener. (b) Thermoforming simulation of inner beltline stiffener. (c) Before forming. (d) Cavity driver touch lower tool. (e) Tool closed condition. Source: Clemson University.

Cost-Modeling Summary

The generative cost model and parametric cost model were developed to estimate the total cost of the door. The generative cost model was developed for the production version of the composites door that comprises both the UD and woven composite ply layup in the two structural parts inner panel and beltline stiffener. The developed cost model is based on the following assumptions: (a) the total cost is assumed to be a function of material, labor, equipment, tool, energy, and overhead cost; (b) the parameters identified for cost-estimation are independent of each other; (c) the data is collected and normalized using experience and literature review; (d) the rate of the overhead (e.g., 20% of the total cost) is assumed by experience; (e) the production volume per year is assumed to be around 80,000; (f) the cost of carry-over parts (~\$181) is assumed to be constant; and (g) the number of workers working on each machine are assumed to be four. The total cost calculated for the latest design of the door is \$935.26. The weight and cost of the door, made with UD and woven composite ply, are compared with a baseline steel door on a different component-level in Table II.2.3.5. The structural weight saved by the ultra-lightweight composite door is 45% as compared to the baseline door, while there is a cost increase of \$4.02 for each lb. saved. Weight-reduction of 47% is obtained for non-structural parts when compared with the baseline door with cost increase of \$4.18/lb. saved. The other carry-over parts, such as the window frame and the seals, are not considered for weight-reduction due to stringent constraints provided by Honda on these parts. In addition, the cost of painting on the composite door was determined, which is higher by \$32.79 than the baseline door. The total weight-reduction achieved by the composite door is approximately 37% of the baseline door weight with the total cost increase of \$5.40/lb. saved, which is slightly higher than DOE's target of \$5/lb. saved. Cost of the material, tooling, equipment, labor, energy, building, maintenance, overhead, and capital were all considered to calculate the cost of each individual parts. As observed, 46% of the total cost is the cost of the material itself while the overhead cost, labor cost, and tooling cost contribute 11%, 5%, and 4%, respectively. The cost distribution based on the individual door subsystems is presented in Figure II.2.3.15. The inner panel is the most expensive component of the car-door with a cost of \$391, which is 42% of the total cost.

Table II.2.3.5. Comparison of Weight and Cost Distribution of Composite Door (Production Version) with the Baseline Door

Results	Baseline Door Weight (kg)	Composite Door Weight (kg)	% Weight-Reduction	\$/Lb-Saved
Door structural parts	15.44	8.44	45%	4.02
Door non-structural parts	9.37	4.97	47%	4.18
Other carry-over parts	6.29	6.29	0%	0
Total	31.1	19.7	36.66%	5.40

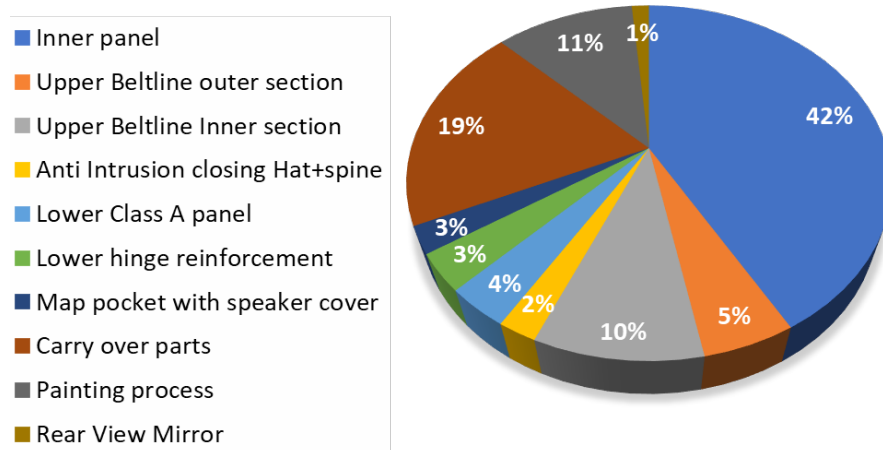


Figure II.2.3.15. Cost distribution of the individual parts of the door. Source: Clemson University.

The development of the generative cost model to estimate the total cost of the door was followed by the development of the parametric cost model to find how individual parameters influence the total cost. Parametric cost-modeling is carried out in three steps: (i) development of cost-estimating relationships; (ii) parameterization of the door design; and (iii) creating user interface to perform tradeoffs and estimate cost of individual parts. At first, individual parameters that influence the overall cost of the door were identified, which are electricity cost per kWh, scrap rate, mold life, equipment life, labor wage, production volume per year, overhead rate, and material cost. Then, a relationship between these parameters with the total cost is determined using mathematical and statistical tools. Assuming the normal distribution of the identified parameters when all are taken together to study overall variation in the door, it is found that the total cost of the door may vary between \$873 to \$996, as presented in Figure II.2.3.16.

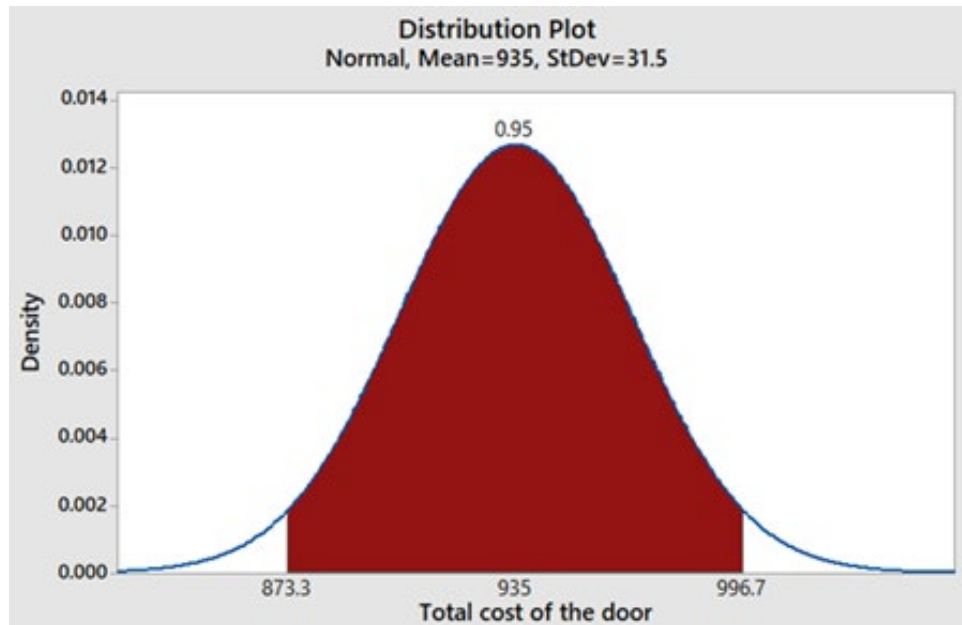


Figure II.2.3.16. Normal distribution of total cost of door. Source: Clemson University.

As a further cost-saving strategy, the team also evaluated costs by adopting a glass fiber-based composite instead of a C composite system because the cost of the glass fiber is almost 1/10th of CF cost; therefore, glass fiber-based composite plies are considered for trials of thermoforming analysis. Keeping the same design, the total cost of a glass-based composite door is obtained as \$805, while the weight-reduction is 28%, which gives a cost increase of \$0.21/lb. saved. The static performance of the glass fiber-based composite system is also evaluated, which lies in the tolerable range satisfying most of the static load cases. However, the glass fiber-based design needs to be further optimized for static and crash load cases. Therefore, it can be concluded that the glass fiber-based composite system has a potential of reducing approximately 25% of the door weight while equally satisfying DOE's cost constraints.

Conclusions

The research focus during FY 2021 involved the finalizing of door design by employing an iterative processing that involved feedback from static and crash simulations, cost analysis, and manufacturing constraints, all while trying to comply with the aggressive weight targets. The final door design met and exceeded expectations from the viewpoint of static and crash targets. This was further validated by experimental tests performed on a subcomponent. A detailed overview of the tooling and manufacturing strategy was discussed in consultation with our material suppliers and tooling partners was presented. Last, from a cost perspective, the door was slightly above the cost targets primarily due to high input material costs, and strategies are being evaluated in order to meet this requirement. With the granting of the no-cost extension, the team will spend the early half of 2022 on tooling and manufacturing, and the latter half on the assembly and testing of the door.

Key Publications

1. Kothari, A.; A. Yerra, M. Limaye, S. A. Pradeep, G. Dalal, G. Li, S. Pilla, L. Fuessel, B. Haque, S. Yarlagadda, S. Malcolm, and D. I. Detwiler, 2021, “A finite element design study and performance evaluation of an ultra-lightweight carbon fiber-reinforced thermoplastic composites vehicle door assembly,” SAE Technical Paper 2021-01-0203.
2. Limaye, M.; S. A. Pradeep, S. Kothari, G. Li, and S. Pilla, 2020, “Thermoforming process induced structural performance of carbon fiber-reinforced thermoplastic composite part through a novel manufacturing-to-response pathway,” Society of Plastics Engineers ACCE Conference, 4-6 September 2020, Novi, MI, USA.
3. Mittal, A., A. Kothari, S. A. Pradeep, S. Savla, M. Limaye, G. Li, S. Pilla, P. Swaminathan, S. Yarlagadda, R. Hahnen, and D. Detwiler, 2021, “Designing a production-ready ultra-lightweight carbon-fiber-reinforced thermoplastic composites door,” *SAE Int. J. Adv. Curr. Pract. Mobil.*, Vol. 3, No. 4, pp. 1915–1922.

References

1. Kelly, J. C., J. L. Sullivan, A. Burnham, and A. Elgowainy, 2015, “Impacts of vehicle weight-reduction via material substitution on life cycle greenhouse gas emissions,” *Environ. Sci. Technol.*, Vol. 49, No. 20, pp. 12535–12542.
2. Mi, H.-Y., X. Jing, J. Peng, L.-S. Turng, and X.-F. Peng, 2013, “Influence and prediction of processing parameters on the properties of microcellular injection-molded thermoplastic polyurethane based on an orthogonal array test,” *J. Cell. Plast.*, Vol. 49, No. 5, pp. 439–458.
3. Chang, S. H. and S. S. Cheon, 2006, “In-plane directional mechanical properties of carbon fabric skins in sandwich structures after thermoforming,” *Compos. Struct.*, Vol. 75, Nos. 1–4, pp. 577–581.
4. Yu, Y., J. Ye, Y. Wang, B. Zhang, and G. Qi, 2013, “A meso-scale ultrasonic attenuation FE model of composites with random-distributed voids,” *Compos. Sci. Technol.*, Vol. 89, pp. 44–51.

II.2.4 High-Temperature Carbon Fiber Carbonization via Electromagnetic Power (Oak Ridge National Laboratory)

Eng Felix L. Paulauskas, Principal Investigator

Chemical Sciences Division
Oak Ridge National Laboratory
1 Bethel Valley Road
Oak Ridge, TN 37831-6053
E-mail: paulauskasfl@ornl.gov

H. Felix Wu, DOE Technology Manager

U.S. Department of Energy
E-mail: felix.wu@ee.doe.gov

Start Date: November 17, 2020 End Date: September 30, 2022
Project Funding (FY 2021): \$2,000,000 DOE share: \$2,000,000 Non-DOE share: \$0

Project Introduction

High-temperature carbonization (HTC) of polymer-fiber via electromagnetic (EM) power is a project that aims to develop an innovative and scalable process for the final stage of CF conversion by reaching sufficiently high coupling and temperature elevation of the material. It is the continuation of a former project dedicated to low-temperature carbonization (LTC).⁶ This project will complete the portfolio of technologies developed by DOE and ORNL that are intended to replace the conventional carbonization technology used in the CF industry. This HTC project is a joint development research project carried out by ORNL and 4XTechnologies, LLC (formerly RMX Technologies), and is fully funded by DOE. Preliminary work on EM carbonization was initiated at ORNL with the Microwave Assisted Plasma (MAP) project⁷, and then jointly continued with 4XTechnologies since 2013. This report covers the progress made on the HTC project during FY 2021.

ORNL and 4XTechnologies have recently completed the development of a new LTC technique for CF manufacturing. This successful LTC project demonstrated that close proximity electromagnetic carbonization (CPEC) technology is feasible and scalable,⁸ and produces CF with the tensile strength meeting or exceeding 500 kilopound per square inch (ksi)⁹ after subsequent conventional HTC processing. This novel technology has the potential to significantly reduce the cost of CF manufacturing by reducing energy consumption and processing time, while decreasing maintenance, capital, and labor requirements. This new method utilizes an EM heating technique that operates at atmospheric pressure. Nevertheless, this process still requires a final HTC stage to produce completed CF, which itself is highly energy-intensive and requires high maintenance. The recent achievements and the need for cost reduction in CF production justify the effort with this HTC project.

EM processing is, in general, characterized by direct deposition of the energy into the material by dielectric coupling. This leads to faster and more efficient energy deposition than conventional processing, as long as the dielectric properties are adequately aligned with the coupling requirements. This was the case with the LTC project. With HTC, a different technical approach will be required due to the electric conductivity of the partially carbonized fibers. Current progress with EM LTC already shows residence time of less than a minute,

6. The Low Temperature Carbonization project was a project jointly conducted by ORNL and 4XTechnologies (FY 2016–FY 2020)

7. Microwave assisted plasma carbonization was a one stage carbonization project conducted solely by ORNL (FY 1997–FY 2007). This technology required vacuum.

8. The last prototype built with the CPEC technology (LTC project) was rated to 1.0 annual metric ton of CF.

9. Details about the mechanical performances of the CF produced with the CPEC technology can be seen the third quarterly progress report of the LTC FY2020 covering the performance period of April–June 2020 (issued in July 2020).

yielding fiber that, once conventionally HTC-carbonized, produces CF with tensile properties above 500 ksi. Related to energy efficiency deposition per unit mass in the EM LTC, the experimental work showed that it is possible to decrease the energy consumption compared to the lowest value of a benchmark¹⁰ by approximately 40% under certain conditions. These conditions include the limitation of the controlled volume to the applicator¹¹ only.

The goal of this new project is to develop an EM-based technology to replace the conventional HTC stage while producing CF with comparable mechanical properties. This new project will exclusively focus on HTC and will capitalize on the knowledge and experience gained from former successful projects, such as LTC and MAP. Compared to those prior works, the HTC apparatus will operate at a higher power level with a novel coupling mechanism than LTC and, unlike MAP, will operate at atmospheric pressure while being scalable. This will make this technology unique and implementable at a large-scale in industrial production lines.

To achieve this, a modular hardware implementation will be introduced, where physical HTC processing modules can be fastened to the output side of the current LTC CPEC furnace.¹² There is the challenge of fiber tensioning in this approach, where there are different stretch conditions implemented for LTC versus HTC during conventional processing. Therefore, a stretcher may need to be inserted between the CPEC LTC and HTC stages. Work will be performed both with and without this intermediate stretcher to determine the minimum hardware required. Additional HTC modules can be added as well to achieve the desired final CF properties. As the project progresses, this consideration will be addressed.

Objectives

The objective of the HTC project is to develop a faster and more efficient carbonization process than the actual conventional process. The concept is to focus the energy deposition on the material and limited parts of the furnace with the goal to reduce the unit energy consumption (in kWh/kg) by approximately 20%, while producing the same (or better) CF quality. This achievement would represent about a 5% cost reduction of the overall CF manufacturing process. The HTC furnace will be designed to treat up to 4 tows of 24,000 filaments.

Approach

The HTC project is split into four phases over a two-year effort. The first three phases are dedicated to the design and construction of the experimental setup and represent year one of the operation of this HTC program. The second and last year will be dedicated to the experimental work, which includes testing as well as all needed upgrades. The four phases are summarized and described in Table II.2.4.1. The HTC technology is co-developed by ORNL and 4XTechnologies.

10. Details about the performance evaluation and benchmark used as a reference are available in the last milestone report (M16) of the Low Temperature Carbonization report released on October 2020.

11. If the controlled volume is extended to include the generator and its cooling system, the energy yield per unit mass of the experimental setup becomes greater than lowest value of the benchmark.

12. CPEC: Close Proximity Electromagnetic Carbonization is the given name to the technology developed for the LTC EM.

Table II.2.4.1. Phased Approach to HTC Project

Phase	Name	Date	Status (Sept. 2021)	Description
1	Modeling and design	FY 2021	Completed	Evaluation, modeling and design, sourcing.
2	Construction	FY 2021	Completed	Construction of the setup with all its subsystems.
3	Commissioning	FY 2021	Completed	Performance test and adjustment of each subsystem. This phase includes the safety evaluation.
4	Operation	FY 2022	Not started	Testing, upgrade, and energy evaluation of the setup.

Results

Start/Initial Delay

The HTC effectively began in the second half of November 2020 because of an administrative delay.¹³ The HTC project was delayed by more than a month and a half compared to the initial schedule proposed in its annual operating program (AOP). This initial delay had a negative impact on the milestone schedule at the end of this first FY.

Personnel Change

A redefinition of the project members and their tasks was done in the first weeks of the project due to the cancellation of the commercial relationship with a third-party. This third-party had previously provided support with the modeling and design activities. This partner had been a full-time team member on the LTC project until April 2018.

As a result, the modeling activity has been redistributed to the existing engineering team. This required the team to acquire some additional skills with the Dassault Systems CST Studio Suite modeling software. Despite this unanticipated human resource change, the modeling activity was successfully completed within the amount of time initially planned, but its completion was shifted by two months, mostly because of the initial delay.

Sourcing and Equipment Preparation

Since this project involves the construction of an experimental setup, sourcing and equipment preparation was expected to be one of the major tasks of this HTC project. The effort dedicated to the hardware was anticipated to take approximately nine months scattered along the first year of this project.

At the inception of the project, the sourcing was identified as one of the major risks for the following reasons:

- This project is based on the construction of an experimental setup that requires a large number of custom parts from multiple suppliers.
- Suppliers related to EM power equipment typically have a long lead time (e.g., months) and frequently exceed them (e.g., months).
- Some parts are not readily available on the market, especially when purchased for R&D purposes; this is the case for the oxidized precursor fiber (OPF) feedstock material.

In addition to the risks related to the sourcing that are specific to the project, the circumstances related to COVID-19 are also relevant. Over this past year, it was observed that supplier lead times were impacted in a random manner. On average, the lead times increased.

13. The contract between the two main project participants (e.g., ORNL and 4XTechnologies, LLC) was signed on November 18, 2020.

Because of the aforementioned reasons, the sourcing was started as soon as possible, in parallel to the evaluation of the LTC equipment. It began as early as December 2020 with the following pieces of equipment:

- Reactivation of the computational electromagnetic modeling (CEM) software license to an upgraded version and its support contract.
- Specification of the power measurement system.
- Specification and shipping of conventional ancillary furnaces (e.g., subsystems of the ORNL pilot line) for refurbishing. These furnaces will be used later in this project for performance evaluation. This equipment will either be used to supply conventional LTC material, or to generate baselines with the same feedstock material for control purposes.
- The first weeks of this project were also dedicated to the critical task of the OPF acquisition. The leftover material inherited from the former LTC project was not sufficient to complete this HTC project. As expected, it took several attempts and almost a month to get a quote from a manufacturer.

All other subsystems were taken care of during the design phase when possible or once the design was completed.

The EM-based HTC setup requires several subsystems and laboratory space organization. Fortunately, some subsystems from the former LTC project could be repurposed to the current project. This is the case for the generator and its chilling system, the exhaust system, part of the control system and its sensors, and the power supply. Nonetheless, some of the existing subsystems still needed important modifications. This included the custom-made fiber handling system. Originally designed in 2018 to operate with two working zones, the fiber handling system was built to match the need of that time with one working zone only. This system had to be sent back to its manufacturer to implement a second working zone. As of September 30, 2021, the laboratory space has been set up in such a way that all equipment is appropriately installed and ready for operation.

In addition to the system using an EM power source, the HTC project includes some work involving conventional carbonization equipment, as observed in Figure II.2.4.1. The purpose of this conventional equipment is to produce some conventional LTC material as a feedstock material for the EM HTC furnace and HTC as a baseline. This task requires some conventional furnaces, similar to those used in industry. ORNL was already in possession of this type of equipment. However, due to aging, these two furnaces of interest were needed:

- A complete refurbishment of their insulation and their heating elements, as well as a renewal of most of its cables.
- Replacement of two controllers.
- Modification of the flanges and nitrogen purge implying the fabrication of a new subsystem.
- A relocation to 4XTechnologies.

The refurbishment and upgrades of the two furnaces were specified and the equipment was crated and then shipped to a furnace manufacturer. The HTC furnace control panel has been serviced and additional upgrades were done on-site. At their return, the two furnaces were installed at 4XTechnologies. This installation required a substantial effort in laboratory space preparation. On September 30, 2021, the system was tested and is ready for operation.



Figure II.2.4.1. A set of conventional LTC and HTC furnaces of the existing pilot line from ORNL. This set of furnaces was refurbished prior to its relocation at 4XTechnologies. Laboratory space has been altered and ancillary equipment installed to make this system operational. (NOTE: Portions of this photograph have been covered due to export control requirements.) Source: ORNL.

Experimental Work: Evaluation of Existing Equipment

The HTC project is a second/further step of the initial successful LTC project. Because the EM energy source is the same for both projects, it is possible to capitalize on the experience gained from the past. Hence, the first main task was to evaluate the existing setup inherited from the former LTC project and assess its best performance and limitation to decide the path to be followed based on the observations. An evaluation of CPEC-4 Configuration #2¹⁴ was completed with seven tows at extended residence times using all available power. As expected, measurements showed that the density increases with the residence time, as observed in Figure II.2.4.2. With a single-stage using EM power and an extended residence time, the produced fiber can reach the density of typical CF; the longest residence time provided a material with a density of 1.76 g/cc.¹⁵ It is expected that an even higher density could be achieved at the tradeoff for a longer residence time, which would not be acceptable at an industrial-scale.

On the other hand, when the residence time of the CPEC-4 Configuration #2 for the EM LTC only was reduced to equal the total residence time of the fully conventional carbonization process for LTC and HTC, it was found that the mechanical performances of the fiber are drastically unfavorable for the EM LTC process, as shown in Figure II.2.4.3. In this case, the only differences between the two processes are the power source and the temperature. Indeed, for equal residence times, the conventional process can produce CF surpassing 600 ksi, while the material produced by the single EM LTC process barely exceeded 200 ksi. The observation that the target density can be reached with the sole EM LTC process, whereas the fact that the mechanical properties cannot was a major indication considered for the design of the HTC furnace.

14. CPEC-4 Configuration #2 is the name of the last reactor built in the LTC project (FY 2015–FY 2020).

15. Most of commercial CF have a density in the 1.77 g/cc to 1.81 g/cc range, but some could be as low as 1.73 g/cc.

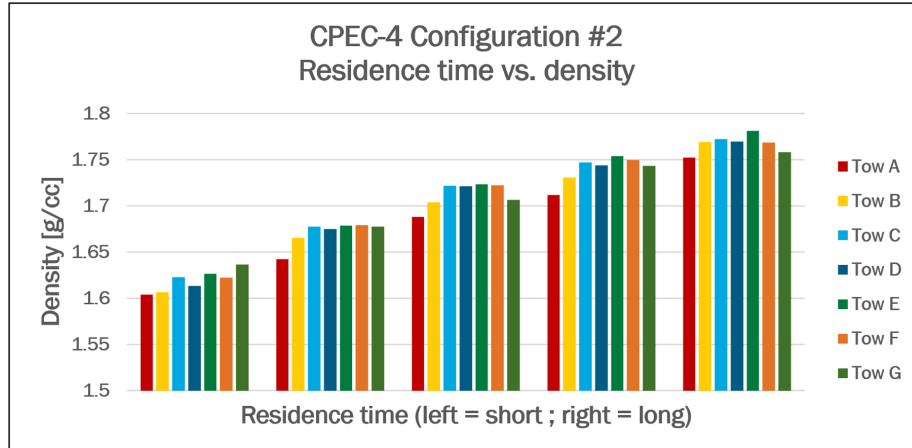


Figure II.2.4.2. Density measurements of seven tows processed with “CPEC-4 Configuration #2” with several residence times of process. The density of 1.76 g/cc can be achieved with this device with long residence times (economically unrealistic). Source: ORNL.

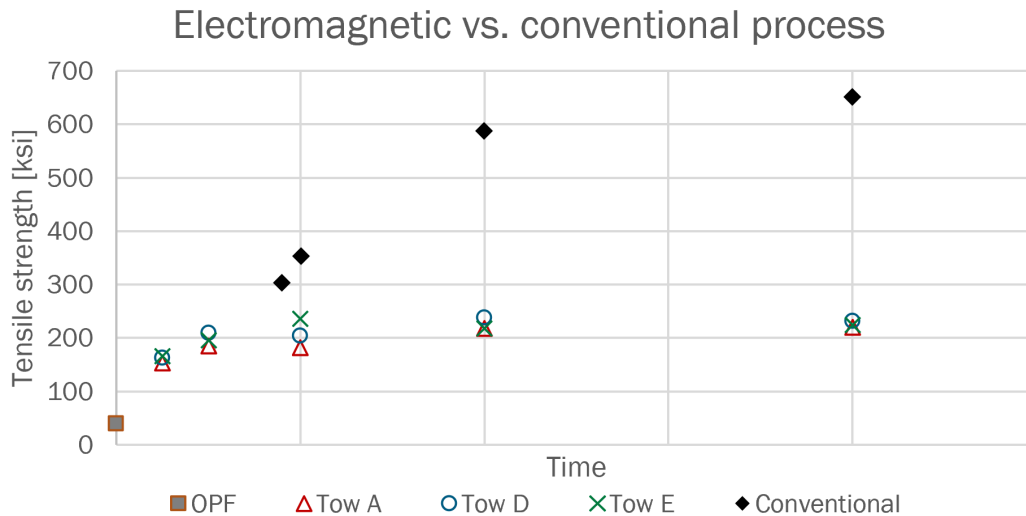


Figure II.2.4.3. Full carbonization test where the performance of the existing EM process operating at 100% of its available power is compared with a modified conventional process. During this test, the EM LTC setup was tested with seven tows (only mechanical properties of tows A, D, and E are reported), whereas the conventional process was limited to a single tow by design (series “Conventional”). Tension per tow in both systems is comparable. Several residence times were tested. The mechanical properties of the OPF feedstock material are indicated at time = 0. Over the time span investigated, the EM process underperforms the altered conventional process. At short residence times, due to technical reasons, no data is available with the conventional process. At long residence time, none of these two processes is economically viable. Source: ORNL.

Just like for the LTC project, modeling using a CEM is a critical phase in the development of the HTC technology. CST software was used for this task. The reactivation and the upgrade of the existing license and its support took several weeks. This activation procedure was done while the evaluation of the LTC equipment was performed. As of March 31, several geometrical configurations had already been explored with the CEM and the first interesting results were already available. Figure II.2.4.4 shows an example of reflection analysis, which results from the simulation of a parametric study of one model with the CEM. A low reflection is one of the criteria that must be satisfied for validation of a design.

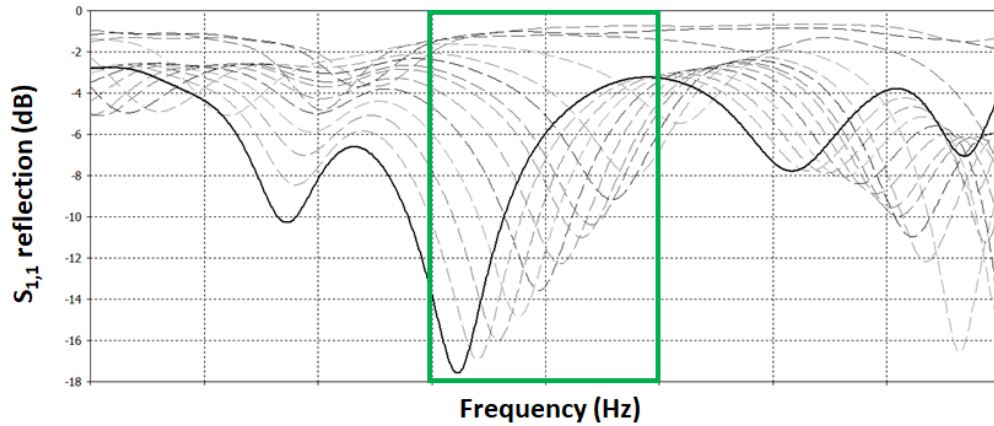


Figure II.2.4.4. Theoretical values of $S_{1,1}$, the coefficient of reflection. The green frame represents the band of operation of the generator system. The CEM modeling allows parametric studies. This figure shows a parametric study where a minimum of reflection goes lower while shifting to lower frequencies. In this configuration, $S_{1,1}$ can reach -17.5 dB while being relatively broad and remaining in the band of interest.
Source: ORNL.

The following months were dedicated to refining the model. Eventually, configurations showing acceptable reflection values, as shown in Figure II.2.4.5, and energy deposition patterns, as shown in Figure II.2.4.6, on the tow were found by the end of May 2021. At this date, it became possible to:

- Create a CAD model.¹⁶
- Order all material and custom parts for the construction of the reactor from vendors and machine shops.
- Design and build appropriate framing to hold the reactor.
- Finalize the laboratory spaces configuration, set all hardware to its final location, and perform electrical wiring.

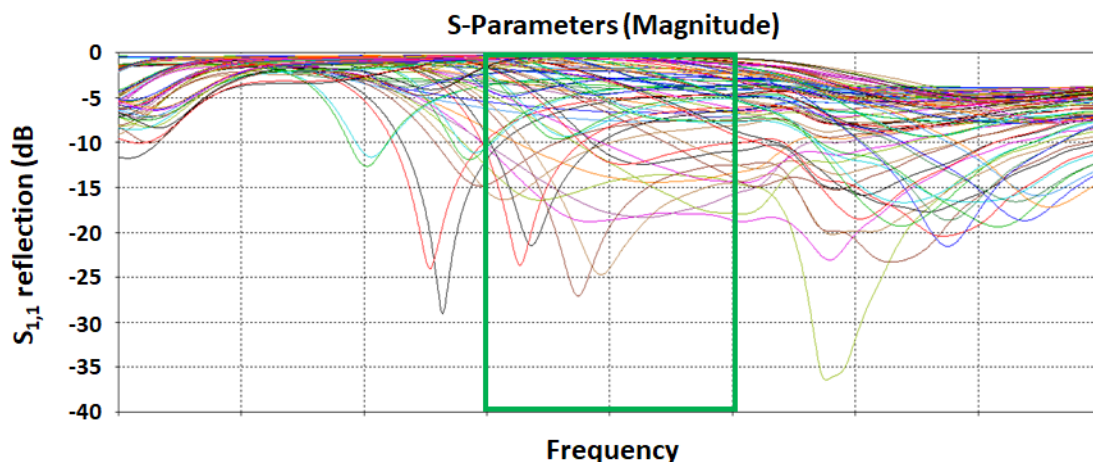


Figure II.2.4.5. Calculated S_{11} parameter values of the future reactor across a frequency spectrum at a point where the material becomes conductive. Each curve represents the calculation of the S_{11} parameter for a given position of the tuning system of the cavity. This figure shows that it will be still possible to find bands of low reflection in the band of operation (green frame) of the generator system until the end of the process.
Source: ORNL.

16. Due to export control and proprietary information, no CAD images can be displayed in this document.

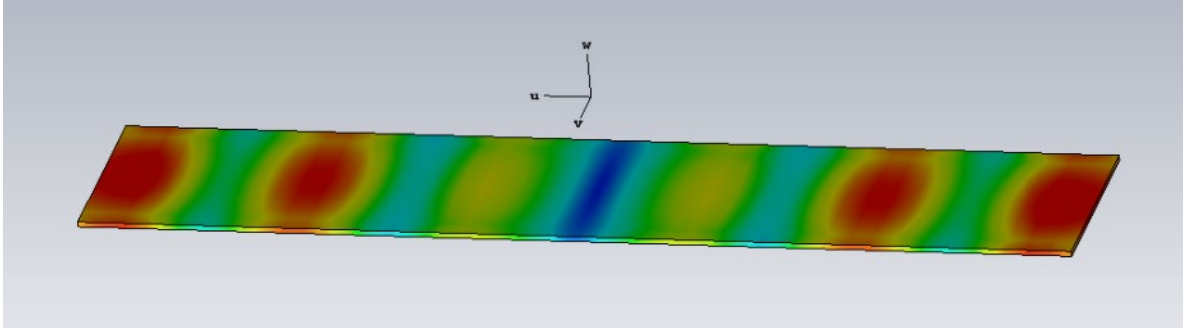


Figure II.2.4.6. Pattern prediction of energy deposition on a ribbon of 4 tows of 50k filaments each. Propagation of the tows is along u, width along v, and thickness along w axes. Image generated by CEM modeling. Source: ORNL.

Safety Management

The safety concerns are identical to those encountered with the former LTC project and were addressed at that time. Aside from regular electrical hazards inherent to any equipment powered with high-power and high voltage (480 VAC, 3 phases), the two additional concerns needed special care:

- **Toxic offgassing:** this hazard is well-known. The existing ventilation system needed an upgrade: a new hood, able to catch all the fumes, has been added. The existing control system already had gas detectors.
- **EM radiation:** the hazard related to the leakage of non-ionizing radiation is certainly the most sensitive one, because it is not perceptible. Such types of EM leakage were measured with the apparatus built for the former LTC project. Despite all the measurements at that time showing values under the limit of population exposure,¹⁷ it has been decided to improve the construction of the new reactor. On the other hand, an existing set of sensors connected to the control system inherited from the former LTC project was repurposed. These sensors have been appropriately relocated. And, to complete this safety system, the team also has an EM sniffer probe as well as a mobile spectrum analyzer.

The management of the hazards related to the current HTC project was substantially eased thanks to the legacy of the LTC project. Indeed, this effort was limited to modification and upgrades, allowing substantial resource savings.

Fiber Production Delayed

In July 2021, a critical supplier of the machined parts of the reactor experienced a significant delay of five weeks due to the COVID-19 pandemic. In August and September, the team was infected by COVID-19. Because of these late circumstances, the HTC project experienced an additional month and a half of delay so that, at the end of the FY, the delay accumulation reached approximately three months.

As of September 30, 2021, the construction phase and the commissioning were completed and the HTC system was declared ready for the experimental work, which will validate milestone M3¹⁸. However, the initial milestone calendar of the first FY involved the successful process of fiber by the end of the first FY, which was milestone M4.¹⁹ Consequently, the criteria of milestone M4 are not satisfied, and the delay of three months compared to the initial schedule set in the AOP FY 2021 imposed to revisit the milestone schedule in the AOP FY 2022. In this new schedule, the production of fiber (milestone M4) is set to begin December 30, 2021, and the three following milestones deadlines have been amended. Nonetheless, the overall timeline and resources of the HTC project remain unchanged, with a planned completion date of September 30, 2022, and the same budget.

17. Based on International Commission on Non-Ionizing Radiation Protection (ICNIRP) recommendation.

18. Milestone M3: Commissioning of HTC hardware and demonstration of stable/proper operation of all subcomponents for 15 min.

19. Milestone M4: Successfully carbonize material on a continuous basis in the HTC process with carbonized material achieving a minimum density of 1.6g/cc, a minimum mechanical properties of 300 ksi tensile strength, and 25 Msi modulus.

Conclusions

This year has been focused on the preparation of the experimental work. Indeed, the process of fiber at HTC requires the construction of a new setup. Hence, most of the effort was planned and has effectively been dedicated to the design, specification of parts, and assembly. At the end of FY 2021, the HTC setup is built and ready for commissioning.

The project experienced two major delays: the first, due to administrative procedures (contract settings between the parts) of more than a month and a half at its beginning. This initial delay was maintained even until a second contingency occurred by the end of July, when a supplier, then the team were infected by COVID-19. At the end of the FY, the project cumulated a delay of approximately three months. Because of these delays, the commissioning is completed, but no fiber has been processed, leaving the criteria of the fiber production milestones (milestone M4) unsatisfied. The milestone schedule for FY 2022 has since been re-evaluated accordingly.

Acknowledgments

This research was sponsored by DOE-EERE VTO, performed at ORNL, and managed by UT-Battelle, LLC, for DOE under AOP project contract DEAC05-00OR22725.

II.2.5 Continuous Fiber, Malleable Thermoset Composites with Sub-1-minute Dwell Times: Validation of Impact Performance and Evaluation of the Efficacy of the Compression-Forming Process (Malinda LLC)

Philip Taynton, Co-Principal Investigator

Mallinda LLC
7270 Gilpin Way Ste 180
Denver, CO, 80229
E-mail: philip@mallinda.com

Michael Larche, Co-Principal Investigator

Pacific Northwest National Laboratory
902 Battelle Blvd.
Richland, WA, 99354
E-mail: michael.larche@pnnl.gov

Bo Song, Co-Principal Investigator

Sandia National Laboratories
1515 Eubank Blvd SE
Albuquerque, NM, 87123
E-mail: bsong@sandia.gov

Bob Norris, Co-Principal Investigator

Oak Ridge National Laboratory
5200 1 Bethel Valley Rd
Oak Ridge, TN, 37831
E-mail: norrisrejr@ornl.gov

H. Felix Wu, DOE Technology Manager

U.S. Department of Energy
E-mail: felix.wu@ee.doe.gov

Start Date: October 1, 2018	End Date: September 30, 2021	
Project Funding (FY 2021): \$200,000	DOE share: \$100,000	Non-DOE share: \$100,000

Project Introduction

In spite of the significant impact that CFC materials have on lightweighting, performance, and efficiency in the aerospace industry, the adoption of these materials has been slow in high-volume industries such as automotive. Two major barriers to adoption are the cost and production cycle time. Current approaches to thermoset composite part production are dependent on in mold curing of thermosets, which are not optimal for high-volume, high-throughput production due to limitations and inefficiencies associated with the in mold cure itself. In addition, ancillary activities such as transport and storage of shelf-life-limited uncured, or B-staged prepreg materials typically necessitate refrigerated transport and storage, which significantly impacts the economic and energy costs associated with manufacturing. Furthermore, limited out-life means that trimmings cannot typically be used as they partially cure during initial production leading to high scrap rates (>20% is common). Finally, the need to cure in mold drives cycle times to multiple minutes in the best cases, and tens of minutes to hours in most cases.

Mallinda is developing polyimine malleable thermoset prepreg composite materials with excellent mechanical properties (e.g., 100 GPa tensile modulus, 2 GPa tensile strength, 2.4% elongation at break) and high operating temperatures ($T_g > 200^\circ\text{C}$). At scale, polyimine resins are commensurate in price with commodity epoxy resins. What distinguishes malleable thermoset prepreg from traditional thermoset prepreg materials is that they are fully cured during Mallinda's roll-to-roll production of prepreg laminate. This results in five key value-differentiating benefits. First, it simplifies manufacturing logistics by enabling ambient transportation and storage, and by significantly extending out-life and shelf life almost indefinitely. Second, elimination of autoclave curing reduces the economic and energy costs to the customer. Third, scrap rates can be reduced as malleable thermoset prepreg materials are directly reusable. Fourth, the manufacturing consolidation step can be roughly 10x faster than traditional thermosets, because the resin is already cured. Parts can be made via compression-forming by the application of heat and pressure to quickly vitrify and consolidate a multilayer part—easily leading to sub-3-minute cycle times. In fact, at the laboratory-scale, we have demonstrated a 20-second dwell time, with room for further optimization. Finally, the closed-loop cradle-to-cradle solution-based recyclability of malleable thermoset composites can also contribute significantly to the future of sustainable lightweight materials.

Objectives

The focus of this project was the development, optimization, and validation of malleable thermoset composite materials that exhibit manufacturing cycle times of 3 minutes or less, high-speed impact performance on par with incumbent technologies, and defect-free consolidation of 3D parts.

Approach

The national laboratory resources utilized for this project are highly specific to DOE, and are very difficult to replicate in the private sector:

1. *Compression-forming and composite manufacturing capabilities.*

The composite manufacturing and processing capabilities at ORNL are well connected to the automotive industry through the Institute for Advanced Composites Manufacturing Innovation—specifically the high-pressure molding capability, which is needed for this project. This unique combination of capabilities and expertise is difficult to find in a collaborative environment.

2. *High-speed impact material characterization.*

High-speed impact material characterization of the composite materials was conducted at Experimental Impact Mechanics Laboratory located at Sandia National Laboratories (SNL), which has unique experimental capabilities for material and structure characterization in combined mechanical (from low-, intermediate-, to high-speed impact) and thermal (-100 to $1,200^\circ\text{C}$) environments. The proposed test strain rates covered from ~ 50 to $1,000\text{ s}^{-1}$ (in compression) or 400 s^{-1} (in tension), which exactly fall into the region of automotive low-to-high-speed collision. Test temperatures ranging from -40 to 60°C were combined with impact mechanical testing to simulate automotive environmental temperatures. From this series of tests, the new composite materials were fully evaluated in terms of stress-strain response, ultimate strength, elongation at break, and failure/fracture mode at different impact loading speeds and modes, as well as different environmental temperatures. Effects of strain rate and temperature on the material performance was also determined for developing strain rate- and temperature-dependent material models for numerical simulation of automotive collision.

3. *Nondestructive defect analysis via scanning acoustic microscopy.*

The combination of measurement and analytics capabilities is unique to the national laboratories in the LightMAT Consortium. Commercial-off-the-shelf scanning acoustic microscopy measurement capabilities do not compare with the custom capabilities developed at PNNL. Additionally, the teaming of experts in nondestructive examination, simulation and modeling, materials science, and mathematics on prior research efforts produced proven algorithms and analysis approaches that are ready to be applied to new problem spaces. The capabilities, collection of experts, and experience of the national laboratories

in this project distinctly separate them from industrial counterparts. Having these resources co-located in one organization aided in meeting the project objectives.

Results

ORNL Results

Mallinda shipped in samples of their material and some industry standard glass mat thermoplastic (GMT) from Hanwha for comparison. ORNL set up and ran tests in the above configuration at velocities of nominally 125, 250, 500, and 1,000 cm/sec (e.g., 50, 100, 200, and 400 in/sec), with corresponding strain rates of approximately 1.0, 2.1, 4.2, and 8.3/sec. Data is plotted in Figure II.2.5.1 shows maximum recorded stress versus speed. Although plans were to run more samples to get more detailed test statistics, the test machine platen extensometer was destroyed during the first test at 400 in/sec. The project period of performance expired before the extensometer could be replaced and the entire planned test matrix completed. However, the collected data appears to show relatively small scatter and slight strain rate effects with mildly increasing stress as a function of speed for the GMT material tested both in machine direction and transverse to that direction. For the Mallinda unidirectional carbon coupons, the stress at failure was significantly higher as expected regardless of speed. However, the greater data scatter along with small number of samples prevents us from drawing firm conclusions as to failure stress as a function of speed, although it appears that there is not a significant speed effect.

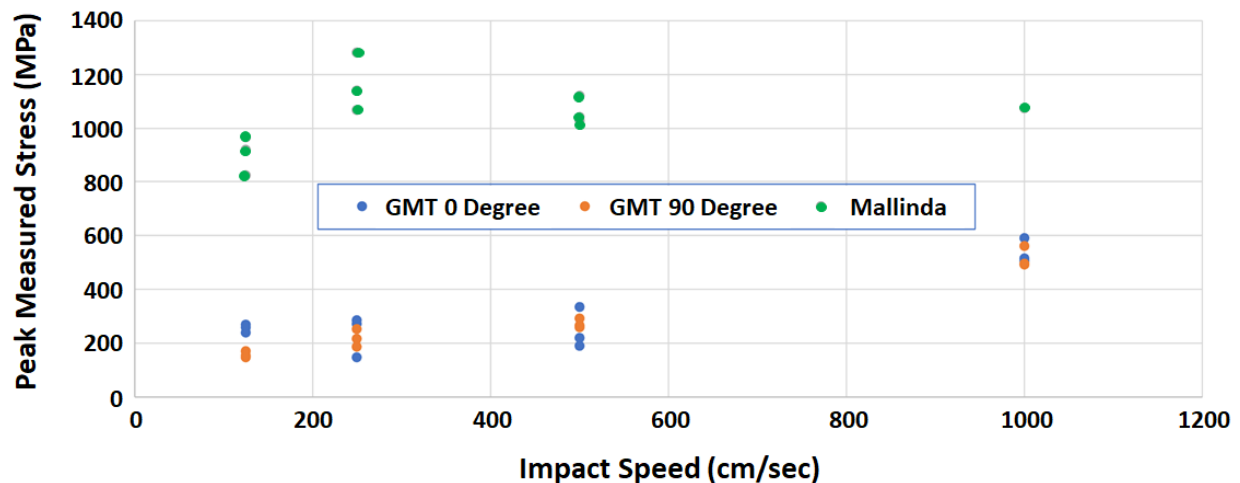


Figure II.2.5.1. Dynamic test data comparing Mallinda CF material with commercial GMT. Source: ORNL.

A secondary objective had been to also provide test data from high-speed tensile testing of the unidirectional carbon-fiber-reinforced Mallinda resin system. Since this system is unidirectionally reinforced, it was not expected that data would be strongly influenced by choice of resin system or by testing strain rate beyond factors such as fiber strength translation factor that can be obtained in static testing. However, it had been planned to obtain this data for the Mallinda system to provide input to future modeling. Based on earlier testing, it was estimated that a sample thickness of up to a standard ASTM coupon thickness of about 0.040 in could be adequately gripped and pulled to failure using the slack adapter in the High-Speed Coupon Tester configuration. However, tests were unsuccessful due to severe slippage in the grips and the funding authorization expired while the machine was down for repair of the machine Temposonics displacement measuring device.

SNL Results

The dynamic compressive characterization of the unidirectional CFC followed the same testing procedure as that for the woven composite. For the in-plane direction, the loading direction is parallel to the fiber direction (e.g., 0°). Figure II.2.5.2(a) shows the dynamic stress-strain curves along the in-plane, while Figure II.2.5.2(b) shows the dynamic stress-strain curves along the out-of-plane directions. The material along the in-plane

direction showed a higher modulus but lower failure strength and strain than those along the out-of-plane direction. The strain rate effect along both directions are insignificant. Under dynamic compression, the material along in-plane direction showed a splitting failure mode, whereas the material along the out-of-plane direction showed a shear failure mode.

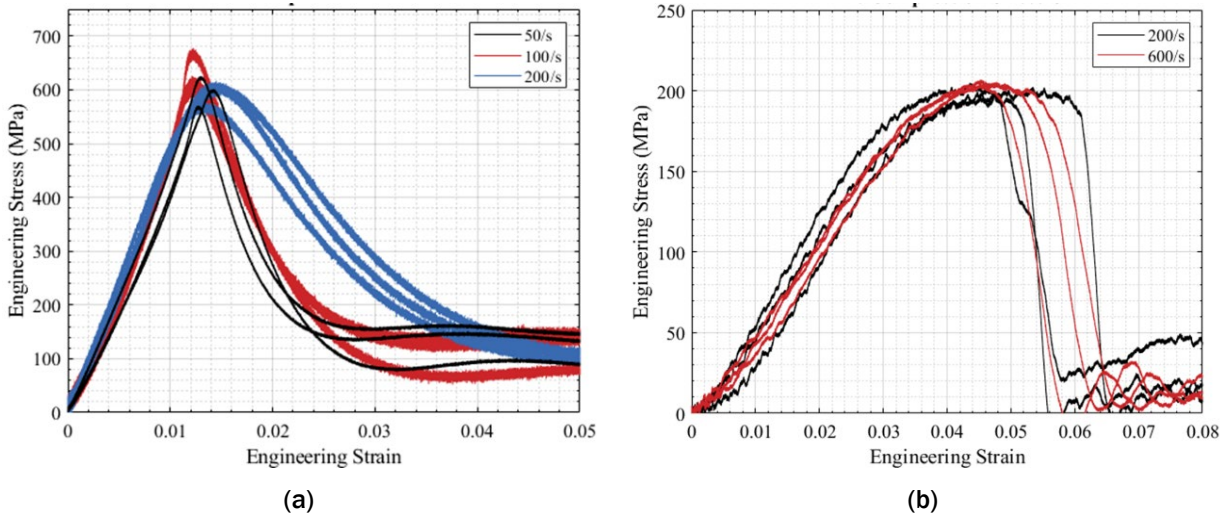


Figure II.2.5.2. Dynamic compressive stress-strain curves of unidirectional composite for (a) in-plane and (b) out-of-plane. Source: SNL.

Dynamic three-point bending tests of the unidirectional composite was conducted with the same Kolsky compression bar with the fixture. The length direction of the beam specimen aligns with the fiber direction. However, the flexural modulus was observed to be impact velocity (or strain rate) dependent, as shown in Figure II.2.5.3. Under dynamic three-point bending, the composite beam specimen was failed via delamination first and then tensile failure with increased load.

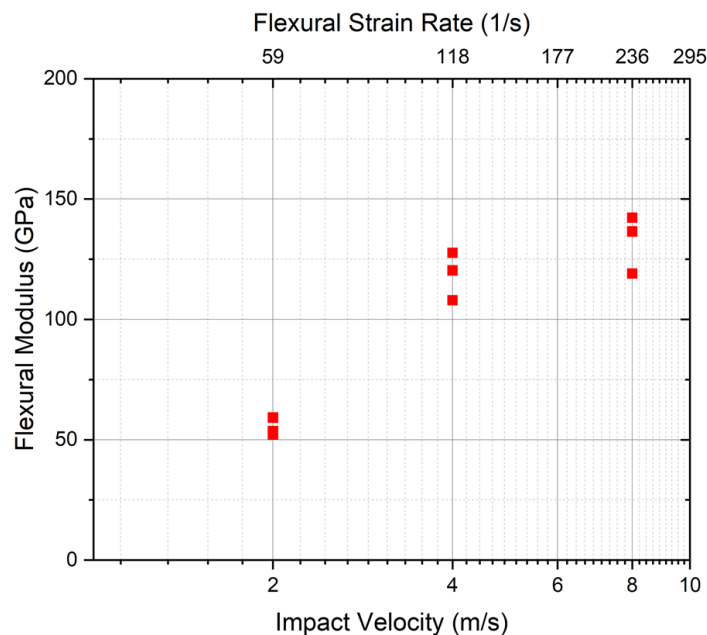


Figure II.2.5.3. Effect of impact velocity (strain rate) on flexural modulus. Source: SNL.

PNNL Results

The second set of panels was submitted to PNNL in May 2021. Table II.2.5.1 summarizes the processing parameters used for each panel. These panels were sealed by Mallinda on the top and bottom surfaces and on all edges. Rust-Oleum® Ultra Cover gloss clear paint was used to seal the top and bottom surfaces, and silicone was used to seal the edges.

Table II.2.5.1. Process Parameters for Panel Set #2

Panel	Ply Count	Cure Temp (°C)	Cure Time (min)	Consolidation Temp (°C)	Consolidation Time (sec)	Consolidation Pressure (psi)	Edge Condition
1	12	115, 150, 180	60, 40, 20	180	60	400	Trimmed and Sealed
2	12	115, 150, 180	60, 40, 20	200	300	200	Trimmed and Sealed
3	12	115, 150, 180	60, 40, 20	200	60	100	Trimmed and Sealed

Figure II.2.5.4 shows, from left to right, the resulting joint entropy images. Each is comprised of nine sub-images produced using the nine sub-scans acquired as described above. The overlap region has not been edited from the image to enable inspection for possible edge effects. Inclusion of the overlap regions is evident from the apparent double imaging of certain features such as the brass nut placed on top of the composite plate during scanning to produce a fiduciary marker to orient scan images relative to the physical plate. It is remarked that no edge effects are observable in the composite image.

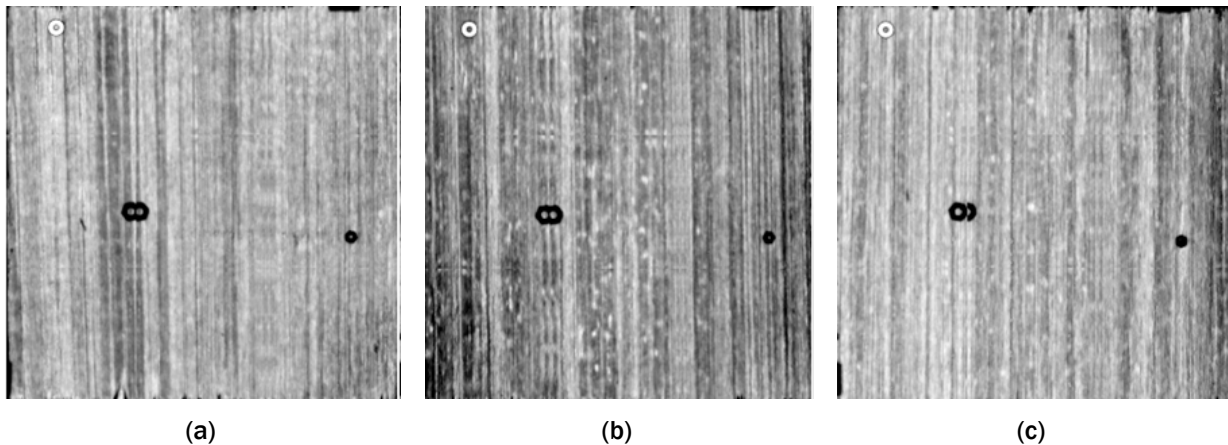


Figure II.2.5.4. Entropy images of all three specimens in this study. $H_{f,g}$ images for specimens (a) SB01, (b) SB02, and (c) SB03. Source: SNL.

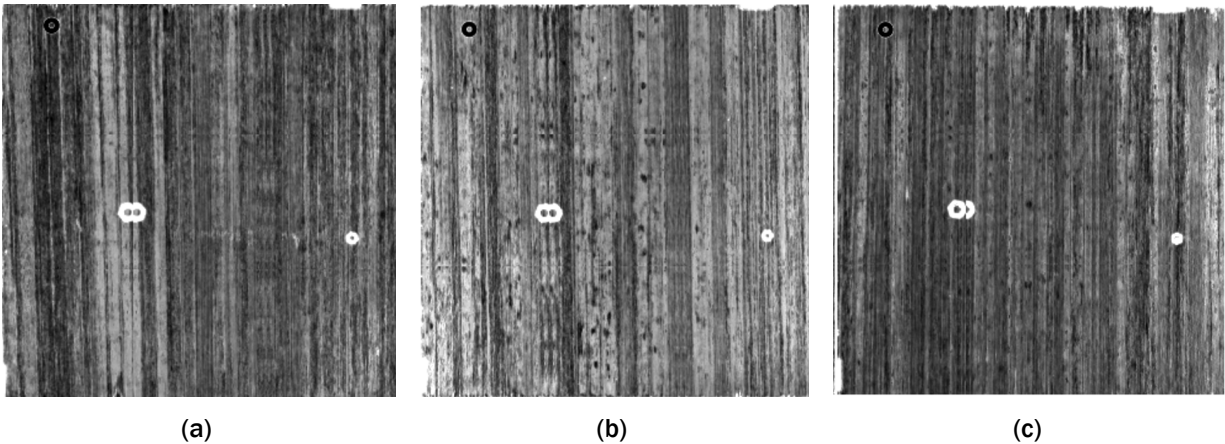


Figure II.2.5.5 shows the corresponding signal energy images. It is observed that the images are essentially the same up to inversion of the gray-scale lookup tables used to produce each image. Moreover, these images do not exhibit the usual cross-hatching pattern that has been observed in all previous studies of graphite/epoxy composites [1-5]. The reasons for this are unclear. However, inspection of the raw RF, resulting in exclusion of the front and backwall echoes indicates that the image structure is generated by the internal scattering architecture of the specimens. We remark also that this behavior differs drastically from specimen (SB0—not shown), which has the expected scattering behavior of a well-consolidated graphite/epoxy specimen, and which seems to have been fabricated using different techniques than those used to manufacture SB01–SB03.

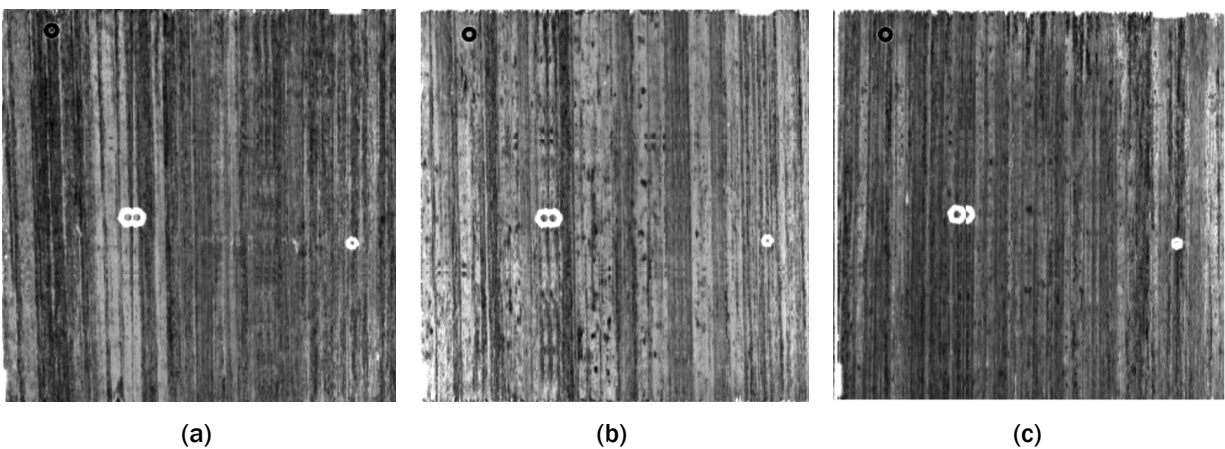


Figure II.2.5.5. A joint signal energy image of all three specimens in this study. $H_{f,g}$ images for specimens (a) SB01, (b) SB02, and (c) SB03. Source: ORNL.

Conclusions

This LightMAT-funded project concluded in FY 2021 and involved the first of its kind evaluations of: (1) the strain rate response of vitrimer matrix composite material; (2) the nondestructive and destructive analysis of the efficacy of welding via bond-exchange mechanism in vitrimer matrix composites; and (3) the mechanical performance compared to existing automotive composite structures. Four organizations successfully collaborated to complete the effort.

References

1. Hughes, M. S., J. N. Marsh, C. S. Hall, D. Savery, G. M. Lanza, and S. A. Wickline, 2005, "Characterization of digital waveforms using thermodynamic analogs: applications to detection of materials defects," *IEEE Trans. Ultrason. Ferroelectr. Freq. Control*, Vol. 52, No. 9, pp. 1555–1564.

2. Hughes, M. S., J. E. McCarthy, J. N. Marsh, and S. A. Wickline, 2013, “Joint entropy of continuously differentiable ultrasonic waveforms,” *J. Acoust. Soc. Am.*, Vol. 133, No. 1, pp. 283–300.
3. Hughes, M. S., J. E. McCarthy, P. J. Bruillard, J. N. Marsh, and S. A. Wickline, 2015, “Entropy vs. energy waveform processing: A comparison based on the heat equation,” *Entropy*, Vol. 17, No. 6, pp. 3518–3551.
4. Hughes, M. S., 1992, “A comparison of Shannon entropy versus signal energy for acoustic detection of artificially induced defects in Plexiglas,” *J. Acoust. Soc. Am.*, Vol. 91, No. 4, pp. 2272–2275.
5. Hughes, M. S., 1993, “Analysis of digitized waveforms using Shannon entropy,” *J. Acoust. Soc. Am.*, Vol. 93, No. 4, pp. 892–906.

Acknowledgments

Authors also acknowledge the critical contributions of Dr. L. Fifield of PNNL to the technical work, coordination, and aid with the overall management of this CRADA.

II.2.6 Ultra-Lightweight, Ductile Carbon Fiber-Reinforced Composites (Oak Ridge National Laboratory)

Vlastimil Kunc, Principal Investigator

Oak Ridge National Laboratory
1 Bethel Valley Road
Oak Ridge, TN 37831
E-mail: kuncv@ornl.gov

H. Felix Wu, DOE Technology Manager

U.S. Department of Energy
E-mail: felix.wu@ee.doe.gov

Start Date: October 1, 2018

End Date: December 31, 2023

Project Funding (FY 2021): \$500,000

DOE share: \$500,000

Non-DOE share: \$00

Project Introduction

CFRP composites are known for their high stiffness-to-weight ratio and hence are of great interest in diverse modern engineering fields. CFRP metamaterials with rationally designed architectures can be realized through AM technologies. Among many additive fabrication approaches, the light-based technique is most suitable for micro-architected metamaterials due to its high-resolution and robust mechanical properties of photopolymers. In the previous project phase, we developed a multi-material optical AM technique for multi-phase materials, which enabled the production of a group of CFRP microlattice that simultaneously exhibited high stiffness and high structural damping. Most high-precision AM techniques are limited by the tradeoff between printing area and resolution. The projection stereolithography process is capable of achieving unmatched feature sizes below 100 microns, but the overall dimension is limited to a few centimeters. This limits their application to produce critical components that require high surface finish, precision multiscale feature sizes over large volumes.

This year, we designed and constructed a novel 3D printer integrated with an optical scanning system and a material switching system to produce large-scale parts with micro-scale resolution. This technique offers possibilities for producing multi-phase architectures that can be applied to structural metamaterials, 3D battery architectures, and large antenna arrays that are not achievable in current AM techniques.

Objectives

This work aims to enable high-speed, large-area, and high-resolution printing of CFRP composites. The following milestones were proposed and accomplished:

- Milestone 1. Demonstrate parallel optics system for large-area ultraviolet (UV) curing.
- Milestone 2. 3D printing of high-strength CFRP closed-cell foams and mechanical property measurement.
- Milestone 3. Integrate multi-extrusion nozzles for multi-material extrusion and switching.
- Milestone 4. Demonstrate high-resolution CFRP lattice materials with size spans from 10 cm to 25 cm.

Go/no-go milestone decision point criteria. Properties of the microlattice must be density of $<500 \text{ kg/m}^3$, high specific strength of $>1 \text{ kPa}/(\text{kg/m}^3)$ with the size of $>10 \text{ cm}$ span.

Approach

This section documents the materials and methods used herein:

1. *Material preparation.*

A UV curable CFRP composite, made of a UV-sensitive resin reinforced with short carbon fibers (~70 μm), was developed for the fabrication. A high-energy ball mill was used to mix the monomer (Rigid 4000, Formlabs), photo-initiator (Irg 819, Sigma-Aldrich), and carbon fiber (PC 100, E&L Enterprises).

2. *Mechanical properties measurement.*

Structural properties were investigated by performing quasi-static compression/tensile tests using an INSTRON 5944 test frame. A strain rate of $10^{-3}/\text{s}$ was adopted to ensure that all tests were performed in a quasi-static regime (to suppress the mass inertia effect). From the measured stress-strain hysteresis loop, we computed the effective modulus from the slope of a loading curve in the linear region.

3. *Simulation methods.*

All simulations were performed under the quasi-static condition (the kinetic energy of the whole system is assumed to be less than 5% of the internal energy in the same system) with mass scaling (scale elements that have a smaller stable time increment to the target time increment 0.005 s at the frequency of every increment) using explicit dynamic FE analyses in the commercial software Dassault Systemes Abaqus 2018. We investigated the mechanical response of the bi-material cubic+octet isotropic plate-lattices under compression by applying quasi-periodic boundary conditions via smooth step amplitude in the time duration of 100 s to simulate the response of an infinite cellular material. To obtain the effective modulus E , peak strength σ_{peak} , and energy absorption U of the plate-lattices, we first extracted the effective stress-strain (σ - ε) curve such that $\sigma = F/L^2$ and $\varepsilon = \delta/L$, where F denotes reaction force due to the applied compressive displacement δ . Then, the effective modulus E was obtained by computing a slope at an initial linear region, the peak strength σ_{peak} was taken at its maximum stress, and U was computed by calculating the area under the curve.

Results

1. *Demonstrate parallel optics system for large-area UV curing.*

A large-area high-resolution UV curing printer with an integrated infinity-corrected projection system was designed and constructed, as shown in Figure II.2.6.1 (Milestone 1). Figure II.2.6.1(a) shows the basic working principle of the proposed infinity-corrected design. Here, light rays emitted from the digital micro-mirror device (DMD) chip pass through a collimating lens, which do not form an image and enter as an infinity parallel beam in the focusing lens, forming an intermediate image. The intermediate image is then relayed and formed a projection image with the prescribed resolution through a projection lens. In contrast to a conventional projection lens in digital light processing printing technology where the focused image will be out of focus as soon as the lens moves, the infinite corrected projection system allows the translation of a projected image over a large distance while keeping the focus and intensity—the image size stays constant even if the distance between the collimating lens and the focusing lens is changed. Thus, the projection images can be translated via a high-speed motion axis with high-resolution, as shown in Figure II.2.6.1(b). A light engine equipped with a DMD chip of 1024 x 768 pixels was used as a demonstration. Figure II.2.6.1(c) shows the schematic of the printer and the optical design: the light engine (where the DMD chip is mounted) is fixed on the ground, while the scanning optics move along the x-y directions, sequentially projecting images onto extended areas of a large format resin vat, extending the build size to 50 cm and above (depending on the stroke of the motion axis that is being employed here). The scanning mirrors are mounted onto two high-speed motion stages to provide a fast-scanning process.

Another advantage of the infinity-corrected design is that the projection area/resolution can be adjusted easily by simply tuning the position of the projection lens. The overall magnification ratio can be adjusted as: $M = f_f/f_c \cdot f_p/(d_o - f_p)$, where f_c , f_f , and f_p are optics' effective focal length, and d_o is the distance

between the projection lens to the intermediate image. To print a structure, a 3D model is created and sliced into layers. Next, every single layer is separated into several sub-images, which are sequentially projected onto the vat when the stage moves along x-y directions. The projected UV images initiate the polymerization of the resin, converting it to a solid single layer part. Figure II.2.6.1(d) shows the current optical system setup.

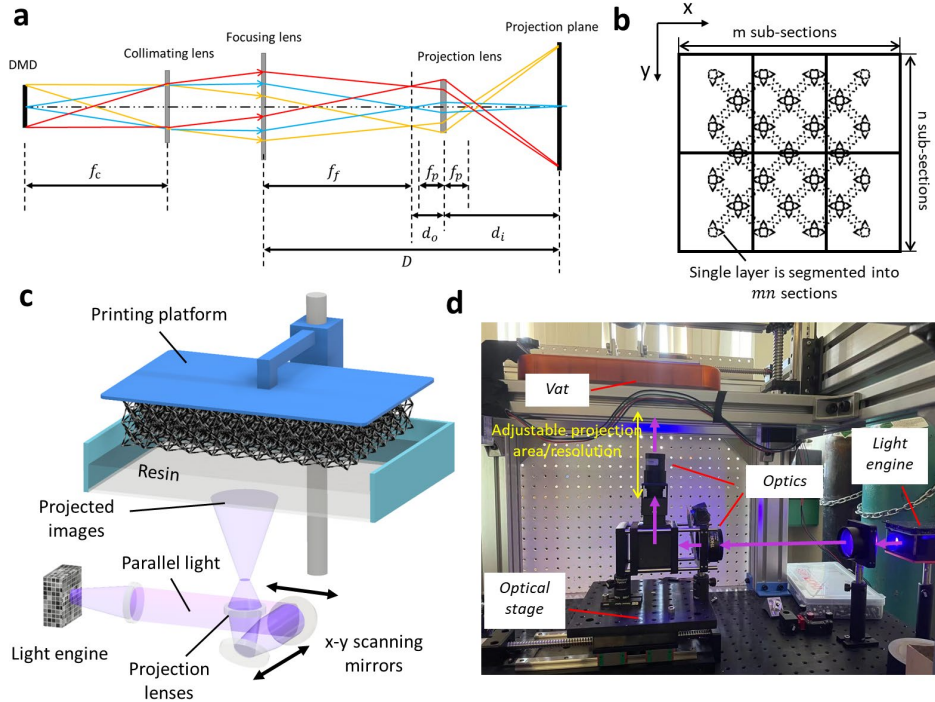


Figure II.2.6.1. (a) Optical path diagram of the infinity-corrected projection system. (b) Segmentation of a single projection image. (c) A schematic of the large-area high-resolution projection stereolithography system. (d) The current optical system with adjustable projection area/resolution. Source: ORNL.

2. 3D printing of high-strength CFRP closed-cell foams and mechanical property measurement.

To highlight the capability of the developed technique, we fabricated plate-lattice structures and measured their mechanical properties. As shown in Figure II.2.6.2(a), a group of such structures having a range of relative densities is fabricated. Unidirectional compression tests were performed to capture the stress-strain curves, as shown in Figure II.2.6.2(b) of the samples, and their stiffness was measured accordingly (Milestone 2). The normalized stiffness of such plate-lattices dramatically outperformed open cellular lattice at a given relative density, as observed in Figure II.2.6.2(c).

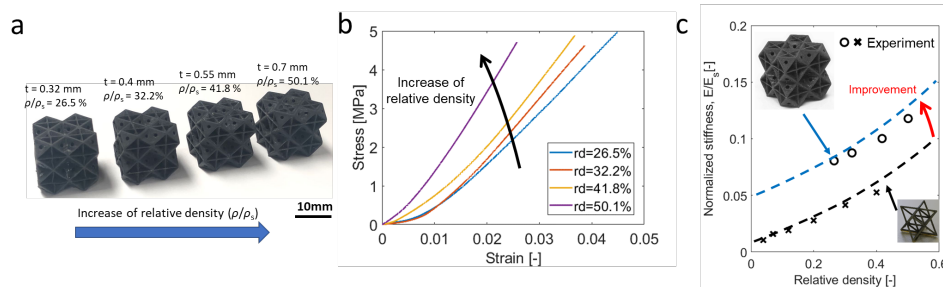


Figure II.2.6.2. (a) Plate-lattices having a range of relative densities. (b) A stress-strain curve of the plate-lattices with different relative densities. (c) A comparison of the stiffness between plate-lattices and truss lattices. Source: ORNL.

Single material lattices, in general, cannot simultaneously achieve high stiffness, strength, and energy absorption because even the most mechanically efficient topological designs (stretching dominated with highest possible Young's modulus and strength [1]) would fail prematurely at small strain through fractures or post-yield softening. Here, we designed a novel isotropic cubic+octet plate-lattice by applying the two material phases (CFRP and soft phases) directly into the lattice topology via a sandwich plate configuration [2] (CFRP-soft-CFRP plies). This improves the energy absorption and maintains the stiffness and strength with almost no change in its mass, as observed in Figure II.2.6.3(a). Figure II.2.6.3(b) shows the CFRP structure before injecting the soft material and after injecting the soft material. Such a configuration allows both stiff and soft material phases to exploit the stretching dominated lattice topology while potentially enhancing the energy absorption from the unique synergy of the constituent materials. We evaluated the energy absorption (e.g., the area under the stress-strain curve) of the designed bi-material isotropic cubic+octet plate-lattice as a function of the volume fraction of the soft phase via FE simulations. Figure II.2.6.3(c) shows the local maxima of the absorbed energy at specific volume fractions of the soft phase for different relative densities. As shown in Figure II.2.6.3(d), we found that the maximum absorbed energy obtained from all of the modeled relative densities (indicated by the round black dots in the figure) was improved by approximately a factor of 2.5, as compared to the plate-lattices entirely made of the CFRP phase (indicated as black triangles in the figure). Our bi-material plate-lattices show favorable strength-energy absorption characteristics against recently reported two-phase CF octet truss (an advantage in $(U/E_s)/\bar{\rho}$ of 190% and in $(\sigma_{\text{peak}}/\sigma_{\text{ys}})/\bar{\rho}$ of 140%), making them an excellent candidate for a stiff, lightweight material for impact isolation and energy dissipation.

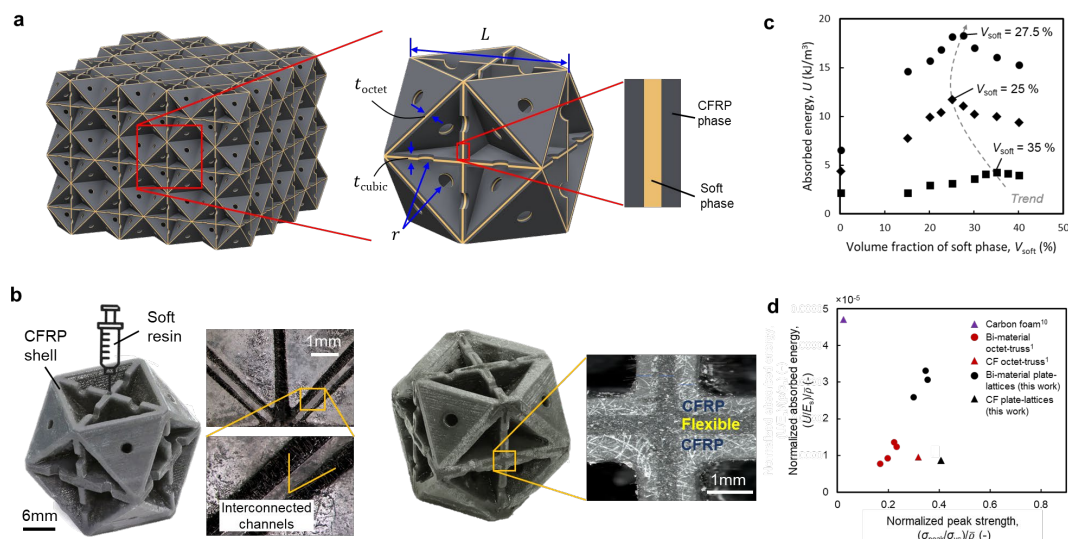


Figure II.2.6.3. Design, fabrication, and evaluation of bi-material isotropic cubic+octet plate-lattice. (a) Each plate is designed as a sandwich plate (CFRP-soft-CFRP). **(b)** Post thermal curing fused the soft-stiff phase. The unit cell has a relative density of 30% after injection. **(c)** The absorbed energy, U , under compression of bi-material isotropic cubic+octet plate-lattices having different volume fractions of the soft phase for several relative densities. **(d)** Assessment of energy absorption performance against previously reported materials. Source: ORNL.

3. Integrate multi-extrusion nozzles for multi-material extrusion and switching.

The potentials of these multi-material AM technologies allow for extending the design space beyond the complex geometries of a single material. However, most of the reported techniques are limited to a small printing area (<40 mm) due to the tradeoff between resolution and printing size. In this work, based on the system proposed above, we developed a material exchanging system for large-scale multi-material printing for CFRP composite with high-resolution and multi-material compositions.

As shown in Figure II.2.6.4(a), custom multi-material channels were designed to enable the switch of resins and ethanol (which cleans the previous material). Peristaltic pumps, pipes, and nozzles were used to enable the extrusion of the multiple resins. If another material needs to be printed in the next layer during the printing process, the locking gate lifts, allowing the resin to flow into the recycling vat. To avoid contamination between resins, ethanol was used to clean uncured resins off solidified parts and the printing vat, followed by air-blowing to dry the ethanol residual. The process was repeated layer-by-layer, combining multiple materials into a 3D structure. Figure II.2.6.4(b) shows the current setup, where the black vat in the middle is specially designed to facilitate resin switching. *Figure II.2.6.4(d) demonstrates an as-fabricated large multifunctional material (polyethylene glycol diacrylate [PEGDA], charged resin) sample as a transmit array (3D antenna) after being selectively deposited with a copper layer (Milestone 3).*

While peristaltic pumps can provide sufficient pressure for resins with high fluidity, clogging/insufficient pressure could arise when processing highly viscous resins mixed with CFs. A commercial ceramic 3D printing kit (StoneFlower), as observed in Figure II.2.6.4(c), was modified for use in the project. The kit has been assembled and will be connected to extrusion nozzles. Nozzles with different designed geometries were printed and tested for the study and optimization of fiber alignment. Preliminary results show promising results. This work is ongoing and will be completed based on the project schedule.

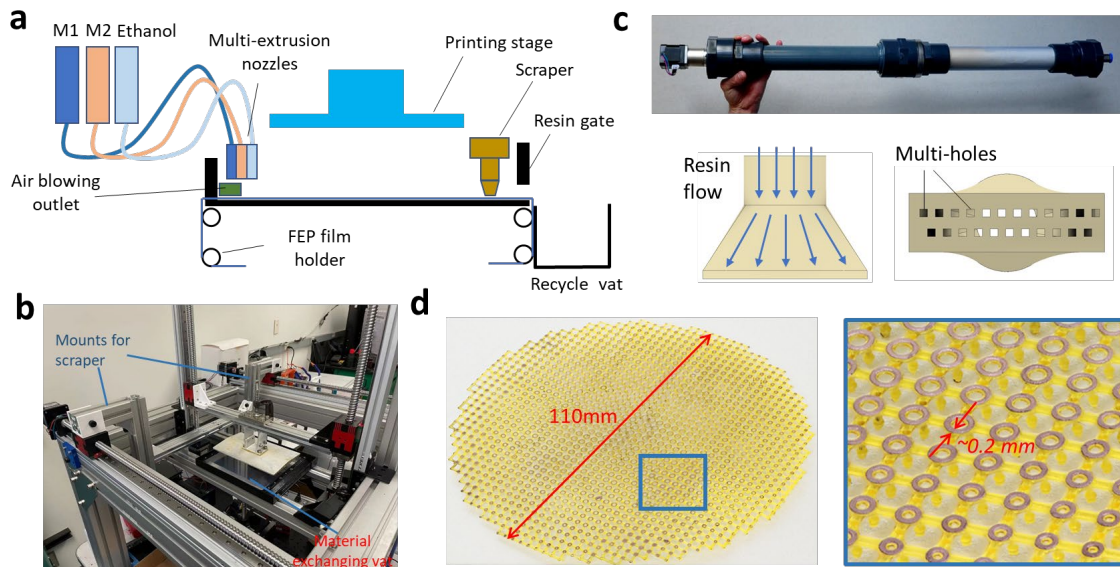


Figure II.2.6.4. (a) Schematic of the multi-material exchanging system, cleaning system, and resin recycling system. (b) The overall system setup. (c) Ram extruder and custom extrusion nozzles with multiple outlets. (d) A large antenna array made of two different resins and copper was deposited onto the charged resin.

Source: ORNL.

4. Demonstrate high-resolution CFRP lattice materials with size spans from 10 cm to 25 cm.

To 3D print objects using the developed system, first, a 3D model is created and sliced into layers. Next, every layer is split into a number of sub-images, which are then sequentially projected onto the vat when the stage moves along the x-y directions. Polymerization initiates at the light-exposed areas, converting it into a solid single layer part and sticking it to the build platform. The build platform elevates to replenish resin and repeat the cycle. *With the developed printer, we managed to print lattices with CFRP with a size of 10 cm to 25 cm, as shown in Figure II.2.6.5 (Milestone 4).* Figure II.2.6.5(a) features a group of hierarchical CFRP lattice material, which is comprised of the octet of octahedra trusses. The overall size of the sample is as large as 18 cm, and the radius of the struts is as thin as 150 μm . Such a group of material is nearly isotropic and have high structural connectivity within stretch-dominated architectures.

Figure II.2.6.5(b) demonstrates the 3D printing of a group of plate-lattice materials using CFRP, which features a more efficient architecture with higher energy absorption capability than truss lattices. The as-fabricated plate-lattice has a length of ~10 cm.

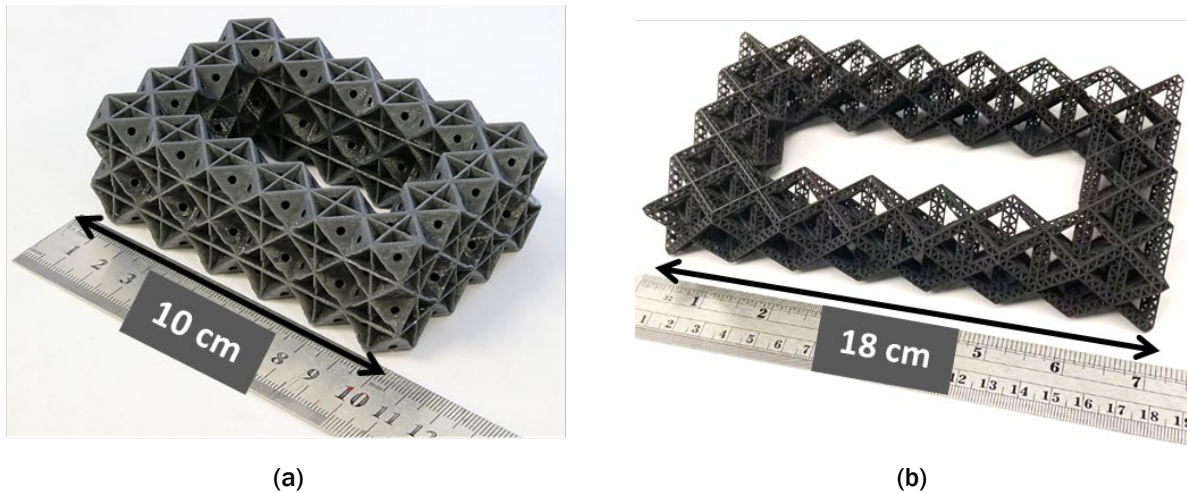


Figure II.2.6.5. (a) Hierarchical CFRP truss-lattice materials ($l = 18$ cm, strut radius of $150 \mu\text{m}$).
(b) CFRP plate-lattice materials ($l = 10$ cm). Source: ORNL.

5. *Properties of the microlattice should have the density of $< 500 \text{ kg/m}^3$, a high specific strength of $> 1 \text{ kPa}/(\text{kg/m}^3)$, with the size of $> 10 \text{ cm}$ span.*

A cubic+octet plate-lattice design in this work has a higher stiffness per unit weight than truss-based lattice, resulting in better mechanical performance. As shown in Figure II.2.6.6(a), the $4 \times 4 \times 2$ lattice weighs only 20 g, while it can withstand the weight of a typical adult, which is $\sim 4,000$ times its weight. Through calculation, the specific strength of such a lattice is larger than $1.2 \text{ kPa}/(\text{kg/m}^3)$, with a density of only 185 kg/m^3 .

Numerical simulations were performed to verify the experimentally measured results. Compressive stress-strain curves of the CFRP isotropic plate-lattices, obtained from the simulations, for relative densities of 10%, 20%, and 30% are shown in Figure II.2.6.6(b). Then, we captured the ultimate strength of the stress-strain curve until fracture. It is found that the ultimate strength increases with the increase of relative density while the fracture strain remains the same. In Figure II.2.6.6(c), we normalize the ultimate strength with the lattice density, and *the results show that such a group of plate-lattice have a specific strength of $\sim 6.2 \text{ kPa}/(\text{kg/m}^3)$ with a density of less than 400 kg/m^3 (meeting the go/no-go)*, making them an excellent candidate for a strong, lightweight material for impact isolation and energy dissipation.

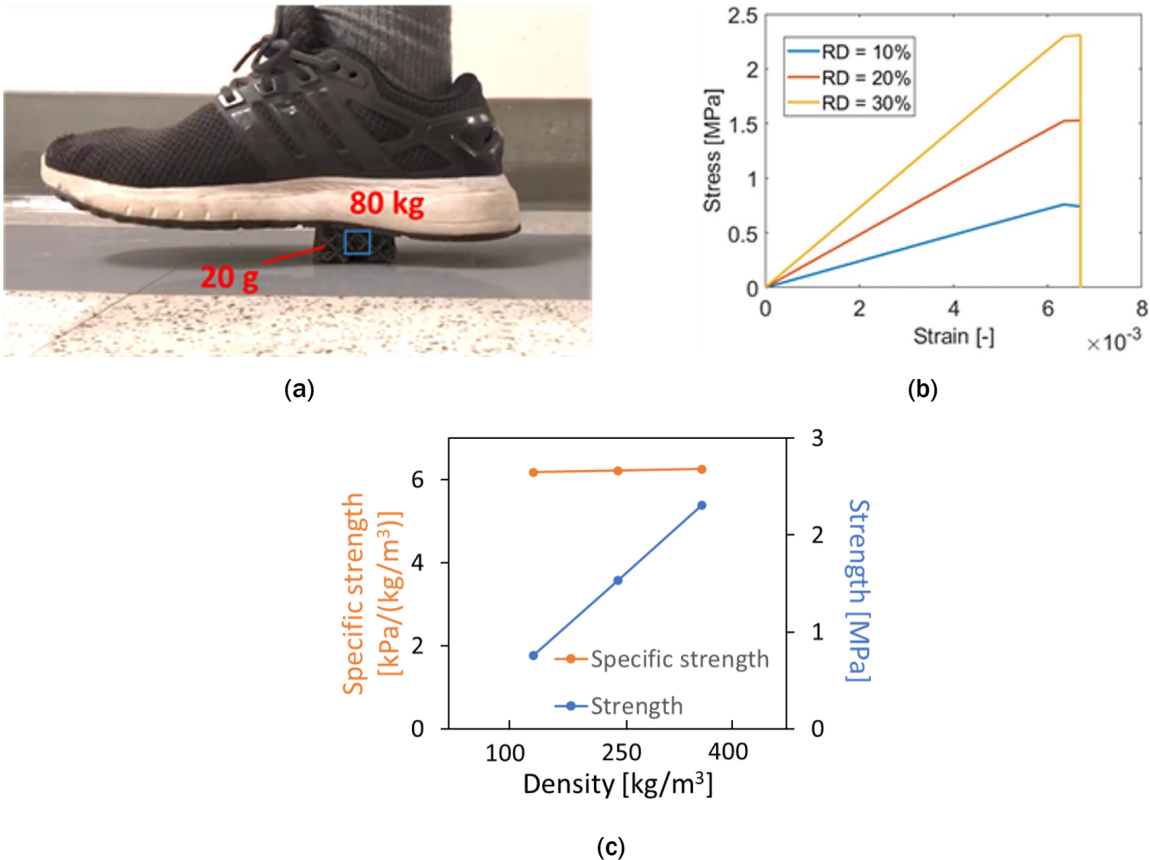


Figure II.2.6.6. (a) Demonstration of the high-strength of the cubic+octet plate-lattice ($4 \times 4 \times 2$). The lattice weighs only 20 g, and it can withstand the weight of an adult. The schematic below shows the unit cell design of such a group of plate-lattice. (b) Simulated compressive stress-strain curves of the cubic+octet plate-lattices for different relative densities, $\bar{\rho}=10\%$, 20%, and 30%. (c) UCS and specific strength of the plate-lattices (The data points correspond to the simulated cases with different relative densities). Source: ORNL.

Conclusions

In this work, we presented a high-speed, large-area, and high-resolution projection stereolithography printer integrated with moving optics and a material switching system to print large-scale structural materials and devices. The developed optical scanning strategy is the key to enlarging a printing area while maintaining a high-resolution of $\sim 50 \mu\text{m}$. Using such a system, we demonstrated the printing of large lattice material made of regular polymer and CFRP with a size up to 50 cm. Furthermore, we integrated a material exchanging system into the printer and demonstrated the printing of a multi-material antenna array larger than 10 cm. Moreover, we demonstrated a group plate-lattices structure that can be additively manufactured by our system. Through experiment and simulation, these plate-lattices show favorable strength characteristics that meet the requirement of the milestone.

Key Publications

- Xu, Z., C. Ha, R. Kadam, J. Jindahl, S. Kim, H. Wu, V. Kunc, and X. Zheng, 2021, "Additive manufacturing of two-phase lightweight, stiff and high damping carbon fiber-reinforced polymer microlattices," *Addit. Manuf.*, Vol. 32, No. 1, Art. 101106.
- Hsieh, M. T., C. S. Ha, Z. Xi, S. Kim, H. F. Wu, V. Kunc, and X. Zheng, 2021, "Stiff and strong, lightweight bi-material sandwich plate-lattices with enhanced energy absorption," *J. Mater. Res.*, Vol. 36, pp. 3628–3641.

References

1. Deshpande, V. S., M. F. Ashby, and N. A. Fleck, 2001, “Foam topology: Bending versus stretching dominated architectures,” *Acta Mater.*, Vol. 49, No. 6, pp. 1035–1040.
2. Salari-Sharif, L., L. Valdevit, and T. A. Schaedler, 2014, “Energy dissipation mechanisms in hollow metallic microlattices,” *J. Mater. Res.*, Vol. 29, No. 16, pp. 1755–1770.

Acknowledgments

This project was performed in collaboration with Prof. X. Zheng’s group at the University of California—Los Angeles (UCLA).

II.2.7 Carbon Fiber Technology Facility (Oak Ridge National Laboratory)

Merlin Theodore, Co-Principal Investigator

Oak Ridge National Laboratory
1 Bethel Valley Road
Oak Ridge, TN 37831
E-mail: theodore@ornl.gov

Amit Naskar, Co-Principal Investigator

Oak Ridge National Laboratory
1 Bethel Valley Road
Oak Ridge, TN 37831
E-mail: naskarak@ornl.gov

Rich Davies, Co-Principal Investigator

Oak Ridge National Laboratory
1 Bethel Valley Road
Oak Ridge, TN 37831
E-mail: daviesrw@ornl.gov

H. Felix Wu, DOE Technology Manager

U.S. Department of Energy
E-mail: felix.wu@ee.doe.gov

Start Date: March 1, 2011	End Date: Project continuation evaluated annually
Project Funding (FY 2021): \$1,000,000	DOE share: \$1,000,000 Non-DOE share: \$0

Project Introduction

In March 2009, DOE-EERE issued a competitive call for proposals to construct and operate a highly flexible, highly instrumented, Carbon Fiber Technology Facility (CFTF) for demonstrating and evaluating low-cost carbon fiber (LCCF) and new low-cost manufacturing technologies at a pilot-scale. Construction began in March 2011 and the CFTF was commissioned for operations in March 2013.

The CFTF is a national treasure and the only open-access state-of-the art CF manufacturing research facility in the U.S. The CFTF offers a unique, highly flexible, highly instrumented CF and melt spinning precursor processing line with a capacity of 25 and 65 tons per year, respectively. The facility is used for demonstrating advanced technology scale-up and for producing market development volumes of prototypical advanced fibers, for example, CFs. The CFTF's unique capabilities, including the flexibility to process a range of feedstocks and product forms, are unmatched anywhere in the world. The CFTF fills a critical need for supporting industrial competitiveness in the manufacture of advanced fibers in this nation by serving as a national resource assisting industry in overcoming the barriers associated with cost and technology scaling of low-cost advanced fibers and its composites including product and market development. The CFTF allows new advanced fiber related technologies to commercialize effectively by bridging research and development to demonstration, deployment, and validation of such technologies using low-cost precursors and energy-efficient advanced conversion processes at an industrial relevant scale. The CFTF also serves as a conduit for testing and validating new technologies in digital and/or smart manufacturing.

ORNL operates the CFTF and works with leading companies to overcome technology barriers to reduce the cost and energy consumption of advanced fiber manufacturing to reveal the strength and energy saving benefits of these new materials. CF is one example of an advanced fiber. Due to its exceptional strength and low density, CF is an enabling material for many applications, such as fuel-efficient automobiles, large wind-turbine blades, and lightweight compressed hydrogen or natural gas tanks. DOE is interested in increasing the availability and affordability of CF and CF composites to increase energy efficiency and product performance. The major obstacles to CF and other advanced fibers are the availability in high-volume industries at a high cost relative to materials currently used, limited availability or a lack of domestic sources, and the lack of compatible materials and processes for manufacturing its composites. In order for advanced fibers to achieve widespread use in vehicle and industrial markets, the cost of these advanced fibers production must be reduced by 30% to 50%.

CF is a strong, stiff, and lightweight material used as a reinforcement for polymer-based composites to enable improved product performance in many applications. However, CF's use in cost-sensitive, high-volume industrial applications is limited because of today's relatively high cost of production. Half of the cost in manufacturing lies in the precursor material, as seen in Figure II.2.7.1. Current methods for manufacturing CF and CF-reinforced composite structures are slow and energy-intensive. New, innovative manufacturing processes for low-cost precursor development and conversion technologies hold the key to reducing CF cost for energy applications.

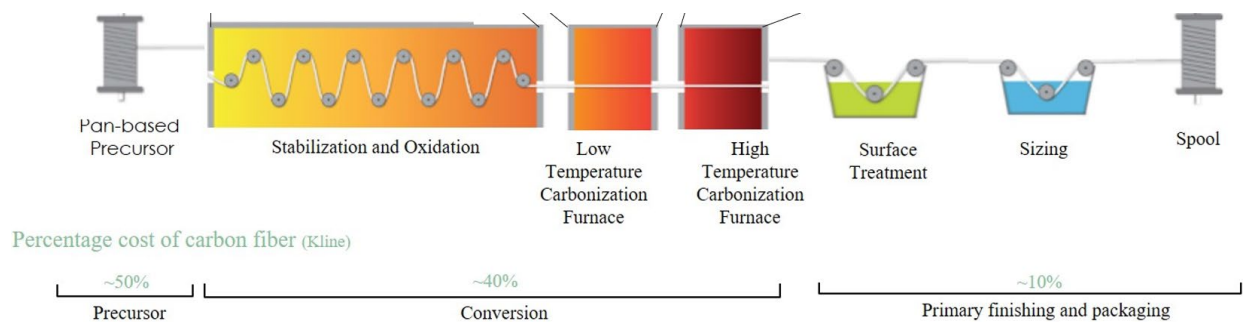


Figure II.2.7.1. CF manufacturing process and cost analysis. Source: ORNL.

The high cost of commercially available CF is due largely to the high cost of specialty precursor materials and the energy- and capital-intensive nature of the conversion process. ORNL was the successful proposer of a DOE-EERE issued a competitive solicitation in 2009 for advanced research, development, and demonstration of CF production and build a semi-production-scale facility with capability to handle various feedstock materials, to integrate advanced energy-efficient conversion technologies, and to produce enough finished fiber to supply end-users for R&D of improved composite manufacturing methods. The proposed capability was focused on four critical areas: (1) the development of low-cost feedstocks (precursors); (2) the development of more affordable feedstock conversion methods; (3) the integration of developed technologies into an industry-scalable demonstration facility to reduce risk of investment; and (4) the development of CF composite material and processing technologies. The project objective will be addressed through the third task in the CFTF annual operating plan.

The objective of this project is to accomplish the safe and reliable operation of CFTF and to further DOE objectives for large-scale LCCF commercialization. ORNL's Advanced Fibers Manufacturing Group functioning at CFTF supports EERE's efforts toward transitioning technologies to industry by focusing on developing scale-up science and technologies for advanced fiber manufacturing and associated fabrication of functional components for high-energy volume energy applications at the CFTF.

In FY 2021, ORNL continued its R&D efforts to further reduce the cost of CF using other alternative precursors or advanced processes. Table II.2.7.1 depicts a list of alternative precursors and advanced processes, along with their advantage and disadvantage for use and the estimated reduction in cost and embodied energy.

Table II.2.7.1. Alternative Precursor and Advanced Conversion Processing Estimated Reduced Cost and Embodied Energy

Precursor/Process	Advantage	Disadvantage	Conversion Yield	Cost	Energy
Standard polyacrylonitrile (PAN) precursor	Strength, elongation, knowledge base, and fiber architecture.	Feedstock price, volatility, capital cost, energy, yield, and processing.	50%	0%	0%
Bio-PAN	Renewable; pricing decoupled from oil.	Knowledge base and scale.	TBD	TBD	TBD
Polyolefin/polyamide precursor	Feedstock price and stability, spinning, yield, and fiber architecture.	Conversion process and equipment, knowledge base, and capital cost.	65% to 75%	-20%	-50%
Mesophase pitch-based precursor	Feedstock price and stability, spinning, yield, knowledge base, properties develop w/o stretching, moderate capital. Pitch-based precursor offers the highest potential cost and energy reduction potential.	Elongation, compression strength, and fiber strength.	80% to 85%	-70%	-70%

Preliminary estimations depicted in Figure II.2.7.2 show a significant reduction potential in coal pitch CF embodied manufacturing from a lower raw material, embodied energy, and higher process yield. Additionally, pitch CF potentially offers the lowest cost/stiffness among CF; hence, a compelling value in cost-sensitive, stiffness-driven, and high-volume applications. ORNL will initiate R&D efforts in other advanced fibers in the near future.

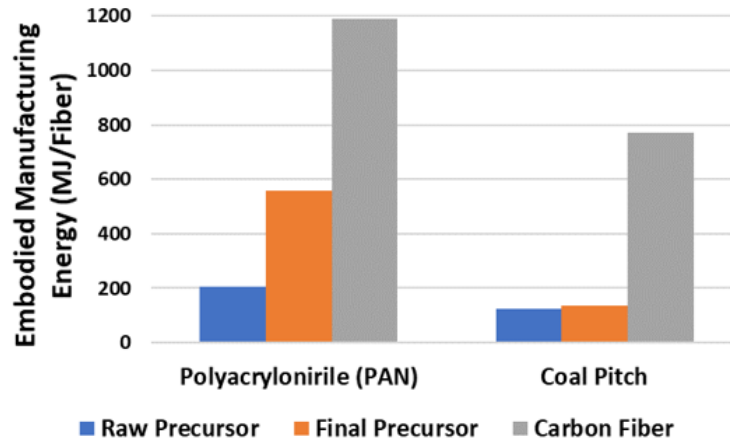


Figure II.2.7.2. Embodied energy for PAN and coal pitch precursor and CF manufacturing. Source: ORNL.

Objectives

The project's objective is to develop low-cost fibers from alternative precursors and accomplish the safe and reliable research and development projects to further DOE objectives for large-scale commercialization of LCCFs. The tasks covered under these agreements are co-funded by the VTO and the Advanced Manufacturing Office (AMO) in support of the efforts by DOE-EERE in transitioning technologies to industry. The CFTF serves as a national resource to assist industry in overcoming the barriers of CF cost, technology scaling, and product and market development. The CFTF provides tours so that industry and others can see the technology and the process science being developed to produce LCCF with industry-appropriate mechanical properties from alternative precursor materials.

Approach

The ORNL team recently modified the strategic plan that resulted in a diverse and comprehensive multiscale integrated plan delivering impactful R&D efforts from basic-to-applied technical readiness level research encompassing "conception to commercialization" or "precursor to part."

Currently, no commercial manufacturer exists for LCCF, so the CFTF plans to identify cost-effective alternative sources of precursors based on availability, C yield, cost, and spinnability. Once the chemistry of the precursor is developed and baseline properties of 250 Ksi tensile strength and 25 Msi modulus are met, a sufficient amount of material will be produced for scaling up to the next level. Results generated from the bench scale studies are then used to develop a baseline condition or starting point for scaling to the next scale. The CFTF staff will then develop process conditions for converting the precursor material into LCCF that will exceed baseline properties. The fibers' performance will be characterized and evaluated in a variety of resins systems at a coupon level utilizing various composting methods. Sufficient amounts of CF will be produced for deployment to industry to evaluate, thereby showcasing the quality of LCCF on a multitude of end-user platforms. This work is intended to produce industry demand for the technology. The CFTF staff continues to hold discussions with industrial partners that are interested in scaling the processes being developed at CFTF. The financial investment for industry to scale-up the technology is significant and, thus, not a subject for quick decision.

The CFTF's integrated CF and its composites research portfolio, within the intricate ORNL ecosystem, shown in Figure II.2.7.3, was developed to maximize the impact in the U.S. economy. ORNL is the only National Laboratory that can deliver a multiscale strategic approach from precursor to part with technology readiness levels (TRLs) ranging from TRL 1 through TRL 7 at handoff to collaborating partners. The vision was developed to drive innovation in R&D from precursor to part for structural and non-structural applications across various technology areas, especially automotive.

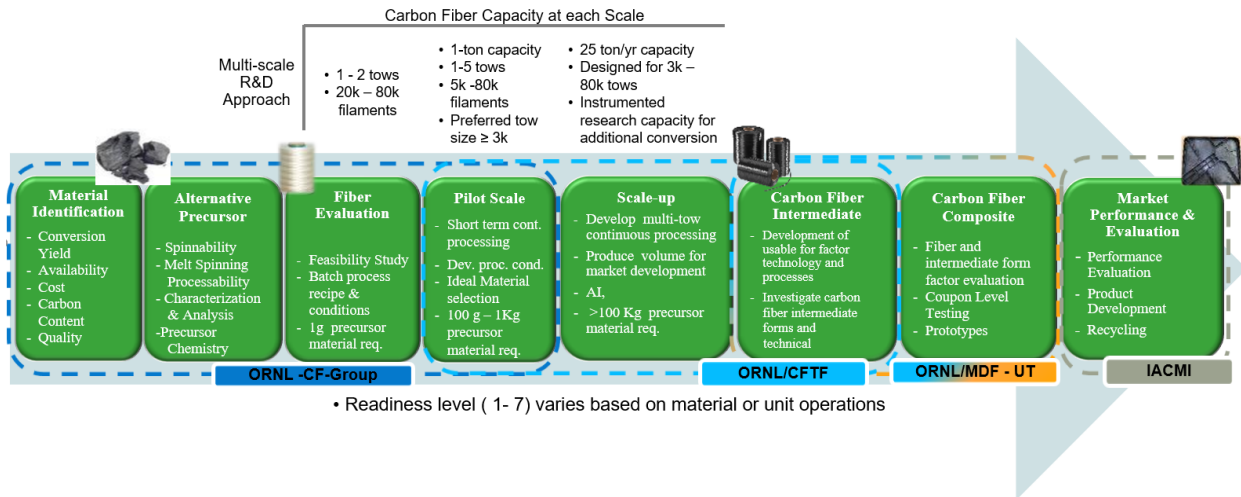


Figure II.2.7.3. Multiscale R&D approach. Source: ORNL.

The CFTF’s mission is to transition technology to industry for scaling, but many technical challenges remain that must be overcome to further reduce the risk for industry to implement the technology. These technical challenges are being addressed in collaboration with industry to reduce uncertainties implementation risks associated with scaling technologies. These challenges include handling the various form factors of fibers processed from the alternative precursors and developing appropriate sizing for LCCFs for specific composite applications. The CFTF continues to be a training ground for any technical staff involved in CF production. Key strategies implemented by the project in FY 2021 supported by VTO were labeled under Task 3 titled “Investigate potential alternative CF precursors” of the CFTF annual operating plan with defined milestones. The milestones and their status at the end of FY 2021, as shown in Table II.2.7.2, were to investigate potential alternative CF precursors. This will allow for the selection of a candidate precursor not previously studied and an investigation of supplier-to-supplier variation effects in precursor chemistry, physical characteristics on product variability, and performance.

Table II.2.7.2. Task 3 Milestones, Task Descriptions, and Status

Milestone	Title or Short Description	Original Plan	Revised Plan	Percent Complete
3.1	Feasibility study of melt blowing ACP mesophase pitch at scale. Characterization and analysis of batch process samples report.	12/31/20	12/31/21	0%; CRADA executed 15 September 2021.
3.2	Develop and demonstrate spinnability of Polyamide precursor at scale. A pilot production demonstration of 12,000 filament tows will be at ORNL CFTF.	03/31/21	06/30/21	100%
3.3	Develop and demonstrate spinnability of mesophase pitch material from Kopper’s Industry partners at scale. Produce CF from 5 kg to 8 kg batch of PP mesophase exhibiting >25 Msi modulus and >250 ksi on multi-filament melt spinning equipment (Q3).	06/30/21	Completed at bench scale	100%
3.4	Develop and demonstrate spinnability of bio-PAN precursor and identify formulations of pre-ceramic polymers that provide >40% silicon carbide yield at 1,000 °C. Spin and oxidize bio-PAN tow for carbonization at CFTF exhibiting >25 Msi modulus, >250 ksi strength and >1% elongation. Provide technical report on formulations of pre-ceramic polymers.	09/31/21		100%

Results

Visitors/Tours

In FY 2021, ORNL operated under a limited work scenario to ensure the safety of the employees and reduce the risks associated with the COVID-19 pandemic. The laboratory operated with a reduced staff level and visitation to the laboratory was restricted to a certain level, throughout the end of the FY. A total of 165 visitors from 14 organizations toured the CFTF in FY 2021.

Alternative Precursor and Carbon Fiber Development

Petroleum Isotropic Pitch Carbon Fiber

The team successfully scaled and developed the process conditions for melt blowing a petroleum-based isotropic pitch material into precursor material which was then processed into pitch CF at CFTF. This research effort was in lieu of receipt and scaling of industry partners pitch material to develop a baseline criteria for processing pitch material at scale. Images of the fiber being processed through the oxidation and carbonization stages are depicted in Figure II.2.7.4.



Figure II.2.7.4. Pitch-based precursor processed through the CFTF CF line. Source: ORNL.

Petroleum Mesophase Pitch Carbon Fiber

Meanwhile at the bench scale, pitch material from other sources is being researched, developed and evaluated for scalability to CFTF. For example, several variations of a Koppers petroleum-based mesophase pitch material was evaluated for spinnability and conversion into precursor and CF at ORNL.

The material was prepared into appropriately sized chunks for feeding through the extruder and continuously melt spinning above the softening point. The green fiber was taken up onto rolls at various draw down ratios to produce contrasting diameters shown in Figure II.2.7.5. The fibers were removed from the rolls and sectioned into lengths suitable for the conversion equipment. Following oxidation, the fiber bundles were carbonized and graphitized. Carbonized filaments exhibit strengths and modulus above the DOE target values, as observed in Table II.2.7.3, while graphitization nearly doubled the modulus to 47.00 ± 2.87 Msi but reduced peak strength slightly to 227.3 ± 2 ksi. These results clearly show the capability of the petroleum mesophases in this study to reach the project property target. Additional work is needed to improve the processing to make higher performance fibers and control the development of nanotexture in the CF to tune the property sets toward applications of interest.

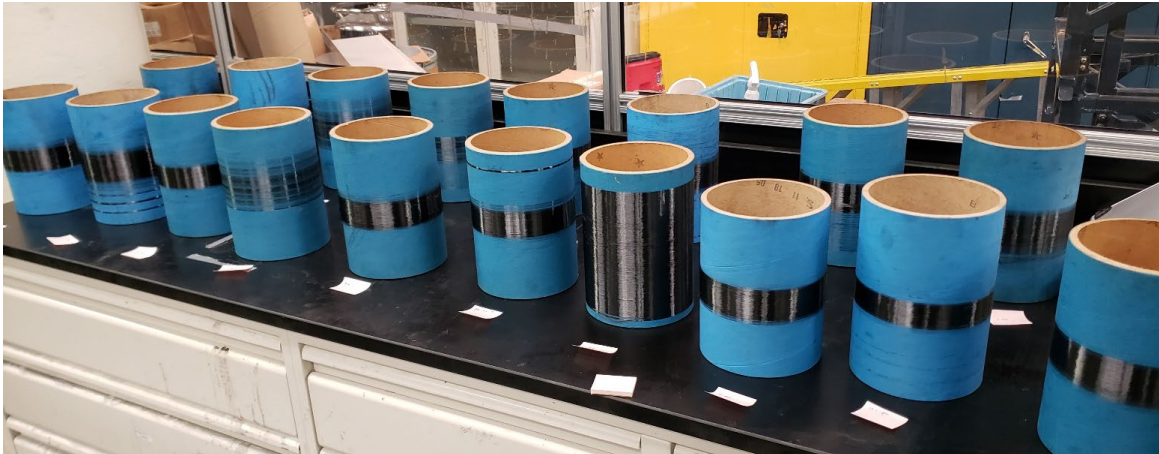


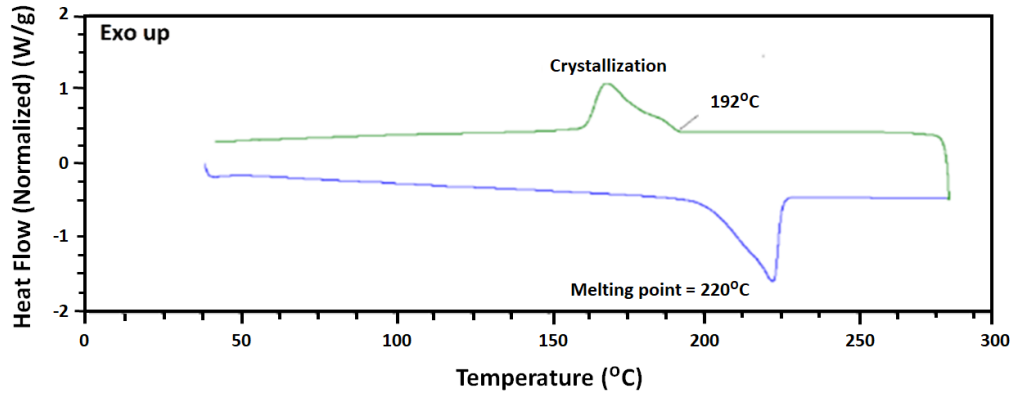
Figure II.2.7.5. Melt-spun petroleum mesophase pitch fibers of different diameters. Source: ORNL.

Table II.2.7.3. Petroleum Mesophase Property

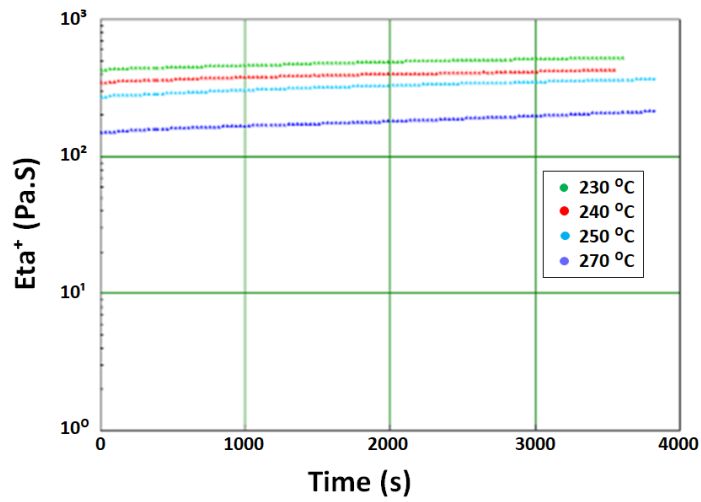
Sample	Break Stress (ksi)	Diameter (μm)	Modulus [in. Modulus] (Mpsi)	Strain (%)
2824	258.84 (39.63)	23.35 (1.27)	25.28 (3.93)	1.21 (0.14)

Polyamide 6 Fiber

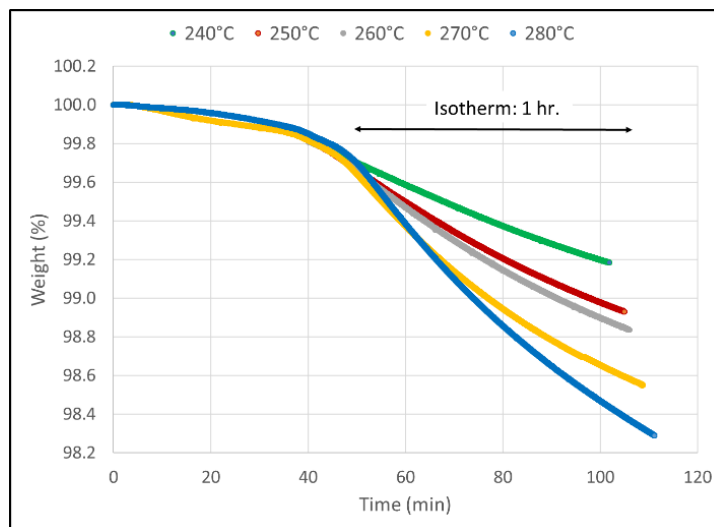
This milestone was completed. In lieu of future projects and/or projected scaling of new alternative precursor material, the team successfully scaled-up and developed a baseline for melt spinning Polyamide 6 material into precursor fibers from the bench scale to CFTF scale. The raw material was characterized using DSC, TGA, and a rotational shear rheometer to determine the melting point, the thermal stability of the polymer at melting processing temperatures, the minimal thermal degradation of the polymer occurs at the processing temperatures, and the appropriate melt spinning conditions and polymer viscosity for the recommended processing temperatures, respectively. Images of the analysis of each technique are shown in Figure II.2.7.6(a)–(c).



(a)



(b)



(c)

Figure II.2.7.6. (a) DSC analysis of the commercial Polyamide 6 sample. (b) Isotherms in nitrogen at different temperatures (TGA). (c) Rotational shear rheology temperature sweeps of Polyamide 6 material. Source: ORNL.

The first melt spinning attempt involved a laboratory mixing extruder from Dynisco. This one filament bench scale extruder can process limited amount of material to get an initial understanding of the precursor behavior. The successful trial was processed at 250°C and two spools were fabricated over a period of 10 mins. Another melt spinning trial was then carried out with the laboratory multi-filament extruder at the aforementioned temperatures. The trial was very stable, the polymer flow was consistent, and Polyamide 6 fibers could be spun for 1 hour. Several conditions regarding the speed of the rotating drum and of the metering pump were tested to obtain different values for the fiber diameter. The bench scale data was utilized to develop the spinning condition at CFTF scale. The CFTF team successfully scaled the Polyamide 6 fiber to produce ~15 spools over a couple hours equaling >12,000 filaments. The process and precursor fibers produced at the different scale are shown in Figure II.2.7.7.

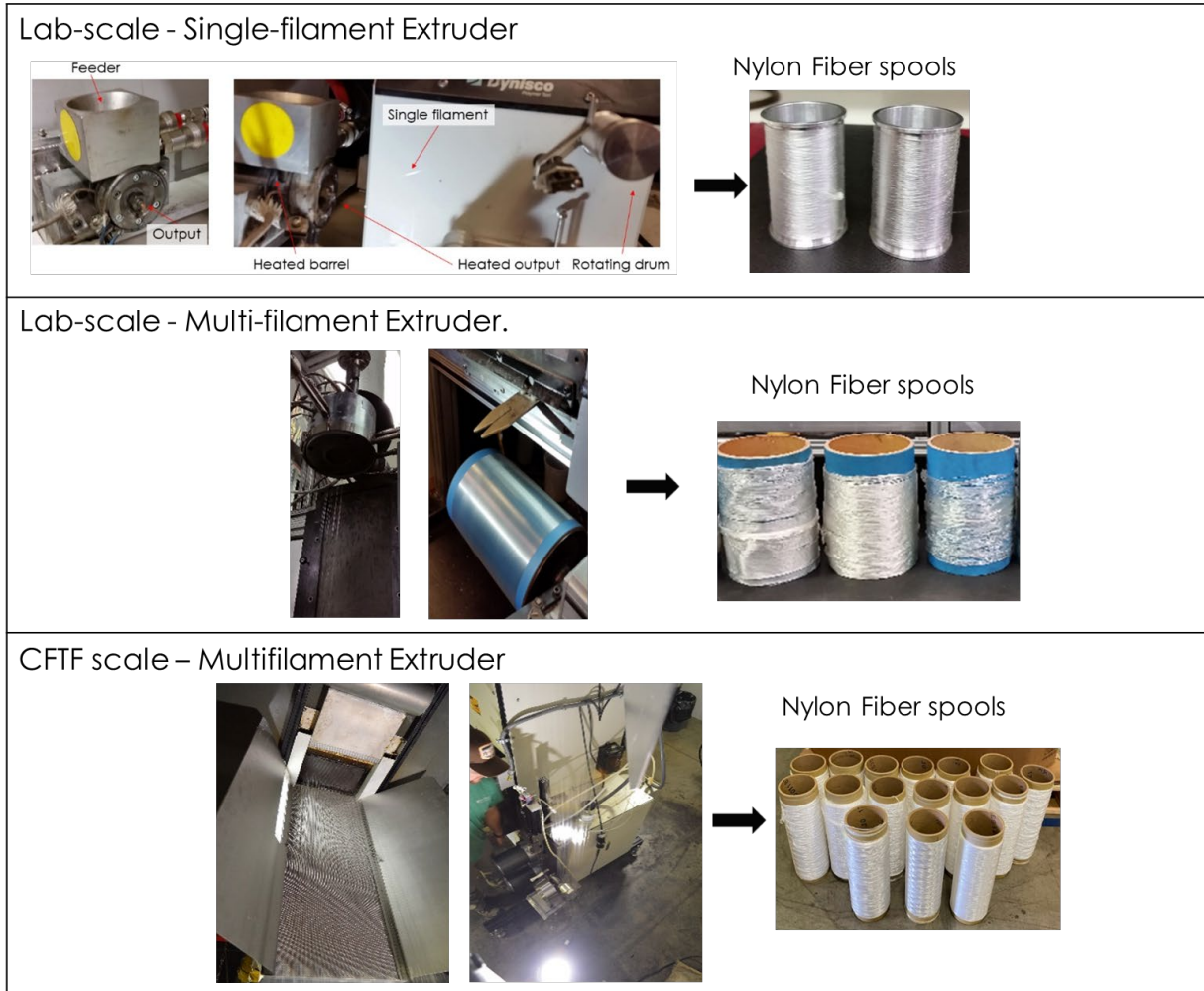


Figure II.2.7.7. Melt-spun Polyamide 6 fibers using a single-single filament and a multi-filament extruder. At the laboratory-scale and a multi-filament extruder at CFTF scale. Source: ORNL.

The melt-spun fibers were characterized to determine the diameter and tensile properties. The fiber diameter was examined and compared between both scales. The diameters pictured in Figure II.2.7.8 at bench scale was 21.3 μm, and 20.3 μm at CTF scale. The tensile properties of the single filaments were evaluated as shown in Figure II.2.7.9. The average properties are listed in Table II.2.7.4.

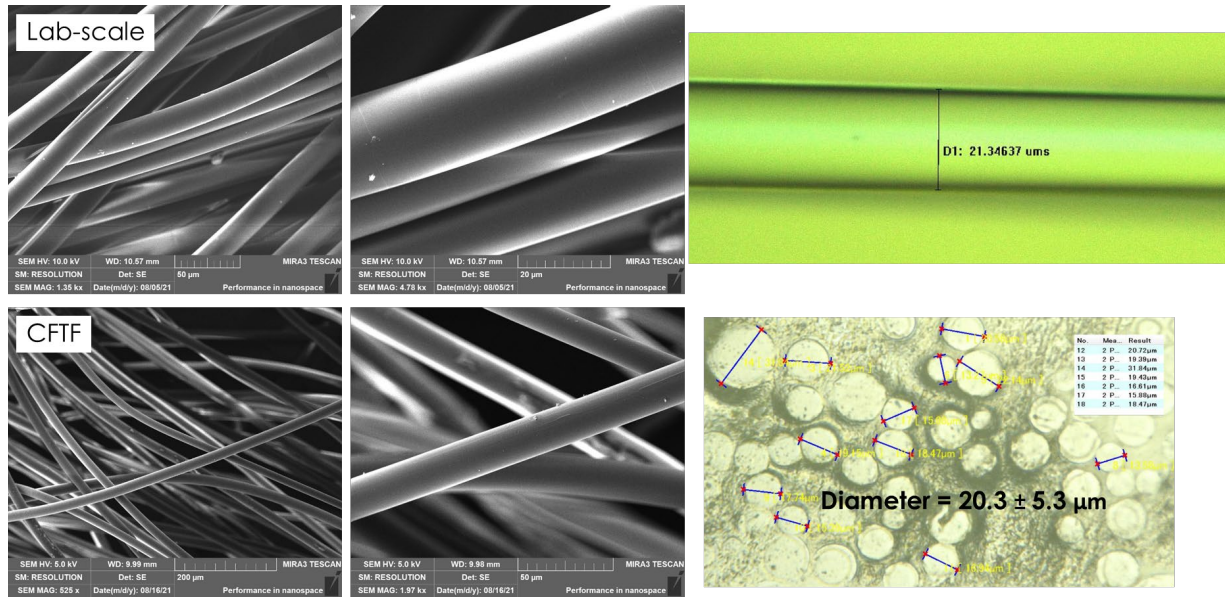


Figure II.2.7.8. Microscopy Images and measurement of the fiber diameter at the laboratory and CFTF scale. Source: ORNL.

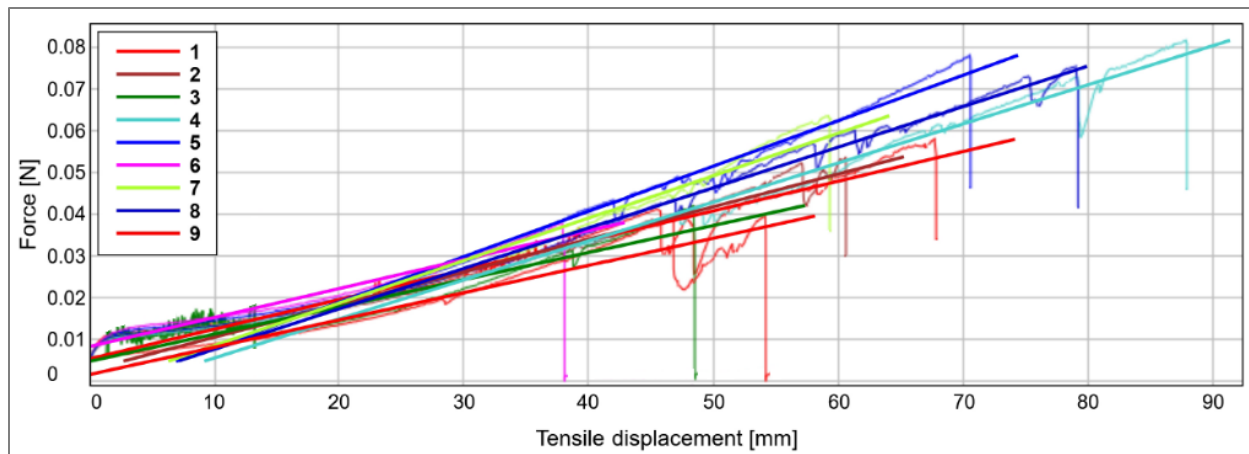


Figure II.2.7.9. Single fiber mechanical test results. Source: ORNL.

Table II.2.7.4. Polyamide 6 Tensile Properties

Sample	Tensile Stress at Maximum Force [GPa]	Modulus Segment (20 - 100%) [GPa]	Strain at Failure [%]
Average	0.14	0.05	230.10
Standard. Deviation	0.04	0.02	78.13

Bio-PAN Fibers

Two bio-PAN dope was prepared and melt-spun into precursor fibers exhibiting over 90 ksi break strength and 14% elongation at break. The resultant fiber properties are consistent with highly drawn specialty acrylic formulations. Pictures are provided in a separate technical report. Once the team achieved the target OPF density, the fiber was deemed to be ready for carbonization. A moderate carbonization, compatible with the processing envelope available at CFTF, was then performed on the OPF to produce a CF, shown in Figure II.2.7.10, achieving the milestone target property set of 289 ksi tensile strength, 27 Msi tensile modulus, and 1.06% elongation at break.



Figure II.2.7.10. CF produced with the OPF at CFTF. Source: ORNL.

Silicon Carbide Fiber Formulation

In the infant stages of this research area, three carbosilane formulations were explored for the spinning of silicon carbide fibers, with the goal of attaining precursors capable of achieving >40% yield at 1,000°C. The precursors explored in this work (SiCP1, SiCP2, and SiCP3) were allylic polycarbosilanes having different molecular weights. Figure II.2.7.11(a) shows the results of TGA of cured SiCP1, SiCP2, and SiCP3 samples in nitrogen with a heating rate of 10°C/min. Figure II.2.7.11(b) shows the DSC thermograms for the precursors used.

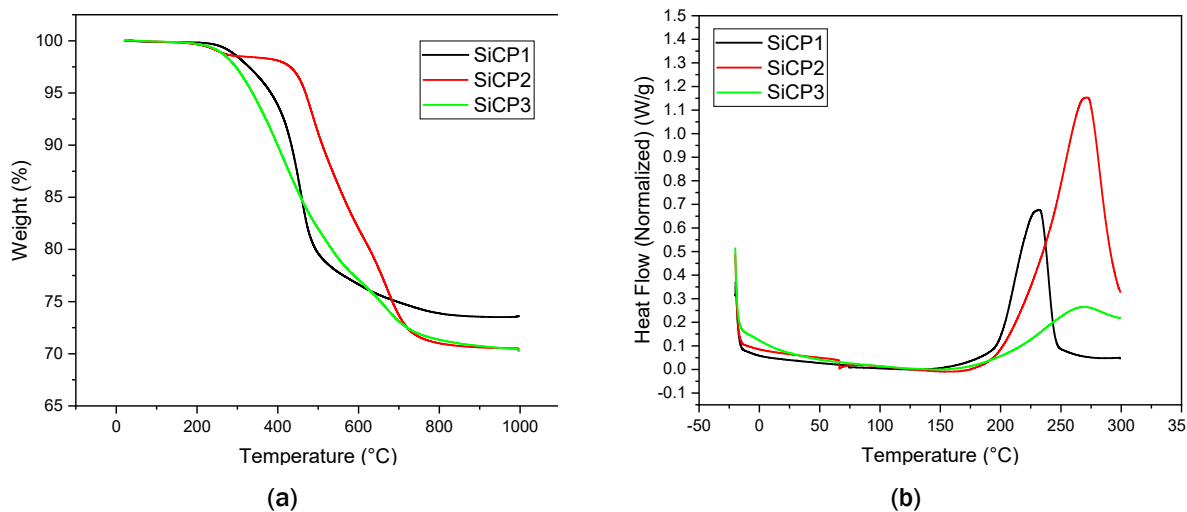


Figure II.2.7.11. (a) Thermogravimetric analysis of silicon carbide precursor polymers in nitrogen (10°C/min), (b) DSC profile of silicon carbide precursor polymers on heating (10°C/min). Source: ORNL.

Conclusions

The multiscale integrated strategy is working seamlessly for scaling and reducing the energy and cost of advanced fiber production using new alternative precursor materials. Despite the ongoing challenges of the COVID-19 pandemic, the team managed to obtain meaningful results and met 80% of the milestones. The team was able to demonstrate successful melt blowing and conversion of isotropic pitch precursor into CF at CFTF using data generated from the research and development efforts at the bench scale in FY 2020. In addition, Polyamide 6 fibers were successfully translated and melt-spun at CFTF scale into spools of precursor fibers.

Other alternative precursor materials such as petroleum-based mesophase pitch, bio-PAN material, and polycarbosilanes are under development at the laboratory-scale for scaling and fabrication of advanced fibers. The spinnability of the petroleum mesophase pitch material and the bio-PAN material into a precursor material was demonstrated including the development of the process condition for fabricating CF from those materials. The process conditions were developed for compatible within the processing envelope available at CFTF for future scaling. The next steps are to conduct research and development efforts to determine the ideal process conditions for continuous processing at scale, minimize material and process variations, utilize advanced processes to further reduce cost, and evaluate the performance of the resulting fibers in a variety of resins systems at a coupon level. Mechanical properties of the fabricated CFs at the laboratory-scale show promising results and can be further enhanced at scale.

Key Publications

1. Kore, S., V. S. M. D. Murthy, N. Hiremath, M. Theodore, S. Young, D. Penumadu, and U Vaidya, 2021, "Textile-grade carbon fiber-reinforced polycarbonate composites: Effect of epoxy sizing," *Ind. Eng. Chem. Res.*, Vol. 60, No. 10, pp. 3981–3991.
2. Kumar, V., N. Hiremath, P. S. Yeole, R. Spencer, K. M. M. Billah, M. Hasanian, M. Theodore, A. A. Hassen, A. Barnes, U. Vaidya, and V. Kunc, 2021, "Internal arcing and lightning strike damage in short carbon fiber-reinforced thermoplastic composites," *Compos. Sci. Technol.*, Vol. 201, Art. 108525.
3. Hiremath, N., S. Young, H. Ghossein, D. Penumadu, U. Vaidya, and M Theodore, 2021, "Low-cost textile-grade carbon fiber epoxy composites for automotive and wind energy applications," *Compos. B. Eng.*, Vol. 198, Art. 108156.
4. Yeole, P., S. Alwekar, N. Veluswary, S. Kore, N. Hiremath, U. Vaidya, and M. Theodore, 2021, "Characterization of textile-grade carbon fiber polypropylene composites," *Polym. Polym. Compos.*, Vol. 29, No. 6, pp. 652–659.
5. Singh, D. K., A. Vaidya, V. Thomas, M. Theodore, S. Kore, and U. Vaidya, 2021, "Finite element modeling of the fiber-matrix interface in polymer composites," *J. Compos. Sci.*, Vol. 4, No. 2, Art. 58.
6. U.S. Non-Provisional Patent Application No. 17/398,063, "Low-Cost Carbon Fiber- Based Lightning Strike Protection."

Key Presentations

Key conference presentations that showcase the R&D efforts at CFTF were given at the Society for the Advancement of Material and Process Engineering (SAMPE) Nexus and Women in Clean Energy conference. The panelists for each conference are shown in Figure II.2.7.12.

SAMPE neXus JUNE 29-JULY 1, 2021

INTERACTIVE FEATURED SESSION

THURSDAY, JULY 1 | 8:00 AM - 9:30 AM PT

Manufacturing of Structures with Composite Materials and Advanced Processes

Moderated by Dr. Thomas Kurfess, Oak Ridge National Laboratory

Register Today:
bit.ly/sampenexus-event

Speakers:

- Dr. Merlin Theodore, Oak Ridge National Laboratory (Fibers and Feedstocks)
- Dr. Vladimir Kunc, Oak Ridge National Laboratory (Composites)
- Dr. Thomas Kurfess, Oak Ridge National Laboratory (Moderator)
- Dr. Thomas Palfreman, Oak Ridge National Laboratory (Hybrid, Integrated Processes)
- Prof. May Weber, The University of Tennessee Knoxville (Workforce Development)

Careers in Clean Energy Innovation

Women in Clean Energy Innovation

Webinar | March 24, 2021 | 1-2 PM Est

Speakers:

- Kerri Hickenbottom, Assistant Professor, Department of Chemical & Environmental Engineering, The University of Arizona
- Jena Holtberg-Benge, General Manager, John Deere Reman at Deere & Co
- Merlin Theodore, Advanced Fibers Manufacturing Group Lead, Oak Ridge National Laboratory
- Joannie Harmon, Director of Workforce, IACMI - The Composites Institute

Sponsors: RAPID, IACMI, REMADE INSTITUTE

Figure II.2.7.12. Single fiber mechanical test results. Source: ORNL.

Acknowledgments

The CFTF Team would like to acknowledge our DOE sponsors, Dr. H. Felix Wu, DOE VTO Technology Development Manager; J. Leong and K. Kort, DOE AMO Technology Manager; the ORNL Management/Team, C. Blue, W. Peter, L. Love, X. Sun, M. Khaleel, Dr. V. Uday, E. Lara-Curzio, V. Kumar, K. Subhri, N. Gallejo, R. Paul, F. Vautard, J. Klett, A. Blankenship, D. Garrett, T. Reagan, F. Crowson, J. Carpenter, L. Lee, R. Strong, and R. Davies for their sponsorship, contributions, and/or support of the ORNL CFTF program.

II.2.8 Low-Cost, High-Throughput Carbon Fiber with Large Diameter (Oak Ridge National Laboratory)

Felix L. Paulauskas, Principal Investigator

Oak Ridge National Laboratory
1 Bethel Valley Road
Oak Ridge, TN 37831
E-mail: paulauskasfl@ornl.gov

H. Felix Wu, DOE Technology Manager

U.S. Department of Energy
E-mail: felix.wu@ee.doe.gov

Start Date: October 1, 2020

End Date: September 30, 2023

Project Funding (FY 2021): \$500,000

DOE share: \$500,000

Non-DOE share: \$0

Project Introduction

ORNL and its partners are demonstrating and evaluating the effects of combining textile PAN fibers produced via dry spinning at substantially larger diameters and oxidized with Atmospheric Plasma Oxidation (APO) in order to produce CF that meets automotive requirements at significantly lower costs while also enhancing processing characteristics. CFCs have been gaining interest from automotive designers due to the potential benefits offered by their high stiffness and low density. It has been projected that CFCs could possibly reduce the weight of vehicle structures by greater than 50% and that fuel economy can be increased by as much as half of the percentage of weight-savings. The high cost of the fiber remains the largest hurdle to production implementation of CFCs as a vehicle structural material. Automotive vehicle manufacturers have consistently indicated that fiber costs approaching \$5/lb. are necessary to achieve substantial inroads into automotive utilization in mass-marketed vehicles where fuel economy can significantly affect national petroleum usage. The costs to produce industrial grade CF with properties similar to those of interest to these automotive applications have been estimated at \$7/lb. to \$10/lb., almost equally split between the cost of the precursor itself and cost of the conversion. To achieve the necessary cost reduction of 30% or greater, most industry insiders concede that a combination of precursor and conversion cost reductions must be implemented. Fortunately, automotive engineers indicate that they are willing to give up some performance in order to get this cost reduction as well. This initiative intends to take advantage of all these factors in order to achieve necessary cost reduction.

Essentially all PAN-based CF is currently produced from precursors manufactured expressly for CF production. While acrylic fiber produced for carbon fiber precursor is very similar chemically to acrylic fiber produced for textile applications, textile acrylics have not been involved in widespread CF manufacturing. ORNL has made significant progress in demonstrating pathways to CF production utilizing textile products, and that approach is being exploited further in this project. It is also worth noting that although PAN fibers are commonly utilized in textile applications worldwide, all acrylic fiber produced for CF conversion and the majority of PAN fibers produced for textiles are solution-spun. Dry spinning is a more challenging approach, but infrequently utilized variant, in textile acrylic fiber production. Dry spinning utilizes significantly less solvents in producing the fiber and requires less equipment and energy to extract and recover the solvents. These differences allow for greater production speeds as well, meaning this approach is less costly than wet spinning as described in IACMI Report IACMI/R-0006-2020/6.06 [1]. The dry spinning process is also being demonstrated and exploited in this project. Conventional oxidation takes place in large open chamber ovens that heat PAN in air. This process typically takes ~90 minutes for commercial CFs. Note that CF manufacturers do not allow their exact residence times to be published. APO was jointly invented by ORNL and 4X Technologies (4XT) and is currently being scaled and commercialized by 4XT and its

commercialization arm, 4M Carbon Fiber. It involves the indirect exposure of PAN to atmospheric plasma in an oven at temperatures similar to conventional oxidation. It has been shown to enhance the oxidation process in CF conversion, especially since it has been shown to be at least three times faster than conventional approaches.

ORNL's acrylic fiber manufacturing partner, Dralon, has indicated that producing larger diameter fibers is not technically challenging and can significantly enhance production economics by up to 30% on their end. However, practical limitations in textile applications and/or the drastic time penalties associated with diffusion time requirements of large diameters in the oxidation process in carbon fiber conversion continue to be the limitation on acrylic fiber diameters for them until this approach is conclusively demonstrated for CF. Success in our approach has the major benefit of dramatically increasing the throughput of both precursor production and CF conversion, leading to significant cost decreases in both stages.

Objectives

The objective of this work is to demonstrate the effects of combining textile PAN fibers produced via dry spinning at substantially larger diameters and oxidized with APO to produce lower-cost CF that meets automotive requirements at significantly lower costs while enhancing processing characteristics. While several of these factors have been considered individually, or in combination with a single factor in past DOE programs, this is the first time that all four approaches have been combined. Ultimately, the team intends to demonstrate this approach can produce CF meeting mechanical performance minimums of 375 ksi, 33 Msi, and 1% strain along with 25% to 30% or greater savings. Scaled-up CF production at the ORNL CFTF for composite panel evaluation and/or demonstration part fabrication in the third year of this project will demonstrate overall advantages of this approach along with providing more detailed assessment of cost/performance tradeoffs.

Approach

During Project Year 1, the team established a baseline for this approach with CF converted from the dry spun textile precursor from Dralon along with a fiber effectively at least 25% larger in diameter. Note that since the dry spun fibers are not round, it is more appropriate to cite the fiber dtex (or mass per unit length in g/10,000 m) rather than the diameter. For example, a round 2.0 dtex PAN fiber would be in the range of 14.5 microns in diameter. Performance of these fibers will be assessed utilizing single filament testing such that cost information will be generated for inclusion into the existing ORNL cost models. The cost of the project baseline fiber will be compared with modeled commercial industrial fiber cost data and preliminary cost projections for larger diameter fiber trends to demonstrate cost-savings for this approach. In order to meet the go/no-go decision point, baseline fiber must exceed the performance of DOE minimum requirements established many years ago for the LCCF Program of 250 ksi strength, 25 Msi modulus, and 1% strain to failure. The ORNL team has established a higher requirement for this project go/no-go of 300 ksi strength, 30 Msi modulus, and 1% strain to failure, along with a projected cost-savings of 20% versus modeled commercial fiber.

In FY 2022, we will focus on producing fiber effectively at least 50% larger than the project baseline along with performance minimums of 375 ksi, 33Msi, and 1% strain, while developing and scaling fiber post-treatment processes to CFTF level production. The cost target for Year 2 is to demonstrate 25% to 30% or greater savings are potentially achievable with this approach and to project optimal diameter targets for scaled-up production at CFTF in late Project Year 2 or early Project Year 3 for composite panel evaluation and/or demonstration part fabrication to demonstrate overall advantages of this approach. In FY 2023, we will focus on demonstrating and evaluating the attractiveness of the new CF produced in late Project Year 2 and/or early Project Year 3. Much of the effort will be expended on making and testing the composite articles required to fully evaluate and define the advantages of this approach. Cost models will be completed and utilized to evaluate the cost vs. performance benefits in combining effects of the textile PAN fibers produced via dry spinning and at substantially larger diameters and oxidized with APO to produce significantly lower-cost CF.

Project partner Dralon was initially to be responsible for all precursor production utilizing their well-established, world-class dry spinning process currently used commercially in producing acrylic fiber exclusively for textile applications. 4XT is responsible for all of the oxidative stabilization portion of the conversion of the dry spun precursor. 4XT will develop oxidation protocols specifically for the unique dry spun precursors in order to oxidize the fiber and provide increments to ORNL for completion of conversion and evaluation of these variants in Years 1 and 2. ORNL has independently, and in collaboration with others, established unique conventional and advanced low and HTC capabilities at a variety of scales from gram quantities of research materials up to 25 tons per year large-scale demonstration levels. To simplify effort for this project, we will focus on utilizing the most appropriate conversion capabilities in the middle of these production scales while acknowledging that the other capabilities might be beneficial in even better exploiting the approaches identified in this project in follow-on efforts. Oxidized fiber from 4XT will be provided to the ORNL Carbon and Composites Group in Years 1 and 2 to develop appropriate carbonization and post-treatment protocols for completing the CF process and then transferring responsibility to the CFTF to complete conversion of the fiber for the composite demonstrations in Year 3.

Similar to capabilities in conversion, ORNL has independently—and in collaboration with others—established post-treatment capabilities at a variety of scales from gram quantities of research materials up to 25 tons per year large-scale demonstration levels. Minimal effort will be expended in this effort in Year 1, but beginning in Year 2, the ORNL Carbon and Composites Group will develop appropriate surface-treatment and sizing protocols for completing the carbon fiber post-treatment process and then transferring responsibility to CFTF to complete post-treatment of the fiber in late Year 2 for making the larger quantity of fiber required for composite demonstrations in Year 3.

Initial fiber testing will be done at the single filament level in Year 1 and early Year 2 to provide basic strength, modulus, and strain data. Later in Year 2, fiber testing will transition to focus on impregnated strand testing, which allows more direct comparison with commercial fibers and gives some insight into how well the fiber tows infuse and how the fiber performs due to compatibility with the ultimately intended composite resin system.

ORNL is generally considered as the preferred source for DOE technical modeling of CFCs for vehicle technologies applications. The project team will utilize the established results of this ongoing effort to evaluate what is expected to be a major impact in the approach for making lower-cost CF.

Going into this project, the project team has identified several composite processing methods and variants that might be utilized in characterizing this fiber's performance in composite systems of interest for automotive applications. The plan is to choose the most appropriate process for demonstrating economic and technical advantages for this new fiber manufacturing approach from the following composite manufacturing processes listed in order of currently perceived attractiveness:

1. CFC Sheet Molding Compound – Thought to be a promising introduction point for lower-cost CF due to similarities with existing commercial utilization of fiberglass, the cutting process and minimal amount of post-treatment optimization may mask advantages provided by continuous fibers.
2. Resin Film Infusion (RFI) – Not quite as cost-effective for automotive applications, this process utilizes continuous fibers, but requires separate preforms and resin films.
3. Resin Transfer Molding – Similar to RFI, but eliminates the resin filming step. Infusion is more difficult but would provide more information on infusion characteristics.
4. Prepreg Molding – Probably offers the best information on overall fiber performance capabilities, but is the costliest to execute and the least applicable to the automotive industry.

The project team plans to consult extensively with automotive industry representatives in Year 1 and early Year 2, while also reviewing new and/or improved equipment capabilities expected to be available at ORNL and partner facilities in the interim before making final decisions on the focal process for Year 3. Primary testing includes composition/composition uniformity, primary direction tensile strength, modulus, strain, and similar transverse direction properties.

Results

Due to a significant downturn in business conditions largely due to COVID-19 limitations, Dralon production over the last 1+ year was significantly curtailed. Fortunately, Dralon had already produced samples adequate for our initial needs for our other partner to utilize for other purposes. 4XT offered us access to materials they had in reserve that have attributes equivalent to those we were targeting for this work. We are now executing planned experimental activities. These plans include the experimental work to evaluate process conditions and associated economic/performance tradeoffs, as well as some equipment adaptations, we believe will facilitate process control and overall production attractiveness.

During this reporting period, we completed most of the work in converting 2.2, 3.3, and 5.5 dtex Dralon fibers made available to us by 4XT, utilizing APO and conventional carbonization, as shown in Table II.2.8.1, Table II.2.8.2, and Table II.2.8.3. The highest tensile strength achieved for each of those fibers was 394 ksi, 337 ksi, and 317 ksi, respectively. While this is probably adequate for us to do the initial cost versus performance tradeoffs outlined for the next milestone, these tensile strengths are a little lower than expected and more importantly, the highest modulus values achieved were about 28 Msi, 26 Msi, and 24 Msi for each of those same fibers respectively. For this reason, we are doing more exploratory work utilizing steam stretching and conventional conversion to determine what limits exist for those materials, as shown in Table II.2.8.4 and Table II.2.8.5.

Table II.2.8.1. Plasma Oxidized/Conventional Carbonized 2.2 dtex Precursor

Favimat #	Diameter (µm)	Diameter Gravimetric	Density (g/cc)	Break Stress (Ksi)	Modulus (Msi)	Strain (%)
3005 Oxidized	10.92 (1.27)	10.88	1.3509	33.85 (1.20)	0.98 (0.02)	24.46 (1.85)
3025 A	6.44 (0.46)	7.04	1.7422 (.0005)	366.69 (65.03)	27.96 (0.76)	1.28 (0.20)
3026 A	6.38 (0.51)	6.33	1.7374 (.0005)	364.57 (71.25)	26.83 (1.61)	1.33 (0.20)
3027 A	6.41 (0.41)	6.33	1.7482 (.0005)	316.92 (35.44)	26.45 (0.46)	1.18 (0.13)
3028 A	6.34 (0.40)	6.28	1.7569 (.0007)	351.43 (56.55)	26.11 (0.63)	1.31 (0.18)
3029 A	6.59 (0.42)	6.33	1.7541 (.0003)	393.73 (63.12)	26.22 (0.58)	1.46 (0.21)
3030 A	6.82 (0.53)	6.37	-	388.07 (36.08)	27.16 (1.06)	1.05 (0.11)
3032 B	6.75 (0.58)	-	-	289.78 (40.13)	26.53 (0.65)	1.07 (0.12)
3051 B	6.13 (0.54)	6.57	1.6558 (0.0018)	351.99 (54.23)	25.86 (0.62)	1.33 (0.20)
3052 C	6.57 (0.40)	-	-	339.97 (64.13)	25.43 (0.40)	1.31 (0.22)
3053 C	6.43 (0.50)	-	-	293.96 (52.88)	24.84 (0.59)	1.16 (0.19)

Table II.2.8.2. Plasma Oxidized/Conventional Carbonized 3.3 dtex Precursor

Favimat #	Diameter (µm)	Diameter Gravimetric	Density (g/cc)	Break Stress (Ksi)	Modulus (Msi)	Strain (%)
3019 Oxidized	13.21 (0.88)	-	1.3562	33.56 (1.37)	0.95 (0.03)	24.57 (2.31)
3106	8.14 (0.54)	-	1.7391 (.0026)	284.54 (44.94)	25.14 (0.56)	1.12 (0.17)
3107	8.20 (0.88)	-	1.7364 (.0003)	337.43 (65.03)	24.99 (0.71)	1.28 (0.24)
3108	8.06 (0.63)	-	1.7357 (.0002)	324.98 (81.49)	26.17 (0.77)	1.22 (0.29)
3109	8.45 (0.55)	-	1.7381 (.0006)	329.48 (82.72)	23.88 (0.44)	1.35 (0.32)
3112	8.13 (0.73)	-	1,7381 (.0006)	330.59 (68.21)	24.23 (0.52)	1.34 (0.26)

Table II.2.8.3. Plasma Oxidized/Conventional Carbonized 5.5 dtex Precursor

Favimat #	Diameter (µm)	Diameter Gravimetric	Density (g/cc)	Break Stress (Ksi)	Modulus (Msi)	Strain (%)
3118 Oxidized	17.79 (1.27)	-	1.3514	32.90 (1.76)	0.98 (0.02)	20.18 (3.31)
3121	10.95 (0.45)	11.02	1.7361 (.0009)	277.43 (76.45)	23.30 (0.50)	1.17 (0.28)
3122	11.27 (0.66)	10.81	1.7362 (.0005)	255.82 (34.82)	23.32 (1.59)	1.09 (0.16)
3129	10.61 (0.87)	10.94	1.7340 (.0011)	298.23 (66.07)	24.31 (0.56)	1.21 (0.26)
3130	10.70 (0.61)	-	-	239.94 (82.33)	25.44 (0.79)	0.95 (0.31)
3131	11.33 (1.07)	-	-	317.11 (71.94)	24.14 (0.39)	1.30 (0.28)
3132	11.04 (0.79)	-	-	274.07 (50.52)	25.02 (0.49)	1.09 (0.19)
3133	10.95 (0.56)	-	-	292.69 (45.66)	24.07 (0.49)	1.16 (0.17)

Table II.2.8.4. Steam Stretched, Conventionally Converted 2.2 dtex Precursor

Favimat #	Diameter (µm)	Calc. Diameter (µm)	Density (g/cc)	Break Stress (Ksi)	Modulus (Msi)	Strain (%)
2887 Precursor	12.24 (1.27)	12.30	1.180	73.94 (3.86)	1.77 (0.07)	9.91 (1.00)
2903 Oxidized	11.03 (0.91)	10.66	1.3247 (.0007)	43.03 (10.09)	1.27 (0.03)	18.87 (4.68)
2923 A	5.96 (0.31)	5.97	1.8054 (.0188)	436.78 (48.13)	33.04 (1.49)	1.29 (0.15)
2929 A	5.71 (0.46)	5.77	1.8117 (.0001)	520.34 (72.64)	33.47 (0.96)	1.50 (0.19)
2919 A	6.07 (0.71)	6.03	1.8106 (.0004)	517.48 (45.31)	34.25 (0.50)	1.47 (0.13)
2930 A	6.12 (0.37)	-	-	469.76 (72.22)	32.86 (2.23)	1.39 (0.16)
2932 B	6.11 (0.38)	6.02	1.8120 (.0005)	457.957 (79.15)	32.12 (1.32)	1.38 (0.21)
2933 B	6.19 (0.46)	6.19	1.8191 (.0002)	462.49 (47.24)	32.32 (0.72)	1.39 (0.13)
2934 C	6.21 (0.43)	6.20	1.8132 (0.004)	453.54 (67.06)	32.15 (0.49)	1.36 (0.19)
2936	6.14 (0.43)	-	-	401.02 (50.94)	30.15 (0.45)	1.30 (0.14)

Table II.2.8.5. Steam Stretched, Conventionally Converted 3.3 dtex Precursor

Favimat #	Diameter (µm)	Calc. Diameter (µm)	Density (g/cc)	Break Stress (Ksi)	Modulus (Msi)	Strain (%)
2884 Precursor	17.40 (1.12)	16.91	1.1787 (.0002)	54.80 (2.38)	1.55 (0.05)	17.91 (1.71)
2872 SS Precursor	14.05 (0.60)	14.08	1.1787	75.29 (2.61)	1.80 (0.05)	11.26 (0.58)
2896 Oxidized	12.39 (0.93)	11.58	1.3581 (.0002)	37.79 (2.20)	1.20 (0.02)	19.77 (3.06)
2901	6.99 (0.36)	-	-	403.80 (109.52)	34.16 (0.65)	1.16 (0.29)
2907	6.81 (0.38)	6.90	1.7935 (.0004)	425.87 (74.11)	31.67 (0.71)	1.31 (0.22)
2908	6.99 (0.47)	6.96	1.7891 (.0004)	445.09 (62.34)	32.09 (0.52)	1.35 (0.17)
2909	7.08 (0.50)	7.20	1.7391 (.0157)	427.21 (55.91)	31.18 (0.67)	1.34 (0.15)
2910	7.39 (0.33)	7.12	1.7901 (.0006)	433.99 (72.08)	32.40 (0.62)	1.31 (0.18)

Due to continued uncertainty of the reliable supply of dry spun fiber from Dralon, ORNL has continued looking for alternative sources for comparable fiber while executing earlier plans utilizing the fiber provided by 4XT. During this time, we were able to identify another source for dry spun fiber in Peru (South America) from Sudamericana De Fibras (SDF), whom we found to have a license based on a very similar process as utilized by Dralon with exception that their comonomer of choice is vinyl acetate versus Dralon utilized methyl acrylate. We believe the performance difference will be relatively small due to the different comonomer and likely more influenced by other characteristics of their production approaches. Fortunately, we were able to procure a substantial supply of SDF-produced fibers in similar diameter ranges as we had from Dralon. These samples were delivered at the end of FY 2021 to begin assessment in early FY 2022.

Conclusions

This year, significant technical progress has been achieved despite the severe impact of materials availability limitations due to COVID-19 and the resulting business impacts to our project partners. The project team is now catching up to schedules after more than six months of delay at project initiation and have identified both short and longer term mechanisms for meeting our materials supply needs. Technically the project team is very close to project mechanical performance goals for the first year and anticipate being able to fully meet those goals during FY 2022.

References

1. Wego, A., "Development of a lower-cost, high-volume, commercially available, precursor for lower-cost carbon fiber for automotive and wind blade applications," IACMI Report IACMI/R-0006-2020/6.06.

Acknowledgments

ORNL leaders would like to recognize technical contributions by A. Wego from Dralon; T. Bonds, D. Martin, and J. Nowak from 4XT, and F. Z. Xiong and D. McConnell from ORNL.

II.2.9 Self-Sensing Fiber-Reinforced Composites (Oak Ridge National Laboratory)

Christopher Bowland, Principal Investigator

Oak Ridge National Laboratory
1 Bethel Valley Road
Oak Ridge, TN 37831
E-mail: bowlandcc@ornl.gov

H. Felix Wu, DOE Technology Manager

U.S. Department of Energy
E-mail: felix.wu@ee.doe.gov

Start Date: October 1, 2019	End Date: March 31, 2021	
Project Funding (FY 2021): \$300,000	DOE share: \$150,000	Non-DOE share: \$150,000

Project Introduction

The Technology Commercialization Fund (TCF) project aimed to demonstrate a scalable coating process to adhere nanoparticles to the surface of fibers and fabricate composites with *in-situ* damage detection abilities and simultaneous mechanical performance enhancements. CF composites have the inherent problem of hiding damage within the structure with no visual indications on the surface. Therefore, a technique to monitor for damage or excessive stress on the composite is necessary to ensure its safety and avoid catastrophic failure. This capability will be desired in future transportation vehicle designs, such as in cargo and surveillance drones developed by Dronesat, LLC, (Dronesat) who was the industrial partner on this project.

Prior work showed that SiC nanoparticles embedded in a thin polymer layer on the surface of CF can result in multifunctional composites that have increased mechanical performance and enhanced self-sensing behavior [1]. Specifically, the composite's interlaminar shear strength was improved, which demonstrates better adhesion between the fiber layers. This fiber-to-fiber adhesion is typically the weak property of fiber-reinforced composites and is the mechanism for composites to fail catastrophically. The nanoparticles also enhanced the electrical resistance change of the bulk composite structure when subjected to applied stress, thus giving it better structural health monitoring capabilities. The nanoparticle deposition technique utilizes a continuous feed-through process that is compatible with existing commercial CF processing lines, thus enabling potential commercial deployment. This prior work resulted in a patent-pending fiber-coating technology titled, "Carbon Fiber-Nanoparticle Composites with Electromechanical Properties" (non-provisional patent application number 16/280,268). Within this project, the prior work was leveraged to extend the fiber-coating process to another material system (i.e., titanium dioxide [TiO₂] nanoparticles on CF) to create composites with embedded active sensing abilities.

Working with Dronesat, this project also involved the design and initial fabrication of self-sensing composite components for a prototype drone. Dronesat has developed a tethered drone system for prolonged flight times. To improve drone safety, Dronesat wants to integrate sensing composites into their drones to detect damage before catastrophic failure. The ultimate result would reduce maintenance time by early detection of cracks or damage, thus mitigating costly effects of unexpected failures, which could result in vehicle loss. Materials that could detect damage and provide timely information about critical components—in particular, ducted fan blades, disks, open rotors, ducts, propellers, airframe, control surfaces, horizontal and vertical stabilizers, and wings—are highly desirable for product safety. Dronesat collaborated with ORNL on this project to help integrate multifunctional composites into their structures. Dronesat offered its drone system as a testbed to demonstrate the application of multifunctional composites in real-world scenarios. Dronesat has one of the most unique power infrastructure concepts for a drone in development that is positioning it to become a highly sought-after drone manufacturer. Safety is one of the biggest challenges in this type of drone market, so

Dronesat partnered with ORNL to integrate sensors that could solve some of the safety challenges. To meet these safety challenges, ORNL has further developed the nanoparticle coating process within this project to achieve improved mechanical and sensing performance.

Objectives

This research work aimed to demonstrate self-sensing CF composites that can be deployed in transportation vehicles using a patent-pending process developed at ORNL. The embedded nanoparticles result in multifunctionalities that increase mechanical performance and enhance self-sensing behavior through electrical resistance change of the bulk composite structure when subjected to applied stress, thus giving it better structural health monitoring capabilities. The specific objectives include homogeneously coating CF with nanoparticles using a continuous processing method, improving mechanical performance through interlaminar shear strength characterization, and enhancing sensing capabilities by utilizing nanoparticles with piezoresistive behavior.

Approach

To achieve the project objectives, nanoparticles were coated on CF using a continuous feed-through process to be able to generate a sufficient length of fiber to fabricate into composites. This process consists of a two-step coating process. The bare CF was first submerged into an aqueous suspension of TiO₂ nanoparticles with subsequent drying. These coated fibers were then dipped in a second coating bath with a commercially sourced aqueous epoxy sizing emulsion. Sizing is a typical coating that is applied to CF in industrial settings. This polymer layer is 100 nm to 200 nm and serves multiple functions. It enhances the adhesion between the fiber and the matrix, protects the fiber surface during composite fabrication, and aids in handling of the fibers. This project aimed to utilize the sizing layer as a carrier matrix for nanoparticles in that the sizing helped bond the nanoparticles to the fiber surface. The goal of the nanoparticles was to enhance the mechanical interlocking at the composite interphase to increase the interlaminar shear strength, as well as increase the piezoresistive response of the composites. This piezoresistive response was quantified by measuring the electrical resistance of composite beams during repeated strain cycles.

Results

The dip-coating procedure was successful in homogeneously dispersing TiO₂ nanoparticles on the surface of a CF tow and subsequently coating it with sizing as shown in by the SEM images in Figure II.2.9.1(a)–(e). This process allowed the concentration of TiO₂ nanoparticles to be easily modified by changing the concentration of nanoparticles in the coating bath. The fibers and composites in the figures are designated by the concentration of nanoparticles in the solution bath (i.e., the “1-wt. %” fibers were dip coated through a water bath with 1 wt. % nanoparticles). Fibers were dip coated with 0.1 wt. % to 4 wt. % nanoparticle mixtures. Using these various fibers, unidirectional composites were fabricated using a filament winding technique followed by compression molding during epoxy curing. The resulting composites were short-beam shear tested to quantify the interlaminar shear strength as summarized in Figure II.2.9.1(a). For most composites, the nanoparticles enhanced the interlaminar shear strength with the most significant improvements in the 0.5 wt. % to 1.5 wt. % composites as shown in Figure II.2.9.1(b). Overall, the best performing sample was the 1 wt. % composites, which was 14.7% stronger than the composites with no nanoparticles.

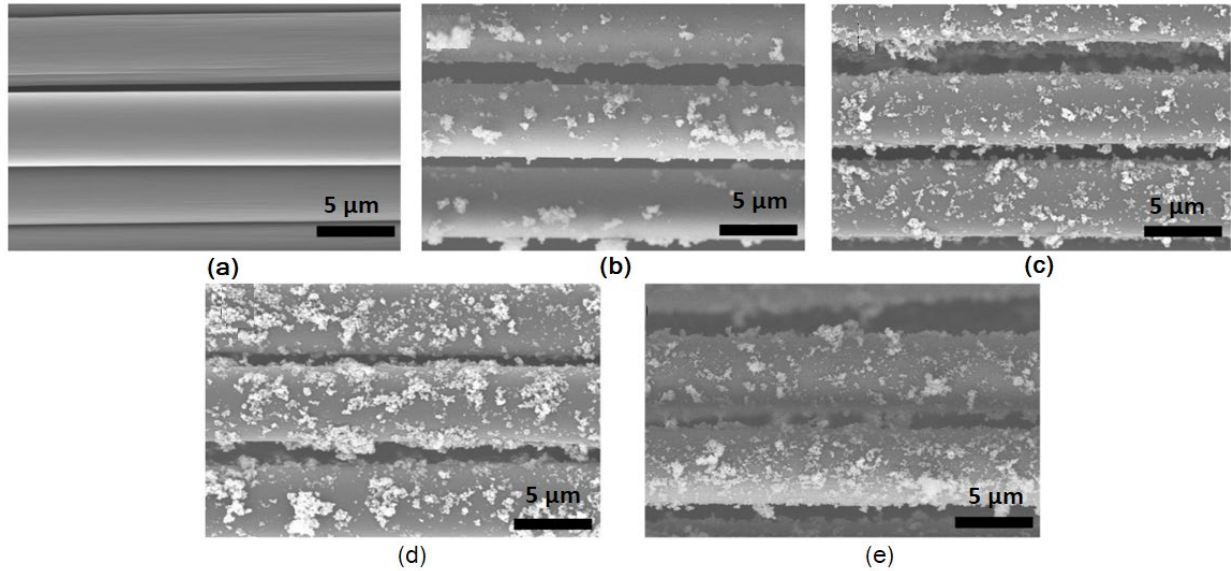


Figure II.2.9.1. SEM images of TiO_2 on CF after a dip-coating process with mixtures containing: (a) 0 wt.%; (b) 1 wt.%; (c) 2 wt.%; (d) 3 wt.%; and (e) 4 wt.% TiO_2 nanoparticles [2]. Source: ORNL.

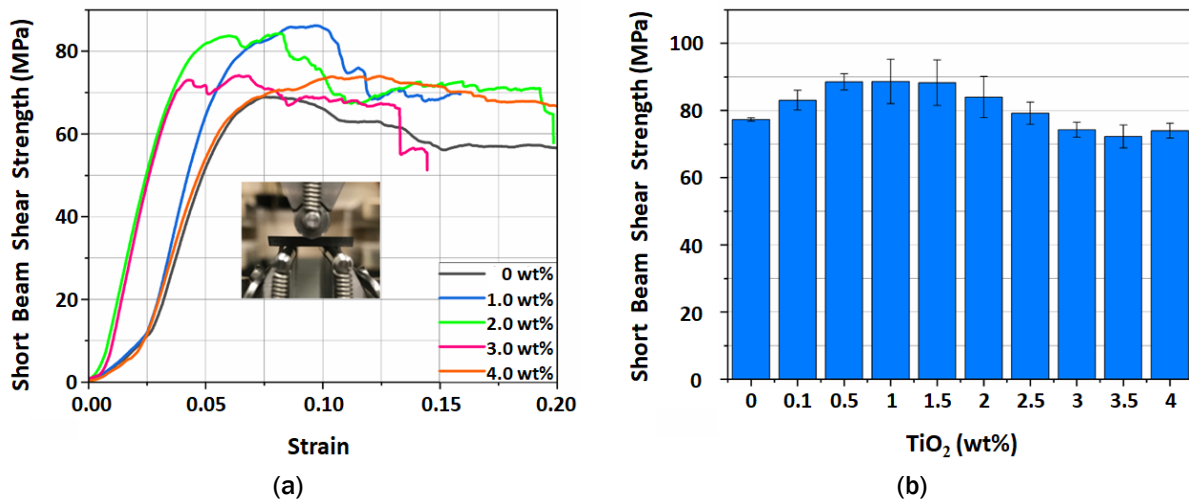


Figure II.2.9.2. Results of the interlaminar shear strength testing showing: (a) the representative strength vs. strain curves; and (b) the average strength values versus the nanoparticle concentration in the coating mixture. The error bars signify one standard deviation [2]. Source: ORNL.

To characterize the structural health monitoring capabilities of the composites, the unidirectional composites were electroded in an out-of-plane through-thickness configuration, as observed in Figure II.2.9.3(a) and placed in a dynamic mechanical analyzer using a single cantilever clamp. The composites were subjected to cyclic strain loading and unloading at different strain magnitudes, as shown in Figure II.2.9.3(b), while capturing the change in electrical resistance, as shown in Figure II.2.9.3(c). An overlay of the strain input and resulting electrical resistance change can be seen in Figure II.2.9.3(d).

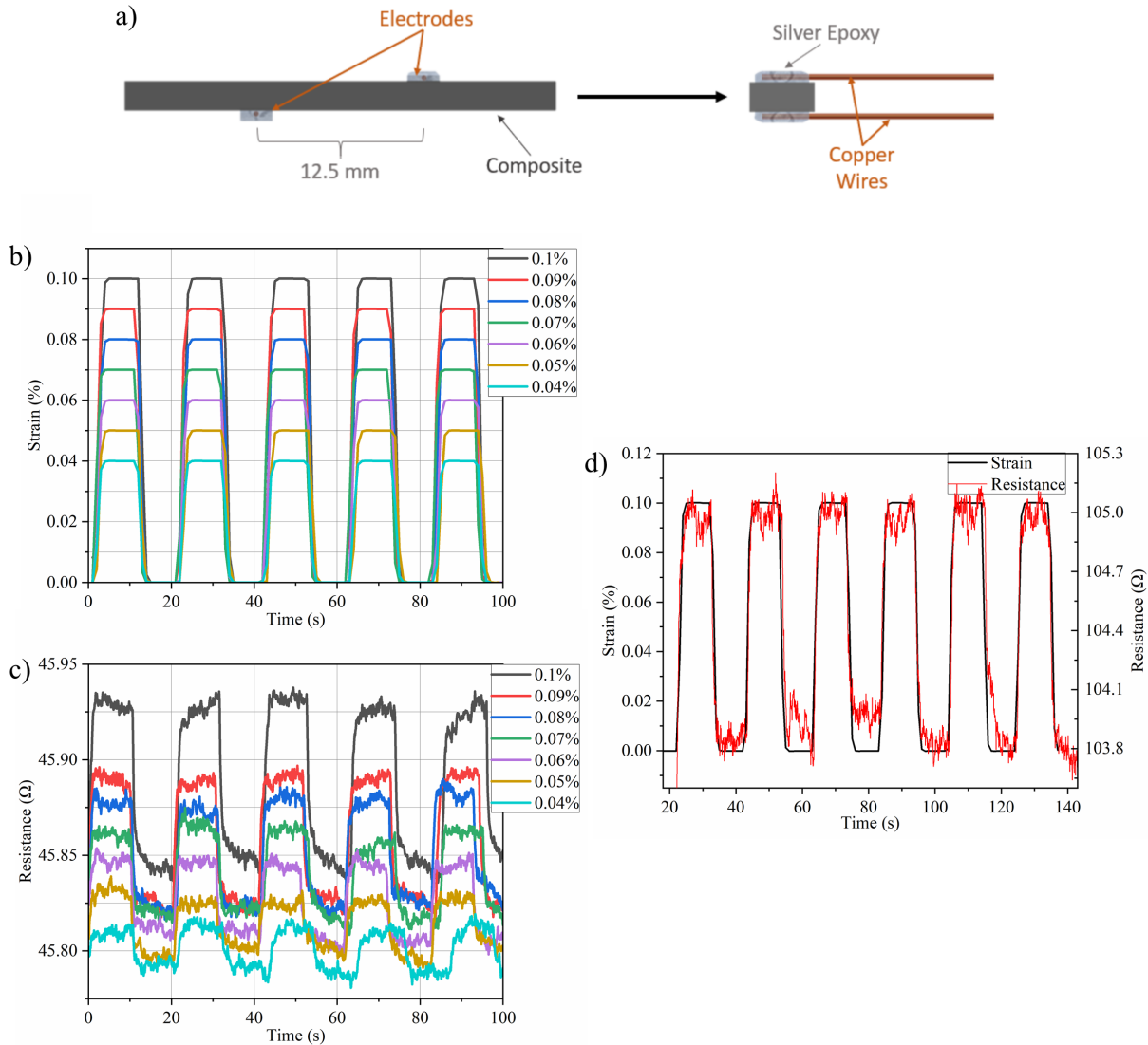


Figure II.2.9.3. (a) Electroded sample schematic in which the CFs run in the x-direction and the thickness is in the y-direction. (b) An overlay of the different strains placed on the composite beam. (c) Representative curves of the electrical resistance in response to the different strain cycles. (d) Overlap of a representative input strain and the electrical resistance response [2]. Source: ORNL.

At least 10 strain cycles were repeated for each strain level and the corresponding electrical resistance change was averaged over the 10 cycles to create the plot in Figure II.2.9.4(a), which shows the average electrical resistance change at each strain level for every composite. To quantify the structural health monitoring sensitivity, the gauge factor for each composite was calculated by dividing the relative electrical resistance change by the strain. The average gauge factor for each composite is shown in Figure II.2.9.4(b), where a larger value represents a better performing composite. This showed that the composites with 1 wt.% to 3 wt.% nanoparticles exhibited enhanced structural health monitoring sensitivity. The best performing composites in terms of gauge factor was the 2.5 wt.% composites with a gauge factor of 7.14, which equates to 186% increase in sensitivity as compared to the composites without nanoparticles.

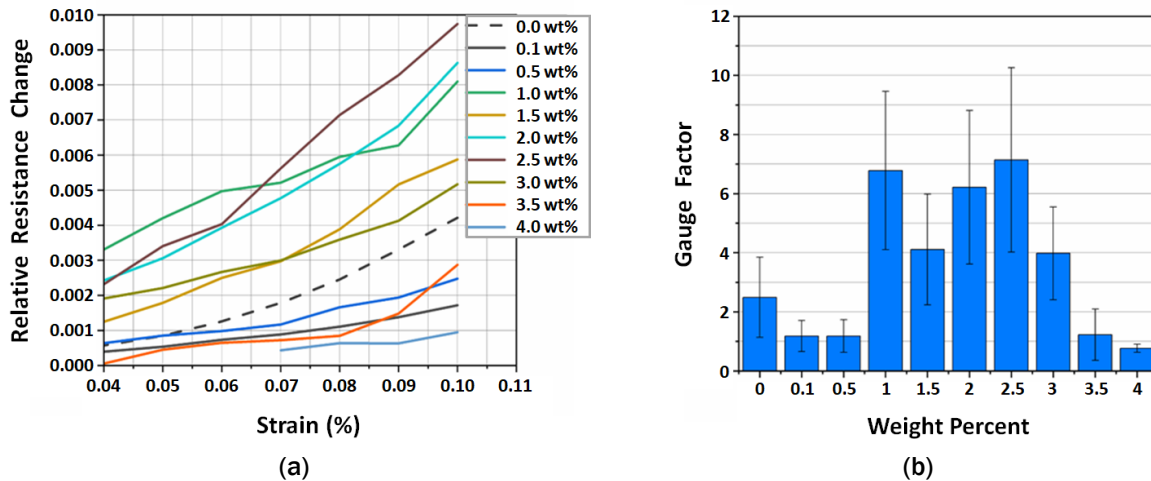


Figure II.2.9.4. (a) Relative resistance change versus percent strain. (b) Gauge factor for each composite averaged over all the strain levels tested. Error bars signify one standard deviation [2]. Source: ORNL.

The overall performance of the composites is summarized in Figure II.2.9.5, which plots both the interlaminar shear strength and gauge factor for each composite. The targeted area of the plot is the highlighted upper-right quadrant, which represents improvements in both mechanical and sensing performance as compared to the composites with no nanoparticles. As shown in Figure II.2.9.5, the composites with 1 wt.% to 2.5 wt.% nanoparticles saw enhancements in both properties. The best performing sample was the 1 wt.% composites with improvements of 14.7% and 172% in interlaminar shear strength and gauge factor, respectively, as compared to the composites with no nanoparticles.

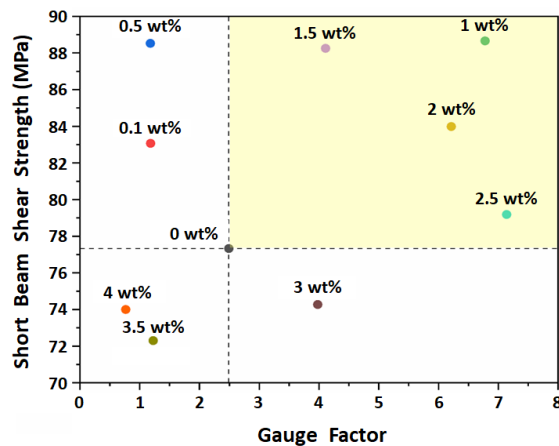


Figure II.2.9.5. Plot of the different composites showing the average interlaminar shear strength versus the average gauge factor. The dashed lines show the values for the composite without nanoparticles with the highlighted region signifying simultaneous improvements in both properties [2]. Source: ORNL.

The next step of the project was working with Dronesat to design the prototype components that could be made from the developed nanoparticle-enhanced composites. Figure II.2.9.6 shows one example of many parts that were designed by Dronesat. The example here shows the fan blade assembly with different viewpoints. The critical part of this assembly would be the point at which the blade is attached to the base. This attachment point is the most prone to failure, so it was targeted as an ideal location to place the sensing composites. These nanoparticle-enhanced composites would both enable sensing of this joint and offer increased strength to reduce composite failure. The implementation of these composites in the drone prototypes is ongoing work.

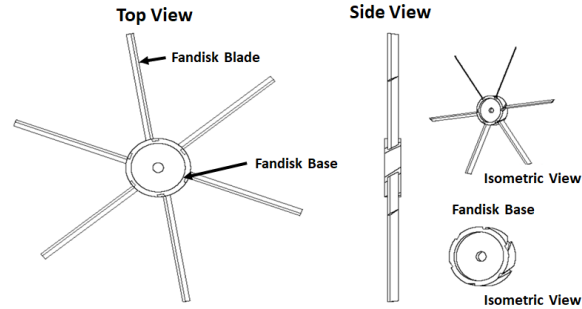


Figure II.2.9.6. Schematic design of the fan blade assembly prototype where the multifunctional composites will be integrated. Source: Dronesat.

As an extension of the dip-coating process, barium titanate (BaTiO_3) particles were coated on basalt fibers. A unidirectional composite was fabricated with tows of BaTiO_3 coated basalt sandwiched between layers of bare CF tows and embedded in an epoxy matrix. The use of two different fibers within the same composite classifies this as a hybrid composite. Placing the basalt in the middle of the composite created a hybrid composite that was not electrically conductive through its thickness, thus enabling a passive sensor to be demonstrated. An electrically insulating composite is required to allow charge accumulation between the electrodes during excitation. For testing, the two CF layers were electroded with silver epoxy, as shown in the schematic in Figure II.2.9.7(a). For the proof-of-concept of the power generation, a composite beam was clamped on one end and manually flexed by hand at the free end, as observed in Figure II.2.9.7(b). The resulting voltage generated during flexing was captured using a digital multimeter. Figure II.2.9.7(c) shows the voltage generated from different excitation events. It is seen that the composite has baseline noise vibration from the environment when not flexed, but when flexed at various magnitudes and frequencies, a corresponding voltage is generated. The zoomed-in plot in Figure II.2.9.7(c) highlights the voltage generated during the excitation events. This final task of the project demonstrated that a passive sensing composite could be synthesized using the dip-coating method developed throughout the project.

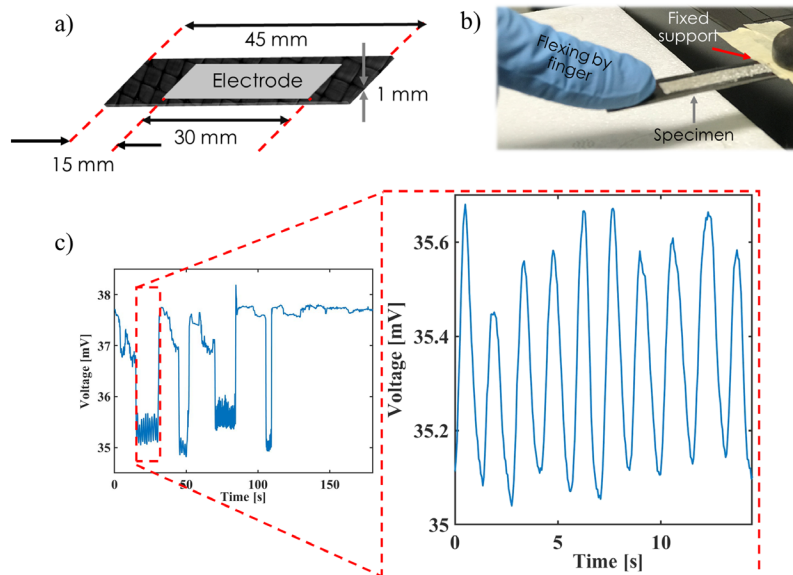


Figure II.2.9.7. (a) Schematic of the hybrid multifunctional composite. (b) Picture of the flexing test method with c) the corresponding voltage output from the composite. Source: ORNL.

Conclusions

This TCF project demonstrated that the continuous fiber dip-coating process developed at ORNL could be used to homogeneously disperse TiO₂ nanoparticles on CF to produce multifunctional composites. The interlaminar shear strength was selected as the metric for mechanical performance. Most of the composites showed increased strength, and the highest performing composite was the 1 wt.% nanoparticle composite, which showed a 14.7% increase. The structural health monitoring capabilities were evaluated by measuring the piezoresistive behavior of the composites and calculating the gauge factor for each composite. It was shown that composites with 1 wt.% to 3 wt.% nanoparticles exhibited increased gauge factor with the highest performing sample being the 2.5 wt.% composite, which had a 186% improvement. In comparing the performance of all the composites based on these two properties, the 1 wt.% composite performed the best overall with 14.7% and 172% improvements in interlaminar shear strength and structural health monitoring sensitivity, respectively. The final tasks of the project showed that the dip-coating process could be used with basalt fiber and BaTiO₃ microparticles to create a passive sensing hybrid composite. Therefore, this project produced CF coated with TiO₂ nanoparticles as well as basalt fibers coated with BaTiO₃ microparticles using a continuous feed-through dip-coating process that significantly enhanced the multifunctional performance of the composites and demonstrated both active and passive sensing composites.

Key Publications

1. Rankin, S. M., M. K. Moody, A. K. Naskar, and C. C. Bowland, 2021, "Enhancing functionalities in carbon fiber composites by titanium dioxide nanoparticles," *Compos. Sci. Technol.*, Vol. 201, Art. 108491.

References

1. Bowland, C. C., N. A. Nguyen, and A. K. Naskar, 2018, "Roll-to-roll processing of silicon carbide nanoparticle deposited carbon fiber for multifunctional composites," *ACS Appl. Mater. Interfaces*, Vol. 10, pp. 26576–26585.
2. Rankin, S. M., M. K. Moody, A. K. Naskar, and C. C. Bowland, 2021, "Enhancing functionalities in carbon fiber composites by titanium dioxide nanoparticles," *Compos. Sci. Technol.*, Vol. 201, Art. 108491.

Acknowledgments

The author would like to acknowledge S. Rankin and M. Moody for their work on this project as part of their ORNL internships, as well as A. Naskar for his supervision and assistance with this research.

II.2.10 Industrialization of Carbon Fiber Composite Wheels for Automobiles and Trucks (Oak Ridge National Laboratory)

Brian Knouff, Co-Principal Investigator

IACMI Scale-up Research Facility
Oak Ridge National Laboratory
1400 Rosa Parks Boulevard
Detroit, MI 48216
E-mail: knouffbj@ornl.gov

Michael Hayes, Co-Principal Investigator

ESE Industries
675 Ponce de Leon Avenue Northeast, Suite 8500
Atlanta, GA 30308
E-mail: m.hayes@ese-industries.com

H. Felix Wu, DOE Technology Manager

U.S. Department of Energy
E-mail: felix.wu@ee.doe.gov

Start Date: May 1, 2020	End Date: December 31, 2022	
Project Funding (FY 2021): \$1,000,000	DOE share: \$500,000	Non-DOE share: \$500,000

Project Introduction

ESE Carbon Company

ESE Carbon Company (ESE) is on track to be the second manufacturer in the world—and the first in North America—of one-piece CF composite wheels to market, behind Australia’s Carbon Revolution. ESE has invested in this technology with an engineering team comprising experts in composite materials, mechanics, design, and manufacturing. With a prototype factory in Jasper, GA, houses considerable capital investment including computer numerical control machines, an eight-head tailored-fiber placement machine, a ply cutting table, an industrial press, wheel test machines, a FARO laser scanner, and an industrial robot.

ESE brings considerable experience in wheel design and manufacturing with composite materials. The combination of its composite design and manufacturing know-how, knowledge of the wheel-specific design challenges, and understanding of the passenger vehicle wheel market are unique and unsurpassed in North America. ESE is interested in scaling from aftermarket sales to passenger car OEM’s specification and to HD truck and military applications.

Oak Ridge National Laboratory

ORNL brings capabilities crucial to meeting the goals of the team, which has decades of experience in industrial composite automotive design and optimization, as well composite materials characterization and testing. ORNL is interested in integrating LCCF into our materials portfolio, using ORNL’s Manufacturing Science Group to provide materials testing and characterization, assist in process improvement, and aid in the virtual simulation including the use of high-performance computing.

ORNL Composite Materials Characterization and Modeling

The Composites Group is part of the Manufacturing Science Group at ORNL and has established leading-edge technologies in composites processing and testing.

Objectives

The primary objective of this LightMAT project is to couple ESE's existing passenger car wheel design and manufacturing process with ORNL's expertise in materials characterization, composites processing, and computational methods to accelerate the current development phase and the subsequent commercialization phase. These phases are not sequential and may overlap.

Approach

Task 1: Baseline Materials Characterization (First and Second Year)

In Year 1, ESE developed the plaque fabrication tool for this characterization and ORNL had initiated cutting of samples for testing. The first set of testing included tensile and flexural samples. Due to delays testing caused by the pandemic, the materials testing has continued into Year 2 of the program. In Year 2, fatigue testing has been initiated and will be reported here.

The original tasks included design optimization for Year 2. ESE was able to bring these tasks forward to Year 1 during the pandemic and will be reported here.

Results

Task 1. Baseline Materials Characterization

ESE provided cross-ply [0/90/90/0] and unidirectional [0] flat panels of 9.42 in. × 9.42 in. × 0.13 in. to evaluate the baseline mechanical properties. Unidirectional tensile and flexural properties were obtained as shown in Table II.2.10.1.

Table II.2.10.1. Fiber Properties (From Manufacturer) and Mechanical Testing Properties of the Plaques Provided by ESE

Sample Type	Tensile Strength, ksi	Tensile Modulus, ksi	Flexural Strength, ksi	Shear Strength, ksi	Flexural Modulus, ksi
Fiber	808	37,000	—	—	—
Plaque	260	21,000	221	10	19,000

Tensile strength results were used to back calculate fiber volume fraction resulting in 32%, which is much lower than anticipated. Using tensile modulus, however, resulted in a fiber volume fraction of 57%, which is in-line with expectations (actual $V_f = 55\%$). That study found that the various strength parameters were up to 50% lower than handbook data for similar composites. ESE initiated a root cause failure analysis under the assumption that the stitching process affects the strength of the fibers, or the plaques and ESE is currently researching this effect. Data collected to date has demonstrated several ways to improve strength including stitching parameter changes and different backing materials. The study is ongoing.

Static compression and fatigue test coupons were extracted from cross-ply panels to generate fully reversed RT fatigue data. For fatigue mechanical testing, test coupons were extracted from cross-ply, 0° unidirectional, and 90° unidirectional composite panels using a waterjet.

Cross-Ply Static Compression Testing

Unidirectional linear strain gauges were placed on compression samples to evaluate the compressive strength to guide the choice of stress levels for fatigue testing, as observed in Figure II.2.10.1. The average compressive strength and modulus of cross-ply sample were 53.24 ± 2.12 ksi (367.08 ± 14.64 MPa), and 5.93 ± 1.26 Msi (40.85 ± 8.66 GPa), respectively. The sample failed in through-thickness mode within the gauge area shown in Figure II.2.10.1.

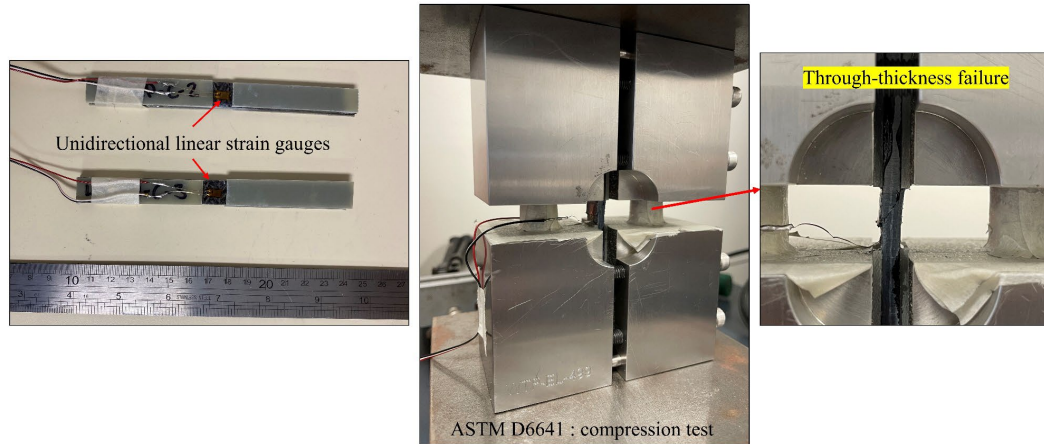


Figure II.2.10.1. Showing prepared compression samples with linear strain gauges, compression testing using CLC fixture, and through-thickness failure mode. Source: ORNL.

Fatigue Testing

The first cross-ply fatigue sample was tested in tension/compression with $R = -1$ at 70% UCS, 37.27 ksi (256.96 MPa) and with 1 Hz frequency. Due to the sample undergoing Euler column buckling, however, the sample failed during the first cycle. The gauge length was altered to prevent this from occurring and the test was rerun, resulting in no failure even after 1,821,351 fatigue cycles. The test was stopped since the sample was able to achieve over 1 million fatigue cycles (ESE's desired fatigue cycle target). ESE then suggested to test fatigue the sample at a higher stress level of 80% UCS and to eliminate the remaining fatigue testing at lower stress levels of 50% and 60% UCS.

The modified fatigue sample of 0.5 in. \times 3.5 in. with a gauge length of 0.5 in. was tested in tension/compression with $R = -1$ at 80% UCS, 42.59 ksi (293.67 MPa), and at 5 Hz frequency. The sample observed 88,881 fatigue cycles prior to multimode failure due to through-thickness and transverse shear.

Unidirectional Tension Testing

Tensile testing was performed for the 0° and 90° unidirectional composite showed average tensile strength and modulus of 186.92 ± 13.02 ksi (1288.77 ± 89.77 MPa) and 19.35 ± 0.15 Msi (133.39 ± 0.96 GPa), respectively. The 90° unidirectional composite showed average tensile strength and modulus of 4.51 ± 0.03 ksi (31.10 ± 0.23 MPa) and 1.09 ± 0.04 Msi (7.50 ± 0.26 GPa), respectively.

Unidirectional Compression Test

The average compressive strength and modulus of the 0° unidirectional sample were 90.27 ± 14.41 ksi (622.42 ± 99.34 MPa) and 18.43 ± 1.29 Msi (127.08 ± 8.91 GPa), respectively. Similarly, the average compressive strength and modulus of the 90° unidirectional sample were 15.49 ± 0.11 ksi (106.82 ± 0.78 MPa) and 1.36 ± 0.07 Msi (9.38 ± 0.46 GPa), respectively.

Virtual Simulation

ESE was able to perform much of the modeling in Year 1 during the first year of the pandemic. The models are intended to simulate the SAE International (SAE) engineer practices²⁰ albeit using simplified approaches. Figure II.2.10.2, Figure II.2.10.3, and Figure II.2.10.4 show schematics of the FEM performed in Abaqus by ESE: SAE J328 Cornering Fatigue, SAE J175 Curb Impact, and AK-LH 08 Radial (Pothole) Impact analyses. The cornering fatigue test applies a bending moment to the mounting surface of the wheel through a simulated axle ("moment arm") with the inboard flange of the wheel clamped to a rotating table. In the analysis, ESE treats the test as a quasi-static load for a relatively quick simulation and iteration. A design margin is applied to the resulting stresses to account for fatigue life.

20. A newly published version of these engineering practices, SAE J3204 "Aftermarket Composite Wheels Made of Matrix Material and Fiber Reinforcement Intended for Normal Highway Use—Test Procedures and Performance Requirements", adopts these tests to composite wheels.

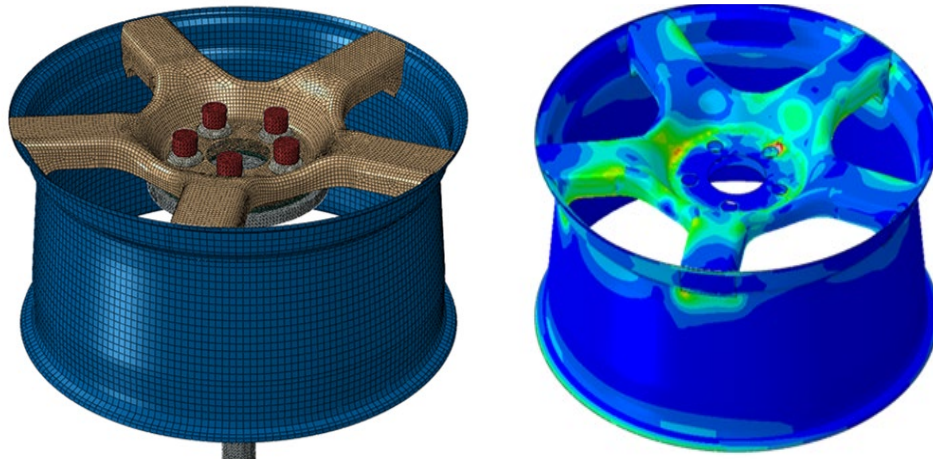


Figure II.2.10.2. Mesh and static analysis results of cornering fatigue showing stiffness of 400 kN-m/rad. Source: ESE.

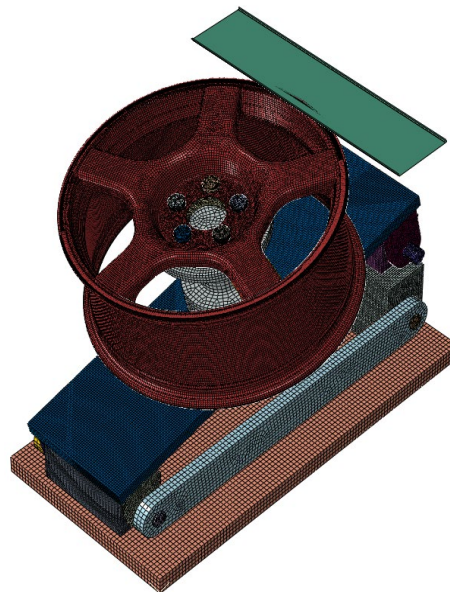


Figure II.2.10.3. Curb impact analysis of the composite wheel without the tire. Source: ESE.

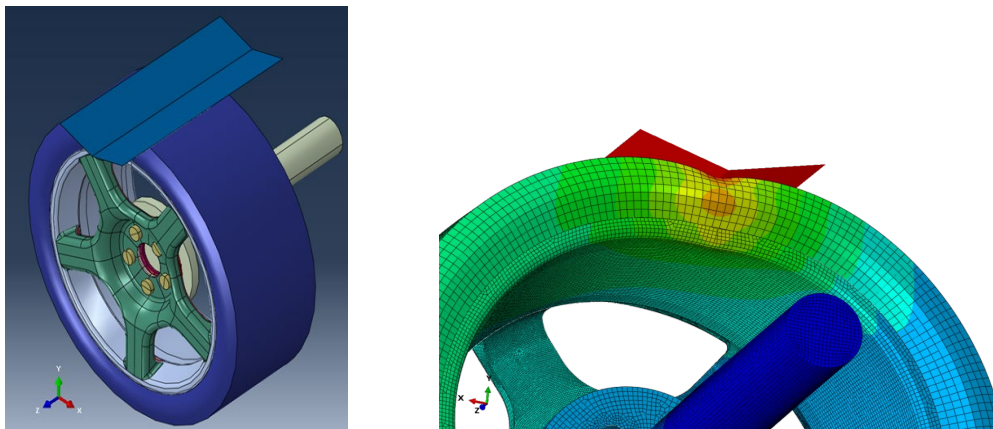


Figure II.2.10.4. Radial (pothole) impact analysis of the composite wheel with the tire. Source: ESE.

In the case of the impacts, simulations are performed in Abaqus Explicit to capture dynamic effects. A full dynamic explicit analysis was used to model curb impact using an SAE J175 support fixture, which includes steel components and rubber compression mounts intended to simulate a car's suspension/chassis response. In the absence of a proper tire model, the tire is currently omitted for simplicity and to allow direct impact to the outboard flange. The analysis has shown reasonable correlation with design changes in the wheel despite the actual material strength parameters being much lower than the assumed handbook material properties used in the analysis. ESE is working to improve the model by incorporating a more sophisticated rubber material model for the compression mounts and a better composite damage model.

The pothole analysis model requires the use of a tire and is, therefore, still in early development. A simplified tire model with homogenized linear elastic properties has been incorporated to allow for some analysis. While still in its infancy, the model has provided mechanics insight and a means of comparing different designs.

Conclusions

Testing: In conclusion, fatigue testing parameters were modified to obtain fully reversed RT fatigue data. Cross-ply static compression, fatigue, unidirectional tension, flexural, and compression testing were successfully conducted. Iosipescu testing will be conducted as per ASTM standard to evaluate the shear properties as shown in Figure II.2.10.5.

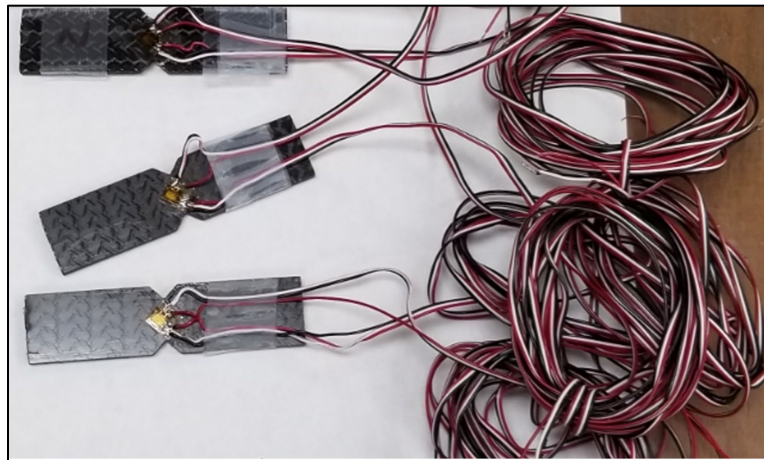


Figure II.2.10.5. Iosipescu samples strain gauged and ready for testing. Source: ORNL.

Modeling: Virtual modeling was performed using Abaqus in Year 1 to design the wheel for cornering fatigue, curb impact, and radial (pothole) impact.

Acknowledgments

The authors would like to thank S. Alwekar, A. Haug, and U. Vaidya from the Fibers and Composite Manufacturing Facility at the University of Tennessee for preparing the fatigue samples, interpreting the results, and assisting in the writing of this report, in addition to D. Erdman from ORNL for performing much of the testing.

II.2.11 LightMAT: A Novel Manufacturing Process of Lightweight Automotive Seats – Integration of Additive Manufacturing and Reinforced Polymer Composite (Oak Ridge National Laboratory)

Vlastimil Kunc, Principal Investigator

Oak Ridge National Laboratory
1 Bethel Valley Road
Oak Ridge, TN 37830
E-mail: kuncv@ornl.gov

H. Felix Wu, DOE Technology Manager

U.S. Department of Energy
E-mail: felix.wu@ee.doe.gov

Start Date: February 21, 2020 End Date: November 20, 2022
Project Funding (FY 2021): \$1,000,000 DOE share: \$500,000 Non-DOE share: \$500,000

Project Introduction

Thinner, lighter weight seats offer multiple benefits to vehicle OEMs in terms of cost-savings from various aspects, including less material usage, more integrated processes, and avoiding CAFE civil penalties. For this reason, OEMs are focused on innovative opportunities for lightweight automotive seats. In this project, a novel manufacturing technology will be developed for a lightweight car seat that involves multiple novel composite manufacturing processes including large-scale AM, discontinuous reinforced composite, AM metal insert attachment, and topology optimization. The car seat back panel will be made with tailored microstructure and hence tailored performance. Design and distribution of the panel reinforcement ribs will be optimized via proven adaptive core optimization technology. The optimizations for the core structure will be based on computational stress analysis to maximize the stiffness and minimize the weight. AM metal inserts for the recliner connection will be integrated into the composite structure during the manufacturing process. All the seat components will be consolidated under pressure to form the final seat geometry in one step. A database will be generated during the manufacturing process to enhance the quality control system using an artificial intelligence (AI) framework.

Objectives

The aim of this LightMAT project is to develop a novel manufacturing technique to produce lightweight car seats by combining AM and conventional techniques. Note that the scope of the project is limited to the primary structure of the seat assembly. This does not include any electric motors, sensors, actuators, or seat coverings that represent the bulk of the seat assembly mass. Instead, this project focuses on the developing AM and overmolding methods that not only apply to seat structures but would also be relevant to a broad range of structural applications across all vehicle subsystems. The newly developed materials and processes will:

- Reduce the mass of the primary seat structure.
- Allow for new/smart seat designs via topology optimization, which cannot be achieved through any other conventional processing methods.
- Produce seats with improved performance.
- Allow for in-line integration of sensing and smart systems that will be used for process monitoring. The collected data will be used within an AI framework for discontinuous reinforced composite manufacturing processes to optimize the processing conditions and part performance.

Approach

The innovative approach for seatback manufacturing to be developed for this project is illustrated in Figure II.2.11.1, which integrates three major manufacturing techniques: (1) adaptive lattice structure generation; (2) AM preform with controlled deposition direction; and (3) overmolding on metal inserts.

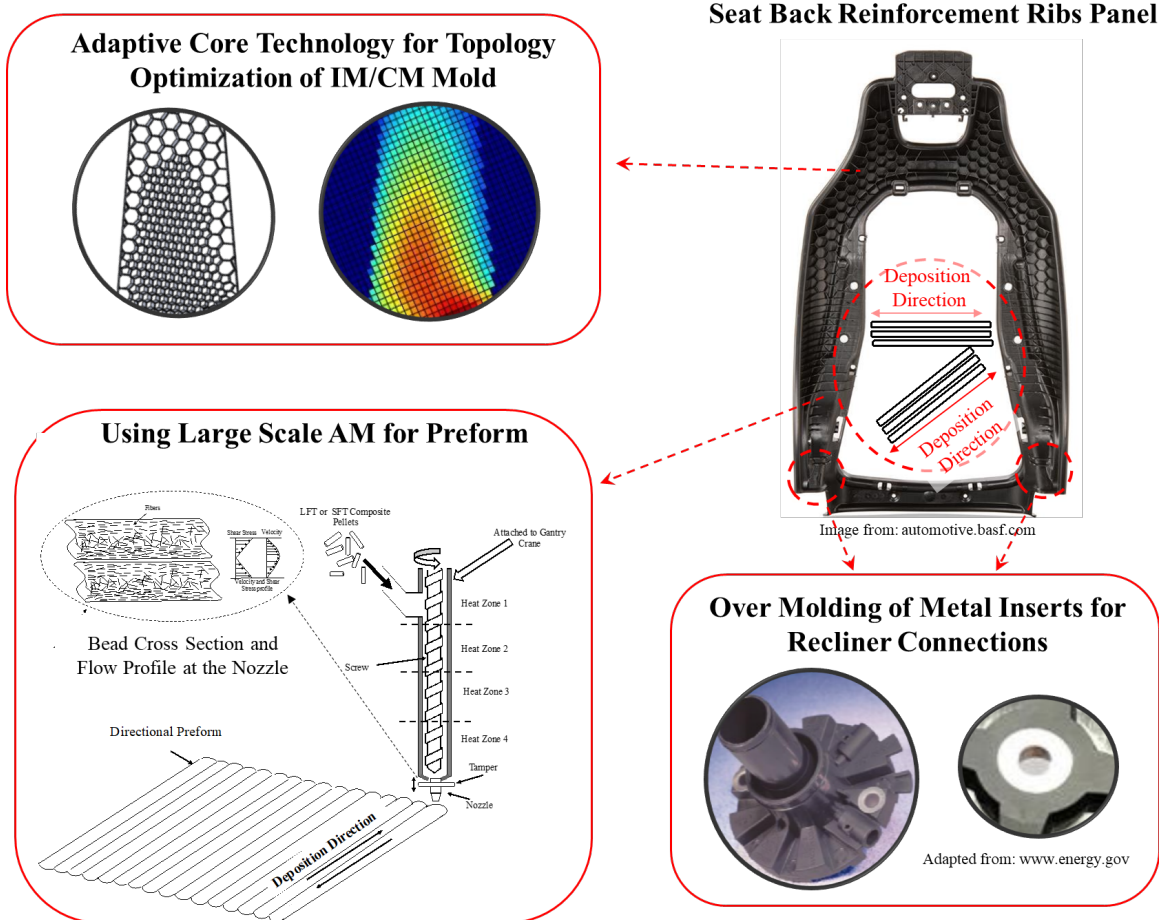


Figure II.2.11.1. An innovative approach for seatback manufacturing that integrates adaptive lattice structure generation, AM preform with controlled deposition direction, and overmolding on metal inserts. Source: ORNL.

Stage I: Topology Optimization of a Seatback Panel, Including ORNL’s Recently Developed Adaptive Lattice Method

- In this stage, the design of the seatback frame is topologically optimized, including ORNL’s recently developed adaptive lattice generation method [1]. Using this method, the structure with its lattice densities can be optimized based on a stress applied to the structure. The local density of the lattice cells is determined based on the stress profile. The infill geometry is mathematically generated using a circle packing algorithm.

Stage II: Manufacturing of the Seatback Panel Via Large-Scale AM

- In this stage, a large-scale AM system (i.e., capable of greater than 100 lb/h deposition rate and a size up to 20 ft × 8 ft × 6 ft) is used to form a preform of the seatback panel. The process is highly capable of producing preforms with highly aligned fibers at the deposition direction. Optimization and control of the tool path (i.e., deposition direction) allows the fabrication of preforms with tailored microstructure and properties. The system also can be used to deposit multi-materials to help reduce the weight of the

seat even further. As an example, the preform can be made from a reinforced thermoplastic for load bearing areas where foams can be deposited at locations where there are no load bearing requirements.

Stage III: Overmolding Process (Integration of the Seatback Panel Preform, Molding of the Reinforcement Features, and Placement of the Metal Inserts)

- In this stage, the AM preform manufactured in Stage I is transferred to a compression mold for consolidation under pressure. After placing the preform and the metal inserts for the recliner connection into the mold, the mold is heated up to the molding temperature. An extrusion compression molding process is used to mold the seat reinforcement features. Extruded charges will be strategically placed on the top of the AM preform in the mold and then all components are consolidated under pressure to form the final seat geometry in one step.

Results

This LightMAT project started in February 2020, and soon after, the project team had major delays and limitations in our laboratory facility access and getting resources after we started the project due to the COVID-19 pandemic. A 9-month extension was requested and granted. The project team is catching up on the delayed work during the extended time.

We have developed an optimal design of the subcomponent of the seatback where the stress is the highest as shown in Figure II.2.11.2 during the previous FY. The design involves a novel hybrid manufacturing technique including overmolding of polymer AM preform with long fiber onto a metal AM mesh. The deflection of this subcomponent (7.6 mm) was predicted by simulation to be much less (53%) than the original design (16.3 mm).

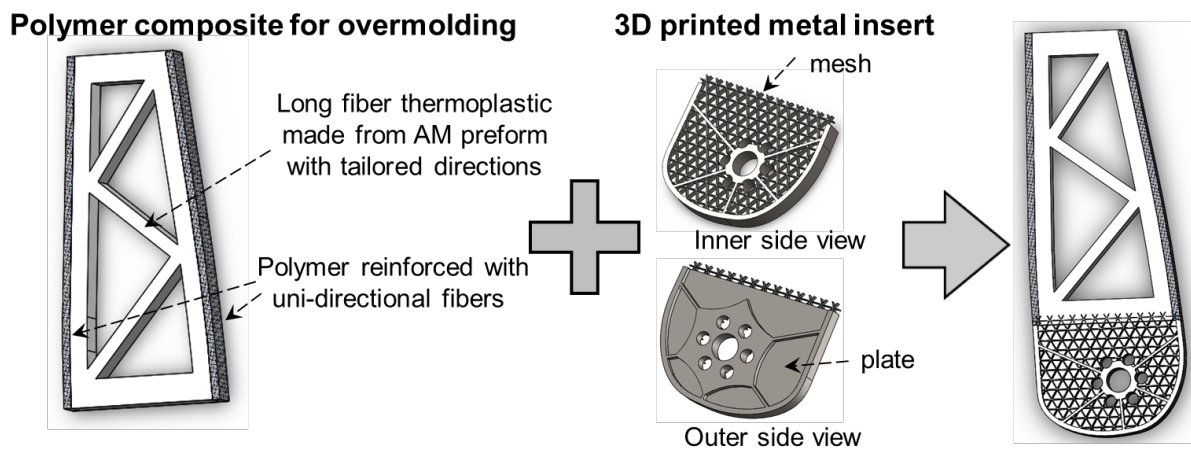


Figure II.2.11.2. Design developed in a previous FY involving a novel hybrid manufacturing process using overmolding of polymer AM onto metal AM. Source: ORNL

Efforts in FY 2021 focused on the development of *Stage II: Manufacturing of the Seat Back Panel via Large-Scale AM*. One of the most important areas of the seat back is the overmolded component, and there is no clear understanding in the literature for the manufacturing process of overmolded AM metal mesh with long fiber thermoplastic (LFT) composites. To understand the process, we designed an experiment that was conducted on flat panels to simplify the processes (i.e., decouple the manufacturing process effect from the shape complexity). We designed and evaluated several mesh sizes to understand the material flowability, as shown in Figure II.2.11.3(a). In addition, several different tensile test designs were made as shown in Figure II.2.11.3(b) to represent/understand different sections of overmolding locations and different loading conditions the component will be subjected to. The meshes in Figure II.2.11.3(b) are for overmolding on a metal mesh: (b.1) with no backing plate; (b.2) with a backing plate; and (b.3) with half mesh and backing and half LFT without a backing plate.

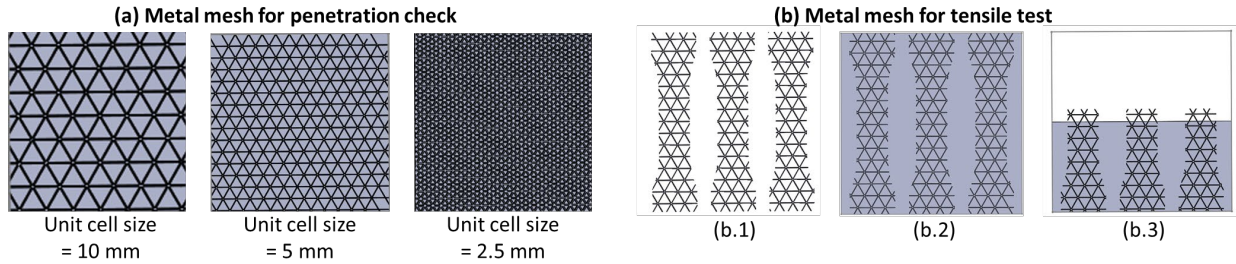


Figure II.2.11.3. Design of several metal AM parts. (a) Meshes with different unit cell sizes. (b) Meshes for tensile tests. Source: ORNL.

We have also designed an experimental shear test setup. A typical shear test focuses on adhesives between one or two materials, and therefore, the upper and lower substrate bars are typically made of the materials, and the adhesive is used to bond the material. The shear test in this project is unique, because we do not have an adhesive, and we are not testing the adhesive, but rather the thin sample should be tested. Therefore, there is no off-the-shelf method for the experimental test setup. We have designed the manufacturing method for the shear test sample manufacturing as shown in Figure II.2.11.4.

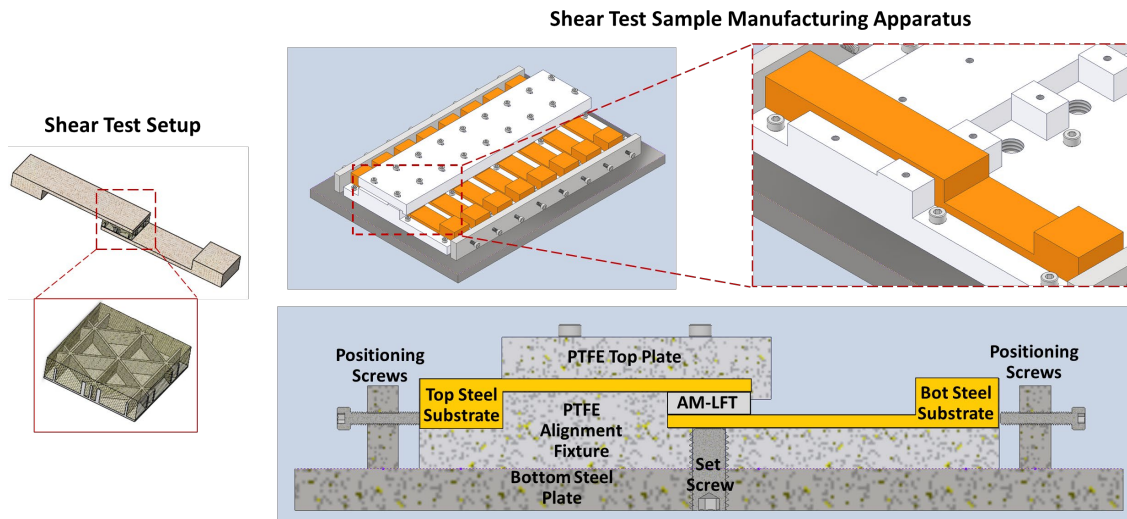


Figure II.2.11.4. Experimental shear test setup and the apparatus of manufacturing shear test samples. Source: ORNL.

Figure II.2.11.5 shows the AM processes from a metal powder laser system and a polymer composite extrusion system. Figure II.2.11.5(a) shows the laser process for metal AM Laser Powder Bed System (AddUp) that was used in this work. The parts were manufactured using maraging steel. Figure II.2.11.5(b) shows the preform made from the big area additive manufacturing (BAAM) system.

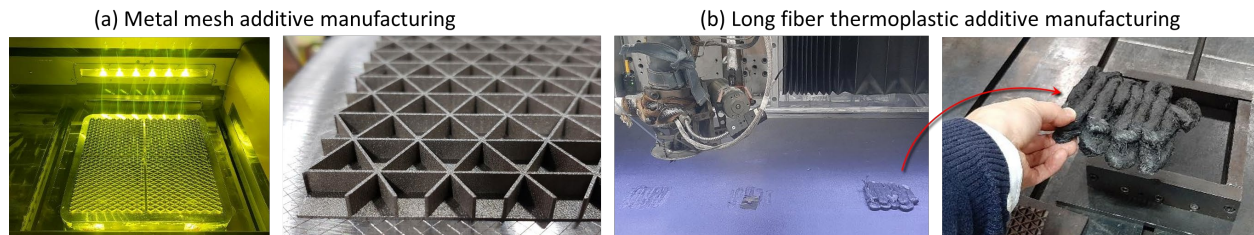


Figure II.2.11.5. (a) Metal mesh AM using (b) a metal powder laser AM system (AddUp) with the LFT. Source: ORNL.

Figure II.2.11.6 shows the proposed overall overmolding process. The overmolding process consists of three stages: (i) AM metal mesh manufacturing as in Figure II.2.11.6(a), (ii) AM polymer composite preform manufacturing as in Figure II.2.11.6(b) (We produced 152-mm x 152-mm preforms, and the material used for the preforms were LFT PA66/CF with 30% CF loading), and (iii) a compression overmolding process. The metal mesh was placed on the mold and then the AM preform was placed on the top and inserted into the press, as shown in Figure II.2.11.6(c). The mold was heated up to PA66 melting temperature, then a 147 kN (15-ton) load was applied for 15 mins. The part was then cooled and demolded. The cycle time for one overmolded part was around 45 mins to one hour. Notably, the processing parameters went through multiple optimization trials (e.g., optimizing material flash, low consolidation pressure, and parts with short mold fills), as shown in Figure II.2.11.7.

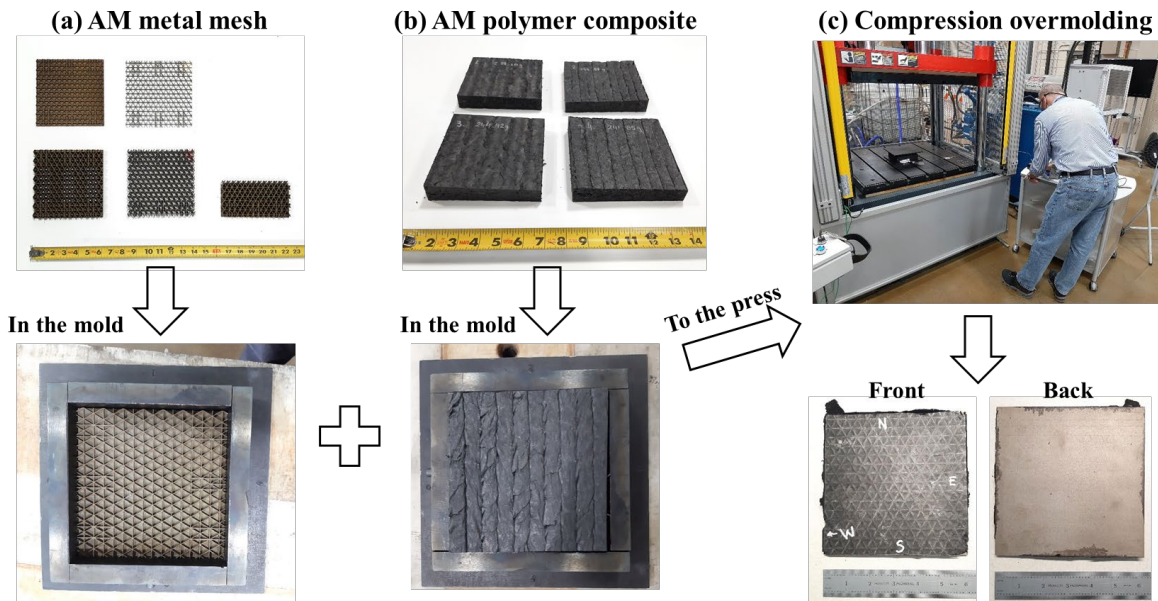


Figure II.2.11.6. Overmolding process (a) AM metal mesh; (b) AM LFT preform on top of the AM metal mesh; and (c) compression overmolding. Source: ORNL.

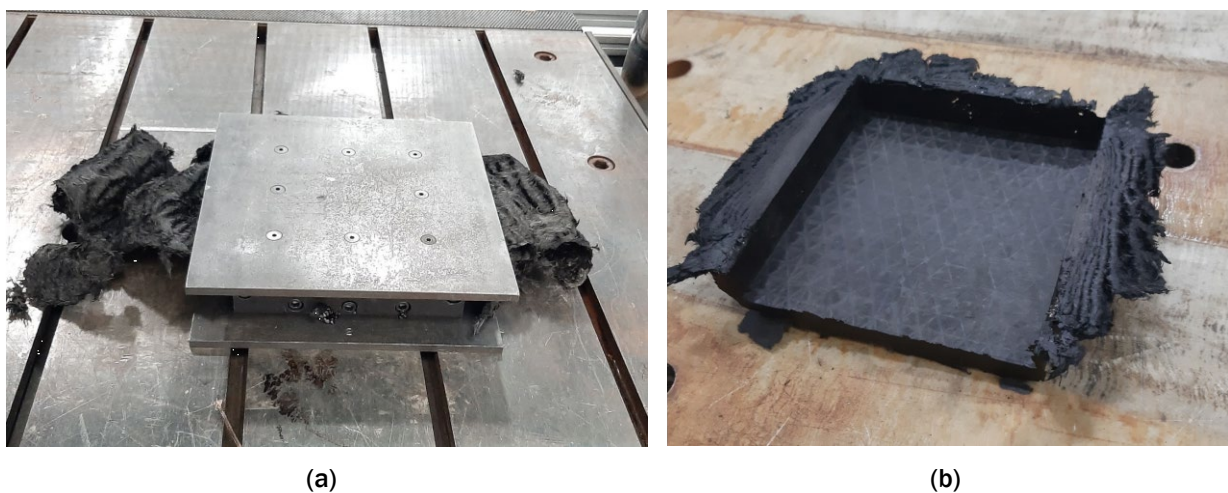


Figure II.2.11.7. Optimization process for the molding parameters. (a) Excess pressures and temperatures. (b) Good consolidation; however, excess materials flash. Source: ORNL.

The material penetration is affected by the depth of the mesh. Figure II.2.11.8(a) shows a cross-section for the molded part with a 4-mm depth mesh. The cross-section view shows a good penetration, and therefore, a good bonding between metal and polymer composites. The 13-mm depth mesh, however, showed a poorly penetrated polymer from the back side, as shown in Figure II.2.11.8(b).

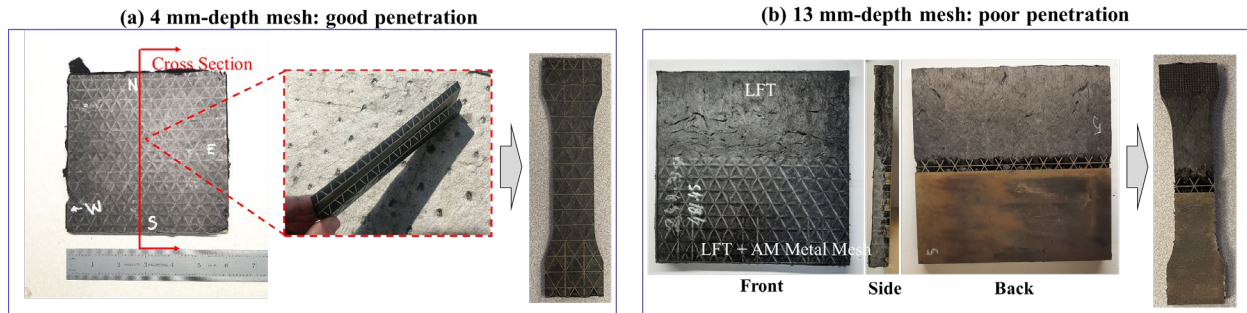


Figure II.2.11.8. (a) Cross-section for the 4-mm depth overmolded sample showing good material penetration into the mesh. (b) Cross-section of a 13-mm depth mesh with poorly penetrated polymer on the back side. Source: ORNL.

We machined the samples into dogbone-type tensile bars and performed tensile tests. Figure II.2.11.9 shows the dogbone-type tensile bars from the two different meshes. For a 4-mm depth mesh, we obtained the modulus of 9.1 GPa and the strength of 76 MPa. For a 13-mm depth mesh, we obtained the modulus of 6.9 GPa and the strength of 45 MPa. For a 13-mm depth mesh with half LFT and half mesh backed LFT, due to a poor penetration especially at the transition, very poor mechanical properties were obtained (0.16 GPa modulus and 6.5 MPa strength). The results suggest that the mesh depth should be carefully chosen for manufacturing, and 4-mm depth gives good bonding between the polymer and the metal mesh.

Process scaling up is currently ongoing to reduce the cycle time of the process. We manufactured 356-mm x 356-mm AM preforms and AM metal mesh structures, see Figure II.2.11.9. To reduce the cycle time, we will use a conveyor belt oven to heat the preform and transfer it to a fast-acting press to be overmolded over the metal mesh (cycle time will be less than 10 minutes).



Figure II.2.11.9. AM preform made of long carbon fiber-reinforced PA66 (356-mm x 356-mm). Source: ORNL.

We are also working on a sub-scale mold design for the seatback. In this process the complex-geometry will be molded with the addition of unidirectional tapes for locally reinforcing weak spots of the overmolded part. Using the optimized subpart, we optimized the overall seatback from the first iteration of the topology optimization as shown in Figure II.2.11.10. We will continue this effort on the entire seatback optimization while finding weak spots and proposing reinforcing methods. We will also design the mold according to the findings from this study.

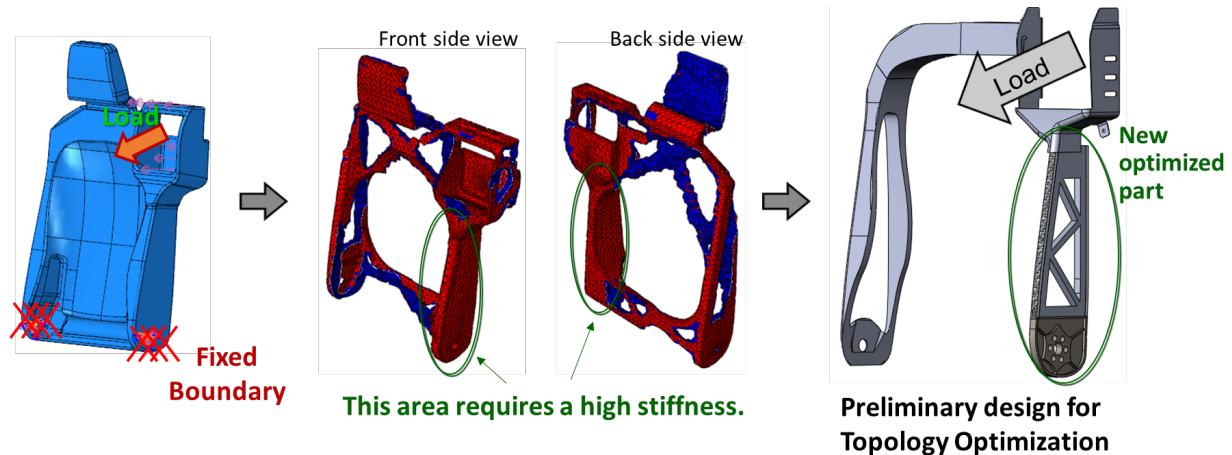


Figure II.2.11.10. Preliminary design of a seatback with the new optimized subpart for hybrid manufacturing technologies. Source: ORNL.

Conclusions

This year's effort focused on manufacturing of the seat back panel via large-scale AM. We have additively manufactured metal meshes with various depths using a metal powder laser system, and also additively manufactured preforms using a BAAM system with a long CF-reinforced nylon (CF/PA66). A higher CF loading (30%) was used for higher stiffness. After multiple iterations, we successfully printed the preforms and overmolded the preforms on the metal meshes. Low-depth meshes (4 mm) showed good bonding. High-depth meshes (13 mm) showed poor penetration, resulting in low mechanical properties, especially for the transition sample from metal mesh to a complete LFT. An experimental shear test setup was specially designed for this project and the manufacturing method was also designed. The overall seatback design was optimized with the previously designed subcomponent. We will design the mold for subcomponent manufacturing based on the findings from this FY's study.

References

1. Gounley, J., M. Vardhan, E. W. Draeger, P. Valero-Lara, S. V. Moore, and A. Randles, 2022, "Propagation Pattern for Moment Representation of the Lattice Boltzmann Method," *IEEE Trans. Parallel Distrib. Syst.*, Vol. 33, No. 3, pp. 642–653.

Acknowledgments

This project was performed in collaboration with Ford Motor Company.

II.2.12 Multi-Functional Smart Structures for Smart Vehicles (Ford Motor Company)

Patrick Blanchard, Principal Investigator

Ford Motor Company
2101 Village Road
Dearborn, MI 48121
E-mail: kuncv@ornl.gov

H. Felix Wu, DOE Technology Manager

U.S. Department of Energy
E-mail: felix.wu@ee.doe.gov

Start Date: October 1, 2020 End Date: December 31, 2023
Project Funding (FY 2021): \$1,399,891 DOE share: \$839,935 Non-DOE share: \$559,956

Project Introduction

Composite materials offer engineering solutions for novel lightweight structures. However, these are typically passive structures and offer little in the way of additional functionality. Consequently, this project seeks to develop a new class of multifunctional composite materials and processing technologies that can lead to lightweight fully integrated smart structures and surfaces. These new materials and processing methods promise to have application to a broad range of automotive applications thus magnifying the impact on the ability to achieve long-term improvements in fuel economy and/or vehicle driving range.

Objectives

This project will develop a new class of recyclable multifunctional composite materials to produce lightweight smart structures and surfaces. Functional high stiffness conductive composites will be processed using novel water assisted injection molding, while integrating continuous fiber and additively manufactured hard points for optimized load transfer. Methods for integration of sensing functionality and controls will be developed to reduce system cost while providing a new capability for structural health monitoring. Final part performance and processing parameters will be optimized using AI ML methods. This new class of composites is applicable to a broad range of vehicle interior, exterior, and battery enclosure systems. By way of demonstration, a vehicle instrument panel cross car beam (XCB) will be developed to provide a 40% mass savings compared to the baseline steel component while maintaining a cost penalty of less than \$3 per pound saved. These technologies will be validated for implementation by a uniquely qualified project team comprising a Ford Motor Company (Ford) (OEM) and Yanfeng Global Automotive Interiors (Yengfen) (Tier 1), with key contributions from ORNL, Purdue University (Purdue), and Michigan State University (MSU).

Approach

To manage project complexity, the 11 workstreams in Figure II.2.12.1 have been created to support various aspects of the technology development. The design work stream serves as the lead activity with all other work streams acting as dependents.

RASIC Chart: Multi-Functional Smart Structures For Smart Vehicles						
R: Responsible: The Institute/Company Responsible for this task A: Approve: The company/institute giving the approval S: Supporting: The Company/Institute giving support for the completion of the task I: Informed: The Compaby/Institute to inform about this task C: Consulted: The company/institute that can act as expert in regard to the task						
	Michigan State University	Purdue University	Oak Ridge National Lab	Ford Motor Company	Yanfeng	
Task 0. Program Management				R		
Task 1. Component Design, Analysis & Prove-Out	I	S	S	R, A	S	
Task 2. Formulation/Compounding of novel materials	I	I	R	S, A	R	
Task 3. Water-Assist Injection Molding (WAIM) Process Development	S	I	S	R	S	
Task 4. Tow/Tape Placement of Continuous Fiber	I	R	S	S	S	
Task 5. Sensor Integration	I	S	S	R	S	
Task 6. Additive Manufactured Hardware Attachment Points	S	S	R	S	S	
Task 7. High Volume Manufacturing Concept Feasibility Demonstration (sub-scale)	S	S	S	S	R	
Task 8. Process Scale Up & Demonstration	S	S	S	S, A	R	
Task 9. Additive Manufacturing of Segmented Tooling	I	S	R	S	I	
Task 10. Artificial Intelligence/Machine Learning For Process Optimization		I	R	I	S	
Task 11. Closed Loop Recycling		I	R	S	S	

Figure II.2.12.1. Project task breakdown. Source: Ford.

The work plan is divided into three BPs:

- **Budget Period 1 (October 2020–December 2021): Concept Design & Development:** The team has established design data, CAD details, functional attributes, and load case data for an existing benchmark design. Design concepts for a multifunctional structure have since been developed with a single design concept for an XCB to be selected at the end of Budget Period 1.
- **Budget Period 2 (January 2022–December 2022): Design, Materials, & Process Optimization:** Further refinements will be made to the XCB design based on manufacturing feasibility trials, material, and process optimization. Unit cell operations for overmolded structural inserts and sensors will be demonstrated.
- **Budget Period 3 (January 2023–December 2023): Prototype Validation & Testing:** The final budget period will focus on fabrication of prototype tooling to manufacture XCBs for testing and validation. Materials and processing optimization will continue. Full-scale injection molding will be demonstrated. The ability to place inserts and continuous fiber during injection molding will be demonstrated.

Results

Task 1. Component Design, Analysis, and Prove-Out

The design activities in Budget Period 1 were broken down into subtasks 1.1 to 1.4. Milestones scheduled in Budget Period 1 for Tasks 1.1, 1.3, and 1.4 are shown in Table II.2.12.1.

Table II.2.12.1. Milestones for Task 1 Work Stream Activities

Milestone (Project Month)	Lead Organization	Description
1.1.1 Concept Development (M1)	Ford	Compile attribute/functional requirements for XCB and establish initial design concepts.
1.1.3 Design Sections (M9)	Ford	Transfer design sections to water-assist and sensor integration teams. Complete two manufacturing feasibility assessment cycles.
1.1.4 Performance Targets (M9)	Purdue	Establish cost and performance targets. Develop framework for realistic manufacturing alternatives based on performance and cost targets for the selected application.

Task 1.1 and Task 1.2

At the commencement of the project in October 2020, the Ford engineering team identified the instrument panel XCB system shown in Figure II.2.12.2 and Figure II.2.12.3 as representative of the current state-of-the-art. This baseline architecture was used as a platform to establish all functional requirements while finalizing new technologies to be integrated into the XCB structure. During this study, a review of system interfaces was performed to capture all inputs, controls, and noise factors. This led to a list of primary interfaces and associated hardware that need to be accommodated during the final demonstration phase of the project in Budget Period 3. Per Milestone 1.1.1, this information was disseminated to the project team to allow appropriate targets for dependent tasks to be established. Key interfaces and hardware modules that require ongoing consideration, or are to be packaged in the new design include:

- Vehicle body in white (BIW) mounting locations and volume capacity
- Instrument panel cluster/displays
- Entertainment/navigation unit
- Wiring harnesses
- Steering column subassemblies
- Heating ventilation and air-conditioning unit
- Instrument panel Class A trim components
- Center console subassembly
- Pedal box subassembly
- Air bag systems
- Glove box
- Hood release.

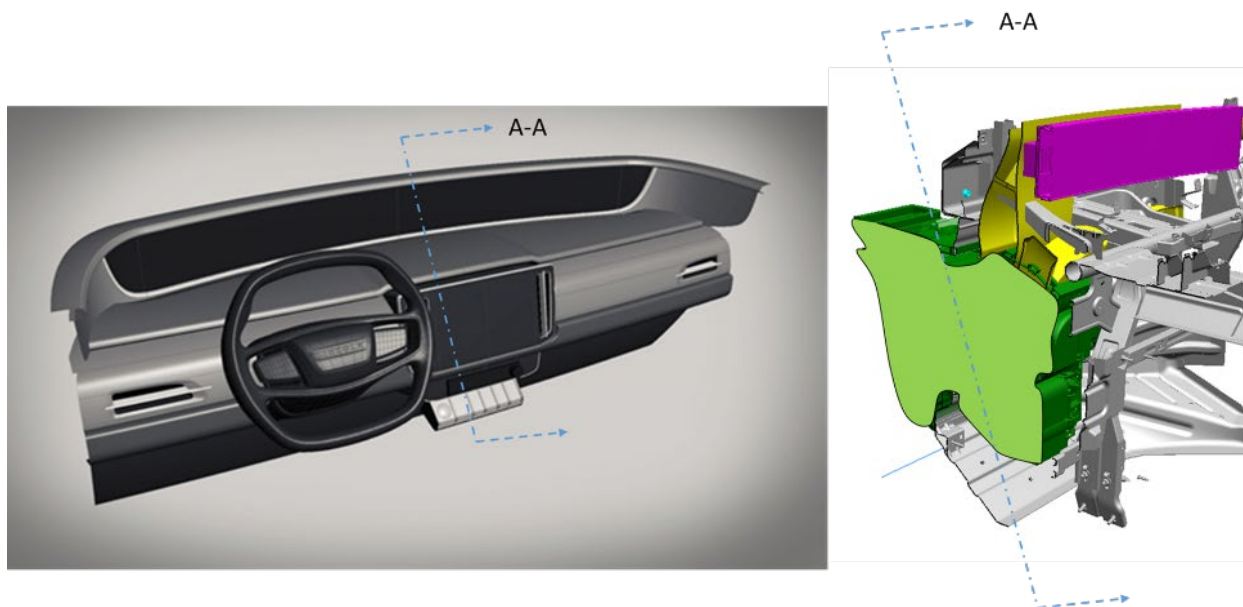


Figure II.2.12.2. Instrument panel XCB system to be adapted to accommodate the new multifunctional XCB structure. Source: Ford.

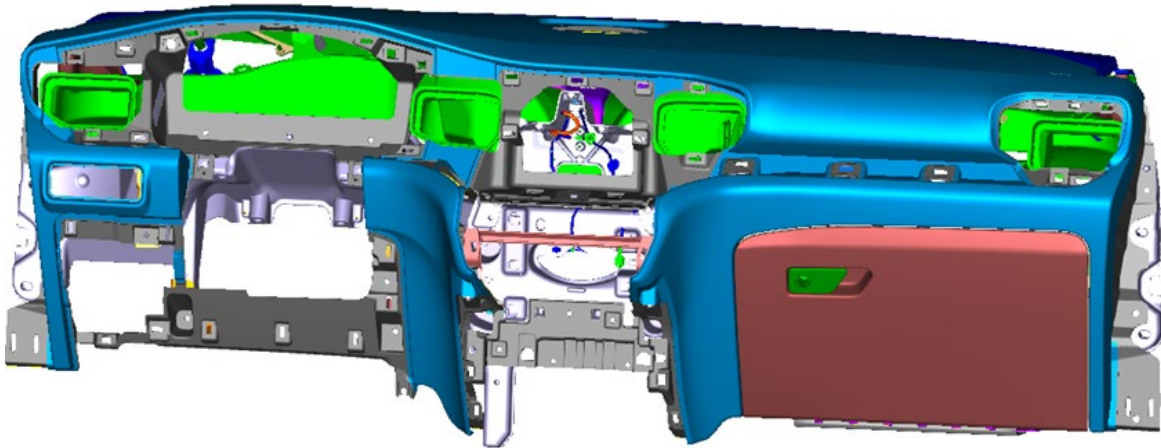


Figure II.2.12.3. CAD rendering of a representative instrument panel structure highlighting surrounding system hardware. Source: Ford.

Since establishing the system requirements, the team has focused on developing 3D CAD models for the XCB structure. An iteration loop was established whereby geometry was developed in 3D CAD before conversion into a mesh model for subsequent CAE model analysis. Table II.2.12.2 shows an example of a series of design/CAE iteration loops that has been completed to support the ongoing concept development. An example of CAE design and analysis results are shown in Figure II.2.12.4(a)–(b).

Table II.2.12.2. Task 1.2 CAE Iterations in Support of the XCB Structural Design

Iteration	Analysis Steps
1	Receive CAD and converted CAE Model.
2	Add the steering column model into structure.
3	Update thickness of water-assist channels.
4	Perform topology optimization for vertical natural frequency targets.
5	Perform topology optimization for lateral natural frequency targets.
6	Remove upper water channel (front surface removed).
7	Remove lower water channel (front surface removed).

Optimization runs indicated that the stiffening features proposed for the XCB are providing the necessary structure towards meeting system requirements. However, updates will continue through the end of Budget Period 1 to represent the location of the closed sections, continuous fiber reinforcements, and the hardware attachment points more accurately under development in Task 1, Task 4, and Task 6 respectively. These CAE model updates will be performed throughout the final quarter of Budget Period 1 ahead of a Go/No-Go gateway review.

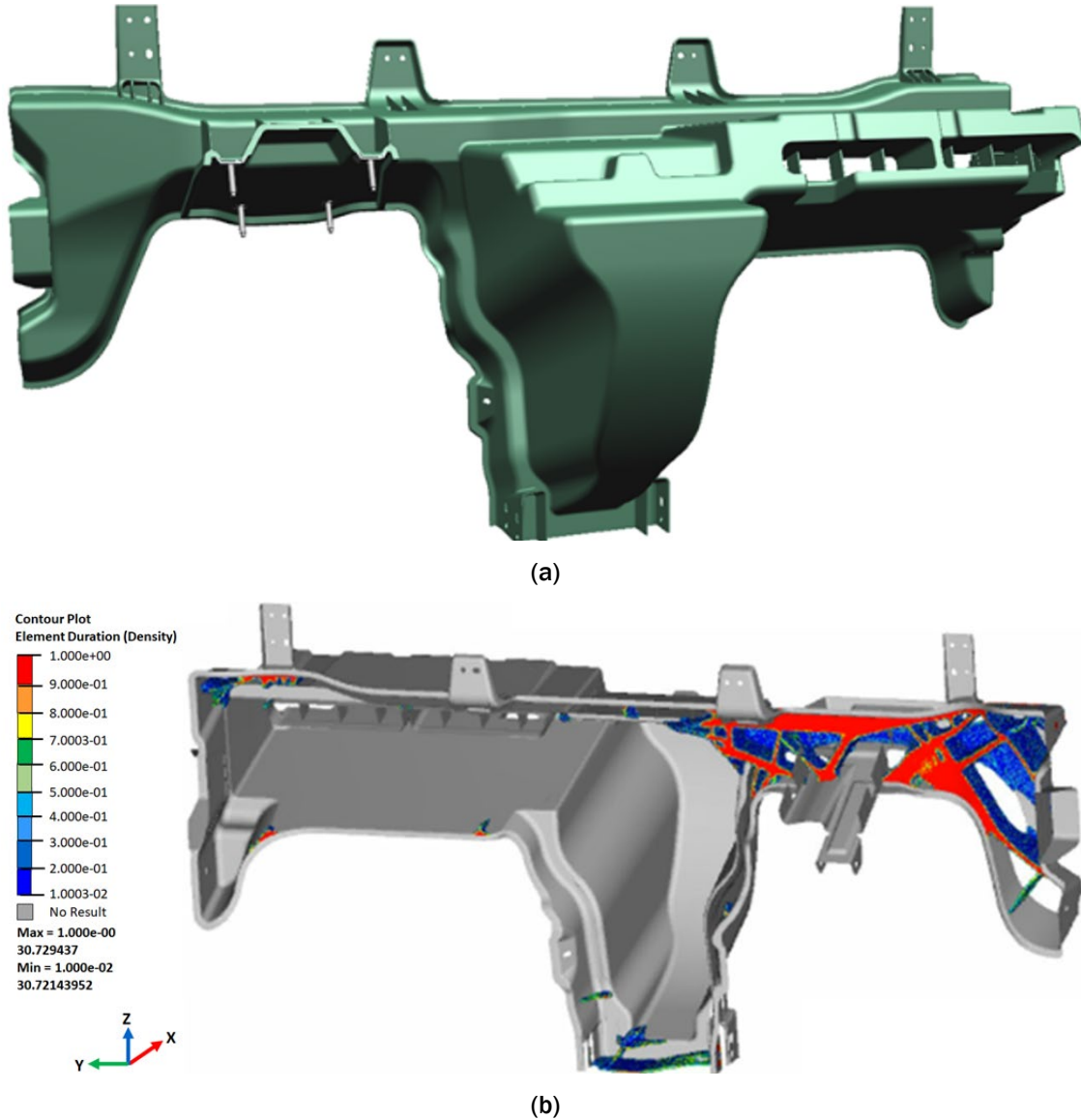


Figure II.2.12.4. (a) CAE design and (b) analysis of instrument panel XCB. Source: Ford.

Task 1.3 Manufacturing Feasibility Assessment

An evaluation of manufacturing feasibility has been made throughout the concept design progression. By example and in support of Milestone 1.1.3, design cross-sections of proposed features have been transferred to the relevant dependent work streams. In the case of water-assist injection molding (WAIM) (Task 3), the proposed location of two closed section stiffening channels is shown on the left-hand side of Figure II.2.12.5.

This has permitted predictions to be made regarding the length of the closed channels, variation in cross-section shape, and subsequent impact on the injection molding tool design. Wall thickness considerations have also been accounted for as it relates to cooling of the part during the injection molding process and any potentially negative effects on cycle time. A summary of the experimental investigations related to these activities falls under Task 3 and are included in later sections of this report. However, from a design perspective, the manufacturing feasibility loop will continue throughout Budget Period 1 prior to downselection to a finalized concept. Budget Period 2 will then be dedicated to further optimization of the design geometry before freezing the CAD ahead of prototype tool fabrication.

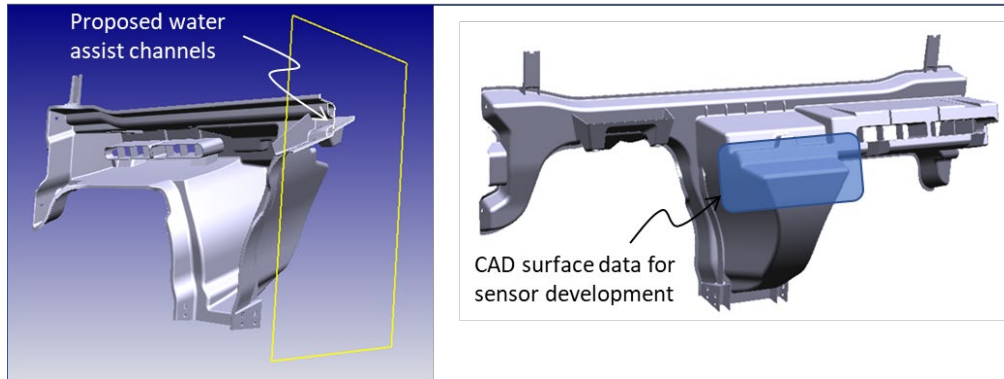


Figure II.2.12.5. Design sections proposed for the WAIM and sensor placement. Source: Ford.

This has permitted predictions to be made regarding the length of the closed channels, variation in cross-section shape, and subsequent impact on the injection molding tool design. Wall thickness considerations have also been accounted for as it relates to cooling of the part during the injection molding process and any potentially negative effects on cycle time. A summary of the experimental investigations related to these activities falls under Task 3 and are included in later sections of this report. However, from a design perspective, the manufacturing feasibility loop will continue throughout Budget Period 1 prior to downselection to a finalized concept. Budget Period 2 will then be dedicated to further optimization of the design geometry before freezing the CAD ahead of prototype tool fabrication.

In a similar manner, design sections and CAD surfaces targeted for sensor integration have also been transferred to the respective sub-team. The right-hand image in Figure II.2.12.5 highlights the CAD surface that has been designated for overmolding of sensors or electrical circuits. This has enabled processing investigations to be performed to determine feasibility of incorporating proposed functionality into these surfaces of the XCB. More specifically, the Task 5 work stream has conducted an experimental program to develop electrical circuits that can tolerate the high-temperature processing of engineering thermoplastics. This work originally commenced on flat panel tooling. However, with development of the geometry in Figure II.2.12.5, new tooling has since been produced to evaluate viability as the shape complexity increases. A final strategy for sensor integration will be proposed as part of the gateway at the end of Budget Period 1.

Task 1.4 Technoeconomic Analysis

The team at Purdue has created a technical cost model to determine the commercial viability of technologies under development. The modular nature of the analysis tool captures each step of the manufacturing process along with materials and purchased parts. This enables key cost drivers to be identified and sensitivity of final cost projections to the various input data. An example of the data input is shown in Figure II.2.12.6. As indicated, considerations are made for annual production volume, variable costs such as those for raw materials in addition to fixed costs such as capital expenditures. A demonstration of the technical model was presented in a review with DOE representatives on July 21, 2021. Since that time, the team at Purdue has been building a baseline model to enable a comparison of the multifunctional XCB design with that of the steel baseline. Results are scheduled to be presented as part of the end of Budget Period 1 Go/No-Go gateway review.

Final Part

Material Costs

Volume and Production Amount

Final Part Volume	5,101,279.10 mm ³	Annual Production	100,000 / year
		Production Years	5 years

MTOW & Inserts

Length of MTOW	3.50 m
----------------	--------

	Cost of Each	#	Volume of Each	Density
Metal Inserts	\$2.00 ea	0	0.014 dm ³	2.71 kg/dm ³
Bushings	\$0.50 ea	5	0.014 dm ³	2.71 kg/dm ³

Overmolding

Overmolding Material Cost	\$3.00/kg	Overmolding Material Density	1.145 g/cm ³
---------------------------	-----------	------------------------------	-------------------------

Capital Expenses

Equipment & Tool Costs

Line Investment	\$2,000,000.00	Jig Price	\$20,000.00
		Mold Price	\$700,000.00

Interest Rate	0.50%	Depreciation Years	5 years
---------------	-------	--------------------	---------

Figure II.2.12.6. Input data screen for XCB techno-economic analysis model. Source: Purdue.

Task 2. Formulation/Compounding of Novel Materials

The goal of the Task 2 work stream is to design a novel, multifunctional material that can replace a traditional steel XCB with a lightweight alternative. However, this transition from steel to a CF-based material results in reduced conductive properties which can negatively impact the grounding, static dissipation, and electromagnetic interference (EMI) shielding that is offered with a metallic design. To ensure conductive properties are met, the materials team has explored bulk modification of the polymer matrix using conductive fillers as well as local integration of conductive pathway through overmolding, as outlined in Task 4.

Per Milestone 1.2.1, the team identified four carbon-based conductive nanofillers to be compounded in a PA66 polymer matrix: carbon nanofibers (CNF), carbon nanotubes (CNT), graphene oxide (GO), and MXene (MX). In addition, five reinforced materials have been compounded in conjunction with the conductive filler materials: 50% short glass fiber (GF), 50% long GF, 40% CF, 25% CF/15% basalt fiber (BF), and 20% CF/10% BF. Using these compounds, ISO test bars were molded in May 2021 for the following: 1%, 3%, and 5% GO/PA66, 1%, 3%, and 5% CNT/PA66 materials. Subsequently, electrical conductivity testing has been completed at ORNL and mechanical and thermal property testing at Ford.

Figure II.2.12.7 summarizes the electrical conductivity results for the GO and CNT conductive materials. The CNT materials have higher electrical conductivity values than the GO materials, with the 5% CNT material exhibiting the best electrical conductivity overall. This is because GO is a 2D structure and CNT is a 1D structure thus, GO has a lower aspect ratio than the CNT materials. The CNT material can reach the percolation threshold of electrical conductivity at lower loadings compared to the GO material. The team anticipates that higher loadings of GO material may result in improved conductivity. The electrical conductivity of samples reaching as low as 10⁻⁶ S/cm was due to the limitation of the multimeter used to measure the resistance, their actual electrical conductivity could be even lower. However, any material having electrical conductivity lower than 10⁻⁶ S/cm is considered insulating.

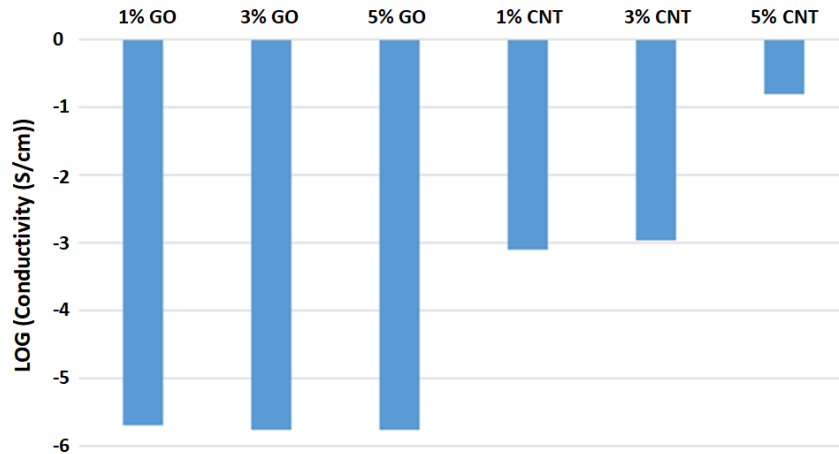


Figure II.2.12.7. Electrical conductivity results for conductive filler materials. Source: Ford.

Figure II.2.12.8 summarizes the electrical conductivity results for matrix materials with either conductive fillers and/or fiber reinforcement. Note the 5% CNT material achieves a similar conductivity to the 40% CF material (0.16 S/cm and 0.32 S/cm, respectively). The team is now investigating whether higher conductivities with formulations comprising combinations of both conductive filler and CFs can be achieved.

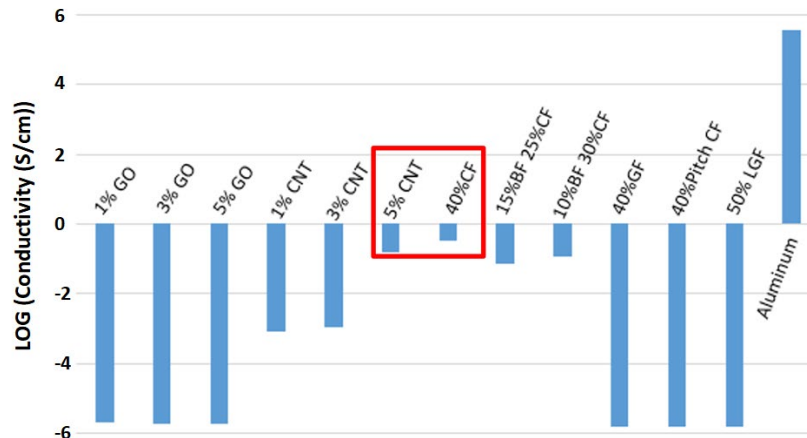


Figure II.2.12.8. Electrical conductivity measurements of candidate fillers compounded in PA66. Source: Ford.

Figure II.2.12.9 contains the mechanical test results for PA66 composites using different degrees of carbon, basalt, and GF. These results align with expectations except for the 40% Pitch CF which resulted in lower values. This is attributed to the fibers being milled to a fiber length shorter than the “critical fiber length.”

Figure II.2.12.10 shows the mechanical test results for the conductive materials. The tensile modulus results are similar for all conductive materials and the modulus for the GO materials increase with increased filler loading. Due to issues with a binder present in the CNT materials, the team was not able to mold enough 3% and 5% CNT samples to perform mechanical testing. However, additional samples will be produced at future molding trials. Figure II.2.12.11 depicts the thermal conductivity of the conductive materials. The thermal conductivity increases with increased loading for GO formulations. The team anticipates that this trend will continue with the 10% and 20% GO loadings.

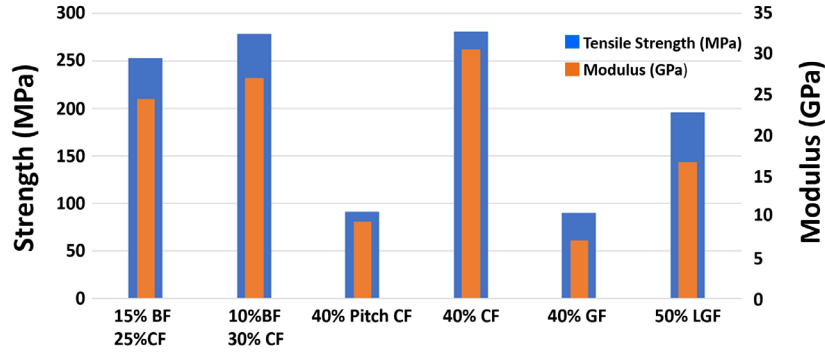


Figure II.2.12.9. Mechanical testing results for the reinforcement materials. Source: Ford.

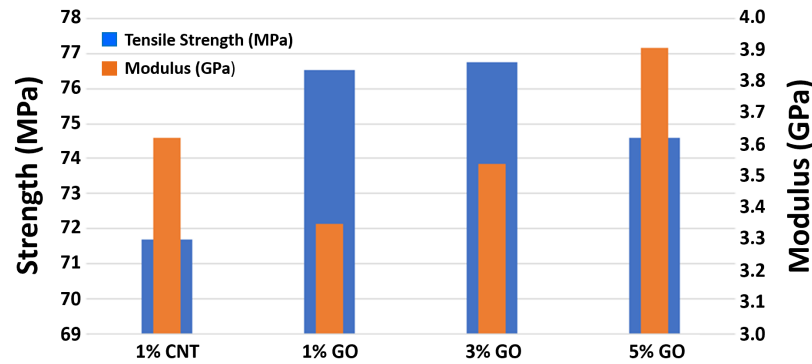


Figure II.2.12.10. Conductive materials mechanical testing results. Source: Ford.

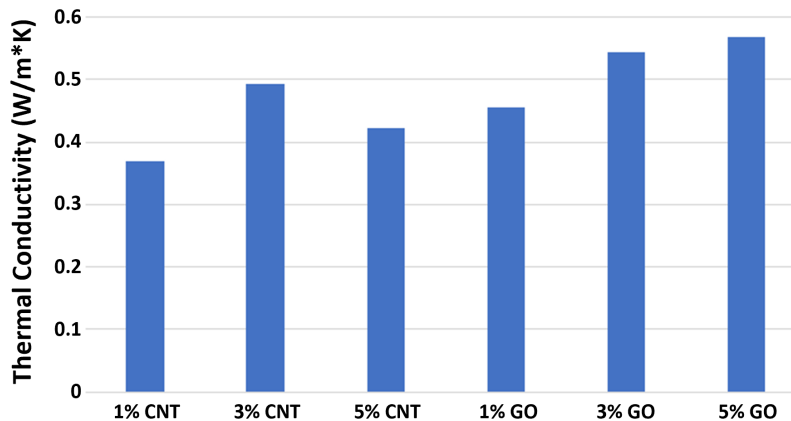


Figure II.2.12.11. Thermal conductivity results for conductive materials. Source: Ford.

Task 3. Water-Assist Injection Molding Process Development

WAIM technology is being developed to enable continuous closed (i.e., hollow) sections to be incorporated into the XCB structure. These offer a weight efficient means of adding stiffness to the XCB within the available design volume. Budget Period 1 has been focused on commissioning a water-assist unit to enable subsequent processing studies. In parallel, design and fabrication of a new demonstrator tool was completed to verify equipment functionality while also testing process feasibility of the materials under development in Task 2. A chronology of key events in Budget Period 1 are as follows:

- WAIM training on-site with equipment, April 19–21, 2021.
- Demonstrator tool build complete on May 27, 2021, per Milestone 1.3.1.1, as observed in Table II.2.12.3.

- Molding technology demonstrator components with WAIM cell, June 2021.
- Commissioning of WAIM equipment complete, June 30, 2021.
- Run at rate parts were produced to demonstrate the capability to create parts with hollow sections per Milestone 1.3.1.2 in July 2021, as observed in Table II.2.12.3. Processing studies continue to support the design feasibility assessment.

Table II.2.12.3. Task 3 Milestones for Budget Period 1

Milestone (Project Month)	Lead Organization	Description
1.3.1.1 Design freeze (M8)	Ford	Complete design freeze and build of tooling to be fabricated for manufacturing feasibility studies.
1.3.1.2 WAIM process tryout (M9)	Ford	Mold 30 tryout parts on Functional Demonstrator Tool to determine manufacturing feasibility of proposed hollow sections.

Figure II.2.12.12(a)–(b) show the two halves of the demonstrator tool mounted in the injection molding press. Albeit a simple tubular geometry, this tooling has been used to investigate the impact of material and process on part performance and dimensional capability. Figure II.2.12.13(a) highlights the transition features on both ends of the part that manage the water injection and coring out of the part during processing. Figure II.2.12.13(b) shows a part that has been cut down the length of the component, revealing the hollow cavity. Figure II.2.12.13(c) shows a batch of 30 parts produced as part of process capability study.

During Budget Period 2 processing investigations will continue based upon materials downselected for the XCB application. Modifications are also planned to an existing injection molding tool to allow scale-up of the WAIM studies to more represent the complexity of the hollow sections proposed in the XCB design.

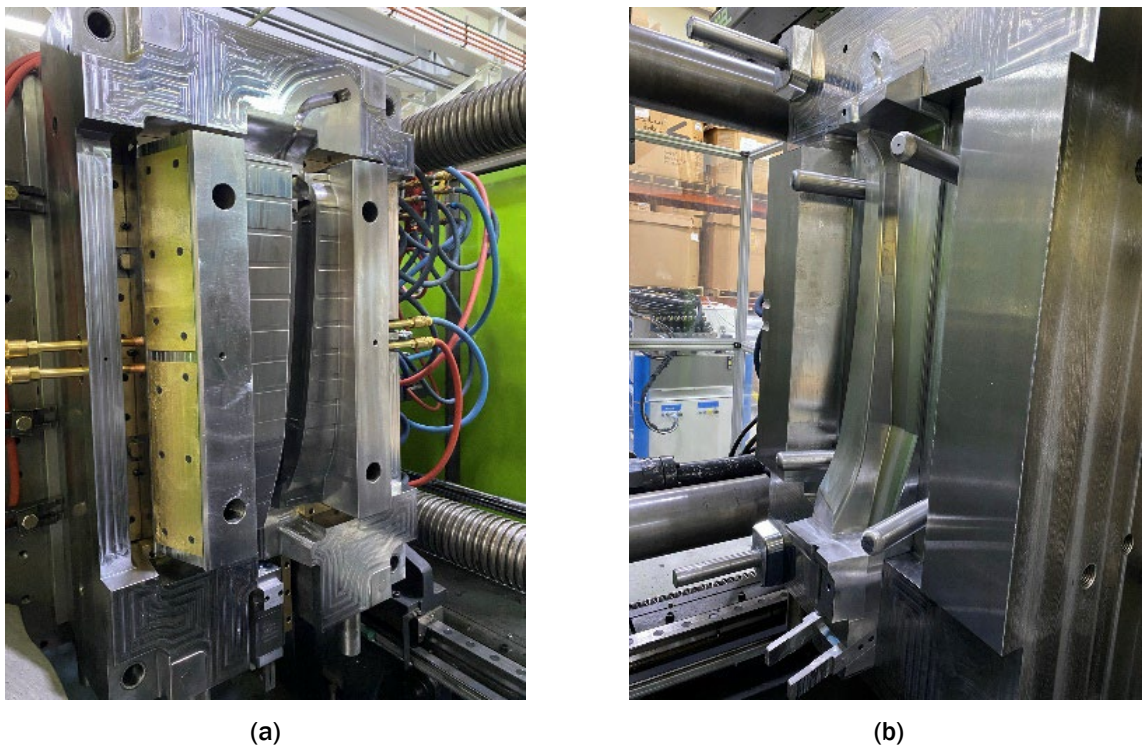


Figure II.2.12.12. Technology demonstrator mold for (a) the moving half and (b) the fixed half. Source: Ford.

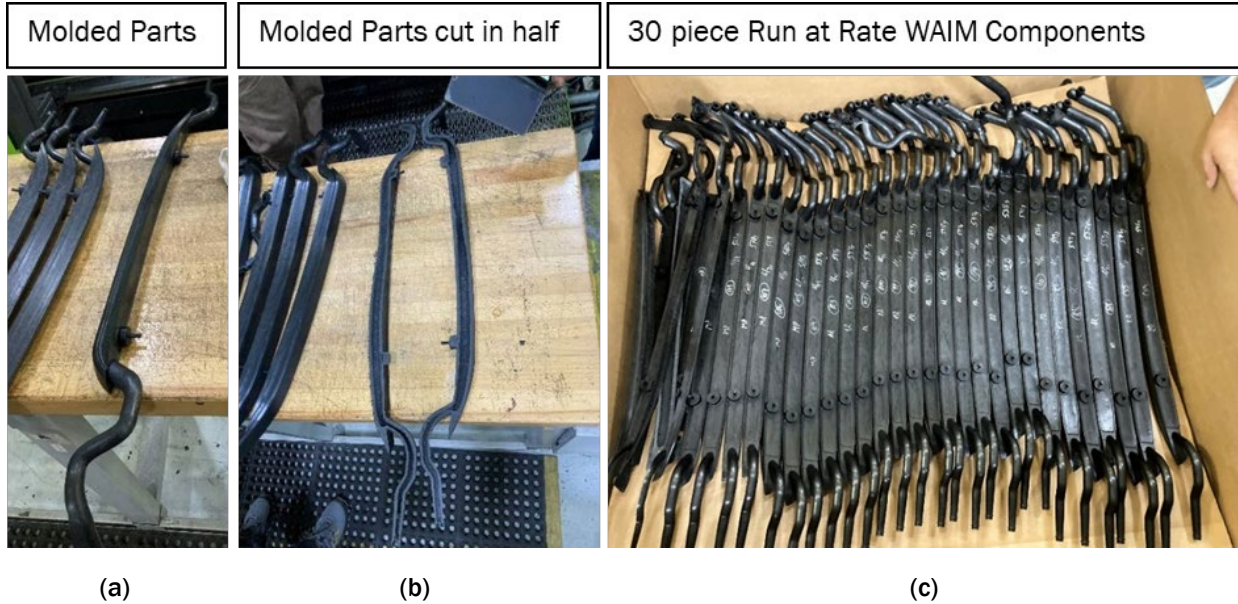


Figure II.2.12.13. Technology demonstrator components. (a) Transition features on both ends of the part that manage the water injection and coring out of the part during processing. (b) A part that has been cut down the length of the component revealing the hollow cavity. (c) A batch of 30 parts produced as a part of the process capability study. Source: Ford.

Task 4. Tow/Tape Placement of Continuous Fiber

The team at Purdue has completed modification of a tape production line for processing of candidate fiber reinforcements. Per the milestones in Table II.2.12.4, this work has progressed with a production run of 300 m of a GF/PA66 prepreg tape being produced in Q2 2021, as observed in Figure II.2.12.14.

In addition to providing enhanced structural performance, the feeding and consolidation stages of the equipment were adapted to allow integration of sensing and electrical conductivity. The results from feasibility studies are shown in Figure II.2.12.15. The image at the top shows the use of a conductor that is braided over the continuous fiber to create a dedicated grounding path along the length of the tow. The middle image shows the concept of introducing an axial conduit within the fiber bundle which can be used to convey fluids. Finally, the lower image shows the integration of the sensing capability using fiber optics and piezoelectric sensors.

Table II.2.12.4. Task 4 Milestones for Budget Period 1

Milestone (Project Month)	Lead Organization	Description
1.4.1 Tape production (M6)	Purdue	Produce 100 m of tape <25 mm wide at < 1 mm thickness for the downselected fiber and polymer system and further adapt for compatibility with multi-tow (M-TOW®), QEE-TECH® and molding cells.
1.4.2.1 Feeding adaptation (M12)	Purdue	Redesigned and adapted feeding and consolidation system of the M-TOW line allowing direct embedment of functional ducts/system into the structural M-TOW. M-TOW targets: diameter 6 mm to 12 mm, >50 v/o fiber content and at a line speed of 0.5 mm to 1.0 m/min.



Figure II.2.12.14. Thermoplastic prepreg tapes produced for continuous tow development. Source: Ford.

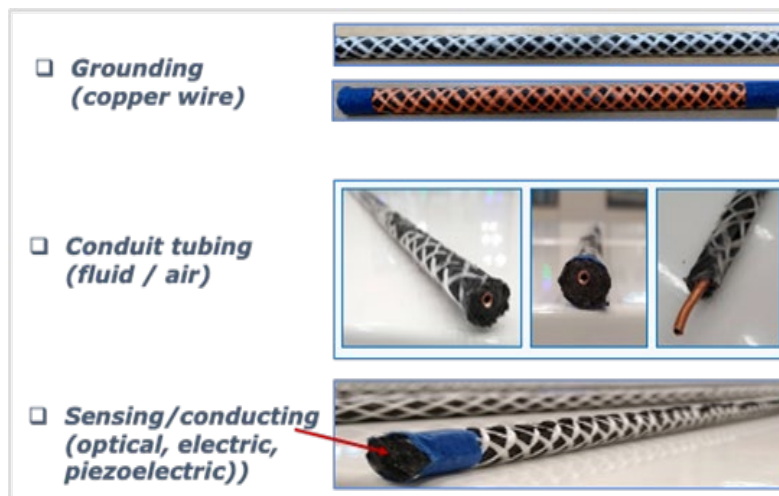


Figure II.2.12.15. Integrated functionality in continuous tow reinforcements. Source: Ford.

Processing studies are planned throughout the remainder of Budget Period 1 and into Budget Period 2 to establish a scalable robust manufacturing methodology. This work will be performed in parallel to the design activities which will dictate the final routing of the continuous tow materials in the XCB structure.

Task 5. Sensor Integration

A cross functional team identified several sensing and electrical system technologies to be investigated for integration into the XCB structure. In particular, dead front, capacitive switching, and swappable modular interfaces were technologies identified. In these use cases, printed wiring and connector termination were determined to be key enablers for integration of this capability into the XCB structure.

Based upon this assessment, Yanfeng conducted injection molding trials using printed circuits and various polymers for overmolding to understand survivability when processed with higher melt temperature polymers. Several sensing circuits including capacitive touch and force sensitive resistors were overmolded with a surrogate 15 wt.% GF reinforced PA6. These trials were conducted using a flat panel injection molding tool (125 mm × 125 mm) to produce the panels shown in Figure II.2.12.16. The following conclusions were developed based upon the results:

- Single layer capacitive touch circuitry is most probably feasible
- Force-sensing resistor technology is not directly compatible with mold-behind injection molding processes

- Higher melt temperature PA6 could potentially be used directly as a mold-behind material
- Formulation of specific inks and films will be required to ensure compatibility with the back molding material.

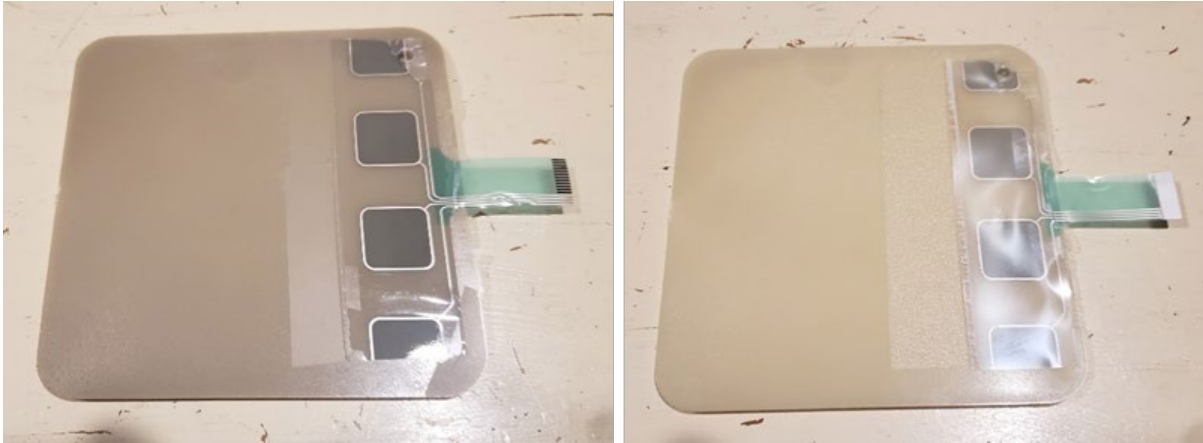


Figure II.2.12.16. Screen printed silver ink and poly (ethylenedioxythiophene) on a polyethylene terephthalate (PET) substrate behind 15 wt.% GF/PA6. Source: Ford.

Subsequent investigations were conducted to evaluate film substrate and conductive ink options for compatibility with the higher temperature processing of polyamide. A list of candidate film substrates and conductive inks is contained in Table II.2.12.5. It should be noted that the use of this existing tooling at Yanfeng has enabled the team to progress the R&D studies without the need to design and develop the new tooling as specified in Milestone 1.5.1.1, and as shown in Table II.2.12.6. Consequently, approval was requested and received from DOE to forgo the second part of Milestone 1.5.1.1. With the initial work on 2D substrates complete, the project team is now focused on fabrication of a prototype thermoforming and molding tool to scale the technology to a more complex 3D surface.

Table II.2.12.5. Materials Used in the Initial Molding Trial

Conductive Links	Substrates		Modeling Materials
Silver, nanoparticle	PET	PI	PC
Silver, particle free	PEN	PEI	PC/ABS
	PC	PA	PA + GF

Note: Industry standard polymer abbreviations are PET, polyethylene naphthalate (PEN), polycarbonate (PC), polyimide (PI), polyethyleneimine (PEI), polyamide (PA), acrylonitrile-butadiene-styrene (ABS), and GF.

Table II.2.12.6. Task 5 Milestones for Budget Period 1

Milestone (Project Month)	Lead Organization	Description
1.5.1.1 Function identification (M6)	Ford	Identify functions in XCB and complete design of a 3D demonstrator (~150 × 150 × 50 mm) for integrated sensors/circuits/electronics.
1.5.2 Prototype tool (M12)	Ford	Fabricate prototype tooling, form/mold 3D demonstrator components and complete functional electrical testing (resistance, continuity, sensor function) of integrated sensors/circuits/electronics.

Task 6. Additive Manufactured Hardware Attachment Points

This task is focused on the development of additively manufactured attachment points as an overmolded insert to provide more efficient load transfer from the surrounding structure into the XCB. Figure II.2.12.17 shows a generalized depiction of the design load cases. The key body attachment points are located at each end. Therefore, the Task 6 work stream is focused on the development of a weight efficient solution that also provides a connection point for overmolded continuous fiber bundles under development in Task 4.

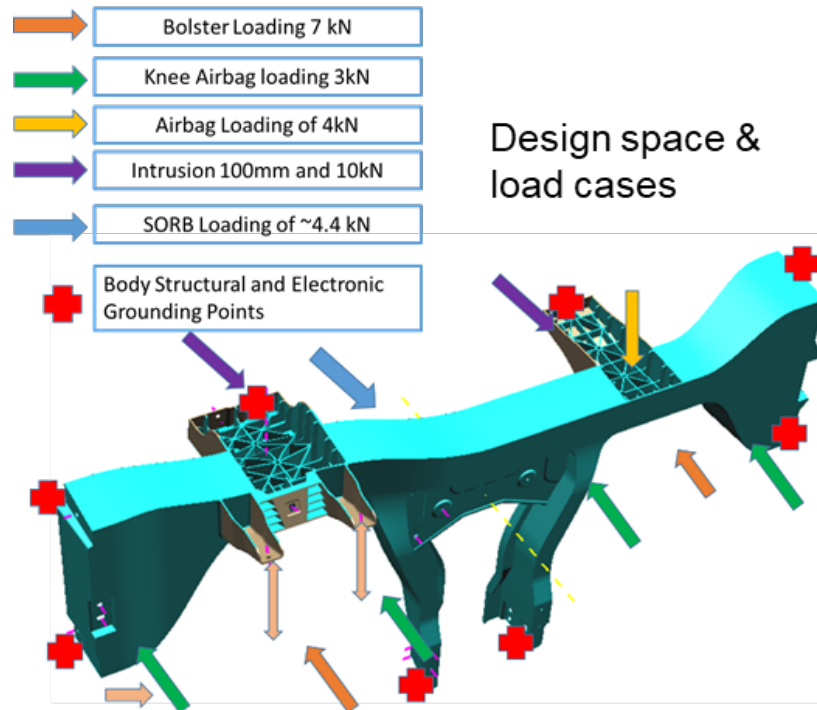


Figure II.2.12.17. Design volume and key load cases for the XCB structure. Source: Ford.

Initial focus has been on assessing overmolding feasibility of additively manufactured inserts rather than on specific design of the lattice structure. Therefore, to support the experimental investigations, ORNL completed printing of additively manufactured meshes with different metals (maraging steel and Inconel). Overmolding trials were subsequently conducted using facilities at Yanfeng. The overmolding was accomplished by taping the additively manufactured mesh into the injection molding tool as shown in the left-hand image of Figure II.2.12.18. As can be observed, the initial process setup resulted in an incomplete fill of the mesh structures. However, using some material offsets in the tool and improved drying of the polymer, the team was able to eliminate the air entrapment and promote flow on the back side of the mesh.

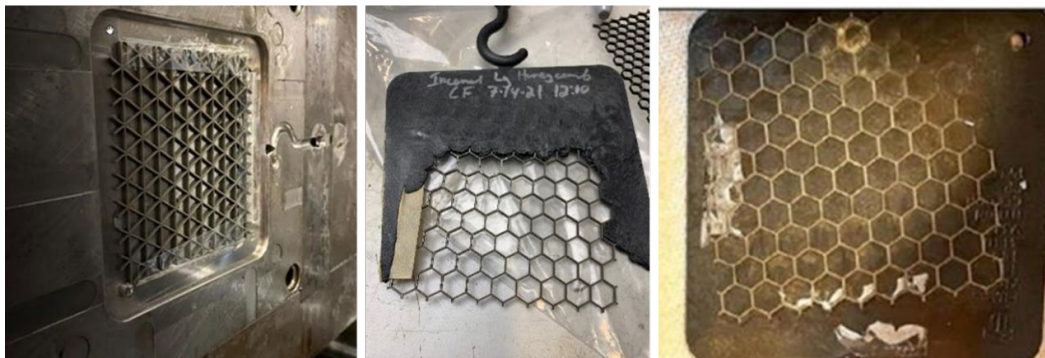


Figure II.2.12.18. 3D printed meshes produced for injection overmolding. Source: Ford.

Since completing the manufacturing trials, the Task 6 work stream has turned their attention to the detailed design of the insert intended for the XCB structure. CAE analysis is set to commence in October 2021 to quantify the performance of the concepts referenced in Milestone 1.6.1.2, and as observed in Table II.2.12.7. It is anticipated that this work will be completed as part of the concept design selection at the end of Budget Period 1.

Table II.2.12.7. Task 6 Milestones for Budget Period 1

Milestone (Project Month)	Lead Organization	Description
1.6.1.2 Attachment concept (M9)	ORNL	Design concepts for attachment points on XCB. Three concepts with 80% load transfer to discontinuous and continuous composite with 30% weight-savings as compared to stamped steel hard point.

Task 7. High-Volume Manufacturing Concept Feasibility Demonstration

Based upon studies being conducted within Task 4, “Tow/Tape Placement of Continuous Fiber,” and Task 6, “Additive Manufacturing Hardware Attachments,” the team at Yanfeng has been developing a material handling strategy for prospective inserts that are to be overmolded during the injection molding process. To assist with these activities, a new injection molding tool was designed, fabricated, and commissioned. This “W” tool has been designed to incorporate the following features, as observed in Figure II.2.12.19.

- Three different tow retention features
- Two bobbins are used to help preshape the fiber tow and hold the shaped tow within the injection mold
- Three different AM hardware attachment designs which demonstrate XCB to A-pillar connection points.

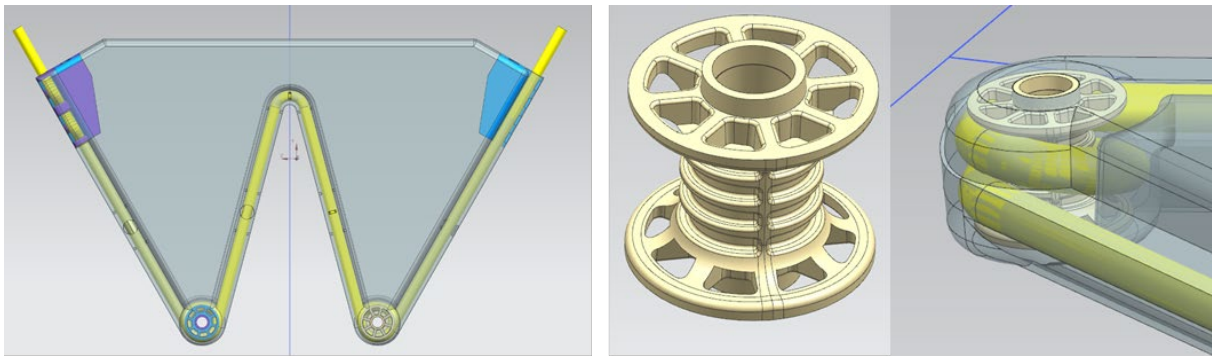


Figure II.2.12.19. W tool for sub-scale tow retention prove-out. Source: Yanfeng.

As the features listed above indicate, this tooling is being used to evaluate the handling characteristics of continuous fiber smart preforms under development at Purdue and how best to optimize the end of arm tooling for insertion into an injection molding tool. Figure II.2.12.19 shows an example of the bobbin that could be used to capture the continuous fiber preform while also allowing retention in the molding tool.

Pick and place studies have also been performed using the fixture shown in Figure II.2.12.20. This is providing the automation team feedback on how to proceed with the end of arm tooling design to transfer items efficiently and robustly into the molding cell. These capability studies will continue through the end of Budget Period 1, leading to a proposed manufacturing strategy for the XCB structure.



Figure II.2.12.20. Fixture to conduct preliminary end-effector capability studies. Source: Yanfeng.

Regarding the milestones for Budget Period 1 listed in Table II.2.12.8, processing studies are ongoing using the “W” mold for the additively manufactured hardware attachment. Samples have been printed at ORNL and received at Yanfeng for injection molding studies. The work required to support Milestones 1.7.1.1 and 1.7.1.2 is scheduled to be complete by the end of Budget Period 1.

Table II.2.12.8. Task 7 Milestones for Budget Period 1

Milestone (Project Month)	Lead Organization	Description
1.7.1.1 Technology Downselection (M8)	Yanfeng	Down-select to one design concept for attachment points on XCB with 80% load transfer to discontinuous and continuous composite with 30% weight-saving compared to stamped hard point.
1.7.1.2 EOAT Studies (M9)	Yanfeng	Complete EOAT studies and establish a material handling strategy for inserts and continuous fiber tows allowing a three-minute cycle time.

Task 8. Full-Process, Automation, Scale-Up, and Demonstration

There are no activities to report in Budget Period 1. This task will commence in Budget Period 2.

Task 9. Additive Manufacturing of Segmented Tooling

Task 9 and the corresponding milestone in Table II.2.12.9 was established to provide tooling support for experimentation being conducted by parallel work streams. Early in Budget Period 1, this need was mitigated through leverage of existing tooling at both Ford and Yanfeng. However, as the sensor work stream (Task 5) has progressed, a request for thermoforming tooling was received to determine whether printed circuit designs could conform to Class A geometry under review. This relates to the region of the XCB structure that was designated for sensor development as shown previously in Figure II.2.12.4.

In response to this request, the team at ORNL completed design and printing of the tooling shown in Figure II.2.12.21. This has subsequently been shipped to Yanfeng for processing trials that are scheduled in October 2021. In Budget Period 2, a provision has been made to produce two additional AM tools to assist with validation of the final design of the XCB structure.

Table II.2.12.9. Task 9 Milestones for Budget Period 1

Milestone (Project Month)	Lead Organization	Description
1.9.1.2 Sub-scale Mold Integration (M6)	ORNL	Complete design of sub-scale molds for sensor, hardware, tow placement, and water-assist work streams.

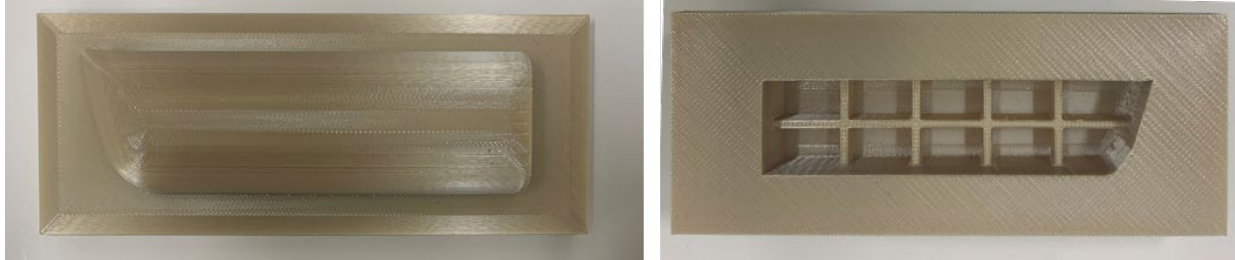


Figure II.2.12.21. Fixture to conduct preliminary end-effector capability studies. Source: Yanfeng.

Task 10. Artificial Intelligence/Machine-Learning for Process Optimization

Task 10 will establish a digital thread to capture each step the component development, ranging from feedstock compounding, geometrical design, processing optimization, *in-situ* monitoring, and material characterization. As a start, a review of the sensor infrastructure at the Tier 1 molding facility in addition to data collection was completed. The goal of this task is to develop a better understanding of the injection molding process via data-driven techniques, allowing real-time interaction with the process for anomaly correction or process optimization. Per Milestone 1.10.1.1 in Table II.2.12.10, a review of the equipment infrastructure and data collection capabilities was completed at Yanfeng. An example of the molding data available from each of the production cells is shown in Figure II.2.12.22. Using this data structure, Task 10 activities will establish an interface to both the machine and the tooling to allow real-time and remote data extraction and manipulation. In advance of this work a new CRADA has been established with Cincinnati Milacron to facilitate upgrades to the ORNL processing equipment.

Table II.2.12.10. Task 10 Milestones for Budget Period 1

Milestone (Project Month)	Lead Organization	Description
1.10.1.1 Infrastructure Review (M6)	ORNL	Complete lab and Tier 1 infrastructure review to determine process sensing capability for AI model development.

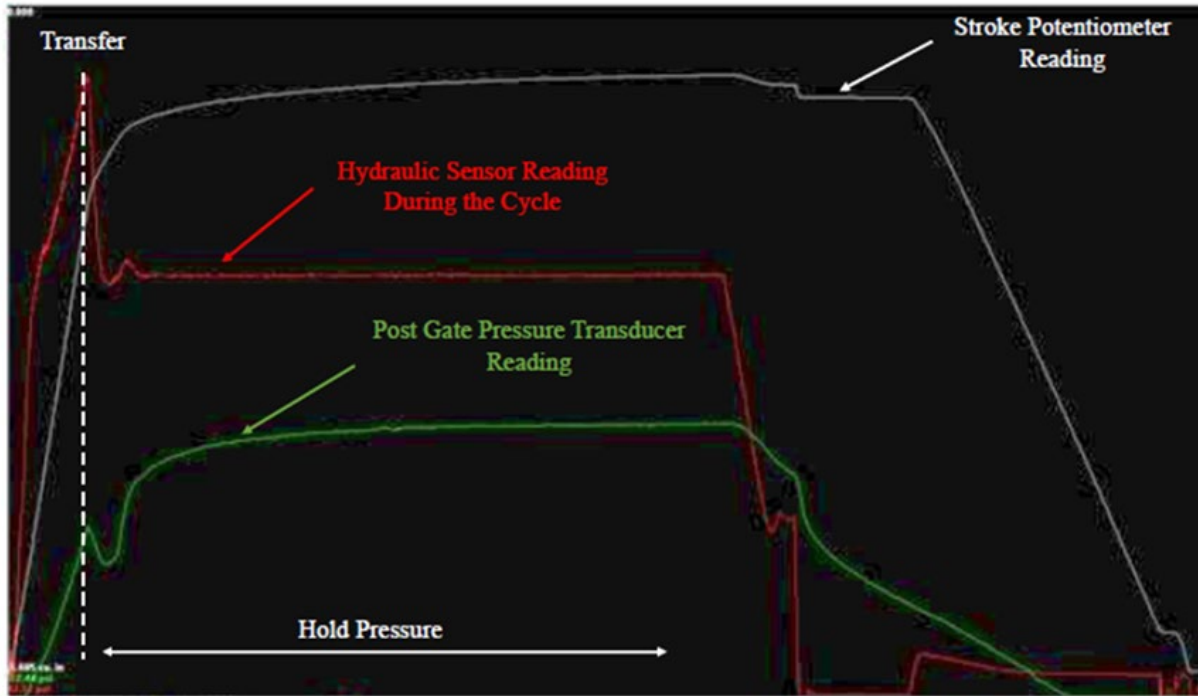


Figure II.2.12.22. Data recording for a standard injection molding cycle. Source: Yanfeng.

Task 11. Closed-Loop Recycling

This task will develop and demonstrate all compounds and materials in terms of circular economy with demonstration of recycling materials specified for the XCB structure. The task will also demonstrate the breakdown of materials into feedstocks for reprocessing. Thermal characterization of candidate materials has been conducted using DSC. Results of this analysis are contained in Table II.2.12.11 including crystallization temperature, enthalpy, percent crystallinity, and melting temperature. Upon the first heating cycle, there were no crystallization peaks indicating that the pellets were already semicrystalline. Compared to neat PA66, the introduction of fillers, either conductive or reinforcing, increased the crystallization temperature during cooling. However, not much change in percentage crystallinity (X_c) of the conductive fillers was observed while the reinforcing fillers decreased X_c . The conductive fillers are on the nanoscale while the reinforcing fillers are on the micron-length scale. The larger reinforcing fillers hindered crystallization while length scale of the conductive fillers was small enough to have no effect.

In addition to DSC measurements, thermomechanical and mechanical properties of injection-molded samples were generated. The purpose here has been to understand the effect of replacing a proportion of CF content with BF in addition to using CNTs versus CNFs as a conductive filler. To understand these effects four different formulations (e.g., 7.5 wt.% BF - 12.5wt.% CF/2.5 wt.% CNT, 7.5 wt.% BF - 12.5 wt.% CF/5 wt.% CNF, 20 wt.% CF/2.5 wt.% CNT, and 20 wt.% CF/5 wt.% CNF) were chosen. Dynamic mechanical analysis was performed to determine the glass transition temperature (T_g), DSC was performed to determine crystallization temperature (T_c), change in enthalpy (ΔH_m), X_c , and melting temperature T_m , thermogravimetric analysis was performed to determine the degradation temperature (T_d). Tensile testing was performed to determine elastic modulus (E), tensile strength (σ), and strain to failure (STF). Conductivity testing was performed to determine the conductivity (κ). The results for each test are shown in Table II.2.12.12.

Table II.2.12.11. Thermal Characterization of Pellet Materials

Material	Crystallization Temperature, T _c (°C)	Enthalpy, ΔH _m (J/g)	% Crystallinity, X _c	Melting Temperature, T _m (°C)
Neat PA66	225.88	70.88	35.98	264.53
1 wt.% GO/PA66	247.34	68.13	34.93	266.665
3 wt.% GO/PA66	245.44	64.93	33.98	263.71
5 wt.% GO/PA66	248.08	63.72	34.05	266.115
1 wt.% CNT/PA66	245.97	61.2	31.38	267.305
3 wt.% CNT/PA66	245.23	62.68	32.80	265.12
5 wt.% CNT/PA66	246.94	58.36	31.18	265.47
40 wt.% Pitch CF/PA66	247.42	42.74	21.70	263.465
40 wt.% CF/PA66	240.32	41.4	21.02	265.505
50 wt.% Long GF/PA66	241.39	32.6	16.55	262.42
40 wt.% GF/PA66	214.61	21.26	10.79	251.705
25 wt.% CF-15 wt.% BF/PA66	241.68	46.77	23.74	264.11
30 wt.% CF-10 wt.% BF/PA66	238.37	40.41	20.51	262.165

Table II.2.12.12. Thermal and Mechanical Properties of Injected Molded Samples

Material (formulation #) (Dry Blended)	T _g (°C)	T _c (°C)	ΔH _m (J/g)	X _c (%)	T _m (°C)	T _d (°C)	E (GPa)	σ (MPa)	STF (%)	κ (S/cm)
7.5BF-12.5CF/2.5CNT/PA66 (#26)	77.94	245.4	48.6	25.3	265.37	390.6	16.3	148.2	1.42	4.193
7.5BF-12.5CF/5CNF/PA66 (#28)	81.34	246.6	50.6	27.03	263.7	432.5	12.9	173.1	2.19	0.203
20CF/5CNF/PA66 (#8)	81.35	247.5	53.5	28.59	266.1	415.8	16.9	188.6	1.83	0.169
20CF/2.5CNT/PA66 (#5)	78.9	246.0	47.9	24.95	265.6	383.9	21.6	152.9	1.25	4.72

Regarding the milestones listed in Table II.2.12.13, considerable testing and characterization has been completed. However, the Task 11 milestones remain dependent upon a final downselection of the candidate materials as directed in Task 2. Therefore, once these selections have been made, the Task 11 sub-team will complete all necessary testing required for these milestones. It is anticipated that work will be completed as scheduled prior to the conclusion of Budget Period 1. In Budget Period 2, the recycling activity will be scaled-up to the component-level to establish a strategy for recycling of the entire XCB structure.

Table II.2.12.13. Task 11 Milestones for Budget Period 1

Milestone (Project Month)	Lead Organization	Description
1.11.1.1 Recycling baseline identification (M12)	ORNL	Identify suitable short-fiber reinforced thermoplastic (SF-TP) material and prepare 5 to 10 injection-molded samples. Prepare six tensile testing specimens (ASTM D638) and test them for tensile strength and elastic modulus measurements.
1.11.1.2 Short-fiber recycled material testing (M15)	ORNL	Prepare recycled short-fiber reinforced thermoplastic samples via mechanical shredding/grinding and injection molding. Prepare at least six tensile testing samples (ASTM D638) and document mechanical properties.

Conclusions

During Budget Period 1, the design work stream has been steadily progressing towards a new composite-based solution for the instrument panel XCB. Early on, system-level requirements were established which provided a baseline for performance and design volume constraints. This has enabled each of the parallel work streams to provide input into material, processing and sensor selection, leading to a finalized concept for review at the end of Budget Period 1. The analysis to date concludes that the mass savings are converging upon the program targets. Furthermore, manufacturing studies have demonstrated feasibility for inclusion of localized tow reinforcements as well as embedded electronics. There have been some concerns over the level of electrical conductivity that can be achieved with the novel fillers under evaluation. However, as an alternative, studies at Purdue have shown that the continuous fiber tow reinforcements can be modified to provide localized electrical conductivity where needed. Therefore, a final determination on whether to adopt bulk modification of the overmolding composites or use of localized conductive pathways has yet to be decided.

From a commercial perspective, the Purdue team has also completed the assembly of a technical cost model to provide insights into cost drivers and help decision-making on filler and reinforcement selection. Early analysis would suggest the overall cost targets for the program will be met. A cost analysis for the current design concept will be subject to review at the Go/No-Go gateway at the end of Budget Period 1.

References

1. Blanchard, P., 2021, "Multifunctional smart structures for smart vehicles," *U.S. Department of Energy 2021 Vehicle Technologies Office Annual Merit Review*. DOE, Washington, D.C., USA. Available at: <https://www.energy.gov/eere/vehicles/vehicle-technologies-annual-merit-review> (last accessed 20 January 2022).
2. Mansson, J. A., 2021, "Towards cost-effective composites," SAMPE Conference 2021, 23 September 2021, Charleston, SC, USA.

Acknowledgments

The project team would like to recognize C. Schell from the AMO for his continued support and guidance throughout Budget Period 1.

II.2.13 Development of Tailored-Fiber Placement, Multifunctional, High-Performance Composite Material Systems for High-Volume Manufacture of Structural Battery Enclosure (General Motors)

Venkateshwar Aitharaju, Principal Investigator

General Motors Global R&D
30470 Harley Earl Blvd.
Warren, MI 48092
E-mail: venkat.aitharaju@gm.com

H. Felix Wu, DOE Technology Manager

U.S. Department of Energy
E-mail: felix.wu@ee.doe.gov

Start Date: April 1, 2021 End Date: June 30, 2024
Project Funding (FY 2021): \$1,000,000 DOE share: \$500,000 Non-DOE share: \$500,000

Project Introduction

The automotive industry is currently in a major transition from internal combustion engines to a new era of EVs. Increasing the driving range of EVs, minimizing the cost of the battery system, and optimizing the vehicle architecture to meet new performance requirements imposed by electric propulsion, while meeting all safety criteria, are some of the new challenges posed during this significant transition. In this endeavor to meet the above challenges, lightweighting by using high-performance materials for EVs has become paramount. Composite materials, in addition to having lower densities, have significant benefits compared to metals by: (1) allowing deep draw, complex shape part manufacturing; (2) combining multiple parts into a single part (i.e., parts consolidation); and (3) varying part thicknesses to reduce the component mass. These benefits have allowed the automotive industry to design innovative components made of composites for improved efficiency. Despite these excellent benefits, composites still face significant challenges for large-scale implementation in automobile production. These challenges are: (1) the inability to be truly multifunctional to stand apart from metals; (2) the lack of predictive tools to eliminate trial-and-error evaluations; (3) the inability to optimize the design parameters; and (4) the high cost for volume manufacturing.

Composite materials were long touted to provide various benefits other than performance (i.e., strength and stiffness), but the technology was never pushed to cover the additional area of multifunctionality. Virtual design of structures using predictive modeling tools is challenging due to the complex behavior of composites caused by heterogeneity at the microstructural level that affects the damage progression. Since accurate prediction is a challenge, optimization of the variables in the composite design has become a remote possibility. High-volume composite material manufacturing is still a challenge in the industry due to high preforming costs (e.g., from hand operations and waste generation) and slow resin curing times. As a result, the opportunities for a good business case for composites in automotive structural areas are limited due to the cost pressure. In this project, we will address the above challenges and provide solutions to make a strong business case for stiff, strong, and smart composites for large-scale implementation in automobiles.

Objectives

The objective of the project is to develop advanced composite materials systems with game-changing technologies such as hybrid fiber systems at the lamina or tow level (commingled), strategic tailored-fiber placement (TFP), self-health monitoring, and multifunctional and high-volume manufacturing-friendly production for the automotive industry. The material systems will be selected appropriately based on the structural requirements, and they will meet or exceed the performance metrics provided by DOE (e.g., fiber strength >25 ksi, fiber modulus >250 Msi, STF >1%) to achieve the necessary weight-savings and cost

targets. High-pressure resin transfer molding (HP-RTM) will be chosen as the high-volume manufacturing process for the components with fast-curing resins that can provide cycle time lower than three minutes. Computational tools for both the manufacturing process and structural performance based on an ICME approach will be developed and validated for the chosen material systems. Using these ICME tools, the project team will design a structural composite battery enclosure for a battery EV. Manufacturing tools will be built entirely based on the virtual simulations. The composite battery enclosure structure will be tested to compare the performance with the baseline metallic assembly. The weight-savings, cost of materials, cost of components, and cycle times for a production volume of 85,000/year will be evaluated and compared with the DOE metrics.

Approach

Several key technology developments are proposed in this project under the following categories.

Materials

The newly developed TFP technology will be advanced to the next level in this project by creating hybrid fiber reinforcements (e.g., carbon, glass, or other fibers), and using them in a single preform or commingled in a tow to enhance the material properties significantly, as observed in Figure II.2.13.1. Based on the limited works cited in the literature, incorporating GFs along with CFs enhances the ductility of the hybrid composite significantly, leading to higher specific energy absorption for the same cost. We propose to study this phenomenon by conducting detailed experiments with various load cases and ratios of fibers to determine optimum commingling fiber parameters. Overall, the material systems developed in the project will lower material and manufacturing costs significantly, meeting the DOE metric of a maximum increase of \$5 per pound saved compared to the steel baseline. Innovative sensor technologies will be embedded within the composite preforms for monitoring the structural health and environmental conditions (temperature and humidity) in self-sustained mode (energy-harvesting). For the damage sensor, a separate CF tow will be embedded in the fabric in a specially designed strain gauge-like pattern. Any damage in the CFRPs, such as CF breakage or polymer matrix cracking, will cause the wire to deform or break, resulting in a change of the wire's electrical resistivity. Therefore, by measuring the electrical resistance of the wires, damage to the CFRP structure can be detected. Furthermore, the damage location can be identified by dividing the monitoring area into multiple sub-areas, each being embedded with separate wires.

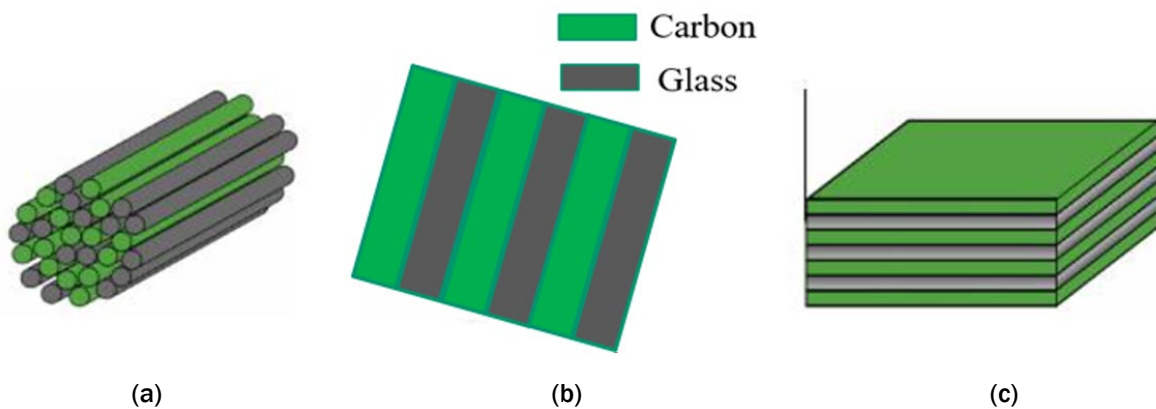


Figure II.2.13.1. Hybridization of fiber commingling in (a) a tow, (b) a layer, and (c) a laminate. Source: GM.

Process/Design

Computational models will be developed to optimize the microstructure of composite preforms (i.e., tow size, tow spacing, stitch density) to maximize their drapability and permeability. The TFP technology explored in the project will provide greater flexibility to vary the geometry of the microstructure spatially, providing an opportunity for next level optimization. HP-RTM is the chosen process in this project due to its advantages for volume manufacturing (notably fast cycle time) seen in our previous DOE-funded project (e.g., contract number DE-EE0006826). For the HP-RTM process design, developed simulation models will be enhanced to

engineer the processing conditions (e.g., molding temperature, injection location, vent, injection pressure, flow rate profile) for a fast-curing resin (with a cycle time of three minutes as we previously demonstrated). Variability in the preform material properties, preform placement, and process molding conditions are the major sources of defects and scrap in this process. To address this issue, we will develop models based on AI/ML to correlate the data from sensors embedded in the mold (e.g., resin arrival time, pressure, temperature, etc.) with the probability of dry spot occurrence in the manufactured parts. This will significantly improve on our current achievements in probabilistic learning on manifolds [1].

Structure/Performance

Predictive tools for the structural performance of the hybrid carbon and glass composites will be developed by extending the existing ICME multiscale models developed previously in our DOE-funded project (contract number DE-EE0006826). The models will be calibrated using coupon level tests and validated by using component-level tests. Further, a method will be developed to optimize the layup fiber directions and thickness of the lamina for minimal fiber use and mass. Using these ICME models, we will be able to exactly predict the optimum fiber make-up, fiber architecture, fiber volume fraction, resin type, manufacturing process, and processing conditions to manufacture components that meet the required structural performance for the components of the composite battery tray.

Results

The project progress during FY 2021 is provided in the following sections.

Task 1.1. Baseline Functional Requirements

Based on internal discussions with GM's vehicle engineering groups, the baseline battery enclosure design was chosen to be the one GM is developing for a production 2023 battery EV. This makes our current project relevant to a new generation of battery EVs. The baseline battery enclosure was made using steel. The critical impact load cases corresponding to 5th pole and 50th pole were simulated, and the intrusion values were extracted for the baseline steel assembly. These baseline values will serve as the reference values for the design of future composite battery enclosures. Due to the protected nature of this data, the details of the results are not presented in this report.

Task 1.2. Materials, Process Models, Technology Development for Future Composite Assembly

Under this task, the development of materials, process simulation models, and structural design tools will be carried out for use with the design of future composite battery enclosure. Accomplishments under each of the development subtasks are provided in the subsections that follow.

Task 1.2.1. Evaluate and Develop an Optimized Hybrid Material System

Under this task, advanced hybrid materials (LatticeTM) (carbon and glass) proposed for the chosen battery enclosure components will be investigated to determine the optimum hybrid ratios for maximizing the balance between structural performance and material cost. Structural property evaluation of LatticeTM preforms were performed on commingled CF and GFs. The purpose of commingling was to utilize the enhanced ductility phenomenon observed in the literature with the hybrid fiber systems to maximize the performance of the design while minimizing the material cost. In addition, using computational tools developed earlier, GM will strategically incorporate the costly CF where it is required structurally, and use the GF in other areas.

Optimum Material Systems for Structural Performance

Three methods of commingling of CF and GF materials were planned, as shown previously in Figure II.2.13.1:

- Commingling in a tow
- Commingling in a layer
- Commingling in a laminate.

In addition to the above material systems, we have also tested other traditional commercially available material systems to compare the performance of the hybrid systems versus mass and cost. Table II.2.13.1 shows the various material systems considered for the study.

Table II.2.13.1. Material Systems Considered for the Study

Material	Epoxy Resin	Reinforcement	Construction
G1	Hexion 06170	Glass	NCF
C2	Hexion 06300	Carbon	NCF
C3	Hexion 06300	Carbon	Twill
C5	Hexion 06170	Carbon	NCF
H1	Hexion 06170	Glass/Carbon (81:19)	Lattice
H2	Hexion 06170	Glass/Carbon (51:49)	NCF

Figure II.2.13.2 shows stress versus strain plot of these material systems under tensile loading.

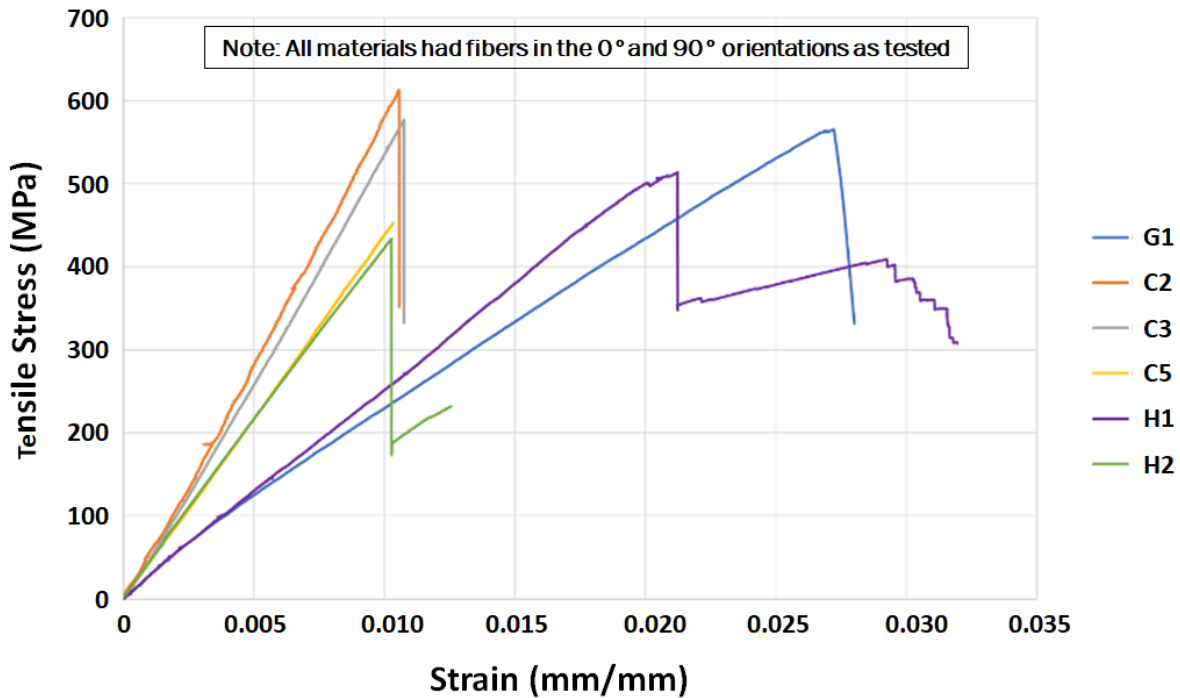


Figure II.2.13.2. Stress versus strain measured for glass, carbon, and Hexion material systems considered in the study. Source: GM.

Several metrics such as stiffness, strength, STF, and energy absorption were evaluated to rank these material systems. Figure II.2.13.3 shows the radar chart of the performance versus specific gravity calculated for each of the material systems. One can see from the chart that for the stiffness and strength, CF material system is the optimum. For the STF and energy absorption, the Lattice™ hybrid system provides the best performance. Figure II.2.13.4 shows the radar chart of performance versus cost. In this case, for the specific gravity, CF yields the optimum solution, and for all other metrics, GF only provides the optimum solution with the hybrid being second.

Based on the above results, the hybrid CF and GFs system provides a balanced optimal material system for structural performance for automotive requirements for mass savings and cost.

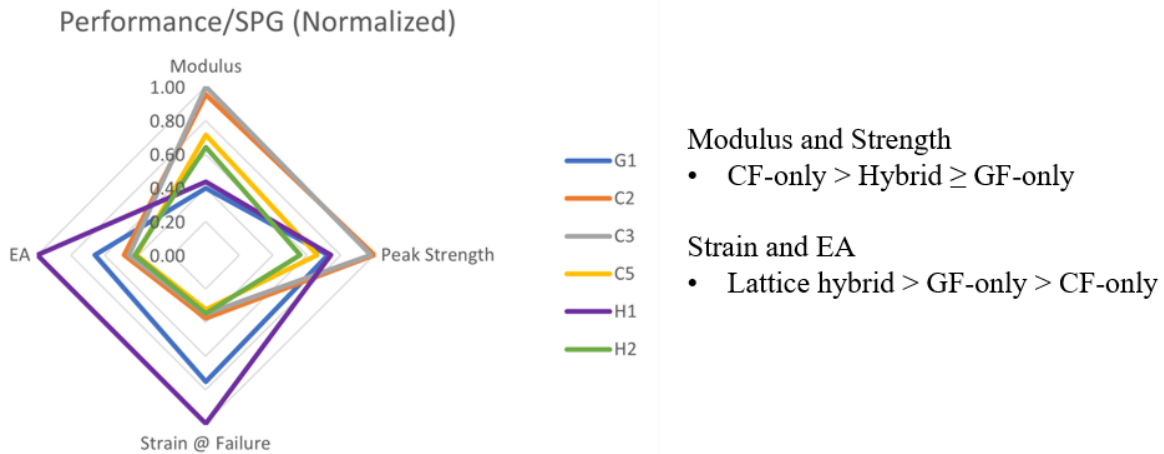


Figure II.2.13.3. Radar chart of performance/SPG for various other metrics. Source: GM.

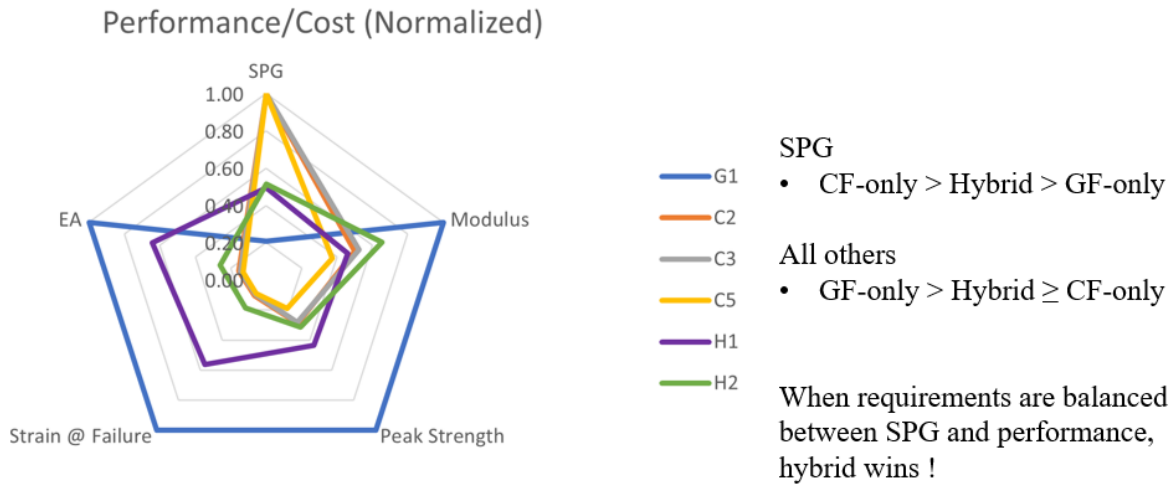


Figure II.2.13.4. Radar chart of performance/cost for various other variables. Source: GM.

Optimum Material Systems for Manufacturing Performance

Bias-extension (BX) samples were prepared with +45°/-45° layup and the fabrics were tested in the tension loading to evaluate the shear stiffness. Lower shear stiffness is better for drapability. For the hybrid Lattice™ material systems, the backing material and stitch density were considered as variables for optimization.

Figure II.2.13.5 shows the force versus deflection of Lattice™ compared with various other fabrics in a bias-extension experiment. The figure shows that the hybrid material system considered in this study has higher stiffness at lower strain values. We have attributed this stiffening effect to the backing material. Towards this, we have evaluated a total of six backing material types and tested them for further downselection. Among the six backing material types, we chose Nylon, chopped glass, and glass veil as future candidates.

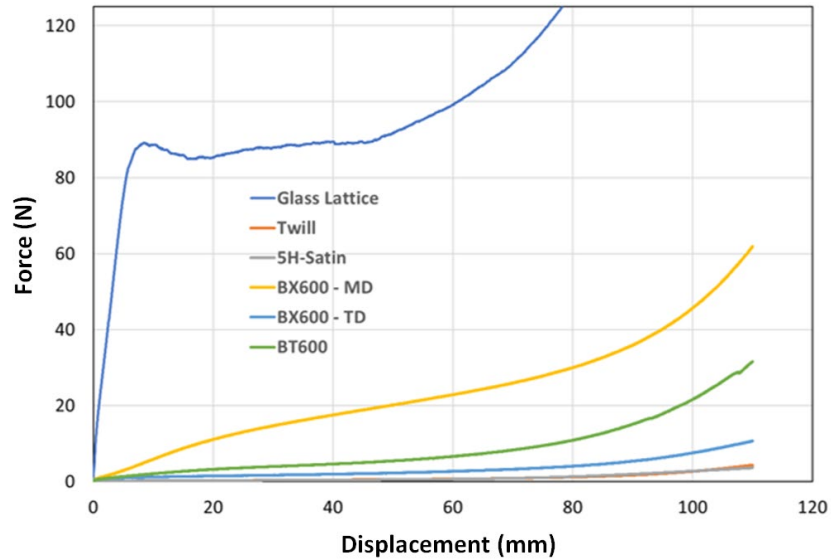


Figure II.2.13.5. Bias-extension results of various preform materials. Source: GM.

Figure II.2.13.6 shows the bias-extension results for the chosen backing materials compared to the other commercially available materials. The glass veil offers the lowest shear resistance among the three candidates and is comparable to the BX-0 fabric. This material will be used as the mainstream material for our future work.

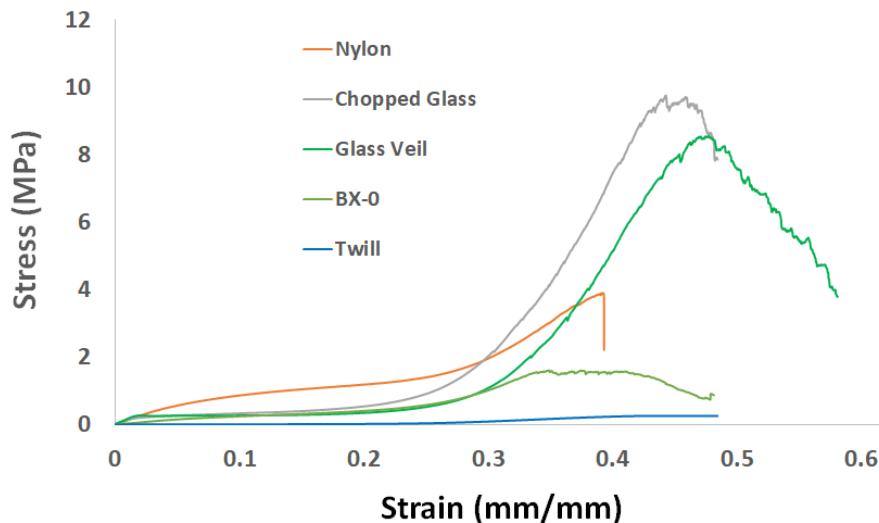


Figure II.2.13.6. Bias-extension results with various backing materials through final downselection. Source: GM.

With the above study, we have optimized the material system for both structural and manufacturing performance, and thus accomplished goals and milestones proposed for this task.

Task 1.2.2. Evaluate and Develop Required Manufacturing Model

Under this task, the manufacturing models to design the HP-RTM process for battery enclosure components will be carried out. The computational model development [1] involves solving complex coupled nonlinear differential equations modeling the heat transfer and fluid flow through porous media. For the model development, calibration, and validation, we performed various experiments collecting the pressure rise during the injection, temperature evolution during the injection, and tracking the flow front in the mold.

Accomplishments

Temperature data were collected on two plaques molded with pure resin and GF preform. A thermocouple was taped in place near the injection port and at the midplane of the preform stack, as shown in Figure II.2.13.7. Data was recorded during the full injection and cure cycle. An example temperature profile is shown in Figure II.2.13.8.

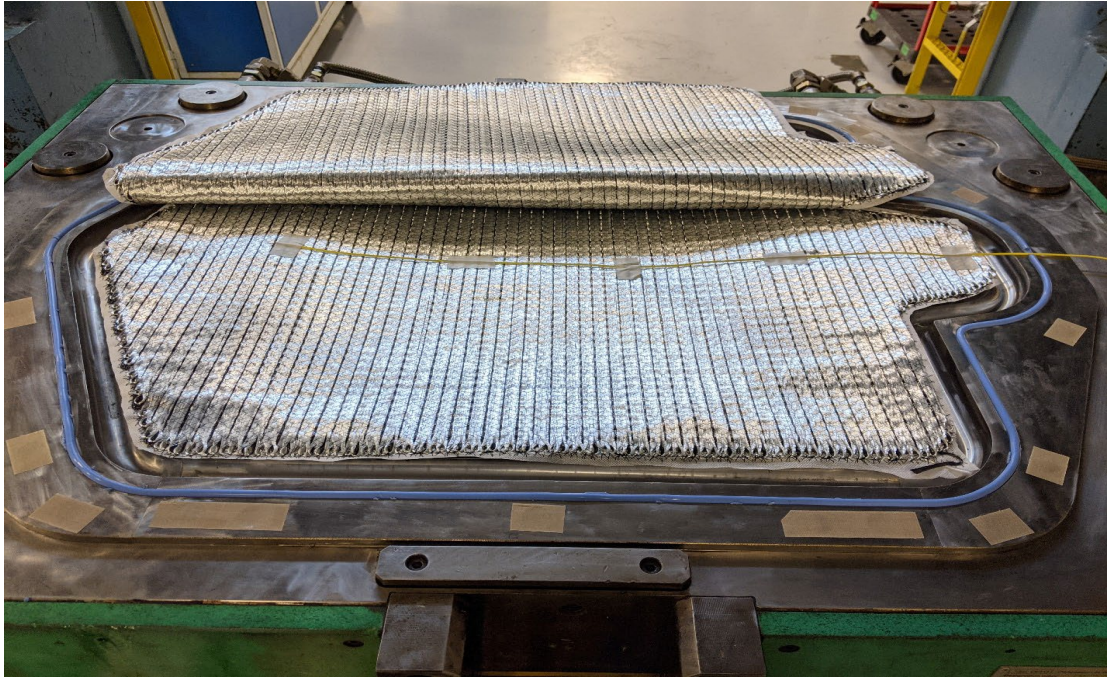


Figure II.2.13.7. Hybrid Lattice™ preform with thermocouple wire (yellow) taped into place. Source: GM.

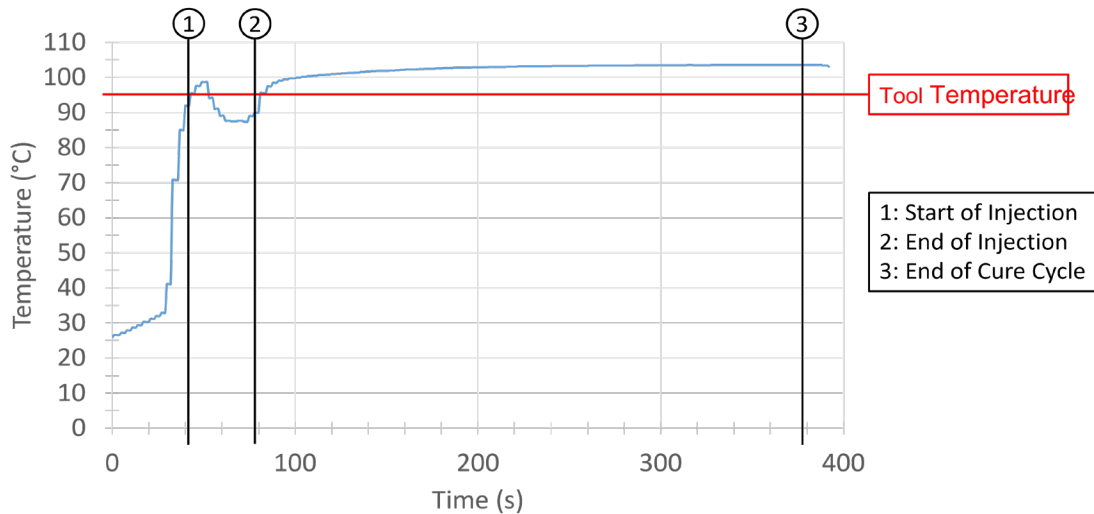


Figure II.2.13.8. Temperature versus time data for one experiment. Source: Michigan State University.

Regarding the collection of experimental data of flow front and pressure, injection experiments were conducted using the HP-RTM machine at the MSU Scale-Up Research Facility (SuRF). Baseline characterization was conducted using a Hexion 06170 epoxy resin system which was chosen for its fast cycle time of under three minutes. The baseline correlation flow results are shown below. The geometry of the molding tool is shown in Figure II.2.13.9(a) and the panel dimensions and instrumentation setup are shown in

Figure II.2.13.9(b). The molded panels with different amounts of injected resin are shown in the following Figure II.2.13.10. Panel to panel quality and repeatability were also verified as shown in Figure II.2.13.11. Units shown in the following figure are thickness of the panel in thousandths of an inch as measured by micrometer (ball-flat) in respective corners of the panel. Pressure data was obtained by GM using Kistler 6161AA pressure transducers embedded in the tool and a National Instruments data acquisition system. Figure II.2.13.12 shows the variation of pressure at the middle transducer in the mold.

The yellow and dark green curves show the resulting pressure signatures in a panel with no patch. The difference in signatures will be further evaluated in future efforts and will be used to evaluate the initial AI/ML control approach.

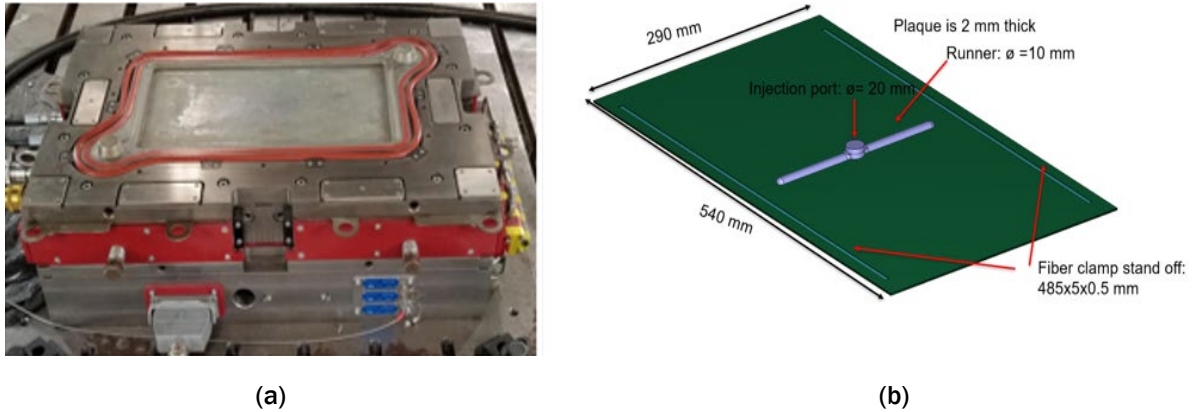


Figure II.2.13.9. (a) Molding tool and (b) instrumentation setup. Source: Michigan State University.



Figure II.2.13.10. Flow front progression for molded panels with different amounts of injected resin. Source: Michigan State University.



Figure II.2.13.11. Process repeatability and dimensional checks for a 200 g injected at 50 g/sec.
Source: Michigan State University.

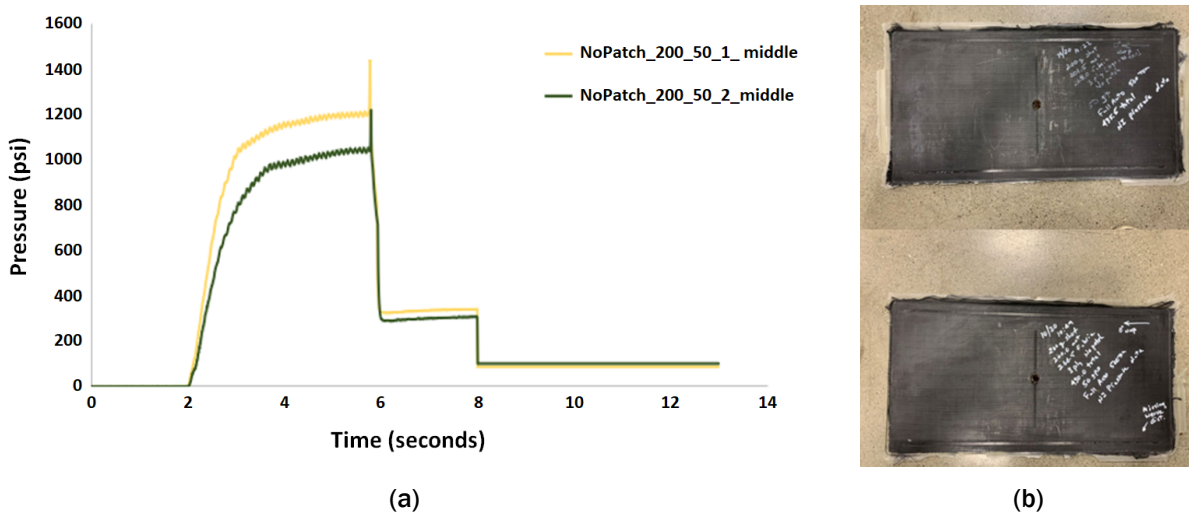


Figure II.2.13.12. (a) In-tool pressure signature summary at the middle of two samples from a 200 g injection at 50 g/sec with no patch. (b) Images of Sample 1 (top) and Sample 2 (bottom).
Source: Michigan State University.

During the high-volume automotive production using HP-RTM processes, variability in the preform placement and process conditions are common. This variability can potentially lead to high scrap rates in the overall process, mainly due to the poor fill and/or wet-out of the part. To understand the influence of variability and to validate the flow front prediction in the model development, an experiment involving accidental addition of a patch was conducted. Figure II.2.13.13 shows the setup and dimensions of the patch/artificial constriction in the panel. The injection point is located at the center of the panel and is distributed by a small runner shown in light green running from top to bottom in Figure II.2.13.13. The flow front then progresses from the panel midline towards the left and right edges.

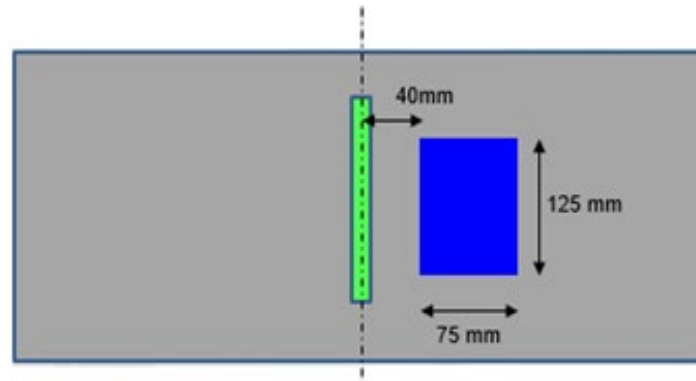


Figure II.2.13.13. Molding experiment target parameters with accidental addition of a patch.
Source: Michigan State University.

Various patch sizes were investigated. The experimental setup also yielded satisfactory results for AI/ML model correlation and validation. The AI/ML process model that is under development senses the deviation of process by comparing the pressure with the baseline and it will adjust the flow rate on the fly to mitigate the defect. Towards this, experimental flow studies were conducted at 50 g/sec and 20 g/sec (the lower bound attainable with MSU's SuRF Hennecke system). The 50 g/sec flow rate is a standard production setting within the automotive industry and with the accidental patch showed significant dry spot in the molded panel. On the contrary, the 20 g/sec flow rate yielded a reduced size of the dry spot in the molded panel. A reduction of dry spot volume by 38% was demonstrated, as shown in Figure II.2.13.14. These experiments were crucial in developing the AI/ML strategy that is currently under development.

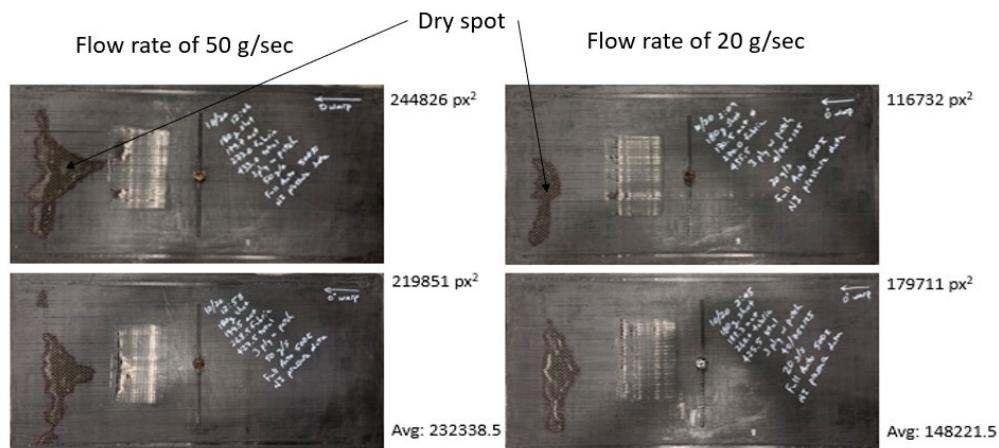


Figure II.2.13.14. Results of flow rate reductions on dry spot area. Source: Michigan State University.

The reduction in dry spot area due to strategic reduction of flow rate will be further confirmed in future efforts under this program. The findings listed above were utilized to develop AI/ML rationale and establish an approach for a phase I implementation on MSU's SuRF HP-RTM machine and will be discussed further in the writeup for Task 1.2.5.

Manufacturing simulation work was focused on two main activities this year: (1) calibration and correlation work for experiments performed at MSU (plaque HP-RTM injections); and (2) meso-scale modeling of composite preforms for predicting the drapability. Experiments were conducted at GM.

Manufacturing Simulation Work – HP-RTM Plaque Tool

MSU conducted the HP-RTM experiments using the flat plaque tool shown in Figure II.2.13.10 and described earlier were used in calibrating and validating the models. The process parameters used to mold the panels are shown in Table II.2.13.2.

Table II.2.13.2. Process Parameters

Flow rate [cc/s]	17.24 43.1	Resin System	Hexion 6170
Resin Temperature [°C]	68.1	Reinforcement	Chomarat BT600 T3.3
Tool Temperature [°C]	120	Layup	0/0/0
Vacuum pressure [bar]	0.3	Thickness [mm]	2
Flow rate [cc/s]		Fiber ratio [%]	50

In addition, during the experiment, significant amount of race tracking in the surrounding channels was observed. The model was updated to account for this zone and an equivalent permeability for the race tracking area was computed based on the tool thickness in this area. The values for the race tracking permeability used in the simulation is provided in Table II.2.13.3. Figure II.2.13.15 shows the FEM used for the correlation work. Two experimental setups were performed, injection at 20 g/s and at 50 g/s. Both the scenarios were simulated. The value of pressure as a function of time at a sensor located at the center of the lower tool is compared with the experimental results. Figure II.2.13.16 shows the comparison of experimental results with simulation. A good correlation was observed.

Table II.2.13.3. Equivalent Permeability of the Surrounding Channel

Fiber Volume ratio	0%
K1[m ²]	3.63E-10
K2[m ²]	3.63E-10
K3[m ²]	3.63E-10
Permeability Angle [°]	0

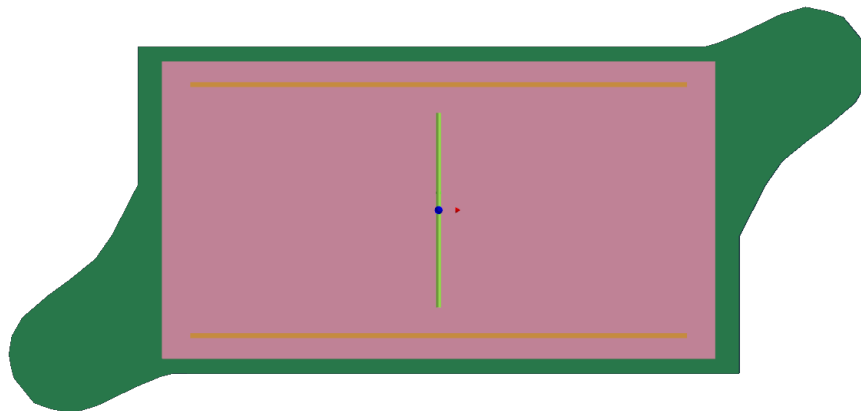


Figure II.2.13.15. FEM representation of the plaque (mesh size 2.5 mm). Source: Michigan State University.

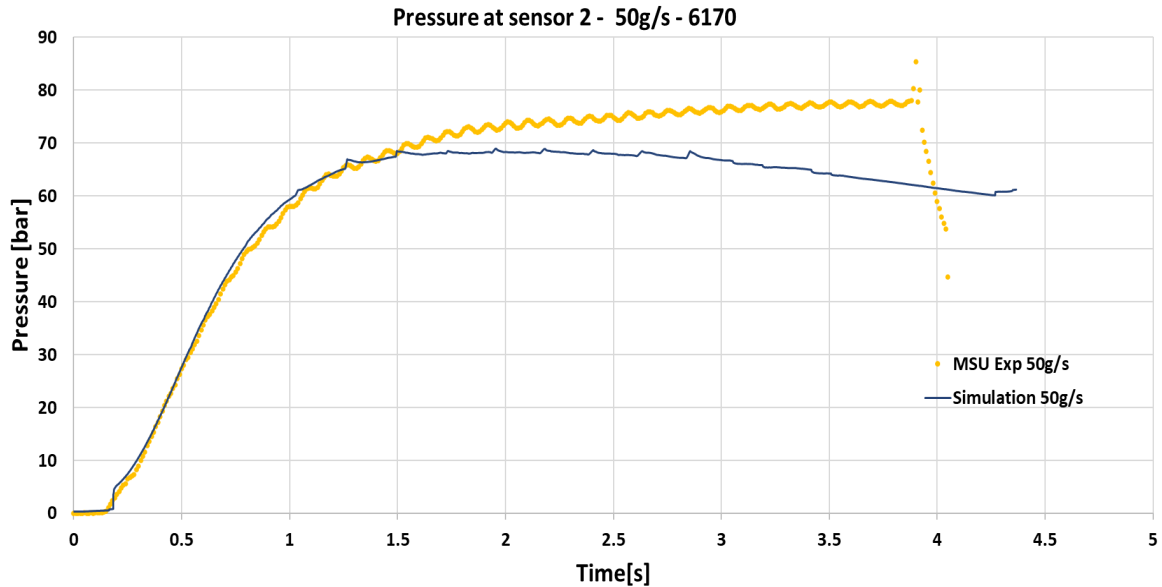


Figure II.2.13.16. Pressure as function of time at the middle sensor. Source: Michigan State University.

Manufacturing Simulation Work – Draping

Another key challenging aspect of manufacturing the composite parts is the draping of the fabrics where the 2D flat shape is converted to the complex 3D shape of the final component. The Lattice™ TFP preforms used in the project offer significant flexibility in terms of design and manufacturability. However, TFP preforms are challenging to model due to the complexities in the stitch pattern, fiber patch, and the backing material.

Two approaches are being investigated for modeling the draping of Lattice™ fabrics. In the first approach, a combination of shell representing fiber tows and backing material, and bar elements modeling the stitches of the preform. In the second approach, a meso-scale approach utilizing the solid elements for modeling the fiber tows, and bar elements for modeling the stitches. Contact conditions will be utilized to tie the fiber tows with the stitch. (As of this writing in November 2021, we expect to finalize the model by the end of December 2021.)

Task 1.2.3. Evaluate and Develop Required Structural Model

Under this task, we will develop state-of-the-art computational models to predict the performance of hybrid composites. Plaques were molded, as described under Task 1.2.1, to generate the experimental data to develop the structural performance model.

Figure II.2.13.17 shows the framework of multiscale structural model compared with the previous model developed under the DOE-funded project DE-EE0006826 [1]. In the present model, an NN-based surrogate model will replace the meso-scale model for the computational efficiency. The NN concept for multiscale modeling of composites is quite novel, and we believe that the technology will be game-changing in improving the computational efficiency and accuracy.

A closed form analytical model to determine the ratio of CF and GF in the composite was developed with the condition that: (a) CF failure precedes the failure of GF; and (b) the final failure load of the composite with GF alone is greater than the load at which CF fails. Utilizing the optimum ratio of CFs and GFs, composite preforms were prepared by commingling them in the three forms, as shown in Figure II.2.13.18. Plaques were molded and samples were prepared for conducting tension and three-point bend experiments. In parallel, multiscale computational models were developed, calibrated, and validated using the experimental data that were generated.

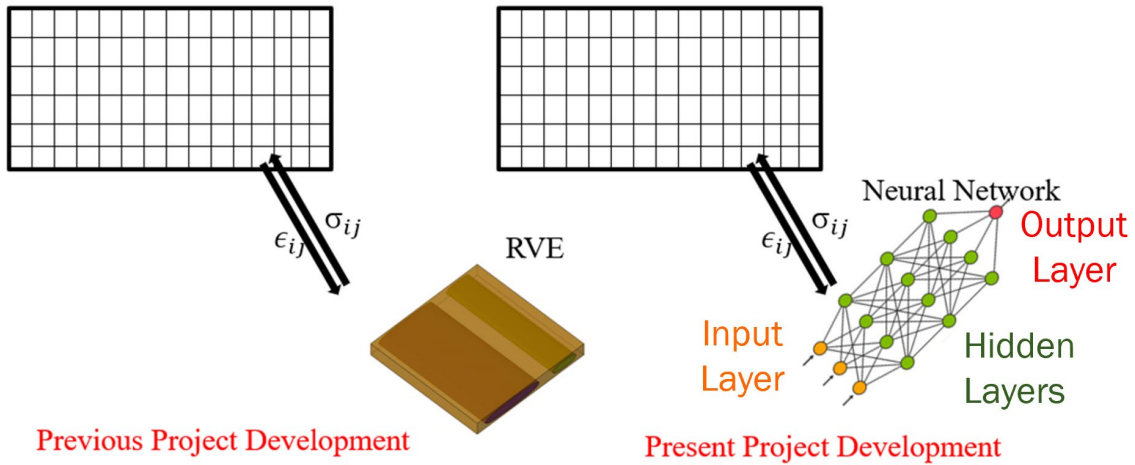


Figure II.2.13.17. Multiscale model development. Source: Michigan State University.

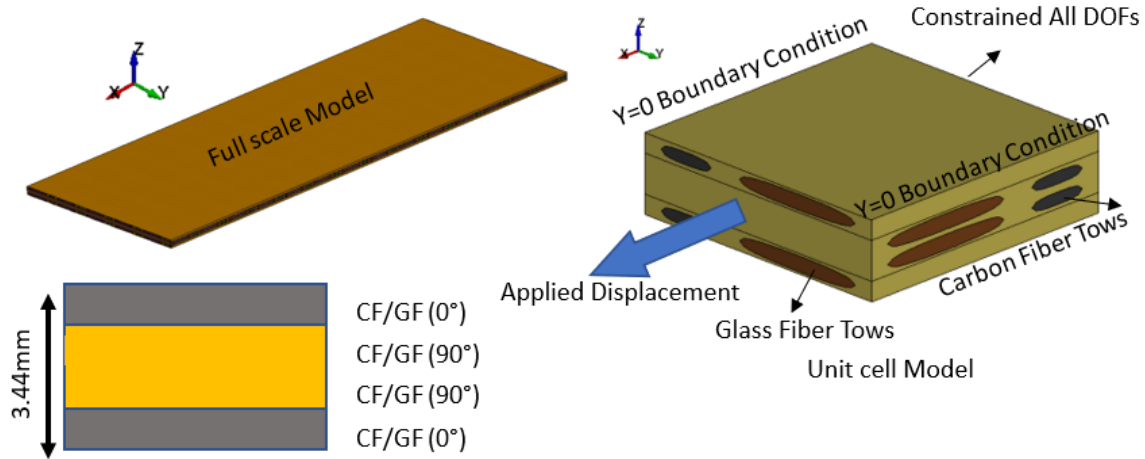


Figure II.2.13.18. Description of the meso-scale model developed for the tensile load case. Source: Michigan State University.

Multiscale Models for Hybrid Composites (CF and GF)

For this task, a layup with 0°/90°/90°/0° hybrid composite was considered under tensile load. The micro-scale model of the CF and GF tows including the resin is shown in Figure II.2.13.18. Suitable symmetry and fixed boundary conditions were applied on the X-Z faces to simulate periodic boundary conditions. The volume fraction of fiber tows and resin considered in the meso-scale model is reported in Table II.2.13.4. The total thickness of the laminate was 3.44 mm. Simulation results predicted the failure of CF tows first, followed by the failure of GF tows. The FEM predictions of force versus displacement were compared with the experimental results which are shown in Figure II.2.13.19. The predictive results showed a high grade of correlation with the experimental results.

Table II.2.13.4. Fiber and Resin Volume Fraction Information in the Unit Cell Model

Sample Number	Carbon Volume Fraction %	Glass Volume Fraction %	Matrix Volume Fraction %
1	11.4	33.4	55.2

Hybrid Lattice (0/90/90/0, CF:GF 19:81) Tensile

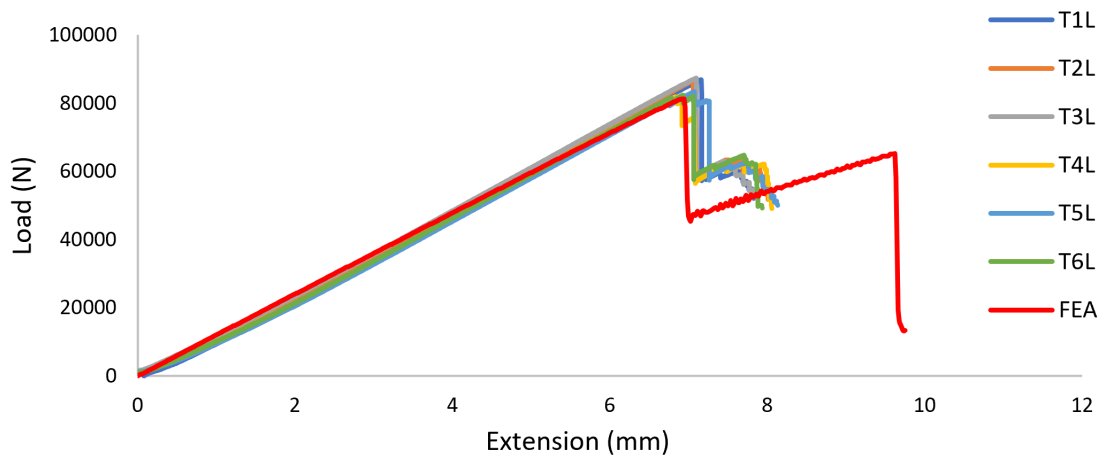


Figure II.2.13.19. Force vs. displacement for the hybrid composite subjected to tensile load case.
Source: Michigan State University.

Validation of Material Models for Hybrid Material Under Flexural Load

The calibrated material models from the tension test were utilized to validate the models by comparing the predictions with the experimental results for the flexural loading. The description of the flexural model is provided in Figure II.2.13.20. The length and width of the specimen considered for study were 150 mm and 40 mm, respectively. The thickness of the specimen was same as the tensile specimens i.e., 3.44 mm. The support span length in the flexural experiments was kept as 100 mm. In the FEM, the element size was kept in the range of 0.21 mm to 0.4 mm while discretizing the fiber tow and resin areas. Material models #54 and #24 available in the LS-DYNA computer program [2] were used for modeling the fiber tows and the resin portions, respectively. Fully integrated element formulation was used for solid elements. The force versus displacement from the simulation was compared with the experimental results, and they are shown in Figure II.2.13.21. The FEM predictions captured the flexural stiffness and the failure displacement of such composites with high accuracy, thereby validating the meso-scale model.

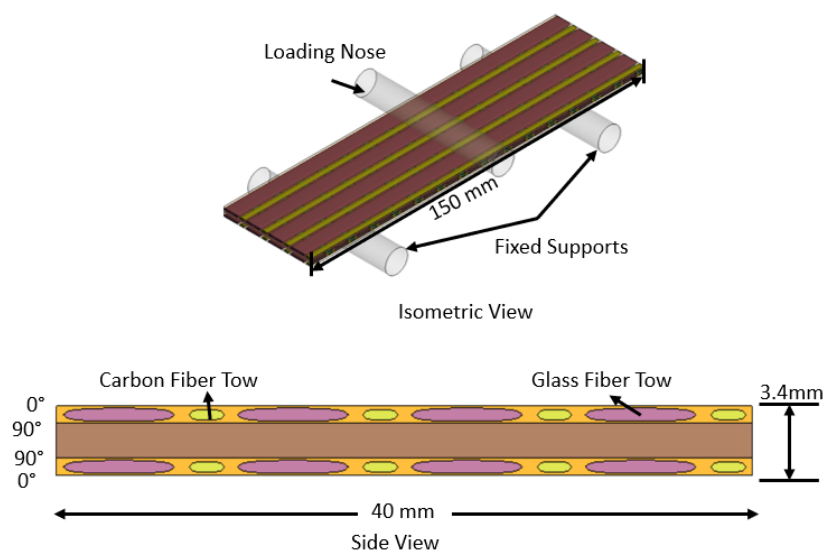


Figure II.2.13.20. Description of the meso-scale model developed for the flexural load case.
Source: Michigan State University.

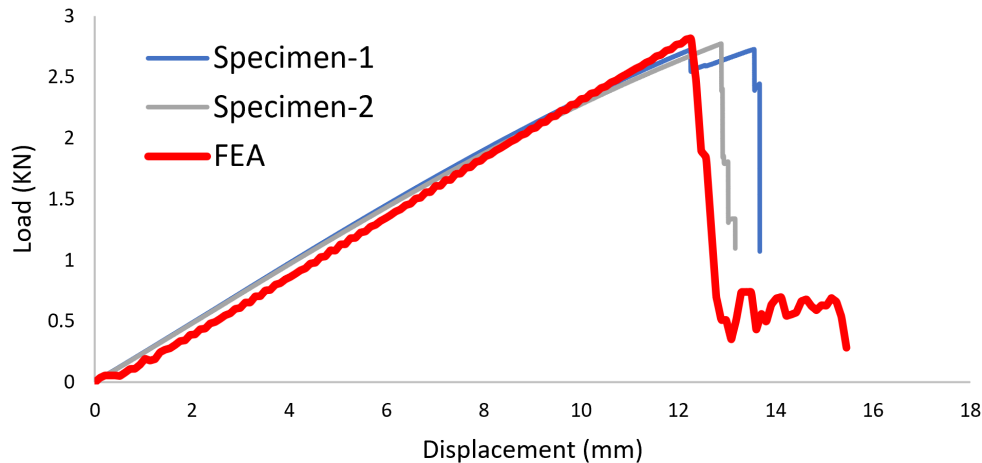


Figure II.2.13.21. Force vs. displacement plot for the hybrid composite subjected to flexural load.
Source: Michigan State University.

Unit Cell Analysis of Hybrid CF and GF Composites

Following the development of the meso-scale model for the hybrid composite, we needed to develop an efficient way to generate a database for the surrogate NN model as per the framework, as shown previously in Figure II.2.13.17. In this process, for a given strain input from the macro-scale model, we need to automatically extract the effective stress from the unit cell after performing calculations with periodic displacement boundary conditions. Towards this, we have developed the associate methodology in the LS-DYNA framework. For greater computational efficiency, we have adopted a nonlinear implicit FEM analysis of the unit cell including the damage. Figure II.2.13.22 shows the meso-scale model of the hybrid composite (GF and CF) with periodic boundary conditions.

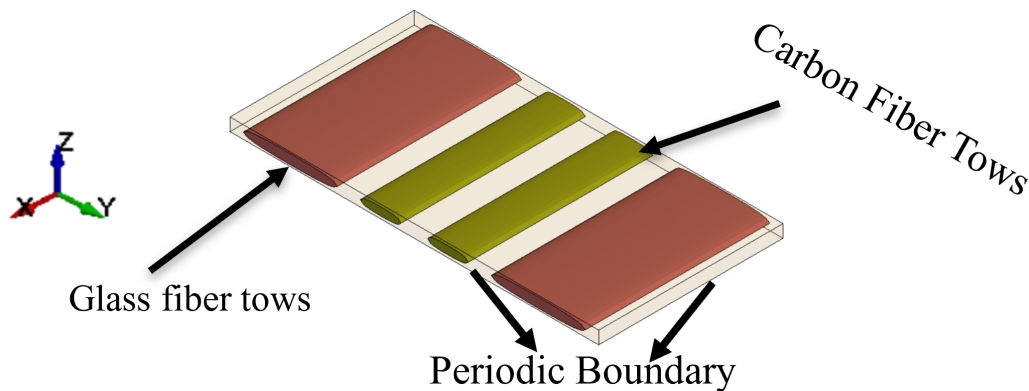


Figure II.2.13.22. Unit cell model for CF/GF hybrid composites (showing fiber tows).
Source: Michigan State University.

The unit cell model was verified by conducting simulations with uniaxial load, biaxial load, and shear load. Figure II.2.13.23 shows the loading conditions. The plot of force versus displacement is shown in Figure II.2.13.24. The correlations of these simulation results are expected to be completed by the end of December 2021.

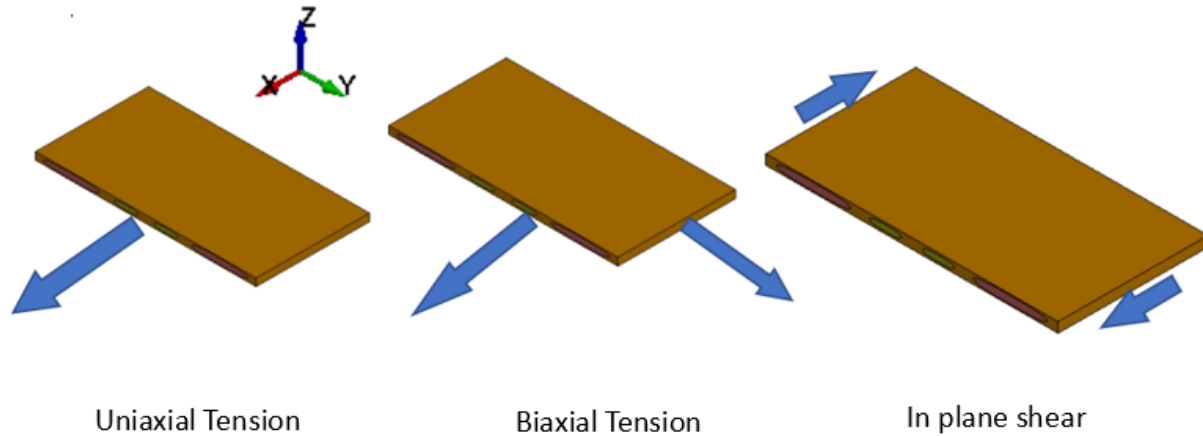


Figure II.2.13.23. Different load cases studied with the unit cell analysis. Source: Michigan State University.

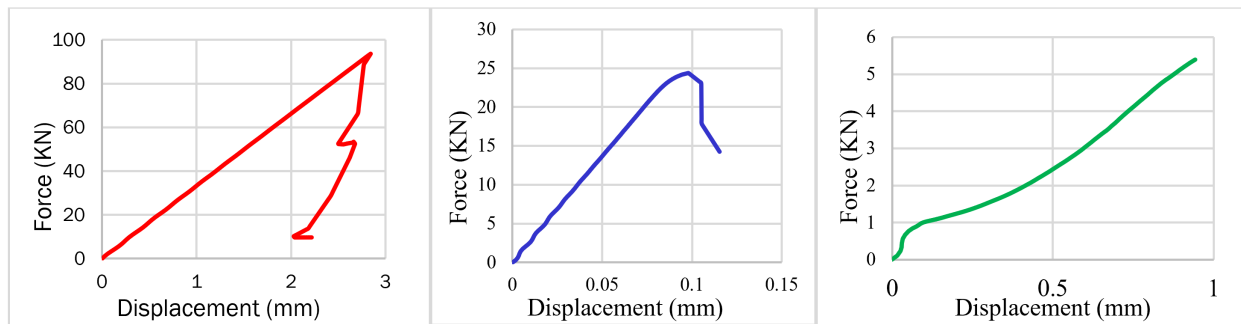


Figure II.2.13.24. Force vs. displacement for the three load cases in the RVE analysis. Source: Michigan State University.

Task 1.2.4. Evaluate and Develop Self-Health Monitoring Technologies

Under this task, we will develop SHM technology by embedding electronic circuitry in the composites. SHM technologies utilize a low-cost conductive wire in the CF tow to detect and locate composite damage, and a temperature/humidity sensor system (T/H sensor, described below), to monitor the health of battery cells for the battery enclosure. The following sections describe the accomplishments in this area.

SHM Sensor

For sensing the damage, the resistance of the sensor was utilized. The resistance is measured by applying a small voltage and measuring the value of the resulting current. This implicit relation between the strain and resistivity of the composite will be used to determine the strain state/damage in the composite.

Figure II.2.13.25 shows the plot of resistance versus strain in the composite. The following two approaches were pursued in developing the SHM sensor:

1. The pass-fail method. Composite damage will break the sensing wire and disconnect its electrical current path.
2. The piezoresistive strain sensor method. Composite strain is monitored by measuring the electrical resistance of the sensing wire, and the composite damage is detected when the resistance exceeds a threshold.

Figure II.2.13.26 shows the experimental results of the tensile sample with an embedded composite wire and CF tow as sensor. The Y axis was plotted with both stress and percentage of resistance change. Among the various conductive sensing wires, the CF tow sensor showed the highest promise. The tensile test results demonstrated a high correlation between the composite strain and the measured electrical resistance, with the resistance increasing rapidly before the composite failure. Therefore, this CF tow sensor can be used not only

to monitor the strain of the composite structure, but also detect damage and provide early warning of structural failure. The tensile tests also demonstrated that the sensitivity of the strain sensor can be increased through a multi-loop design.

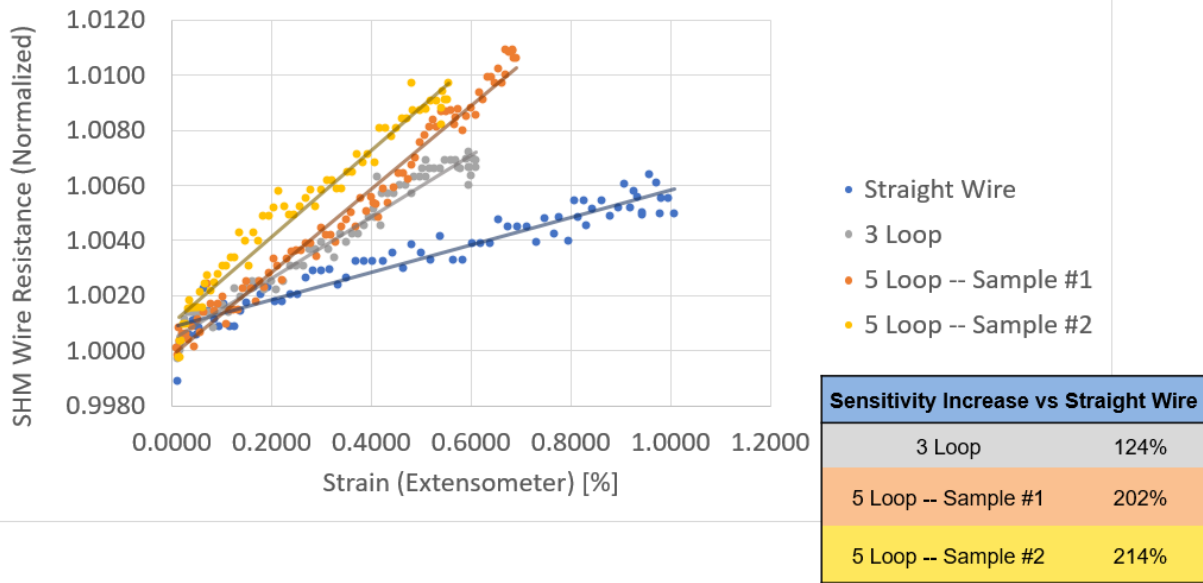


Figure II.2.13.25. Plot of resistance versus strain in the composite. Source: Michigan State University.

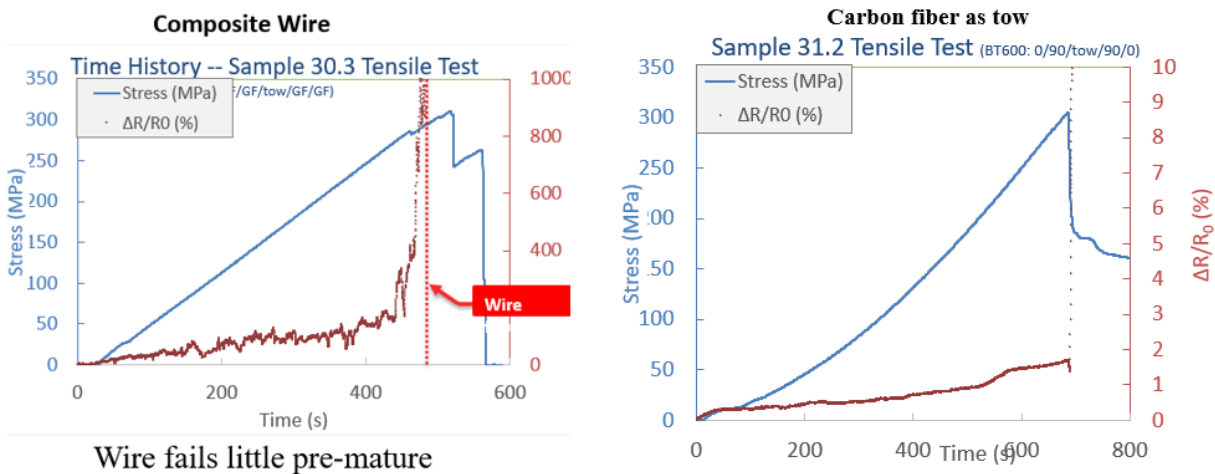


Figure II.2.13.26. Plot of resistance versus strain in the composite wire and CF tow. Source: Michigan State University.

Additionally, a novel low-cost damage location method was developed that requires only one circuit to measure multiple sensing branches and locate the damaged branch. The team formulated and solved an optimization problem that produced a layout design of the sensor branches with required sensitivity and spatial resolution. Based on the design, a specimen was fabricated that successfully demonstrated the damage location method.

T/H Sensor

The project team has developed an embedded temperature sensor for monitoring the temperature of the component. There are several advantages of embedded sensors in the composite versus bonded sensors: removing the need for a sensor housing and thus eliminating the associated weight penalty and cost while

providing more packaging space. A search was conducted for various types of off-the-shelf T/H sensors that can be embedded in the composite enclosure to monitor the battery cell temperature. The search was driven by the required temperature and humidity range with emphasis on the reduction of the overall manufacturing cost. In addition, digital sensors are desired to reduce electrical noise. Based on these requirements, the team has downselected the Sensirion SHT40 sensor as it showed the best performance in terms of response time and presented the optimum tradeoff between the performance and dimensions. This T/H sensor was embedded in a CFRP specimen. During the curing process of the specimen, the sensor successfully measured the temperature and humidity data. Experimental temperature results showed a small lag of temperature measurement between the surface-mounted sensor and the embedded thermal sensor during heating and cooling stages of a composite component, as observed in Figure II.2.13.27. Since the difference is small and the embedded sensor carries all the signatures of the temperature profile from the surface-mounted sensor, an inverse calibration should be able to compensate this difference adequately.

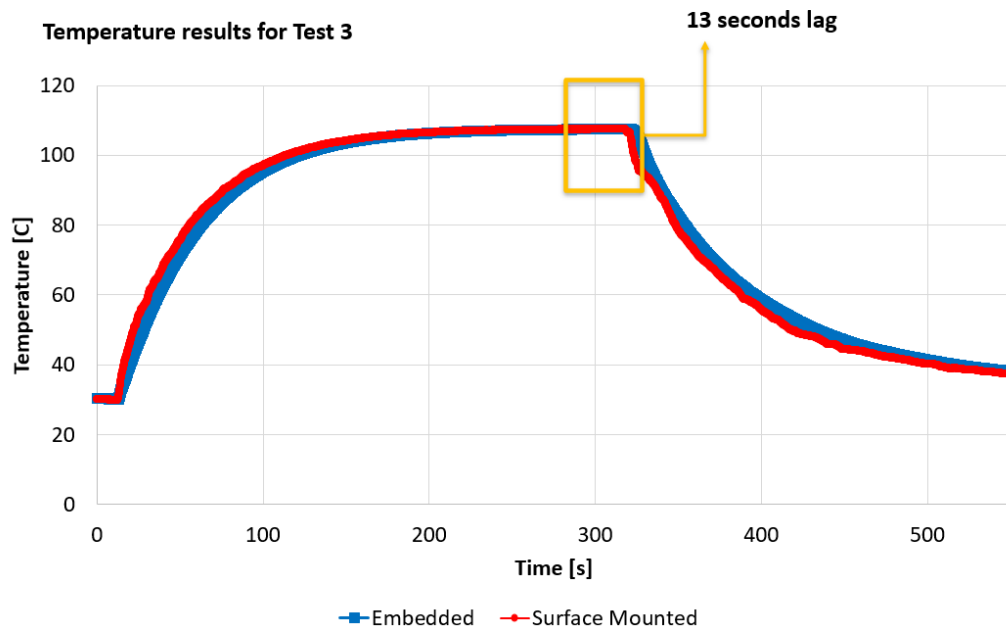


Figure II.2.13.27. Difference between temperature measured using surface-mounted and embedded thermal sensor. Source: Michigan State University.

Task 1.2.5. Evaluate and Develop AI/ML Technologies for Monitoring Manufacturing Process

Under this task, we developed the AI/ML technology for monitoring the manufacturing process. In the event of any abnormalities noticed based on readings from the strategically located pressure sensors, the AI/ML system will automatically determine the required changes to the injection pressure and flow rate to mitigate the risk and produce a quality part.

The developed AI/ML system was applied for composite structural analysis that is trained and informed from three distinct scales: 1) **microconstituents** including volume fraction and fiber/resin mechanical properties; 2) **meso-scale** properties including layup geometry and averaged mechanical properties of lamina, required as input to LS-DYNA computer program; and 3) **laminata structure** properties including elastic moduli, strength and absorbed energy. All observables in the ML system are described as random variables, allowing the team to make inferences about their probability distributions. The prior models for these ML analyses were obtained by a random selection of 500 samples featuring statistical variations of fiber and resin properties, lamina orientations, and volume fraction. These statistical variations are modeled as a beta distribution for the random variables with specified range and shape parameters.

These micro-scale properties are then analyzed through a rule of mixture procedure to produce the lamina-scale properties required as input to LS-DYNA computer program. Each sample of rule of mixture properties thus obtained were propagated through LS-DYNA and a load-deflection curve is obtained. Eight indicators are extracted from each load-deflection curve: four secant moduli of elasticity at different strain levels in the elastic regime, maximum load, deflection at maximum load, absorbed energy at two different levels of strain. A total of 81 observables for each of the 500 samples (13 micro-scale variables, 15 LS-DYNA input parameters for each of four layers, and eight indicators from the laminate-scale force-deflection diagram), are saved and used for the ML training exercise. The training is used to construct a joint density function of all 81 observables which is subsequently used in the following way: observing the force-deflection curves during experiments, some of the eight performance indicators are extracted and used to condition the joint density function to obtain the marginal probability density function (PDF) of the remaining variables. Figure II.2.13.28 below shows the conditional PDF thus obtained by one of the Poisson ratios of the LS-DYNA input deck. The prior PDF was obtained from the 500 samples in the training set. It was clear that the specific experiment used in the conditioning is capable of discerning specific values of Poisson ratio. Figure II.2.13.29 shows similar results associated with predicting the value of tensile strain at failure. Here again, we note that conditioning was able to significantly narrow the uncertainty in the value of the tensile failure strain. The procedure just described could just as easily be used to predict composite properties by conditioning on either LS-DYNA inputs or microconstituents. This would represent the forward uncertainty propagation case.

Constructing a joint density function over 81 dimensional spaces, using the above procedure, is a significant challenge that is addressed within the probabilistic learning on manifolds by embedding the 500 samples of 81 observables in a low-dimensional space and pursuing an Ito sampling [3] in that space to generate several million samples of the 81 observables. With this augmented dataset, statistical inference in high dimension becomes possible with higher accuracy.

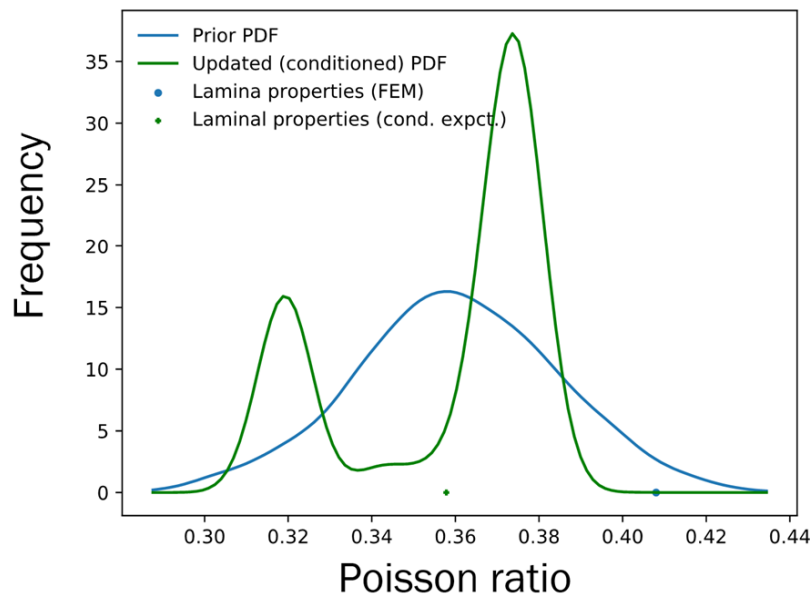


Figure II.2.13.28. Predicting PDF of Poisson ratio conditioned on experimental observations of moduli, energy, maximum force, and displacement. Source: Michigan State University.

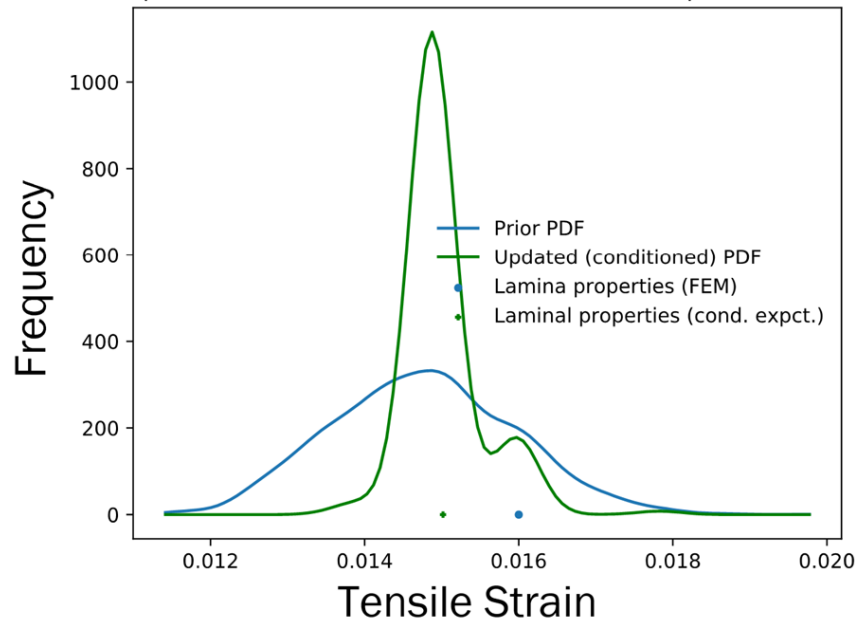


Figure II.2.13.29. Predicting PDF of tensile strain at failure (input to LS-DYNA) conditioned on experimental observations of moduli, maximum force, and displacement. Source: Michigan State University.

For the process monitoring side, we have developed an optimization code to assimilate experimental data into a functional including viscosity represented using Castro-Macosko model. We have described the parameters in this model as random variables, allowing us to inject a model error component in the training set to be used for ML. We have also, with assistance from collaborators at ESI Group, NA, developed a workflow (a series of Python scripts) to generate samples of meshes and input files for PAM-RTM that exhibit variation in permeability due to placement of a patch of certain size at a location, in permeability over each node, and in Castro-Macosko parameters. All these variations are modeled as independent beta distribution for the random variables with range exhibiting 10% to 20% fluctuations around the mean value, and symmetrical shape parameters.

Conclusions

During FY 2021, the project team successfully designed and manufactured hybrid CF and GF preforms in various forms of commingling. These hybrid preforms are very novel and new to the industry. Using the preforms, we have molded composite plaques using the HP-RTM process and extracted coupon samples. The coupon samples were tested for various loading conditions. We have observed an interesting phenomenon called “enhanced ductility,” where the failure strain of CF is increased in the presence of a ductile GF. After characterizing the material systems, we have optimized the ratio of CF and GF to maximize the ratio of performance and cost. From the manufacturing side, the variables such as type of backing material and stitch length of the hybrid preform were optimized to maximize the draping performance. From the modeling standpoint, multiscale, ICME-based structural models were developed where the unit cell model is replaced with a novel NN model to improve the computational effort. We believe this innovative approach is game-changing to the industry. The multiscale structural models were validated by comparing the predictions with experimental results. Manufacturing models were developed and validated for the HP-RTM process considering a state-of-the-art fast-curing resin. SHM technology for damage detection was developed using a CF tow and embedded thermal/humidity sensor was tested for environment observation. A preliminary AI/ML technology for process monitoring was developed and validated for three-point bending experiments. Finally, the assembly chosen for demonstration of technology is a battery enclosure of GM’s production vehicle (2022 Cadillac Lyriq model). The baseline assembly was made with high-strength steel. We have determined the structural performance requirements such as peak load, intrusion, etc., of battery enclosure for the critical load case of side pole impact, and this information will be used in designing the future composite battery enclosure.

Overall, the first year of this project is very productive, and we believe our project outcome will be a significant benefit to the entire automotive industry and will accelerate the implementation of advanced composite materials for next level of lightweighting of automobiles.

References

1. ESI Group, 2022, “PAM-COMPOSITES 2020.6 Software.” Available at: <https://myesi.esi-group.com/downloads/software-downloads/pam-composites-2020.6> (last accessed 7 March 2022).
2. Livermore Software Technology Corporation, 2007, *LS-DYNA Keyword User’s Manual, Vol. II*, Livermore, CA, USA.
3. Soize, C., and R. Ghanem, 2016, “Data-driven probability concentration and sampling on manifold,” *J. Comput. Phys.*, Vol. 321, pp. 242–258.

Acknowledgments

The project team is extremely grateful to the valuable technical and administrative support from DOE managers F. Wu, A. Yokum, and C. Schell.

II.2.14 Ultra-Lightweight Thermoplastic Polymer/Polymer-Fiber Composites for Vehicles (Pacific Northwest National Laboratory and Oak Ridge National Laboratory)

Kevin Simmons, Co-Principal Investigator

Pacific Northwest National Laboratory
902 Battelle Blvd.
Richland, WA 99352
E-mail: kl.simmons@pnnl.gov

Amit Naskar, Co-Principal Investigator

Oak Ridge National Laboratory
902 Battelle Blvd.
Oak Ridge, TN 37831
E-mail: naskarak@ornl.gov

H. Felix Wu, DOE Technology Manager

U.S. Department of Energy
E-mail: felix.wu@ee.doe.gov

Start Date: August 17, 2020	End Date: September 30, 2023	
Project Funding (FY 2021): \$320,000	DOE share: \$320,000	Non-DOE share: \$0

Project Introduction

PNNL and ORNL teamed to develop ultra-lightweight polymer/polymer composites to reduce vehicle component mass. The project will address production of low-cost, high-volume components using high-performance composites. The objective is to demonstrate homo- and heterogeneous polymer-fiber composites that have higher strength and stiffness-to-weight ratios than current thermosetting E-glass and CF composites. Polymer/polymer composites have several advantages over traditional thermosetting glass and CF composites due to their high specific strength and stiffness ratios, impact performance, recyclability, and elimination of galvanic corrosion with Al and Mg joints.

The approach is built on the fact that mechanical properties of plastic materials such as polypropylene (PP) (density $\sim 0.9 \text{ g/cm}^3$) can be improved by introducing structural alignment of polymer chains and crystals during solid-phase processes like uniaxial stretching. The resulting self-reinforced fibers or highly oriented morphology can then be formed into high-strength components suitable for passenger vehicles. As a result, lightweighting and cost reduction can be attained due to removal of higher density fibers (e.g., CF $\sim 1.6 \text{ g/cm}^3$, GF $\sim 2.6 \text{ g/cm}^3$) with lower density fibers and matrices.

Objectives

The project objective is to develop ultra-lightweight polymer/polymer (thermoplastic) composites, comparable to CF composites, to reduce vehicle weight. More specifically, this project will develop a thermoplastic composite with polymer fibers that reduces weight by 30%, has a <3-minute cycle time, and meets the lower-cost target ($< \$15/\text{kg}$ of composite). The research aims to exploit melt- and solution-spun high-performance polymer fibers that have unique mechanical properties, chemical resistance, and thermal stability. With a new composite system that is more recyclable, the project will also demonstrate a scalable, adaptable approach for recycling into new products with lower-cost and higher manufacturing efficiency.

Approach

This project leverages existing processing methods and commercially available materials, promising low-cost and a short path to commercialization. The concept uses fiber spinning capabilities at ORNL for solid-phase uniaxial fiber processing to improve mechanical properties of performance polymers by inducing molecular alignment during the forming process. The project objectives will be met by developing ultra-high-strength, low-cost, lightweight polymer fibers from commodity plastics such as PP and polyester, and their highly drawn controlled crystallinity product with >700 MPa strength. A major challenge in manufacturing polymer-polymer composites is avoiding dimensional instability during fabrication caused by shrinkage force from misorientation/relaxation of fiber polymers. To achieve this, partial crosslinking in fibers will be induced and new chemistries will be developed.

PNNL will develop fabrication techniques with high-quality temperature controls for controlling the rheological behavior of the polymer matrix and cooling for development of polymer morphology to minimize void fractions and maximize material property performance while achieving continuous compression molding or injection molding under three-minute cycle times.

Results

Summary of PNNL Results

Project milestones PM1, PM3, and PM5 in Table II.2.14.1 were completed by PNNL in FY 2021.

Table II.2.14.1. FY 2021 PNNL Milestones

Milestone Name/Description	Criteria	End Date
PM1: Demonstrate with commercially available isotactic PP material powder coating impregnation and mold 6"x6" plaques.	Obtain less than 2% void fraction	12/31/2020
PM3: Surface modification of polymer-fiber for interfacial adhesion to matrix.	Show a 30% change in surface energy from the baseline surface	07/31/2021
PM5: Demonstrate fiber surface interfacial adhesion to thermoplastic matrix materials by evaluating the composite fiber, strength, modulus, and thermal stability	Achieve a 10% increase over untreated baseline	12/31/2021

Commercially available polyethylene, PP, and nylon thermoplastic resin and fiber materials were acquired in support of this project. Thermal analysis and morphological evaluations were completed on the materials to guide the processing trial parameters. Several panel fabrication methods were explored such as solution spraying, immersion coating, and dry powder coating. Ultimately, it was determined that dry powder coating with the use of a doctor blade was the most efficient and consistent method of fabricating single pre-impregnated plies with the target matrix to fiber ratio. These single pre-impregnated plies were then consolidated in a heated platen press to create a test plaque. Test plaques were also fabricated through the film stacking process, where films were prefabricated from polymer powders or pellets and then combined in a stacking sequence with fabric layers.

Milestone PM1 entitled, "Demonstrate with Commercially Available Isotactic PP Material Powder Coating Impregnation and Mold 6 in. × 6 in. Plaques," was achieved by December 31, 2020. Panels were fabricated using two combinations: (1) polyethylene resin and PP fabric; and (2) isotactic PP resin and PP fabric. A fiber content of 45 weight-percent (wt.%) and a void fraction of 1.8% was achieved. The crystallinity of the resin did not significantly change with the processing parameters chosen.

Milestone PM3 entitled, "Surface Modification of Polymer-Fiber for Interfacial Adhesion to Matrix," show a 30% change in surface energy from the baseline surface" was achieved by March 31, 2021. The objective of this milestone was to identify plasma treatment methods that would increase the surface energy of

thermoplastic fibers by at least 30%. This surface energy improvement will result in greater adhesion of the fibers to the thermoplastic matrix, thus resulting in improved mechanical properties of the composite laminate. The milestone was demonstrated using a PP fiber manufactured by Tencate. High-power air plasma and low power (45 W) oxygen plasma treatment methods were both evaluated. The contact angle of water and diiodomethane on the treated and untreated fibers were obtained using a Kruss Surface Energy Analyzer. Surface free energy was calculated according to Owens, Wendt, Rabel, and Kaelble method [1].

The high-power air plasma treatment was evaluated at several height and rate settings to find the optimal plasma treatment. All the high-power air plasma test settings evaluated resulted in heating of the fiber sample, and no surface energy improvement was observed. The low power oxygen plasma treatment was evaluated at different time durations keeping the height and rate constant. The goal of a 30% improvement in surface energy was achieved at the lowest time duration of three minutes. A treatment time of seven-minutes resulted in a surface energy almost twice that of the baseline. The surface energy results are displayed in Figure II.2.14.1.

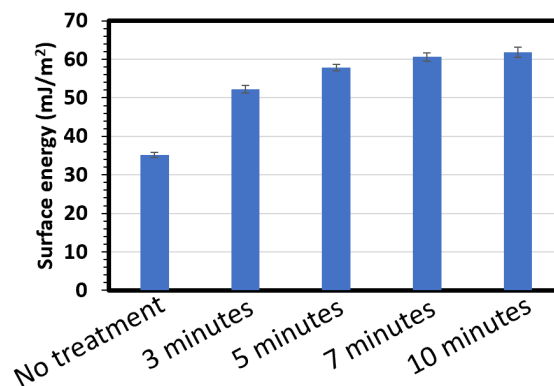


Figure II.2.14.1. Surface energy of PP fiber treated by low power oxygen plasma at varying durations.
Source: PNNL.

Milestone PM5 entitled, “Demonstrate Fiber Surface Interfacial Adhesion to Thermoplastic Matrix Materials with a 10% Increase Over Untreated Baseline,” was completed by September 30, 2021. The objective of this milestone was to quantify the increase in fiber to matrix adhesion when specific surface treatments are applied to the fiber. Increased adhesion of the fibers to the thermoplastic matrix will result in improved mechanical properties of the composite laminate.

A fiber pull-out test method to evaluate the adhesion of a single fiber embedded in a thermoplastic matrix was developed. Baseline values of untreated Tencate PP fiber in high density polyethylene (HDPE) matrix have been compared to values for the plasma-treated Tencate PP fiber. Nominal interfacial shear strength (IFSS) with embedded fiber length is shown in Figure II.2.14.2(a). Helium ion microscopy was used to obtain the fiber dimensions, allowing the IFSS to be calculated by dividing the maximum load by the surface area of the embedded fiber. The nominal IFSS for the untreated Tencate PP fiber embedded in HDPE was 0.43 MPa. The nominal IFSS for the plasma-treated Tencate PP fiber embedded in HDPE was 0.53 MPa. A micrograph of tested single Tencate PP fiber with high magnification in Figure II.2.14.2(b) shows a smooth surface with significantly less HDPE matrix bonding to the surface after testing. On the other hand, Figure II.2.14.2(c) shows plasma-treated surface of PP fiber with more bonded HDPE matrix remaining after testing.

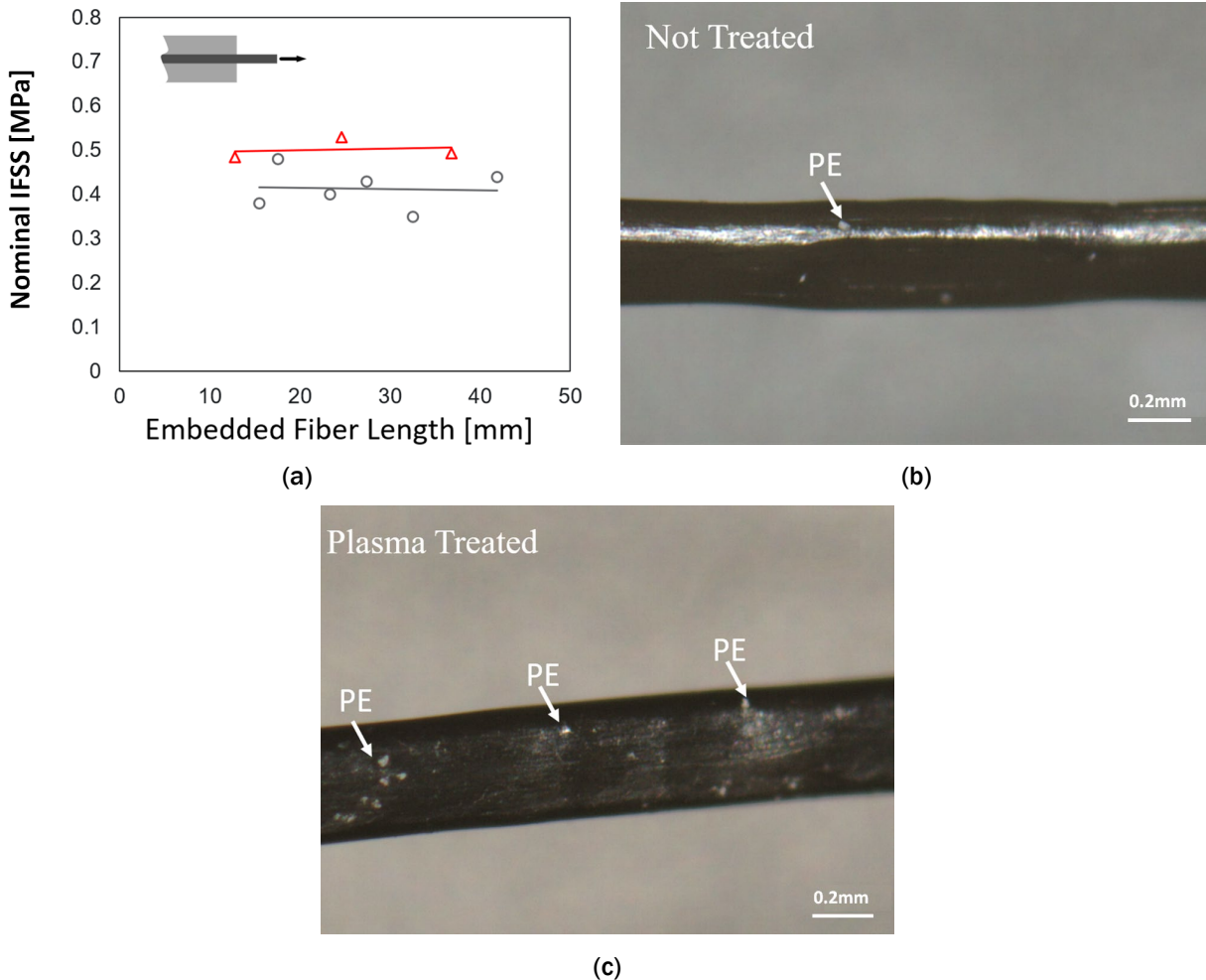


Figure II.2.14.2. (a) Nominal IFSS vs. embedded length for untreated (black) vs. treated (red) PP fiber in a HDPE matrix. (b) Untreated PP fiber. (c) Plasma-treated PP fiber pulled out from HDPE matrix. Source: PNNL

In support of understanding how the processing parameters and fiber-matrix interaction contribute to laminate level mechanical properties, several thermoplastic composite panels have been fabricated and tested. A summary of the panels is shown in Figure II.2.14.3. The fibers in these panels were untreated, and all panels were fabricated using the film stacking method. Note that Panel 3 was fabricated from commercially available, self-reinforced PP composite sheets (trade name Propex) and was tested for comparison purposes only.

Tensile dog bones were machined from each panel in accordance with ASTM D638. The normalized tensile test results (using the rule of mixtures) based on 50 wt.% fiber content are summarized in Table II.2.14.2, and the raw data (unnormalized form) obtained from the tests are shown in Figure II.2.14.3. Panel 1 with 33 wt.% Tencate fiber demonstrated a 27% increase in elastic modulus and 125% increase in tensile strength when compared to the measured properties of neat HDPE matrix (elastic modulus = 1.1 GPa, tensile strength = 31 MPa). Panel 2 with 50 wt.% Innegra fiber demonstrated a 180% increase in elastic modulus and 450% increase in tensile strength when compared to the measured properties of neat syndiotactic PP matrix (elastic modulus = 0.4 GPa, tensile strength = 20 MPa). Also, based on normalized data shown in Figure II.2.14.3 at 50 wt.% fiber content, Panel 1 has the highest Young's modulus, and Panels 1 and 2 have similar tensile strengths.

Table II.2.14.2. List of Fabricated Panels, Material Details, and Normalized Mechanical Properties Based on 50 wt% Fiber Content

Sample Number	Matrix	Fiber	Fiber Form	Fiber Weight Fraction (wt.%)	Young's Modulus based on 50 wt.% (GPa)	Normalized Tensile Strength based on 50 wt.% (MPa)
1	HDPE	Tencate PP	Plain Weave Fabric	33	2.1	108
2	Syndiotactic PP	Innegra PP	Satin Weave Fabric	50	1.1	110
3	PP	PP	Satin Weave Fabric	80	0.9	88

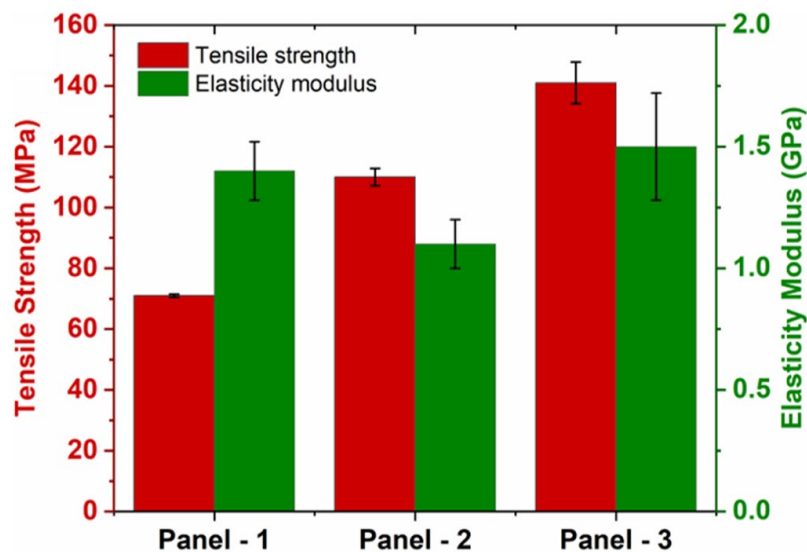


Figure II.2.14.3. A summary of tensile data on panels fabricated by film stacking method with untreated fibers. Source: PNNL.

Summary of PNNL Results

Project milestones PM2 and G/NG1 (Go/No-go) were achieved by ORNL in FY 2021. The detailed milestones and corresponding criteria are listed in Figure II.2.14.3.

Table II.2.14.3. FY 2021 ORNL Milestones

Milestone Name/Description	Criteria	End Date
PM2: Develop 1st thermoplastic fiber (PP) solution-based spinning system, spin and draw 10 meters of polymer-fiber for testing.	Demonstrate spun fiber of 10-meter length for subsequent characterization.	03/30/2021
G/NG1: Demonstrate a fiber with 500 MPa fiber strength and 5 GPa modulus with a 10% STF.	Methodology of sample preparation will be documented. Fibers will be mechanically tested.	09/30/2021

The key milestones for ORNL in FY 2021 are to fabricate a polyolefin fiber, which has high mechanical properties of >500 MPa strength, >5 GPa modulus, and >10% strain to be used as a reinforcing material over a polymer matrix. The milestones are achieved with a gel-spun ultra-high molecular weight polyethylene (UHMWPE), which has a failure strength of 652 MPa, Young's modulus of 18.4 GPa, and elongation at break of 11%. Figure II.2.14.4 presents the UHMWPE gel preparation, fiber spinning, and hot drawing process.

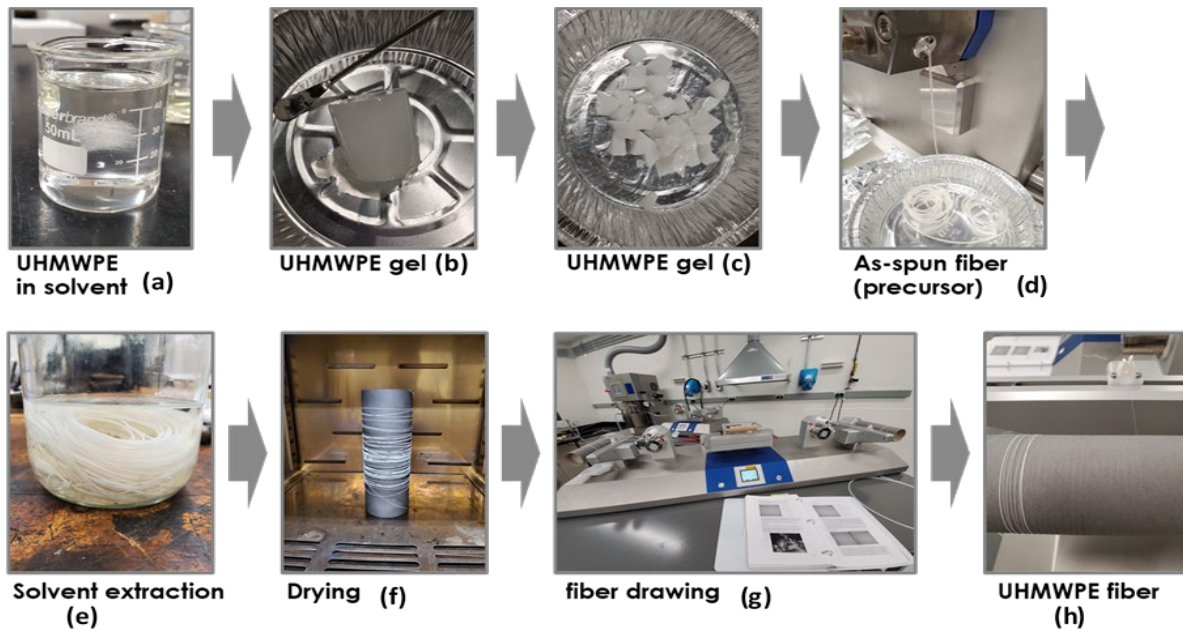


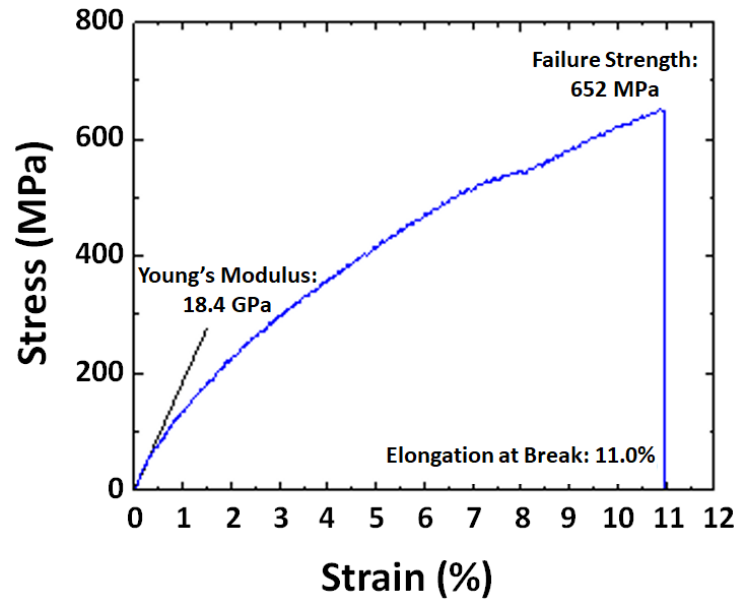
Figure II.2.14.4. UHMWPE solution/gel preparation, fiber spinning, and hot drawing process. Source: ORNL.

First, UHMWPE was dissolved in a solvent. The transparent UHMWPE solution was quickly crystallized in a few minutes at RT, as observed in Figure II.2.14.4(a). A block of UHMWPE gel, as shown in Figure II.2.14.4(b), was cut into small pieces using a razor blade to feed into a micro-compounder, as can be seen in Figure II.2.14.4(c). Spinning was performed using a twin-screw micro-compounder. The UHMWPE gel was fed into a barrel and homogeneously mixed for ~10 minutes at a screw speed of 100 RPM, followed by solvent-assisted melt extrusion through a 0.5 mm die at a low screw speed, as observed in Figure II.2.14.4(d), to minimize filament irregularities by elastic solution fracture. To remove solvent from the as-spun UHMWPE filament, the solvent was extracted for ~1 day as shown in Figure II.2.14.4(e). The remaining solvent was subsequently dried in an oven, as can be seen in Figure II.2.14.4(f). Finally, the as-spun UHMWPE filament was stretched with different drawing ratio using a conditioning unit presented in Figure II.2.14.4(g). The final diameter of the collected UHMWPE fiber was ~150 microns, as observed in Figure II.2.14.4(h).

The mechanical properties of the UHMWPE fiber are presented in Figure II.2.14.5. The tensile test of the UHMWPE fiber was performed by winding both fiber ends around two wood sticks, as shown in Figure II.2.14.5(a), because the sample thickness was too thin to firmly hold using pneumatic grips. Figure II.2.14.5(b) shows a representative stress-strain curve monitored at the strain rate of 20 mm/min. The Young's modulus was determined at 0.2% strain. The failure strength, Young's modulus, and elongation at break of the UHMWPE fiber were 652 MPa, 18.4 GPa, and 11%, respectively, meeting the critical milestones in FY 2021.



(a)



(b)

Figure II.2.14.5. (a) A picture of the UHMWPE fiber being tensile tested. (b) The stress-strain curve monitored at the strain rate of 20 mm/min. The Young's modulus was determined at 0.2% strain. Source: ORNL.

Conclusions

PNNL and ORNL achieved all FY 2021 milestones towards the development of a high-performance thermoplastic fiber/thermoplastic composite material system.

Key Publications

1. Seo, J., et al., 2022, "Controlling interfacial stability and formation of polyamide 66 fibril reinforced polypropylene composite for upcycling of wastes," manuscript in preparation.
2. Qiao, Y., L. Fring, M. Pallaka, and K. Simmons, 2022, "A review on the fabrication methods and mechanical behavior of thermoplastic polymer-fiber/polymer-matrix composites," to be submitted.

References

1. Owens, D., and R. Wendt, 1969, "Estimation of the surface free energy of polymers," *J. Appl. Polym. Sci.*, Vol. 13, pp. 1741–1747.

Acknowledgments

This project was performed in collaboration with Ford Motor Company.

II.2.15 Additive Manufacturing for Property Optimization for Automotive Applications (Oak Ridge National Laboratory)

Seokpum Kim, Principal Investigator

Oak Ridge National Laboratory
2350 Cherahala Blvd
Knoxville, TN 37932
E-mail: kimsp@ornl.gov

H. Felix Wu, DOE Technology Manager

U.S. Department of Energy
E-mail: felix.wu@ee.doe.gov

Start Date: October 1, 2020

End Date: September 30, 2023

Project Funding (FY 2021): \$500,000

DOE share: \$500,000

Non-DOE share: \$0

Project Introduction

This project is aimed at using advanced manufacturing for developing property optimized structures for applications in passenger vehicles. The primary objective of this project is to develop lightweight structures with tailored mechanical responses by utilizing multiple technologies associated with polymer and composites AM. The primary AM technologies developed in this work include multi-material printing using material extrusion AM process, out-of-plane printing (OPP) using a multi-axis robotic arm printer, and toolpath optimization associated with the printing systems. In addition to material selection and optimization, design flexibility offered by AM process will be leveraged in this project by developing novel lattice structures with tailored responses in AM parts. Some of the key steps towards attaining these goals include lattice structure optimization, ML for design selection, toolpath optimization, multi-axis robot arm control, and part fabrication and testing steps.

Objectives

With the primary focus being developing tailored structures with high-performance for applications in passenger vehicles, two target parts/components have been chosen in this project, in collaboration with Ford Motor Company (Ford). The first part is a front bumper, and the second is a door panel arm rest.

To develop a front bumper that meets the performance requirements, research will be conducted on fabricating parts with multi-material printing. Therefore, our studies involve printable material properties and optimizing material combinations. In the design space, novel 2.5D lattice structures with tailored mechanical responses will be developed in collaboration with the University of California-Los Angeles (UCLA) using ML techniques. The final printed bumper is aimed to incorporate both material and design optimized structures, thereby being a customized lightweight structure with high-performance.

In the case of a door arm rest, research will be conducted on OPP technique using a robotic arm printer. Extrusion and control techniques in the OPP system require research and development in this project including slicing technology development, toolpath planning and optimization, robotic arm control and extrusion control optimization, and material property evaluation and optimization. For OPP technology development, a single material with optimized structures will be explored to obtain lightweight high-performance components.

Approach

The proposed work is divided into three major tasks, with various subtasks for each. The first task will provide a large-scale structure optimized for structural design and multi-material placement printed in the BAAM system. In the second task a control technique for OPP will be developed, and the subcomponent of a vehicle will be fabricated. The third task will focus on the ML algorithm development for a subcomponent structure

with tailored energy absorption characteristics in collaborations with Prof. Rayne Zheng at UCLA. Below is the list of tasks and subtasks in FY 2021:

1. Multi-material large-scale printing of optimized structures (bumper)
 - 1.1. Initial design selection and performance criteria with load conditions
 - 1.2. Mechanical property evaluation and for BAAM materials
 - 1.3. Property optimization and the demonstration of printing of property optimized structure
2. OPP of optimized structures (arm rest)
 - 2.1. Design optimization through topology optimization.
 - 2.2. Performance simulation for the out-of-plane structure.
3. Tailored lattice structures using ML
 - 3.1. Simulation technique development for 3D-printed lattice structures
 - 3.2. Simulation verification and parameter calibration through experimental comparison
 - 3.3. Perform simulations for multiple lattice structures and material combinations (small-scale)

Results

Task 1. Multi-Material Large-Scale Printing of Optimized Structures (Bumper)

Task 1.1. Initial Design Selection and Performance Criteria with Load Conditions

A front bumper of a passenger vehicle was chosen for Task 1 of this project involving multi-material printing on the large-scale BAAM 3D printer. Upon discussions with industry partner Ford, along with literature reviews, a bumper design was identified to be used as the reference design for this project. The bumper design comprises three parts: (i) bumper base; (ii) long and thin fins; and (iii) short and thick fins.

Standard tests for full-sized bumpers include testing at both low and high speeds. The two test methods that will be employed for the final part testing for this task are (i) Pendulum intrusion test and (ii) Leg flexion test. The bumper chosen here has two conflicting performance requirements. The pendulum intrusion test, which is used for creating scenarios such as the impact of the vehicle with another vehicle, is conducted at a low speed of 2.5 mph using a large footprint impactor. For the bumper to perform successfully under such impact conditions, the energy absorber (EA) portion of the bumper should be stiff (deformation < 22 mm). On the other hand, for the leg flexion test, which replicates the scenario of impact with a pedestrian's leg, test speeds are higher at 25 mph. In this case, the EA allows larger deformation (deformation < 85 mm). Therefore, these automotive passive safety parts must be fabricated such that they have an adaptive footprint size as well as adequate impact speed. The conflicting performance requirements for a bumper must be achieved using a combination of lattice designs and multiple materials.

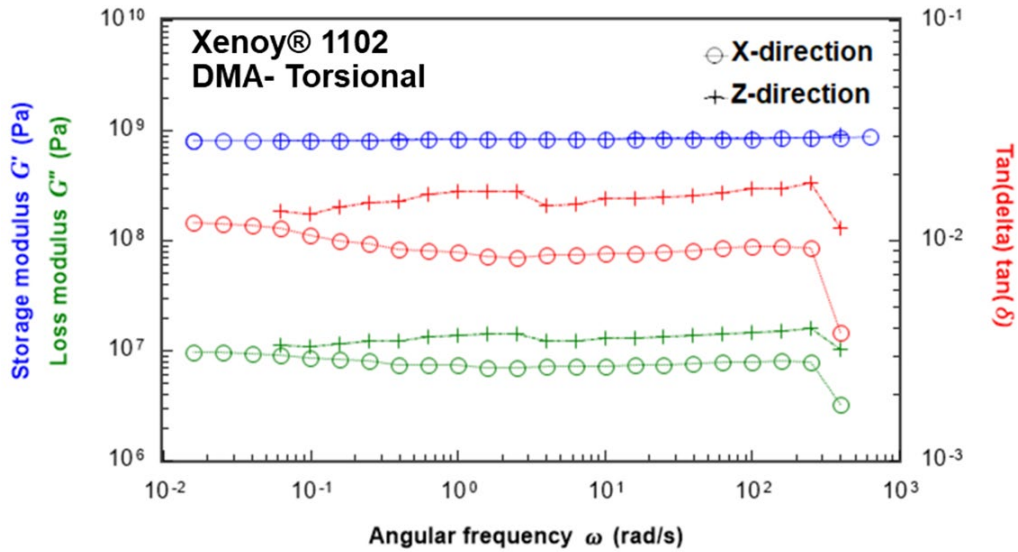
Task 1.2. Mechanical Property Evaluation and for BAAM Materials

Table II.2.15.1 shows material characterization (modulus) data for five different material systems measured from parts printed on the BAAM system. The materials were chosen such that they ranged from a highly stiff printable material, such as 20 wt.% CF reinforced ABS, to a highly elastomeric material such as thermoplastic polyurethane (TPU) 70 Shore A, as well as blends of these two materials which exhibited a range of intermediate properties. Xenoy® 1102, a material commonly used in bumper manufacturing, was chosen to characterize some baseline material properties.

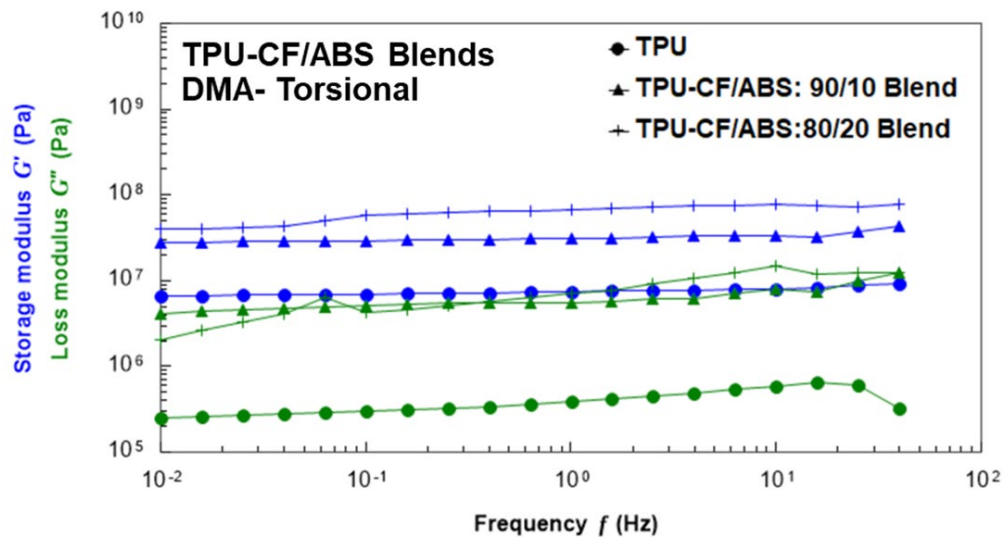
Figure II.2.15.1(a) represents data from dynamic mechanical analysis and tensile testing for Xenoy® 1102 and Figure II.2.15.1(b) for TPU-CF/ABS blends which were utilized as inputs for subsequent material property optimization.

Table II.2.15.1. Modulus Evaluated for Five Materials Printed on Large-Scale AM System

Materials	Property	Values
Xenoy® 1102	E (GPa)	2
TPU (70 Shore A)	E (MPa)	16
20 wt.% CF/ABS	E ₁₁ (GPa)	12.47
	E ₃₃ (GPa)	2.58
Blend 1: 20 wt.% CF/ABS and TPU (20:80)	E ₁₁ (GPa)	0.41
Blend 2: 20 wt.% CF/ABS and TPU (10:90)	E ₁₁ (MPa)	98



(a)



(b)

Figure II.2.15.1. DMA properties in a frequency sweep for (a) Xenoy and (b) TPU and CF/ABS blends (90/10 blends and 80/20 blends). Source: ORNL.

Task 1.3. Property Optimization and the Demonstration of Printing of Property Optimized Structure

We have obtained the anisotropic mechanical properties from a limited experimental dataset. First, based on the experimentally measured E_{11} and E_{33} values, we have utilized micromechanics models to calculate anisotropic mechanical properties, and obtained the effective composite properties with aligned fibers. Second, based on the aligned properties and modulus in the flow direction and cross-flow direction, we have dehomogenized the composite materials and obtained fiber orientation distributions and modulus tensors for the following materials: (1) CF/ABS composite; (2) the blend of CF/ABS 20% and TPU 80%; and (3) a blend of CF/ABS 10% and TPU 90%. The details of the dehomogenization technique are shown in reference [1].

Mechanical properties of blend materials with the blending ratio ranging from 0% to 100% were estimated as shown in Figure II.2.15.2 for ABS/CF/TPU blend materials using interpolations based on the obtained anisotropic mechanical properties shown previously in Table II.2.15.1. The four data points are from the experiments in the material: (1) 100% TPU; (2) 10% CF/ABS + 90% TPU; (3) 20% CF/ABS + 80% TPU; and (4) 100% CF/ABS. The optimal blending ratio of 85% CF/ABS + 15% TPU was selected based on the geometry and thickness of the fin.

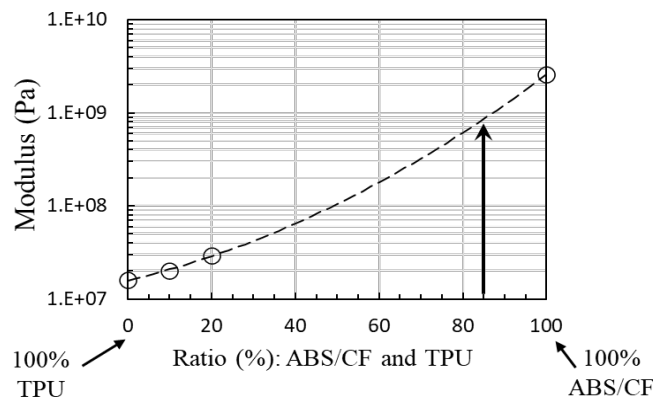


Figure II.2.15.2. Moduli of ABS/CF/TPU blend materials. Circle data are from the experiments. Source: ORNL

The projected performance of the bumper with the selected blend material was obtained using a finite element analysis (FEA) method. The reference design for Xenoy material was modified for the new material blend. Because the blend material has fibers, and therefore the anisotropic directionally should be accounted for, the fiber alignment direction was assigned in the geometric model. The simulation shows that the bumper with the selected blend material (85% ABS/CF + 15% TPU) is slightly (by 11%) stiffer than the reference bumper with Xenoy as shown in Figure II.2.15.3. The results show that the selected blend is the optimal ratio for the bumper design that can replace the baseline reference bumper for 3D printing.

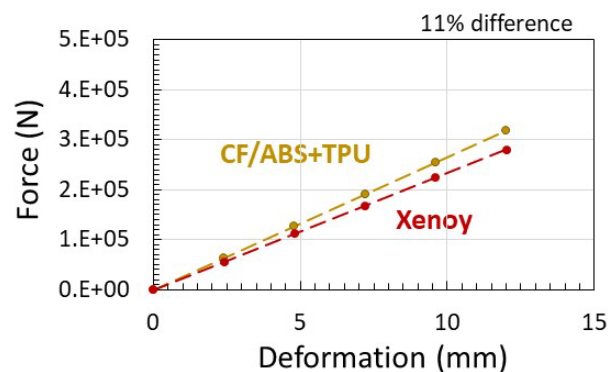


Figure II.2.15.3. Deformation–force curves during loading bumpers made of the blend material and Xenoy. The bumper with the blend material is slightly (~11%) stiffer than the bumper with Xenoy. Source: ORNL.

We printed a sub-portion of the bumper using the selected material blend and CF/ABS (achieving the Go/No-go Milestone). Figure II.2.15.4 depicts a bumper subcomponent that was printed on the BAAM using two materials (20 wt.% CF/ABS and a blend of TPU with 20 wt.% CF/ABS) with the material ratios and site-specific properties determined from material property optimization process. As shown in Figure II.2.15.4, the bumper has long fins and short fins (the image of the 3D printed bumper was blurred due to proprietary info of Ford's design). The long fins were 3D printed with the blend material (CF/ABS 85% and TPU 15%), and the short fins were 3D printed with CF/ABS.

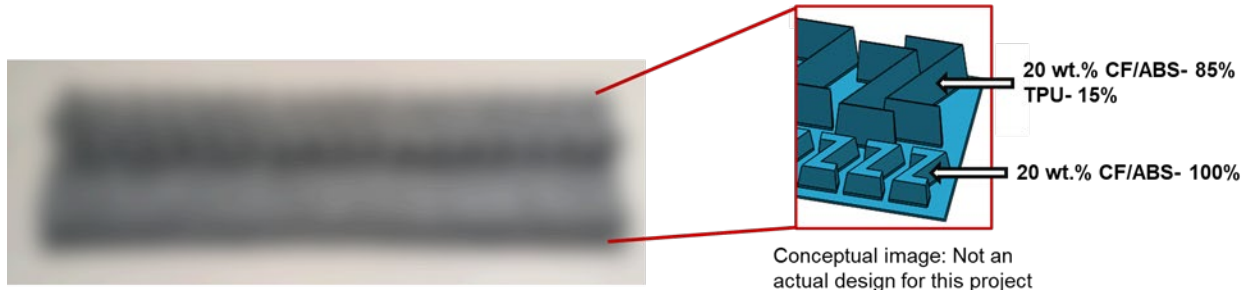


Figure II.2.15.4. Bumper subcomponent printed with property optimized material combinations. The image of the 3D printed bumper was blurred due to proprietary info of Ford's design. Source: ORNL.

Task 2. Out-of-Plane Printing of Optimized Structures (Arm Rest)

Task 2.1. Design Optimization Through Topology Optimization

Load cases and the deflection criteria were identified for a door arm rest. Figure II.2.15.5(a) shows the load cases and the deflection requirement. A FEA was performed to obtain a stress distribution in the design space as shown in Figure II.2.15.5(b). A topology optimization was performed, which is an iterative process between a simulation and the material removal until the target volume is achieved. Figure II.2.15.5(c) shows the topology-optimized structure. The volume has reduced by 75% (volume change: 3430 cc --> 790 cc) because of topology-optimization. From the topology-optimized design, we have further modified the design to a shell design. The result of the entire process of design optimization is shown in Figure II.2.15.5(d). The final design consists of a 1 mm-thick shell throughout the part with a weight of 271 g and a volume of 219 cc.

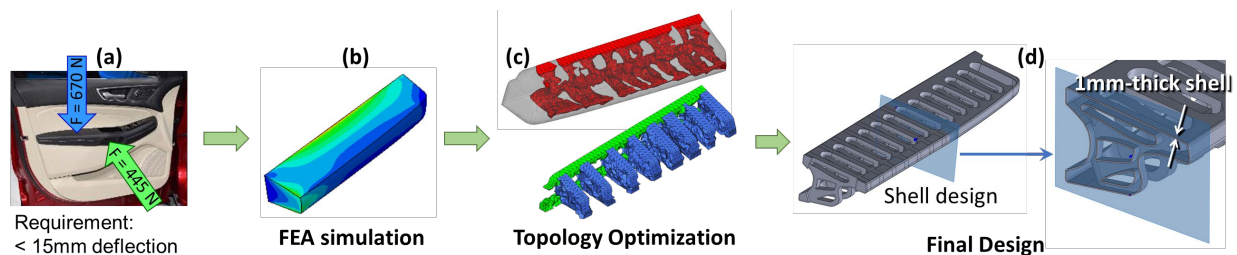


Figure II.2.15.5. (a) Load cases and deflection requirement for a door arm rest. (b) Stress distribution via FEA. (c) Topology optimization with 30% volume fraction target. (d) Final shell design. Source: ORNL.

Task 2.2. Performance Simulation for the Out-Of-Plane Structure

Performance simulations were conducted via FEA assuming the material is neat polylactic acid ($E = 2.3$ GPa). For given loading conditions, the maximum deflection is shown as 6.8 mm, which satisfies the requirement (< 15 mm deflection) as shown in Figure II.2.15.6.

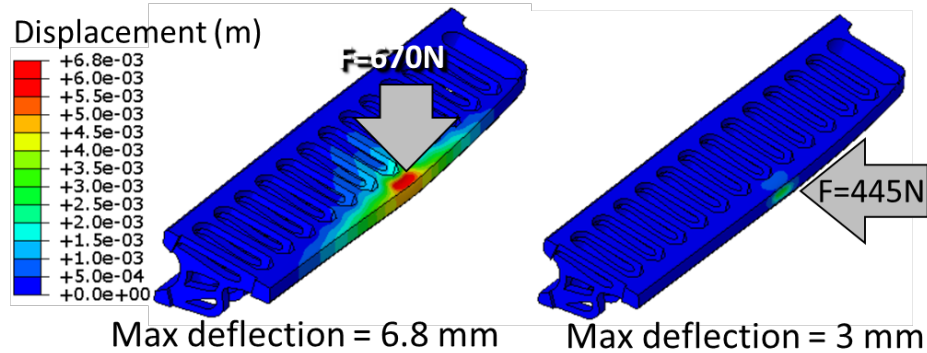


Figure II.2.15.6. Performance simulation of the optimized design. The maximum deflection for the given load cases (6.8 mm) satisfies the requirement (<15 mm). Source: ORNL.

Task 3. Tailored Lattice Structures Using Machine-Learning

Task 3.1. Simulation Technique Development for 3D-Printed Lattice Structures

A simulation framework has been developed to model the compression behavior of a lattice structure using a FEA approach. The framework utilizes three stages to capture accurate buckling failures: (1) material anisotropy assignment; (2) perturbation (modal analysis); and (3) compression simulation, as shown in Figure II.2.15.7. Material properties for orthotropic elasticity and Hill plasticity were used. Fracture was modeled as element deletion. Element deletion occurred if the maximum principal stress exceeded the strength of the material. Element-element contact detection/repulsion was accounted for with a penalty friction.

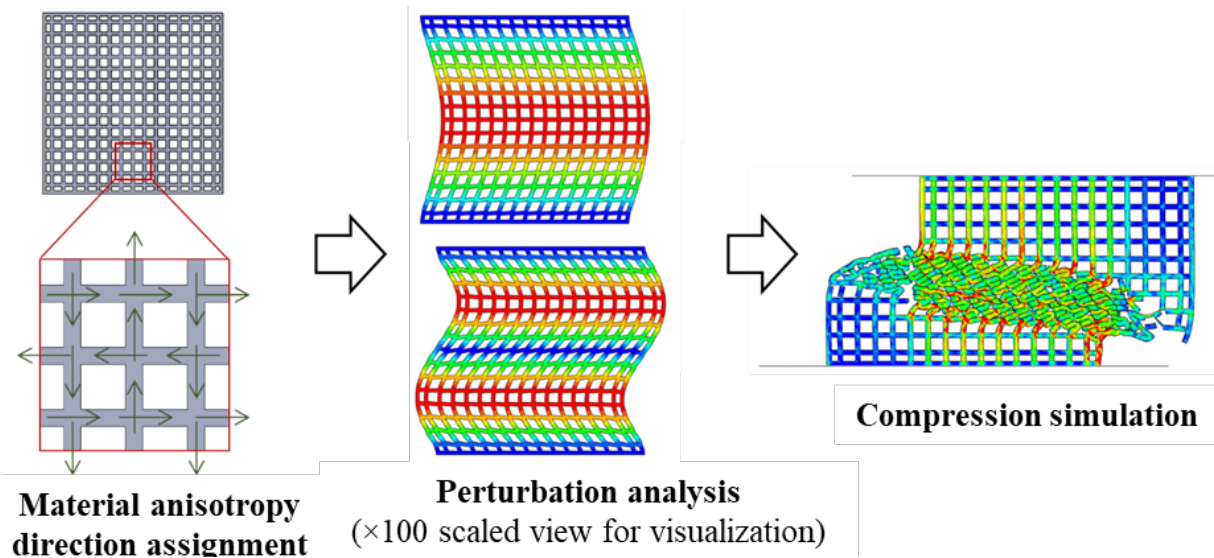


Figure II.2.15.7. Simulation workflow for lattice crush using FEA. Source: ORNL.

Task 3.2. Simulation Verification and Parameter Calibration Through Experimental Comparison

We have calibrated our simulation parameters based on literature values [2] and performed crush simulations on various lattices and compared the results with experiments. The failure patterns are in a good agreement with experiments as shown in Figure II.2.15.8.

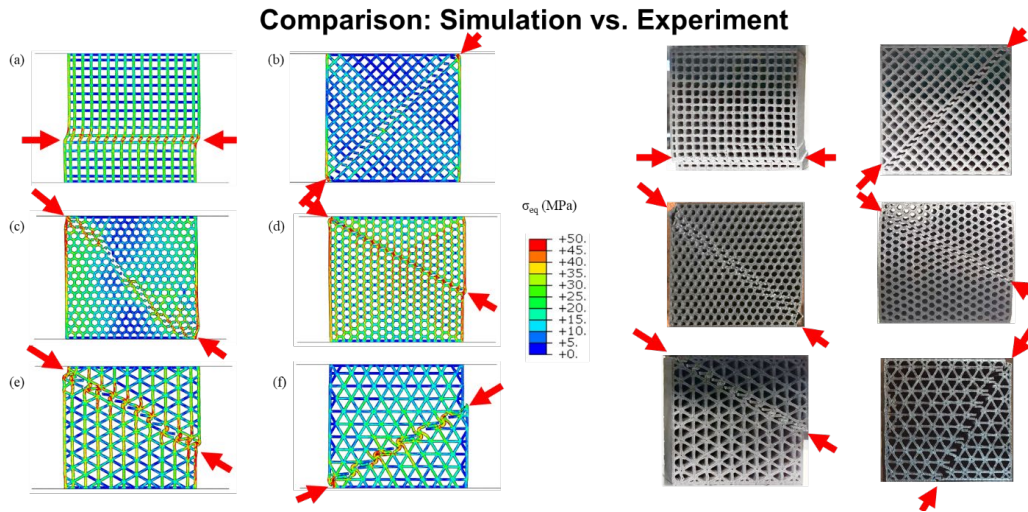


Figure II.2.15.8. Crush simulation on six different lattice orientations and comparison with experiments. Source: ORNL.

Task 3.3. Perform Simulations for Multiple Lattice Structures and Material Combinations (Small-Scale)

Figure II.2.15.9 presents the simulation results of multiple lattice structures and multiple materials. In terms of materials, we have used CF/ABS/TPU blends, Formlab Tough, and trimethylolpropane triacrylate (TMPTA). In terms of lattice structures, we have used a square grid (0°), an isogrid (-30°), and a honeycomb grid (30°). We have also introduced a wall thickness gradient in four steps: (1) 0.6 mm to 1.6 mm; (2) 0.8 mm to 1.4 mm; (3) 1.0 mm to 1.2 mm; and (4) no gradient (uniform). The results are shown in Figure II.2.15.9.

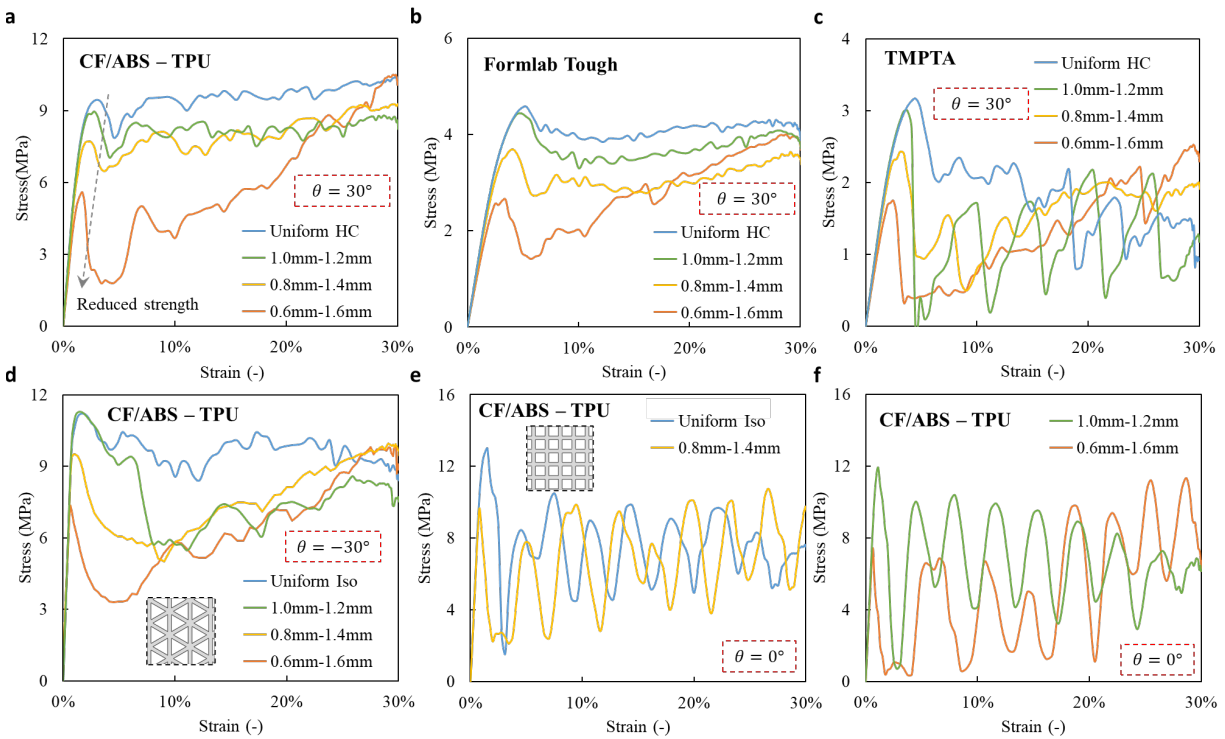


Figure II.2.15.9. Compressive responses with various cell wall thicknesses. (a) Honeycomb ($\theta=30^\circ$) lattice with CF/ABS/TPU blends. (b) Honeycomb ($\theta=30^\circ$) lattices with Formlab Tough. (c) Honeycomb ($\theta=30^\circ$) lattices with TMPTA. (d) Isogrid ($\theta=-30^\circ$) lattice. (e)–(f) Box Infill ($\theta=0^\circ$) lattice with CF/ABS/TPU blends. Source: ORNL.

Conclusions

In FY 2021, for Task 1 involving multi-material printing development for an automobile bumper, material property evaluation for chosen printable materials was conducted. In addition, multi-material property optimization was performed for a bumper and the bumper subcomponent was printed on the BAAM system. For an arm rest, a topology optimization was performed, and a shell design was proposed based on the topology optimization. The deflection of the shell design predicted via simulation satisfies the requirement. For lattice crush responses, an FEA framework for lattice crush simulation was developed, and the results show a good agreement with experiments. Based on the framework, we have obtained lattice crush responses with various materials and lattice shapes. The results will be used for training an ML framework.

Key Publications

1. Kim, S., A. Nasirov, V. Kishore, C. Duty, and V. Kunc. “Compression characteristics of additively manufactured lattice composite structures,” manuscript in preparation.

References

1. Kim, P., H. Baid, A. Hassen, A. Kumar, J. Lindahl, D. Hoskins, C. Ajinjeru, C. Duty, P. Yeole, U. Vaidya, F. Abdi, L. Love, S. Simunovic, and V. Kunc, 2019, “Analysis on part distortion and residual stress in big area additive manufacturing with carbon fiber-reinforced thermoplastic using dehomogenization technique,” *The Composites and Advanced Materials Expo (CAMX 2019)*. TP19-0694, Available at <https://www.osti.gov/biblio/1607087> (last accessed 8 March 2022).
2. Jiang, D., and D. E. Smith, 2016, “Mechanical behavior of carbon fiber composites produced with fused filament fabrication,” *Solid Freeform Fabrication 2016: Proceedings of the 26th Annual International Solid Freeform Fabrication Symposium*. pp. 884–898.

Acknowledgments

The work performed in this project in FY 2021 involve contributions from teams at ORNL, UCLA, and Ford Motor Company. The key personnel who contributed to project progress in the past year include V. Kishore, S. Simunovic, T. Smith, V. Kunc, T. Feldhausen, R. Kurfess and B. Knouff from ORNL; X. (R.) Zheng, and D. Yao from UCLA; and E. Lee, I. Farooq, R. Baccouche, S. Chowdhury, Z. Pecchia, and M. Rebandt from Ford Motor Company.

II.2.16 Additively Manufactured, Lightweight, Low-Cost Composite Vessels for Compressed Natural Gas Fuel Storage (Lawrence Livermore National Laboratory)

James P. Lewicki, Principal Investigator

Lawrence Livermore National Laboratory
7000 East Ave.
Livermore, CA 94550
E-mail: lewicki1@llnl.gov

H. Felix Wu, DOE Technology Manager

U.S. Department of Energy
E-mail: felix.wu@ee.doe.gov

Start Date: July 1, 2020	End Date: September 30, 2023	
Project Funding (FY 2021): \$460,000	DOE share: \$460,000	Non-DOE share: \$0

Project Introduction

CF/polymer composites are a transformative class of high-performance, lightweight material, where high aspect ratio CFs reinforce a polymer matrix and exceed the strength of steel alloys at a fraction of the density. Despite the advantages of such a class of material, the broader implementation of CF composites in a range of automotive, aerospace, and energy applications is hindered by limitations of current manufacturing methods. These current techniques (e.g., hand layup, wet filament winding) are costly and impose severe limitations on fiber placement, orientation, and angle, and thus a composite's ultimate properties. Today's CF composites are expensive to manufacture, limited in form factor, and utilize costly and sub-optimal continuous filament CF. Advanced AM processes, combined with computational design optimization and new approaches to resin development, offer alternative design and manufacturing paradigms that have the realistic potential to lift these constraints. Such integrated AM approaches could thus help to realize the full potential of CF composite materials.

One relevant application of CF composite materials where manufacturing constraints limit the cost-benefit ratio is in the manufacture of high-performance composite pressure vessels for onboard compressed natural gas (CNG) storage. Current CNG storage vessels (Types 3–5) are made from load bearing filament-wound CF composite and are ~3.5 times as expensive as an all-metallic Type-1 vessel. This cost is invariably tied to the complex and labor-intensive nature of conventional filament winding processes and the large volumes of expensive high-tensile strength CF tow feedstock required in manufacture. Our proposed approach to CNG storage vessel manufacture is based on a combination of AM technologies for CF composite printing and design optimization tools that were pioneered at Lawrence Livermore National Laboratory (LLNL), with advances in resin/composite formulation enabled by chemical and nanomaterial modification. Through the successful development of this technology, LLNL seeks to demonstrate the capability for advanced CNG storage vessel manufacture at reduced cost with no reduction in performance versus the most advanced, extant Type-5 designs.

Objectives

The proposed work addresses three objectives that are critical to the additive manufacture of next-generation CF composites:

- **Objective 1:** Enhance resin properties via chemical and nanomaterial modifications to yield an improved resin matrix with significantly increased mechanical performance over baseline winding resins. (*Enables reductions in CF content without detriment of performance.*)

- **Objective 2:** Realize compositionally graded CF composites. Apply novel AM and design methodologies to combine continuous and short-fiber structures in a graded, computationally optimized tank design which maximizes performance while minimizing mass and cost. (*Hybrid, optimized design enables increased performance at lower relative volume fraction of expensive continuous CF filament.*)
- **Objective 3:** Additively manufacture and test a contoured hybrid CF vessel having all the major design elements of a Type-5 CNG Tank, providing validation of the materials and design concepts within a relevant laboratory-scale environment (*Enables the development of a technology data package including a cost to benefit assessment for the demonstrated technology and will form a starting point for further maturation [post-project] at scale.*)

Approach

This project will develop a process to combine AM (via direct ink writing [DIW]) technology for CF composite printing and use design optimization tools pioneered at LLNL, with advances in resin/composite formulation enabled by chemical and nanomaterial modification to produce lightweight low-cost CNG tanks. Our approach will yield sub-scale prototype composite pressure tanks equivalent to Type-5 CNG vessel designs that demonstrate a potential cost-benefit advantage. Central to our vision is using agile AM and design based on computationally informed DIW of both short and continuous CF, further coupled with high-performance thermoset polymer matrixes modified by emergent nanomaterials. Our single-stage, multi-material AM technology, combined with a decreased volume fraction of CF and an increased proportion of economically advantaged short-fiber, all together drive the reduction in manufacturing time and overall cost. Importantly, reductions in continuous fiber and overall fiber volume fraction will be achieved without detriment to the mechanical strength of the composite vessel. This will be achieved by employing a single process, multi-materials grading involving the following: a thermoset resin ‘ink’ modified with aligned nanoplatelets to leverage the efficient tortuous-path gas barrier effect, printed as an inner flexible gas barrier as the initial stage in our manufacturing process before compositionally grading the AM feedstock in real-time to transition to a rigid, structural CF-filled resin. The proposed hybrid construction is projected to achieve pressure ratings (2,900 psi to 3,600 psi service range with a 3 times burst safety factor) comparable to conventional filament-wound composite tanks with an estimated 30% to 50% reduction in total manufacturing cost. The cost reductions are based on a reduction in the levels of CF required and process streamlining achieved via a hybrid DIW manufacturing method, as observed in Figure II.2.16.1.

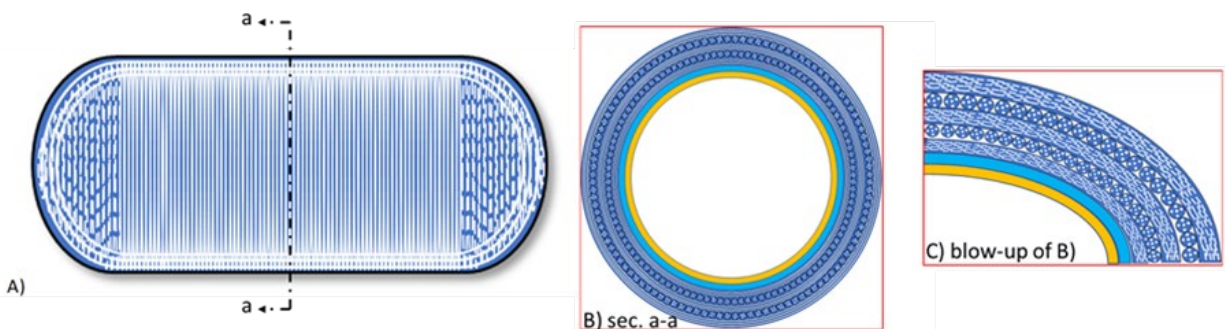


Figure II.2.16.1. Schematic of an AM-CNG storage vessel concept. (a) External rigid structural layers of the vessel: load bearing resin filaments (blue) filled with short and continuous CF (white). (b) Continuous filament material is applied to the midbody yielding maximum hoop strength. (c) Short-fiber extrusion used to fabricate complex end caps. (b) and (c) Flexible and cross-linkable polymer compositions reinforced with nanoplatelets will be printed to serve as the inner layers of a vessel (yellow and blue layers represent the inner gas barrier and transition to structural layers respectively). Source: LLNL.

A core advantage of our approach over existing technology lies within our high-performance thermosetting resins that are both ultraviolet (UV) gellable and thermally curable. They are specially formulated to be compatible with the DIW process and to engender enhanced gas barrier and mechanical performance in the

final printed material. We will base our gas barrier resin technology on the development of a UV-gel/thermal-post-cure epoxy network that is chemically modified for flexibility and physically modified with 2D graphene nanoplatelets. Our structural resin will be based on a family of LLNL high-performance polymers characterized by hybrids of cyanate ester and aromatic epoxy segments in a contiguous network. To overcome the ubiquitous challenges in CF composites relating to weak polymer matrices and fracturing at CF-matrix interfaces, we will introduce additional hierarchical reinforcement elements based on 1D nanomaterials. Our non-acrylate-based, UV-gel/thermal-cure technology is found in both resin families. This similar chemistry enables a single-stage, multi-materials deposition process wherein one resin can be covalently blended into the next at a range of compositional gradients.

Through hybridizing continuous and short-fiber printing we will enable the manufacture of novel graded composites. This will realize printing with tunable and enriched concentrations of continuous filament in the center of the vessel body to maximize radial hoop strength while minimizing the overall use of expensive continuous filament fibers. A unified resin deposition process seamlessly blends portions of the build requiring rich continuous filament with short-fiber material to accommodate conformal and open geometries problematic for standard continuous filament techniques (e.g., vessel endcaps). To realize this hybrid composite approach, a new print head is required to be developed (based on LLNL’s Patent’s and extant breadboard demonstrations in the area). The design, manufacture and testing of a hybrid print head, that enables the laydown of both long fiber tows and short-fiber ‘ink’ within a single AM structure will be carried out in collaboration with our industrial partner – Materials Sciences LLC (MSC). MSC will design and manufacture a practical hybrid head prototype, based on LLNL breadboard concepts that may be integrated into LLNL’s current AM printing platform, participate in the integration and testing of the system and execute any improvements/modifications that are necessary after completion of the prototype trials. (MSC will also participate in the design of the hybrid test vessels under Task 3 of this project).

We will maintain optimal mechanical performance of our composite vessel walls using a multiscaled, hybrid composite structure—realized in a rationally designed manufacturing form derived from DIW. Leveraging our advanced DIW printing technology for short and continuous fiber, we will develop unique capabilities to manufacture the main body of the vessel within one consolidated, cost-efficient process.

A series of burst and performance tests of manufactured articles will form the basis of the validation of our design and manufacturing approach. A breakdown of our project schedule at a task level is shown in Figure II.2.16.2.

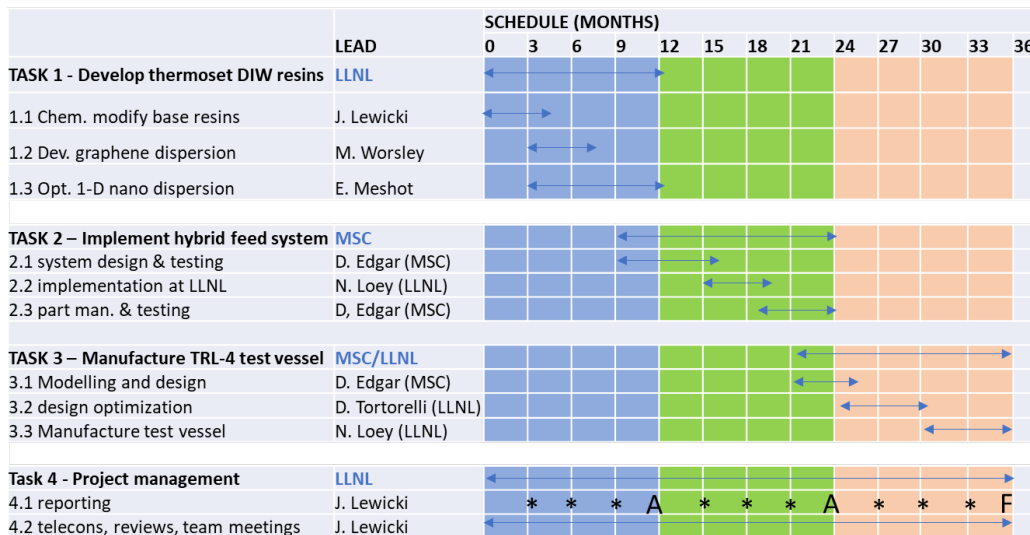


Figure II.2.16.2. Project schedule. Source: LLNL.

Results

Significant progress was made in FY 2021 in the development, testing, and modification of nano-enhanced resin phases optimized for use in our DIW CF composite printing process: We have demonstrated the successful incorporation of GO platelets, ceramic nanofibers, and functional nano silicas into our base UV gellable DIW resin systems and quantified the resultant effects on the matrix mechanical performance of each.

The effects of GO on the strength of a UV gellable cyanate ester based DIW resin were studied over a range of GO loadings (from 0.0 wt.% to 0.5 wt.%). The GO dispersion in the uncured resin was achieved through a roll-milling-based compounding approach, with dispersion efficiency being assessed via rheology, as observed in Figure II.2.16.3.

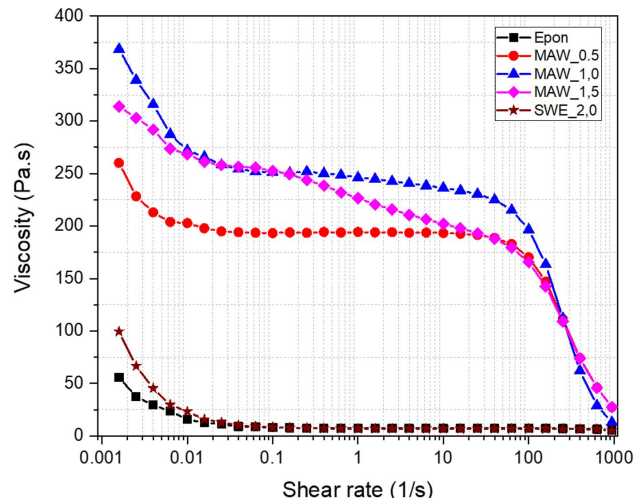


Figure II.2.16.3. Rotational rheometry of a range of base and modified resins. The 'Hexon EPON' and 'SWE2.0' are unmodified epoxy and cyanate ester bases respectively. 'MAW 0.5–1.5' are 0.5 wt.%–1.5 wt.% dispersions of GO in cyanate ester. Note that the DIW modified GO resins have a clear thixotropic response with a shear-thinning profile at higher shear rates. Note that 'SWE' and 'MAW' are notebook tracking names for test formulations based in the initials of the researchers who produced the samples Source: LLNL.

The GO/resin base was then modified for the DIW process through the addition of necessary thixotropes and catalysts—both with and without loadings of short CF to yield a range of GO modified model short-fiber 'test' inks. From these inks, test coupons for tensile testing to failure were printed on LLNL's DIW carbon composite printing platform, as can be seen in Figure II.2.16.4. The results of tensile tests of the prepared samples are given in Table II.2.16.1.

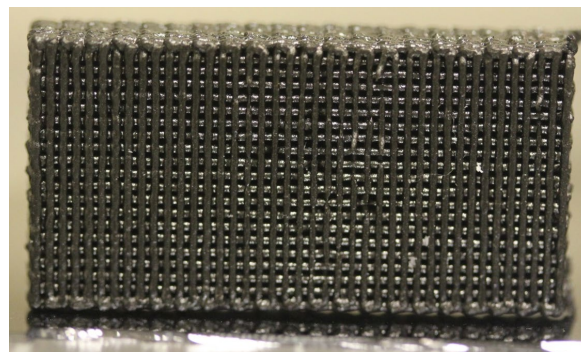


Figure II.2.16.4. Experimental shear test setup and the apparatus of manufacturing shear test samples. Source: ORNL.

Table II.2.16.1. Percentage Increase in Tensile Strength and Stiffness of a Cyanate Ester Based, Printed Short CF Composite as a Function of GO Loading

GO wt.% Added	Strength (MPa) Increase (%)	Modulus (GPa) Increase (%)
0	--	--
0.025	11.5	36.7
0.050	8.2	18.0
0.100	7.9	36.7
0.174	12.2	0.6
0.500	2.7	21.0

From these data it is apparent that GO both has a significant beneficial effect of the strength and stiffness of the DIW resin system as-printed and cured, and that there is a clear optimum loading of GO on the system of 0.025 wt.%. At levels above 0.025 wt.% we saw a decline in the mechanical reinforcement effects. These data suggest a strong validation of the nano-reinforcement effect whereby ultra-low loadings of high aspect ratio materials can have correspondingly large effects on the bulk properties of the matrix. However, as higher loadings were approached, the nano-phase morphology of the composite breaks down and an agglomerated micro composite regime is entered, whereby larger domains of agglomerated nanoparticles may simply act as defects and stress concentrators on the matrix. Regardless, achieving a ~37% increase in modulus and a 11% increase in strength through an extremely low loading of a relatively inexpensive nanomaterial is a positive result as well as an overall validation of the nanomodification objective.

Further approaches to nanomodification were carried out in FY 2021. Both ceramic nanofibers and functional nano-silica colloids were assessed to determine their effects on the mechanical properties of our DIW resins. Utilizing a preparation and compounding approach similar to that employed for the GO study, a broad loading range of printed tests coupons of nanofibers in a cyanate ester base and functional nano-silica in an epoxy DIW base were prepared and tested. Given in Figure II.2.16.5 and Figure II.2.16.6, respectively, are the summarized results of the effects of these nano modifiers on the mechanical properties of the bases.

From the data summarized in Figure II.2.16.5, it is apparent that the nanofiber modifier can considerably alter the mechanical properties of the DIW resin base. At low loadings (~1 wt.%) in the ‘nano regime’ we observed up to a 37% increase in strength with no change in modulus. In the bulk regime (~20%) we observed up to 120% increase in Young’s modulus with no increase in strength.

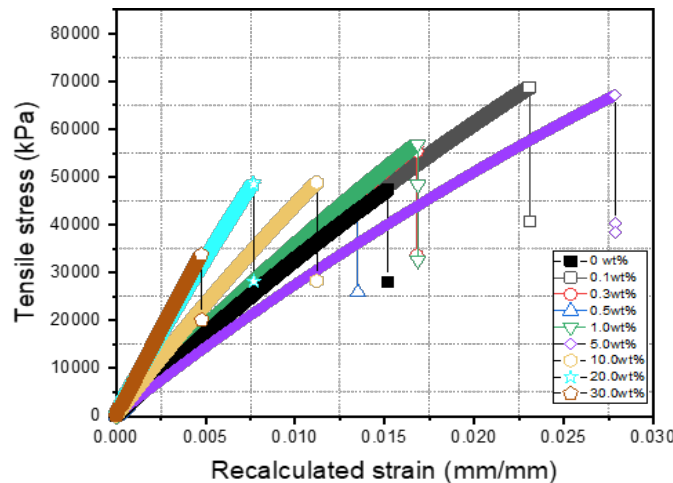


Figure II.2.16.5. Tensile stress vs. STF of DIW cyanate ester resins modified with up to 30 wt.% nanofibers. Source: LLNL.

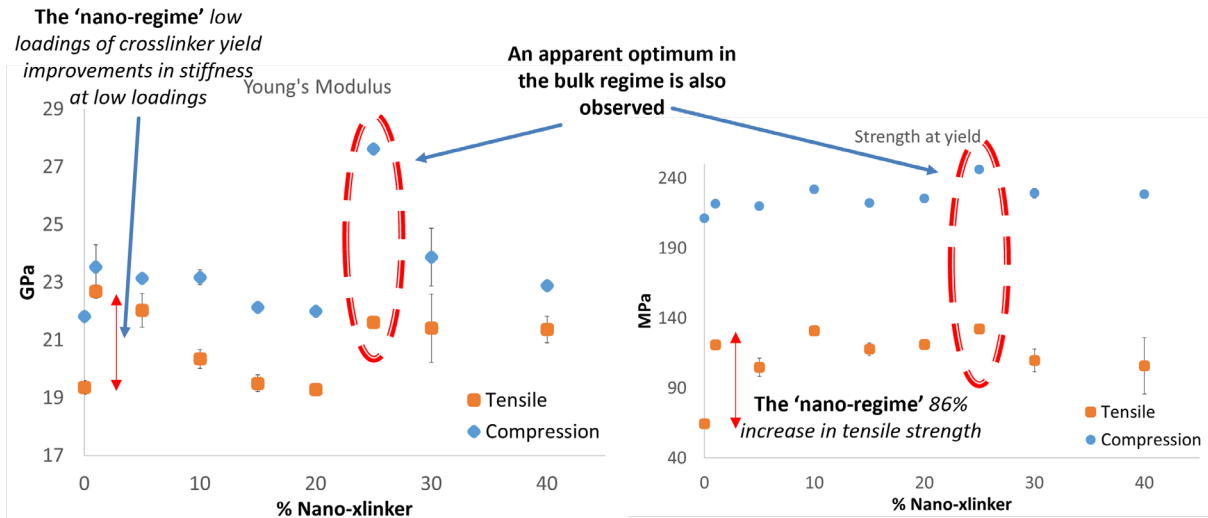


Figure II.2.16.6. Overmolding process (a) AM metal mesh; (b) AM LFT preform on top of the AM metal mesh; and (c) compression overmolding. Source: ORNL.

From the data presented in Figure II.2.16.6, it is once again apparent that the base mechanical properties of the DIW Resin (in this case an epoxy-based material) can be significantly improved and modified by the inclusion of a relatively inexpensive nano modifier—here a colloidal nano-silica capable of chemically crosslinking in the network. Positive effects were observed in both tension and compression. Two regimes are again evident: a nano-reinforcement regime (~1 wt.%) and a bulk regime ~20 wt.%. In the nano regime we observe 86% improvement in tensile strength and 32% increase in modulus and in the bulk loading regime we observe a 103% increase in strength and a 16% increase in modulus, as compared to the unmodified short-fiber loaded baseline DIW resin.

Conclusions

In FY 2021 we successfully demonstrated the ability to modify custom DIW-processable thermoset resins with three classes of relatively inexpensive nanofiller. We successfully printed each with and without a short-fiber phase on our customized CF AM platform, further demonstrating concept viability. Though characterization and testing we identified optimal loadings of each in our base resins and further identified transitions to bulk micro composite regimes at higher loadings. Individually, GO, colloidal nano-silica, and ceramic nanofibers all present process compatibility for CF AM and impart significant improvements in strength and stiffness of the base resin materials fulfilling a primary project milestone and providing a path forward for an optimized nanomodified resin base for FY 2022 vessel design and initial test article printing. Uncertainties remaining in the nanomodification approach include the possibility of potential synergistic or antagonistic behavior of the various nanophases with each other in such an optimized resin and the yet uncharacterized effects of the nano modifiers on the important second order physical properties including, but not limited to fracture toughness, hardness, fatigue resistance, and crack propagation. Obtaining experimental data to address these uncertainties will be a further target of FY 2022 activities.

Acknowledgments

Dr. M. A. Worsley (LLNL), Dr. S. Chandrasekaran (LLNL), and Dr. E. Meshot (LLNL) are all gratefully acknowledged for their extensive scientific contributions to resin development and testing. Ms. S. Mabery (LLNL), Mr. Taylor Bryson (LLNL), and Ms. K Baron (LLNL) are all greatly acknowledged for their technical support of material's preparation, printing, testing, and characterization. This work was performed under the auspices of DOE by LLNL under DOE contract DE-AC52-07NA27344.

II.2.17 3D-Printed Hybrid Composite Materials with Sensing Capability for Advanced Vehicles (Oak Ridge National Laboratory)

Rigoberto C. Advincula, Principal Investigator

Oak Ridge National Laboratory
1 Bethel Valley Road
Oak Ridge, TN 37830
E-mail: advincularc@ornl.gov

H. Felix Wu, DOE Technology Manager

U.S. Department of Energy
E-mail: felix.wu@ee.doe.gov

Start Date: October 1, 2020

End Date: September 30, 2023

Project Funding (FY 2021): \$500,000

DOE share: \$500,000

Non-DOE share: \$0

Project Introduction

ORNL and collaborators at University of North Texas (UNT) pursued research on 3D-printed CF composites for vehicle lightweighting with sensing functionality. The objectives were to (1) enhance the organic–inorganic interface for long-term performance via covalent bonding between CF and the polymer matrix; and (2) conduct real-time evaluation of material properties with embedded sensors. This involves advanced AM and synchronous sensor fabrication/embedding toward next-generation vehicle structures and materials. The PIs are Advincula at ORNL, an expert in AM and nanocomposite materials, and Choi at UNT, an expert in carbon nanomaterials and sensors. They, along with their co-researchers, engaged in the following efforts:

- Synthesis, modification, and characterization of CF–polymer composites using low-cost CFs, surface modifiers, and optimized resin formulations and chemistry.
- Dynamic studies of curing control and characterization guided by simulations on multifunctional polymer-based composites—feedback loop materials development protocol.
- Advanced AM and 3D printing of continuous CF–polymer composite geometries.
- Assembly of sensor-embedded CF–polymer composites via multi-material 3D printing.

Objectives

The project focused mainly on: (1) enhancing the interfacial interaction between CF and polymer; and (2) enabling monitoring of the material’s performance. To meet these objectives, the group pursued the following and their respective outcomes:

- Investigate chemical reactions at CF–polymer interface and long-term thermomechanical performance to achieve mechanical properties with Young’s modulus >15 GPa and tensile strength >250 MPa.
- Conduct simulation and computational studies to establish structure–process–property relationships and evaluate interfacial failure mechanisms with FEA.
- Fabricate 3D-printed composite parts with controlled fiber orientation, multi-axis capabilities, and enhanced fiber-polymer interfacial adhesion at various test geometries and parts design.
- Incorporate and test sensor-embedded CF–polymer composites: Use 3D printing to embed piezoelectric sensor layers *in-situ* with designed vehicle component geometries that can be monitored for stress and fatigue with time.

Approach

Although CF–polymer composites have been used in the vehicle industry to compete with metal parts, this has not been demonstrated with 3D-printed CF–thermoset polymer composites [1, 2]. While weight-to-strength ratio advantages have been demonstrated, long-term material creep, poor Class A surface finish, and high cost prevent wider adoption. Materials chemistry studies reveal that interfacial interaction of CF and the polymer matrix remains a challenge. AM or 3D printing should enable rapid prototyping, lightweighting, and use of new materials. There is interest in new functionality for vehicle parts by combining multiple parts into a unibody design with real-time fatigue assessment. 3D printing of familiar thermoset epoxy resins is the main direction of this project. Epoxy blends with polybenzoxazine, polyurethane, vinyl esters are of high interest and can also be explored with 3D printing of CF–polymer composites. ORNL and UNT have partnered to advance the DOE VTO mission toward next-generation materials and vehicles. Co-PIs at ORNL and UNT bring strengths in synthetic chemistry, composite materials, and AM. UNT developed simulations and embedded sensors using nanomaterials and 3D printing capabilities. The project is divided into four tasks, as described below.

Task 1. Precise Chemical Reaction Control in Resin Materials

Objective: Develop CF–polymer with enhanced inorganic–organic interface covalent interaction.

End-of-project goal: Develop composites with optimum chemistry and processability and high-performance.

CF-based composite materials with poor interfacial adhesion between individual fibers and polymer present a challenge for long-term stability and performance. This project will pursue CF-reinforced polymer composites with enhanced inorganic–organic interfaces via covalent bonds. Bisphenol A diglycidyl ether resins will be selected for base study. Options include epoxyphenol novolak and aliphatic glycidyl epoxy resins, along with amine-based hardeners in specific ratios of accelerators/retarders. The project is pursuing blending of copolymers with benzoxazine dimer, polyether amines, polyurethane epoxy, and amine telechelics of various molecular weights, providing a wider range of curing temperatures for kinetics studies. *The most important objective is interfacial enhancement of CF–polymer resin using new reactive silane surface modifiers.* Systematic studies with simulation of different epoxy resin systems will determine their critical parameters, e.g., viscosity, curing temperature and time, and additive ratios. Properties will be characterized through analysis using the following method types: (a) spectroscopic (NMR, IR, and Raman spectroscopy), (b) microscopic (SEM and EDXS), (c) rheological, (d) thermal (DSC and thermogravimetric analysis), and (e) thermomechanical (dynamic mechanical analysis). Control experiments include the use of chopped fiber compositions (5 wt.% to 50 wt.%). Optimizing the CF-containing resin for 3D printing parameters with their final thermomechanical properties will be a challenge.

Task 2. Computational Studies of Interfacial Interaction between Polymer Matrix and CF

Objective: Conduct simulations of interfacial properties and optimum reactive chemical species.

End-of-project goal: Achieve a high correlation of printed components with predictive tools.

To optimize resin composition, establish process parameters, predict structure-property relationships, and understand interfacial failure mechanisms, the project team is using computational and simulation tools to perform FEA with Abaqus-customized computational subroutines for simulating composites under different loading conditions. Each component is defined with experimentally derived properties, with interfacial properties modeled via traction-separation (T-S) relations. MATLAB/Python–Abaqus iterations will be used for systematic geometric designs. DFT methods will be used to optimize interfacial interactions and define structure-property relationships. Semi-empirical *ab initio* calculations (Hartree-Fock) and molecular dynamics will be used to identify optimum reactive chemical species based on new telechelic multifunctional groups and monomers that will be synthesized.

Task 3. 3D Printing of Continuous CF–Epoxy Composite with Enhanced Fiber-Polymer Adhesion

Objective: Develop 3D printing of a continuous CF–epoxy matrix with optimal fabrication parameters.

End-of-project goal: Achieve an AM process and materials combination for high-performance.

3D printing gives unprecedented freedom in geometric design and materials fabrication. 3D-printed chopped CF–epoxy composites have been demonstrated to exhibit a Young’s modulus of 5 GPa and a tensile strength of 110 MPa with a 20% loading. A publication on this research is being prepared. Double printing heads modified for fused deposition modeling will enable controlled CF distribution and orientation; one extrudes epoxy-wetted CF (CF-head), and another deposits only epoxy (E-head). The project team will initially use viscosity optimized epoxy resin (EPON 826 epoxy/EPIKURE W crosslinker) with silica nanoparticles (rheology/thixotropy modifier). Optimized resin reactivities will be guided by DFT and *ab initio* molecular dynamics simulation. Nanomaterials such as graphene, carbon nanotubes, and nanocellulose will be used to modify crosslinking reactivities and nanostructure (de-aggregation and network formation) to improve thermomechanical properties of 3D-printed parts up to 200%. *These optimized compositions will be matched with FEA simulation for optimized 3D printing parameters, as outlined in Task 2.* The printing geometries and materials dispensing will be programmed (G-code modification). CF orientation can be controlled with the CF-head moving path routes (X-Y plane) and use of multi-axis build platforms. Test bars and cubes (with control sample) will first be validated using tensile, compression, and flexural strength tests. Multi-axis printing and gradient or step printing will be further investigated toward low-cost and high-throughput fabrication. Varied composite densities and zoned mechanical strengths will be fabricated to satisfy different geometrical stresses and vehicular assembly function in the future.

Task 4. Continuous Sensor-Embedded Polymer/CF Composite 3D Printing

Objective: 3D print continuous CF–polymers with embedded sensor geometries and testing.

End-of-project goal: Achieve sensing capability in continuous CF–epoxy 3D-printed parts.

3D printing gives unprecedented freedom in geometric design and materials fabrication. 3D-printed chopped CF–epoxy composites have been demonstrated to exhibit a Young’s modulus of 5 GPa and a tensile strength of 110 MPa with a 20% loading. A publication on this research is being prepared. Double printing heads modified for fused deposition modeling will enable controlled CF distribution and orientation; one extrudes epoxy-wetted CF (CF-head), and another deposits only epoxy (E-head). The project team will initially use viscosity optimized epoxy resin (EPON 826 epoxy/EPIKURE W crosslinker) with silica nanoparticles (rheology/thixotropy modifier). Optimized resin reactivities will be guided by DFT and *ab initio* molecular dynamics simulation. Nanomaterials such as graphene, carbon nanotubes, and nanocellulose will be used to modify crosslinking reactivities and nanostructure (de-aggregation and network formation) to improve thermomechanical properties of 3D-printed parts up to 200%. *These optimized compositions will be matched with FEA simulation for optimized 3D printing parameters, as outlined in Task 2.* The printing geometries and materials dispensing will be programmed (G-code modification). CF orientation can be controlled with the CF-head moving path routes (X-Y plane) and use of multi-axis build platforms. Test bars and cubes (with control sample) will first be validated using tensile, compression, and flexural strength tests. Multi-axis printing and gradient or step printing will be further investigated toward low-cost and high-throughput fabrication. Varied composite densities and zoned mechanical strengths will be fabricated to satisfy different geometrical stresses and vehicular assembly function in the future.

Results

Task 1: Precise Chemical Reaction Control in Resin Materials

- Performed a comprehensive study of epoxy–chopped CFs. The sample with 50 μm CFs showed promising results, which is good for the fundamental study.
- Investigated model epoxy resins along with optimized protocols for grafting of surface functional groups in CFs, as shown in Figure II.2.17.1.
- Improved the performance of composites that achieved the desired strength of 200 MPa, even with chopped CFs. The initial targets for a modulus of 10 GPa and a tensile strength of 200 MPa were achieved.

- Determined that the mechanical strength of a sample with 1 wt.% CF is comparable to that of pristine polymer but decreases with further increase of CF loading (i.e., 5 wt.%, 20 wt.%).
- Observed the phase separation for the samples with 1 and 5 wt.% CF.
- Determined that the uniform distribution of CFs into the system during the whole process was critical.

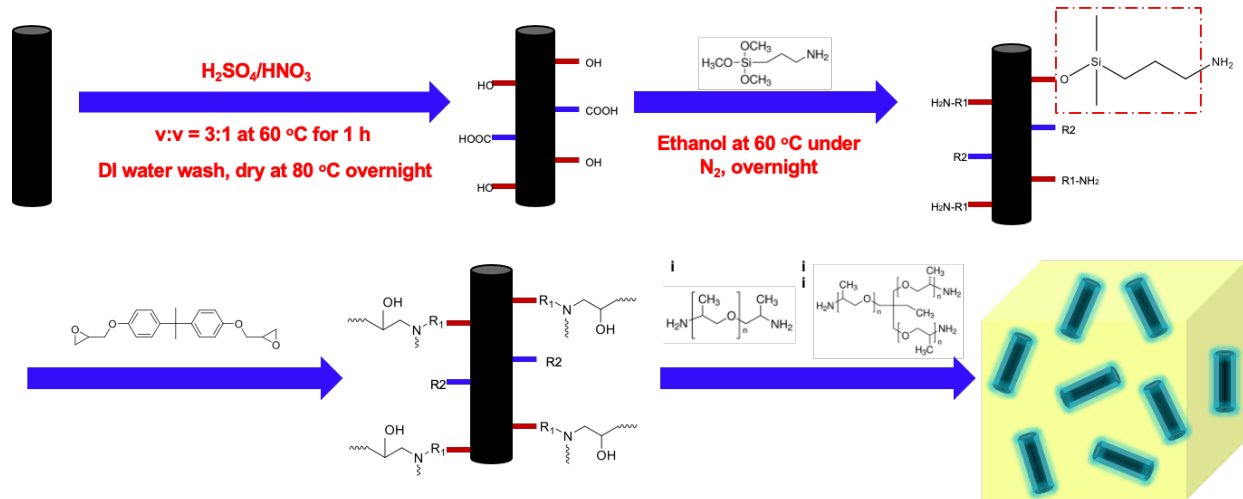


Figure II.2.17.1. Schematic of fiber modification showing surface silanization followed by crosslinking with epoxy. Source: ORNL

Task 2: Computational Studies of Interfacial Interaction between Polymer Matrix and CF

- Established data-driven ML models to precisely predict the interface adhesion properties and identify imperfections along interfaces from FEA and standard experiments whose relations are shown in Figure II.2.17.2.
- Performed preliminary FEA simulations on fiber-reinforced composites with multiscale fibers.
- Developed algorithms for material programming of crack design and high-toughness and high-strength composites. These efforts are ongoing.
- Established genetic algorithm and FEA iterations for crack propagation simulations with designed composites.
- Experimentally characterized the interface between epoxy, epoxy–CF, and polymer–silicone interfaces and obtained force-displacement data. SEM images of the epoxy with 10 wt.% silane-treated CF are shown in Figure II.2.17.3(a), and the resulting stress-strain curve showing an achieved strength of 207 MPa is shown in Figure II.2.17.3(b).
- Predicted and evaluated T-S laws at interfaces at the micro/nanoscale using the experimental force-displacement data using FEA to compare with experimental data.
- Developed a crack propagation model. Initial tests using an atomic fluctuation electron microscopy method allowed failure across the composite plate.

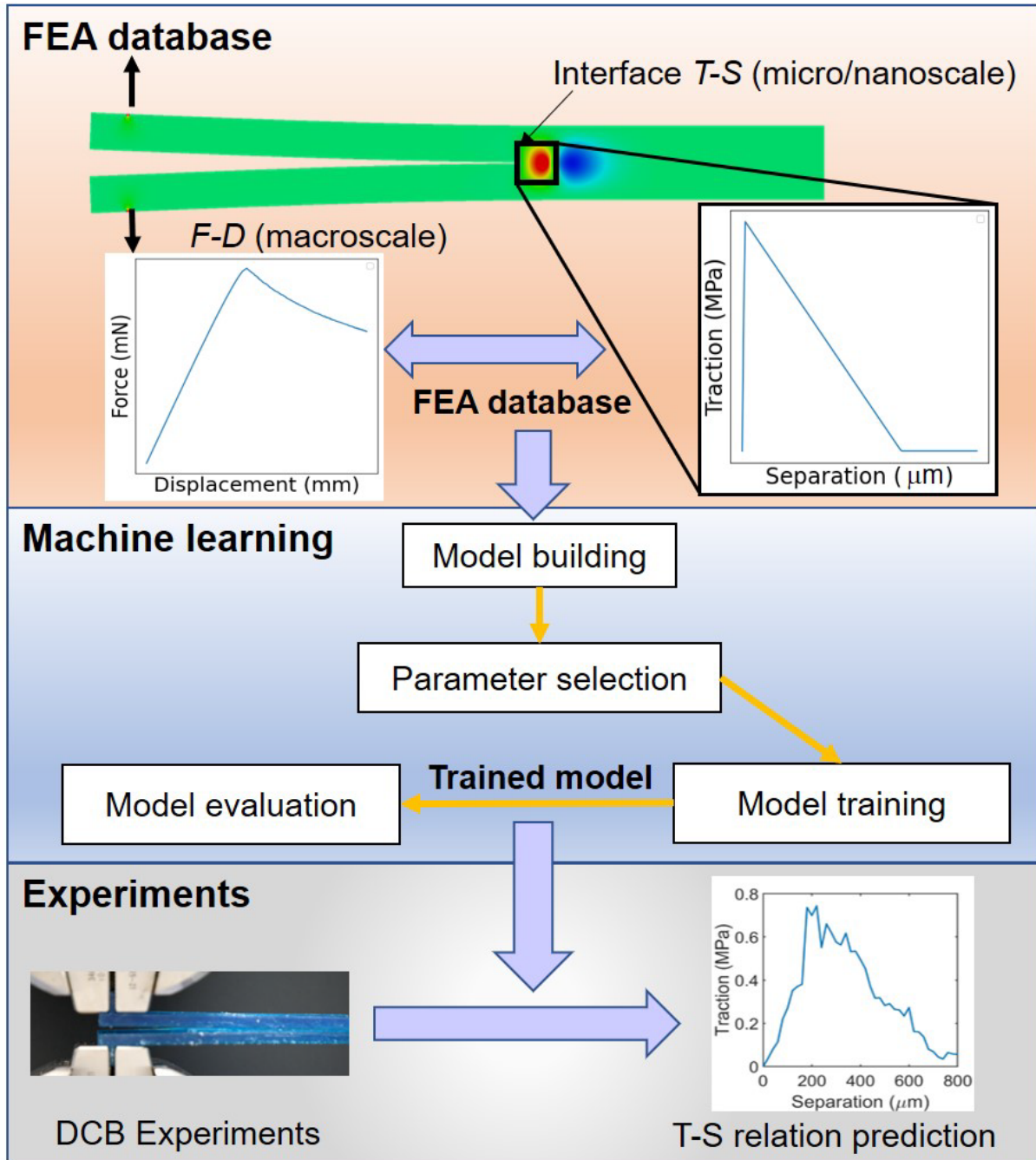
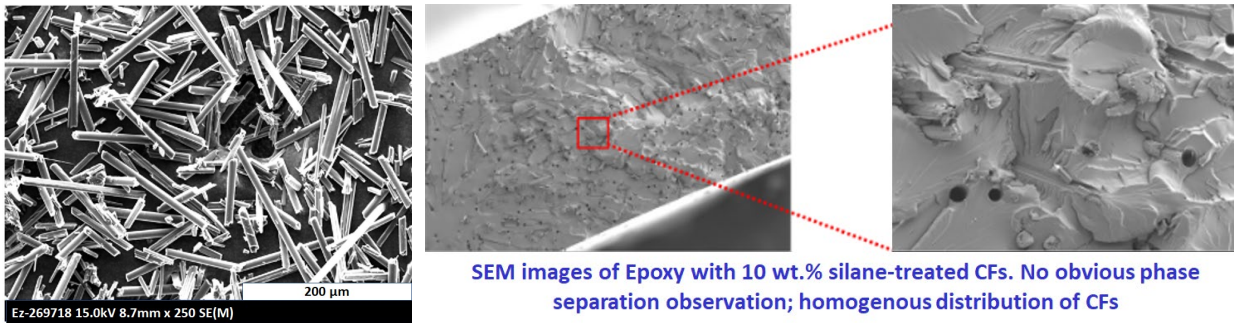
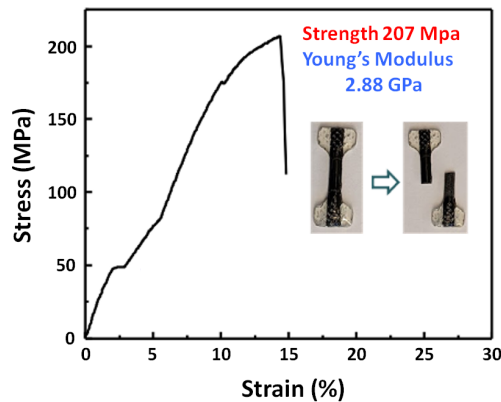


Figure II.2.17.2. Schematic of the data-driven ML model used to precisely predict the interface adhesion properties and identify imperfections along interfaces from FEA. The modeling and actual data are compared for the separation and displacement on a test composite strip. Source: ORNL



(a)

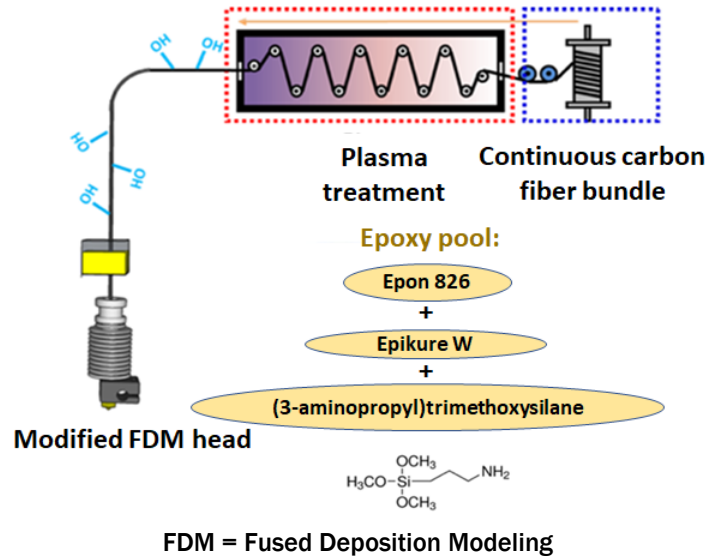


(b)

Figure II.2.17.3. (a) SEM images of chopped CFs and their incorporation into the epoxy matrix. (b) A strength of 207 MPa and a Young's modulus of 2.88 GPa were achieved. The printing and layering method is prepared over several coats of the materials. Failure mechanism can be attributed to a slip-disk model. Source: ORNL.

Task 3: 3D Printing of Continuous CF-Epoxy Composite with Enhanced Fiber-Polymer Adhesion

- Achieved 3D printing of epoxy-CF composite using a viscous solution printing-based method and studied the composition up to 40 wt.%.
- Demonstrated process scale-up using the rheology and mixing of commercial-based epoxy and chopped CF with EPON, EPIKURE, and silica nanoparticles added, as shown in Figure II.2.17.4.
- Demonstrated that a loading of CF at 40 wt.% produced a tensile strength of 73 MPa and a modulus of 2.8 GPa but the elongation decreased to 3%. The toughness maximized at 20 wt.%.
- Investigated the multi-material 3D printing with a CF mat prepreg.



(a)

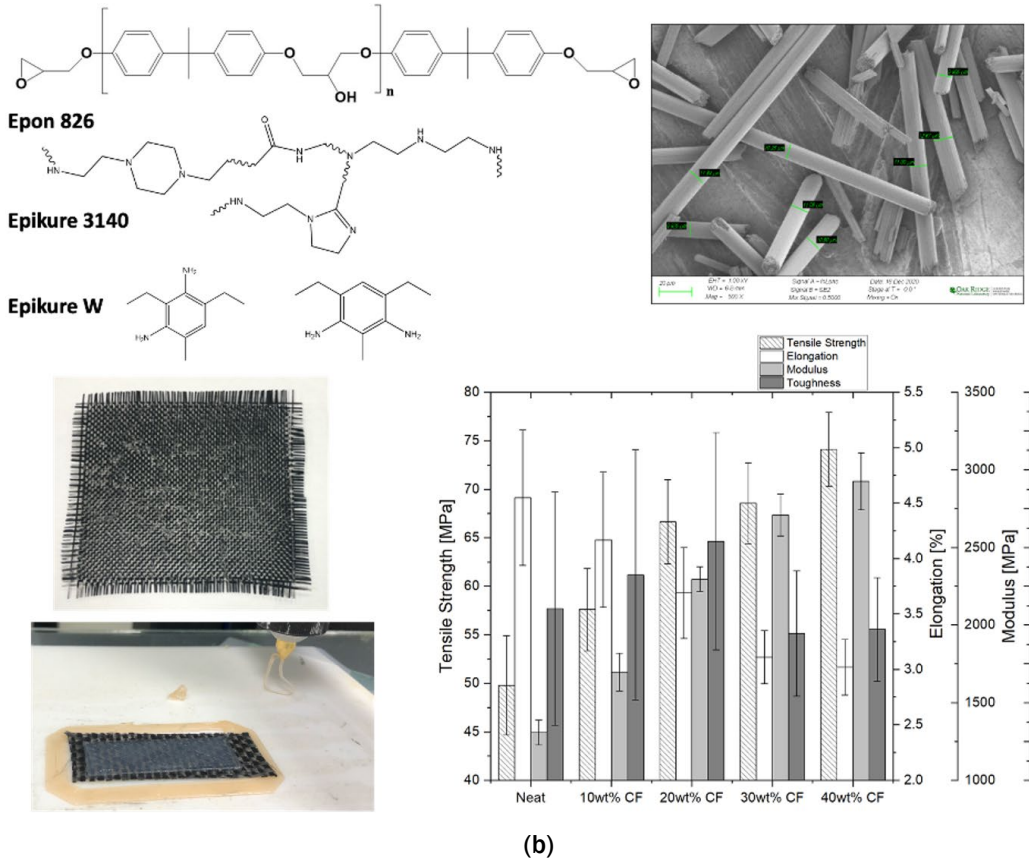


Figure II.2.17.4. (a) 3D printing of epoxy and chopped CF was demonstrated for the ability to scale-up the process. EPON 826, EPIKURE 3140, EPIKURE W, and silica nanoparticles were added with the CF. (b) Loading of CF at 40 wt.% gave a tensile strength of 73 MPa and a modulus at 2.8 GPa, but elongation decreased to 3%. The toughness is maximized at 20 wt.%. These results were obtained for multi-material 3D printing with CF mat prepreg sheets. Source: ORNL.

Task 4: Continuous Sensor-Embedded Polymer–CF Composite 3D Printing

The end goal is to design and demonstrate multi-material 3D printing to incorporate *in-situ* and embedded sensors, in support of the concept of printing vehicle components that can be monitored with stress and time:

- Developed protocol and 3D printing inks for embedded sensors and Zn-ion battery, as shown schematically in Figure II.2.17.5(a).
- Designed and 3D-printed porous structures of Zn-anode with a high surface area for a high-efficiency Zn-anode with the characteristics shown in Figure II.2.17.5(b). Macropore structures in 3D-printed anodes show homogeneous distribution of ink materials with no agglomeration in the printed structure, as exhibited by the images in Figure II.2.17.5(c). Carbon particles act as bridges between zinc particles, improving conductivity.
- Successfully fabricated a flexible Zn-anode with a high specific capacity of 650 mAh/g. Full cell characterization was performed. High reaction kinetics with increasing surface area were observed, as shown by the data in Figure II.2.17.5(d). The series resistance did not differ significantly, and the Zn-plate exhibited high charge transfer resistance, as shown in Figure II.2.17.5(e). A high specific capacity of 650 mAh/g at 0.2 A/g C-rate was achieved, as shown by the data in Figure II.2.17.5(f). The 3D anode maintained stability and high-capacity during a long-term stability test, as shown in Figure II.2.17.5(g).

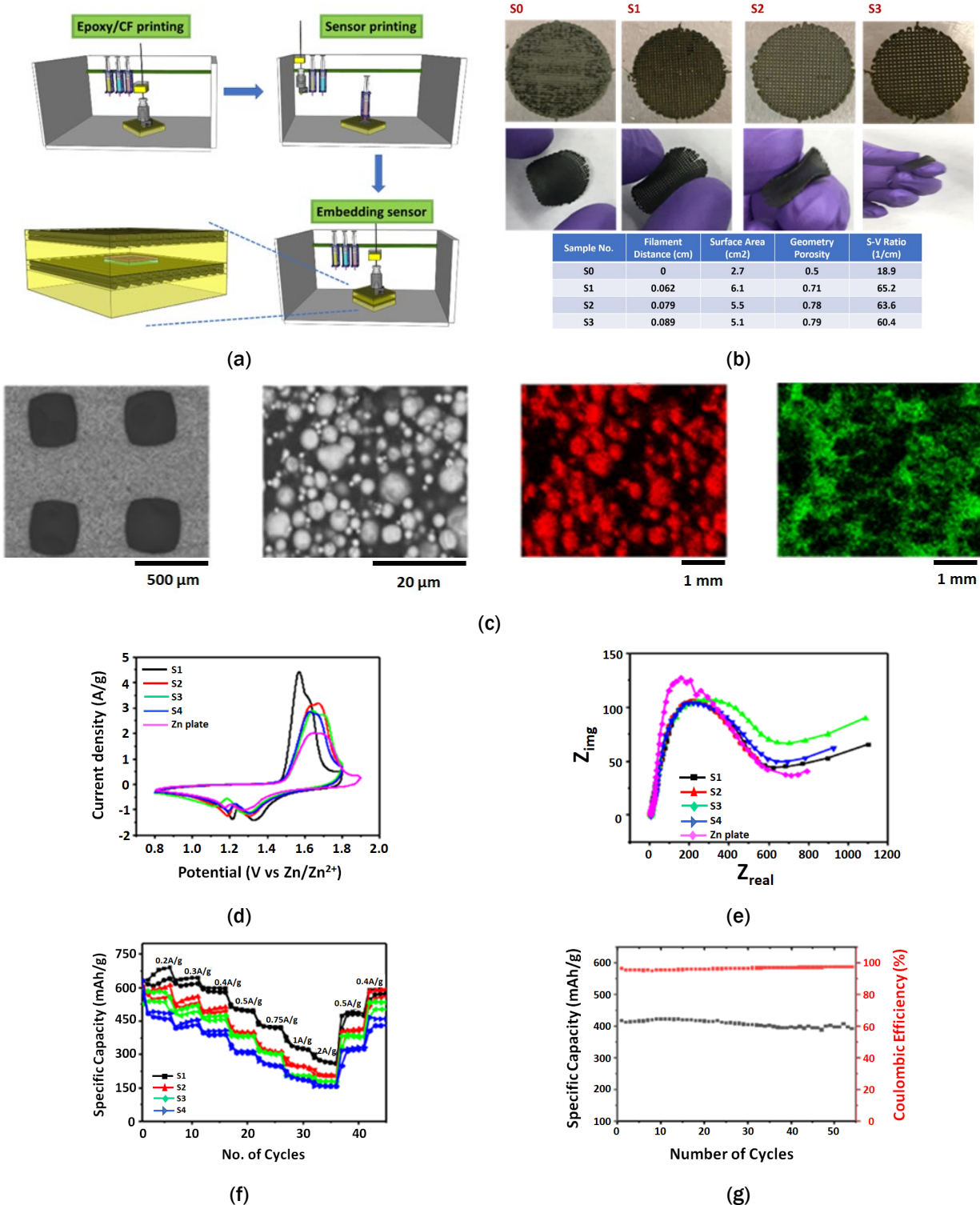


Figure II.2.17.5. (a) Process for 3D printing inks for embedded sensors. (b) Fabrication of Zn-anode based with carbon black particle additives and PVDF. (c) SEM and fluorescence spectroscopy imaging of the composite. Full characterization by electrochemical methods: (d) high reaction kinetics with increasing surface area; (e) no significant difference in series resistance; Zn-plate with high charge transfer resistance; (f) high specific capacity of 650 mAh/g at 0.2 A/g C-rate; and (g) stable and high-capacity 3D anode maintained in the long-term stability test. Source: ORNL.

Conclusions

The project team achieved the following:

- Performed a comprehensive study of epoxy–chopped CFs. Investigated model epoxy resins, along with optimized protocols for grafting surface functional groups in CFs.
- Established data-driven ML models to precisely predict the interface adhesion properties and identify imperfections from FEA and standard experiments. Developed algorithms for material programming of crack design and high-toughness and high-strength composites.
- Achieved 3D printing of epoxy–CF composite using a viscous solution printing-based method as well as continued development of continuous CF printing. Device fabrication for continuous fiber 3D printing remains a priority.
- Developed a protocol and 3D printing inks for embedded sensors using a flexible Zn-ion anode and battery to enable high-resolution sensor 3D fabrication with the epoxy–CF composite. Future work will be done using other 2D materials with PVDF compositions.

The project initiated in 2020 with four tasks is on schedule, and a path forward has been planned for FY 2022. A cohesive team between ORNL and UNT has been established to conduct the research.

Key Publications

1. Ferdousi, S., Q. Chen, M. Soltani, J. Zhu, P. Cao, W. Choi, R. Advincula, and Y. Jiang, 2021, “Characterize traction-separation relation and interfacial imperfections by data-driven machine-learning models,” *Scientific Reports*, Vol. 11, 14330.
2. Khatri, N. R., M. N. Islam, P.-F. Cao, R. C. Advincula, W. Choi, and Y. Jiang, n.d., “Integrating helicoid channels for passive control of fiber alignment in direct-write 3D printing,” paper accepted for publication by *Additive Manufacturing*.

References

1. Sun, J., F. Zhao, Y. Yao, Z. Jin, X. Liu, and Y. Huang, 2017, “Highly efficient and continuous surface modification of carbon fibers with improved tensile strength and interfacial adhesion,” *Applied Surface Science*, Vol. 412, pp. 424–435.
2. Hao, W., Y. Liu, H. Zhou, H. Chen, and D. Fang, 2018, “Preparation and characterization of 3D printed continuous carbon-fiber-reinforced thermosetting composites,” *Polymer Testing*, Vol. 65, pp. 29–34.

Acknowledgments

We appreciate collaborations with the N. Zhou group at the University of Tennessee at Knoxville, Civil Engineering Department, for the extensional tensile testing methods and equipment. We acknowledge technical support with Hyrel on the fabrication of the 3D printing attachment.

II.2.18 New Frontier in Polymer Matrix Composites via Tailored Vitrimer Chemistry (Oak Ridge National Laboratory)

Tomonori Saito, Principal Investigator

Oak Ridge National Laboratory
1 Bethel Valley Road
Oak Ridge, TN 37830
E-mail: saitot@ornl.gov

H. Felix Wu, DOE Technology Manager

U.S. Department of Energy
E-mail: felix.wu@ee.doe.gov

Start Date: October 1, 2020

End Date: September 30, 2023

Project Funding (FY 2021): \$500,000

DOE share: \$500,000

Non-DOE share: \$0

Project Introduction

The project aims to develop fast-processable, repairable, recyclable, and affordable carbon-fiber-reinforced polymer composites (CFRPs). The project is incorporating dynamic covalent chemistry into the fibers and resins so that materials exhibit superior mechanical properties while maintaining recyclability. The current epoxy-based CFRP manufacturing process is time-consuming, is not cost-effective, and is not ideal for efficient mass production in the industry. In addition, the current CFRPs and resins are not readily repairable or recyclable/reprocessable; the latter is due to the presence of irreversible thermoset moieties, which ultimately end up in a landfill without an option for recycling. In this project, novel vitrimer-based resins will be designed and synthesized using a fast and robust dynamic exchange chemistry, enabling the cross-linked network to be (re)processable and healable. The dynamic covalent bond allows rapid manufacturing, similar to thermoplastic resins, but provides mechanically robust networks, similar to epoxy-based resins. In addition to providing a rapid manufacturing process, the resins' recyclability and healability will reduce the manufacturing cost of CFRPs.

Vitrimers consist of a cross-linked network with dynamically exchangeable groups. The cross-linked network provides high mechanical strength, and the dynamic crosslinking gives facile reprocessability. While several epoxy-based vitrimers have been reported, they typically require high temperatures and long annealing times, which inevitably lead to loss of mechanical properties and an increase of production cost. Here we report a new design of readily scalable resins for CFRPs, the new vitrimers with exchangeable disulfide cross-links, that produces excellent mechanical properties and facile processability. Compared to a conventional disulfide epoxy vitrimer, the ORNL vitrimer exhibits a stress relaxation time faster at 160°C while maintaining the mechanical strength. Owing to the rapid exchange reactions and the efficient chain rearrangement, the ORNL resin exhibits excellent reprocessability under a moderate temperature and a short annealing time. The ORNL vitrimer resin can fully recover the mechanical strength for many cycles, while the dynamic epoxy loses ~64% of the mechanical strength after six cycles. Additionally, the prepared CFRPs with the ORNL vitrimer show excellent reprocessability and recyclability. An ideal vitrimer for industrial applications needs the characteristics of: (1) high mechanical strength; (2) facile reprocessability (e.g., low-temperature and short annealing time); and (3) mechanical or chemical recyclability. The simple strategy of a tailored resin combination presented here is effective in preparing mechanically strong and readily reprocessable vitrimers and their CFRPs. Here we chose disulfide dynamic bonds, since disulfide bonds are easily cleavable, and the cured thermoset materials become malleable and reprocessable under external stimuli (e.g., a moderate temperature). Owing to the fast exchange of disulfide bonds, the mechanical properties can be easily recoverable. Therefore, the use of disulfide bond as dynamic crosslinker is a promising way to enable facile reprocessability and maintain mechanical properties in thermoset materials.

Objectives

CFRPs are lightweight with extremely high structural strength, sufficient for aerospace and automobiles. The use of CFRPs for vehicles is currently limited because of the high manufacturing costs of carbon fibers, as well as the time-consuming curing process of manufacturing CFRP parts. Carbon-fiber-reinforced thermoset epoxy composites are widely used for good thermal and mechanical properties; however, these epoxy resins require long processing times and cannot be repaired, remolded, reprocessed, or recycled. This study ventures into a new frontier of CFRPs based on novel vitrimer materials, which will give outstanding mechanical and chemical resistance similar to that of thermosets. However, unlike thermosets, vitrimers can be reprocessed/recycled and repaired. Vitrimers are covalently cross-linked polymeric materials able to shuffle chemical bonds through exchange reactions and thus can be thermally processed without losing their network integrity. To overcome the existing limitations of current CFRPs, we are pursuing the following objectives: designing vitrimer-based matrix resins from inexpensive and readily available precursors; developing manufacturing technology for the novel CFRPs; and manufacturing fast-processable, recyclable, and repairable or healable resins and CFRPs.

Approach

To achieve the project objectives, the project team tailored a resin combination of polymer A and epoxy in preparing mechanically strong and readily reprocessable vitrimers and their CFRPs by taking advantage of facile disulfide metathesis and the high mechanical strength of epoxy. The ORNL vitrimers were synthesized by reacting component A and epoxy monomer B using disulfide containing building block C. The team investigated their thermal, mechanical, and rheological properties and compared them with the conventional epoxy and dynamic epoxy vitrimers. Because of the rapid exchange reactions and the efficient chain rearrangement, the ORNL vitrimer resins exhibited superior reprocessability compared to the dynamic epoxy vitrimers while maintaining the mechanical strength. In contrast, the dynamic epoxy vitrimers demand a much higher temperature and a longer annealing time, which causes the loss of mechanical strength over multicycle recycling. The CFRPs made of the ORNL resin formulation maintained excellent mechanical properties, comparable to those of the conventional epoxy-based CFRPs. Furthermore, the ORNL vitrimer resins and their CFRPs displayed outstanding chemical resistance to classical solvents, including dimethyl formamide, dimethylacetamide, and N-methyl pyrrolidone, while providing a path of chemical recycling by using a thiol-containing solvent.

Results

The ORNL vitrimers were prepared with controlled weight ratios of component A to epoxy resins at 1:0, 2:1, 1:1, 1:2, and 0:1, where C acted as a dynamic crosslinker. To examine the mechanical properties of the dynamic resins, we first fabricated the dumbbell-shaped specimens using a liquid-based method and cured them in an oven to obtain fully cross-linked dynamic networks. As shown in Figure II.2.18.1(a), the tensile stress of samples monotonously increased with more loading of epoxy from the dynamic polymer A to the dynamic A epoxy to the dynamic epoxy. In contrast, the tensile strain exhibited an opposite trend. Both the tensile strength and strain values of samples are summarized in Figure II.2.18.1(b). For example, the tensile strength of the dynamic polymer A was obtained as 39.2 ± 1.7 MPa, while that of the ORNL vitrimer network with a weight ratio of 1:1 increased to 56.8 ± 3.8 MPa. The dynamic epoxy exhibited a tensile strength of $67.8 \text{ MPa} \pm 4.6 \text{ MPa}$, a tensile strength similar to that of the conventional epoxy. The ORNL vitrimer, especially 1:1 and 1:2, maintained the high tensile strength, close to that of conventional epoxy.

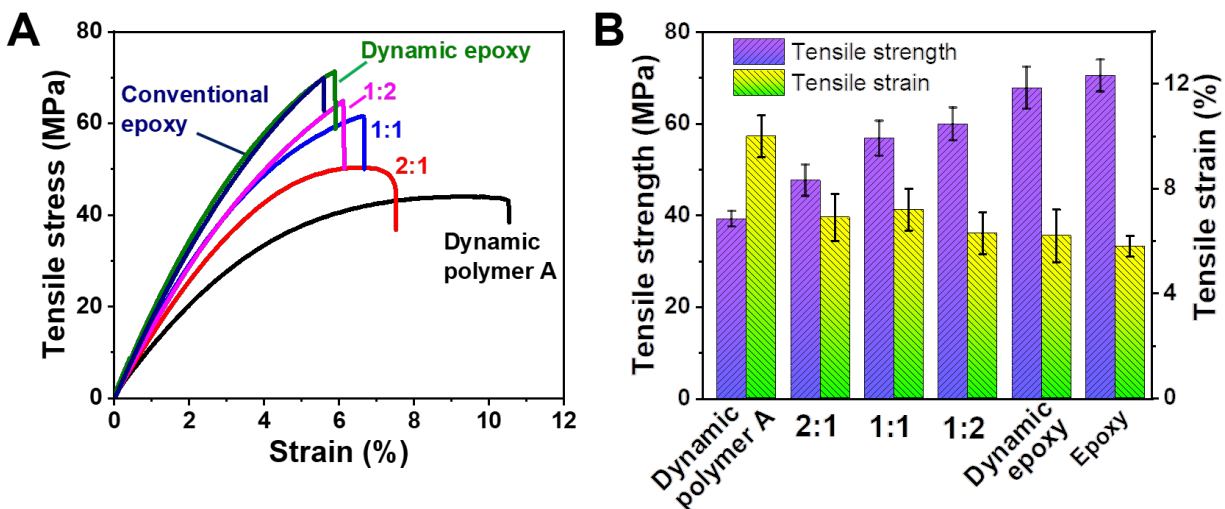


Figure II.2.18.1. Mechanical properties of ORNL vitrimer. (a) Tensile stress-strain curves; three different weight ratios of A to epoxy resins: 1:2 (pink), 1:1 (blue) and 2:1 (red). (b) Summarized tensile strength and strain values [1]. Source: ORNL.

To determine the thermomechanical properties of these vitrimers, the project team used dynamic mechanical analysis to characterize the storage modulus and tan delta values for different weight ratios of dynamic polymer A to epoxy resins, as observed in Figure II.2.18.2(a)–(b). All the samples exhibited a rubbery plateau storage modulus at a temperature higher than the glass transition temperature (T_g), indicating the occurrence of dynamic exchange, which is a typical behavior for vitrimer materials. T_g of ORNL vitrimer resin is $\sim 100^\circ\text{C}$ at a weight ratio of 1:1, which is much lower than that of the dynamic epoxy at $\sim 140^\circ\text{C}$. To study the exchange reaction of the ORNL vitrimers, we measured the stress relaxation using a rheometer; the typical normalized stress relaxation curves at a temperature of 160°C are shown in Figure II.2.18.2(c). The ORNL vitrimer has a stress relaxation time six times faster than that of the dynamic epoxy at 160°C , allowing much faster processing at the moderate temperature. The relaxation times of the dynamic epoxy and ORNL vitrimer network follow the Arrhenius law, as shown in Figure II.2.18.2(d), confirming the dynamic disulfide exchange reaction and the formation of dynamic vitrimer resins.

To illustrate the effective reprocessability of our dynamic vitrimers, we compared them to a traditional epoxy cross-linked with unexchangeable covalent bonds, as shown in Figure II.2.18.3(a), and an epoxy dynamically cross-linked with exchangeable covalent bonds, as observed in Figure II.2.18.3(b)–(c). As a result of the permanently cross-linked networks, the traditional epoxy cannot be reprocessed or recycled at elevated temperatures. As expected, the traditional epoxy specimens remained broken after hot-pressing at 200°C , as can be seen in Figure II.2.18.3(a). In contrast, owing to the exchangeable disulfide bonds, both dynamic epoxy and ORNL vitrimer were hot-pressed and successfully reformed into homogenous, compact films, as observed in Figure II.2.18.3(b)–(c). Importantly, the reprocessing of the ORNL vitrimer can be performed at a moderate temperature of 160°C , coupled with a low pressure of 100 psi and a short annealing time of 1 minute, while the dynamic epoxy requires a higher temperature of 200°C and a long annealing time of 5 minutes. To ensure the reprocessability, tensile tests on both the dynamic epoxy and ORNL vitrimer resins were repeated up to six times, as shown in Figure II.2.18.3(d), and the samples' mechanical properties were measured. The results demonstrate that both the dynamic epoxy and ORNL resin can recover their tensile strength, with even slight improvements, after the first reprocessing. The tensile strength of the dynamic epoxy started to decrease after the second reprocessing and dramatically dropped after the sixth reprocessing to approximately 36% of the initial tensile strength. This significant loss of tensile strength could be due to the degradation of disulfide bonds and oxidation of the epoxy–amine network at the high reprocessing temperature of 200°C . In contrast, the ORNL resin maintained its mechanical strength, indicating that it was readily reprocessed multiple times at 160°C for 1 minute without any degradation of the disulfides.

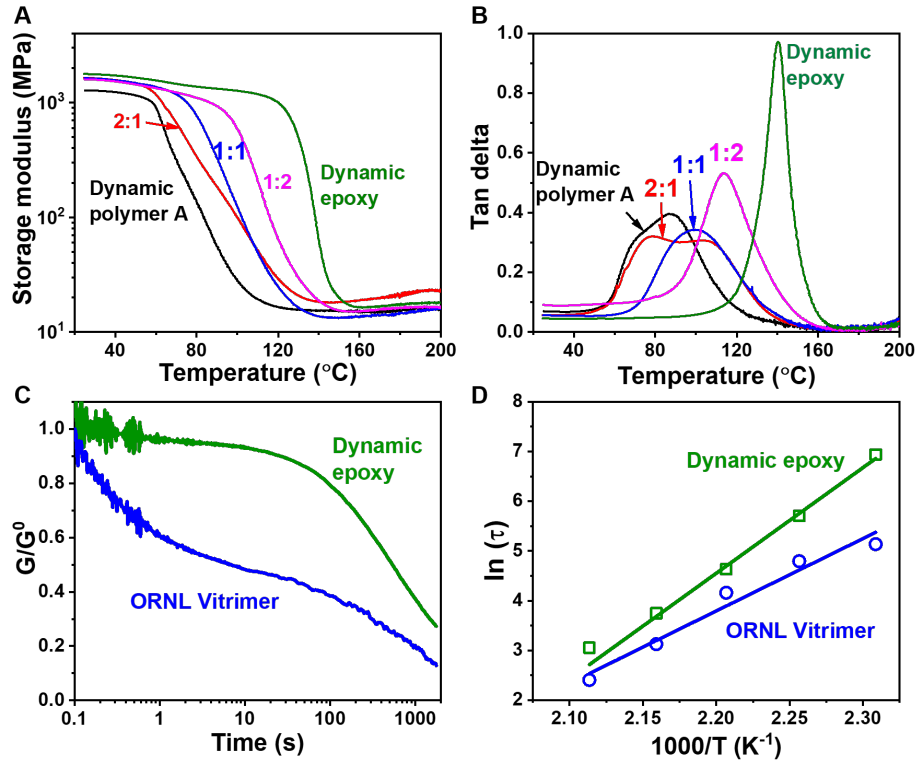


Figure II.2.18.2. Dynamic properties: (a) storage modulus, (b) tan delta versus temperatures, (c) normalized relaxation modulus of the dynamic epoxy and the ORNL vitrimer networks at 160 °C, (d) linear Arrhenius behavior of the dynamic epoxy and the dynamic ORNL vitrimer networks [1]. Source: ORNL

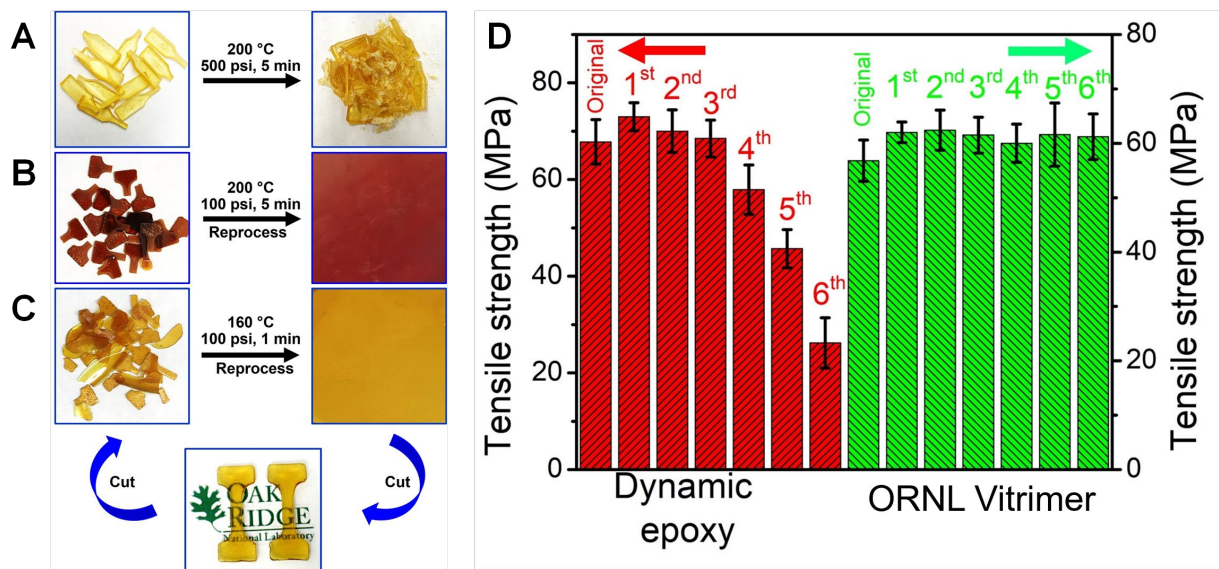


Figure II.2.18.3. Reprocessing by hot-pressing. (a) Traditional epoxy samples with cross-linked unexchangeable bonds were processed in a hot press at 200 °C and 500 psi for 5 minutes, resulting in broken pieces. (b) Dynamic epoxy specimens were processed at the same hot-pressing conditions as traditional epoxy and formed a compact film. (c) ORNL vitrimer pristine samples were hot-pressed at 160 °C and 100 psi for 1 minute to obtain a recycled compact film. The ORNL vitrimer film was easily cut to dumbbell-shaped specimens. (d) Summarized tensile strength values of reprocessed dynamic epoxy (red) and ORNL vitrimer samples (green) [1]. Source: ORNL

We used a simple thermoformation of cured composite laminate for CFRP fabrication, as can be seen in Figure II.2.18.4. First, three individual CF fabric sheet composites with dimensions of 120 mm × 120 mm were soaked in a ORNL resin solution and cured in an oven at 120°C for 2.5 hours, as shown in Figure II.2.18.4(a). After curing, the three composite sheets were placed together and carried out in the hot press. After hot-pressing at 160°C and 500 psi for 1 minute, these three sheets formed a compact multilayer composite film Figure II.2.18.4(b), which further demonstrates the excellent reprocessability of the ORNL composite. The multilayered composite film was then placed inside a compression molding press to quickly obtain a three-dimensional shaped composite Figure II.2.18.4(c)–(d). Such a fast-thermoforming process signifies the great promise of the ORNL vitrimer for new CFRP manufacturing that leads to scalable, low-cost production.

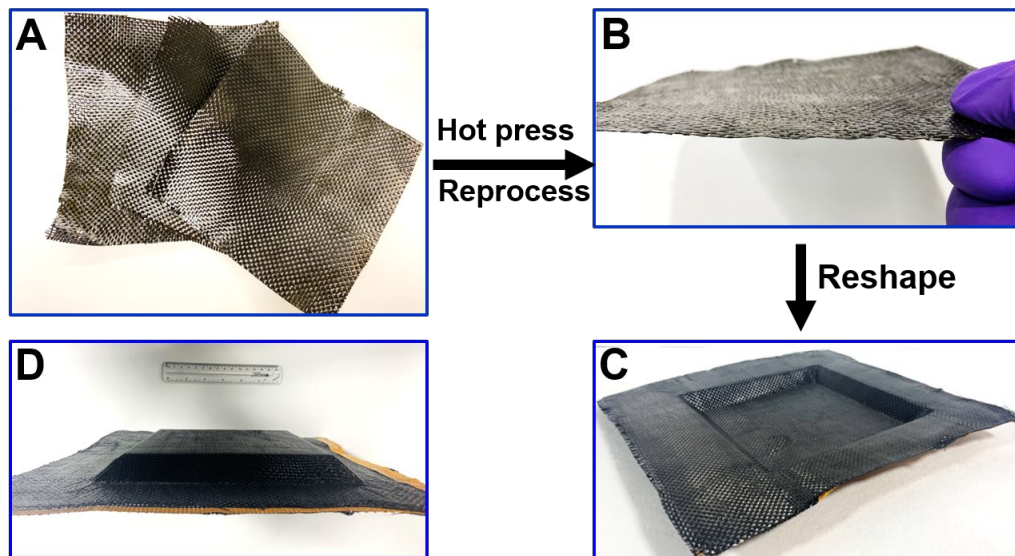


Figure II.2.18.4. Thermoformation of cured composite laminate. (a) Three individual CF fabric composite sheets with the ORNL vitrimer. (b) After being hot-pressed at 160°C and 500 psi for 1 minute to obtain a compact multilayered composite sheet. Reshaping the multilayered film under hot-pressing: (c) bottom view and (d) top view of multilayered composite sheet [1]. Source: ORNL.

We used a short-beam shear test method in accordance with ASTM D2344 to characterize the interlaminar shear strength of the CFRPs. As shown in Figure II.2.18.5(a), the flexural strength of the ORNL vitrimer composite reached 903 ± 53.6 MPa, ~80% of flexural strength of the dynamic epoxy composite. Figure II.2.18.5(b) shows the representative shear-stress-strain curves for the regular epoxy, dynamic epoxy and the ORNL vitrimer composites with unidirectional CFs (Hexcel IM7, 12K). The ORNL composite exhibits a high interlaminar shear strength of 50 ± 1.2 MPa, which is ~67% of that of the dynamic epoxy composite. Both high interlaminar shear and flexural strengths, coupled with high recyclability and rapid processing capability, signify the great potential of the tailored resin combination with dynamic disulfide crosslinkers to design and prepare mechanically robust, readily reprocessable CFRPs.

The ORNL vitrimer samples also showed good solvent resistance properties and remained unaltered in common organic solvents, e.g., ethanol, acetone, tetrahydrofuran, toluene, and chloroform, even under sonication for 5 hours. Importantly, the ORNL resins can be chemically recycled by dissolving in binary solvents in the presence of an excess thiol group, including 1-dodecanethiol (DDT) and 3-mercaptopropionic acid (3-MPA), owing to the thiol-disulfide exchange reaction with the cross-linked disulfides. Similarly, carbon fiber from CFRPs can be recycled or recovered. Such high-efficiency of chemical recycling of the ORNL vitrimer composites opens new possibilities for the sustainability of composites and fibers as well as reduces the overall cost for CFRP fabrications.

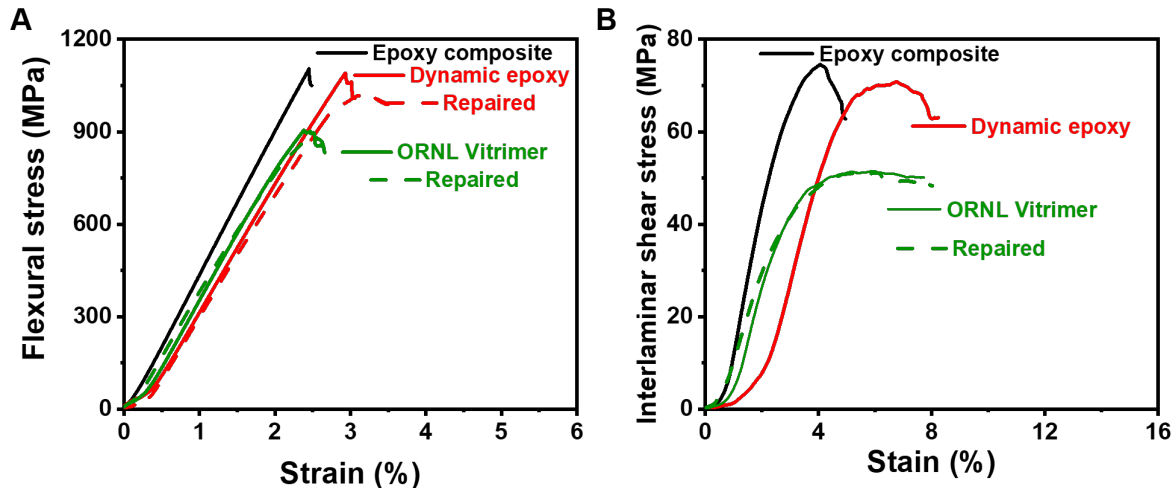


Figure II.2.18.5. Mechanical properties of the unidirectional CFRPs. Representative stress-strain curves obtained from (a) the short-beam shear and (b) flexural tests for pristine and repaired samples of epoxy composite, dynamic epoxy and ORNL vitrimer composites [1]. Source: ORNL.

Conclusions

This project demonstrated that the ORNL vitrimer with exchangeable disulfide bonds as dynamic cross-links are superior vitrimers for addressing the two long-lasting challenges: high mechanical strength and facile reprocessability. The ORNL vitrimer exhibited a stress relaxation time at 160°C six times faster than that of the dynamic epoxy. The time reduction was enabled by the synergy of the rapid exchange reaction of disulfide metathesis and the efficient chain rearrangement. Importantly, the ORNL vitrimer retained its mechanical strength for many cycles because of facile reprocessability at moderate temperature with a short annealing time. In contrast, the mechanical strength of the dynamic epoxy dramatically decreased after four cycles. Notably, the CFRPs with the ORNL vitrimer exhibited excellent reprocessability and recyclability while maintaining mechanical strength. Moreover, the ORNL vitrimer resins and their CFRPs displayed outstanding chemical recycling, leading to excellent recyclability for carbon fibers, while maintaining good chemical resistance to common solvents. The findings provide a solution to circumventing the common challenges of poor recyclability and low mechanical strength for other vitrimers. The capabilities of the ORNL vitrimer composites with high mechanical strength and facile reprocessability demonstrated in this work will enable the development of advanced CFRPs.

Key Publications

1. Zhou, Z., S. Kim, C. C. Bowland, B. Li, N. Ghezawi, E. L. Lara-Curzio, A. Hassen, A. Naskar, M. A. Rahman, and T. Saito, 2022, "Unraveling a path for multicycle recyclability in robust dynamic fiber-reinforced vitrimer composites," draft manuscript.

References

1. Zhou, Z., S. Kim, C. C. Bowland, B. Li, N. Ghezawi, E. L. Lara-Curzio, A. Hassen, A. Naskar, M. A. Rahman, and T. Saito, 2022, "Unraveling a path for multicycle recyclability in robust dynamic fiber-reinforced vitrimer composites," draft manuscript.

Acknowledgments

This research was sponsored by the DOE-EERE VTO. We thank the team members of this project: Drs. A. Rahman, C. Bowland, A. Naskar, Z. Zhou, S. Kim, and M. Arifuzzaman; Mr. Bingrui Li; and Ms. N. Ghezawi.

II.2.19 Adopting Heavy-Tow Carbon Fiber for Repairable, Stamp-Formed Composites (Oak Ridge National Laboratory)

Amit Naskar, Principal Investigator

Oak Ridge National Laboratory
1 Bethel Valley Road
Oak Ridge, TN 37830
E-mail: naskarak@ornl.gov

H. Felix Wu, DOE Technology Manager

U.S. Department of Energy
E-mail: felix.wu@ee.doe.gov

Start Date: October 1, 2020

End Date: September 30, 2023

Project Funding (FY 2021): \$500,000

DOE share: \$500,000

Non-DOE share: \$0

Project Introduction

This research focuses on interface engineering and high-throughput manufacturing methods for heavy-tow CFs—having >100,000 filaments in a single bundle—and tailoring its interactions with thermoplastic matrices to develop new stamp-formed layered structures. This approach involves the integration of fundamental understanding, application of modern scattering-based characterization tools, and computation to achieve the rational molecular-level design and control of the mechanical properties in thermoplastic composites. State-of-the-art automotive parts [1, 2] produced from the thermoplastic composite at a high production rate (>250,000 parts/year) usually cost >\$50/kg [3]. As a part of this project, technologies that enable a significant cost reduction in composite parts will be developed. The project will lead to the elimination of several processing steps and of costly shipment and storage requirements for intermediates.

The work builds upon the team's prior success with experiments and modeling of polymer composites and extends that to time and length scales comparable to polymer matrix composite material design to enable the significant cost reductions in CF-reinforced thermoplastic composite parts for cars [4, 5]. The research leverages recent advances made in structural CF manufacturing at ORNL and the laboratory director's R&D investment with an *in-situ* characterization of polymer composites and strengthens the link between basic research and applications of composites.

Objectives

The objective of this research is to develop and commercialize new interfacial engineering methods for efficient reinforcement of thermoplastic matrices by heavy-tow CFs and demonstrate that the chemistry and processing allow the formation of multilayer laminate structures rivaling the rapid stamping rate of metals. The project will deliver repairable low-cost thermoplastic composites with a multilayered stamp-formed structure containing 40 vol.% to 60 vol.% fiber and outstanding mechanical performance (e.g., 0.8 GPa to 1.4 GPa unidirectional tensile strength, 50 GPa to 100 GPa Young's modulus). High-throughput processing technologies for thermally recyclable or repairable CF composites of thermoplastic matrices will enable a new paradigm toward cost-competitive lightweight materials for automotive fuel efficiency without compromising their mechanical performance and crashworthiness.

Approach

The overarching goal of this early-stage research is to connect the key physicochemical relationships at different length scales (including surface adsorption or bonding, polymer interfacial dynamics, and fiber–fiber interactions) to the key process engineering considerations, along with macroscopic rheological and mechanical properties of thermoplastic polymer matrix composites. To this end, we combine polymer and interfacial chemistry, x-ray scattering, rheology, thermomechanical characterization of intermediates and

formed samples, and spectroscopy (on the experimental side) with molecular dynamics simulations (on the high-performance computation side). Specifically, the project team is: (1) developing new interfacial chemistries under the guidance of a computationally defined framework to optimize polymer-fiber interaction; (2) revealing the interplay of the interfacial interactions on the processability and composites' response to load by using mechanical testing and *in-situ* x-ray scattering; and (3) elucidating the relationship between fiber volume fraction, matrix morphology, and performance of the stamp-formed multilayered structures.

Results

To develop the understanding and processing conditions needed to make the thermoplastic composites, the project started by evaluating the baseline properties of thermoplastic matrix composites reinforced with standard or commercial fibers without any specific interfacial chemistry. The project team aimed to maximize properties of the “baseline” composites by mere use of simple process parameters. Such enhancement in properties needed a deep understanding of fiber-matrix interface structures at different length scales. Once such understanding was developed, the goal was to exercise simple compression molding or apply the stamping process. The project milestones associated with these specific tasks: M1.0, M2.0, M3.0, and M4.0, as observed in Table II.2.19.1, were completed during FY 2021.

Table II.2.19.1. FY 2021 Milestones

Milestone/Deliverable Name/Description	End Date	Status
M1.0: Develop composite performance data for CF–epoxy commercial materials and compare with CF–polypropylene (PP) performance	12/31/2020	Complete
M2.0: Exhibit PP matrix discontinuous CFRPs with 100 MPa tensile strength	03/30/2021	Complete
M3.0: Establish intermediates' morphology at 100 nm to 500 nm and 5 mm to 100 mm length scales	06/30/2021	Complete
M4.0: Demonstrate CFRP stamping process for multilayered structures	09/30/2021	Complete

To establish composite performance baseline data for milestone M1.0, a HexTow[®] IM7 (IM7) unsized, untreated fiber of 12,000 tow size was procured and continuously processed with the PP, HDPE, LDPE, and ABS copolymer thermoplastic matrices to make thermoplastic tow-pregs, as shown in Figure II.2.19.1. The plastics were extruded and allowed to impregnate the tow, as shown in Figure II.2.19.1(a). The prepared tow-preg strands represent baseline thermoplastic composite, as observed in the samples shown in Figure II.2.19.1(b); the CF interface has not been modified or tailored. The unidirectional mechanical properties of these “baseline” unidirectional composite strands were measured by tensile testing, as observed in Figure II.2.19.2(a). The fiber fraction in composite strands was measured by TGA, as shown in Figure II.2.19.2(b). The properties were compared with unidirectional epoxy composite performance on these IM7 CFs (>1 GPa tensile strength and >100 GPa modulus). Based on industry feedback, the project team established a goal for unidirectional thermoplastic composites of 750 MPa tensile strength. Nonetheless, the project team also aims to make discontinuous CF-reinforced thermoplastic composites with isotropic properties. Specifically, this study will use such composites to understand the morphology of polymers at the fiber-matrix interface vs. the bulk of the matrix.

The fiber volume fraction in the PP composite was estimated using a thermogravimetric analyzer. The PP tow-preg had 10 volume fraction of CF and exhibited 60 MPa strength. Therefore, a 50 vol.% CF-PP composite is expected to have 300 MPa tensile strength (assuming a linear relationship for mechanical performance against fiber volume fraction for unidirectional composites). Our goal for unidirectional thermoplastic composites is to achieve 750 MPa tensile strength. Therefore, our goal in tailoring interfacial morphology is to improve the properties at least by 150%. In the first quarter of FY 2021, we recorded our baseline properties and established our target for improvement.

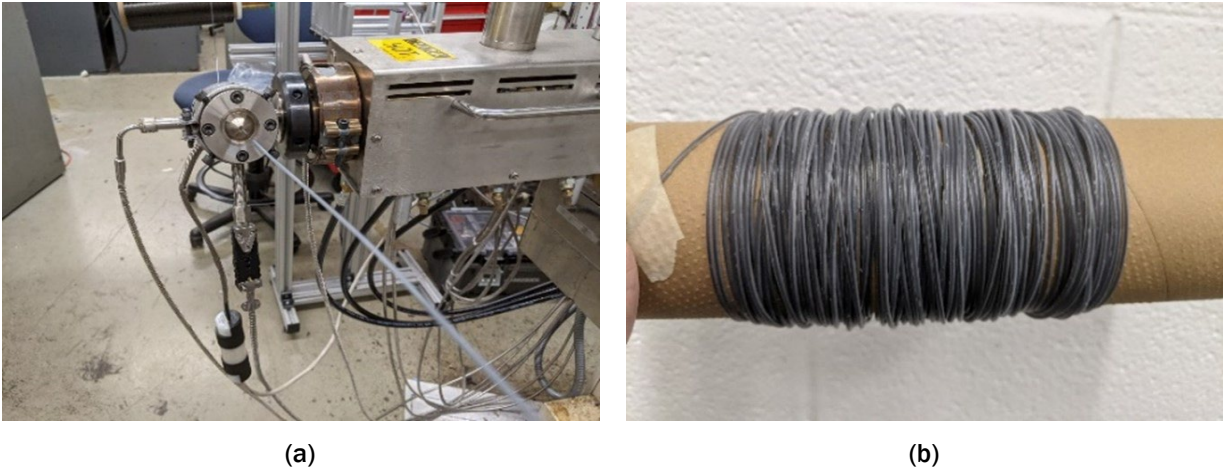


Figure II.2.19.1. Representative photographs of (a) the continuous CF tow processing system and (b) the spooled thermoplastic tow-preg. Source: ORNL.

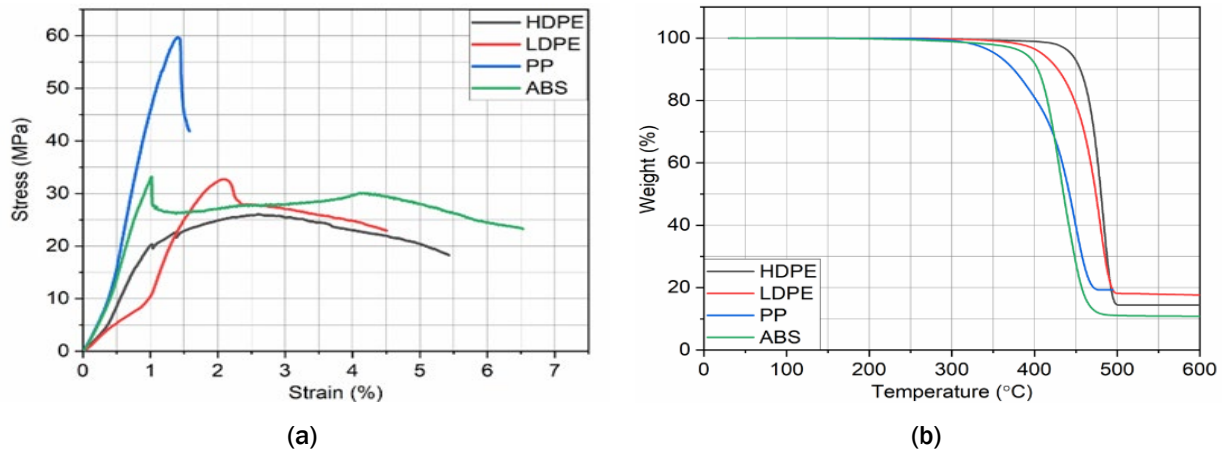


Figure II.2.19.2. (a) Representative stress-strain plots of the prepared tow-pregs. (b) TGA thermograms, showing 12 wt.% to 17 wt.% CF loading in composites. Source: ORNL

Part of milestone M2.0 involved exhibiting PP matrix discontinuous CFRPs with 100 MPa tensile strength. To this end, the project team developed a method that enhances fiber–PP matrix interactions. Methods with and without the need for chemicals were studied. Figure II.2.19.3 shows the electron micrographs for CFs processed in the laboratory. The processing technique can be adopted for a continuous operation and can be readily tuned to tailor fiber surface chemistry and topology.

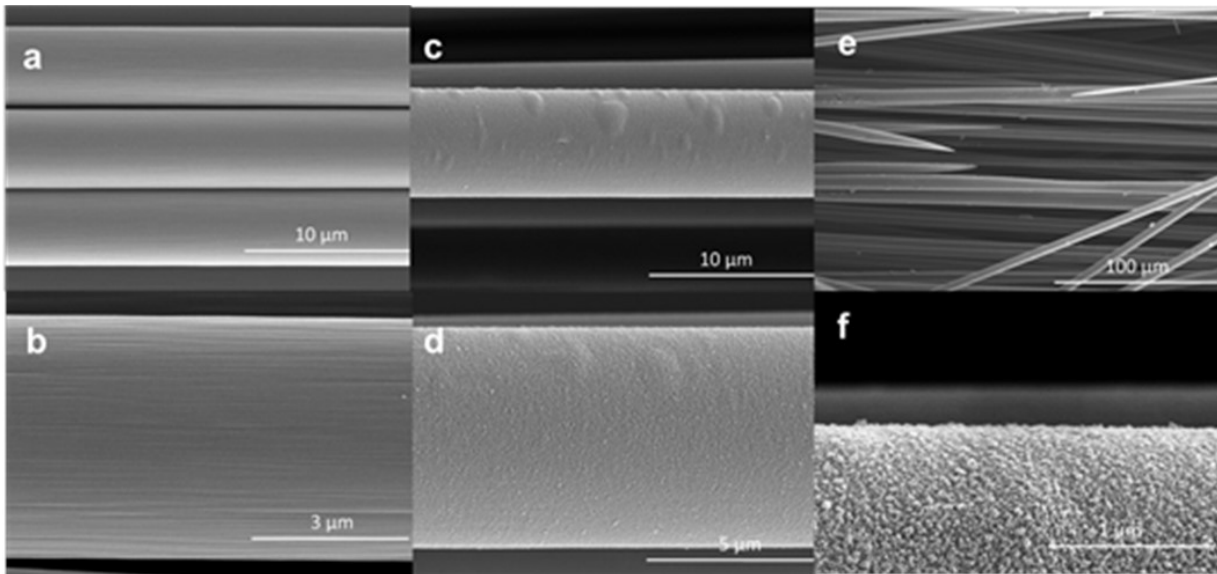


Figure II.2.19.3. Electron micrograph of (a)-(b) pristine, (c)-(d) mild treated, and (e)-(f) excessively treated CF surfaces. Source: ORNL.

Figure II.2.19.4 below shows the tensile stress-strain profile of composites from unsized discontinuous fibers from heavy-tow CF manufactured at ORNL. Specific polyolefin composite specimens exhibited significantly higher tensile strength than the 100 MPa milestone and were observed to be considerably stronger and tougher than the control specimens. This proves the effectiveness of the fiber processing developed as part of this milestone.

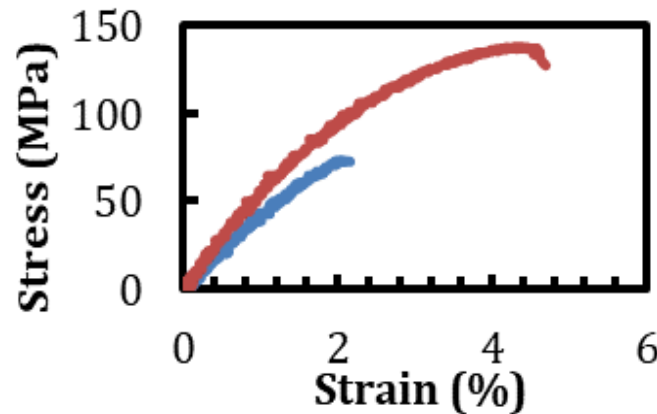


Figure II.2.19.4. Tensile stress-strain profile of composites from unsized discontinuous filaments from heavy-tow CF. Treated fiber composite specimens (red) are stronger and tougher than the control composite specimens (blue). Source: ORNL.

Part of milestone M3.0 was to establish CF-PP morphology at 100 nm to 500 nm and 5 nm to 100 nm length scales. To this end, the project team used several different techniques such as DSC, wide-angle x-ray diffraction (WAXD) and polarized optical microscopy (POM). From the DSC analysis on different weight fractions of CF-PP composites, it was observed that the CF surface offers an excellent nucleating site. However, the epitaxial growth of PP limits crystal growth. Isothermal crystallization of the PP matrix loaded with clean, unmodified CF shows that the presence of CF accelerates PP crystallization and the crystallization half-time reduces as the CF weight fraction in PP is increased, as observed in Figure II.2.19.5.

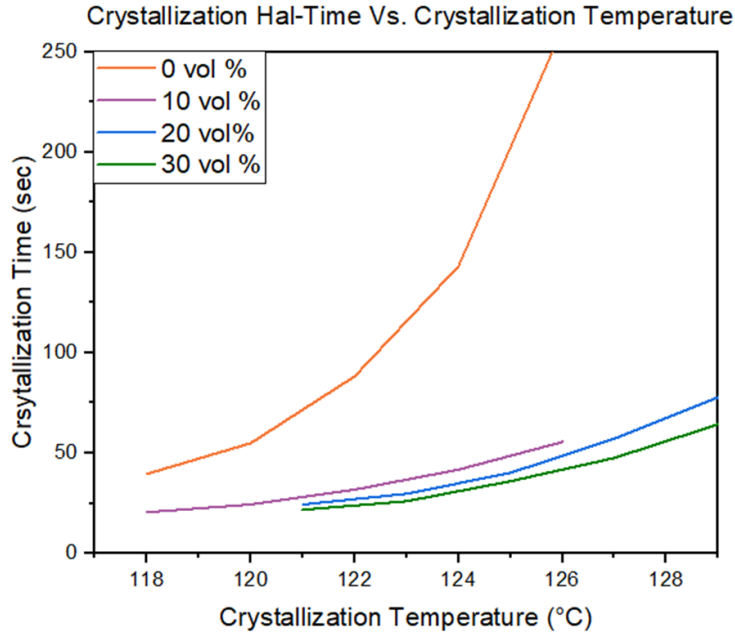


Figure II.2.19.5. Plot showing crystallization half-time vs. crystallization temperature, suggesting crystallization rates become faster with increasing fiber loadings for all temperature ranges studied. Source: ORNL.

WAXD was used to study the crystallographic attributes of the isotactic PP systems as a function of CF loadings with the goal of analyzing the morphologies quantitatively. The project team observed seven diffractions (110), (040), (130), (111), (060), (200), and (220) of the α -crystal system, in addition to two (300) and (301) of the β -crystal systems, as observed in Figure II.2.19.6. However, as fiber loadings scale-up, β -crystal systems either disappear (300) or become less distinct (301) because the rate of undercooling during crystallization decreases. This finding is supported by the DSC data, which showed that the temperature at which crystallization initiates (onset temperature) increases proportionally to fiber loading, where nucleation initiates at temperatures closer to melting temperature.

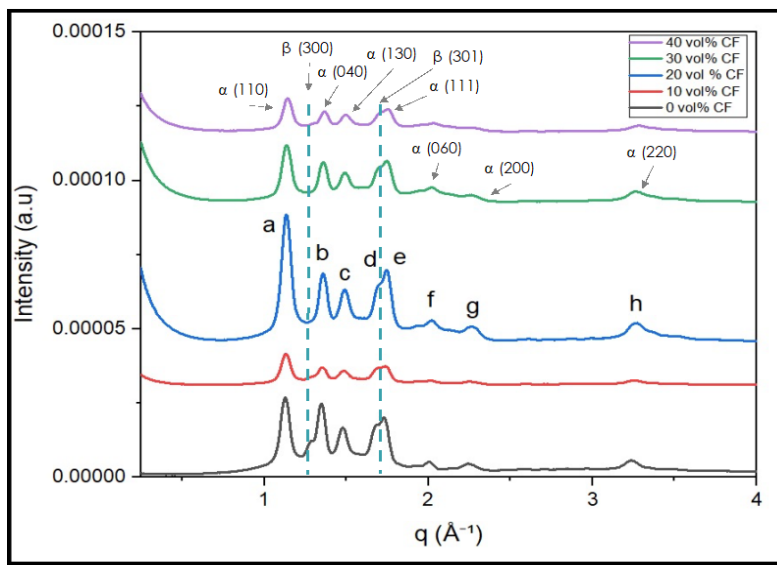


Figure II.2.19.6. Wide-angle X-ray diffractograms of PP and CF composites. Source: ORNL.

Using a polarized OM, the researcher team observed crystallization of PP in bulk polymer and on the CF surface, as observed in Figure II.2.19.7 where Figure II.2.19.7(a) shows spherulitic crystal growth in neat PP polymer and Figure II.2.19.7(b) shows an abundance of individualized PP crystals on the CF surface since it offers an excellent nucleation site. However, the epitaxial growth of PP limits crystal growth, and the crystal size is significantly smaller on the surface of the CF than in the bulk polymer. The fiber surface is filled with nuclei, and as a result, a layer of transcrystallinity forms, restricting the growth of the crystals to a normal size at the surface of the fiber. The bulk crystal spherulites are of $\sim 100\ \mu\text{m}$ diameter and consist of sub-micrometer lamellae and the spherulites grown near fibers are restricted to $10\ \mu\text{m}$ to $30\ \mu\text{m}$ radii with thinner lamellae.

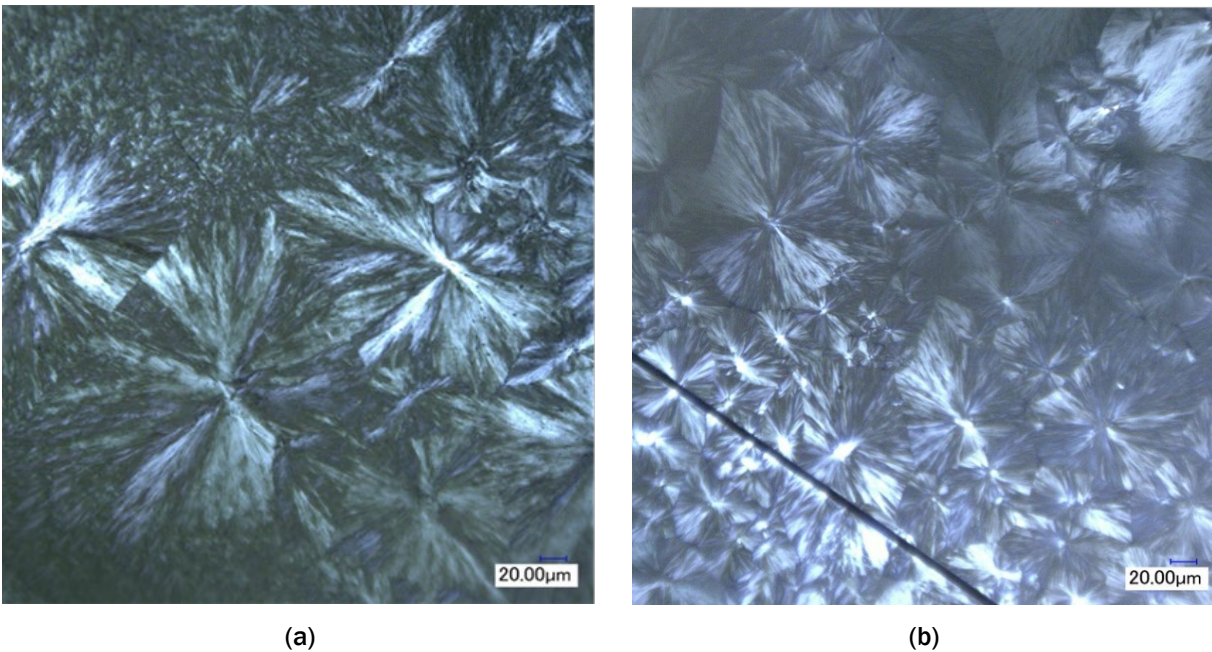


Figure II.2.19.7. POM images showing (a) spherulitic crystal growth in neat PP and (b) fiber surface with transcrystallinity due to an abundance of nucleation sites, leading to restricted crystal growth around fiber.

Source: ORNL.

As part of milestone M4.0, the project team developed a novel process for fabricating multilayered composite structures with the goal of achieving thorough fiber wetting and resin penetration, resulting in enhanced mechanical performance. First, an air-blowing setup was used to fabricate chopped CF mats with randomly oriented fibers. After the air-blowing process is complete, the CF mat is formed and utilized to make composite structures. In the second step of the fabrication process, alternate layers of PP films and chopped CF mats are stacked on top of each other and hot-pressed between steel plates in a 10-ton press at 190°C for 30 minutes, as can be seen in Figure II.2.19.8(a). The resulting multilayered CF-PP composites exhibited a smooth surface finish. The microstructure observed using SEM showed good resin penetration and fiber wettability, as shown in Figure II.2.19.8(b).

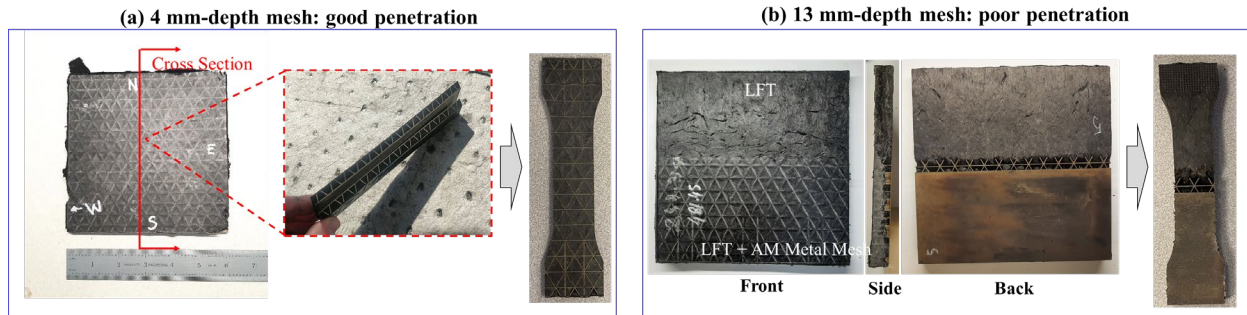


Figure II.2.19.8. Schematic of the fabrication process for multilayered composite structures: (a) the hot-pressing process for fabricating the multilayered CF-PP composite and (b) an SEM micrograph of the CF-PP microstructure. Source: ORNL.

Conclusions

The project team began the FY 2021 work by evaluating CF composite performance data for different thermoplastics (e.g., LDPE, ABS, HDPE, PP) to obtain baseline properties for CF composites with no surface treatments or interfacial modifications. Following this, researchers developed a novel fiber processing method to engineer the interface in polymer matrix composites, observing significantly higher strength and stiffness compared to control composites. An in-depth study of the crystallization behavior, along with nano- and micro-scale morphology of the composites, revealed that crystallization rates increase with CF loading, as CF surfaces provide an abundance of nucleation sites for semicrystalline matrix crystal growth. Researchers also observed that the matrix forms a transcrystalline region at the fiber surfaces with an abundance of individualized crystals on the surface since it offers an excellent nucleation site. However, the epitaxial growth limits matrix crystal growth, and the crystal size is significantly smaller on the fiber surface than in the bulk polymer. In addition to understanding interfacial morphology, researchers developed a novel fabrication process and successfully fabricated multilayered composite structures with good fiber wetting and resin penetration and a void-free microstructure.

Key Publications

1. Allen, K., et al., 2022, "Morphology optimization in isotactic polypropylene carbon fiber composites," draft manuscript.
2. Datta, S., et al., 2022, "Carbon-fiber-reinforced thermoplastic composites with enhanced functionalities," draft manuscript.

References

1. Milberg, E., 2018, "GMC reveals carbon fiber truck bed in new 2019 Sierra Denali," *Composites Manufacturing*, Available at: <http://compositesmanufacturingmagazine.com/2018/03/gm-carbon-fiber-truck-bed-2019-sierra-denali/>. (last accessed 7 December 2021).
2. Malnati, P., 2019, "High-speed, high-rate thermoplastic composites manufacturing," *CompositesWorld*, August 2, Available at: <https://www.compositesworld.com/blog/post/high-speed-high-rate-thermoplastic-composites-manufacturing> (last accessed 8 March 2022).

II.2.20 Soft Smart Tools Using Additive Manufacturing (Savannah River National Laboratory)

Jay Gaillard, Co-Principal Investigator

Savannah River National Laboratory
Bldg. 999-2W
Aiken, SC 29808
E-mail: jay.gaillard@srnl.doe.gov

Srikantha Pilla, Co-Principal Investigator

Clemson University International Center for Automotive Research
4 Research Dr.
Greenville, SC 29607
E-mail: spilla@clemson.edu

Richard Czerw, Co-Principal Investigator

Mainland Solutions, LLC
409 W. Maple St.
Yadkinville, NC 27055
E-mail: czerwr@mainlandsolutions.com

H. Felix Wu, DOE Technology Manager

U.S. Department of Energy
E-mail: felix.wu@ee.doe.gov

Start Date: October 1, 2020

End Date: September 30, 2023

Project Funding (FY 2021): \$500,000

DOE share: \$500,000

Non-DOE share: \$0

Project Introduction

Tooling is an integral part of composites manufacturing. Composite tools, also called soft tools, are more easily constructed than “hard” metal tools and, because they are made from materials similar to the manufactured composite part, they can be made in-house and have a good CTE match. However, as the “soft” designation suggests, they are more vulnerable to wear and typically find application in relatively low-volume production. AM of thermoplastics has proven to be a lucrative option that can help improve the tooling functionalities, as it offers more design flexibility. Owing to the inherent nature of AM, the possibility of printing sensors within the tool material and at proximity to otherwise inaccessible areas of the tool become a reality. CCF-reinforced 3D printing of engineering thermoplastics has proven to be a viable option to strengthen a part well beyond the ideal moduli of unmodified thermoplastic. Furthermore, adding nanotubes or graphene to the thermoplastic matrix will also improve both the thermal conductivity and interlaminar shear strength within the tool. CNTs and CFs are microwave susceptors; exploiting the physics of Joule heating to increase the energy efficiency of tool hardening and cure rates is a core goal of this project. Because of the rapid volumetric heating enabled by the absorption of microwave or RF EM annealing presents an attractive opportunity to significantly reduce manufacturing cycle times while improving part performance.

The introduction of integrated sensors such as thermocouples and strain gauges allow for real-time feedback to the end-user, resulting in improved process controls such as thermal management. Strain gauges provide valuable information about when the tooling becomes warped beyond tolerance and needs to be scrapped. Thermocouples help with reducing wasted processing time because the tooling temperature can be monitored for optimized cure schedules and out-of-tolerance thermal gradients. AM principles allow these integrated

smart sensors to be printed simultaneously with production of the soft tool. Incorporation of integrated sensors into composite tools enables process controls that will further improve cycle times and reduce scrap rates.

Objectives

The goal of this project is to develop high-toughness, wear-resistant CCF nanocomposite tooling with embedded sensors for vacuum bag molding or autoclaving of automotive parts. Using EM post-annealing of 3D-printed CCF and nanotube composite structures will improve the tooling’s strength and thermal conductivity as compared to traditionally annealed soft composite tools. AM allows for integration of printable smart sensors to continuously monitor temperature, strain, and pressure within the tool itself, enabling improved process controls and lower inter-part variability. If successful, this technology will decrease soft tooling costs by 30%, increase process throughput by 50%, and reduce failures in the molding process.

Approach

To increase process throughput, reduce scrap rates, and lower soft tooling costs, the project is prototyping soft smart tooling using AM techniques incorporating the following concepts:

- Nanomaterial-filled thermoplastics to improve thermal conductivity with added tool strength in 3D continuous fiber printing. This allows for thinner tooling with less thermal gradient and thermal lag.
- Post-curing and -annealing performed by coupling microwave or induction RF energy directly to the susceptor-enhanced nanomaterials, resulting in reinforcement and improved polymer crystallinity for greater mechanical and thermal properties.
- Temperature, heat flux, strain, and pressure sensors printed into the tool to monitor cure kinetics, voids (especially for resin transfer molding), and spring-in.

Our approach seeks to 3D-print nanomaterial-enhanced CCF soft tooling with embedded sensors. Incorporating nanomaterials into the soft tooling adds toughness and improved thermal conductivity; EM annealing increases polymer crystallinity, further increasing mechanical and thermal properties; and adding sensors allows the user to monitor temperature and pressure during part manufacturing. Process controls implemented using sensor feedback allows the user to identify when a tool needs to be scrapped and replaced.

Figure II.2.20.1 provides a detailed schematic of our approach. The CCF tow, prepared with a thermoplastic prepreg containing our nanomaterials, is printed by the layup head. The nanomaterials incorporated within the prepreg are designed to be EM susceptors are added at a concentration at which percolation theory leads to an inherent increase in thermal conductivity between z-direction layers; this is a major challenge in AM. During printing of the layers using the CCF tow enhanced with nanomaterial-embedded thermoplastic substrate, secondary reservoir heads with conductive inks are used to print thermocouple and/or strain gauge sensors *in-situ*. Table II.2.20.1 provides the milestones, go/no-go decision, and status for FY 2021.

Table II.2.20.1 Milestones and Go/No-Go

Milestone Name/Description	Milestone Status
M1.1: Demonstrate proof-of-concept of significant mechanical/thermal property enhancements using EM coupled heating.	Complete
M1.2: Design smart sensor for integration into 3D printing.	Complete
M1.3: Obtain sufficient evidence of >10% increase in tensile strength and >10% increase in thermal conductivity for small test coupons.	Complete
M1.4: Demonstrate smart sensor integration of at least two sensors into a test coupon.	Complete
Phase 1 (Year 1) go/no-go milestone: Demonstrate >20% higher modulus/strength and thermal conductivity with at least one integrated smart sensor.	Complete

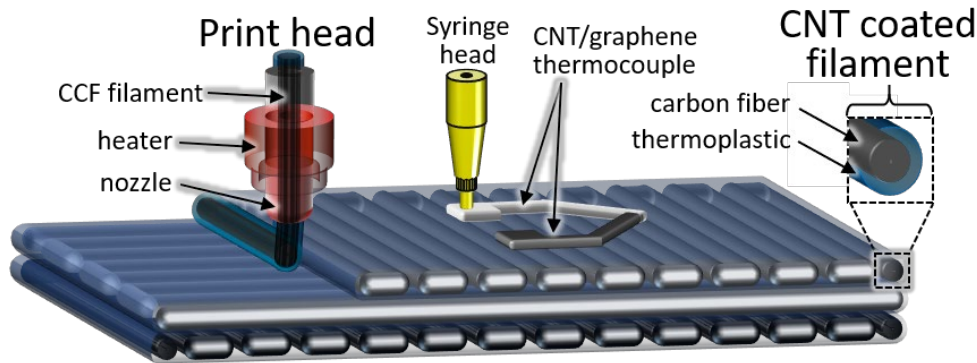


Figure II.2.20.1. Diagram of 3D printing equipment for CCF composites: Source: SRNL.

Results

3D Printing CCF Test Coupons

Samples used for tensile and thermal conductivity testing were printed into ASTM-compliant dog bones or coupons using Savannah River National Laboratory's (SRNL's) Markforged X7 CCF 3D printer. Initially, a 3D-printed object (e.g., an ASTM-compliant dog bone) was drawn within a CAD program and then sliced into layer sections using Markforged's Eiger software to generate the toolpath code for each printer head.

Figure II.2.20.2(a) shows the Eiger-generated schematic of a tool path for a dog bone. White lines indicate the path followed for the nylon filament, while blue lines indicate the tool path followed by the head laying up the CCF tow. Figure II.2.20.2(b) shows a CCF 3D-printed dog bone.



Figure II.2.20.2. (a) 2D rendering of the top and side build path and slicing diagrams of dog bones and (b) CCF 3D-printed dog bone. Source: SRNL

Initial experiments used a sandwiched structure wherein layers of nanotube-filled filament were alternated with layers of CCF tow. Neat nylon samples were printed using the same method. Both samples were then subjected to microwave annealing. Later experiments replaced the alternating interlayer structure of nylon-carbon fiber-nylon with structures of solid nylon-prepregged CCF tow. As the CF is itself a microwave susceptor, samples were microwave-annealed and evaluated for their mechanical strength and thermal transport enhancements.

Microwave Annealing with Mechanical/Thermal Testing Results

Microwave annealing experiments were performed in a CEM Mars6™ microwave, which contains a large volume cavity capable of receiving a wide variety of sample sizes and shapes. Microwave power levels ranging from 50 W to 250 W were surveyed for annealing, determined separately for both the dog bone- and coupon-shaped samples. Powers surveyed for EM annealing that showed maximum mechanical enhancement ranged from 170 W to 200 W, resulting in dwell temperatures ranging from 90°C to 120°C, as shown in Figure II.2.20.3. Initial annealing experiments were performed on a sandwiched structure wherein layers of

nanotube-filled filament were alternated with layers of CCF tow. As shown in Figure II.2.20.3(a) and Figure II.2.20.3(b), we demonstrated an improvement in mechanical properties (>10% modulus and tensile strength), and as shown in Figure II.2.20.3(c), the thermal properties (>5% heat transfer) after only five minutes of annealing, as compared to traditional curing and annealing times of two to eight hours in 3D-printed structures. This experiment demonstrates the advantages of microwave annealing 3D-printed nylon specimens, both for increasing mechanical properties and reducing annealing time.

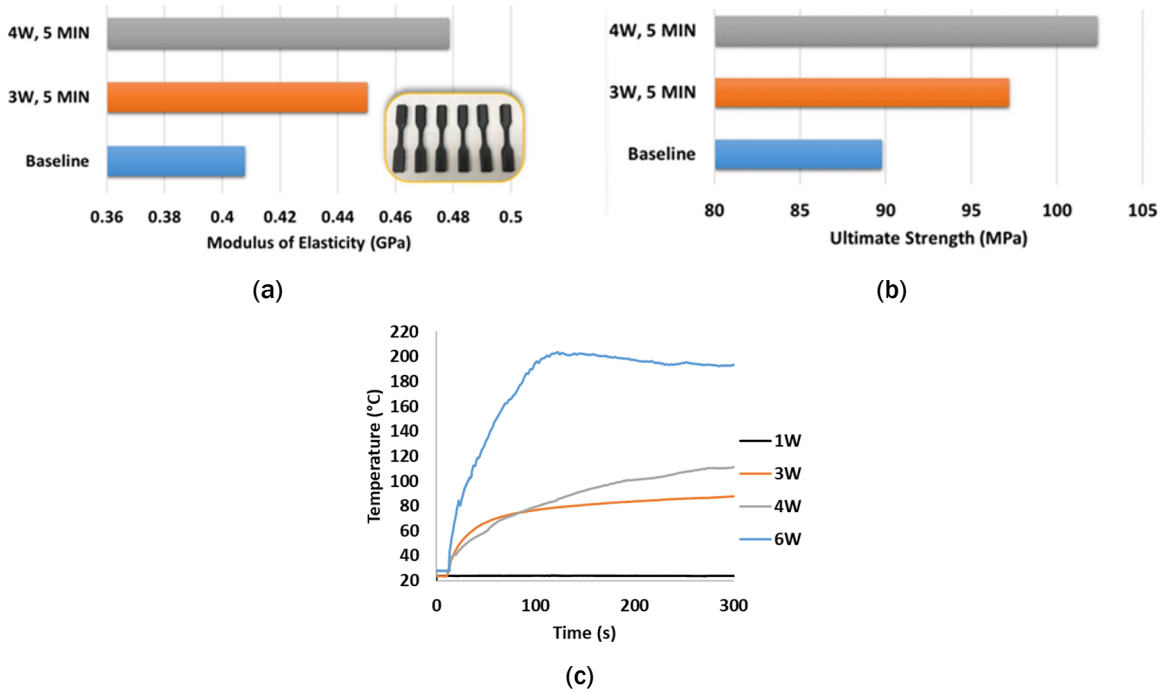


Figure II.2.20.3. Microwave annealing of chopped CF dog bones shows enhancement of tensile properties after five minutes of irradiation at constant power. Source: SRNL.

EM annealing of dog bones composed of solid nylon-prepregged CCF tow showed a 21.2% increase in tensile strength, as observed in Figure II.2.20.4, relative to the baseline sample. Similarly, coupons printed with CCF tow showed a 22.9% increase in the rate of temperature change for EM-annealed samples, demonstrating a significant increase in thermal conductivity.

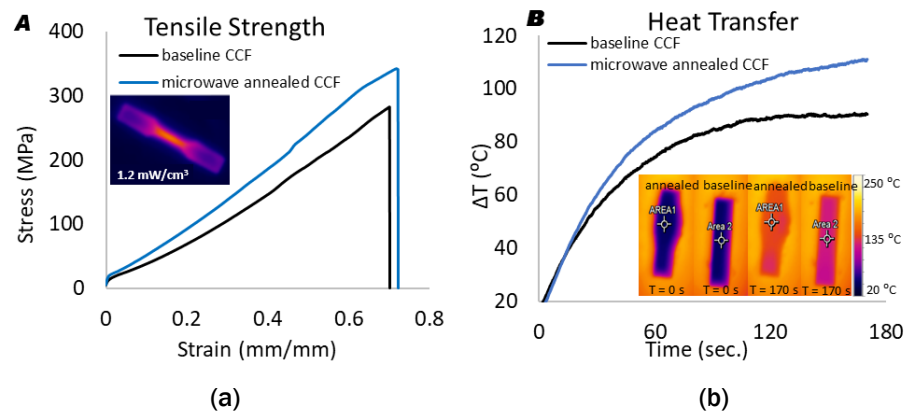


Figure II.2.20.4. (a) Tensile strength measurements and (b) heat transfer measurements for 3D-printed CCF composite dog bone samples showing the effect of EM annealing (inset) forward-looking infrared (FLIR) camera images of 3D-printed CCF composite samples on a hotplate set to 200°C. Source: ORNL.

Compounding and Filament Production with CNTs

Mainland Solutions, LLC produce the baseline filament material, without any nanomaterial additives, by extruding neat Nylon 12 powder through a 1.75 mm die at the outlet of a HAAKE MiniLab, as shown in Figure II.2.20.5(a). CNTs were then compounded from 1 wt.% to 20 wt.% to form the CNT–nylon melt mixes, from which printable filaments were produced. Initial experiments showed poor intermixing of the nanotubes within filaments. It was found that a triple pass of the composite produced sufficiently dispersed nanotubes in the filament. Results of the mechanical testing are shown in Figure II.2.20.5(b).

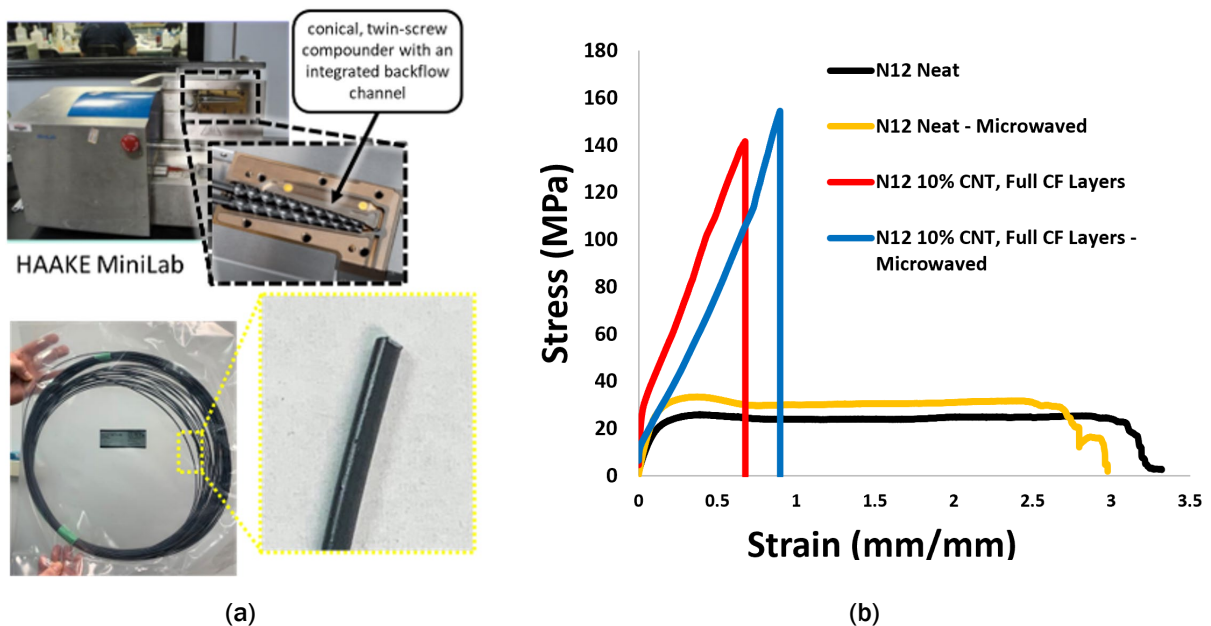


Figure II.2.20.5. (a) Metal mesh AM using (b) a metal powder laser AM system (AddUp) with the LFT. Source: ORNL.

Characterization of CNT–Thermoplastic and CNT–CF Filaments

Clemson University performed materials characterization to identify the processing properties of the different composite materials and determine whether a significant deviation in printing parameters between the base

material and the composite mixes could be expected. As the annealing temperature must be held between the glass transition temperature (T_g) and the melting temperature (T_m), it is critical to know these temperatures so that the annealing produces optimal mechanical properties. Sample characterization showed that no significant changes were observed in the melt temperature with the addition of varying ratios of CNT or CF to the nylon, as shown in Table II.2.20.2. However, the addition of CNT to the thermoplastic filament blend did lead to increases in the glass transition temperature for both thermoplastics. Nylon 12 was found to have the highest glass transition temperature, followed by Dupont Zytel®.

Table II.2.20.2 Specific Heat Capacity at Key Temperature Points

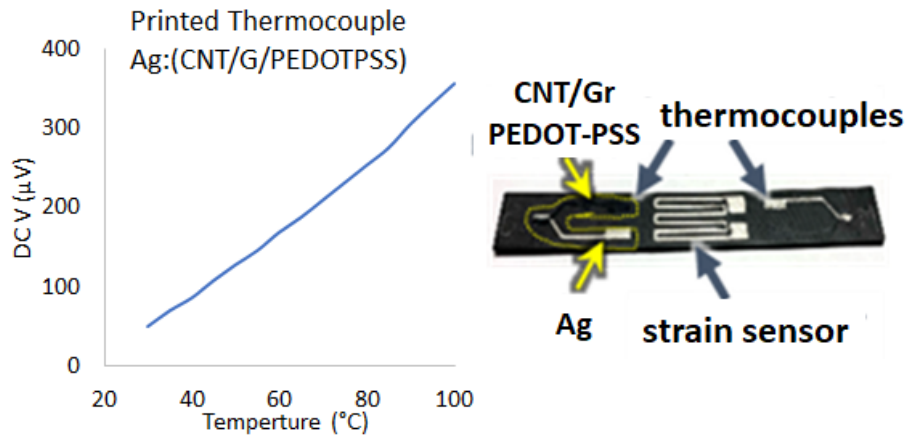
Sample Composition	Glass Transition T_g (°C)	C_p at T_g (J/kg*K)	Melting Point T_m (°C)	C_p at T_m (J/kg*K)	Enthalpy of Crystallization (J/g)
Neat Nylon 12	99.97	2.586	181.17	7.744	36.27
5% CNT_Nylon 12	102.19	1.913	180.47	7.182	33.062
10% CNT_Nylon 12	111.27	2.439	180.54	8.373	33.825
5% CNT_Nylon 12_10% CF	103.74	2.161	180.22	6.682	35.859
5% CNT_Nylon 12_35% CF	101.12	2.113	179.9	3.519	11.038
5% CNT_Nylon 12_45% CF	109.4	2.133	179.73	3.884	12.199

Smart Sensor Design, Testing, and Evaluation

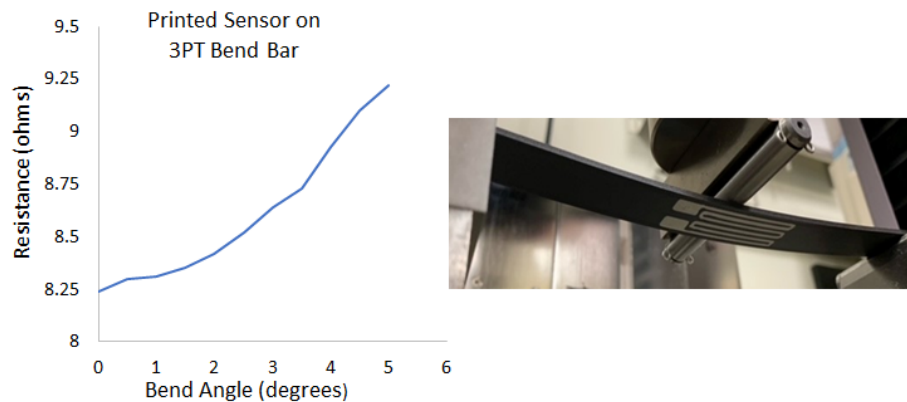
Smart sensor integration was demonstrated by 3D printing silver (Ag) paint onto two 3D-printed CCF test coupons. The smart sensors targeted were a strain gauge and a thermocouple, as shown in Figure II.2.20.6(a). The strain gauge sensor is a resistive-type strain gauge, where the resistance changes based upon the bend angle. Strain gauges provide the amount of force applied to a material whether under tension or compression. Figure II.2.20.6(b) shows the change in resistance of a printed strain gauge on a specimen in three-point bend. The strain gauge sensor, along with two working thermocouples, were all printed on the face of a 20-cm-long specimen for a three-point bend test. One of the primary challenges in syringe ink printing is ensuring consistent, continuous material flow during the print. The G-code governing printer movement was optimized for the extrusion rate based on both the viscosity of the material and the selected nozzle tip diameter.

The printed strain gauge sensor was evaluated as follows. After printing and drying, a loading nose was applied to the opposite side of the strain gauge, causing it to bend. A trend of increased resistance with increased loading was measured. The silver trace strain gauge demonstrated an increase in resistance of 12% over a 5° arc in response to the bending angle, as measured on an MTS® load frame equipped with a three-point bending head and a 100 kN load cell.

The thermocouple design consisted of two dissimilar materials meeting at a junction. As temperature changes at that junction, compared to a cold junction, a voltage is generated due to the Seebeck effect, which can be correlated to a temperature. The project used this thermocouple layout for ink printing. The layout consisted of two material traces joined together at a point to form the temperature-sensing junction. Two materials were printed consecutively to avoid having the first trace dry before the second was laid over it. The traces consisted of a silver ink and a carbon nanotube:Graphene in PEDOT:PSS. The nanotubes were produced by a modified chemical vapor deposition process to obtain 800- μ m-long nanotubes. The thermocouples were printed on a Hyrel Engine HR printer with a reservoir-based print head using a 5 mL syringe. Two layers were applied to each trace to ensure sufficient material distribution. Using Ag/(CNT:Graphene in PEDOT:PSS) for the two different leg materials allowed for ambient processing without any anneal. A heater tape was placed onto the tip of the printed thermocouple mounted on the bend bar. Two traditional thermocouples, one measuring the tape temperature and the other measuring the temperature of the bar, were placed to record reference temperatures. Figure II.2.20.6(a) shows the voltage response over a range of temperatures, demonstrating a functional temperature sensor.



(a)



(b)

Figure II.2.20.6. (a) Voltage response of the thermocouple to temperature where the thermocouples and strain gauge were consecutively printed on a 3D-printed three-point bend bar. (b) Change in resistance as a function of bend angle in a silver three-point bend apparatus with a printed strain gauge.

Source: Clemson University.

Conclusions

In FY 2021, our team proposed to incorporate printable smart sensors into high-strength, high thermal conductivity composite tools to measure temperature, strain, and pressure during manufacturing processes such as vacuum bag molding or autoclaving. Targeted metrics included tooling costs, process throughput, and failure rates in the molding process, addressed through improved mechanical and thermal properties attained through EM annealing and improved process controls such as thermal management.

Microwave annealing of 3D-printed CCF composite dog bones demonstrated a 21.2% increase in tensile strength and a 22.9% increase in the rate of temperature change, compared to control specimens without annealing. The tensile strength of CCF-reinforced samples with carbon nanotube-filled filament increases after microwave annealing. Integrating nanotubes into the print design followed by EM annealing is ongoing work.

Smart sensor integration was demonstrated by 3D printing different tailored inks to incorporate strain and thermocouple sensors onto a CCF 3D-printed coupon. The traces were made from silver ink and a carbon nanomaterial dispersion in PEDOT:PSS. Use of Ag/CNT:Graphene in PEDOT:PSS allowed for ambient processing without annealing.

This effort has laid the groundwork for commercially relevant smart tooling, increasing the usage of CF and nanomaterial additives in composite parts. Initial results showed significant improvements to tensile strength and thermal conductivity through incorporation of nanomaterials and EM annealing while integrating sensors through AM. This work is continuing to make progress toward our goal of decreasing soft tooling costs by 30% and increase process throughput by 50% while reducing significant failures in the molding process.

Acknowledgments

SRNL would like to acknowledge our DOE VTO sponsor, as well as H. F. Wu, the DOE VTO Technology Manager. This work was performed at SRNL and managed by Battelle Savannah River Alliance, in collaboration with Clemson University's International Center for Automotive Research and Mainland Solutions, LLC.

II.2.21 Multi-Material, Functional Composites with Hierarchical Structures (Oak Ridge National Laboratory)

Christopher Bowland, Principal Investigator

Oak Ridge National Laboratory
1 Bethel Valley Road
Oak Ridge, TN 37830
E-mail: bowlandcc@ornl.gov

H. Felix Wu, DOE Technology Manager

U.S. Department of Energy
E-mail: felix.wu@ee.doe.gov

Start Date: October 1, 2020

End Date: September 30, 2023

Project Funding (FY 2021): \$500,000

DOE share: \$500,000

Non-DOE share: \$0

Project Introduction

The aim of this project is to develop approaches to modify fiber surfaces with nano- and microstructures to improve composite strength through better fiber-matrix adhesion. Stronger composites require less material to meet strength specifications, thus leading to better vehicle efficiency. As reported by DOE, a 10% reduction in vehicle weight equates to a 6% to 8% increase in vehicle efficiency [1]. To further enhance vehicle efficiency, this work aims to enhance the mechanical properties of fiber-reinforced composites by at least 10% to 20% using hierarchical structures with different fiber-matrix combinations. Based on DOE efficiency estimates, this 10 to 20% increase of the composite strength-to-weight ratio leads to a 12% to 16% increase in vehicle efficiency.

Fiber surface modification via added functional groups or nanomaterials has shown promising lab-scale results in the literature for enhancing the fiber-matrix interface, but not many approaches have been successful in going beyond lab-scale demonstrations. Process scalability is one key aspect of fiber production and composites manufacturing that limits a good deal of research from making the transition from lab-scale demonstrations to commercial scale applications. The fibers in this project are processed using different scalable methods and integrated into both thermosets and thermoplastics, covering a wide performance range to meet specifications for both semi-structural and structural automotive applications with added functional properties. Specifically, the structural automotive components of interest for the thermoset matrix are the frame components, such as A-, B- and C-pillars and roof rails, where high specific strength and stiffness are paramount. The thermoplastic composites will be used in semi-structural composites on the automobile's exterior, such as the door panels, bumpers, pickup truck bed, and trunk lid/deck lid.

Objectives

The tasks laid out for this research offer routes toward vehicle lightweighting by increasing the strength of the composites. The overall goal is to present versatile methods to deposit nano- and microstructures on the fiber surface for both high-performance structural composites and low-cost, high-volume semi-structural composites. Beyond mechanical performance enhancements, the high-performance structural composites will be capable of embedded *in-situ* sensing and structural health monitoring, owing to the design of the added structures. Even though the main focus of this research is to increase the strength of fiber-reinforced composites to meet the DOE VTO vehicle lightweighting goal, there are other functional properties that the surface-adhered structures can provide to the composites.

Approach

The processing routes developed for this project are versatile, as they offer compatibility with different fibers and a wide variety of nano- and micro-sized particles using a continuous feed-through process. Based on the type of sensor (i.e., passive or active), the electrical conductivity of the composite needs to match the requirements for that sensing system. Therefore, it is advantageous to have this continuous dip-coating technique that is compatible with different fibers to be able to change the electrical conductivity of the bulk composites. For this first year of the project, the focus of the work was on the dip-coating process. This technique was very successful in depositing spherical particles on the fiber surface. However, high aspect ratio particles have not been successfully made to adhere to the fiber surface using the dip-coating technique. Therefore, subsequent work in this project will investigate different coating processes to facilitate high aspect ratio particles' adherence to different fibers.

Results

A two-step fiber-coating process was used to deposit barium titanate (BaTiO_3) particles (200 nm in diameter) on the surface of BF. This was performed in a continuous feed-through fashion to process larger volumes of fiber (versus a batch process). The first step in the process consisted of a mixture of water and BaTiO_3 particles, in which the BaTiO_3 concentration ranged from 0.5 wt.% to 4 wt.%. The second step in the process was an epoxy sizing emulsion bath in which the particles adhered to the fiber surface. The coating of the BaTiO_3 on basalt is shown in Figure II.2.21.1. It is seen that the particles agglomerate slightly in areas, but overall, the particles coat every fiber in the tow homogeneously.

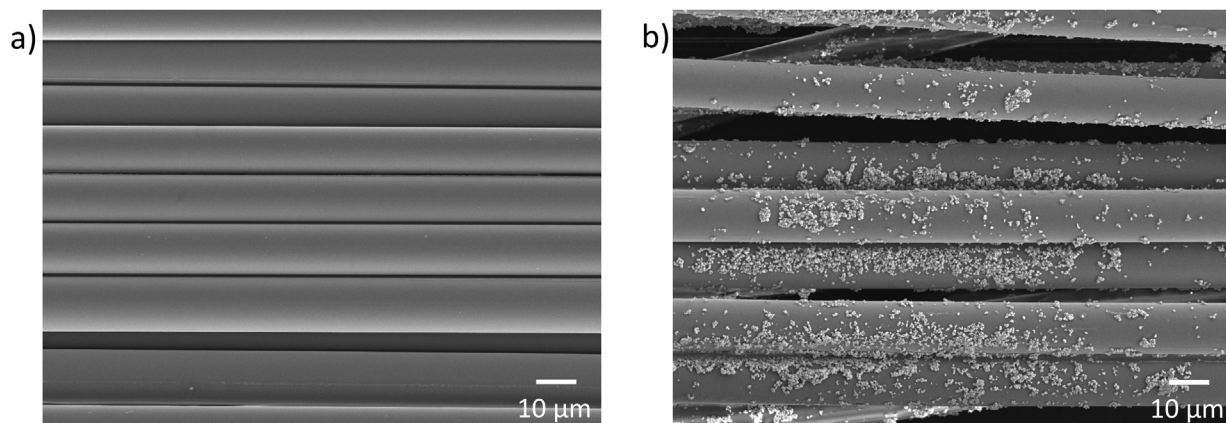


Figure II.2.21.1. SEM images of (a) as-received basalt (with commercial sizing) and (b) BF coated with BaTiO_3 particles using the 2 wt.% BaTiO_3 coating bath [2]. Source: ORNL.

To evaluate the mechanical performance of the coated fibers, unidirectional composites were fabricated using a filament winding approach. These composites were composed of roughly 60 vol.% fibers embedded in a commercial epoxy (Hexion EPON 862 with EPIKURE Curing Agent W). A composite sample set was fabricated for the bare BFs, as well as for the 0.5 wt.% to 4 wt.% BaTiO_3 -coated fibers, in which the weight-percent values represent the concentration of BaTiO_3 in the first coating bath. These composites were sectioned into smaller samples for short-beam shear testing following ASTM D2344 to quantify the apparent interlaminar shear strengths (ILSSs). Representative stress vs. strain plots for selected composites are shown in Figure II.2.21.2(a), and the average ILSS for each composite is summarized in the bar graph in Figure II.2.21.2(b). Overall, the highest performing composite was 1.5 wt.% BaTiO_3 , with an ILSS of 81.9 MPa. This equates to an improvement of 19.6% compared to the as-received basalt fiber composite, thus meeting one of the milestones for this project.

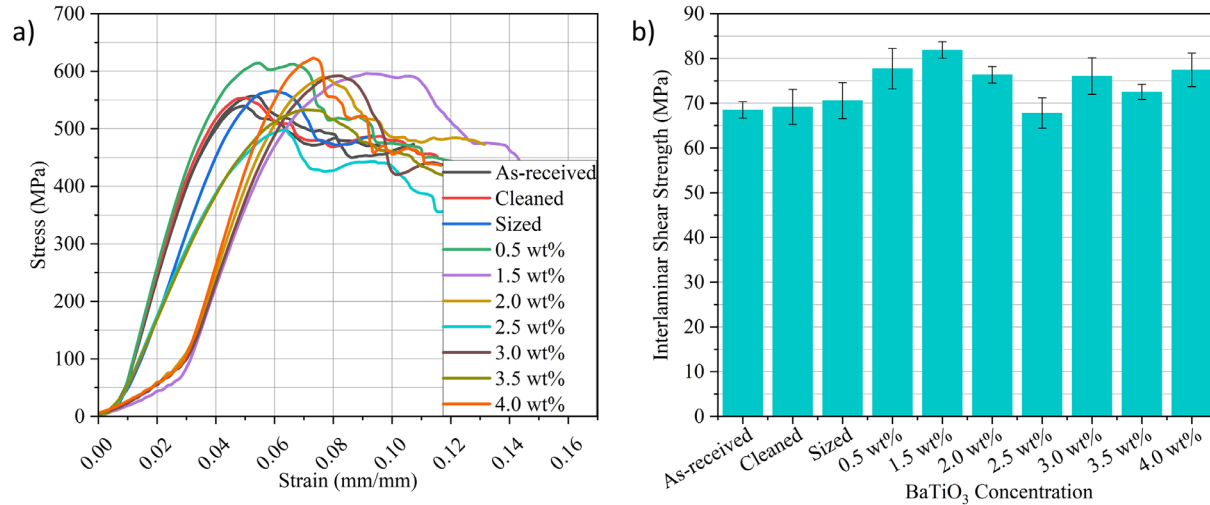


Figure II.2.21.2. (a) Representative stress versus strain plots for selected composites. (b) The average apparent interlaminar shear strength for each composite [2]. Source: ORNL

The BaTiO₃ microparticle-coated basalt fibers were also fabricated into thin unidirectional composite beams for passive sensing characterization. Similar to the short-beam shear strength test specimens, the thin beams were fabricated using approximately 60 vol.% fiber loading in an epoxy matrix with a beam thickness of ~0.65 mm. For this initial proof-of-concept, the composite architecture consisted of a layer of 4 wt.% BaTiO₃-coated basalt fibers with two layers of bare basalt fibers on top, as shown in Figure II.2.21.3(a). These composites were electroded with silver epoxy paint in a configuration shown in Figure II.2.21.3(b). The electrodes were connected to a digital multimeter to measure the through-thickness voltage generation of the composites during vibrations. Prior to electromechanical testing, the samples were poled using a 10 kV voltage held on the electroded faces of the samples for four hours at RT. This process was necessary to orient the electric dipoles in the BaTiO₃ microparticles. Two different testing setups were built to investigate both the sensor sensitivity and power-harvesting capabilities of the composite. Figure II.2.21.3(c) shows the sensing setup consisting of securely anchoring one end of the composite and attaching the free end of the composite to a permanent magnet shaker that could deflect the beam and induce a controlled strain. For energy-harvesting characterization, the beam was attached to the same permanent magnet shaker, and the other end was left unconstrained, thus creating a cantilever beam that could vibrate from input accelerations generated by the permanent magnet shaker, as shown in Figure II.2.21.3(d).

The initial results from the sensing setup are shown in Figure II.2.21.4(a). The plot shows the voltage generated from the composite when subjected to various 5 Hz sinusoidal input accelerations from the shaker. It clearly indicates that a measurable voltage is generated and has a sensitivity of 0.18 mV/g. The testing went one step further and quantified the power generated from the composite using the energy-harvesting test setup. These results in Figure II.2.21.4(b) show a peak power output of 1.5 nW/cc from a 30 Hz sinusoidal excitation waveform at 0.7 g input acceleration. Therefore, these results achieved the milestone of demonstrating an electromechanical property of the composite. Further optimization with varying degrees of BaTiO₃ loading and composite architectures were also performed.

After validating their superior ILSS, passive sensing, and energy-harvesting characteristics, the project team investigated the BaTiO₃ microparticle-enabled composites' damping and tensile properties. Here, the 0.0 wt.% and 0.5 wt.% BaTiO₃ specimens were selected since the 0.5 wt.% specimen showed a 10% improvement in ILSS over the 0.0 wt.% specimens. For the damping characterization, composite specimens were placed in a dynamic mechanical analyzer in a three-point bend configuration and subjected to a 10 Hz sinusoidal wave with a 0.01% strain amplitude from a temperature of -100°C to 225°C at a ramp rate of 2°C per minute. This test measures the beam's storage and loss moduli that are used to calculate the loss tangent, which represents

the damping property of the composite. The loss tangent as a function of temperature can be seen in Figure II.2.21.5(a) for the 0.0 wt.% and 0.5 wt.% BaTiO₃ specimens. It was observed that the loss tangents for the samples at RT were 0.03259 and 0.03975 for the 0.0 wt.% and 0.5 wt.% samples, respectively. These results equate to a loss tangent improvement of 22%, which met the milestone of increasing the damping by at least 20%. Instead of tensile testing unidirectional composites, which simply tests the fiber strength when tested in the axial direction of the composite, the fibers were chopped to roughly 5 mm in length and then mixed into the epoxy matrix at a 1.0 wt.% fiber loading to create dog bone tensile testing specimens. The representative strain versus stress graphs from these composites can be seen in Figure II.2.21.5(b). The ultimate tensile strengths were 55.8 MPa and 66.7 MPa for the 0.0 wt.% and 0.5 wt.% BaTiO₃ samples, respectively. This represents a 19.5% improvement in tensile strength and meets the milestone for tensile strength improvement target.

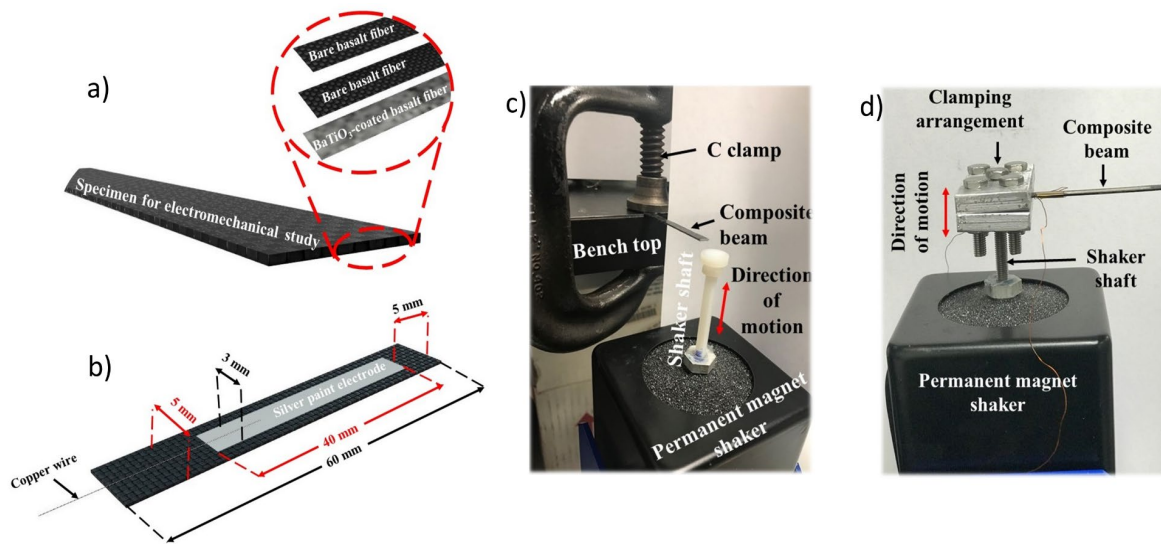


Figure II.2.21.3. (a) Schematic of the composite layering. (b) Schematic of the composite electroding scheme. Pictures of the (c) sensing setup configuration and (d) energy-harvesting setup [2]. Source: ORNL.

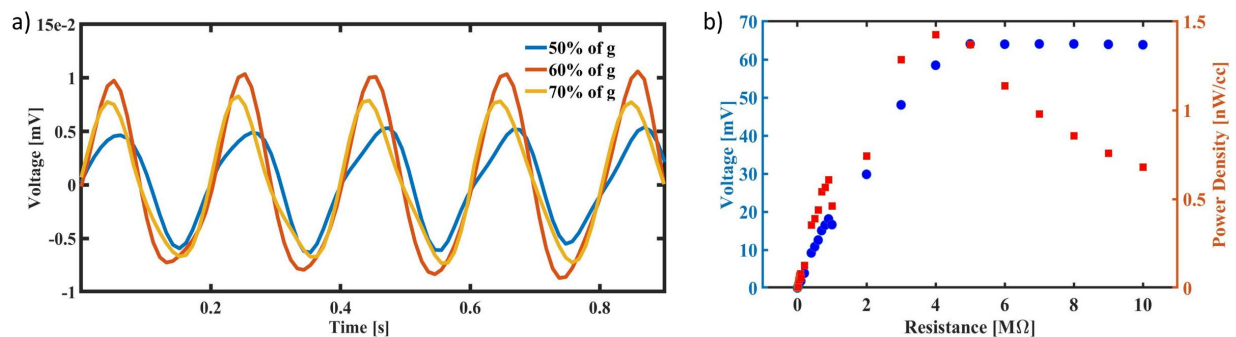


Figure II.2.21.4. (a) The voltage generated from the composite in the sensing setup under three different input accelerations. (b) The voltage and power generated from the composite in the energy-harvesting setup from 0.7 g of acceleration [2]. Source: ORNL.

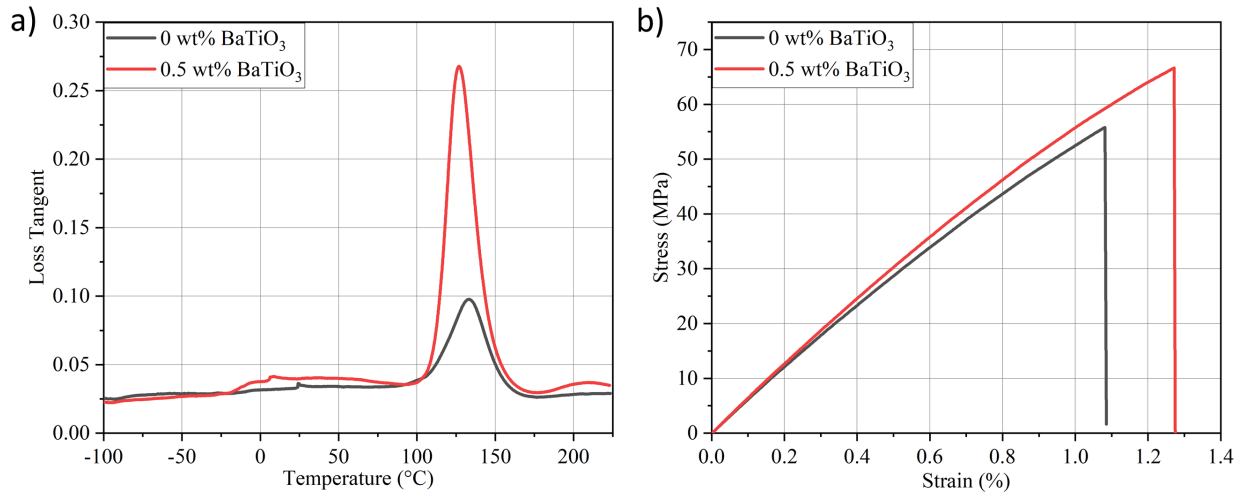


Figure II.2.21.5. (a) The loss tangent from the dynamic mechanical analyzer testing of the 0.0 wt.% and 0.5 wt.% BaTiO₃ samples as a function of temperature. (b) Representative stress versus strain curves for the 0.0 wt.% and 0.5 wt.% BaTiO₃ chopped fiber samples. Source: ORNL.

Conclusions

This work demonstrated a scalable, low-cost dip-coating method for depositing BaTiO₃ microparticles on basalt fibers to produce multifunctional fiber-reinforced composites. This continuous feed-through deposition procedure can produce a large volume of multifunctional fibers. Homogeneous deposition of microparticles on the fiber surfaces was confirmed through SEM imaging. The mechanical performance enhancement of the BaTiO₃-enhanced composites was realized through ILSS tests. While most composites showed an increase in the apparent ILSS, 1.5 wt.% specimens exhibited a ~20% improvement in apparent ILSS compared to the pristine composites. There was also a ~22% increase in the damping properties for the 0.5 wt.% BaTiO₃ coated fiber composite as compared to the pristine fiber composite. Furthermore, a ~22% increase in tensile strength was exhibited by the composites reinforced with 1.0 wt.% BaTiO₃-coated chopped basalt fibers. To characterize the electromechanical properties of the BaTiO₃-enhanced composites, the project team carried out strain-controlled vibration tests. It was found that composites containing 4 wt.% BaTiO₃-coated fibers demonstrated passive self-sensing (sensitivity = 0.18 mV/g) and energy-harvesting (maximum power output = 1.5 nW/cc) abilities. Overall, this research was able to produce BaTiO₃-coated basalt fibers using a continuous feed-through dip-coating method to integrate multifunctionality in the composites while simultaneously increasing the mechanical performance. Future studies will establish the optimal BaTiO₃ concentration through extensive computational modeling and experiments to produce a composite with the best electromechanical properties with enhanced mechanical performances.

Key Publications

1. Bowland, C. C., S. Gupta, S. M. Rankin, and A. K. Naskar, 2021, "Passive sensing of a microparticle modified hybrid, fiber-reinforced composite," *Nondestructive Characterization and Monitoring of Advanced Materials, Aerospace, Civil Infrastructure, and Transportation XV*, Vol. 11592, Art. 115920B.
2. Gupta, S., A. K. Naskar, and C. C. Bowland, 2022, "An engineered multifunctional composites for passive sensing, energy-harvesting, and *in-situ* damage identification with enhanced mechanical performance," manuscript in review.

References

1. Joost, W. J., 2012, “Reducing vehicle weight and improving U.S. energy efficiency using integrated computational materials engineering,” *JOM*, Vol. 64, pp. 1032–1038.
2. Bowland, C. C., S. Gupta, S. M. Rankin, and A. K. Naskar, 2021, “Passive sensing of a microparticle modified hybrid, fiber-reinforced composite,” *Nondestructive Characterization and Monitoring of Advanced Materials, Aerospace, Civil Infrastructure, and Transportation XV*, Vol. 11592, Art. 115920B.

Acknowledgments

The authors would like to acknowledge Dr. Sumit Gupta, who is working as a postdoctoral research associate under my supervision. I would also like to thank Dr. Amit K. Naskar for his supervision and assistance with this research.

II.2.22 Efficient Synthesis of Kevlar and Other Fibers from Polyethylene Terephthalate (PET) Waste (Pacific Northwest National Laboratory)

Lelia Cosimbescu, Principal Investigator

Pacific Northwest National Laboratory
908 Battelle Blvd.
Richland, WA 99354
E-mail: lelia.cosimbescu@pnnl.gov

H. Felix Wu, DOE Technology Manager

U.S. Department of Energy
E-mail: felix.wu@ee.doe.gov

Start Date: July 1, 2020 End Date: September 30, 2023
Project Funding (FY 2021): \$270,000 DOE share: \$270,000 Non-DOE share: \$0

Project Introduction

Lightweighting of automotive components has become of paramount importance, not only to reduce the carbon footprint of final automotive products but also to conserve valuable and depleting resources. Existing approaches of substitution and structure redesign with traditional materials have reached their limits, but an urgent need exists to explore non-metallic, but equally functional, sets of materials to achieve more aggressive fuel savings targets. Lightweight fiber-reinforced plastics have become the material of choice due to their flexibility, functionality, and formability into intricate hybrid and multipart designs. CF is the reinforcement of choice for many applications in the aerospace industry, as CF composites have the most weight-reduction potential. However, CF composites have an extremely brittle nature, so CF cannot be considered for applications in which impact performance is a principal design requirement. Aramid fiber, such as Kevlar, fills this niche, providing superior impact performance while preserving the high-strength-to-weight ratio.

Carbon and aramid fiber composites have yet to be fully exploited in the automotive industry because of the high cost associated with the manufacture of such high-performance fibers. Presently, Kevlar fibers cost \$12/lb, which is comparable to the cost of CF. In the context of automotive parts, aramid fibers can improve the safety, performance, and durability of automotive components for a wide variety of vehicles, from passenger cars to light-duty trucks. Components of specific interest include those which demand excellent fatigue and impact performance. For example, belts, tires, and hoses that are subjected to continuous stress cycling require good fatigue properties; fore posts, hoods, and underbody components that are subject to rock impact require excellent impact properties. Replacement of metal components or GFs offers additional lightweighting opportunities, owing to the low density of aramid polymers (1.4 g/cm³ for aramid versus at least 2.5 g/cm³ for glass).

We propose to achieve the formation of Kevlar-like materials from waste PET, an approach that has not been reported in the published literature. This methodology not only contributes to enabling an inexpensive starting material for the fiber production but also provides a means of addressing our plastic waste problem and a novel, exciting pathway to PET chemical upcycling.

Objectives

The objective of this project is to demonstrate waste PET as an inexpensive alternative source feedstock for Kevlar and other aramid fibers. The polymer will then be formed into fibers by processes analogous to those used in the production of high-performance Kevlar fiber. PET will be sourced from the current waste stream at minimal cost. Using a waste source is projected to greatly reduce the overall cost of producing high-performance aramid fibers, which could dramatically reduce the current cost barrier to implementing aramid fiber composites in automotive applications. Specifically, we aim to form aramid fibers with a minimum

molecular weight of 10 kDa in the first year of performance and 20 kDa by the end of the project. The aramid fibers will be tested against Kevlar 29, a commercial product, with respect to tensile strength, modulus, and elongation. By the end of Year 2, we aim to produce fibers that have a tensile strength of 1,500 MPa and a modulus of 40 GPa, and by the end of Year 3, we aim to produce fibers that have a tensile strength of 2,900 MPa and a modulus of 80 GPa.

The main objective for FY 2021 was to explore synthetic pathways and demonstrate feasible methodologies to generate high molecular weight aramid polymers from waste PET.

Approach

Before fibers and composites could be produced, we needed to identify suitable conditions to prepare aramid polymers made from PET waste, terephthalic acid derived from PET waste, or terephthaloyl chloride generated from terephthalic acid, a more reactive starting material. Our original aramid synthetic strategy involved the direct concerted depolymerization/repolymerization reaction, as observed in Figure II.2.22.1, via C-O bond cleavage and C-N bond formation. This methodology, if successful, was projected to provide a considerable advantage in the cost of aramid polymers, as the starting material is inexpensive PET waste.

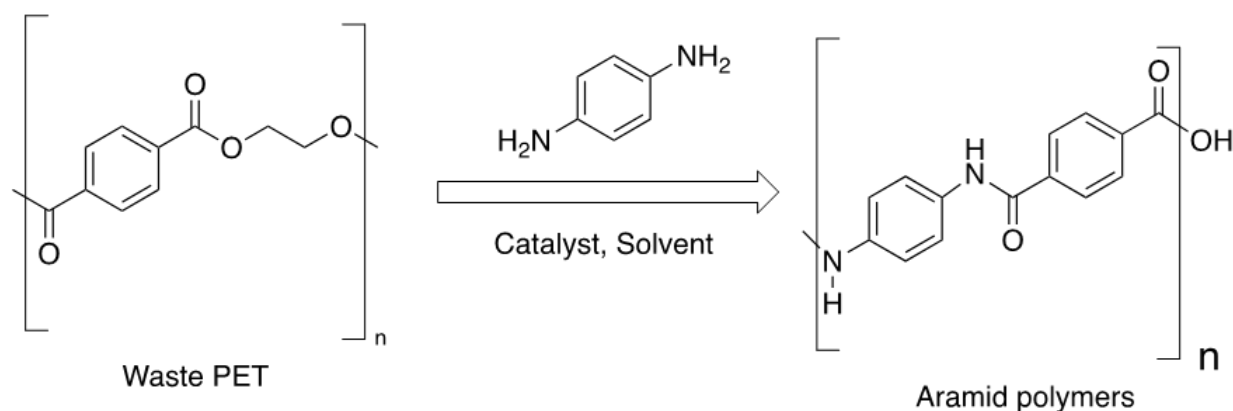


Figure II.2.22.1. Direct depolymerization of PET waste and concerted repolymerization. Source: PNNL.

The main challenge is PET insolubility in all non-reactive, relatively inexpensive organic solvents such as dimethylmethanamide, dimethylsulfoxide, hexamethylphosphoramide, N-Methylpyrrolidone (NMP), and dichlorobenzene, therefore making the solution chemistry difficult. Moreover, the reaction is unlikely to go to completion, and separation of insoluble starting materials (unreacted PET) from products (aramid) would be very challenging. Furthermore, this approach is especially unfeasible for mixed waste because of the presence of impurities that might deactivate the catalyst, thereby hindering the reaction dynamics and interfere with the separation process. Given these considerations, other methodologies were explored to achieve an efficient synthesis of aramid polymers. Those strategies are briefly discussed in the results section.

Results

Because of the challenges of direct depolymerization of PET, we decided to depolymerize PET under basic conditions to generate terephthalic acid (TPA) in high yield, even from mixed waste PET (published results). We explored melt polymerization of TPA with various diamines. These amines were employed as model compounds to probe the chemistry, as they are much more nucleophilic than aromatic amines and more likely to react; if the reaction is unsuccessful with such moieties, it is very unlikely to be successful with aromatic diamines typically found in Kevlar-like structures. However, there are challenges associated with this approach as well, as piperazine and phenylene diamines (para and meta derivatives) sublime around 100°C, while TPA is a very high-melting solid (at 300°C) that starts slowly subliming around 180°C. First attempts were conducted in a round bottom flask, which allowed researchers to visually observe the reaction mixture, but the sublimation of the amines essentially escaped the mixture. Therefore, we transitioned to a closed Swagelok-

type reactor. Given that the solid or melt chemistry proved challenging (not unexpectedly, considering that TPA is a deactivated diacid, among other challenges), we decided to investigate Higashi–Ogata methodology for direct polycondensation, shown in Figure II.2.22.2.

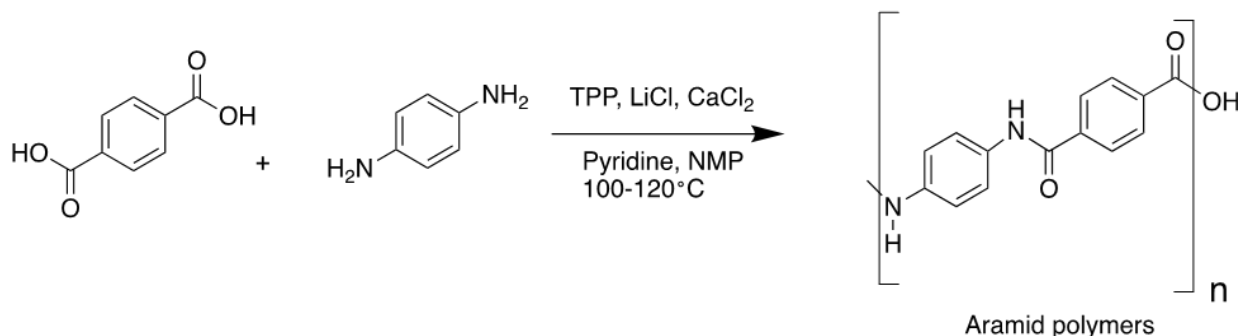


Figure II.2.22.2. Direct polycondensation of TPA and aromatic amines. Source: PNNL

This method produced low-molecular-weight oligomers, as identified spectroscopically. It became apparent that to generate relatively high molecular weight polymers, we had to apply the commercial/traditional approach of aramid polymer synthesis, via terephthaloyl dichloride. Terephthaloyl dichloride was generated in quantitative yield from the reaction of TPA with thionyl chloride, as can be seen in Figure II.2.22.3. Several compounds were prepared via this method to ascertain the solubility of the resulting polymers, as solubility is a real challenge both in characterizing the polymers and in limiting the solvents that can be subsequently used for fiber spinning.

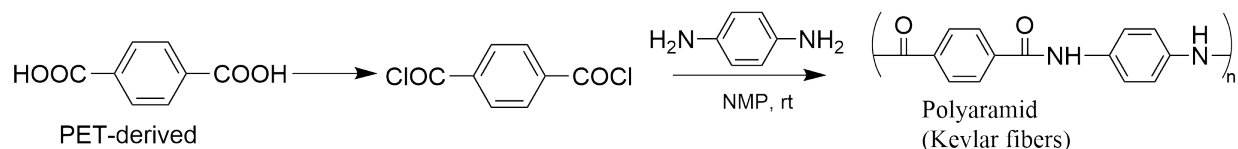


Figure II.2.22.3. Representative example of aramid polymer synthesis from TPA (Kevlar is illustrated herein). Source: PNNL.

Even with a promising synthetic strategy in place, reaction conditions had to be optimized to achieve a high-degree of polymerization, and thus many conditions with several diamines were explored, as shown in Table II.2.22.1. Structures of the various amines employed in these reactions are shown in Figure II.2.22.4.

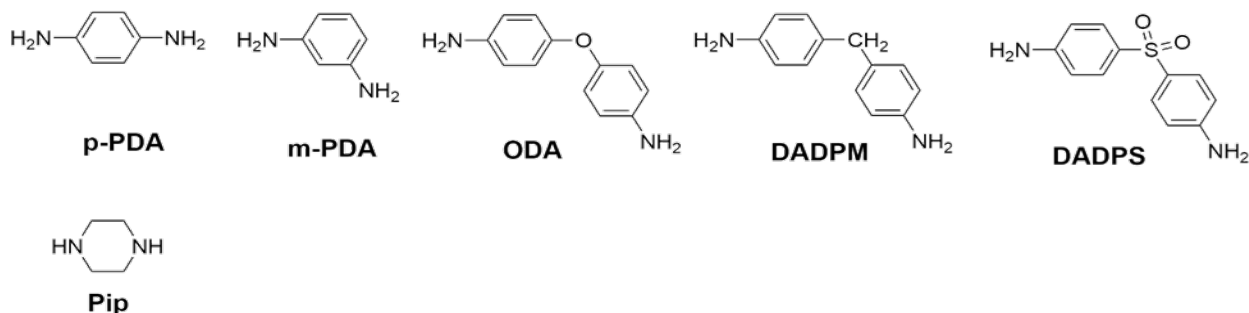


Figure II.2.22.4. Structures of various amines employed in the synthesis of polymers P1–P15. Source: PNNL.

Table II.2.22.1 Amines and Conditions Employed in the Preparation of Aramid Polymers

Polymer	Method	Amine (Molar Ratio)	Additives Conc. (g/ml)	°C	Observations
---------	--------	------------------------	---------------------------	----	--------------

P1	TPA; Higashi	p-PDA: 1	none	100	Solid precipitated after 2 hours
P2	TPA; Higashi	p-PDA: 1	CaCl ₂ (6%)	100	Scale-up of 25; solid precipitated after 1 hour
P3	TPA Chloride	p-PDA: 1	LiCl (2%)	rt	Solid precipitated in 5 minutes
P4	TPA Chloride	p-PDA: 1	LiCl (2%)	rt	Cloudiness, no precipitation
P5	TPA Chloride	Pip: 1	none	rt	Cloudiness, no precipitation
P6	TPA Chloride	m-PDA: 1	none	rt	No precipitation
P7	TPA Chloride	Pip: 1	none	rt	Repeat of P5; no precipitation
P8	TPA Chloride	m-PDA: 1	none	rt	More concentrated than P6; no precipitation
P9	TPA Chloride	OPDA: 1	none	rt	Viscous solution; no precipitation
P10	TPA Chloride	NapDA:1	none	rt	Precipitation upon addition
P11	TPA Chloride	p-PDA:1	none	0; rt	Viscous solution; no precipitation
P12	TPA Chloride	m-PDA:1	CaCl ₂ (5%)	0; rt	Viscous solution; no precipitation
P13	TPA Chloride	p-PD:OPDA; 0.75:0.25	CaCl ₂ (5%)	0; rt	Slightly viscous solution; no precipitation
P14	TPA Chloride	p-PD:OPDA; 0.9:0.1	CaCl ₂ (5%)	0; rt	Highly viscous solution; no precipitation
P15	TPA Chloride	DADPM	CaCl ₂ (5%)	0; rt	Slightly viscous solution; no precipitation

PDA (o - ortho and p - para) phenylene diamine, OPDA - 4,4'-diaminodiphenyl ether, Pip - piperazine, DADPM - 4,4'-diaminodiphenylmethane, NapDA - 1,5-diaminonaphthalene

Herein, we discuss in some depth the Kevlar polymers prepared from para-phenylenediamine (p-PDA) and TPA. All polymers were analyzed using NMR to evaluate differences among various batches and reaction conditions. Unfortunately, conversion or number of repeating units is impossible to assess from the aromatic region where all peaks overlap. However, the broadness of the peaks and absent or undetectable terminal units are empirical indicators of degree of polymerization and hence molecular weight. Figure II.2.22.5 illustrates polymers **P1–P4** and **P11**. Compounds **P1** and **P2** were prepared via the Higashi method, and they appear to have a lower molecular weight. That is evident by the more defined splitting of peaks in the aromatic region. Furthermore, compound **P1** appears to be an oligomeric species, where terminal terephthalic unit appears at ~8.2 ppm and the protonated terminal amine at ~7.2 ppm. The internal PDA groups appear at ~7.7 ppm. Integration appears to suggest that there are four repeating units (four TPAs and four PDAs), based on the rough integration of the overlapped peaks. Analogs **P3**, **P4**, and **P11** appear to have similar spectra, with **P3** displaying the broadest peaks, and these are expected to have similar molecular weights.

The isolated solids/polymers were analyzed via TGA and DSC to evaluate their decomposition onset, identify relative differences among identical structures prepared via various conditions, and determine their melting points or glass transition temperatures (T_g). The maximum temperature the sample was subjected to for TGA analysis was 700°C. The TGA data generally shows a high thermal stability, as expected from aramid polymers, with high percentage char values, indicative of a high thermal stability up to 700°C. Most of the materials did not reach a char state per the definition of char and still appeared as the original solids, slightly colored. In contrast, the same composition polymers prepared via TPA chloride, **P3**, **P4**, and **P11**, are much more stable with $T_{10}\%$ values well over 500°C. **P1** and **P2** are spectroscopically similar, and therefore we expected similar thermal behaviors. Surprisingly, **P1** appears very different from the rest of the analogs, while **P3**, **P4**, and **P11** are very similar, displaying high thermal stabilities and similar char yields. The team is still

investigating the potential reason for such discrepant thermal behavior for the oligomeric polymer **P1**. The TGA plots are illustrated in Figure II.2.22.6.

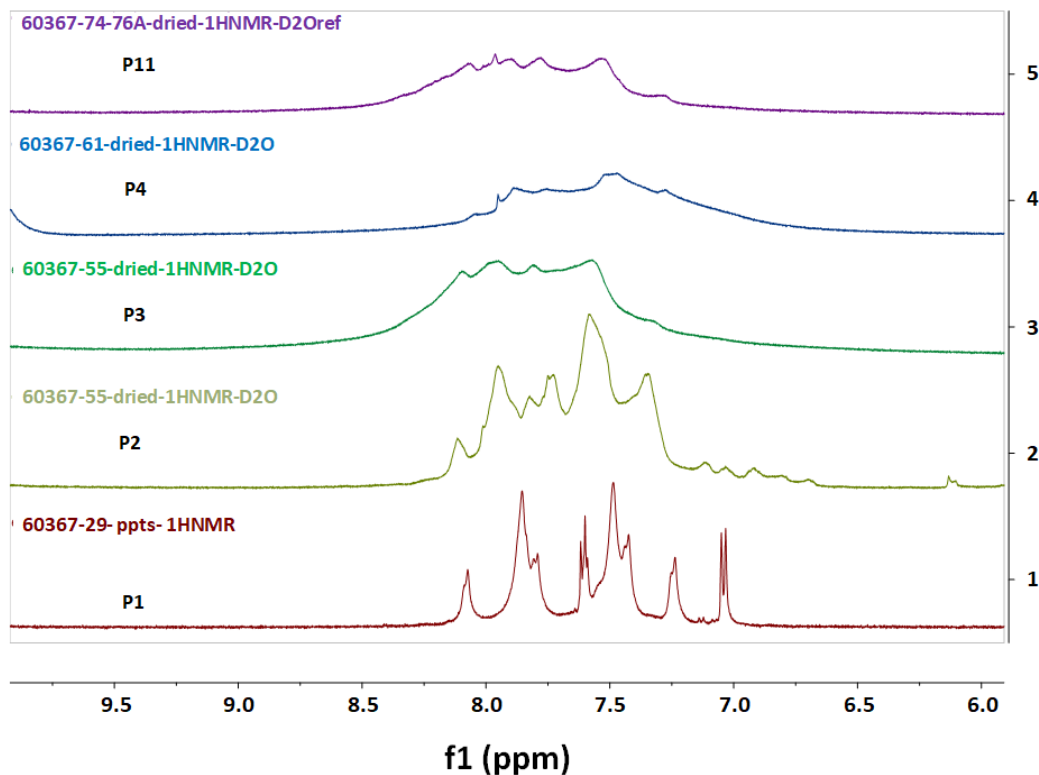


Figure II.2.22.5. Stacked ¹H NMRs of polymers P1–P4 and P11. Source: PNNL.

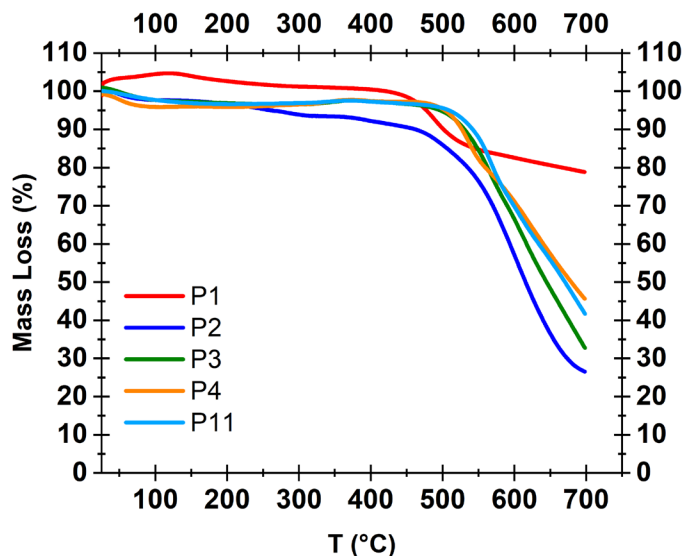


Figure II.2.22.6. TGA plots of polymers P1–P4 and P11. Source: PNNL.

Conclusions

automotive composites, although the original strategy was modified. Reaction conditions were optimized to enable high molecular weight polymers. The prepared polymers have a high thermal stability, as expected from

aramids. The remaining challenge is to evaluate the molecular weight of the polymers via gel permeation chromatography (GPC) to determine number of repeating units in the polymer chain. This is a daunting task, as the polymer insolubility hinders normal GPC operations; a new solvent system was devised, composed of N-methylpyrrolidone and a proprietary additive, to enable even the slight solubility of most polymers in Table II.2.22.1 in something other than concentrated sulfuric acid. The medium in which aramid polymers are dissolved for processing and wet spinning is typically concentrated sulfuric acid, but this is not a suitable solvent for GPC analysis.

Key Publications

1. Cosimbescu, L., D. R. Merkel, J. Darsell, and G. Petrossian, 2021, “Simple but tricky: Investigations of terephthalic acid purity obtained from mixed PET waste,” *Ind. Eng. Chem. Res.*, Vol. 60, No. 35, pp. 12792–12797.
2. Cosimbescu, L., D. Malhotra, M. R. Pallaka, and M. S. Swita, 2022, “Kevlar-like aramid polymers from mixed PET waste,” manuscript in preparation.

Acknowledgments

The authors would like to offer their thanks to the following contributors who made this work possible: D. Malhotra, D. Merkel, and M. R. Pallaka of PNNL.

II.2.23 Bio-Based, Inherently Recyclable Epoxy Resins to Enable Facile Carbon-Fiber-Reinforced Composite Recycling (National Renewable Energy Laboratory)

Nicholas A. Rorrer, Co-Principal Investigator

National Renewable Energy Laboratory
15013 Denver West Parkway
Golden, CO 80401
E-mail: nicholas.orrer@nrel.gov

Gregg T. Beckham, Co-Principal Investigator

National Renewable Energy Laboratory
15013 Denver West Parkway
Golden, CO 80401
E-mail: gregg.beckham@nrel.gov

H. Felix Wu, DOE Technology Manager

U.S. Department of Energy
E-mail: felix.wu@ee.doe.gov

Start Date: October 1, 2020

End Date: September 30, 2023

Project Funding (FY 2021): \$500,000

DOE share: \$500,000

Non-DOE share: \$0

Project Introduction

The use of CFRCs in vehicles is promising, as CFRCs exhibit a superior strength-to-weight ratio and stiffness-to-weight ratio relative to that of steel, at 60% to 70% of steel's weight, thus increasing vehicle fuel efficiency. Despite these promising features, CFRCs have not been widely implemented in vehicles because of the high cost of CF and challenges with repairing the composites when they are damaged. To this end, this project is developing bio-based, inherently recyclable, high-performance resins for CFRCs using covalent adaptable networks (CANs, otherwise known as vitrimers). These covalent adaptable network-based CFRCs (CAN-CFRCs) will enable facile CF recycling and improve CFRC mechanical properties and performance.

Objectives

Overall, the proposed project aims to increase the use of reinforced composites in vehicles by enabling the recovery of CF via the use of CAN chemistry. We further aim to demonstrate that:

- The proposed chemistry can reuse CF in multiple material lives without detriment to the performance of the CFRCs, as measured by their thermomechanical properties.
- The proposed chemistry can reuse CF in multiple material lives without detriment to the performance of the CFRCs, as measured by their thermomechanical properties.
- The use of bioderivable building blocks can result in the requisite performance across multiple lives.
- The use of bioderived building blocks can result in a cost-competitive resin while simultaneously lowering the associated supply chain energy and GHG emissions.
- The reuse of CF across multiple lives can reduce the impacts associated with CF manufacture.

To accomplish these goals, the project work is divided into four tasks:

- Synthesis of CAN-CFRC.
- Sizing of fiber reinforcements for enhanced performance, reparability, and durability.

- Validation and scale-up for manufacturing automobile parts.
- TEA, life cycle assessment, and supply chain modeling of the materials relative to incumbent composite materials.

Approach

To accomplish our objectives, the first year of this project was aimed at initially demonstrating that our resin could be used alongside CFs to produce CFRCs with thermomechanical properties that are comparable to the industry standard epoxy–amine chemistries and could be depolymerized without damaging the fiber. Post-depolymerization, the fibers were reused alongside virgin resin to demonstrate that properties can be obtained across multiple lives. This approach is summarized in Figure II.2.23.1 and was complemented by TEA and supply chain analysis focused on calculating the cost, supply chain energy, and GHG emissions of the resin and composites.

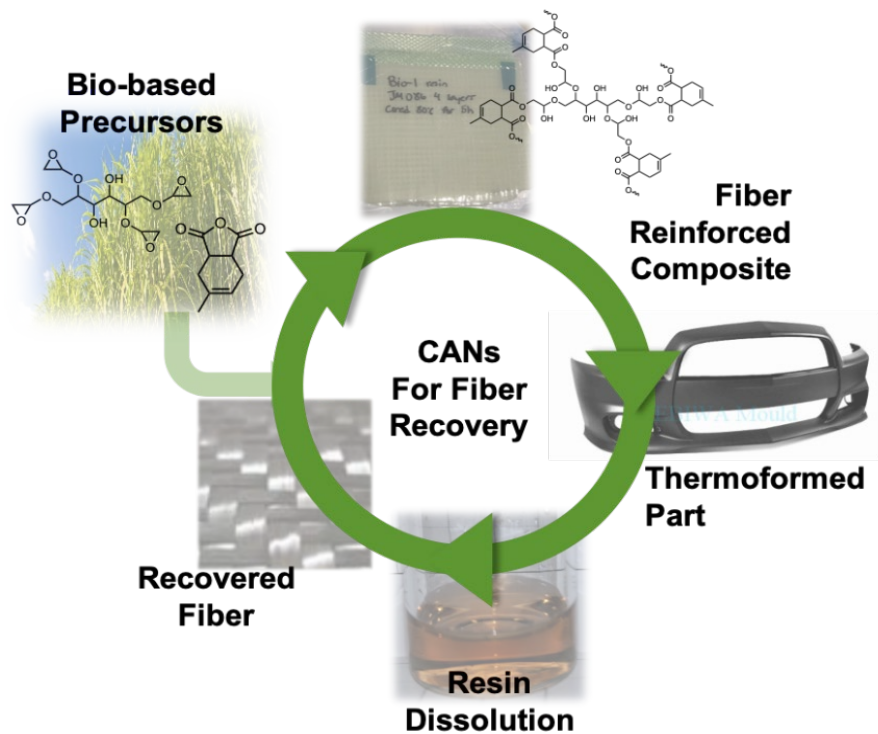


Figure II.2.23.1. Project overview. Source: NREL.

To demonstrate the reuse of the CF across multiple lives, it was necessary to develop a recyclable resin, unlike today's standard epoxy–amine resins. To these ends, we implemented a polyester-based covalently adaptable network (PE-CAN), which comprises both epoxy components and anhydride components. Akin to today's standard resins, the PE-CAN possesses epoxies that enable for a quick reactivity; however, the PE-CAN uses an anhydride hardener instead of an amine hardener, so the resultant chemical bonds are esters instead of amides. Esters can be recycled by hydrolysis or alcoholysis. The epoxy and hardener components are bio-based. Figure II.2.23.2 provides chemical structures of the materials.

As outlined below and demonstrated in our project milestones, the first year of this project was successful and demonstrated that the PE-CAN resin can enable the use of CF across multiple lives with little degradation to material properties. With the results from FY 2021, we will continue to build upon this project, with activities including (but not limited to) the use of different reinforcements to augment material properties, the TEA and supply chain analysis of subsequent material lives, the thermoforming of the material, and the demonstration of material repair.

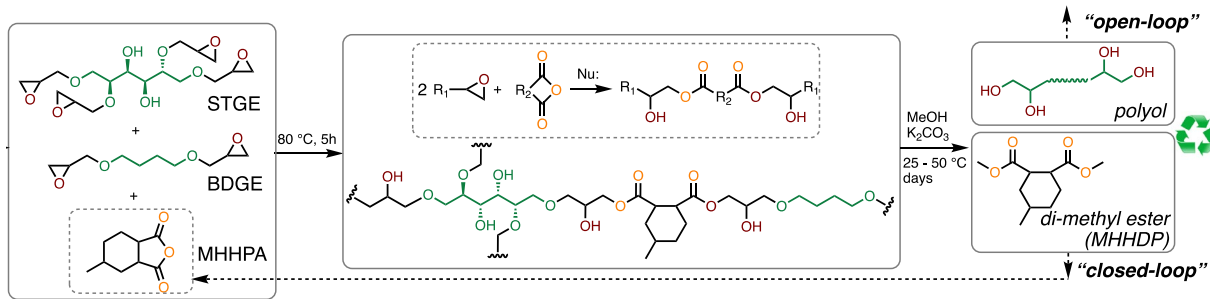


Figure II.2.23.2. Design developed in a previous FY involving a novel hybrid manufacturing process using overmolding of polymer AM onto metal AM. Source: NREL

Results

All results that follow are covered by U.S. Provisional Patent Application No. 63/087,547. Additionally, this project has experienced minimal delays due to the COVID-19 pandemic, aside from limited laboratory time and space. The results summarized below were reflected in our peer review presentation and in quarterly milestones culminating in achieving a go/no-go milestone at the end of FY 2021.

Initially, it was important to demonstrate that the PE-CAN (also called bio-resin) could be formulated to possess properties that were on par with industrial resins. We procured a Hexion epoxy-amine resin (also called petro-resin) and compared it to our in-house resins. Initially, CFRCs were prepared by infusing double-ply woven carbon fiber via vacuum-assisted resin transfer molding (VARTM) and cured at 80 °C for six hours. Post-curing, the CFRCs were analyzed via dynamic mechanical analysis (DMA) to ascertain their thermomechanical properties and by TGA to determine resin content. For both CFRCs, the fiber loading was ~50 wt.%. DMA revealed that both resins possessed near-identical storage moduli on the order of 30 GPa and comparable glass transition temperatures of 80 +/- 5 °C, as measured by the maximum in the tanδ.

Figure II.2.23.3(a)-(b) provides the storage modulus and tanδ of the petro-resin and bio-resin CFRCs.

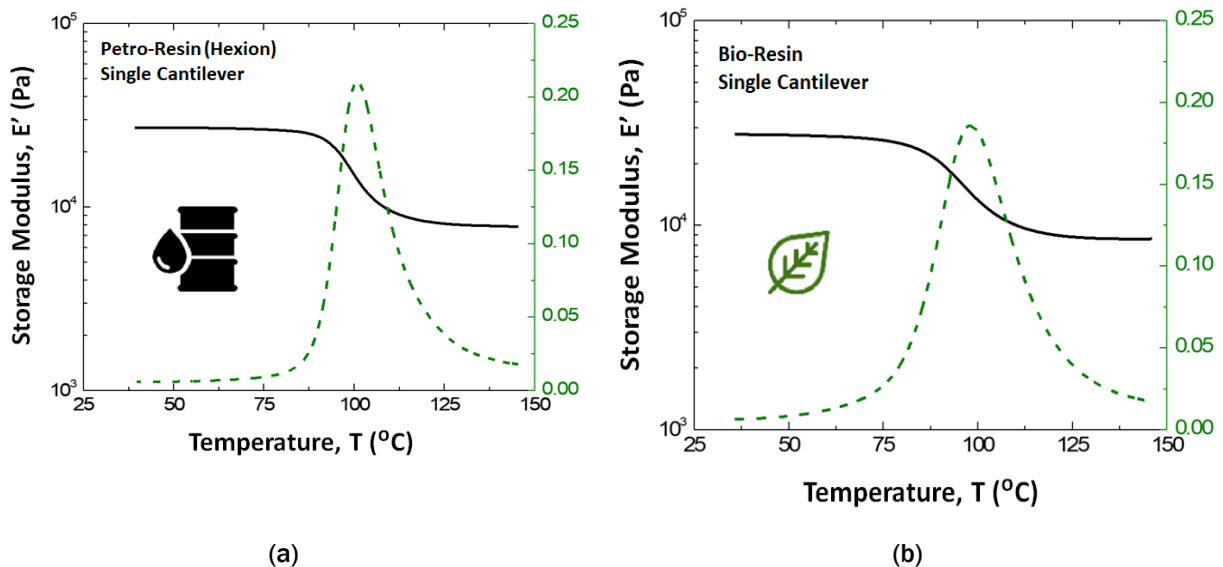


Figure II.2.23.3. DMA of (a) an industry-relevant epoxy-amine CFRC and (b) the bio-derivable PE-CAN. Source: NREL.

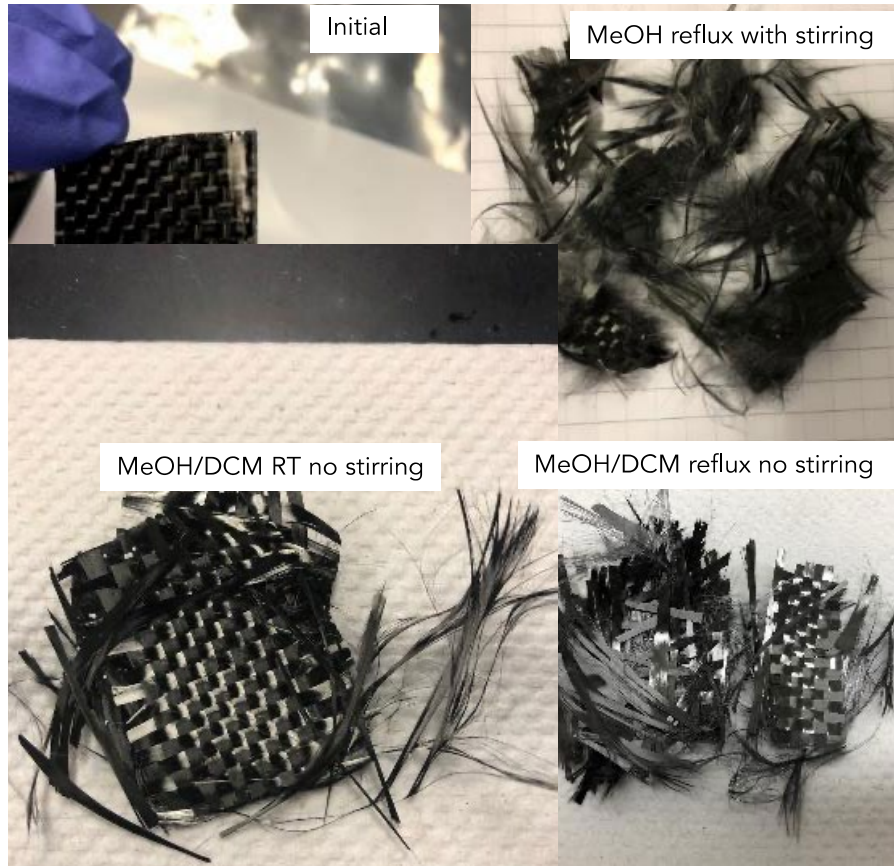
Following formation of the CFRCs, we endeavored to develop a recycling strategy that would depolymerize the resin while leaving the fibers intact. Initially, we demonstrated that refluxing in methanol with either acidic or basic catalysts would result in a removal of the resin; however, the vigorous reflux and stirring resulted in a loss of fiber alignment and destruction of fiber quality. To maintain fiber alignment, we investigated lower temperature processes, which resulted in an ideal depolymerization system of DCM and MeOH as a solvent with K_2CO_3 as a catalyst [1]. With this depolymerization system, we were able to depolymerize the CFRCs at RT with no stirring, which maintained fiber alignment, as shown in Figure II.2.23.4(a). TGA revealed that nearly all the resin was removed post-depolymerization, leaving the fiber intact, as shown by the data in Figure II.2.23.4(b). At RT, the depolymerization took up to a week, depending on composite thickness. Future work could investigate further optimization of the depolymerization conditions (e.g., slight use of temperature, scaling depolymerization, alternative solvents), However, as fiber orientation was maintained, this depolymerization allows for the fiber to be reclaimed and used across multiple lives.

Following depolymerization, the CF was washed to remove residual resin and catalyst, then dried. After workup, the CF was re-infused with fresh resin and cured using the previous conditions. The depolymerization, wash, and repolymerization process was repeated once more for a total of three material generations, as shown in Figure II.2.23.5(a)-(c) for the DMA of the CFRCs across the multiple generations. Across all three generations, the storage moduli are within measurement error and is 30 ± 3 GPa, and the glass transition temperatures, as measured by the maximum of $\tan \delta$, were $80 \pm 6^\circ C$. Interestingly, the materials may exhibit enhanced performance on subsequent lives, but further investigation is needed into the mechanisms that may enable enhanced performance (e.g., residual resin acting as a fiber sizing and aiding compatibility). Supplemental studies were also conducted with virgin fibers and the depolymerization mixture to ensure that the depolymerization solution does not affect CFRC properties. Demonstrating that PE-CAN could result in CFRCs with consistent properties (<20% variation) across multiple lives was our FY 2021 go/no-go milestone and was successfully met, as demonstrated here.

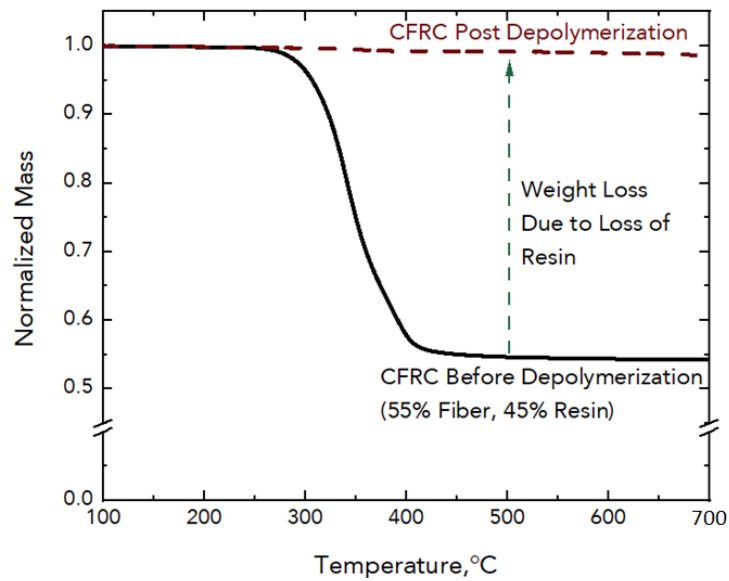
In addition to the experimental results, this project was supported by TEA and supply chain analysis to determine the minimum selling price of the PE-CAN resin, as well as the supply chain energy and GHG emissions associated with the production of the PE-CAN resin relative to petrochemical manufacture. TEA was conducted via the development and use of Aspen Plus® process models, while supply chain analysis was conducted using the materials flow through industry (MFI) tool. Results are summarized in Table II.2.23.1. It is important to note that the process developed aimed at determining the individual monomer and polymer contributions as the sum of their input in a consistent methodology and framework. Additionally, the results presented here do not account for the carbon that is sequestered during biomass cultivation. The PE-CAN resin is within 10% the cost of the petroleum resin while possessing a >33% lower supply chain energy and >18% GHG emissions. These results indicate that even resin production can result in decarbonization relative to current epoxy-amine manufacture while maintaining a competitive cost. Further TEA and MFI analysis will examine the potential cost reductions and decarbonization that is afforded to subsequent material generations.

Table II.2.23.1 Technoeconomic and Supply Chain Analysis Results for the PE-CAN Resin

Resin Components	Supply Chain Energy, MJ/kg	GHG Emissions, kg CO ₂ -e/kg	Minimum Selling Price, \$/kg
Petroleum-Based Resin – Overall	129	5.7	2.03
Biologically Derivable Resin (PE-CAN) – Overall	86	4.7	2.17
Carbon Fiber	467 [2]	29 [2]	21.50 (Variable)



(a)



(b)

Figure II.2.23.4. The depolymerization, wash, and repolymerization process was repeated for a total of three material generations. (a) The fiber alignment in various depolymerization techniques. (b) TGA results, demonstrating the removal of resin. Source: NREL.

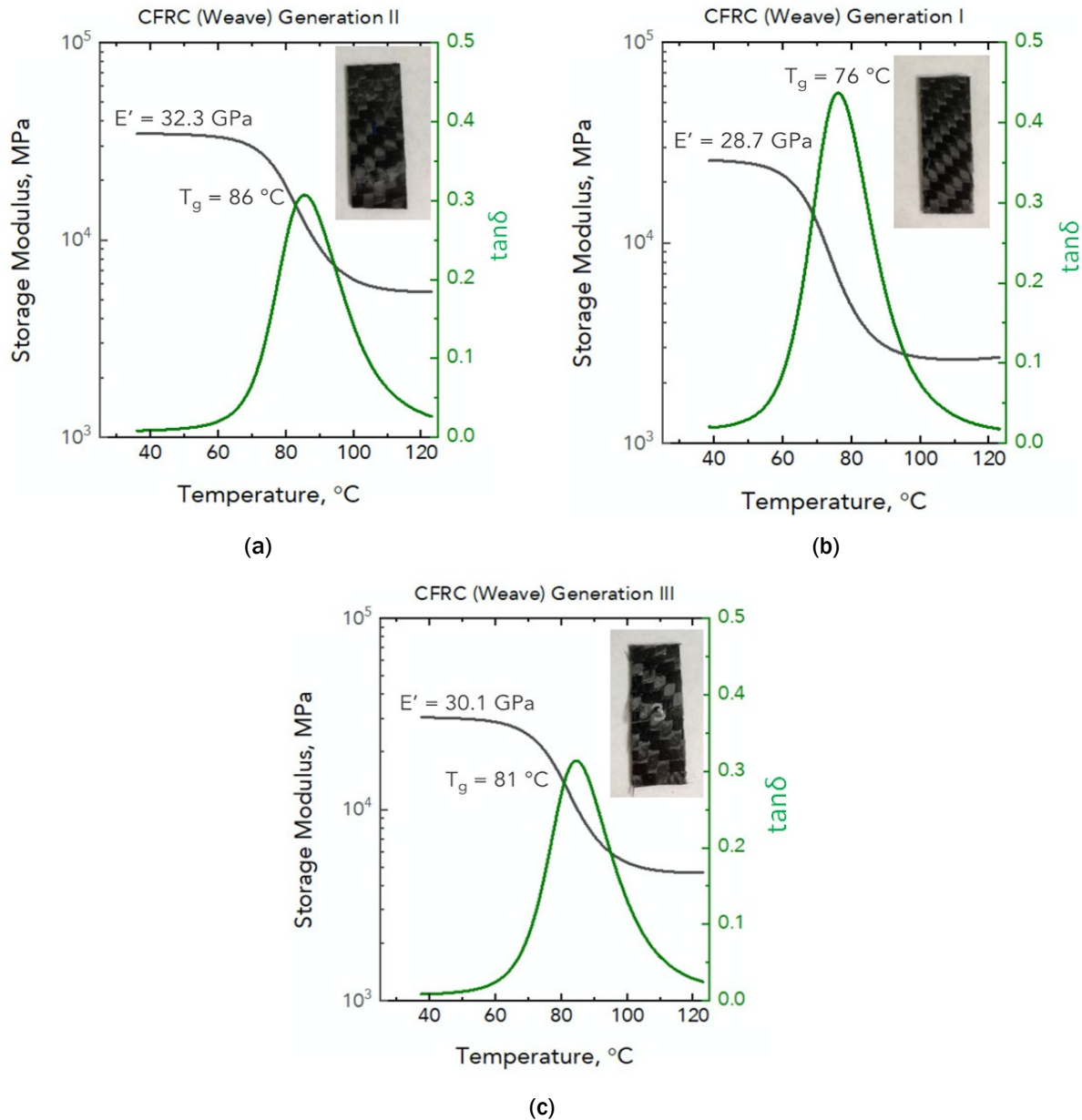


Figure II.2.23.5. Results of the depolymerization, wash, and repolymerization process for (a) Generation I ($E' = 28.7 \text{ GPa}$); (b) Generation II ($E' = 32.3 \text{ GPa}$); and (c) Generation III ($E' = 30.1 \text{ GPa}$). Source: NREL.

Conclusions

The first year of this work demonstrated that a PE-CAN can be used as a replacement for epoxy-amines in CFRC applications and enable the reuse of CF across multiple material lives without any degradation in material performance. The consistent performance was obtained by virtue of our resin combined with the RT depolymerization procedure, which maintained fiber integrity across multiple lives. Use of a bio-derivable resin achieves near cost parity with petroleum-based epoxy-amine resins while reducing supply chain energies by $>33\%$ and GHG emissions by $>18\%$. The work conducted in the first year of this project has enabled all subsequent work, including the study of additives in the PE-CAN resin, the thermoforming of PE-CAN-based CFRCs, the *in operando* repair of the PE-CAN-CFRCs, and the TEA and supply chain analysis of the CFRCs across multiple lives.

Key Publications

1. Rorrer, N., G. Beckham, et al., 2022, “Bioderived recycle epoxy–anhydride thermosetting polymers and resins,” U. S. Provisional Patent Application No. 63/087,547.
2. Wang, C., R. Murray, A. Singh, G. Musgrave, E. G. Rognerud, M. Skala, P. Murdy, S. R. Nicholson, A. Shapiro, J. Miscall, R. Beach, R. D. Allen, N. A. Rorrer, and G. T. Beckham, 2022, “Recyclable-by-design fiber-reinforced composite materials via bio-derivable polyester matrices,” manuscript in preparation.

References

1. Pham, D. D., and J. Cho, 2021, “Low energy catalytic methanolysis of poly(ethyleneterephthalate),” *Green Chem.*, Vol. 23, No. 1, pp. 511–525.
2. Nicholson, S. R., N. A. Rorrer, A. C. Carpenter, and G. T. Beckham, 2021, “Manufacturing energy and greenhouse gas emissions associated with plastics consumption,” *Joule*, Vol. 5, No. 3, pp. 673–686.

Acknowledgments

The authors would like to thank the contributors to this work. E. Rognerud is currently the lead experimentalist on this work. A. Singh and S. Nicholson were instrumental in the analysis component of this work. R. Murray and her team were instrumental in demonstrating the scalability of the CFRCs using industrially relevant VARTM techniques. C. Wang served as a postdoctoral researcher on this project for eight months; A. Shapiro and M. Skala also contributed to this project as interns with a focus on the depolymerization work.

II.3 Multi-Material Joining

II.3.1 A Multiscale Computational Platform for Predictive Modeling of Corrosion in Al-Steel Joints (University of Michigan)

Mihaela Banu, Principal Investigator (2019–2021)

University of Michigan
2350 Hayward Street
Ann Arbor, MI, 48109
E-mail: mbanu@umich.edu

S. Jack Hu, Principal Investigator (2018–2019)

University of Michigan
2350 Hayward Street
Ann Arbor, MI, 48109
E-mail: jackhu@umich.edu

Sarah Kleinbaum, DOE Program Manager

U.S. Department of Energy
E-mail: sarah.kleinbaum@ee.doe.gov

Start Date: January 24, 2019	End Date: December 31, 2021	
Project Funding: \$1,978,423	DOE share: \$1,500,000	Non-DOE share: \$478,423

Project Introduction

The goal of this project is to develop multiscale models for predicting the location and extent of corrosion and the impact of such corrosion on the performance of dissimilar materials joints. The selected joining technologies are RSW, SPR, and rivet-welding that are applied to coupons made of AA 6022, 2.0-mm-thick, and HDG HSLA 340 steel, 1.2-mm-thick. The performance models will include joint strength and fatigue life predictions. These models will be validated by experiments with the goal of achieving strength and fatigue prediction accuracy within 10% of experiments.

Objectives

To achieve the project goal, three objectives are considered: (1) to develop the models at the micro-scale level starting from DFT and simulating the initiation of the corrosion; (2) to develop corrosion mesoscopic models by bridging the scales from atom to grain structure, with the meso-scale material properties being homogenized using uncertainty quantification; and (3) to develop FE performance and fatigue life predictions by integrating models at different scales. These models will be validated as they are developed.

Approach

The multiscale models will integrate: (1) the atomic-phase level modeling with new high-throughput DFT and CALPHAD simulations; (2) the mesoscopic level modeling of corrosion evolution with a FEM, material property homogenization, and uncertainty quantification; (3) the macro-level modeling of joint performance with experimental validations; and (4) the integrations of these models into a computational platform. The models will be validated by the experiments with the goal of achieving an accuracy in strength and fatigue life prediction within 10% of the experiments.

Results

Integration of Micro-scale and Continuum Models into the Finite Element Models

Experimental lap-shear tests of RSW and SPR joints with different levels of corrosion indicate a change in the behavior from ductile to brittle (e.g., from 48–104 cycles under accelerated corrosion tests, GM Best Practices

No. 14872). The developed atomic-phase models are able to predict this complex dynamic behavior through the calculation of ideal shear-stress (ISS, τ_{IS}) for dilute Al-based and dilute Fe-based alloys, and stable and unstable stacking fault energy (USFE, γ_{US}) of dilute Al alloys and surface energy. Predicted values of these two material parameters in the joining area are used in identification of the material behavior of the finite element model of joining performance. Thus, ISS is directly correlated with the maximum strength of the material, the ratio of the USFE, and the surface energy and indicates the ductility of the material and the fracture toughness. The details of the ISS and USFE for the phases that are formed in RSW and SPR of Al-Fe joints are presented in the following sections.

Prediction of ISS and USFE Using First Principles Calculation and Machine-Learning

An ML approach was used to understand and correlate the DFT-predicted ideal shear strength and USFE in terms of the pure shear deformation and supercells for the body-centered cubic (bcc), face-centered cubic (fcc), and hexagonal close-packed (hcp) lattices. The typical changes of shear-stress and stacking fault energy as a function of engineering strain, are shown in Figure II.3.1.1(a)-(b) and Figure II.3.1.1(c)-(d), respectively, for fcc Al and bcc Fe. With increasing shear-strain, the shear-stress curve shows a sudden drop for the case of bcc Cr and a smooth or near-smooth change for fcc Pt. When the stress equals to zero, the energy reaches the maximum (i.e., the peak value of the USFE that is marked by the red symbols).

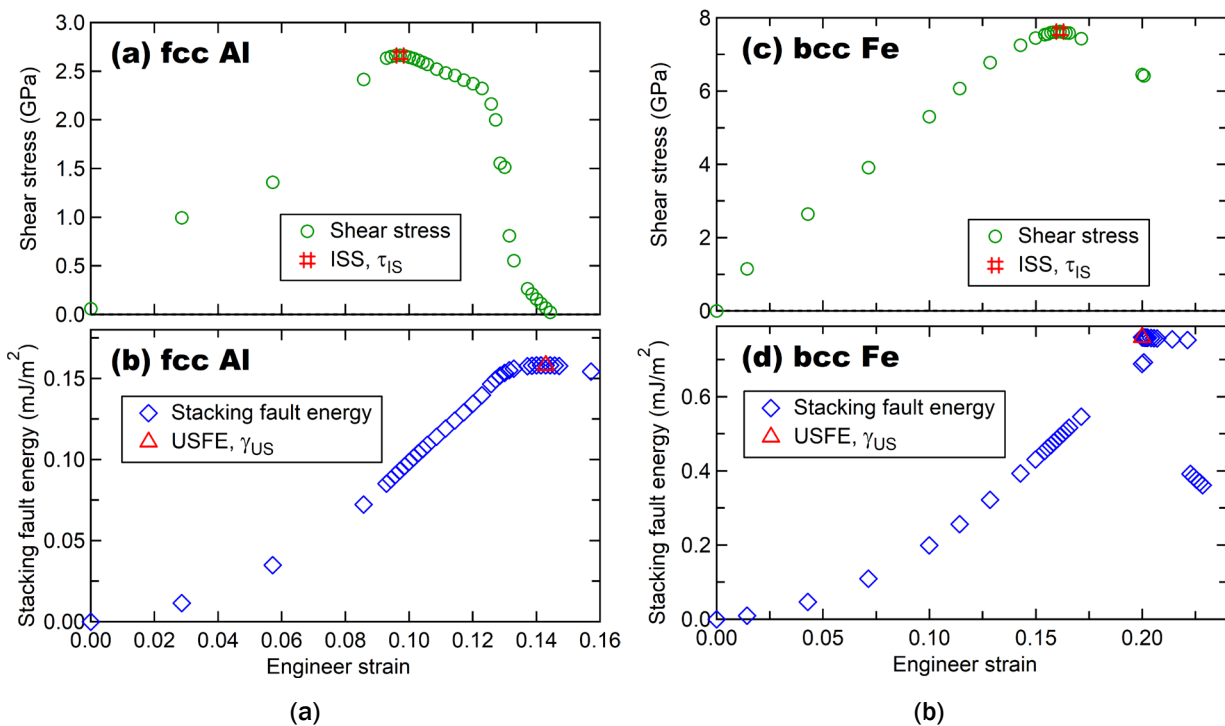


Figure II.3.1.1. Variations of shear-stress and stacking fault energy as a function of engineer strain for fcc Al in (a) and (b) and for bcc Fe in (c) and (d), where the red symbols representing ISS (τ_{IS}) and USFE (γ_{US}).

Source: Penn State University.

Figure II.3.1.2(a) shows the correlation between the DFT-predicted USFE (γ_{US}) and ISS (τ_{IS}) using the Rice model [1], which uses the equation of $\gamma_{US} = \tau_{IS}b/3.125$ (b is the Burgers vector). The resulting linear fit score is $R^2 = 0.78$ which indicates that the results reasonably agree with the suggestions by Rice [1]. As another example, Figure II.3.1.2(b) shows the correlation between the DFT-predicted vacancy activation energy, VaQ [2], and the experimental measured Brinell hardness, HB , displaying a linear fit score of $R^2 = 0.79$. This indicates that VaQ is one of the key features to correlate the hardness.

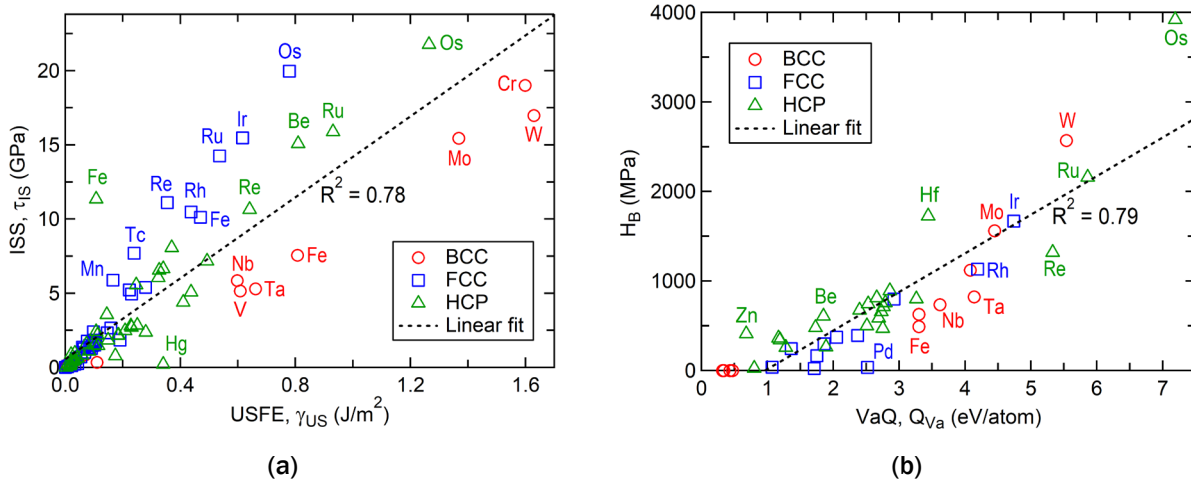


Figure II.3.1.2. (a) Correlation between the DFT-predicted USFE (γ_{US}) and ISS (τ_{IS}) with the linear fit R² score = 0.78. (b) Correlation between the DFT-predicted vacancy activation energy VaQ and the experimental measured Brinell hardness HB with a linear fit R² score = 0.79. Source: Penn State University.

Figure II.3.1.2(a)-(b) show that the R² score for the combined effects with several features is higher than the maximum individual effect. R² scores for DFT-predicted results (e.g., ISS, USFE, VaQ) are higher than the experimental results, since DFT predictions are usually performed on equal footing, while the conditions for the experimental measurements are in general, different, thus resulting in scattered results. By predicting at least one parameter among ISS and ISFE, the other can be determined through these correlation functions and further, calculate strengths, ductility, and fracture toughness, as shown in Figure II.3.1.3.

- Ideal shear strength (τ_{IS}):** Yield stress (σ_y) $\leftarrow \tau_{CRSS} \leftarrow$ Peierls stress (σ_p)

$$\sigma_y = \frac{\tau_{CRSS}}{m_{max}}, \tau_{CRSS} = \tau_p \text{ at } 0 \text{ K}$$

$$\tau_p = \frac{Kb}{a} \exp(-2\pi\zeta/a) \text{ and } \zeta = \frac{Kb}{4\pi\tau_{IS}}$$

CRSS: Critical resolved shear stress
 m_{max} : Max value of Schmid factor
 K: Elastic factor
 b: Burgers vector
 a: Spacing distance of slip place
- Unstable stacking fault energy (γ_{usf}) over surface energy (γ_s):** Ductility of the material ($\frac{\gamma_s}{\gamma_{usf}} \rightarrow$ Ductility)
- Fracture toughness**

$$K_{Ic} = \frac{\sqrt{\frac{2G\gamma_{usf}}{1-\nu}}}{\cos^2\left(\frac{\theta}{2}\right) \sin\left(\frac{\theta}{2}\right)} \text{ (Rice, 1992)}$$

G or μ - Shear modulus for sliding along slip plane
 γ_{usf} - Unstable stacking fault energy
 ν - Poisson's ratio
 θ - Slip plane inclination angle

Figure II.3.1.3. Calculation of material properties using atomic-level predicted ISS and USFE. Source: Penn State University.

Integration of a Probabilistic Confidence-based Adaptive Algorithm into Corrosion Evolution

Corrosion in SPR and RSW joints are subject to different sources of uncertainty with an impact on the variation of force-displacement response in lap-shear tests (e.g., variation of the thickness of the metal sheets, misalignments of the electrode with the sheets during RSW or SPR leading to crevice gap variations, or variation of the coupons' exposure position in the chamber). The meso-scale models are developed for the prediction of the corrosion evolution in the joints and the adjacent areas. The models include the effects of the couplings' various geometric and environmental factors, such as: (1) uneven distribution of the electrolyte; (2) effects of roughness of the Al coupon; (3) effects of crevice distance; (4) effects of Al crystal microstructure; and (5) synergetic effects of the combinations of the couplings. In addition, simulations of stress corrosion cracking in the RSW joint where the cracking is characterized by the growth of the crack at the interface in a corrosive environment and is induced by the corrosion process along with residual stress or stress concentration have been performed. Geometric parameters such as variation of the roughness of the samples, waviness of the samples, positioning of the electrodes during welding were identified as sources of uncertainty of the performance of the joint. Consequently, their effect on the corrosion evolution was considered in modeling through coupling equations that consider not only their absolute value but also their interaction effects on accelerating corrosion. Furthermore, a systematic parametric investigation has been conducted to provide the dataset for developing the predictive model, which can help clarify the phenomenon and give the joint probabilistic distribution for UQ in the future study. Different ML algorithms have been trained and compared to determine the candidate predictive model.

Uncertainty Quantification Study

The second part of the UQ study was the development of the Gaussian Process Regression ML model for material loss study, and this model will be used in the Probabilistic Confidence-Based Adaptive sampling approach, which will help in exploring the whole design space while reducing the overall number of FE simulations required. Based on the sensitivity analysis done previously, it was found that crevice gap, temperature, pH, and thermal conductivity are the main parameters that affect the material loss. Twenty initial simulations, with random values of selected parameters were created and run to calculate the material loss. Some of the response surfaces of the parameters and the material loss are given in Figure II.3.1.4.

The above-described atomic-level and meso-scale models are integrated in the macro-scale modeling of the lap-shear tests of the SPR and RSW joints for prediction on the performance of the joint. An overview of the process flow is shown in Figure II.3.1.5.

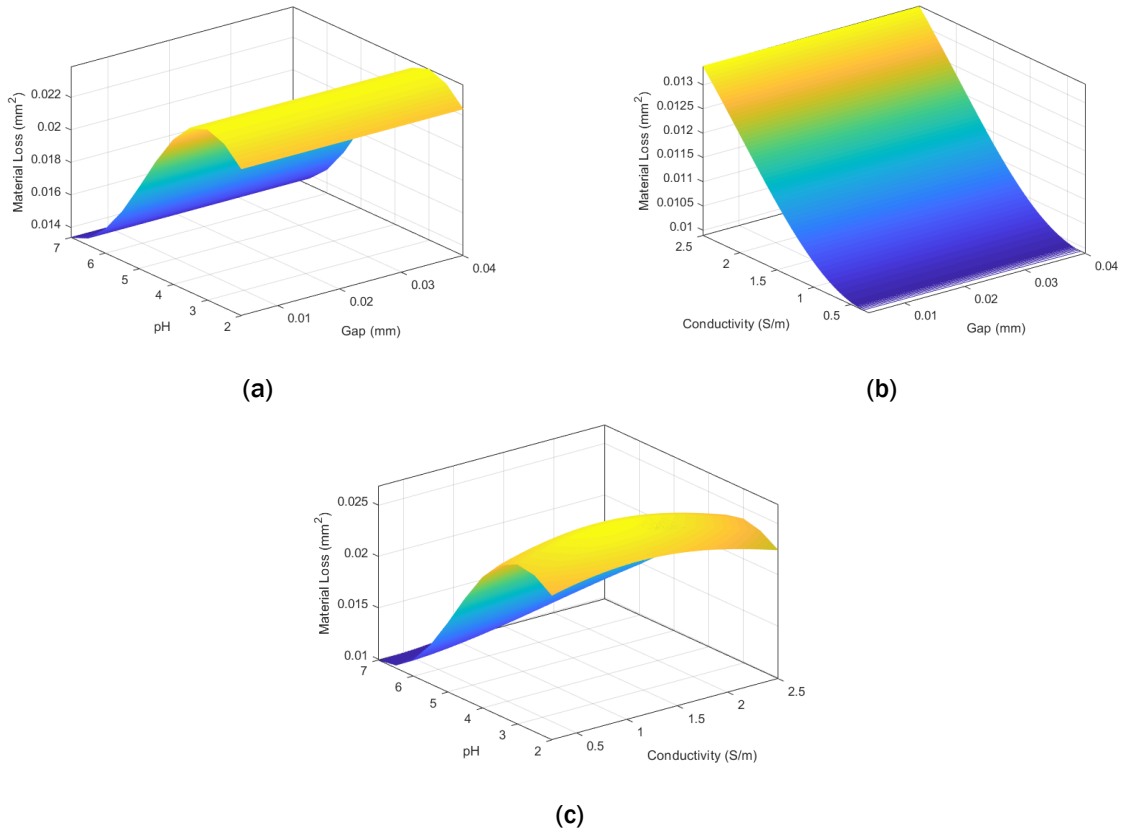


Figure II.3.1.4. Response surfaces for material losses over different input parameters: (a) pH and crevice gap; (b) conductivity and crevice gap; and (c) pH and conductivity. Source: University of Illinois Urbana Champaign.

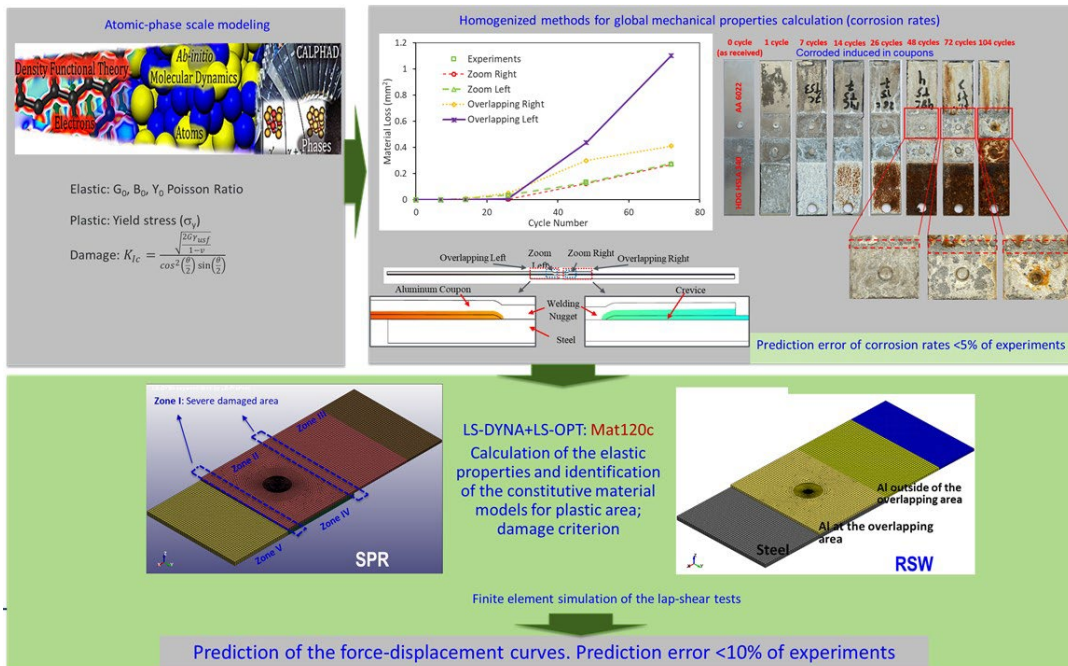


Figure II.3.1.5. The integration of the atomic-phase and meso-scale predictions in FEM of a lap-shear test. Source: University of Michigan.

Fatigue Prediction of the Joints through Modeling S-N Curves

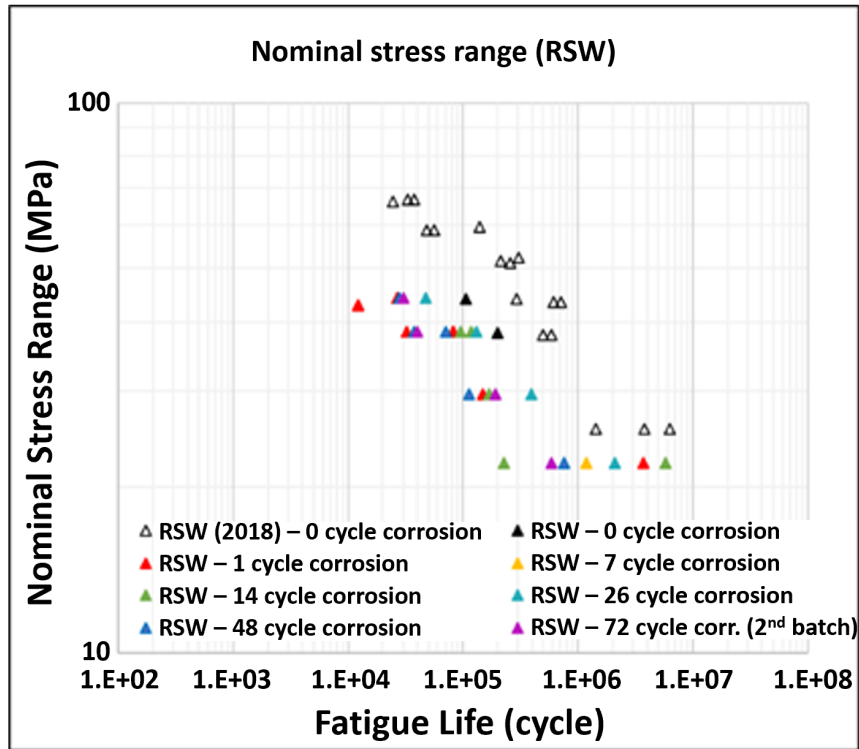
RSW and SPR joints uncorroded and corroded have been tested for fatigue to create the validation sets of data for the model developed for prediction of the stress-number of cycles (S-N) curves. Corroded samples exhibited the same trend in fatigue as non-corroded samples but about 10% lower nominal stress value. Figure II.3.1.6(a) shows the nominal stress range versus cycles to failure for corroded samples with different corrosion cycles and non-corroded. Note that the slight discrepancy between the filled triangles and empty triangle symbols can be attributed to the slight difference between the two batches of specimen geometry, which cannot be differentiated by the use of the nominal stress range (load range divided by load-carrying cross-section area). Regardless of corrosion duration, i.e., with corrosion cycles varying from 1 to 48 or 72, Figure II.3.1.6(a)-(b) show that these test data are situated in a shared scatter band without showing separate trends. The scatter band is consistent with available literature test data for joining steel to steel spot welds [3], in which a typical fatigue life variation range between 6%–8% normal stress.

To increase the database for prediction of the fatigue tests, the data obtained in Figure II.3.1.6(a) were combined with the ones presented in the literature, for a similar couple of Al-steel materials [4] and the results are shown in Figure II.3.1.7(a). Nominal stress is the traditional method for presenting fatigue test data, which is defined as $\sigma_n = F/A$, where F is the load applied and A is the cross-section area. The mixed database was used for obtaining the correlation function of the structural stress and fatigue cycles in Figure II.3.1.7(b). It is noticed that at increasing the corrosion exposure (e.g., from 14 cycles to 72 cycles) the fatigue resistance measured in fatigue cycles drops about 100 cycles. Thus, corroded samples show a significant fatigue resistance degradation compared to uncorroded samples, as shown in Figure II.3.1.7(a) for RSW joints. The reduction in fatigue resistance for corroded specimens is similar among specimens subjected to 1 cycle to 48 cycles of corrosion. This is explained through observations of the fatigue failure modes. There are two main fatigue failure modes, namely Mode A and Mode B, identified based on the cracking starting position and the crack propagation direction. For RSW, Mode A refers to fatigue cracking originating from the weld nugget interfacial notch that propagates into sheet thickness, while Mode B refers to the fatigue cracking originating from the weld nugget interfacial notch and propagating into weld nugget approximately along the Al-Steel interface. Thus, the fatigue resistance degradation is explained through a reduction of the effective nugget size which promotes a failure mode transition from Mode A to Mode B, where Mode B failure typically exhibits a lower fatigue life than that for Mode A due to corrosion-induced smaller nugget size. A schematic of these modes is shown in Figure II.3.1.8. According to the observations of fracture surface characteristics, a three-stage crack development can be inferred. By using nominal specimen geometry information in our FE models, the structural stress method [4, 5] showed its ability in incorporating corrosion effects on stress concentration and predicting fatigue lives for Mode A failure related tests.

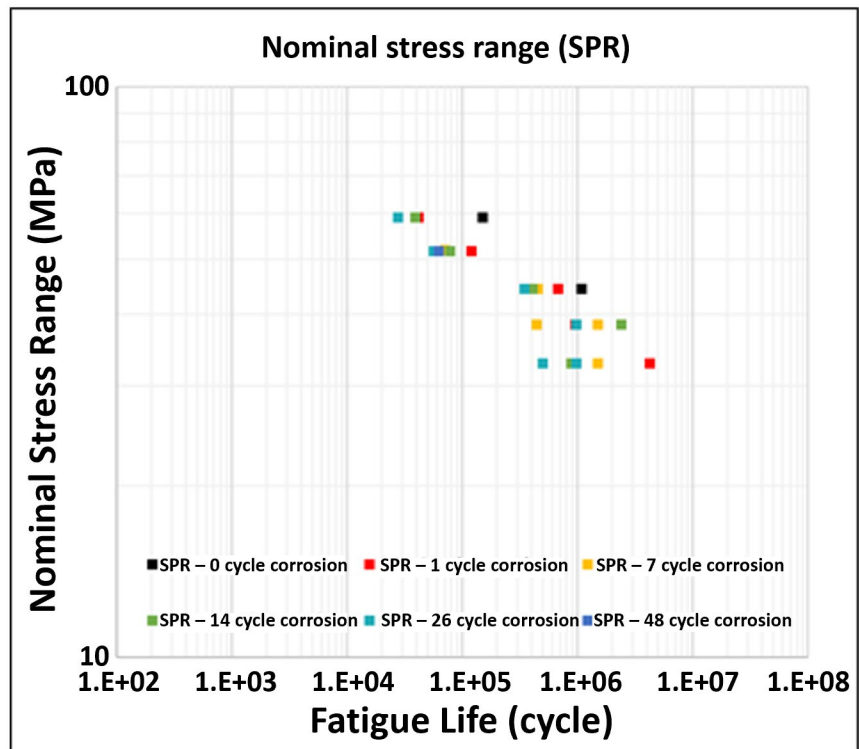
Structural stress based on the stress concentration factor (SCF) is used to predict the S-N curves because the load is transferred through the weld nugget. If the nugget size and position remain the same, a small overlap geometry change will not influence the SCF in any significant manner. Similar to the RSW joints, the corroded specimens showed degradation in fatigue lives in SPR specimens.

Based on the above observations, all test data with corrosion cycles from 1 to 48 or 72, can be grouped together since they do not show any distinct trends due to different corrosion cycles. In other words, for each joint type, data were divided into two groups: uncorroded and corroded and analyzed each group separately.

After grouping, the amount of degradation can be estimated for the corroded specimens. By calculating a fitted equation of each group, about 78% reduction of fatigue life under 40MPa nominal stress range load of RSW joints and about 77% reduction of fatigue life under 50MPa nominal stress range load of SPR joints are obtained as shown in Figure II.3.1.9(a) for RSW and Figure II.3.1.9(b) for SPR.

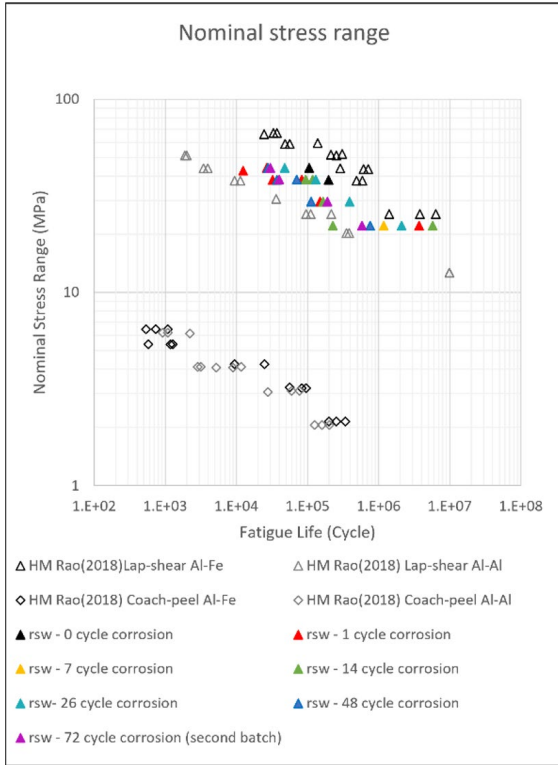


(a)

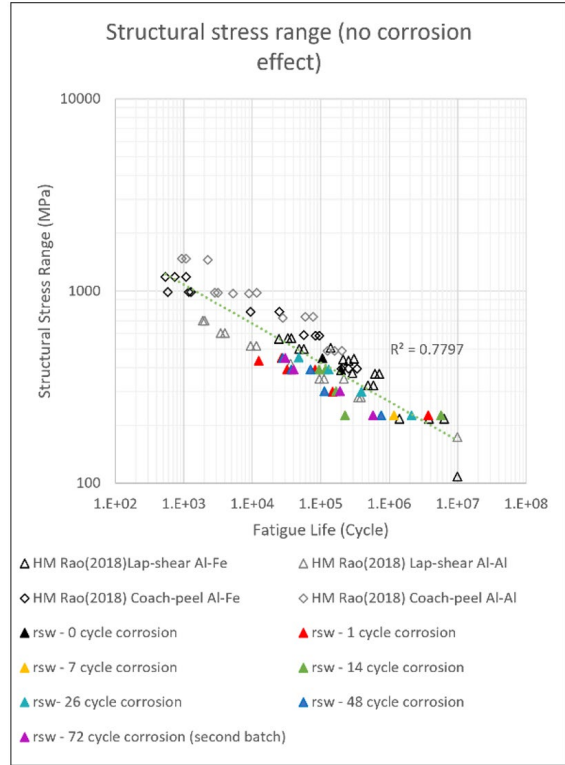


(b)

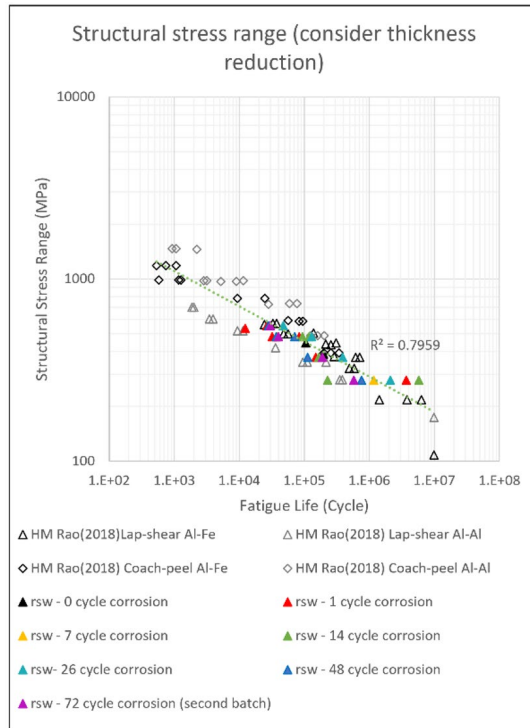
Figure II.3.1.6. S-N charts of the nominal stress range versus failure life for non-corroded and corroded samples: (a) RSW and (b) SPR. Source: University of Michigan.



(a)



(b)



(c)

Figure II.3.1.7. S-N chart correlation for (a) the nominal stress, (b) the structural stress without considering corrosion effects, and (c) the structural stress considering corrosion effects. Source: University of Michigan.

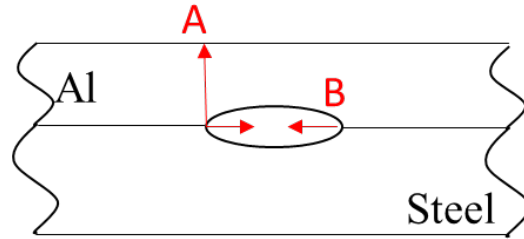


Figure II.3.1.8. Illustration of Mode A and Mode B fatigue failure modes. Source: University of Michigan.

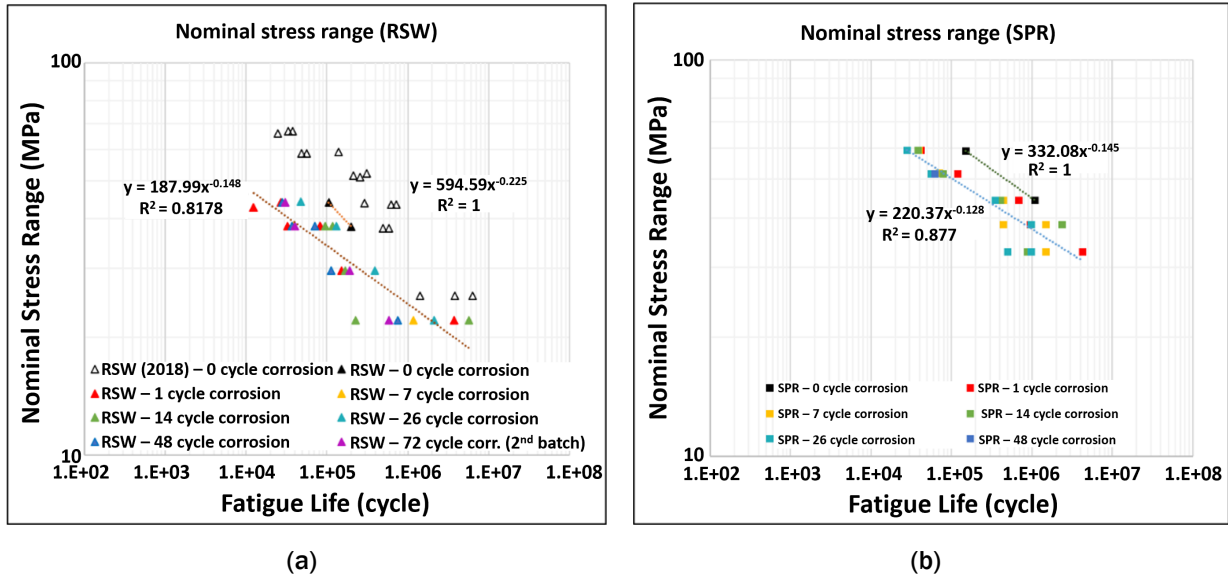


Figure II.3.1.9. Degradation of the fatigue resistance illustrated through fitted curves of the nominal stress range versus fatigue life for (a) RSW and (b) SPR. Source: University of Michigan.

Two characteristics are associated with SPR fatigue failure modes: A1 and A3, as shown in Figure II.3.1.10. A1 shows similar characteristics to those observed in the RSW specimens, while A3 has two simultaneous cracks growing near both sides of the rivet. Uncorroded specimens all have the A1 type of failure mode. Corrosion effects caused joint loosening and a ‘bolt’ type of connection. Load transfer to the Al sheet through the remaining ligament results in the A3 failure mode.

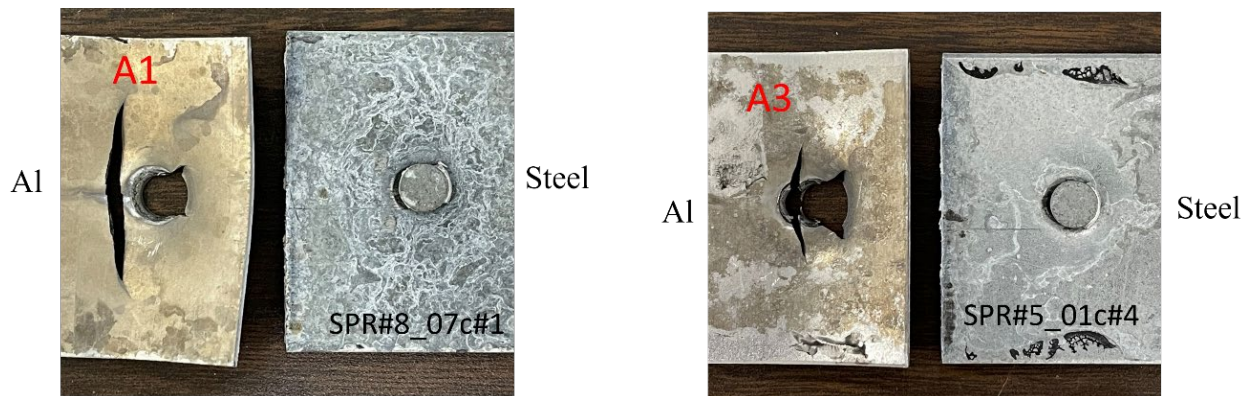


Figure II.3.1.10. Failure characteristics of SPR joints. Source: University of Michigan.

To analyze the structural stress-state of the SPR joints, a FE model with shell elements was established. The rivet was modeled by a ‘fastener’ with a radius of 3.2 mm in ABAQUS. Some differences exist in the geometric dimensions between the nominal design and the as-received specimens.

However, the difference in the resulting structural stress SCFs is only at about 2%. To represent the corrosion effect, the notch depth of SPR was measured from six microscopic images of three SPR 48-cycle corrosion specimens. There is an average reduction of 0.181 mm or 0.15 t, where “t” is the thickness of the Al sheet. This thickness reduction using nominal geometry will result in an increase in SCF of 29%. Incorporating these structural stresses provides the data correlation shown in Figure II.3.1.11(a). Similar to RSW, considering corrosion-induced thickness reduction leads to an improved data correlation of the fatigue test data. The fatigue predictions integrated in the multiscale platform for joining performance prediction under corrosion conditions are shown in Figure II.3.1.11(b).

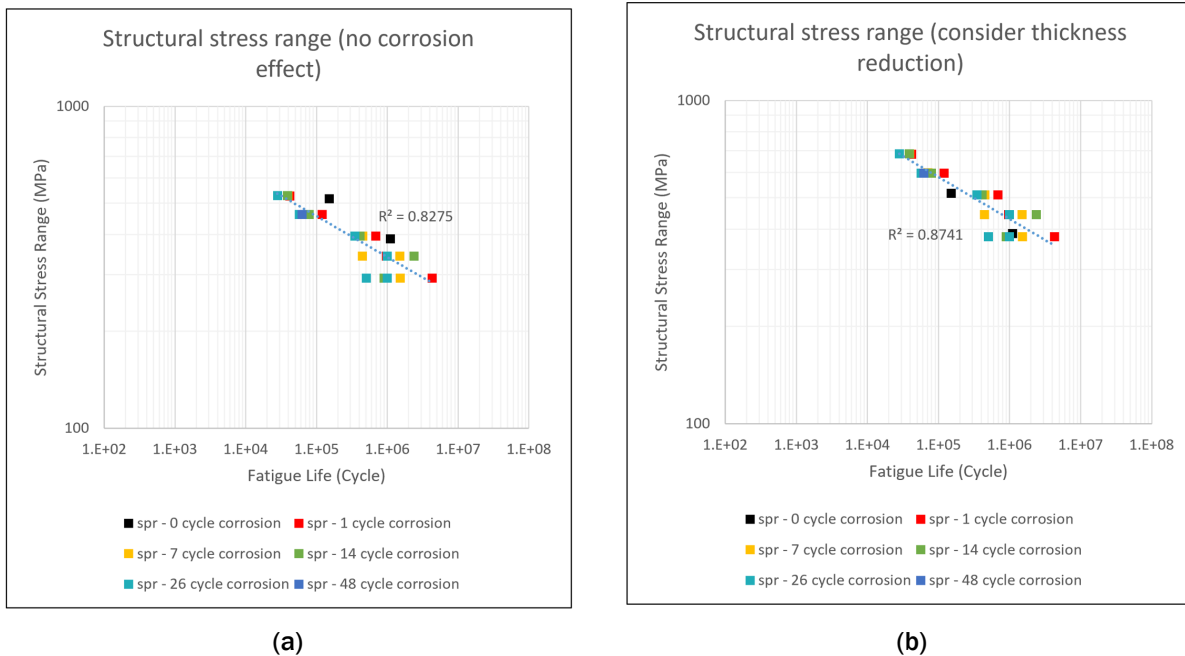


Figure II.3.1.11. S-N chart correlation for: (a) structural stress without considering corrosion effects; and (b) structural stress considering corrosion effects. Source: University of Michigan.

Conclusions

Atomic, meso-scale, and macro-scale models were developed for the prediction of the corrosion evolution and its impact on the joining performance for RSW and SPR technologies. The atomic and meso-scale results were integrated in the macro-scale finite element model of a lap-shear configuration to predict the force-displacement curves before and after corrosion. Using this platform for Al-HSLA RSW and SPR joints, the force-displacement predictions are less than 10% error comparing with experiments. An overview of the integrated platform is presented in Figure II.3.1.12.

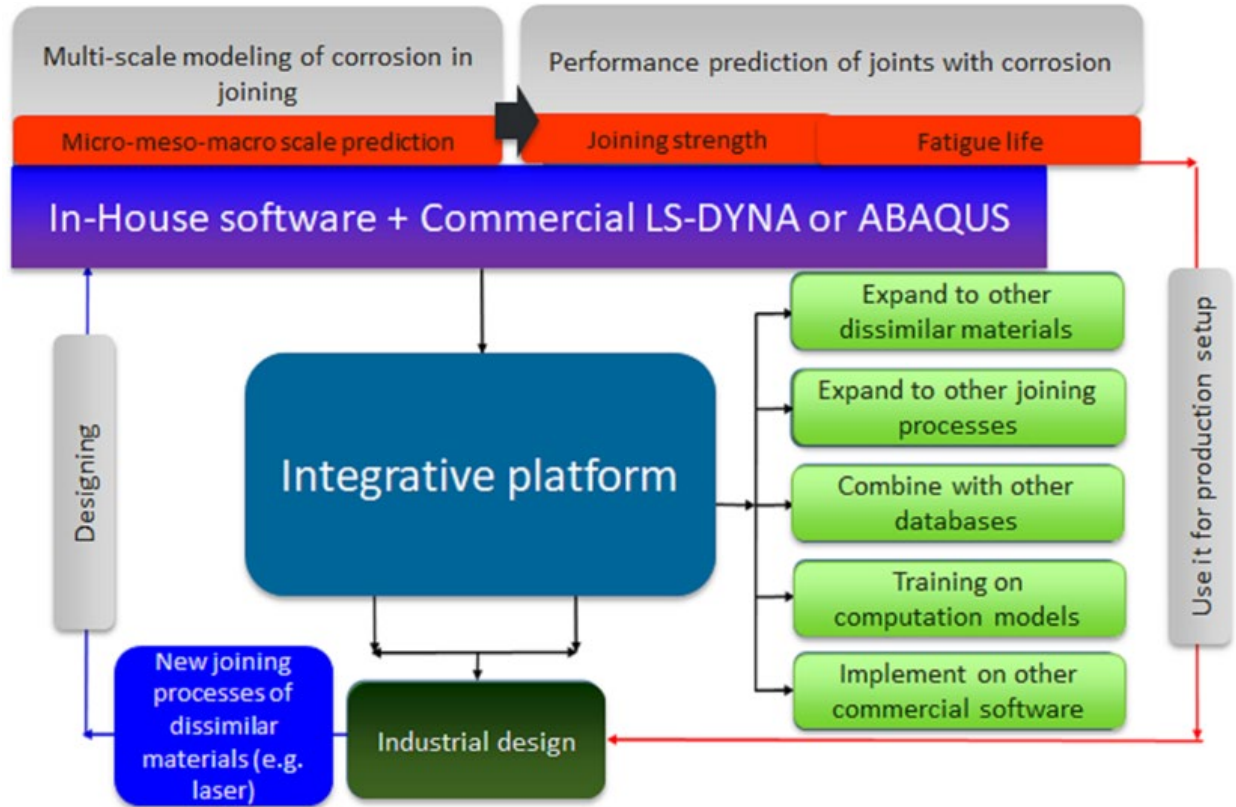


Figure II.3.1.12. Integrative platform for prediction of the location and extent of corrosion in Al-steel joints and its impact on joint strength and fatigue life. Source: University of Michigan and University of Georgia.

The innovative aspects of the developed models, as well as their performance are the following:

- Atomic modeling from DFT-based first principles calculations and phase-scale modeling from the CALPHAD approach were developed to predict welding and corrosion products and their mechanical properties (e.g., 5% error prediction compared with the experiments).
- Mesoscopic corrosion models were developed based on the FE method and improved by incorporating stress corrosion cracking modeling and data-driven methods for UQ of factors influencing joining processes. Material loss and corrosion rates were predicted with an error of < 5% compared with the experiments.
- At the macroscopic level, the FE models were built for simulation of lap-shear tests applied to RSW and SPR joints. Thus, the performance of the joints with and without corrosion compare well with the results from the experiments. An average of 4% error compared with the experiments was achieved with the RSW joints. A simulation of the lap-shear tests applied to the SPR joints are in progress.
- Failure of the SPR joints was successfully predicted, showing that the model approaches that were developed for RSW and applied to SPR are providing a high accuracy with the simulated results at a prediction error of < 5% up to 48 cycles and 10% for 72 cycles.
- At the macroscopic level, a fatigue model was developed to predict the S-N curves, which is added to a complete prediction of the RSW and SPR joining performance.

Key Publications

1. Wang, Y., M. Q. Liao, B. J. Bocklund, P. Gao, S. L. Shang, H. J. Kim, A. M. Beese, L. Q. Chen, and Z. K. Liu, 2021, "DFTTK: Density functional theory toolkit for high-throughput lattice dynamics calculations," *CALPHAD*, Vol. 75, Art. 102355.

2. Pan, B., H. Sun, S. L. Shang, W. L. Wen, M. Banu, J. C. Simmer, B. E. Carlson, N. N. Chen, Z. K. Liu, Z. Y. Zheng, P. F. Wang, and J. J. Li, 2021, “Corrosion behavior in aluminum/galvanized steel resistance spot welds and self-piercing riveting joints in salt spray environment,” *J. Manuf. Process.*, Vol. 70, pp. 608–620.
3. Shang, S. L., H. Sun, B. Pan, Y. Wang, A. M. Krajewski, M. Banu, J. Li, and Z.-K. Liu, 2021, “Forming mechanism of equilibrium and non-equilibrium metallurgical phases in dissimilar materials: Illustrated with aluminum/steel (Al-Fe) joints,” *Sci. Rep.* Available at: <https://doi.org/10.21203/rs.3.rs-745143/v1> (Accessed 21 December 2021).
4. Wen, W., T. Liu, J. Simmer, B. Carlson, S. J. Hu, and M. Banu, 2020, “Corrosion evolution in Al-steel dissimilar joints,” *Proceedings of the ASME 2020, the 15th International Manufacturing Science and Engineering Conference, MSEC 2020*, 22–26 June 2020, Cincinnati, OH, USA.
5. Wang, K. F., S. L. Shang, Y. X. Wang, A. Vivek, G. Daehn, Z. K. Liu, and J. J. Li, 2020, “Unveiling non-equilibrium metallurgical phases in dissimilar Al-Cu joints processed by vaporizing foil actuator welding,” *Mater. Des.*, Vol. 186, Art. 108306.
6. Chong, X. Y., S. L. Shang, A. M. Krajewski, J. D. Shimanek, W. H. Du, Y. Wang, J. Feng, D. Shin, A. M. Beese, and Z. K. Liu, 2021, “Exploring materials properties by machine-learning: Illustrated with stacking fault energy from first principles calculations in dilute Al-, Ni-, and Pt-based alloys,” *Acta Mater.* (submitted).
7. Liu, Z. K., 2020, “Computational thermodynamics and its applications,” *Acta Mater.*, Vol. 200, pp. 745–792.
8. Zheng, Z., P. Bansal, P. Wang, C. Shao, and Y. Li, 2021, “Corrosion modeling and prognosis of the Al-steel SPR joints,” *Proceedings of the International Mechanical Engineering Congress & Exposition, IMECE 2021*, 15–19 November 2021, Portland, OR, USA.
9. Liu, Z.-K., 2001, “Fundamentals and predictions of cross phenomena,” *International Materials, Applications, & Technologies (IMAT) 2021*, 13–16 September 2021, St. Louis, MO, USA.
10. Krajewski, A. M., J. Siegel, S.-L. Shang, Y. Wang, J. Xu, and Z.-K. Liu, 2021, “MPDD (Material-Property-Descriptor Database),” *International Materials, Applications & Technologies (IMAT) 2021*, 13–16 September 2021, St. Louis, MO, USA.
11. Liu, Z.-K., 2021, “High-throughput tools for data generation, process, and rational and inverse design of materials,” *International Materials, Applications & Technologies (IMAT)*, 13–16 September 2021, St. Louis, MO, USA.
12. Liu, Z.-K., 2021, “CALPHAD for materials design enhanced by high-throughput computations,” *International Materials, Applications, & Technologies (IMAT)*, 13–16 September 2021, St. Louis, MO, USA.

References

1. Rice, J. R., 1992, “Dislocation nucleation from a crack tip: An analysis based on the Peierls concept,” *J. Mech. Phys. Solids.*, Vol. 40, pp. 239–271.
2. Shang, S.-L., B.-C. Zhou, W. Y. Wang, A. J. Ross, X. L. Liu, Y.-J. Hu, H.-Z. Fang, Y. Wang, and Z.-K. Liu, 2016, “A comprehensive first principles study of pure elements: Vacancy formation and migration energies and self-diffusion coefficients,” *Acta Mater.*, Vol. 109, pp. 128–141.
3. Kang, H. T., P. Dong, and J. K. Hong, 2007, “Fatigue analysis of spot welds using a mesh-insensitive structural stress approach,” *Int. J. Fatigue*, Vol. 29, No. 8, pp. 1546–1553.
4. Beber, V. C., B. Schneider, and M. Brede, 2018, “On the fatigue behavior of notched structural adhesives with considerations of mechanical properties and stress concentration effects,” *Procedia Eng.*, Vol. 213, pp. 459–469.

5. Dong, P., 2001, “A structural stress definition and numerical implementation for fatigue analysis of welded joints,” *Int. J. Fatigue*, Vol. 23, pp. 865–876.
6. Dong, P., and J. K. Hong, 2006, “A robust structural stress parameter for evaluation of multiaxial fatigue of weldments,” *J. ASTM Int.*, Vol. 3, pp. 1–17.

Acknowledgments

The authors would like to recognize the following individuals whose contributions to this project have been greatly appreciated:

- Co-PI B. Carlson, and J. Simmer, GM
- R. Chinoski, H. W. Wen, T. H. Lee, and T. Liu, UM
- Co-PI J. Li, S. Shang, Z.-K. Liu, H. Sun, and B. Pan, PSU
- Co-PI C. Shao, P. Wang, and Y. Li, Post-Doc Z. Zheng, and Graduate Students Y. Meng, P. Bansal, and Y. Yang, University of Illinois Urbana-Champaign
- Co-PI Jack Hu, University of Georgia
- Co-PI M. S. Pigazzini, and Co-PI D. Lyu, LSTC.

II.3.2 Phase-Field Modeling of Corrosion for Design of Next-Generation Magnesium-Aluminum Vehicle Joints (Worcester Polytechnic Institute)

Adam C. Powell, IV, Principal Investigator

Worcester Polytechnic Institute
100 Institute Road
Worcester, MA 01609
E-mail: acpowell@wpi.edu

Sarah Kleinbaum, DOE Program Manager

U.S. Department of Energy
E-mail: sarah.kleinbaum@ee.doe.gov

Start Date: October 1, 2018	End Date: January 15, 2023	
Project Funding (FY 2021): \$433,394	DOE share: \$366,859	Non-DOE share: \$66,535

Project Introduction

The next frontier in vehicle body lightweighting could make extensive use of a Mg alloy sheet for its outstanding stiffness and strength-to-weight ratio with an Al alloy sheet providing low-cost paintable Class A finish surfaces. The Lincoln MKT and Chrysler Pacifica liftgates have used cast-Mg inner and Al outer sheet components, and next-generation doors could also benefit from using these materials. Corrosion in Al-Mg fusion welds must be addressed to consider widespread use of this material pair in a vehicle's body structure.

FSW leads to significant grain refinement, second-phase refinement, homogenization, and densification—all characteristics known to have beneficial effects on the corrosion resistance of light metals [1–3]. Similarly, FSW in wrought Mg-Yttrium RE and AA5083 Al alloys shows potential for improved corrosion resistance likely due to the breakdown and dispersion of intergranular precipitates [4].

However, there is no quantitative link between microstructure and corrosion performance. Closing this missing link in our current understanding will facilitate the design of cost-effective processes for making robust joints whose geometry and microstructure reduces corrosion and joint failure, even when coatings fail.

Objectives

The objective of this project is to provide a quantitative link between FSW microstructure and corrosion performance. In particular, the team aims to develop and validate a phase-field model of micro-galvanic corrosion, as well as a coupled micromechanics model of mechanical failure, in FSW Al-Mg alloy joints to predict strength and fatigue lifetime of corroded joints within 10% of measured performance.

The case study for this project is based on the hem joints in the Magna-Fiat Chrysler Automobiles U.S. LLC ultra-lightweight door project. Applying FSW to this configuration requires these welds go through 6022 Al sheet into ZEK100 Mg alloy sheet. This is difficult because the welds are usually through the softer material into the harder material.

Approach

The phase-field corrosion model starts with an expression for free energy vs. composition in the metal, electrolyte, oxide, and hydroxide corrosion product phases, following the method of Pongsaksawad et al. [5]. This expression begins with a fit to thermodynamic data on Al and Mg alloy systems, including the base metals and IMCs. The electrolyte is an aqueous solution with Al^{3+} and Mg^{2+} ions and dissolved oxygen. Using a representation of the full Al-Mg system free energy function both produces the correct compositions at phase boundaries, and leads to correct chemical potential of both species at metal-electrolyte boundaries, which creates electronically mediated micro-galvanic corrosion reactions.

The corrosion model is validated through the fabrication of diffusion-bonded and welded joints. Diffusion-bonded sheets of pure Mg and Al provide an ideal model system for understanding the fundamentals of galvanic corrosion. Diffusion-bonded alloy sheets deepen this understanding to include additional phases in each alloy. When the phase-field diffusion and phase transformation model is proven for diffusion-bonded couples, we can then try to use it to describe corrosion in a complex FSW microstructure.

Prediction of FSW microstructure is beyond the scope of this study. Instead, characterization techniques, such as SEM with EDS and EBSD, will produce maps of composition and grain orientation across a FSW joint. This includes using *in-situ* FIB etching to expose and characterize multiple layers in a joint leading to a 3D microstructure, which will provide the initial condition for the corrosion model. The change in geometry due to corrosion then informs the mechanical failure model.

This project consists of four tasks with an end goal of a validated model of corrosion and mechanical failure:

1. **Produce Diffusion-Bonded and Welded Coupons for Testing:**
Produce coupons with joints between pure and alloyed Mg and Al sheets by diffusion-bonding and/or friction stir and/or fusion welding.
2. **Conduct Corrosion and Mechanical Testing:**
Run accelerated corrosion tests and tensile and fatigue tests to determine corrosion morphology and its effect on mechanical performance of Mg-Al joints.
3. **Characterize Welded Joints and Corrosion and Mechanical Test Samples:**
Use advanced characterization methods including SEM with EDS and EBSD, as well as small-angle neutron scattering, to understand the structure of corrosion products and fracture surfaces and provide input geometry/morphology as an initial condition for models.
4. **Develop Corrosion and Mechanics Model:**
Use phase-field and mechanical deformation modeling software to build a model of corrosion and mechanical deformation of Al-Mg joints.

Results

Results are presented here by task, as listed above.

Task 1. Produce Weld Coupons for Testing

In FY 2019 to FY 2020, the PNNL team learned to produce consistently strong linear friction stir welds through a 1.27 mm 6022 Al into a 1.5 mm ZEK100 Mg sheet, as described in a prior report. Using a triflute pin, the welds showed 160 N/mm lap-shear strength, which is 35% of the tensile strength of the 1.5-mm-thick ZEK100 sheet (300 MPa for 1.5-mm thickness) [6].

In the second quarter of FY 2021, the ZEK100 Mg sheet supplier changed from 1.5 mm thickness to 1.2 mm thickness, and the team needed to change their procedure to produce a strong joint. In the end, the triflute pin with a single rectangular scroll shown on the left side of Figure II.3.2.1 led to joint lap-shear strength consistently above 170 N/mm, which is 47% of ZEK100 tensile strength at this thickness. However, crown surface roughness increased with this tool. Figure II.3.2.1 also shows a welded panel and the new tool used to make the weld. Figure II.3.2.2 shows load-displacement curves for coupons cut vertically across a weld.



Figure II.3.2.1. FSW tool used to weld Al and Mg sheet and the Al side of the linear FSW Al-Mg welded panel. Source: PNNL.

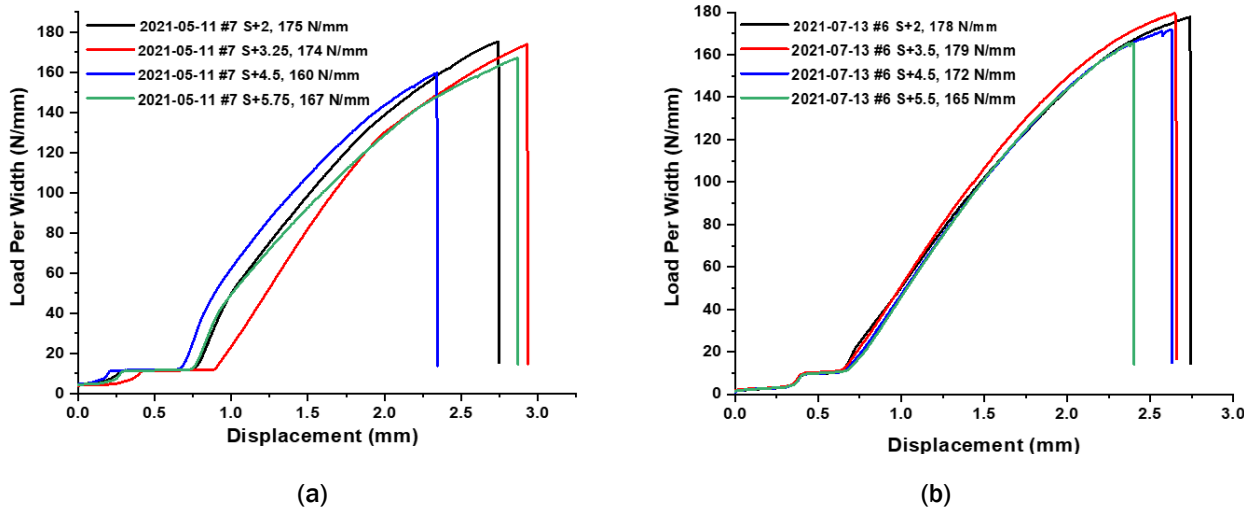


Figure II.3.2.2. Load vs. displacement plots for coupons cut from two welded panels showing improvement in lap-shear strength and consistency between samples welded in (a) May vs. (b) July. Source: PNNL.

Task 2. Corrosion and Mechanics Testing

The Western Polytechnic Institute (WPI) team performed two types of corrosion tests—a polarization resistance test and a partial cyclic corrosion test with a hold in a desiccator. Lap-shear tests of as-received material and material from the cyclic corrosion test determined the effect of corrosion on strength. A microindentation mapping study characterized the hardness distribution of a whole weld cross-section for use in developing the model of mechanical deformation and failure. Procedures and results are described below.

Cyclic Corrosion Testing

A cyclic corrosion test (CCT) following the SAE J2773 standard ran for five weeks. A study hypothesis has been that galvanic corrosion is limited by the cathode reaction at the Al. Figure II.3.2.3(a) shows the samples cut to varying Al lengths, while Figure II.3.2.3(b) shows the corresponding weight loss over five weeks. The observed trend of higher weight loss corresponding to higher Al:Mg surface ratio agrees with the cathode limitation hypothesis.

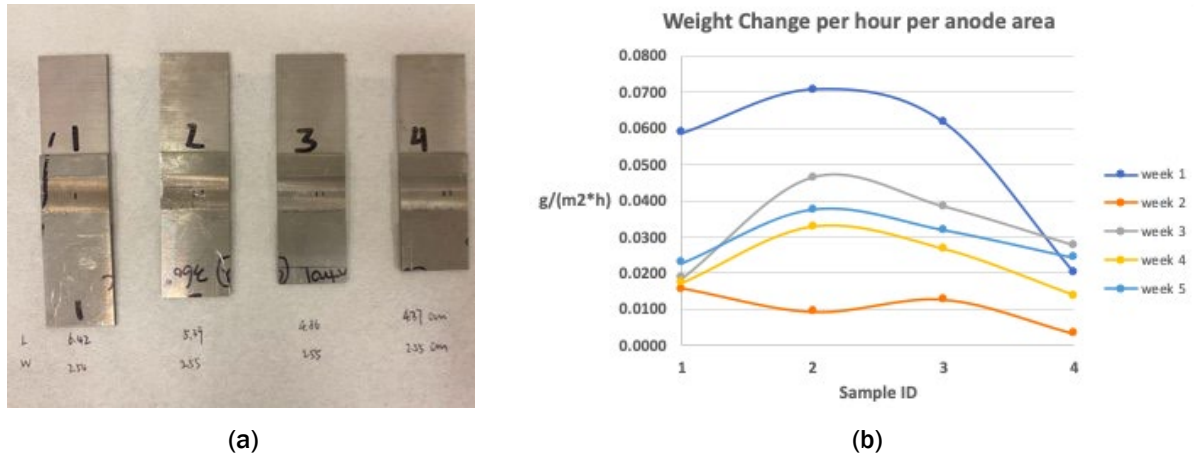


Figure II.3.2.3. (a) FSW joint coupons used as CCT sample geometries with varying surface area ratios of 6022 Al (bottom) to ZEK100 Mg (top). (b) Weight change during CCT testing by sample ID. Source: WPI.

Lap-Shear Testing

The team tested both as-received samples and those that had gone through CCT processing for five weeks. The CCT samples were stored in a desiccator for five months prior to testing. The measured strengths of the four samples shown in Figure II.3.2.3 were 41.2, 130.3, 86.2, and 75.4 N/mm, respectively. These are well below the 160-170 N/mm strength range for newly welded samples. As of the end of FY 2021, it is not known whether the reduction in strength was caused by the CCT process or because of storage in the desiccator. The team plans to run longer CCT experiments with lap-shear tests immediately following, with a larger number of samples to produce meaningful statistics for each cathode:anode (i.e., Al:Mg) surface area ratio.

Microindentation Testing

Hardness distribution was measured in a weld cross-section using a Vicker's indenter on an automated array sampling device. Measurements covered the overlap region of the two sheets—particularly the weld nugget and HAZ. Figure II.3.2.4 shows the hardness distribution. Base 6022 Al hardness is somewhat higher than the ZEK100 Mg, as expected. But the Al nugget zone hardness is low, comparable with the base Mg value. This and the equiaxed grain structure in the nugget described below are consistent with recrystallization, which would remove work hardening introduced in the sheet rolling process. In contrast, Mg in the nugget zone is slightly hardened relative to the base sheet. This may be in part due to mixing and IMC formation.

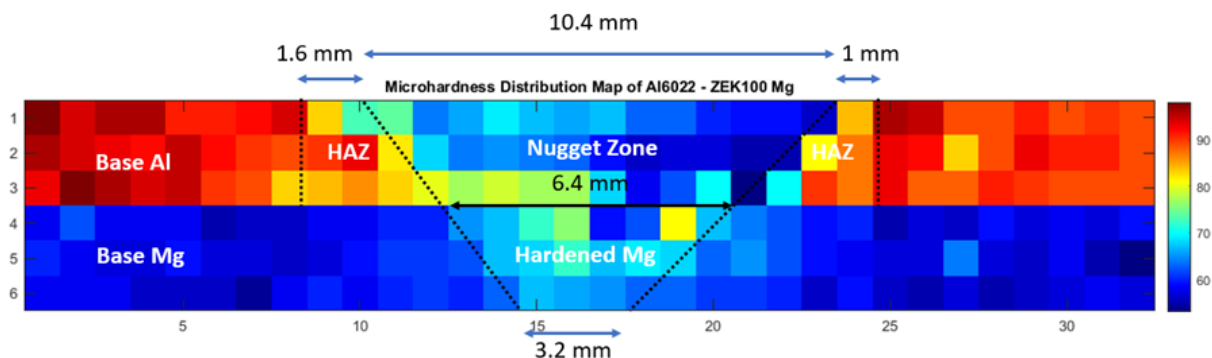


Figure II.3.2.4. Hardness distribution map of an Al-Mg FSW joint cross-section dilated in the vertical direction, with each box measuring 1 mm horizontal by 0.4 mm vertical. Source: WPI.

The hardness distribution and measured shape of the Al-Mg interface form the basis for a model geometry of the weld cross-section showed in Figure II.3.2.5. This includes base Mg, hardened Mg in the weld, base Al, softer (likely recrystallized) Al in the weld, and a HAZ in the Al next to the weld.

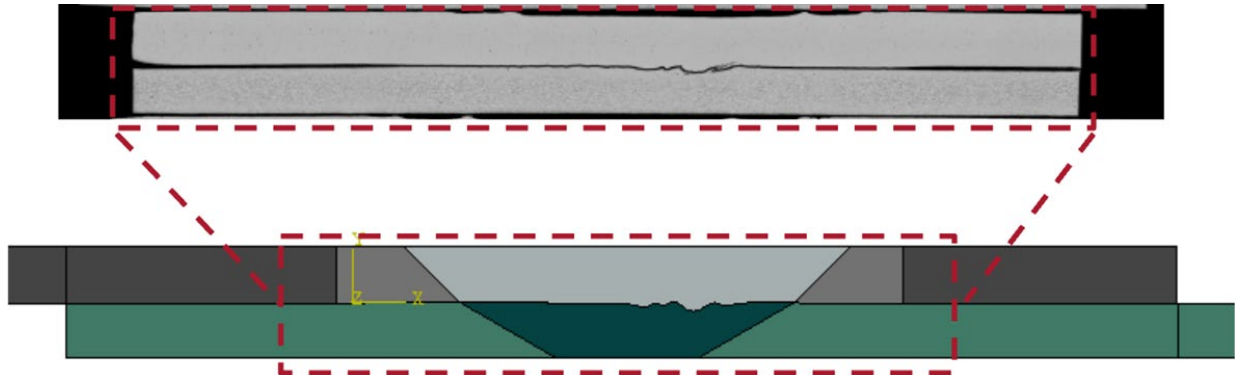


Figure II.3.2.5. Linear FSW cross-section (top image) with Al sheet on top and Mg beneath, and model geometry (bottom image) showing region of reduced strength in the Al nugget. Source: WPI.

Task 3. Characterize Welded Joints and Corrosion Test Samples

Large-area maps (LAMs) using SEM characterized centimeter-scale regions of the FSW joint with sub-micron resolution. This technique involved automated motion of the SEM stage to take multiple images and knit them together into a single map. Figure II.3.2.6 shows two LAM analyses of the FSW joint polished down into the Al side. The EBSD orientation map in Figure II.3.2.6(a) shows equiaxed grains in the weld nugget zone, which are much smaller than the base metal, with considerable texturing as indicated by color bands; this is consistent with recrystallization as described above. Between the nugget and base metal, grains are heavily sheared.

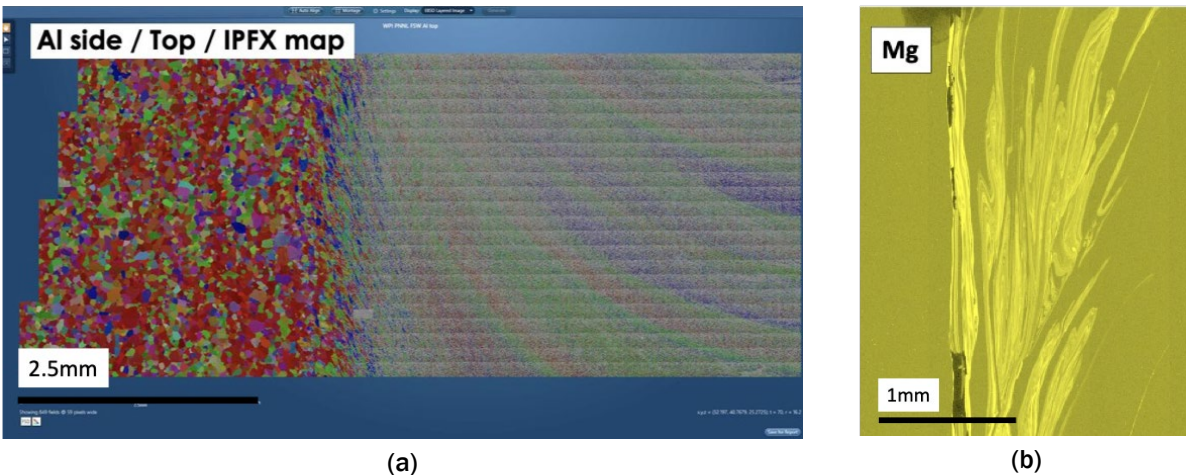


Figure II.3.2.6. The SEM studies of the 6022 Al side of the joint polished down. (a) The EBSD orientation map showing distribution of grain sizes and texture. (b) The EDS map of Mg concentration. Source: ORNL.

The EDS map of Mg concentration in Figure II.3.2.6(b) shows a swirling pattern of mixing into an Al nugget zone, with several distinct shades indicating a tendency to form specific concentrations rather than a continuum of Al-Mg mixtures. A small FIB lift-out was then analyzed using transmission Kikuchi diffraction with results shown in Figure II.3.2.7(a). At the interface between the Mg and Al, two IMC layers form as shown as yellow and purple grains in Figure II.3.2.7(b), which explains the distinct shades in EDS as IMC concentrations. This is similar to the IMC layers in diffusion bonds as described in our previous annual report.

It is not clear what role these IMC layers play in mechanical failure, as fracture follows the Al-Mg interface rather than the nugget zone.

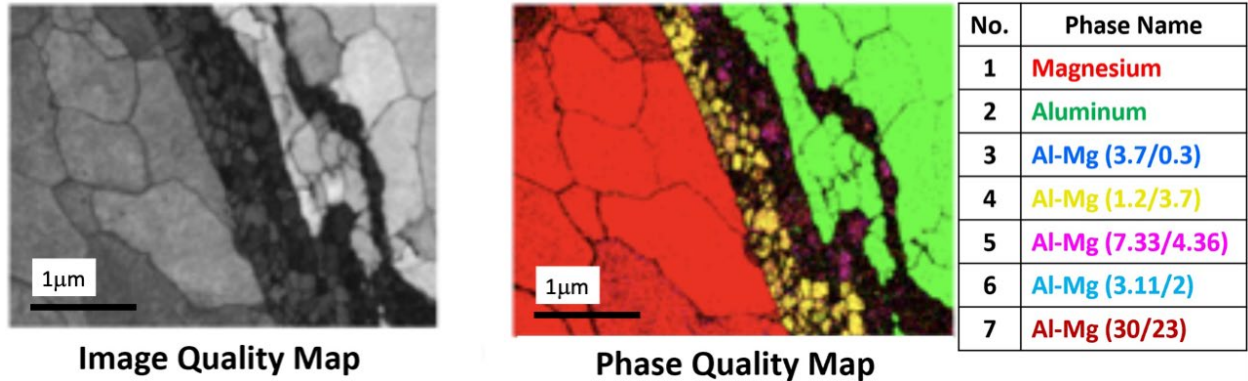


Figure II.3.2.7. (a) Transmission Kikuchi diffraction image quality and (b) phase map with the identified phases from a FIB lift-out in an Al-Mg interfacial region of the Al nugget. Source: ORNL.

Task 4. Develop Corrosion and Mechanics Model

The WPI team developed a model of lap-shear failure of the Al-Mg FSW joints based on literature. This is a 2D stationary FEA model of mixed elastic-plastic deformation, with damage accumulation and fracture occurring as the sample is continuously extended from its ends. The work began by reproducing the results of a published model of steel-Mg FSW joint lap-shear failure [7] as a verification study, which was adapted to the stress-strain behavior of the Al-Mg FSW zones as shown previously in Figure II.3.2.5.

Figure II.3.2.8 shows the FEA model output, indicating deformation geometry and von Mises stress at initial, intermediate, and final stages. The model predicts that the largest stresses and fractures occur along the deformed interface between the Al and Mg sheets, in good agreement with the experimental observations.

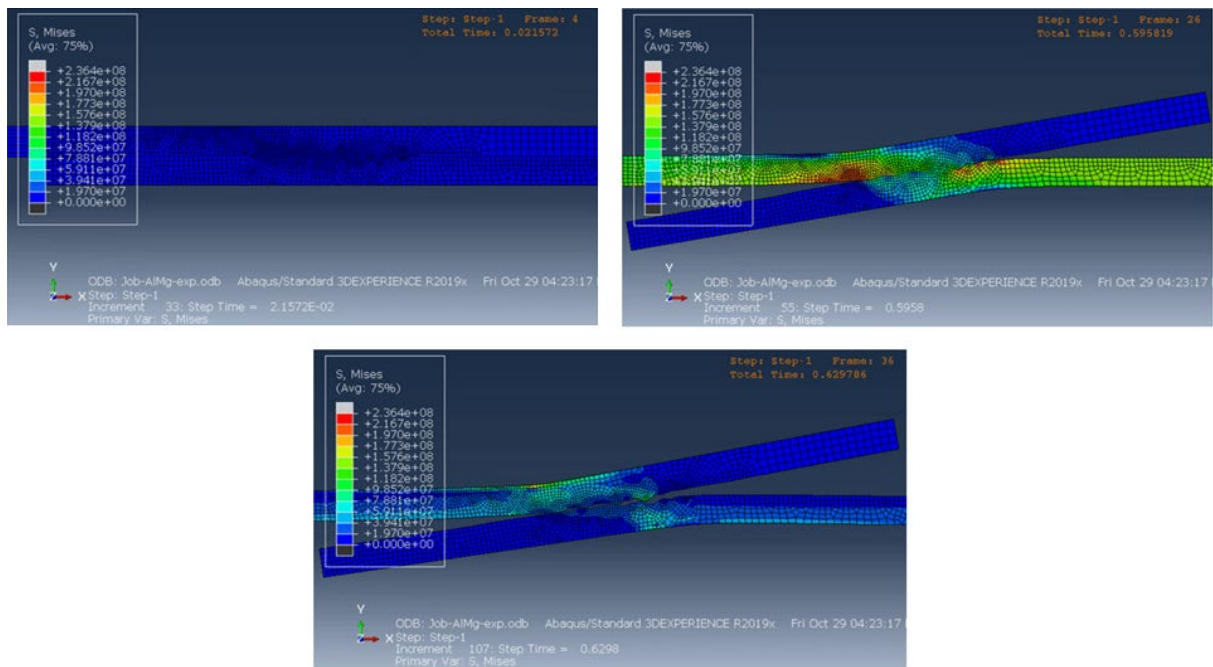


Figure II.3.2.8. Output of FEA mechanical failure model of Al-Mg FSW joint (Al sheet on top, Mg sheet on bottom) showing mesh and von Mises stress at initial, intermediate, and final stages of elongation. Source: WPI.

Figure II.3.2.9 shows FEA model predictions of load vs. displacement under two conditions. As shown in Figure II.3.2.9(a), the model of the uncorroded joint predicts 160 N/mm strength that is in good agreement (<10%) with the results shown previously in Figure II.3.2.2. The model of the corroded joint begins with a shorter bonded interface between the two sheets, roughly corresponding to the fracture surface observed on the four samples exposed to five weeks of CCT and five months in a desiccator (as described above). The model prediction of corroded joint lap-shear strength corresponds to the strongest of the four corroded joints, as shown in Figure II.3.2.9(b) but is more than 50% stronger than the mean of the four corroded samples' strengths as described above.

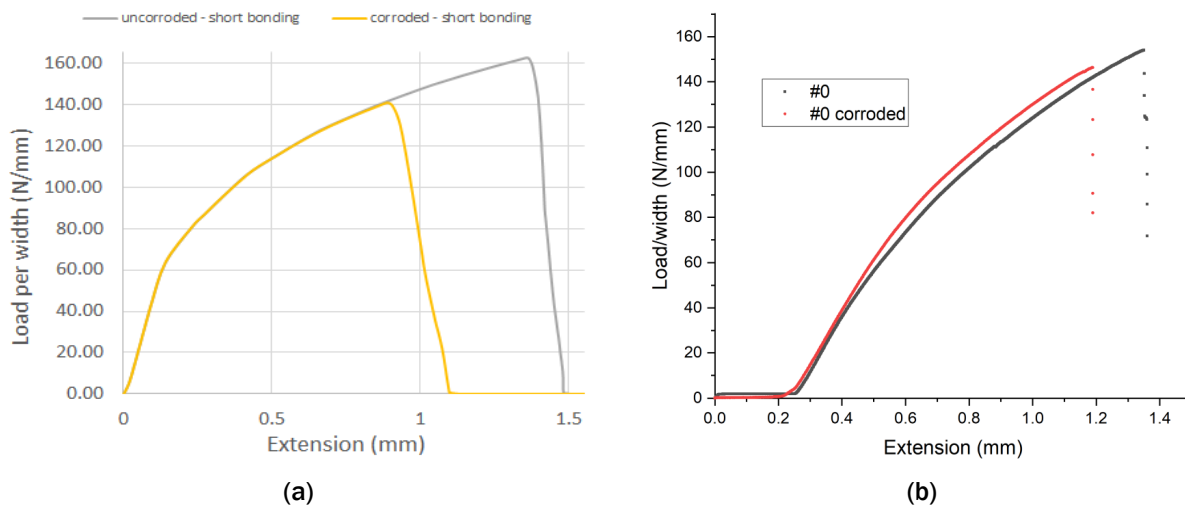


Figure II.3.2.9. (a) Predicted and (b) actual corroded and uncorroded load-extension curves. Source: WPI.

Conclusions

The team has successfully completed several project objectives in FY 2021:

- Developed a method, tooling, and parameters for linear FSW through a hard material into a softer one with high joint strength.
- Used a model of Al-Mg intermetallic formation at interfaces based on diffusion-bonding studies to study swirl structures found in the FSW joint.
- Characterized corrosion of Al-Mg FSW joints in CCT.
- Developed a FEA model of deformation, damage, and mechanical failure of Al-Mg FSW joints, included joints corroded by CCT plus static holding in the desiccator.

Going forward, the team plans to continue to develop the corrosion model and couple it more strongly with the mechanical failure model. The relative effects of CCT vs. subsequent static corrosion over time (in the desiccator as described above) will be explored in more detail, including the influence of the adhesive/sealant in the door design. The corrosion and mechanical failure model will also be extended to cyclic loading.

References

1. Savguira, Y., T. H. North, and S. J. Thorpe, 2016, "Effect of grain size and residual stress on the corrosion resistance of friction stir spot welded AZ31B joints," *Mater. Corros.*, Vol. 67, No. 10, pp. 1068–1074.
2. Kish, J. R., G. Williams, J. McDermid, J. M. Thuss, and C. Glover, 2017, "Effect of grain size on the corrosion resistance of friction stir welded Mg alloy AZ31B joints," *J. Electrochem. Soc.*, Vol. 161, No. 9, Art. C405.

3. Guan, Q., J. Sun, W. Y. Wang, J. Gao, C. Zou, J. Wang, B. Tang, H. Kou, H. Weng, J. Hou, J. Gao, J. Ma, and J. Li, 2019, "Pitting corrosion of natural aged Al-Mg-Si extrusion profile," *Materials*, Vol. 12, No. 7, Art. 1081.
4. Mofid, M. A., and E. Loryaei, 2020, "Effect of bonding temperature on microstructure and intermetallic compound formation of diffusion-bonded magnesium/aluminum joints," *Materialwissenschaft und Werkstofftechnik*, Vol. 51, No. 4, pp. 413–421.
5. Pongsaksawad, W., A. Powell, and D. Dussault, 2007, "Phase-field modeling of transport-limited electrolysis in solid and liquid states," *J. Electrochem. Soc.*, Vol. 154, No. 6, Art. F122.
6. Li, Y., 2021, "Mechanical properties of ZEK100 Mg alloy," Ryerson University Ph.D. Thesis. Available at: <https://www.semanticscholar.org/paper/Mechanical-properties-of-ZEK100-Mg-alloy-Li/9af19cafab1fd392cf13bfb939c563cda2754cf3> (last accessed 3 March 2022).
7. Wang, T., D. R. Tamayo, X. Jiang, P. Kitsopoulos, W. Kuang, V. Gupta, E. Barker, and P. Upadhyay, 2020, "Effect of interfacial characteristics on magnesium to steel joint obtained using FAST," *Mater. Des.*, Vol. 192, No. 1, Art. 108697.

Acknowledgments

This material is based upon work supported by the DOE-EERE VTO under award number DE-EE0008454.

II.3.3 A Hybrid Physics-Based Data-Driven Approach to Model Damage Accumulation in Corrosion of Polymeric Adhesives (Michigan State University)

Roozbeh Dargazany, Principal Investigator

Michigan State University
428 S. Shaw Lane, Room 3567
East Lansing, MI 48824
E-mail: roozbeh@msu.edu

Sarah Kleinbaum, DOE Program Manager

U.S. Department of Energy
E-mail: sarah.kleinbaum@ee.doe.gov

Start Date: October 1, 2018 End Date: December 31, 2022
Project Funding (FY 2021): \$1,005,397 DOE share: \$817,016 Non-DOE share: \$188,381

Project Introduction

Degradation of polymeric adhesives in dissimilar joints is a menace to electric and structural components of the automotive industry. Often in polymeric adhesives, failure occurs due to damage accumulated from discrete environmental sources—thermal degradation, oxidation, hydrolysis, radiation, and moisture—that are combined with progressive damage mechanisms, such as aging and fatigue. Because most damage mechanisms that lead to degradation act in parallel, estimation of the lifetime of a polymeric material becomes a significant reliability issue. No study currently exists that can simultaneously consider even two of these phenomena. Most current efforts are directed toward a single-phenomenon, single-model approach in which a model is developed to cover one specific damage mechanism. While this approach is advantageous in exploring single mechanisms, it is strongly inconclusive for degradation that occurs by multiple damage mechanisms. Our team has taken a fresh perspective by designing a hybrid constitutive/data-driven approach that allows models of different damage mechanisms to be integrated into one model and then used to explore degradation-induced failure of polymeric adhesives. The theoretical-computational part of this work is divided into four research components as described in the Approach section below.

Objectives

The objective of this project is to develop and validate a model to predict degradation-induced failure in polymeric adhesives with respect to damage accumulated by different degradation and fatigue mechanisms within 10% of measured performance. Models of different damage mechanisms will be integrated into one platform and used to explore the degradation-induced failure of polymeric composites. Initially, the focus will be on modeling and coupling of viscoelasticity, thermo-oxidation, photo-oxidation, and moisture degradation. The platform output will be given to a NN engine to calculate remaining service life. Using the NN, a new fatigue failure model will be developed that considers the effect of degradation.

Approach

This report covers our results for FY 2021 where our focus was on understanding, characterizing, and modeling individual degradation mechanisms. The modeling part of this project consists of four major tasks that focus on the multiscale modeling of each of the following damage mechanisms based on the substructural changes associated with them:

- The **vibration-induced** model was developed based on MSU's quasi-static [1] and visco-elastic [2] models in FY 2020.
- The **thermo-oxidative** model was finished in FY 2020.
- The **hydrolysis** model was finished in FY 2020.

- **Thermo + photo-oxidation** modeling, which is modeled with the continuous network hypothesis concept as the implementation process for the dual network hypothesis. In this hypothesis, we assume that strain energy of the totally aged network in dual network hypothesis is not constant anymore and can be considered as a function of time.
- The **thermo + hydrolysis** modeling (also referred to as ‘hydrothermal’) results indicate that hygrothermal aging can be considered because of damage accumulation in two concurrent aging mechanisms, namely: (i) thermo-oxidative; and (ii) hydrolytic aging. We assumed that each of the aging phenomena can be superimposed upon each other.
- The **thermo + vibration** model, which was composed of thermo-oxidative and vibration mechanisms separately through its sub-mechanisms, were then coupled using the network alteration platform concept. Kinetic equations describing damage of each sub-mechanisms are coupled into the network alteration modular concept to allow calculation of synergies on the strain energy of the matrix.
- The proposed **machine-learned** model introduces a novel physics-informed multi-agent constitutive model to predict quasi-static constitutive behavior of cross-linked elastomer and the loss of mechanical performance during environmental aging.
- Upon the successful completion of the development and validation of the **FE implementation for Endurica** failure model, the framework will be implemented as a new module of the base Endurica durability code. Base Endurica is a commercial code that is currently used by automotive OEMs for design and reliability analysis of polymeric components.

Results

Thermo + Photo-Oxidative Degradation

The proposed model should be able to capture the constitutive behavior of polymers in both thermo- and photo-oxidative aging scenarios simultaneously. The experimental data suggests that the dual network hypothesis cannot be scaled-up to model the complexities that arise in the presence of photo-oxidative aging. Therefore, we offered the continuous network hypothesis to complement the dual network one. In this hypothesis, we assume that the strain energy of the totally aged network in the dual network hypothesis is not constant anymore and can be considered as a function of time. The rate of oxidation during aging can be expressed as:

$$-d[P]/dt = k[P]^q \quad (1)$$

where $[P]$ is the concentration of the chemical compound P , k is the reaction rate coefficient, and q is the reaction order. By assuming the homogeneous condition and abundance of oxygen throughout the matrix for the reactions to take place, k would be a function of temperature T and light intensity I . According to the Arrhenius function:

$$k = \tau I^\alpha e^{(-E_{a1})}, E_{a1} = E_a/RT. \quad (2)$$

In most polymeric systems, homogeneous cross-link formation reduces the average end-to-end chain distance across the matrix, while increasing the cross-link density. Bond scission usually induces the reverse effect.

Representing the changes in the average end-to-end chain length in un-deformed material R , one can write the normalize contribution of cross-link formation on end-to-end distance by $-R_c^*$ and that of scission by $+R_s^*$ which yields:

$$R(t) = R_0 - R_c^* [1 - \exp(-\tau_1 \exp((-E_{a2})/RT) \Gamma^\alpha)] + R_s^* [1 - \exp(-\tau_1 \exp((-E_{a2})/RT) \Gamma^\beta)], \quad (3)$$

$$R_c^* = R_c + R_{I1}, R_s^* = R_s + R_{I2}$$

where E_{a2} is the activation energy needed for photo-oxidation reactions, and R_c and R_s are relative weight factors that describe the contribution of cross-link formation and scission due to thermo-oxidation on R , respectively. R_{I1} and R_{I2} are the relative weight factors due to ultraviolet (UV) radiation. Here, α and β define the rate of each reaction due to the UV effect. Using the same concept, we define the contribution of cross-link formation and scission density $C_r(t)$ as:

$$C_r(t) = C_{r0} - C_{r_c^*} [1 - \exp(-\tau_1 \exp(-E_{a2}/RT) \Gamma^\alpha t)] + C_{r_s^*} [1 - \exp(-\tau_1 \exp(-E_{a2}/RT) \Gamma^\beta t)]. \quad (4)$$

$$C_{r_c^*} = C_{r_c} + C_{r_{I1}}, \quad C_{r_s^*} = C_{r_s} + C_{r_{I2}}.$$

Validation

So far, the evolution of an aging network within the polymer matrix has been formulated.

Experimental status: For thermo + photo-oxidative degradation, specimens were aged under UVA-340 fluorescent lamps in three temperatures (e.g., 45°C, 60°C, and 80°C), four aging durations (e.g., 24, 240, 1440, and 3600 hrs.), five reliability tests, five test types, and four compounds (i.e., one silicone, two polyurethanes, and styrene-butadiene rubber (SBR) as a control-set). The 100% pilot rubric matrix has been finished. 1200 tests should be performed (~1200 were finished). Figure II.3.3.1 shows the results of these tests.

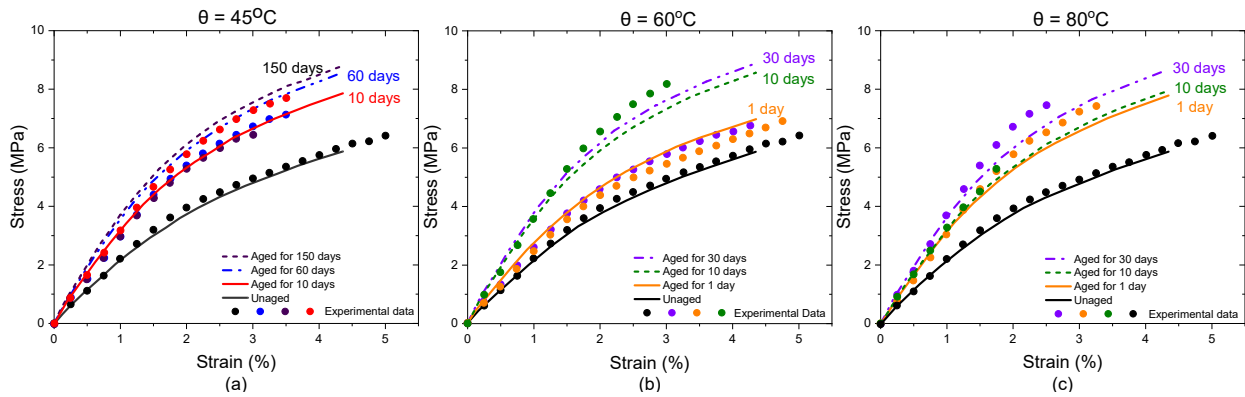


Figure II.3.3.1. The proposed model is validated through three different aging times and three different aging temperatures for black polyurethane. Source: Michigan State University.

Thermo + Hydrolysis (Hygrothermal)

Constitutive Model

The strain energy of the polymer matrix under hygrothermal condition is written with respect to three independent mechanisms: (i) the shrinking original matrix that has neither been attacked by water nor oxygen; (ii) the conversion of the first network to two new networks due to the reduction and formation of cross-links; and (iii) the energy loss from network degradation due to water attrition to polymer active agents. We defined two end-states of the material as the state-of-the-polymer matrix at the initial state, Ψ_0 , and the fully aged state at time infinity, Ψ_∞ . The end-states are considered as extreme points of aging. The strain energy of the material in all states of aging can be calculated through predefined shape functions, $N(t, T)$ and $N'(t, T)$, as:

$$\Psi_M(t, T, RH, \mathbf{F}) = N(t, T)\Psi_0 + N'(t, T)\Psi_\infty; \quad N'(t, T) = 1 - N(t, T). \quad (5)$$

where $N(t, T)$ is the shape function that represents the contribution of each initial state in the current state. In most solo aging of the polymeric systems, the evolution of the shape function can be well captured by the Arrhenius decay function:

$$N(t, T) = \exp(-\gamma \exp(-E_a/RT)t), \tag{6}$$

where γ is the underlying degradation rate, E_a is the activation energy, and R is the universal gas constant.

Based on the theory of network decomposition, we assume that the fully aged polymer matrix decomposes into two different networks; one of them resulted from the diffusion of oxygen to the polymer matrix, Ψ_t^∞ , and the second one modeled the effect of water on the polymer matrix, Ψ_h^∞ . The infinity state-of-the-polymer matrix can be written as:

$$\Psi_\infty = (1 - \beta)\Psi_t^\infty + \beta\Psi_h^\infty, (0 \leq \beta \leq 1), \tag{7}$$

where $\beta(t, T, RH)$ defines the portion of each network, which contributes to the complete aging of the polymer matrix for a certain amount of temperature and humidity. The hydrolysis Ψ_h^∞ network itself decomposes into two independent sub-networks, namely morphed Ψ_m^∞ and deactivated Ψ_d^∞ , and can be written as:

$$\Psi_h^\infty = \alpha\Psi_m^\infty + (1 - \alpha)\Psi_d^\infty, (0 \leq \alpha \leq 1), \tag{8}$$

where α depicts the contribution of each sub-microstructural phenomenon and is considered as a fitting parameter. The aging parameter, β , is a function of water absorption. We assume that the contribution of the water network in the total entropy of polymer matrix is linearly related to the amount of water in the matrix. Here, one can define the function $\beta(t, T, RH)$ as:

$$\beta(t, T, RH) = \text{erf} \left(\frac{RH}{Q} \right) \sqrt{\theta \exp[-E_b/RT]t}, \tag{9}$$

where Q and θ are adjusting parameters that keep the range of $\beta(t, T, RH)$ between 0 and 1.

Validation

Experimental status: For hygrothermal degradation, the 100% pilot rubric matrix has been finished on three temperatures (e.g., 60°C, 80°C, and 95°C), three humidity percentages (e.g., 30%, 50%, and 80%), three aging times (e.g., 24, 240, and 720 hrs), five reliability tests, five test types, and four compounds (e.g., one silicone, two polyurethanes, and SBR a as control-set). 2700 tests should be performed (~2700 were finished). Figure II.3.3.2 shows the results of these tests. We fitted our model based on unaged data and one set of temperature, humidity, and aging time. The model's prediction to experimental data is within the acceptable range (<10%).

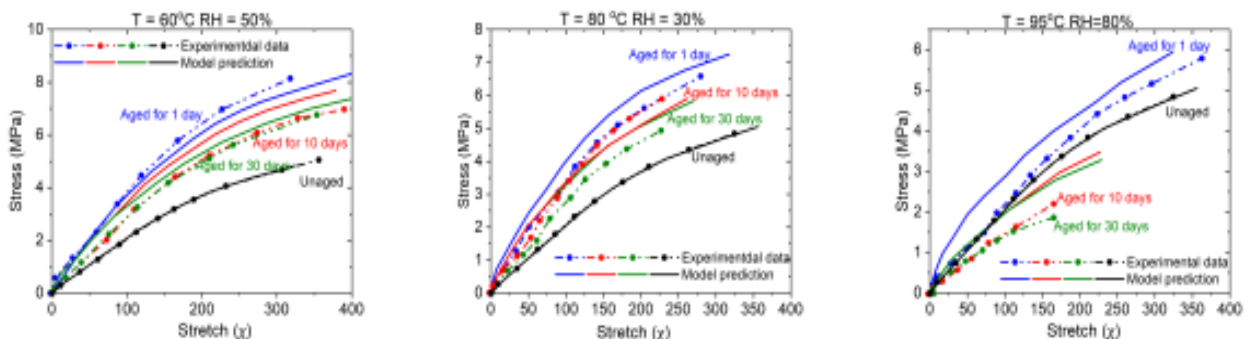


Figure II.3.3.2. The proposed model is validated against rubric of environmental conditions for black polyurethane. Source: Michigan State University.

Thermo + Vibration

Constitutive Model

The main assumption is that the mechanical and environmental aging collaborate to induced damages and consequently they can be modeled as two parallel damage mechanisms. The proposed model is a kind of modular platform to describe damage accumulation during thermo-oxidation aging and vibration-induced damages. To model the effects of thermo-oxidative aging, it is assumed that the mechanical and environmental damages are independent and as a result, they could be superposed on each other. During thermal aging, we assumed changes in the chains' density are equal to the alteration of peroxide cross-link density by:

$$\rho_{ev}^d = \rho_{\infty} - \rho_0 \exp(-\gamma \exp(-E_a/RT)t). \quad (10)$$

In the absence of environmental damages, mechanical damage leads to detachments of the weakened bonds, and consequently, results in two microstructural phenomena namely: (i) increase in the average length of the polymer chain n ; and (ii) decrease in the density of the polymer chains, ρ^d . These two phenomena are a function of maximum stretches in direction, \mathbf{d} , previously reached by the material and they can be best modeled via exponential functions. Having the evolution of chain density during environmental and mechanical damages, one can rewrite the chain density due to the accumulated damage as:

$$\rho^d = \rho_{\infty} \exp(-\mu \lambda_m^d) - \rho_0 \exp(-\gamma \exp(-E_a/RT)t - \mu \lambda_m^d). \quad (11)$$

The constitutive equation for an incompressible polymer matrix (e.g., the strain energy function) is postulated:

$$\Psi = \Psi(\mathbf{F}) - p(J - 1). \quad (12)$$

The first Piola-Kirchhoff tensor, \mathbf{P} , can be written as:

$$\mathbf{P} = K_B T \sum_{i=1}^k \rho_r^{di} \sqrt{\bar{n}^{di}} \mathcal{L}^{-1}(\lambda^{di} / \sqrt{\bar{n}^{di}}) \frac{\omega_i}{\lambda^{di}} J^{-1/3} \bar{\mathbf{F}}(\mathbf{d}^i \otimes \mathbf{d}^i) - p \mathbf{F}^{-T}. \quad (13)$$

Experimental Status: For thermo + vibration, the 100% experiments on unaged specimens finished with three reliability tests, two test types (e.g., cyclic and vibration), three compounds [i.e., SBR as a control-set, silicone (DOWSIL-7091), and polyurethane (3M-590 black)]. Furthermore, experimental characterization of aging + fatigue for the pilot adhesives in each aging environment (e.g., thermo-oxidation, hydrolysis, hygrothermal) is an extension of the vibration fatigue failure model that we used earlier for validation of the cyclic fatigue without any aging. Here we aim that environmental degradation will be coupled with mechanical fatigue damage and validated through modifications in the fatigue failure model.

Machine-Learned

Constitutive Model

The model was proposed to solve the problem of significant missing data in finite deformation constitutive behavior through a physics-driven order-reduction approach by implementing microsphere concept, network decomposition theory, continuum mechanics compatibility equations, and general rules provided by polymer physics on matrix behavior. L-agent response is computed using a feed-forward algorithm for a given set of hyper-parameters (n_l , n_n). Each L-agent can be represented by a CondNNs:

$$\mathcal{A}_j^i = \mathcal{D}^{d_i}(E^{d_i}) \psi_j^d(\mathbf{M}_j^i, S_j^i). \quad (14)$$

Environmental Damage: $\mathcal{D}_j^i = \text{CNN}_e(\mathbf{W}_e, \mathbf{E}^i)$, Mechanical Damage $\psi_j^d = \text{CNN}_m(\mathbf{W}_m^j, \mathbf{M}_j^i, S_j^i)$.

For the CondNNs structure of L-agents, we considered one input layer, one hidden layer with four neurons, and three activation functions (e.g., soft plus, sinusoid, hyperbolic tangent). Internal parameter λ_{j-max} to capture the deformation of the rubbers with full memory:

$$\mathbf{M}_1^{d_i} = [\lambda_1^{d_i}], \mathbf{S}_1^{d_i} = [\lambda_{1-max}^{d_i}], \mathbf{E}^{d_i} = [t, \theta], \mathbf{M}_2^{d_i} = [\lambda_2^{d_i}], \mathbf{S}_2^{d_i} = [\lambda_{2-max}^{d_i}], \mathbf{E}^{d_i} = [t, \theta], \quad (15)$$

where $\lambda_1^{d_i} = \sqrt{\mathbf{d}_i \mathbf{C} \mathbf{d}_i}$, $\lambda_2^{d_i} = \sqrt{\mathbf{d}_i \mathbf{C}^{-1} \mathbf{d}_i}$, $\mathbf{C} = \mathbf{F}^T \mathbf{F}$, $\lambda_1^{d_i}$, $\lambda_2^{d_i}$ are related to I_1 , I_2 , as the first and second invariants of \mathbf{C} . We used identical engines, a relatively simple engine built by $N_d = 21$ teams, where each team has $N_s = 2$ agents. The final cost function:

$$\mathcal{L}(W_m^1, W_m^2, W_e) = \frac{1}{2} \sum_{n=1} [g_1 \left(\sum_{i=1}^{21} \sum_{j=1}^2 \omega_i \frac{\partial \mathcal{A}_j^i}{\partial \mathbf{F}} - p \mathbf{F}^{-T} \right) g_1 - P_n^{11}]^2. \quad (16)$$

Validation

Figure II.3.3.3 shows the results of these tests.

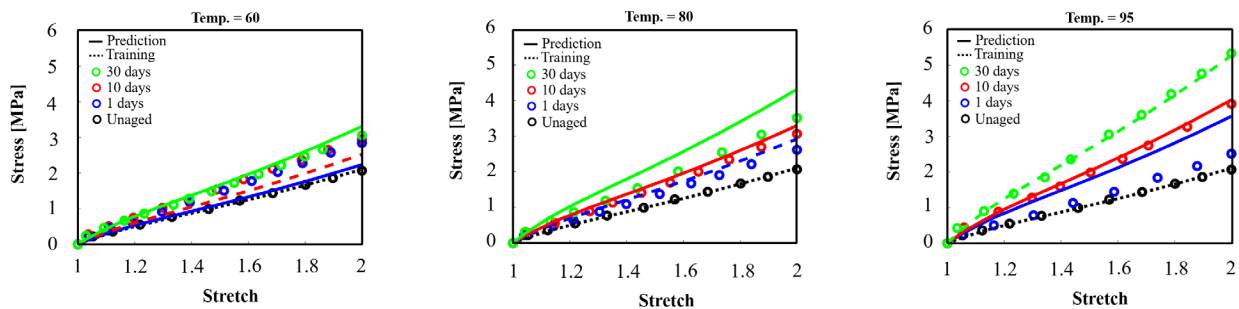


Figure II.3.3.3. Validation of proposed model on thermo-oxidative aging of black polyurethane. Source: Michigan State University.

FE Implementation for Endurica

This step involves the implementation of the user-defined mechanical material behavior subroutine (UMAT) in Abacus and software design. The Endurica suite of fatigue analysis tools currently comprise both the base fatigue solver Endurica CL and the incremental solver and co-simulation add-on Endurica DT. Both tools implement critical plane analysis. Endurica’s critical plane analysis is founded on the observation that polymer microstructures contain crack precursors that tend to grow under cyclic loading. In FY 2022, Endurica will be responsible for coupling fatigue model to the platform, software development, and reliability analysis. Endurica will also oversee the joint efforts for UMAT implementation of the hybrid framework. The additional capabilities of the project’s corrosion model will expand Endurica’s existing capabilities and will enable users to assess all aspects of durability more completely and accurately.

Conclusions

We developed an integrated experimental, computational, and analytical approach to understand and model the mechanisms of degradation in polymeric adhesives through a set of constitutive models that was supported by an extensive experimental program. This approach should provide predictive capabilities on the state of damage accumulation for cases in which degradation is induced by multiple parallel mechanical and environmental loads. The proposed platform can also provide guidance for future durability research of compounds. The micro-mechanical concepts and modeling strategies employed in this project are evolving to reflect best practices to provide the most confidence in predicted results. In view of the experimental tests provided on different adhesives, most adhesives with cross-linked networks are highly susceptible to damage when environmental loads are combined with mechanical loads.

Key Publications

1. Alazhary, S., H. Mohammadi, and R. Dargazany, 2020, “Thermo-oxidation analysis of structural adhesives: An experimental study,” In: *American Society of Mechanical Engineers International Mechanical Engineering Congress and Exposition*, Vol. 84607, pp. V012T12A003.
2. Bahrololoumi, A., V. Morovati, M. Shaafaey, and R. Dargazany, 2021, “A multiphysics approach on modeling of hygrothermal aging and its effects on constitutive behavior of cross-linked polymers,” *J. Mech. Phys. Solids*, Vol. 156, Art. 104614.
3. Morovati, V., A. Bahrololoumi, and R. Dargazany, 2021, “Fatigue-induced stress-softening in cross-linked multi-network elastomers: Effect of damage accumulation,” *Int. J. Plast.*, Vol. 142, Art. 102993.
4. Bahrololoumi, A., H. Mohammadi, V. Morovati, and R. Dargazany, 2021, “A physically-based model for thermo-oxidative and hydrolytic aging of elastomers,” *Int. J. Mech. Sci.*, Vol. 194, Art. 106193.
5. Mohammadi, H., V. Morovati, A. E. Korayem, E. Poshtan, and R. Dargazany, 2021, “Constitutive modeling of elastomers during photo-and thermo-oxidative aging,” *Polym. Degrad. Stab.*, Vol. 191, Art. 109663.

References

1. Dargazany, R., and M. Itskov, 2009, “A network evolution model for the anisotropic Mullins effect in carbon black filled rubbers,” *Int. J. Solids Struct.*, Vol. 46, No. 16, pp. 2967–2977.
2. Khalili, L., V. Morovati, R. Dargazany, and J. Lin, 2017, “Micro-mechanical modeling of visco-elastic behavior of elastomers with respect to time-dependent response of single polymer chains,” *Constitutive Models for Rubber X*, 28–31 August 2017, Munich, Germany, Vol. 10, Art. 523.
3. Mohammadi, H., and R. Dargazany, 2019, “A micro-mechanical approach to model thermo-oxidative aging in elastomers,” *Int. J. Plast.*, Vol. 118, pp. 1–16.
4. Mohammadi, H., and R. Dargazany, 2018, “Micro-mechanical model for thermo-oxidative aging of elastomers,” In: *American Society of Mechanical Engineers 2018 International Mechanical Engineering Congress and Exposition*, Art. V009T12A028–V009T12A028.
5. Carter, H. G., and K. G. Kibler, 1978, “Langmuir-type model for anomalous moisture diffusion in composite resins,” *J. Compos. Mater.*, Vol. 12, No. 2, pp. 118–131.
6. Khalilili, L., A. I. Azad, J. Lin, and R. Dargazany, 2019, “Modular platform to model parallel inelastic mechanisms in rubber-like materials,” *Rubber Chem. Technol.*, Vol. 92, No. 1, pp. 51–68.
7. Morovati, V., and R. Dargazany, 2019, “NET v1.0: A framework to simulate permanent damage in elastomers under quasi-static deformations,” *Softwarex*, Vol. 10, Art. 100229.
8. Beyer, M. K., and H. Clausen-Schaumann, 2005, “Mechanochemistry: The mechanical activation of covalent bonds,” *Chem. Rev.*, Vol. 105, No. 8, pp. 2921–2948.
9. Ishida, T., R. Kitagaki, H. Hagihara, and Y. Elakneswaran, 2020, “Challenges in prediction of significant structural changes during photochemical ‘degelation’ of acrylic-urethane network,” *Polymer*, Vol. 186, Art. 122035.
10. Gillen, K. T., and H. Kudoh, 2020, “Synergism of radiation and temperature in the degradation of a silicone elastomer,” *Polym. Degrad. Stab.*, Vol. 181, Art. 109334.

Acknowledgments

We thank Ms. S. Kleinbaum, DOE VTO Technology Manager, for her comments and suggestions on the experimentation procedure and continuous feedback, as well as Mr. J. Terneus from NETL for managing the project. This material is based on work supported by DOE-EERE under award number DE-EE0008455.

II.3.4 High-Strength Steel-Aluminum Components by Vaporizing Foil Actuator Welding (The Ohio State University)

Glenn Daehn, Co-Principal Investigator

Department of Materials Science and Engineering
The Ohio State University
295 Watts Hall
2041 College Road North
Columbus, OH 43210
E-mail: daehn.1@osu.edu

Anupam Vivek, Co-Principal Investigator

Department of Materials Science and Engineering
The Ohio State University
348 MacQuigg Labs
105 West Woodruff Avenue
Columbus, OH 43210
E-mail: vivek.4@osu.edu

Sarah Kleinbaum, DOE Program Manager

U.S. Department of Energy
E-mail: sarah.kleinbaum@ee.doe.gov

Start Date: October 1, 2016	End Date: April 30, 2021	
Project Funding (FY 2021): \$289,948	DOE share: \$4,702	Non-DOE share: \$285,246

Project Introduction

This project aims to address the challenge of effectively welding dissimilar materials—high-strength steel and high-strength Al—for creating lightweight, multi-material automotive components. Traditional fusion-based welding between dissimilar combinations of Al and steel is difficult due to starkly disparate melting points and usually leads to the formation of brittle intermetallic compounds at the weld interface. Such joints are weak and cannot be implemented in crash-sensitive components. Structural adhesives and mechanical fasteners of various types including self-piercing rivets, flow-drilled screws, friction element welds, and RIVTAC® are currently being utilized to address this issue. Solid-state welding techniques, like friction stir and impact welding, offer an elegant alternative solution for joining dissimilar metals without the use of a third body, such as rivets. This project utilizes Vaporizing Foil Actuator Welding (VFAW), an impact welding method developed at The OSU [1]. Details on this process can be found in the Materials 2017, 2018, 2019, and 2020 Annual Progress Reports [2–5], as well as several journal articles published on this technology.

VFAW has demonstrated much success in welding a wide range of alloys, including Mg-Al, Al-Cu, Ti-Cu, bulk metallic glass-Cu, and Ni-Ti. In this project, the focus is on welding specific grades of steel and Al that are relevant to automotive subframes and developing the technology to a level at which it can be transitioned to an automotive supplier or an OEM. Besides the research on weldability of different material combinations and determination of ideal parameters through experiment and simulation, the project also includes design, production, and testing of a prototype subframe component, as well as production equipment. Robustness of the process for application in a serial production setting is demonstrated via robotic implementation.

Fully automated VFAW joints were achieved with the automation work cell. Construction, assembling, testing, and optimizing of the prototype weld head was complete. The work in FY 2021 was focused on the production

of prototype subcomponents with the equipment developed in the previous years. Two sets of engine cradles were complete and are currently under characterization and testing at Magna. More sets of engine cradles were planned for production at OSU.

Objectives

This project accelerated and focused the development of VFAW to produce an automotive component. At project completion, the technology will be ready for adoption within the R&D groups of Tier 1 and OEMs for assembly of mixed, advanced material bodies.

The overall objectives of the project are:

- A 20% weight-reduction of the current all-steel automotive component from a 2017 mid-size sedan at a cost premium of \$3/lb-saved by developing a mixed material joining technology capable of high-volume production.
- The produced component that meets or exceeds the strength and durability of the incumbent component.
- To develop a predictive modeling capability for relating the process, structure, and properties of VFAW joints.

The specific objectives for FY 2021 were:

- To produce prototype Al-steel engine cradles using the weld head that meets automotive performance objectives of strength, durability in corrosion, durability in fatigue, and stiffness.
- To evaluate the quality and performance of the VFAW engine cradle products via subcomponent-level testing and characterization.

Approach

The overall approach for this project is to perform coupon scale testing at OSU, develop welding systems and part fixtures at OSU and Coldwater, prototype-scale manufacture and testing at Magna, and process simulation at PNNL. Ashland, Arconic, Hydro, Novelis, and Magna are providing material. The pre-prototype welding heads and final welding head were fabricated at Coldwater and tested at OSU. Coupon data were imported into the design of the prototype component, while simulated testing and design iterations will lead to the final part. After the prototype design was released, OSU produced subcomponents and Magna will perform the assembly at its prototype facility. The assembled prototypes will be tested for durability and corrosion performance at Magna.

Coupon Testing

The Al-steel combination was finalized as hot-rolled 4-mm to 5-mm-thick 5xxx Al alloys and 2-mm to 3-mm-thick high-strength low alloy (HSLA) 340, based on the screening results in FY 2017 and FY 2018 and actual material inventory at Magna's material supplier, Novelis. For this project, VFAW requires a 1-mm-thick AA3003-H14 intermediate layer (interlayer). Standoff gaps between the interlayer and target were provided by dimpling the target sheet. Geometry of the pre-formed dimples was finalized based on the trials conducted to generate the strength and durability data used in the prototype design simulation. As the final welding parameters, two welds are required to create a weld: the first joins the interlayer with the pre-deformed target, as shown schematically in Figure II.3.4.1(a), while the second joins the Al flyer to the target at the pre-welded interlayer as shown schematically in Figure II.3.4.1(a).

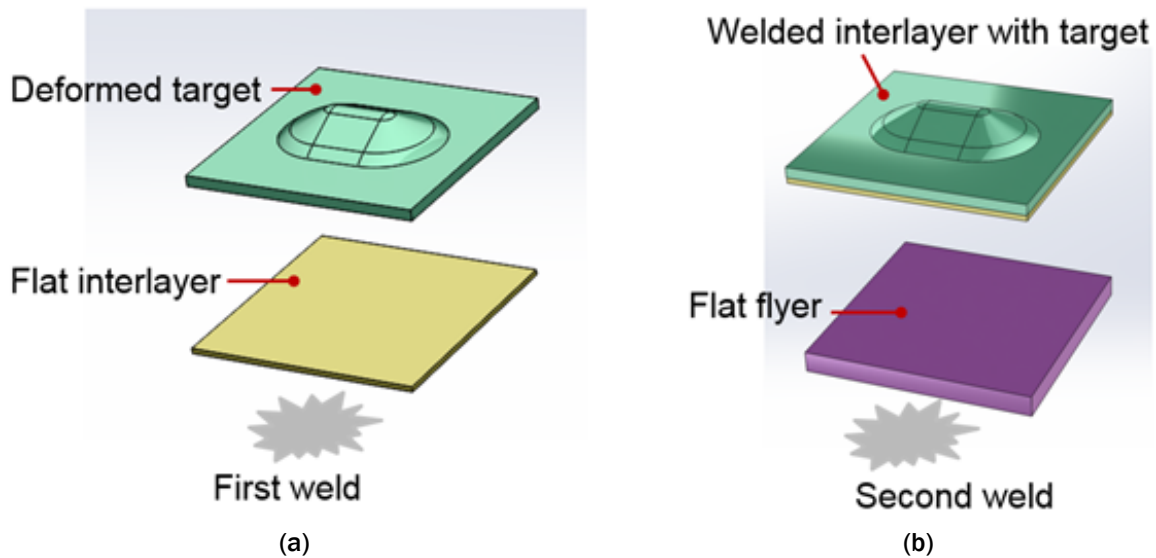


Figure II.3.4.1. Illustrations of the two-shot VFAW showing: (a) the first shot welds the flat interlayer to the deformed target; and (b) the second shot welds the flyer to the welded flyer-target stack-up.
Source: The Ohio State University.

Prototype Weld Head Test

The prototype weld head was designed and “pre”-prototyped in FY 2019, and constructed, assembled, tested, and optimized in FY 2020, and shown in Figure II.3.4.2(a). Installed at OSU, the weld head was validated and optimized through coupon welding tests, as shown in Figure II.3.4.2(b). Lap-shear tests were performed to determine the weld quality. Current and voltage trace during welding was acquired using an oscilloscope as the reference system parameters. A noise resisting chamber was constructed for the prototype weld head test.

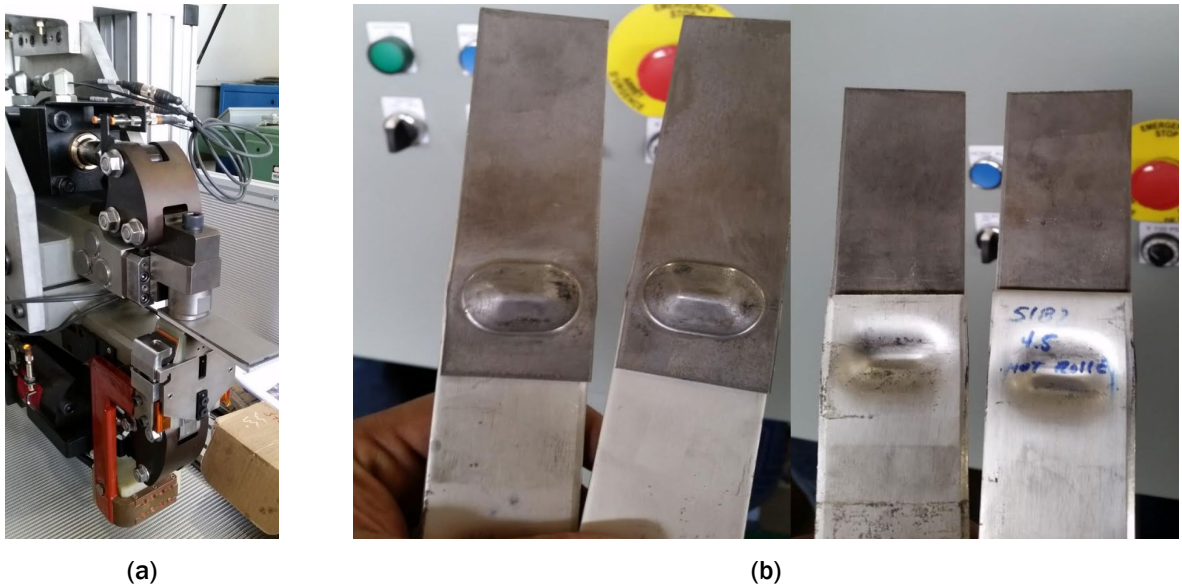


Figure II.3.4.2. Prototype weld head test: (a) the fixture during welding; and (b) the AA 5183-HSLA340 coupon welds created by the system. Source: The Ohio State University.

Development of Automation Work Cell

The automation work cell was complete in FY 2020, as shown in Figure II.3.4.3. Fully automated VFAW joints of 1-mm-thick AA5052 and 1-mm-thick dual-phase (DP) 590 steel coupons were created using the automation work cell including hybrid samples with automated epoxy adhesive dispersion and VFAW only samples. Lap-shear tests were performed to validate the VFAW automation process.

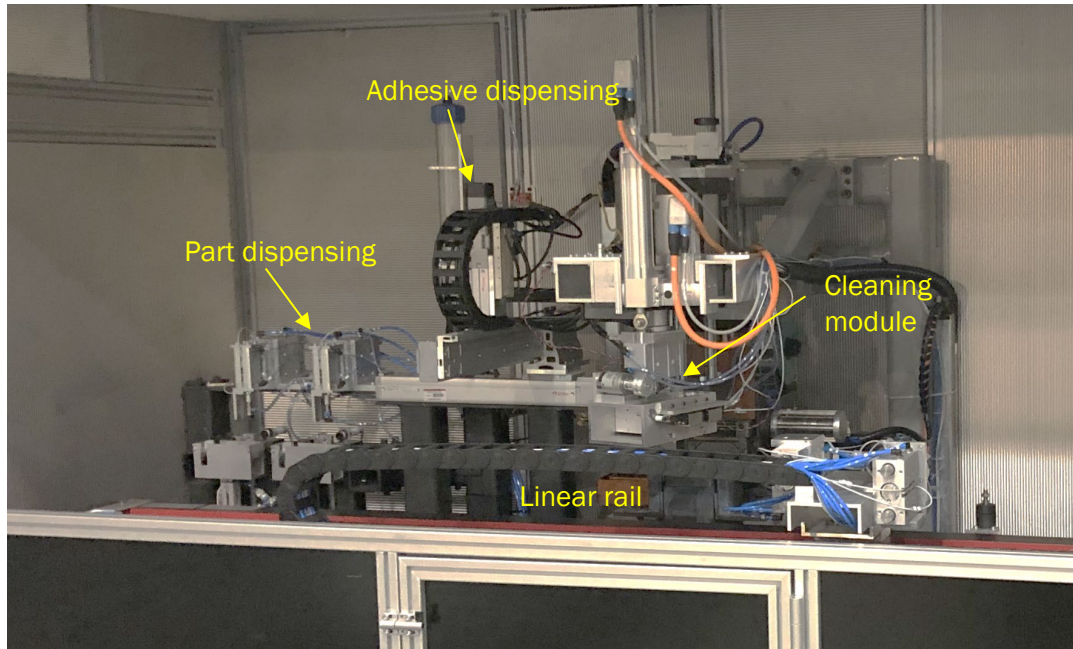


Figure II.3.4.3. Pedestal welder with automated part handling, adhesive dispense, and cleaning.
Source: The Ohio State University.

Upgrade of Capacitor Bank-Prototype Weld Head System

Interference on the communication signal from the PLC to the HMI was detected and characterization using voltage probe and oscilloscope indicated it was caused by induced electromagnetic field at discharge. Mitigation approaches including adding extra electric components to shield or counteract the induced field were developed. Arcing issues inside the system were also detected. Analysis and redesign of the related components of the weld head were performed accordingly.

Prototype Production of Engine Cradles

Using the developed prototype welding head, Al-steel prototype engine cradles were produced. Figure II.3.4.4(a) shows joining interlayers to steel parts during the first batch and Figure II.3.4.4(b) joining the Al part to the steel part during the second batch. Trace of discharge current was monitored by an oscilloscope during the welding process to ensure the weld quality. To better apply VFAW into the production, subassembly fixturing was planned. The VFAW production was divided into three batches: (1) all the interlayer welds, (2) part of the Al-steel welds joining the subcomponents, and (3) the rest of the Al-steel welds. The subassembly fixturing was performed by Magna before the production of each batch.

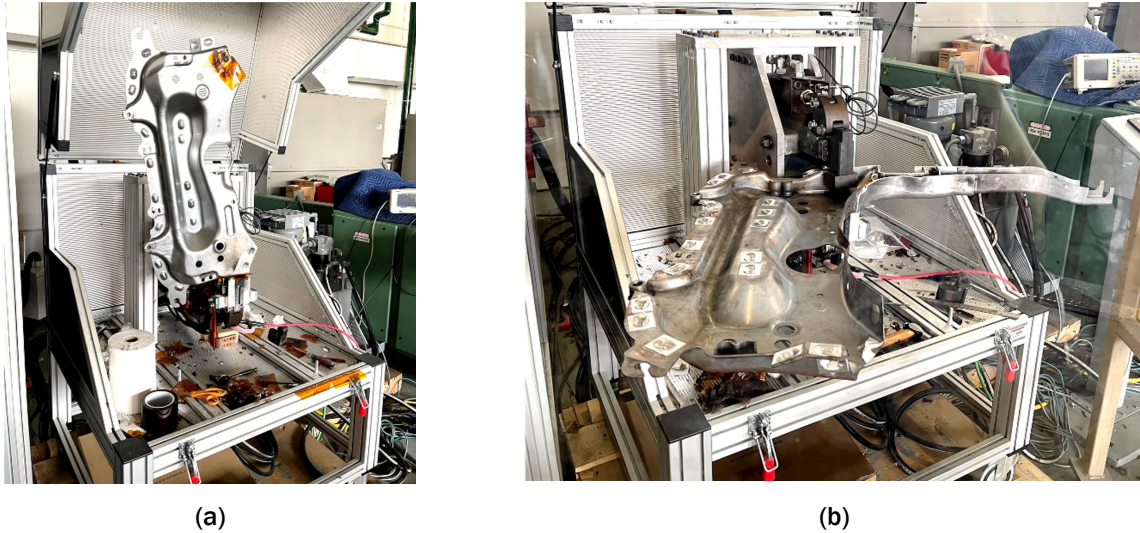


Figure II.3.4.4. Robotic prototype system: (a) a schematic of VFAW prototype production showing a 4.2kJ capacitor bank, robotic arm, prototype welding head, prototype components, and fixture table; (b) procured KUKA 6-axis welding robot; and (c) a holding fixture. Source: The Ohio State University

Results

COVID-19 Impacts

The testing of the prototype welding tool, described next, was delayed due to COVID-19 related shutdowns in March 2020. Testing resumed at OSU in July 2020 and the overall project has been given a no-cost extension of six months to complete the remaining tasks of prototype production, testing, and cost analysis.

Upgrade of Capacitor Bank-Prototype Weld Head System

The interference on the communication signal from the PLC to the HMI was solved. With the oscilloscope, a voltage spike around 100 V was detected in the communication signals between the PLC and the HMI at discharge. The voltage spike was caused by a ground loop and electromagnetic field induced by high-amplitude current. The spike proved to be damaging for the control system. To diminish the voltage spike, various approaches were tested including additional wire shielding, optical isolator, surge protection port, etc. An RS232 optical isolator was finalized as the solution with the spike decreased to around 40 V.

The arcing issues in the system were solved. Three locations where most of the arcing occurred, shown in Figure II.3.4.5, were redesigned: (1) the terminal connection to the coaxial cable was redesigned as shown in Figure II.3.4.5(a); (2) the hot bus bar area where there are lots of close edges of the bar and anvil was resolved by creating extra space in between by separating them with an extra G10 piece, as shown in Figure II.3.4.5(b); and (3) the fasteners of the terminals on the welding head where the two through holes caused arcing from the hot copper terminal to the anvil and the copper bar to the metal screw was solved by adding space with rubber O-rings, thicker G10 fiberglass sheets, and Teflon blocks, as shown in Figure II.3.4.5(c). The system thus modified proved to be robust and functional for VFA welding.

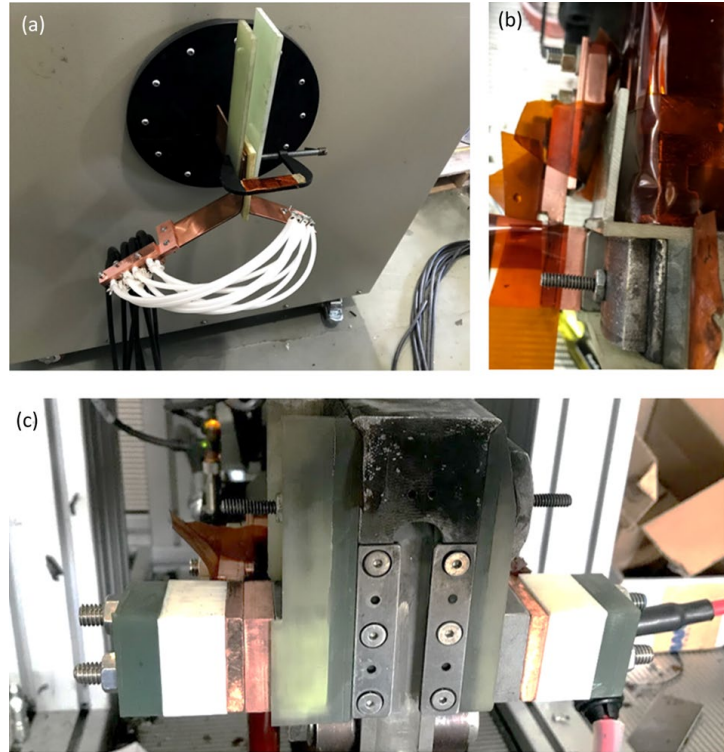


Figure II.3.4.5. Regions of arcing issues and redesign solutions: (a) the terminal connection to the coaxial cable; (b) the hot bus bar area where there are lots of close edges of the bar and the anvil; and (c) the terminals on the welding head where the two through holes caused arcing from the hot copper terminal to the anvil and copper bar to the metal screw. Source: The Ohio State University.

Prototype Production of Engine Cradles

The VFAW prototype production of two sets of engine cradles are complete. The front and back sides are shown in Figure II.3.4.6(a) and Figure II.3.4.6(b), respectively. Each cradle contains 56 VFA welds. The parts were sent to Magna for further characterization and testing. More engine cradle sets are in production at OSU.

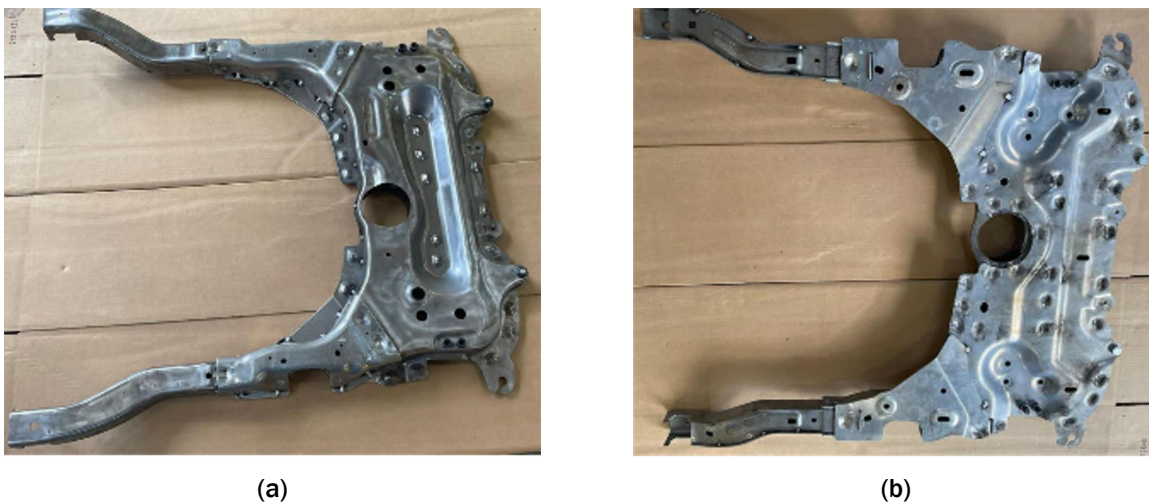


Figure II.3.4.6. VFA-welded thick 5000 series Al coupon with HSLA 340 subcomponents: (a) steel side shows no damage; and (b) Al side shows successful welds of first weld (yellow) and second weld (blue). Source: The Ohio State University.

Conclusions

With the upgraded system, VFAW prototype production was achieved. The prototype components are undergoing mechanical testing for comparison with baseline performance of an all-steel component.

Key Publications

1. Thurston, B. P., A. Vivek, B. S. Nirudhoddi, and G. S. Daehn, 2019, “Vaporizing foil actuator welding,” *MRS Bull.*, Vol. 44, No. 8, pp. 637–642.
2. Sridharan, N., J. Poplawsky, A. Vivek, A. Bhattacharya, W. Guo, H. Meyer, Y. Mao, T. Lee, and G. S. Daehn, 2019, “Cascading microstructures in Al-steel interfaces created by impact welding.” *Mater. Charact.*, Vol. 151, pp. 119–128.
3. Gupta, V., T. Lee, A. Vivek, K. S. Choi, Y. Mao, and X. Sun, 2019, “A robust process-structure model for predicting the joint interface structure in impact welding,” *J. Mater. Process. Tech.*, Vol. 264, pp. 107–118.
4. Mao, Y., V. Gupta, B. Ufferman, A. Vivek, K. S. Choi, X. Sun, and G. S. Daehn, 2018, “On process, structure, property relationships in impact welding of Aluminum 6061 and Steel 4130,” *Eighth International Conference on High-Speed Forming*, 14–15 May 2018, Columbus, OH, USA.
5. Gupta, V., X. Sun, K. Choi, A. Vivek, Y. Mao, and G. Daehn. 2017, “A computational modeling approach to predict the interfacial characteristics obtained in high velocity impact welding of metals,” *Materials Science & Technology 2017*, 8–12 October 2017, Pittsburgh, PA, USA.
6. Gupta, V., K. Choi, A. Vivek, Y. Mao, X. Sun, and G. Daehn, 2018, “Prediction of joint properties obtained in the high velocity impact welding of dissimilar metals,” *TMS 2018 Annual Meeting & Exhibition*, 11–15 March 2018, Phoenix, AZ, USA.

References

1. Vivek, A., S. R. Hansen, B. C. Liu, and G. S. Daehn, 2013, “Vaporizing foil actuator: A tool for collision welding,” *J. Mater. Process. Tech.*, Vol. 213, No. 12, pp. 2304–2311.
2. DOE-EERE Vehicle Technologies Office, 2018, “Materials 2017 Annual Progress Report,” DOE-EERE VTO Report No. DOE/EE-1711, May 2018.
3. DOE-EERE Vehicle Technologies Office, 2019, “Materials 2018 Annual Progress Report,” DOE-EERE VTO Report No. DOE/EE-1827, April 2019.
4. DOE-EERE Vehicle Technologies Office, 2020, “Materials 2019 Annual Progress Report,” DOE-EERE VTO Report No. DOE/EE-1990, April 2020.
5. DOE-EERE Vehicle Technologies Office, 2021, “Materials 2020 Annual Progress Report,” DOE-EERE VTO Report No. DOE/EE-2336, April 2021.

II.3.5 Machine-Learning for Automated Weld Quality Monitoring and Control - Joining Core Program (Oak Ridge National Laboratory)

Zhili Feng, Co-Principal Investigator

Oak Ridge National Laboratory
1 Bethel Valley Road
Oak Ridge, TN 37831
E-mail: fengz@ornl.gov

Keerti Sahithi Kappagantula, Co-Principal Investigator

Pacific Northwest National Laboratory
908 Battelle Boulevard
Richland, WA 99352
E-mail: keertisahithi.kappagantula@pnnl.gov

Blair Carlson, Co-Principal Investigator

General Motors LLC
30500 Mound Road
Warren, MI 48090
E-mail: blair.carlson@gm.com

Sarah Kleinbaum, DOE Program Manager

U.S. Department of Energy
E-mail: sarah.kleinbaum@ee.doe.gov

Start Date: October 1, 2020 End Date: September 30, 2021
Project Funding (FY 2021): \$600,000 DOE share: \$600,000 Non-DOE share: \$0

Project Introduction

The use of lightweight material combinations has been highly demanded in manufacturing automotive structures. However, making robust dissimilar material joints of such lightweight materials is still challenging. A significant barrier to achieving high-quality and repeatable joint performance is a deficient understanding of the relationship between the welding process, joint attributes, and joint performance. In this context, welding factors refer to material, equipment, environment, and process parameters, while joint features comprise specific microstructural attributes of the weld such as (but not limited to) nugget size, HAZ topology, intermetallic layer thickness, and sheet thickness reduction. Joint performance is quantified in terms of strength (e.g., tensile shear, coach peel, cross-tension), weld size, and hardness, among other factors. While there have been many attempts to establish this process-structure-property relationship by developing a model derived from the associated physics and first principles, the complexity of the joining processes compounded by the complex interactions with different materials, in the context of an automotive assembly line environment, has hindered the usefulness of such attempts. The complexity is further exacerbated by the use of different stacking materials, especially comprising dissimilar material combinations. In practice, the common approach has been the laborious process of creating welds, characterizing them, and then physically testing them through the design of experiments.

With the emergence of AI methods, an alternative pathway to eliciting the desired process-structure-property relationship at an accelerated pace is to use a data-driven approach by employing ML techniques. This approach is benefited by the availability of large streams of data, generated through years of research and testing by OEMs, in the form of material, process, environmental, equipment, microstructural, and bulk-scale

performance information from multimodal, multiscale sensors making measurements from laboratory-scale to production-scale processes.

Objectives

In this project, we will develop and apply a ML/AI-based program to analyze in-line and post-processed joint data from existing and novel sensor streams to achieve automated weld quality monitoring and control.

Specific goals include:

1. The identification of data streams with the greatest impact on joint performance by developing a data-driven understanding of process/structure/property associations.
2. Translation of ML/AI tools from a test case to parallel configurations/materials/processes using generalized learning methodologies.
3. Application of control programs to maintain process parameters within optimal limits for manufacturing joints with desired performance.

Approach

Project objectives will be achieved by demonstrating the application of a suite of ML and AI tools to analyze in-line and post-processed joint data for manufacturing assemblies with optimal performance. Joints manufactured by RSW of Al alloy sheets to different types of steels will be evaluated for applications in automotive manufacturing. Data being assessed, as well as the performance targets, were provided by GM, the industry partner of the project. The large dataset from GM covers a wide range of welding data associated with Al and steel resistance spot welded joints, comprised of material specifications, welding process parameters such as voltage, current, pressure, and duration; microstructural features such as hardness, interface topology, and IMC; and bulk performance in terms of peak load, elongation, and energy under different loading/mechanical testing conditions (e.g., coach peel, lap-shear, cross-tension tests). Figure II.3.5.1 summarizes the weld data in terms of different materials, thicknesses, and surface treatments.

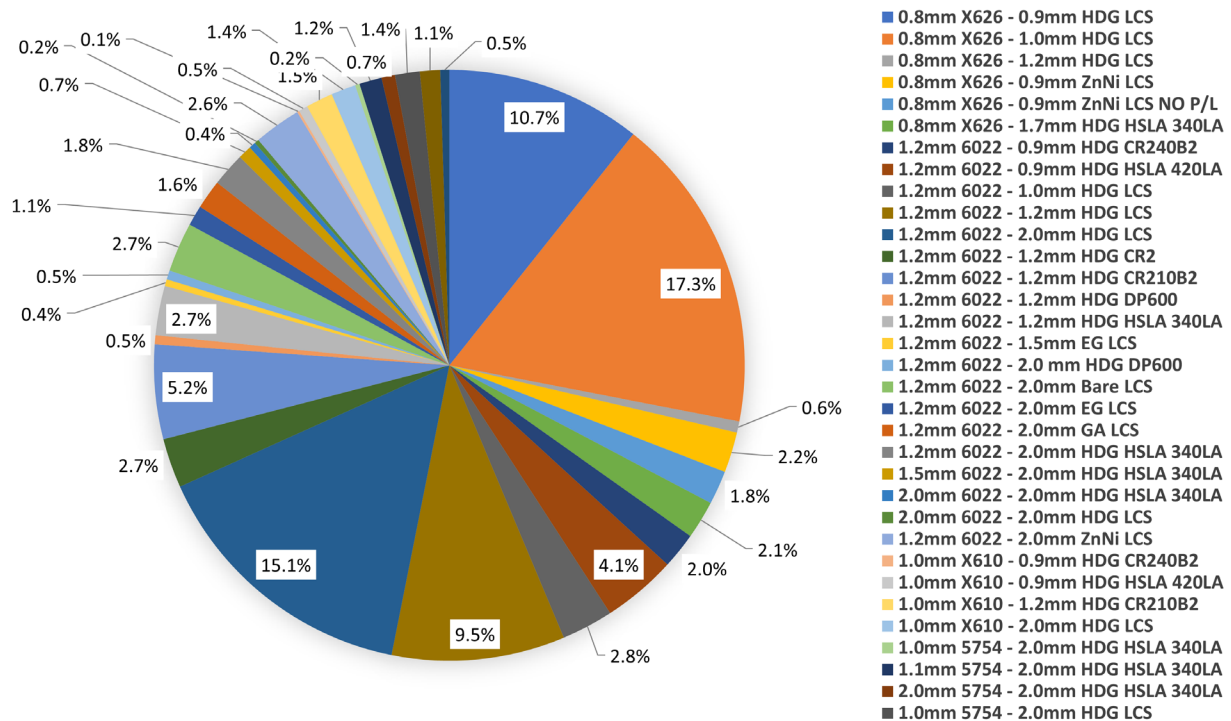


Figure II.3.5.1. Summary of 2T weld stack-ups in terms of materials, thicknesses, and surface treatments. Source: ORNL.

Two different ML approaches are explored to establish associations among process parameters, weld attributes, and weld performance, as shown in Figure II.3.5.2. PNNL focused on establishing the process parameter and property correlations in Approach-I, while ORNL focused on establishing weld attribute and joint performance relationships, as well as the weld process-attribute-performance property relationships, in Approach-II. This will lead to the construction of a cohesive model in the next phase of the project, from the two different sets of findings from the two National Laboratories collated with literature and physics-based model predictions. Finally, we predict the process conditions for making optimized RSW samples per GM's performance metrics using the cohesive set of findings.

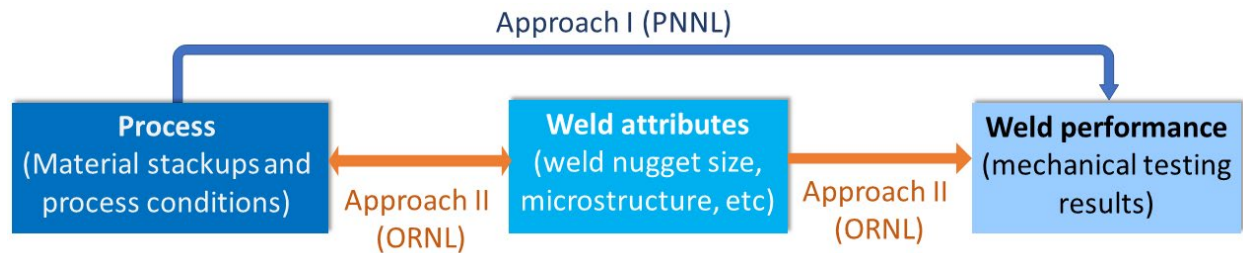


Figure II.3.5.2. Two approaches to establish associations among process parameters, weld attributes, and weld performance. Source: PNNL/ORNL.

Results

Date Collection, Preparation and Standardization for ML (ORNL, PNNL, GM)

The first step of the project was to standardize and transform the experimental forensic data provided by GM into readable formats for ML through knowledge-guided quality assurance, quality control, and normalization. To this end, the data was labeled with identified independent variables (i.e., weld process parameters for PNNL and weld attributes for ORNL) and dependent variables (i.e., weld mechanical performance properties under lap-shear, coach peel, and cross-tension). Data acquisition, arrangement, and spreadsheet creation was done using Microsoft Excel, R, and Python software. Process parameters were split into 41 columns of data streams corresponding to 41 distinct predictors. The independent data streams that were analyzed include an RSW sample ID corresponding with the different experiments, different preheating and RSW welding stages, cathode- and anode-facing material thickness, material coating, and bake conditions. Performance data was in the form of coach peel test metrics, such as peak load, extension during loading, and total energy. Following data labeling, the subset of AA6022/LCS and X626 Al/LCS joints provided the greatest number of data points.

Deep Neural Networks Approach for Weld Attributes-Performance Relationship (ORNL)

ORNL employed deep neural networks (DNNs) to mathematically explore the relationship between weld attributes and mechanical performance of the RSW joints. The weld attributes, including nugget size, button sizes, material indentation, expulsion, IMC, and hardness formed during RSW, together with the weld conditions (e.g., bake, adhesive, aging), materials (e.g., type and thickness of Al and steel alloys), and coupon geometry, were adopted as independent data streams in the form of input data to the ML model. The dependent variables (e.g., the output/prediction from ML model) included the peak load, extension at break, and the total energy observed during the cross-peel test, in the triple-object DNN model. The design of the DNN model architecture was guided by the welding physics knowledge to properly handle cases such as weld stack-ups of various materials, thicknesses, and weld conditions, etc. Consistent with PNNL's effort, two subsets of data comprising AA6022/LCS and X626/LCS joints were selected for the *initial* DNN model development. The DNN model was then progressively expanded to cover ~60% of the dataset from GM, which included 12 additional weld stack-ups of various material combinations. The architecture of DNNs was optimized regarding the model accuracy, efficiency, trainability, and understandability. The DNN model was trained ten times with different random splits of data, while the maximum number of epoch iterations for each ML training was 1000 which was found to be adequate to determine the best prediction performance. The training process of NNs was conducted using Pytorch [1].

Accuracy of ML Model (ORNL)

Figure II.3.5.3(a) summarizes the material combinations analyzed in FY 2021 where HDG is hot-dip galvanized, HSLA is high-strength low alloy, EG is electro-galvanized, and GA is galvanized. The box plots in Figure II.3.5.3(b)-(d) show the distribution of error of prediction (EoP) (calculated by $(\hat{y}_i - y_i)/y_i$, where y_i is the measured value, and \hat{y}_i is the predicted value) for joint mechanical performance of peak load, extension at break, and total energy for the 15 analyzed weld stack-ups, respectively. Note each weld stack-up contains tens or hundreds of welds that were fabricated through different welding processes. For training the ML model, the transformed datasets were randomly categorized into training and validation testing, with the ratio of 8:2 for training:testing. The box plot is constructed of a box (drawn between first and third quartiles of the dataset) and a set of whiskers (minimum and maximum of the dataset without outliers). The spacings between the different parts of the box indicate the degree of skewness in the data. For ease of understanding, the distribution of individual prediction is plotted together with the box plot for EoP of peak load in Figure II.3.5.3, showing that ML prediction results follow the Gaussian distribution with ~50% population of dataset within 5% EoP and gradually reduced population when the EoP increases. The narrow box of EoP for peak load, extension at break, and total energy indicates that ML prediction yields good accuracy with most of the population located around the median of near-zero EoP. The mean absolute accuracy for peak load, extension at break, and total energy is calculated as 90.0%, 86.2%, and 80.6% for training, and the DNN model keeps good accuracy of 89.4%, 85.9%, and 77.7% for peak load, extension at break, and total energy, when the ML model was generalized to the unseen validation testing dataset. The consistent accuracy between training and validation testing indicates that the DNN architecture in this project is appropriately designed with neither overfitting nor underfitting of GM's provided experimental data. The EoP for total energy shows wider dispersion than that of peak load and extension at the break, which was mainly attributed to the presence of extremely low total energy (e.g., < 0.01 J) in some welds failed by interfacial failure.

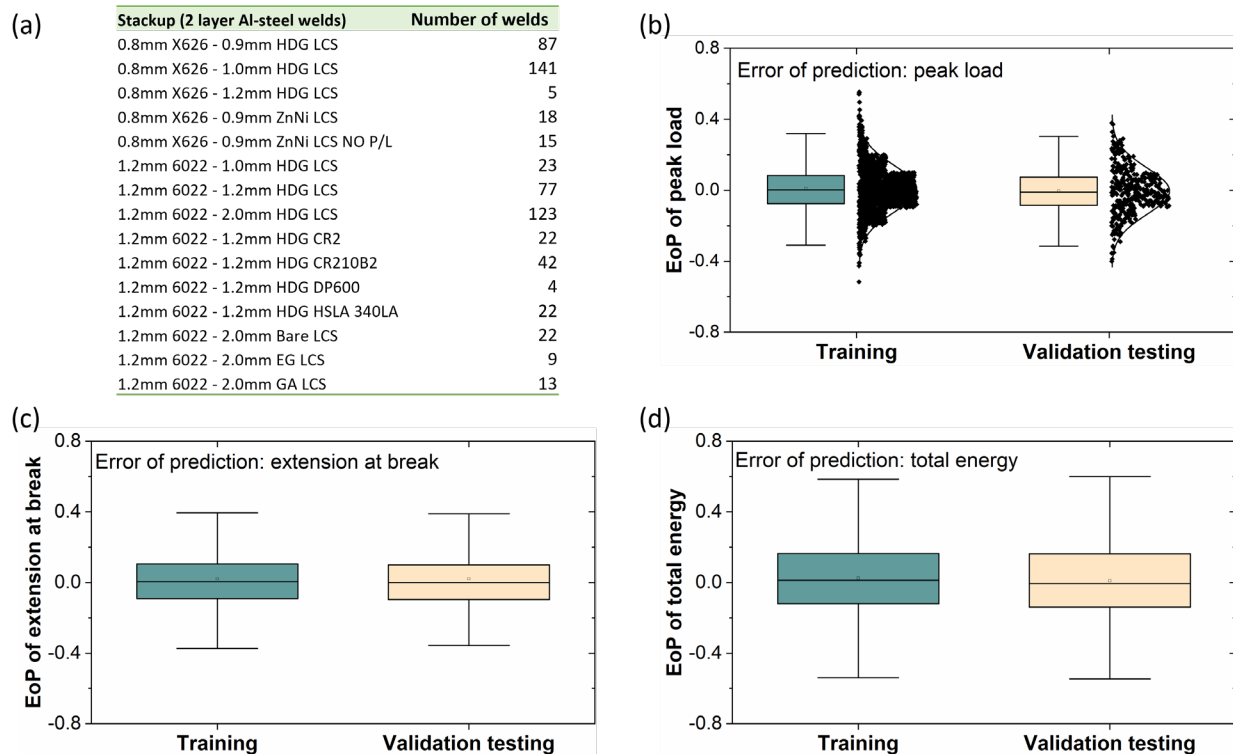


Figure II.3.5.3. (a) Summary sheet showing the GM weld stack-ups analyzed by the unified ML model, and box plots of (b), (c), and (d) showing the EoP for weld mechanical performance of peak load, extension at break, and total energy, respectively, of both training and validation testing. Source: ORNL.

Figure II.3.5.4 shows the regression analysis between the measured and ML predicted results of mean peak load, extension at break, and total energy for each individual weld in different weld stack-ups for the validation testing results only. The measured and predicted values are located around the perfect prediction line (i.e., $y=x$) in a scattered manner. Pearson’s correlation coefficients between the measured and predicted peak load, extension at break, and total energy are 0.964, 0.948, and 0.945, respectively. The high correlation coefficients suggest that there is a strong relationship between measured and predicted results, that is, the ML model with the DNNs architecture constructed in this project is capable to identify the high-dimensional correlations among the welds attributes and performance of RSW joints. It is important to note that the ML model learns the nature of interfacial failed welds and yields the similar trend prediction of low total energy.

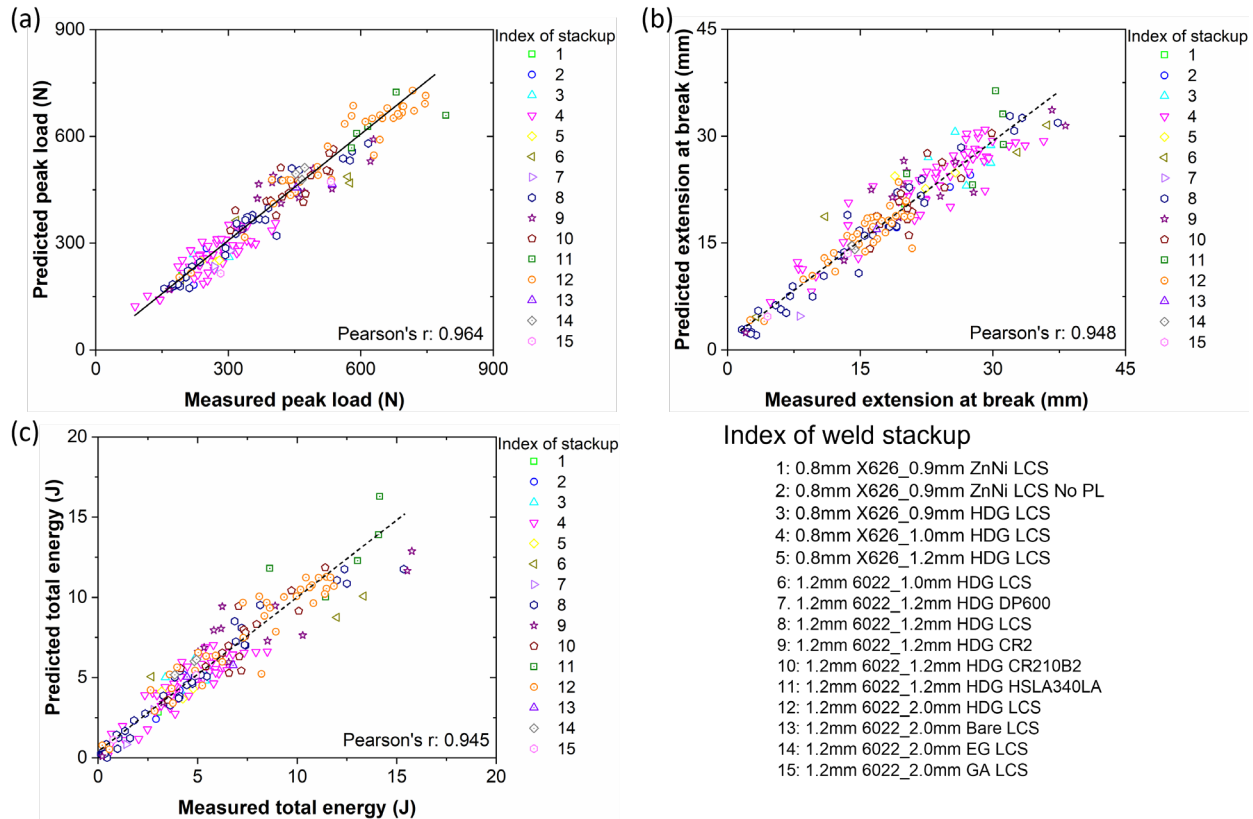


Figure II.3.5.4. Validation testing results of ML prediction in comparison with experiment measurement for the mean value of (a) peak load, (b) extension at break, and (c) total energy, respectively, for each individual weld in the 15 analyzed GM's weld stack-ups. The high-value of Pearson's correlation coefficient for peak load, extension at break, and total energy indicates the DNN model learns the high-dimensional correlations between weld attributes and weld performance. Source: ORNL.

The comparison between measured and ML predicted mechanical performances in terms of mean value and standard deviation for each weld stack-up is presented in Figure II.3.5.5 for the validation testing results only. The plot shows the direct comparison of mechanical performances for different weld stack-ups. The weld stack-up made with 1.2-mm 6022 Al with 1.2-mm HDG HSLA 340LA exhibits the combination of the highest peak load, extension at break, and total energy, while those made by 0.8mm X626 Al and LCS show the lowest peak load and total energy. The ML prediction results capture the variation of mechanical performances for different weld stack-ups in terms of both mean value and standard deviation. Conversely, the ML prediction for the stack-up of 1.2-mm 6022 Al with 1.0-mm steel showed relatively larger error, which was attributed mainly to the limited number of welds, with only eight welds available from GM with both mechanical and metallurgical measurements. Still, the smaller error bars for the ML model also means that the model is capable to predict the measured value with good confidence. Note that the ML model developed so

far has focused on connecting the weld performance properties (e.g., strength, extension, energy) to the weld attributes (e.g., weld nugget size, intermetallic layer, weld expulsion, etc.). Their association to weld process parameters (e.g., weld schedule, electrode features, clamp load, etc.) will be established in the next phase of research at ORNL.

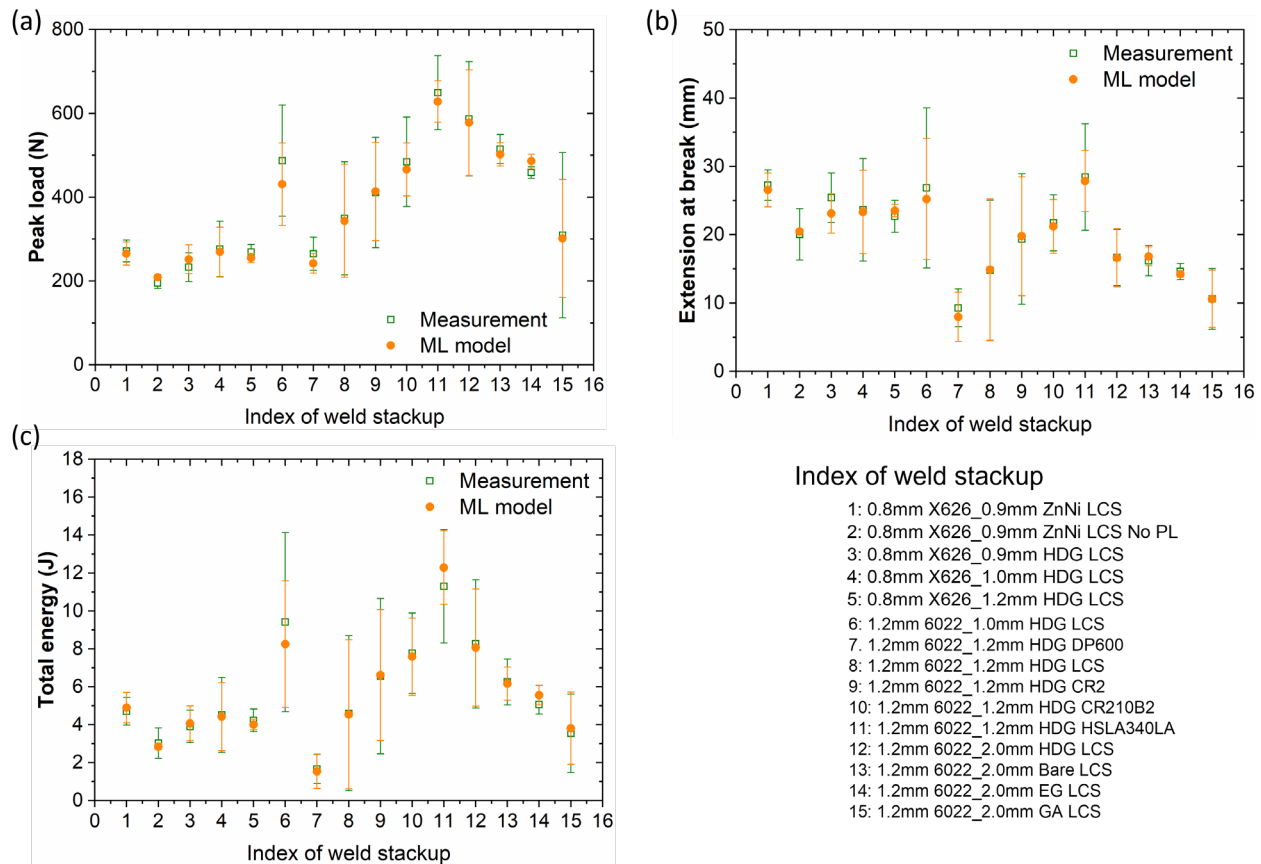


Figure II.3.5.5. Validation testing results of ML prediction in comparison with experiment measurement for mean value and standard deviation of (a) peak load, (b) extension at break, and (c) total energy, respectively, for GM's 15 weld stack-ups. Source: ORNL.

'Unknowns' revealed by ML Model

Our DNNs-based ML model has been developed and extensively trained based on ~60% of the GM-provided dataset of Al-steel dissimilar resistance spot welds. The predictive capability has been demonstrated through generalization to the unseen validation testing dataset. With the extensive training and testing, the ML model identifies several interesting findings, which have puzzled the welding community.

Effect of Adhesive on Weld Performance: It has been reported that more desirable joint performance could be produced by joule heat and an adhesive layer acting simultaneously in RSW of two steel sheets, since adding adhesive into the interfaces can lead to the increase of contact resistance and nugget size [1–3]. A similar argument has been made for RSW of dissimilar materials of Al and steel alloys. Interestingly, the extensively trained ML model reveals a contrary phenomenon that the adhesive leads to reduced peak load when a weld is not baked (NBK), as is shown in Figure II.3.5.6. Note that the conclusion was drawn based on the welds of the same material combination and fabricated through the same welding process, where the only difference is with/without the adhesive. The physical mechanism responsible for the “puzzling” effect of the adhesive on the mechanical performance needs to be further investigated via coupling ML and experimental study of dissimilar RSWs of steel with Al alloys and other lightweight materials.

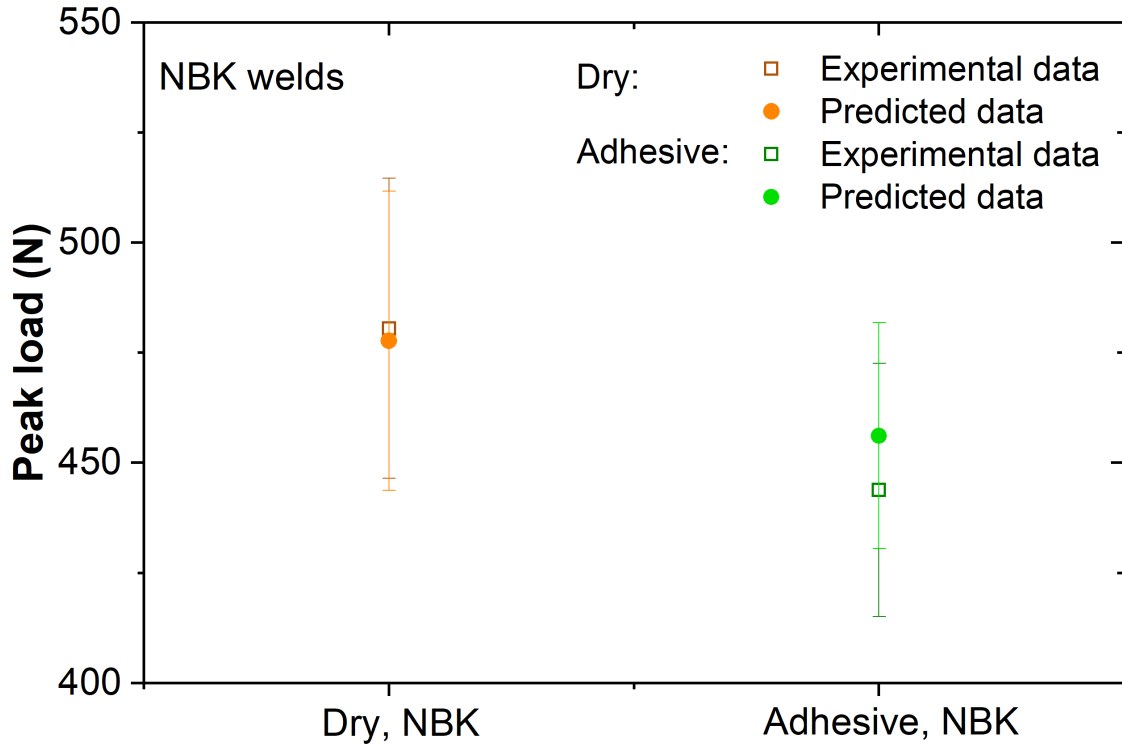


Figure II.3.5.6. The ML model reveals that the adhesive leads to reduced peak load when an Al-steel resistance spot weld is not baked. Source: ORNL.

Effect of Baking on Weld Performance: The ML model identifies that the baking effect for weld performance shows a dependence on material thickness, as is shown in the data summarized in Figure II.3.5.7(a)-(c). Contrary to the fact that Al can be strengthened by baking, ML reveals that the joint mechanical performance is degraded after baking—especially for the welds fabricated from a thinner steel sheet, as evidenced by the significantly reduced peak load, extension at break, and total energy in welds made with 1.2-mm 6022 Al and 1.0-mm or 1.2-mm HDG LCS. The baking effects could be associated with the mismatch of the thermal expansion coefficient between Al and steel. A solid mechanics simulation has been performed to provide the mechanistic understanding of the intriguing baking effect that has been identified by the ML model. As shown in Figure II.3.5.7(d), the mismatch of thermal expansion leads to very high stresses on the intermetallic layer in welds made with thinner steels. Such high stress may cause brittle failure of IMCs and potentially break the bond formed during RSW. With the increase of steel thickness, the stress magnitude gradually decreases as the thicker steel sheet provides a large structural stiffness that better resists the expansion of Al.

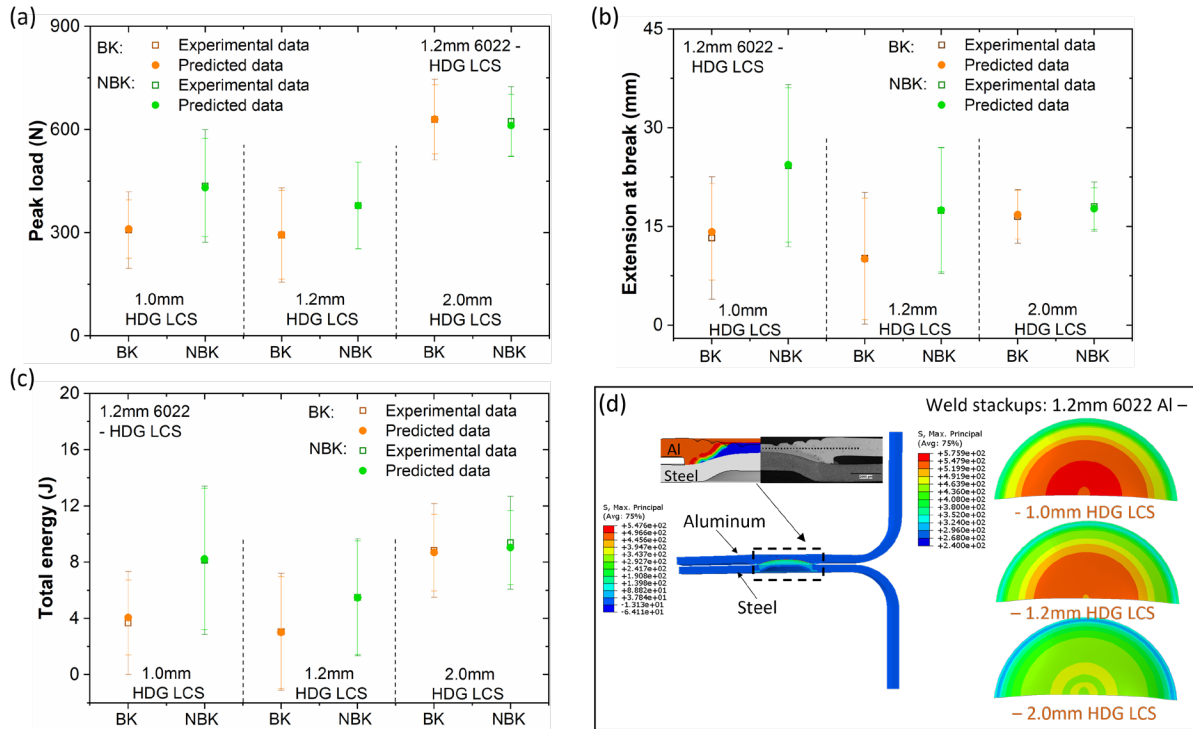


Figure II.3.5.7. The ML model identifies the thickness-dependent baking effect on weld mechanical performance of (a) peak load, (b) extension at break, and (c) total energy. (d) Solid mechanics simulation provides the mechanistic understanding of the ML-identified baking effect. Source: ORNL.

Random Forest Regression Approach for Weld Process-Performance Relationship (PNNL)

A series of experiments were conducted by constructing 500 trees accommodating 41 independent and correlated process variables, referred to as predictors, using the regression type of Random Forest where the number of variables tried at each split was 13. The data from GM was split into training/testing portions where the divisions were varied as 80/20, 75/25, 70/30, 65/35, and 60/40. Using these data splits, predicted error was calculated in determining peak load and total energy of the RSW joints, as shown in Table II.3.5.1. The variation of predicted error of the peak load is presented in one as a representative result. Subsequently, the 60/40 data split was identified as able to decrease the predicted error to the lowest value of 14.9%.

Table II.3.5.1 Split in Training and Testing Data Portions in the AA6022/LCS RSW Data Set to Determine the Prediction Error in the Random Forest Model for Predicting Peak Load

Training Data Portion/Testing Data Portion	Prediction Error In The Random Forest Model
60/40	14.965
65/35	15.887
70/30	15.175
75/25	15.268
80/20	15.026

Subsequently, peak load and total energy was determined for each joint using the training and testing data. The predicted peak load is presented in Figure II.3.5.8 as a representative image. It was seen that the Random Forest model was generating predictions for the experimental conditions within the data spread available for each of the properties.

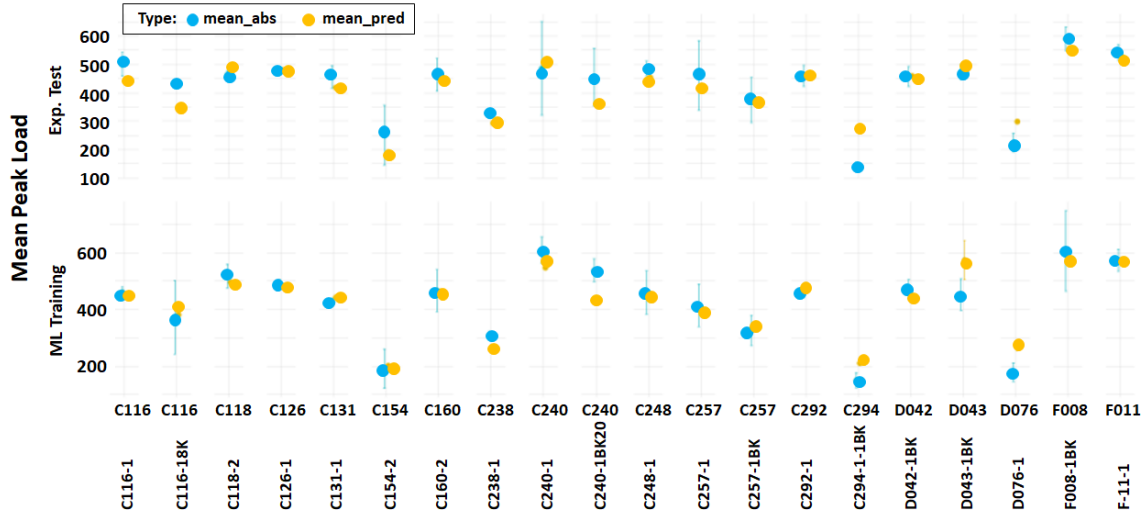


Figure II.3.5.8. Peak load predictions made by the Random Forest model contrasted against the experimental data spread showing the accuracy of the ML model. Source: PNNL.

Following this, the 60/40 data split was established as an ideal practice for subsequent model development. The next stage of model development was geared towards identifying the most important manufacturing process parameters among the 41 independent data streams identified previously. This was a necessary step to finally make predictions for these parameters. Figure II.3.5.9 presents the factors of importance of the 41 predictors arranged in the decreasing order. It was identified that the RSW heating stages were the data streams that had the highest effect on the peak load, as determined from the Random Forest analysis with an accuracy of ~80%.

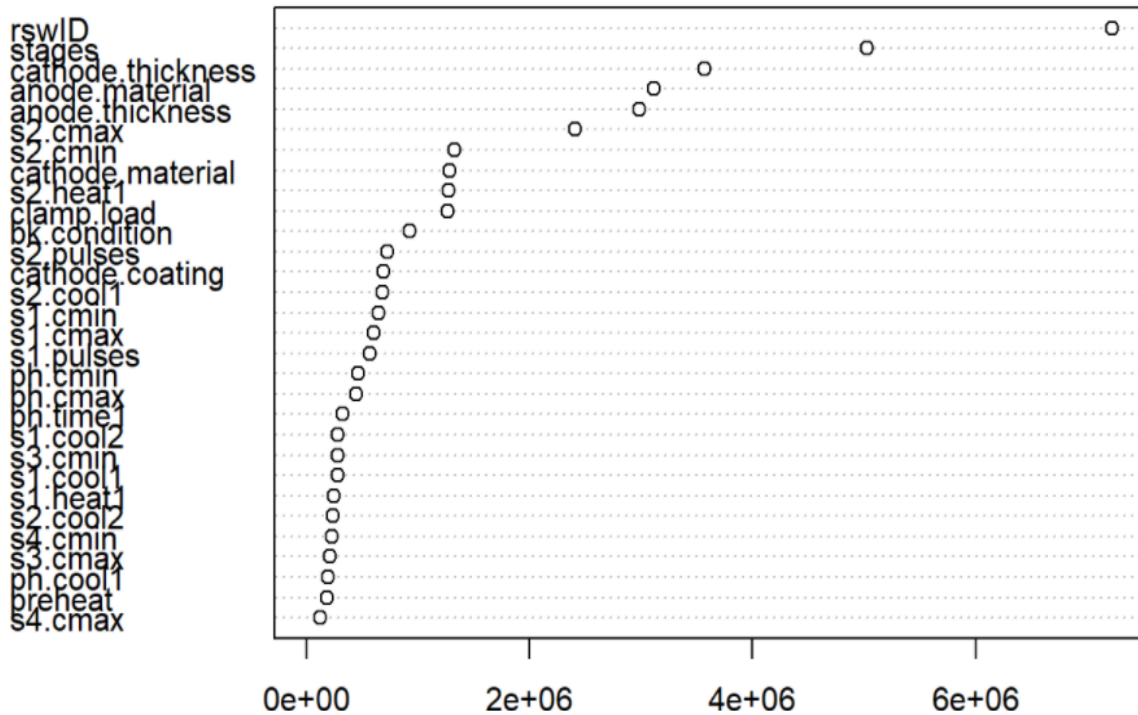


Figure II.3.5.9. Importance scores of the Random Forest nodes corresponding to the independent process variables that were used to make the 6022/LCS and X626/LCS coach peel peak loads with ~80% accuracy. Source: PNNL.

Subsequently, to identify the physical relationships between the dependent and independent variables as supported by the RSW literature, associative plots were developed between the independent process variables and the dependent RSW coach peel peak load. A representative plot between the different RSW preheating stages and its effect on coach peel peak load is presented in Figure II.3.5.10. Here, for the 6022/LCS joint made with high copper 6022, the highest peak loads were achieved for the samples that were not subjected to Stage 1 heating. Conversely, for the joint made with low copper 6022 and LCS, the highest peak loads were observed when only preheating and Stage 1 heating was performed. Interestingly, for the X626/LCS, the same process conditions resulted in low peak loads, which are around half of those observed in the high copper 6022/LCS joints. Similar associative plots were developed for other independent process parameters and other coach peel attributes, such as total energy and elongation at break.

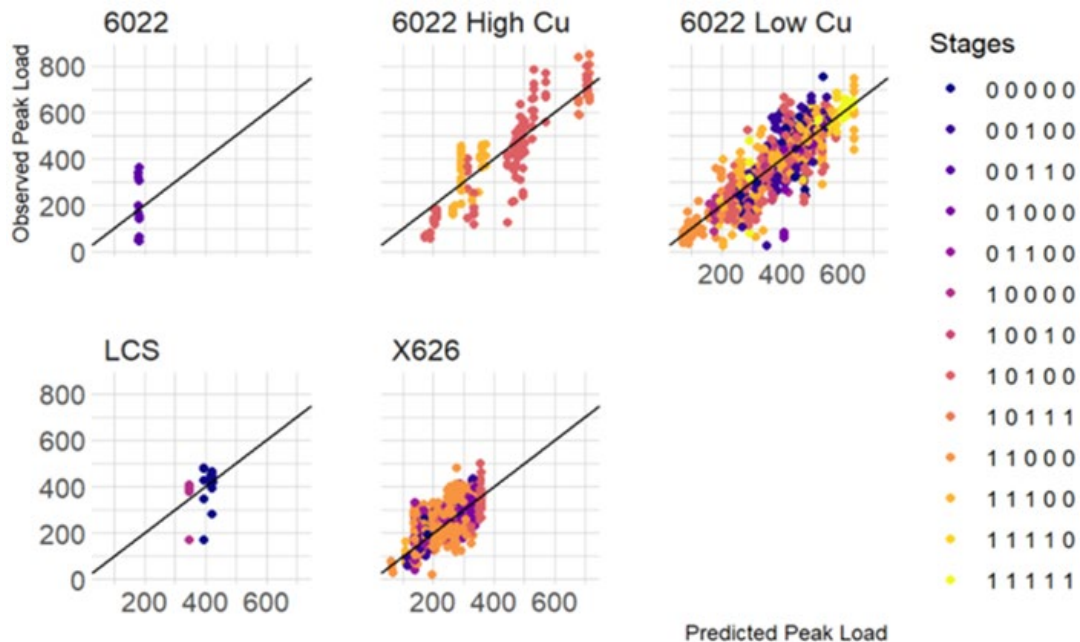


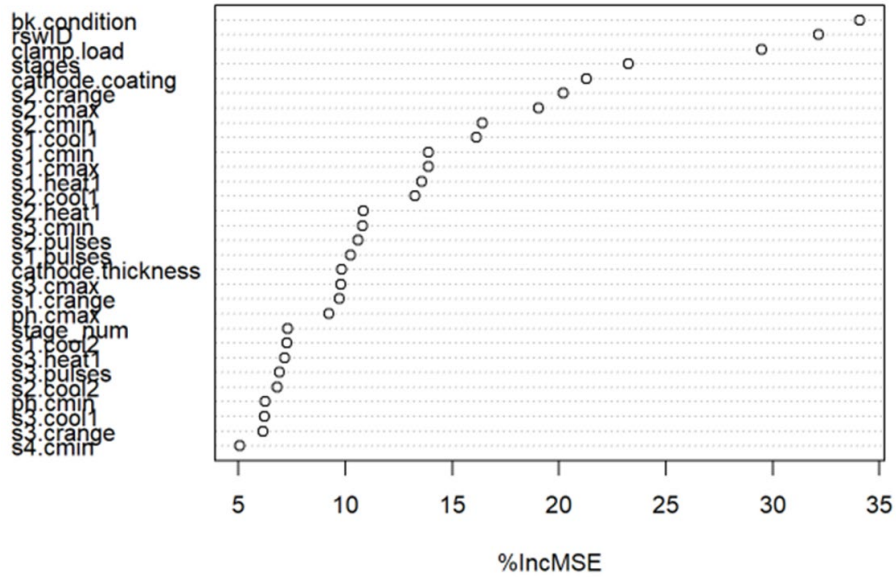
Figure II.3.5.10. Observed and predicted coach peel test peak loads for AA6022/LCS and X626/LCS samples as a function of the different RSW heating stages. Source: PNNL.

At this stage, owing to the number of predictors to be accommodated and the variations in data spread, the analysis was confined to only the AA6022/LCS data streams. After the predictor and dependent-variable correlations were made for the AA6022/LCS RSW joints, we commenced activities to develop values for the independent and correlated process variables that result in the highest peak load and total energy individually. Prior to this, the Random Forest model was reconstructed to simulate peak load and total energy using 10 predictors with the highest importance scores. The parameters used for the new total energy model with the 41 and 10 predictors, as well as the importance scores, are provided as representative results in Table II.3.5.2 and Figure II.3.5.11. Interestingly, the percent variance decreased marginally when the number of predictors was reduced to 10 for all the models indicating that the reduced order models captured the dependent-variable relationships effectively.

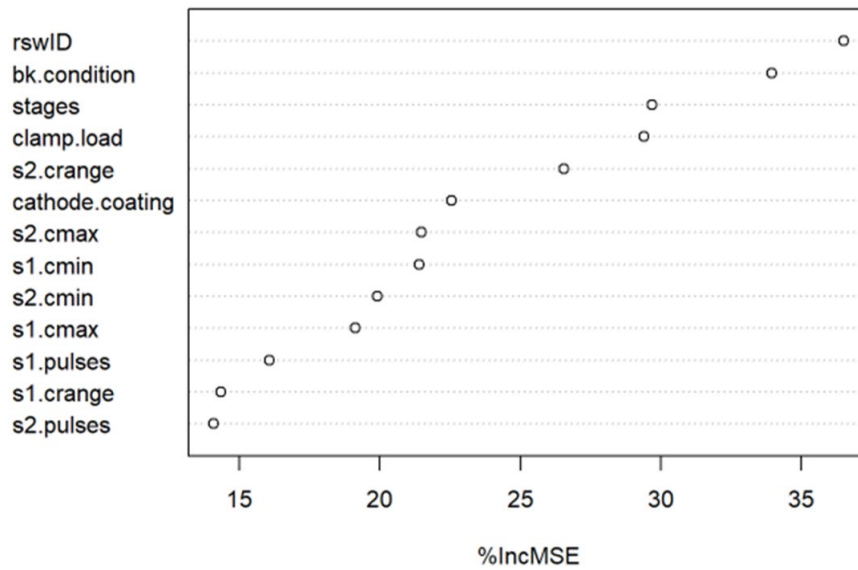
Following this, 5,000 experiments were simulated to predict peak load and total energy over the 10-dimensional parameter (predictor) space within the ranges provided in the GM dataset for the AA6022/LCS RSW joint manufacturing parameters. The results from the experiments are shown in Figure II.3.5.12. Among the 5,000 simulations, process conditions corresponding to the 10 highest peak loads, as well as the 10 highest total energy values, were consolidated and provided to the GM team for their consideration in performing model validation experiments. These values are provided in Figure II.3.5.12.

Table II.3.5.2 Random Forest Coefficients Used for Building Total Energy Models Using 41 and Top 10 Most Important Predictors

Parameter	Value 1	Value 2
Model Coefficients	41 Predictors	10 Predictors
Number of Trees	500	500
Number of Variables at Each Split	13	4
Mean of Squared Residuals	5.93	5.93
% Variance Explained	50.13	50.08



(a)



(b)

Figure II.3.5.11. Importance of scores for Random Forest model with (a) 41 predictors and (b) 10 predictors. Source: PNNL.

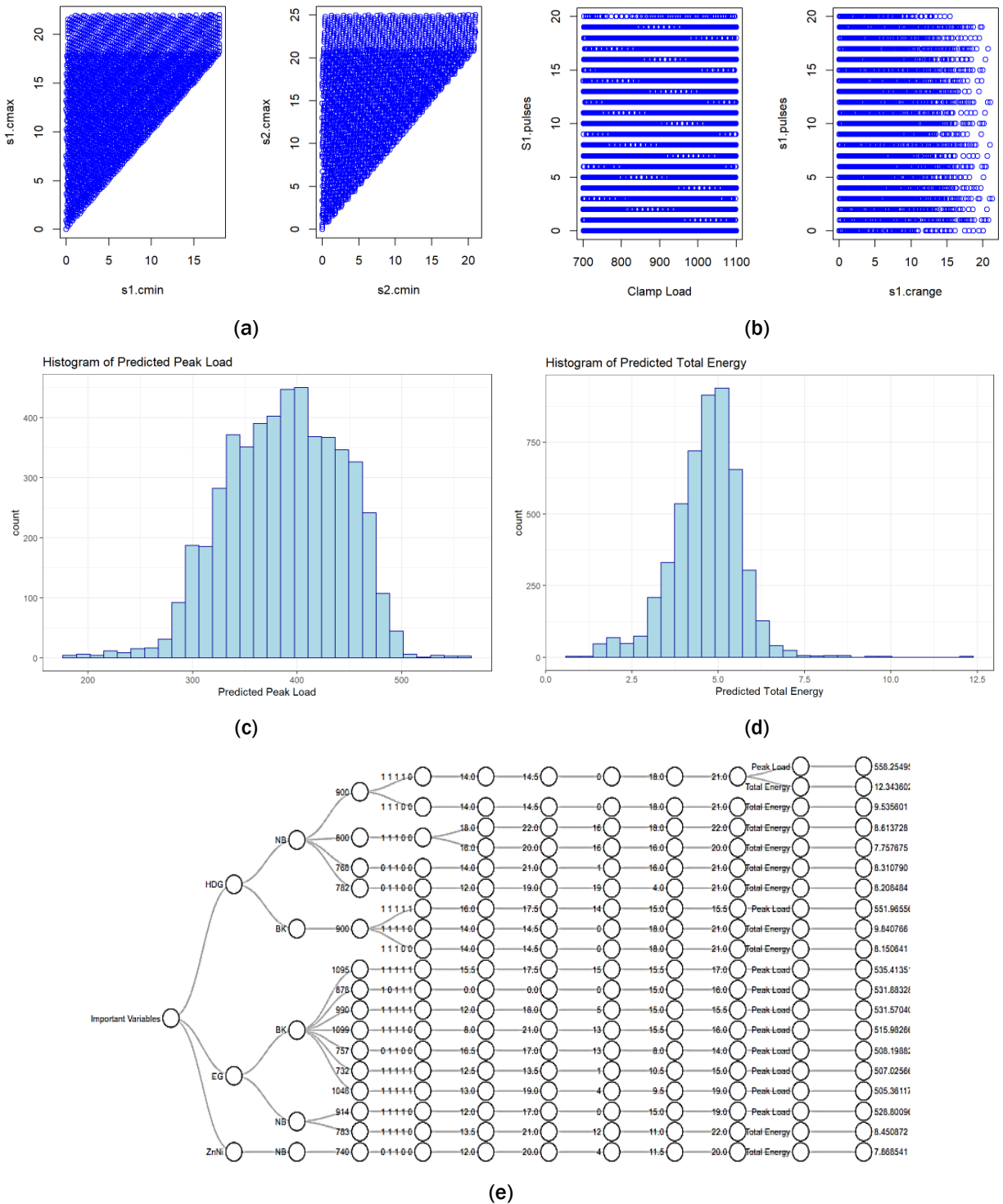


Figure II.3.5.12. Representative parametric space explored for the 5,000 completed experiments for: (a) the maximum and minimum current used in preheating stage of the RSW process; (b) the number of pulses and clamp load applied on the joint during RSW; (c) the peak load; and (d) the total energy predicted by the Random Forest models developed using the predictors with the 10 highest importance scores. (e) A schematic depicting the various process conditions corresponding to the hierarchy shown in the key to be used for manufacturing AA6022/LCS RSW joints with the highest peak loads and total energies.

Source: PNNL.

Conclusions

Two ML models have been built and used to investigate the relationships between the process parameter, weld attributes, and joint performances. The high-dimensional correlations have been established through recursive learning from GM's provided dataset for RSW of various combinations of Al and steel alloys. The key findings and conclusions were:

1. Both the Random Forest and DNN models are capable of predicting the relationships between process parameter/weld attribute and performance with over 80% accuracy.
2. The Random Forest model provided an optimal balance between flexibility and interpretability to model the RSW process parameter and performance relationships in order to identify the parameters of interest.
3. Only 10 of the 41 different independent variables (predictors) used for performing RSW joint experiments had a significant effect on joint performance, as identified by the Random Forest analysis.
4. It was possible to predict the process conditions necessary to be used in order to achieve the highest peak load and highest total energy in the RSW joints for AA6022/LCS 2T stack-ups using the ML architecture developed in this project.
5. The ML model utilizing a DNN architecture is highly expandable. It has been successfully expanded to ~60% of the GM dataset without degradation of prediction accuracy.
6. The DNN approach revealed the intriguing effect of weld conditions on weld performance, such as adhesive and baking can cause a significant reduction of joint performance under identified conditions.

References

1. Paszke, A., S. Gross, F. Massa, A. Lerer, J. Bradbury, G. Chanan, T. Killeen, Z. Lin, N. Gimeshein, L. Antiga, A. Desmaison, A. Köpf, E. Yang, Z. DeVito, M. Raison, A. Tejani, S. Chilamkurthy, B. Steiner, L. Fang, J. Bai, and S. Chintala, 2019, "PyTorch: An imperative style, high-performance deep learning library," *Adv. Neural Inf. Process. Syst.*, Vol. 32, pp. 8024–8035.
2. Vogler, M., and S. Sheppard, 1993, "Electrical contact resistance under high loads and elevated temperatures," *Weld. J. Res. Suppl.*, Vol. 6, pp. 231s–238s.
3. Song, Q., W. Zhang, and N. Bay, 2005, "An experimental study determines the electrical contact resistance in resistance welding," *Weld. J. Res. Suppl.*, Vol. 84, No. 5, pp. 73s–76s.
4. Rogeon, P., P. Carre, J. Costa, G. Sabilia, and G. Saindrenan, 2008, "Characterization of electrical contact conditions in spot-welding assemblies," *J. Mater. Process. Technol.*, Vol. 195, No. 1–3, pp. 117–124.

II.3.6 Prediction of Al-Steel Joint Failure (Pacific Northwest National Laboratory)

Kyoo Sil Choi, Principal Investigator

Pacific Northwest National Laboratory
902 Battelle Blvd.
Richland, WA 99352
E-mail: kyoosil.choi@pnnl.gov

Sarah Kleinbaum, DOE Program Manager

U.S. Department of Energy
E-mail: sarah.kleinbaum@ee.doe.gov

Start Date: December 1, 2018 End Date: December 31, 2021
Project Funding (FY 2021): \$500,000 DOE share: \$500,000 Non-DOE share: \$0

Project Introduction

GM has developed a RSW process for joining Al to steel for several different joint configurations (i.e., alloys and material thicknesses). For RSW, one of the common metrics for an acceptable joint is for the weld nugget to remain on the steel sheet upon completion of a destructive tensile test. This is referred to as button pull-out (BP) failure mode. Conversely, an unacceptable RSW failure occurs through the nugget at the interface between the two materials, referred to as an interfacial failure (IF). Development efforts to determine viable process parameters for any new joint configuration can be very costly; as such, predictive models for the process could significantly reduce these efforts. This project was proposed and initiated with the objective to develop a model that could predict failure mode of the weld coupon under various destructive test configurations. Destructive test configurations included typical ones used in the automotive industry for RSW—including coach peel (CP), cross-tension, and lap-shear (LS). Additionally, automotive components are often painted and subsequently processed through a paint-bake process. This exposes the RSW to additional thermal history, which has been demonstrated to influence the joint failure mode.

Objectives

While the overall objective of this project is to develop a validated FE model that can predict the failure mode of Al to steel RSW, there were four more detailed objectives to support this effort:

1. Fabrication and Destructive Testing of Al to Steel Spot Welded Coupons. This was a GM-led effort that involved creating weld coupons in five joint configurations. Post-weld destructive testing included LS, CP, and CT tests. In addition, microhardness testing and metallography were included.
2. Detailed Characterization of the Al to Steel RSW Joints. This was a PNNL-led effort focused on microstructural characterization and local material property measurement. Outputs from this effort are inputs to the FE model.
3. Weld Joint Simulation FEM. This was a PNNL-led effort toward the development of FE models to simulate the three destructive test configurations using material property data inputs.
4. Validation. These efforts will be performed to determine the accuracy of the developed model. By comparing the failure modes of the actual samples versus the model prediction and analyzing discrepancies, additional refinement activities were performed to improve the accuracy of the model.

Approach

The approach taken for this project is similar to other simulation development efforts. The first involved test coupon creation, which was followed by characterization of the RSW (input data for the model) with initial model creation performed in parallel. Finally, an iterative validation and model refinement process was performed. A more detailed description of the approach follows:

- Fabrication and Destructive Testing of Al to Steel Spot Weld Coupons:
 - RSW coupons were created in multiple joint configurations to allow for a range of input conditions for the model. Five predominant weld joint configurations in GM were chosen that included a single Al alloy in a single thickness and three hot-dipped galvanized steel alloys in three different thicknesses.
 - Destructive testing of the coupons was performed in three common test configurations used by the automotive industry for characterizing RSW joint performance. These included LS, CP, and CT testing. The failure mode and load-displacement curve output from these tests were used for model validation.
- Joint Characterization:
 - It was anticipated that local material properties at a fine resolution would be required as inputs to the finite element model to enable accurate model output and failure mode prediction. The approach taken was first to rank and then select test methods to generate local material property data. Cost and alignment of the test method output to model input needs were the most important criteria. Test methods were selected for creating input data or for use as validation data.
 - Joint characterization was then performed with prioritization based on model input needs.
- Simulation Development:
 - FE models for CP, CT, and LS tensile testing were developed. Information from optical and SEM images were used to generate the finite element models with various geometric features observed near the weld nugget. The IMC layer was modeled using solid elements to represent the damage, since the fracture parameter is rather easily defined for solid elements.
 - FE models for uniaxial tensile testing were also developed to determine the fracture strain level of Al alloy under tension. To consider the stress-triaxiality dependency of the fracture strain of Al, FE models for limiting dome-height (LDH) tests were developed, which provided the fracture strain level under higher stress-triaxiality levels.
- Validation:
 - Load-displacement data from simulations for multiple joint and test coupon configurations was generated. Using data generated from the destructive testing and joint characterization efforts, the accuracy of the model was assessed and opportunities for improvement identified. In an iterative fashion, model refinements and output were reassessed for accuracy.

Results

Initial model validation efforts in the last quarter of FY 2020 indicated a relatively high-level of accuracy (e.g., ~80%) for predicting the CP and CT failure modes, while the predicted LS failure mode was less so. With this, efforts in FY 2021 focused on model refinement activities toward improving the failure mode prediction. An additional effort was placed on modeling and comparing the load-displacement curve for these tests as well. Initial comparisons of the model's predicted load-displacement curve indicated that additional refinement activities would be necessary. In the end, the objective was to obtain accurate model predictions for both the failure mode, as well as the peak load and shape of the load-displacement curves.

Weld simulation finite element models were generated based on the actual weld geometry and the observations of microstructures. Stress-strain curves estimated from microhardness values were assigned for different zones of Al and steel within the weld nugget, HAZ, and base material. Strain-based ductile damage was adopted for Al, which depends on stress-triaxiality. The IMC layer was modeled using solid elements and the stress-based brittle fracture criteria.

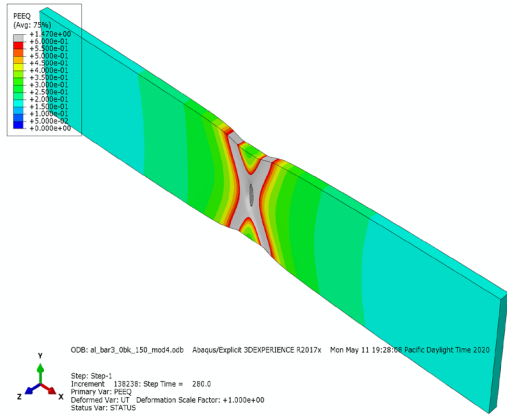
First, simulation tasks were performed for predicting the matched failure modes of the selected material combination for different conditions (i.e., CP/CT/LS, and baking conditions). The model was refined to improve failure mode prediction via different fracture criteria and adjusting their critical values (e.g., fracture strength). With sufficient accuracy obtained, the team transitioned to the development of a finite element model to predict the load-displacement curves.

Initial tasks of load-displacement curve simulation development and validation were conducted using Al fracture strain curves based on standard tensile test results of the Al base materials in the unbaked (0BK) and double-baked (2BK) conditions. Figure II.3.6.1 shows the simulated models for tensile loading and the Al fracture strain curves assumed based on the obtained simulation results for 0BK and 2BK conditions. It is noted that the tensile fracture strain levels were evaluated from the tensile simulations. The stress-triaxiality dependency is assumed as shown in Figure II.3.6.1 based on the literature data [1].

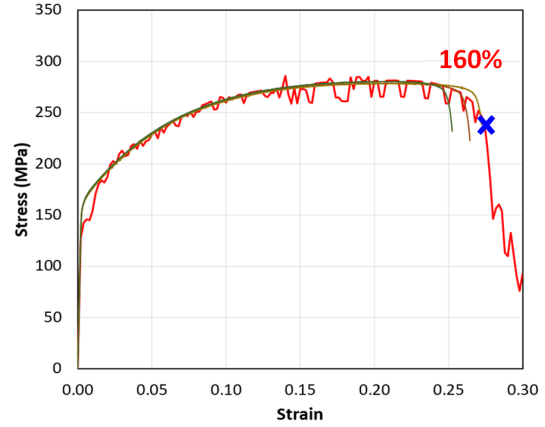
Initial simulations of the CP, CT, and LS coupon load-displacement curves were started using the curves in Figure II.3.6.1. While the peak load would match in some cases, other cases contained up to 50% in error - this much error seemed to be attributed mainly to the use of inaccurate Al fracture strain curves. A similar finding was associated with the shape of the curves, with the CT test model simulation performing the best. The CP load-displacement simulation curves had less accuracy than the CT curves. The initial shape/slope of the load-displacement curve exhibited the most dramatic difference in the case of the CP test. Last, the LS simulation results were the most discrepant, similar to the initial failure mode prediction. Example model outputs versus experimental results are presented in Figure II.3.6.2.

As mentioned above, a strain-based ductile damage simulation approach was adopted for the Al, which depends on the stress-triaxiality. To aid in determining more accurate triaxiality data for Al fracture strain curves, LDH testing was performed. To aid this effort, a FE simulation of the LDH test was also created. Initially, Al fracture strain curves were modified only considering results from the LDH testing. A literature review was also performed on the Al fracture behaviors, which suggested complex-shaped stress-triaxiality dependency of Al fracture strain curves could be necessary (e.g., a “W” shape fracture strain curve) [2-4]. With additional model refinement efforts, “W” shaped fracture strain curves were eventually implemented. In order to improve the model’s accuracy, several refinement efforts were pursued, including but not limited to:

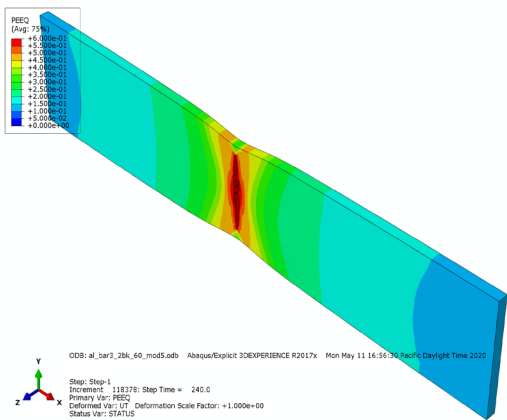
- Efforts to further refine the fracture criteria and levels
- Confirmation that geometry of the coupons entered into the model was accurate
- Inclusion of residual stress, due to the differential thermal expansion coefficient between Al and steel
- Inclusion of a weakly bonded area (anulus) at the exterior of the nugget. This is referred to as a kissing bond
- Consideration for a “W” shaped Al fracture strain curve, as noted above.



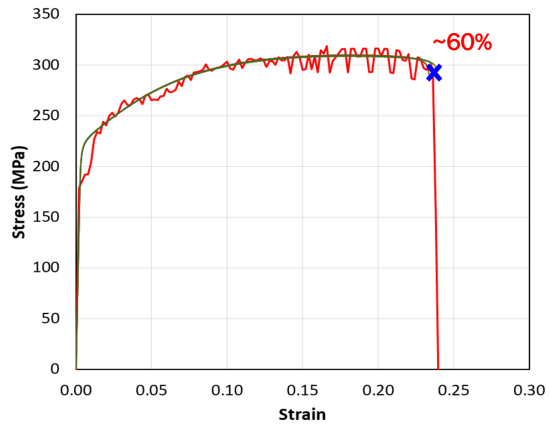
(a)



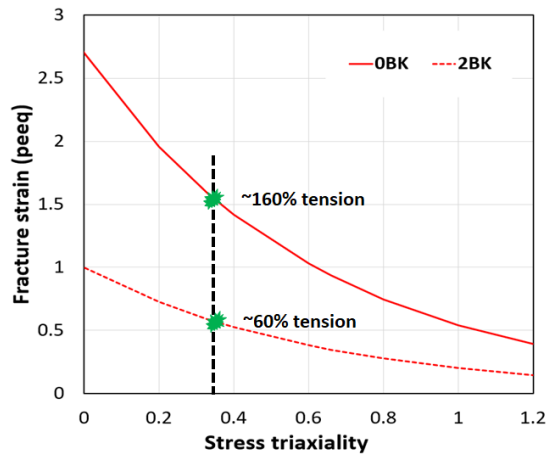
(b)



(c)



(d)



(e)

Figure II.3.6.1. Example of initial AI fracture strain curves estimation. (a) Equivalent plastic strain from a simulated model for OBK condition with 160% tensile fracture strain. (b) Stress-strain curve comparison between simulation and experiment for OBK condition. (c) Equivalent plastic strain from a simulated model for 2BK condition with 60% tensile fracture strain. (d) Stress-strain curve comparison between simulation and experiment for OBK condition. (e) Initially assumed AI fracture stress-strain curves based on tensile simulations. Source: PNNL.

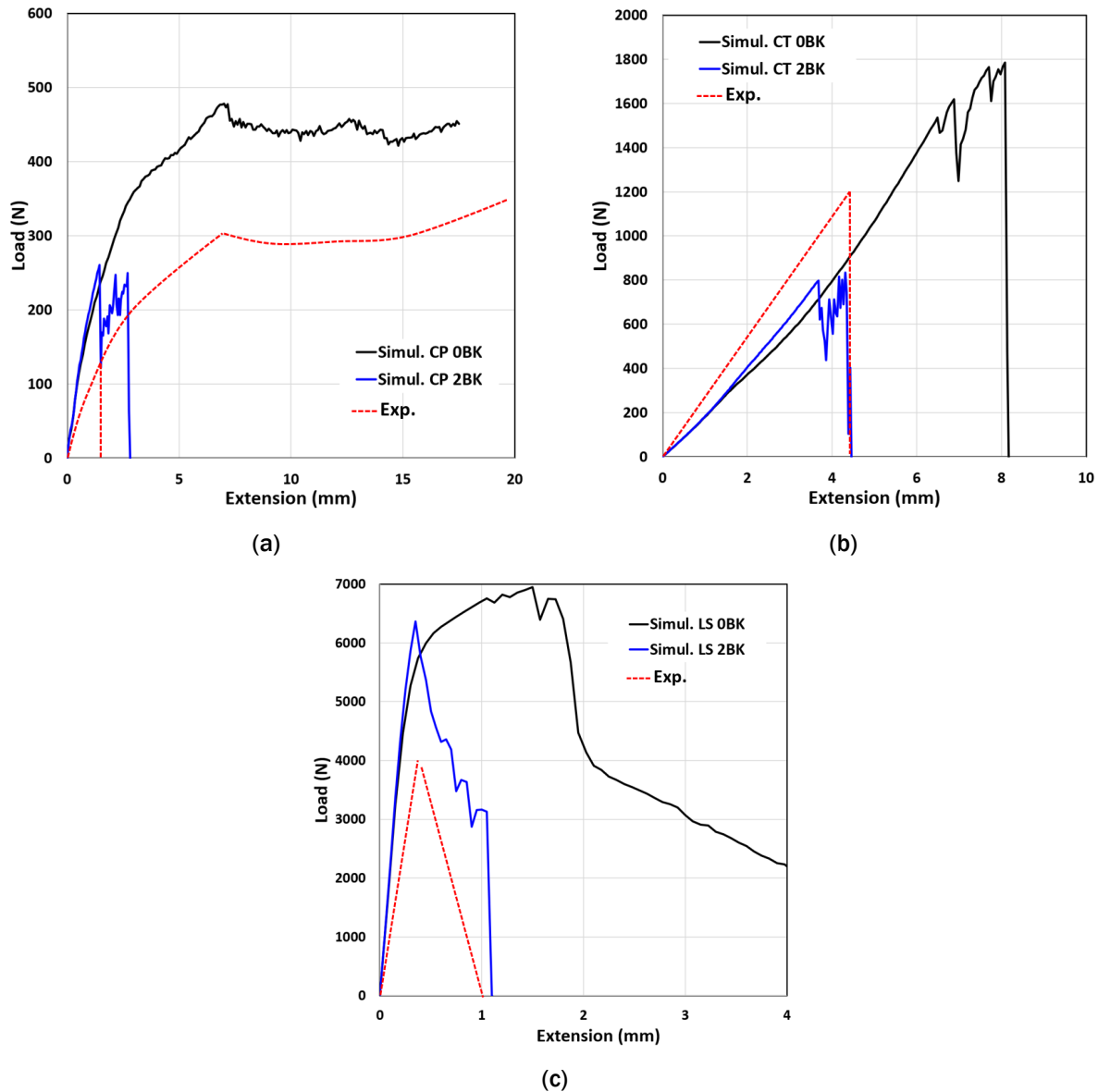


Figure II.3.6.2. Examples of early load-displacement curve simulation versus experimental results for the (a) CP, (b) CT, and (c) LS tests. Source: PNNL.

The following observations were made because of these activities:

- Further refinement of the fracture criteria and levels had a significant effect, mostly affecting the peak loads. Model accuracy was improved.
- Some geometry entered into the model was slightly inaccurate. For example, the distance from the weld to the flange on the CP test. However, these changes had little, if any, effect towards improving the model prediction.
- The geometry of the actual CP coupons, specifically the flange angle, varied significantly. The implementation of a varied flange angle had a significant effect on the initial shape (elastic region) of the CP simulation helping to improve accuracy.

- The inclusion of the kissing bond or region of lower bond strength at the edge of the nugget did have some effect and improved the peak load and curve shape, most prominently for the LS coupons.
- Efforts to include the residual stress data included initial estimations of the stress levels. These calculations indicated that residual stress levels are likely non-trivial. Attempts at implementing into the model were not complete due to budget funding limitation and will require additional user subroutine development. Initial efforts suggest residual stress inclusion may have a significant effect.

An example of the model output versus the experimental data and failure mode from late in the project is presented in Figure II.3.6.3. As can be observed in Figure II.3.6.3(a) for the CP model, the peak load and overall shape of the predicted load-displacement curve matched generally well with the experimental curves, except for the initial slope of the curve that may be affected by the flange angle. For the LS model shown in Figure II.3.6.3(b), the predicted load-displacement curves exhibited similar energy absorption to those of the experiments, although the peak loads do not match well in these example cases. In the end, significant improvements in the accuracy have been achieved via the refinement activities.

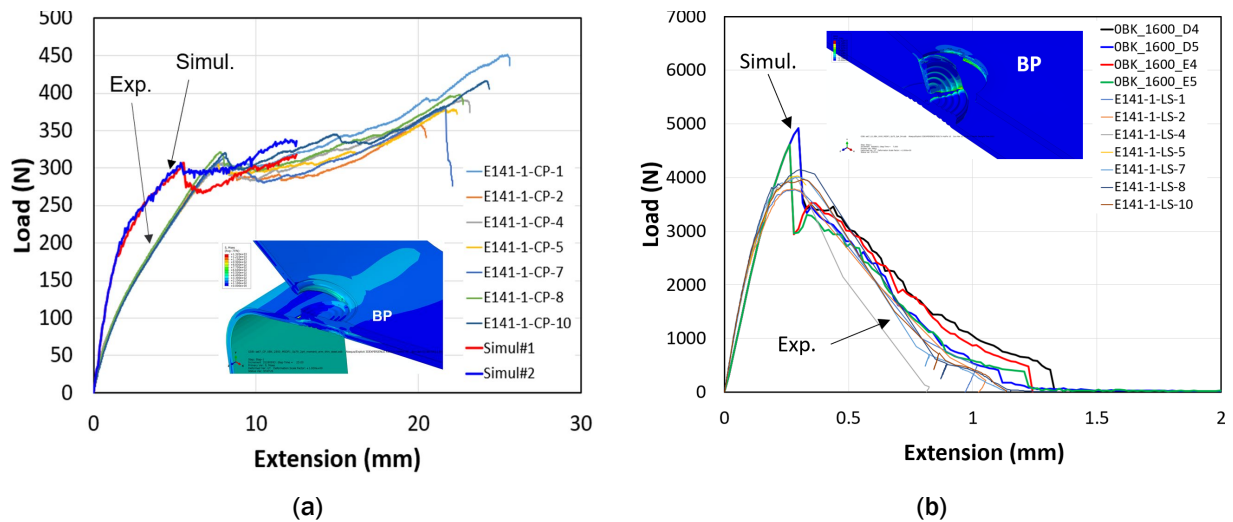


Figure II.3.6.3. Examples of load-displacement curves and failure mode simulation versus experimental tests after refinement activities for (a) CP, and (b) LS. Source: PNNL.

While the model accuracy is not 100% satisfactory, significant strides towards the development of a model to predict failure mode, as well as load-displacement curves, has been made. With this, further refinement activities were identified, including:

- completion of the implementation of the residual stress FE into the model
- finer tuning of Al fracture strain curves and kissing bond strength
- consideration of material anisotropic behavior
- examination of Al properties near the edge of the weld nugget and the interface of the Al/steel
- perform model/experimental result comparisons for additional joint configurations.

Conclusions

For FY 2021, model validation activities were completed against the selected material combination for different testing configurations and baking conditions. From the FY 2021 and related final project efforts, the conclusions below have been made:

- In this modeling effort, the failure mode (i.e., BP or IF) observed in the experiments can be matched via adjusting the Al and IMC fracture strength levels.
- It is found that the predicted failure modes can better match the experimental failure modes for all conditions by assuming a lower IMC fracture strength with baking process. This indicates that possible weakening in the bonding strength of the IMC layer due to local cracking during the baking process may be one of the important factors influencing the fracture mode.
- The Al fracture strain curve modified based on the LDH tests, along with a strong enough IMC fracture strength, was an important model enhancement to enable accurate prediction of the load-extension curve and BP failure mode of CP/0BK samples. Weaker IMC fracture strength appears to be a key factor influencing the load-extension curve and IF failure mode of CP/2BK samples.
- Off-normal bend angles of actual CP samples can have significant effects on the initial portion of load-extension curves.
- W-shaped Al fracture strain curves as a function of stress-triaxiality appear to enable accurate prediction on the overall shape of the load-extension curve and partial button failure mode of LS/0BK samples.
- Consideration of weaker bonding in the kissing zone can help improve the prediction of the peak load of the LS/0BK samples. Similar to the case of CP/2BK, weak IMC fracture strength can also be a key factor influencing the load-extension curve and IF failure mode of the LS/2BK samples.
- The calibrated material parameters from the LS/0BK modeling and kissing zone concept are theoretically expected to predict the matched load-extension curves and failure mode for CP/0BK samples. However, the newly predicted load-extension curves for the CP/0BK samples show a noticeable discrepancy as compared to the experimental curves. Further fine-tuning efforts appear necessary to enable model to accurately predict load-extension curves for the LS tensile test.
- Model validation and refinement efforts demonstrated alignment between model and experimental results is possible in a large percentage of cases, but alignment is yet to be universal. This can be attributed to the complexity of predicting both the failure modes and load-extension curves for different sample configurations and baking conditions. The authors have identified several opportunities for improvement of the model that should enable a better understanding of the failure mechanisms of spot-welding of dissimilar materials.
- The developed modeling method in this study is recommended to be applied to other material combinations and destructive test configurations to understand additional fundamentals and the key factors influencing the failure mode of Al to steel spot-welding.

References

1. Hu, X. H., K. S. Choi, X. Sun, and S. F. Golovashchenko, 2014, "Edge fracture prediction of traditional and advanced trimming processes for AA6111-T4 sheets," *J. Manuf. Sci. Eng. Trans. ASME*, Vol. 136, Art. 021016-1-11.
2. Bao, Y., and T. Wierzbicki, 2004, "A comparative study on various ductile crack formation criteria," *J. Eng. Mater. Technol.*, Vol. 126, pp. 314–324.
3. Ha, J., M. Baral, and Y. P. Korkolis, 2018, "Plastic anisotropy and ductile fracture of bake-hardened AA6013 aluminum sheet," *Int. J. Solids Struct.*, Vol. 155, pp. 123–139.
4. Li, Z., S. Lu, W. Yang, and T. Zhang, 2019, "Study on the ductile fracture rule of 6061-T6 aluminum alloy sheet under different strain conditions," *Trans. Indian Inst. Met.*, Vol. 72, pp. 2721–2728.

Acknowledgments

The author would like to thank and recognize the following team members for their valuable input, including N. Overman who provided material science expertise, as well as the experimental direction; W. Kuang and X. Ma for nano-hardness testing and insight; C. Smith for project management; and S. Riechers for atomic force microscopy testing and input. Additionally, all team members would like to thank GM and their team, specifically W. Cai, A. Haselhuhn, and B. Carlson, for their valuable insight, guidance, and providing test coupons and data.

II.3.7 Extending High-Rate Riveting to New Material Pairs (Pacific Northwest National Laboratory)

Kevin Simmons, Co-Principal Investigator

Pacific Northwest National Laboratory
902 Battelle Blvd.
Richland, WA 99352
E-mail: kl.simmons@pnnl.gov

Amit Naskar, Co-Principal Investigator

Oak Ridge National Laboratory
902 Battelle Blvd.
Oak Ridge, TN 37831
E-mail: naskarak@ornl.gov

Sarah Kleinbaum, DOE Program Manager

U.S. Department of Energy
E-mail: sarah.kleinbaum@ee.doe.gov

Start Date: August 16, 2020	End Date: September 30, 2023	
Project Funding (FY 2021): \$683,000	DOE share: \$683,000	Non-DOE share: \$0

Project Introduction

PNNL, ORNL, and ANL are teaming to develop a combination of adhesive-based bonding and high velocity mechanical joining methods for multi-material systems to reduce vehicle component mass.

Objectives

This project aims to develop a hybrid adhesive-mechanical joining method to efficiently join multi-materials of two and three thickness configurations that exceed LS strengths by 50% and cross-tension strength by 30% beyond what is possible with adhesive bonding alone and demonstrate its effectiveness as a robust approach that has improved joint integrity. The project will combine state-of-the-art riveting techniques with adhesive bonding and focus on adhesive curing, thermal stability, and wettability issues both by experimental and modeling to enhance the performance of hybrid and non-hybrid joints. Ultimately, the project will develop and demonstrate an adhesively bonded multi-material joint that has high velocity-formed rivets and high-friction rivets that will increase the performance and reliability of the joined dissimilar material sets.

Approach

The approach will investigate adhesively bonded and non-bonded joints with 2T and 3T material sets of high-strength steel (DP590), Al alloys (5052 and 6061), Al castings (<12 mm), polyphthalamide, and polyamide 66 (PA66) CF composites from sheets up to 3 mm in material thickness. These material combinations are relevant for use in vehicle structural joints. The project will evaluate the use of cured and uncured adhesively bonded joints to determine the effect of the riveting process on the adhesive. Modeling simulations will be performed to optimize rivet design and process parameters. The experimental data is then compared to simulations to improve the model prediction to allow for optimum conditions to reach the fullest potential of the joint strength. The material joint evaluations then will be mechanically tested and characterized to develop both a physical and chemical understanding of the bonding strengths and external effects.

Results

Adhesive Bonding

Adhesive bonding of metal/metal, metal/CFRP, and CFRP/CFRP material combinations under shear load condition was investigated via lap-shear tests. As illustrated in Figure II.3.7.1, lap-shear strength (LSS) of

metal/metal combinations was in the range from 20 to 24 MPa. LSS of metal/CFRP combinations was in the range from 7 to 15 MPa. The lowest bond strength was found in the CFRP/CFRP combinations with values in the range from 4 to 12 MPa.

The results were compared to joints with air plasma-treated surfaces to quantify the improvement on shear behavior due to plasma treatment. Treatment parameters of the tip-to-surface distance (d) and tip speed (v) producing a maximum surface energy were used for the plasma treatment on Al alloys (d=6.4 mm, v=3.2mm/s), steel (d=3.2 mm, v=1.6mm/s), and CFRPs (d=3.2 mm, v=100 mm/s). Details of the effect of plasma treatment parameters on surface energy, surface roughness, wettability, and surface chemistry are reported in Section II.3.9, “Surface Modifications for Improved Joining and Corrosion Resistance.” Air plasma treatment improved the LSS of the metal/metal, metal/CFRP, and CFRP/CFRP combinations. In Figure II.3.7.1 with the plasma-treated combinations highlighted red, the improvement of LSS is about 3% to 10% for the different metal/metal combinations. Improvements of 11% to 23% was observed for the different metal/CFRP and CFRP/CFRP combinations.

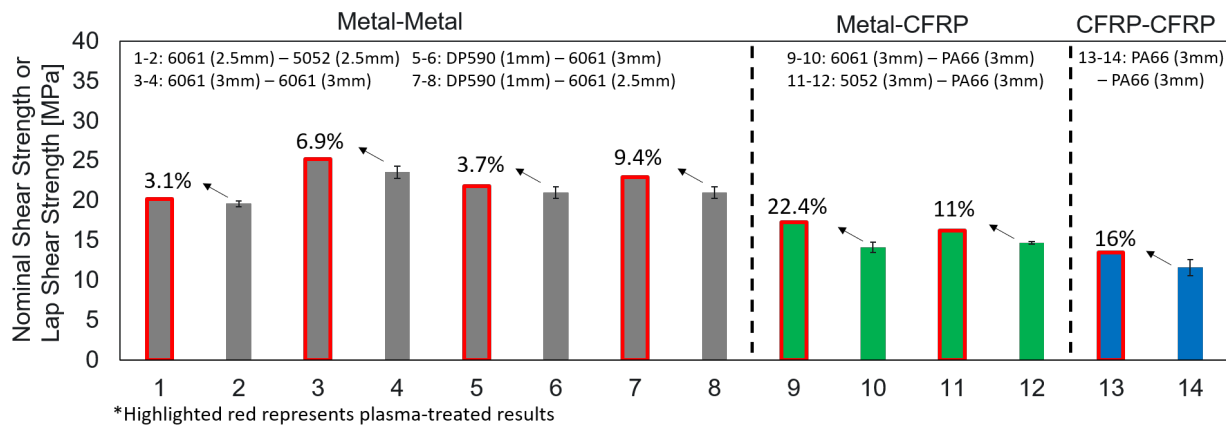


Figure II.3.7.1. LSS of non-treated and air plasma-treated metal/metal, metal/CFRP, and CFRP/CFRP combinations. The in-plane dimension of each material is 25 mm × 100 mm with a 645 mm² bond area. Source: PNNL.

Mechanisms for the improvement on shear failure behavior after plasma treatment was evident in the surface morphology of the bonded materials after the LS testing. As illustrated in Figure II.3.7.2, plasma-treated surfaces of CFRP composites retained more adhesive compared to non-treated CFRP surfaces. In the A6061/PA66 combination, the matrix and fiber was physically removed from the PA66 surface during lap-shear failure, thus dissipating more energy and leading to better LSS performance compared to the non-treated case. The failure morphology of the surface confirms the improvement of adhesive bonding on combinations with different materials via air plasma treatment.

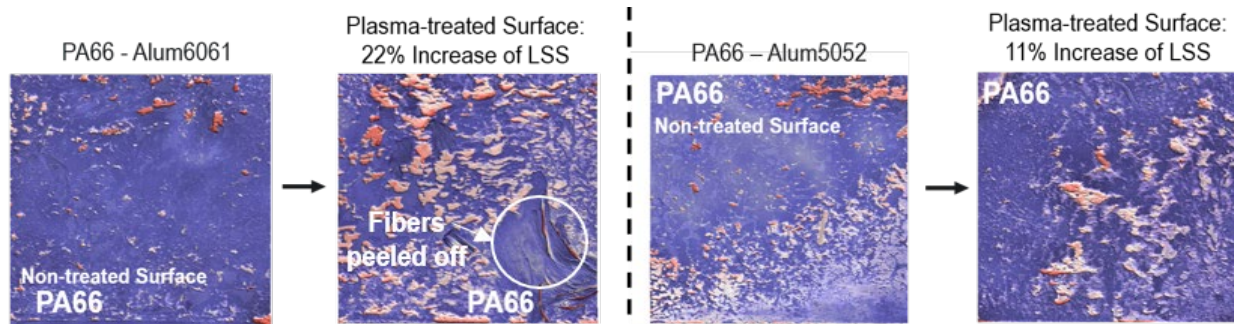


Figure II.3.7.2. Colorized surface morphology of non-treated and air plasma-treated CFRP after LS failure. The PA66-A6061 and PA66-A5052 combinations are shown on the left and right, respectively. The CFRP surface is shown in blue, while the adhesive remaining on the surface is shown in pink. Source: PNNL.

Adhesive Curing

The cure kinetics of the epoxy-based adhesive (XP-0012 batch YL230) were determined using a classical Kissinger model. Activation energy for the adhesive was calculated to be 88.3 kJ/mol. Based on the cure instructions of 175°C for 25 minutes, curing profiles were constructed at various heating rates using a semi-empirical cure kinetics model, as observed in Figure II.3.7.3. Experimental cure data obtained from the DSC experiments also indicate a similar profile, although some deviations at lower temperatures are present.

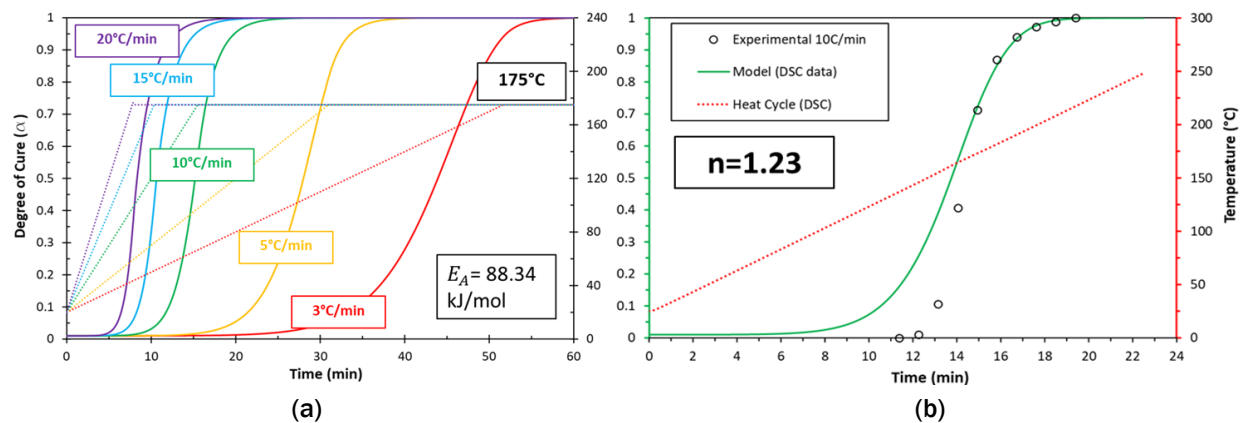


Figure II.3.7.3. (a) The degree of cure of the adhesive at different cure rates. (b) Model vs. experimental data at a rate of 10 °C/min. Source: ORNL.

Rheological characterization was carried out at RT to determine the flow characteristics of the uncured adhesive. The adhesive was subject to a flow profile at varying shear rates and the viscosity and shear-thinning behavior was determined. As seen in Figure II.3.7.4(a), the adhesive is highly shear-thinning at RT, which could potentially lead to adhesive flow-out during the high-shear riveting processes. In Figure II.3.7.4(b), the adhesive was subjected to flow at increasing temperatures. Gelation of the adhesive occurs at 150°C, at a temperature similar to the beginning of the curing exotherm in Figure II.3.7.4(b), leading to increased viscosity. This suggests that the ideal time to carry out the riveting on the adhesive joints would be at the beginning of the curing process.

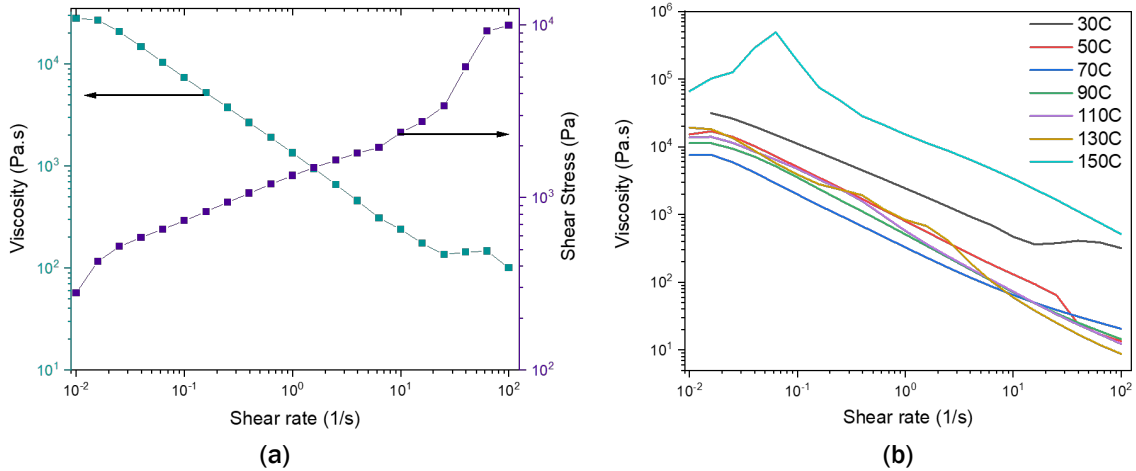


Figure II.3.7.4. (a) RT shear profile of adhesive subject to flow. (b) Viscosities of adhesive at increasing temperatures. Source: ORNL.

High Velocity Riveting

Joints created in multi-material stack-ups were successfully formed via high velocity riveting (HVR) with commercially available nail type fasteners and custom flathead type rivets. Utilizing a commercially available nail/riveting powder gun, the rivets were accelerated at different ballistic velocities which allowed the rivets to penetrate the material stacks. The rivets velocity was decelerated by the faying surfaces and ultimately terminated in the back of the material stack and into a steel die and backing plate. The dynamic processes induced in both the rivet and the target material introduced both metallurgical and mechanical bonding, as shown in Figure II.3.7.5(a). Initial trials were performed using 1040 steel and commercial rivets developed by Ramset[®]. These joints were then characterized by LS testing and compared to baseline flow-drill screw techniques. Various stack-up combinations of Al alloys 6061-T6 and 5052-H32 were successfully joined via 7075-T6 and 1040 steel rivets. Figure II.3.7.5(b) shows the results of commercial rivets used in this study on two 3 mm 6061-T6 plates. The 1040 steel rivets exhibited consistent and repeatable bonding behavior and produced desirable LS performance over traditional flow-drill screw joints of similar material combinations.

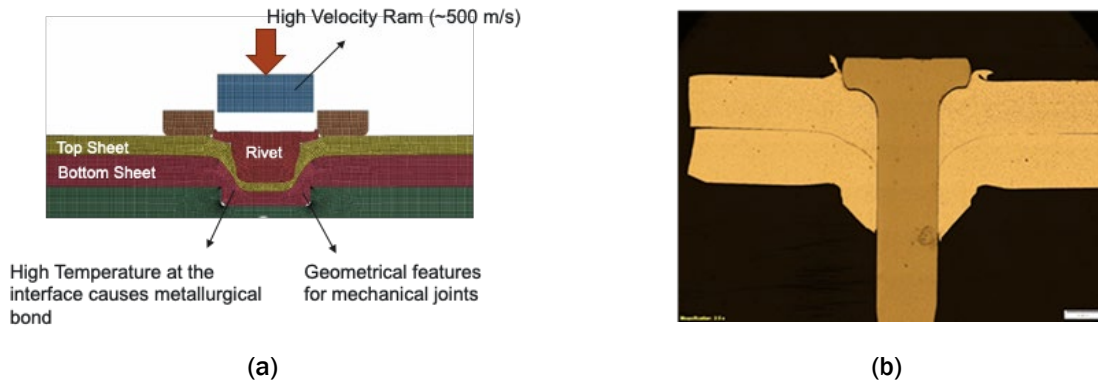


Figure II.3.7.5. (a) Concept of HVR. (b) Optical cross-section of 6061-T6 bonded using a commercial rivet. Source: PNNL.

A 3D thermomechanical coupled finite element model was developed in Abaqus to gain a full understanding of the HVR process, such as heat generation, plastic deformation, thermal stresses, and joint integrity with various processing parameters. Figure II.3.7.6 shows a comparison of the experimental and computational results for a 6 mm Al 7075-T6 rivet and a stack of two Al 6061-T6 3.18 mm plates, which are in good agreement. During the HVR process, striker kinetic energy was transferred to material plastic deformation and

heat energy to increase the joint temperature and pressure between the plates. The increase in temperature and the magnitude of the pressure between the plates may favor the formation of a metallurgical bond.

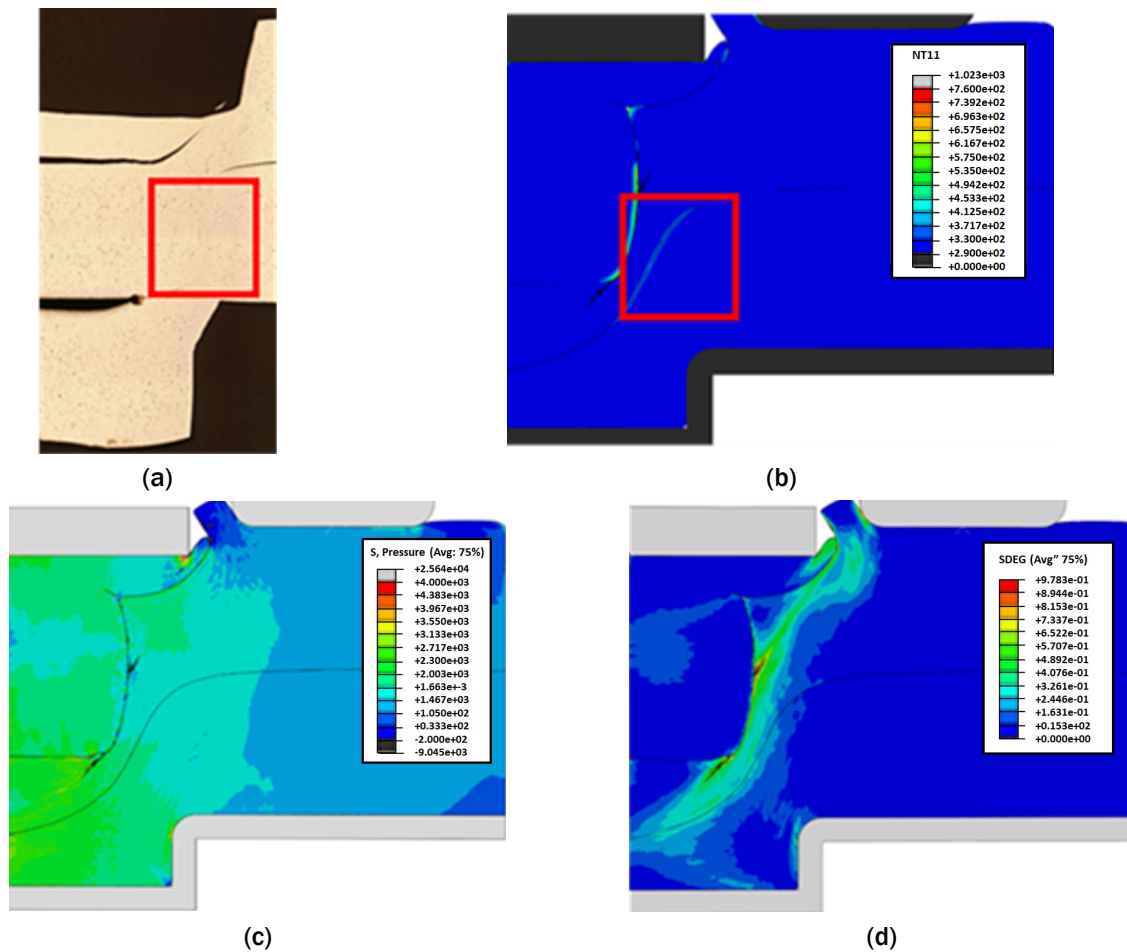


Figure II.3.7.6. Results of the 150 m/s rivet speed, 6 mm solid rivet, and 1.5-mm deep die with a 3.5 mm hole for (a) the experimental value, (b) the temperature profile, (c) the pressure profile, and (d) the material damage. Source: PNNL.

Al – DP590 and CFRP Joints

Al to DP590 steel trials were also performed utilizing the commercial nail. The 3-mm Al 6061-T6 plates were bonded to the 1-mm DP590. The orientation of the material stack-up was important to the success of the joint. For example, when the 1-mm DP590 was on top of the 3-mm 6061-T6, it was observed that the rivet consistently penetrated fully through the plate. The inverse of this stack-up proved successful when bonding via HVR. For the Al to CFRP, the joints were similarly successful when the CFRP acted as the bottom plate in the material stack-up. However, the Al-CFRP joint proved difficult due to catastrophic failure of the CFRP plate during the rivet process. The stress induced from the rivet caused the plate to fracture. Optimizing the rivet geometry and die backing can potentially alleviate the causes of failure. By limiting the overall penetration of the rivet into the material stack-up, the amount of deformation in the CFRP plate can be controlled.

Nondestructive absorption contrast x-ray tomography was utilized to characterize these joints in 3D. Figure II.3.7.7(a) shows a AA6061 plate in blue joined with a CFRP plate in green using a steel rivet appearing red. The plates undergo significant deformation during the HVR process leading to extrusion. Figure II.3.7.7(b) shows a region of contact via green arrows between two riveted plates wherein conclusive evidence of a metallurgical bond was observed. This region of contact between the two plates was present

throughout the extruded portion of the top plate indicating the likely presence of the metallurgical bond throughout the regions of contact between the two plates.

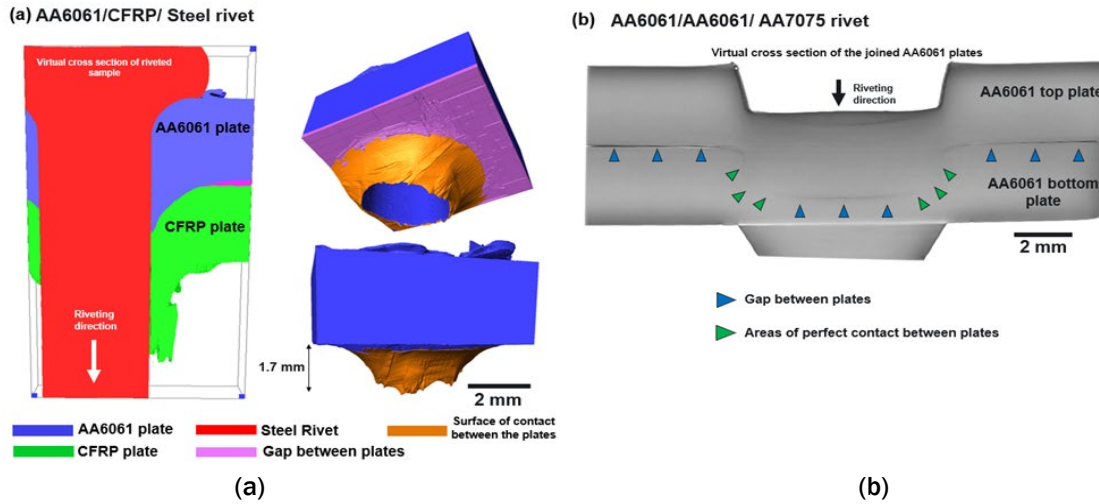


Figure II.3.7.7. (a) An AA6061 plate joined to a CFRP plate with a steel rivet showing the extrusion of the two plates. Yellow and pink labels show the areas of contact and gap areas between the two plates, respectively, (b) AA6061 plates combined with an AA7075 rivet showing the areas of perfect contact. Source: PNNL.

Lap-Shear Performance

Performance of the Al-Al joints showed considerable improvement over the flow-drill screw joints during LS testing, as shown in Figure II.3.7.8(a)-(b). LS testing was performed on 3-mm 6061-T6 Al stacks bonded by HVR. Two samples—one with the adhesive applied to the overlap area of the 6061-T6 plates and another without an adhesive applied—were joined using commercial steel nails for use in powder-actuated systems. Figure II.3.7.8(c) exhibits the load vs. cross-head extension plots as compared to the literature values of flow-drill screw (FDS) joints. HVR showed a 14.3% and 50.1% increase in maximum load over FDS for both the adhesive and non-adhesive joints, respectively. The HVR joints also showed a significant increase in total work before fracture (e.g., 49% and 97% increase with and without adhesive).

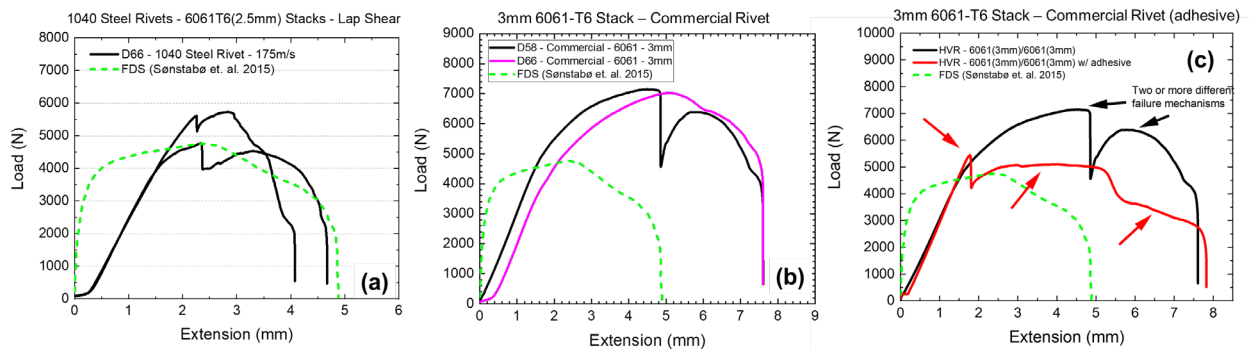


Figure II.3.7.8. (a) LS load-extension curves for 1040 steel flat head rivets. (b) Commercial nail LS tests. (c) 6061-T6 commercial nail with and without adhesive bonding. Source: PNNL.

High-Rate Friction Riveting

High-rate Friction Riveting (HFR) is a multi-material joining method where a rotating cylindrical rivet is driven into a joint assembly, typically in an overlap configuration. The rotating rivet joins the plates in the assembly through a combination of mechanical fastening and friction welding to form the final joint. It is predicated on the FricRiveting process developed by Helmholtz Zentrum Geesthacht [1]. Existing methods,

such as self-piercing riveting [2] and friction bit joining [3], would require a separate joining tool and a consumable part where the part is inserted into the joint assembly while the tool is retracted after the joining process. On the contrary, during HFR similar to the FricRiveting process, the consumable rivet alone is driven into a joint assembly without the need for a separate tool.

In FY 2021, HFR was used to join Al alloys to CFRP, a dissimilar Al alloy, and steels using Al and steel rivets. Rivet design was optimized to develop HFR joints with minimal gaps between the joint assembly. Specific process conditions were developed for each stack-up/rivet combination with the parameter optimization being driven by the ability to generate laboratory-scale samples with minimal macro-scale defects, such as cracking or interfacial separation. Figure II.3.7.9 shows the perspective and cross-sectional images of the Al/CFRP and Al/steel joints. AA6022 was used for making the Al/CFRP joints while AA6061, AA5052, A356, and DP590 were used in the Al/steel joints. AA6022 plates were also joined to each other using the HFR process. The rivet material was AA7075 in the T6 condition for the Al/CFRP joint. Al/steel joints used M42 and HS C300 alloy steel rivets.

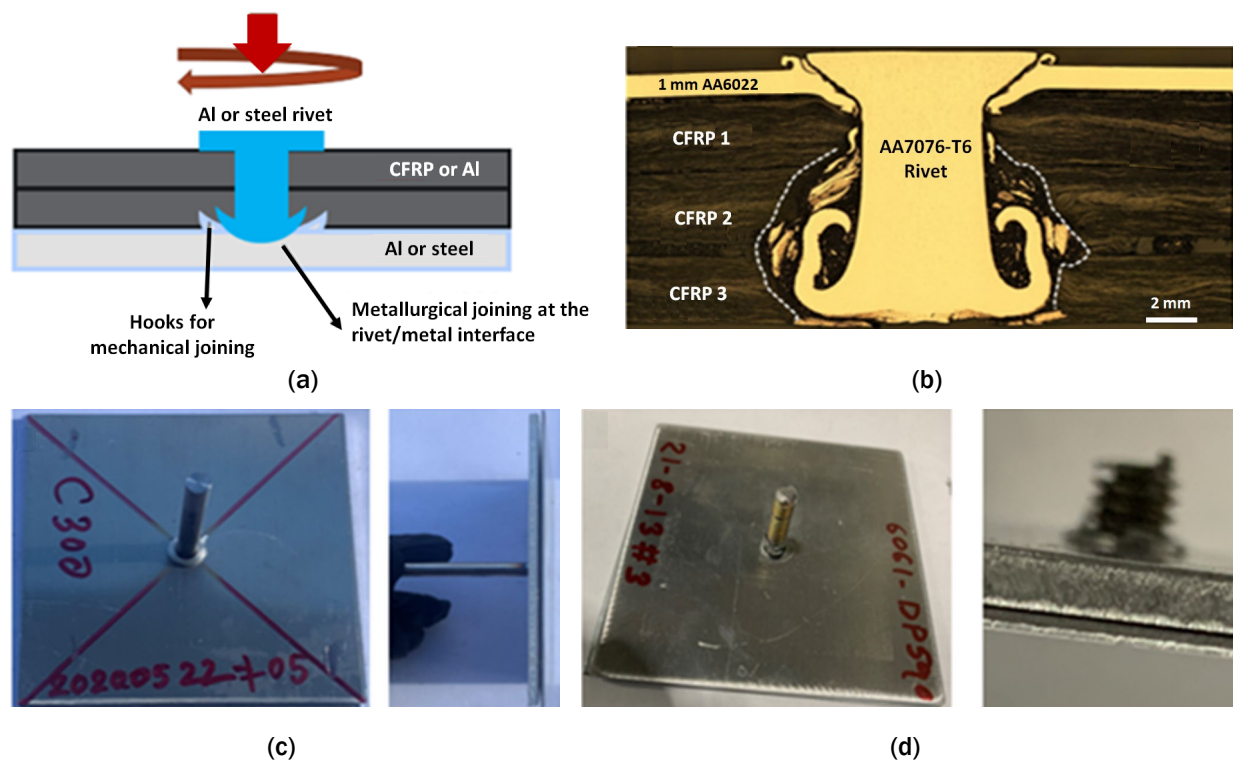


Figure II.3.7.9. (a) Schematic demonstrating the HFR process for multi-material stack-ups. (b) A micrograph of the cross-section of an Al/CFRP joint comprising AA6022 joined to three CFRP plates using an AA7075-T6 rivet. (c) Top and side views of an Al/Al HFR joint made with an HS C300 alloy steel rivet. (d) Orthogonal and side views of the Al/steel HFR joint with AA6061 and DP590 plates, as well as an M42 steel rivet.

Source: PNNL.

Al/steel joints were manufactured with and without adhesive and tested in the LS tensile configuration. The results are summarized in Figure II.3.7.10. The results from the LS tensile test were compared with the Al/steel joints made of AA5052 and galvanized low carbon steel plates manufactured by resistance spot-welding (RSW) [4] and AA5083/340LA joints manufactured with FDS [5]. Normalized peak stresses of the three Al/steel HFR joints without an adhesive were 65% to 99% higher than the RSW joints and comparable to the FDS joints. Here, LS tensile load obtained from tensile testing was normalized by the interfacial area, since the failure mode was through the interface. For the HFR joints, the interfacial area was not clearly defined since

the adhesive was also load bearing. Therefore, to better compare the performance of the HFR joints with and without adhesive with RSW joints, normalized fracture energy was determined from the tensile test. Table II.3.7.1 gives the results of these tests. Compared to the Al/steel RSW joint, Al/steel HFR joints without an adhesive demonstrated 30% to 80% higher normalized fracture energy, while the HFR joints with an adhesive were over 300% better in performance. Normalized fracture energy of Al/steel HFR joints manufactured without an adhesive was comparable to the FDS joints. On the contrary, the addition of adhesive enhanced the normalized fracture energy to over 300% of the FDS joints.

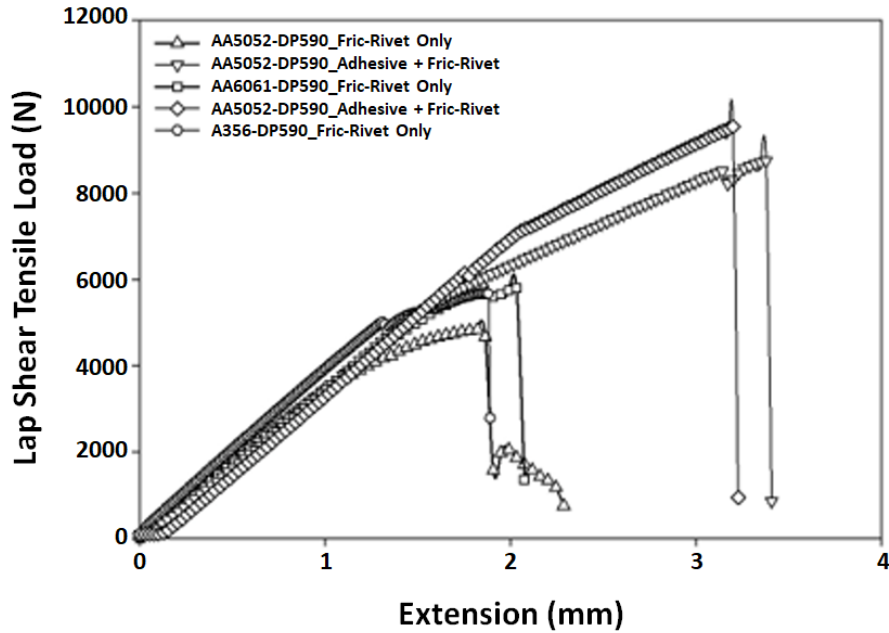


Figure II.3.7.10. LS tensile load of Al/steel joints manufactured using HFR as a function of joint extension. Source: PNNL.

Table II.3.7.1. Normalized Peak Stress and Normalized Fracture Energy of Various Al/Steel HFR Joints with and without Adhesive as Compared to An Al/Steel Joint Manufactured Using RSW as the Baseline

Stack-up	Peak Stress ¹ (MPa)	Fracture Energy ² (J/mm)
AA5052/DP590	157.5 ± 17.6	1.4
AA6061/DP590	190.2 ± 7.9	1.8
A356/DP590	185 ± 5.4	1.3
AA5052/DP590 + Adhesive	N/A*	4.2
AA6061/DP590 + Adhesive	N/A*	4.4
AA5052/GI-LCS	95.7	1
AA5083/HC340La	204.9	1.6

¹Normalized properties; ²Interfacial area different from other configurations and not estimated for adhesive joints.

Conclusions

Air plasma treatment improved the LSS of metal/metal, metal/CFRP, and CFRP/CFRP combinations. The improvement of LSS is about 3% to 10% for different metal/metal combinations. Improvements of 11% to 23% was observed for the different metal/CFRP and CFRP/CFRP combinations.

Uncured adhesive is highly shear-thinning at RT, which could potentially lead to adhesive flow-out during high-shear riveting processes. Gelation of the adhesive occurs at 150°C, which is a temperature that is similar to the beginning of the curing exotherm, leading to increased viscosity. This suggests that the ideal time to carry out riveting on the adhesive joints would be at the beginning of the curing process.

Coupled with intensive modeling activities, dies, velocities of the projectiles (rivets), and dimensions of the rivets for the HVR process have been optimized. The HVR process demonstrated a 14.3% and 50.1% increase in maximum load over FDS for both the adhesive and non-adhesive joints, respectively. The HVR joints also showed a significant increase in total energy absorption before fracture (49% and 97% increase with and without adhesive).

Normalized peak stresses of the three Al/steel HFR joints were 65% to 99% higher than the RSW joints and comparable to the FDS joints. Al/steel HFR joints demonstrated 30% to 80% higher normalized fracture energy, while the HFR joints with adhesive were over 300% better in performance. Normalized fracture energy of Al/steel HFR joints manufactured without an adhesive was comparable to the FDS joints. On the other hand, the addition of adhesive enhanced the normalized fracture energy to over 300% of the FDS joints.

References

1. Amancio-Filho, S. T. and J. F. dos Santos, 2008, "Development of FricRiveting as a new joining technique for polymer and lightweight alloys," *Materwiss. Werksttech.*, Vol. 39, No. 11, pp. 799–805.
2. Settineri, L., E. Atzeni, and R. Ippolito, 2010, "Self-piercing riveting for metal-polymer joints," *Int. J. Mater. Form.*, Vol. 3, pp. 995–998.
3. Miles, M., S.-T. Hong, C. Woodward, and Y.-H. Jeong, 2013, "Spot-welding of aluminum and cast-iron by friction bit joining," *Int. J. Precis. Eng. Manuf.*, Vol. 14, No. 6, pp. 1003–1006.
4. Arghavani, M. R., M. Movahedi, and A. H. Kokabi, 2016, "Role of zinc layer in resistance spot-welding of aluminum to steel," *Mater. Des.*, Vol. 102, pp. 106–114.
5. Graf, M., S. P. Sikora, and C. S. Roider, 2018, "Macroscopic modeling of thin-walled aluminum-steel connections by flow-drill screws," *Thin-Walled Struct.*, Vol. 130, pp. 286–296.

Acknowledgments

The authors from PNNL recognize Y. Qiao, Y. Shi, A. Ortiz, and D. Merkel for the adhesive bonding work; Z. Yu, and N. Kanbargi for the adhesive curing work; B. Schuessler, M. Rhodes, R. Seffens, S. Niverty, A. Guzman, and V. V. Joshi for the HVR work; R. M. Rabbi, and K. Kappagantula for the HFR work; and A. Soulami, L. Li, and L. D. R. Tomayo for the computational simulations.

II.3.8 Solid-State Joining of Multi-Material Autobody Parts Toward Industry Readiness (Pacific Northwest National Laboratory and Oak Ridge National Laboratory)

Piyush Upadhyay, Co-Principal Investigator

Pacific Northwest National Laboratory
900 Battelle Blvd.
Richland, WA 99352
E-mail: piyush.upadhyay@pnnl.gov

Yong Chae Lim, Co-Principal Investigator

Oak Ridge National Laboratory
One Bethel Valley Rd.
Oak Ridge, TN 37831
E-mail: limy@ornl.gov

Sarah Kleinbaum, DOE Program Manager

U.S. Department of Energy
E-mail: sarah.kleinbaum@ee.doe.gov

Start Date: October 1, 2020 End Date: September 30, 2023
Project Funding (FY 2021): \$1,150,000 DOE share: \$1,150,000 Non-DOE share: \$0

Project Introduction

PNNL and ORNL are teaming to further advance and mature friction-based solid-state joining technologies toward industry readiness for the high-volume production of multi-material autobody structures. Two solid-state joining technologies—friction-self-piercing rivet (F-SPR) and friction stir linear welding (FSLW)—have been under development at the two national laboratories and have been proven to apply to a wide range of material stack-ups at the laboratory coupon level. We intend to overcome identified technical barriers related to robustness, joint function to process correlation, and equipment scale-up to sufficiently advance joining technologies for industry adoption with support from a partnering OEM, Honda R&D Americas (HRA); a Tier 1 supplier, Magna; Eagle Bend Manufacturing (EBM); and a material supplier, Arconic Inc.

The ability to join dissimilar materials with specific property needs is critical for lightweight multi-material design. In a body-in-white construction, replacing the steel passenger cage with an appropriately designed stamped Al assembly and using CFRCs to stiffen AHSS in front/rear end sections is an approach to achieving this goal. This approach comes with two joining challenges: (1) the ability to effectively assemble dissimilar stamped Al subassemblies; and (2) the ability to join the Al subassembly to the AHSS/CFRC subassembly.

This need requires the development of technologies that can join different material sets in a cost-effective, robust manner, in addition to minor modifications to assembly lines that can meet high-volume demands. Friction stir derived linear and spot-joining technologies provide a solution.

In FY 2021, we initiated this collaborative project by performing baseline joint developments for dissimilar Al alloys, Al-Steel, and Al-CFRP. FSLW was successfully transferred from a gantry-based machine to a robotic platform. 3T (three separate stacked sheets) Al FSLW joints produced in the robot exceeded the coupon level strength target at high-speed. As a single joining process, the F-SPR process was refined for different material combinations to achieve high joint strength in LS and cross-tension testing in the laboratory coupon level.

Objectives

The goal of this multi-lab, multi-year project is to mature two friction-based joining technologies and to demonstrate joining of dissimilar Al components and Al to steel/CFRC subassemblies. The outcomes will be process parameters, machine control strategies, and a clamping and fixturing design, all necessary to advance the FSLW and F-SPR joining methods from the lab-scale plaque and coupon levels to component-level demonstrations geared toward high-volume production.

Approach

Two friction stir-based joining processes—FSLW and F-SPR—at two national laboratories are being leveraged to develop and demonstrate multi-material joining in a relevant automotive component. The material stacks to be joined and characterized in this project for both processes are shown in Figure II.3.8.1. The materials, as well as their temper and thicknesses, were established in consultation with the collaborating industry.

FSLW-stack 1	FSLW stack 2	FSPR	FSPR
7055-T76 – 2.5 mm	6111-T4 – 2.5 mm	CFRP- 1.9 mm to 3.2 mm	7055 – 2.5 mm
7055-T76 – 2.5 mm	6111 –T4 2.5 mm	6111-T4 7055-T76 – 2.5 mm	AHSS – 1.2 mm to 1.6 mm
6022-T4 –1 mm	6022-T4 –1 mm		

Figure II.3.8.1. Material arrangements for the four material stacks to be joined and characterized. Source: PNNL.

The overall tasks to be performed each year and their interactions, as illustrated in Figure II.3.8.2, are:

- Linear (short stitches and long continuous welds): friction stir welding of dissimilar Al alloys
- Spot-welding: spot/tack welding for Al structures before linear friction stir welding
- F-SPR: spot-welding of Al-CFRP and Al to AHSS.

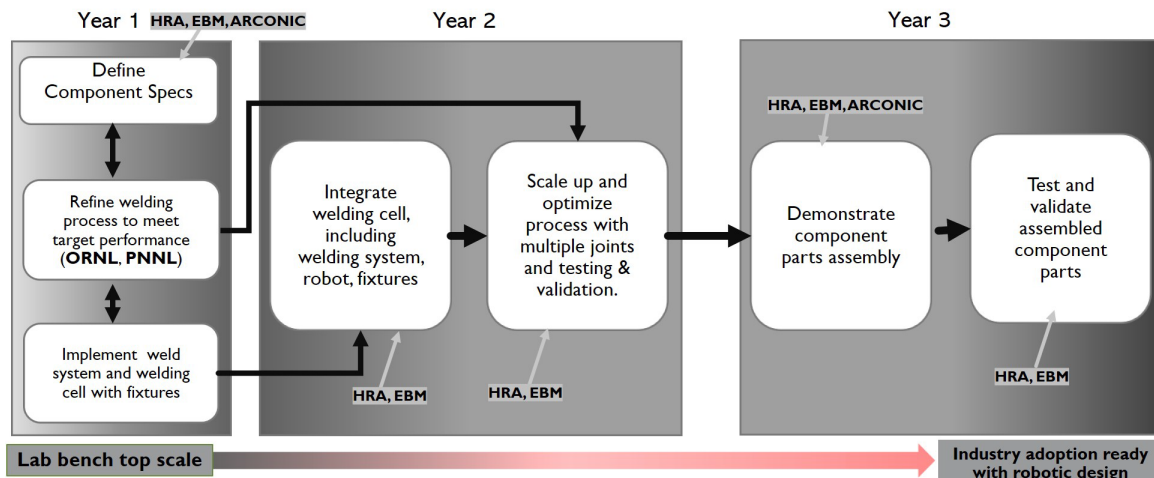


Figure II.3.8.2. Overview of project approach. Source: ORNL.

The R&D activities during this first FY were to define material stack-up and refine joining processes to meet target performance by implementing welding system and fixtures at each national laboratory.

Results

FSLW Process Development in Robot

This year, we transferred the FSLW process to produce 3T Al assembly joints from a gantry system to a robotic platform, as shown in Figure II.3.8.3(a). The stiffness of the robotic end-effector varies depending on robot posture and the location of the weld line relative to the robot base. Stiffness also determines the extent of

Z-force and allowable speed. Thus, a campaign of robot-based process development was performed to adapt the FSLW process to produce the 3T Al joint coupons. Rapid coding language was used to code the welding program in the robot. Welding parameters, including RPM, welding speed, plunge RPM velocity, and tool tilt, were varied using the baseline FSLW tool, as observed in the inset of Figure II.3.8.3(b), from prior work. A welding speed of 0.5 m/min to 2 m/min and a 1200 rpm to 3000 rpm range were used to produce many welded coupons. Continuous clamping was used to produce long linear welds for the LS sample, as shown in Figure II.3.8.3(c), while the curve welds, observed in Figure II.3.8.3(d), and the discrete clamping bolts, outlined in Figure II.3.8.3(e), were used to produce the T-peel samples. Process variables were recorded and correlated with each joint's macro structure and resulting mechanical performance.

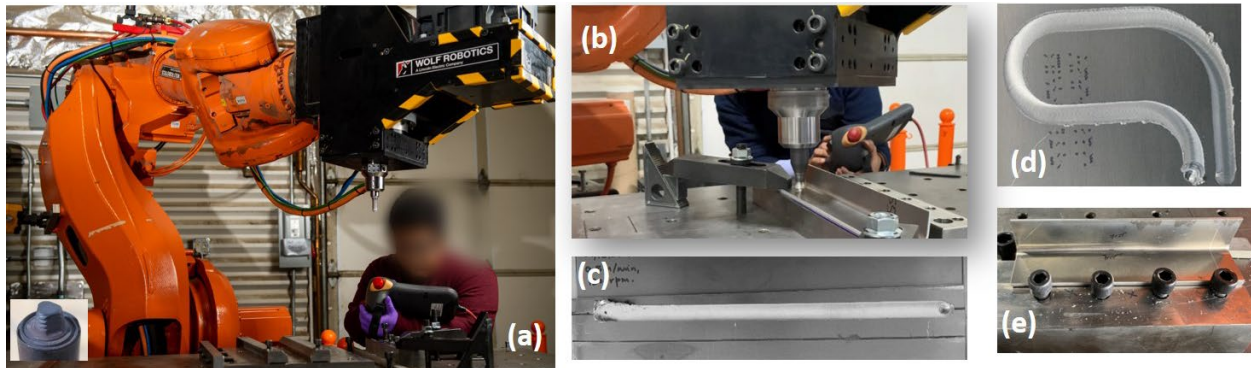


Figure II.3.8.3. (a) Robotic platform (inset: the baseline tool). (b) T-peel sample welding. (c) Linear lap weld. (d) Curve weld. (e) Clamping scheme for the T-peel sample. Source: PNNL.

After several rounds of process development, we were able to identify the welding parameters to produce 3T FSLW joints at a welding speed of 1 m/min that exceeded minimum strength requirements stipulated by our collaborating OEM (e.g., 375N/mm for the LS and 112.5N/mm for the T-peel). This was demonstrated for both the 3T multi-alloy Al combinations being developed in this project:

- Stack 1: 7055-T6 (2.5 mm) - 7055-T6 (2.5 mm) - 6022 (1.0 mm)
- Stack 2: 6111-T4 (2.5 mm) - 6111-T4 (2.5 mm) - 6022 (1.0 mm).

For Stack 1, an average LSS of 652 ± 74 N/mm, as observed in Figure II.3.8.4(a), and T-peel strength of 119 ± 5 N/mm, as shown in Figure II.3.8.4(b), was achieved. For Stack 2, average LSS of 519 ± 45 N/mm and T-peel strength of 122 ± 9 N/mm was achieved. The LS tests were performed on 1 in. wide samples extracted from the long linear welds. The T-peel samples were tested in the form of a 50 mm long stitch weld. The bar chart in Figure II.3.8.4(c) shows the average strength values, deviations, and number of samples tested. Having achieved this milestone, our teams now are working towards performing a large set of welding campaigns for both the LS and T-peel configurations to prove process repeatability.

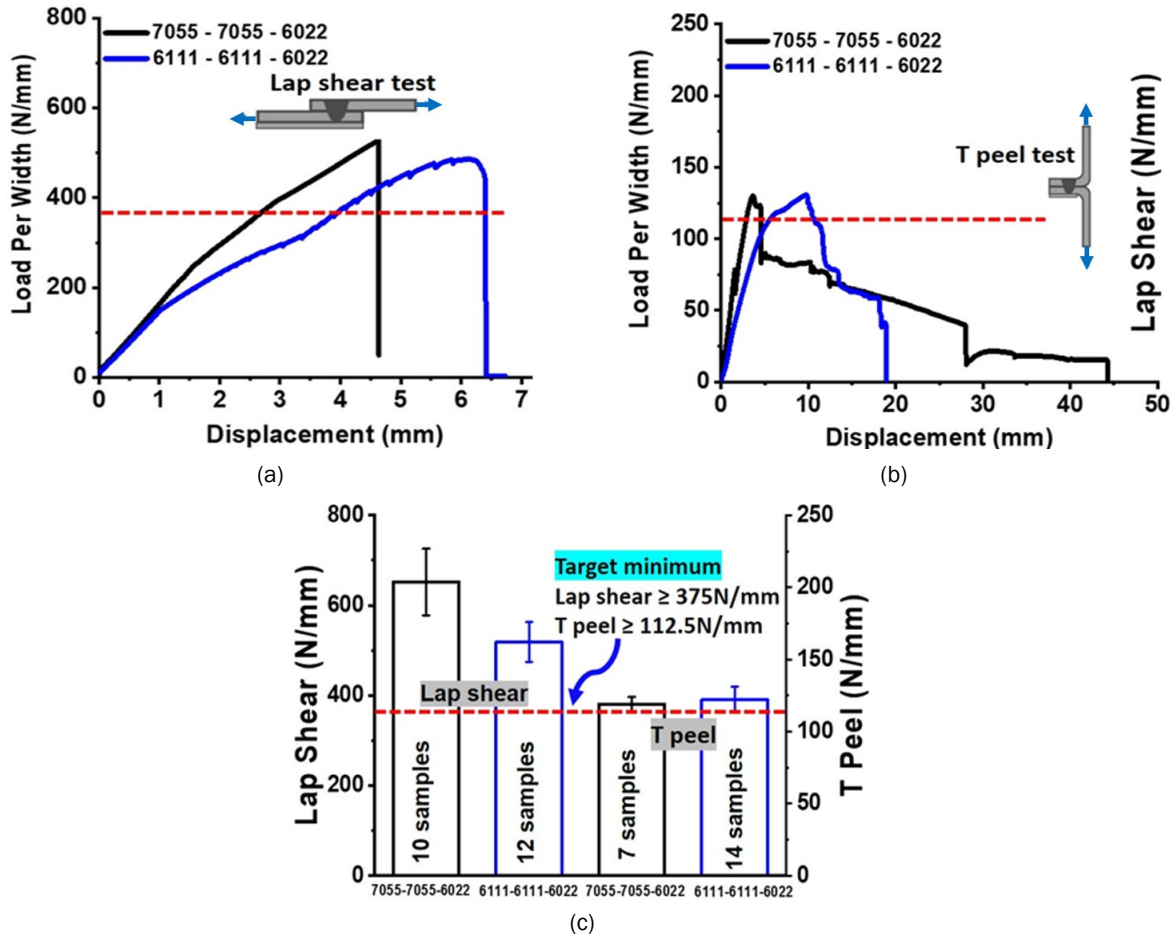


Figure II.3.8.4. Load per unit width vs. cross-head displacement plot for 3T FSLW joints: (a) LS; (b) T-peel; and (c) bar chart compilation of several tested samples. Source: PNNL.

Stack 1 typically fractured at the interface of the nugget and HAZ either on the top or middle 7055 sheet, as shown in Figure II.3.8.5(a). Where micron-size weld defects were observed, fractures occurred via the nugget while still retaining joint strength, as shown in Figure II.3.8.5(b). For Stack 2, typical fracture modes for both the T-peel and LS loading is interfacial fracture between the 6111 sheets, as seen in Figure II.3.8.5(c). Figure II.3.8.5(d) shows an as-polished, unetched joint cross-section for reference. Fracture modes and joint cross-sections—including hook morphology—provide input parameters for structure-property modeling.

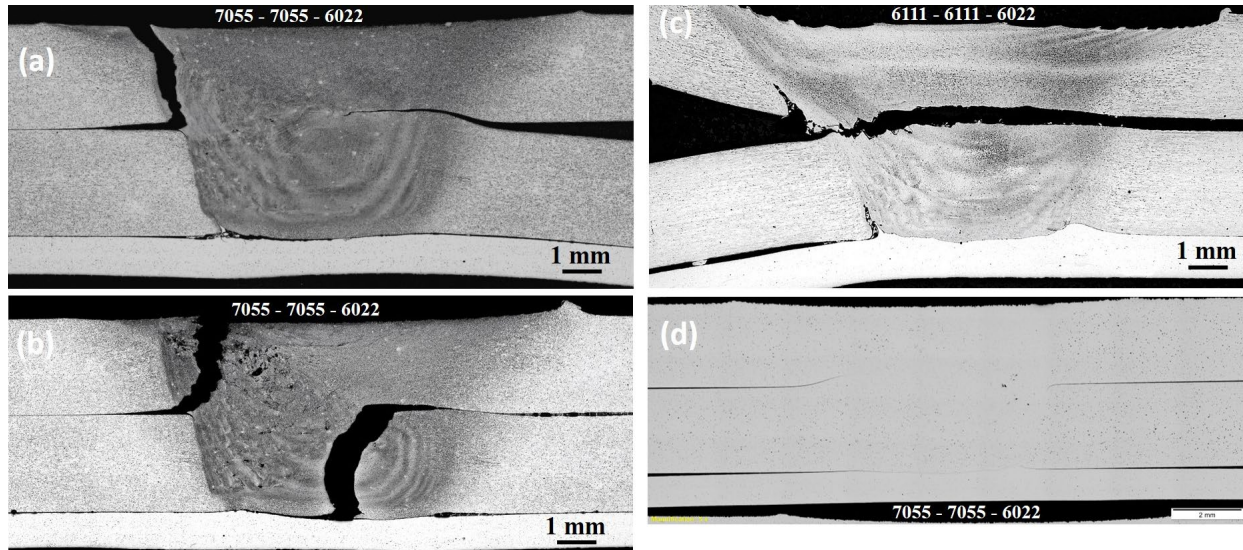


Figure II.3.8.5. Representative fracture mode for both LS and T-peel of (a) and (b) the 7055-7055-6022 stack; (c) the 6111-6111-6022 stack; and (d) the optical micrograph of the 7055-7055-6022 stack (e.g., 1350 rpm at 0.5 m/min). Source: PNNL.

Several unique aspects of robotic FSLW as opposed to gantry-based welds were observed. For instance, in certain intermediate rpms for a given welding speed, the planar forces had significant oscillations (e.g., 1700 rpm at 0.5 m/min). Upon further characterization, the joints were observed to contain large defects; thus, mechanical performance was poor. Resonant frequency of the robotic arm may have matched that of the process frequency, thereby resulting in excessive vibration of the welding head [1]. In addition, a change in the joining characteristics near the plunge-in location of the FSLW was made in the robot vs. the gantry. Using similar welding parameters, the joint strength near the plunge-in location was lower in comparison to “steady-state” locations (~2 in. away from the plunge-in location). As such, we are investigating variations to plunge-in parameters to increase joint performance. While the addition of power (e.g., increasing the rpms, decreasing the plunge-in velocity) can enable greater mixing of materials, this can also lead to surface overheating—especially in the 7055 sheets. We are exploring the effect of concave shoulder design to minimize overheating.

Figure II.3.8.6 highlights the effects of the plunge-in parameters needed to make a weld of a given weld length. While welding speed is a criterion for high-volume production, we are also mindful that time for plunge-in can contribute to the overall time needed to complete a joint. For instance, a plunge-in velocity of 0.5 m/sec vs. 5 mm/sec (e.g., maximum using the PNNL robot) shows a plunge-in time of 35 seconds, as observed in Figure II.3.8.6(a), vs. 5 seconds, as shown in Figure II.3.8.6(b). In a mass production context, it is ideal to minimize the time during plunge-in. However, the plunge-in sequence facilitates shoulder/tool seating and mixing of the cold material during a startup. Thus, an ideal tradeoff of plunge speed/plunge rpm combination for each material set to minimize plunge time without compromising mixing is required.

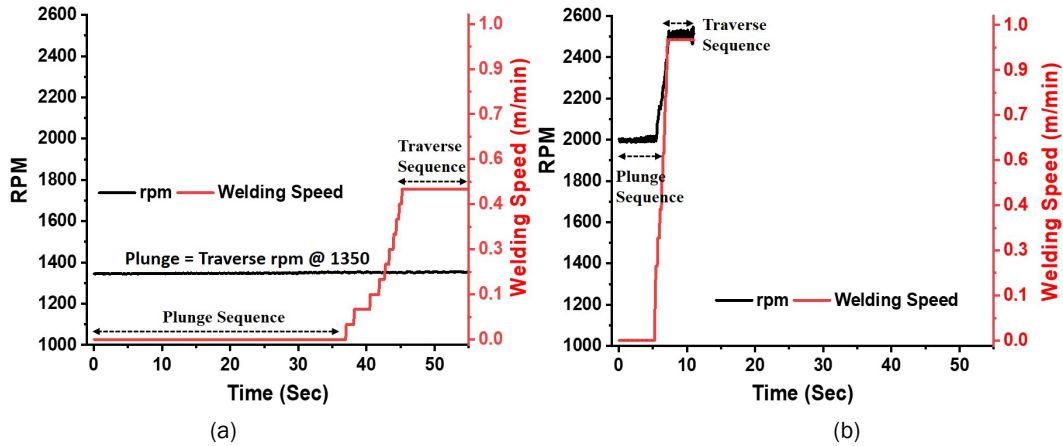


Figure II.3.8.6. Comparison of welding time (including plunge-in and traverse time) per plunging speed. Source: PNNL.

Sufficient clamping is critical to produce defect-free, flash-free FSLW. One requirement for FSLW is to apply a high enough clamping force to prevent any movement and to have tight material contact during the joining process. Excessive clamping force on the part is not viable with a robotic application in an industrial production line. While we are continually working to minimize clamping needed to produce T-peel coupons, we are also collaboratively leveraging ORNL's F-SPR capability to explore using tack welding prior to FSLW.

Friction Stir Welded Joint Strength Modeling (PNNL)

Typical FSLW joints contain microstructural features, such as voids, oxide layers, and unavoidable cracks that interface with the base metal and nugget. Also, the welding process alters the material properties around the joint. Thus, the effect of joint features on desired mechanical properties needs to be understood so that it is possible to design a FSLW assembly for a component and predict fracture conditions. Figure II.3.8.7 below summarizes the modeling work conducted to determine these structure-property relationships and predict the mechanical behavior of a 3T Al assembly.

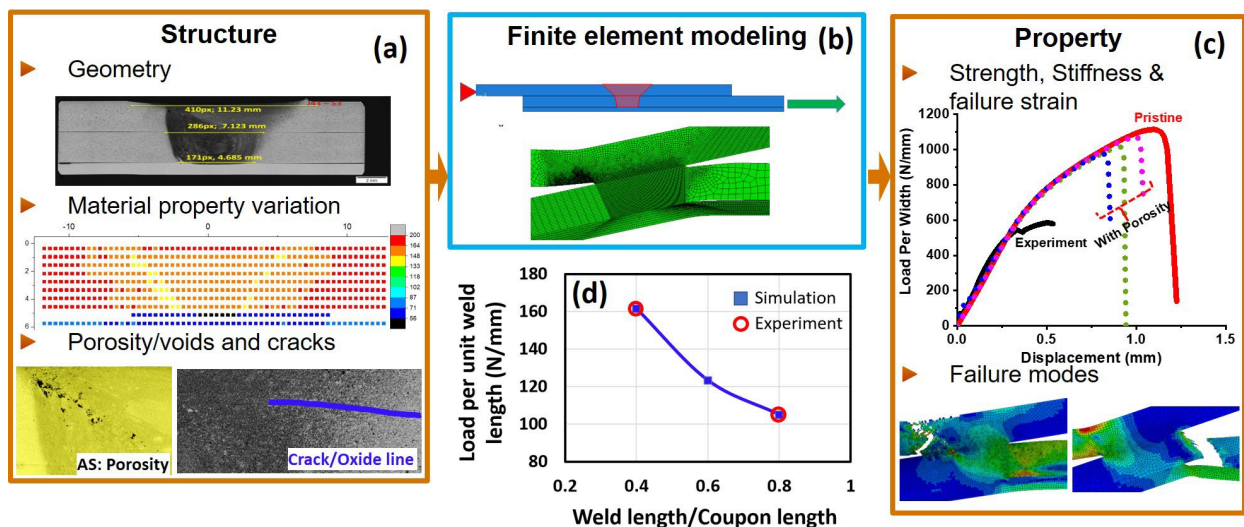


Figure II.3.8.7. (a) The approach that was used starting with the material properties and (b) using a finite element model to determine (c) the structure-property relationships in a FSWL joint. (d) The simulated and experimentally determined strengths of the T-peel joints of various weld lengths. Source: PNNL.

FEA informed by characterization data from the FSLW joint was used to simulate the A17055 joint's response to uniaxial tensile loading. A 2D geometry with the assumption that all transverse weld cross-sections have the same microstructure is used. Initial simulations use uniform base material properties (e.g., 7055-T67) to determine the effect of the joint's geometry alone. Later, material heterogeneity inferred from microhardness testing and microstructural features inferred from the micrographs are gradually introduced. Behaviors such as a ductile fracture through the growth of porosity are also considered.

This approach enabled an investigation of the influence of individual aspects of the joint's structure on the resulting strength. Both porosity and FSW-induced softening affect the failure modes and significantly reduce the joint's strength. These results, in combination with additional simulations supported by fracture toughness characterization, will lead to a predictive capability for coupons and component-level joints and guide improvements in the FSLW process.

Aspects of the joint's 3D structure, such as the length of the weld stitch, also affect the strength of the T-peel and U-peel joints. 3D models of the A17055 T-peel joint were constructed; in addition to using the microstructure properties, the fracture properties were determined by calibrating to an experimental data point. Figure II.3.8.7(d) shows the simulated strengths for T-peel joints with various weld lengths. A trend of increasing load-carrying capacity of the joint per unit length of the weld can be observed. These results will help optimize the weld time.

F-SPR Process Development for Various Material Combinations (ORNL)

As a collaboration effort with PNNL for FSLW in Al-Al, ORNL has refined the F-SPR process for spot-joining of high-strength A17055 to A17055. For the F-SPR joints, the mechanical interlocking distance between the flared rivet and the bottom sheet is critical for performance. In addition, frictional heating is important to prevent cracking of A17055 due to low ductility at RT. Frictional heat and axial plunge force also will promote solid-state joining between the rivet and the surrounding material if they are metallurgically compatible. This solid-state bonding will add to the mechanical strength.

Computational modeling with a sequentially coupled 3D Coupled Eulerian-Lagrangian (CEL) model and an equivalent 2D axisymmetric model was developed to determine the necessary processing parameters to achieve mechanical interlocking in F-SPR joints. Figure II.3.8.8(a) shows the basic modeling procedure, where the overall temperature (~200°C to 300°C) of the Al sheets was predicted by the 3D model, showing good correlation with the evolution of the microstructure characterization results. By mapping the temperature and applying shear load caused by rotational friction, the 2D model can provide full-process simulation at reasonable computational cost. Figure II.3.8.8(b) shows the computational cases with different rivet tip angles and die cavity depths. Table II.3.8.1 summarizes the interlocking distance for each case. Under the same remaining bottom sheet thickness, the Design 2 rivet provides wider mechanical interlocking than the Design 1 rivet, where a shallower die cavity tends to make the rivet leg thicker due to large hydrostatic pressure. By reducing the remaining thickness from 0.5 mm to 0.35 mm, the interlocking distance can be increased by 60%. With a shallower die having a cavity depth 1.0 mm, the interlocking performance becomes even better as compared with a die having a cavity depth of 1.5 mm.

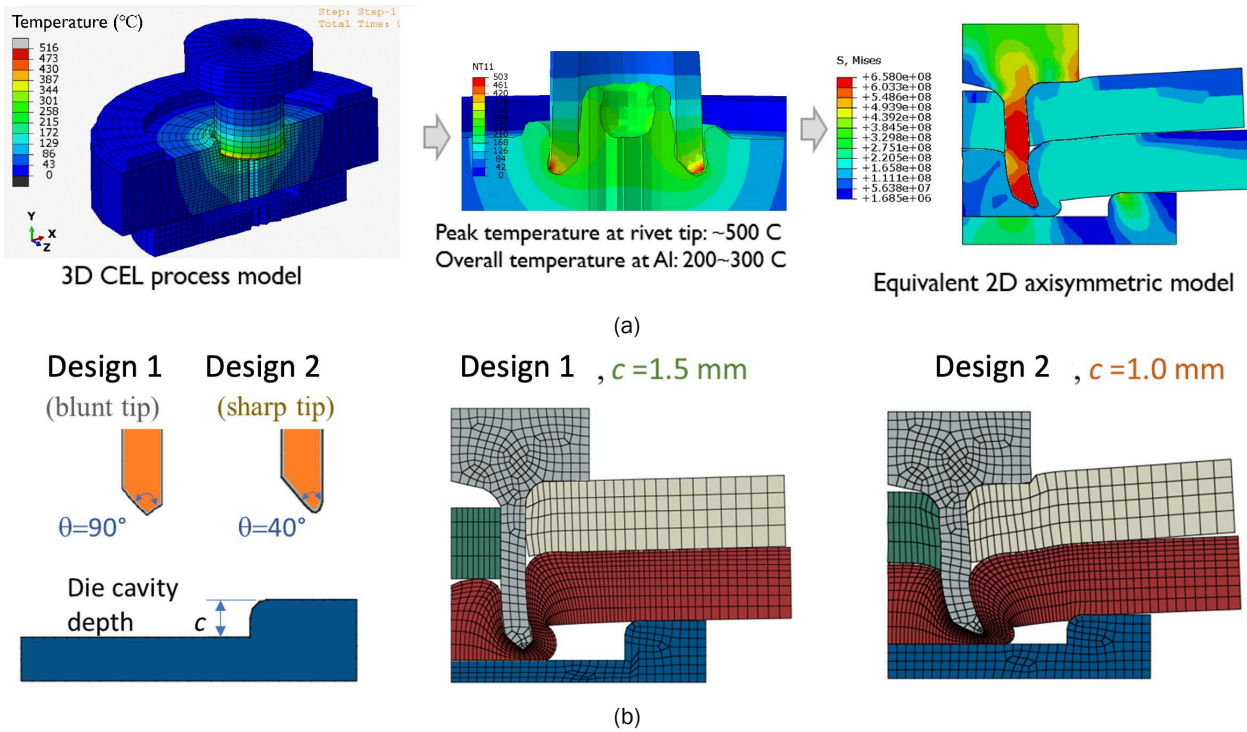


Figure II.3.8.8. Process modeling of an Al-Al F-SPR joint to optimize rivet tip and die cavity depth. (a) The computational approach by 3D CEL model and a 2D axisymmetric model. (b) The simulated rivet shape for a different tip angle and die cavity. Source: ORNL.

Table II.3.8.1. Effect of Rivet Design/Die Cavity Depth on Predicted Mechanical Interlocking Distance

Location	Design 1 Rivet ($c = 1.5$ mm)	Design 2 Rivet ($c = 1.5$ mm)	Design 2 Rivet ($c = 1.0$ mm)
Remaining Bottom Sheet Thickness, $t = 0.5$ mm	0.12 mm	0.31 mm	0.33 mm
Remaining Bottom Sheet Thickness, $t = 0.35$ mm	0.20 mm	0.49 mm	0.52 mm

A F-SPR joint performance model was also developed to evaluate the LSS and cross-tension strength of Al-Al F-SPR joints towards refined rivet design. In particular, rivet shape and strength were examined by the numerical modeling. Figure II.3.8.9 shows the comparisons of fracture mode of the joint and load-displacement curve for different rivet shank diameters (e.g., 5.2 mm vs. 7.8 mm) and rivet material strengths (e.g., 560 MPa vs. 760 MPa). The model shows that a weaker rivet with a tensile strength of 560 MPa will result in rivet failure, as well as having lower strength, as shown in Figure II.3.8.9(a)-(b). Here, interlocking distance was assumed to be 0.6 mm based on initial characterization results. In addition, a larger rivet tensile strength of 760 MPa can improve the tensile failure load by 25%. By using a heat-treated and large-shank rivet, predicted LSS of the joint can reach as high as 12 kN. Comparing the two different interlocking distances, the 0.6 mm measurement can contribute as much as 15% overall LSS. Such information has been referenced by the experimental design to improve joint performance.

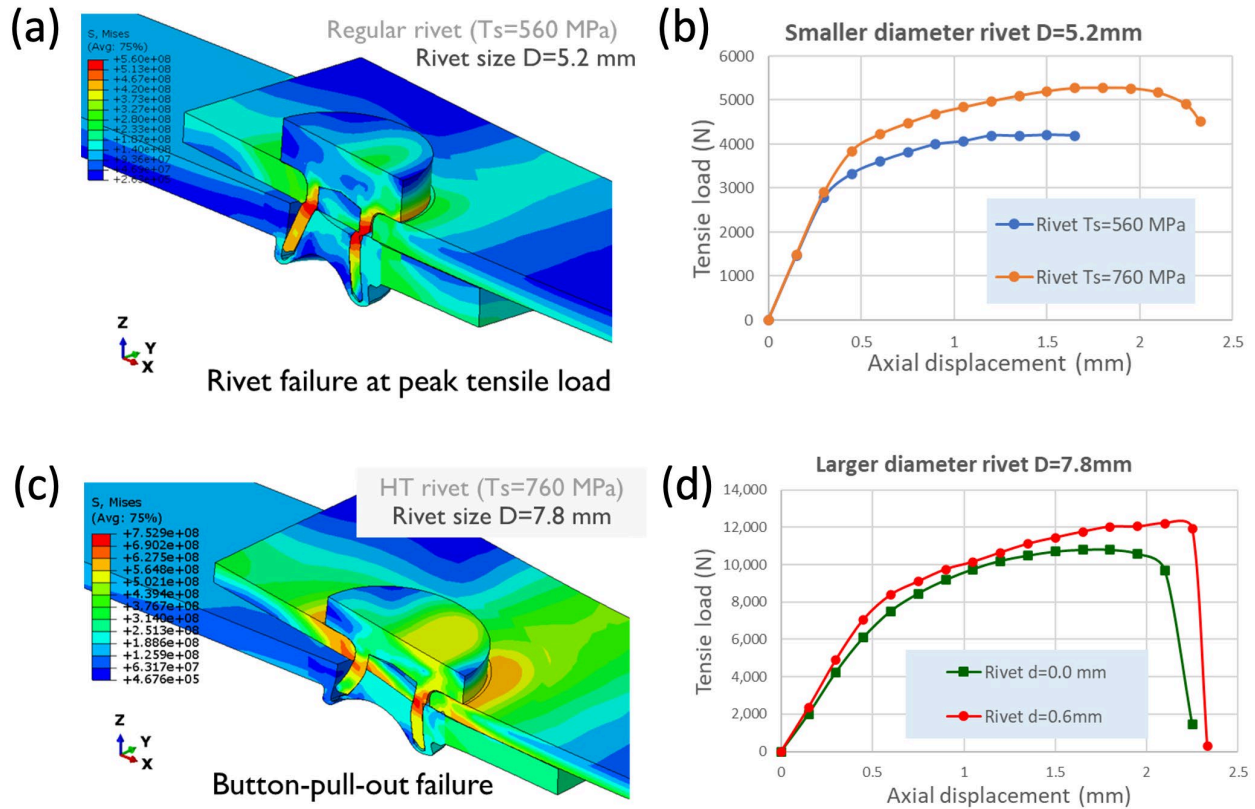


Figure II.3.8.9. Performance modeling of Al-Al F-SPR joint for the LS test: (a) the von Mises stress [Pa] in a joint with a regular rivet; (b) the effect of rivet strength on LSS; (c) the von Mises stress [Pa] in a joint with a heat-treated and larger-shank rivet; and (d) the effect of interlocking distance on joint strength.

Source: ORNL.

To reduce the material in the rivet, a performance model simulating a cross-tension test was employed to optimize the rivet head height, which was originally set as 2.54 mm for non-heat-treated steel. A minimum head thickness is required to sustain the torque during the joining process, as well as the external load during the mechanical test. Figure II.3.8.10(a) depicts the plastic strain distribution for the rivet under a 10 N-m torque and a 5 kN plunging force, suggesting the 1-mm-thick rivet head with a large fillet can carry the processing load without excessive plastic deformation. Figure II.3.8.10(b)-(c) show stress and plastic strain for the rivet at peak load during the cross-tension test, with the fillet region of the rivet showing a high stress distribution due to reduced head thickness. For a thicker rivet head, the predicted cross-tension failure load is larger and saturated at 1.5 mm for the same rivet material strength. By increasing rivet material strength by heat-treatment, predicted cross-tension failure load is increased more than 10% at the same rivet head thickness. All cases have a constant interlocking distance of 0.6 mm since the process condition and rivet leg shape are the same. After the Al-Al computational model was developed as a basis, this numerical approach can be further applied for joining process optimization for different material combinations.

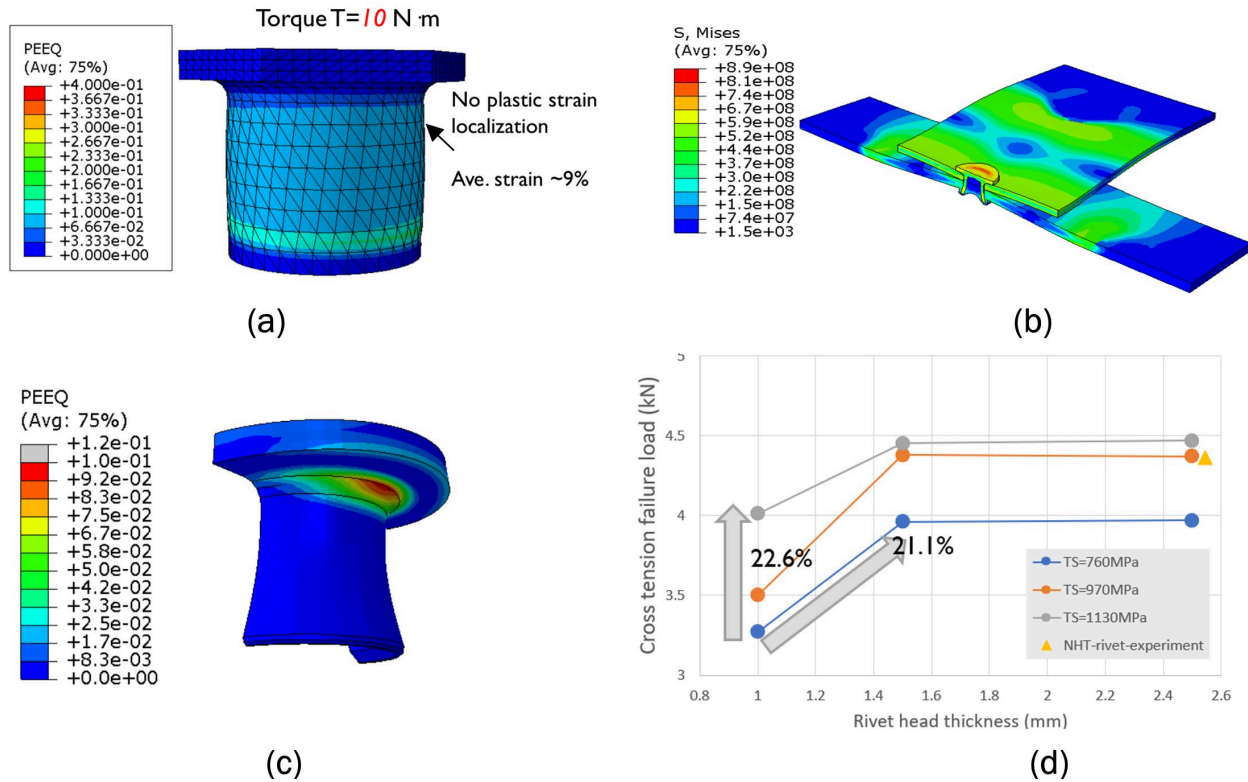


Figure II.3.8.10. Cross-tension modeling of an Al-Al F-SPR joint to optimize rivet head and material strength: (a) the rivet under combined torque and compression load; (b) the von Mises stress [Pa] distribution at peak load of cross-tension; (c) the plastic strain localization at the fillet region of the rivet; and (d) the dependence of joint load on rivet head thickness and tensile strength. Source: ORNL.

With guidance from computational modeling, the optimized rivets and dies were fabricated for joining Al7055–Al7055 by F-SPR. Different joining process conditions—such as spindle rotational speeds and axial plunge depths and speeds—were used to produce Al7055–Al7055 in a LS joint configuration of $40 \text{ mm} \times 120 \text{ mm}$ with a 20 mm overlap. After achieving the highest LS failure load, the same joining process condition was used for cross-tension specimens of $50 \text{ mm} \times 150 \text{ mm}$ with a 50 mm overlap. Figure II.3.8.11 summarizes the load and displacement curves from the LS and cross-tension testing. Four samples were tested for each mechanical testing to study joining process consistency. Averaged LS fracture was $11.2 \pm 0.24 \text{ kN}$, while averaged cross-tension failure load was $5.82 \pm 1.35 \text{ kN}$, thus achieving 51.9% of LS failure load. It is noted that one scattering result from the cross-tension testing could be a shorter rivet leg length during fabrication. Nevertheless, cross-tension fracture load exceeded the evaluation criteria suggested by our industry partner (e.g., 30% of LSS). All tested LS and cross-tension coupons showed a fracture at the bottom of the Al7055 sheet, indicating strong mechanical interlocking between the flared rivet leg and the bottom sheet. Achieved mechanical joint performances were close to the predicted computational modeling results.

LS on the Al7055–Al7055 joint was cross-sectioned for microstructure characterization at the joint interface, as shown in Figure II.3.8.12. A macrograph of the cross-sectional image is provided in Figure II.3.8.12(a), indicating a crack-free joint. Al7055 has a low ductility ($\sim 9\%$) at RT, so it is easy to form a crack during forming or conventional mechanical fastening (e.g., self-piercing riveting) at ambient temperature. However, frictional heat is generated during the F-SPR process so that it locally softens the material to produce a crack-free joint. It was reported that heating the 7xxx Al alloy above 200°C can minimize cracking during the forming process. Therefore, the estimated temperature during the joining process can be above 200°C , which shows good correlation with the predicted temperature in numerical modeling. This is one of the advantages of the F-SPR process for joining low ductility materials without an auxiliary heating system and an additional

joining step. Mechanical interlocking distance between the flared rivet leg and the bottom Al sheet, which is identified by the yellow dot circle in the figure, was measured at 0.6 mm, thus resulting in good mechanical joint performance. Figure II.3.8.12(b) shows magnified optical images at the left side joint interface, identified in the figure by the yellow box, after etching. Approximately more than 100 μm of solid-state bonding between the upper and lower Al sheet near the joint, identified by the horizontal white box in the figure, was observed. This solid-state bonding can contribute further joint strength in addition to mechanical interlocking and can serve as a physical barrier to prevent infiltration of the corrosion medium into a joint interface. In addition, Al grain refinement at the joint interface was observed due to dynamic recrystallization during the joining process. Furthermore, additional solid-state joining was observed between the steel rivet and the surrounding Al material, identified by the white box in the figure, due to frictional heat generation during the joining process. Similarly, grain refinement and solid-state bonding between the Al sheet at the rivet cap, steel rivet, and surrounding Al can be observed in Figure II.3.8.12(c). These additional solid-state joining attributes contribute to the overall mechanical joint performance, leading to failure at the bottom Al sheet.

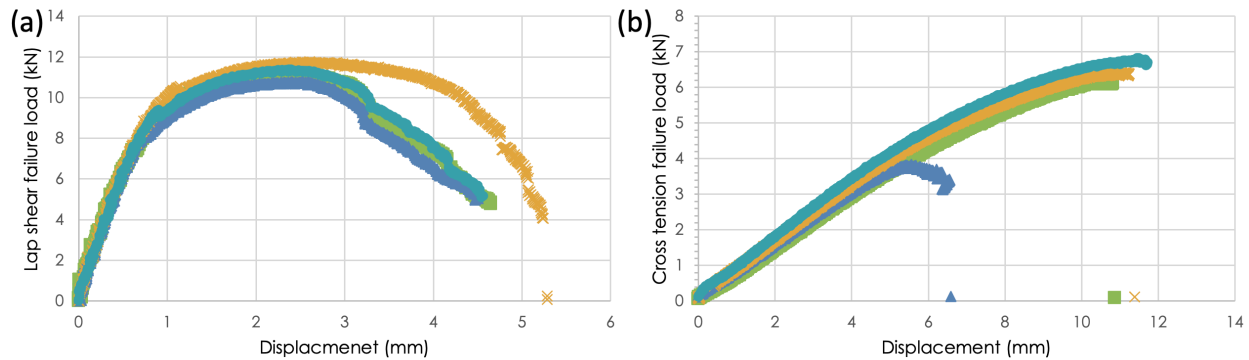


Figure II.3.8.11. Summary of mechanical joint performance for F-SPR Al7055-Al7055 joints from (a) lap-shear tensile testing and (b) cross-tension testing. Source: ORNL.

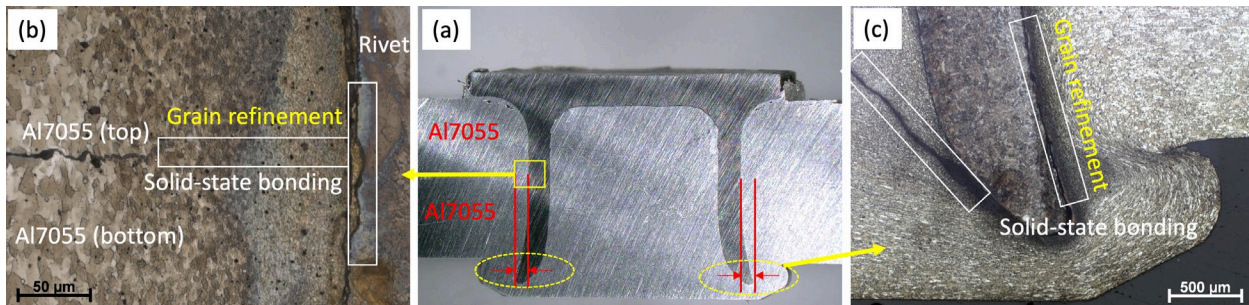


Figure II.3.8.12. (a) Optical image of the Al7055-Al7055 F-SPR joint cross-section. (b) Magnified optical image at the joint interface (yellow box) showing grain refinement and solid-state bonding between the upper and lower Al sheet (horizontal white box), as well as the steel rivet and surrounding Al sheets (vertical white box). (c) Magnified optical image at flared rivet tip and bottom Al sheet, showing grain refinement of the Al sheet at the cap near the joint interface (left white box) and solid-state bonding between the steel and the bottom Al sheet (right white box). Source: ORNL.

Upon successful joining process development for the Al-Al coupons, F-SPR was further applied for CFRC-Al joints where 2.5-mm-thick thermoset CFRC was stacked on the bottom of Al7055. The same coupon dimensions for the Al-Al coupon were used for the CFRC-Al joints. Figure II.3.8.13 summarizes the lap-shear tensile (4 samples) and cross-tension (3 samples) testing of the TS CFRC-Al7055 joint. As shown in Figure II.3.8.13(b), the averaged failure load from the lap-shear tensile testing process was 5.33 kN, exceeding the milestone target strength of 5 kN. The averaged fracture load for the cross-tension coupons was 3.12 kN, higher than the target milestone value of 30% of LSS, as depicted in Figure II.3.8.13(b). The failure mode for

the LS coupons was consistently shear out failure of the CFRC, which would then pull the rivet out of the bottom Al sheet. This shear out failure of CFRC is commonly observed from mechanical bolting when the joint is close to the edge of the coupon [2]. LS failure load can be further increased when stronger CFRC and larger overlap are used at fixed rivet shank diameter. Currently, overlap size was fixed by 20 mm as suggested by the project team. Failure mode for the cross-tension tested coupons was rivet pull-out of the bottom Al sheet.

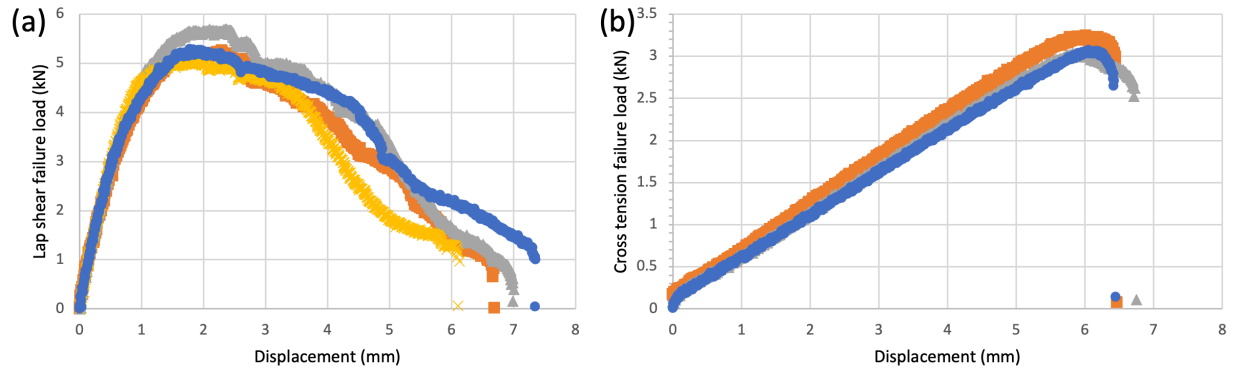


Figure II.3.8.13. Summary of mechanical joint performance for F-SPR TS CFRC-Al7055 joints from (a) LS tensile and (b) cross-tension testing. Source: ORNL.

Figure II.3.8.14 shows a macrograph of a CFRC-Al7055 joint cross-section by F-SPR. The crack-free joint on the bottom Al sheet was achieved due to frictional heat during the joining process. Mechanical interlocking distance between the flared rivet leg and the bottom Al sheet, identified by the red dot circle in the figure, was approximately 0.6 mm. When the rotating rivet was plunged into the bottom Al sheet surface, the partial Al sheet was embedded into the CRFC layer, showing additional mechanical interlocking. The microscopic gap at the joint between the rivet and the Al sheet was filled by CFRC due to material flow during joining process.

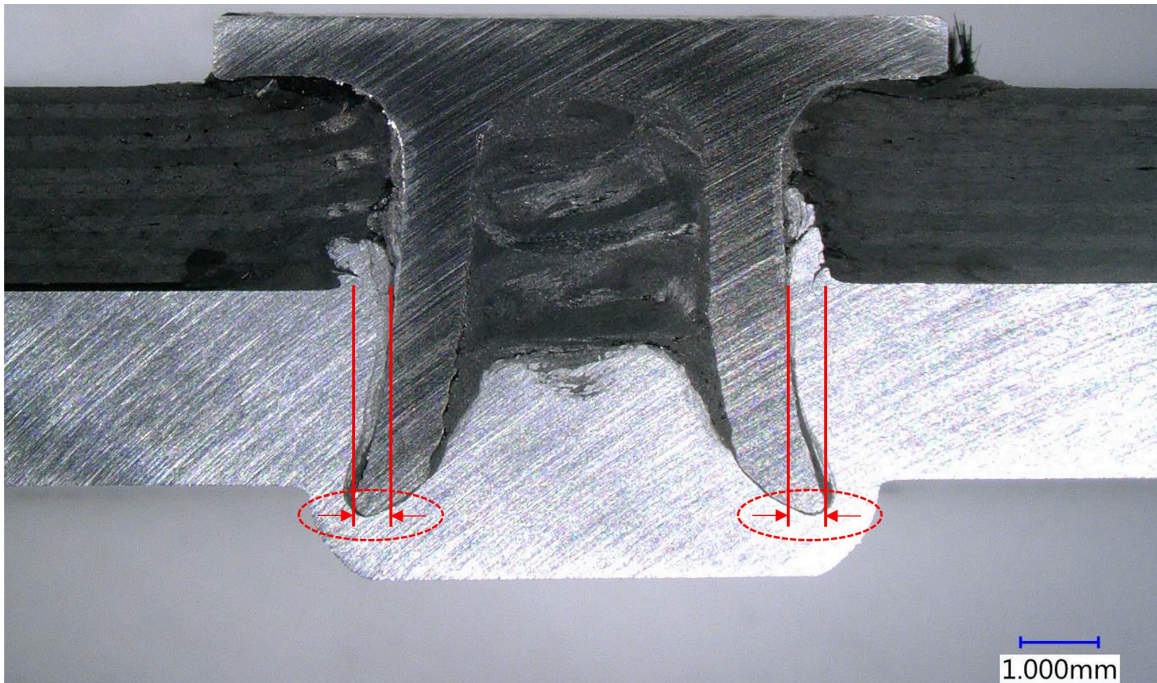


Figure II.3.8.14. Optical image of TS CFRC-Al7055 F-SPR joint cross-section, showing mechanical interlocking between the flared rivet leg and bottom Al7055 sheet, as well as the crack-free joint on the Al sheet.

Source: ORNL.

Conclusions

This multi-laboratory project is aimed at maturing two solid-phase joining techniques to overcome several identified technological barriers towards enabling dissimilar Al assembly with Al/CFRC and Al/Steel joining in high-volume applications. In FY 2020, the project team at PNNL (developing FSLW for 3T Al joints) and ORNL (developing F-SPR for 2T material stacks) focused on refining the joining technology, demonstrating higher coupon level mechanical joint performance on industry-selected material stack-up.

FSLW was successfully transferred to a robotic platform at a commercially viable welding speed. Structure to property model that includes porosity and hardness distribution was built and provided promising correlation with the experiments. Having met the coupon level milestone in the robotic platform, our team now is working towards the goals of the second year of the project, which includes assessing repeatability and robustness of the process, as well as the ability to make a curved welding towards a demonstration prototype part.

With computational modeling support, the F-SPR process was further refined for spot-joining of high-strength Al-Al and CFRC-Al as a single joining process. Friction heat generated during the joining process suppresses the formation of cracking for high-strength and low ductility on the Al sheet. Superior mechanical joint properties from LS and cross-tension testing also were achieved in the laboratory coupon level.

Key Publications

1. Upadhyay, P., and Y. Lim Y, 2021, "Solid-state joining of multi-material autobody parts toward industry readiness," U.S. Department of Energy Vehicle Technologies Office Annual Merit Review, 21–25 June 2021, Virtual. Available at: <https://www.energy.gov/eere/vehicles/annual-merit-review-presentations> (Accessed 20 December 2021).
2. Upadhyay P., H. Das, and D. Graff, 2021, "Three-sheet Al alloy assembly for automotive application," In: *TMS 2021 Virtual, Friction Stir Welding and Processing XI*. pp. 13–20. Available at: https://doi.org/10.1007/978-3-030-65265-4_2 (Accessed 20 December 2021).

References

1. Upadhyay, P., and Y. Lim Y, 2021, “Solid-state joining of multi-material autobody parts toward industry readiness,” U.S. Department of Energy Vehicle Technologies Office Annual Merit Review, 21–25 June 2021, Virtual. Available at: <https://www.energy.gov/eere/vehicles/annual-merit-review-presentations> (Accessed 20 December 2021).
2. Galinska, A., 2020, “Mechanical joining of fiber-reinforced polymer composites to metals—A review. Part I: Bolted joining,” *Polymers*, Vol. 12, No. 10, Art. 2252.

Acknowledgments

At PNNL, the welding and data analysis activities were supported by H. Das in association with M. Frank and W. Choi. Modeling work was performed by K. Balusu, in association with A. Soulami. C. Smith provided robotic welding guidance and support. T. Roosendaal, R. Seffens, and E. Nickerson performed the mechanical testing. A. Ortiz, A. Guzman, and M. Blazon performed the metallography and hardness testing.

The co-PI at ORNL would like to acknowledge R. Davies, Z. Feng, and A. Hayes for their leadership and technical guidance. In addition, great efforts from project team members at ORNL, including H. Huang for modeling and Y. Li and Y. Wang for characterization, are appreciated. Technical guidance and material support from E. Boettcher at Honda R&D America; R. Long at Arconic; and J. K. Kang at EBM is also acknowledged.

II.3.9 Surface Modifications for Improved Joining and Corrosion Resistance (Oak Ridge National Laboratory and Pacific Northwest National Laboratory)

Yong Chae Lim, Co-Principal Investigator

Oak Ridge National Laboratory
1 Bethel Valley Rd.
Oak Ridge, TN 37831
E-mail: limy@ornl.gov

Vineet V. Joshi, Co-Principal Investigator

Pacific Northwest National Laboratory
900 Battelle Blvd.
Richland, WA 99352
E-mail: vineet.joshi@pnnl.gov

Sarah Kleinbaum, DOE Program Manager

U.S. Department of Energy
E-mail: sarah.kleinbaum@ee.doe.gov

Start Date: October 1, 2020 End Date: September 30, 2021
Project Funding (FY 2021): \$1,000,000 DOE share: \$1,000,000 Non-DOE share: \$0

Project Introduction

PNNL, ORNL, and ANL are teaming to develop a combination of adhesive-based bonding and high-rate mechanical hybrid joining methods (i.e., utilizing adhesives along with mechanical fastening joining techniques) for multi-material systems to reduce vehicle weight. Specifically, this project will demonstrate the potential of laser or atmospheric plasma surface treatments to achieve high-quality Al alloy-galvanized steel and Al-CF composite joints that also offer improved bulk substrate and galvanic corrosion resistance. We will utilize several joining techniques, including ultrasonic spot-welding, friction-based fastener joints, and adhesive bonding, which were developed as a part of the first phase of Joining Core Program (JCP), for this effort. The team will also collaborate with other projects in Phase 2 of the JCP to leverage the understanding of the surfaces and improve joint performance.

Corrosion mitigation (general and galvanic corrosion) in the joints of dissimilar materials is a key technical challenge that must be overcome to successfully integrate candidate lightweight autobody structures from materials such as Al alloys, CFRP composites, Mg alloys, and steels [1–3]. Galvanic couples forming at the joint interface of two different materials can greatly accelerate the corrosion of the more anodic material (i.e., Al alloys can suffer from accelerated corrosion when coupled with steels and stainless steels) [4]. If a mechanical fastener is utilized in the joining process, additional galvanic coupling interfaces can be formed [5]. Surface modification strategies can potentially be used to enhance the general corrosion resistance of the bulk substrate [6], as well as to form the electrical isolation between the joint materials to minimize the galvanic effects [7]. However, surface modifications change the surface chemistry and surface morphology of the substrates. These chemical and/or morphology changes on the surface change the surface energy that affects adhesive wetting and bonding performance. The key challenge is to define the extent to which corrosion protection and galvanic isolation can be achieved without compromising joint quality utilizing surface modification processes that are also amenable to high-volume vehicle production.

Laser and atmospheric plasma (AP) surface treatments are being investigated as an effective way to clean local surfaces for improved joining characteristics as compared with conventional chemical cleaning. Additionally, these methodologies can be scaled-up for high-volume automotive production by an integration with automatic translation stages or a robotic system. These treatments are also capable of controllably growing oxide and related ceramic phases on substrate alloys that can offer enhanced corrosion protection. Three key aspects will be addressed: (1) how the chemistry, morphology, and thickness of these surface-modified layers evolve on selected Al alloys (or galvanized steel) and CFRP composite surfaces; (2) how they impact joining processing and adhesive adherence; and (3) if they can significantly reduce bulk corrosion resistance and also mitigate galvanic coupling effects between the Al and the galvanized steel by electrically insulating the interface(s).

Approach

In this project, we will specifically focus on optimizing the surfaces of different faying surfaces to improve the corrosion resistance, as well as adhesion. The surface optimization techniques being utilized are laser and AP surface treatments. These techniques are becoming established as an effective way to clean local surfaces for improved joining characteristics as compared with conventional chemical cleaning and can also offer enhanced corrosion protection as aforementioned. The project will also evaluate the effect of the riveting process on cured and uncured adhesively bonded joints. Corrosion properties of metal surfaces are being evaluated in post-laser- and AP-treated Al alloys and steel using both macroscopic and microscopic electrochemical measurement techniques. SECCM is being employed to probe microscopic corrosion response of pre- and post-treated surfaces. Tafel and EIS are recorded in the bulk and locally modified regions. Advanced characterization techniques including optical profilometry, X-ray photoelectron spectroscopy (XPS), Fourier-transform infrared spectroscopy (FTIR), STEM, and contact angle measurement are used to study pre- and post-surface-modified samples. Experimental data will be compared to corrosion modeling and joint strength simulations to improve the model prediction to allow for optimum conditions to reach the fullest potential of the joint strength.

Results

Surface-Treatment on 7xxx Al by Laser and AP Processes (ORNL)

The control of surface chemistry is critical to achieve high-quality, adherent joints and minimize the impacts of galvanic coupling of dissimilar materials on corrosion susceptibility. In this project, we focused on Al-CFRP and Al-steel joints to further optimize joining and corrosion mitigation purposes. First, the cleaning of Al surfaces, as well as controlled growth of aluminum oxide (Al_2O_3) and related oxides for improved corrosion resistance, were pursued by laser and AP techniques, with benchmarking to anodized Al surfaces. Figure II.3.9.1 shows the Nd:YAG laser system and AP system at ORNL.

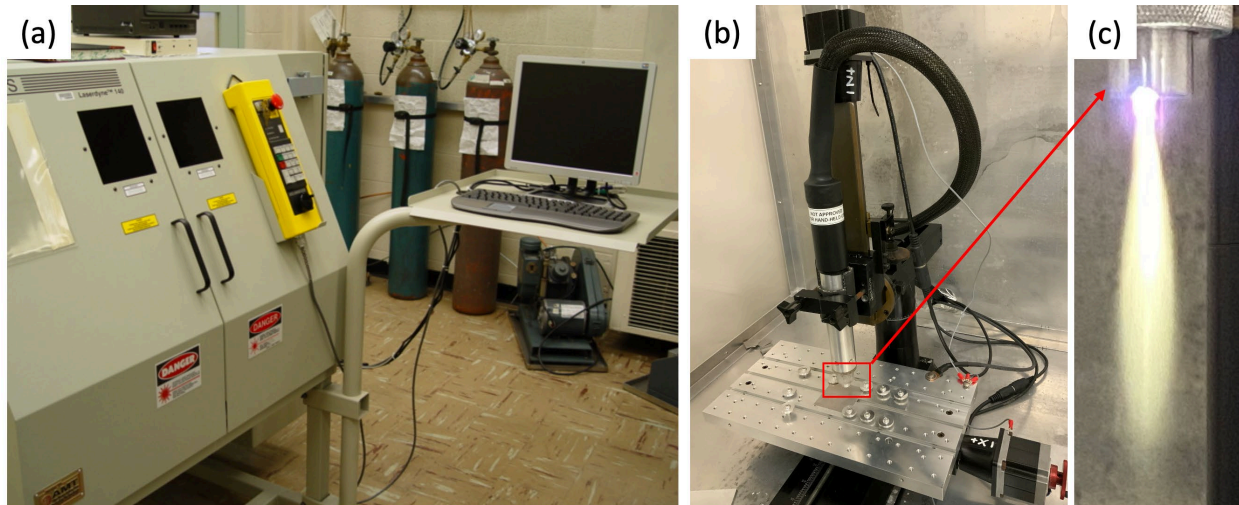


Figure II.3.9.1. (a) The Nd:YAG laser system at ORNL. (b) The atmosphere plasma system at ORNL. (c) The atmosphere plasma jet from the nozzle. Source: ORNL.

Cleaning and oxide growth on Al alloy surfaces were studied by varying the laser process parameters, such as laser power, pulse duration, scan speed, and overlap. Initially, a single-pass surface-treatment was applied on Al7075-T6 with different processing conditions by using the Nd:YAG (wavelength of 1064 nm) laser system at ORNL. Because Al7075-T6 is well-known for hot cracking, crack-free surface-treatment condition was downselected for scanned surface-treatment as a next step. For the laser scanned area, 2 in. \times 2 in. Al coupons were cut and cleaned with alcohol to remove any dirt or oil residue. Then, laser surface-treatment was applied in a 1 in. \times 1 in. scan area that is large enough for EIS measurement to study the effectiveness of corrosion improvement. Examples of laser-treated Al7075 with different laser pulse energies are shown in Figure II.3.9.2. To study the surface profile changes from laser surface processing, surface roughness of the as-received Al7075, the 600-grit surface-finished, and laser-treated samples were measured by optical profilometry and summarized in Figure II.3.9.3. Figure II.3.9.3(a-c) shows optical image and vertical surface profile measured for the as-received, 600 grit, and laser pulse energy of 1.2 J. Figure II.3.9.3(d) summarizes the R_a and R_z values; where R_a is the arithmetical mean deviation of the measured surface profiles and R_z is the maximum peak to valley height of the measured profile; for four different surface conditions of Al7075. 600-grit surface finish is smoother than the as-received and laser-treated samples. Also, the laser treatment created a rougher surface than the as-received and 600-grit conditions.

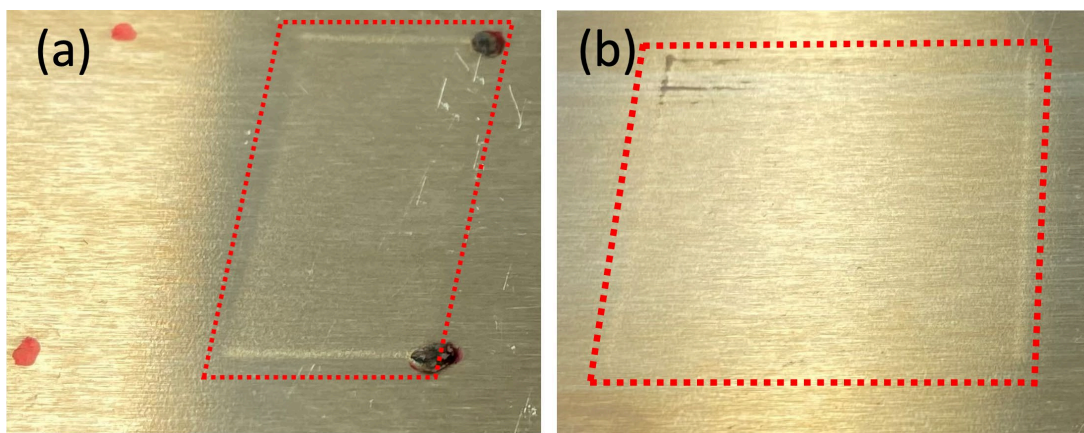


Figure II.3.9.2. Optical images of laser-surface-treated Al7075 with different laser pulse energies: (a) $E_p=1.2J$; and (b) $E_p=1.6J$. The areas in dotted boxes are approximately (a) 1 \times 0.5 in. and (b) 1 \times 1.0 in. Source: ORNL.

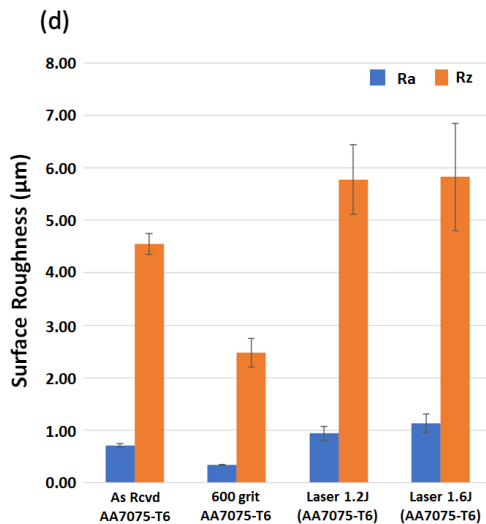
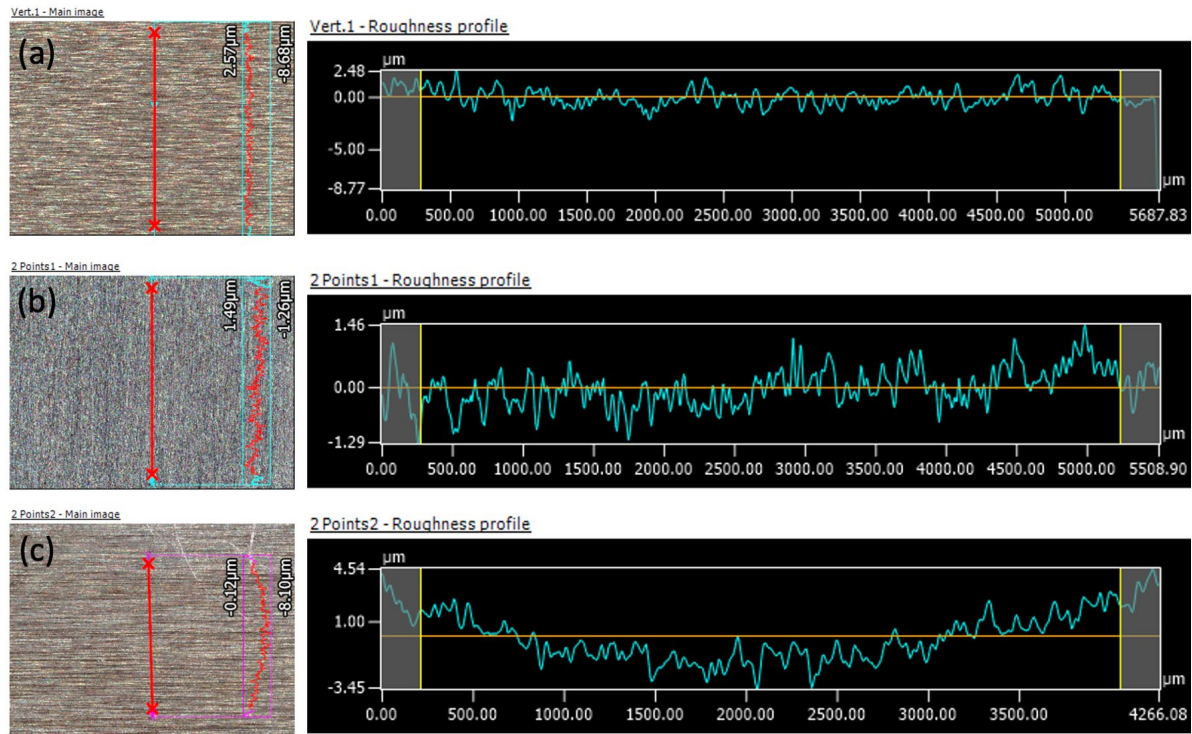


Figure II.3.9.3. Summary of surface roughness on (a) as-received Al7075, (b) 600-grit surface-finished Al7075, and (c) laser-treated Al7075 at $E_p = 1.2J$. (d) Summary of Ra (arithmetical mean deviation of the measured surface profiles) and Rz (maximum peak to valley height of the measured profile) for four different surface conditions. Source: ORNL.

In parallel to the laser surface modification studies, open to lab air/atmospheric AP surface treatments were evaluated as a second method for surface-cleaning and oxide growth on the Al alloy surface, as a function of process conditions, such as nozzle height to substrate, scan speed, and overlap spacing. All AP treatment was conducted on the same coupon size with the same scan area used for laser processing. Figure II.3.9.4 provides optical images of AP-treated AA7075 with different nozzle heights ranging from 0.5 in. to 1.0 in. at fixed scan speeds of 32 inches per minute (ipm). When the nozzle height was near the Al substrate, a noticeable plasma process mark was observed on the Al top surface. Also, some deformation of Al sheet was observed due to

excessive heat input from the plasma. However, as the plasma nozzle height was increased, the distortion of the Al sheet was greatly minimized, and any noticeable surface change by visual inspection finally disappeared at the 1 in. nozzle height. Surface temperature at the 1 in. nozzle height was measured by an infrared camera, which recorded a temperature of $\sim 200^{\circ}\text{C}$ during the process. Therefore, changing nozzle height, scan speed, and scan spacing can affect process temperature on the substrate.

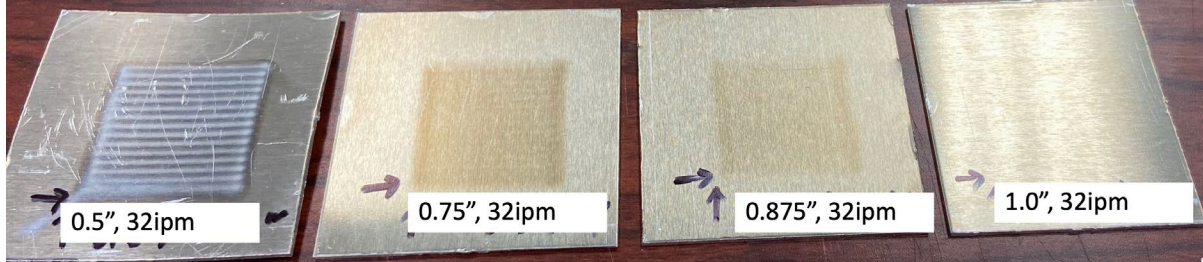


Figure II.3.9.4. Optical images of AP-treated AA7075 with different nozzle heights ranged from 0.5 in. to 1.0 in. at a fixed scan speed of 32 ipm. Source: ORNL.

Corrosion evaluation of laser- and plasma-treated Al7075 sheets was conducted by macroscopic EIS measurement using 3.5wt.% NaCl solution at RT. The impedance data from the measurements were fitted using equivalent circuit models to determine corrosion reaction resistance, R_2 or $R_2 + R_3$. In the two equivalent circuits, R_1 indicates solution resistance, R_2 and R_3 are charge transfer resistance in single and double Resistance-Constant Phase Element ($R//CPE$) models, respectively, and R_2 in double $R//CPE$ model indicates film resistance. The Nyquist impedance plot of baseline 600-grit silicon carbide finish and 1.2J laser-treated Al7075 sheets are compared in Figure II.3.9.5(a). The impedance spectra of the laser-treated Al7075 exhibited two arcs, unlike the baseline Al7075 with depressed semi-circles, suggesting that the laser-treated samples had both corrosion interface and film resistance elements while the resistance of baseline samples was primarily from corrosion interface without any effective film resistance. The impedance scales were greater in laser-treated Al7075 due to the presence of the second arcs associated with film resistance. Other Al7075 samples treated with the 1.4J and 1.6J laser pulses also exhibited two impedance arcs.

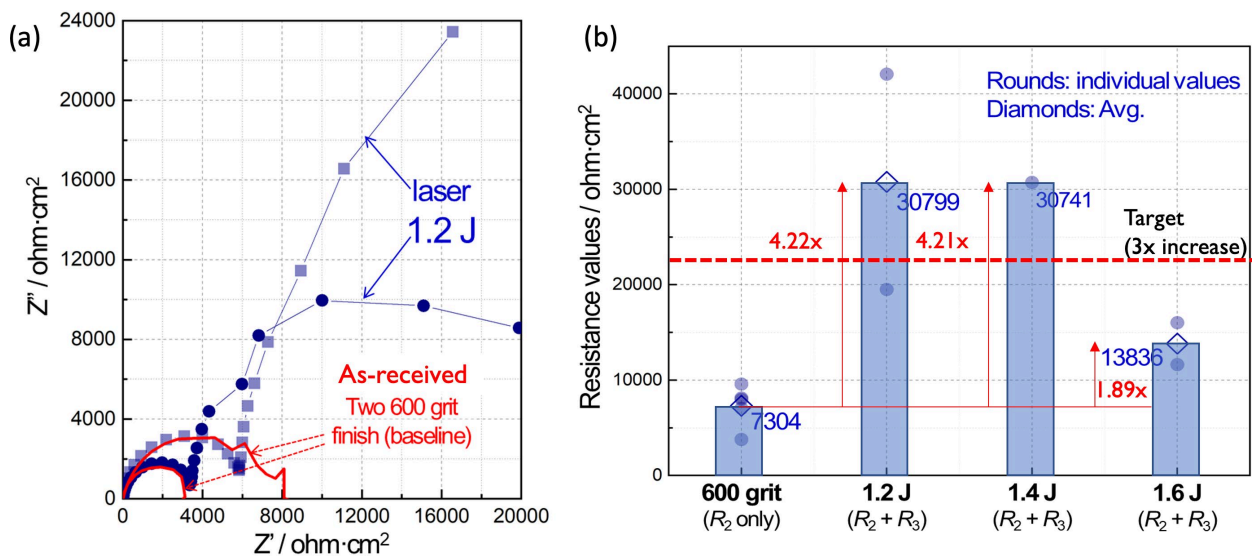


Figure II.3.9.5. (a) Nyquist plots of laser-treated (1.2 J) and baseline 600-grit finish Al7075 surfaces with the exposure area of 0.833 cm^2 . (b) A comparison of corrosion reaction resistance values from laser-treated (1.2, 1.4, and 1.6 J) samples and the baseline Al7075. Source: ORNL.

Impedance data fitting was performed to determine R_2 for the baseline and $R_2 + R_3$ for the laser-treated samples as their corrosion reaction resistance values. These resistance values are summarized in Figure II.3.9.5(b). The average resistance values of all laser-treated samples were greater than the values of baseline A17075, and more importantly, the resistance values of two laser treatment conditions, 1.2 J and 1.4 J, were approximately 4.2 times the baseline resistance value. Per the criteria of FY 2021 JCP task 1C, the laser surface treatments with 1.2 J and 1.4 J have surpassed the task goal of three times the baseline corrosion resistance.

Nyquist impedance plots of AP-treated A17075 sheets are presented with an impedance spectra of baseline A17075 with a 600-grit finish in Figure II.3.9.6. The shape and scale of impedance spectra were not substantially different between 5 ipm and the baseline shown in Figure II.3.9.6(a), which indicates that the AP treatment with 5 ipm speed did not improve corrosion resistance of A17075. With 10 ipm scanning speed, the AP-treated sample showed a second impedance arc and marginal increase of impedance scale as compared to the baseline sample shown in Figure II.3.9.6(a), which suggests this AP treatment developed a somewhat resistive surface film on A17075. For faster plasma scanning speeds, 20 and 32 ipm (maximum speed of current motion stages), the second arcs at a higher impedance regime were larger than the one in the sample with a 10 ipm condition, indicating the film resistance was increased. The real impedance portion of 20 and 32 ipm AP-treated samples extends over 12000 ohm (for the surface area of 0.833 cm²) for the respective frequencies designated in Figure II.3.9.6(b). These results suggest that a faster scanning speed (to 32 ipm) of AP can be more effective on increasing corrosion resistance of A17075 within the processing window used in this work. At the lower scan speeds, more intensive plasma interaction (cleaning surface rather than growing oxide layer) and more surface heat can potentially have an adverse effect on the local surface chemistry. Further optimization of AP treatment processes will be performed to achieve a higher corrosion resistance of A17075 surface. In addition, N₂ feed plasma also will be used to treat the A17075 surface to promote the formation of N- and O-rich Al compounds that could offer corrosion protection for the alloy.

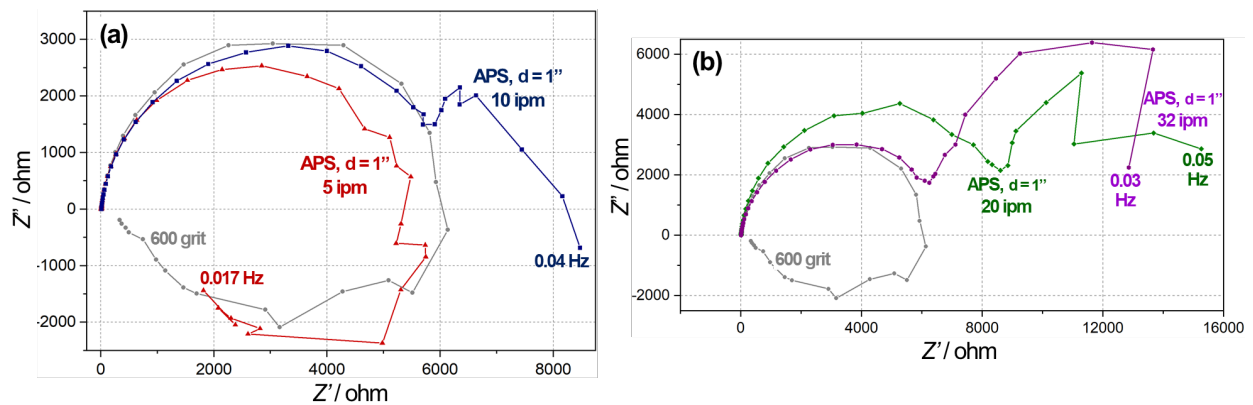


Figure II.3.9.6. Nyquist plots of AP-treated A17075 with the scanning speed of (a) 5 and 10 ipm and (b) 20 and 32 ipm in comparison with the baseline 600 grit finish A17075. Source: ORNL.

To observe the morphological and compositional changes at the surface of the A17075 sheet that arise from processing with a 1.2 J laser pulse energy and a 1.8 kW AP, site-specific lift-out with a focused ion beam was employed. The lift-out samples of the A17075 surfaces shown in Figure II.3.9.7 are representative of the cross-section view of the top surface of the processed samples. The 200-nm scale bar shows that any change in the surface morphology from dissolution or deposition during processing was on the nanoscale. The Guinier-Preston (GP) zones of the A17075-T6 alloy are observed along with the Cr-rich second-phase particles. The η -phase (MgZn₂), AlZnMgCu, Al₂CuMg, and even Al₂Cu phases also have been reported in the literature [8]. The differences in fine details of the A17075 alloy in each micrograph of Figure II.3.9.7 needs to be understood further. A stark difference in bulk microstructure for each of the laser and AP processing scenarios can be seen. Changes in aqueous or micro-galvanic corrosion can be influenced by the different composition of second phases being present on the A17075 surface during processing. A 100 nm band, which was below the

film formed during AP processing, was observed in the bright-field and HAADF micrographs and with EDS to be a region depleted of Mg. It was hypothesized that this region, void of GP zones, was changed through diffusion of Mg to the surface. Small nanoscale particles were also observed in this AP-formed surface layer. At the resolution of this study, the nanoscale particles in the surface film were not resolved well, nor was their structure or composition determined. Comparison with the XPS data taken from these samples would help elucidate the surface chemistry feature and may help to understand the nanostructures formed during the AP processing.

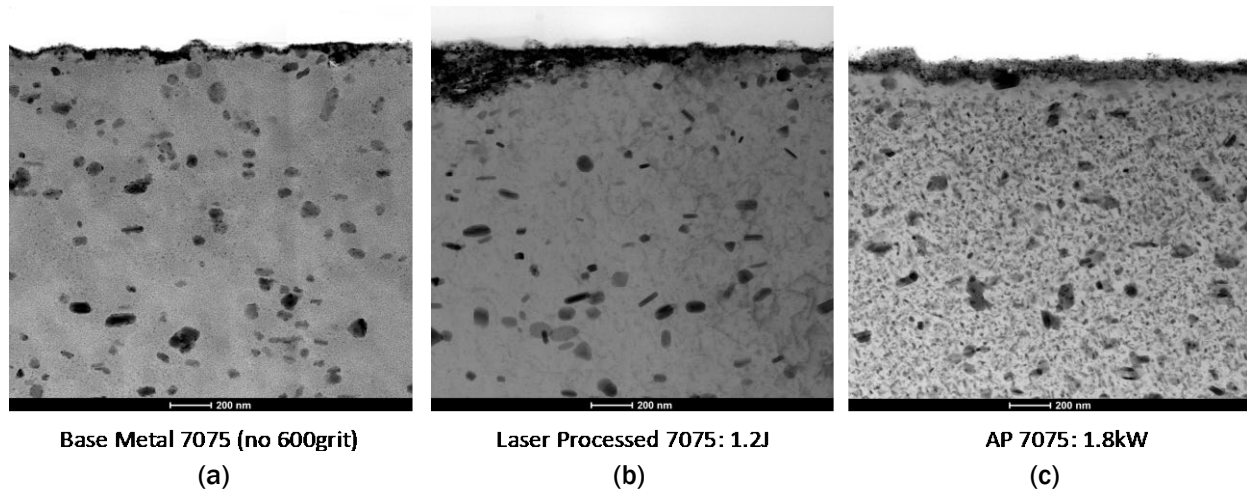


Figure II.3.9.7. Cross-section STEM bright-field micrographs of the (a) as-received Al7075, (b) the laser-processed Al7075 at 1.2J, and (c) the AP-processed Al7075. The AP sample shows a band under the formed surface film that is depleted of GP zones. Source: ORNL.

To better understand the elemental distribution in the surface films of the as-received base metal and the laser and AP-processed samples, X-ray maps were acquired from each specimen. The EDS maps of Figure II.3.9.8 show that O, Mg, Cu, and Si were present in the film formed at the surface of the as-received Al7075 sample. The surface film measures less than 100 nm thick and appeared conformal to the surface of the sample.

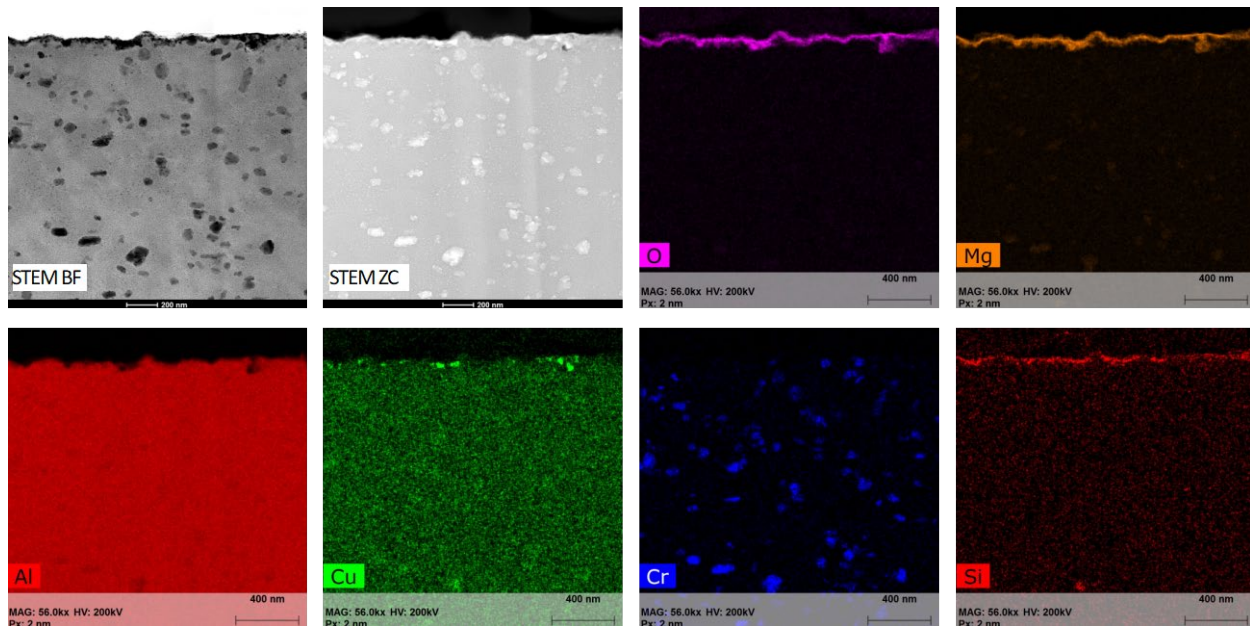


Figure II.3.9.8. STEM/EDS data from the Al7075 as-received base metal sample. The native oxide film contains O, Mg, Cu, and Si. Source: ORNL.

Figure II.3.9.9 shows the X-ray maps of the surface film on the Al7075 after laser processing at 1.2 J pulse energy. These X-ray maps show O, Mg, Cu, and Si at the Al7075 surface, as well as a surface film measuring less than 100-nm thick. Note the Cr-rich second-phase particles in the sample, which was typical for this alloy. Also note that the Mg and O signal does show up ~300 nm below the top surface of the sample. Further study is needed to determine whether this processing caused subsurface oxygen penetration of the surface or if these regions exist *a priori*.

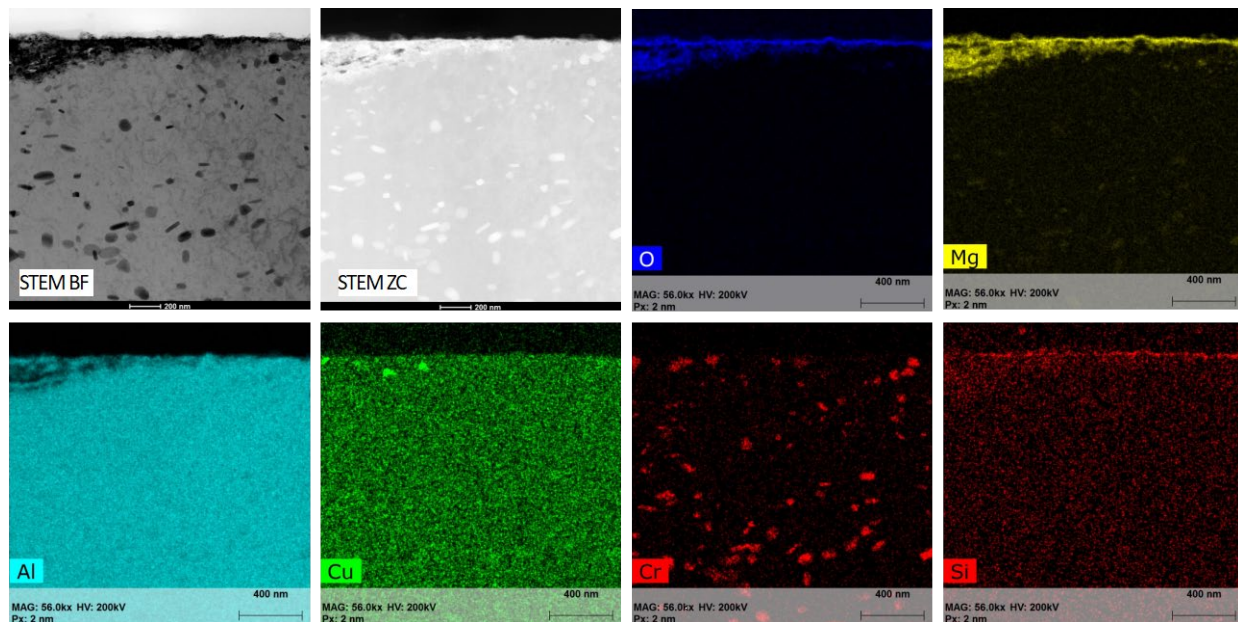


Figure II.3.9.9. STEM/EDS data from the Al7075 1.2 J laser-processed sample. The formed film contains O, Mg, Cu, and Si. Source: ORNL.

The AP-processed Al7075 surface, as shown in the cross-section view of Figure II.3.9.10, contained a film formed at the top surface, but also a subsurface layer void of the nanoscale precipitates (GP zones) that are typical in this heat-treated Al alloy sheet. The surface film formed during 1.8 kW plasma treatment contained O, Mg, and Si. A quantified EDS line scan from the metal across the surface film showed that the subsurface band observed in the HAADF (Z-contrast) micrograph is a region where the base composition of the alloy has been changed. This is likely due to the strong chemical potential for Mg to diffuse to the surface and form the O-rich film.

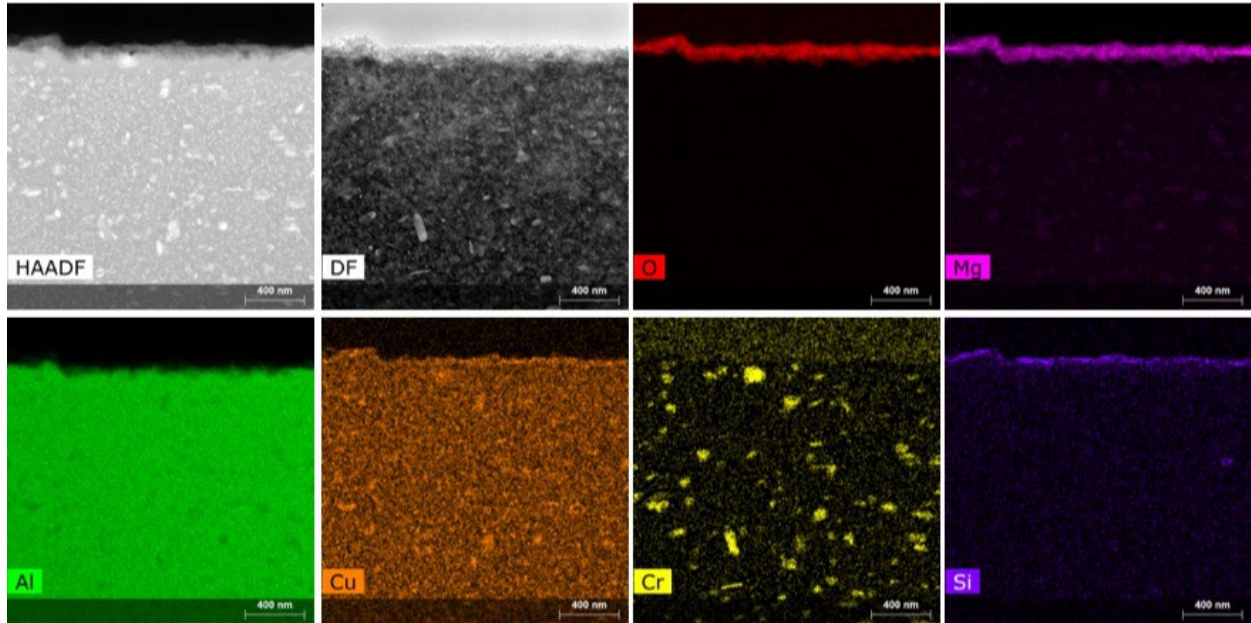


Figure II.3.9.10. STEM/EDS data from the Al7075 1.8 kW AP-processed sample. The formed film contains O, Mg, Cu, and Si. Source: ORNL.

Plasma Treatment of 6XXX, 5XXX, and CFRP (PNNL)

Initial efforts focused on finding process parameters, such as plasma tip-to-surface (d) and tip speed (v) to optimize the processing condition of air plasma treatment of Al6061 and CFRP-PA66 surfaces. Based on the optimum surface energy and stability for each combination of process parameters, the best process condition was $d=3.2$ mm and $v=3.2$ mm/s for Al6061 and $d=3$ mm and $v=100$ mm/s for CFRP-PA66. One of the key issues in plasma-treated surfaces is transient stability of activated surface energy in air, which can decay within minutes of treatment. The stability of selected Al6061 and CFRP-PA66 was tested in air and the enhanced surface energy by air plasma treatment very quickly decreased, as observed in Figure II.3.9.11(a)-(b). After exposure to air for about 30 min., the surface energy of Al6061 was close to that of the as-received surfaces. Likewise, after 5 min. to 10 min. in air, the surface wettability of Al6061 was significantly decreased. In all materials, the polar component was dominantly decreased while the dispersive component remained stable. This indicates that adhesive joining of two different surfaces should be performed immediately after air plasma treatment to avoid radical deactivation of polar functional groups, as can be seen in Figure II.3.9.11(c)-(d). In the case of plasma-treated CFRP-PA66, the total surface free energy was higher than that of as-received CFRP-PA66, but after 20 min exposure to air, the wettability of the adhesive was outside the wetting envelope, which means the adhesive cannot completely wet the surface, as shown in Figure II.3.9.11(d).

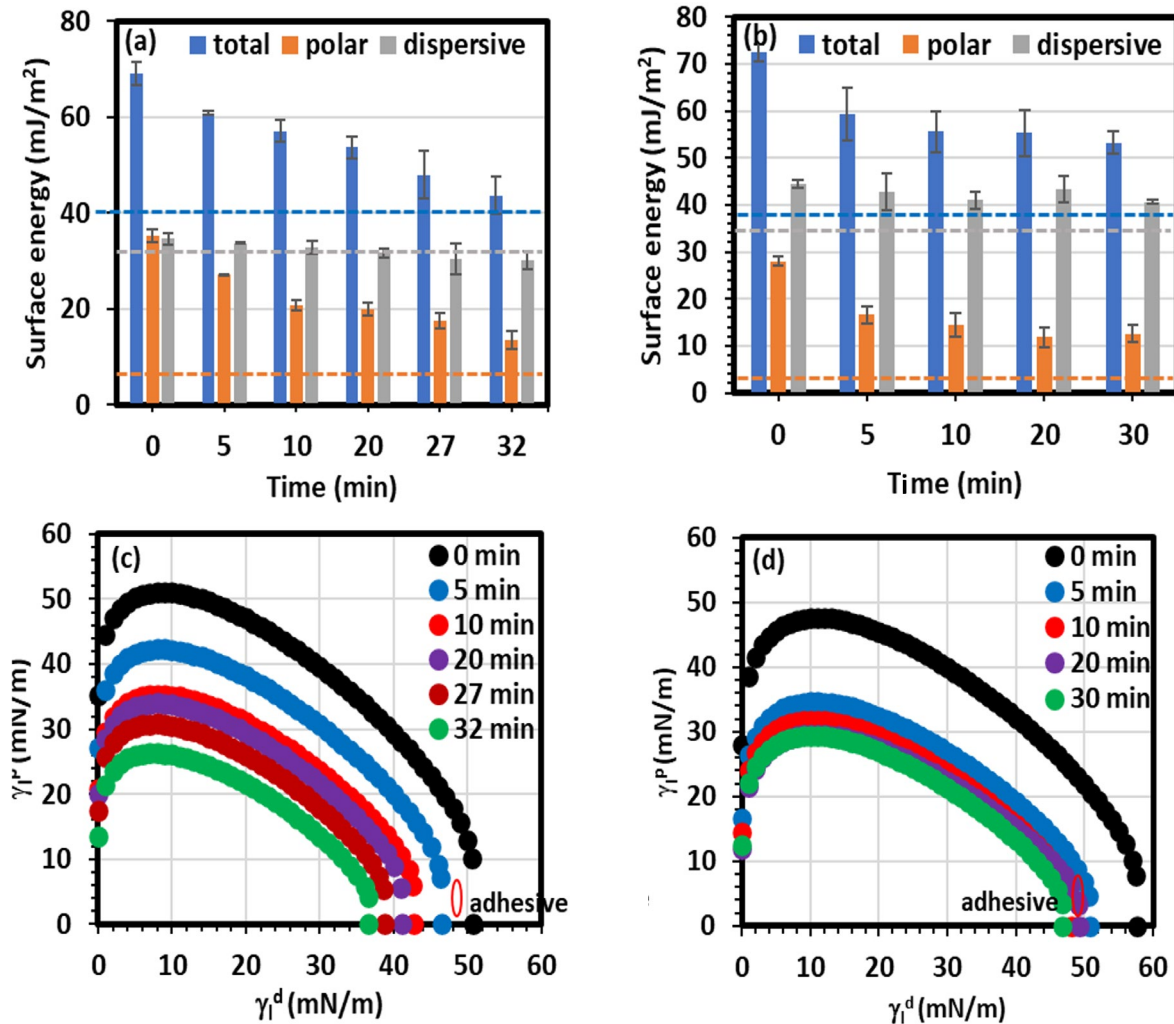


Figure II.3.9.11. Surface energy stability of (a) Al6061 and (c) CFRP-PA66 as a function of time in air and the wetting envelopes of (b) Al6061 and (d) CFRP-PA66. Dotted lines of surface energy plots indicate total, polar, and dispersive component of as-received surfaces. Source: PNNL.

XPS was used to investigate elemental composition and bonding on Al6061 and CFRP-PA66 surfaces. Al₂p spectra of Al6061 showed an increase in surface oxide after plasma treatment. As-received Al6061 showed 15.1% Al metal and 84.9% octahedral Al₂O₃ at 73.08 eV and 74.58 eV, which changed to 2.3% Al and 97.7% Al₂O₃ after air plasma treatment, as shown in Figure II.3.9.12(a)-(b), respectively. O1s spectra showed a transition from an Al₂O₃ dominant to a MgO dominant surface. The as-received Al6061 showed 59.1% Al₂O₃ at 531.38 eV and 40.9% MgO at 532.18 eV, but after the plasma treatment, a significant amount of MgO migrated to the surface (i.e., 91.1%), as shown in Figure II.3.9.12(c)-(d). A high portion of Mg coverage on the Al6061 surface would protect or minimize the corrosion issue of the Al surface. As-received CFRP-PA66 showed normal hydrocarbon distribution (80% to 90% of C-C), but after air plasma treatment, a significant amount of surface carbon (C-C at 284.68 eV: C1s) was oxidized (85.1% to 64.3%). Surface hydrocarbon mainly changed to carbonyl and carboxylate group at 286.18 eV, which is critical to change the surface hydrophilicity, as observed in Figure II.3.9.12(e)-(f). N1s of as-received CFRP-PA66 showed 61.4% amide group (-NH-C=O) at 399.58 eV and divalent N (C=N-C) at 397.88 eV, but after plasma treatment, the easily oxidizing divalent nitrogen converted to nitrate at 409.68 eV by plasma oxidation, as shown in Figure II.3.9.12(g)-(h).

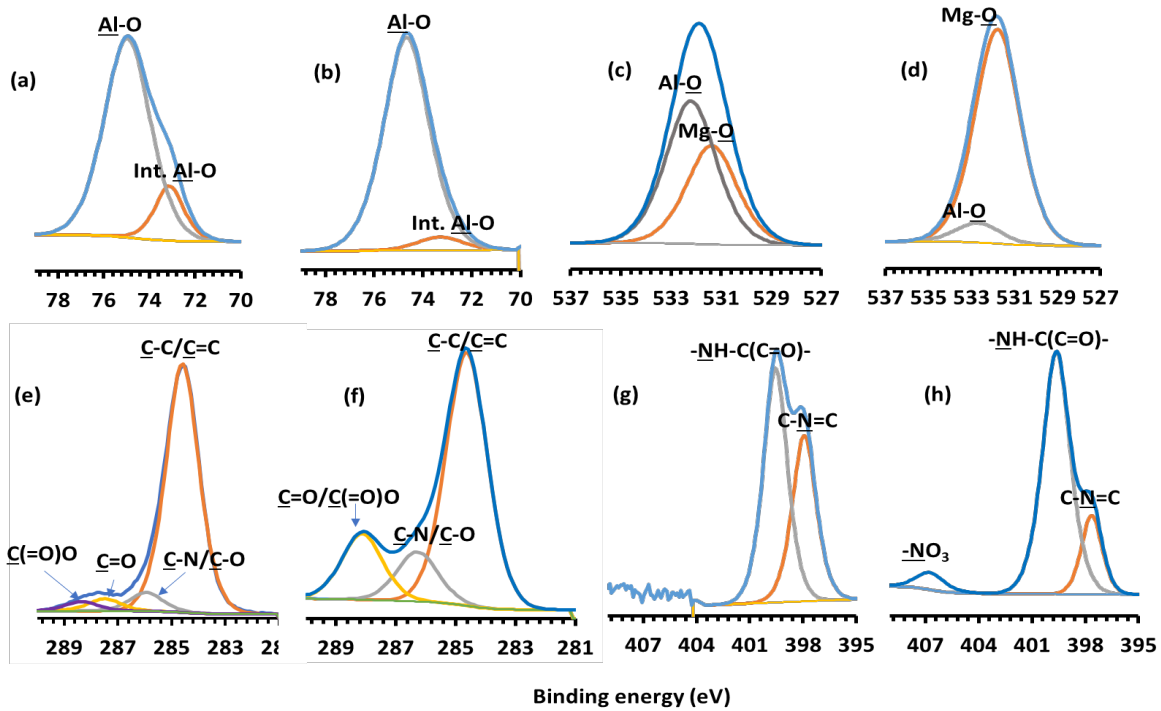


Figure II.3.9.12. XPS Al2p spectra of Al6061 and CFRP-PA66 before and after air plasma treatment: (a) Al6061_AR, as-received; and (b) AL6061_air plasma. O1s: (c) Al6061_AR; and (d) Al6061_air plasma. C1s: (e) CFRP-PA66_AR; and (f) CFRP-PA66_air plasma. N1s: (g) CFRP-PA66_AR; and (h) CFRP-PA66_air plasma. Source: PNNL.

The adhesive that was manufactured by L&L Products was characterized by FTIR spectroscopy and found to contain two main chemicals of bisphenol A type epoxy resin and dicyandiamide curing agent along with a small amount of adhesion promoters. These components reacted with each other through an epoxide ring opening polymerization and rearrangement on Al6061 and CFRP-PA66 surfaces when cured at 150°C for about 40 min. It was also found that the epoxide ring opening polymerization is mainly responsible for the adhesive bond to Al6061 and CFRP-PA66 surfaces. In addition to epoxide-enabled bond, plasma-treated Al6061 and CFRP-PA66 surface hydroxyl group (-OH) interacts with cyano group (-C≡N) of dicyandiamide to form amide bonding, which is likely responsible for the improvement in bond strength observed in LS testing. Details of bond strength improvement are discussed previously in II.3.7, “Extending High-Rate Riveting to New Material Pairs.”

Corrosion Measurements

Localized microscopic electrochemical properties were measured on plasma-treated samples using SECCM. Figure II.3.9.13 shows the Tafel plots for pre- and post-plasma-treated surfaces for A15052, Al6061, and DP590 steel. There is a significant improvement of pitting corrosion observed in plasma-treated samples. Figure II.3.9.14 shows the Nyquist plots for pre- and post-plasma-treated surfaces for A15052 and Al6061 alloys. Nyquist plots were fitted to get charge transfer resistance (R₂) using an equivalent circuit diagram. Overall resistance increased significantly for both the Al samples after plasma treatment. The charge transfer resistance values are increased by ~5 times in the A15052 sample and ~23 times in the Al6061 sample after plasma treatment. The resistance values for both pre- and post-plasma treatment are shown in Table II.3.9.1. The equivalent circuit diagram used to fit the EIS data is also shown in Figure II.3.9.14.

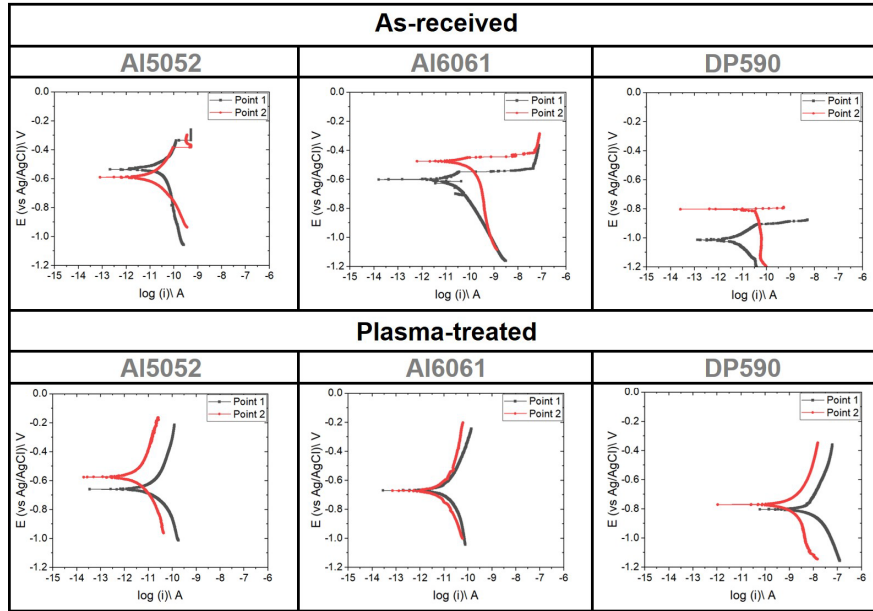


Figure II.3.9.13. Tafel plots measured on pre- and post-plasma-treated surfaces of Al5052, Al6061, and DP590 steel. Source: PNNL.

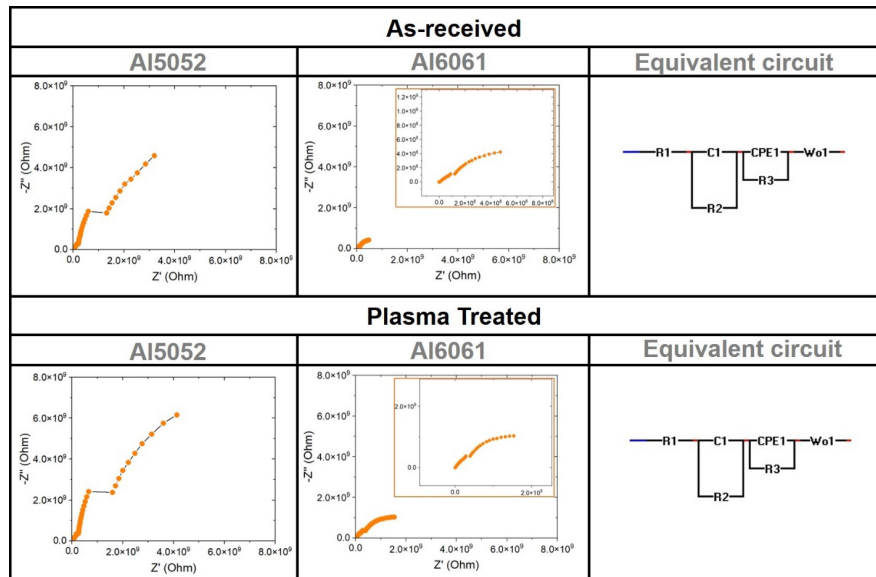


Figure II.3.9.14. Nyquist plots measured on pre- and post-plasma-treated surfaces of Al5052 and Al6061 sample and their equivalent circuit diagram used for resistance value calculation. Source: PNNL.

Table II.3.9.1. Resistance Values Calculated from EIS Using the Equivalent Circuit Diagram

Alloy	Al5052			Al6061		
Resistance	R1 (Ω)	R2 (Ω)	R3 (Ω)	R1 (Ω)	R2 (Ω)	R3 (Ω)
As-Received	99854	2.3×10^9	9.6×10^{10}	1.0×10^5	2.7×10^7	8.3×10^8
AP-Treated	37676	1.0×10^{10}	4.6×10^9	1.0×10^5	6.4×10^8	1.0×10^9

Figure II.3.9.15 shows the potentiodynamic curves of the different material combinations/alloys being investigated for joining studies as a part of this project. This study systematically compared the galvanic potentials of these alloys in a 0.1M NaCl solution. The galvanic potential of DP590 is due to the Zn coating and not the underlying steel substrate. The COMSOL multiphysics modeling tools are being used to predict current density in joint interfaces. Figure II.3.9.16(a) shows the current density at rivet and sheet with positions for different Al sheet materials. In the case of rivets, the minimum current density was observed in the AA5052 alloy. Whereas, in the sheet materials, the minimum current density was observed in the AA5052, AA5182, and AA5083 alloys. Figure II.3.9.16(b) shows the current density map for the AA5083 and AA6063 sheet at the near interface. The modeling data showed the greatest current density in the AA6063 alloy as compared to the AA5083 alloy.

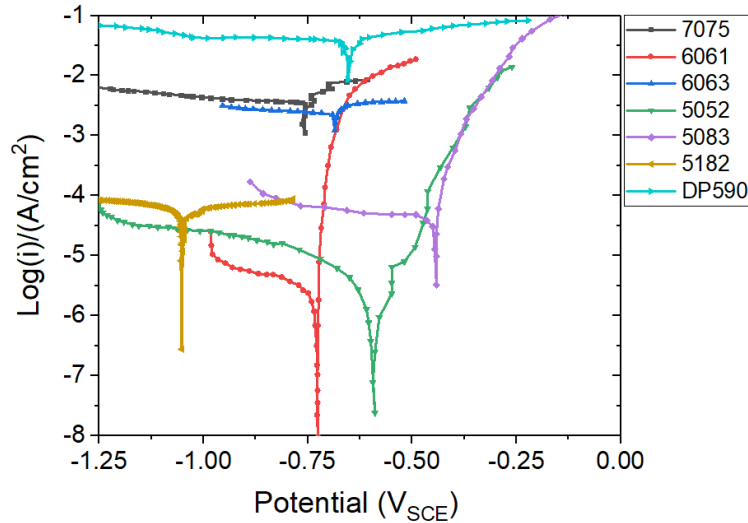


Figure II.3.9.15. Potentiodynamic curves of the different Al alloys and steel that are being used for the JCP 2.0 project. Source: PNNL.

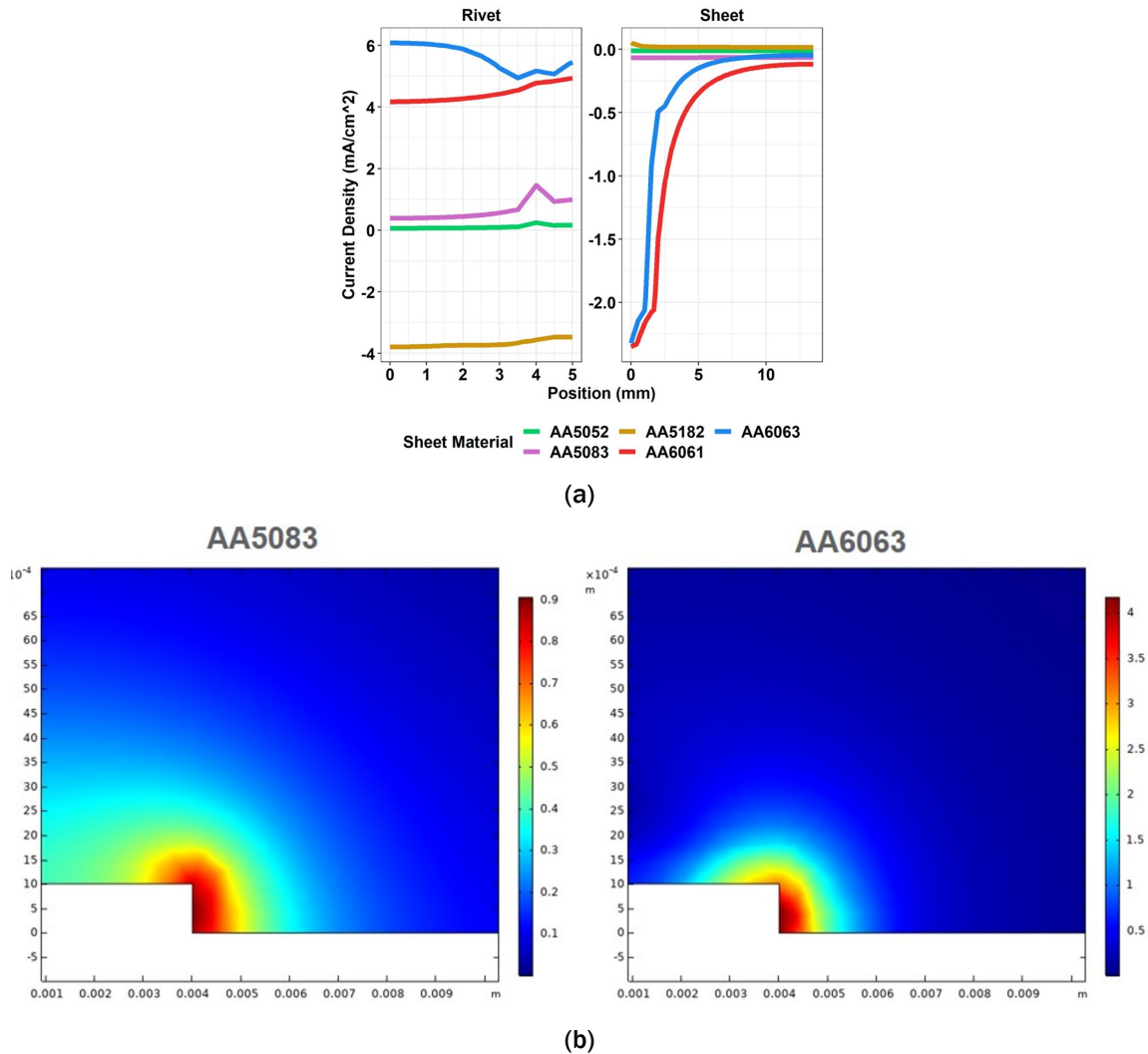


Figure II.3.9.16. (a) The current density of the rivet and sheet for the AA5052, AA5182, AA6063, AA5083, and AA6061 alloys with distance. (b) The current density map at the rivet region for the AA5083 and AA6063 alloys. Source: PNNL.

Conclusions

1. Both laser- and AP surface treatments on AA7075 showed improved corrosion resistance compared to the base material. For the laser treatments, the increase of corrosion reaction resistance was significant for energy input conditions of 1.2J and 1.4J, resulting in resistance values over four times of the value measured from the base material. For the AP treatments, faster scanning speeds of 20 and 32 ipm resulted in a higher impedance scale than the base material. From the impedance spectra data, it is speculated that both the laser and AP treatments can promote the formation of resistive surface film contributing to improved corrosion resistance. Advanced electron microscopy characterizations show the formation of multiple oxides including Al, Mg, and Si after surface-treatment.
2. Corrosion properties improved after air plasma treatment. Significant improvement of pitting corrosion observed in surface treated samples. EIS analysis indicates significant improvement of corrosion resistance after surface-treatment.
3. Modeling studies are providing useful insights into the corrosion mechanisms as well as the rivet and sheet material systems and combinations most vulnerable for corrosion.

Key Publications

1. Lim, Y. C., J. Jun, D. Leonard, H. Meyer III, J. K. Keum, M. Brady, and Z. Feng, 2022, “Atmospheric plasma surface processing of a 7xxx Al alloy surface to improve corrosion resistance,” *TMS Conference*, 27 Feb.–3 Mar. 2022, Anaheim, CA, USA. Accepted for presentation.
2. Jun, J., J. Chen, Y. L. C. Lim, M. Brady, D. Leonard, and Z. Feng, 2021, “Galvanic corrosion of AZ31B ultrasonically welded with bare and Zn-coated steels,” *MS&T 2021*, 17–20 Oct. 2021, Columbus, OH, USA.
3. Lim, Y. C., J. Jun, J. K. Keum, Y. Li, D. Leonard, M. Brady, and Z. Feng, 2021, “Galvanic corrosion mitigation of CFRP-AZ31B dissimilar joint,” *MS&T 2021*, 17–20 Oct. 2021, Columbus, OH, USA.
4. Lim, Y. C., V. Joshi, et al., 2021, “Surface modification for improved joining and corrosion resistance,” DOE VTO Annual Merit Review, 21–25 Jun. 2021, Virtual.

References

1. Lim, Y. C., J. Chen, J. Jun, D. N. Leonard, M. P. Brady, C. D. Warren, and Z. Feng, 2021, “Mechanical and corrosion assessment of friction self-piercing rivet joint of carbon fiber-reinforced polymer and magnesium alloy AZ31B,” *J. Manuf. Sci. Eng.*, Vol. 143, No. 3, Art. 031106.
2. Lim, Y. C., H. Park, J. Jang, J. W. McMurray, B. S. Lokitz, J. K. Keum, Z. Wu, and Z. Feng, 2018, “Dissimilar materials joining of carbon fiber-polymer to dual-phase 980 by friction bit joining, adhesive bonding, and weld-bonding,” *Metals*, Vol. 8, No. 11, Art. 865.
3. Lim, Y. C., L. Squires, T.-Y. Pan, M. Miles, G.-L. Song, Y. Wang, and Z. Feng, 2015, “Study of mechanical joint strength of aluminum alloy 7075-T6 and dual-phase steel 980 welded by friction bit joining and weld-bonding under corrosion medium,” *Mater. Des.*, Vol. 69, pp. 37–43.
4. Mansfeld, F., and J. V. Kenkel, 1976, “Laboratory studies of galvanic corrosion of aluminum alloys,” In: Baboian, R., W. France, L. Rowe, and J. Rynewicz (eds.), *Galvanic and Pitting Corrosion—Field and Laboratory Studies*, ASTM International, West Conshohocken, PA, USA. pp. 20–47.
5. Mandel, M., and L. Kruger, 2013, “Determination of pitting sensitivity of the aluminum alloy EN AW-6060-T6 in a carbon-fiber-reinforced plastic/aluminum rivet joint by finite element simulation of the galvanic corrosion process,” *Corros. Sci.*, Vol. 73, pp. 172–180.
6. Liu, Z., Y. Dong, Z. Chu, Y. Yang, Y. Li, and D. Yan, 2013, “Corrosion behavior of plasma sprayed ceramic and metallic coatings on carbon steel in simulated seawater,” *Mater. Des.*, Vol. 52, pp. 630–637.
7. Lim, Y. C., J. Jun, M. P. Brady, and Z. Feng, 2021, “Methodology to avoid accelerated corrosion of dissimilar material fastener joints using alloys forming surface oxides,” ORNL invention disclosure No. 81920635.
8. Gharbi, O., S. K. Kairy, P. R. De Lima, D. Jiang, J. Nicklaus, and N. Birbilis, 2019, “Microstructure and corrosion evolution of additively manufactured aluminum alloy AA7075 as a function of aging,” *NPJ Mater. Degrad.*, Vol. 3, Art. 40.

Acknowledgments

The co-PI at PNNL would like to acknowledge Y. Shin, D. Merkel, K. Simmons, Y. Qiao, B. Schuessler, R. Kalsar, A. Guzman, M. Rhodes, V. Prabhakaran, V. Viswanathan, L. Strange and A. Crawford for surface processing, characterization, and modeling activities for this project. The co-PIs at ORNL would like to acknowledge R. Davies, Z. Feng, and A. Hayes for their leadership and technical guidance. Also, great efforts from the project team members at ORNL are acknowledged as well, including J. Jun, A. Frederick, D. Kyle, H. Meyer III, J. K. Keum, M. Brady, N. Kanbargi, Z. Yu, and A. Naskar are greatly appreciated. The co-PIs at ORNL appreciate L&L Products for providing adhesives for this project.

II.3.10 Ultrasonic-Based Multi-Materials Joining – Joining Core Program (Oak Ridge National Laboratory)

Jian Chen, Co-Principal Investigator

Oak Ridge National Laboratory
1 Bethel Valley Rd.
Oak Ridge, TN 37831
E-mail: chenj2@ornl.gov

Zhili Feng, Co-Principal Investigator

Oak Ridge National Laboratory
1 Bethel Valley Rd.
Oak Ridge, TN 37831
E-mail: fengz@ornl.gov

Sarah Kleinbaum, DOE Program Manager

U.S. Department of Energy
E-mail: sarah.kleinbaum@ee.doe.gov

Start Date: October 1, 2020	End Date: September 30, 2023	
Project Funding (FY 2021): \$584,000	DOE share: \$584,000	Non-DOE share: \$0

Project Introduction

Modern multi-material vehicles require joining various lightweight materials together—such as Al and Mg alloys, CFRPs, and AHSSs—to form a high-performance and lightweight body structure. A variety of joining methodologies (e.g., RSW, adhesive bonding, linear fusion welding, hemming, clinching, bolting, and riveting) have been attempted by the automotive industry to join these different materials together. Often, these joining techniques are limited to only certain material combinations. For capital and operational costs, auto OEMs need to limit the number of joining technologies implemented in their assembly lines.

In Phase I of the JCP, we investigated and successfully demonstrated the versatility of ultrasonic-based spot-joining (UJ) processes to join different material combinations [1, 2]. USW is one of the major UJ processes. It is a solid-state joining method that produces weld joints by localized high-frequency tangential vibration under moderate clamping pressure. The temperature rise during a USW process is generally not sufficient to melt the material. Instead, the high-temperature and pressure at the interface induces rapid diffusion between the substrates to form the joint. In Phase I of the JCP, the USW method has been successfully applied to join DP590 steel and AZ31B Mg alloys with reasonably high-strength.

However, it is still very challenging to apply USW to join large metal structures consisting of multiple spot joints due to the lack of understanding of the vibration wave propagation and structural response. Consistent joint quality through the entire structural component is difficult.

Objectives

The objective of this R&D activity aims to further explore, understand, and extend the unique characteristics of UJ to various lightweight material combinations in an assembly of lightweight multi-material vehicles. Particularly in FY 2021, our goal was to join large DP590-AZ31B samples consisting of multiple USW joints to obtain an average joint strength that was at least 80% of the strength obtained on single-joint coupons.

Approach

The project was divided into three major tasks to ensure risk mitigation and successful completion, which are:

- FY 2021—Making multiple USW joints in large steel-Mg coupons and obtaining an average joint strength that was at least 80% of that obtained in single-joint coupons.
- FY 2022—Extending the USW method to join large Al-steel and Al-Mg coupons consisting of multiple joints and obtaining an average joint strength that is at least 80% of that obtained in single-joint coupons.
- FY 2023—Using one UJ variant to join polymer-metal structural stack-ups.

The following subtasks were planned to meet the FY 2021 milestones:

- Subtask 1: Conduct *in-situ* measurements of the structural thermomechanical responses and post-weld characterizations of the resultant joint quality.
- Subtask 2: Establish a model-based engineering tool to understand the influence of process conditions and structural response on the joint quality.
- Subtask 3: Optimize USW processes with the assistance of the model-based engineering approach and demonstrate the effectiveness of joint quality improvement.

Results

Single-joint LS USW coupons (e.g., 1-mm Zn-coated DP590 and 2-mm AZ31B) were produced using varying welding conditions (e.g., ultrasonic energy from 200 J to 2500 J on five coupons per welding condition), as shown in Figure II.3.10.1(a). The LSS of these samples was tested and Figure II.3.10.1(b) plots the peak LSS as a function of the ultrasonic energy. The joints welded using 200 J had a minimum average strength at approximately 1 kN. The average peak strength increases to approximately 4.9 kN with the energy increased from 200 J to 2000 J. There is no obvious increase of the peak LSS with a further increase of the input energy up to 2500 J.

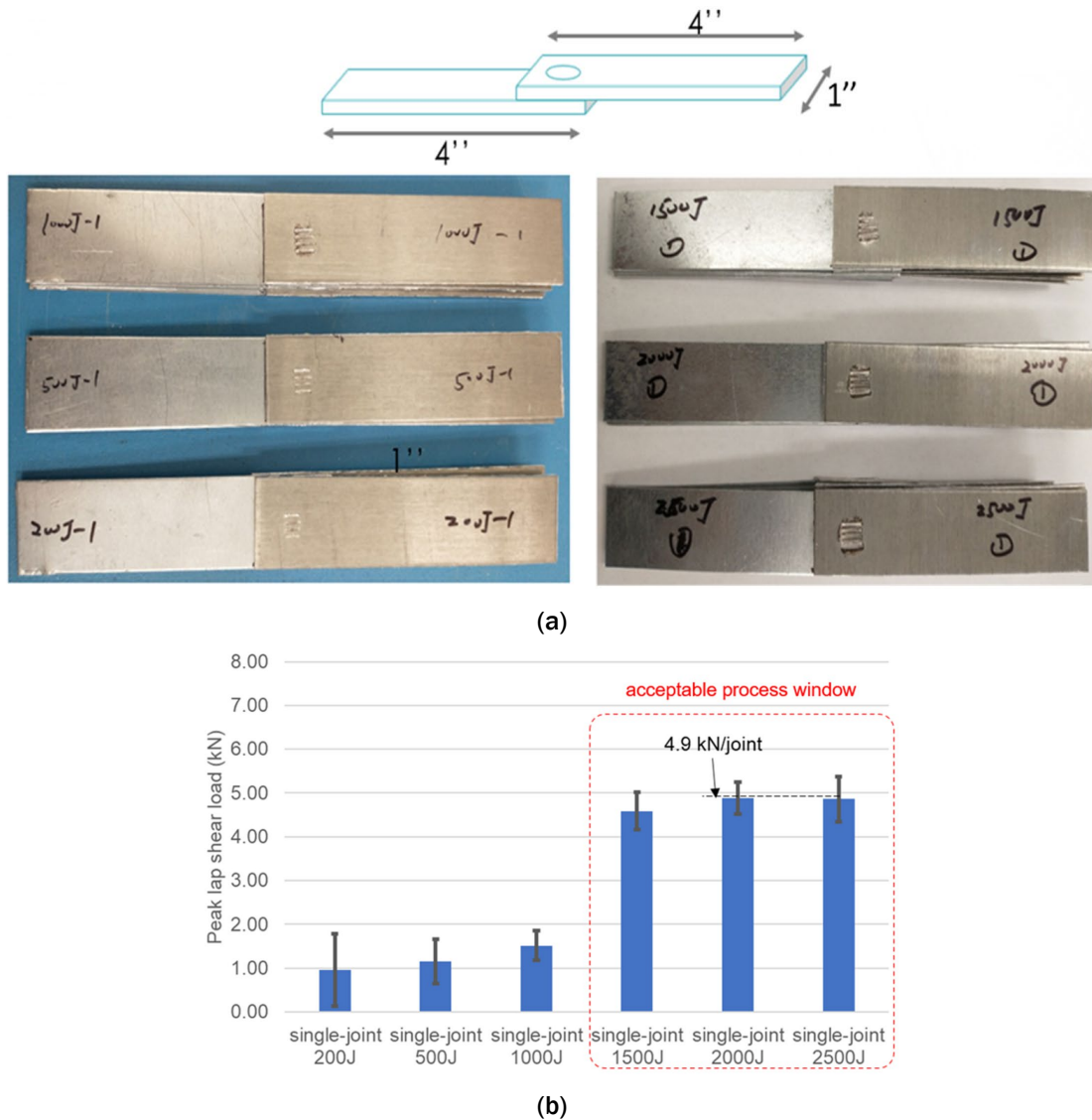


Figure II.3.10.1. (a) Single-joint LS coupons welded by varying ultrasonic energies. (b) Peak LSS as a function of ultrasonic energy. Source: ORNL.

Since the welding condition of 2000~2500 J ultrasonic energy yields the best joint quality in the single-joint coupons, a constant energy at 2500 J was then applied to join a large DP590-AZ31B coupon consisting of five USW joints, as shown in Figure II.3.10.2(a). Each USW joint was then cut out and tested individually as a single-joint LS coupon. Figure II.3.10.2(b) shows the peak LSS of each individual USW joint. The strength is below what was obtained on the single-joint coupon and varies in a quite large range from 0.6kN to 4kN. The strength of the two joints (e.g., A and E) on the edges are relatively large.

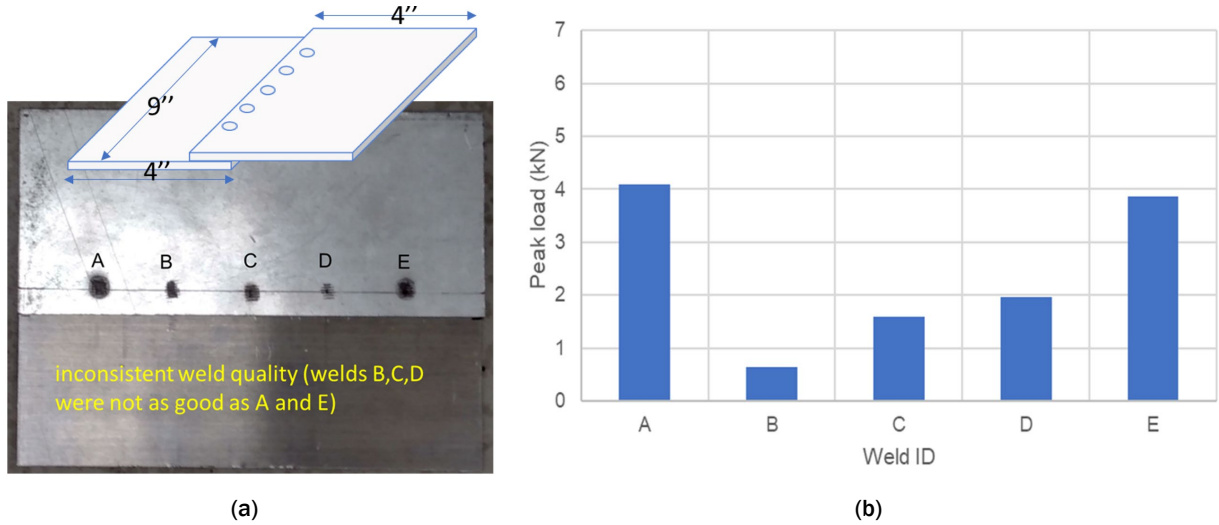


Figure II.3.10.2. (a) Multi-joint sample that was welded using a constant ultrasonic energy input at 2500J. (b) Peak lap-shear strength of each USW joint that was cut out of the large coupon and tested individually. Source: ORNL.

To understand heat generation during joining of each individual USW joint in the large coupon, *in-situ* measurements and numerical modeling were performed. The temperature distribution was measured via an infrared camera. A high-emissivity coating was uniformly coated on the top of the sample to facilitate the temperature measurement. A constant ultrasonic energy was applied to all five joints. Figure II.3.10.3 shows the measured and predicted temperature fields adjacent to the sonotrodes (steel side) when the maximum is reached during welding on joints w1 through w5. The measured peak temperatures of welding joints w4 and w5 are much higher than those on joints w1-w3 (e.g., 437°C to 443°C versus 194°C to 226°C). The prediction is consistent with the experimental measurements.

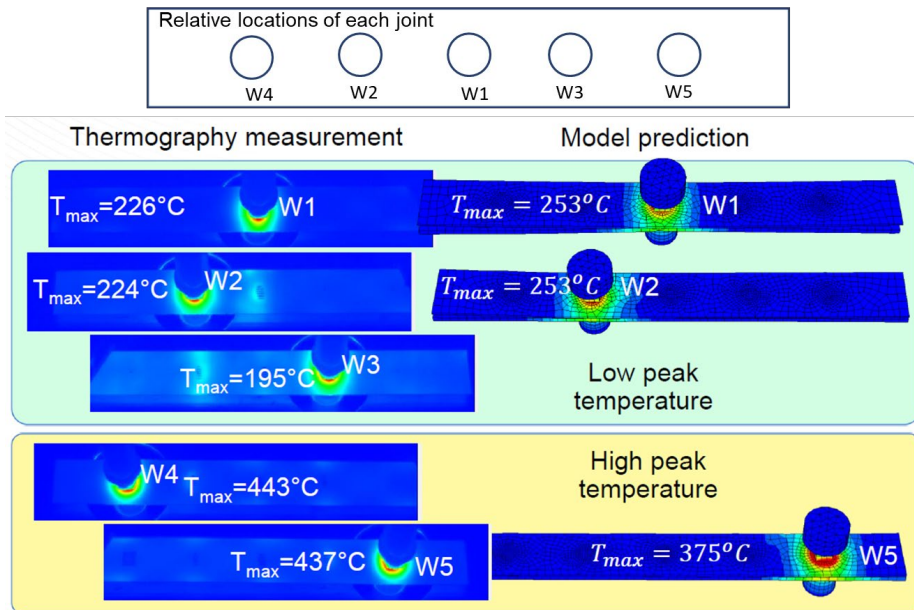


Figure II.3.10.3. Measured and predicted temperature fields when surface temperature reaches the maximum during the welding of each joint as labeled w1-w5. Source: ORNL.

Both measured and predicted temperature fields suggests that a constant ultrasonic welding parameter set (i.e., energy input) may not necessarily yield a consistent temperature field as well as the resulting joint strength. Thus, an adaptive energy input or varying energy levels as a function of joint location may be required to achieve consistent temperature fields. Figure II.3.10.4 demonstrates the predicted temperature fields when making USW joints at different locations (e.g., on the middle versus the edge of the plates) using different ultrasonic energies. Both the high-energy of 7800 J for the middle joint shown in Figure II.3.10.4(a) and the low energy of 2300 J for the edge joint shown in Figure II.3.10.4(b) yielded a similar peak temperature distribution of 427°C that was above the Mg-Zn eutectic reaction to form an effective metallurgical bond.

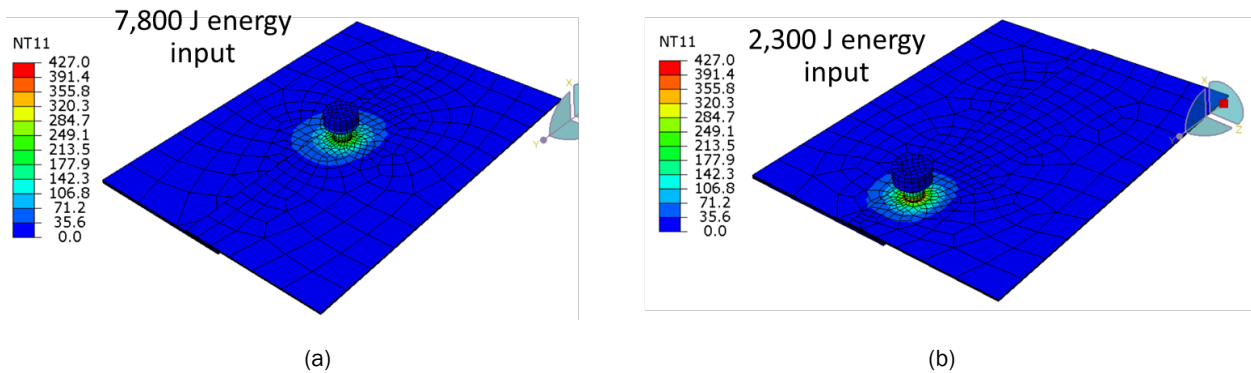


Figure II.3.10.4. Prediction of similar temperature fields when making joints at different locations using different ultrasonic energies of: (a) 7,800 J; and (b) 2,300 J. Source: ORNL.

Experimentally, the strategy of adaptive energy input was applied to make USW joints through the entire large coupon. As shown in Figure II.3.10.5, a relatively small energy of 3200 J was used to weld two joints adjacent to the edges. Next to these two joints, an increased energy of 6000 J was used. Finally, a maximum energy of 10000 J was used to weld the joint in the middle. Although the exact energy levels are different from those used in the finite element models, the overall trend of low energy at the edges with high-energy in the middle is similar.

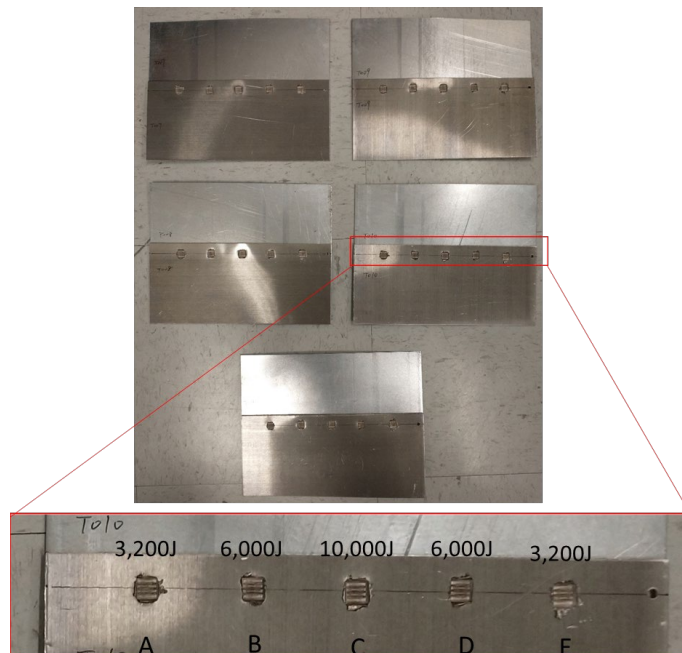


Figure II.3.10.5. Adaptive energy inputs used to make consistent USW joint quality throughout the entire large coupon. Source: ORNL.

Five such large coupons were produced. Each USW joint was cut out of the large coupons and tested individually. Figure II.3.10.6 plots the average peak LSS of each USW joint (e.g., A through E) that was cut out of the large multi-joint coupon, as shown in Figure II.3.10.5. Average peak strength is quite consistent within the five joints; more importantly, there is no observable reduction compared to the strength obtained on the single-joint coupons.

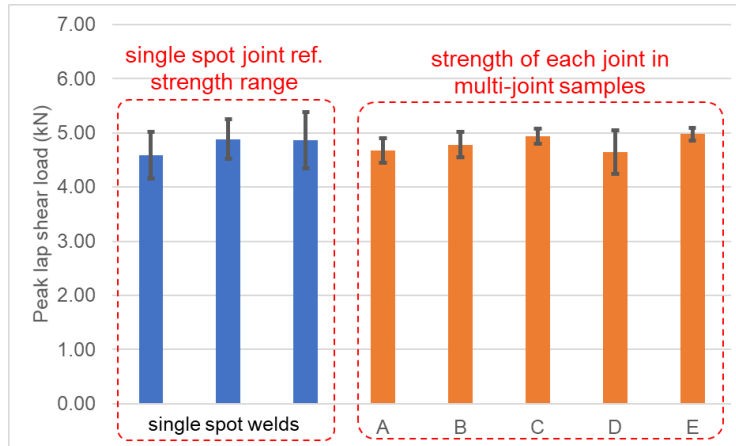


Figure II.3.10.6. Peak LSS of each USW joint (e.g., A through E) cut out of the large multi-joint coupon, as shown in Figure II.3.10.5, and the comparison with the peak strength obtained on the single-joint coupons.
Source: ORNL.

Conclusions

Through our FY 2021 work, the following conclusions can be made:

- The USW process is not only material-dependent but also geometry-dependent. A process parameter set developed on single-joint small coupons cannot be readily applied to join large structures consisting of multiple joints.
- Inconsistent joint quality is expected for welding USW joints at different locations in large structures using constant parameter sets.
- Adaptive welding process parameters that are location- and geometry-dependent are required to consistently achieve high-quality joints throughout entire large structures.

Key Publications

1. Chen, J., Y. C. Lim, D. Leonard, H. Huang, Z. Feng, and X. Sun, 2020, “*In-situ* and post-mortem characterizations of ultrasonic spot welded AZ31B and coated dual-phase 590 steel joints,” *Metals*, Vol. 10, No. 7, Art. 899.
2. Chen, J. Y. C. Lim, H. Huang, Z. Feng, and X. Sun, 2019, “Ultrasonic welding of AZ31B magnesium alloy,” *MRS Bull.*, Vol. 44, No. 8, pp. 630–636.
3. Huang, H., J. Chen, Y. C. Lim, X. Hu, J. Cheng, Z. Feng, and X. Sun, 2019, “Heat generation and deformation in ultrasonic welding of magnesium alloy AZ31,” *J. Mater. Process. Technol.*, Vol. 272, pp. 125–136.
4. Chen, J., Y. C. Lim, H. Huang, and Z. Feng, 2019, “Ultrasonic welding of AZ31B magnesium and DP590 steel,” *AWS Annual Professional Program*, 11–14 November 2019, Chicago, IL, USA.
5. Huang, H., J. Chen, Y. C. Lim, Z. Feng, and X. Sun, 2019, “Enhance heat generation and joint strength in dissimilar metal ultrasonic welds by surface engineering,” *AWS Annual Professional Program*, 11–14 November 2019, Chicago, IL, USA.

6. Jun, J., J. Chen, Y. C. Lim, M. Brady, D. Leonard, and Z. Feng, 2020, “Corrosion behavior of ultrasonic-welded AZ31B and dual-phase steel with and without galvanize layer,” *TMS Coatings and Surface Engineering for Environmental Protection II*, 23–27 February 2020, San Diego, CA, USA (Invited).
7. Xiong, L., A. Chuang, D. Singh, J. Chen, Y. C. Lim, and Z. Feng, 2020, “Synchrotron x-ray diffraction and computed tomography studies of ultrasonic welding dissimilar Mg-Fe metals,” *TMS Coatings and Surface Engineering for Environmental Protection II*, 23–27 February 2020, San Diego, CA, USA.
8. Chen, J., Y. C. Lim, H. Huang, and Z. Feng, 2021, “A method to consistently produce high-quality ultrasonically welded spot joints in large structures,” Oak Ridge National Laboratory Invention Disclosure 202104997.

References

1. Upadhyay, P., H. Das, J. Chen, Z. Feng, H. Huang, Y. C. Lim, Y. Li, D. Leonard, X. Sun, L. Xiong, C. A. Chuang, and D. Singh, 2021, “Solid-state joining of magnesium sheet to high-strength steel,” DOE-EERE Vehicle Technologies Office Joining Core Program. Available at: <https://info.ornl.gov/sites/publications/Files/Pub152244.pdf> (Accessed 17 December 2021).
2. Chen, J., R. W. Davies, Z. Feng, X. Hu, H. Huang, and S. Xin, 2020, “Ultrasonically assisted self-piercing riveting,” 2 April 2020, U.S. Patent Application No. 16/585,754.

II.4 Small Business Innovation Research (SBIR)

II.4.1 Self-Sensing, Self-Sustaining Carbon-Fiber-Reinforced Polymer (S4CFRP) Composites for Next-Generation Vehicles (Newport Sensors, Inc.)

Masato Mizuta, Principal Investigator

Newport Sensors, Inc.
2102 Business Center Dr., Ste. 208D
Irvine, CA 92612
E-mail: info@newportsensors.com

H. Felix Wu, DOE Technology Manager

U.S. Department of Energy
E-mail: felix.wu@ee.doe.gov

Start Date: June 29, 2020	End Date: March 28, 2021	
Project Funding (FY 2021): \$200,000	DOE share: \$200,000	Non-DOE share: \$0

Project Introduction

This project is to develop self-sensing, self-sustaining carbon-fiber-reinforced polymer (S4CFRP) composites for automotive vehicle structural applications. Lightweight high-strength CFRP composites have emerged as the next-generation materials for automotive vehicle structures. In addition to the improvement of fuel efficiency and reduction of CO₂ emissions, CFRP composites offer a great degree of freedom in car design, enabling lower numbers of parts, reduced manufacturing/tooling costs, and enhanced vehicle performance. However, high CF cost and reliability concerns, coupled with high inspection and maintenance costs, have been identified as the most significant obstacles to widespread commercial adoption of CFRP composites in automotive vehicles. Fiber-reinforced composite structures are susceptible to impact damage, which can propagate and drastically reduce the structural strength and stiffness without any visible sign on the surface, which makes it difficult to detect such damage through visual inspection. In addition, there is concern about unknown aging effects of CFRP composites. These challenges necessitate frequent inspections by trained technicians using expensive nondestructive testing and subsurface imaging equipment.

This project aims to overcome these major obstacles, thereby accelerating the commercial deployment of lightweight CFRP composites in the automotive industry. To this end, the project proposes an intelligent CFRP composite integrated with *in-situ* self-health monitoring, real-time damage detection, and energy-harvesting, in addition to the composite's basic functionality as a lightweight structural material. In Phase I, the project focuses on addressing the challenge of damage inspection, while the high fiber cost will be tackled in Phase II by hybridizing low-cost natural fiber with CF.

Objectives

The objective of Phase I is to demonstrate the feasibility of transforming structural materials into a spatially distributed piezoelectric sensor and a vibration energy harvester for simultaneous damage detection and energy generation. Specific technical objectives include the following:

- To design and fabricate the S4CFRP composites, including circuitry.
- To demonstrate the feasibility of self-sensing and detection of impact and damage.
- To demonstrate the feasibility of harvesting vibration energy sufficient to power the self-sensing system.

Approach

Our approach is to transform the structural composite material components into a piezoelectric transducer for simultaneous self-sensing and energy-harvesting. As with conventional CFRP composites, our multifunctional CFRP composite is a laminate of carbon fiber layers in polymer matrix, except that the polymer is the PVDF polymer, which is equipped with piezoelectric properties. Taking advantage of the electric conductivity of CFs, the two layers of CFs sandwiching the PVDF polymer layer are used as electrodes. Through this design, the CFRP composite is transformed into a spatially distributed piezoelectric transducer that can serve as a sensor, without requiring the insertion of any additional sensors, as is necessary in a conventional structural health monitoring system. Impact loads and initiation or propagation of any damage in the composite—such as fiber breakage, fiber-polymer debonding, polymer cracking, and interlayer delamination—will generate elastic waves that cause deformation in the polymer, resulting in detectable electric signals. Because every point in the laminate structure is a sensor, any damage event, no matter where it occurs, can be detected.

Furthermore, the same piezoelectric transducer can also serve as an energy harvester to power the self-sensing and monitoring system. The basic design of this integrated S4CFRP system is shown in Figure II.4.1.1. Vehicle vibration causes deformation of the piezo transducer, generating electricity that will be stored in a battery to power the sensor system. Using the stored energy, the sensor system can stand-by 24/7, even when the vehicle is not in operation, so that no damage event will be missed. To save energy, a low power electric circuit must be developed.

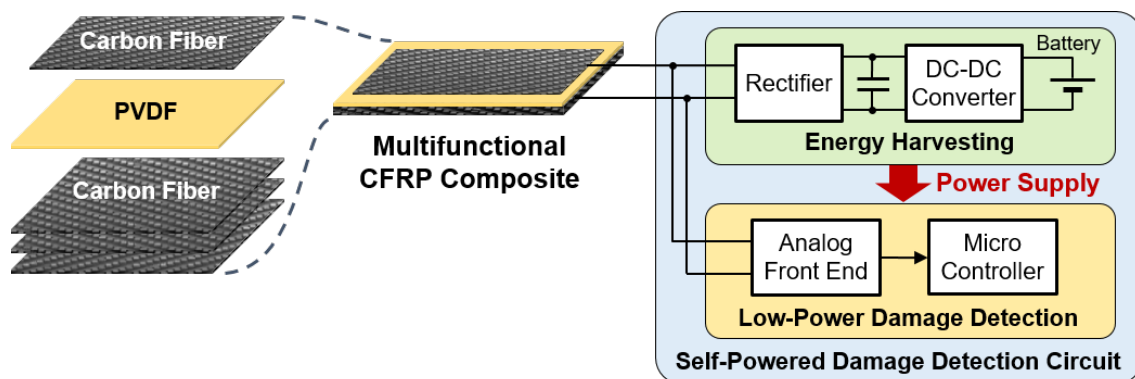


Figure II.4.1.1. Concept of S4CFRP composite system. Source: Newport Sensors, Inc.

Simultaneous Sensing and Energy-Harvesting Circuit

This circuit functionality is the key innovation of this project. The most significant technical challenge is how to create a single circuit that: (1) can distinguish an instantaneous damage signal from the continuously harvested vehicle vibration signal; and (2) can be powered by the vibration energy harvested by the circuit itself. The Phase I effort successfully met the technical challenge and developed a circuit that senses and harvests energy simultaneously. The project used circuit simulation to confirm these functionalities, then prototyped and integrated the circuit with the fabricated composite material specimens. Figure II.4.1.2 shows the circuit block diagram of the proof-of-concept system created in Phase I.

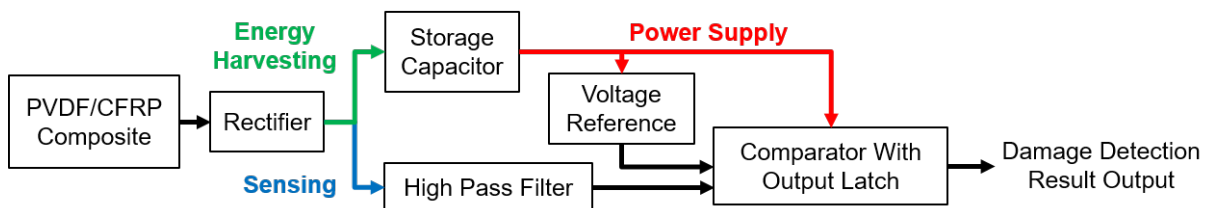


Figure II.4.1.2. Circuit block diagram of the proof-of-concept system. Source: Newport Sensors, Inc.

Results

Prototype of Multifunctional CFRP Composite Specimens

The project team prototyped multifunctional CFRP composite test specimens. Figure II.4.1.3 shows the specimen fabrication process using the hand layup and vacuum bagging method. The project team used epoxy resin (applied by hand) to stack trimmed CF preforms and a piece of PVDF film. The laminated structure was placed in a vacuum bag, and the bag was transferred to an oven. The bag was placed in a vacuum at the oven temperature of 60°C. After three hours of curing, the formed CFRP plate was cut into individual specimens.

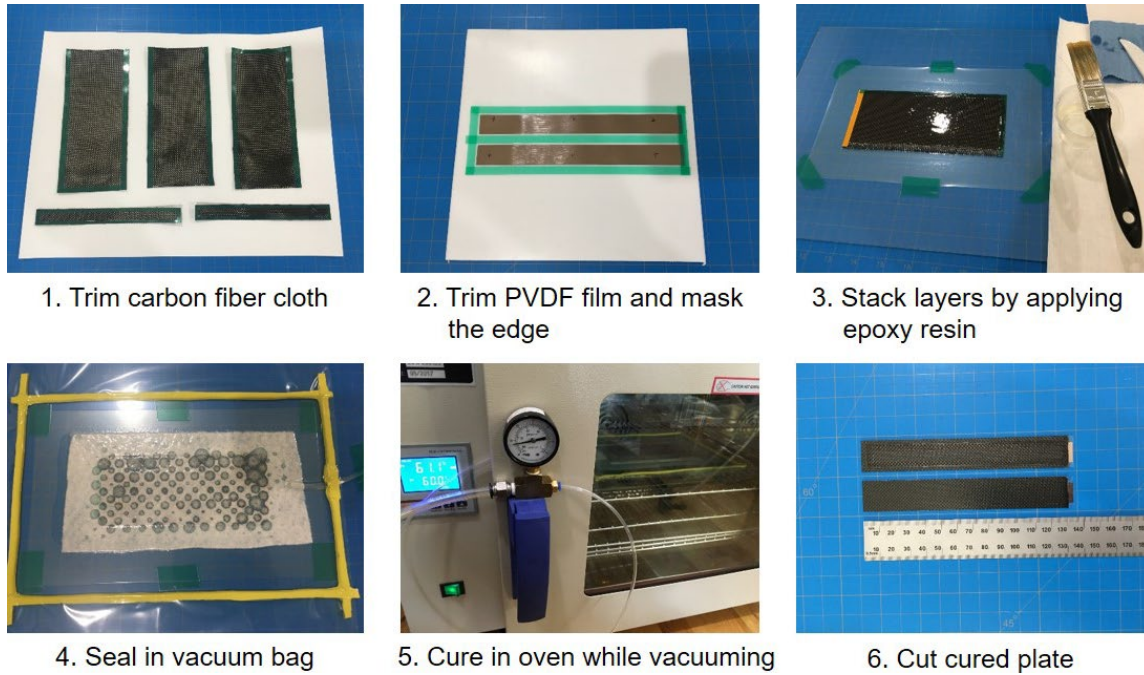


Figure II.4.1.3. Process for fabrication of test specimens. Source: Newport Sensors, Inc.

Experimental Evaluation

Integrated with the prototype circuit, the fabricated CFRP composite specimens were experimentally tested to evaluate the self-sensing and energy-harvesting functionalities. The project team carried out different types of test setups, as shown in Figure II.4.1.4. The free vibration testing was used to evaluate the energy-harvesting functionality. The pencil damage and the hammer impact tests were used to validate the self-sensing functionality. In addition, simultaneous sensing and energy-harvesting experiments were also conducted.

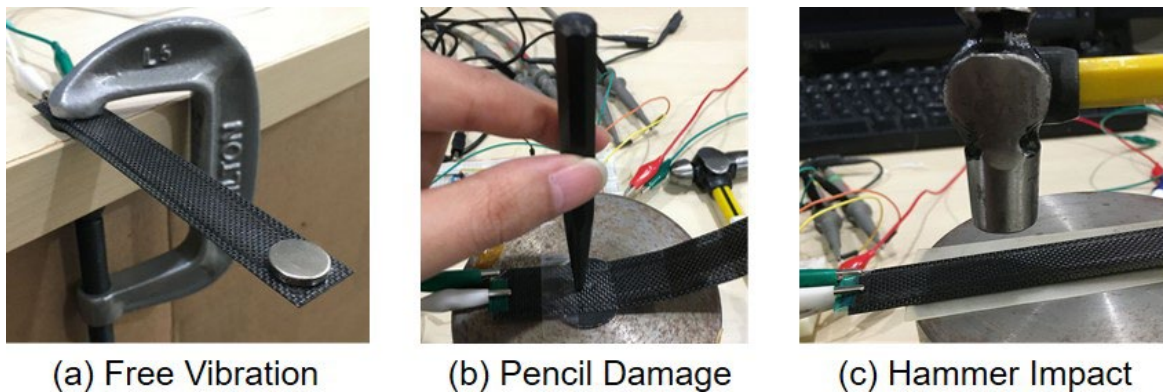
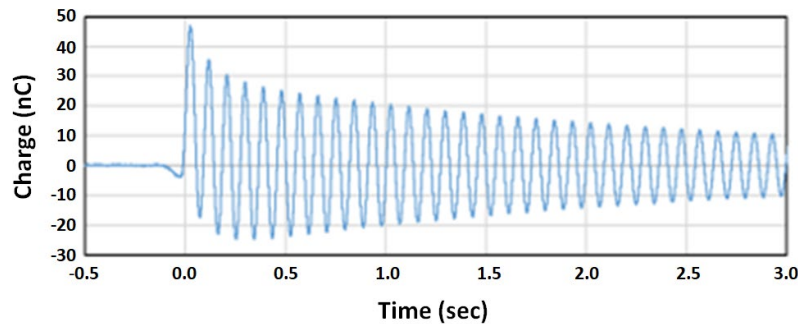


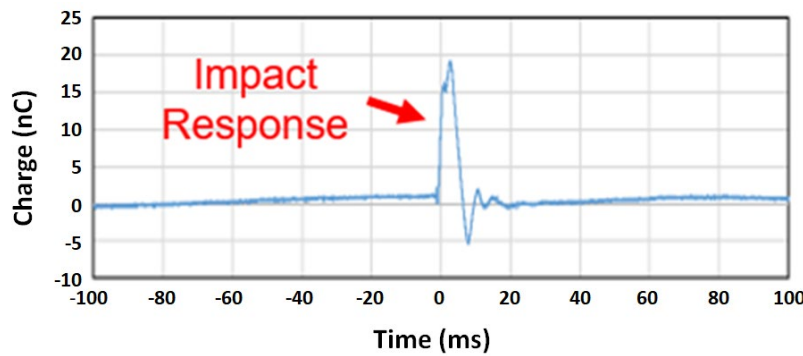
Figure II.4.1.4. Experimental evaluation setups: (a) fixture for free vibration, (b) fixture for damage from stylus, and (c) setup for impact with a hammer. Source: Newport Sensors, Inc.

Piezoelectric Signals under Ambient Vibration, Impact Load, and Combined Conditions

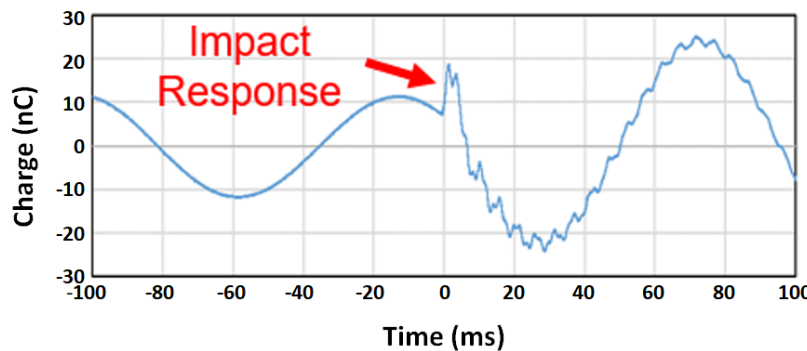
The piezoelectric signal results are shown in Figure II.4.1.5. Figure II.4.1.5(a) shows the signal time history measured from the piezoelectric transducer, when the CFRP specimen was under free vibration. The oscillation, which can simulate vehicle ambient vibration, was successfully measured. Figure II.4.1.5(b) shows the measured piezoelectric signal when a hammer impact was applied to the specimen. As expected, the test measured a pulse that was clearly different from the free vibration. The third chart shows the measured piezoelectric signal when the free vibrating specimen was subjected to a hammer impact. Although the signals are mixed, the high-frequency pulse caused by the impact can be distinguished from the oscillatory free vibration signal. These experimental results validated the feasibility of separating the shock signal from ambient vibration using a high-pass filter.



(a)



(b)



(c)

Figure II.4.1.5. Measured piezoelectric signals of the specimens from: (a) the free vibration test, (b) the impact test, and (c) the impact during free vibration. Source: Newport Sensors, Inc.

Evaluation of the Vibration Energy-Harvesting Functionality

Figure II.4.1.6 demonstrates the system’s capability of harvesting energy using self-generated power from vibration. Vibration frequencies of traveling vehicles depend on road surface conditions and the natural frequency of the suspension system (estimated to be in the range of 2 to 20 Hz). The project tested the energy-harvesting characteristics under vibrations of different frequencies, using the free vibration test setup. Within the anticipated vibration frequency range of a traveling vehicle, the energy generated by the piezoelectric PVDF material should be sufficient to power the self-sensing system.

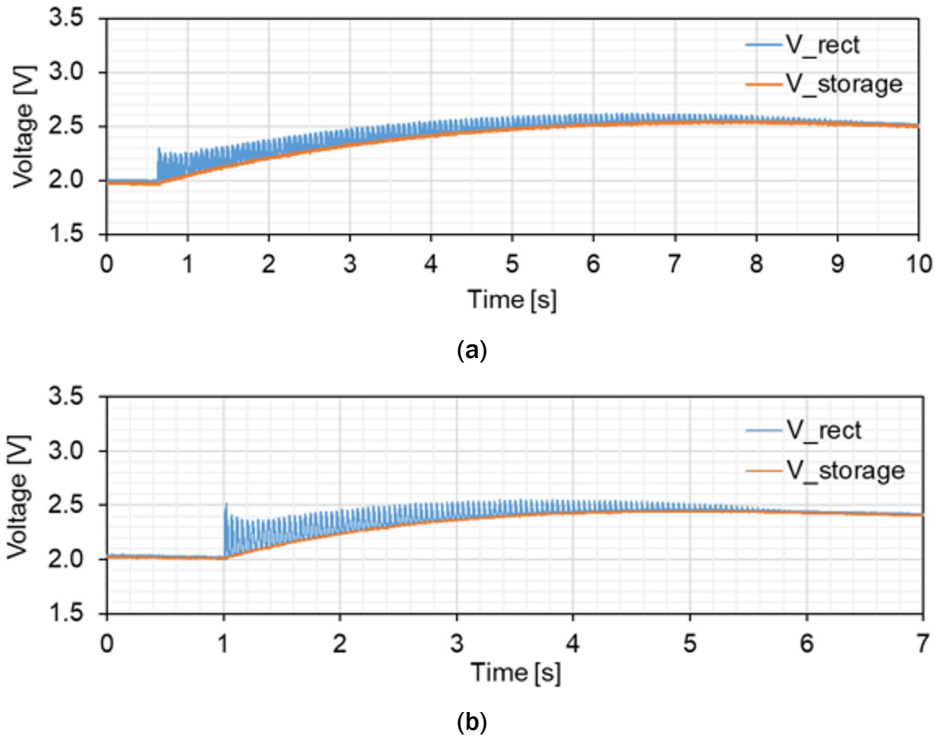


Figure II.4.1.6. Energy-harvesting results at (a) 8 Hz and (b) 11 Hz. Source: Newport Sensors, Inc.

Evaluation of the Damage Detection Functionality

The project conducted the hammer impact test on the specimen. The hammer impact was applied, causing a permanent punch damage to the specimen, as shown in Figure II.4.1.7(a). The voltage time histories measured at the three outputs of the circuit, as shown in Figure II.4.1.7(b), indicate that the damage event was successfully detected by the circuit.

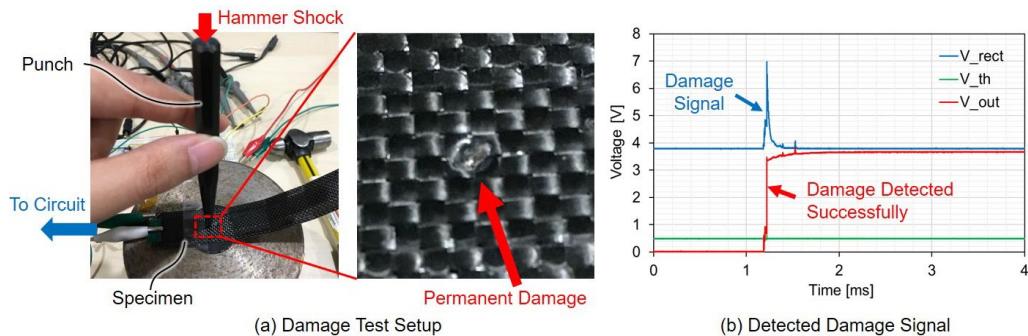


Figure II.4.1.7. (a) Damage detection test setup and (b) results of the damage detection test. Source: Newport Sensors, Inc.

Evaluation of the Simultaneous Sensing and Energy-Harvesting

The project also evaluated the simultaneous sensing and energy-harvesting functionality, as shown in Figure II.4.1.8, using the time history of the circuit output voltage measured when the free vibrating CFRP specimen was subjected to a hammer impact load. The impact signal event was successfully detected. Therefore, the impact/damage event can be detected while harvesting energy from free vibration. Again, the pulse signal caused by the hammer impact can be clearly distinguished from the oscillatory ambient vibration.

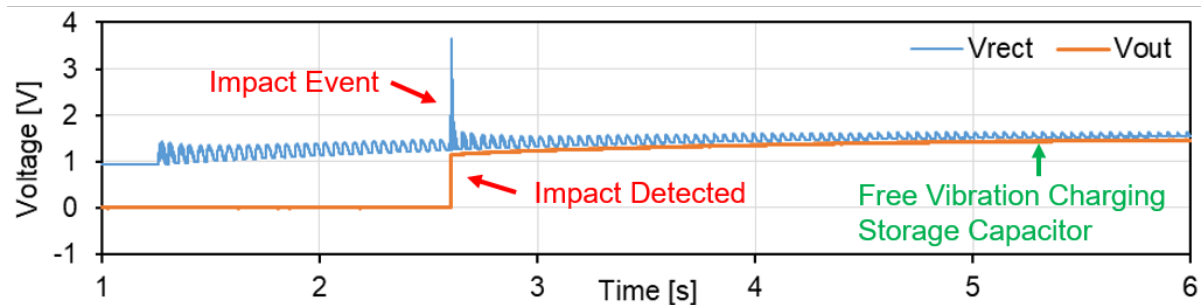


Figure II.4.1.8. Simultaneous sensing and energy-harvesting result. Source: Newport Sensors, Inc.

In Phase I, the tests were focused on impact loads and impact damage, which are important for vehicle structural materials. In Phase II, the proposed S4CFRP technology will be evaluated under more realistic structural damage scenarios.

Conclusions

This SBIR project is developing an innovative multifunctional CFRP composite integrated with self-powered *in-situ* self-health-monitoring functionalities. The purpose is to address difficulties with damage inspection of CFRP, a major obstacle to the material's widespread commercial adoption by the automotive industry.

Major outcomes and conclusions are summarized as follows:

1. In Phase I, the project successfully created a laminated CFRP composite that can double as a distributed piezoelectric sensor and a vibration energy harvester.
2. The Phase I effort developed an electrical circuit for simultaneous detection of impact loads and structural damage and harvesting of vehicle vibration energy. This was the first such circuit developed for practical use.
3. The multifunctional CFRP specimens and circuit were experimentally evaluated through free vibration, impact, and damage tests.
4. The experimental results demonstrated the feasibility of distinguishing the impact and damage signal from the ambient vibration signal measured by the piezoelectric PVDF transducer.
5. The efficiency of the energy harvester was also demonstrated. The amount of energy harvested was sufficient to power the sensor circuit.
6. The amount of energy harvested was almost constant for each cycle of vibration, regardless of the frequency of vibration.

In summary, this project has demonstrated the technical feasibility of the proposed self-powered, self-health-monitoring CFRP composite, successfully achieving the Phase I objective. Building upon the success of Phase I, Phase II will further expand the material's functionalities by adding a novel complementary piezoresistive sensor to enhance the reliability of *in-situ* damage detection and enable damage location. Natural fibers will be incorporated not only to reduce cost but also to improve crashworthiness—the most critical and distinct requirement for automotive vehicle structural materials. Because of the new functionalities to be added

in Phase II, the proposed technology will be named Sustainable Lightweight Intelligent Composite (SLIC). By delivering the proposed SLIC technology to address the two most significant obstacles to widespread CFRP adoption (i.e., high fiber cost and difficult damage inspection), SLIC aims to accelerate commercial adoption of lightweight fiber composites in automotive vehicles, which will result in enormous environmental and economic benefits due to reduced vehicle weight and greenhouse gas emissions.

Key Publications

1. Mizuta, M., 2021, “Self-sensing self-sustaining carbon-fiber-reinforced polymer composites (S4CFRP) for next-generation vehicles,” 2021 DOE VTO Annual Merit Review, 25 June 2021.

Acknowledgments

This project is supported by the DOE SBIR program under Award No. DE SC0020707. The author is grateful for the support provided by the DOE SBIR program.

II.4.2 Integrated Self-Sufficient Structurally Integrated Multifunctional Sensors for Autonomous Vehicles (Acellent Technologies, Inc.)

Amrita Kumar, Principal Investigator

Acellent Technologies Inc.
835 Stewart Drive
Sunnyvale CA 94085
E-mail: akumar@acellent.com

H. Felix Wu, DOE Technology Manager

U.S. Department of Energy
E-mail: felix.wu@ee.doe.gov

Start Date: June 29, 2020	End Date: March 28, 2021	
Project Funding (FY 2021): \$111,111	DOE share: \$111,111	Non-DOE share: \$0

Project Introduction

The DOE VTO has identified a need for novel multifunctional composite materials and structures for the automotive industry that have the capability to reduce weight and volume, as well as costs of conventional structural components, by performing engineering functions beyond load-carrying. The multifunctionality that couples structural performance and additional functionalities (e.g., electrical, magnetic, optical, thermal, chemical, biological, etc.) is critical to the growth of AI in the automotive industry. Multifunctional structures can sense, diagnose, and respond, thereby adapting to environmental changes with minimum external intervention, allowing alternation of shape functionality and mechanical properties on demand, and enabling structural integration of power harvest/storage/transmission capabilities for “self-sustaining” systems. There is currently a need to reduce the demands of whole systems. For example, a pedestrian protection system (PPS) is of paramount importance for a city car, and 98% of the required energy needs are associated with weight. Adopting composites provides the capability to integrate sensors needed by a PPS into the structure and provides significant weight-savings, especially with multifunctionality built in to store electrical energy and to carry mechanical load.

Objectives

Acellent Technologies, Inc. (Acellent) is developing an integrated AUTO-SMART sensor system for the automotive industry. The system will be able to provide multifunctional capabilities and help make vehicles self-sufficient. The primary focus is on how multifunctionalities in composites can affect vehicle design to provide increased pedestrian safety, weight-savings and structural efficiencies. The proposed development will focus on development of two multifunctionalities:

- PPS
- Battery monitoring system (BMS).

Approach

The following developments were targeted in this project, with Phase I focusing on developing a complete design for the AUTO-SMART sensor system:

1. Developing the design for a pedestrian crash-sensing system that has the capability to detect any impact event occurring on the front bumper of an automobile within a very short duration and generate the proper response signal to a built in protection system. A primary challenge in this effort was to design and develop an impact event detection technique that can work efficiently, even for complex structures with local property variation. Conventional impact detection systems have long response times because of the slow response of traditional sensors. The proposed system utilized lead zirconate titanate (PZT)

sensors to generate the impact signal immediately after the impact event happens. The quicker response allows the passive safety systems (such as air bags and pyrotechnic restraints) to be activated in time to save lives.

2. Developing the design of a system for monitoring the state of health (SOH) and state of charge (SOC) of a typical battery pack for use in automobiles. Key issues such as sensor locations were developed for the battery.
3. Performing preliminary testing. The design developed in Phase I was also tested during Phase I to check on the multifunctionalities. The final configuration will be determined in Phase II.

Results

Pedestrian Protection System

An automotive PPS is generally used to protect pedestrians from harm caused by frontal collisions. In Phase I, the project system was demonstrated on a stationary bumper, and methods for design and installation of sensors on the bumper were developed.

Sensor Network Design for Pedestrian Crash-Sensing

In Phase I, Acellent used its previously developed SMART Layer sensors for the bumper. The technology is well-established in the field and is currently known for its unique ability to provide a large structural coverage for gathering data with a network of sensors/actuators embedded on a layer, thus eliminating the need for each sensor to be installed individually, as shown in Figure II.4.2.1 [1–4]. The layer consists of a network of embedded, distributed PZT discs acting as both sensors and actuators for monitoring structural conditions in real-time. The SMART Layer manufacturing process uses the printed circuit technique to connect a number of sensors and actuators embedded in the layer. The SMART Layer is treated as an extra ply that can be embedded between composite plies during the composite layup process or surface-mounted on both metallic structures and composite structures using a secondary adhesive, such as epoxy.

For this application, Acellent choose small-size disc-shaped PZTs. The PZT sensors, capacitors, and wiring can all be embedded in a thin dielectric film, as shown in Figure II.4.2.1. Additional shielding layers and wiring was also added to the sensor layer to minimize external EMI and crosstalk between sensors. All SMART Layer strips have a copper layer that shields one side of the circuit from EMI. The small-size of the PZTs ensures they can be embedded in the bumper during manufacturing and do not protrude from the bumper.

To find an optimal sensor density and spacing for the sensor network, the project team looked at several factors. Speed and accuracy requirements play a critical role in making this determination. Ideally, sensors should be instrumented along the entire length of the bumper, with minimal spacing between each sensor, to account for impacts at every location (as discussed in the requirements above). However, cost and practicality issues necessitate a minimum sensor density [5, 6].

Based on previous work done at Acellent on similar structures, a conservative sensor spacing of 6 in. between the sensors was chosen for the Phase I testing. A total of 10 PZTs were designed into the layer, based on typical bumper sizes. The SMART Layer sensor locations for the bumper were designed based on this spacing.

Acellent tested a prototype PPS on a test car bumper. The bumper, with sensors installed, was fastened securely to two poles. The sensors were connected to the impact data collection hardware through cables. The data were sent to a laptop via ethernet connection for analysis. Figure II.4.2.2 shows the test setup. Two types of impacts were tested: one using a golf club (non-pedestrian) and another using a prosthetic leg (pedestrian simulation).



Figure II.4.2.1. SMART Layer sensors. Source: Acellent.

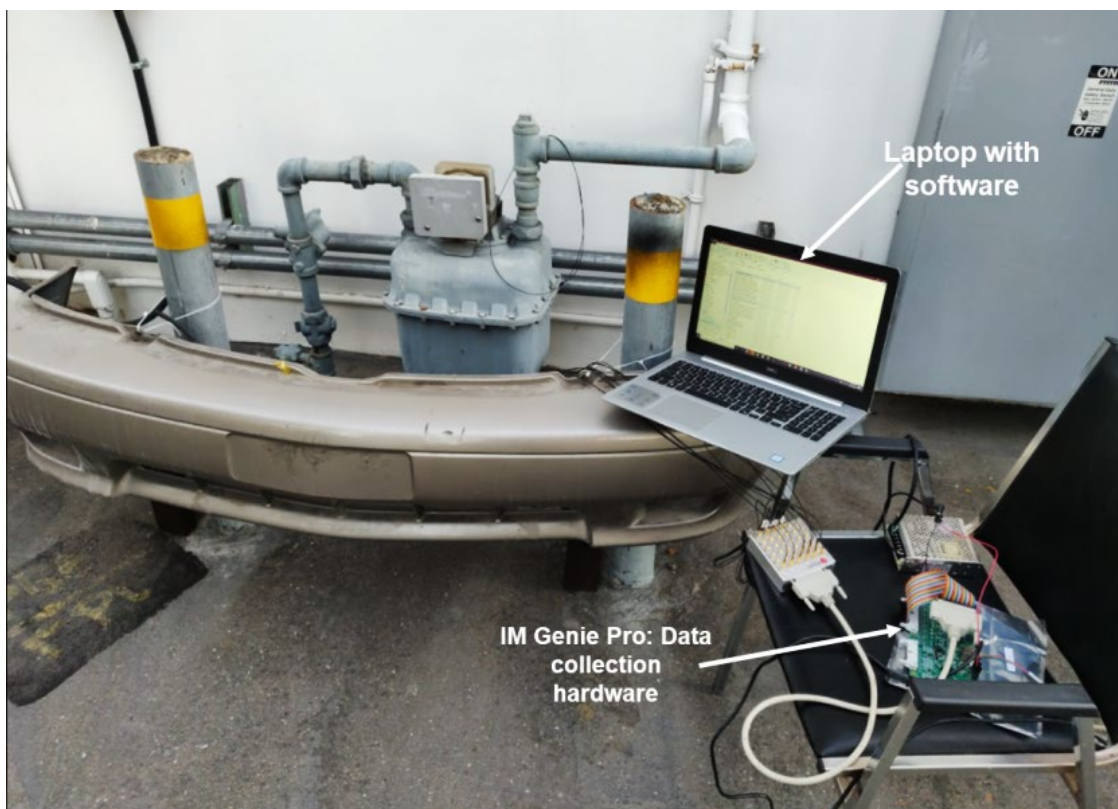


Figure II.4.2.2. Circuit block diagram of the proof-of-concept system. Source: Acellent.

Impact with a golf club. The researchers used a golf club to hit the car bumper near the center line, as shown in Figure II.4.2.3. The impact triggered the system to collect data from the sensors. The image on the right shows the signals received from the sensors. As the figure shows, the Structural Health Monitoring (SHM) system successfully captured the impact.

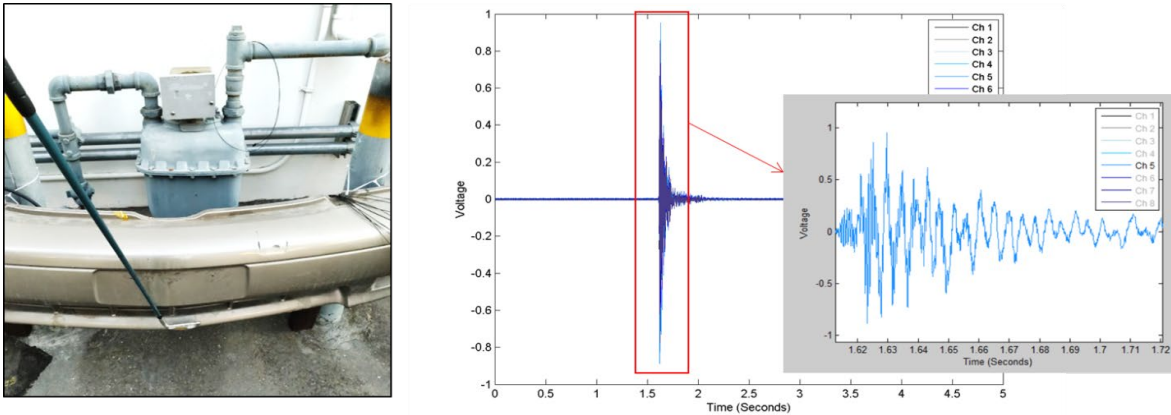


Figure II.4.2.3. Voltage impulse received upon an impact with a golf club. Source: Acellent.

Impact with a prosthetic leg. The researchers hit the car bumper with a prosthetic leg to simulate hitting a pedestrian, as shown in Figure II.4.2.4. The impact triggered the system to collect data from the sensors. The image on the right shows the signals received from the sensors. The figure shows that the SHM system successfully captured the impact.

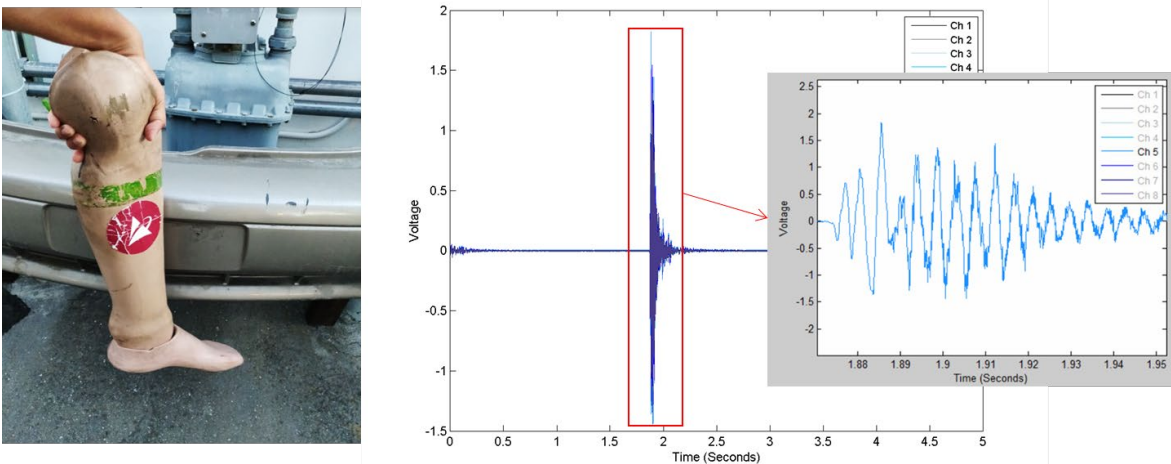


Figure II.4.2.4. Experimental evaluation setups: (a) fixture for free vibration, (b) fixture for damage from stylus, and (c) setup for impact with a hammer. Source: Acellent.

As can be seen from the data obtained, the impact signals obtained from the golf club (non-pedestrian) and prosthetic leg (simulated pedestrian) are significantly different. During Phase II, Acellent will use data obtained from further tests to identify the frequency responses due to impacts of various objects on the bumper. Based on the results, software will be developed to meet the requirements for detection of pedestrians.

Battery Monitoring System

BMSs are used to monitor and control battery energy storage systems, ensure the health of the battery cells/pack. Lithium-ion (Li-ion) battery technology has performed magnificently and has improved over the last decade; however, the chemistry inside the battery is very susceptible to certain risks such as overheating, over-voltage, deep discharge, over-current, pressure, and/or mechanical stress. To prevent battery failure and

mitigate potential hazardous situations, there is a need for a BMS that ensures that batteries function properly in the final application. The BMS can provide SOC, SOH, and end-of-life monitoring of the battery.

During Phase I, Acellent and Stanford University conducted testing on a Li-ion pouch cell, as shown in Figure II.4.2.5(a) that was equipped with Acellent's single-sensor SMART Layer PZTs, which can serve as actuators and sensors. One of the piezoelectric discs can be chosen as an actuator to generate acousto-ultrasonic guided waves. The other piezoelectric disc then serves as a receiver to receive the transmitted guided wave signals, as shown in Figure II.4.2.5(b)-(d). The project team aims to correlate the guided wave signals from piezoelectric sensors with battery SOC and SOH through both experiments and data analysis. The results are imperative for evaluating the efficacy of SOC and SOH prediction using guided waves with built in sensors/actuators. The proposed technique was evaluated on indicative commercial Li-ion pouch cells (graphite/NMC chemistry; 3,650 mAh capacity; $135 \text{ \AA} \sim 45 \text{ \AA} \sim 5 \text{ mm}$; free-standing and stationary conditions). The results are shown in Figure II.4.2.5(e).

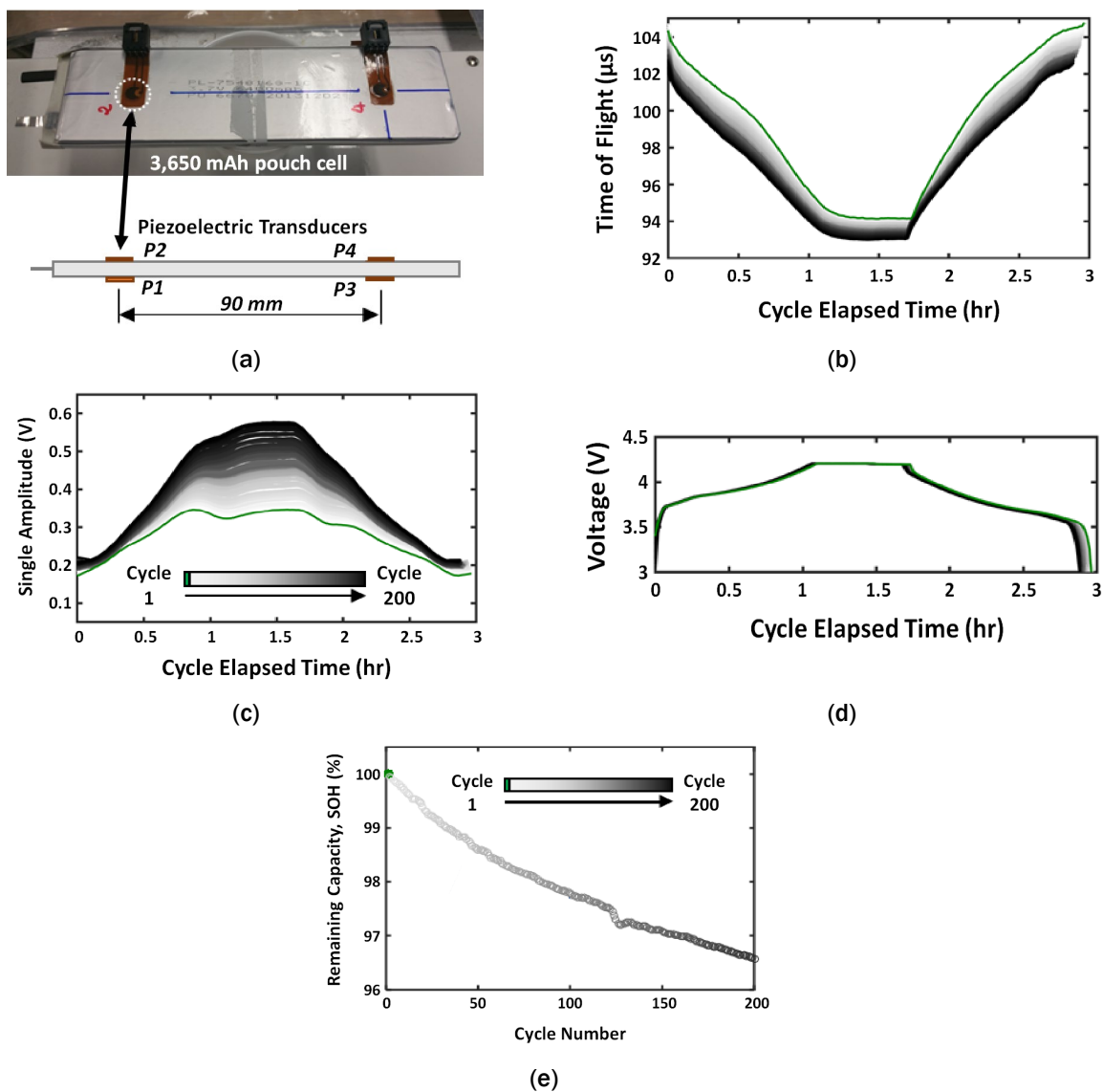


Figure II.4.2.5. (a) The 3,650 mAh pouch cell that underwent cycle life aging; (b), (c), and (d) schematics of the experimental guided wave propagation inspection setup in Li-ion batteries; and (e) the indicative results for the SOH [7]. Source: Stanford University.

Pitch–catch guided wave propagation experiments were performed on commercial Li-ion pouch batteries using surface-mounted piezoelectric disc transducers. The research team identified sensitive ultrasonic features that correlated with the distribution of electrode moduli and densities during cycling and aging, and thus with SOC and SOH. The physical relationships between the ultrasonic signature and electrochemical process were thoroughly analyzed. An analytical acoustic model was developed to validate the guided wave response to the changes in electrode moduli and densities during cycling. The results and physical insights from the experiments and analysis were then used in the preliminary statistical study to evaluate the efficacy of SOC and SOH prediction. The team established a statistical framework to explore the feature-rich multipath nature of guided wave signals for improving prediction accuracy and robustness, as well as for reducing computational complexity.

The experimental setup for battery charge and discharge is shown in Figure II.4.2.6. Acellent’s data acquisition (DAQ) system was used for all data acquisition, along with the SMART Layer PZT sensors installed on the battery pouch.

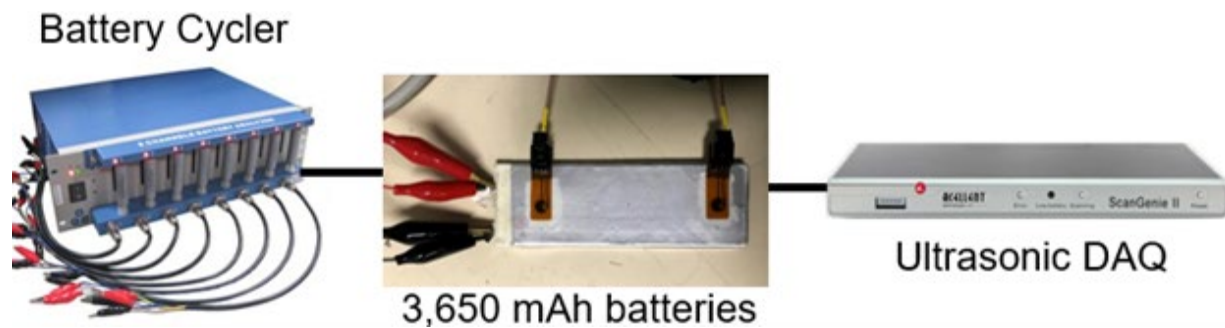
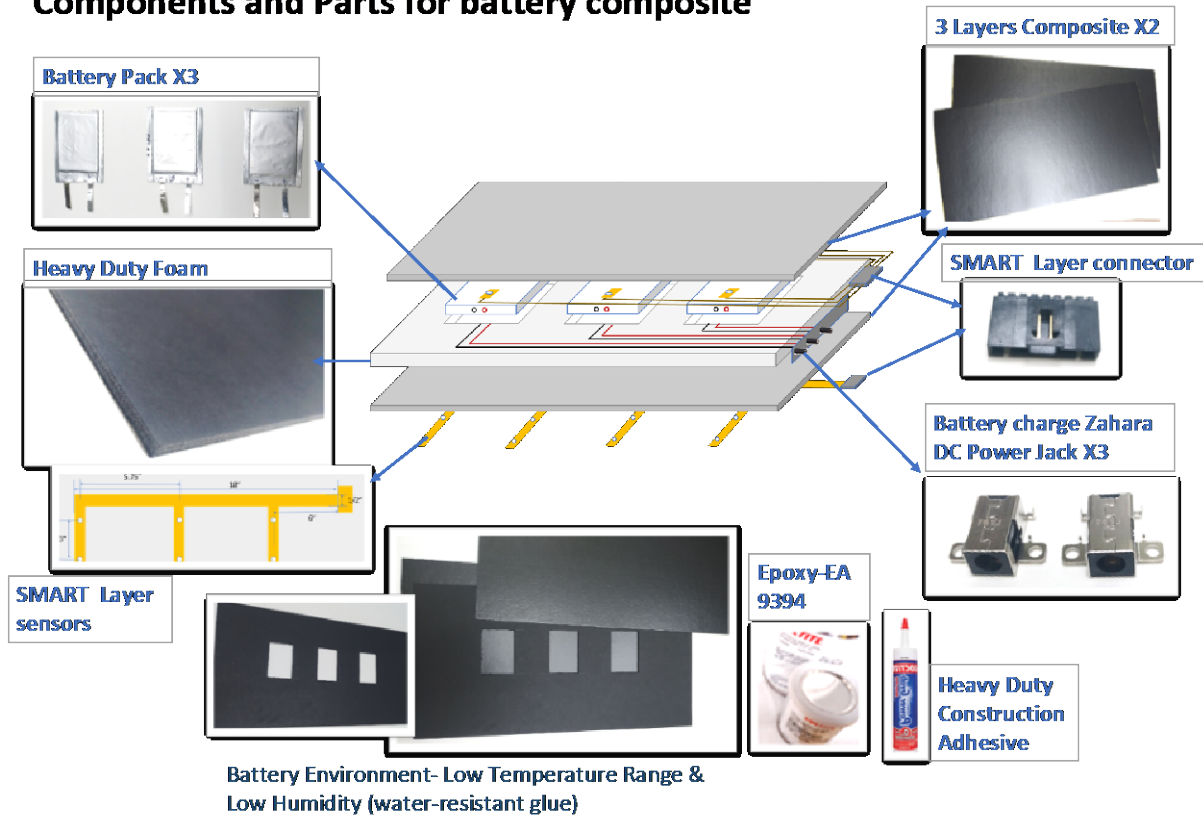


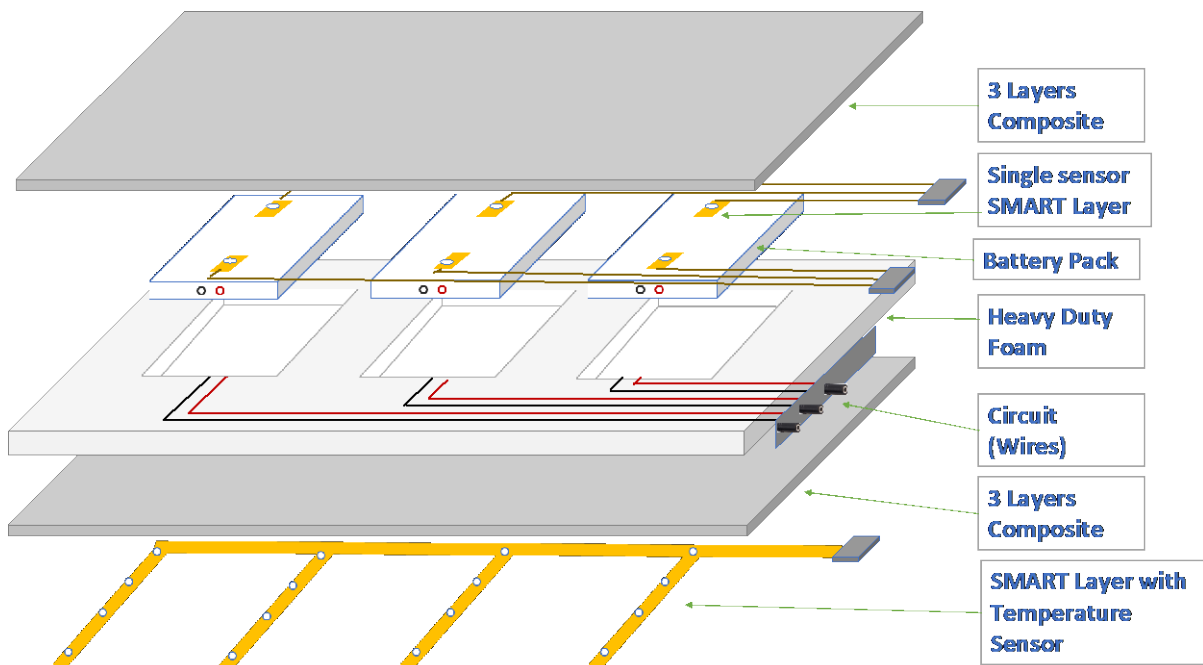
Figure II.4.2.6. Experimental setup showing the battery cyclier connection to the 3,650 mAH battery and the DAQ. Source: Stanford University.

Under an ARPA-E-funded project, Stanford University is developing multifunctional energy storage composites (MESCs) for the energy-efficient design of lightweight electric vehicles [8–12]. The MESCs constitute a multifunctional structural battery system that embeds Li-ion battery materials into high-strength structural composite materials. During SBIR Phase I, Acellent designed a complete sensing system for the MESC batteries; the work included installing sensors directly on the battery and on the composite. The research team created a design for the MESC with the embedded sensors and manufactured a complete testbed to test the sensors for use in SOH and SOC determination. Figure II.4.2.7(a) shows the components required for the MESC battery testbed. The MESC battery was embedded between two layers of composite material. SMART Layer sensors were manufactured and installed on the composite layer to monitor the performance of the battery. Figure II.4.2.7(b) shows the design and installation of the sensors in the MESC battery.

Components and Parts for battery composite



(a)



(b)

Figure II.4.2.7. MESC battery monitoring components and layout. Source: Stanford University.

Conclusions

During Phase I of this project, Acellent developed an innovative sensor suite that was designed, developed, and integrated with automotive vehicle structures during the manufacturing process itself to create a structurally integrated sensor network. The focus was primarily on demonstrating the following two multifunctionalities:

- A PPS that is critical for driverless cars.
- A BMS for: (1) typical battery packs; and (2) a structurally integrated battery developed by Stanford University and licensed exclusively by Acellent, leveraged for use in power delivery and management.

In SBIR Phase I, Acellent successfully demonstrated a complete PPS in a laboratory environment. Sensors were designed for installation on a bumper. The system was tested for impact detection using a non-pedestrian object (golf club) and a pedestrian proxy (prosthetic leg). The signals due to the impacts with each were clearly discernable.

In collaboration with Stanford University, Acellent also demonstrated the ability to use piezoelectric transducers to monitor the SOC and SOH for battery cells, both independently and when embedded inside a composite structure. Using practical usage design, the researchers created and manufactured a testbed for testing in Phase II.

References

1. Acellent website, n. d., “Smarter structures, safer world,” Available at: <http://www.acellent.com> (last accessed 10 March 2022).
2. Kumar, A., H. Chung, T. Singhal, S. Yadav, C. Gray, G. Chang, and I. Li, 2019, “Industrial IOT-enabled SHM systems,” In: Chang, F.-K., and F. Kopsaftopoulos (eds.), *Proceedings of the 12th International Workshop on Structural Health Monitoring*, 10–12 September 2019, Stanford, CA, USA. Available at: <https://10.12783/shm2019/32216> (last accessed 10 March 2022).
3. Qing, X. P., S. J. Beard, A. Kumar, I. Li, M. Lin, and F.-K. Chang, 2009, “Stanford Multiactuator–Receiver Transduction (SMART) layer technology and its applications,” *Encyclopedia of Structural Health Monitoring*, Wiley, Chichester, UK.
4. Qing, X. P., S. J. Beard, R. Ikegami, F.-K. Chang, and C. Boller, 2009, “Aerospace applications of SMART layer technology,” *Encyclopedia of Structural Health Monitoring*, Wiley, Chichester, UK.
5. Kim, A. C., and F.-K. Chang, 2005, “Rapid detection and identification of pedestrian impacts using a distributed sensor network,” *Proceedings of SPIE Smart Structures and Materials 2005: Smart Structures and Integrated Systems*, Vol. 5764, 17 May 2005. Available at: <https://doi.org/10.1117/12.600433> (last accessed 10 March 2022).
6. Kim, A., 2006, “A rapid method for identifying and characterizing structural impacts using distributed sensors: an application for automotive pedestrian protection,” Ph. D dissertation, Stanford University, Stanford, CA, USA.
7. Purim, L., F. Kopsaftopoulos, and F.-K. Chang, 2018, “Estimating state of charge and health of lithium-ion batteries with guided waves using built in piezoelectric sensors/actuators,” *J. Power Sources*, Vol. 384, pp. 342–354.
8. Wang, Y., and F.-K. Chang, 2021, “Numerical and experimental evaluation of mechanical performance of the multifunctional energy storage composites,” *J. Compos. Mater.*, Vol. 56, No. 2, pp. 199–212.
9. Liu, P., R. Ross, and A. Newman, 2015, “Long-range, low-cost electric vehicles enabled by robust energy storage,” *MRS Energy Sustain.*, Vol. 2, Art. E12.

10. Ladpli, P., R. Nardari, F. Kopsaftopoulos, Y. Wang, and F.-K. Chang, 2016, "Design of multifunctional structural batteries with health monitoring capabilities," *8th European Workshop on Structural Health Monitoring (EWSHM)*, 5–8 July 2016, Bilbao, Spain.
11. Ladpli, P., R. Nardari, R. Rewari, H. Liu, M. Slater, K. Kepler, Y. Wang, F. Kopsaftopoulos, and F.-K. Chang, 2016, "Multifunctional energy storage composites: Design, fabrication, and experimental characterization," *ASME 2016 Energy Storage Forum*, American Society of Mechanical Engineers, 26–30 June 2016, Charlotte, NC, USA, V002T01A004.
12. Ladpli, P., R. Nardari, Y. Wang, P. A. Hernandez-Gallegos, R. Rewari, H. T. Kuo, F. Kopsaftopoulos, K. D. Kepler, H. A. Lopez, and F.-K. Chang, 2015, "Multifunctional energy storage composites for SHM distributed sensor networks," *10th International Workshop on Structural Health Monitoring*, 1–3 September 2015, Stanford, CA, USA.

Acknowledgments

Accellent Technologies would like to acknowledge the guidance of F. Wu, DOE Technology Manager during the program. This work was conducted under DOE SBIR Phase I Award #DE-SC0020714.

II.4.3 Active Monitoring of Composite Structures through Embedded Synthetic Fiber Sensor (Intellisense Systems, Inc.)

Yong Chae Lim, Co-Principal Investigator

Intellisense Systems, Inc.
21041 S. Western Ave.
Torrance, CA 90501
E-mail: htran@intellisenseinc.com

H. Felix Wu, DOE Technology Manager

U.S. Department of Energy
E-mail: felix.wu@ee.doe.gov

Start Date: June 29, 2020	End Date: March 28, 2021	
Project Funding (FY 2021): \$200,000	DOE share: \$200,000	Non-DOE share: \$0

Project Introduction

Current and future automobiles will increasingly use composite materials in their structures to reduce vehicle weight and increase fuel/energy efficiency. These structures, especially the critical parts such as battery housing, must be monitored for safety. The vehicle's outer body structure, often exposed to extreme conditions and potential mechanical impacts, should also be closely monitored for its safety and failure prevention. Innovative methods of monitoring thermomechanical changes to these composite parts will help provide early warning of any imminent failures and allow for the execution of precautionary measures to ensure safety. This project aims to address this need.

During Phase I, Intellisense Systems, Inc., demonstrated the feasibility of its Active Monitoring of Composite Structures through Embedded Synthetic Fiber Sensor (AMCOS) technology. AMCOS technology is a smart fiber sensor that can be either woven into composite materials or laid out between CF layers. The technology can sense temperature and mechanical impacts by directly monitoring changes to the filament's electrical resistive and reactive properties.

Objectives

The overall goal of this project is to develop and demonstrate, for the first time, the feasibility of AMCOS, which could then be used to address DOE's need for novel multifunctional composite materials to perform engineering functions beyond load-carrying. The following specific objectives have been established to reach this goal:

- Objective 1. Design and analyze the AMCOS smart sensor system.
- Objective 2. Characterize the embedded synthetic fiber strain sensor in composite materials.
- Objective 3. Build, test, and demonstrate an AMCOS prototype.
- Objective 4. Explore the commercialization and technology transition opportunities for AMCOS.

Approach

In Phase I, the project team developed and demonstrated the feasibility of AMCOS technology by embedding electrically conductive coaxial synthetic fiber yarn in composites to monitor structural integrity and fiber electrical resistance. The feasibility study included repeated tensile, impact, and thermal tests in a laboratory environment. An initial model was developed to distinguish between different test modalities. The test results demonstrated that AMCOS technology can detect mechanical strains, impacts, and temperature changes in the composite material. The project team also developed a technology transition and commercialization plan.

Results

In Phase I, synthetic polymer (nylon) smart fiber yarns were successfully embedded in woven composite panels, demonstrating the AMCOS technology's compatibility with the composite manufacturing process for automotive applications. Electrically conductive fiber sensor yarns were embedded in test coupons and electrically terminated for real-time continuous sensor readout. The sensors' responses to external events, such as strain, impact, and temperature changes, were experimentally measured.

Intellisense Systems, Inc., successfully met all the Phase I objectives. The following list summarizes Phase I work and major achievements in demonstrating the AMCOS technology:

- Task 1. Develop AMCOS System Architecture:
 - Analyzed DOE requirements for AMCOS and defined target applications and system properties, focusing on automotive components from composite materials.
 - Designed the AMCOS Phase I system, considering the desired specifications.
 - Performed tests to determine the need for fiber twisting, connector type, and optimal fiber length.
 - Built a heat transfer model in COMSOL Multiphysics® software to evaluate the heat transfer capabilities of fibers embedded into composite materials.
- Task 2. Investigate Fiber Response and Placement:
 - The project team performed a comparison of fiber sensor formulations for their electrical and mechanical properties and based on the findings, selected a fiber type that provided batch measurements of 241 k Ω for 10 bundles of 144 threads at a length of 1 foot.
 - Single fiber bundles of lengths of up to 30 feet were tested for noise level. To maintain a noise error of under 5%, the length of the double-twisted sensor line should be limited to approximately 12 ft., which is sufficient for automotive parts.
- Task 3. Develop Electronic Reader and Software:
 - The data acquisition speed of the electronic reader was increased from 1 kHz to 4 kHz to better capture impact events, which happen on (or close to) the millisecond timescale. This sampling frequency was sufficient to capture impact events in detail during operation in an automotive environment and generate structural failure warnings in real-time.
- Task 4. Assemble the AMCOS Benchtop Prototype and Perform Preliminary Tests:
 - The project team assembled test coupons to test the response of fibers embedded in woven carbon-fiber-reinforced plastics to tensile loading, impacts, and temperature changes.
 - The researchers improved the manufacturing method. They developed an electrical interface for the sensors through the surface, and they used an approach in which the fiber's ingress and egress points are on the side of the composite, thereby increasing the manufacturing method's reliability.
 - The team performed five tensile tests and compared the strain to the resistance readings of the fibers. The sensor fibers follow the strain readings within $\sim 0.3\%$ strain. The change in resistance depends on the baseline resistance and needs to be calibrated accordingly.
 - The team performed impact tests on three test coupons, with four sensor lines read in parallel at different distances from the impact location at increasing impact energies, which were below the damage threshold. The sensors clearly show each impact up to ~ 3 in. distant from the impact site.
 - Environmental tests were performed; test coupons were placed in an environmental chamber, and the temperature was increased and decreased stepwise, with and without humidity control. To achieve repeatable readings, the sensor fibers were temperature-cycled before testing.

- Task 5. Demonstrate Feasibility of the AMCOS System:
 - Using the temperature and tensile test results, the team established a calibration curve based on the baseline resistance (before the resistance test) that allows the correlation of strain and temperature to resistance measurements.
- Task 6. Explore the Commercial Potential and Product Viability:
 - The team conducted market research and held active dialogues with composite and fiber-drawing experts Dr. S. Nutt (University of Southern California) and Dr. C. Bowland (ORNL) to identify the most promising applications of the AMCOS technology. The University of Southern California and ORNL provided letters of support for Phase II AMCOS development collaboration.

Figure II.4.3.1, Figure II.4.3.2, Figure II.4.3.3, Figure II.4.3.4, and Figure II.4.3.5 illustrate highlights of the Phase I results summarized above. A full description of the technical results and methods applied to obtain these results can be found in the Phase I Final Technical Report.

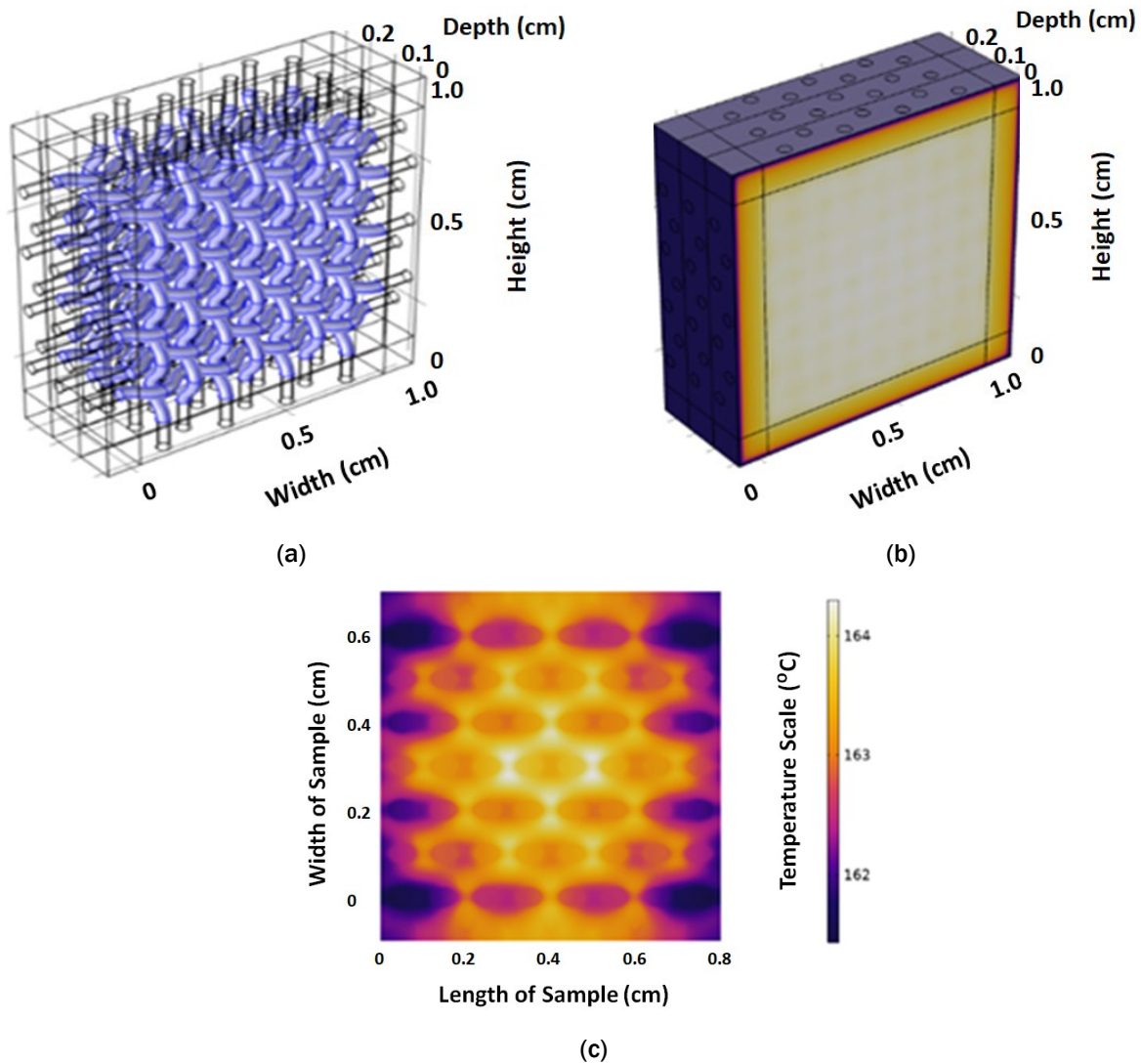


Figure II.4.3.1. (a) Heat transfer model for the oven composite structure. (b) Heat source (100 W/cm^2) on one face of the material block. (c) Thermal heatmap of the improved nylon sample showing a temperature of approximately 163°C around the center of the panel. Source: Intellisense Systems, Inc.

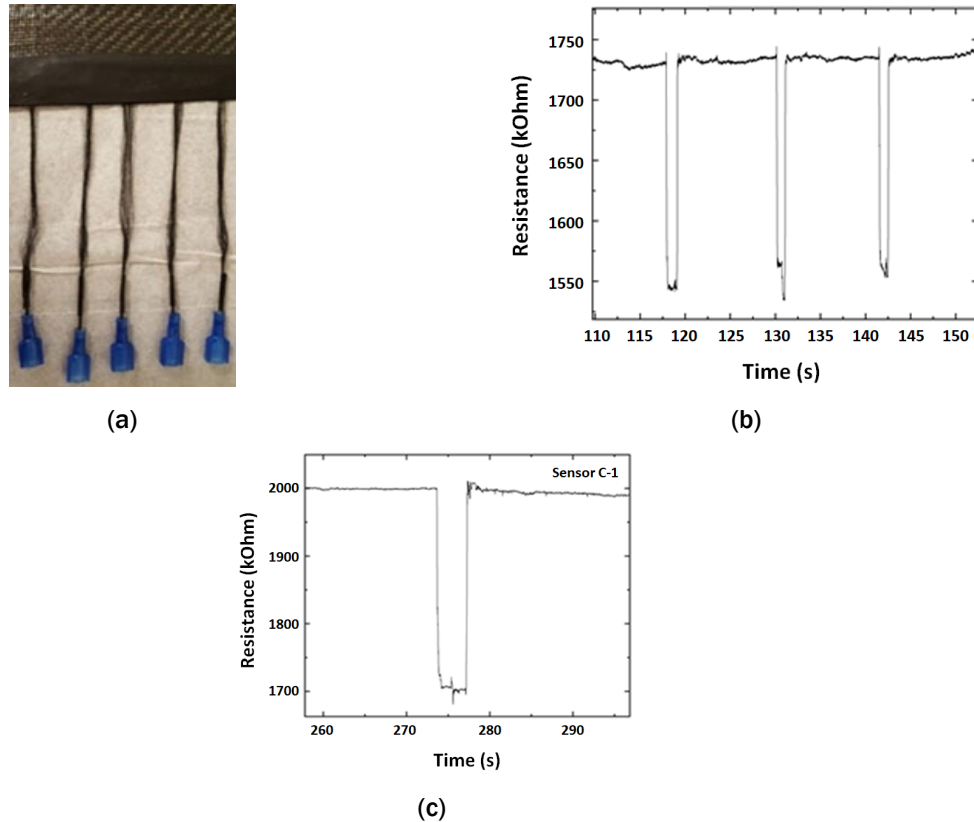


Figure II.4.3.2. (a) Connectorized fibers of the composite test panel. A comparison of impact points from two tests using (b) 500 Hz and (c) 4,000 Hz sampling rates on the DAQ board. Both were impact tests in an Instron Dynatup machine with an impact energy of <10 joules. The impact caused the resistance to spike downward, and after a delay of several seconds, the resistance returned to its initial position.

Source: Intellisense Systems, Inc.

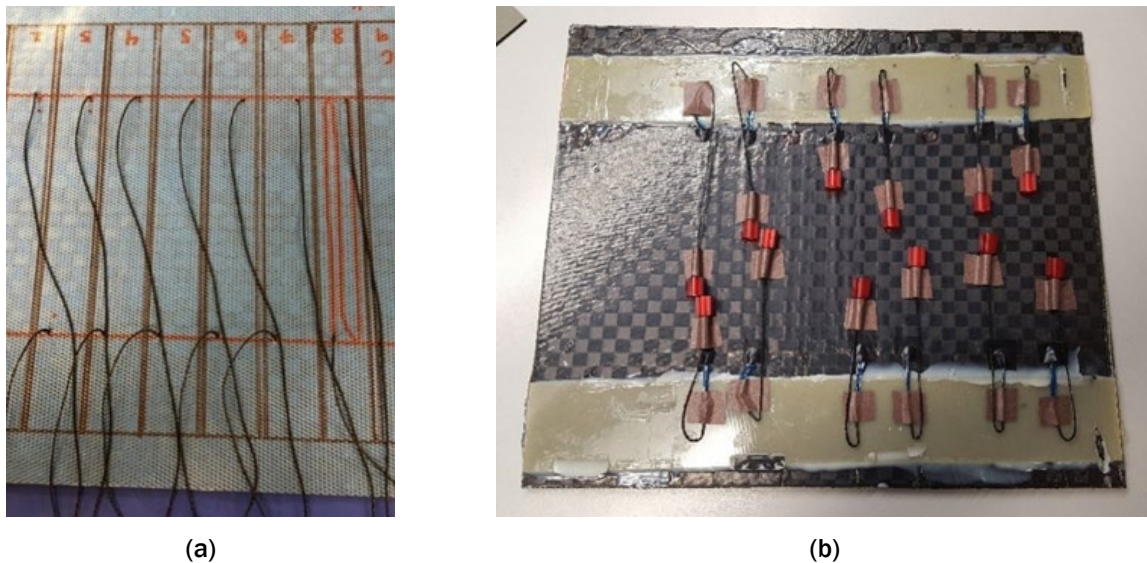


Figure II.4.3.3. (a) Layup of the tensile panel with sensor lines exiting through the blue backing paper. (b) The composite panel containing six tensile coupons, three thermal coupons, and two reference coupons in which the sensor ends have been cleaned and connectorized. Source: Intellisense Systems, Inc.

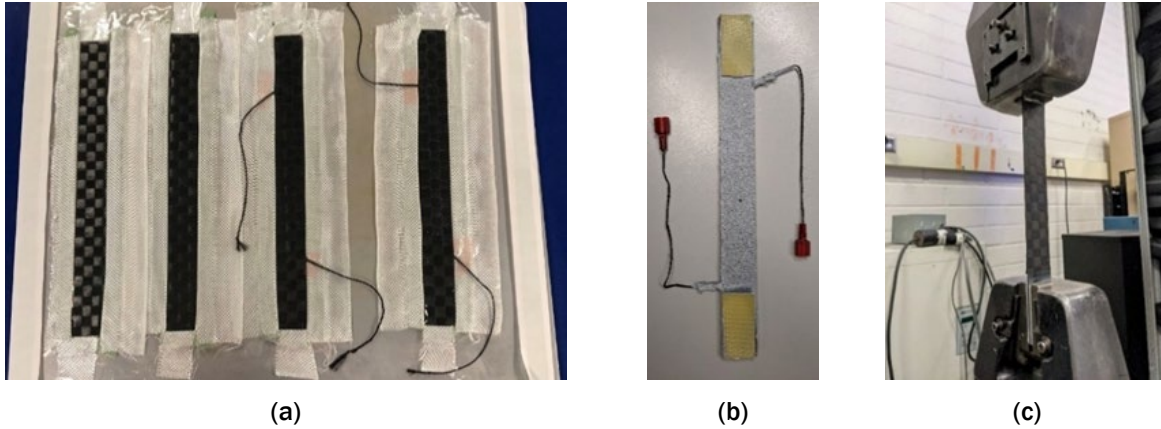


Figure II.4.3.4. (a) Tensile coupon made by leading the sensor out the sides rather than threading through the top, eliminating the need for cutting. (b) One of the three new sensor coupons in which the end tabs were adhered to the coupon after fabrication. This may have reduced the gripping strength of the end tabs and adhesive. The sensor lines and end tabs were covered in tape, and a spackle dot pattern was sprayed along the front of the coupon. (c) A control coupon mounted in the Instron tensile clamps.

Source: Intellisense Systems, Inc.

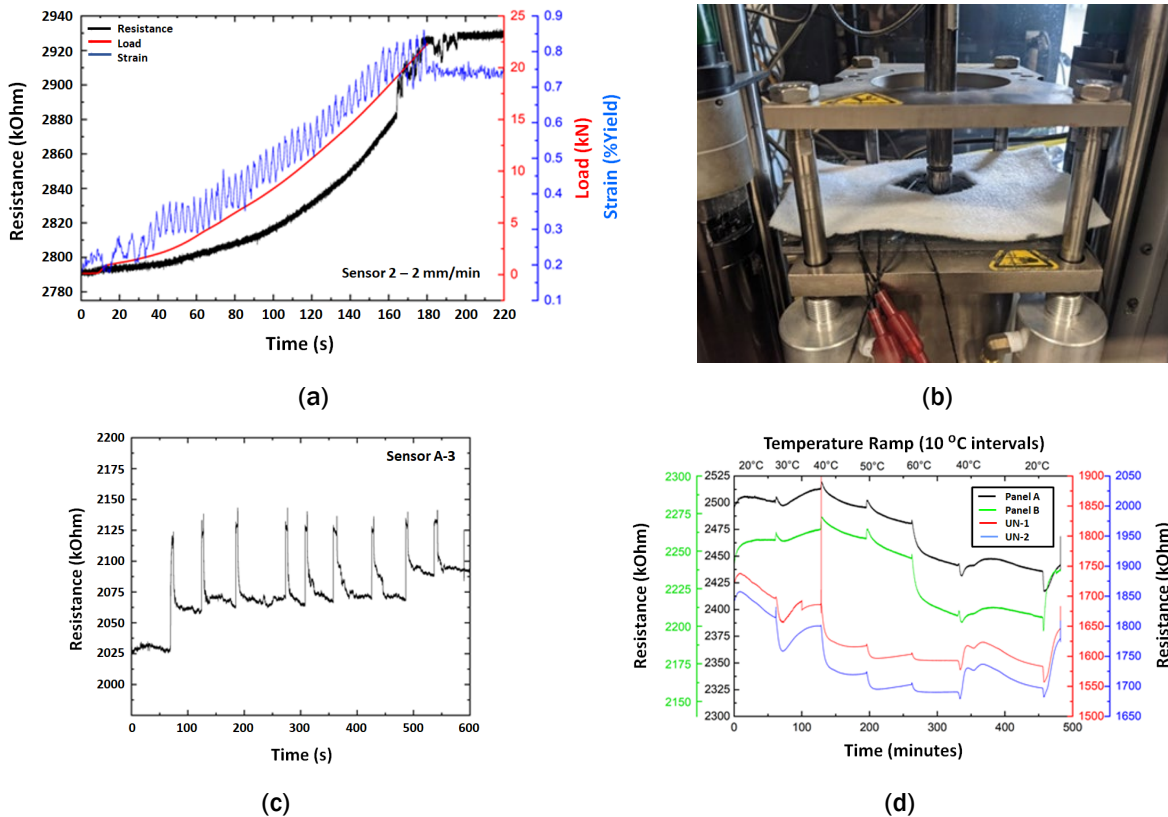


Figure II.4.3.5. (a) A graphical representation of the resistance, load, and strain data versus time. (b) Impact coupon loaded into the uncompressed test frame, with a breather cloth to protect the sensors. A hole was cut in the center where the tip impacts the coupon. (c) Impact test results. (d) Thermal ramp-step test, repeated. The chamber was heated from 20 °C to 60 °C at 10 °C intervals, and back down to 40 °C and 20 °C. Each step involved a brief heating or cooling period, followed by a 60-min. waiting period.

Source: Intellisense Systems, Inc.

Conclusions

Intellisense successfully met all the SBIR Phase I project objectives. Synthetic polymer (nylon) smart fiber yarns were successfully embedded in woven composite panels, demonstrating the AMCOS technology's compatibility with composite manufacturing process for automotive applications. Electrically conductive fiber sensor yarns were embedded in test coupons and electrically terminated for real-time continuous sensor readout. Their response to external events, such as strain, impact, and temperature changes, were experimentally measured.

The testing results show that the sensing fibers repeatably detect strain, impacts and temperature and that calibration procedures can be used to establish a quantitative relationship between resistance and strain as well as resistance and temperature. An algorithm was developed to automatically identify impacts and distinguish them from other events.

The SBIR Phase I development have laid a solid foundation for further development and improvements to be realized in the future.

II.4.4 Short-Fiber Preform Technology for Automotive Part Production – Phase II (Composites Automation, LLC)

Roger Crane, Co-Principal Investigator

Composites Automation, LLC
7 McMillan Way, Ste. 1
Newark, DE 19713
E-mail: roger.crane@compositesautomationllc.com

Dirk Heider, Co-Principal Investigator

Composites Automation, LLC
7 McMillan Way, Ste. 1
Newark, DE 19713
E-mail: dirk.heider@compositesautomationllc.com

H. Felix Wu, DOE Technology Manager

U.S. Department of Energy
E-mail: felix.wu@ee.doe.gov

Start Date: July 1, 2019 End Date: August 23, 2022
Project Funding (FY 2021): \$1,299,489 DOE share: \$1,299,489 Non-DOE share: \$0

Project Introduction

CFCs exhibit superior properties and enable part consolidation, reduced system weight, and reduced emission benefits for automotive applications. Lack of affordable and high-rate-capable CFC materials and processes limit the materials' widespread implementation. Studies during a Composites Automation (CA) project sponsored by DOE-EERE—Ultra-Light Composite Door, with participation of our academic partner, the University of Delaware Center for Composite Materials (UD-CCM), and vehicle OEM, GM—have shown that a key obstacle to widespread CFC adoption is the ability to manufacture complex-geometry CF preforms that meet performance, cost, and rate targets in infusion processes while minimizing scrap. Single-piece, continuous CF preforms are restricted to simple geometries, as the continuous CF layup cannot be easily and cost-effectively formed into doubly curved or complex-geometry parts, limiting the application of CF preforms to a few components. Multipiece preforms are complex to manufacture, require joining, are difficult to handle prior to molding, have inconsistencies in mold filling, and have limited rate production, all of which increase part cost. Another challenge is the high cost and embodied energy of the CF material itself. With current composite processing approaches, lower-cost recycled or waste stream short CFs, currently available only in discontinuous form, cannot be converted into high-fiber-volume and high-performance CFCs.

Our team (CA, UD-CCM, and Vartega, Inc. [Vartega]), with the support of GM and the U.S. Automotive Materials Partnership (USAMP), is addressing these shortcomings through a novel aligned, short-fiber material called Tailorable universal Feedstock for Forming (TuFF). TuFF was developed in a four-year UD-CCM program, sponsored by the Defense Advanced Research Projects Agency (DARPA). TuFF production uses low-cost short virgin, waste stream, or recycled fibers. (The recycled CF is optimized and provided by Vartega). The material has significant in-plane extensibility and exhibits metal-like formability with full property translation, compared to continuous fiber composites. CA has produced composite panels with 46% fiber volume fraction using \$11/kg (\$5/lb) CF from waste stream sources and wet compression processing that exhibited tensile properties sufficient for primary structural automotive applications.

The CF TuFF material has unique properties that make it amenable to the automotive stamp-forming typically used for metals. These properties include 1) the ability to stretch up to 50% without losing material integrity, allowing net-shape preforming, 2) enabling a near-zero waste process with full recovery and reuse of CFs, as is possible with metals, and 3) potential to use recycled/waste stream CFs to produce structural parts with reduced cost and embodied energy efficiency. One issue being addressed in this project is the ability to handle TuFF preforms in the mechanized material handling typically used in automotive part production. To address this challenge, CA is developing methods to automate the stabilization of the TuFF preforms. CA is also evaluating the use of recycled fibers to further improve cost and embodied energy and will be scaling the process to demonstrate automotive part production at rate and with lower-cost. The ability to process short-fiber into stretchable preforms with rapid conversion to high-performance, complex-geometry, and low-cost CFC structures creates opportunities to replace automotive metal structures.

Objectives

- The objective of this SBIR Phase II effort is to evaluate the use of low-cost, discontinuous CFs from a variety of sources to produce TuFF preforms that can be used in high-rate formation of the TuFF material into composite automotive parts. The CF sources include virgin material from commercial and government sources (low-cost CFs from ORNL will be considered), waste stream fibers, and recycled fibers from Vartega. The specific technical objectives of Phase II SBIR are as follows:
 - Identify low-cost short-fiber and resin systems that can be used to produce TuFF prepreg material that can be fabricated into components at production rates approaching those of metal stamping.
 - Evaluate and address challenges with recycled CF materials, such as entanglement, adhesion, and fiber length distribution.
 - Develop and scale stabilization methods, such as electrospinning veil surfaces, onto the TuFF preforms; methods must be compatible with resin systems, such as snap cure resin systems, that have minimal or no effect on TuFF composite fiber volume fraction.
 - Demonstrate that the veil materials enable handling of blanks in automated processes (transfer to infusion line, placement in tooling etc.).
 - Fabricate TuFF preforms using low-cost (waste/recycled) fibers and stabilize the preforms using the electrospinning process for infusion processing.
 - Demonstrate formability of dry TuFF preforms for complex part production.
 - Demonstrate performance.
 - Meet automotive microstructure requirements such as fiber volume fraction (>50%).
 - Measure mechanical properties for a property database.
 - Demonstrate at rate fabrication, performance, and cost for an automotive component (intent is to leverage EERE door tooling and data).
 - Evaluate insertion opportunities with GM and USAMP.

Approach

This effort is developing the requirements for fiber geometry (fiber length and distribution), demonstrating the ability to disperse the various fiber systems in water to produce TuFF preforms, developing an environmentally friendly electrospinning material and process that will allow for the TuFF preform to be handled without disrupting the fiber orientations, and developing resin process conditions that will allow for high-rate or snap curing of the TuFF composite material. To provide handleability, the project team is developing a method for using an electrospun veil on the TuFF preform. The system is scalable and potentially can be integrated into the TuFF pilot-scale facility. Commercial veils are being evaluated but lack the customization afforded by veils produced from electrospun equipment. This customization will ensure compatibility with snap cure resin chemistry that is envisioned for use with the TuFF preforms. In addition,

with the electrospun materials, mechanical properties can be maintained by minimizing the areal weight and tailoring the equipment to match the TuFF sheet width. Once the electrospun material is selected, the project team will determine the minimum areal weight required to make the material handleable.

This veil solution will be used to fabricate material for compaction studies to verify 50% fiber volume fraction is maintained. TuFF composite panels will be produced for mechanical testing, and an extensive mechanical property test plan similar to a recent EERE door program will be executed. These TuFF composite panels will initially be fabricated from TuFF prepreg material produced using a film infusion process.

In addition, CA will investigate the use of high-pressure RTM for impregnation for the TuFF preform. To demonstrate the potential for high-rate production, the use of snap cure epoxy resin will be investigated as the resin for the prepregging process, as well as with a wet compression process. The project team will establish the process conditions that enable infusion of the resin into the TuFF material without advancing the cure.

Once the team validated that the TuFF prepreg with the snap cure resin has the demonstrated mechanical properties, feature-based parts (such as sections of the door impact beam or inner/outer door panel) will be investigated for fabrication demonstration. The intent is to use the mechanical property database and apply it to the EERE door design to provide a TuFF solution that demonstrates weight, cost, and performance metrics comparable or superior to the continuous CFC. The designs for tooling to produce a component will be developed and fabricated. Door components will then be manufactured and tested (based on availability of existing EERE tooling). The team will conduct a trade study to assess the material and final part cost and compare the results to the EERE findings, as well as the current steel baseline.

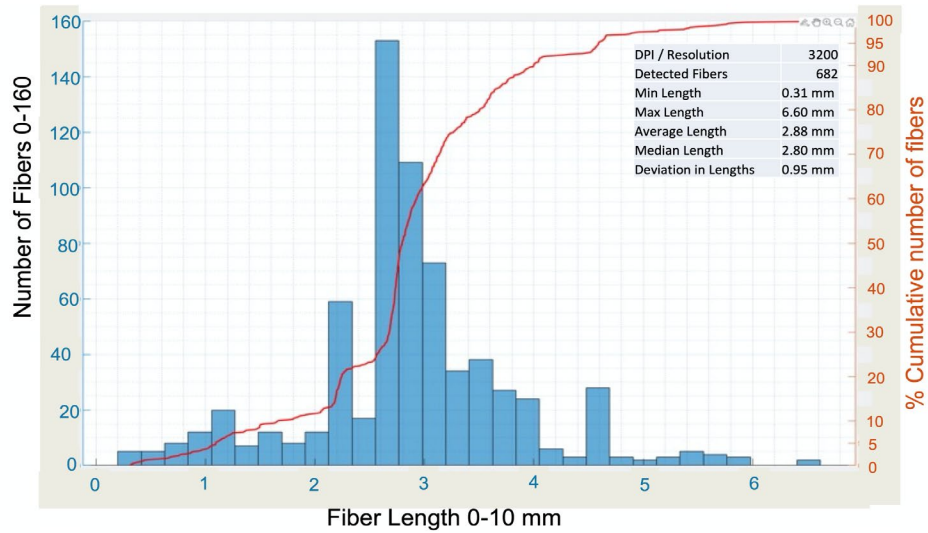
During this process, we will continue to brief our OEM partners GM and USAMP and expect to engage their supply chains throughout the effort to evaluate potential technology insertion opportunities.

Results

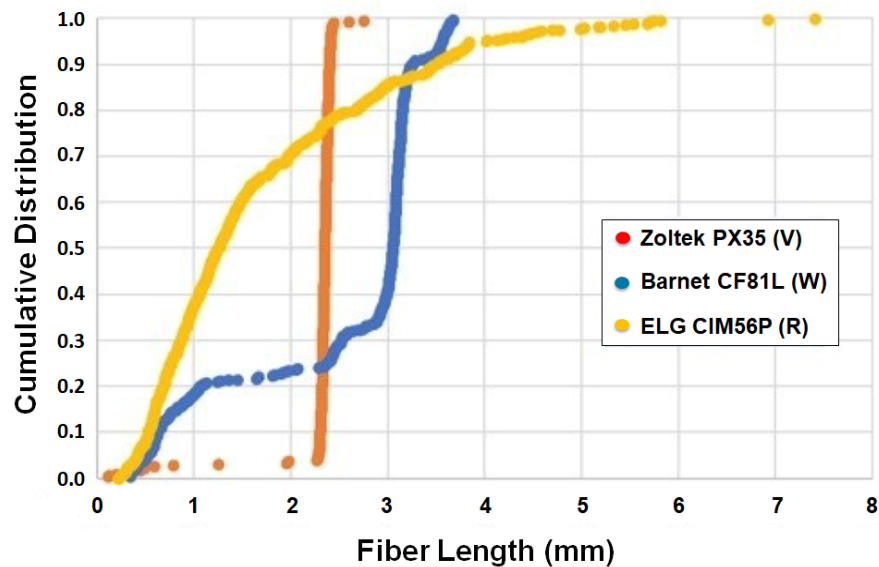
This SBIR project is working toward three advances to enable more general use of composite materials for general automotive structural applications: (1) low material costs; (2) material that can be compression- or stamp-formed, as metals are; and (3) high-rate fabrication similar to metals. From the survey of sources of low-cost short fibers, CA has selected T-800 waste stream fibers from Barnett, T-800 recycled fibers from Vartega, and P35 low-cost commercial CFs from ZOLTEK. The cost of these fiber systems currently ranges from \$5/lb. to \$10/lb., but for large quantities, the cost has been projected to be as low as \$3/lb.

To produce the highly aligned TuFF fiber preforms using the above-mentioned fibers, several attributes must be met. The fibers must: (1) be a specific length with a narrow distribution; (2) have an aspect ratio between 600 and 1,000; and (3) be able to be well-dispersed in water. This project selected a fiber length of 3 mm. T-800 virgin fibers were cut to length by Engineered Fibers Technology. ZOLTEK was able to provide fibers of this length. The recycled and waste stream fibers were provided by our industry partner, Vartega.

The project team conducted fiber length studies on all these fibers. The fiber lengths were determined by first dispersing the specific fibers in water using a laboratory mixing tank, which has been designed to replicate the mixing that is used in the TuFF material fabrication process. ImageJ analysis is then used to mark the ends of a sampling of fibers that have been dispersed and deposited on a high-resolution scanner. Figure II.4.4.1(a) shows the results of the fiber length study on the T-800 fibers. This analysis has also been performed with the ZOLTEK P35 fiber, which ZOLTEK provided already cut to the 3 mm length. Figure II.4.4.1(b) shows the results of the fiber length study for the ZOLTEK fibers. The laboratory-scale dispersion setup is also used to assess the dispersion of the fibers of interest at the water-to-fiber dilution ratio of 37.5k:1, typically used in the TuFF manufacturing process. The T-800 waste fiber and ZOLTEK fiber disperse well at the 37.5k:1 dilution ratio. The Vartega recycled fiber did not disperse well in the laboratory-scale dispersion testing, showing noticeable fiber clumps. Examination of these clumped fibers revealed residue remained on the fibers after the resin removal processing that Vartega typically conducts for recycled prepreg material.



(a)



(b)

Figure II.4.4.1. Fiber length investigation for: (a) the Vartega T-800 waste fiber; and (b) the ZOLTEK P35 fiber. Source: Composites Automation, LLC.

After verifying that the fibers can be well-dispersed in the laboratory setup, the project team produced TuFF material using the processing line set up at CA. The TuFF material produced using the T-800 waste fiber and the ZOLTEK fiber showed good quality with no defects, while the TuFF material produced using the Vartega recycled fiber had visible defects or flocks, as can be seen in Figure II.4.4.2. The defects resulted from the residual resin on the fibers. Vartega and CA are investigating methods to remove the residue, as well as the potential use of two dispersants, Blusil and Silcolapse, that have previously been shown to aid in the dispersion of the 3 mm CFs.

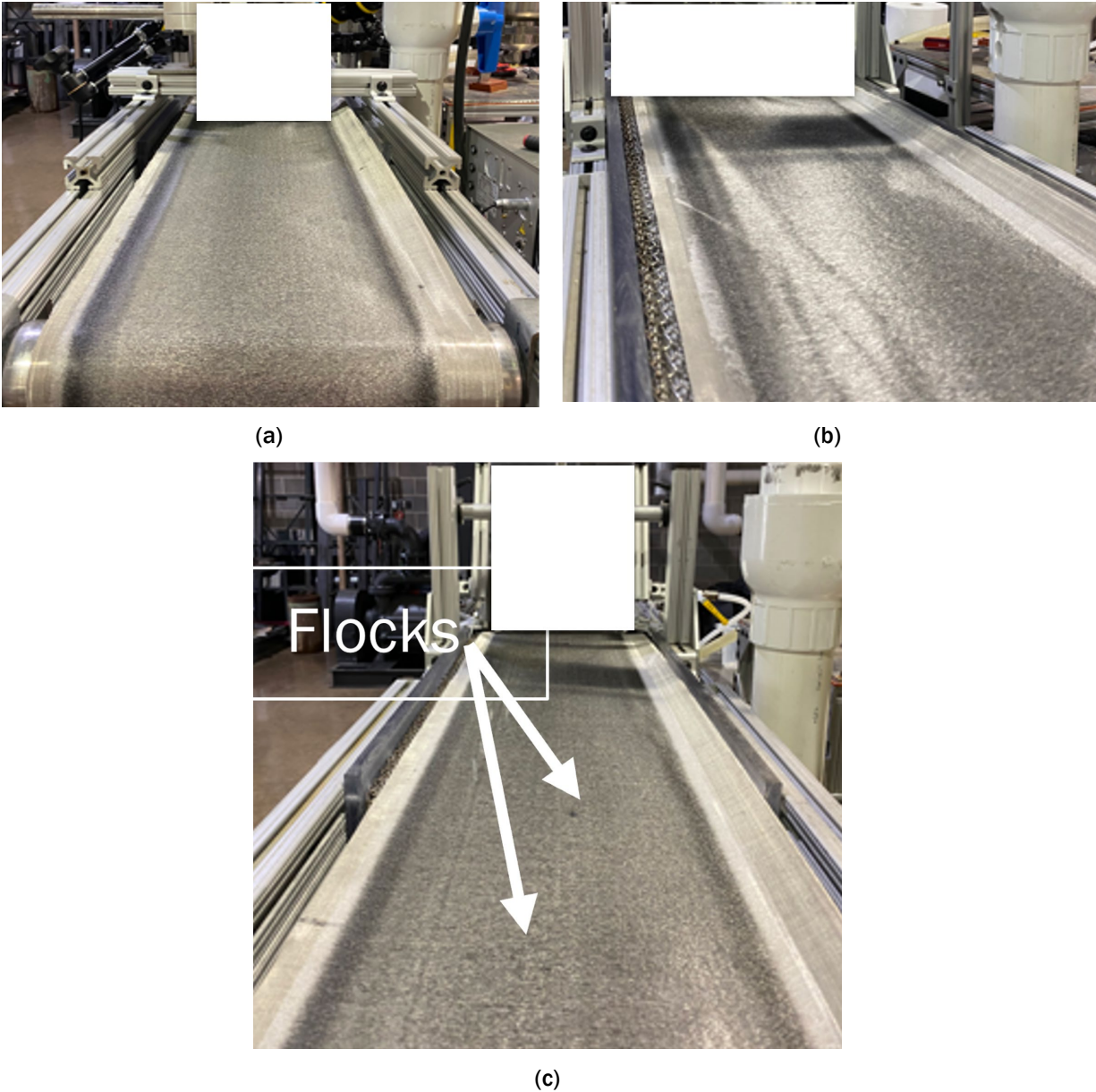


Figure II.4.4.2. TuFF processing using the (a) T-800 waste fiber, (b) ZOLTEK P35, and (c) Vartega recycled fiber. (NOTE: Proprietary information is covered by the white squares). Source: Composites Automation, LLC.

The stabilization of the TuFF material is key for handling the material for subsequent processing steps. Both commercial and electrospun veil material were investigated as methods for stabilizing the TuFF material. The use of an electrospinning process has been selected as the best solution for stabilizing the TuFF material since: (1) it can potentially be placed in-line with the TuFF fabrication assembly, creating a way to seamlessly produce a material that is easy to handle, (2) the areal weight can be tailored to minimize detrimental effects on compaction and therefore fiber volume fraction of the TuFF composite, and (3) the electrospun veil can potentially provide improved toughness as a interlaminar toughening material.

Of the materials investigated to date, polyvinyl alcohol (PVA) was selected as the best solution. The electrospun solution of the PVA is water-based and therefore is environmentally friendly. In addition, the PVA can be obtained in various molecular weights, thereby enabling electrospun areal weights as low as 0.1 grams per square meter (gsm). Figure II.4.4.3(a) shows the laboratory-scale electrospinning apparatus, and Figure II.4.4.3(b) shows a SEM image of the PVA electrospun material at a deposition of 0.1 gsm PVA on the T-800 TuFF ply. In addition to providing stability and handleability to the TuFF preforms, the electrospun veil material needs to allow for the TuFF material to deform while keeping the preform fibers intact. Preliminary testing showed that the TuFF material stabilized with the 0.1 gsm PVA held the fibers in place while being stretched 50% transverse to the fibers, as shown in Figure II.4.4.3(c).

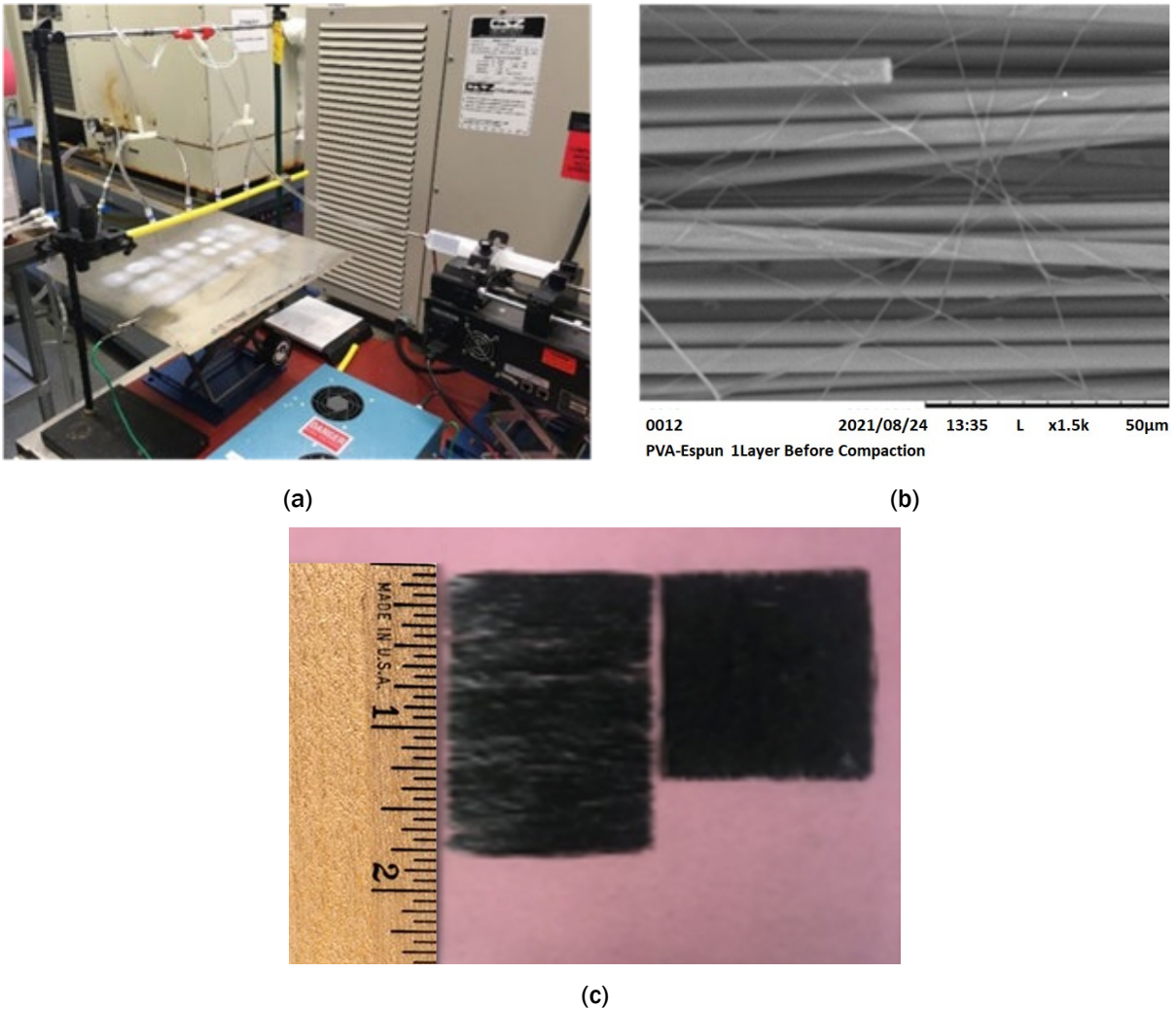


Figure II.4.4.3. Electrospinning of PVA with (a) a laboratory-scale four-needle electrospinning apparatus, (b) the SEM image of a 0.1 gsm electrospun PVA on TuFF preform, and (c) the TuFF material with 0.1 gsm PVA showing 50% stretching. Source: Composites Automation, LLC.

Compaction studies were carried out to verify that the PVA electrospun material does not affect the fiber volume fraction of the TuFF material. Figure II.4.4.4 shows these results, comparing the compaction of 8- and 16-layer TuFF material with and without the electrospun PVA. This shows that the use of the electrospun material will not adversely affect fiber volume fraction and will therefore not affect mechanical properties of the TuFF composite.

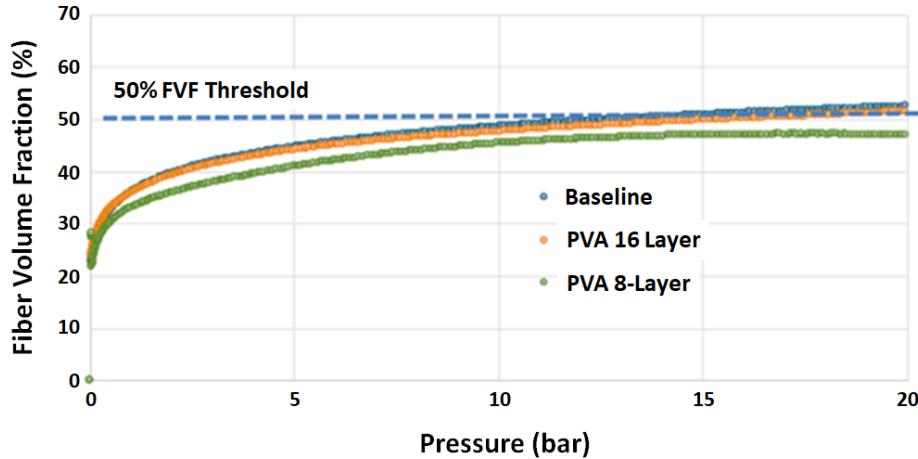


Figure II.4.4.4. Results of the compaction studies of the TuFF material that has been stabilized with PVA electrospun material (1% by weight). Source: Composites Automation, LLC.

Thermoset resin systems that can be used to infuse the TuFF material and enable high-rate curing of the composite are being investigated. For the initial infusion and processing of the TuFF material, the project team used Axiom Materials, Inc. (Axiom) epoxy resin in film form. Rheology studies were conducted using non-isothermal DSC heating ramps to develop the process conditions to prepreg the multilayer TuFF preforms with the Axiom resin. In addition, the team experimentally determined temperature conditions to minimize processing time of the prepreg while ensuring 95% conversion.

From prior work, the research team knew that it is possible to achieve complete infiltration of a dry TuFF preform with resin viscosities <1,000 Pa-S. When considered together, the DSC and rheology data, as shown in Figure II.4.4.5(a), proved that using a temperature range of 35°C to 50°C for impregnation of the dry TuFF preform will ensure no change in the state of resin cure. Once the TuFF material is prepregged, it can be stored in a freezer for later use. The project team produced the material under these conditions and cured it using the predictions for the percentage conversion as a function of time for isothermal cure temperatures ranging from 100°C to 150°C, as shown in Figure II.4.4.5(b). Under such conditions, the TuFF/Axiom prepreg should be curable in 15 min. to 70 min. when heated to a temperature of 150°C.

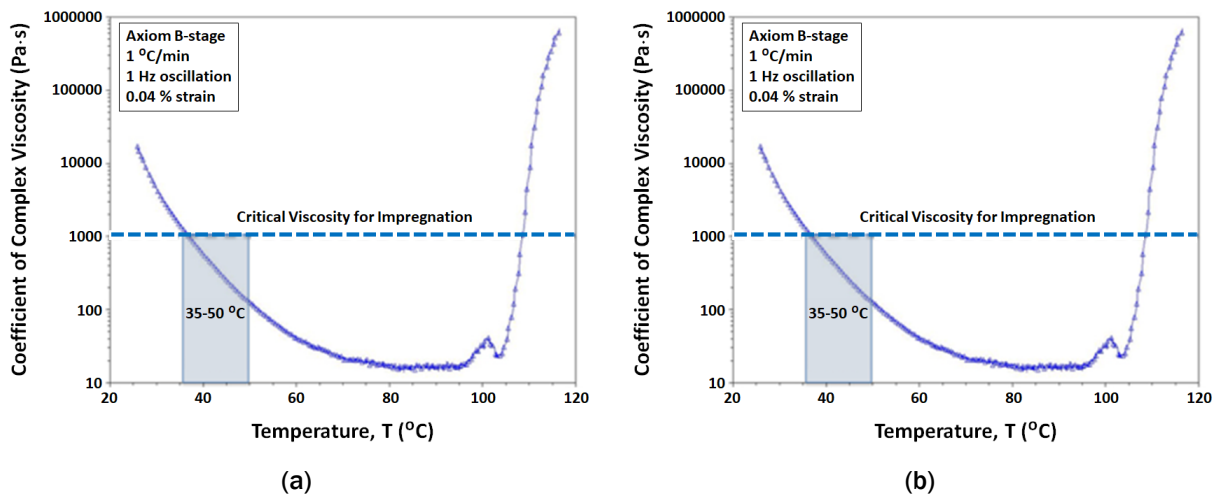


Figure II.4.4.5. Results of the rheology study of Axiom resin. (a) Viscosity as a function of temperature for a heating ramp of 1°C/minute and (b) percentage conversion versus time predictions for isothermal cure temperatures ranging from 100 °C to 150 °C. Source: Composites Automation, LLC.

To produce a TuFF composite with reduced required processing time, the project team procured Hexion EPIKOTE™ snap cure resin for impregnation and curing trials. With this resin, the project team considered two processes: (1) performing wet compression with resin dispensing and immediate forming; and (2) making blanks in a press with controlled resin dispensing where process conditions are controlled to produce B-staged blanks that can be processed later in a press.

The team has procured the equipment required to perform the wet compression method: the TuFF material is placed on an automated indexing table that moves the material through the various processing stations; a high-pressure RTM machine is used for calibrated mixing, dispensing, and distributing the epoxy resin onto the TuFF material; and a twin press is used either to create prepreg blanks or to cure the TuFF composite material. Both the snap cure Hexion Epikote™ and the Axiom epoxy resin system can be used in this system.

Figure II.4.4.6 shows the manually operated equipment that was used to process a TuFF panel. The automation of the equipment/process will be done in the next phase of the project. Trial runs have been done by manually moving the material on the table, manually indexing the resin dispensing on the preform, and manually moving the impregnated TuFF material into the twin press, where it was cured.

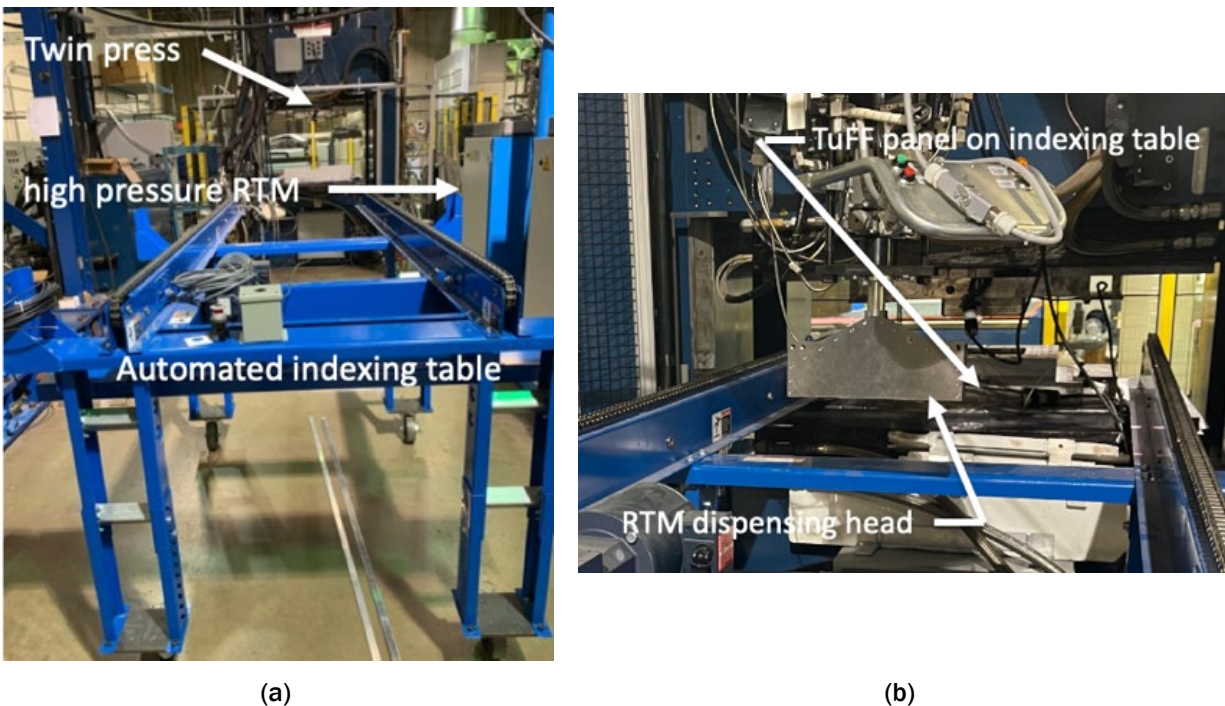


Figure II.4.4.6. Wet compression equipment: (a) Indexing table, high-pressure RTM, and twin press; and (b) the high-pressure RTM head, ready for dispensing epoxy on TuFF preform.

Source: Composites Automation, LLC.

In addition, TuFF composite material has been processed using a heated press using the Axiom film infusion. The tooling for processing TuFF using the T-800 and P35 CFs is shown in Figure II.4.4.7. After fabrication, tensile test specimens and specimens for micrographic inspection were cut from the processed panels. The microscopy specimens were used to examine microstructure and determine the fiber aligned properties. Table II.4.4.1 shows the tensile properties achieved using the T-800 and ZOLTEK fibers impregnated with the Axiom resin. The project team compared the resultant properties to the anticipated properties based on the fiber volume. The team determined that the tensile properties of the T-800 TuFF material had 100% strength translation compared to the continuous fiber composite and the ZOLTEK TuFF material had 99% strength translation compared to the continuous fiber composite. This shows that handling and recycling the fibers did not result in fiber property degradation. This excellent property translation is also the result of the alignment

achieved, shown in Figure II.4.4.8 for the T-800 waste fiber and ZOLTEK P35 fibers. The tensile properties achieved with both these fiber systems are appropriate for automotive applications.

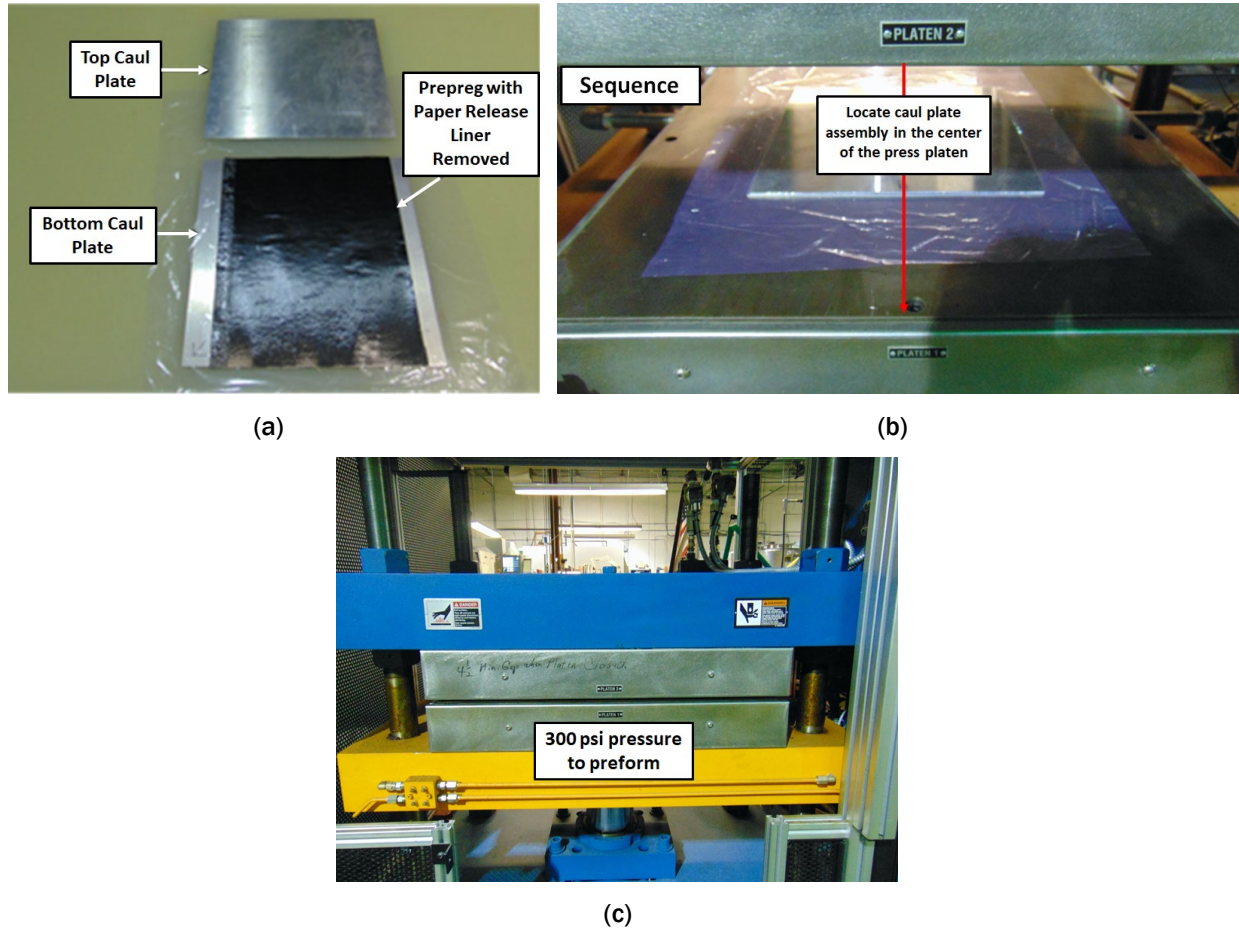


Figure II.4.4.7. TuFF processing with Axiom film: (a) prepregging TuFF with film; (b) locating the prepreg in a heated press with caul plates; and (c) application of heat and pressure to cure the panel. Source: Composites Automation, LLC.

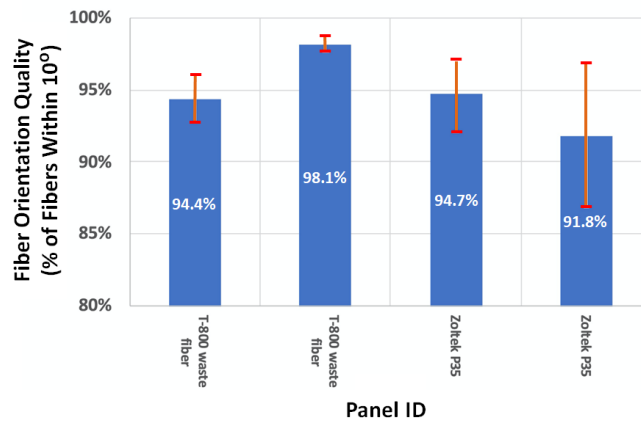


Figure II.4.4.8. Fiber alignment properties of TuFF panels produced using T-800 waste fiber and ZOLTEK P35. Source: Composites Automation, LLC.

Table II.4.4.1. Tensile Properties of TuFF Panels Produced Using T-800 Waste Fiber and ZOLTEK P35

	T-800 Waste Fiber		ZOLTEK P35	
	Tensile strength (psi)	Tensile Modulus (Msi)	Tensile strength (psi)	Tensile Modulus (Msi)
Average	310	18.5	175.03	15.03
Std Dev	9.40	0.292	9.79	0.28
COV (%)	3.03	1.57	5.6	1.9

Conclusions

Composite solutions for structural automotive applications require that the material be cost-competitive with metal, have mechanical properties similar to metals, be handleable using automated equipment and be processable using stamp-forming type processes at similarly high rates. All of these attributes are required to transition the TuFF material technology to the automotive production environment, and all have been addressed in this effort. The further scale-up and demonstration of the material performance and processes and verification of the high-rate manufacturing will require additional work.

Acknowledgements

The authors would like to acknowledge the support of A. Maxey and K. Van Aken from Vartega for their support in providing recycle and waste fiber for this project, and J. Dietzel from the University of Delaware for his support in developing the electrospinning of veil material for TuFF preform stabilization.

II.4.5 Multifunctional Composites for Vehicles (Trimer Technologies, LLC)

Evan Schaefer, Co-Principal Investigator

Trimer Technologies, LLC
45800 Mast St.
Plymouth, MI 48170
E-mail: eschaefer@trimerllc.com

Henry A Sodano, Co-Principal Investigator

Trimer Technologies, LLC
45800 Mast St.
Plymouth, MI 48170
E-mail: hsodano@trimerllc.com

H. Felix Wu, DOE Technology Manager

U.S. Department of Energy
E-mail: felix.wu@ee.doe.gov

Start Date: June 29, 2020 End Date: June 28, 2021
Project Funding (FY 2021): \$200,000 DOE share: \$200,000 Non-DOE share: \$0

Project Introduction

Multifunctional materials are integrated material systems that serve multiple roles, such as structural load bearing, energy absorption, thermal management, sensing, power generation, vibration control, etc. The advancement of this field has been rapid because of the significant safety and performance benefits that can be achieved when using this class of materials. While many multifunctional materials have been developed, carbon nanotubes (CNTs) have received tremendous interest because of their high-strength and conductivity, which can be used to endow a composite with a range of functionalities. However, after three decades of research, CNTs are still costly and difficult to disperse into a polymer composite, which has led to limited commercial applications of the material. Graphene has emerged as a promising alternative to CNTs, and significant progress has been made in its production and use as a reinforcement in polymer matrix composites. More recently, the manufacture of graphene has been made compatible with prepregs and continuous films through the LIG process. This method uses pulsed laser irradiation from a low-cost carbon dioxide (CO₂) infrared laser to photothermally convert the surface of polyimide or other thermoplastic to a three-dimensional network of graphene. Trimer Technologies, LLC (Trimer) has shown the graphene network can be repeatable, grown through photothermal carbonization of polyimide and transferred to a tacky prepreg, as shown in Figure II.4.5.1(a). Laser irradiation can also be applied directly to thermoplastics, resulting in the formation of graphene on the surface, as shown in Figure II.4.5.1(b) for polyether ether ketone (PEEK). Unlike vertically aligned CNTs, LIG can be grown at atmospheric conditions using a low-cost CO₂ laser and can provide significantly improved fracture toughness, as well as being compatible with automated tow placement and filament winding manufacturing procedures.

As graphene is highly conductive, it provides an ideal mechanism to integrate electrical conductivity into a composite material such that multifunctional behavior can be obtained. This Phase I SBIR project has demonstrated low-cost automotive composites that use LIG coatings to produce embedded sensors, electrical interconnects, and EMI shielding. The project has also shown that improved thermal conductivity will provide a step change in vehicle energy efficiency, particularly for electric drive and autonomous vehicles. The compatibility of the process with existing thermoplastics and prepreg materials allows Trimer to effectively market the multifunctional composites without the requirement for costly capital equipment and will furthermore allow automotive manufacturers to maintain their existing supply chains.

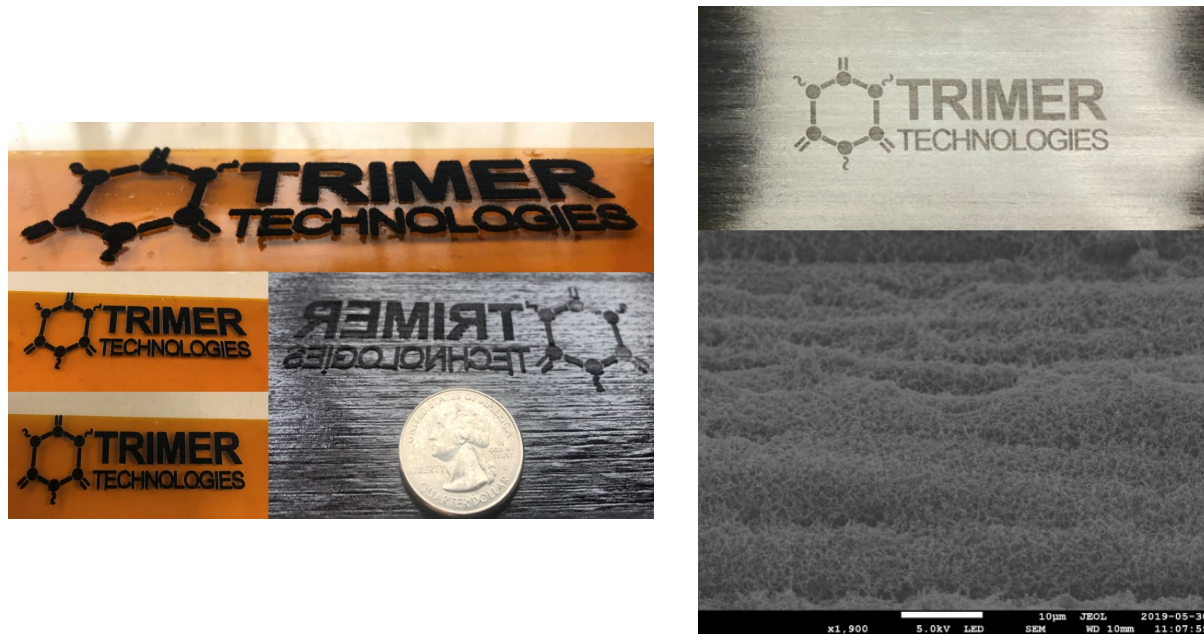


Figure II.4.5.1. (a) Laser-induced graphene on a Kapton polyimide film and IM7/8552 prepreg with the transferred graphene (note the transfer process yields the mirror of the graphene) and PEEK/IM7 prepreg coated with an LIG array. (b) SEM image of the graphene structure form on the PEEK matrix.

Source: Trimer LLC.

Objectives

The objective of the proposed SBIR project is to demonstrate the manufacture of multifunctional composites using LIG and its application for embedded sensing and EMI shielding. Trimer's work has shown that functional LIG deposited on the surface of a prepreg or sheet molding compound (SMC) yields composites with improved toughness due to interlaminar reinforcement while maintaining the in-plane properties of the composite. The interlaminar region of a composite is critical since it controls delamination, which is one of the primary failure modes in laminated composites. However, no current technology adequately addresses its weaknesses, therefore creating a critical need and excellent commercial opportunity. The current technology gap in interlaminar reinforcement and the high demand for improved composites provides numerous opportunities to insert the technology into a wide range of applications. As the proposed reinforcement simultaneously adds functional properties to the composite, it offers a unique solution to improve automotive composites; provide methods for *in-situ* nondestructive evaluation (NDE) sensors to track loading, allowing lifetime predictions; and provide EMI shielding for the sensitive electronics used in current electric vehicles and future autonomous vehicles.

Approach

Phase I research focused on demonstrating the manufacturing processes required to produce large-scale graphene coatings and the functional properties that are enabled by the highly conductive interlaminar treatment. Trimer worked with both thermoset SMCs and thermoplastic prepreps to produce functional composites to validate the mechanical and functional properties. While CNTs have received significant attention for high-strength polymers, they are costly and difficult to apply to existing materials. Therefore, we propose an alternative approach that forms graphene arrays directly on the surfaces of thermoplastics, such as polyimide Kapton, or PEEK, using a low-cost CO₂ laser. The graphene array can be used directly on the thermoplastic materials or transferred to the surface of a thermoset prepreg or SMC, pressing the two surfaces together such that the prepreg, which is tacky, sticks to the graphene and transfers it when peeled away.

The LIG treatment improves interlaminar strength while simultaneously providing functional properties to the material. Phase I has demonstrated embedded strain sensing and EMI shielding through the high conductivity of graphene. Strain sensing was accomplished through piezo resistivity, which defines a material's change in resistance under strain, and was shown to enable the tracking of loading cycles and amplitudes such that material lifetimes can be predicted based on fatigue data. A critical technology for future vehicles, embedded sensing will require increased state awareness and the ability to monitor structural performance. Strain sensing can also be used for crash detection and in applications for active control techniques to address NVH. EMI shielding has emerged as another critical technology for electric vehicles, as the high voltage and current required for electric motors can cause interference with sensors and electronics around the vehicle. Autonomous vehicles rely on measurement and data fidelity, and therefore, insulating these components from electrical interference is critical to ensuring safety. Furthermore, composite materials can be used to reduce the weight of battery packages; however, the materials' limited electrical conductivity can cause static grounding issues, which may be solved through the use of graphene coatings.

Results

Phase I of this SBIR project began by optimizing the graphene coating and then demonstrating the functionality that could be endowed to the structure. This report focuses on the multifunctionality rather than the processing conditions. The project team demonstrated the potential use of the LIG treatment for both multifunctionality and strength by patterning the LIG in the form of a strain gauge on the surface of a fiberglass composite and measuring the dynamic response of a cantilevered composite beam. The experimental setup, shown in Figure II.4.5.2, consisted of a fiberglass composite beam mounted to an electrodynamic shaker, which was instrumented with an accelerometer and load cell. The composite was further instrumented with a commercial Micro-Measurements strain gauge with a gauge factor of 2.0. The LIG strain gauge was transferred to the beam's surface prior to cure and was electrically connected via a set of magnet wires bonded to the beam using silver paint. The resistance change under cyclic strain was measured by applying a constant current from an ICP current supply, which resulted in a varied voltage drop as the resistance of the gauge changed under strain. The beam was excited at a constant frequency while the amplitude of the response was measured with the LIG sensor and the commercial strain gauge. The sensitivity to a base acceleration, shown in Figure II.4.5.3, shows that the LIG sensor had a gauge factor 2.5 times greater than the commercial strain gauge. This result demonstrates that the LIG interlaminar treatment can provide both significant electrical conductivity and piezoresistive behavior to enable multifunctional automotive structures. (Note that multifunctionality is a critical technology in the U.S. DRIVE Materials Technical Team Technology Roadmap). These results demonstrate that the approach developed here can not only provide increased toughness, but also embed functionality.

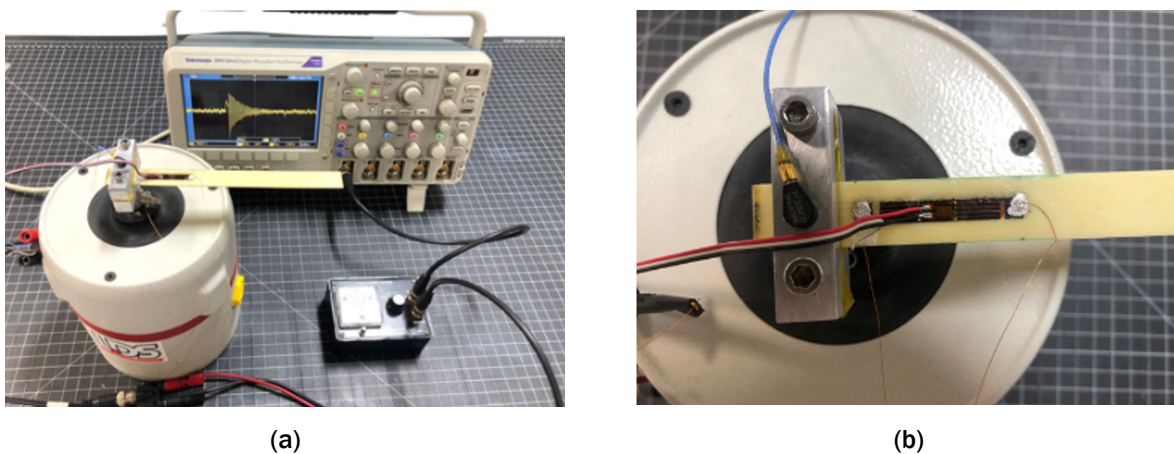


Figure II.4.5.2. (a) Experimental setup of the piezoresistive LIG strain sensor and (b) a Micro-Measurements strain gauge with a gauge electrically connected via a set of magnet wires bonded to the beam using silver paint. Source: Trimer LLC.

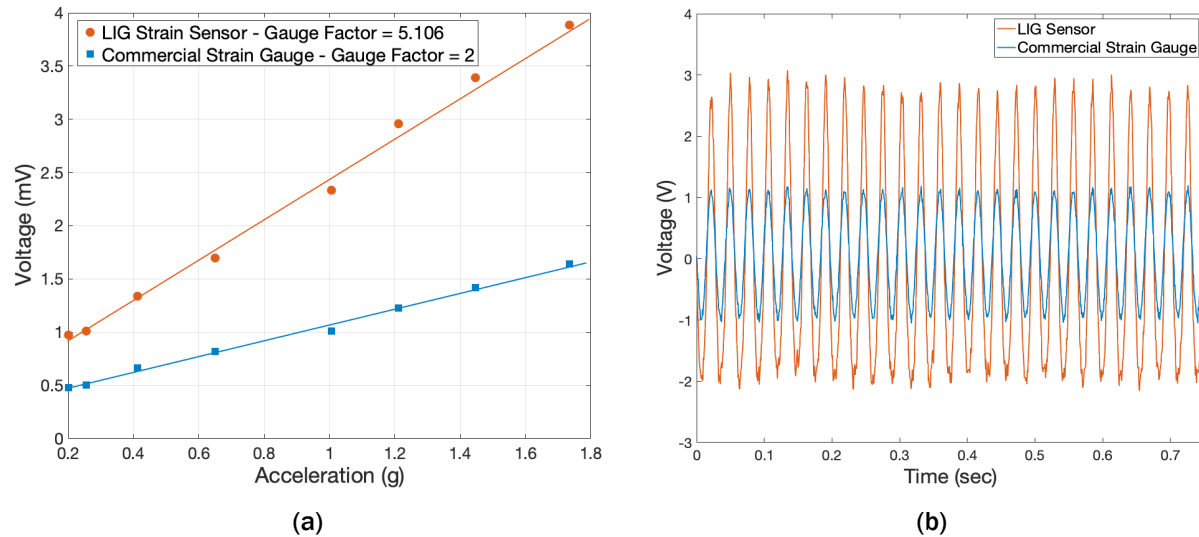


Figure II.4.5.3. (a) Voltage amplitude as a function of acceleration showing device sensitivity, which was 2.5 times greater for the LIG sensor than a commercial strain gauge, and (b) the time domain response to a sinusoidal excitation. Source: Trimer LLC.

Trimer worked with Rhein Tech Laboratories, Inc. to perform EMI shielding effectiveness testing according to a modified IEEE standard: IEEE 299.1-2013 *Standard Method for Measuring the Shielding Effectiveness of Enclosures and Boxes Having all Dimensions between 0.1 m and 2 m*. The project team evaluated the effectiveness of shielding to radio frequencies from 200 MHz to 6 GHz, with bandwidths of 100 kHz and 1 MHz for frequency ranges of 200 MHz to 1,000 MHz and 1 GHz to 6 GHz, respectively. A log periodic antenna and double ridge guide horn were used for the respective frequency ranges.

The shielding effectiveness testing apparatus, shown in Figure II.4.5.4, uses a shielded room to block any signals from external sources, with an opening for the SUT to be the only source of electromagnetic energy to pass into the room housing the receiving antenna. The transmitting antenna outside the room and the receiving antenna were placed one meter apart and at the same height and orientation. Before Trimer's LIG EMI shielding was placed into the bulkhead opening, a reference field was produced and collected by the transmitting and receiving antennae using a continuous wave signal without modulation. The results served as reference measurement data for the subsequent shielding testing. Data points were recorded for each frequency tested between 200 MHz and 6 GHz. The LIG coated shielding sample was then placed into the bulkhead, and the test was repeated through the same frequency range. This shielded data were then subtracted from the reference data for each frequency being tested. Results showed the shielding effectiveness of the LIG throughout the tested frequency range. The LIG-treated EMI shield was tested initially for both horizontal and vertical polarity. The test setup for each antenna and data plot for the initial testing is shown in Figure II.4.5.4.

From these initial data, EMI shielding effectiveness is quite low, in the range of 200 MHz to 1,000 MHz, which is attributed to the small-size of the sample provided relative to the wavelength of the signal. The effective opening in the bulkhead needs to be one-quarter the wavelength of the electromagnetic field for proper penetration; meaning the 70 mm × 70 mm opening only allows for accurate reference measurements to be made using frequencies greater than 1 GHz. The shielding effectiveness varied relative to the polarization of the electromagnetic field, showing that the average shielding effectiveness for horizontal polarization and vertical polarization is 21.2 dB and 18.4 dB, respectively. This was an unexpected result. Further testing was done to analyze the root cause of the discrepancy. Each surface and orientation of the shield was referenced, labeled A and B, with orientations labeled 0°, 90°, 180° and 270°, as shown in Figure II.4.5.5.

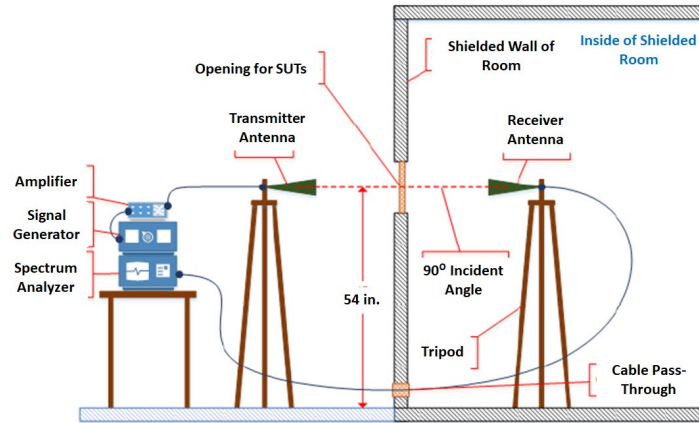


Figure II.4.5.4. EMI shielding effectiveness test configuration. Source: Trimer LLC.

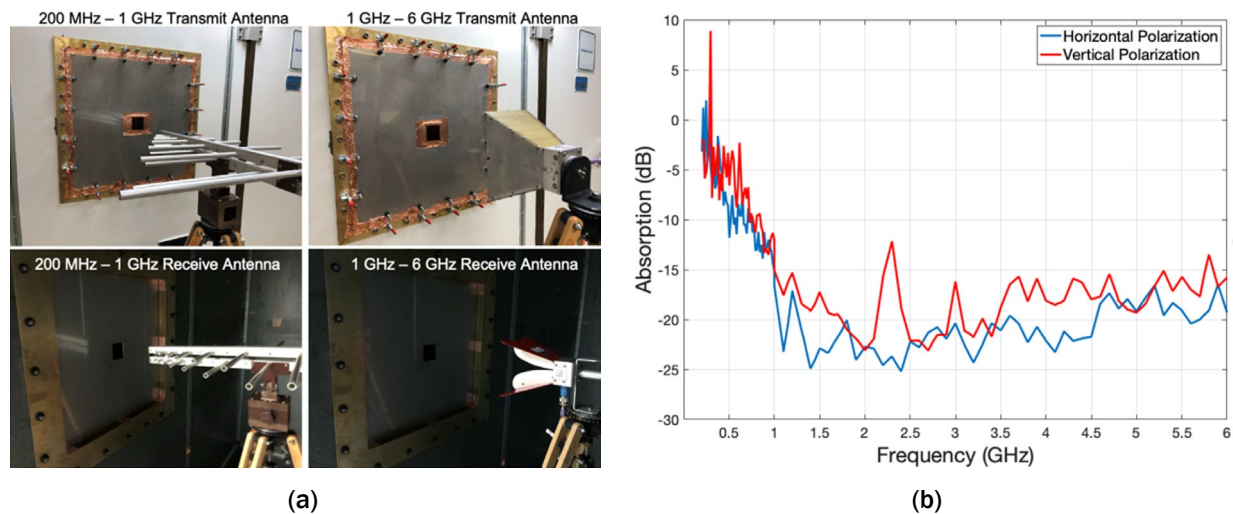


Figure II.4.5.5. (a) Testing configuration using both antenna and (b) the EMI shielding effectiveness testing results showing both horizontal and vertical polarization. Source: Trimer LLC.

Conclusions

The development of advanced lightweight materials is essential to boosting the fuel economy of modern automobiles, and the U.S. DRIVE Materials Technical Team has identified low-cost, high-volume manufacturing of CF composites as one of the most critical challenges in need of R&D needs. This project directly addresses this goal through the development and characterization of a new low-cost technique to create multifunctional composites with embedded sensors, electrical interconnects, and EMI shielding, as well as improved thermal conductivity, and will provide a step change in vehicle energy efficiency, particularly for electric and autonomous vehicles. Multifunctional materials are integrated material systems that serve multiple roles: structural load bearing, energy absorption, thermal management, sensing, power generation, vibration control, etc. The rapid advancement of this field has been due to the significant safety and performance benefits that can be achieved when using this class of materials. Multifunctionality can come in many forms, ranging from embedded sensing to EMI shielding, and can also be designed to overcome certain limitations in the use of composite materials. For instance, the manufacture of composite materials involves more challenging quality control than that required for metal manufacturing; therefore, methods for NDE of composite materials must be developed to ensure they meet design and safety specifications. Furthermore, composite materials have greatly reduced thermal conductivity, which can lead to increased stress in bonded joints and poor heat removal from components under-the-hood. Additionally, composite materials exhibit poor

electrical conductivity, which is required for EMI shielding of electrical components or the dissipation of static electricity. With electric and hybrid electric vehicles, the EMI issue is magnified by the large magnetic field between the cables of the battery and the engine, as well as the battery and the charger, which can negatively affect other electronic systems in the vehicle. Incoming EMI is also a source of concern, as it can harm the battery and its circuits. Multifunctional composites can be designed to eliminate these limitations and enable additional value-added properties.

Trimer's Phase I work has shown that the graphene treatment can greatly improve fracture toughness, which reduces commercialization risk and provides the ultimate multifunctional solution, one that increases strength while simultaneously embedding additional functionality. Furthermore, Phase I has shown that sensors can be manufactured to provide measurement of strain and pressure, thereby enabling the application of the technology to provide embedded measurements. The sensors can be produced directly on the surface of a thermoplastic composite, therefore, requiring no additional raw material cost and providing a means to increase the value of components being manufactured. The process proposed by Trimer is advantageous to other multifunctional methodologies because the treatment is directly applied to the prepreg, making it compatible with current manufacturing processes, and is low-cost since the process can be applied to commercial thermoplastic films or currently used thermoset materials. Furthermore, the process is performed at atmospheric pressure using low-cost CO₂ lasers and therefore can be scaled far more easily than vertically aligned arrays of CNTs, which are costly to produce and require chemical vapor deposition reactors that make scaling to automotive structures unrealistic. Unlike other treatments, the proposed graphene interleave process is low-cost, environmentally benign, and compatible with SMC or thermoplastic processing; the process can be grown at a production-scale and does not require advanced tooling or resin transfer equipment. The application of graphene arrays to the interlaminar region will produce lightweight composites with increased strength and toughness, as evidenced by the preliminary results showing significantly improved interlaminar toughness, ultimately leading to higher performance materials.

II.4.6 Low-Cost Resin Technology for the Rapid Manufacture of High-Performance Fiber-Reinforced Composites – Phase II (Trimer Technologies, LLC)

Megan Dunn, Co-Principal Investigator

Trimer Technologies, LLC
45800 Mast St.
Plymouth, MI 48170
E-mail: mdunn@trimerllc.com

Henry A Sodano, Co-Principal Investigator

Trimer Technologies, LLC
45800 Mast St.
Plymouth, MI 48170
E-mail: hsodano@trimerllc.com

H. Felix Wu, DOE Technology Manager

U.S. Department of Energy
E-mail: felix.wu@ee.doe.gov

Start Date: August 24, 2020 End Date: August 23, 2021
Project Funding (FY 2021): \$1,150,000 DOE share: \$1,150,000 Non-DOE share: \$0

Project Introduction

Lightweighting of vehicle structures clearly represents a significant opportunity for energy savings. However, traditional composite manufacturing technologies offer either high-volume or significant weight-savings—but not both. Over the past decade, automotive composites have focused on SMC, which enables high-volume manufacturing but is produced with chopped fibers and therefore inefficiently capitalizes upon the strength of the reinforcement, leading to materials with poor specific properties. For instance, AOC Aliancys' (now AOC) PALAPREG P18-03 vinyl ester SMC with 30% GF obtains a tensile strength of only 100 MPa, which is below most neat (without reinforcement) epoxies used in the aerospace industry. The tensile strength of CF SMCs can be double that of fiberglass SMCs but is still roughly four times lower than that of a composite using continuous CF reinforcement. Manufacturing processes using continuous fiber reinforcement would fully capitalize upon the greater cost and lightweighting potential of CF.

Recently, high-pressure resin transfer molding (HP-RTM) has emerged as an alternative approach to manufacture composite materials with continuous fiber reinforcement. HP-RTM was demonstrated to be cost-effective and compatible with high-rate manufacturing through BMW's i-series vehicle program, which achieved a 50% weight-reduction compared to traditional steel designs. HP-RTM injects a catalyzed resin into a heated mold containing draped woven or non-crimp fabric at pressures as high as 200 bar. In the BMW i3 program, HP-RTM enabled cycle times of approximately five minutes (versus several hours for standard RTM processes used in the fabrication of large components such as wind-turbine blades). However, while a five-minute cycle time is acceptable for lower volume production in high-performance vehicles, it is too slow to realize the use of low-cost composite materials required by the automotive industry for mass market vehicles.

The DOE VTO is targeting a 25% glider weight-reduction at less than \$5/lb.-saved by 2030, which will require innovative new materials that achieve both rapid-cure and significantly improved mechanical properties. Current HP-RTM resins include polyesters, vinyl esters, snap cure epoxies, and polyurethanes. However, the low-cost polymers employed for automotive parts have properties inferior to those employed in the aerospace industry. Trimer has identified the catalysts required to enable snap cure (<45 seconds) while maintaining aerospace-grade performance. Furthermore, the resin has an infusion viscosity (at 65°C) of less than 25 cP,

which will enable rapid infusion to further reduce manufacturing time. In addition to the manufacturing benefits and aerospace-grade strength, the cured polymer achieves a glass transition temperature greater than 700°F (375°C) and is non-flammable without additives, providing unique commercialization opportunities. Table II.4.6.1 provides a comparison of the material properties for two snap cure epoxies and two vinyl esters and demonstrates that the proposed Trimer polymer greatly outperforms state-of-the-art materials while simultaneously offering significantly reduced cost.

Table II.4.6.1. Comparison of Trimer’s RTM Polymer with Current Low-Cost Rapid-Cure Resins

Material Property	Trimer RTM Resin	Dow Voraforce 5300	Huntsman Araldite LY 3585/ Aradur 3475	AOC VIPER FO10 BIS-A VE	Reichhold DION IMPACT 9102-75
Polymer Type/Chemistry	-	Epoxy	Epoxy	Vinyl Ester	Vinyl Ester
Glass Transition, T _g Dry (°C)	375	120	110	130	99
Tensile Strength (MPa)	105	68	77.5	88	79.2
Tensile Modulus (GPa)	4.0	2.8	2.8	3.2	2.9
Tensile STF (%)	4.0	7	9	6.2	4.5
Compressive Strength (MPa)	149	-	-	121	108.9
Flexural Strength (MPa)	140	-	-	153	144
Fracture Toughness, K _{1c} (MPa/m ^{1/2})	1.03	1.22	0.85	0.6	-
Viscosity (cP at 23°C)	200	500	1,000	3,200	170

Objectives

The objective of this SBIR Phase II project is to demonstrate the manufacture of high-strength CF composites with a full molding and injection cycle time below 60 seconds for thin parts and a cycle time under 120 seconds for thick chassis structures such as leaf springs. This aggressive goal is enabled by Trimer’s patent-pending thermosetting resin, which has been shown to achieve aerospace-grade mechanical and thermal properties through a 30-second cure. The polymer is ideally suited for integration into the automotive industry since the raw material cost is below vinyl esters, and the polymer’s high-strength and stiffness will enable further reduction of component weight. The high-performance-to-cost ratio of Trimer’s resin is revolutionary and will drive its commercial adoption in an industry where value is critical. The product is non-flammable, with a glass transition temperature greater than 700°F (375°C) and mechanical properties that rival the highest-performance aerospace resins. No competing technology exists that can match the cure time, strength, and cost.

Approach

To achieve DOE’s ambitious weight targets, there exists a critical need to implement new resin technologies that are compatible with high-rate industrial manufacturing approaches yet provide the mechanical properties of aerospace resins. In this Phase II SBIR project, Trimer has demonstrated that its low-cost RTM resin exhibits high-strength and a cure time as fast as 23 seconds with a 3.5-mm-thick panel and under 60 seconds with a 10-mm-thick panel. These rapid-cure results were obtained through liquid compression molding with an unheated resin and unheated fiber preform, which indicates that significantly faster cure times should be achievable with an HP-RTM system. Cycle times under 60 seconds are possible because of the very low resin viscosity (25 cP at 65°C), which reduces the infusion time, combined with preheating the resin, which quickens the cure. While other resin systems can cure in 60 seconds, they are compatible with only very thin parts. These systems exhibit a highly exothermic reaction that, in parts thicker than a couple millimeters, leads to thermal runaway and server degradation of the cured polymer or, in some cases, combustion. The Trimer resin can cure 28-mm-thick parts in 90 seconds, which is eight times faster than state-of-the-art epoxy resins. The proposed polymer will enable both high-volume manufacturing and significant weight-savings in vehicle structures through the realization of unprecedented low cycle times.

Trimer is working with the Institute for Advanced Composites Manufacturing Innovation (IACMI) SuRF to demonstrate production-scale HP-RTM manufacturing with a focus on minimizing the cycle time. Trimer's efforts with the IACMI-SuRF used its Hennecke HP-RTM system and Schuler 4,000-ton press equipped with a Cannon DMC flat plate mold to manufacture panels with non-crimp CF reinforcement for evaluation. The project is working with both high-pressure injection resin transfer molding and high-pressure compression resin transfer molding processes to optimize cycle time. Researchers are further characterizing the infusion process through analysis of reinforcement wet-out, void content, and dimensional stability of the cured part.

Results

Trimer performed extensive mechanical testing to show that the resin performance greatly exceeds that of currently used resins. Test results were shown in Table II.4.6.1 above, while Figure II.4.6.1 shows a representative set of tensile data for the polymer showing a tensile strength of 108 MPa, modulus of 3.7 GPa, and STF of 4.0%. This combination of properties exceeds many aerospace resins and greatly outperforms automotive epoxies. HP-RTM manufacturing is a cyclic process in which it is advantageous to avoid applying an external mold release using internal mold release (IMR) agents that enable efficient removal of the cured part from the mold. Given the importance of the IMR for HP-RTM, Trimer spent considerable effort developing a suitable IMR. In addition to providing a weak adhesive strength, one of the critical IMR parameters is that it leave the mold surface clean and without residue. The testing used a small pultrusion die fabricated such that an Instron could be used to pull a CF tow through the die while the pull force was measured. This methodology allowed Trimer to identify several effective IMRs and isolate one for production manufacturing. Trimer has also found the IMRs do not affect the tensile properties of the resin but lead to a significant improvement in the fracture toughness, with the K_{IC} increasing by as much as 36% because of a plasticizing effect. Another critical requirement for polymers used in the automotive industry is the capacity to withstand prolonged exposure to various automotive fluids. Tensile specimens were immersed in various automotive solvents for 24 hours and then tested. Figure II.4.6.2 shows these results, which indicate that the resin is generally unaffected by the various automotive fluids tested, which is critical for automotive applications.

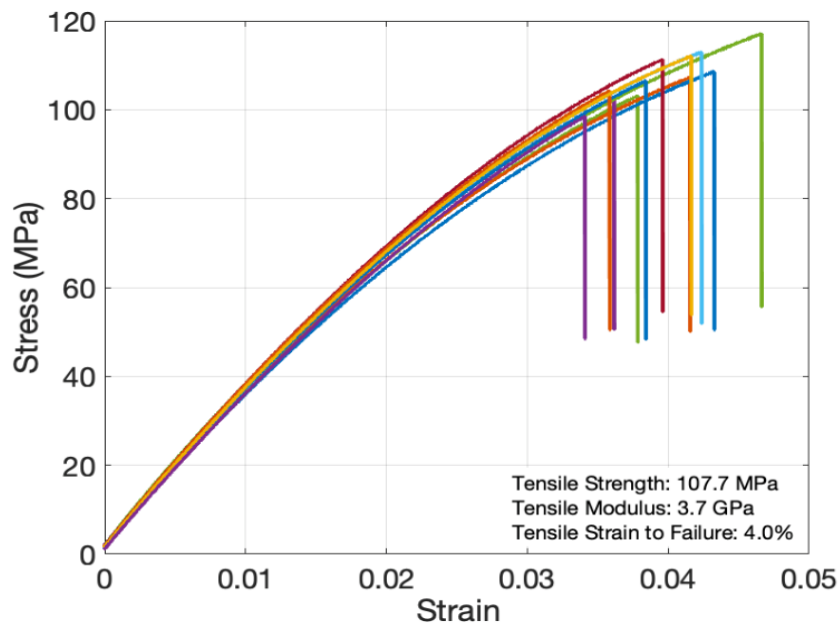


Figure II.4.6.1. Tensile strength of the neat resin tested according to ASTM D638, demonstrating high-strength of the resin. Source: Trimer LLC.

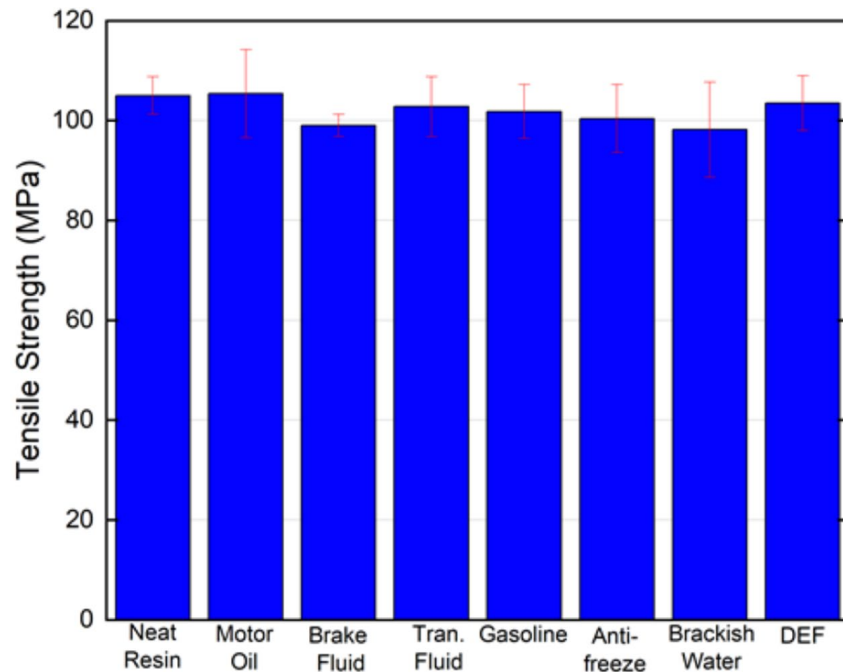


Figure II.4.6.2. Tensile strength after a 24-hour immersion in common automotive solvents.
Source: Trimer LLC.

The project has also performed testing on composite panels manufactured using Trimer's RAPID infusion resin and Scott Bader's Crestapol 1250 resin, a low-viscosity and fast-curing resin system that is currently used by Shape Corp. in the manufacture of the Chevrolet Corvette bumper. Composite panels were prepared using VARTM and E-glass non-crimp fabric from Vectorply (weave ELA2412), and samples were cut and tested in accordance with ASTM standards for tensile strength (ASTM D3039), compressive strength (ASTM D6641), in-plane shear response (ASTM D3518), Mode I fracture toughness (ASTM D5528), Mode II fracture toughness (ASTM D7905), and tensile and compressive translaminar fracture toughness (ASTM E1922). The cure cycle for the RAPID resin was three minutes before de-molding; the Crestapol 1250 resin required a 60-minute cure time. The Crestapol 1250 resin was cured at a lower temperature but required a 60-minute cure time compared to the three-minute cure time of the RAPID parts, which would greatly reduce the cycle time in a production setting. The results, provided in Table II.4.6.2, show significant performance improvements (emphasized in red text) over the Crestapol 1250 resin, with notable improvement to compressive strength. The axial compressive strength of Trimer's RAPID resin was 966.02 MPa, compared to 568.71 MPa for the Crestapol 1250 resin. The transverse strength was 99.5 MPa for Crestapol 1250 and 184.3 MPa for Trimer's RAPID resin, which is 70% higher under axial loading and 85.2% under transverse loading. In addition to the compressive strength, RAPID performed extremely well in both Mode I and Mode II fracture toughness. The average G_{IC} of 0.473 kJ/m² is more than twice the value of Hexcel 8552, a toughened aerospace resin. The RAPID pre-cracked Mode II fracture toughness, a G_{IIC} value of 1.51 kJ/m², is nearly three times higher than Hexcel 8552. This testing was not only beneficial for highlighting the strength of the resin system being developed in this project but also allowed Trimer to further populate its data sheet for future commercial partners and benchmark a competing resin system.

Table II.4.6.2. Material Properties Form VARTM E-Glass Composites

Property	Standard	Trimer RAPID	Crestapol 1250
0° Tensile Strength, GPa	ASTM D3039	1.04	1.03
0° Tensile Modulus, GPa	ASTM D3039	44.2	46.45
0° Compression Strength, MPa	ASTM D6641	966.0	568.70
0° Compression Modulus, GPa	ASTM D6641	47.2	43.90
90° Tensile Strength, MPa	ASTM D3039	36.4	19.50
90° Tensile Modulus, GPa	ASTM D3039	14.3	14.90
90° Compression Strength, MPa	ASTM D6641	184.3	99.50
90° Compression Modulus, GPa	ASTM D6641	31.0	12.90
In-Plane Shear Strength, MPa	ASTM D3518	64.7	57.77
In-Plane Shear Modulus, GPa	ASTM D3518	3.4	2.66
Mode I Fracture Toughness, J/m ²	ASTM D5528*	437	809
Mode I Fracture Toughness, J/m ²	ASTM D7905†	1,510	1,640
Translaminar Fracture Toughness, MPa-m ^{1/2}	ASTM E1922	60.64	51.87

To meet the project's Phase II objective for reduced manufacturing cycle time of composite parts in a production environment, we worked with an OEM to perform a series of RTM trials on thick chassis composites. State-of-the-art snap cure epoxies require ~12 minutes to cure a 28-mm-thick composite because of the highly exothermic reaction, which, if pushed, will cause the resin to overheat and thermally degrade or even combust. Trimer's resin provides the ability to cure thick composites in under 120 seconds since the resin has very little exotherm. During our trials, a dielectric cure monitoring (DCM) system was used to establish cure times of the RTM composite panels. The DCM system measures the ion viscosity velocity, which increases as the press is closed and decreases back to baseline once the polymer is cured, stopping ion mobility. Figure II.4.6.3 shows the cure monitor data for injection into a production part, with a 60-second vacuum followed by a fast 23-second injection and a 90-second cure. The cycle time demonstrated in the RTM trials is much faster than state-of-the-art epoxies. Trimer is now working with IACMI-SuRF to demonstrate HP-RTM manufacturing in which higher injection pressure can be used to further reduce molding time. We will mold the same chassis component, which is a production part, and will evaluate the cycle time using production injection tooling. The initial trials will focus on cycle time reduction through optimization of the infusion viscosity (controlled through temperature) and pressure. IACMI-SuRF's tooling does not have cure monitor hardware, so the degree of cure will be analyzed on molded parts. Because of delays at IACMI-SuRF, it is anticipated that the manufacturing trials will occur in the second quarter of FY 2022.

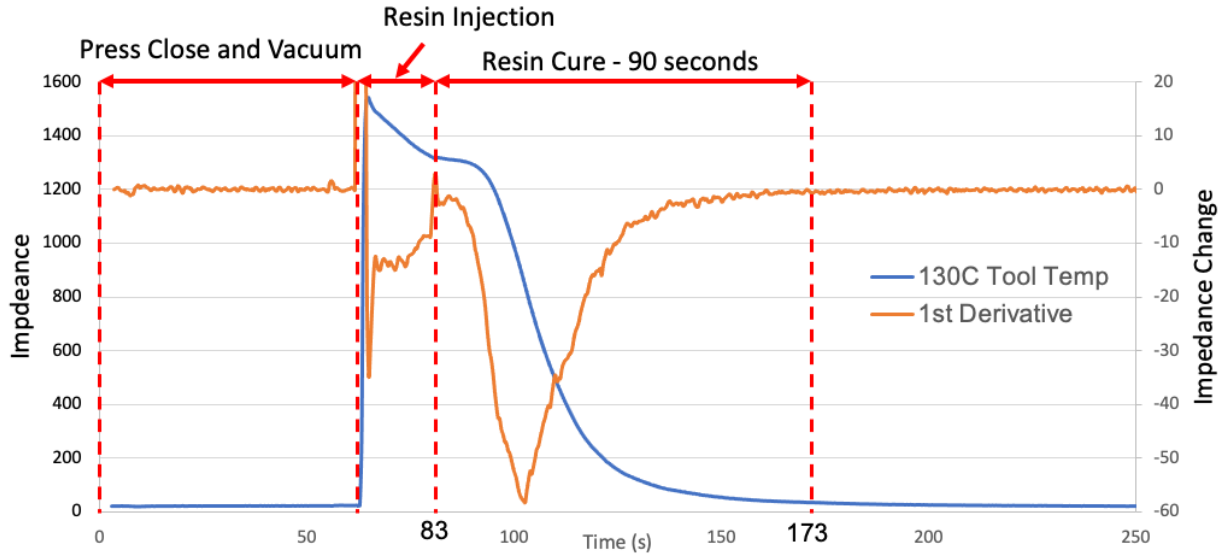


Figure II.4.6.3. Dielectric cure monitor data from the molding of a 28-mm-thick composite part demonstrating a 90-second cure time. Source: Trimer LLC.

The composite panels molded during the trials were tested for both static and fatigue properties, with the results showing results similar to or better than epoxies, yet with significantly improved cycle time. The fatigue testing specification required the part to exhibit less than 5% load loss after 200,000 cycles at 200 MPa; however, our composites were tested at 450 MPa, and after 8 million cycles, the composite exhibited only 2.1% load loss, as shown in Figure II.4.6.4. Given that our specimens were tested at more than 100% higher load and far greater cycle count, this result clearly demonstrates our resin is well within the range of acceptable fatigue for automotive chassis systems.

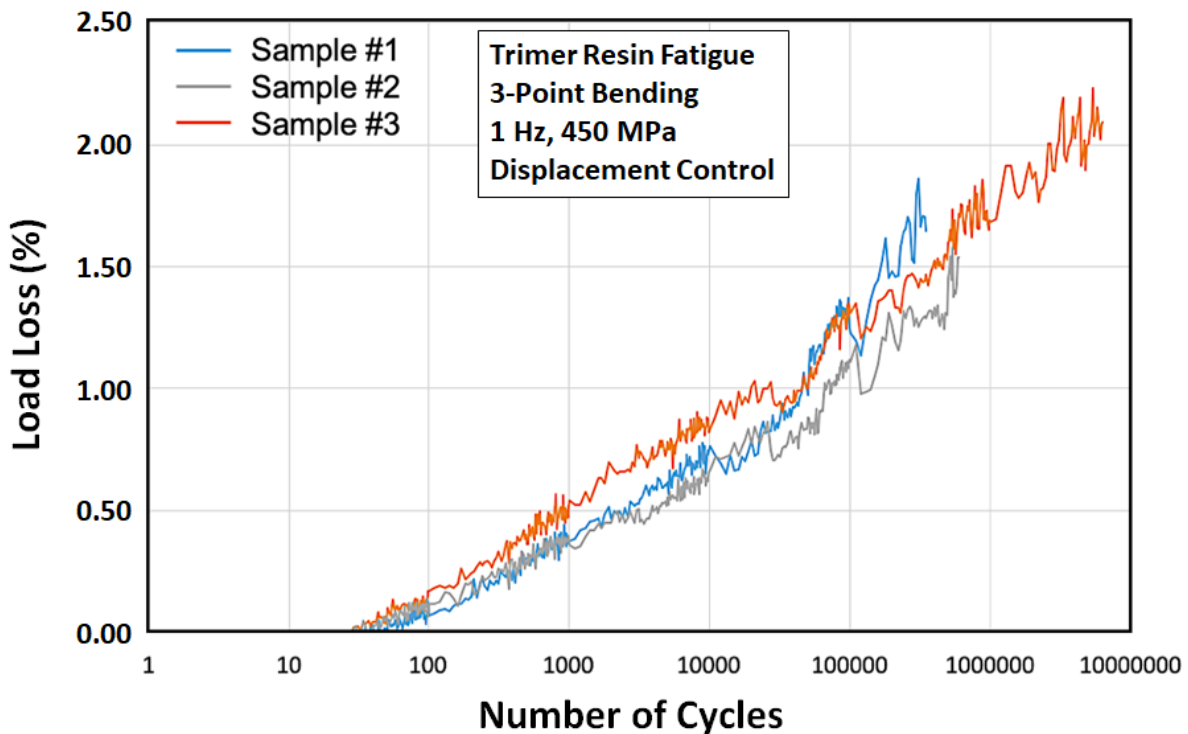


Figure II.4.6.4. Fatigue testing of fiberglass composites manufactured. Source: Trimer LLC.

In addition to mechanical testing of the resin, the Phase II work has also demonstrated the fire performance of Trimer's resin system. Trimer performed thermal analysis through DMA to identify the glass transition temperature (T_g), which showed an extreme T_g of 707°F (375°C) with a high storage modulus of ~2.5 GPa at 300°C. While the extreme T_g obtained here is not critical for automotive applications, the high T_g does enable the resin to be compatible with the E-coat process and potentially opens the door to under-the-hood applications such as composite engine blocks. Furthermore, these extremely high thermal properties make the resin suitable for even faster cure since it does not degrade when heated to extreme temperatures and expands the use in a broader range of commercial applications. This high T_g also contributes to the resin's non-flammable nature, which is critical for vehicle applications and is a particular need for battery enclosures.

Trimer worked with University of Dayton Research Institute (UDRI) to perform oxygen consumption calorimetry under ASTM E-1354/ISO 5660 to characterize the fire performance, with results at a heat flux of 50 kW/m² shown in Figure II.4.6.5. These data show a very low peak heat release rate (HRR) of 81 kW/m², a long time to ignition of 258 seconds, and a low average HRR of 46 kW/m². We have further performed testing according to ASTM D635, and the polymer passed the horizontal burning test after 30 seconds' exposure to flame. To further demonstrate the polymer's non-flammable properties, we have subjected the polymer to a 60-second burn time under significantly more intense flux than the ASTM requires. Figure II.4.6.5 provides images of the results. From the figure, the polymer can self-extinguish in under 20 seconds following exposure to the flame. Trimer has performed similar torch testing on a 3-mm-thick fiberglass composite panel in which the flame was positioned normal to the composite surface for 60 seconds before removing the flame and allowing the composite to self-extinguish undisturbed. Figure II.4.6.5 shows the results of the test and demonstrates the panel can effectively self-extinguish in under 10 seconds. Following testing, the composite showed no significant geometrical change, and the resin was able to prevent burn-through. As the test results show, Trimer's resin is able to resist ignition even under an extreme forced fire condition, and while it is not obvious from the images, very little smoke was generated during and after the test. According to smoke density testing [1], the composite has a smoke density of only 5, which is 40 times lower than required for application to aircraft. All testing on both neat polymer specimens and composites showed self-extinguishing behavior without halogenated compounds or mineral additives and zero flame growth after removal of the ignition source. This property of Trimer's resin enabled the development of fire-resistant battery enclosures for electric vehicles.

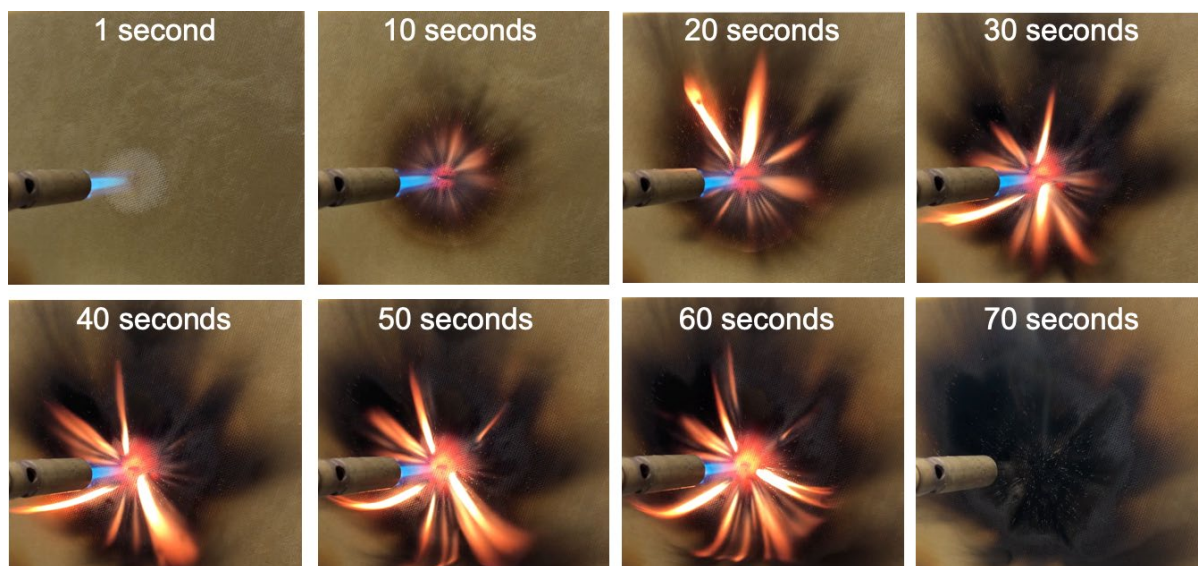


Figure II.4.6.5. Propane torch testing on a 3-mm-thick fiberglass composite panel with a 60-second flame exposure, after which the composite was able to self-extinguish in under 10 seconds. Source: Trimer LLC.

Conclusions

Trimer has developed a new resin system that can enable unprecedented cycle time while producing fire-resistant composites with the strength and stiffness of more costly aerospace-grade materials. Through the first year of this SBIR Phase II project, Trimer demonstrated RTM manufacture of composite structures and validated their fatigue performance while reducing the cycle time eight-fold. The next year of the project will focus on HP-RTM manufacturing of chassis components and further refinement of the fire-resistant properties.

References

1. Code of Federal Regulations, 1991, "Compartment Interiors," 14 14 CFR § 25.853(d), Appendix F, Part V, Amdt. 25-116.

(This page intentionally left blank)

U.S. DEPARTMENT OF
ENERGY

Office of
**ENERGY EFFICIENCY &
RENEWABLE ENERGY**

For more information, visit:
energy.gov/eere/vehicles

DOE/EE-2615 August 2022